

Lecture Notes in Mechanical Engineering

Tezeswi Tadepalli
Vijayabaskar Narayanamurthy *Editors*


Recent Advances in Applied Mechanics

Proceedings of Virtual Seminar
on Applied Mechanics (VSAM 2021)

 Springer


Lecture Notes in Mechanical Engineering

Series Editors

Francisco Cavas-Martínez , Departamento de Estructuras, Construcción y Expresión Gráfica Universidad Politécnica de Cartagena, Cartagena, Murcia, Spain

Fakher Chaari, National School of Engineers, University of Sfax, Sfax, Tunisia

Francesca di Mare, Institute of Energy Technology, Ruhr-Universität Bochum, Bochum, Nordrhein-Westfalen, Germany

Francesco Gherardini , Dipartimento di Ingegneria “Enzo Ferrari”, Università di Modena e Reggio Emilia, Modena, Italy

Mohamed Haddar, National School of Engineers of Sfax (ENIS), Sfax, Tunisia

Vitalii Ivanov, Department of Manufacturing Engineering, Machines and Tools, Sumy State University, Sumy, Ukraine

Young W. Kwon, Department of Manufacturing Engineering and Aerospace Engineering, Graduate School of Engineering and Applied Science, Monterey, CA, USA

Justyna Trojanowska, Poznan University of Technology, Poznan, Poland

Lecture Notes in Mechanical Engineering (LNME) publishes the latest developments in Mechanical Engineering—quickly, informally and with high quality. Original research reported in proceedings and post-proceedings represents the core of LNME. Volumes published in LNME embrace all aspects, subfields and new challenges of mechanical engineering. Topics in the series include:

- Engineering Design
- Machinery and Machine Elements
- Mechanical Structures and Stress Analysis
- Automotive Engineering
- Engine Technology
- Aerospace Technology and Astronautics
- Nanotechnology and Microengineering
- Control, Robotics, Mechatronics
- MEMS
- Theoretical and Applied Mechanics
- Dynamical Systems, Control
- Fluid Mechanics
- Engineering Thermodynamics, Heat and Mass Transfer
- Manufacturing
- Precision Engineering, Instrumentation, Measurement
- Materials Engineering
- Tribology and Surface Technology

To submit a proposal or request further information, please contact the Springer Editor of your location:

China: Ms. Ella Zhang at ella.zhang@springer.com

India: Priya Vyas at priya.vyas@springer.com

Rest of Asia, Australia, New Zealand: Swati Meherishi at swati.meherishi@springer.com

All other countries: Dr. Leontina Di Cecco at Leontina.dicecco@springer.com

To submit a proposal for a monograph, please check our Springer Tracts in Mechanical Engineering at <https://link.springer.com/bookseries/11693> or contact Leontina.dicecco@springer.com

Indexed by SCOPUS. All books published in the series are submitted for consideration in Web of Science.

More information about this series at <https://link.springer.com/bookseries/11236>

Tezeswi Tadepalli · Vijayabaskar Narayanamurthy
Editors

Recent Advances in Applied Mechanics

Proceedings of Virtual Seminar on Applied
Mechanics (VSAM 2021)

 Springer

Editors

Tezeswi Tadepalli
Civil Engineering
National Institute of Technology
Warangal, Telangana, India

Vijayabaskar Narayanamurthy
Research Centre Imarat
Hyderabad, Telangana, India

ISSN 2195-4356

ISSN 2195-4364 (electronic)

Lecture Notes in Mechanical Engineering

ISBN 978-981-16-9538-4

ISBN 978-981-16-9539-1 (eBook)

<https://doi.org/10.1007/978-981-16-9539-1>

© The Editor(s) (if applicable) and The Author(s), under exclusive license to Springer Nature Singapore Pte Ltd. 2022

This work is subject to copyright. All rights are solely and exclusively licensed by the Publisher, whether the whole or part of the material is concerned, specifically the rights of translation, reprinting, reuse of illustrations, recitation, broadcasting, reproduction on microfilms or in any other physical way, and transmission or information storage and retrieval, electronic adaptation, computer software, or by similar or dissimilar methodology now known or hereafter developed.

The use of general descriptive names, registered names, trademarks, service marks, etc. in this publication does not imply, even in the absence of a specific statement, that such names are exempt from the relevant protective laws and regulations and therefore free for general use.

The publisher, the authors and the editors are safe to assume that the advice and information in this book are believed to be true and accurate at the date of publication. Neither the publisher nor the authors or the editors give a warranty, expressed or implied, with respect to the material contained herein or for any errors or omissions that may have been made. The publisher remains neutral with regard to jurisdictional claims in published maps and institutional affiliations.

This Springer imprint is published by the registered company Springer Nature Singapore Pte Ltd. The registered company address is: 152 Beach Road, #21-01/04 Gateway East, Singapore 189721, Singapore

Preface

Greetings from Indian Society for Applied Mechanics.

The papers appearing in this special issue *Recent Advances in Applied Mechanics* under Springer's *Lecture Notes in Mechanical Engineering* are selected from more than 80 peer-reviewed papers presented in the field of solid mechanics, fluid mechanics, material science and engineering, design engineering, biomechanics and bio-medical engineering, at the Virtual Seminar on Applied Mechanics 2021. This event was held in three spells during 28–29 May, 04–05 June and 30–31, July 2021, and conducted by the Indian Society for Applied Mechanics (ISAM) and supported by team of professors and research scholars from three different NITs, viz. National Institute of Technology Warangal; Motilal Nehru National Institute of Technology, Allahabad; and National Institute of Technology Jamshedpur, in India.

All submissions have undergone a two-stage peer review. Authors have initially submitted two-page extended abstracts each of which were scrutinized by two independent reviewers. Based on the stage-1 review comments, authors have submitted the full length papers which were reviewed by a large team of professors, scientists and engineers from IITs, NITs, research laboratories and industries. The reviews were focussed on technical content, originality and presentations by authors. Based on reviewers' comments and recommendations, 57 papers were selected for publication in this special issue. There are 11 papers in fluid mechanics and 5 in biomedical engineering and remaining 41 papers in broad areas of solid mechanics covering computational solid mechanics, mechanics of impact, fracture mechanics, material modelling, experimental mechanics, composites and structural health monitoring. Our sincere thanks to all reviewers who are listed at the end of this preface for their valuable time and review comments which helped in the inclusion of good quality papers in this special issue.

We would like to express our sincere gratitude to the organizing team comprising Prof. C. Lakshmana Rao (IITM), Prof. Puneet Mahajan (IITD), Prof. K. K. Shukla (NIT Jamshedpur), Prof. A. K. Upadhyay (MNNIT), Prof. Deepak Kumar (NITJ), Prof. Vineet Sahoo (NITJ), Dr. B. Ramakrishna (DMRL) and research scholars Mr. Ashish Pandey (IITM), Mr. Rishabh Shukla (IITD), Mr. Yatish Baghel

and Mr. Saurabh Kureel from MNNIT, Ms. Harika Vasamsetti and Mr. V. Guru from NITW and Mr. Bipin Kumar Chaurasia, Mr. Ravi Sinha, Mr. Abhishek Kumar Yadav and Mr. Ashish Ranjan Pradhan from NITJ.

Thanks to Springer Nature for readily accepting our proposal and agreeing to bring out this special issue. This publication would not have been possible without constant support from Ms. Muskan Jaiswal (Assistant Editor—Applied Sciences & Engineering) from its initiation to completion. Our sincere appreciations on the background work carried out by the team from Springer Nature comprising Ms. Sushmitha Shanmuga Sundaram (Project Coordinator—Books Production), Mr. Karthik Raj Selvaraj (Project Coordinator—Total Service) and Mr. Hemanth M. V. N. (Project Manager—Scientific Publishing Services).

The chapters in this book encompass up-to-date research in the field of applied mechanics, and we believe that this will be helpful to researchers and scholars across the broad spectrum of engineering involving the application of mechanics in civil, mechanical, aerospace, automobile, bio-medical, material science and more.

Tezeswi Tadepalli
Vijayabaskar Narayanamurthy

Organization

List of Reviewers

C. Lakshmana Rao
Ramsharan Rangarajan
A. K. Upadhyay
Viswanath Chintapenta
Vagesh Narasimhamurthy
Sundararajan Natarajan
Ashok Pandey
Sitikantha Roy
Ajey K. Patel
Bharghavi
K. Supradeepan
Jayakrishna
Rajesh P. Nair
V. K. Patel
Abhishek Tiwari
Tejas Kotkinde
Bishweshwar Babu
K. Surendra
Hari Ponnamma
M. V. N. Sivakumar
Anita Priyadarshini
Anubhab Roy
K. Senthil
Nomesh Kumar
Gurunathan
Madhan Kumar Vasudevan
B. Ramakrishna
Rahul Dixit

K. Lakshmi
C. Ramadass
Janardhan Reddy
Ramesh Gupta
Sajan Kumar Wahi
Rajendra Bahadur
G. Vamsi Krishna
Manabendra M. De
Vivek Kumar Patel
Vishwanath Managuli
Swathika Meenraj
Sri Krishna Sudhamsu Kambhammettu
Agesh Markose
Sandeepan Roy
B. T. Kannan
Harsha Praneeth Pavani
M. Sree Ramana
S. Veerabhadra Reddy
Poojari Yugendar
Adnan Ahmed
Gaurav Watts
Rajendra Maurya
Amit Yadav
Ashish Pandey
Rishabh Shuka
Noushad Bin Jamal M.
K. Manoj
A. Karthik

Uday Kumar
 N. V. N Rao Pasalapudi
 K. Gopinath
 M. Umakanth
 Manoj Kumar Behera
 Vineeth Ravulapalli
 A. V. N. S. Swathi Kiran
 Paleti Mohan Krishna
 Rashmiranjan Mohapatra
 Nagendranath
 Ramesh Babu Vaddi
 Firoz Khan
 Akhileshwar Pandey
 Gangisetty Venkatesh
 Sajal Kumar Babu Degala
 Kamal Tewari
 Vipin Kumar
 Mogili Sudhakar
 Tandel Dhananjay
 V. B. Brahmadathan
 Anoop Kumar Pandouria
 M. D. Hasan
 Mirza Shariq Beg
 B. Raja Rajeshwari
 Parvez Ahmad

Swarna Swetha Kolaventi
 Padakanti Rakesh
 Kuldeep Yadav
 Devashish Rajpoot
 Peddi Sai Rama Narayana
 Sumit Kumar
 H. V. Kalekar
 Asish Ranjan Pradhan
 Polu Sathish
 Ravi Sinha
 Bipin Kumar Chaurasia
 Swaroop Kumar Mandal
 Abhishek Kumar Yadav
 Tahseen Alam
 Jayaprakash K.
 Abhilash Awasthi
 Helan Satish
 Umesh Gautam
 P. M. G. Bashir Asdaque
 Yadwinder Singh Joshan
 Praveen Oggu
 Purnashis Chakraborty
 Ajay Kumar Jaiswal
 P. Krishna Menon
 V. Guru Prathap Reddy

Contents

Numerical Studies on Propagation of Non-linear Lamb Waves Through Delaminated Surfaces in Stiffened Composite Plate Structures	1
Rajat Gethe, Ramadas Chennamsetti, and Avinash Hood	
Excitation Bandwidth Dependence of Cantilever Energy Harvester	15
K. Manoj, V. Narayanamurthy, and S. Korla	
A Review on Phase-Field Models Applied to Fracture in Solids	33
P. C. Sidharth and B. N. Rao	
A Simulation Study on Propagation of Action Potential in Epicardial Tissue Due to SCN5A L812Q Gene Mutation	57
Helan Satish and Machireddy Ramasubba Reddy	
Evaluation of Outflow Boundary Conditions in DNS of Turbulent Jet Flows	69
Prince Charles and Vagesh D. Narasimhamurthy	
Effect of Fluidic Injection on the Core Length of Rectangular Sonic Jet	87
G. Kailash and S. M. Aravindh Kumar	
Stress Distribution in Infinitely Long Plate with Circular Hole Loaded by Concentrated Loads	95
Kannan Kulavan Mohammed Shafeeque and K. V. N. Surendra	
Re-deployable Smart Sensor Concept for Modal Estimates of Bridges Subjected to Random and Vehicle Excitations	109
Vasamsetti Sri Harika and Jayakumar Prawin	
Ballistic Study of Shear Thickening Fluid Impregnated Unidirectional Ultra-High Molecular Density Polyethylene Fabric	125
Vagish D. Mishra, Ashish Mishra, Avinash Singh, Luv Verma, and G. Rajesh	

Effect of Steel Fibre Content on the Information Entropy of Acoustic Emission Waveforms Generated During Mode I Fracture Process in Cementitious Composites	135
Indrashish Saha and R. Vidya Sagar	
3D Non-linear Finite Element Analysis of a Naturally Corroded Beam	151
Ankita Suman Mohanty and B. N. Rao	
A Review of Stage Separation Systems for Launch Vehicles	161
Shyamala Iyer and V. Narayanamurthy	
Testing and Numerical Simulations on Fracture Behavior of Fresh Quartzite Rock Using the Discrete Element Method	183
G. V. Ramana, Jaisingh Verma, and P. Ravi Prakash	
Feasibility of Composite Compressor Blade Using Sub-element Level Bird Strike Tests and Analysis	195
Prakash Jadhav	
Influence of Invertube's Thickness on Crash Energy Absorption	211
Velugubantla Dushyanth Rudra Mahesh and V. Narayanamurthy	
Maximizing the Energy Absorption Capacity of Thin Walled Box Structures Using Ultra High Strength Steels (UHSS) at Sensitive Zones	223
Peddi Sai Rama Narayana, Raghu V. Prakash, Srinivas Gunti, and Kanugula Raghu	
A Non-model Damage Diagnostic Technique for Online Structural Health Monitoring	235
K. Lakshmi	
Simulation of Mixed-Mode Fracture in a Single Phase and Two-Phase Composite Material	247
Subrat Senapati, Anuradha Banerjee, and R. Rajesh	
Comparable Safety Margins of the Ulnar Fingers When the Thumb Remains on an Unsteady Slider	261
Banuvathy Rajakumar and S. K. M. Varadhan	
Identification of Crack Parameters Using XFEM-QPSO	275
M. Surendran, J. Prawin, and S. Natarajan	
Computational Study of Hydrodynamics of Mixing Tank with Non-Newtonian Fluids	291
Aishwarya Mulampaka and Rajmohan Soundararajan	
Development of a 100 mm-Diameter Split-Hopkinson Pressure Bar for High Strain Rate Characterization of Concrete	305
S. Ranjithkumar, S. N. Khaderi, and S. Suriya Prakash	

Numerical Investigation of Bistable Laminates on Geometric Scaling 321
 G. S. Srikanth, S. Scheffler, P. M. Anilkumar, B. N. Rao, and R. Rolfes

Theory of Shape for Living and Non-living Things–Based on Thin Fluid Flows in Hele-Shaw Cell 337
 Vijayakumar Mathaiyan, R. Vijayanandh, S. Srinivasamoorthy, Tharikaa Ramesh Kumar, Sivaranjani Sivalingam, and Dong Won Jung

Investigation on Impact Characteristics of Concrete Under Varying Drop Height of Pendulum Impact 353
 K. Senthil, R. Sharma, A. Thakur, M. A. Iqbal, and A. P. Singh

Axial Stiffness of a Slot-Nut Type Conformal Segment Joint 367
 M. Umakanth, P. Uday Kumar, V. Narayanamurthy, and S. Korla

Simulation and Analysis of Natural Gas Pipe Network for MNNIT (Allahabad) Staff Colony 379
 Ashwin Pandey, Ankit Prakash, Ramesh Pandey, and Anubhav Rawat

To Predict Frictional Pressure-Drop of Turbulent Flow of Water Through a Uniform Cross-Section Pipe Using an Artificial Neural Network 397
 Vaibhav Srivastava, Ankit Prakash, and Anubhav Rawat

Dynamic Analysis of 3D Printed Polylactic Acid Bolted Joint Beams 413
 K. P. Sibivivek and Ashok Kumar Pandey

Effect of Longitudinal Unstiffened Cut-Outs on Buckling Behavior of Metal-FRP Hybrid Airframe Shell 423
 G. Vamsi Krishna, V. Narayanamurthy, and C. Viswanath

Vibration Perception Threshold Tuning Curve Towards Early Diagnosis of Diabetic Peripheral Neuropathy 431
 V. Madhan Kumar, S. Natarajan, and M. Manivannan

Effect of Elevated Finger Temperature on Active Force JND 441
 V. Madhan Kumar, A. Ashwath, and M. Manivannan

Fatigue Crack Growth Study in Miniature Single Edge Notch Tension Specimen Using Acoustic Emission Technique 451
 Raghu V. Prakash, Prathmesh Pokharkar, and Chandan K. Mukhopadhyay

Numerical Investigations on the Pelton Turbine Jet 465
 Firoz Khan and Arun Kumar

Electromechanical Modelling of Ring Type of MEMS Gyroscopes 479
 Sunrit Samanta and Ashok Kumar Pandey

Material Parameter Identification for Brain Tissue Using Open-Source Platforms - GIBBON and FEBio	495
Abhilash Awasthi, Umesh Gautam, and Sitikantha Roy	
Porosity/Distributed Resistance (PDR) Modelling in the CFD Solver PDRFOAM	503
Manish Dhiman, V. Meysiva, P. Sathiah, and Vagesh D. Narasimhamurthy	
Design of Experimental Setup for Investigation of Leakage in O-Rings	521
Ambrish Biredar, Sri Krishna Sudhamsu Kambhammettu, and Lakshmana Rao Chebolu	
Development of Digital Twin for Polycrystalline BCC α-Fe	535
Gopi Gulivindala, Madhu Kiran Karanam, and Viswanath Chintapenta	
Interaction of Shock Waves in a Multi-material System	547
Satyendra Pratap Singh, Harpreet Singh, and Puneet Mahajan	
Analytical Modeling of Electro-Mechanical Linear Actuator for Control Pedal of Unmanned Ground Vehicle	561
R. Prem Chand, P. Chellapandi, and C. Lakshmana Rao	
Evaluation of Population-Based Metaheuristic Methods for Optimization of Truss Structures	571
K. Akanksh and B. N. Rao	
Effectiveness of Polyurea Based Foams as Seat Cushion to Reduce Spinal Compression Injury of Occupant in Vehicle During Mine Blast Using Finite Element Analysis	585
Basa Jsk Kalyan Subrahmanyam, Venkatesh Balasubramanian, and C Lakshmana Rao	
Numerical Analysis of a Vibration Isolator Under Shock Load	597
Ameena Nazeer, Rajesh P. Nair, and D. D. Ebenezer	
Finite Element Analysis of OGrid Lateral Bracing System	613
V. J. Farhana, Beena Mary John, and Rajesh P. Nair	
Active Vibration Model Predictive Control for a Smart Flexible Beam	625
A. R. Prashant, Arun K. Tangirala, C. Lakshman Rao, and M. V. V. S. Murthy	
Effect of Notch-to-Depth Ratio and Steel Fiber Volume Fraction on Acoustic Emissions Generated During Mode I Fracture Process in Steel Fiber Reinforced Concrete	637
Sardar Abhijit Samadhan and R. Vidya Sagar	

Delamination Buckling of Composite Conical Shells 653
 A. Nagendranath, Sanjay A. Khalane, R. K. Gupta,
 and C. Lakshmana Rao

Comparative Study of 2D Heat Transfer Models for a Wankel Expander 663
 Gautam Subburaj, Vipin V. Gopal, and Satyanarayanan Seshadri

A Novel Desiccant-Based Cooling System for Hot and Humid Climates 673
 Sandeep Koundinya and Satyanarayanan Seshadri

Development of Heat Exchanger Models for Predicting Heat Transfer Behaviour of Mixed Refrigerants 687
 Alfred Emmanuel, Satyanarayanan Seshadri, and Sandeep Koundinya

Dispersion of Love Waves in a Dry Sandy Layer Imperfectly Attached to a Microcontinuum Substrate: An Analysis with Stress-Free and Clamped Top Surface Conditions 697
 Shikha Deep and Vikas Sharma

Importance of Boundary Conditions in Multi-Physics Analysis of One-Dimensional ‘smart’ Beam 711
 P. M. G. Bashir Asdaque and Sitikantha Roy

Numerical Investigation of Sweet Spot of Cricket Bat 719
 Hari Vignesh, S. M. Srinivasan, and Ashish Pandey

Comparative Study of Ballistic Performance Parameter of Kevlar/Epoxy Composite Laminate 725
 A. Balaji Shunmugam and R. Velmurugan

Creep Failure Estimation of Nickel-Based Superalloys Using Unified Mechanics Theory (UMT) 737
 Kambhammettu Sri Krishna Sudhamsu and Chebolu Lakshmana Rao

Experimental Studies on the Effect of Blast Loading on Scaled Down Plates 745
 Aagesh Markose and C. Lakshmana Rao

About the Editors

Dr. Tadepalli Phanirama Tezeswi is currently Assistant Professor at National Institute of Technology (NIT) Warangal, India. He obtained B.Tech. from Karnataka University and M.S. and Ph.D. from University of Mississippi, USA. He has a background in structural engineering and mechanics. His areas of expertise include structural dynamics, nonlinear finite element analysis, composite materials, vibration testing, photoelastic testing, high strain rate SHPB testing, shock testing, multi-scale modelling, micro-mechanics and non-destructive evaluation. He works in the area of experimental characterization and analytical modelling of materials and structure response to shock and high strain rate loading. He has publications in various journals, holds a US patent and has an EIT certification from Michigan. He is a reviewer for several international journals. He is a member of ASME, ASCE, ASC, APS and Chi Epsilon Honor Society.

Dr. Vijayabaskar Narayanamurthy is Scientist at Research Centre Imarat, Hyderabad, India. He obtained B.Tech. from Pondicherry University, M.Tech. from Indian Institute of Technology (IIT) Madras and Ph.D. from University of Edinburgh and Heriot-Watt University, UK. His research interests include theoretical and computational impact mechanics, modelling of hybrid beams, plates and shells, flight structures–mechanisms–configurations, mechanics of fastenings and interfacial fracture mechanics. He has published his works in patents, journals and conferences. Presently, he is serving as Secretary of Indian Society for Applied Mechanics and reviewer for several international journals.

Numerical Studies on Propagation of Non-linear Lamb Waves Through Delaminated Surfaces in Stiffened Composite Plate Structures



Rajat Gethe , Ramadas Chennamsetti, and Avinash Hood

Abstract This paper examines the propagation characteristics of non-linear Lamb waves through delamination surfaces in the stiffened composite plate structures. Finite Element based simulations were performed by introducing contact non-linearity in the structure. The contact interface modeled at a delaminated surface shows the generation of higher harmonics when the A_0 mode interacts with it. The effect of presence and absence of spar was analyzed through amplitude ratio. It was observed that the amplitude ratio decreases with the presence of spar. Due to which there is a decrease in fundamental peak amplitude with the presence of a defect in the structure and energy is distributed in the form of subharmonic or higher-order harmonics. It is identified that as delamination length increases the amplitude ratio also increases. Delamination length greater than the wavelength of excitation frequencies introduces subharmonic in the signal whereas the amplitude ratio decreases when delamination length approaches wavelength in the structure. Based on this, we can infer relative size of the delamination length.

Keywords Contact nonlinearity · Delamination · Higher harmonics · Lamb waves · Subharmonics

1 Introduction

Initiation of delamination in a composite structure is one of the major failure modes. From an external view, it is barely visible, since the delamination is frequently embedded in the composite structure. Delamination arises during manufacturing, wear and tear during use, or by external factors like incomplete wetting. Small damage in a

R. Gethe (✉)

Department of Technology, Savitribai Phule Pune University, Pune, India

R. Chennamsetti · A. Hood

Composite Research Centre, R&DE(E) DRDO, Pune, India

© The Author(s), under exclusive license to Springer Nature Singapore Pte Ltd. 2022

T. Tadepalli and V. Narayanamurthy (eds.), *Recent Advances in Applied Mechanics*,

Lecture Notes in Mechanical Engineering, https://doi.org/10.1007/978-981-16-9539-1_1

structure over a period of time may lead to failure [1]. For the safety and reliability of a structure, it is important to detect damage at an early stage in the structure before reaching its critical limit. Structural Health Monitoring (SHM) helps to provide information in real-time to identify the damage or health status of the component. SHM systems employing guided waves such as Lamb waves, Rayleigh waves have received special attention over the past decades [2]. Lamb waves are one of the promising techniques for damage detection. Lamb wave has the ability to examine the entire structure, thereby detecting internal damage as well surface defects with low energy consumption. Lamb wave-based SHM is highly sensitive to locate the damage in the engineered components. Lamb wave-based method is classified into two types, linear and nonlinear. In the linear method, the presence of damage is indicated by velocity, attenuation, reflection, and transmission of waves. In the case of the nonlinear method, the presence of damage is shown by the generation of sub and higher harmonics in the structures. There are basically two types of nonlinearities, classical and non-classical which are introduced by damage and wave interaction phenomenon. The classical nonlinear response is concerned with damage such as micro-cracks in the material field. Whereas, the non-classical nonlinearity is introduced by various mechanisms like the Luxemburg-Gorky effect, stress-strain hysteresis, contact nonlinearity, and rough surfaces contact [3]. Yelve et al. [4, 5] have demonstrated delamination in a laminate by using a non-linear technique. A new hybrid method was proposed to locate the actual location of the delamination. Hammami et al. [6, 7] studied the effect of increasing the delamination length on the linear and non-linear behavior of laminate. Ramadas et al. [8, 9] widely addressed that Lamb wave-based features such as mode conversion, amplitude ratio, time of flight for locating and detecting the damage in composite materials.

In the present study, finite element (FE) based simulations were performed to detect and simulate propagation characteristics of A_0 wave mode through delamination in the laminate (skin) and in stiffened composite structure (skin and spar) with various excitation frequencies. The delamination length varied from 5 to 30 mm. Furthermore, the presence and absence of spar element in the structure and delamination length equal to wavelength are investigated on amplitude ratio. Moreover, the effect of various delamination length and input excitation frequencies is implemented to do sensitivity analysis on the amplitude of fundamental frequency, first-order harmonics, and amplitude ratio. Data were examined by a signal processing tool (Matlab) in time and frequency domains.

2 Numerical Simulations

Finite Element (FE) simulations were carried out to simulate propagation of linear and nonlinear Lamb waves through contact delaminated interface in laminate (skin) and stiffened structure with various excitation frequencies.

2.1 Numerical Modelling

Skin (Composite Flat Laminate): Finite Element (FE) simulation of the Lamb wave propagation in a laminate was carried out using ANSYS. Laminate was modeled using 2-D 8 node quadrilateral structural solid (PLANE183) assigned with orthotropic properties and plane strain condition was assumed. Model specifications were 2 mm in thickness and 350 mm in length with 8 plies and all were oriented in zero direction. Figure 1 shows the geometry of the model.

The orthotropic properties for 2D skin, 2D stiffened structure are listed in Table 1.

Skin and Spar (Stiffened Composite Structure): Lamb wave propagation through structural inhomogeneity (e.g. stiffener, bolt and rivet) imposed on a composite structure was simulated using ANSYS. Model specifications are skin is 2 mm thick 350 mm with 8 plies and zero degree orientation and spar is 130 mm in height 2 mm thick and 35 mm in length bonded onto the skin with the same laminate properties as mentioned in Table 1. Figure 2 shows the geometry of model.

Fig. 1 Schematic representation of skin with delamination

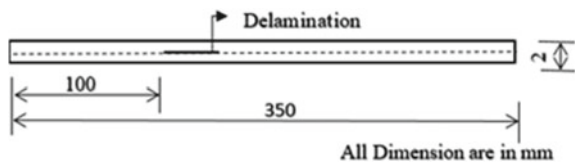
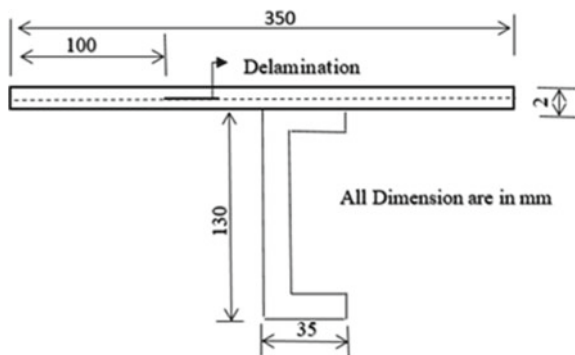


Table 1 Composite laminate material properties

Material	E_{11} (GPa)	E_{22} (GPa)	ν_{13}	ν_{23}	G_{13} (GPa)	$\rho(kg/m^3)$
Carbon/epoxy	126	8.7	0.2	0.3	8.96	1500

Fig. 2 Schematic representation of stiffened structure with delamination



2.2 Modelling the Contact Nonlinearity

In the present numerical study, the crucial part is to model a delamination and contact at the delamination in the laminate and composite structure. When a Lamb wave passes through the delamination, the surfaces with contacts should interact with each other giving rise to energy transfer between the surfaces. Here, delamination was modeled between 6th and 7th plies by demerging the nodes at that interface. After creating the delamination, contact elements were introduced at the delaminated surfaces. Hence, it was modelled by contact type elements- surface-to-surface CONTA172 and TARGE169. The contact problem was solved by using Augmented Lagrangian (AL) algorithm [10], which contributes to benefits like penetration control, governing equations and constraint satisfying finite penalties. As Lamb wave propagates through the delaminated surfaces, it starts opening and closing in multiple ways shown in Figs. 3 and 4.

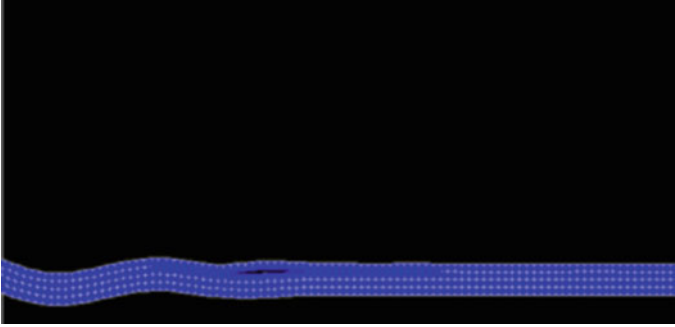


Fig. 3 Opening at contact delaminated interface

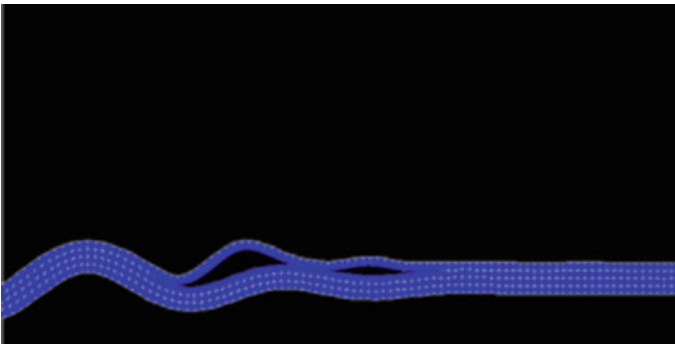


Fig. 4 Closing at contact delaminated interface

2.3 Excitation Details of A_0 Mode

A_0 mode was excited from one end of the laminate and response time history was to capture in out-of-plane direction (displacement in y-direction). To simulate Lamb wave propagation in the composite structure, the input excitation signal consisted of five cycles was modulated using Hanning window. The input excitation signal (0.1 MHz) consists of five cycles sinusoidal tone bursts modulated with a Hanning window and its corresponding energy spectrum obtained by Fast Fourier Transform is shown in the Figs. 5 and 6.

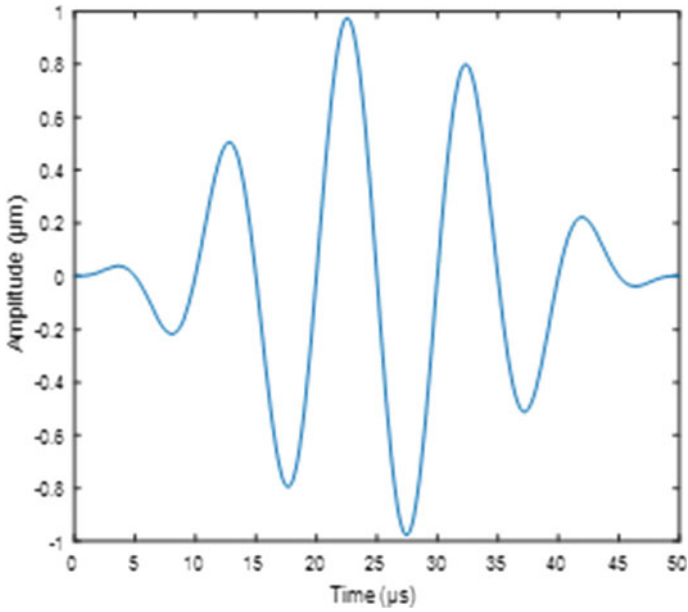


Fig. 5 Time domain signal of Lamb wave

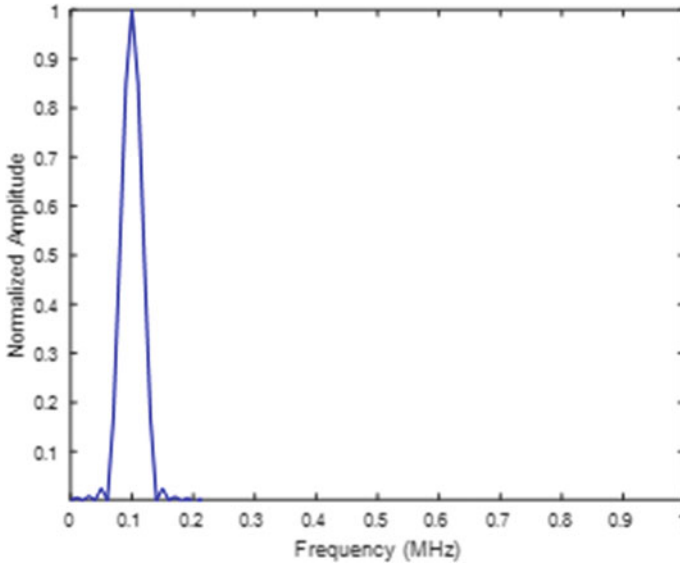


Fig. 6 Frequency domain signal of Lamb wave

3 Result and Discussions

Numerical simulations were performed without contact (linear) and with contact (non-linear) in a flat laminate and a composite structure consisting of skin and spar replicating a typical wing structure. To study the effect of wavelength on delamination length various cases were analysed. All such cases such as delamination length is less than wavelength, delamination length is equal to wavelength and delamination length is greater than wavelength were identified. Data was examined by signal processing tools in time and frequency domains. Non-linearity in the Lamb wave signal is not clearly analyzed in the time domain analysis. FFT gives detailed insight on the non-linearity in the signal in terms of higher order harmonics. If A_1 is the amplitude of the fundamental peak and A_2 is the peak amplitude of the first harmonic then the amplitude ratio associated with it is expressed as below.

$$A_r = A_2/A_1 \quad (1)$$

The wavelength of the wave was found out by using following expression

$$\lambda = v/f \quad (2)$$

where,

λ = wavelength of the wave;

v = phase velocity of the wave;

f = input excitation frequency.

Figures 7 and 8 show time and frequency domain analyses for 0.1 MHz excitation frequency for 20 and 25 mm delamination lengths. Due to the presence of the delamination in the structure, nonlinearity in the signal was present in the form of higher

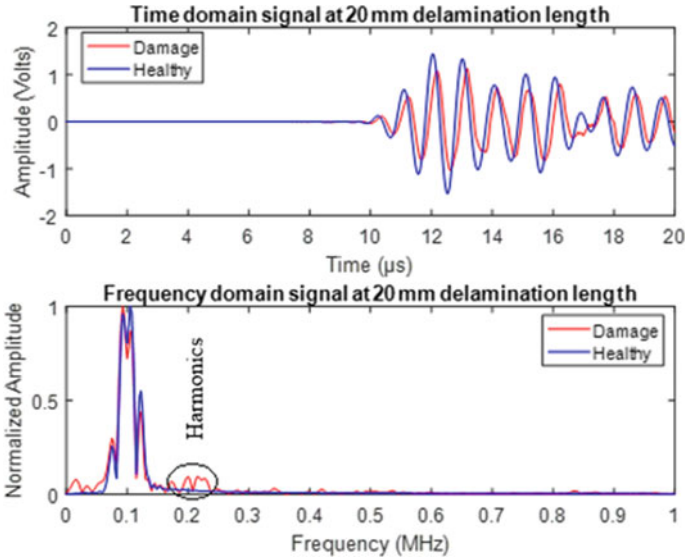


Fig. 7 Response for 20 mm delamination length

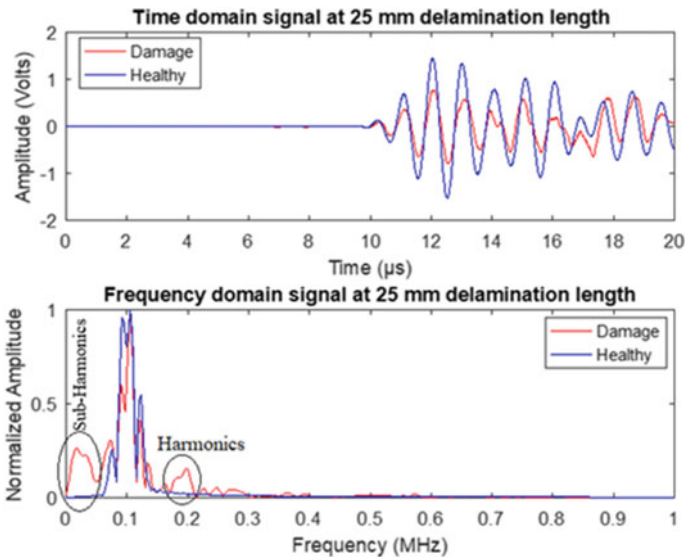


Fig. 8 Response for 25 mm delamination length

order harmonics. When the delamination length exceeds the wavelength (22 mm) the sub-harmonics generation is observed in frequency domain signal.

3.1 Delamination Length Equal to Wavelength

For 0.1 MHz input excitation frequency wavelength is 22.5 mm. Here the phase velocity was calculated as 2250 m/s. The amplitude ratio shows increasing trend till delamination length approaches to wavelength. Further, when delamination length is equal to wavelength, amplitude ratio decreases and when delamination length is greater than wavelength, it shows an increase in amplitude ratio again, as shown in Fig. 9. When the delamination length is greater than wavelength the amplitude ratio of sub-harmonics increases drastically as shown in Fig. 12.

For 0.15 MHz excitation frequency wavelength is 16 mm. Here the phase velocity was calculated 2400 m/s. The amplitude ratio shows increasing trend till delamination length approaches to wavelength. Additionally, when delamination length is equal to wavelength, amplitude ratio decreases at that point and when delamination length is greater than wavelength, it shows an increase in amplitude ratio again, as shown in Fig. 10. When the delamination length is greater than wavelength the amplitude ratio of sub-harmonics increases drastically as shown in Fig. 12.

For 0.2 MHz excitation frequency wavelength is 12.5 mm. Here the phase velocity was calculated as 2450 m/s. The amplitude ratio shows increasing trend till delamination length approaches to wavelength. Moreover, when delamination length is equal

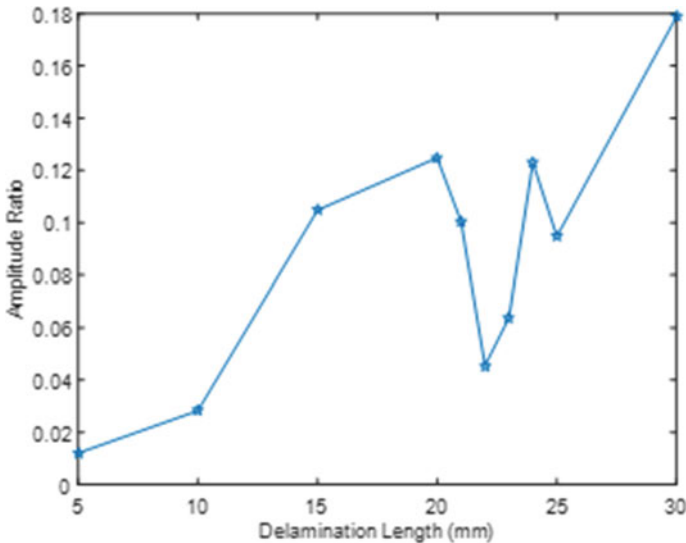


Fig. 9 Sensitivity graph for 0.1 MHz input excitation frequency

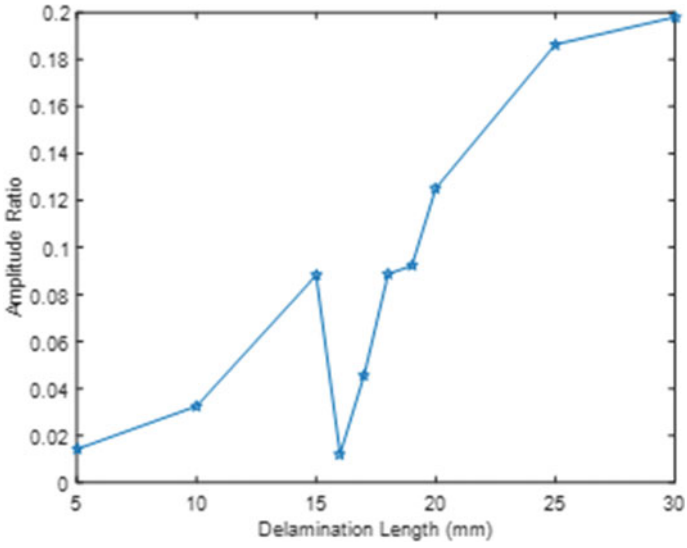


Fig. 10 Sensitivity graph for 0.15 MHz input excitation frequency

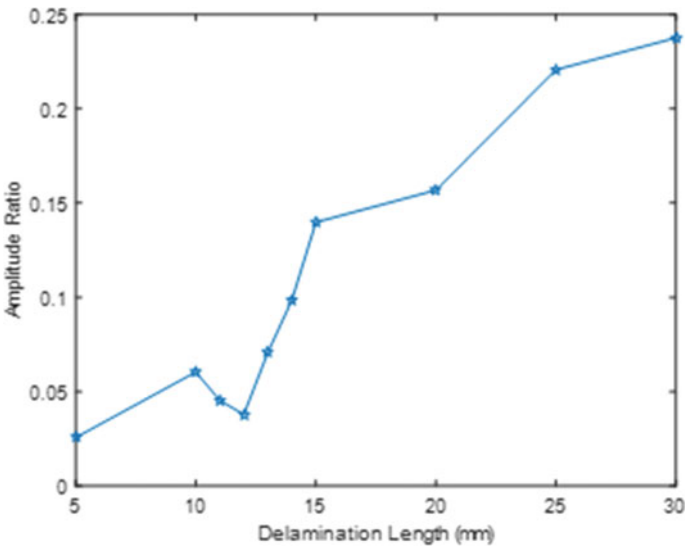


Fig. 11 Sensitivity graph for 0.2 MHz input excitation frequency

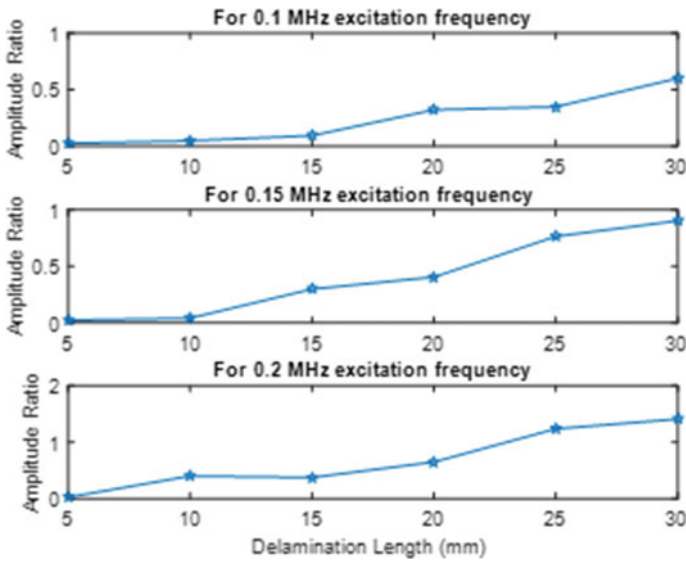


Fig. 12 Sensitivity graph for sub-harmonics

to wavelength, amplitude ratio decreases at that point and when delamination length is greater than wavelength, it shows an increase in amplitude ratio again, as shown in Fig. 11. When the delamination length is greater than wavelength the amplitude ratio of sub-harmonics increases drastically as shown in Fig. 12.

From the above, it is inferred that amplitude ratio decreases when delamination length approaches to wavelength. This could be due to generation of sub-harmonics, which carry part of the energy of the fundamental frequency.

3.2 Variation in Frequency for Flat Laminates

Excitation frequencies selected in the current study were 0.1, 0.15 and 0.2MHz. From the results, it is observed that for a given frequency, with increase in delamination length, there is an increase in amplitude ratio, as shown in Fig. 13, except at a particular length of the delamination, which is equal to wavelength.

3.3 Variation in Frequency in Skin-Spar Structure

In case of skin-spar geometry also, for a given excitation frequencies viz. 0.1, 0.15 and 0.2MHz as the size of the delamination increases, amplitude ratio also increase, as shown in Fig. 14, except when size of delamination is equal to wavelength of the Lamb mode.

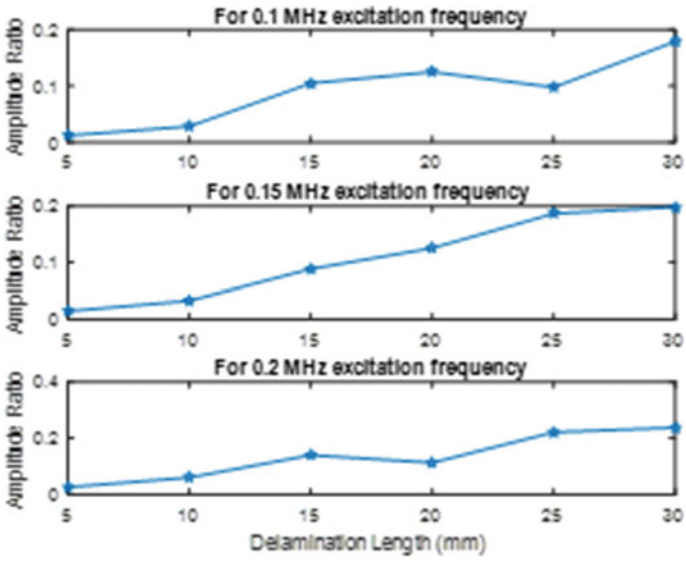


Fig. 13 Sensitivity study graph for skin

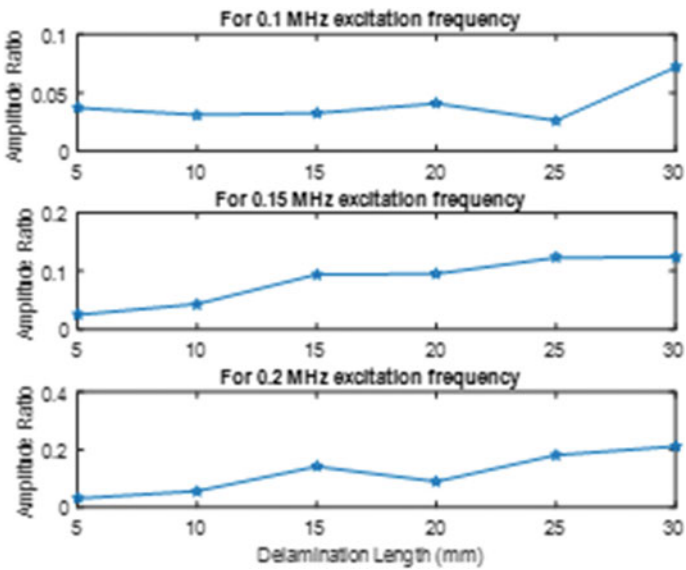


Fig. 14 Sensitivity study graph for stiffened structure

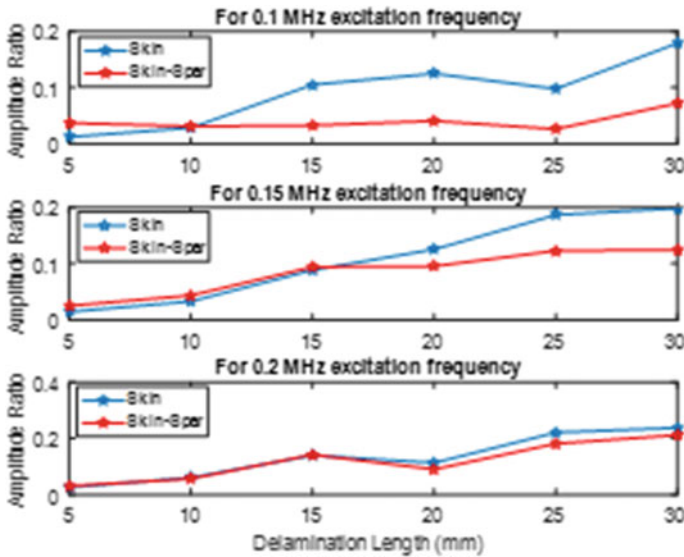


Fig. 15 Effect of presence and absence of spar on amplitude ratio parameter

3.4 Effect of Presence and Absence of Spar

In flat laminate structure, the amplitude ratio increases for 0.1 MHz is shown in Fig. 15. Due to absence of spar in the structure, energy transfer does not take place. In skin-spar structure there is presence of spar, the amplitude ratio decreases due to reflection and transmission of wave groups in the structure at the spar. Same pattern was seen at various frequencies viz. 0.15 and 0.2 MHz. From above, it is concluded that due to presence of spar in the structure the amplitude ratio is reduced in comparison with flat laminate (skin).

4 Conclusion

Numerical modelling employing A_0 mode and non-linear contacts was carried out to study the effect of variation in frequency and delamination size in flat laminates and skin-spar like structure. It is observed that amplitude ratio of harmonics increases with increase in size of delamination. When the size of delamination is equal to the wavelength of A_0 wave mode, amplitude ratio has a lower value. For higher delamination sizes, which are beyond wavelength of the Lamb mode, sub-harmonics are getting introduced. Hence we can infer relative size of the delamination length. Comparison of numerical simulations with and without spar have revealed that, presence of structural features like spar reduces amplitude of first order harmonic

and amplitude ratio due to reflection and transmission of incident wave group on the structural feature. Presence of sub-harmonic indicates that the size of defect is more than wavelength of Lamb mode.

Acknowledgements The first author is grateful to all the scientist and staff working at Composite Research Centre (CRC) in R&DE(E), DRDO for their guidance and timely support as well as administrative staff for providing me with an opportunity to work with the scientists of a prestigious research institute.

References

1. Kessler Seth S et al (2002) Damage detection in composite materials using frequency response methods. *Compos B Eng* 33(1):87–95
2. Su Z, Lin Y (2009) Identification of damage using Lamb waves: from fundamentals to applications, vol 48. Springer, London
3. Yelve NP, Mitra M, Mujumdar PM (2017) Detection of delamination in composite laminates using Lamb wave based nonlinear method. *Compos Struct* 159:257–266
4. Yelve NP, Mitra M, Mujumdar PM (2015) Detection of stiffener disbonding in a stiffened aluminium panel using nonlinear Lamb wave. *Appl Acoust* 89:267–272
5. Yelve NP et al (2016) A hybrid method based upon nonlinear Lamb wave response for locating a delamination in composite laminates. *Ultrasonics* 70:12–17
6. Hammami M et al (2016) Experimental analysis of the linear and nonlinear behaviour of composites with delaminations. *Appl Acoust* 108:31–39
7. Bermes C et al (2008) Nonlinear Lamb waves for the detection of material nonlinearity. *Mech Syst Signal Process* 22(3):638–646
8. Ramadas C et al (2010) Delamination size detection using time of flight of anti-symmetric (Ao) and mode converted Ao mode of guided Lamb waves. *J Intell Mater Syst Struct* 21(8):817–825
9. Ramadas C et al (2010) Interaction of guided Lamb waves with an asymmetrically located delamination in a laminated composite plate. *Smart Mater Struct* 19(6):065009
10. Simo JC, Laursen TA (1992) An augmented Lagrangian treatment of contact problems involving friction. *Comput Struct* 42(1):97–116

Excitation Bandwidth Dependence of Cantilever Energy Harvester



K. Manoj , V. Narayanamurthy, and S. Korla

Abstract Significant research has been carried out on cantilever energy harvester (CEH) when subjected to harmonic or random excitations in stand-alone configuration. But the performance of this CEH is unknown when this harvester is subjected to different bandwidth of random excitations at the base. In the present research, experiments have been carried out to investigate the influence of frequency bandwidth of the random base excitation on the output of the CEH when the harvester is mounted inside an airframe section. Further, the harvesters' performance is studied at different loads at each frequency bandwidth and under different acceleration levels. The results demonstrated that the CEH produces more power at lower base excitation frequency bandwidths when acceleration levels are higher and load resistances are minimal.

Keywords Vibration · Cantilever energy harvester · Random excitation · Experiments · Power output

1 Introduction

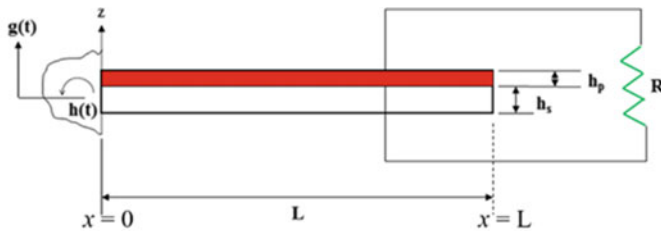
Vibration energy harvesting is one of the promising applications in the field of unconventional energy sources. The idea of venturing to vibration energy harvesting was originally initiated for powering the micro-electro mechanical based systems in flight vehicles [1–5] in order to overcome several issues associated with conventional power supply systems such as frequent charging and discharging of secondary batteries, disposal of chemical waste after the shelf life of chemical batteries, periodical replacement of primary batteries, slow rate of installation and necessity for separate cables for communication to and from different subsystems in the flight. Studies were carried out on different transduction mechanisms for converting vibrations into electrical signals [6–10, 12, 13, 15]. The cantilever energy harvester (CEH)

K. Manoj (✉) · S. Korla
National Institute of Technology, Warangal 506004, Telangana, India

K. Manoj · V. Narayanamurthy
Research Centre Imarat, Hyderabad 500069, Telangana, India

uses the cantilever beam over which piezoelectric material is glued. When CEH is subjected to vibration, the strain induced piezoelectric material generates electric power. The schematic diagram is shown in Fig. 1.

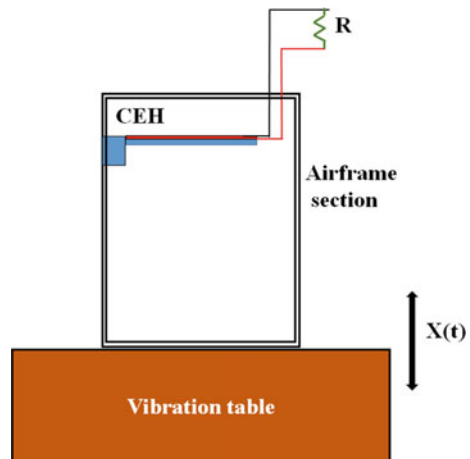
Considerable amount of research has been carried out on this harvester in stand-alone mode in the past when subjected to harmonic and random excitations [11, 14, 16–21]. Few researchers [22, 23] have developed computational models to study the performance of CEH subjected to random excitation. But the performance of this CEH is unknown when this harvester is subjected to different bandwidth of random excitations at the base. In the present research, experiments have been carried out to investigate the influence of frequency bandwidth of the random base excitation on the output of the CEH when the harvester is mounted inside an airframe section. The schematic diagram of CEH mounted in airframe is shown in Fig. 2. Further, the



g(t): translational force; h(t): rotational force; R: Load resistance; h_s : Thickness of Al substructure; h_p : Thickness of Piezoelectric material; L: length of CEH ;

Fig. 1 Schematic diagram of CEH under base excitation

Fig. 2 Schematic diagram of airframe with CEH under base excitation

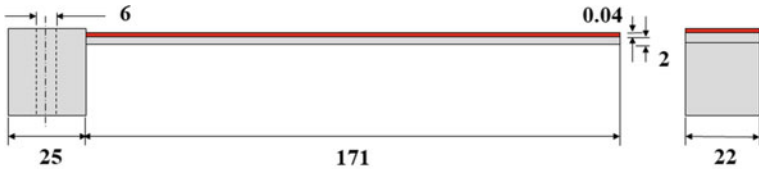


Where, R is load resistance and X(t) is base excitation

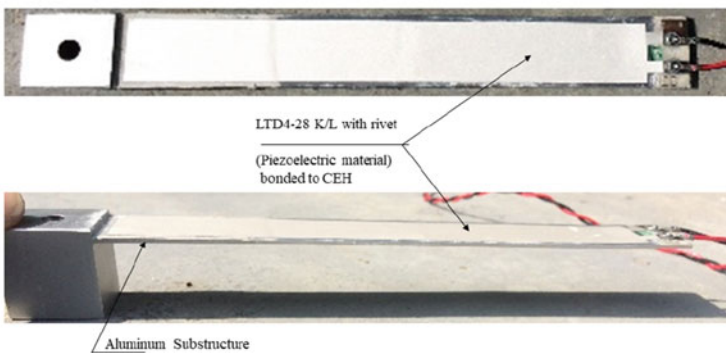
harvesters’ performance is studied at different loads at each frequency bandwidth and under different acceleration levels.

1.1 Properties of CEH

The configuration of CEH in the present study is similar to that of the one studied in [23]. The Energy harvester consists of a cantilever beam structure with piezoelectric patch glued to the upper surface. The piezoelectric patch used is a PVDF having part No. LTD4-28K/L. The patch has a thickness of 40 μm . It is glued to the Al alloy material (IS 24345) cantilever beam whose dimensions are shown in Fig. 3(a). In the figure, The Piezoelectric material is indicated by red colour and the Al alloy beam is indicated by grey colour. The base kind of structure is provided to the beam so that the beam can be clamped to the vibration table and airframe section using M6 fastener. Mbond 200 is used for gluing PVDF to Al alloy beam. The hardware of the CEH is shown in Fig. 3(b). The Table 1 gives the details of the properties of piezoelectric material that is provided by manufacturer. The same properties are used during the Finite Element Analysis.



(a) Dimensions of cantilever energy harvester in mm



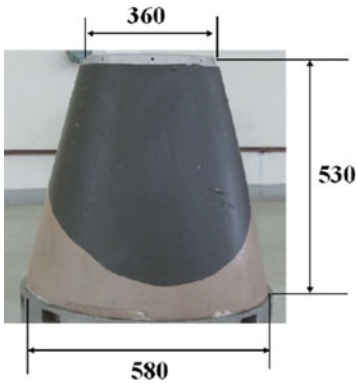
(b) Actual hardware

Fig. 3 Unimorph cantilever energy harvester

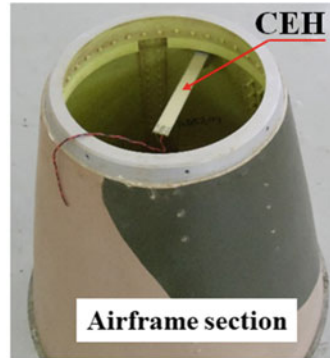
Table 1 Properties of piezoelectric material

S. No.	Property	Value	Unit
1	Density	1780	kg/m ³
2	Strain constant (d_{31})	23×10^{-12}	C/N
3	Strain constant (d_{33})	-33×10^{-12}	C/N
4	Piezoelectric stress constant (g_{31})	216×10^{-3}	Vm/N
5	Piezoelectric stress constant (g_{33})	-330×10^{-3}	Vm/N
6	Electromechanical coupling factor (k_{31})	12.0%	–
7	Electromechanical coupling factor (k_t)	14.0%	–
8	Modulus of elasticity (E)	4.0	GPa
9	Capacitance (C)	11.0	nF

Further, the CEH is mounted in airframe section. The airframe section is made up of aluminium alloy IS 24345. The dimensions of airframe section and configuration for experiment are detailed in Fig. 4(a) and (b) respectively. The properties of IS 24345 is shown in Table 2. The CEH is mounted in airframe section using M6 fasteners at its front bulkhead.



(a) Dimensions of airframe section



(b) CEH mounted on FBH of airframe

Fig. 4 Airframe section with CEH

Table 2 Properties of Al alloy material

S. No.	Property	Value	Unit
1	Density	2650	kg/m ³
8	Young’s modulus of elasticity (E)	70	GPa
9	Poissons ratio	0.3	–

2 Research Objectives

The research objectives and significance are to experimentally investigate:

- The performance of CEH mounted in an airframe section and subjected to random base excitations; and
- The relative performance of this CEH when subjected to different bandwidths of random excitations at three different loads and at different magnitudes of random excitations.

3 Experiment on CEH Under Harmonic and Random Excitation

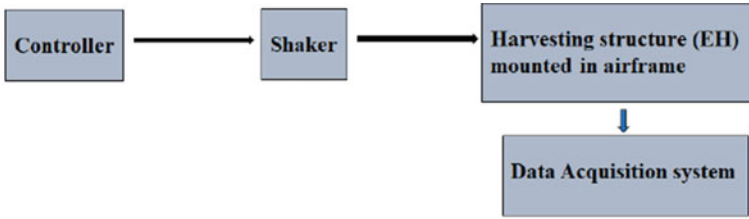
The experiments are carried out on the CEH in stand-alone mode for determining its natural frequency. This is performed by giving harmonic excitation to its base. Later the CEH is mounted in airframe section by fasteners and the airframe is subjected to harmonic and random excitation. The experiments on CEH along with airframe is conducted at different magnitudes of vibration. Here the experiments are carried out on CEH connected to different load resistances namely 100, 1000 and 10,000 k Ω . The airframe is subjected to different frequency bandwidths during random excitation of airframe.

3.1 Experimental Setup

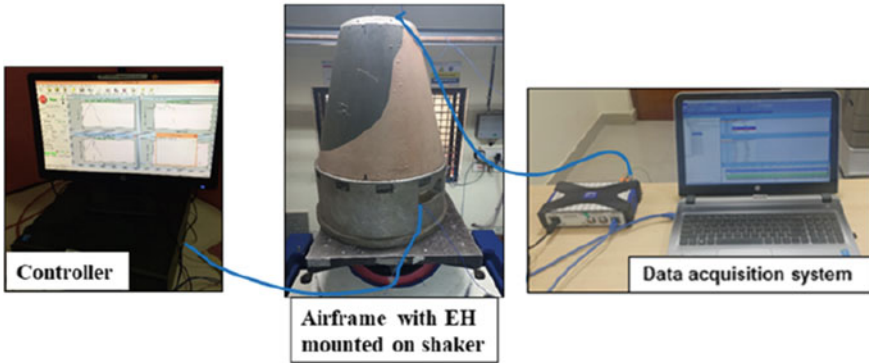
The block diagram as shown in Fig. 5(a) is taken as a reference for setting up the experiment. The setup for experiments on CEH with airframe is displayed in Fig. 5(b) and the Fig. 5(c) shows the mounting details of CEH in airframe.

The vibration levels to the airframe during experiments is controlled by using an accelerometer. It is mounted on the vibration fixture. The various equipment used during the experiment are mentioned below.

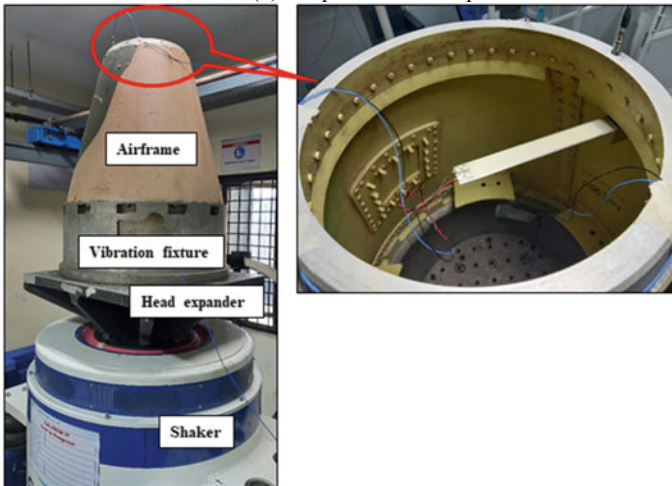
Shaker with Controller: The vibration shaker with inbuilt controller is used for imparting the specified vibration. The shaker is electrodynamic type in which the vibrations are generated from electricity influencing the magnetic flux generated in armature. The details of vibration shaker are make: Sdyn, model: SEV 360, and capacity: 3.5 tonnes.



(a) Block diagram for experiment



(b) Experimental set up



(c) CEH in airframe during experiment

Fig. 5 Airframe on shaker



Fig. 6 Electric circuit

Data Acquisition System (DAS): The DAS is employed to measure the voltage across the circuit and record the same when the CEH is subjected to specified vibrations. The details of DAS are make: HBM make, model: MX1601B.

The two resistors having value R_1 are connected in series to measure the voltages V_1 and V_2 across the circuit, as shown in Fig. 6. The value V_2 , the voltage across the single resistor, is used for calculation of power and current.

3.2 Experiments

The experiments are performed in three stages that is 1. Analysis of CEH in stand-alone mode under harmonic excitations, 2. Analysis of CEH mounted in airframe section and subjected to harmonic excitation and 3. Analysis of CEH mounted in airframe section and subjected to random excitation. In stage-1, the Energy harvester in stand-alone mode is subjected to a harmonic excitation of 1 g at the fixed end. The frequency is swept from 10 to 40 Hz without any load. The first natural frequency of the Energy harvester is determined from its frequency response. In stage-2, the experiments are performed by mounting CEH in airframe section and exciting the airframe structure at its base, at natural frequency of Energy harvester. Here the airframe section is subjected to simple harmonic motion from 1 to 5 g with 0, 100, 1000 and 10,000 $k\Omega$ loads. In stage-3, keeping the set up same as in stage-2, the excitation is changed to random from harmonic. The frequency bandwidths for this excitation are chosen so that the fundamental frequency of CEH lie within. The experiment is conducted at vibration levels from 1 to 5 g_{RMS} .

Harmonic Excitation of CEH in Stand-Alone Mode at 1 g with No Load. The energy harvester is mounted on the Shaker. The shaker simulates the source of base excitation for the energy harvester. An accelerometer is fit to the shaker on its top near to base of CEH to measure and control the base excitation so that the specified vibration levels could be transmitted to the CEH. The details are shown in Fig. 7.

Fig. 7 Accelerometer on shaker

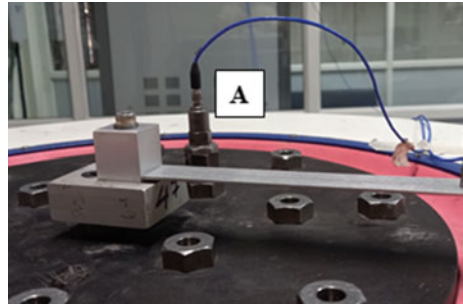
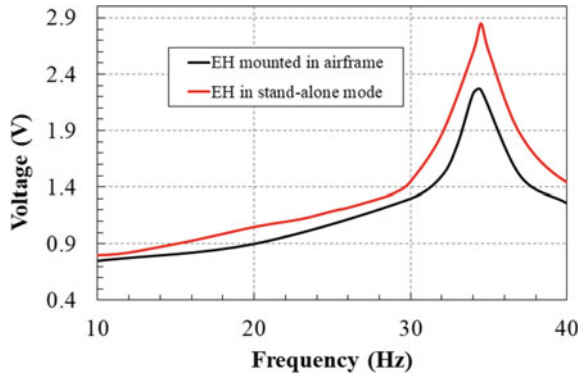


Fig. 8 Comparison of voltage across CEH



The piezoelectric material which is glued to the harvesting structure, is connected to DAS as shown in experimental set up. The Energy harvester is subjected to simple harmonic motion from 10 to 40 Hz with a magnitude of 1 g. It is inferred from the results of simulations and experiments [40] that the energy harvester is efficient and effective when the harvesting structure is excited at its natural frequency. In the present study the harvester is efficient at 34.5 Hz. The voltage across the circuit in CEH is recorded and is shown in Fig. 8.

Harmonic Excitations of CEH Mounted in Airframe from 1 g–5 g. Further, the CEH is mounted in the airframe and the airframe in turn is mounted on the shaker with the help of head expander as shown in Fig. 5(c). The piezoelectric material which is glued to the harvesting structure in CEH, is connected to DAS. The Airframe section assembly is subjected to simple harmonic motion from 10 to 40 Hz with a magnitude of 1 g. The voltage generated across the channel V_1 was measured, recorded and is showed and compared with that of CEH in stand-alone mode as shown in Fig. 8.

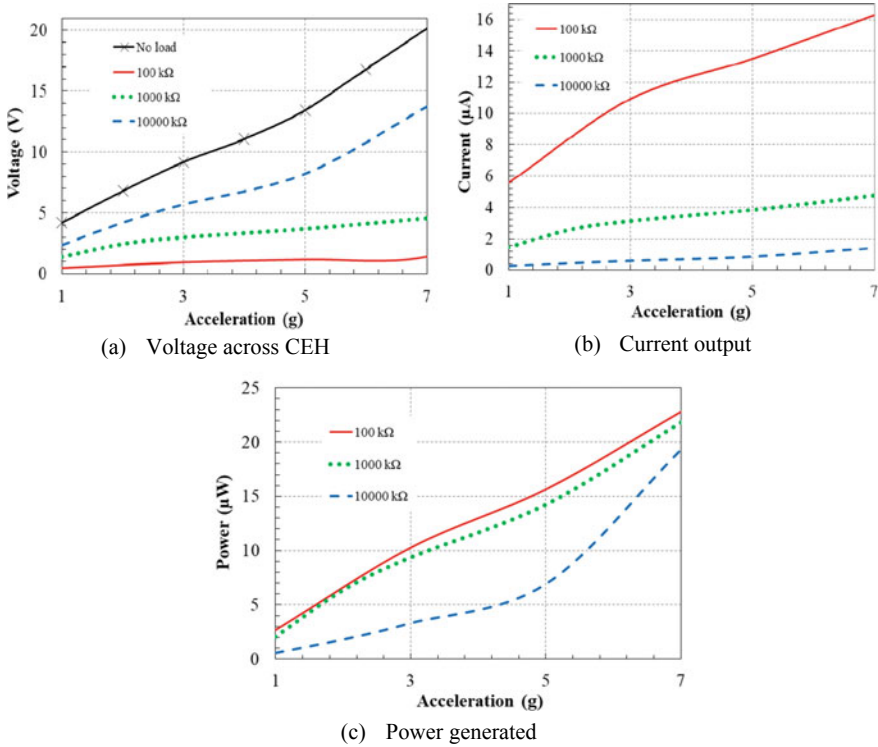


Fig. 9 Acceleration response (Harmonic excitation) of CEH mounted in airframe

Based on the results of the experiments performed in this Sub-section as well as in previous Sub-section, the airframe was base excited harmonically from 1 to 5 g at 34.5 Hz i.e. at natural frequency of CEH with 100 kΩ for generating maximum power. The voltage V_1 across the circuit is measured and recorded. The current ‘i’ is calculated through Ohm’s law as $i = V_1/2R_1$ and hence the power $P = i^2 * 2R_1$. The voltage across the circuit and power generated by CEH are plot in Figs. 9(a–c). The procedure is repeated with two more resistances of 1000 and 10,000 kΩ to investigate the harvested energy at different acceleration levels and loads. The voltage across the circuit, current and power generated from CEH at different values of excitation varying from 1 to 5 g for three different loads 100 kΩ ($R_1 = 50$ kΩ), 1000 kΩ ($R_1 = 500$ kΩ) and 10,000 kΩ ($R_1 = 5000$ kΩ) are plot in Figs. 9(a–c).

Table 3 Calculation of ASD from g_{RMS}

Sl. No.	Frequency bandwidth (Hz)	Magnitude of excitation (g _{RMS})	Acceleration Spectral Density (g ² /Hz)
1	20–50	1	0.03
		3	0.30
		5	0.83
2	20–250	1	0.004
		3	0.039
		5	0.10
3	20–500	1	0.002
		3	0.018
		5	0.052
4	20–800	1	0.001
		3	0.01
		5	0.03

Random Excitation of CEH Mounted in Airframe from 1–5 g_{RMS}. The airframe section with CEH is further studied by conducting more experiments in which the assembly is subjected to base random excitation with four frequency bandwidths ranging from 20 to 50, 20 to 250, 20 to 500 and 20 to 800 Hz with acceleration magnitudes 1 to 5 g_{RMS}. The input to the vibration table is in terms of Acceleration Spectral density (ASD). The magnitude of ASD for the same magnitude of excitation in terms of g_{RMS} changes for different bandwidths. The calculation is shown in Eq. (1) and the values are mentioned in Table 3.

$$g_{RMS} = \sqrt{BW * ASD} \tag{1}$$

$$ASD = \frac{(g_{RMS})^2}{BW} \tag{2}$$

where, ASD: Acceleration spectral density in g²/Hz,
 BW: Frequency bandwidth in HZ &
 g_{RMS}: Acceleration in g.

The bandwidth of frequencies is chosen to consider the frequencies of all the vehicles that move in air, water and land. The 20–50, 20–250, 20–500 & 20–800 Hz are experienced by automobiles and ships, helicopters, aeroplanes and missiles respectively. The procedures mentioned in the Subsection **Harmonic excitations of CEH mounted in airframe from 1–5 g** is opted for measuring voltage, calculation of

current and power from voltages with same experimental set up for the studies. Here, the airframe section assembly is subjected to different values of excitation (1, 3 & 5 g_{RMS}) connected to a load of 100 $k\Omega$ in a frequency bandwidth 20–50 Hz. The process is repeated with another two loads of 1000 and 10,000 $k\Omega$ in above mentioned frequency bandwidths.

The acceleration response of CEH from random excitation are shown in Figs. 10(a–c) and frequency bandwidth response of CEH are shown in Fig. 11(a–c). The power generated increases with the increase in magnitude of vibration levels irrespective of loads. The voltage across the circuit increases, the current and power generated decreases with increase in load. This trend is observed in all the frequency bandwidths but the magnitude of power generated is relatively high in low frequency bandwidth with low magnitude that is 20–50 Hz.

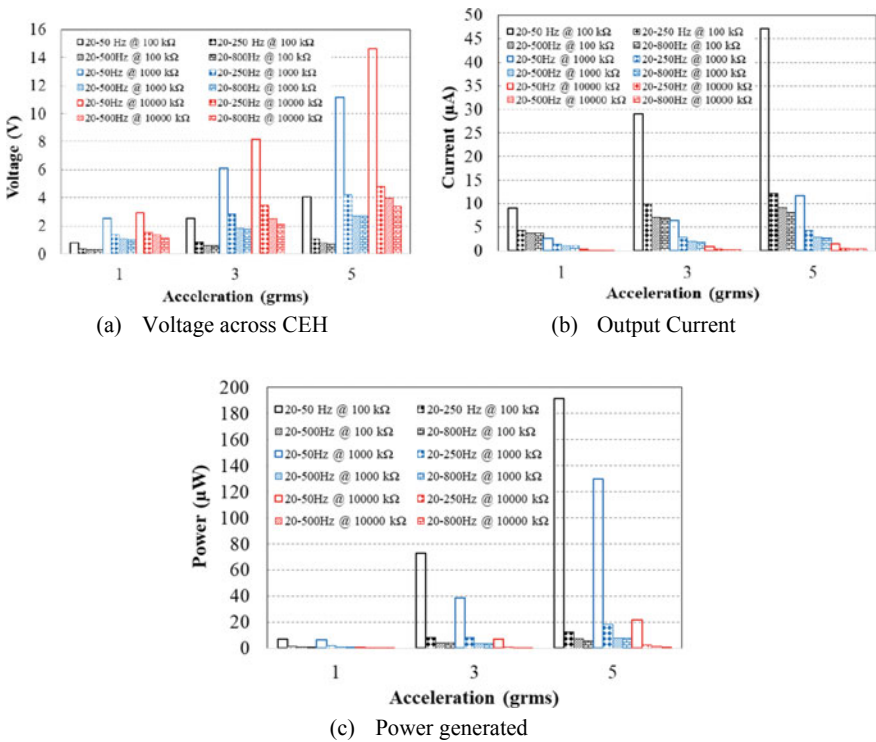


Fig. 10 Acceleration response (Random excitation) of CEH mounted in airframe

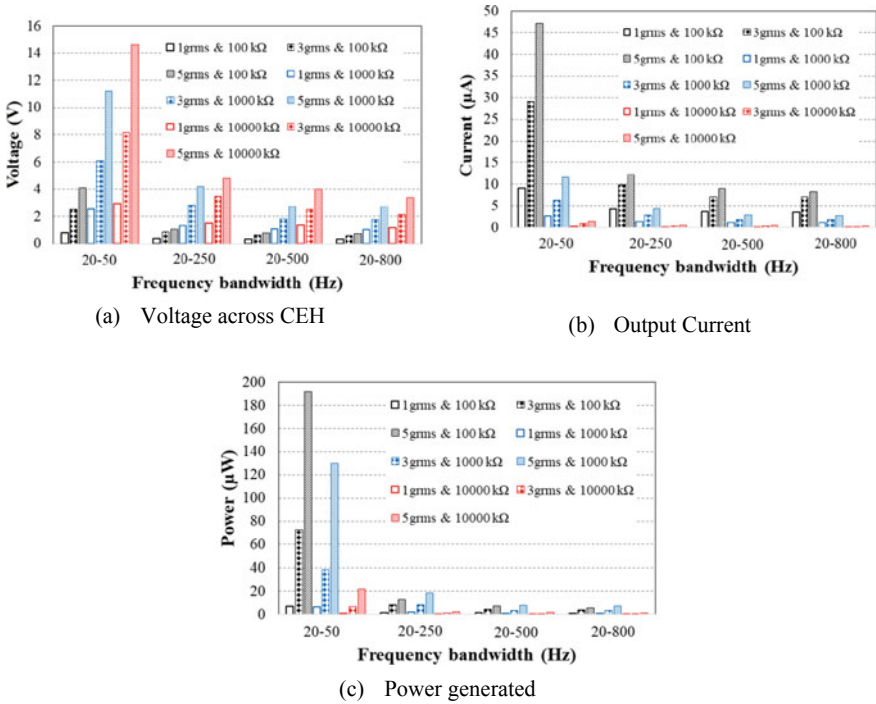


Fig. 11 Frequency bandwidth response (Random excitation) of CEH mounted in airframe

4 Comparison of Harvested Energy under Harmonic and Random Vibrations

The power generated by CEH mounted in airframe section under the influence of harmonic and random vibrations connected to three different loads are recorded. It is to be noted that the random excitation is given to the system at four bandwidths that is 20–50, 20–250, 20–500 and 20–800 Hz. The comparison of energy harvested during random excitation in bandwidths of 20–50 and 20–800 Hz which are smallest and largest in the experiment with harmonic excitation are shown in Figs. 12(a–c) and 13(a–c). These comparisons clearly demonstrate that random excitation with small frequency bandwidth yields higher power output as compared to that in the case of large frequency bandwidth. It is also demonstrated that the power generated in the former case is comparatively higher than that in harmonic excitation unlike the latter case in which power generated in harmonic excitation is more than that in the case of random excitation. The Fig. 14 shows the power ratio of random excitation in

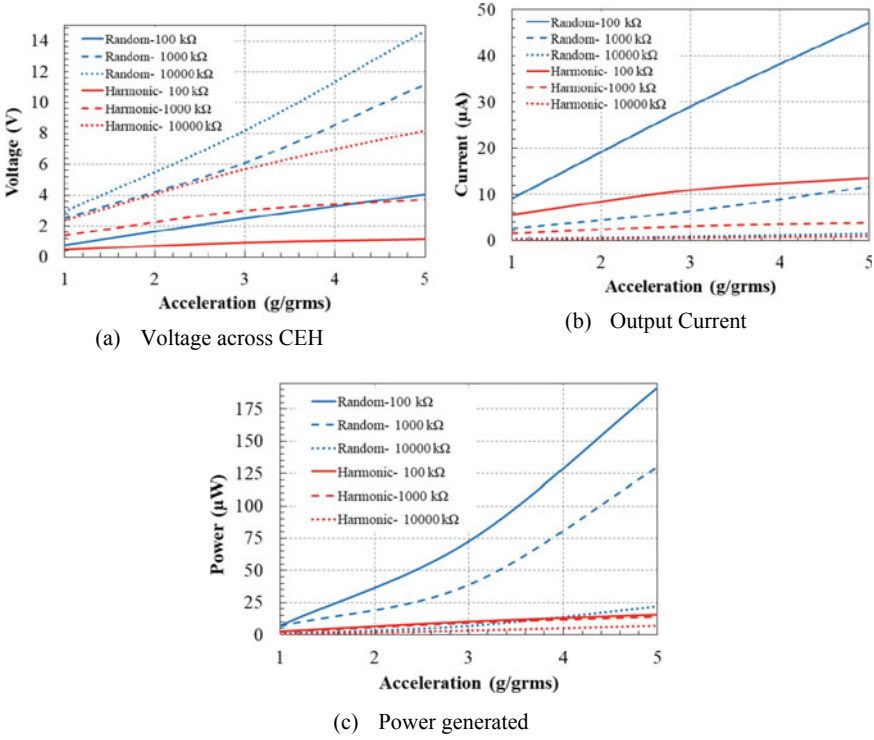


Fig. 12 Comparison of acceleration response of CEH in airframe under harmonic & random (20–50 Hz) excitation

lowest frequency bandwidth—to—equivalent harmonic excitations for three loads. The power generated during random vibration is 2.6–12 times higher for 100 kΩ, 3.2–9 times higher for 1000 kΩ and 1.6–3 times higher for 10,000 kΩ as compared to that under equivalent harmonic motion. This demonstrate that maximum power can be generated when the Energy harvester is installed on structures experiencing random as well as harmonic vibrations depending on the frequency bandwidths. Lower the frequency bandwidth, higher the power generated in random vibration and higher the frequency bandwidth higher the power generated in harmonic vibration. The values of voltage across the circuit, current and power generated by CEH when subjected to harmonic and random vibration is summarised in Table 4 and 5 with increasing load resistances and base accelerations.

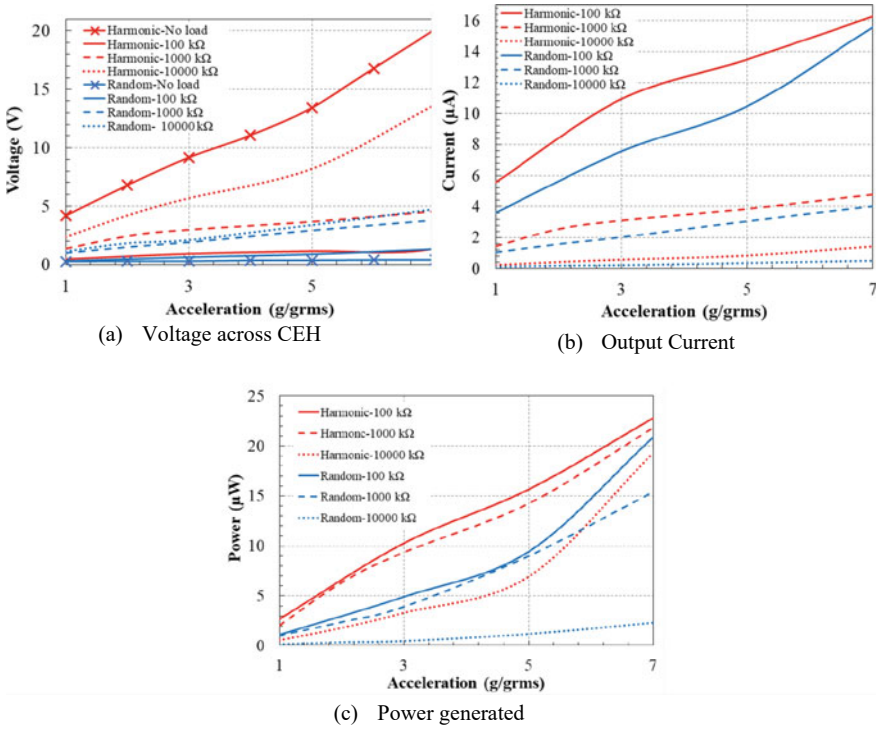


Fig. 13 Comparison of acceleration response of CEH in airframe under harmonic & random (20–800 Hz) excitation

Fig. 14 Power ratio of random and equivalent harmonic excitations

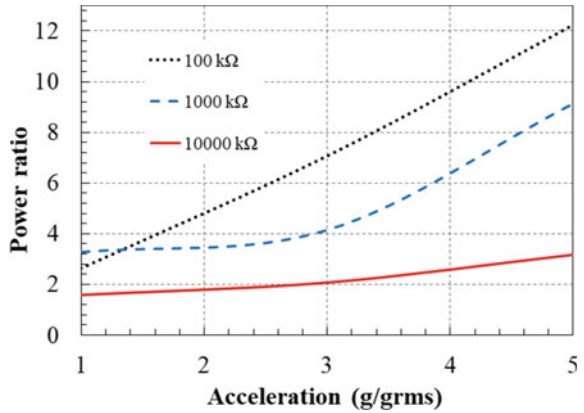


Table 4 Energy harvested under harmonic and random excitations: Acceleration -1 to 5 g; Frequency bandwidth-20–50 Hz

S. No.	Load (k Ω)	Harmonic excitation			Random excitation		
		Voltage (V)	Current (μ A)	Power (μ W)	Voltage (V)	Current (μ A)	Power (μ W)
1	100	0.48–1.16	5.6–13.5	2.6–15.6	0.78–4.06	9.06–47.2	7.0–191.0
2	1000	1.4–3.7	1.40–3.8	2.0–14.2	2.5–11.17	2.6–11.6	6.6–129.7
3	10,000	2.35–8.2	0.2–0.8	0.56–6.9	2.96–6.60	0.3–1.5	0.9–21.9

Table 5 Energy harvested under harmonic and random excitations: Acceleration -1 to 5 g; Frequency bandwidth-20–800 Hz

S. No.	Load (k Ω)	Harmonic excitation			Random excitation		
		Voltage (V)	Current (μ A)	Power (μ W)	Voltage (V)	Current (μ A)	Power (μ W)
1	100	0.48–1.16	5.6–13.5	2.6–15.6	0.3–0.7	3.6–8.1	1.1–5.7
2	1000	1.4–3.7	1.40–3.8	2.0–14.2	1.0–2.7	1.0–2.8	1.0–7.5
3	10,000	2.35–8.2	0.2–0.8	0.56–6.9	1.15–3.4	0.1–0.35	0.13–1.18

5 Conclusions

The paper presented the investigations on the performance of CEH mounted in airframe section subjected to harmonic and random excitation. The airframe assembly was subjected to random excitation in four different frequency bandwidths that are having same amplitude of acceleration (a_{GRMS}). In this study, more clarity observed about the amount of power generated under the influence of random excitation as compared to that in equivalent harmonic excitations which was not understood in literature. The present research highlighted the work carried out for quantification of energy harvested under harmonic excitations at natural frequency of CEH and random excitation in different frequency bandwidths. This is done by conducting experiments on CEH by subjecting it to the increasing values of excitation (1 to 5 g) for different loads 100, 1000 and 10,000 k Ω . Subsequently, the experiments on CEH are extended to study the relative performance under harmonic and equivalent random excitations in different frequency bandwidths. The following important points can be concluded from the present paper.

- The results indicate that the voltage and power generated is maximum when the frequency of base excitation matches with the natural frequency of CEH (34.5 Hz) whether it is in stand-alone mode or assembled to any structure. The natural frequency of airframe and CEH are 876 and 34.5 Hz respectively.
- The voltage generated by CEH is relatively high when excited in stand-alone mode than in assembled condition. The loss of voltage across CEH in assembled condition may be attributed to the damping properties of airframe structure.

- The voltage across CEH increases with increase in load resistance and the harvested current and power decrease with increase in load resistance irrespective of type of excitation.
- The Voltage across CEH, output current and power generated is relatively higher when it is subjected to random excitation in a smaller bandwidth with low frequencies(20–50 Hz) compared to larger bandwidth with high frequencies (20–800 Hz).
- The increase in power generated by CEH connected to different loads under the influence of increasing magnitude of random vibration in smaller frequency bandwidth is relatively higher than in simple harmonic motion which is recorded as 2.6–12 times.
- The increase in power generated by CEH connected to different loads and subjected to increasing magnitude of harmonic motion is comparatively higher than that during random excitation in larger frequency bandwidth and quantified as 1.8–5.8 times.
- It is recommended that the cantilever energy harvester can be used for aerospace applications like missiles and rockets in smaller frequency bandwidth that includes its own natural frequency.

Acknowledgements The authors thank 1) Directorate of Power Supply Systems team at Research Centre Imarat (RCI) for providing the piezoelectric material, 2) Directorate of Flight Instrumentation team at RCI for preparing the specimen, and 3) M/s. SSPL test house, Hyderabad, for providing the infrastructure required for conducting the experiments.

References

1. Roundy S, Wright PK, Rabaey J (2003) A study of low-level vibrations as a power source for wireless sensor nodes. *Comput Commun* 26:1131–1144. [https://doi.org/10.1016/S0140-3664\(02\)00248-7](https://doi.org/10.1016/S0140-3664(02)00248-7)
2. Beeby SP, Tudor MJ, White NM (2006) Energy harvesting vibration sources for microsystems applications. *Meas Sci Technol* 17:R175–R195. <https://doi.org/10.1088/0957-0233/17/12/R01>
3. Priya S (2007) Advances in energy harvesting using low profile piezoelectric transducers. *J Electroceram* 19:167–184. <https://doi.org/10.1007/s10832-007-9043-4>
4. Anton SR, Sodano HA (2007) A review of power harvesting using piezoelectric materials (2003–2006). *Smart Mat Struct* 16:R1–R21. <https://doi.org/10.1088/0964-1726/16/3/R01>
5. Cook CKA, Thambi N, Sastry AM (2008) Powering MEMS portable devices—a review of non-regenerative & regenerative power supply systems with special emphasis on piezoelectric energy harvesting systems. *Smart Mat Struct* 17:3001. <https://doi.org/10.1088/0964-1726/17/4/043001>
6. Hudak NS, Amatucci GG (2008) Small-scale energy harvesting through thermoelectric, vibration, & radiofrequency power conversion. *J Appl Phys* 103:101301–101324. <https://doi.org/10.1063/1.2918987>
7. Amirtharajah R, Chandrakasan AP (1998) Self-powered signal processing using vibration-based power generation. *IEEE J Solid-State Circuits* 33:687–695. <https://doi.org/10.1109/4.668982>

8. Mitcheson PD (2004) MEMS electrostatic micro power generator for low frequency operation. *Sens Actuators A Phys* 115:523–529. <https://doi.org/10.1016/j.sna.2004.04.026>
9. Dutoit NE, Wardle BL, Kim SG (2005) Design considerations for MEMS-scale piezoelectric mechanical vibration energy harvesters. *Integr Ferroelectr* 71:121–160. <https://doi.org/10.1080/10584580590964574>
10. Wang L, Yuan FG (2008) Vibration energy harvesting by magnetostrictive material. *Smart Mat Struct* 17:45009–45014. <https://doi.org/10.1088/0964-1726/17/4/045009>
11. Erturk A, Inman DJ (2009) An experimentally validated bimorph cantilever model for piezoelectric energy harvesting from base excitations. *Smart Mat Struct* 18:25009. <https://doi.org/10.1088/0964-1726/18/2/025009>
12. Mann BP, Sims ND (2009) Energy harvesting from the nonlinear oscillations of magnetic levitation. *J Sound Vib* 319:515–530. <https://doi.org/10.1016/j.jsv.2008.06.011>
13. Stanton SC (2010) Non-linear piezoelectricity in electroelastic energy harvesters: modeling & experimental identification. *J Appl Phys* 108:074903. <https://doi.org/10.1063/1.3486519>
14. Friswell MI, Adhikari S (2010) Sensor shape design for piezoelectric cantilever beams to harvest vibration energy. *J Appl Phys* 108:014901. <https://doi.org/10.1063/1.3457330>
15. Bai X, Wen Y, Yang J, Li P, Qiu J, Zhu Y (2012) A magneto-electric energy harvester with the magnetic coupling to enhance the output performance. *J Appl Phys* 111:07A938. <https://doi.org/10.1063/1.3677877>
16. Nechibvute A, Albert C, Pearson L (2013) Design & characterisation of a piezoelectric bimorph energy harvesting device. *Int J Eng Technol* 3:608–614
17. Yu H, Zhou J, Deng L, Wen Z (2014) A vibration-based MEMS piezoelectric energy harvester & power conditioning circuit. *Sensors* 14:3323–3341. <https://doi.org/10.3390/s140203323>
18. Litak G, Friswell MI, Adhikari S (2010) Magneto-piezo-elastic energy harvesting driven by random excitations. *Appl Phys Lett* 96:214103. <https://doi.org/10.1063/1.3436553>
19. Leng Y, Tan D, Liu J, Zhang Y, Fan S (2017) Magnetic force analysis & performance of a tri-stable piezoelectric energy harvester under random excitation. *J Sound Vib* 406:146–160. <https://doi.org/10.1016/j.jsv.2017.06.020>
20. Erturk A, Inman D (2008) Issues in mathematical modeling of piezoelectric energy harvesters. *Smart Mat Struct* 17:065016. <https://doi.org/10.1088/0964-1726/17/6/065016>
21. Shu YC, Lien IC (2006) Analysis of power output for piezoelectric energy harvesting systems. *Smart Mat Struct* 15:1499. <https://doi.org/10.1088/0964-1726/15/6/001>
22. Adhikari S, Friswell MI, Inman DJ (2009) Piezoelectric energy harvesting from broadband random vibrations. *Smart Mat Struct* 18:5005. <https://doi.org/10.1088/0964-1726/18/11/115005>
23. Manoj K, Narayanamurthy V, Korla S (2021) Performance of a cantilever energy harvester under harmonic and random excitations. *Def Sci J* 71:231–240. <https://doi.org/10.14429/dsj.71.15772>

A Review on Phase-Field Models Applied to Fracture in Solids



P. C. Sidharth  and B. N. Rao 

Abstract In circumstances with complicated crack topologies, computer modelling of fracture processes in solids that consider cracks as sharp discontinuities are found to be inadequate. It is possible to address this by a diffusive approximation of cracks based on a crack phase-field introduction. The phase-field model (PFM) thus presents a diffusive representation of fracture geometry that avoids abrupt discontinuities. The advantage of such a model over models having discrete descriptions of cracks is that numerical monitoring of discontinuities is no longer needed. The complexity of implementation is substantially reduced as a result of this. These features allow PFM to describe crack propagation more efficiently, especially for complicated crack patterns, as compared to numerical approaches based on a discrete crack model. These methods have also been shown capable of predicting fracture initiation and propagation in two and three dimensions without requiring any additional criteria. The phase-field model is a promising alternative to sharp crack models as it can cope with complicated crack patterns. Crack merging, fragmentation, and also branching patterns are successfully predicted by this model. An effort has been made to provide a brief overview of the phase-field model in the prediction of solid fractures and to concentrate on certain recent studies on the subject. We also present several noteworthy findings as well as suggestions for future research topics in this subject.

Keywords Phase-field model · Fracture · Diffusive crack modelling

1 Introduction

In engineering materials and structures, fractures are often encountered and their prevention is a major design constraint. Numerical modelling of fracture processes is commonly used to make design decisions. However, most design guidelines use significant safety factors to prevent it from manifesting. Fracture is indeed a challenging event to describe in reality since it is generally a complicated phenomenon.

P. C. Sidharth · B. N. Rao (✉)

Department of Structural Engineering, Indian Institute of Technology Madras, Chennai 600036, India

e-mail: bnrao@iitm.ac.in

As a result, it is crucial to use computer models to simulate and forecast the start, development, and branching of potential fractures for real engineering applications.

When an elastic solid body is deformed by a set of surface forces, the equilibrium condition is identified as the state such that the potential energy of the entire system is a minimum, from the well-known ‘theorem of minimal energy’. A new rupture criterion is obtained by adding to this theory an assertion regarding the broken state of the body. That is if at all an equilibrium is feasible; the equilibrium position must correspond to a ruptured state. Here, the assumption is made that a process involving a continuous decrease in potential energy is possible for the system to transition from unbroken to the broken state. Griffith [31] and Irwin [38] stated that a crack propagates when the energy release rate exceeds a threshold value. This theory became to be accepted as the classical theory of brittle fracture in elastic materials. They associated the presence of cracks to surface energy, which is a macroscopic manifestation of lattice debonding. The spread of cracks is then conceptualised as a competition between bulk energy of the domain elsewhere from the crack and surface energy on the crack as the crack length increased infinitesimally. This is, to say that crack propagation will occur if the rate of loss of elastic energy per unit surface area exceeds a critical energy release rate G_c . If the rate reaches the critical rate, however, it becomes unstable.

The Griffith theory does offer a fracture propagation criterion; however, it falls short in predicting crack kinking or branching and determining curved crack pathways. Such a hypothesis is also unable to anticipate fracture onset. These flaws in the traditional fracture theories can be addressed using variational techniques, as proposed by Francfort and Marigo [26]. In such an approach, the total energy is minimised concurrently for the crack geometry and displacement field. This formulation is significantly better than conventional Griffith theory since it determines the whole development of fractures, including their start and branching, without requiring any additional criteria.

However, because the displacement field is discontinuous in the presence of fractures, a straightforward implementation is problematic. Numerical techniques are essential in a fracture scenario not only because of the inherent complexity in solving the problem but also because fracture processes are encountered very often in engineering applications. Finite element techniques, in particular, are frequently employed in combination with the conventional linear elastic fracture mechanics (LEFM) models put forth by Griffith. The virtual crack closure approach [47] and, more recently, Moës et al.’s extended finite element method [73] are some of the most often utilised finite element models. These methods depict fractures as discrete discontinuities, either by utilising remeshing procedures to insert discontinuity lines or by introducing discontinuities in the displacement field using Babuška and Melenk’s partition of unity method [7]. However, these approaches have the disadvantage of being overly time consuming and tedious in tracing the evolution of complicated fracture surfaces. Not to mention the difficulties when it comes to complex geometries in three dimensions.

Alternative techniques of numerical modelling of brittle fracture have recently been developed [15, 26, 48, 70], to mention a few. In strong contrast to previous

models, discontinuities are not introduced explicitly in these methods. Instead, an additional field is used to represent the fracture surface, smoothing the crack’s border across a limited area. This method is known as the phase-field model and was originally employed for problems involving a change in physical states, such as solidification problems. In general, the phase-field methods are used for modelling systems with sharp discontinuities or interfaces and does so by embodying a continuous field variable called the field order parameter. Numerous physical phases in the system can then be distinguished by this parameter via a smooth transition. In a fracture problem’s context, such an order parameter is renamed as the crack field and is meant to depict the smooth transition between totally fractured and un-fractured material phases. This approximates the sharp crack discontinuity in a diffused manner. The advantage of such a model is that fracture description not requiring numerically monitoring of discontinuities. The complexity of implementation is substantially reduced as a result of this. Such an approach also enables bypassing the time-consuming effort of tracking complex fracture surfaces in 3D makes implementation much easier. Needless to say, phase-field modelling of fracture has undergone considerable theoretical and computational research since the late 1990s.

2 Phase-Field Approximation of Crack Topology

Consider an endlessly extended bar $L = [-\infty, +\infty]$ occupying the domain $B = \Gamma \times L$ where Γ is the cross-section and positioned along x axis. Assume that the bar has a crack in the axial direction, at $x = 0$. The fully broken crack surface is represented in Fig. 1.

For representing the sharp crack topology diffusively, an auxiliary field variable d (or u or ϕ), $\in [0, 1]$ can be made use of. For $d = 0$ and $d = 1$, the implication being the intact and fully broken states of the material respectively. (some authors use the reverse notion, in accord with their implementation). This approximation of the crack surface is visualised in Fig. 2.

In a one-dimensional setting, the discontinuous function of Fig. 2 can be approximated by the following exponential function, Where l_0 is the internal length scale parameter.

$$d(x) = e^{-|x|/2l_0} \tag{1}$$

Fig. 1 Sharp crack at $x = 0$

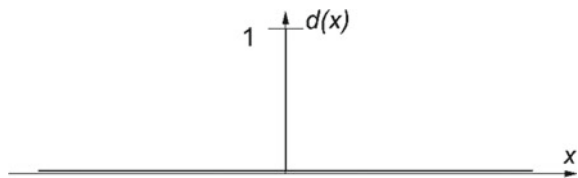
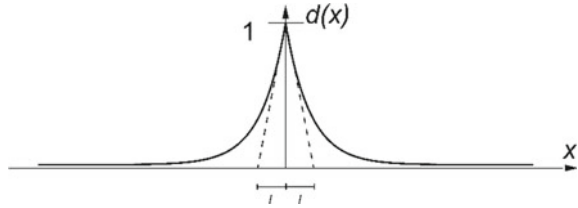


Fig. 2 Diffusive crack at $x = 0$ modelled with the length scale l



To proceed with the explanation in 2D, we consider a domain $\Omega \subset R$ with a crack Γ and $\partial\Omega$ representing the boundary. The domain chosen is linearly elastic as well as being homogeneous and isotropic. This is shown in Fig. 3.

The crack geometry in Fig. 3 can now be represented in a smeared manner by the phase field variable, $\phi(x) \in [0, 1]$, $x \in \Omega$. This is illustrated in Fig. 4.

Phase-field models has been used to model a variety of different problems. Dynamic fracture [11, 36, 93], quasi-brittle fracture [104], ductile fracture [4, 9, 62, 100], fractures of cohesive nature [12, 13, 101], rubbery polymers [72], hydraulic fracture [84], thin films [67], saturated porous media [55, 84, 88], and thin shells [4, 44, 99]. By accounting for an additional variable, that is the phase-field parameter, a fracture may be reformulated as an energy minimization problem [15].

As a result, complicated fracture characteristics including crack branching, crack initiation from random locations, and multiple crack coalescence are preserved naturally [9, 11, 66]. The approach is getting widespread popularity, and applications of

Fig. 3 Sharp interface topology

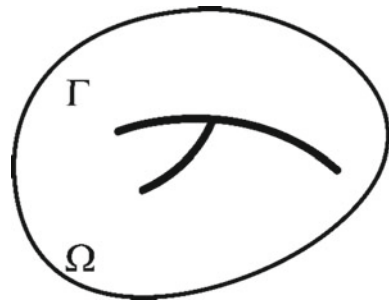
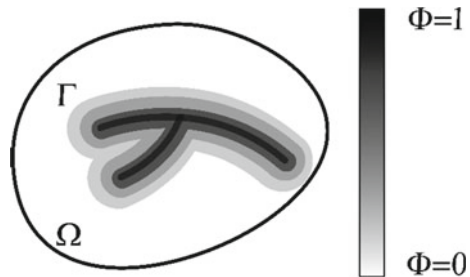


Fig. 4 Phase-field model of the interface



the model have risen dramatically. Hydrogen embrittlement [23, 64], fatigue damage [2, 19], lithium-ion battery cracking [69, 109], fracture in rock specimens [111], fracture of functionally graded materials [35], delamination of composites [89, 90] are only few of the recent instances. The method was shown capable to simulate crack onset and propagation in real materials like concrete, by Nguyen et al. [81, 82]. Direct images of the material microstructure, such obtained by 3D X-Ray computed tomography images were made use in their simulation. In [101], a cohesive phase-field model was developed and numerically examined in [14].

3 Theoretical Aspects

Several phase-field methods have emerged from the physics and mechanics communities to study brittle. Although the conceptual and technical bases for them are vastly different. Models created in the physics community are generated by modifying Landau and Ginzburg's phase transition formalism [54]. Whereas the models presented within the mechanics community are based on the variational formulation of Francfort and Marigo for brittle fracture [26]. This formulation was later regularised by Bourdin et al. [16]. The formulation can be seen as an extension to the conventional Griffith's theory of fracture, rendering the capability to now tackle problems involving more complexity. The latter group of models are focused in this study, due to their close ties to Griffith's theory which is well understood and extensively utilised by engineers.

In the mechanics community, a lot of effort has gone into further improving phase-field models. Amor et al. [5] had performed tension-compression partition in variational principle for fracture [26] and Miehe et al. [70, 71] in its regularised approximation [15]. This split was required to discriminate fracture behaviour in tension from those in compression. The fundamental concept is to express total elastic energy as the sum of active and passive energy components. The active energy component arising from tensile stresses contributes to fracture growth, but the passive energy component, which is derived from compressive stress levels, does not. This feature is explained further in the discussions which follow.

Improving computing efficiency is an important subject for phase-field modelling. A hybrid formulation was presented by Ambati et al. [3] which preserves the linearity of momentum balancing equations. This formulation was computationally efficient while having the ability to prevent fractures in compressive stress levels. The capacity of exponential shape functions to capture the analytical stationary solution of the fracture field was revealed by Kuhn and Muller [51]. The findings were relevant, since a coarser mesh may be employed along with exponential shape functions without compromising the ability to model possible cracks.

A regularisation parameter directly connected to the diffusive approximation of the sharp crack is introduced by all of the modern phase-field models. This parameter has length dimensions in the mechanics community's models and is understood as the breadth of the regularised crack. For obvious reasons, this parameter is referred to

as the length scale parameter or simply regularisation length. When the length scale parameter approaches zero, several of these models converge to Griffith's theory. This feature of phase-field models is called as Γ -Convergence. The size of the elements in a finite element formulation must be chosen sufficiently smaller than the length scale parameter to properly resolve diffuse crack. The additional computational cost caused by the use of a very tiny mesh, on the other hand, can be mitigated by using an adaptive local mesh refinement and coarsening method.

3.1 Phase-Field Models for Brittle Fracture

Although traditionally phase-field models are implemented in finite element settings, a combined finite volume method was proposed in Sargado et al. [68]. Their proposed framework had claimed to achieve fewer restrictions regarding mesh refinement. In contrast to the traditional implementation where fine meshes had to be used, employing coarser meshes does allow for a significant reduction in computational cost.

The phase-field methods to fracture that are preferred in the mechanics community are discussed in this section. The models are shown in the sequence in which they were created. As previously stated, the phase-field models produced in the mechanics community are based on the variational formulation of Griffith theory proposed by Francfort and Marigo's [26] and its subsequent regularisation by Bourdin et al. [15]. The 'phase-field regularised cohesive zone model' of Wu et al. [104, 106] was extended to thermoelastic solids by Mandal et al. [41]. The problem subsequently became a three-field problem, with temperature as an extra field, which was solved using monolithic BFGS methods.

Francfort and Marigo [26], 1998

In this model, the minimization of energy functional E is expected to govern the entire fracture phenomena including initiation, branching and propagation.

$$E(u, \Gamma) = \int_{\Omega} \psi_0(\varepsilon(u)) dx + G_c \int_{\Gamma} ds \quad (2)$$

In Eq. (2), the material fracture toughness G_c and the elastic energy density function ψ_0 and are included. It yields an admissible crack set $\Gamma \subset \Omega$ and a displacement field $u : \Omega \rightarrow R$, that is discontinuous across the cracked domain Γ . The limitations of Griffith's traditional brittle fracture theory are shown to be addressed by formulating Eq. (2). Bourdin et al. [16] proposed a regularised version of Eq. (2) to allow for an efficient numerical treatment which reads as,

$$\begin{aligned}
 E(u, s) &= \int_{\Omega} (s^2 + \eta) \psi_0(\varepsilon(u)) dx \\
 &+ G_c \int_{\Omega} \left(\frac{1}{4\epsilon} (1 - s^2) + \epsilon |\Delta s|^2 \right) dx
 \end{aligned} \tag{3}$$

In this expression, s is the crack field parameter. Its value ranges from 0 to 1, which respectively mean undamaged material and damaged material. A parameter $\epsilon > 0$ having the dimensions of length is critical to the formulation which represents the transition zone width. To avoid numerical issues, the broken phase's artificial residual stiffness is required to be simulated and is done so by a tiny dimensionless parameter η . In the sense of Γ -Convergence, when $\epsilon > 0$, Eq. (2) is approximated by Eq. (3) and demonstrating the connection between regularised and free-discontinuity fracture energy. This means that the original crack set Γ is recovered when the length scale parameter is set to zero. To solve for (u, s) , the functional E_ϵ is directly minimised, utilising the famous alternative minimization along with back-tracking methods in numerical implementations [15, 16].

Kuhn and Müller Model [48], 2008

Gurtin's theory on the thermodynamics of models which employ an order parameter [32] inspired Kuhn and Müller to rework the minimization problem in Eq. (3) to generate a system of stress equilibrium equations, $-div \sigma(u, s) = 0$ where

$$\sigma(u, s) := (s^2 + \eta) \frac{\partial \psi_0(\varepsilon)}{\partial \varepsilon} = (s^2 + \eta) \mathbb{C} : \varepsilon \tag{4}$$

and an evolution equation of the Ginzburg–Landau type for s :

$$\dot{s} = -M \left[2s \psi_0(\varepsilon) - G_c \left(2\epsilon \Delta s + \frac{1-s}{2\epsilon} \right) \right] \tag{5}$$

The irreversibility limitation on crack development was also added to the mix. The dissipation during steady crack development is controlled by the so-called mobility parameter $M \geq 0$. In the limit scenario $M \rightarrow \infty$, quasi-static fracture propagation is approximated, yielding

$$0 = 2s \psi_0(\varepsilon) - G_c \left(2\epsilon \Delta s + \frac{1-s}{2\epsilon} \right) \tag{6}$$

Amor et al. Model [5], 2009

Equation (3) does not discriminate between fracture behaviour in compression and tension. Unrealistic fracture patterns in compression have been observed in [15].

Additively decomposing the elastic energy density ψ_0 into volumetric and deviatoric contributions as in [5] was a successful modification to the regularised formulation of Eq. (3). This adaptation avoided such scenarios and also prevented the interpenetration of compression crack sides.

Thus, with $\psi_0 = \psi_0^+ + \psi_0^-$, where

$$\begin{aligned}\psi_0^+ &= \frac{1}{2}K_n \langle \text{tr}(\varepsilon) \rangle^2 + \mu(\varepsilon^{dev} : \varepsilon^{dev}) \\ \psi_0^- &= \frac{1}{2}K_n \langle \text{tr}(\varepsilon) \rangle^2\end{aligned}\quad (7)$$

$$\text{in turn } K_n = \lambda + \frac{2\mu}{n}, \langle a \rangle_{\pm} := \frac{1}{2}(a \pm |a|) \quad (8)$$

$$\text{and } \varepsilon^{dev} := \varepsilon - \frac{1}{3}\text{tr}(\varepsilon)I \quad (9)$$

And replaced the energy functional in Eq. (3) by

$$\begin{aligned}E(u, s) &= \int_{\Omega} (s^2 + \eta)\psi_0^+(\varepsilon) + \psi_0^-(\varepsilon) dx \\ &+ G_c \int_{\Omega} \left(\frac{1}{4\epsilon}(1 - s^2) + \epsilon|\Delta s|^2 \right) dx\end{aligned}\quad (10)$$

In this model, like in Henry and Levine's [56], but unlike Eq. (3), only the positive energy portion is permitted to deteriorate, while the negative energy part remains unchanged.

Miehe et al. Model [70, 71], 2010

A phase-field model, which is thermodynamically consistent, was proposed by Miehe and colleagues for brittle fracture. The model is derived using thermodynamic considerations along with continuum mechanics concepts. The formulation may be seen as a complement to the frameworks of Bourdin et al. [15, 16] and Francfort-Marigo [26]. In the suggested formulation, the crack phase-field variable is $d \in [0, 1]$, where $d = 0$ correspond to the unbroken state and $d = 1$ for the broken state. The thickness of the transition zone between the two states is accounted for by the length scale parameter l present. In this formulation, additive decomposition of the elastic energy as $\psi_0 = \psi_0^+ + \psi_0^-$ is achieved by spectral decomposition of the strain tensor. Ultimately,

$$\psi_0^{\pm} := \frac{1}{2}\lambda \langle \text{tr}(\varepsilon) \rangle_{\pm}^2 + \mu(\varepsilon_{\delta}^2) \quad (11)$$

The system of the balance equation $-div\sigma(u, s) = 0$ is the governing system of equations in this case, where

$$\sigma(u, d) := [(1 - d)^2 + k] \frac{\partial \psi_0^+(\varepsilon)}{\partial \varepsilon} + \frac{\partial \psi_0^-(\varepsilon)}{\partial \varepsilon} \quad (12)$$

and the evolution equation is

$$\eta \dot{d} = 2(1 - d)\psi_0^+(\varepsilon) + \frac{G_c}{l}(d - l^2 \Delta d) \quad (13)$$

Here, k is the broken phase's tiny artificial residual stiffness, and $\eta \geq 0$ is the viscosity value. The following is the fundamental originality of the Miehe et al. model: it solves some of the inherent implementation challenges associated with the previous phase-field models. The authors introduced a history field variable $H(x, t)$ of the highest positive reference energy acquired in a loading process, $H(x, t) := \max_{\tau \in [0, t]} \psi_0^+(\varepsilon(x, \tau))$ in the formulation. The observation that the value of d is determined by the load term ψ_0^+ entering Eq. (10) was the basic inspiration behind this. They get the evolution equation by replacing ψ_0^+ in Eq. (13) with H as

$$\eta \dot{d} = 2(1 - d)H + \frac{G_c}{l}(d - l^2 \Delta d) \quad (14)$$

This equation is to be used in conjunction with Eq. (9). In the first place, the incorporation of H took care of the irreversibility of the development of fracture phase-field. Lu et al. [63] used Miehe's method to model various fracture propagation issues in two-dimensional (2D) isotropic linear elastic materials. The effects of the force-displacement curve and fracture propagation trajectory on loading type and crack location were also studied. A thorough investigation of numerical instances can be found in the mentioned paper.

Higher-Order Model, Borden et al. [10], 2014

To impart momentum to the search of obtaining quicker converging solutions to the variational problem of brittle fracture, Borden et al. [10] proposed a higher-order phase-field model. The proposed energy functional is based on Bourdin's formalism and Miehe et al.'s concept of the fracture surface density function. Although this formulation resembles Eq. (10) in the elastic energy portion, crack phase-field's higher-order derivatives were also incorporated into the corresponding surface energy integral. This demands the energy functional be written as,

$$\begin{aligned} E_\varepsilon(u, s) = & \int_{\Omega} (s^2 + \eta)\psi_0^+(\varepsilon) + \psi_0^-(\varepsilon) dx \\ & + G_c \int_{\Omega} \left(\frac{1}{4\varepsilon}(1 - s^2) + \frac{1}{2}\varepsilon|\Delta s|^2 \right. \\ & \left. + \frac{1}{4}\varepsilon^3(\Delta s)^2 \right) dx \end{aligned} \quad (15)$$

Either Eq. (7) or (11) can be utilised to obtain ψ_0^+ . A fourth-order partial differential equation now describes the evolution equation for s as:

$$\dot{s} = -M[2s\psi_0^+(\varepsilon)] - G_c \left(\frac{-\varepsilon^3}{2} \Delta^2 s + \varepsilon \Delta s + \frac{1-s}{2\varepsilon} \right) \quad (16)$$

3.2 Input Parameters in the Simulations

All variations of modern phase-field models can simulate fracture problems in both 2D and 3D without the need for ad hoc numerical treatment. However, the approach necessitates the selection of certain parameters. Be it the regularisation parameter related to smeared discontinuity approximation, mesh size of the implementation or the load and time increment, they are required to be determined ahead of time. The following discussion is devoted to the sensitivity of the phase-field models towards these input parameters.

Choice of the Regularization Parameter

Regularization in phase-field models causes the model to have a characteristic length that must be determined by the user. The length scale is not just an arbitrary tiny parameter that has limited importance. Instead, this parameter may reflect in the solution itself and it must be determined with care. This makes interpreting the length scale parameter challenging for the phase-field model. The choice of a characteristic length parameter is still up for debate among academics and is generally acknowledged that a proper assumption of this parameter is necessary for a solution to be found. The authors of [5] shown that the parameter may be calculated using at least two additional material parameters. This hypothesis was backed by simulations of fracture initiation on drilled plaster samples by Nguyen et al. [83]. On the one hand, it was introduced based on the mathematics of the problem, separate from the mechanical field problem. It, on the other hand, behaves as a material parameter when connecting the mechanical field and the phase-field. Setting the length scale to a small enough value allows for accurate fracture path modelling. Although an effort was made in [11, 17, 52], where formula was provided to evaluate this parameter, there is no commonly recognised technique for calculating it for phase-field modelling. The said formula was obtained from a basic one-dimensional crack problem analytically. Zhang et al. [108] used fracture experimental testing on concrete to support the correctness of the above-mentioned formulation.

Influence of Mesh Size

The size of the elements must be smaller than l_0 , the characteristic length, enough to sufficiently resolve the damaged region for achieving numerically stable crack propagation. Miehe et al. [70] demonstrated that satisfying the requirement $h < l_0/2$ leads to a clear convergence and produces mesh independent results for a given l_0 .

A phase-field model of the fourth-order was developed by the same authors in [10] to relieve the mesh size constraints for l_0 . Higher-order derivatives of the phase-field included in the fourth-order model resulted in a more regular crack description. It was shown to improve the convergence rate and accuracy. Mesh bias analyses suggested in [15, 16, 70, 104, 106] and in [40] revealed that if suitably refined meshes are employed, none of the PFMs is mesh biased. Furthermore, if less refined meshes are used, all models demonstrate mesh bias sensitivity but to varying degrees. The AT2 model [15, 16, 70] exhibits the greatest, while the PF-CZM [104, 106] exhibits the least. The PF-CZM was shown to be mesh bias for quasi-brittle fracture. Recently, meshless methods for the implementation of phase-field models have been proposed. For instance, ‘a consistent meshless method’ [74], and the ‘element free Galerkin method’ [95] both produced results without mesh dependence. The need for finer mesh near the crack path was addressed in Kasirajan et al. [42] by ‘a mesh-free natural neighbour Galerkin method’.

Influence of the Load Increments

Usage of sufficiently small loading steps can guarantee the stability of phase-field solvers. Using too large steps lead to delayed initiation of damage in the simulation and thus harden the overall response of the structure.

4 Finite Element Discretization and Solvers

Spatial discretization using finite elements is discussed in this section. Conventional Lagrange elements and isogeometric elements are in use. The phase-field variables and the nodal displacements are treated as unknowns in a conventional Bubnov–Galerkin finite element technique. Iterative solvers are employed to solve the coupled non-linear problem. Solvers that are both monolithic and staggered are presented.

4.1 Finite Element Discretization

As mentioned earlier, the element size within the fracture process zone has to be set smaller than the characteristic length. This is done so to achieve stable crack propagation and to accurately estimating the fracture energy. It is shown in numerical simulations that for brittle fracture, elements sizes inside the crack band should be such that $h < l_0/2$ [11, 71]. In comparison, a lower mesh size $h < l_0/5$ is recommended for cohesive fracture [104, 106]. Identical basis functions are generally employed for both displacement and the phase-field parameter. However, to prevent stress oscillations and numerical locking, it is preferable to employ uneven interpolation orders for them. It is suggested that the damage interpolation order be one order lesser than the displacement interpolation order. While considering linear-linear elements, stress oscillations and possible numerical locking are found to have

only minimal influence on the overall numerical results, given that linear shape functions are used for both displacement and damage. Smoothed finite element technique [60, 87] is another option.

For problems with numerous fractures scattered across the domain, the discretisation of the process zone must correspond with the computational domain as a whole. However, for localised failures, this zone can be chosen to be substantially narrower, as long as it includes possible crack propagation pathways. This may be accomplished by using PFM with both displacement and crack phase-field *dof*'s for a single subdomain that will be damaged, i.e., the damage domain. For the remainder of the domain, a less expensive elastic model with merely displacement degrees of freedom is utilised.

Linear finite elements are often used in the literature to discretize both phase-field and stress equilibrium and equations. However, modelling the phase-field using P1 Lagrange shape functions is not ideal since the latter has cusps for fully formed fractures. They become evident at positions that correspond to Gauss points in the finite element model. Because such a feature is difficult to replicate properly with low order elements, element sizes must be kept modest with the phase-field regularisation parameter to ensure mesh convergence. Sargado and colleagues [68] used a cell-centred finite volume (FV) approximation of the phase-field evolution equation combinedly with the standard linear FE discretization of stress equilibrium. The suggested framework resulted in looser mesh refinement limitations on the phase-field length scale as compared to a pure finite element formulation using linear components. In comparison to the typical approach, the option to use coarser meshes results in considerable cost savings.

A phase-field model for simulating brittle fracture in originally straight Euler-Bernoulli beams that were proposed Lai et al. [53], with generalisation to curved beams. They simplified the issue to a one-dimensional field variable minimization. The suggested technique has the advantage of being able to depict the fluctuation of phase-field inside the cross-section without discretizing it, allowing them to model fractures partially passing through the thickness due to bending and axial stresses.

4.2 Irreversibility of the Crack Phase-Field and Its Boundedness

It is critical to impose the damage boundedness and irreversibility conditions when numerically implementing phase-field models. Boundedness implies that the phase-field parameter must be between 0 and 1, whereas irreversibility indicates and its rate of change must always be positive. The latter situation has the practical consequence that the fractures do not mend themselves. Though there are different options for specific PFMs, a typical method is to think about the PFM's governing Equations as an optimization problem with the following constraint [5].

$$0 \leq a_{I,n} \leq a_{I,n+1} \leq 1 \quad \forall I = 1, 2, n_p \quad (17)$$

where \bar{a} is the vector of nodal damage *dof*'s. When the above condition is met, the governing Equation becomes a mixed complementarity problem [24, 25], which can be solved using a suitable solver. For example, the MATLAB Optimization Toolbox has a 'quadratic optimization solver' included and was used in [5] and [86]. Miehe et al. [70] recommended that the damage driving force be replaced with a history field variable H . This variable reflected the highest value ever attained during the simulation. It also allows to elegantly decouple the governing system of equations algorithmically, as well as the use of a staggered approach for computing displacement and phase-field parameters. In comparison to the monolithic approach, where the unknowns are concurrently solved, this technique is straightforward and very resilient and is a particularly appealing component of the proposed paradigm. Kristensen et al. [46] demonstrated that the history field must meet the Kuhn-Tucker criteria to assure irreversible development of the phase-field variable. Other techniques have been offered, such as penalty-based methods [28, 102] and crack-sets [86, 97]. The handling of the irreversibility constraint is gaining traction in recent times. A thorough discussion and comparative analyses were given by Gerasimov and Lorenzis [62].

4.3 Solution Strategies

In a typical phase-field implementation, coupled phase-field and displacements must be calculated. They may be solved simultaneously or sequentially in successive time steps, earning them the titles monolithic and staggered schemes, respectively. In recent years, modified monolithic schemes have gained favour as none of the two methods is universally applicable. Since the underlying energy functional being non-convex, monolithic solvers may be more robust. Although, in most methods, the solution is achieved by iteration between the variables, by a process known as alternating minimization [15, 16, 97]. This concept is based on the observation that if one variable is fixed, convexity does appear regarding the other unknown. However, such a partitioned method may need several iterations [27, 65]. [33] proposes a quasi-monolithic method in which the phase-field variable is fixed in the most critical term and extrapolation in time is used. In terms of parallelization, it's worth mentioning [112], which proposes GPU parallelization utilising a partitioned technique. However, studies demonstrate that performance is strongly influenced by the problem configuration, material, and model parameters. The key is a thorough examination of the Newton method's fundamental assumptions, with the expectation that unique changes would result in solutions. In the case of quasi-static fracture, inertial forces associated with nodal accelerations in the governing equation are got rid of, by

ignoring the kinetic energy. The next sections cover both monolithic and staggered solvers.

Monolithic Solvers

Monolithic solvers are only utilised for ordinary PFMs where the boundedness requirement is automatically met and the local history field technique is applied. As mentioned before, because of the non-convexity of energy functional, the Newton Raphson solution performs poorly in the quasi-static situation. Gerasimov and Lorenzis [27] devised to increase the solver's convergence by a line search approach. Heister et al. [33] suggested a technique to convexify the energy functional, among other things. Singh et al. [96] and May et al. [65] both provided continuation or arc-length techniques for PFMs. The multi-field finite element formula established by Kuhn et al. [48] and Miehe et al. [70], as well as the Abaqus-based implementation by Msekhi et al. [76], are examples of monolithic systems.

Staggered Solvers (Alternating Minimization)

This solver is significantly more resilient and versatile than the monolithic solver, although it has a slower convergence rate. In such a solver, called the AM solver, the displacements at nodes a_{n+1} are first solved using the phase-field *dof's* \bar{a}_n at t_n . It is possible to utilise the Newton–Raphson technique. The revised displacements at nodes a_{n+1} are then utilised for solving the bound-constrained optimization problem and get the fracture phase-field *dof's* \bar{a}_{n+1} .

The ‘PETS’ package [91] or the “bound-constrained quadratic optimization solver” inside the “MATLAB Optimization Toolbox” can easily deal with the related irreversibility condition and acceptable range. It's worth noting that the sub-displacement problem can be solved first, then the subphase-field problem. Until a stop criterion is achieved, the aforementioned alternative minimization is repeated. Bourdin et al. [15] utilised a phase-field-based criterion, i.e., $\left| \varnothing_{n+1}^{(k)} - \varnothing_{n+1}^{(k-1)} \right| < \varepsilon$, where a small positive number is considered for ε . A termination criterion based on energy can also be considered as in [4].

Amor et al. [5] suggested a new AM method for generic PFMs, which was then used by Pham et al. [86]. But the model of Pham et al. [85] had a slow convergence rate and had reported 500 iterations for their static fracture analyses to converge. This solver could achieve accelerated performance by using the “composite staggered-monolithic algorithm” of Farrell and Maurini [25] along with an over-relaxed strategy. However, the numerical implementation is tiresome. The first PFM model to apply to both brittle and cohesive fracture [105, 106], used this composite solver as well. More recently, the AM algorithm was updated to include the local arc-length approach with indirect displacement control, resulting in a more robust solution for dealing with localised failure-induced snap-backs. Many researchers, such as Miehe et al. [70], simply utilise one iteration, regardless of whether the answer converges or not. As a result, very modest load and time increments must be utilised.

5 Computational Aspects

In addition to employing parallel calculations, Ziaei-Rad and Shen [112], Li et al. [59] and Liu et al. [61], have developed efficient element technologies, devised innovative solvers, and used adaptive mesh refinement (and coarsening) to minimise the inherent computational cost of PFMs. Another crucial consideration is the code platform for implementing PFMs.

5.1 Computer Codes

Nguyen et al. [83] and Lu et al. [63] had utilised MATLAB to have a functioning implementation of PFMs. Implementing the model in a future proof and established computer platform is also vital, for the sake of being consistent with ongoing research. As a result, a quick survey is done on the platforms where PFM codes are implemented.

[25] and [59] both use the library FENICS to produce open source PFM codes, respectively for static brittle fracture and dynamic fracture. Klinsmann et al. [45] used DEALII to implement the PF model, which included support for adaptive refinement and coarsening. MEF90 Fortran code by Bourdin is also publicly accessible. A Jacobian free Newton–Krylov solver based monolithic solution strategy was built by Chakraborty et al. [20, 21] in MOOSE. Kuhn et al. [48] code was implemented in FEAP using JIVE, while Singh et al. [96] code was implemented in FEAP using NUTIL. It's also worth noting the GPU implementation described by Ziaei-Rad and Shen [112].

Msekh et al. [76], Liu et al. [61], Molnar Gravouil [75], Pillai et al. [88], Bhowmick Liu [8], Jeong et al. [39], and Kristensen et al. [46] all reported Phase-field implementation of brittle fracture in Abaqus, a widely used commercial finite element programme. The structure of the user-defined finite element UEL subroutine was used in these implementations. However, they report only one-pass AM and monolithic and solvers. Zhou [110] had done a multi-pass AM implementation. Gerasimov et al. [29] proposed a nonintrusive global/local PFM implementation, intending to pave the path for widespread use of PFMs in legacy codes. In [42], the cost of computation from the mesh-free ‘natural neighbour Galerkin method’ (NNGM) was compared to the finite element method and found to be almost equal for a required accuracy. But, Natural Neighbour Galerkin method shape functions are smooth and higher-order continuous gave more accurate results for the same quadrature. Navidtehrani et al. [79, 80] presented a new Abaqus implementation that only requires the use of a user material (UMAT) subroutine. This simple yet robust implementation is achieved by taking advantage of the analogy between the heat transfer equation and the phase-field evolution equation. This implementation could take advantage of the many in-built features provided by the commercial package.

5.2 *Element Technologies*

To build phase-field fracture models, standard Lagrange linear components have been widely employed. High order Lagrange components may not be acceptable because they might produce negative damage at integration points. In the literature, works have been proposed to improve the computing efficiency of PF simulations. Kuhn and Muller [51], for example, created shape functions that could explain the fracture phase-field's exponential nature and sensitivity on the length scale parameter. Exponential shape functions were found to perform substantially better than ordinary linear elements in simulations where this value is set low and coarse meshes are used. The technique, however, is confined to straight crack topologies.

Schillinger et al. [92], Hesch et al. [34], Kastner et al. [43] and Borden et al. [9, 10], have utilized smooth B-splines, NURBS, T-splines basis functions in the context of isogeometric analysis. Schillinger et al. [92] proposed an isogeometric collocation formulation to speed up phase-field computations. Aldakheel et al. [1] provided a “virtual element method” (VEM) version of Miehe's isotropic model. They demonstrated that VEM with a Voronoi mesh is equivalent to utilizing higher-order finite elements with a greater computational cost but with one additional parameter, which is the stabilization parameter. Even better, VEM exhibited more mesh creation flexibility and is less prone to mesh distortion [78]. Smooth basic functions such as “H2-nonconforming Morley triangular elements” [98], “subdivision surface finite elements” [57], NURBS [11] and “local maxentropy” [58] have been used to build high order PFMs. However, higher-order derivatives of the phase-field necessitated newer basis functions that were difficult to implement in the standard finite element method [10]. Goswami et al. [30] had implemented a local refinement strategy using “polynomial splines over hierarchical T-meshes (PHT-splines)”. They could overcome the execution difficulty with NURBS basis functions in isogeometric analysis.

5.3 *Solvers*

A PFM's computer implementation is straightforward at the element level, but a more specialised solution should be employed in most cases. Monolithic and staggered solution strategies were discussed earlier. Neither of these two strategies can be regarded as best over the other, instead, the choice is often problem-dependent. Several authors have implemented and further modified these two strategies concerning their speed of convergence. This section provides a brief account of the implementation of such strategies.

- Addressing the boundedness requirements and crack irreversibility, Bourdin et al. (2000)'s alternating minimization technique with ‘bound-constrained optimization solvers’ (Farrell and Maurini [25], Amor et al. [5], Li et al. [59]). Lu et al. [63], Wu et al. [104, 107].

- Path-following methods such as the “local arc-length (or indirect displacement) control” combinedly with alternating minimization (Wu et al. [107]).
- A monolithic solution that employs path-following techniques such as fracture surface management and energy dissipation (May et al. [65]; Singh et al. [96]).
- In the computational mechanics field, Miehe et al. [70]’s staggered approach with a single iteration employing the local history variable has been frequently employed.
- The monolithic solver used by Gerasimov and Lorenzis, [27] and Heister et al. [33].
- BFGS (Broyden-Fletcher-Goldfarb-Shanno) monolithic solution (Wu et al. [106]) is good at solving problems with nonconvex energy functions.

The alternating minimization method is extremely resilient, although it is computationally inefficient. The over-relaxed approach and the composite staggered-monolithic algorithm (Farrell and Maurini, [25]) can speed up the sluggish convergence rate, albeit the numerical implementation is difficult. Snap-back instabilities can be mitigated using staggered solution techniques. They are not, however, absolutely stable, and the time increment must be short enough to avoid straying from the equilibrium solution.

Monolithic systems, on the other hand, maintain unconditional stability, allowing for considerably greater temporal increments. Because of the underlying energy functional being non-convex in terms of total unknowns, it is well known that the monolithic approach utilising the conventional “Newton-Raphson” scheme performs badly. Several approaches have been proposed to improve the robustness of the monolithic solver, including modified Newton schemes (Wick et al. [103], Heister et al. [33]), “line search technique” (Gerasimov and Lorenzis [27]), and path-following methods (May et al. [65], Singh et al. [96]). These approaches, on the other hand, are generally problem-specific and are not always effective.

Regardless, the deployment of more efficient monolithic methods has been hampered by their inability to achieve a converged solution. Wu et al. [106] presented the BFGS quasi-Newton monolithic scheme, which produced equivalent results to the staggered solver but is robust in many cases. This includes both brittle and quasi-brittle failure with a single or many fractures. Convergence, on the other hand, requires many fewer repetitions. Furthermore, the quasi-Newton monolithic approach is significantly more efficient than the staggered solver. The savings in CPU time is roughly a factor of 3 to 7 in representative numerical examples.

The resilience of BFGS quasi-Newton monolithic systems was demonstrated by Kristensen et al. [46], with convergence achieved under both stable and unstable cracking circumstances. In comparison to frequently utilised staggered solution techniques, the solution approach is unconditionally stable, with considerable computing advantages. The adaptive time step method they developed along with their monolithic approach was computationally efficient, with the comparable staggered solution requiring up to 3000 times more load increments. They claimed that significantly larger phase-field fracture simulations could be performed once quasi-Newton monolithic solution methods are popular.

Mandal et al. [41] proposed a monolithic BFGS method for dealing with numerous thermally induced fracture issues. Here coupled equations were three-field with the temperature being the third field. Good accord with prior findings and experiments could be achieved from their prediction using the finite element method. The suggested model demonstrated length scale insensitive responses, and they perform better in cases of thermally induced fractures. BFGS monolithic solution is four to five times quicker than the traditional alternating minimization solver, according to the results. Wu et al. [105], in a recent thorough analysis of phase-field implementations in Abaqus, reaffirmed the superiority of the BFGS method.

5.4 Adaptive Mesh Refinement and Coarsening

Piero et al. [22], Burke et al. [18], Borden et al. [10], Klinsmann et al. [45], Heister et al. [33], Wick [103], Kastner et al. [43], Artina et al. [6], Paggi et al. [85] all reported Phase-field simulations using adaptive mesh refinement. The phase-field parameter was employed as a mesh refinement indication in [10, 22, 33], i.e., elements with $\phi > \phi_c$ for a critical value ϕ_c had at least one quadrature point refined. [45] presented a new refinement/coarsening indication that is more complex. In [10, 33, 45], Elements identified for refinement are split into four new 2-D quadrilateral elements. This resulted in isotropic mesh refinement alone. Appropriate restrictions were also applied to hanging nodes. Artina et al. [6] suggested anisotropic mesh adaptation, in which mesh modifications are carried out along the crack's normal direction rather than along it. Although anisotropic mesh adaption is more efficient than isotropic mesh refinement, it is more difficult to execute. Muixi et al. [77] proposed a novel adaptive refinement methodology based on h-refined elements along with the fractures and standard elements in the rest of the domain, with Nitsche's method imposing continuity between elements of various types in the weak form.

5.5 Modelling of Pre-existing Cracks

Initial (or existing) fractures can be represented using one of three approaches within the context of PFMs:

- Mesh induced initial cracks: Initial cracks are depicted as discrete cracks in the geometry/mesh.
- Phase-field induced initial cracks: Li et al. [59], Lee et al. [55], and Schluter et al. [93], use Dirichlet conditions to simulate first fractures.
- H-induced initial crack: The local history variable is used to represent initial cracks (Borden et al. [11], Klinsmann et al. [45], Strobl and Seelig [94]).

The first technique, especially for 3-D issues, would require a time-consuming pre-processing step for complicated initial fractures. As a result, the other two alternatives

are preferred, especially for PF simulations that use a fixed regular mesh. Klinsmann et al. [45] showed that mesh-induced fracture predictions differ considerably from analytical relationships established in the literature. In contrast to Li et al. [59], the technique of phase-field generated early fractures does not work for the Kalthoff–Winkler experiment, but the method of mesh induced initial cracks does. The choice appears to be highly problem-dependent.

6 Conclusions

This work attempts to introduce the variational approach to fracture or the phase-field model and to justify its widespread acceptance among researchers to simulate fracture related phenomena. The superiority of the model over discrete descriptions of cracks are discussed. The models used are thermodynamically consistent and can forecast fracture propagation in homogeneous materials when diverse loading types, physical fields, and geometrical nonlinearities are taken into account. Even dynamic loading processes are studied, including plastic effects. The key advantages of the phase field models can be summarised as:

- i. Crack growth, nucleation, branching and merging are automatically handled even in 3D problems.
- ii. Straightforward computer implementation.
- iii. Variational structure of the model describing the physics of the fracture problem well.

Still another reason for the popularity of the model is that the concept of phase field is well accepted in the physics domain. The main disadvantage of PFM is clearly their high computation cost. Advancements in computer hardware and implementation strategies such as adaptive remeshing improved solvers etc. will definitely increase the efficiency of phase-field simulations. Despite the large number of references and recent contributions, the theoretical and numerical aspects of PFM are still undergoing improvements. In particular, the model has to be improved to predict global responses which are length scale-independent and for predicting cracks close to external boundaries.

7 Scope for Future Studies

PFMs' theoretical and numerical elements are continuously being improved. The traditional phase-field method may fail when fracture nucleation occurs in the bulk, at borders, or in tiny fractures, according to ongoing research. Mesh modifications and quicker solvers may be beneficial in overcoming the lengthy computing periods

associated with phase-field simulations, perhaps paving the road for the commercialization of the approach. The method's effectiveness in severe situations like explosion or impact loading is still to be investigated.

References

1. Aldakheel F, Hudobivnik B, Hussein A, Wriggers P (2018) Phase-field modeling of brittle fracture using an efficient virtual element scheme. *Comput Meth Appl Mech Eng* 341:443–466
2. Alessi R, Vidoli S, De Lorenzis L (2017) A phenomenological approach to fatigue with a variational phase-field model: the one dimensional case. *Eng Fract Mech* 190:53–73
3. Ambati M, Gerasimov T, De Lorenzis L (2014) A review on phase-field models of brittle fracture and a new fast hybrid formulation. *Comput Mech* 55(2):383–405
4. Ambati M, De Lorenzis L (2016) Phase-field modeling of brittle and ductile fracture in shells with isogeometric NURBS-based solid-shell elements. *Comput Meth Appl Mech Eng* 312:351–373
5. Amor H, Marigo J-J, Maurini C (2009) Regularized formulation of the variational brittle fracture with unilateral contact: numerical experiments. *J Mech Phys Solids* 57(8):1209–1229
6. Artina M, Fornasier M, Micheletti S, Perotto S (2015) Anisotropic mesh adaptation for crack detection in brittle materials. *Comput Meth Sci Eng* 37(4):B633–B659
7. Babuska I, Melenk JM (1996) The partition of unity method. *Int J Numer Meth Eng* 40:727–758
8. Bhowmick S, Liu GR (2018) A phase-field modeling for brittle fracture and crack propagation based on the cell-based smoothed finite element method. *Eng Fract Mech* 204:369–387
9. Borden MJ, Hughes TJR, Landis CM, Anvari A, Lee JJ (2016) A phase-field formulation for fracture in ductile materials: Finite deformation balance law derivation, plastic degradation, and stress triaxiality effects. *Comput Meth Appl Mech Eng* 312:130–166
10. Borden MJ, Hughes TJR, Landis CM, Verhoosel CV (2014) A higher-order phase-field model for brittle fracture: formulation and analysis within the isogeometric analysis framework. *Comput Meth Appl Mech Eng* 273:100–118
11. Borden MJ, Verhoosel CV, Scott MA, Hughes TJR, Landis CM (2012) A phase-field description of dynamic brittle fracture. *Comput Meth Appl Mech Eng* 220:77–95
12. May S, Vignollet J, de Borst R (2015) A numerical assessment of phase-field models for brittle and cohesive fracture: Γ -convergence and stress oscillations. *Eur J Mech A Solids* 52:72–84
13. Vignollet J, May S, de Borst R, Verhoosel CV (2014) Phase-field models for brittle and cohesive fracture. *Meccanica* 49(11):2587–2601
14. de Borst R, May S, Vignollet J (2016) A numerical assessment of phase-field models for fracture. In: Trovalusci P (ed) *Materials with internal structure*. Springer, Cham, pp 17–28. https://doi.org/10.1007/978-3-319-21494-8_2
15. Bourdin B, Francfort GA, Marigo JJ (2000) Numerical experiments in revisited brittle fracture. *J Mech Phys Solids* 48(4):797–826
16. Bourdin B, Francfort GA, Marigo J-J (2008) The variational approach to fracture. *J Elast* 91(1–3):5–148
17. Bourdin B, Marigo J-J, Maurini C, Sicsic P (2014) Morphogenesis and propagation of complex cracks induced by thermal shocks. *Phys Rev Lett* 112(014301):1–5
18. Burke S, Ortner C, Suli E (2010) An adaptive finite element approximation of a variational model of brittle fracture. *Soc Ind Appl Math* 48(3):980–1012
19. Carrara P, Ambati M, Alessi R, De Lorenzis L (2019) A framework to model the fatigue behavior of brittle materials based on a variational phase-field approach. *Comput Meth Appl Mech Eng* 361:112731
20. Chakraborty P, Sabharwall P, Carroll MC (2016) A phase-field approach to model multi-axial and microstructure dependent fracture in nuclear grade graphite. *J Nucl Mater* 475:200–208

21. Chakraborty P, Zhang Y, Tonks MR (2016) Multi-scale modeling of microstructure dependent intergranular brittle fracture using a quantitative phase-field based method. *Comput Mater Sci* 113:38–52
22. Del G, Lancioni G, March R (2007) A variational model for fracture mechanics: numerical experiments. *J Mech Phys Solids* 55:2513–2537
23. Duda FP, Ciaronetti A, Toro S, Huespe AE (2018) A phase-field model for solute-assisted brittle fracture in elastic-plastic solids. *Int J Plast* 102:16–40
24. Facchinei F, Pang J-S (eds) (2004) *Finite-dimensional variational inequalities and complementarity problems*. Springer, New York. <https://doi.org/10.1007/b97544>
25. Farrell P, Maurini C (2017) Linear and nonlinear solvers for variational phase-field models of brittle fracture. *Int J Numer Meth Eng* 109:648–667
26. Francfort GA, Marigo JJ (1998) Revisiting brittle fracture as an energy minimisation problem. *J Mech Phys Solids* 46(8):1319–1342
27. Gerasimov T, De Lorenzis L (2016) A line search assisted monolithic approach for phase-field computing of brittle fracture. *Comput Meth Appl Mech Eng* 312:276–303
28. Gerasimov T, De Lorenzis L (2019) On penalization in variational phase-field models of brittle fracture. *Comput Meth Appl Mech Eng* 354:990–1026
29. Gerasimov T, Noii N, Allix O, De Lorenzis L (2018) A non-intrusive global local approach applied to phase-field modeling of brittle fracture. *Adv Model Simul Eng Sci* 5(14):1–30
30. Goswami S, Anitescu C, Rabczuk T (2020) Adaptive fourth-order phase field analysis for brittle fracture. *Comput Meth Appl Mech Eng* 361:112808
31. Griffith AA (1921) The phenomena of rupture and flow in solids. *Philos Trans Roy Soc Lond* 221:163–198
32. Gurtin ME (1996) Generalized Ginzburg-Landau and Cahn-Hilliard equations based on a force balance. *Phys D Nonlin Phenom* 92(3–4):178–192
33. Heister T, Wheeler MF, Wick T (2015) A primal-dual active set method and predictor-corrector mesh adaptivity for computing fracture propagation using a phase-field approach. *Comput Meth Appl Mech Eng* 290:466–495
34. Hesch C, Franke M, Dittmann M (2016) Hierarchical NURBS and a higher-order phase-field approach to fracture for finite-deformation contact problems. *Comput Meth Appl Mech Eng* 301:242–258
35. Hirshikesh, Natarajan S, Annabattula RK, Martínez-Pañeda E (2019) Phase field modelling of crack propagation in functionally graded materials. *Compos Part B Eng* 169:239–248
36. Hofacker M, Miehe C (2012) A phase field model of dynamic fracture: robust field updates for the analysis of complex crack patterns: a phase field model of dynamic fracture. *Int J Numer Meth Eng* 93(3):276–301
37. Hofacker M, Miehe C (2012) Continuum phase field modeling of dynamic fracture: variational principles and staggered FE implementation. *Int J Fract* 178(1–2):113–129
38. Irwin GR (1958) Fracture. In: Flüge S (ed) *Elasticity and plasticity*. Springer, Heidelberg, pp 551–590. https://doi.org/10.1007/978-3-642-45887-3_5
39. Jeong H, Signetti S, Han T, Ryu S (2017) Phase field modeling of crack propagation under combined shear and tensile loading with hybrid formulation, Ph.D. thesis
40. Kanti T, Phu V, Wu J (2019) Length scale and mesh bias sensitivity of phase-field models for brittle and cohesive fracture. *Eng Fract Mech* 217:106532
41. Kanti T, Phu V, Wu J, Nguyen-Thanh C (2021) Fracture of thermo-elastic solids: phase-field modeling and new results with an efficient monolithic solver. *Comput Meth Appl Mech Eng* 376:113648
42. Kasirajan P, Bhattacharya S, Rajagopal A, Reddy JN (2020) Phase field modeling of fracture in Quasi-Brittle materials using natural neighbor Galerkin method. *Comput Meth Appl Mech Eng* 366:113019
43. Kästner M, Hennig P, Linse T, Ulbricht V (2016) Phase-field modelling of damage and fracture—convergence and local mesh refinement. In: Naumenko K, Abmus M (eds) *Advanced methods of continuum mechanics for materials and structures*. Springer, Singapore, pp 307–324. https://doi.org/10.1007/978-981-10-0959-4_17

44. Kiendl J, Ambati M, De Lorenzis L, Gomez H, Reali A (2016) Phase-field description of brittle fracture in plates and shells. *Comput Meth Appl Mech Eng* 312:374–394
45. Klinsmann M, Rosato D, Kamlah M, Mcmeeking RM (2015) An assessment of the phase field formulation for crack growth. *Comput Meth Appl Mech Eng* 294:313–330
46. Kristensen KP, Martínez-Pañeda E (2020) Phase field fracture modelling using quasi-Newton methods and a new adaptive step scheme. *Theoret Appl Fract Mech* 107:102446
47. Krueger R (2004) Virtual crack closure technique: history, approach, and applications. *Appl Mech Rev* 57(2):109–143
48. Kuhn C, Müller R (2008) A phase field model for fracture: a phase field model for fracture. *PAMM* 8(1):10223–10224
49. Kuhn C, Müller R (2010) A continuum phase field model for fracture. *Eng Fract Mech* 77(18):3625–3634
50. Kuhn C, Müller R (2010) Exponential finite elements for a phase field fracture model. *PAMM* 10(1):121–122
51. Kuhn C, Müller R (2015) A new finite element technique for a phase field model of brittle fracture. *J Theoret Appl Mech* 49(4):1115–1133
52. Kuhn C, Schlüter A, Müller R (2015) On degradation functions in phase field fracture models. *Comput Mater Sci* 108:374–384
53. Lai W, Gao J, Li Y, Arroyo M, Shen Y (2020) Phase field modeling of brittle fracture in an Euler–Bernoulli beam accounting for transverse part-through cracks. *Comput Meth Appl Mech Eng* 361:112787
54. Landau LD, Lifshitz EM (1980) *Statistical physics. Course of theoretical physics, vol 9.* Pergamon Press, Oxford, statistica ed.
55. Lee S, Wheeler MF, Wick T (2016) Pressure and fluid-driven fracture propagation in porous media using an adaptive finite element phase field model. *Comput Meth Appl Mech Eng* 305:111–132
56. Levine H, Henry H (2004) Dynamic instabilities of fracture under biaxial strain using a phase field model. *Phys Rev Lett* 93(10):1–4
57. Li B, Millán D, Torres-Sánchez A, Roman B, Arroyo M (2018) A variational model of fracture for tearing brittle thin sheets. *J Mech Phys Solids* 119:334–348
58. Li B, Peco C, Millán D, Arias I, Arroyo M (2014) Phase-field modeling and simulation of fracture in brittle materials with strongly anisotropic surface energy. *Int J Numer Meth Eng* 102:711–727
59. Li T, Marigo J-J, Guilbaud D, Potapov S (2016) Gradient damage modeling of brittle fracture in an explicit dynamics context. *Int J Numer Meth Eng* 108:1381–1405
60. Liu GR, Dai KY, Nguyen TT (2007) A smoothed finite element method for mechanics problems. *Comput Mech* 39:859–877
61. Liu G, Li Q, Msekh MA, Zuo Z (2016) Abaqus implementation of monolithic and staggered schemes for quasi-static and dynamic fracture phase-field model. *Comput Mater Sci* 121:35–47
62. Ambati M, Gerasimov T, De Lorenzis L (2015) Phase-field modeling of ductile fracture. *Comput Mech* 55:1017–1040
63. Lu X, Li C, Tie Y, Hou Y, Zhang C (2019) Crack propagation simulation in brittle elastic materials by a phase field method. *Theoret Appl Mech Lett* 9:339–352
64. Martínez-Pañeda E, Golahmar A, Niordson CF (2018) A phase field formulation for hydrogen assisted cracking. *Comput Meth Appl Mech Eng* 342:742–761
65. May S, Vignollet J, de Borst R (2016) A new arc-length control method based on the rates of the internal and the dissipated energy. *Eng Comput* 33(1):100–115
66. McAuliffe C, Waisman H (2016) A coupled phase field shear band model for ductile brittle transition in notched plate impacts. *Comput Meth Appl Mech Eng* 305:173–195
67. Mesgarnejad A, Bourdin B, Khonsari MM (2013) A variational approach to the fracture of brittle thin films subject to out-of-plane loading. *J Mech Phys Solids* 61:2360–2379
68. Sargado JM, Keilegavlen E, Berre I, Nordbotten JM (2021) A combined finite element–finite volume framework for phase-field fracture. *Comput Meth Appl Mech Eng* 373:113474

69. Miehe C, Dal H, Schänzel L, Raina A (2016) A phase-field model for chemo-mechanical induced fracture in lithium-ion battery electrode particles. *Int J Numer Meth Eng* 106(9):683–711
70. Miehe C, Welschinger F, Hofacker M (2010) Thermodynamically consistent phase-field models of fracture: variational principles and multi-field FE implementations. *Int J Numer Meth Eng* 83:1273–1311
71. Miehe C, Hofacker M, Welschinger F (2010) A phase field model for rate-independent crack propagation: robust algorithmic implementation based on operator splits. *Comput Meth Appl Mech Eng* 199(45–48):2765–2778
72. Miehe C, Schänzel LM (2014) Phase field modeling of fracture in rubbery polymers. Part I: finite elasticity coupled with brittle failure. *J Mech Phys Solids* 65:93–113
73. Moes N, Dolbow J, Belytschko T (1999) A finite element method for crack growth without remeshing. *Int J Numer Meth Eng* 46(1):131–150
74. Mohammadi V, Dehghan M (2019) Simulation of the phase field Cahn Hilliard and tumor growth models via a numerical scheme: element-free Galerkin method. *Comput Meth Appl Mech Eng* 345:919–950
75. Molnár G, Gravouil A (2017) 2D and 3D Abaqus implementation of a robust staggered phase-field solution for modeling brittle fracture. *Finite Elem Anal Des* 130:27–38
76. Msekh MA, Sargado JM, Jamshidian M, Areias PM, Rabczuk T (2015) Abaqus implementation of phase-field model for brittle fracture. *Comput Mater Sci* 96:472–484
77. Muixí A, Fernández-Méndez S, Rodríguez-Ferran A (2020) Adaptive refinement for phase-field models of brittle fracture based on Nitsche’s method. *Comput Mech* 66:69–85. <https://doi.org/10.1007/s00466-020-01841-1>
78. Natarajan S, Bordas SPA, Ooi ET (2015) Virtual and smoothed finite elements: a connection and its application to polygonal/polyhedral finite element methods. *Int J Numer Meth Eng* 104(13):1173–1199
79. Navidtehrani Y, Betegón C, Martínez-Pañeda E (2021) A simple and robust Abaqus implementation of the phase field fracture method. *Appl Eng Sci* 6:100050
80. Navidtehrani Y, Betegón C, Martínez-Pañeda E (2021) A unified Abaqus implementation of the phase field fracture method using only a user material subroutine. *Materials* 14:1913
81. Nguyen TT et al (2016) On the choice of parameters in the phase field method for simulating crack initiation with experimental validation. *Int J Fract* 197(2):213–226
82. Nguyen TT, Yvonnet J, Zhu Q, Bornert M, Chateau C (2016) A phase-field method for computational modeling of interfacial damage interacting with crack propagation in realistic microstructures obtained by microtomography. *Comput Meth Appl Mech Eng* 312:567–595
83. Nguyen TT, Yvonnet J, Zhu QZ, Bornert M, Chateau C (2015) A phase field method to simulate crack nucleation and propagation in strongly heterogeneous materials from direct imaging of their microstructure. *Eng Fract Mech* 139:18–39
84. Nguyen VP, Lian H, Rabczuk T, Bordas S (2017) Modelling hydraulic fractures in porous media using flow cohesive interface elements. *Eng Geol* 225:68–82
85. Paggi M, Corrado M, Reinoso J (2018) Fracture of solar-grade anisotropic polycrystalline Silicon: a combined phase field cohesive zone model approach. *Comput Meth Appl Mech Eng* 330:123–148
86. Pham KH, Ravi-Chandar K (2017) The formation and growth of echelon cracks in brittle materials. *Int J Fract* 206(2):229–244
87. Pham K, Amor H, Marigo J-J, Maurini C (2011) Gradient damage models and their use to approximate brittle fracture. *Int J Damage Mech* 20(4):618–652
88. Pillai U, Heider Y (2018) A diffusive dynamic brittle fracture model for heterogeneous solids and porous materials with implementation using a user-element subroutine. *Comput Mater Sci* 153:36–47
89. Quintanas-corominas A, Reinoso J, Casoni E, Turon A, Mayugo JA (2019) A phase field approach to simulate intralaminar and translaminar fracture in long fiber composite materials. *Compos Struct* 220:899–911

90. Quintanas-Corominas A, Turon A, Reinoso J, Casoni E, Paggi M, Mayugo JA (2020) A phase field approach enhanced with a cohesive zone model for modeling delamination induced by matrix cracking. *Comput Meth Appl Mech Eng* 358:112618. <https://doi.org/10.1016/j.cma.2019.112618>
91. Zhang H et al (2016) PETSc users manual, ANL-95/11
92. Schillinger D, Borden MJ, Stolarski HK (2015) Isogeometric collocation for phase-field fracture models. *Comput Meth Appl Mech Eng* 284:583–610
93. Schlüter A, Willenbücher A, Kuhn C et al (2014) Phase field approximation of dynamic brittle fracture. *Comput Mech* 54:1141–1161. <https://doi.org/10.1007/s00466-014-1045-x>
94. Strobl M, Seelig T (2016) On constitutive assumptions in phase field approaches to brittle fracture. *Procedia Struct Integrity* 2:3705–3712
95. Shao Y, Duan Q, Qiu S (2019) Adaptive consistent element free Galerkin method for phase field model of brittle fracture. *Comput Mech* 64:741–767
96. Singh N, Verhoosel CV, De Borst R, Van Brummelen EH (2016) A fracture-controlled path-following technique for phase-field modeling of brittle fracture. *Finite Elem Anal Des* 113:14–29
97. Tanné E, Li T, Bourdin B, Marigo J-J, Maurini C (2018) Crack nucleation in variational phase-field models of brittle fracture. *J Mech Phys Solids* 110:80–99
98. Teichtmeister S, Kienle D, Aldakheel F, Keip M (2017) Phase field modeling of fracture in anisotropic brittle solids. *Int J Non-linear Mech* 97:1–21
99. Ulmer H, Hofacker M, Miehe C (2012) Phase field modeling of fracture in plates and shells. *PAMM* 12(1):171–172
100. Ulmer H, Hofacker M, Miehe C (2013) Phase field modeling of brittle and ductile fracture. *PAMM* 536:533–536
101. Verhoosel CV, De Borst R (2013) A phase-field model for cohesive fracture. *Int J Numer Meth Eng* 96:43–62
102. Wheeler MF, Wick T, Wollner W (2014) An augmented-Lagrangian method for the phase-field approach for pressurized fractures. *Comput Meth Appl Mech Eng* 271:69–85
103. Wick T (2017) Modified Newton methods for solving fully monolithic phase-field quasi-static brittle fracture propagation. *Comput Meth Appl Mech Eng* 325:577–611
104. Wu J (2017) A unified phase field theory for the mechanics of damage and quasi-brittle failure. *J Mech Phys Solids* 103:72–99
105. Wu J, Huang Y (2020) Comprehensive implementations of phase field damage models in Abaqus. *Theoret Appl Fract Mech* 106:102440
106. Wu J, Huang Y, Phu V (2020) On the BFGS monolithic algorithm for the unified phase field damage theory. *Comput Meth Appl Mech Eng* 360:112704
107. Wu J, Phu V (2018) A length scale insensitive phase field damage model for brittle fracture. *J Mech Phys Solids* 119:20–42
108. Zhang X, Vignes C, Sloan SW, Sheng D (2017) Numerical evaluation of the phase field model for brittle fracture with emphasis on the length scale. *Comput Mech* 59(5):737–752
109. Zhao Y, Xu B, Stein P, Gross D (2016) Phase field study of electro-chemical reactions at exterior and interior interfaces in Li-ion battery electrode particles. *Comput Meth Appl Mech Eng* 312:428–446
110. Zhou S, Zhuang X, Rabczuk T (2018) A phase field modeling approach of fracture propagation in poroelastic media. *Eng Geol* 240:189–203
111. Zhou S, Zhuang X, Zhu H, Rabczuk T (2018) Phase field modelling of crack propagation, branching and coalescence in rocks. *Theoret Appl Fract Mech* 96:174–192
112. Ziaei-rad V, Shen Y (2016) Massive parallelization of the phase field formulation for crack propagation with time adaptivity. *Computat Meth Appl Mech Eng* 312:224–253
113. Wu J-Y, Nguyen VP, Nguyen CT, Sutula D, Sinaie S, Bordas SPA (2020) Phase-field modeling of fracture. *Adv Appl Mech* 53:1–183

A Simulation Study on Propagation of Action Potential in Epicardial Tissue Due to SCN5A L812Q Gene Mutation



Helan Satish  and Machireddy Ramasubba Reddy 

Abstract Brugada Syndrome is a rare arrhythmia caused due to mutation in genes that encodes sodium ion channels, and it leads to sudden cardiac death in young adults. It is a rare arrhythmia and so there is a need for computational study. A simulation study of SCN5A L812Q gene mutation in sodium ion channel which affects the propagation of action potential in the two dimensional epicardial tissue cell grid is conducted. This paper aims to model a two dimensional SCN5A L812Q mutated epicardial tissue by modifying the model equations for sodium ion channel in the Ten Tusscher model for human ventricular tissue. A two dimensional epicardial cell grid was made and the sodium ion channel properties were modified for the L812Q mutation. Parallel and diagonal excitations were simulated in normal cell grid and mutated cell grid. Results show that propagation of action potential in the mutated cell grid is slower when compared to normal cells. The thickness of the interface of depolarization and repolarization phase of propagating wave in the mutated cell grid is smaller when compared to the normal cell grid.

Keywords SCN5A gene mutation · Sodium ion channel · Brugada syndrome · Cardiac ventricular arrhythmia · Action potential

1 Introduction

Brugada Syndrome (BrS) is a rare cardiac ventricular arrhythmia and is caused due to mutation in sodium ion channels. The mutation is generally loss of function in nature. BrS usually leads to sudden cardiac death in young adults of Asian countries [1]. Antiarrhythmic drugs do not help to prolong the life of the subjects with BrS arrhythmia. It is a genetic disease that has a pattern of autosomal dominant inheritance and incomplete penetrance.

BrS is related to mutations that occur in the gene that encodes alpha subunit of the sodium ion channel (SCN5A). This mutation leads to less sodium current which causes reduction in spike amplitude of the action potential that results in abnormal

H. Satish (✉) · M. Ramasubba Reddy
Indian Institute of Technology Madras, Chennai, India
e-mail: am17d025@smail.iitm.ac.in

ECG. If sodium channel blockers are used for treatment to reduce arrhythmia, further reduction in the sodium current takes place. Many other genes that are related to BrS are also listed and discussed in the literature, but SCN5A is the most prevalent one [2].

NaV is voltage gated sodium ion channel. There are nine NaV isoforms. NaV1.1, NaV1.2, NaV1.3 and NaV1.6 are encoded by SCN1A, SCN2A, SCN3A and SCN8A respectively and are primarily found in central nervous system. NaV1.7, NaV1.8 and NaV1.9 are encoded by SCN9A to SCN11A and they are found in the peripheral nervous system, NaV1.4 which is encoded by SCN4A is found in the skeletal muscle. NaV1.5 encoded by SCN5A is found in cardiac muscle [3].

A sodium ion channel consists of 24 transmembrane segments. They are arranged as 4 domains DI, DII, DIII and DIV. Each domain consists of six segments (S1 to S6). Segments S1 to S4 forms voltage sensing unit and segments S5 and S6 form the pore forming unit.

Initially S4 is found deep in to the intracellular region. When a stimulus is applied, the intracellular region becomes more positive and the voltage sensor S4 that is positively charged moves to the outer region of the cell due to electrostatic repulsion. This is called depolarization and it results in activation state of the sodium ion channel. Later pore formation takes place in the membrane and it allows sodium ions to enter into the cell. This leads to depolarization phase (spike) of the action potential. Finally, closure of the activation gate takes place and the S4 segments goes back to their original locations. This process is called deactivation of the channel and it results in repolarization of the cell.

There are many loss of function mutations that leads to arrhythmia. SCN5A L812Q is one among them [4]. L812Q mutation changes the amino acids of protein found in segment S4 of Domain DII in NaV1.5 sodium channel. Loss of function mutation in exon 16, results in replacement of Leucine (L) to Glutamine (Q) at position 812 that results in decreased I_{Na} [5]. Channels formed with this modified protein allow less number of sodium ions to enter in to the cell that results in less stimulus current to the neighboring cell. This leads to difficulty in formation of electrical signals (action potential) and to propagate them. This mutation causes an amplitude reduction in the sodium ion current and further leads to abnormalities in ECG. As BrS is a rare arrhythmia, experimental study is complex and so there is a need for simulation study. Computational cardiology helps us to understand the changes in ionic currents, the behavior of the ion channel and their mutations at a sub-cellular, cellular and further to the whole heart.

Effect of loss of function mutation on SCN5A gene due to L812Q mutant in the DII-S4 transmembrane region of the sodium channel protein is studied by considering the steady state activation and inactivation, time constants, sodium ionic current and action potential of the epicardial cell. Reduction in the spike of the action potential due to SCN5A L812Q gene mutation is observed. This reduction in the action potential spike is due to the reduced sodium current inflow [6]. In this paper, a model of homogeneous two dimensional normal epicardial tissue grid was made. To study how the action potential propagates from one cell to the another in the mutated

epicardial tissue, SCN5A L812Q gene mutation is introduced in the epicardial tissue grid by modifying the equations of sodium ion channel given by Wang et al. [5].

2 Materials and Methods

The cell membrane is usually represented as a capacitor connected in parallel with variable resistances and batteries that represents different ionic currents and pumps given in the model of squid giant axon by Hodgkin and Huxley in 1952 [7]. The electrophysiological behavior of a cardiac ventricular cell is considered for this study.

There are many biophysical models available for the cardiac ventricular cell model. A biophysical model is a computational study of a biological system using mathematical equations that relates the physical properties of that system. Such models are used to predict the effect of biological and physical factors on these biological systems. These models use the physiology of the organ to get the behavior of the system.

There are many advantages of biophysical models. The ability to study wave propagation in the two dimensional cell grid, which is difficult using experiments, and the ability to analyze the changes in ionic currents due to ion channel mutations and to study the mechanism of arrhythmias that occur in the whole organ (heart) are few of the advantages of biophysical models.

The biophysical model given by Ten Tusscher et al. in 2004 (TNNP model) is considered to be a more realistic model for human ventricular tissue than other models because it is based on experimental data. Therefore, TNNP model is used for the simulation study.

2.1 Model Characterization

Model of a ventricular epicardial cell was made by using the biophysical model given by Ten Tusscher et al. [8] (TNNP model). The following ordinary differential equation (Eq. 1) was used to update the membrane potential in the epicardial cell.

$$\frac{dV_m}{dt} = -\frac{I_{ion} + I_{stim}}{C_m} \quad (1)$$

Where V_m is the membrane potential, t is the time, C_m is the membrane capacitance, I_{stim} is the external stimulus current and I_{ion} is the sum of transmembrane currents given below.

$$I_{ion} = I_{Na} + I_{K1} + I_{to} + I_{Kr} + I_{Ks} + I_{CaL} + I_{NaCa} + I_{NaK} + I_{pCa} + I_{pK} + I_{bCa} + I_{bNa} \quad (2)$$

Where I_{Na} is fast sodium current, I_{K1} is inward rectifier potassium current, I_{to} is the transient outward current, I_{kr} is rapid delayed rectifier current, I_{ks} the slow delayed rectifier current and I_{CaL} the L-type calcium current, I_{NaCa} the sodium calcium exchanger current, I_{NaK} the sodium potassium pump current, I_{pCa} plateau calcium current, I_{pK} the plateau potassium current, I_{bCa} the background calcium current and I_{bNa} the background sodium current.

To study the effects of SCN5A L812Q mutation in the epicardial cells, modification is done in the gating variables of I_{Na} to incorporate the experimentally observed properties given by Wang et al. [5]. The general equation for sodium current is as follows.

$$I_{Na} = G_{Na} m^3 h j (V - E_{Na}) \quad (3)$$

Equations for Normal Cells

$$m_{\infty} = \frac{1}{[1 + e^{(-56.86 - V)/9.03}]^2} \quad (4)$$

$$\alpha_m = \frac{1}{1 + e^{(-60 - V)/5}} \quad (5)$$

$$\beta_m = \frac{0.1}{1 + e^{(V+35)/5}} + \frac{0.1}{1 + e^{(V-50)/200}} \quad (6)$$

$$\tau_m = \alpha_m \beta_m \quad (7)$$

$$h_{\infty} = \frac{1}{[1 + e^{(-71.55 - V)/7.43}]^2} \quad (8)$$

$$\alpha_h = 0 \quad \text{if } V \geq -40 \quad (9)$$

$$\alpha_h = 0.057 e^{-(V+80)/6.8} \quad \text{Otherwise}$$

$$\beta_h = \frac{0.77}{0.13 [1 + e^{-(V+10.66)/11.1}]} \quad \text{if } V \geq -40 \quad (10)$$

$$\beta_h = 2.7 e^{0.079V} + 3.1 \times 10^5 e^{0.3485V} \quad \text{Otherwise}$$

$$\tau_h = \frac{1}{\alpha_h + \beta_h} \quad (11)$$

$$j_{\infty} = \frac{1}{[1 + e^{(-71.55 - V)/7.43}]^2} \quad (12)$$

$$\alpha_j = 0 \quad \text{if } V \geq -40 \quad (13)$$

$$\alpha_j = \frac{(-2.5428 \times 10^4 e^{0.2444V} - 6.948 \times 10^{-6} e^{-0.04391V})(V+37.78)}{1 + e^{0.31(V+79.23)}} \quad \text{Otherwise}$$

$$\beta_j = \frac{0.6e^{0.057V}}{1+e^{-0.1(V+32)}} \quad \text{if } V \geq -40 \quad (14)$$

$$\beta_j = \frac{0.02424e^{-0.01052V}}{1+e^{-0.1378(V+40.14)}} \quad \text{Otherwise}$$

$$\tau_j = \frac{1}{\alpha_j + \beta_j} \quad (15)$$

The equations for gating variables m , h and j of the activation and inactivation gates of the sodium ion channel (I_{Na}) for the mutated cell are from [5].

$$m_\infty = \frac{1}{1 + e^{(-41.24-V)/4.72}} \quad (16)$$

$$h_\infty = \frac{1}{(1 + e^{(-92.40-V)/6.20})} \quad (17)$$

$$j_\infty = \frac{1}{(1 + e^{(-92.40-V)/6.20})} \quad (18)$$

Other gating variables such as r and s for I_{to} , $xr1$ and $xr2$ for I_{kr} , xs for I_{ks} , d , f , and f_{Ca} for I_{CaL} and g for I_{rel} are same as that of TNNP.

2.2 Electrical Activity in Epicardial Tissue

The heart wall consists of three layers. The inner layer of the heart wall is the endocardium, the middle layer is the mid myocardium or M cells and the outer layer is the epicardium. As the study is on propagation of action potential in the epicardial cells, model of epicardial cell was made using the equations given by Ten Tusscher et al. [8]. Modification in the sodium ion current due to the presence of SCN5A L812Q gene mutation is taken from Wang et al. [5].

Simulation of normal epicardial cell was made by using TNNP model and the mutated epicardial cell was made by using modified equations from Wang et al.. MATLAB R2019b was used for the simulation study of the epicardial cell. To observe the propagation of electrical activity in epicardial tissue, a 100×100 cell grid is considered. This cell grid contains 100 rows and 100 columns of cells in which the row on the top is numbered as row 1 and one on the bottom as row 100. The left most column of the cell grid is considered as column 1 and one at the extreme right is column 100. The corner most cells of the array are coupled to three neighboring cells. Five neighboring cells are coupled for the cells at the borders and cells at the inner rows and columns are coupled to eight neighboring cells. Gap junction conductance helps the passage of ionic current from one cell to another when there is a difference in membrane potential between the two neighboring cells. This discrete connection of cells as a grid helps us to observe the behavior of specific cells in the

tissue by varying individual parameters such as initial values, membrane potential and conductance etc.

The cells are interconnected by using uniform gap junction conductance of 0.06 nS which connects the intracellular spaces of two adjacent myocytes. The resting membrane potential of all the cells is considered as -85.7 mV. Propagation of electrical activity from one cell to another of the grid takes place by using the method explained in [9]. The study is conducted on normal tissue and mutated tissue. Colorbar represents the membrane potentials with black color indicating the resting membrane potential and yellow colour as depolarization. The transition from resting membrane potential through the depolarization phase to the repolarization phase is represented as the change in colour from black to yellow.

We start by understanding the normal tissue grid with parallel excitation. The entire first column of the cell grid was excited with a stimulus current of $52 \mu\text{A}$ for a duration of 1 ms. Gating variables and the corresponding ionic currents are calculated using equations given in TNNP as in Eqs. 1 to 15 described in Sect. 2.1 at an interval of 0.8 ms. The excitation wavefront propagates parallelly from left to right of the cell grid. In the same fashion, mutated cell grid is formed and excited at the leftmost column of the cell grid. To calculate the gating variables and the corresponding ionic currents Eqs. 4, 8 and 12 were replaced with Eqs. 16, 17 and 18.

In another type of excitation, a 2×2 group of cells at the top left corner of the cell grid were excited simultaneously with the stimulus current of $52 \mu\text{A}$ for a duration of 1 ms. Gating variables and the corresponding ionic currents for the normal cell grid as well as the mutated cell grid are calculated using appropriate equations from Eqs. 1 to 18. The excitation wavefront propagates diagonally from top left corner to bottom right corner of the cell grid.

3 Results

3.1 Parallel Propagation in a Normal Cell Grid

A normal cell grid is formed as explained in Sect. 2.2. In the parallel excitation, entire first column of cells was excited with the stimulation current and the duration as explained in Sect. 2.2. Cells at the first column take 0.4 ms to depolarize. Once the cells in the first column gets depolarized, a potential difference is formed between the cells present in column 1 and column 2. This allows the cells from column 1 to flow current to column 2 and excite them. A depolarization wavefront is formed that moves from left to right of the cell grid in a parallel manner. 50th row was considered for the observation of wavefront from left to right. Depolarization of 50th column is at 186 ms and 100th column at 382 ms which is shown in Fig. 1a, b respectively.

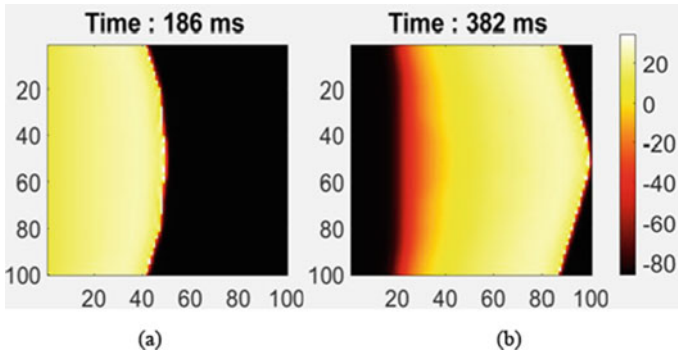


Fig. 1 Parallel propagation of action potential in normal epicardial cell grid **a** cell (50, 50) **b** cell (50, 100)

3.2 Parallel Propagation in a Mutated Cell Grid

In the same fashion explained in Sect. 2.2, mutated cell grid is formed and excited at the leftmost column of the cell grid. To calculate the gating variables and the corresponding ionic currents equations from TNNP and wang et al. were taken. The excited wavefront in the mutated cell grid reaches 50th row 50th column at 630 ms as shown in Fig. 2a. Action potential reaches the 100th column of 50th row at 1386 ms as shown in Fig. 2b.

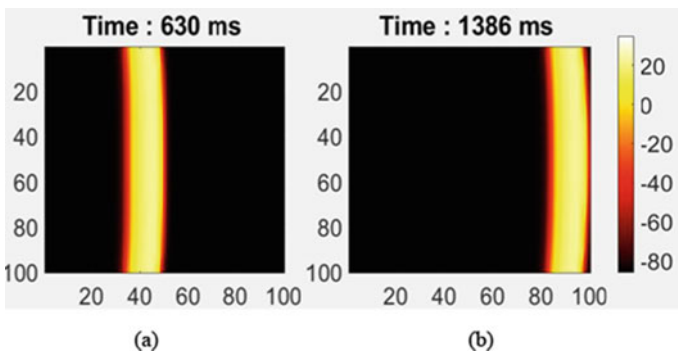


Fig. 2 Parallel propagation of action potential in SCN5A L812Q mutated epicardial cell grid **a** cell (50, 50) **b** cell (50, 100)

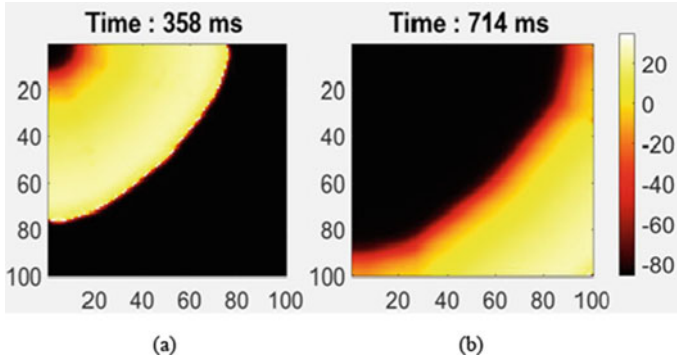


Fig. 3 Diagonal propagation of action potential in normal epicardial cell grid **a** cell (50, 50) **b** cell (100, 100)

3.3 Diagonal Propagation in a Normal Cell Grid

As explained in the Sect. 2.2, a 2×2 group of cells at the top left corner of the cell grid is excited. The 2×2 group of cells depolarizes at 0.4 ms. Similar to the parallel excitation, the cells depolarizes and a potential difference is observed between them and the neighbouring cells. This allows the current to pass through the neighbouring cells in a diagonal manner that forms a depolarization wavefront in the diagonal path from the top left corner of the cell grid to the bottom right corner of the cell grid. The time taken for the action potential to reach cell (50, 50) is 358 ms and cell (100, 100) is 714 ms as shown in Fig. 3a, b respectively.

3.4 Diagonal Propagation in a Mutated Cell Grid

As explained in Sect. 2.2, cells are excited in the mutated cell grid and current is allowed to pass through the neighbouring cells and an excitation wavefront is generated. The excitation wavefront propagates diagonally from top left corner to bottom right corner of the cell grid as earlier but with a delay when compared to the propagation in the normal cell grid. The action potential wavefront took 1339 ms to reach cell (50, 50) in the mutated cell grid as shown in Fig. 4a and 2480 ms to reach the cell (100, 100) as shown in Fig. 4b.

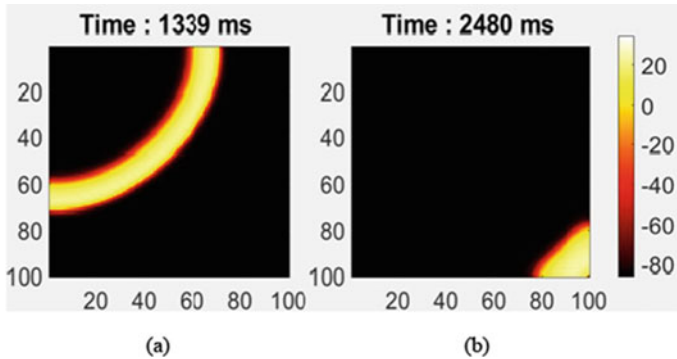


Fig. 4 Diagonal propagation of action potential in SCN5A L812Q mutated epicardial cell grid **a** cell (50, 50) **b** cell (100, 100)

4 Discussion

In parallel excitation, since the uppermost and lowermost cells of each column have smaller number of neighboring cells, propagation takes little more time than all the other cells of the column. This results in a slightly convex pattern in the parallel propagation of the action potential. A delay in the propagation of action potential is observed in these regions.

A delay in the propagation of action potential between normal and mutated tissue is observed. For a parallel excitation in the normal cell grid, the time taken to reach the 100th column of the 50th row is 382 ms whereas the time taken to reach 100th column of the 50th row in the mutated cell grid is 1386 ms. Similarly for a diagonal excitation in the normal cell grid, the depolarization of cell (100, 100) is at 714 ms whereas for a mutated cell grid, the depolarization of cell (100, 100) is at 2480 ms. This delay in propagation between normal and mutated cell grid is due to the reduced spike in the phase 0 of the action potential. This is caused due to inflow of lesser number of sodium ions during depolarization that leads to reduced sodium ion current. This is clearly the effect of SCN5A L812Q gene mutation.

A propagation delay is observed at the diagonal wave front compared to the propagation of the parallel wave front. This is due to the presence of greater number of neighbouring cells in the diagonal path than in the parallel propagation path.

A difference in the width of the interface of depolarization and repolarization phase of propagating wave is noted. This is because, the action potential duration remains approximately same for both the normal and the mutated cells, but the propagation takes larger time when compared to the normal cells. This leads to repolarization of cells in the wave tail at a constant rate but slower depolarization of cells in the wavefront.

5 Limitations and Future Scope

In this study, cardiac ventricular tissue is assumed as a two dimensional, isotropic and homogeneous tissue grid, whereas a real cardiac tissue is three dimensional, anisotropic and heterogeneous in nature. Regional heterogeneity also exists in a real cardiac tissue. Therefore, a three dimensional model can be made to analyse the propagation of action potential in the epicardial tissue due to the SCN5A L812Q gene mutation. Study of propagation of action potential due to the presence of a premature beat in the SCN5A L812Q gene mutated epicardial tissue and generation of reentrant waves such as figure of 8, spiral waves and wave breaks can also be performed.

6 Conclusion

Brugada Syndrome is a hereditary disease caused due to mutation in genes that encodes sodium ion channel. SCN5A L812Q is one among them. This study was conducted to find the effect of SCN5A L812Q gene mutation in an epicardial tissue. A 100×100 cell grid of normal, mutated epicardial tissue is simulated for parallel and diagonal excitation. It is observed that the propagation of action potential is slower in mutated epicardial tissue when compared to the normal epicardial tissue. This delay is due to the reduction in sodium ion current because of the SCN5A L812Q gene mutation. This leads to reduction in total ionic current I_{stim} . Delay in the propagation of diagonal wavefront is observed when compared with the parallel propagating wavefront. It is because the depolarized cells in the diagonal propagating wavefront need to send current to larger number of cells compared to the parallel propagating wavefront. Reduced thickness is observed in the interface of depolarization and repolarization phase of propagating wave. This is because of the constant action potential duration and larger time taken for the wavefront to propagate.

References

1. Antzelevitch C (2012) Genetic, molecular and cellular mechanisms underlying the J wave syndromes. *Circ J* 76:1054–1065. <https://doi.org/10.1253/circj.CJ-12-0284>
2. Zaklyazminskaya E, Dzemeshevich S (2016) The role of mutations in the SCN5A gene in cardiomyopathies. *Biochim Biophys Acta Mol Cell Res* 1863:1799–1805. <https://doi.org/10.1016/j.bbamcr.2016.02.014>
3. Chahine M (2018) Voltage-gated sodium channels: structure, function and channelopathies
4. Li W, Yin L, Shen C, Hu K, Ge J, Sun A (2018) SCN5A variants: association with cardiac disorders. *Front Physiol* 9:1–13. <https://doi.org/10.3389/fphys.2018.01372>
5. Wang L, Meng X, Yuchi Z, Zhao Z, Xu D, Fedida D, Wang Z, Huang C (2015) De novo mutation in the SCN5A gene associated with brugada syndrome. *Cell Physiol Biochem* 36:2250–2262. <https://doi.org/10.1159/000430189>

6. Satish H, Machireddy RR (2021) Computational study of SCN5A L812Q gene mutation in epicardial cells. In: 2020 IEEE-EMBS conference on biomedical engineering and sciences (IECBES), pp 46–50. <https://doi.org/10.1109/IECBES48179.2021.9398756>
7. Hodgkin AL, Huxley AF (1952) A quantitative description of membrane current and its application to conduction and excitation in nerve. *J Physiol* 117:500–544. <https://doi.org/10.1113/jphysiol.1952.sp004764>
8. ten Tusscher KHWJ, Noble D, Noble PJ, Panfilov A (2004) V: A model for human ventricular tissue. *Am J Physiol Heart Circ Physiol* 286:H1573–H1589. <https://doi.org/10.1152/ajpheart.00794.2003>
9. Mayourian J, Sobie EA, Costa KD (2018) An introduction to computational modeling of cardiac electrophysiology and arrhythmogenicity. In: *Methods in molecular biology*. Humana Press Inc., pp 17–35

Evaluation of Outflow Boundary Conditions in DNS of Turbulent Jet Flows



Prince Charles  and Vagesh D. Narasimhamurthy 

Abstract Choice of an outflow boundary condition (BC) for a turbulent free-jet flow simulation in a finite domain is non trivial, where neighbouring boundaries and their BCs may also have an influence. In this work, three different outflow BCs, Neumann BC with back-flow limiter, convective BC and Chapman BC (which is based on Orlanski scheme), were considered. A planar turbulent jet at $Re = 4000$ was simulated using direct numerical simulation (DNS), where an entrainment BC is applied on the lateral sides of the jet. The outflow BC proposed by Orlanski in an explicit form, which was later re-formulated by Chapman, was found to be a good choice in the present problem, where entrainment effects are also present.

Keywords Turbulent free jet · Outflow BC · Chapman BC · Orlanski scheme

1 Introduction

The study of turbulent jets is helpful in applications such as jet-mixing, jet-cooling, jet-cutting, combustion and many other engineering applications. In some cases, like studying the effect of orifice geometry on a jet flow, mixing on swirling jets and the pre-filming process for atomization, researchers are interested primarily in the near-field to intermediate (NIF) region. This region has a range up to $x/D = 30$ downstream of a jet from the nozzle exit, and it has immense contribution in heat, mass and momentum transfer [1]. Numerical simulation of a turbulent jet is helpful to study the physics of such problems and is further valuable for optimizing an experiment before testing. However, choosing a proper outflow boundary condition (OBC) is challenging, especially for a finite domain covering the NIF region. Different kinds

P. Charles (✉) · V. D. Narasimhamurthy

Department of Applied Mechanics, Indian Institute of Technology Madras, Chennai 600036, India
e-mail: vagesh@iitm.ac.in

of OBCs and their effects on a turbulent free-jet simulation with entrainment were investigated in this work.

The conventional Neumann BC could be used as an OBC, but only with an extended numerical domain, which is computationally expensive. In a shorter domain, it is known to exhibit numerical reflections back into the flow [2]. An OBC that is feasible to use in a shorter domain is essential to reduce the computational cost with least compromise on numerical error. Here, a Neumann BC with a limiter for back-flow that sets all velocities into zero except the streamwise component at the boundary (i.e. $U_B = \text{Max}(U_{B-1}, -0.01)$; $V_B = 0$; $W_B = 0$, where B refers to any boundary point), is imposed. As suggested by several researchers, e.g. Akselvoll and Moin [3], Dai et al. [4], Craske and van Reeuwijk [5], convective BC is an option for overcoming the problem of numerical reflections at the outlet boundary. Convective BC equation is given by,

$$\frac{\partial U_i}{\partial t} + U_{conv} \frac{\partial U_i}{\partial x} = 0 \quad (1)$$

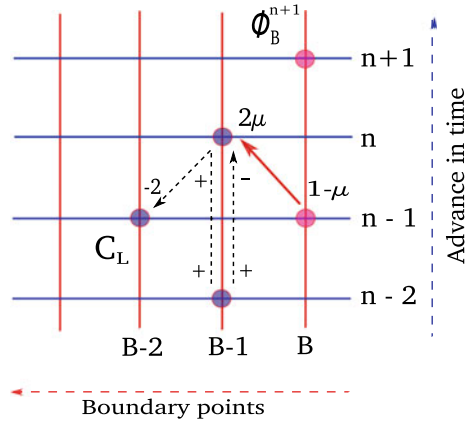
where U_i is an instantaneous velocity vector. In general this convective BC is a good option for free shear flow problems, however, it may cause a numerical error in the region close to the outlet (4–5 orifice widths). Further, the convective BC has a variable U_{conv} , which is either fixed before the simulation or computed during the simulation. As suggested by other researchers [3], there are several ways of applying this condition. One method is by fixing the U_{conv} using linear constant method, that gives $\phi_B^{n+1} = \phi_{B-1}^n$ (where ϕ , B and $n + 1$ refers to any flow variable, boundary point and present time step respectively). Another one is computing U_{conv} as a mean streamwise velocity that is integrated across the exit plane, as suggested by Akselvoll and Moin [3]. The latter one has been chosen for computing U_{conv} in this work. Next, an OBC based on the Orlanski scheme and the formulation for applying the Orlanski scheme [6] in an explicit form by Chapman [7] is used in this work. This OBC is termed Chapman BC from here on.

The Orlanski scheme as OBC can effectively minimize the oscillations from the outlet boundary because of its framework. In this approach, the constant phase velocity or convection velocity, instead of being fixed, is numerically calculated from the ‘propagation velocity’ C_L . Here, C_L itself is estimated from the velocity at the neighbouring grid points at several previous time instants as given below:

$$C_L = \frac{\phi_{B-1}^{n-2} - \phi_{B-1}^n}{\phi_{B-1}^n + \phi_{B-1}^{n-2} - 2\phi_{B-2}^{n-1}} \quad (2)$$

where, $B - 1$, $B - 2$ are neighbouring grid points from the boundary point (B) and n , $n - 1$, $n - 2$ are previous time steps of present time step ($n + 1$). Chapman [7] further suggested that this C_L be used for determining a factor μ as given below:

Fig. 1 Pictorial representation of Chapman BC



$$\begin{aligned} \mu &= 1 \text{ if } (C_L \geq 1) \\ \mu &= C_L \text{ if } (0 < C_L < 1) \\ \mu &= 0 \text{ if } (C_L \leq 0) \end{aligned}$$

which is used to modify the BC as follows,

$$\phi_B^{n+1} = \frac{\phi_B^{n-1}(1 - \mu) + 2\mu\phi_{B-1}^n}{(1 + \mu)}. \tag{3}$$

A pictorial representation of the Chapman BC is given in the Fig. 1 for a better understanding of its calculation method, which is based on the neighbouring grid points along with time advancement. The horizontal lines and the vertical lines in the stencil represent the progress in time and the neighbouring grid points or boundary points, respectively. From the Fig. 1, we can notice that the ‘propagation velocity’ C_L has been calculated using those three points, which is marked with violet in colour. The dashed arrow lines on either side within those three points represent the value of numerator (right side arrow) and the value of denominator (left side arrow) in the C_L calculation, which has already shown in the Eq. 2. Finally, the value of ϕ_B^{n+1} has been calculated using the neighbouring grid points from the previous time steps. This value of C_L has been used for fixing the μ value. When the value of μ equals to 1, the Eq. 3 becomes $\phi_B^{n+1} = \phi_{B-1}^n$ and behave like a convective BC based on the linear constant method as mentioned earlier. When the value of μ equals to 0, the Eq. 3 becomes $\phi_B^{n+1} = \phi_B^{n-1}$, where the flow field variable has been replaced by the value which is two-step down in time. When the value of μ is between 0 and 1, the flow field variable at the boundary point has been calculated with the neighbouring points from the previous time steps considering the propagation velocity (C_L) as a relaxation factor.

In addition to the above OBCs, we have given 4% of inflow bulk velocity as an entrainment BC on either side of the flow domain in the lateral or cross-streamwise

direction as a minimum requirement for the present jet simulations [8]. Boersma [9] reported that no-slip and free-slip boundary conditions at the lateral sides for a jet simulation would lead to divergence of solution for a shorter domain. Furthermore, they suggested that entrainment boundary condition is essential for free shear flow simulations. Many researchers considered the maximum limit of 5–10% of jet inlet velocity as a weak co-flow for their numerical jet studies [10, 11]. However, for a turbulent jet simulation to study the effect of the geometry of the nozzle, such a co-flow condition for a jet will not be helpful. In such cases, entrainment BC is a better choice for the study of nozzle effects on jets. In some turbulent jet experiments, researchers considered the entrainment effect from the lateral sides of their wind tunnel arrangements while studying the effect of nozzle geometry upon the turbulent jet [12–14]. For example, Thomas and Chu [15] used twin confining steel plates extended in the lateral direction and allowed entrainment from the lateral sides with a minimum requirement for their jet flow experiment. In the case of numerical jet studies, Dejoan and Leschziner [16] used Schlichting’s semi-analytical solution for setting up the entrainment velocity from the lateral sides for their wall jet simulation. They found the maximum entrainment velocity was computed as 5% of their maximum inlet velocity and reported that their solution was unaffected by the use of lateral entrainment boundary condition. Kakka and Anupindi [17] in their turbulent wall jet simulation, used 4% of inlet velocity as weak entrainment from the top side of their computational domain. Our main objective is to evaluate different OBCs under the influence of entrainment BC and perform verification and validation study against literature. The numerical methodology used in the present work and the results of comparing different OBCs and their effects are discussed in the following sections.

2 Numerical Methodology

2.1 Solver Details

The fluid is considered Newtonian, and the flow is incompressible and isothermal. In three-dimensional space and time, the Navier-Stokes equation is directly solved numerically (DNS) without modelling turbulence using an in-house parallel finite volume code, MGLT [18]. The code uses a staggered Cartesian grid arrangement. Convective and diffusive fluxes are discretized using a second-order central-difference scheme. Time discretization was done by using a third-order explicit Runge-Kutta scheme. Stone’s strongly implicit procedure (SIP) is used to solve the Poisson equation for pressure at every time step. Parallelization is achieved by using Message Passing Interface (MPI).

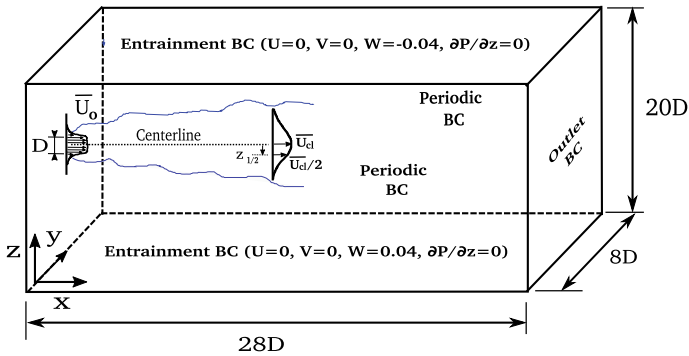


Fig. 2 Flow configuration with boundary conditions

2.2 Computational Domain Details

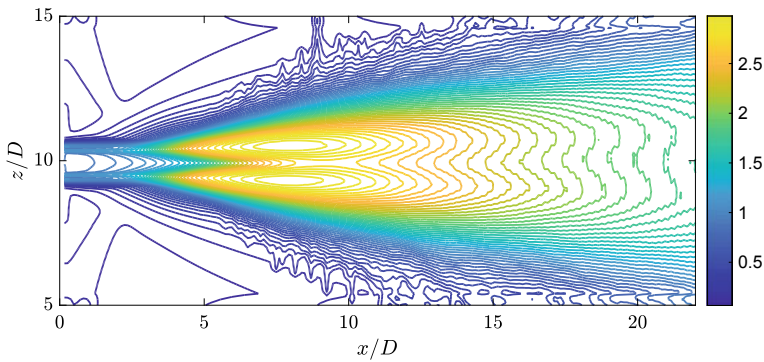
The simulations were performed on a domain similar to that used by Klein et al. [19]. A mesh of $(256 \times 64 \times 256)$ grid points in a computational domain of $(28D \times 8D \times 20D)$ along with the streamwise, spanwise and cross-stream directions, respectively, has been chosen in the present work. Note that the current mesh is somewhat coarser than Klein et al. [19]. The Reynolds number, based on the bulk velocity at the inlet U_o and the jet width D , is $Re = 4000$ (i.e. same as Klein et al. [19]). A hyperbolic tangent profile with momentum thickness of $D/20$ used by Klein et al. [19] for the inflow is also used in the present work. Entrainment BC is given with $W = 0.04U_o$ on the lateral sides [8]. Periodic BC is used in the homogeneous spanwise direction. A three-dimensional flow configuration along with BCs used in the present work is shown in Fig. 2. The jet centerline velocity $\overline{U}_{cl}/2$ and the jet half-width $z_{1/2}$ are also shown in the Fig. 2 which has been used for similarity calculation in the validation study later. Here, the jet half-width is the distance from the jet centerline to the location where the mean axial velocity becomes half of its maximum or centerline velocity (\overline{U}_{cl}). The numerical details used for present simulation compared with Klein et al. [19] are given in Table 1.

2.3 Grid Resolution Check

A criterion proposed for checking the optimum grid resolution of a computational domain for a direct numerical simulation (DNS) by Grötzbach [20] is used. The criterion used is based on the Kolmogorov length scale and the mean grid width of a computational cell. This criterion suits well for a free shear flow problem as well, and it is given by $[(\Delta x \Delta y \Delta z)^{1/3} / \pi \eta] \leq 1$. From the Fig. 3, we can see that Grötzbach's criterion satisfies near all boundaries, and it has higher values only at the interaction region of the turbulent jet, where the dissipation of the turbulent jet comes in to

Table 1 Numerical details

	Klein et al. [19]	Present case (MGLET)
Reynolds no.	$Re = 4000$	$Re = 4000$
Inflow bulk velocity	$U_0 = 1$	$U_0 = 1$
Inflow profile	Hyperbolic tangent profile	Hyperbolic tangent profile
Domain	$20D(x), 8D(y), 20D(z)$	$28D(x), 8D(y), 20D(z)$
Grid	$360 \times 128 \times 512$	$256 \times 64 \times 256$
Equidistant mesh	$\Delta x/D = 1/18, \Delta y/D = 1/16$	$\Delta x/D = 1/9.14, \Delta y/D = 1/8$
Stretching with uniform mesh at core region ($5.5 \leq z/D \leq 14.5$)	$\Delta z/D = 1/50, 450$ cells (core)	$\Delta z/D = 1/25, 225$ cells (core)
Spanwise BC	Periodic	Periodic
Top and bottom BC	Setting pressure as zero and interpolating tangential velocities continuously	Entrainment of 4 % of U_0 used
Outflow BC (OBC)	Neumann BC is used and negative velocities were clipped	1) Neumann BC with back-flow limiter, 2) convective BC, 3) Chapman BC

**Fig. 3** Grid resolution contour based on Grötzbach's criterion

picture. Further, we are only focusing on the effect of boundary condition, thereby, the current grid resolution is suitable for the purpose.

3 Results and Discussion

For testing the BC at the outlet, a free jet with Neumann BC with back-flow limiter is simulated first. While testing, no back-flow appeared in the simulations, but some oscillations were still observed in the cross-stream and the spanwise directions. From the instantaneous data in the region close to the outlet of the domain, numerical

oscillations due to the Neumann BC with back-flow limiter can be observed (refer Fig. 4g). It is more distinctly visible in the second-order statistics. The variation of root mean square (RMS) quantities along the streamwise direction has been chosen for comparing different OBCs (refer Fig. 6). The simulation was first run with the Neumann BC with back-flow limiter for about $4200D/U_o$ time units. The convective BC and Chapman BC were then applied, and all 3 cases were run till $5200D/U_o$. Figures 4 and 5 (instantaneous contours) and Fig. 6 (RMS quantities) clearly demonstrate that this modification can damp the oscillations created by the Neumann BC with back-flow limiter. Generally, an OBC has an impact in all three directions as well as in all three velocities. So, we showed the instantaneous velocity contours near the outlet, especially in the xz -plane at the mid-span location and the xy -plane at the centerline location for all three instantaneous velocities (U , V , W) for our present study and their results and discussions follow in detail.

3.1 Comparison of OBCs

Instantaneous Contours (xz -plane): A comparison of instantaneous U , V , W velocity contours in the xz -plane for different OBCs is shown in Fig. 4. These contours are aligned row-wise as follows U , V and W velocity contours in the first, second and third row, respectively. Then, its corresponding boundary conditions are aligned column-wise as follows Neumann BC with back-flow limiter, Convective BC, Chapman BC in the first, second and third column, respectively. A comparison of instantaneous U velocity contours for different OBCs in the xz -plane near the outlet is shown in the Figs. 4a–c. As we are fixing the streamwise velocity in Neumann BC with a back-flow limiter, no oscillations were found in the contour. The convective BC and Chapman BC follow the same streamwise velocity condition from the previous condition. These conditions are actively doing the convection of streamwise velocity from the domain. These OBCs also do not show any oscillations in their contours. A comparison of instantaneous V velocity contours for different OBCs along the xz -plane is shown in the Figs. 4d–f. From the Fig. 4d, we can see the Neumann BC with back-flow limiter at the outlet give rise to some numerical oscillations near the outlet. Furthermore, we can see the effect of convective BC in the Fig. 4e, which reduces the oscillations, but still, there are some oscillations at the centerline region. From the Fig. 4f, the Chapman BC performs well at the outlet. Here, we can see this BC preserves the jet's flow dynamics as it approaches the outlet, which is a distinct behaviour compared to the other OBCs. A comparison of instantaneous W velocity contours for different OBCs along the xz -plane is shown in the Figs. 4g–i. There are some numerical oscillations found in the Fig. 4g, which has the Neumann BC with a back-flow limiter at the outlet. These oscillations are intruding into the upstream of the jet flow from the outlet. From the Fig. 4h, we can notice that the use of convective BC at the outlet reduces the oscillations compared to the previous BC. This OBC has a similar effect to the earlier OBC, but it has been started to diminishing the oscillations in some more interior points near the outlet.

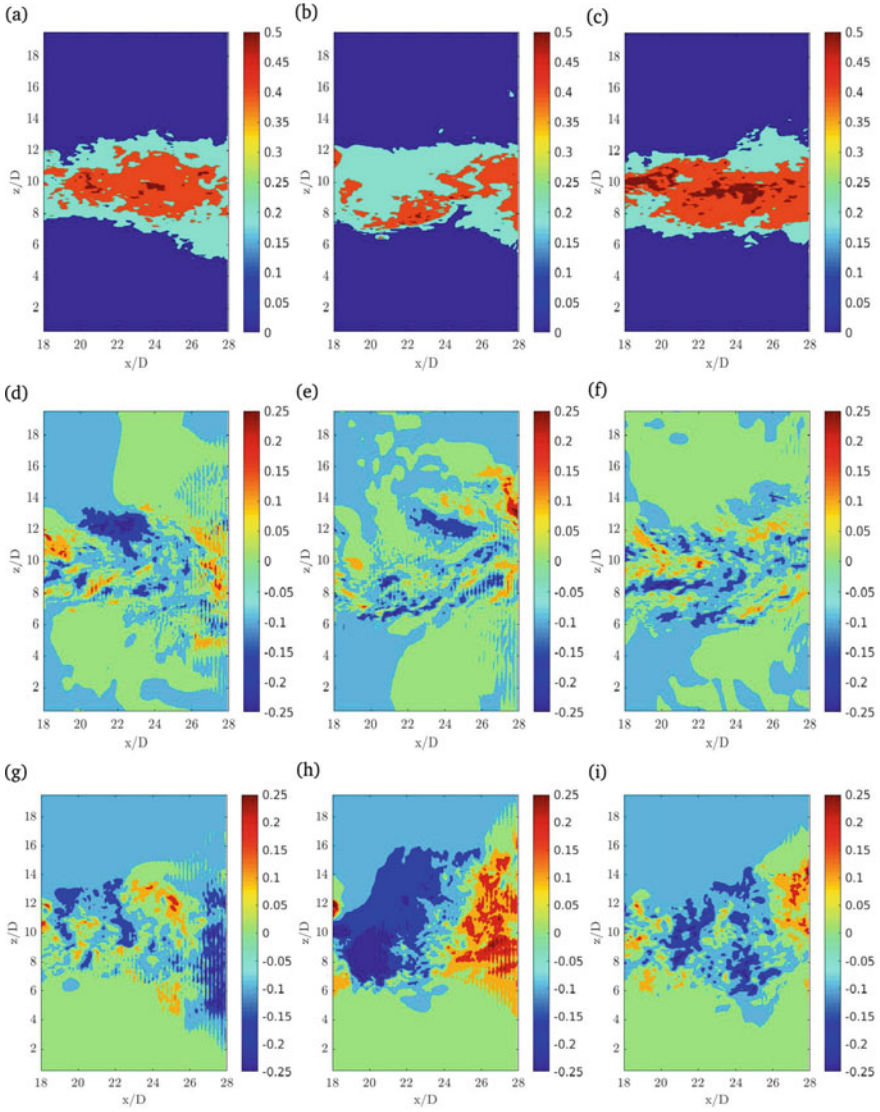


Fig. 4 Comparison of instantaneous U, V, W (in row-wise) velocity contours (xz -plane) near the outlet at the centerline location for different OBCs (in column-wise): **a, d, g** Neumann BC with back-flow limiter, **b, e, h** convective BC and **c, f, i** Chapman BC

From the Fig. 4i, we can observe a significant reduction of oscillations that appeared near the outlet when using the Chapman BC. Here, we can also observe that the effect of OBC is not intruding into the upstream of the jet flow and performing well near the outlet.

Instantaneous Contours (xy -plane): A comparison of instantaneous U velocity contours for different OBCs in the xy -plane near the outlet is shown in the Figs. 5a–c. There are no remarkable differences found in those contours. Still, we can see that the Chapman BC can solve the U velocity uniformly along the spanwise direction that we can observe from the contour's velocity in all ranges compared to the previous OBCs. A comparison of instantaneous V velocity contours for different OBCs along the xy -plane is shown in the Figs. 5d–f. We can see the Neumann BC with back-flow limiter at the outlet (see Fig. 5d) has a weak oscillation effect compare to the previous xz -plane. When we use the convective BC at the outlet (see Fig. 5e), it is showing strong convection takes place and reduces some oscillations, which is better than the earlier one. When we use the Chapman BC, it exhibits that the flow field variables are being convected properly with fewer oscillations compare to the other OBCs (see Fig. 5f). Further, these data were eventually spread along the spanwise direction, which shows the Chapman BC is effectively sustaining the upstream conditions near the outlet using the propagation velocity. Further, it acknowledges the behaviour of the Chapman BC that the neighbouring grid values were used constructively in the calculation of the propagation velocity. A comparison of instantaneous W velocity contours for different OBCs in the xy -plane is shown in the Figs. 5g–i. The oscillations generated by the Neumann BC with back-flow limiter (see Fig. 5g) are as same as the previous one. Nevertheless, it shows the effect of intrusion of oscillation along the spanwise direction from the outlet has less concentration when compared with the previous plane-in contrast, using convective BC at the outlet (see Fig. 5h) has strong oscillations patterns compared with the previous BC. Furthermore, the dispersion of oscillations at the exit is weaker in the Neumann BC with back-flow limiter. However, the visible pattern in the convective BC case clearly shows that a stronger dispersion in oscillations along the spanwise direction has appeared evident. In addition to the oscillation, the magnitude of the flow field variables in the Fig. 5h explains the dominant feature of the convective term in the convective BC while approaching the outlet. When we use the Chapman BC at the outlet, from Fig. 5i, we can observe that oscillations completely suppressed near the outlet, and the pattern of spanwise bands are looking the same as the convective BC contour. We can see that Chapman BC's performance is exceptionally well compared to other OBCs in all velocities in all planes.

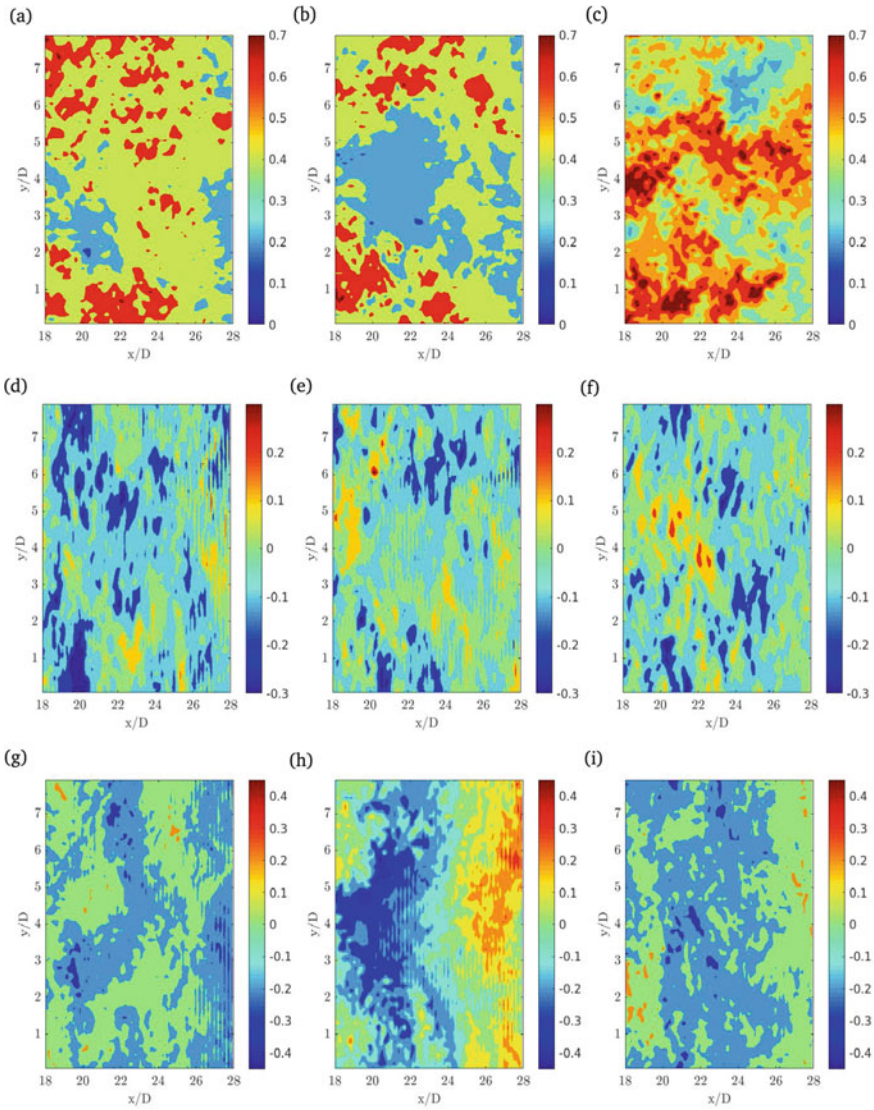


Fig. 5 Comparison of instantaneous U , V , W (in row-wise) velocity contours (xy -plane) near the outlet at the centerline location for different OBCs (in column-wise): **a, d, g** Neumann BC with back-flow limiter, **b, e, h** convective BC and **c, f, i** Chapman BC

RMS Quantities: As discussed earlier, the effect of oscillations is more distinctly visible in the second-order statistics or RMS quantities. Here, a comparison of different OBCs for three different RMS quantities varying along the streamwise direction is shown in the Fig. 6 (refer Fig. 6a). There are no oscillations found in the u_{rms} plot. As the Neumann BC with back-flow limiter formulated based on fixing a common value

Table 2 Comparison of approximate damping percentage range using different OBCs

	v_{rms} variation plot	w_{rms} variation plot
% damped using convective BC	50 to 55	60 to 65
% damped using Chapman BC	75 to 80	80 to 85

in the streamwise direction, it did not exhibit oscillations in the streamwise direction. As convective BC and Chapman BC formulated based on the convective equation, it showed common behaviour near the outlet in the u_{rms} plot. In the v_{rms} variation plot along the streamwise direction (refer Fig. 6b), the effects of the new OBCs are clearly visible. In convective BC, the oscillations were diminished approximately in the range of 50 to 55% compared to the Neumann BC with back-flow limiter. In Chapman BC, the oscillations were reduced approximately in the range of 75 to 80%. The damping effect are stronger in w_{rms} variation plot compared with the v_{rms} variation plot. From the Fig. 6c, we can observe that convective BC reduces the oscillations into 60 to 65%, and the Chapman BC reduces the oscillations into 80 to 85%. These values are listed in the Table 2 showing the comparison of approximate damping percentage range using different OBCs. In this study, the jet flow simulation having homogeneous property in the spanwise and a minimum entrainment effect in the cross-streamwise direction. So, the numerical oscillations generated along the cross-streamwise velocity component is larger than the spanwise velocity component in the Neumann BC with back-flow limiter case. Further, it was damped when we modify the OBC into convective BC, and Chapman BC is evident. Moreover, the Chapman BC is performing better than the convective BC for the present problem.

3.2 Results Using Chapman BC

After comparing different OBCs, the Chapman BC has been chosen as an OBC for further validation and verification study of turbulent free-jet flow simulation with the presence of weak entrainment flow from the lateral sides. The jet simulation was allowed to run till $1300D/U_o$ time units as an initial phase before collecting the samples to remove the initial disturbances due to the flow development. Then, the samples were collected for $1000D/U_o$ time units with the interval time of $0.2D/U_o$ time units. After the flow reached the statistical stationarity, the statistical results were compared against Klein et al. [19], and few more qualitative results also shown and discussed in the following subsections.

Streamline Plot: A streamline plot of mean velocities in the xz -plane is shown in the Fig. 7. Here, we can see that the NIF region up to $22x/D$ downstream of the turbulent jet was unaffected by the Chapman BC. Further, it shows the entrainment condition, which is helping the jet to flow without disturbing the core of the jet.

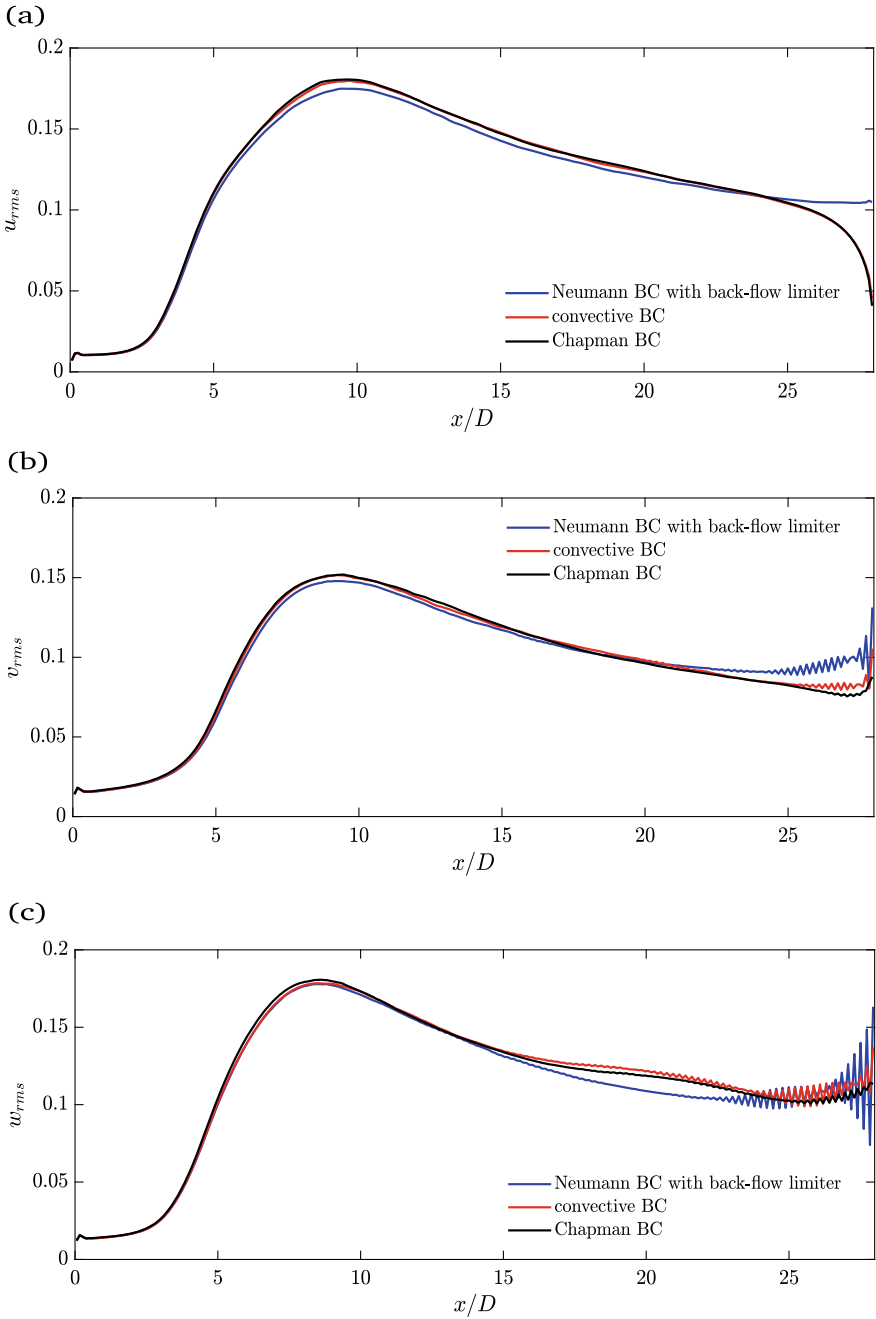


Fig. 6 Variation of **a** u_{rms} and **b** v_{rms} and **c** w_{rms} along the jet centerline for different OBCs

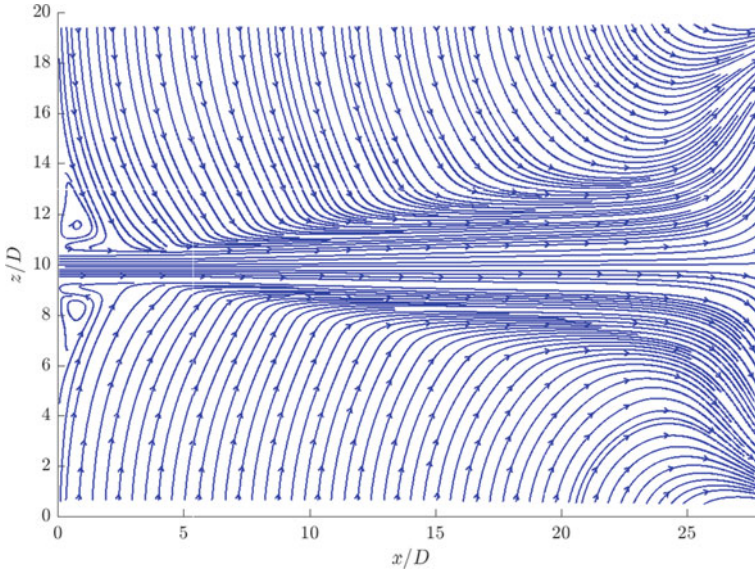


Fig. 7 Streamline plot of mean velocities in xz -plane

Because of the hyperbolic tangent profile at the inlet, the jet formed recirculation zones on either side, which can adversely affect the shear layer of the jet. The size of the recirculation bubble is also a function of the weak entrainment flow from the lateral sides of the flow domain.

Instantaneous Flow: A streamwise velocity contour at the mid-span location (xz -plane) and at the centerline (xy -plane) is shown in Fig. 8a, b respectively. In the xz -plane, we can see the potential core region, interaction region and similarity region. Near the location of $5x/D$ downstream, the jet started to roll up where the potential core of the jet ends. We can see a wavelet form of the jet flow found in the Fig. 8a, it shows the vortex merging happens at the immediate zone next to the potential core region, and it starts to flap in the lateral direction. This effect is somewhat similar to the vortex shedding event which happens in the wake flow. From Fig. 8b, we can see the potential core region ends up near $5x/D$ from the hills and valleys created in the streamwise direction. We can also identify the interaction region using the transition pattern, which happens along the spanwise direction when we go along in the streamwise direction. In this flow, we can see the interaction region ends up near $10x/D$; from that, the flow has been spatially transported more than them-self interacted. In this region, the transition of jet started after the shear layer interaction (see Fig. 8a), and this effect is propagated along the interaction region (see Fig. 8b). Further, we can see that it completely has been broken near $10x/D$ downstream of the jet, which shows the jet getting into the similarity region. Until $22x/D$, we can see the jet flow was not disturbed by the influence of OBC and the presence of entrainment condition not affecting the flow physics of this turbulent free-jet flow.

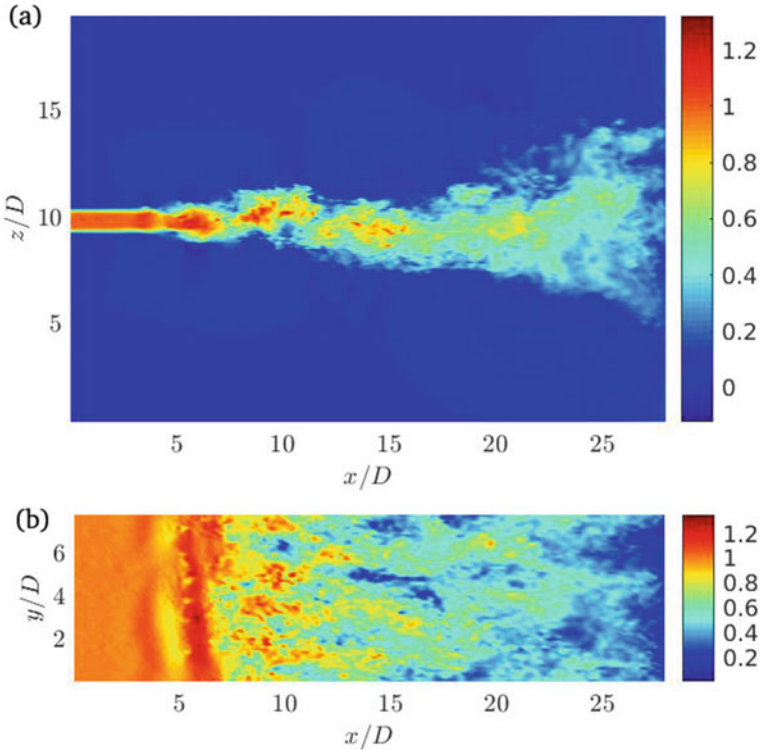


Fig. 8 **a** Instantaneous streamwise velocity contour at the mid-span location (xz -plane), **b** Instantaneous streamwise velocity contour at the centerline (xy -plane)

Thus, the above instantaneous contours clearly show that the Chapman BC for our present problem working fine and can be used for our future studies in turbulent free-jets.

In addition to the instantaneous contour, a three-dimensional iso-contour of spanwise vorticity (ω_y) for Chapman BC is presented in the Fig. 9. Only the core region of the jet was covered in this figure. Further, this figure shows that the structures of vorticity were not affected by the Chapman BC. These vorticity formations also explain the regions of the jet clearly. The region which is covered by the sheet of shear layer starting from the inlet up to the vortex roll-up is called as potential core region (see Fig. 9). In this region, the centerline velocity remains constant, the shear layer developed from either side starts to interact at the point where the potential core ends. Next, the shear layer interaction region or transition region extends up to some peak value of turbulence intensity which can be easily identified from the RMS quantities plot (see Fig. 6c). In this region, we can see the break-up and merge of vortices of the jet happens. Next to this region, the far-field or similarity region starts and extends up to a jet's termination. As we focus only on the near to intermediate field (NIF) region of a jet, this similarity region has been limited to $22x/D$ downstream for

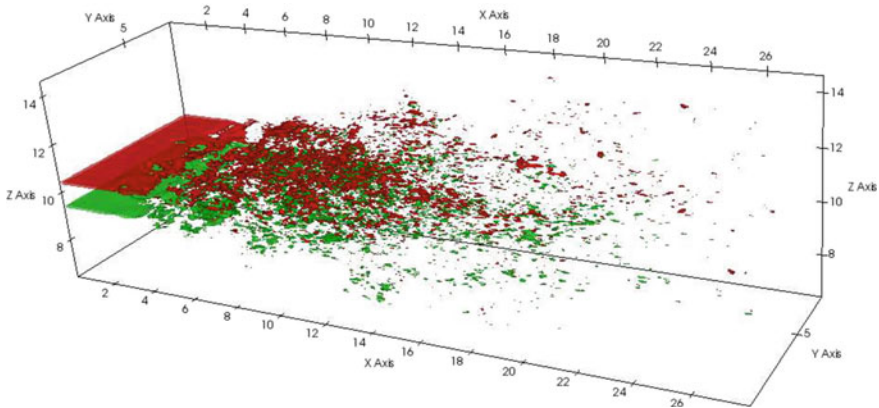


Fig. 9 A three dimensional iso-contour of spanwise vorticity ω_y (green $-0.0009 \omega v/U_o^2$, and red $+0.0009 \omega v/U_o^2$) of a turbulent free-jet using Chapman BC as an OBC

our jet studies. As we can see from the Fig. 9 the NIF region was unaffected by the OBC but, this region can be influenced only at the outer layer of the jet in the lateral direction due to the presence of entrainment flow. Furthermore, this entrainment flow does not have an intense effect over the jet region near the centerline. In addition to it, we can see some nonphysical vortices were formed only near the outlet, which could be due to the effect of artificial boundary condition (Chapman BC) at the outlet.

First Order Statistics: A turbulent planar jet has predominant flow characteristics in the streamwise and cross-streamwise direction of the flow. We already discussed that the jet reaches equilibrium far downstream from the jet inlet and forms a similarity region. This similarity is a characteristic of the flow wherein its velocity profiles at the different downstream locations collapse over each other when adequately scaled. In the current case, local centerline velocity (\bar{U}_{cl}) and jet half-width ($z_{1/2}$) have been used as the suitable scales as same as Klein et al. [19]. In the present work, a weak entrainment flow from the lateral sides is also considered, which is an additional feature to the case of Klein other than OBC. The similarity for mean streamwise velocity and the cross-stream wise velocity at location $15x/D$ is shown in the Fig. 10a, b. The similarity in both directions agrees well with the result of Klein et al. [19]. Further, we can observe a slight offset of similarity profile, especially near the outer layer region ($1.5 \geq z/D \geq 2.5$). This effect shows the flow has the effect of the weak entrainment flow, which comes from the lateral sides of the domain, which is a negligible effect on the predominant behaviour of the jet.

Second Order Statistics: In addition to the previous results, the second-order statistics also plotted and compared against the results of Klein et al. [19]. We showed the turbulence intensities for all velocities and the shear stress normalized by the centerline velocity in the Fig. 11. From the results of turbulence intensities (see Figs. 11a–c), we can see a slight offset in the value of intensities when approaching the outer layer of the jet in the lateral direction. This may be the cause of weak

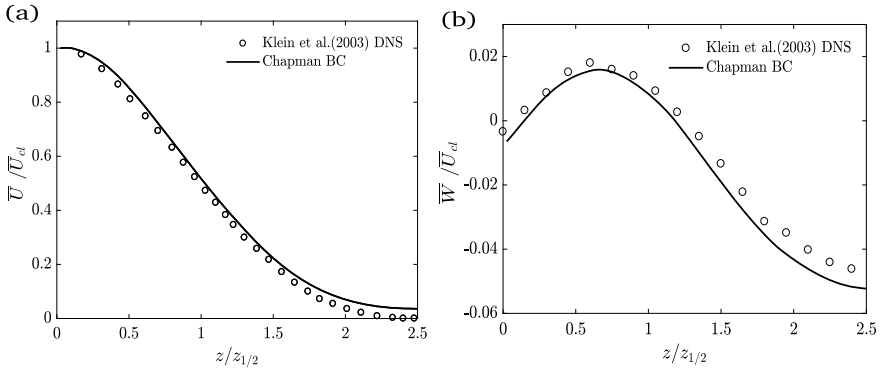


Fig. 10 **a** Similarity for mean streamwise velocity at location $x/D = 15$. **b** Similarity for mean cross-streamwise velocity at location $x/D = 15$

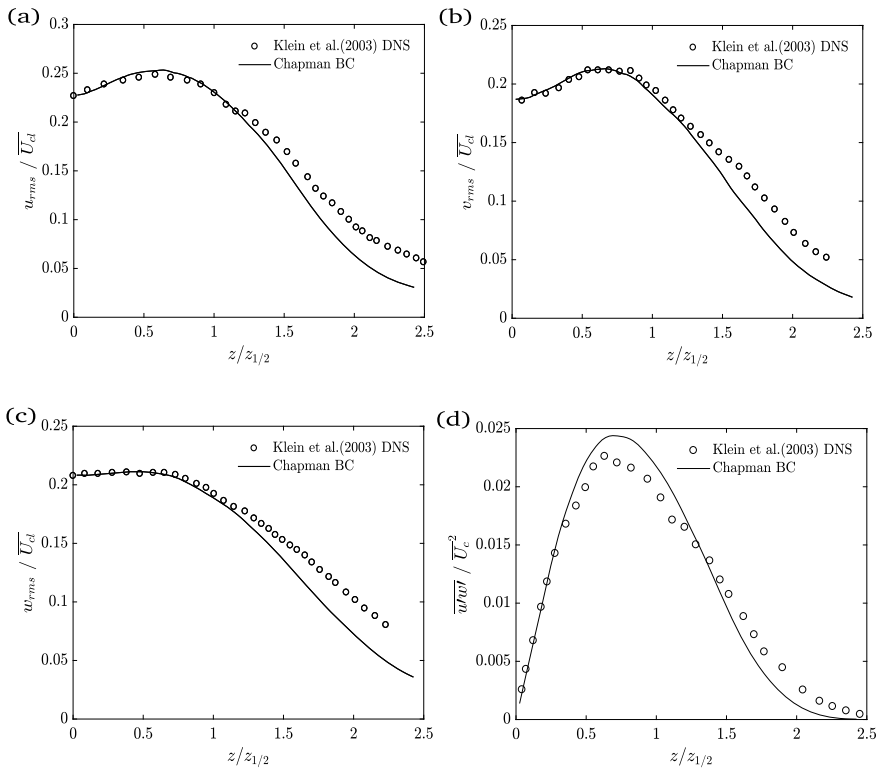


Fig. 11 Lateral profile of **a** u_{rms} , **b** v_{rms} , **c** w_{rms} and **d** shear stress normalized by \bar{U}_{cl} at location $x/D = 15$

entrainment flow; however, this effect does not affect the centerline and shear-layer region intensively, which is a favourable condition for studying the turbulent jet flow. Further, this entrainment effect can be seen clearly in the shear stress plot also. Even with entrainment, we can see the results are comparable in the centerline region and the first half of the shear layer from the centerline. Moreover, the similarity plots at specific locations also agree well with the results of Klein et al. [19]. It shows that the effect of entrainment is negligible for studying the main characteristics of the jet. From the above second-order statistics results, we can conclude that the Chapman BC at the outlet is performing well for the present problem. Also, it does not affect the region up to $22x/D$, which comes under the region of interest for studying the present turbulent free-jet problem.

4 Conclusion

In this study, three different OBCs and their effects on the turbulent free-jet simulation in a finite domain were investigated. The comparison study of different OBCs was evaluated using the instantaneous contours of all three velocities in two different directions and RMS quantities. The Chapman BC, based on the Orlanski scheme in explicit form, has performed well as it reduces the numerical oscillations among other OBCs. And also, the Chapman BC found to be a better OBC for the present case, where an entrainment BC also applied from the lateral sides. The results using the Chapman BC case is further validated with Klein et al. [19]. From the analysis of free turbulent jet results, it has been found that the NIF region of a turbulent jet was unaffected by the use of Chapman BC as an OBC where an entrainment condition is also present. Further, results were analysed using the first-order and second-order statistical data.

References

1. Ball CG, Fellouah H, Pollard A (2012) The flow field in turbulent round free jets. *Prog Aerosp Sci* 50:1–26. <https://doi.org/10.1016/j.paerosci.2011.10.002>. ISSN 03760421
2. Miyauchi T, Tanahashi M, Suzuki M (1996) Inflow and outflow boundary conditions for direct numerical simulations. *JSME Int J, Ser B* 39(2):305–314. <https://doi.org/10.1299/jsmeb.39.305>
3. Akselvoll K, Moin P (1996) Large-eddy simulation of turbulent confined coannular jets. *J Fluid Mech* 315(-1):387–411. <https://doi.org/10.1017/S0022112096002479>. ISSN 00221120
4. Dai Y, Kobayashi T, Taniguchi N (1994) Large eddy simulation of plane turbulent jet flow using a new outflow velocity boundary condition. *JSME Int J Ser B* 37(2):242–253. <https://doi.org/10.1299/jsmeb.37.242>. ISSN 1340-8054
5. Craske J, van Reeuwijk M (2013) Robust and accurate open boundary conditions for incompressible turbulent jets and plumes. *Comput Fluids* 86:284–297. <https://doi.org/10.1016/j.compfluid.2013.06.026>. ISSN 00457930
6. Orlanski I (1976) A simple boundary condition for unbounded hyperbolic flows. *J Comput Phys* 21(3):251–269. [https://doi.org/10.1016/0021-9991\(76\)90023-1](https://doi.org/10.1016/0021-9991(76)90023-1). ISSN 0021-9991

7. Chapman DC (1985) Numerical treatment of cross-shelf open boundaries in a barotropic coastal ocean model. *J Phys Oceanogr* 15(8):1060–1075. [https://doi.org/10.1175/1520-0485\(1985\)015<1060:ntocso>2.0.co;2](https://doi.org/10.1175/1520-0485(1985)015<1060:ntocso>2.0.co;2). ISSN 00223670
8. Pope SB (2000) *Turbulent flows*. Cambridge University Press, Cambridge
9. Bendiks JB (2000) Entrainment boundary conditions for free shear flows. *Int J Comput Fluid Dyn* 13(4):357–363. <https://doi.org/10.1080/10618560008940906>. ISSN 10618562
10. Stanley SA, Sarkar S, Mellado JP (2002) A study of the flow-field evolution and mixing in a planar turbulent jet using direct numerical simulation. *J Fluid Mech* 450:377–407. <https://doi.org/10.1017/s0022112001006644>. ISSN 0022-1120
11. Watanabe T, Sakai Y, Nagata K, Ito Y, Hayase T (2014) Enstrophy and passive scalar transport near the turbulent/non-turbulent interface in a turbulent planar jet flow. *Phys Fluids* 26(10). <https://doi.org/10.1063/1.4898208>. ISSN 10897666
12. Heskestad G (1964) Hot-wire measurements in a plane turbulent jet. *J Appl Mech Trans ASME* 32(4):721–734. <https://doi.org/10.1115/1.3627309>. ISSN 15289036
13. Flora James J, Goldschmidt Victor W (1969) Virtual origins of a free plane turbulent jet. *AIAA J* 7(12):2344–2346. <https://doi.org/10.2514/3.5543>. ISSN 00011452
14. Miller David R, Comings Edward W (1957) Static pressure distribution in the free turbulent jet. *J Fluid Mech* 3(1):1–16. <https://doi.org/10.1017/S0022112057000440>. ISSN 14697645
15. Thomas FO, Chu HC (1989) An experimental investigation of the transition of a planar jet: subharmonic suppression and upstream feedback. *Phys Fluids A* 1(9):1566–1587. <https://doi.org/10.1063/1.857333>. ISSN 08998213
16. Dejoan A, Leschziner MA (2005) Large eddy simulation of a plane turbulent wall jet. *Phys Fluids* 17(2):1–16. <https://doi.org/10.1063/1.1833413>. ISSN 10706631
17. Kakka P, Anupindi K (2020) Assessment of subgrid-scale models for large-eddy simulation of a planar turbulent wall-jet with heat transfer. *Int J Heat Mass Transf* 153:119593. <https://doi.org/10.1016/j.ijheatmasstransfer.2020.119593>. ISSN 00179310
18. Manhart M (2004) A zonal grid algorithm for DNS of turbulent boundary layers. *Comput Fluids* 33(3):435–461. [https://doi.org/10.1016/S0045-7930\(03\)00061-6](https://doi.org/10.1016/S0045-7930(03)00061-6). ISSN 00457930
19. Klein M, Sadiki A, Janicka J (2003) Investigation of the influence of the Reynolds number on a plane jet using direct numerical simulation. *Int J Heat Fluid Flow* 24(6):785–794. [https://doi.org/10.1016/S0142-727X\(03\)00089-4](https://doi.org/10.1016/S0142-727X(03)00089-4). ISSN 0142727X
20. Grötzbach G (1983) Spatial resolution requirements for direct numerical simulation of the Rayleigh-Bénard convection. *J Comput Phys* 49(2):241–264. [https://doi.org/10.1016/0021-9991\(83\)90125-0](https://doi.org/10.1016/0021-9991(83)90125-0). ISSN 10902716

Effect of Fluidic Injection on the Core Length of Rectangular Sonic Jet



G. Kailash and S. M. Aravindh Kumar

Abstract The fluidic injection using air tabs at the nozzle exit is performed along minor axis, and major axis of aspect ratio 2 (AR2) rectangular sonic jet and its effect on the jet is investigated using shadowgraph visualization technique. For nozzle pressure ratios (NPRs) 2, 3 and 4 of rectangular jet, the injection pressure ratio (IPR) is varied from 2 to 4, in steps of 1. The core lengths measured from shadowgraph results indicate that the injection along minor axis has promoted mixing at all the NPRs and the mixing increases with increasing IPR which is evident from reduced core length compared to uncontrolled jet. The injection along major axis reduced mixing as a result the core length elongation is noticed at all the NPRs and IPRs, except at NPRs 2 and 3 at IPR 4, where the core is slightly shorter than uncontrolled jet. With injection along minor axis, the jet at NPR 2 showed higher core length reduction at IPRs 2, 3 and 4 compared to NPRs 3 and 4. The study proves that injection along minor axis of rectangular jet is efficient in promoting the mixing of jet with the ambient as compared to injection along major axis.

Keywords Sonic jet · Core length · Shadowgraph · Rectangular jet · Fluidic injection

1 Introduction

A jet is mainly controlled to enhance mixing with fluid in the surrounding still environment. Better mixing is important for the applications such as increasing acoustic performance, infrared signature reduction, increasing combustor performance and reducing interaction between engine exhaust and after-body. The controlling techniques are classified as active and passive. The passive controls such as geometric modifications, chevrons, solid tabs etc. are permanently fixed and cannot vary the control parameters when needed. Also the passive control of jet results in thrust losses. The experiments conducted by Zaman [1] using solid tabs as the control

G. Kailash · S. M. Aravindh Kumar (✉)
SRM Institute of Science and Technology, Kattankulathur, India
e-mail: aravindm1@srmist.edu.in

system affirmed that the blockage effect produced by solid tabs induces thrust loss in the jet. The results show that the increasing blockage area from 1.1% to 14.1% causes thrust loss of 4.1% to 23.7%. To vary the output parameters of any passive control there is a requirement of rotating parts or additional mechanical systems even to make it switch on or off, so that mostly it is permanently fixed at the time of engine operation [2]. As an alternative to passive controls, active controls are introduced. Active controls involve actuation of any fluid induced into the primary flow. The studies based on active controls always resulted in minimal or no thrust loss. The control parameters of an active control can be varied whenever required.

The literature on uncontrolled rectangular jets explained the enhanced mixing of rectangular jets over circular jets. Rectangular jets are common in military applications due to their reduced infrared signature. The major advantage in rectangular jets is, it has flat and vertex sections along its exit geometry resulting in a differential jet growth [3]. This differential jet growth results in axis switching and jet rotation. The phenomenon of axis switching improves the jet mixing characteristics. Since the nozzle exit height determines the shock cell length of jet [4], the rectangular jet produces shorter shock cell length than equivalent axisymmetric nozzles. There are studies [4] proving that the rectangular jet produces higher level of mixing where it exhibits only 50% of total core length of an equivalent circular jet.

The air tabs as an active control technique to improve jet mixing is a promising technique to achieve better mixing without losing thrust [5]. The air tabs are constant area circular tubes used as the injector of air in a fluid dynamic jet. The air tabs can also enhance the total thrust of the system through mass addition [6]. The mechanism behind the air tab technique is explained by Wan and Yu et al. [7] and Arun Kumar et al. [8]. Wan and Yu et al. [7] conducted experiments on circular jet of Mach 1.3 and concluded that the air tabs positioned at 90° had remarkable effect in enhancing jet mixing. He also showed that the lateral deflection in the primary jet resulted in the initiation of counter-rotating vortex pair right behind the injected jet. Arun Kumar et al. [8] explained that the counter-rotating vortex pairs generated by injection of fluid into the jet become longitudinal vortices while moving towards the jet axis. These vortices promote the penetration of ambient fluid into jet core. The faster penetration makes the jet decay faster ending up with a shorter supersonic core. The fluidic injection also tends to break the shock cells and diminish their intensity. It is seen from the previous studies that lesser the diameter of injector more will be the distortion in primary jet resulting in better mixing [9]. Lesser the number of injectors used will result in higher mixing promoting efficiency [10]. The studies with single injector configuration showed that the single injector is not enough to alter the shock structure of jet [11]. So in the present study two injectors with smaller diameter is employed.

So far in the literature, it can be seen that the majority of studies with fluidic injection technique are considered for jets with circular geometry. The rectangular jet operated at sonic conditions with varying fluidic injection pressure is found to

be missing in the literature. The present work investigates the extent of core length of rectangular sonic jet of aspect ratio (AR) 2 issuing from a convergent nozzle with fluidic injection along major and minor axes. The two air tabs used for fluidic injection are fixed at the nozzle exit along major and minor axes. The jet mixing is quantified from visualization images obtained using shadowgraph.

2 Experimental Details

The present experiments are conducted at Open Jet Facility in High Speed Aerodynamics Laboratory at SRM Institute of Science and Technology. The facility features a primary settling chamber and injection settling chamber for nozzle and air tabs respectively. The stagnation pressure in the primary and injection chambers is controlled to maintain the nozzle pressure ratio and injection pressure ratio. The nozzle pressure ratio (NPR) is the ratio of primary settling chamber stagnation pressure to the ambient pressure. The injection pressure ratio (IPR) is the ratio of injection chamber stagnation pressure to ambient pressure. The model used for the study is aspect ratio 2 (AR2) rectangular convergent nozzle with inlet and exit equivalent diameters (D_e) of 30 mm and 10 mm. The dimensions of nozzle model are shown in Fig. 1. The two air tabs/injectors of inner diameter 1 mm are fixed at the nozzle exit as shown in Fig. 2. For NPRs 3, 4 and 5, the fluidic injection is done along minor axis and major axis (as shown in Fig. 2) with IPRs 2, 3 and 4. The waves present in the jet field are visualized using shadowgraph technique.

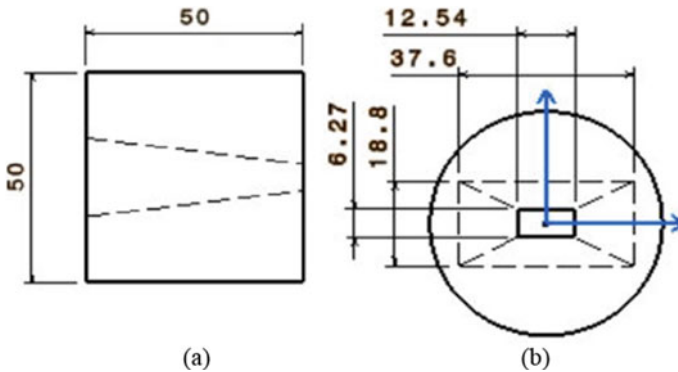


Fig. 1 Side view (a) and front view (b) of rectangular nozzle, (All dimensions are in mm)

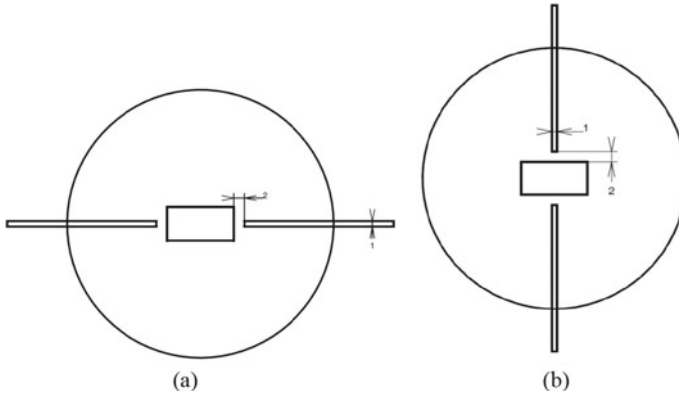


Fig. 2 Injection along major axis (a) and minor axis (b), (All dimensions in mm)

3 Results and Discussions

In supersonic jet studies, the supersonic core length is the axial extent up to which supersonic flow prevails [2]. In the present experimental work the supersonic core length is measured from shadowgraph image [12]. The extent of waves along the jet axis in shadowgraph image is considered as the jet core length.

The shadowgraph results of rectangular jet with air tabs along minor axis at NPR 2 with increasing IPR 1 (no injection), 2, 3 and 4 are presented in Fig. 3a–d. The waves in the core are weak as NPR 2 is close to correct expansion of sonic jet. At NPR 2, the rectangular jet without injection has a core length of $4.5D_e$. With injection, the core length of AR2 jet is found to decrease with increasing IPR. The core length of AR2 jet at NPR 2 with IPRs 2, 3 and 4 is $4D_e$, $3.7D_e$ and $3.1D_e$, respectively. For the same NPR of 2, the injection along major axis has caused elongation of core at IPRs 2 and 3 as shown in Fig. 3e, f. But at IPR 4 (Fig. 3g), the injection along major axis resulted in core reduction which is not as high as compared to injection along minor axis. For NPR 2 with injection along major axis, the core length at IPRs 2, 3 and 4 is $4.9D_e$, $4.7D_e$ and $4.6D_e$. The same trend of core length elongation and reduction was observed for NPR 3 also. At NPR 3, the core length of uncontrolled jet is $6.6D_e$ which got reduced with injection along minor axis, to $6.4D_e$, $6.2D_e$ and $5.8D_e$ at IPRs 2, 3 and 4, respectively. For injection along major axis at NPR 3 the core length at IPRs 2, 3 and 4 is $7.7D_e$, $7D_e$ and $6.5D_e$, respectively. At highest studied NPR 4 (Fig. 4), the injection along minor axis resulted in core reduction and this increased with increasing IPR as in NPRs 2 and 3. The core length at NPR 4 with IPRs 2, 3 and 4 is $8.7D_e$, $8.1D_e$ and $7.6D_e$, respectively as compared to $9.1D_e$ for uncontrolled jet. At NPR 4, the trend in core length variation for injection along major axis (Fig. 4e–g) is not same as NPRs 2 and 3, i.e. at NPR 4, the core has elongated at all the IPRs whereas at NPRs 2 and 3, the core elongated only at IPR 2 and 3, but reduced at IPR 4.

Fig. 3 Shadowgraph images at NPR 2, **a**-uncontrolled jet, **b, c, d**-with injection along minor axis, **e, f, g**-with injection along major axis

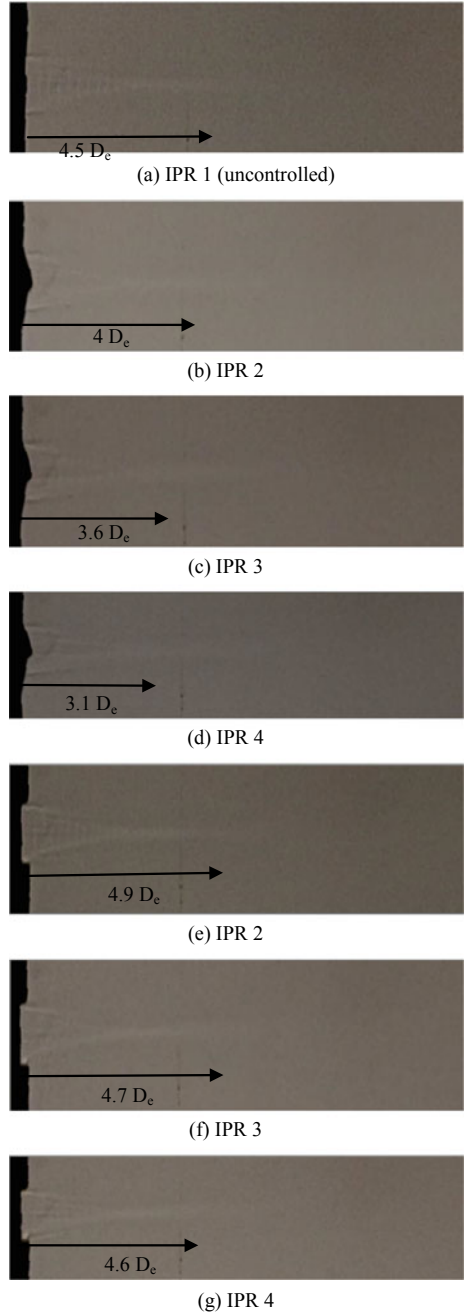
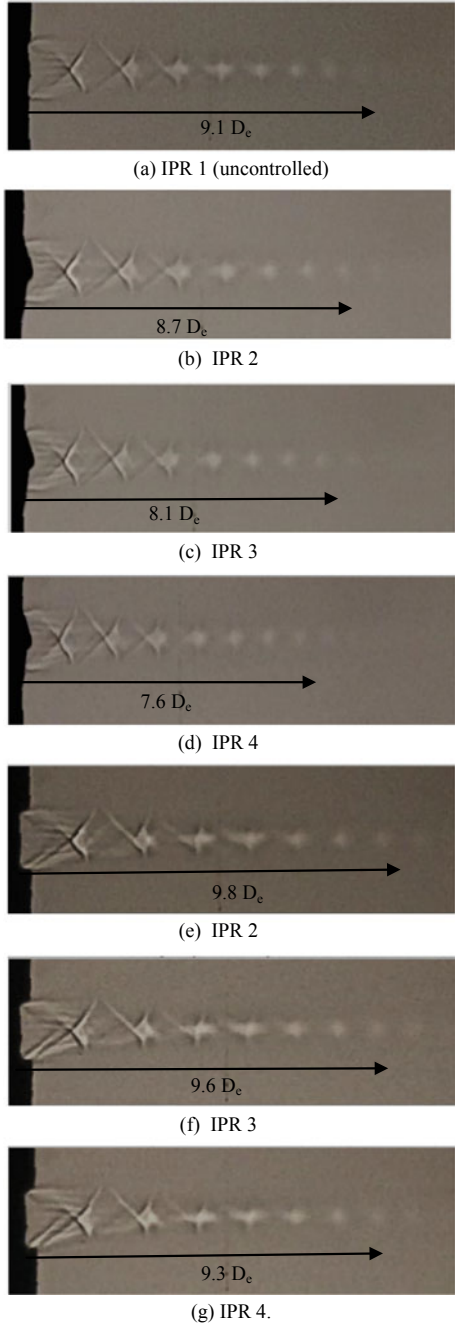


Fig. 4 Shadowgraph images at NPR 4, **a**-uncontrolled jet, **b, c, d**-with injection along minor axis, **e, f, g**-with injection along major axis



From the results it is evident that the rectangular jet can be manipulated by fluidic injection via air tabs. The level of mixing due to fluidic injection depends on the orientation of air tabs. Injection along minor axis caused reduction in core length at all the NPRs and IPRs, which is an indication of increased jet mixing. Injection along jet major axis resulted in core length elongation in almost all the cases, indicating reduced mixing of the jet with the ambient fluid. It is also found that core length reduction due to injection along minor axis increases with increasing IPR at all the NPRs studied. For all NPRs, the maximum core length reduction occurred at the highest IPR of 4.

The percentage reduction in core length between uncontrolled jet and controlled jet is calculated to identify the effectiveness of air tabs on jet mixing. The percentage reduction in core length is quantified as follows,

$$\% \text{ reduction in core length} = \left(\frac{\text{Uncontrolled jet core length} - \text{Controlled jet core length}}{\text{Uncontrolled jet core length}} \right) * 100$$

The percentage reduction in core length caused by injection is significant when injection is carried out along minor axis. Injection along major axis caused reduction at NPRs 2 and 3 at IPR 4 only. The reduction is about 8.8% and 1.51% for NPRs 2 and 3 at IPR 4. For other cases, the injection along major axis does not cause any core length reduction. The percentage reduction in core length for injection along minor axis for NPRs 2, 3 and 4 at IPRs 2, 3 and 4 is shown in Fig. 5. It is clear that the reduction increases with increasing IPR at all NPRs. The maximum reduction at each IPR is achieved when the NPR is 2. With increasing NPR, the core length reduction is found to come down for the IPRs studied.

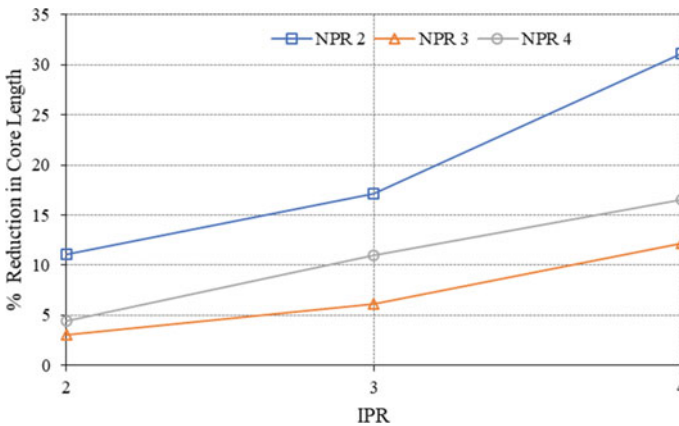


Fig. 5 Percentage reduction of rectangular jet with injection along minor axis

4 Conclusion

The fluidic injection along major axis, and minor axis of AR2 rectangular sonic jet in the present experimental investigation proved to be an effective jet control for noncircular geometry also. Both major and minor axis injection using air tabs resulted in core length changes as evident from the shadowgraph images. The injection along minor axis caused reduction in core length at all the NPRs. The reduction is found to increase with increasing IPR and it is maximum at the highest IPR of 4. Reduced core length is an indication of increased mixing of jet with the ambient fluid. Compared to injection along minor axis, the injection along major axis caused elongation of core at all NPRs and IPRs, except at NPRs 2 and 3 at IPR 4 condition. Injection along minor axis at NPR 2 showed highest reduction in core length at all IPRs compared to NPRs 3 and 4.

References

1. Zaman KBMQ (1999) Spreading characteristics of compressible jets from nozzles of various geometries. *J Fluid Mech* 383:197228. <https://doi.org/10.1017/S0022112099003833>
2. Rathakrishnan E (2019) *Applied gas dynamics*. Wiley, Hoboken
3. Gutmark E, Gutmark E (1997) Mixing enhancement in non-circular jets. In: 4th shear flow control conference. <https://doi.org/10.2514/6.1997-1876>
4. Knowles K, Saddington AJ (2006) A review of jet mixing enhancement for aircraft propulsion applications. *Proc Inst Mech Eng Part G J Aerosp Eng* 220(2):103–127. <https://doi.org/10.1243/09544100g01605>
5. Davis MR (1982) Variable control of jet decay. *AIAA J* 20(5):606–609. <https://doi.org/10.2514/3.7934>
6. Cuppoletti DR, Gutmark E (2014) Fluidic injection on a supersonic jet at various mach numbers. *AIAA J* 52(2):293–306. <https://doi.org/10.2514/1.j010000>
7. Wan C, Yu SCM (2011) Investigation of air tabs effect in supersonic jets. *J Propul Power* 27(5):1157–1160. <https://doi.org/10.2514/1.B340794>
8. Arun Kumar P, Aravindh Kumar SM, Surya Mitra A, Rathakrishnan, E (2018) Fluidic injectors for supersonic jet control. *Phys Fluids* 30:6101. <https://doi.org/10.1063/1.5056209>
9. Arun Kumar P, Verma SB, Rathakrishnan E (2015) Experimental study of subsonic and sonic jets controlled by air tabs. *J Propul Power* 31(5):1473–1481. <https://doi.org/10.2514/1.b35675>
10. Chauvet N, Deck S, Jacquin L (2007) Numerical study of mixing enhancement in a supersonic round jet. *AIAA J* 45(7):1675–1687. <https://doi.org/10.2514/1.27497>
11. Prasad C, Morris P (2019) Effect of fluid injection on turbulence and noise reduction of a supersonic jet. *Phil Trans R Soc A* 377:20190082. <https://doi.org/10.1098/rsta.2019.0082>
12. Kailash G, Aravindh Kumar SM (2020) Control of sonic jets by fluidic injection. *IOP Conf Ser Mater Sci Eng* 912:022012. <https://doi.org/10.1088/1757-899x/912/2/022012>

Stress Distribution in Infinitely Long Plate with Circular Hole Loaded by Concentrated Loads



Kannan Kulavan Mohammed Shafeeque and K. V. N. Surendra

Abstract The title problem is 2-D exterior problem which is solved here by superposing Flamant problems followed by annihilating far-field and boundary tractions using limiting case of Lamé's problem. This method being identical to that used for classical problem of disk under diametral compression (corresponding interior problem), leads to closed-form solution for the exterior problem. Series solution is applicable for distributed loads, which in the limit approaches solution for the title problem. FEM which can model only finite geometries, approximates the infinite domain in the limit. The latter two methods are adopted here for validation of the analytical method by comparison. The analytical method is extended to solve three-point, four-point and n -point loading cases on the circular hole boundary.

Keywords Stress distribution · Infinite plate · Circular hole · Point loads · Three point load · Four point load

1 Introduction

Holes of different shapes are inevitable in many of the structural & machine components. These holes induce stress concentration in the solid revealing in the form of uneven distribution of force transmission paths. The irregularities may be of various shapes according to its use in the design which may be made in different locations of solid. In many cases like huge walls, the geometry is very large in comparison to its irregularity so that it can be assumed as infinite plate with hole. Stress concentration regions are more prone to crack initiation and are studied by various researchers. In the traditional literature, classical solutions are available for infinite plate with a hole subjected to far-field uniform loading [1]. A few researchers attempted the exterior problem with loaded boundary. Various shape of holes in infinite plate were considered. For example, a general analytical solution for an infinite plate with a

K. K. Mohammed Shafeeque (✉) · K. V. N. Surendra
Mechanical Engineering, Indian Institute of Technology Palakkad, Palakkad, Kerala, India
e-mail: 131814002@smail.iitpkd.ac.in

© The Author(s), under exclusive license to Springer Nature Singapore Pte Ltd. 2022
T. Tadepalli and V. Narayanamurthy (eds.), *Recent Advances in Applied Mechanics*,
Lecture Notes in Mechanical Engineering, https://doi.org/10.1007/978-981-16-9539-1_7

traction free elliptical hole subjected to arbitrary far-field biaxial loading is provided by Gao [2]. Ukadgaonker and Rao presented a general solution for the stress distribution around triangular holes in isotropic plate and single and multilayered orthotropic plate [3]. Patel and Desai solved the problem of a large rectangular plate with an elliptical hole subjected to linearly varying in-plane loading on two opposite edges using Muskhilsvili's complex variable method [4]. Simha and Mahapatra [5] used complex variables with conformal mapping to obtain the tangential stress variation around irregular holes in large plates under uniform loading. In many cases, the hole may be subjected to contact loading. Using Muskhilsvili's complex variable formulation a general solution for the stress field around an internally pressurized circular hole in infinite orthotropic plate was obtained by Sharma et al. [6]. Zirka et al. [7] used photo-elastic method to obtain the stress distribution around circular hole in a rectangular orthotropic plate under static and dynamic loading.

In this work, we solve the 2-D exterior problem of infinite plate with circular hole subjected arbitrary number of self-equilibrating point loads acting on the circular edge, for stress distribution. In Sect. 2, the basic problem of pair of collinear loads is stated. To solve this problem within the scope of linear elasticity under isothermal conditions, we use at the simplest, superposition principle and classical solutions of elasticity in Sect. 3. The solution so obtained in case of pair of collinear loads, is compared against the approximate solutions obtained using Michell generalized bi-harmonic series and FEM for validation in Sect. 4. Then the analytical method is extended in Sect. 5 to solve for three-point symmetric normal loading, four point symmetric normal loading and n number of self-equilibrating point loads on the circular hole boundary of an infinitely long plate.

2 Problem Description: Pair of Loads

An infinite plate with a circular hole of radius R , subjected to two concentrated forces (P) at diametrically opposite points as shown in Fig. 1(a) is our basic exterior problem for which the circular disc under diametral compression can be considered as the corresponding interior problem as shown in Fig. 1(c). The primary aim is to find the state of stress in the infinite plate with a circular hole (Fig. 1(a)) subjected to the following conditions.

- Boundary conditions of the problem:
 - Traction free circular hole boundary (except at loaded points): $\sigma_{rr}(r = R) = 0 = \tau_{r\theta}(r = R)$
 - Traction free at far-field: $\sigma_{rr}(r \rightarrow \infty) = 0 = \tau_{r\theta}(r \rightarrow \infty)$
- Other conditions:
 - It has symmetry about x and y axes implying shear free planes along the axes.
 - There are stress singularities at loaded points.

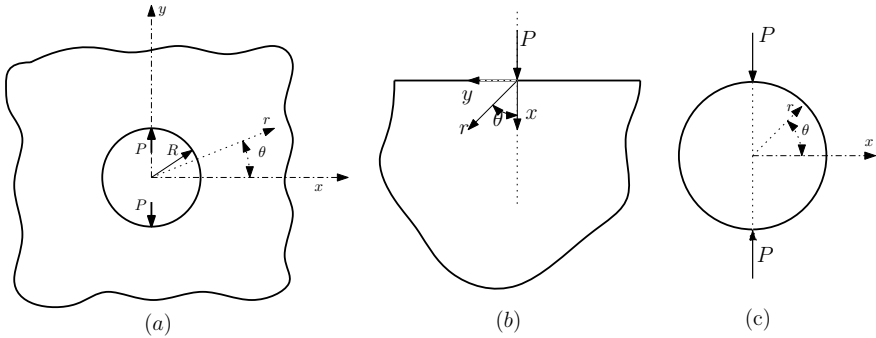


Fig. 1 **a** The exterior problem: infinite plate with a circular hole subjected to diametrical compression on the hole boundary. **b** Flamant problem: semi-infinite plate with concentrated load at the boundary [1]. **c** Corresponding interior problem: disk under diametrical compression [1]

3 Method for Closed-Form Solution

The problem is formulated using the well known Airy stress function, ϕ , which is defined (in polar coordinates) as in Eq. 1.

$$\sigma_{rr} = \frac{1}{r^2} \frac{\partial^2 \phi}{\partial \theta^2} + \frac{1}{r} \frac{\partial \phi}{\partial r}; \quad \sigma_{\theta\theta} = \frac{\partial^2 \phi}{\partial r^2}; \quad \tau_{r\theta} = -\frac{\partial}{\partial r} \left(\frac{1}{r} \frac{\partial \phi}{\partial \theta} \right) \tag{1}$$

Airy stress function itself satisfy the equilibrium equations and the governing equation is obtained from the 2D compatibility conditions without body forces as biharmonic equation as in Eq. (2).

$$\nabla^2 \nabla^2 \phi = 0 \quad \text{where, } \nabla^2 = \frac{\partial^2}{\partial r^2} + \frac{1}{r^2} \frac{\partial^2}{\partial \theta^2} + \frac{1}{r} \frac{\partial}{\partial r} \tag{2}$$

The stated problem of infinite plate with a circular hole subjected to a pair of collinear point loads can be solved by recalling the classical solution for disk under diametrical compression provided by Hertz [1], the corresponding interior problem. The Flamant problem of semi-infinite plate with point load as shown in Fig. 1(b) is traditionally used for solving corresponding interior problem of disk under diametrical compression shown in Fig. 1(c) by Hertz [1].

Flamant solution in terms of Airy stress function is given by Eq. (3) [1].

$$\phi^{(F)} = \frac{-P}{\pi h} r \theta \sin \theta \tag{3}$$

where, h is the width of the plate.

The interior problem of disk under diametrical compression is solved by superposition of two variants of Flamant problem and a hydrostatic tension stress state as

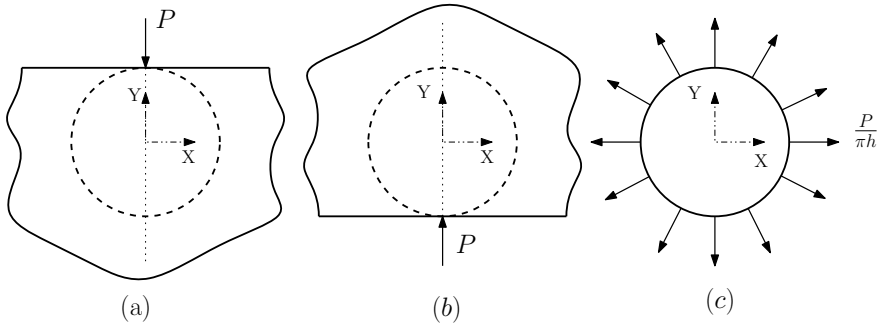


Fig. 2 Superposition solution for disk under diametric compression: **a & b** two Flamant solutions **c** hydrostatic tension [10]

shown in Fig. 2. By superposing two such solutions after relevant coordinate transformations and a hydrostatic tension state as in Fig. 2, the following stress components were obtained for the interior problem in terms of polar coordinates.

$$\begin{aligned} \sigma_{rr} &= \frac{-2P}{\pi h} \left[\frac{(R - r \sin \theta)(r - R \sin \theta)^2}{(r^2 + R^2 - 2rR \sin \theta)^2} + \frac{(R + r \sin \theta)(r + R \sin \theta)^2}{(r^2 + R^2 + 2rR \sin \theta)^2} - \frac{1}{2R} \right] \\ \sigma_{\theta\theta} &= \frac{-2P}{\pi h} \left[\frac{(R - r \sin \theta)R^2 \cos^2 \theta}{(r^2 + R^2 - 2rR \sin \theta)^2} + \frac{(R + r \sin \theta)R^2 \cos^2 \theta}{(r^2 + R^2 + 2rR \sin \theta)^2} - \frac{1}{2R} \right] \quad (4) \\ \tau_{r\theta} &= \frac{-2PR \cos \theta}{\pi h} \left[\frac{(R - r \sin \theta)(-r + R \sin \theta)}{(r^2 + R^2 - 2rR \sin \theta)^2} + \frac{(R + r \sin \theta)(r + R \sin \theta)}{(r^2 + R^2 + 2rR \sin \theta)^2} \right] \end{aligned}$$

The solution given by Eq. (4) satisfies the traction-free circular boundary for both interior and exterior problem. And it captures the stress singularities at the two loaded points for both the problems. At the basic level, it satisfies equilibrium equations and the 2-D compatibility condition as the terms of solution (Eq. (4)) are transformed versions of Airy function solution. With these observations, if we examine the validity of Eq. (4) as the solution for exterior problem, we realize that it leaves uniform tensile radial stress at infinity which needs to be annihilated as shown below.

As $r \rightarrow \infty$

$$\sigma_{rr} = \sigma_{\theta\theta} = \frac{P}{\pi Rh}; \quad \tau_{r\theta} = 0 \quad (5)$$

Lame problem of thick cylinder can be used for annihilation by considering its extreme case of infinite outer radius, under zero inner pressure and an outer pressure. This way, traction at infinity can be made zero while ensuring that hole boundary traction is not disturbed. The outer load must be equal in magnitude to the radial traction induced at infinity in our approach and opposite in sense. Lamé’s solution in terms of stress components in polar coordinates is given by [1]:

$$\begin{aligned}
\sigma_{rr} &= \frac{P_i R_i^2 - P_o R_o^2}{R_o^2 - R_i^2} - \frac{R_i^2 R_o^2}{r^2} \frac{P_i - P_o}{R_o^2 - R_i^2} \\
\sigma_{\theta\theta} &= \frac{P_i R_i^2 - P_o R_o^2}{R_o^2 - R_i^2} + \frac{R_i^2 R_o^2}{r^2} \frac{P_i - P_o}{R_o^2 - R_i^2} \\
\tau_{r\theta} &= 0
\end{aligned} \tag{6}$$

Substituting $P_o = \frac{P}{\pi R h}$, $P_i = 0$ and $R_i = R$ in Eq. (6), we get
As $R_o \rightarrow \infty$

$$\begin{aligned}
\sigma_{rr} &= \frac{P}{\pi R h} \left(\frac{R^2}{r^2} - 1 \right) \\
\sigma_{\theta\theta} &= \frac{-P}{\pi R h} \left(\frac{R^2}{r^2} + 1 \right)
\end{aligned} \tag{7}$$

Required Lamé's solution applicable for infinite plate with circular hole of radius R is given by Eq. (7). By incorporating all these, the final solution for the exterior problem in terms of stress components in polar coordinates is given by Eq. (8).

$$\begin{aligned}
\sigma_{rr} &= \frac{2P}{\pi h} \left[\frac{(R - r \sin \theta)(r - R \sin \theta)^2}{(r^2 + R^2 - 2rR \sin \theta)^2} + \frac{(R + r \sin \theta)(r + R \sin \theta)^2}{(r^2 + R^2 + 2rR \sin \theta)^2} - \frac{1}{2R} \left(\frac{R^2}{r^2} \right) \right] \\
\sigma_{\theta\theta} &= \frac{2P}{\pi h} \left[\frac{(R - r \sin \theta)R^2 \cos^2 \theta}{(r^2 + R^2 - 2rR \sin \theta)^2} + \frac{(R + r \sin \theta)R^2 \cos^2 \theta}{(r^2 + R^2 + 2rR \sin \theta)^2} + \frac{1}{2R} \left(\frac{R^2}{r^2} \right) \right] \\
\tau_{r\theta} &= \frac{2PR \cos \theta}{\pi h} \left[\frac{(R - r \sin \theta)(-r + R \sin \theta)}{(r^2 + R^2 - 2rR \sin \theta)^2} + \frac{(R + r \sin \theta)(r + R \sin \theta)}{(r^2 + R^2 + 2rR \sin \theta)^2} \right]
\end{aligned} \tag{8}$$

4 Verification of the Closed Form Solution

4.1 Finite Element Method

A finite circular plate with a circular hole subjected to collinear point loads is modeled in Ansys mechanical APDL and is solved for stress distribution. The outer radius of the plate is increased in steps so that the extreme case of the problem becomes an infinite plate with circular hole. However, we modeled a finite outer radius although it may be very large compared to hole size. In the simulations, outer radius is taken as $30R_i$ and is shown in Fig. 3(a). By making use of symmetry, only quarter of the

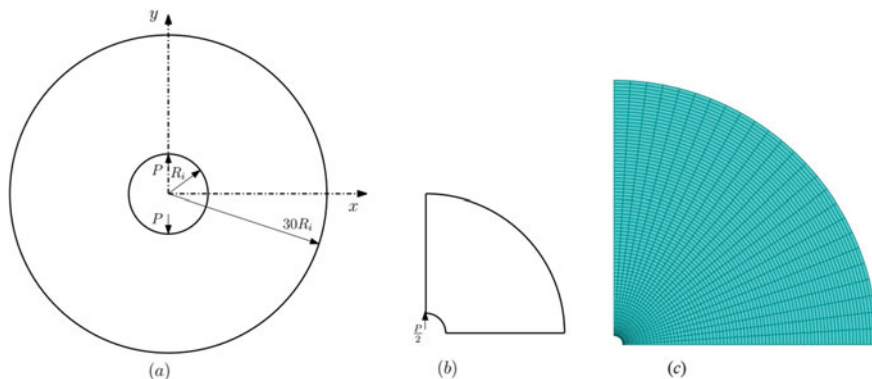


Fig. 3 a Circular plate with circular hole under collinear point loads. b Quarter of the plate (symmetric model). c Finite element meshed model of the plate

plate is modeled as shown in Fig. 3(b). In the model, radius of the circular hole (R_i) was taken as 1 m and hence the outer radius of the plate as 30 m. For the material model elastic properties of steel as Young's modulus, $E = 200$ GPa and Poisson's ratio, $\nu = 0.3$ are considered. Eight-noded 2D plane elements (PLANE183) are used for meshing the plate and a typical mesh pattern generated in Ansys of the plate is shown in Fig. 3(c). There are total 2500 elements and 7751 nodes in the meshed model for which a polar grid pattern is used for generating the mesh, which ensures finer elements near the hole and coarser elements far away as shown in Fig. 3(c). A mesh insensitivity analysis was conducted with same meshing pattern but with different number of elements (divisions) in radial and tangential directions. The stress distribution on x and y axes is plotted in two separate superimposed plots for all cases for comparison, which are not shown here for brevity. Six different cases of number of divisions in the two different directions considered, exhibited a convergent behaviour as total number of elements increased. The meshing parameters for the highest number of elements case is adopted here.

4.2 Series Solution Method

An infinite plate with a circular hole subjected to a uniformly distributed radial traction on the hole boundary as shown in Fig. 4 can be solved using series solution method for various values of loading angle, β . The problem of infinite plate with a circular hole subjected to collinear point loads can be thought as a limiting case of a distributed loading as β approaches zero.

The relevant terms corresponding to the problem of infinite plate with a circular hole subjected to uniformly distributed radial traction is chosen from the generalized solution in terms of Airy stress function given by Michell [1, 8]. Applying symmetry

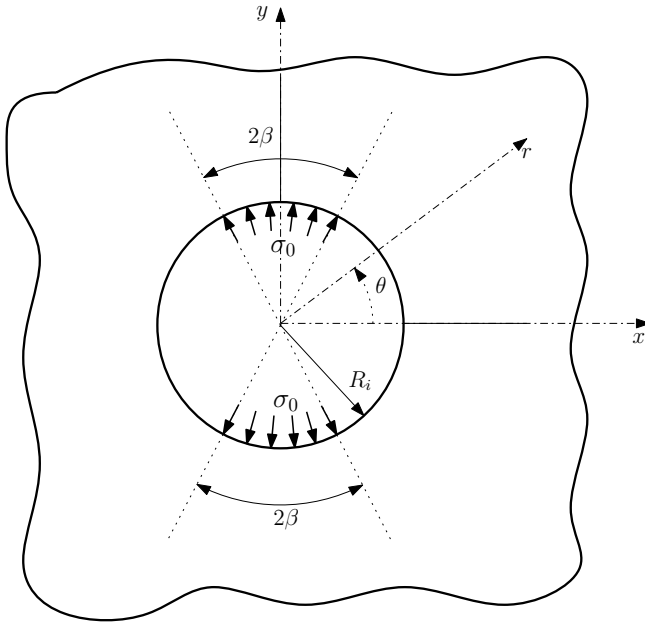


Fig. 4 Infinite plate with a circular hole subjected to a uniformly distributed radial traction with loading angle β

of the problem about both x and y axis, only the even terms of the series will be preserved. And the resulting Airy stress function is given by:

$$\phi = c'_1 \ln r + \sum_{n=2,4,\dots}^{\infty} [c_n r^{-n} + d_n r^{-n+2}] \cos n\theta \tag{9}$$

The stress components can be obtained from the definition of Airy stress function and is given by:

$$\begin{aligned} \sigma_{rr}(r, \theta) &= \frac{c'_1}{r^2} + \sum_{n=2,4,\dots}^{\infty} \left[n(-n-1)c_n r^{-n-2} - (n-1)(n+2)d_n r^{-n} \right] \cos(n\theta) \\ \sigma_{\theta\theta}(r, \theta) &= \frac{c'_1}{r^2} + \sum_{n=2,4,\dots}^{\infty} \left[n(n+1)c_n r^{-n-2} + (n-1)(n-2)d_n r^{-n} \right] \cos(n\theta) \end{aligned} \tag{10}$$

$$\tau_{r\theta}(r, \theta) = \sum_{n=2,4,\dots}^{\infty} \left[-n(n+1)c_n r^{-n-2} - n(n-1)d_n r^{-n} \right] \sin(n\theta)$$

By applying the boundary conditions in the form of Fourier transform the unknown coefficients can be obtained. Boundary condition in terms of Fourier series is given by:

$$\sigma_{rr}(r = R_i, \theta) = \frac{-2\sigma_0\beta}{\pi} + \sum_{n=2,4,\dots}^{\infty} \left[\frac{4\sigma_0}{n\pi} \sin(n\pi/2 - n\beta) \cos n\theta \right] \quad (11)$$

Hence the unknown coefficients are given by:

$$\begin{aligned} c_1' &= \frac{-2\sigma_0\beta}{\pi} \\ c_n &= \frac{2\sigma_0}{n(n+1)\pi} \sin(n\pi/2 - n\beta) \\ d_n &= \frac{-2\sigma_0}{n(n-1)\pi} \sin(n\pi/2 - n\beta) \end{aligned} \quad (12)$$

4.3 Results for Comparison

The results obtained are plotted as stress components along vertical and horizontal axes as shown in Fig. 5. The solution is compared with Finite element method (FEM) and series solutions. In FEM, a finite circular plate with a circular hole can be modeled and the outer boundary size can be increased so that it tends to infinity to represent the actual problem in the limit. However, we can model only finite outer radius although it may be very large compared to hole size. In this simulations, outer radius is taken as $30R$ and plotted in Figs. 5 and 6. In case of series solution, an infinite plate with a circular hole subjected to uniformly distributed radial traction can be solved for various values of loading angle (β), and β can be decreased so that it approximates the point load case of our problem in the limit. The value of β is taken as 1° and plotted in Figs. 5 and 6. The three solutions are compared in the plots of Fig. 5 which indicates a perfect match away from circular boundary. The discrepancies near the circular boundary are due to approximations.

Isochromatic patterns are also obtained from the three methods and plotted to compare as shown in Fig. 6. The contours of $(\sigma_1 - \sigma_2)$ are known as isochromatics. The $(\sigma_1 - \sigma_2)$ is related to the photoelastic isochromatic fringe order, N as

$$(\sigma_1 - \sigma_2) = Nf_\sigma/h \quad (13)$$

where, σ_1, σ_2 are the principal stresses, f_σ is the material fringe constant and h is the thickness of the specimen. Again, it shows a very good matching among the three methods. Figures 6(a) and 6(b) are obtained for the analytical and series solutions respectively which show almost same patterns. Both of them show symmetric pair of isotropic points (IPs) on x-axis at some distance away from the hole boundary. The pattern obtained from the FEM solution is also similar to the other two except

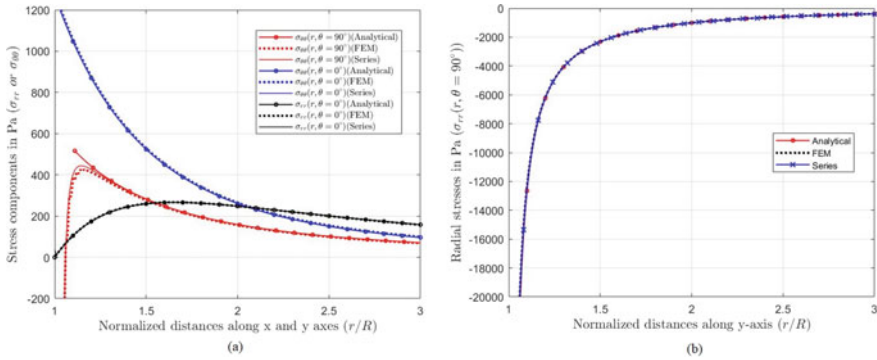


Fig. 5 Stress components: **a** hoop stress along y-axis and along x-axis, radial stress along x-axis; **b** radial stress along y-axis

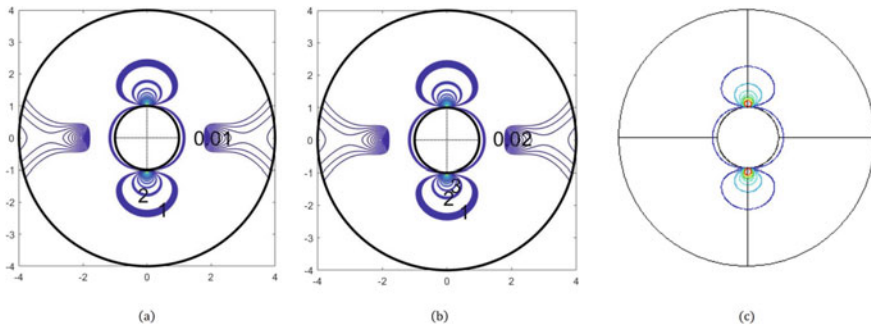


Fig. 6 Isochromatics generated by: **a** analytical solution **b** Michell series **c** FEM. The values on x and y axes of the sub-figures **a & b** are the normalized domain coordinates ($x/R, y/R$)

the absence of IPs. This absence is due to FEM approximation of discretization and interpolation. The FEM solution is for a finite geometry whereas the other two are for infinite geometry.

5 Extension of Analytical Method to More Loading Cases

The closed form solution obtained by superposing particular Flamant problems and Lamé problem can be extended arbitrary number of self-equilibrating point loads acting on the boundary of the circular hole in infinite plate. Two such cases of point loads are solved here. The generalized Flamant solution is used to derive the closed form solutions for all the cases.

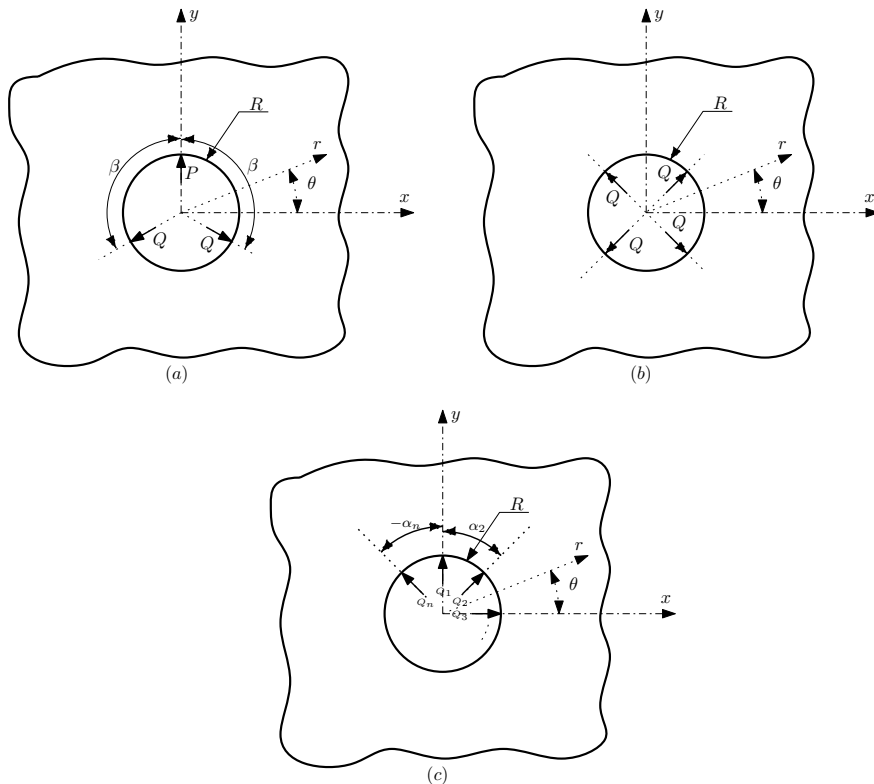


Fig. 7 Infinite plate with circular hole under: **a** three-point symmetric normal loading **b** four-point symmetric normal loading **c** n number of self-equilibrating arbitrary point normal loading

5.1 Infinite Plate with a Circular Hole Subjected to 3-Point Symmetric Normal Loading

The interior problem of three point symmetric normal loading of a circular disk can be solved by superposing three particular cases of Flamant solution and annihilating the hydrostatic state of stress [9]. The corresponding exterior problem of an infinite plate with circular hole as shown in Fig. 7(a) can be solved using the same principle applied to the collinear point load problem. The closed form solution in terms of Airy stress function for the circular disk subjected to three-point symmetric loading is given by [9]:

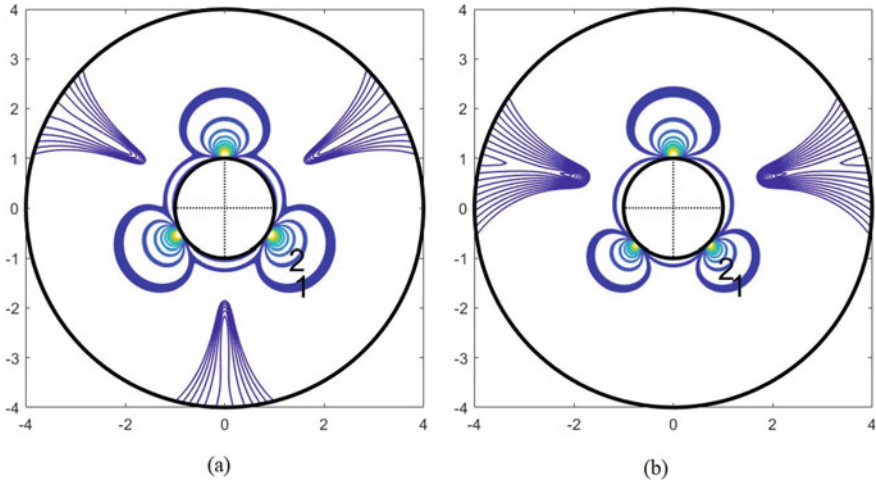


Fig. 8 Isochromatics generated for infinite plate with circular hole under symmetric three-point normal loading for ($P = 2 \text{ kN}$, $h = 1 \text{ m}$, $f_\sigma = 800 \text{ N/m}$): **a** $\beta = 120^\circ$ **b** $\beta = 135^\circ$. The values on x and y axes in each sub-figure are the normalized domain coordinates (x/R , y/R)

$$\begin{aligned} \phi^{(3Nd)} = & \frac{P}{\pi h} r \cos \theta \arctan \left(\frac{r \cos \theta}{r \sin \theta - R} \right) + \frac{Q}{\pi h} r \cos (\theta + \beta) \arctan \left(\frac{r \cos (\theta + \beta)}{r \sin (\theta + \beta) - R} \right) \\ & + \frac{Q}{\pi h} r \cos (\theta - \beta) \arctan \left(\frac{r \cos (\theta - \beta)}{r \sin (\theta - \beta) - R} \right) + \frac{P + 2Q}{4\pi Rh} r^2 \end{aligned} \tag{14}$$

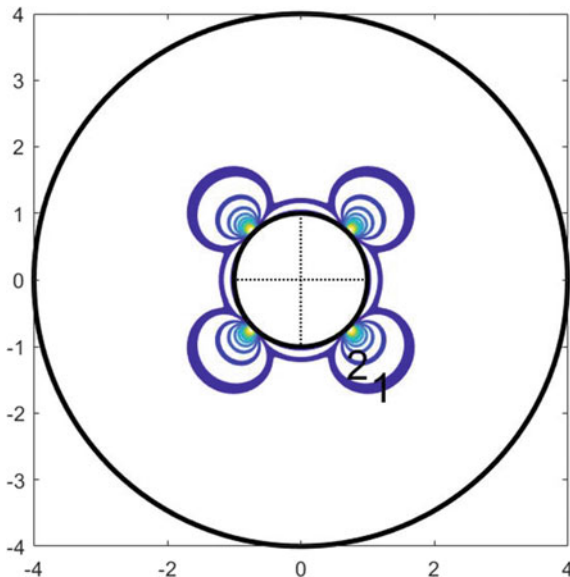
where $P = -2Q \cos \beta$, to ensure the static equilibrium of the disc. It is obvious that this equation will satisfies equilibrium equations and 2-D compatibility conditions. And it also captures the loading point stress singularities. From the definition of Airy stress function, we can derive the stress components in polar coordinates. The stress components give rise to a uniform radial tensile radial stress at infinity which can be annihilated using an extreme case of Lamé problem of thick cylinder (Eq. (6)).

After superposing all the required component solutions, final solution of the problem is given by:

$$\begin{aligned} \phi^{(3N)} = & -\frac{P}{\pi h} r \cos \theta \arctan \left(\frac{r \cos \theta}{r \sin \theta - R} \right) - \frac{Q}{\pi h} r \cos (\theta + \beta) \arctan \left(\frac{r \cos (\theta + \beta)}{r \sin (\theta + \beta) - R} \right) \\ & - \frac{Q}{\pi h} r \cos (\theta - \beta) \arctan \left(\frac{r \cos (\theta - \beta)}{r \sin (\theta - \beta) - R} \right) - \frac{(P + 2Q)}{4\pi Rh} R^2 \log r \end{aligned} \tag{15}$$

The corresponding stress components can be derived using the definition of Airy stress function. The isochromatic pattern of the three point loading for $\beta = 120^\circ$ and $\beta = 135^\circ$ were plotted as shown in Fig. 8.

Fig. 9 Isochromatics generated for infinite plate with circular hole under symmetric four-point normal loading. The values on x and y axes are the normalized domain coordinates (x/R , y/R)



5.2 Infinite Plate with a Circular Hole Subjected to 4-Point Bi-symmetric Normal Loading

An infinite plate with a circular hole subjected to 4-point bi-symmetric normal loading as shown in Fig. 7(b) is analyzed here similar to the three point loading case. It shows a pure radial loading case symmetric to both X and Y axis. The four loads (Q) are equal in magnitude. The corresponding interior problem of a circular disk is solved using four Flamant solutions at the four loading points and annihilating the uniform compressive stress state [9]. The final solution for the circular disk is given by:

$$\phi^{(4Nd)} = \frac{4Q}{4\pi Rh} r^2 + \sum_{\alpha=\beta, (180^\circ-\beta)}^{-\beta, (\beta-180^\circ)} \left[\frac{Q}{\pi h} r \cos(\alpha + \theta) \arctan \left(\frac{r \cos(\alpha + \theta)}{r \sin(\alpha + \theta) - R} \right) \right] \tag{16}$$

By assuming the same solution to the exterior problem, in order to get a traction free boundary condition at far field, an extreme case of Lamé’s thick cylinder problem is used here. And the final solution in terms of Airy stress function is given by:

$$\phi^{(4N)} = \frac{-4Q}{4\pi Rh} R^2 \log r - \sum_{\alpha=\beta, (180^\circ-\beta)}^{-\beta, (\beta-180^\circ)} \left[\frac{Q}{\pi h} r \cos(\alpha + \theta) \arctan \left(\frac{r \cos(\alpha + \theta)}{r \sin(\alpha + \theta) - R} \right) \right] \tag{17}$$

The corresponding stress components can be derived using the definition of Airy stress function. The isochromatic pattern of the four point symmetric normal loading were plotted as shown in Fig. 9.

5.3 *Infinite Plate with a Circular Hole Subjected to Self Equilibrating n -point Normal Loading*

Analytical method demonstrated here can be extended to any number of arbitrary normal point loads on the circular hole boundary, as shown in Fig. 7(c). By superposing required variants of Flamant problem along with Lamé problem, the final solution for the case self-equilibrating n number of point loads acting on the boundary is given by:

$$\phi^{(nN)} = -\frac{\sum_{i=1}^n Q_i}{4\pi R h} R^2 \log r - \sum_{\alpha=\alpha_1, \dots}^{\alpha_n} \left[\frac{Q_i}{\pi h} r \cos(\alpha_i + \theta) \arctan \left(\frac{r \cos(\alpha_i + \theta)}{r \sin(\alpha_i + \theta) - R} \right) \right] \quad (18)$$

6 Conclusion

Using superposition principle applied to classical solutions of elasticity, the problem of an infinite plate with circular hole subjected to a pair of collinear point loads on the hole edge is solved. The same problem is also approximately solved using generalized series method and FEM to compare the results. A good matching is obtained among the three results which validates the solution method. Further, the same procedure is followed for deriving closed form solutions for the case of three point symmetric normal loading and four point symmetric normal loading. Then, using the analytical method a closed form solution for n number of self equilibrating arbitrary point loads on the circular hole boundary of an infinitely long plate is derived.

References

1. Timoshenko SP, Goodier JN (1970) Theory of elasticity, 3rd edn. McGraw-Hill Book Company, Singapore
2. Gao XL (1996) A general solution of an infinite elastic plate with an elliptic hole under biaxial loading. J Press Vessels Pip 67:95–104
3. Ukadgaonker VG, Rao DKN (2000) A general solution for stress around holes in symmetric laminates under in-plane loading. J Compos Struct 49:339–354

4. Patel A (2020) Desai CK (2020) Stress concentration around an elliptical hole in a large rectangular plate subjected to linearly varying in-plane loading on two opposite edges. *Theor Appl Fract Mech* 106:102432
5. Simha KRY, Mahapatra SS (1998) Stress concentration around irregular holes using complex variable method. *Sadhana* 23(4):393–412
6. Sharma DS, Panchal K, Patel N (2011) A general solution for stresses around internally pressurized circular hole in symmetric laminates. In: *NUiCONE 2011* (2011)
7. Zirka AI, Malezhik MP, Chernyshenko IS (2004) Stress distribution in an orthotropic plate with circular holes under impulsive loading. *Int Appl Mech* 40:448–452
8. Barber JR (2009) *Elasticity*, 3rd edn. Springer, Berlin
9. Surendra KVN, Simha KRY (2014) Characterizing frictional contact loading via isochromatics. *Exp Mech* 54:1011–1030. <https://doi.org/10.1007/s11340-014-9865-3>
10. Sadd Martin H (2010) *Elasticity: theory, applications, and numerics*. Elsevier Science, Amsterdam

Re-deployable Smart Sensor Concept for Modal Estimates of Bridges Subjected to Random and Vehicle Excitations



Vasamsetti Sri Harika  and Jayakumar Prawin 

Abstract Mode shapes are the predominant dynamic sensitive features for structural damage identification. However, mode shape estimation requires high fidelity dense sensor network (several accelerometers – remain fixed at certain locations) which incurs huge costs and resource-intensive. This paper proposes a new decentralized modal analysis approach where only two sensors are moved along the monitored bridge and are progressively re-deployed for various segments to obtain continuous mode shape data. A numerically simulated simply supported beam subjected to individually random and vehicle excitation has been considered to demonstrate the proposed re-deployable sensor-based modal estimation concept. The proposed concept estimate mode shapes more reliably using two sensors with a modal assurance criterion value greater than 0.9.

Keywords Re-deployable smart sensors · Mode shapes · Frequency domain decomposition

1 Introduction

Vibration-based methods are the most served method for nondestructive testing and damage identification/structural health monitoring, which can able to detect damages in a different types of structures. The vibration-based techniques are preferred for damage diagnosis as they are global methods, and it does not need a priori information about the damage including its spatial location [1]. In general, the process of damage detection by vibration methods contains different steps that are of recording structural

V. Sri Harika (✉)

Structural Engineering, JNTUK, Kakinada, Andhra Pradesh, India
e-mail: sv712003@student.nitw.ac.in

Structural Engineering, NIT Warangal, Warangal, Andhra Pradesh, India

J. Prawin

CSIR-Structural Engineering Research Centre, Chennai, Tamil Nadu, India
e-mail: prawinj@serc.res.in

time-series data, extracting modal properties, and recognizing damages which are functions of changes in structural dynamic features such as Frequency, Mode shapes. The change of structural vibration mode contains more damage information, which has a significant advantage in determining damage location. It should be mentioned here that in data recording, the source of excitation or vibration can be created from a particular vibrating machine, ambient loading, or vehicle excitation. In addition, both static sensors and mobile sensors are used for data collection. The accurate identification of modal parameters/vibration-sensitive features only pave way for reliable structural damage detection. The traditional method of static sensor network-based mode shape computation involves the huge number of accelerometers placed at multiple locations which can be resource-intensive and incur high costs and handling a large amount of data. This paper presents the concept of decentralized estimation of mode shapes by progressively re-deploying mobile sensors along with the target structure.

Recently, mobile sensors are widely used for data collection rather than using networks of static sensors due to their advantage of high spatial resolution, less field instrumentation, huge cost-saving, feasibility under real-time passing traffic. Re-configurable mobile sensing, which involves repositioning mobile sensors in a series of static configurations which are kept motionless and in-motion sensing that continuously collect measurement data while the sensors traverse the spatial domain of the structure, are the two smart mobile sensor concepts available in the literature. In-situ mobile sensing belongs to the class of indirect structural health monitoring/drive-by monitoring and re-deployable sensor comes under direct structural health monitoring [2]. The present work is limited to re-deployable mobile sensor-based damage-sensitive feature extraction.

Various researchers have developed a decentralized modal analysis that uses independent groups of measurements (i.e., two sensor measurements with re-deployable sensors) with common nodes (at least of one overlapping node) to record local spatial information in stitch-able segments [3–6] and then combined data from each segment to obtain global mode shape. For example, Malekjafarian and O'Brien [3] and Brincker et al. [4] developed Short Time–Frequency Domain Decomposition (STFDD) and Frequency Domain Decomposition (FDD) based techniques which compute mode shapes using the multi-stage process of time history data collection, local mode shape estimation and then connect using common/overlapping points between adjacent segments. Nayak et al. [2] and Sim et al. [5] used both in-situ and re-deployable sensing concepts with different topologies and networks for decentralized mode shape estimation. However, most of the studies use ambient or free excitation and only limited studies consider vehicle bridge interaction. In this paper, the computation of mode shape is attempted using the re-deployable smart mobile sensor concept for the structure subjected to individually both random (i.e., white noise/Gaussian excitation) and vehicle excitation.

The remainder of the paper is organized as: Re-deployable smart mobile sensor concept and Frequency Domain Decomposition method are presented in Sect. 2 and

Sect. 3. Section 4 briefly outlines the Vehicle-Bridge Interaction Formulation and the computation of acceleration records on vehicle loading. Section 5 explains the comprehensive step-by-step procedure of the proposed re-deployable mobile sensor-based mode shape estimation technique. Numerical investigations on the demonstration of the proposed re-deployable sensor concept for mode shape estimation are presented in Sect. 6 followed by conclusions in Sect. 7.

2 Re-deployable Smart Mobile Sensor Concept

A series of acceleration time history response measurements are taken from two accelerometers/two sensors by relocating it from one end of the bridge to the other. The accelerometers are re-deployed to different bridge nodes at different time instants. The position of the accelerometer is independent of the Vehicle loading (i.e., spatial location and speed of the vehicle). It should be mentioned here that each segment has two sensors on the bridge and one overlapping sensor node is assumed between each segment. The bridge acceleration responses from two sensors of each segment undergo a Frequency Domain Decomposition (FDD)/operational modal analysis technique to get local mode shapes. These mode shape data from different segments are then combined using a normalization/re-scaling procedure for the estimation of global mode shape. The re-scaling/normalization procedure is a decentralized procedure that combines the amplitude of the mode shape/dynamic sensitive feature of the common location of various segments to arrive at a single unique value globally.

The global mode shape (Φ_{Ω}^m) is the union of the total ‘n’ number of local mode shapes (i. e., Ω_s^m —‘s’th segment) and mathematically given by

$$\Phi_{\Omega}^m = \bigcup_{s=1}^n R_s \Phi_{\Omega_s}^m; \Omega_s^m = \begin{pmatrix} \Phi_{s,1}^{m,o} \\ \Phi_{s,1}^{m,o} \end{pmatrix}; \Omega_{s+1}^m = \begin{pmatrix} \Phi_{s+1,1}^{m,0} \\ \Phi_{s+1,1}^m \end{pmatrix}; R_s(\Phi_{s,1}^{m,o}) = R_{s+1}(\Phi_{s+1,1}^{m,o}) \tag{1}$$

where the superscript ‘m’ and ‘o’ indicates the ‘m’th mode and the overlapping node. The rescaling factor, R_s , is defined as the ratio of the mode shape amplitude at the ‘s’th segment overlapping node to the mode shape amplitude of the same node of the one at the ‘(s + 1)’th segment. The pictorial illustration of the procedure is presented in Fig. 1.

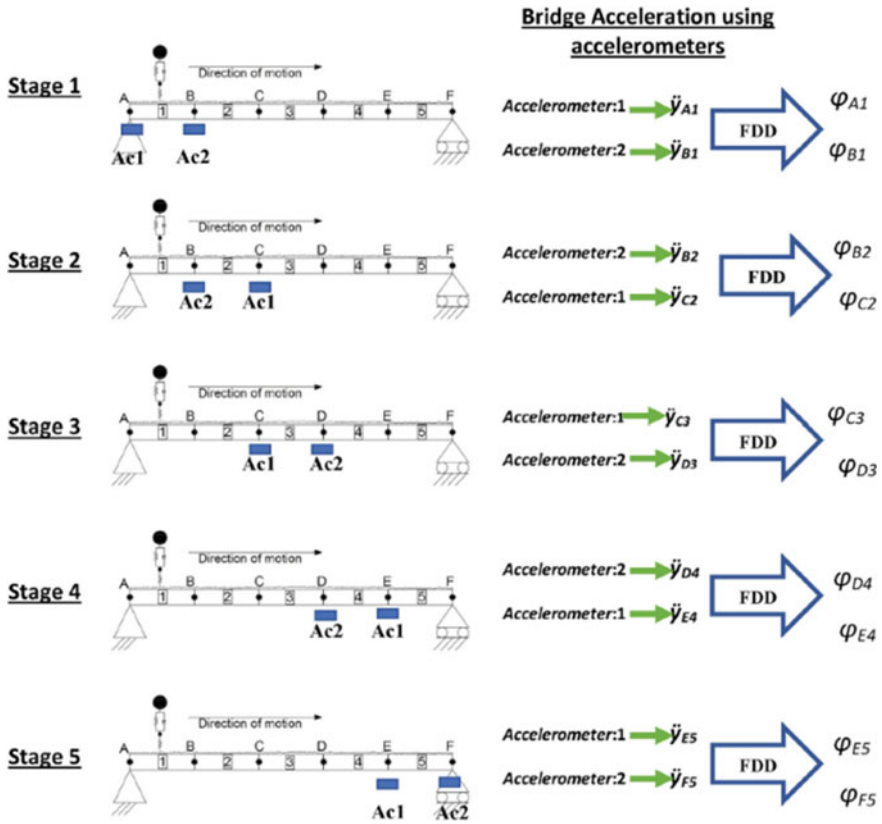


Fig. 1 Re-deployable sensor concept

3 Frequency Domain Decomposition (FDD)

The basic step of the Frequency Domain Decomposition (FDD) approach, is the estimation of the power spectral density (PSD) $G_{yy}(j\omega)$ observed at discrete frequencies $\omega = \omega_i$ and then decomposition of the PSD matrix using singular value decomposition:

$$G_{yy}(j\omega) = \hat{H}(j\omega)G_{FF}(j\omega)H(j\omega)^T \tag{2}$$

$$G_{yy}(j\omega) = U_i S_i U_i^H \tag{3}$$

where G_{yy} and G_{FF} represent the PSD of output and input respectively. The symbols H and \hat{H} indicate the frequency response function and its corresponding complex conjugate. The parameters U_i and S_i are the singular vectors unitary matrix and the singular value diagonal matrix.

The natural frequencies and mode shapes are computed respectively from the singular values and the singular vectors (i.e., U_i matrix). The singular vectors with the largest Modal Assurance Criterion (MAC) values are computed as modes. On the other hand, if none of the singular vectors has a MAC larger than a threshold, the search for matching parts of the spectral density is terminated.

The output PSD (i.e. response) is related to modal parameters by

$$G_{yy}(j\omega) = \sum_{k \in \omega} \frac{d_k \Phi_k \Phi_k^T}{j\omega - \lambda_k} + \frac{\overline{d_k \Phi_k \Phi_k^T}}{j\omega - \overline{\lambda_k}} \tag{4}$$

where d_k is another scalar constant and the parameters ϕ_k and λ_k indicate the mode shape and modal participation factors of the ‘ k^{th} mode.

4 Numerical Simulation of Bridge Response Considering Vehicle Bridge Interaction (VBI)

The simply supported bridge is idealized using the Finite Element Method as a 1D Euler–Bernoulli beam structure. Each beam element has 2 nodes with vertical translation and rotation being the degree of freedom (DOF) per node. It is also assumed that axial deformations are neglected. The beam is considered to be an ‘ n ’ DOF system. The vehicle is considered to be 4-DOF lumped mass system and moving with a constant velocity. It is also Assumed that there is no other vehicle on the bridge. The 4-DOF lumped mass system of the vehicle is popularly referred to as Half Car Model. Vehicle-bridge Interaction (VBI) has been widely studied both theoretically and experimentally to understand the behavior of both the vehicle and bridge during their interaction. VBI has great signification in the design of both the bridges and vehicles and also structural health monitoring. The representation of the considered vehicle model passing over the simply supported beam with constant velocity ‘ v ’ is illustrated in Fig. 2.

The equation of motion used for solving the VBI dynamics [7] is given by

$$M(t)\ddot{Y} + C(t)\dot{Y} + K(t)Y = Q(t) \tag{5}$$

where $[M(t)]$, $[C(t)]$, $[K(t)]$ are the coupled/global mass, damping, and stiffness matrix which are of $(n + 4) \times (n + 4)$ order, $\{Q(t)\}$ represents force matrix where n represents DOF of the bridge and 4 represents DOF of vehicle.

The global system matrices are mathematically given by

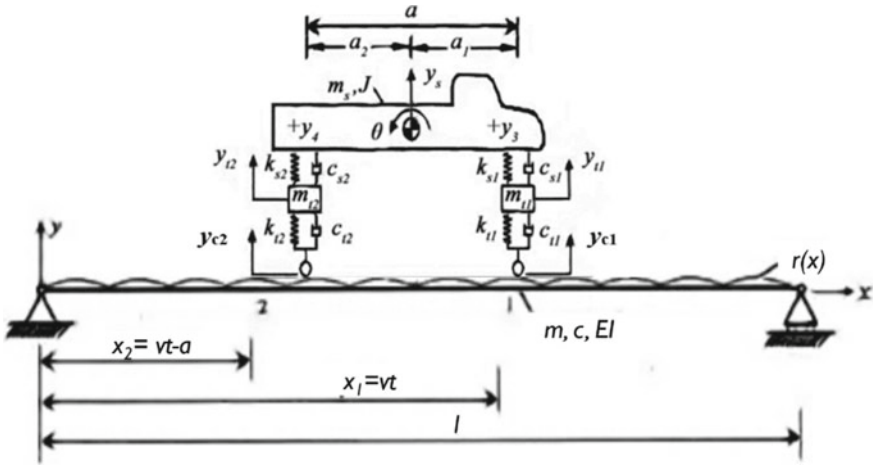


Fig. 2 Numerical modelling - vehicle bridge interaction

$$M(t) = \begin{bmatrix} m_s & 0 & 0 & 0 & 0 & 0 & \dots & 0 \\ 0 & J & 0 & 0 & 0 & 0 & \dots & 0 \\ 0 & 0 & m_{t1} & 0 & 0 & 0 & \dots & 0 \\ 0 & 0 & 0 & m_{t2} & 0 & 0 & \dots & 0 \\ \frac{a_2\varphi_{11}\delta_1 + a_1\varphi_{21}\delta_2}{a} m_s & \frac{\varphi_{11}\delta_1 - \varphi_{21}\delta_2}{a} J & \varphi_{11}\delta_1 m_{t1} & \varphi_{21}\delta_1 m_{t1} & 1 & 0 & \dots & 0 \\ \frac{a_2\varphi_{12}\delta_1 + a_1\varphi_{22}\delta_2}{a} m_s & \frac{\varphi_{12}\delta_1 - \varphi_{22}\delta_2}{a} J & \varphi_{12}\delta_1 m_{t1} & \varphi_{22}\delta_1 m_{t2} & 0 & 1 & \dots & 0 \\ \vdots & \vdots & \vdots & \vdots & \vdots & \vdots & \dots & \vdots \\ \frac{a_2\varphi_{1n}\delta_1 + a_1\varphi_{2n}\delta_2}{a} m_s & \frac{\varphi_{1n}\delta_1 - \varphi_{2n}\delta_2}{a} J & \varphi_{1n}\delta_1 m_{t1} & \varphi_{2n}\delta_1 m_{t2} & 0 & 0 & 0 & 1 \end{bmatrix} \quad (6)$$

$$C(t) = \begin{bmatrix} c_{s1} + c_{s2} & c_{s1}a_1 - c_{s2}a_2 & -c_{s1} & -c_{s2} & 0 & 0 & \dots & 0 \\ c_{s1}a_1 - c_{s2}a_2 & c_{s1}a_1^2 - c_{s2}a_2^2 & -c_{s1}a_1 & c_{s2}a_2 & 0 & 0 & \dots & 0 \\ -c_{s1} & -c_{s1}a_1 & c_{s1} + c_{t1} & 0 & -c_{t1}\varphi_{11}\delta_1 & -c_{t1}\varphi_{12}\delta_1 & \dots & -c_{t1}\varphi_{1n}\delta_1 \\ -c_{s2} & c_{s2}a_2 & 0 & c_{s2} + c_{t2} & -c_{t2}\varphi_{21}\delta_2 & -c_{t2}\varphi_{22}\delta_2 & \dots & -c_{t2}\varphi_{2n}\delta_2 \\ 0 & 0 & 0 & 0 & 2\xi_1\omega_1 & 0 & \dots & 0 \\ 0 & 0 & 0 & 0 & 0 & 2\xi_2\omega_2 & \dots & 0 \\ \vdots & \vdots & \vdots & \vdots & \vdots & \vdots & \dots & \vdots \\ 0 & 0 & 0 & 0 & 0 & 0 & 0 & 2\xi_n\omega_n \end{bmatrix} \quad (7)$$

$$k(t) = \begin{bmatrix} k_{s1} + k_{s2} & k_{sj}a_1 - k_{s2}a_2 & -k_{s1} & -k_{s2} & 0 & 0 & \dots & 0 \\ k_{s1}a_1 - k_{s2}a_2 & k_{s1}a_1^2 - k_{s2}a_2^2 & -k_{s1}a_1 & k_{s2}a_2 & 0 & 0 & \dots & 0 \\ -k_{s1} & -k_{s1}a_1 & k_{s1} + k_{s2} & 0 & (-c_{t1}\dot{\varphi}_{11} - k_{t1}\varphi_{11})\delta_1 & (-c_{t1}\dot{\varphi}_{12} - k_{t1}\varphi_{12})\delta_1 & \dots & (-c_{t1}\dot{\varphi}_{1n} - k_{t1}\varphi_{1n})\delta_1 \\ -k_{s2} & k_{s2}a_2 & 0 & k_{s2} + k_{t2} & (-c_{t2}\dot{\varphi}_{21} - k_{t2}\varphi_{21})\delta_2 & (-c_{t2}\dot{\varphi}_{22} - k_{t2}\varphi_{22})\delta_2 & \dots & (-c_{t2}\dot{\varphi}_{2n} - k_{t2}\varphi_{2n})\delta_2 \\ 0 & 0 & 0 & 0 & \omega_1^2 & 0 & \dots & 0 \\ 0 & 0 & 0 & 0 & 0 & \omega_2^2 & \dots & 0 \\ \vdots & \vdots & \vdots & \vdots & \vdots & \vdots & \dots & \vdots \\ 0 & 0 & 0 & 0 & 0 & 0 & 0 & \omega_n^2 \end{bmatrix} \quad (8)$$

$$Q(t) = \left\{ \begin{array}{c} 0 \\ 0 \\ (c_{t1} \dot{r}_1 + k_{t1}r_1)\delta_1 \\ (c_{t2} \dot{r}_2 + k_{t2}r_2)\delta_2 \\ -[\Phi_{11}W_1\delta_1 + \Phi_{21}W_2\delta_2] \\ -[\Phi_{12}W_1\delta_1 + \Phi_{22}W_2\delta_2] \\ \vdots \\ -[\Phi_{1n}W_1\delta_1 + \Phi_{2n}W_2\delta_2] \end{array} \right\} \quad (9)$$

where $[\delta]_{[0, \frac{a}{v}]} = \begin{bmatrix} 1 \\ 0 \end{bmatrix} \dots \dots [\delta]_{[\frac{a}{v}, \frac{l}{v}]} = \begin{bmatrix} 1 \\ 1 \end{bmatrix} \dots \dots [\delta]_{[l, \frac{(l+a)}{v}]} = \begin{bmatrix} 0 \\ 1 \end{bmatrix}$

$$W_1 = \left(m_s \frac{a_2}{a} + m_{t1}\right)g; \quad W_2 = \left(m_s \frac{a_1}{a} + m_{t2}\right)g \quad (10)$$

where m_s is the mass of the frame and the body of the vehicle, m_{t1} , m_{t2} are the mass of the axle between the front and rear wheelset and the tires, k_{s1} , k_{s2} , c_{s1} , c_{s2} are the stiffness and damping between wheelset and the body of the vehicle, k_{t1} , k_{t2} , c_{t1} , c_{t2} are the stiffness and damping of the tires, W_i Static load of the wheel and the vehicle body gravity of the wheel undertake, g acceleration due to gravity, J mass moment of inertia, a is the total length of the vehicle where a_1 and a_2 are the distance from the center of gravity of the vehicle. The parameters. $\varphi_{ij}, \xi_{ij}, \omega_j$ represents mode shapes, damping ratio and bridge natural frequencies at i^{th} node and j^{th} mode.

The bridge surface roughness profile is also involved in the vehicle-bridge interaction formulation to simulate as close to reality. The bridge surface roughness profile is commonly assumed to be represented by a normal zero-mean, real-valued stationary Gaussian process. It is mathematically given by

Table 1 Bridge surface roughness profiles - ISO

$G_d(n_0)$ (10^6m^3)				
Road class	Description	Lower limit	Geometric limit	Upper limit
A	Very good	-	16	32
B	Good	32	64	128
C	Average	128	256	512
D	Poor	512	1024	2048
E	Very poor	2048	4096	8192

$$R(x) = \sum_{i=0}^N \sqrt{2G_d(n_i)\Delta n} \cos(2\pi n_i x + \Phi_i) \quad (11)$$

$$G_d(n_i) = G_d(n_0) \left(\frac{n_i}{n_0}\right)^{-\omega}; n_i = n_l + i\Delta n; \Delta n = \frac{n_u - n_l}{m}; \omega = 2$$

where N (a value chosen between 100 to 10,000) is the total no. of harmonic waves, Φ_i is the random phase angle with a value chosen based on uniform distribution data between $[0, 2\pi]$. The parameters n indicate the spatial frequency and the subscripts 'o', 'u', and 'l' represent the reference, upper and lower limit respectively. The classification of bridge surface roughness profile as per ISO standard is given in Table 1.

5 Proposed Strategy

The step-by-step process of the proposed strategy of mode shape computation is presented below and also illustrated in the form of a Flow chart in Fig. 3

1. The Simply supported bridge is idealized using 1D Euler Beam element (with 'n' number of elements). The vehicle is modelled using a 4-DOF spring mass damper system referred to as the Half-car model. The coupled equation of motion is established using Vehicle-Bridge Interaction dynamics.
2. The two mobile sensors were placed at the first two nodes for data collection.
3. Frequency Domain Decomposition is applied to the collected data (i.e., acceleration-time history response corresponding to two sensors) to compute mode shapes. These obtained shapes are stated as local mode shapes which are stored until further stages.
4. Relocate/deploy the sensors to the next successive nodes maintaining one node common with the previous stage and step 3 is repeated till the end node of the right end support is reached.
5. All these stored local mode shapes were combined to form a global mode shape by normalization and re-scaling concept discussed in Sect. 2.

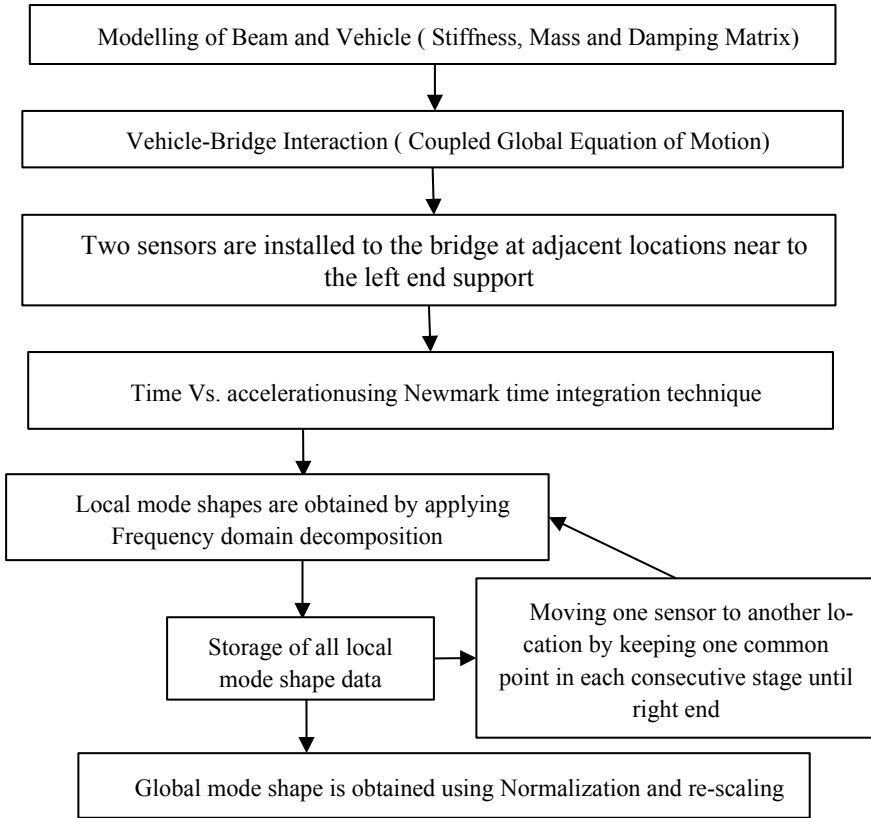


Fig. 3 Step-by-step procedure

6 Numerical Studies

The details of the simply supported beam (modelled using 1D Euler elements) and Vehicle model (Half Car Model – 4 DOF system) are presented in Tables 2 and 3. Implicit Newmark time marching scheme is used to obtain the time-series data measurements at different locations (i.e., acceleration time history measurements at 14 nodes excluding supports) of the beam. The simply supported beam is subjected

Table 2 Properties of bridge

Span/length (m)	Density ρ (kg/m ³)	Flexural rigidity EI (N.m ²)	Damping coefficient per unit length (μ)	Number of Elements
16	7850	2.05e10	0.025	15

Table 3 Properties of vehicle

Properties	Value	Properties	Value
m_s (Kg)	38,500	k_{t2} (N,m-1)	$4.28 * 10^6$
J (kg,m ²)	$2.446 * 10^6$	c_{s1} (N.sm-1)	$1.96 * 10^5$
m_{t1} (Kg)	4330	c_{s2} (N.sm-1)	$1.96 * 10^5$
m_{t2} (Kg)	4330	c_{t1} (N.sm-1)	$9.8 * 10^4$
k_{s1} (N,m-1)	$2.535 * 10^6$	c_{t2} (N.sm-1)	$9.8 * 10^4$
k_{s2} (N,m-1)	$2.535 * 10^6$	a ₁ (m)	4.2
k_{t1} (N,m-1)	$4.28 * 10^6$	a ₂ (m)	4.2
Vehicle speed: 5 and 10 m/s			

to individually random excitation and vehicle excitation. The sampling frequency considered is 1000 Hz.

6.1 Model Assurance Criterion (MAC)

To evaluate the accuracy of the mode shape estimated using the proposed re-deployable smart mobile sensor, mode shape is also estimated using static sensor concept and the results are compared. In addition, to quantify the accuracy of estimation of re-deployable sensor-based mode shape computation, a modal assurance criterion is employed in the present work.

In general, MAC is determined between mode shapes extracted analytically with experimentally. The magnitude of MAC lies between 0 and 1. High MAC (a value near 1) indicates that they are similar and fully consistent. Low MAC (a value near 0) implies that modes do not have any evenness. The MAC between the 'r'th mode and 'q'th mode is given by

$$MAC(r, q) = \frac{|\{\varphi_A\}_r^T \{\varphi_X\}_q|^2}{(\{\varphi_A\}_r^T \{\varphi_A\}_r)(\{\varphi_X\}_q^T \{\varphi_X\}_q)} \quad (12)$$

where $\{\varphi_A\}$, $\{\varphi_X\}$ refer to mode shape being measured analytically and experimentally. In the present work, mode shapes computed using a static sensor network are considered analytical mode shapes, and re-deployable sensor-based mode shapes are referred to as experimental mode shapes.

6.2 *Beam Subjected to Random/White Noise/Gaussian Excitation*

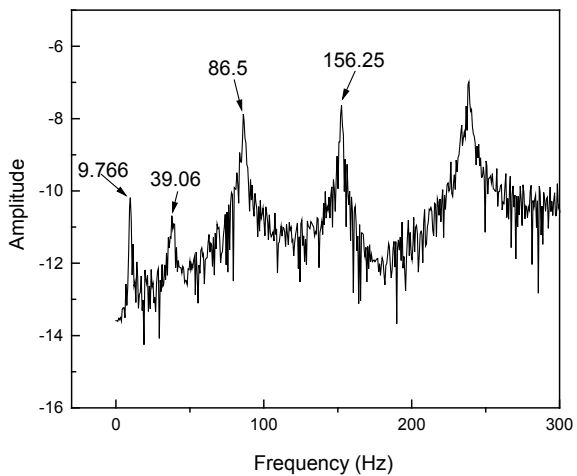
The acceleration Fourier spectrum corresponding to the 5th node for the simply supported beam subjected to random excitation at the center is presented in Fig. 4. The first four natural frequencies, identified from Fig. 4 are 9.766, 39.06, 86.5, and 156.25 Hz.

The first three mode shapes estimated using 16 static sensor measurements by using FDD are presented in Fig. 5. The mode shapes are also estimated using the proposed two sensor-based re-deployable sensing. The local mode shapes are first estimated for each segment (i.e., every two sensors) using FDD. Later, the global mode shape is obtained using the normalization and re-scaling procedure discussed in Sect. 2. The first three global mode shapes estimated using re-deployable mobile sensors are presented in Fig. 5 along with the results of the static sensor network. Figure 5 depicts that the mode shapes estimated using static sensor network (i.e., using 14 sensors) and re-deployable mobile sensors (i.e., using 2 sensors) are matching very well.

Similar to Fig. 5, the results of the mode shape estimated using static and re-deployable mobile sensors for the simply supported beam subjected to random excitation at 1/4th span of the beam are presented in Fig. 6. Figure 6 depicts that the mode shape can be estimated accurately using the proposed re-deployable mobile sensors similar to that of the static sensor network.

The results of the modal assurance criterion values (MAC) for the simply supported beam subjected to random excitation being applied at two different locations are presented in Table 4. It can be noticed from Table 4 that MAC of 1 is achieved for the first mode shape and MAC > 0.9 is achieved for other modes for the beam subjected to random excitation at two different locations.

Fig. 4 Fourier spectrum computed using FFT of 5th node response



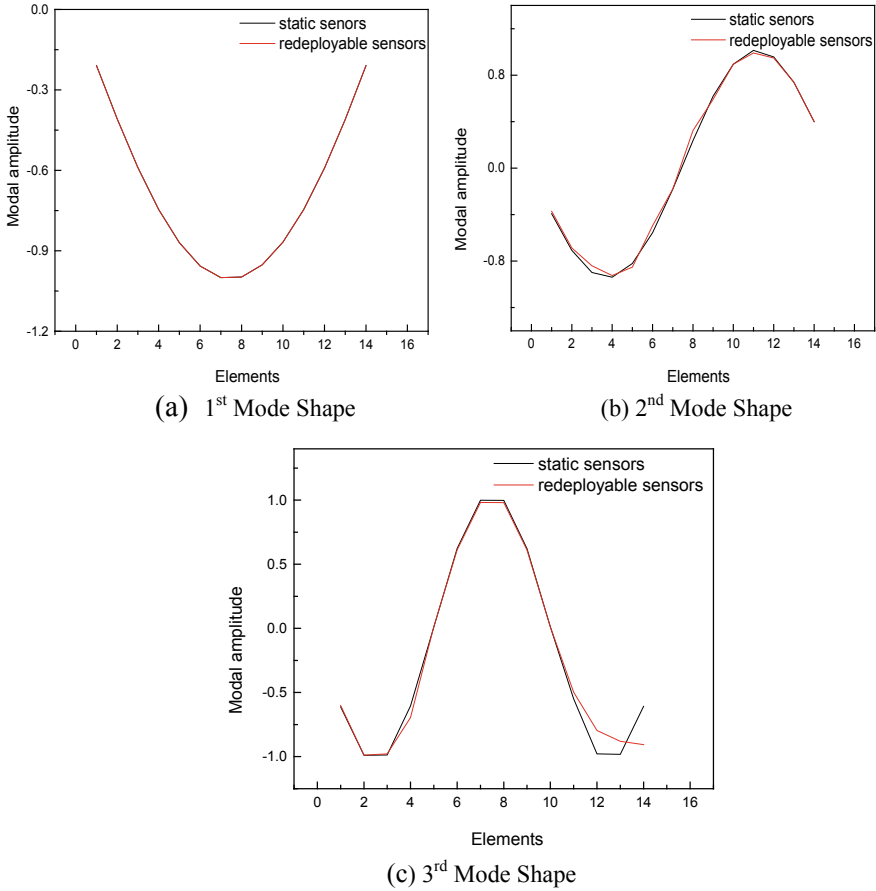


Fig. 5 Mode shapes – estimated for SS beam subjected to random excitation at center

Therefore, it can be concluded from Table 4, irrespective of varying load location and amplitude of random excitation, all the first three mode shapes are estimated with modal assurance criterion greater than 0.9. It should be mentioned here that we have considered a total of 15 sensors in the present work. If the number of local segments (>14 nodes), the accuracy of mode shape estimation accuracy also increases.

6.3 Beam Subjected to Vehicle Excitation

Besides the demonstration of estimation of mode shapes of the beam subjected to random excitation, the proposed re-deployable is also verified for the beam subjected to vehicle excitation (i.e., passing traffic). The Half car Model is considered for

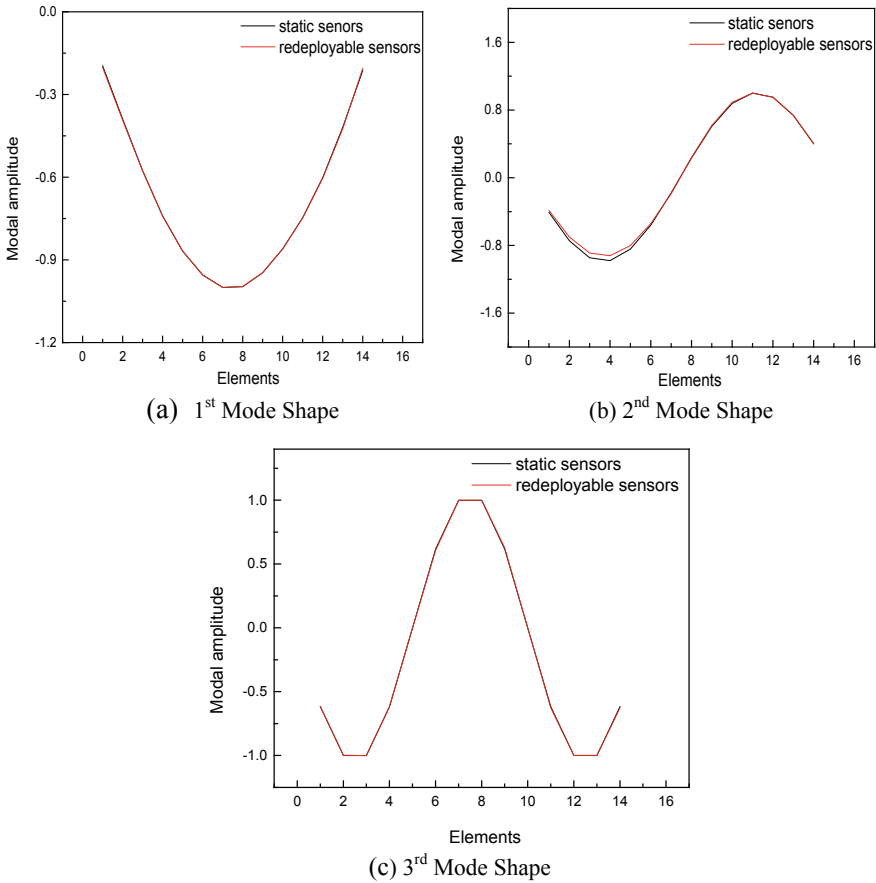


Fig. 6 Mode shapes – estimated for SS beam subjected to random excitation at 4 m from the left support

Table 4 MAC - random excitation

Mode shape	Load at center	Load at 4 m from left-hand support
Mode shape 1	1.00	1.00
Mode shape 2	0.91	0.96
Mode shape 3	0.94	1.00

vehicle loading and the vehicle is running with constant velocity when passing over the target beam. The medium Level of roughness (i.e., Road Class B) defined in Table 1 is considered to simulate bridge surface roughness profile.

Two different cases of vehicle excitations are considered i.e. vehicle being run at two different velocities. The two different velocities of the vehicle considered

are 5 and 10 m/s. It should be mentioned here that the vehicle speed will influence the bridge acceleration records as the interaction of the vehicle with the bridge will be lesser if the vehicle is running at a higher velocity. This in turn influences the estimation of mode shapes to at least a little extent.

The results of the first three mode shapes computed using static sensor network and re-deployable mobile sensing concept with the vehicle running at two different constant velocities while passing the target beam are presented in Fig. 7. It can be observed from Fig. 7 that the mode shapes can be estimated reliably estimated using the re-deployable sensor concept for the beam subjected to vehicle excitation.

The modal assurance criterion of the mode shape estimated between static sensors and the re-deployable mobile sensor concept for the simply subjected beam subjected to vehicle excitation is presented in Table 5.

It can be observed from Table 5 that when the vehicle runs at low velocity, all the mode shapes are estimated with MAC greater than 0.95. In the case of vehicle runs at a high velocity of 10 m/s, the MAC is found to be greater than 0.9 but lesser

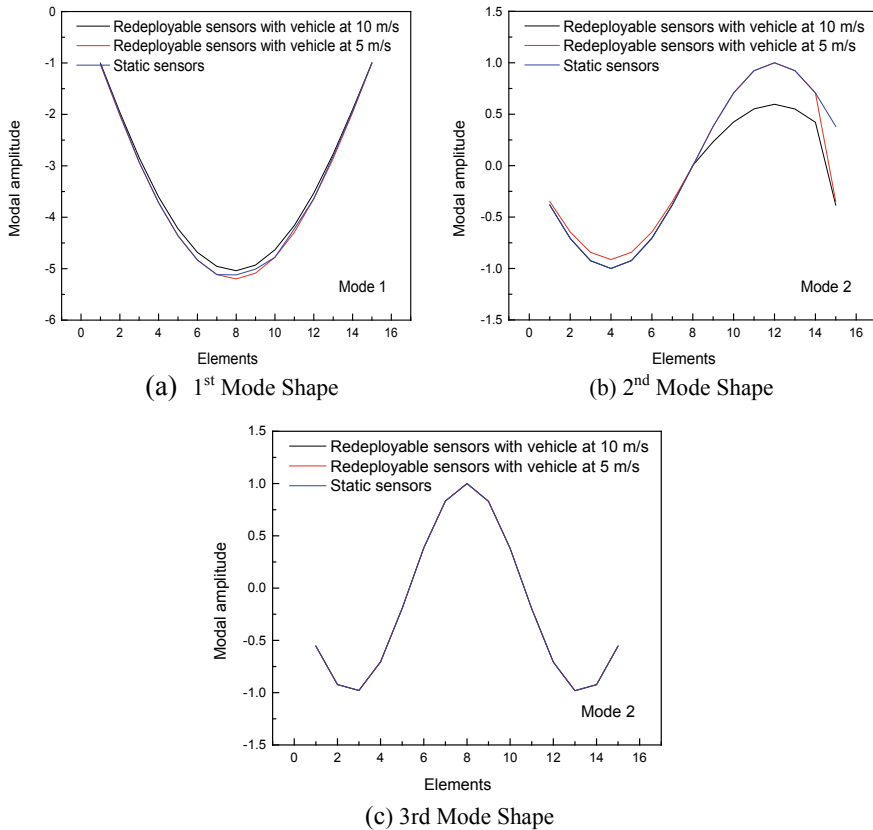


Fig. 7 Mode shapes – estimated for SS beam subjected to vehicle excitation

Table 5 MAC - vehicle excitation

Mode shape	Vehicle velocity	
	10 m/s	5 m/s
Mode shape 1	1.00	1.00
Mode shape 2	0.905	0.96
Mode shape 3	1.00	1.00

than the case of low velocity. This agrees with the physics of the Vehicle Bridge Interaction. Therefore, it can be concluded that the first three mode shapes can be computed using the re-deployable smart mobile sensor concept with an accuracy of MAC value greater than 0.9 irrespective of the target bridge subjected to ambient or passing traffic in practice. The proposed re-deployable mobile sensor concept paves way for the estimation of dynamic sensitive features (i.e., mode shape) in real-time under passing traffic independent of time, the spatial location, and velocity of the vehicle. The accuracy of mode shape estimation increases with the increase in the number of sensor node measurements.

7 Conclusions

The paper presents the application of the re-deployable mobile sensing concept for decentralized mode shape estimation using bridge acceleration records. Numerical investigation on a simply supported beam subjected to individually random and vehicle excitation is considered to compute mode shape using the proposed concept. The results from the numerical simulation demonstrate and quantify the effectiveness of re-deployable mobile sensing in mode shape estimation using two sensors and can be implemented on a network of smart wireless sensors at a wider scale for the SHM of bridge infrastructure. The results also concluded that with the Re-deployable sensor concept, MAC of above 0.9 is achieved when compared to static sensor concept even with medium roughness road profile. It should be highlighted here that the MAC values will increase with the increase in the number of nodes i.e. decrease in the spatial resolution between the two mobile sensors. The proposed re-deployable mobile sensing-based decentralized mode shape estimation approach is robust and reliable irrespective of the type of excitation being random or vehicle excitation. The proposed concept estimates mode shapes more reliably even sensors are moved over time and independent of passing traffic. It is also feasible to extend the proposed concept for structures with localized damage towards the application of structural health monitoring.

References

1. Avci O, Abdeljaber O, Kiranyaz S., Hussein M, Gabbouj M, Inman DJ (2021) A review of vibration-based damage detection in civil structures: from traditional methods to machine learning and deep learning applications. *Mech Syst Sig Process* 147:107077
2. Nayek R, Mukhopadhyay S, Narasimhan S (2018) Mass normalized mode shape identification of bridge structures using a single actuator-sensor pair. *Struct Control Health Monit* 25(11):e2244
3. Malekjafarian A, OBrien EJ (2014) Identification of bridge mode shapes using short time frequency domain decomposition of the responses measured in a passing ehicle. *Eng Struc* 81:386–397. <https://doi.org/10.1016/j.engstruct.2014.10.007>
4. Brincker R, Zhang L, Andersen P (2001) Modal identification of output-only systems using frequency domain decomposition. *Smart Mater Struct* 10(3):441
5. Sim SH, Spencer BF Jr, Zhang M, Xie H (2010) Automated decentralized modal analysis using smart sensors. *Struct Control Health Monit* 17(8):872–894
6. Khan MA, et al. (2021) Re-deployable sensors for modal estimates of bridges and detection of damage-induced changes in boundary conditions. *Struc Infrastruc Eng* 10:1–5
7. Duan R, Yang J (2013) Modelling and simulation of a bridge interacting with a moving vehicle system. Ph.D. Thesis

Ballistic Study of Shear Thickening Fluid Impregnated Unidirectional Ultra-High Molecular Density Polyethylene Fabric



Vagish D. Mishra , Ashish Mishra , Avinash Singh, Luv Verma ,
and G. Rajesh 

Abstract A ballistic test in the velocity range of 280–700 m/s is performed on the target panel comprised of 30 layers of neat and shear thickening fluid impregnated unidirectional (UD) ultra-high molecular weight polyethylene (UHMWP) fabric. The energy absorbed by shear thickening fluid treated panel is higher than their neat counterparts for the nearly identical impact velocities. A maximum improvement of 12.83% is obtained in energy absorbed by shear thickening fluid treated panel at an impact velocity of 691 ± 4 m/s. Also, the ballistic limit of the STF treated panel is increased by 5.2%. Enhancement in the ballistic performance of the target panel is attributed to the increased friction between the layers of STF treated UD UHMWP fabric.

Keywords Ballistic impact · UHMWP fabric · Shear thickening fluid

1 Introduction

Soft armours are generally made up of high-performance fabrics such as aramid or ultra-high molecular density polyethylene (UHMWP). Layers of fabric are stacked to construct the protective armours for the desired level of threat. However, the stacking

V. D. Mishra · A. Singh · G. Rajesh
Department of Aerospace Engineering, Indian Institute of Technology Madras,
Chennai 600036, India

A. Mishra (✉)
Department of Aerospace Engineering, University of Petroleum and Energy Studies,
Dehardun 248007, India
e-mail: ashish.mishra@ddn.upes.ac.in

L. Verma
Department of Applied Mechanics, Indian Institute of Technology Madras,
Chennai 600036, India

can make the protective armour stiff and bulky, thus reducing the wearer's mobility, especially in the combat situation. Energy absorption by protective armour depends on the fabric structure [21, 26]. Fabric arrangements such as unidirectional (UD) [18], woven (2D/3D) [4–6], warp-knitted [17] are used for making soft armours.

An effort has been made to improve the ballistic resistance of these fabrics without affecting the flexibility and weight of the armour through surface treatments [16]. Use of latex/natural rubber [1], polyvinyl acetate [10, 11], and shear thickening fluids (STFs) [7] are some of the coating materials which are explored to improve the structural integrity of the fabric and hence the ballistic performance. The most promising of the above technique is the use of STFs to improve the ballistic performance through surface modification of the fabric. Shear thickening fluids exhibit an abrupt increase in the viscosity with an increase in shear rate or rate of applied mechanical load [16, 23]. Various studies conducted by the researchers to study the influence of STF impregnation on fabric against a threat such as a knife, spike, and low impact velocity [3, 7, 8, 13, 14, 22]. Liu et al. [14] conducted ballistic test on STF impregnated woven fabric at an impact velocity of 244 m/s. They reported that STF impregnated Kevlar fabric improved the ballistic resistance without affecting the flexibility. Sun et al. [22] investigated the effect of silica mass fraction on stab resistance of STF impregnated woven UHMWP fabric. A similar study by Li et al. [13] concluded that the stab resistance of woven UHMWP fabric enhanced through STF impregnation. They reported that the STF impregnation decreases yarn mobility due to increment in the inter-yarn friction, thus prevents slipping of a projectile through the fabric. Fabric structure further affects yarn mobility, and hence the performance of protective armours [3].

Although the UD fabrics have desirable ballistic properties, their complex manufacturing process incurs high manufacturing cost compared to woven fabric that have matured weaving technology and easy processing [19]. Therefore, the latter attracts more attention from the researchers to further enhance the performance of fabric through surface treatment like STF, natural rubber latex etc. Extensive research is done to study the influence of surface treatment on woven fabric; however, a very limited study is found on the UD fabric. For ex., Ahamd et al. [2] revealed that the ballistic resistance of natural rubber coated UD UHMWP fabric is superior to the neat fabric. They reported that the elastomer coating improves the structural integrity of the through friction and results in increased energy absorption against the ballistic impact. A related work by Hassim et al. [9] found that the fabric wetting route influences the impact resistance of the ballistic material. Liu et al. [14] found that the addition of shell particles improves ballistic resistance of UD laminate by 20%. However, to the best of the authors' knowledge, the effect of STF impregnation on the UD UHMWP fabric has been not studied yet. Therefore, the present study explores the impact of STF treatment on the ballistic resistance of UD UHMWP fabric through the deep wetting method.

In UD fabrics, straight fibres are laid in the 0° and 90° orientation which are bonded using an adhesive resin to allow efficient energy transfer on impact. Due to the absence of the cross over points in UD fabrics, the stress waves can propagate to a large area on impact [26]. Mawkhlieng et al. [15] found that placing a few UD-UHMWP fabric layers in the front of stacked STF treated woven fabrics results in the reduction

of amount of back deformation, also known as back face signature (BFS), of ballistic material after impact in comparison to equivalent all woven fabric layers in a hybrid armour system, comprised of layers of both unidirectional UD and 2D woven fabrics. The maximum permissible indent/deformation is 1.73 in. (44 mm) set by the National Institute of Justice (NIJ) for personal body armour [12]. Mawkhlieng et al. [15] further reported that the improvement in the hybrid armour system's ballistic performance is due to the dissipation of energy to the large surface area of UD-UHMWP fabric owing to straight fibre arrangement i.e. free from any undulation or crimp unlike in woven fabric. Ahmad et al. [2] reported that the ballistic limit and energy absorption of UD-UHMWP fabric is improved through natural rubber/latex coating. Zhang et al. [26] found that UD fabric outperforms the woven against ballistic impact due to the absence of the cross over points in the former. They conducted the ballistic test for the impact velocities of about 700 m/s; however, the influence of STF impregnation was not addressed. Therefore, an attempt has been made in the present study to improve the ballistic resistance of UD-UHMWP fabric through STF impregnation and compare their ballistic performance with their neat counterparts.

2 Materials

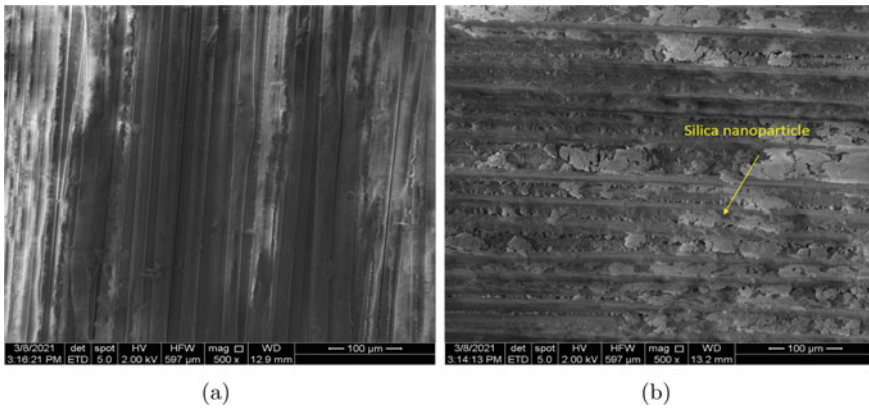
UD-UHMWP fabric used in the present study was procured in the prepreg form, which comprised of a cross-ply arrangement of high tenacity UHMWP fibres bonded using a thermoset resin. The properties of UD-UHMWP fabric are shown in Table 1. Shear thickening fluid (STF) was synthesized by dispersing 40% wt. fumed nanoparticle silica in polyethylene glycol of molecular weight 400 (PEG 400) [24]. The mixture then diluted with ethanol to decrease the viscosity of the solution for efficient impregnation. Figure 1 shows the surface morphology of neat and STF treated fabric examined through a scanning electron microscope (SEM). A small agglomeration of silica particle was observed between the fibres of STF treated fabric; however, this effect can be considered negligible on account of improvement in the ballistic performance [20]. Neat UD-UHMWP fabric sheets of size 150mm × 100 mm² were cut to prepare the panel consisting of total 30 layers (30L). The layers were bonded from their boundaries using epoxy adhesive to avoid slipping during impact. Neat UD-UHMWP layers are first impregnated with the STF solution and then dried in an oven for 40 min at 80°C to remove the ethanol. After that, the impregnated layers of equivalent number as neat UD-UHMWP fabric were stacked to prepare STF treated UHMWP (STF-UHMWP) panel. Table 2 shows the properties of fabricated 30 layers neat and STF treated panel. The projectile consists of aluminium of mass 4 gm and has cylindrical geometry with a nearly hemispherical nose end of a 10 mm diameter.

Table 1 Properties of UD-UHMWP fabric

Areal weight	210 gsm
Breaking tenacity	3.5 GPa
Tensile Modulus	110 Gpa
Elongation at break	3.6%

Table 2 Properties of 30 layer neat and STF treated UD-UHMWP fabric panels

Material	Mass (g)	Areal density (kg/m ²)	Panel thickness (mm)
neat UD-UHMWP	58.34	3.89	4.8
STF-UHMWP	61.80	4.11	5.4

**Fig. 1** SEM images of neat and STF treated UD-UHMWP fabric

3 Experiment and Results

The ballistic evaluation of the target in the present study is performed using an aeroballistic range facility as shown in Fig. 2(a). The target was sighted at a distance of 0.5 m from the exit end of the launch tube and attached to a metallic fixture connected to the pinned rod. The fixture used to support the target is shown in Fig. 2(b). Zeng et al. [25] reported that the fabric with four edges clamped leads to lower energy absorption compared to clamping at two edges. They revealed that reducing the clamping pressure leads to greater transverse deflection of material and thus increases energy absorption. They also reported that fabric target clamped with four edge fails earlier than clamping at two edges as stress waves reflected from all the four edges in the former. Therefore to closely mimic the real situation, the target was clamped only from two edges instead from all four edges. The top and bottom edge of the target panel was fixed to the frame, while the side ends were free from any support. The impact and residual velocities are measured using a high-speed camera, iX camera (model

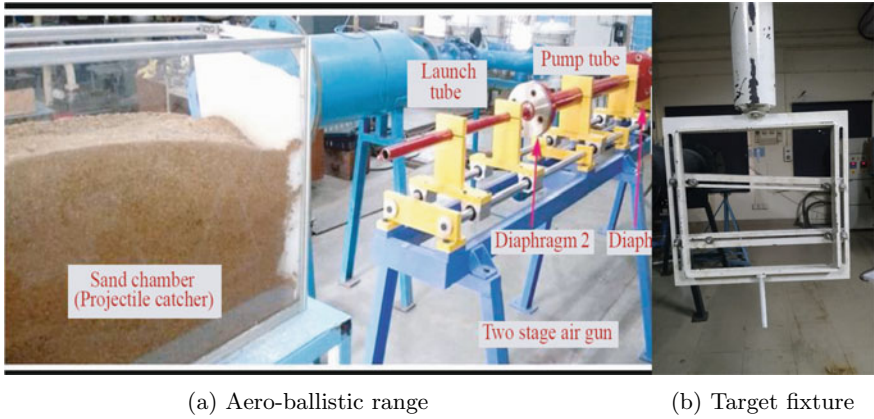


Fig. 2 Experimental setup

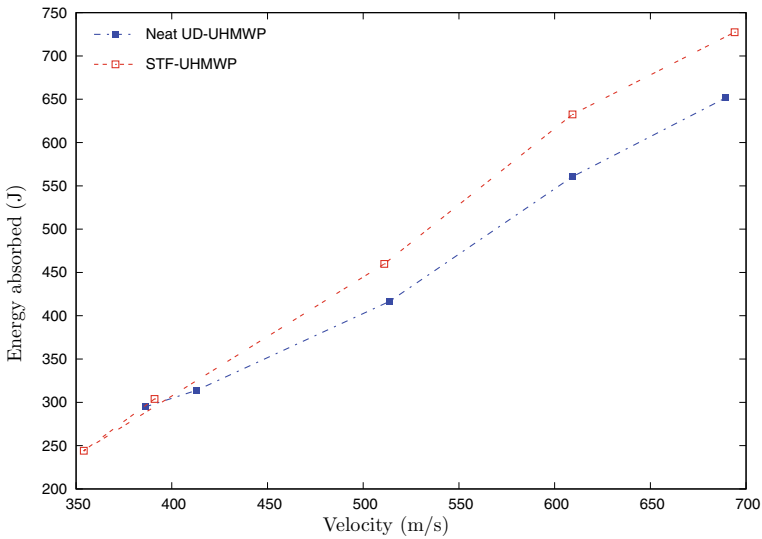


Fig. 3 Variation of energy absorption with impact velocities of neat and STF treated 30L UD-UHMWP fabric panel

i-SPEED 726), which captures the events at a maximum of 1×10^6 frame per second (fps). In the case of complete penetration, the projectile was recovered from the sand chamber placed at the back of the target support. All tests were conducted at room temperature.

4 Results and Discussion

The impact test was performed between the velocity range of 280–700 m/s on both the neat and STF treated UD-UHMWP panel. It was challenging to achieve a similar velocity for both neat and STF treated target; however, the impact velocities were kept in a tight limit enough by regulating the gas pressure and choosing a suitable thickness of diaphragm material so that a fair comparison can be made. The energy absorbed (ΔE) by the completely perforated target was calculated using Eq. 1

$$\Delta E = \frac{1}{2}m_p (V_i^2 - V_r^2), \quad (1)$$

where, m is the mass of the projectile, V_i and V_r denote the impact and residual velocity of the projectile, respectively. Figure 3 shows the energy absorbed by the 30 layers (30L) neat and STF treated completely penetrated panels of UD-UHMWP fabric for impact velocities between 350–700 m/s. The energy absorbed by the STF treated panel is higher than the neat ones for the range of impact velocities. The difference between the energy absorption of the neat and treated panel is more apparent at higher impact velocities with a maximum improvement of 12.83% at an impact velocity of 609 ± 4 m/s. However, the enhancement in the energy absorption of neat and STF treated panels is not monotonous, as there is a decrease in the value was observed at an impact velocity of 692 ± 3 m/s. The drop in energy absorption was due to the high kinetic energy of the projectile. The improvement in energy absorption of 30L STF treated panel at an impact velocity of 512 ± 4 m/s is 10.38%.

To assess the addition of STF on the ballistic performance of UD-UHMWP fabric, the specific energy absorption (SEA) of neat and STF treated UD-UHMWP fabric is determined using Eq. 2.

$$SEA = \frac{\frac{1}{2}m_p (V_i^2 - V_f^2)}{AD}. \quad (2)$$

where, AD is the areal density of the panels (kg/m^2). Figure 4 depicts the SEA of 30L neat and STF treated panel at various impact velocities. SEA of STF treated panel is higher than the neat panels, which indicates that the enhancement in energy absorption overcome the weight addition of STF. The increase in energy absorption is attributed to the increased friction between the layers of the STF treated panel.

Table 3 Ballistic limit and energy absorption of 30L neat and STF treated UD-UHMWP fabric panels

Parameter	Neat UD-UHMWP	STF-UHMWP	Percentage change
Ballistic limit (m/s)	363	382	5.2%
Energy absorbed at ballistic limit (J)	263.39	286.14	10.8%

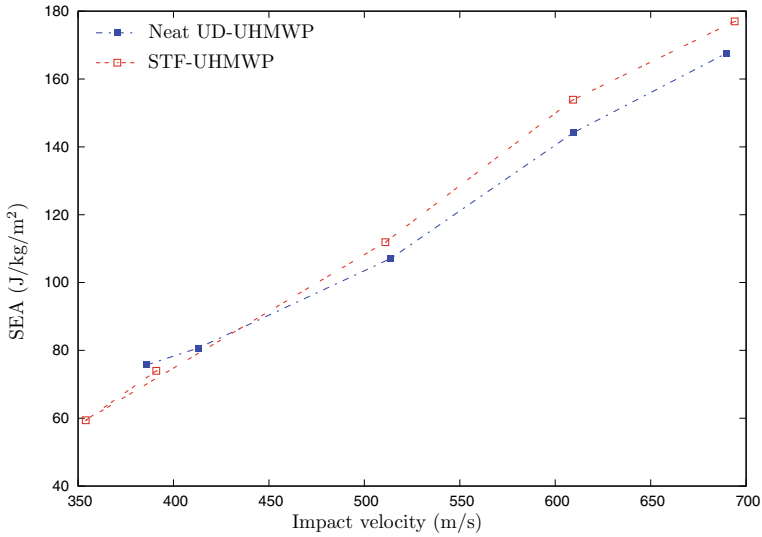


Fig. 4 Variation of specific energy absorption (SEA) with impact velocities of neat and STF treated 30L UD-UHMWP fabric panel

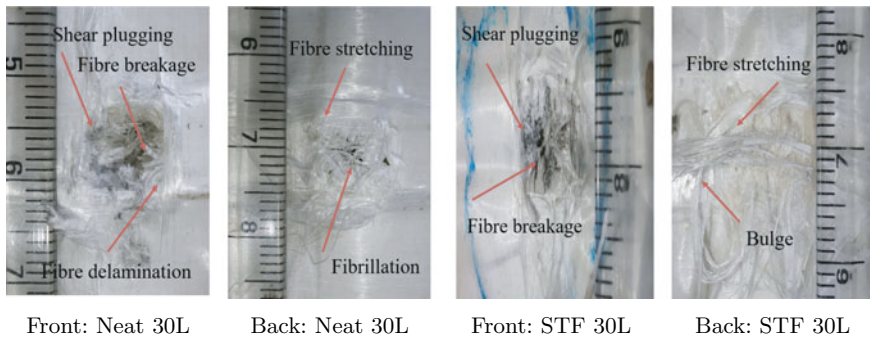


Fig. 5 Post impact front and rear pictures of neat and STF treated 30 layers UD-UHMWP fabric panel at an impact velocity of 512 ± 4 m/s

STF addition, therefore, contributes to an increase in the energy absorption of UD-UHMWP fabric without affecting the flexibility and weight penalty of the target.

The ballistic limit, V_{50} , of the neat and STF treated panel was determined by calculating the average of impact velocities of three partial and three complete penetration events. Table 3 shows the ballistic limit of neat and STF treated 30L UD-UHMWP panel. An increment of 5.2% in the ballistic limit and 10.8% in the corresponding energy absorption was obtained for the STF treated panels.

4.1 Failure Mechanisms

During the ballistic impact, the kinetic energy of the bullet is reduced by the target through various failure mechanisms. Figure 5 shows the post-impact front and rear face of 30L neat and STF treated perforated panel at an impact velocity of 512 ± 4 m/s. The failure events at the front face of the neat and STF treated panel were similar. Both the panels exhibit fibre breakage, shear plugging and fibre delamination at the impact site. The damage events at the rear face of the neat and STF treated panels were different. Distortion of the nearby fibre was severe in the neat UD-UHMWP in comparison to the STF treated panel. Hence, the failure events were more localised in the neat panel compared to the STF impregnated ones. In the STF impregnated panel,

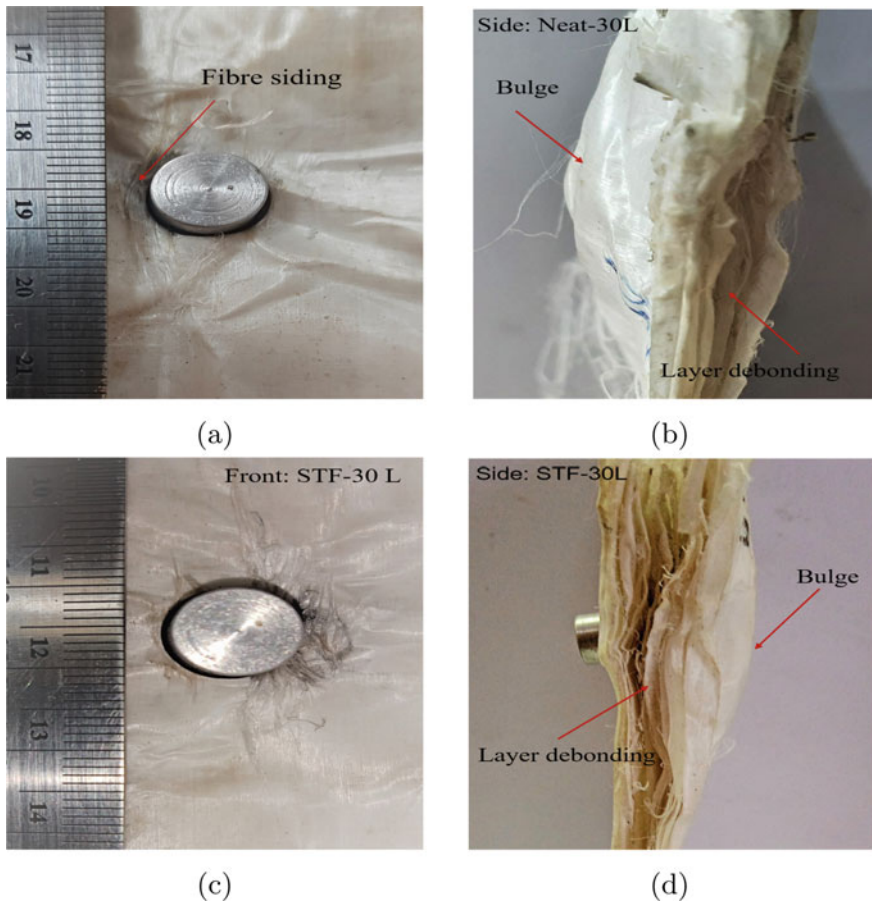


Fig. 6 Front and side face (a, b) of partially penetrated neat 30-layer UD-UHMWP fabric at impact velocity of 312 m/s. Front and side image (c, d) of partially penetrated STF treated UD-UHMWP at impact velocity 316 m/s

the secondary fibres away from the impact site were stretched, with fibre breakage occurred under the impact load. This results in the dissipation of the energy to a large area and renders greater energy absorption of the STF impregnated panel Fig. 6 show the front and side faces of partially penetrated neat and STF treated 30L panel at an impact velocity of 312 and 316 m/s, respectively. 13 layers were perforated in the neat panel while perforation of 11 layers occurred in the STF treated panel. Neat panels offer lower resistance to the projectile. Also, due to the lower friction between the neat UD-UHMWP fabric layers, the projectile pushes the fibre aside during the course of penetration while projectile energy dissipated in the breaking of high tenacity fibre in STF treated panel results in penetration in the lower number of layers.

5 Conclusion

Impact test in the velocity range of 280–700 m/s is conducted on the target panels consist of 30 layers of neat and STF treated fabric. The influence of STF impregnation on the ballistic performance of UD-UHMWP is studied. For a fair comparison, the impact velocities of neat and STF treated panels remained at a close limit. During the ballistic evaluation, the following observation is concluded.

- STF treated panel exhibits superior ballistic resistance for the range of impact velocities.
- The increase in the energy absorption of the STF treated panel is attributed to the enhancement in friction between the STF treated fabric layers and the shear thickening effect.
- Maximum enhancement in energy absorption of STF treated panel was about 12.83 % at an impact velocity of 609 ± 4 m/s. The ballistic limit of the STF treated panel is improved by 5.2%.
- At an impact velocity 512 ± 4 m/s the failure events in neat UD-UHMWP panels were localised with severe fibre breakage at the impact site; however, in STF treated fabric panel, the secondary fibres away from the impact site were also contributed in energy absorption by undergoing transverse deformation through stretching of fibres.

References

1. Ahmad M, Ahmad W, Samsuri A, Salleh J, Abidin M (2010) Blunt trauma performance of fabric systems utilizing natural rubber coated high strength fabrics. In: AIP conference proceedings, vol 1217, pp 328–334. American Institute of Physics
2. Ahmad M, Hassim N, Ahmad W, Samsuri A, Yahya M (2013) Preliminary investigation on the ballistic limit of ultra high molecular weight polyethylene unidirectional coated fabric system. *Fibres Text East Eur* 3(99):89–94

3. Arora S, Majumdar A, Singh Butola B (2020) Interplay of fabric structure and shear thickening fluid impregnation in moderating the impact response of high-performance woven fabrics. *J Compo Mater* 54(28):4387–4395
4. Bandaru AK, Chavan VV, Ahmad S, Alagirusamy R, Bhatnagar N (2016) Low velocity impact response of 2D and 3D kevlar/polypropylene composites. *Int J Impact Eng* 93:136–143
5. Chu CK, Chen YL (2010) Ballistic-proof effects of various woven constructions. *Fibres & Text East Eur* 18: 63–67
6. El Messiry M, Eltahan E (2016) Stab resistance of triaxial woven fabrics for soft body armor. *J Ind Text* 45(5):1062–1082
7. Gürgen S, Kuşhan MC, Li W (2017) Shear thickening fluids in protective applications: a review. *Progr Polym Sci* 75:48–72
8. Hasanzadeh M, Mottaghtalab V (2014) The role of shear-thickening fluids (stfs) in ballistic and stab-resistance improvement of flexible armor. *J Mater Eng Perform* 23(4):1182–1196
9. Hassim N, Ahmad MR, Ahmad WYW, Samsuri A, Yahya MHM (2012) Puncture resistance of natural rubber latex unidirectional coated fabrics. *J Ind Text* 42(2):118–131
10. Ignatova A, Dolganina NY, Sapozhnikov S, Shabley A (2017) Aramid fabric surface treatment and its impact on the mechanics of yarn's frictional interaction. *PNRPU Mecha Bull* 4:121–137
11. Ignatova A, Kudryavtsev O, Zhikharev M (2020) Influence of surface polymer coating on ballistic impact response of multi-layered fabric composites: experimental and numerical study. *Int J Impact Eng* 144:103654
12. of Law Enforcement Standards (OLES), O., of America, U.S.: Ballistic resistance of body armor INJ standard-0101.06 (2008)
13. Li W, Xiong D, Zhao X, Sun L, Liu J (2016) Dynamic stab resistance of ultra-high molecular weight polyethylene fabric impregnated with shear thickening fluid. *Mater Des* 102:162–167
14. Liu S, Wang J, Wang Y, Wang Y (2010) Improving the ballistic performance of ultra high molecular weight polyethylene fiber reinforced composites using conch particles. *Mater Des* 31(4):1711–1715
15. Mawkhlieng U, Majumdar A (2020) Designing of hybrid soft body armour using high-performance unidirectional and woven fabrics impregnated with shear thickening fluid. *Compos Struct* 253:112776
16. Mawkhlieng U, Majumdar A, Laha A (2020) A review of fibrous materials for soft body armour applications. *RSC Adv* 10(2):1066–1086
17. Miao X, Jiang G, Kong X, Zhao S (2014) Experimental investigation on the stab resistance of warp knitted fabrics. *Fibres Text East Eur* 22:65–70
18. Pandya K, Shaktivish S, Gowtham H, Inani A, Naik N (2015) Shear plugging and frictional behaviour of composites and fabrics under quasi-static loading. *Strain* 51(5):419–426
19. Park JL, Chi YS, Kang TJ (2013) Ballistic performance of hybrid panels composed of unidirectional/woven fabrics. *Text Res J* 83(5):471–486
20. Park Y, Kim Y, Baluch AH, Kim CG (2014) Empirical study of the high velocity impact energy absorption characteristics of shear thickening fluid (stf) impregnated kevlar fabric. *Int J Impact Eng* 72:67–74
21. Stempień Z (2011) Effect of velocity of the structure-dependent tension wave propagation on ballistic performance of aramid woven fabrics. *Fibres Text East Eur* 19(4):87
22. Sun LL, Xiong DS, Xu CY (2013) Application of shear thickening fluid in ultra high molecular weight polyethylene fabric. *J Appl Polym Sci* 129(4):1922–1928
23. Wagner NJ, Brady JF (2009) Shear thickening in colloidal dispersions. *Phys Today* 62(10):27–32
24. Wang X, Zhang J, Bao L, Yang W, Zhou F, Liu W (2020) Enhancement of the ballistic performance of aramid fabric with polyurethane and shear thickening fluid. *Mater Des* 196:109015
25. Zeng X, Shim V, Tan V (2005) Influence of boundary conditions on the ballistic performance of high-strength fabric targets. *Int J Impact Eng* 32(1–4):631–642
26. Zhang D, Sun Y, Chen L, Zhang S, Pan N (2014) Influence of fabric structure and thickness on the ballistic impact behavior of ultrahigh molecular weight polyethylene composite laminate. *Mater Des* 1980–2015(54):315–322

Effect of Steel Fibre Content on the Information Entropy of Acoustic Emission Waveforms Generated During Mode I Fracture Process in Cementitious Composites



Indrashish Saha and R. Vidya Sagar

Abstract This article reports the variation of ‘information entropy’ of Acoustic Emission (AE) waveforms in steel fibre reinforced concrete (SFRC) as the volume fraction of the steel fibre (V_f) is increased from 0.0 to 1.6%. Information entropy is the measure of uncertainty in the probability distribution of a random variable. The random variable is the amplitude (volts) of the AE waveforms. Three-point bend tests were performed on notched SFRC beam specimens to record the generated AE waveforms by following EN-14651 recommendations. As the damage in the SFRC specimens developed under the loading, it was observed that the logarithm of the cumulative AE information entropy becomes almost constant. The AE information entropy may be useful to identify the damage in SFRC by observing the change in slope of the logarithm of cumulative AE information entropy curve during structural health monitoring. The reason is due to the existence of a relation between AE based damage index (D) and AE information entropy.

Keywords Fracture · Cementitious composites · Acoustic emission · Information entropy

1 Introduction

The steel fibre reinforced concrete (SFRC) is used in the construction of industrial slabs, tunnel linings and precast members [1]. It is known that when a cementitious structural member cast with SFRC is cracking, deforming, or otherwise becoming damaged, it produces sound waves which are in sonic and ultrasonic frequency range. It is known that damage is the deterioration of the material prior to failure. Deterioration can occur due to the propagation of the microcracks under external load. Detecting, recording, and analyzing the subtle sounds generated due the development

I. Saha (✉) · R. Vidya Sagar
Department of Civil Engineering, Indian Institute of Science, Bangalore, India
e-mail: indrashish@iisc.ac.in

R. Vidya Sagar
e-mail: rvsagar@iisc.ac.in

of damage and fracture in the material through Acoustic Emission (AE) testing can reveal cracks and other flaws that are forming, and which may cause damage. AE parametric analysis is performed with combination of threshold dependent signal features such as count, peak levels, rise time, energy, duration, and amplitude to draw conclusions. These features are also affected by the wave propagation medium and the attenuation characteristics of the material [2].

A relatively new method of AE waveform analysis is the use of information entropy of the AE waveforms [3]. Information entropy of an AE waveform remains independent of threshold and other waveform features by using the time distribution of the AE waveform data. Chai et al. had shown that information entropy is a better method for damage assessment [4]. Chai et al. also conducted studies on three-point bend specimens under fatigue loading and showed that the counts, AE energy and AE information entropy evolve in a similar manner [5]. Das and Leung had used power spectral entropy (PSE) as a damage indicator for strain hardening cement composites which proved to be invariant to the noise level and thresholding [6]. Karimian et al. had used AE information entropy to predict crack initiation in aluminium alloy and observed that the entropy reached minimum values close to crack initiation [7].

Previous studies on monitoring of concrete structures using AE testing were primarily performed using the AE energy, AE counts, and AE hit rate. These parameters are constrained by the specifications of the acquisition system. In this study, an attempt has been made to relate the fracture developed in the material with the AE information entropy by studying the slope change in the log-cumulative AE information entropy curve. The nonlinear behaviour of the material has also been studied using the AE information entropy.

2 Methodology

Entropy is a measure of the uncertainty of a random variable [8]. Suppose X is a discrete random variable and $p(x_i)$ be the probability mass function and is the support of the random variable X (i.e., the probability associated with the value x_i)

$$p(x_i) = P\{X = x_i\}, x_i \in X \quad (1)$$

Then the entropy function (H) can be defined as for a dataset of size n ,

$$H = - \sum_{i=1}^n p(x_i) \log_2[p(x_i)] \quad (2)$$

Various entropy formulations have been introduced by researchers [8]. Shannon's entropy formulation, as given in Eq. (2), is one of them [9]. Unnthorsson et al. had calculated the information entropy from the probability distribution of amplitude and frequency for every 5 min of fatigue testing on carbon fibre reinforced polymers [10].

The information entropies based on the amplitude distribution had a good correlation with the trend of AE hits. Also, Qi et al. had found that the AE information entropy calculated during the tensile test of polymeric material increases with the applied stress [11]. After the material reaches the ultimate strength, the entropy becomes almost constant. Based on these reasons, Shannon’s entropy was selected in this study to calculate the AE information entropy.

It assumes that the consecutive AE events are independent of one another. In this study, the amplitude (in volts) of the AE waveforms is considered as the random variable. To calculate the entropy of each AE waveform data, first, the Pre-trigger Time was removed, and an optimum bin size was selected to obtain the maximum entropy. Figure 1a and 1b shows the AE waveform with the Pre-trigger time and the waveform amplitude distribution with the pre-trigger time, respectively. The time of zeros at the beginning of the AE waveform, as shown in Fig. 1a corresponds to the amount of pre-trigger time and suggests that no data can be recorded in the period where the AE card is re-arming. As a result, the pre-trigger duration does not generate additional AE data because the voltages in the distribution will be zero. This causes the AE amplitude histogram to be biased at zero volts, as shown in Fig. 1b. This bias reduces the information entropy value for the probability distribution of the AE amplitude and thus produces incorrect results. If the Pre-trigger time is removed, then the bias can be eliminated. Figure 2a shows the AE waveform without Pre-trigger Time and Fig. 2b shows the AE amplitude distribution after Pre-trigger time is eliminated.

Fig. 1 a AE waveform with pre-trigger time b Histogram showing the amplitude distribution

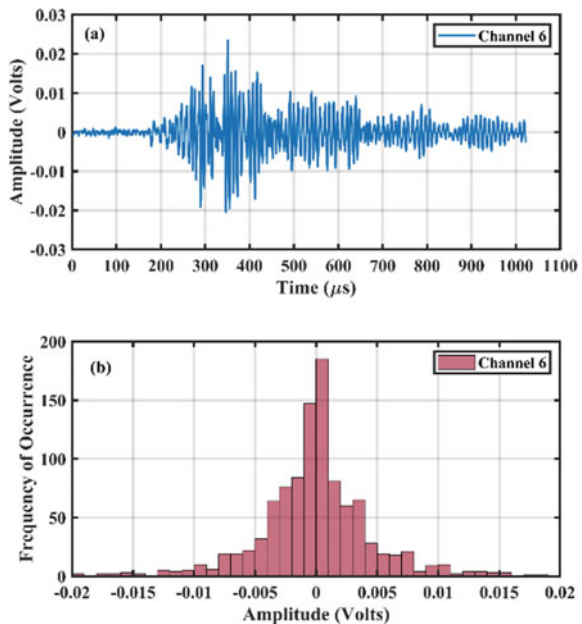
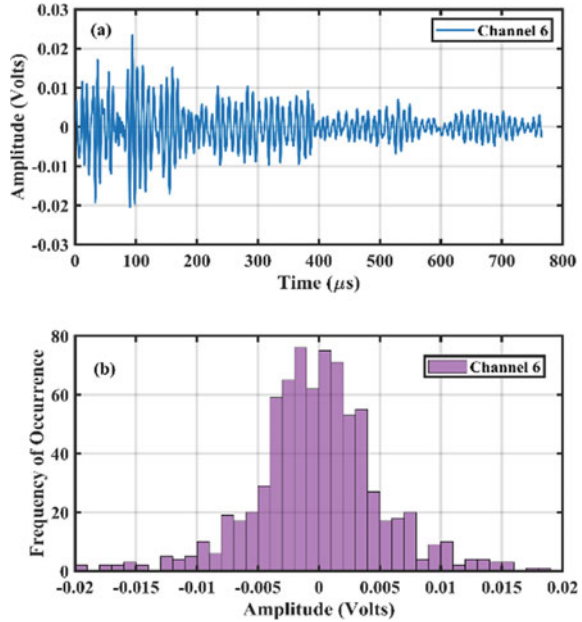


Fig. 2 a AE waveform without pre-trigger time **b** Histogram showing the amplitude distribution



To calculate the value of the probability density function from the histogram data an optimum bin size was selected

$$b_n = k\delta n^{-\frac{1}{3}} \quad (3)$$

where n is the number of datapoints, b_n is the optimum bin size, δ is the standard deviation of the data and k is a constant whose value is taken as 3.49 [12]. Using Eq. (3) the optimum bin size was selected as 0.001 for the test specimens with $V_f = 0, 0.8$ and 1.6%. Figure 3 shows the variation of the standard deviation of entropy with the bin width.

In Fig. 3a for $V_f = 0.0\%$ the standard deviation of bin width 0.001 and 0.0001 was almost the same. However, in Fig. 3b and 3c, it can be observed that for a bin width value of 0.001 the standard deviation of information entropy of AE waveforms was maximum for $V_f = 0.8$ and 1.6%, respectively. To maintain consistency, a bin width of 0.001 was selected to calculate the information entropy of all the specimens. Lower bin width values will give higher variation of the information entropy, thus capturing critical damages in the material. But use of very low bin width values can lead to high computation time for the calculation of the information entropy of the AE waveforms. Thus, an optimum bin width is selected to calculate the information entropy without compromising on the ability to capture critical damages in the material and maintaining a reasonable computation time.

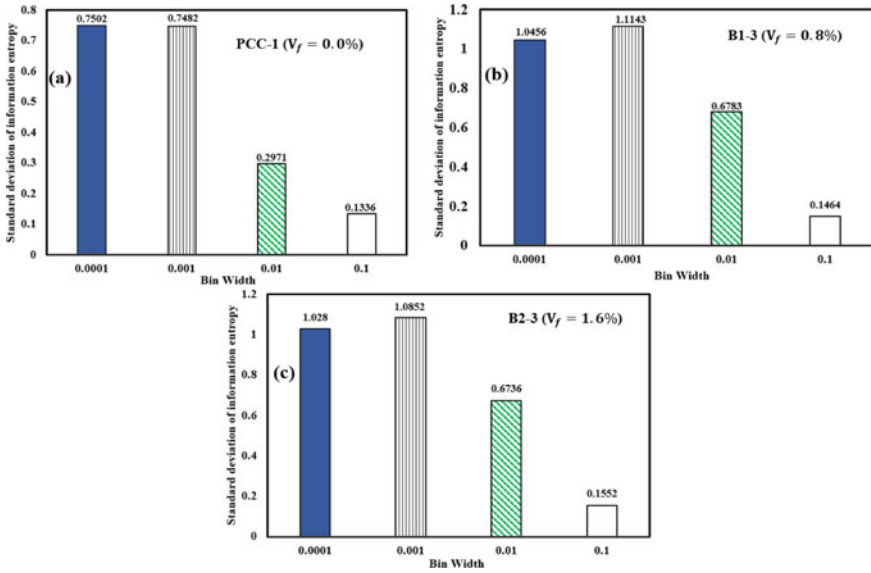


Fig. 3 Variation of standard deviation of information entropy with bin width for **a** $V_f = 0.0\%$ **b** $V_f = 0.8\%$ **c** $V_f = 1.6\%$

3 Experimental Program

The SFRC specimens were tested in the Structures Laboratory, Department of Civil Engineering, Indian Institute of Science, Bangalore, India. The tests were performed under Crack Mouth Opening Displacement (CMOD) control by following the recommendations of EN-14651: 2005, Test method for metallic fibered concrete— Measuring the flexural tensile strength (limit of proportionality (LOP), residual) [13]. Two-stage loading rate was applied on SFRC specimens as explained in Table 1. An LVDT was placed at the underside of the test specimen at midspan to measure the downward displacement. An eight-channel AE monitoring system was used, and only three sensors (resonant type, 57 kHz frequency) were activated. The frequency of the sensor refers to its resonant frequency. Resonant frequency is the frequency at which the piezoelectric material inside the sensor is most sensitive. Generally, frequency of the AE waveforms generated during cementitious materials are around 10 kHz to several kilo Hertz. For applications to plain concrete or other cementitious composites a resonant frequency of 57 kHz is usually selected. The sensor can detect signals of other frequencies. However, its sensitivity to these frequencies is low. Due to the laboratory restrictions only 57 kHz sensors were used for the experiments. 2D XY-planar arrangement was used for mounting AE sensors on the test specimens to record the AE waveforms. Figure 4 depicts the experimental setup used for the

Table 1 Details about the geometric dimensions of test specimens, steel fibre content (V_f) in the specimen and loading rate applied on the test specimens

Specimen	Geometric dimensions of test specimens				V_f (%)	Loading rate (CMOD controlled) (mm/s)
	Length (mm)	Span (mm)	Width × Depth (mm × mm)	Notch depth (mm)		
PCC-1	600	500	150 × 150	25	0.0	0.0008
PCC-2						
B1-1	600	500	150 × 150	25	0.8	(i) 0.0008 mm/s till CMOD = 0.1 mm
B1-2						(ii) 0.0033 mm/s till CMOD = 4.0 mm
B1-3						
B2-1	600	500	150 × 150	25	1.6	(i) 0.0008 mm/s till CMOD = 0.1 mm
B2-2						(ii) 0.0033 mm/s till CMOD = 4.0 mm
B2-3						

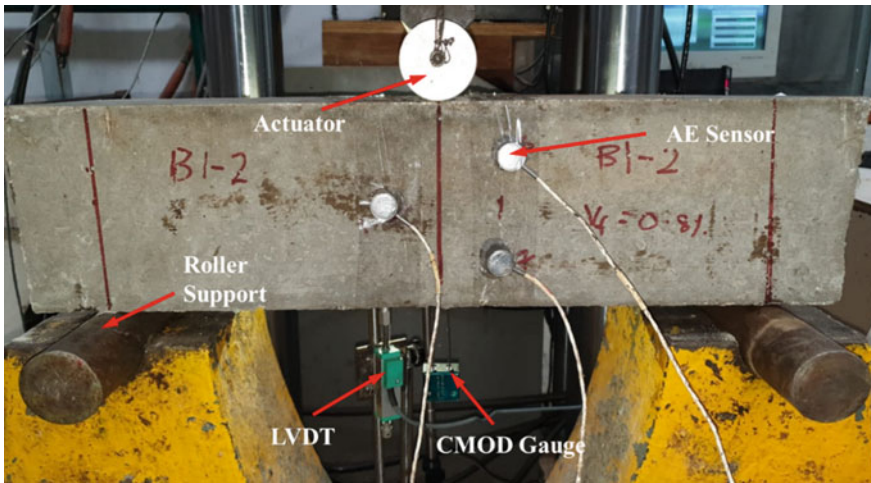


Fig. 4 Experimental setup in structures laboratory, Department of Civil Engineering, Indian Institute of Science, Bangalore, India

present study. The geometric details of the three-point bend test specimens (rectangular cross-section), steel fibre volume fraction (V_f), and the loading rate are given in Table 1.

4 Results and Discussion

4.1 Mechanical Response of the Three-Point Bend Specimens Under Mode I Fracture Process

Figure 5a and 5b, shows the mechanical response of the SFRC specimens, with varying steel fibre content, tested under similar loading conditions, has been presented. Although there is little variation in the limit of proportionality values for the volume fraction of 0.0, 0.8 and 1.6%, the post-peak response shows a noticeable difference. The increase in the steel fibre content (V_f) increases the load-carrying capacity of the SFRC in the post-peak region. The plain concrete specimen collapsed at a CMOD value close to 1.8 mm while the SFRC has a significant load-carrying capacity to a CMOD value of around 4 mm. The load-CMOD curves shown in Fig. 5a depicts the same behaviour as given in the standard namely, EN-14651:2005, thereby validating the correctness of the testing procedure. From Fig. 5a it is seen that the SFRC specimen with 1.6% steel fibre depicts a strain-hardening effect as the TU part continues rising till the peak load is reached and then continues falling. This is due to the formation of multiple microcracks initially, which finally localizes into a major crack. Whereas the SFRC specimen with 0.8% steel fibre shows a strain-softening effect as the PQR part never rises and remains almost constant at around 10 kN till CMOD is 2.5 mm and when CMOD is greater than 2.5 mm, the QR region starts decreasing. The specimen with 0% steel fibre content shows no residual load-carrying capacity, and the AB region in the post-peak response falls with a steep slope and fails at a CMOD value of 1.8 mm. The fracture energy obtained by using the Load–Displacement curve in Fig. 5b showed an increasing trend with the increase in the steel fibre content and shows a similar behaviour as shown in Fig. 5a. For 0.0% steel fibre, it was 357.56 N/m, 0.8% steel fibre it was 4798.7 N/m, and for 1.6% steel fibre, it was 7399.8 N/m.

4.2 AE Characteristics of the Three-Point Bend Specimens

Figure 6 shows the variation of the cumulative AE Energy with the loading history. A semi-log scale has been used for the ease of representing the AE energy of plain concrete and SFRC in the same plot. In Fig. 7a and 7b it can be observed that the AE energy increases for 0.0% and 1.6% and all the major AE activity is observed in the post peak region. However, for $V_f = 0.0\%$ significant AE is generated even

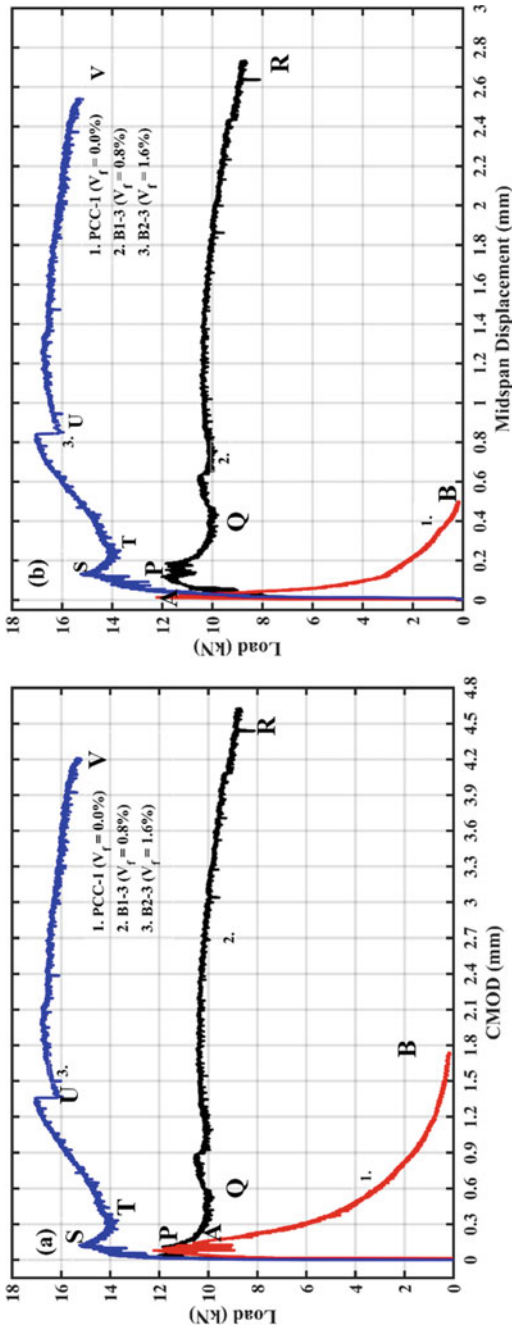


Fig. 5 a Load versus CMOD curves for $V_r = 0.0\%$, 0.8% and 1.6% b Load versus Displacement curves for $V_r = 0.0\%$, 0.8% and 1.6%

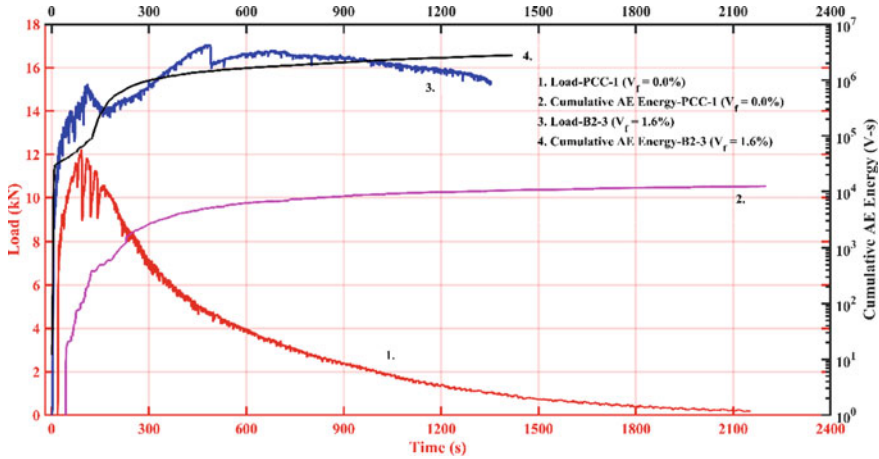


Fig. 6 Cumulative AE energy for $V_f = 0.0\%$ and $V_f = 1.6\%$

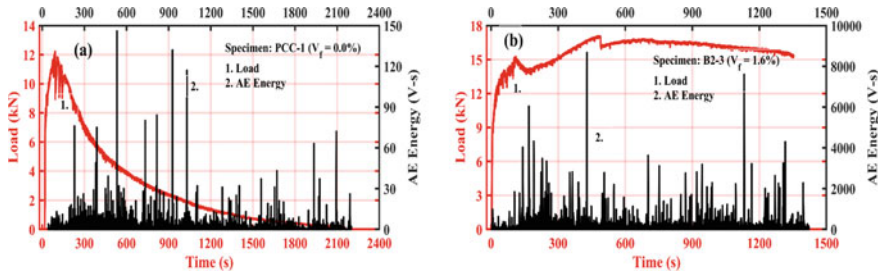


Fig. 7 Load versus AE energy for **a** $V_f = 0.0\%$ **b** $V_f = 1.6\%$

before the peak load as shown in Fig. 7a. Also with the increase in the fibre content of the SFRC specimens it can be observed that the number of high energy AE is also increased, which is caused due to the steel fibre pullout taking place in the post peak region of the SFRC specimens.

4.3 Variation of AE Information Entropy with V_f of Steel Fibres

In Figs. 8 and 9 the log-cumulative AE entropy is shown. As the fracture develops in the material, the slope of the log-cumulative entropy remains almost zero. In the linear part of the load history, the entropy curve remains almost vertical. As the material starts showing nonlinear behaviour, the slope of the log-cumulative AE entropy also changes. As the material fails completely, the slope becomes almost

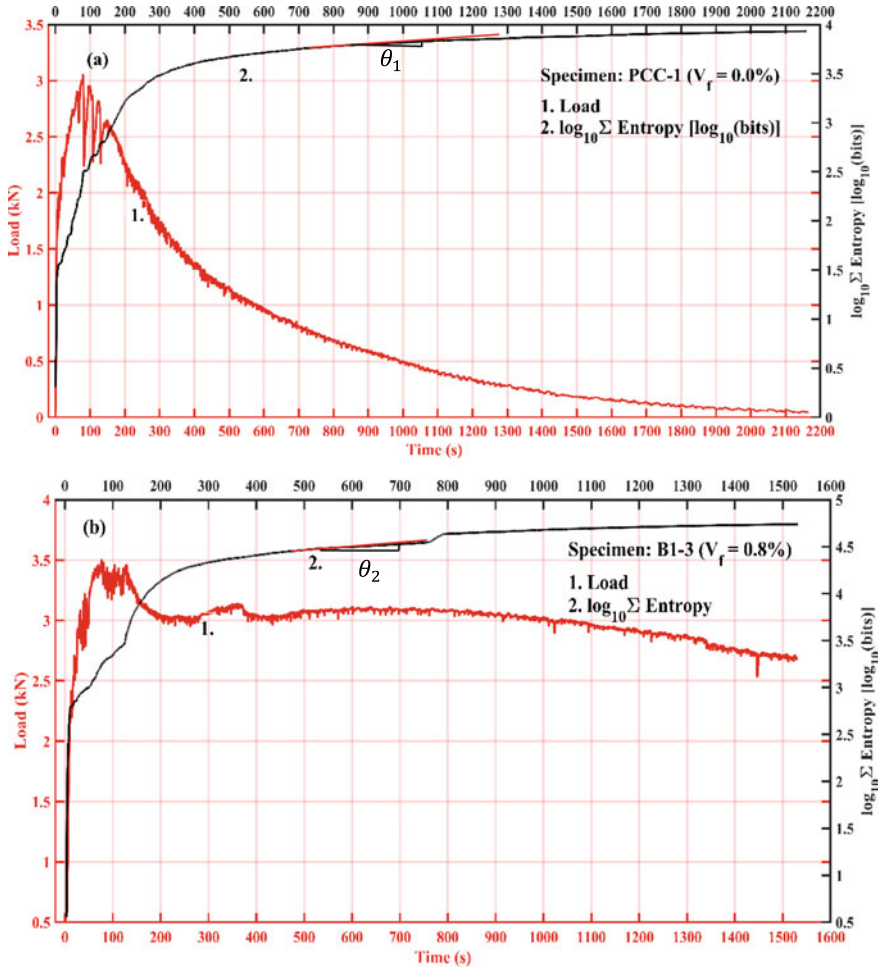


Fig. 8 Variation of log-cumulative AE entropy for **a** $V_f = 0.0\%$ and **b** $V_f = 0.8\%$

horizontal as shown in Fig. 8a. However, the slope of the log-cumulative entropy can be seen to increase as the V_f is increased from 0 to 0.8 and 1.6% in Figs. 8b and 9. The reason behind this can be explained by the superimposition of the acoustic waves generated during the experiment. An AE waveform is a superimposition of all the acoustic waves released during the fracture process at a certain instant. The superimposition can cause the AE waveforms to spread out or remain concentrated around a specific value. A spread-out waveform results in the spreading out of the voltage distribution and thereby increasing the AE waveform entropy. Similarly, a concentrated waveform with a smaller spread has a lower AE information entropy [4].

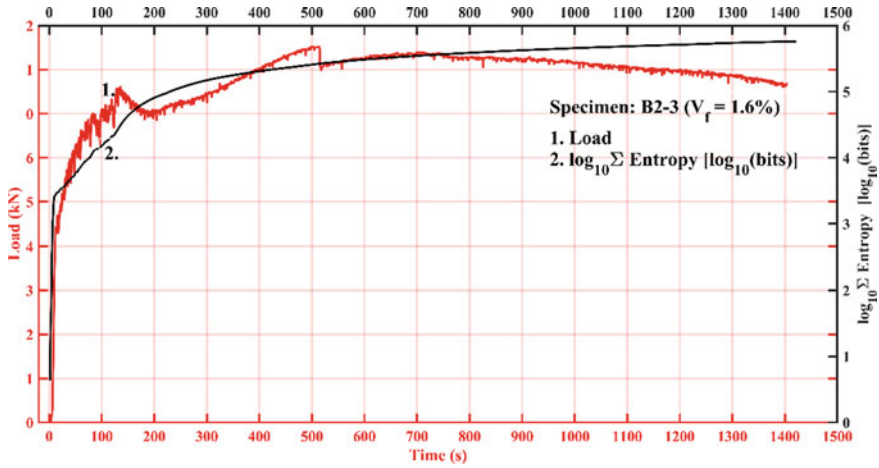


Fig. 9 Variation of log-cumulative AE entropy for $V_f = 1.6\%$

Therefore, during the fracture process in plain concrete, the AE waveforms generated are a superimposition of a single type of event, which results in a waveform concentrated around a specific value. This event is corresponding to cementitious matrix cracking. However, for SFRC beams, one additional event is present in the fracture process which is corresponding to the steel fibre pullout.

The superimposition of AE waveforms generated due to cementitious matrix cracking and steel fibre pullout causes a spread out of the AE waveforms which causes the voltage distribution to spread out, thus increasing the AE entropy value. This increase in the AE entropy value causes the slope of the log-cumulative AE entropy curve to increase. This can be observed in Figs. 8 and 9 where $\theta_1 > \theta_2 > \theta_3$. The slope change study on the AE waveform entropy may be useful in predicting the failure of the material.

4.4 Variation of the Slope of Log-Cumulative AE Information Entropy Curve with AE Based b -value

To predict the failure of the material the studying the slope change of the log-cumulative AE entropy curve maybe useful. The variation of AE based b -value has been shown with the load in Fig. 10a. It can be observed that as soon as the load carrying capacity of the SFRC beam with $V_f = 0.8\%$ drops, there is a sudden drop in the AE based b -value. The drop from A to B in Fig. 10a indicates the transition from

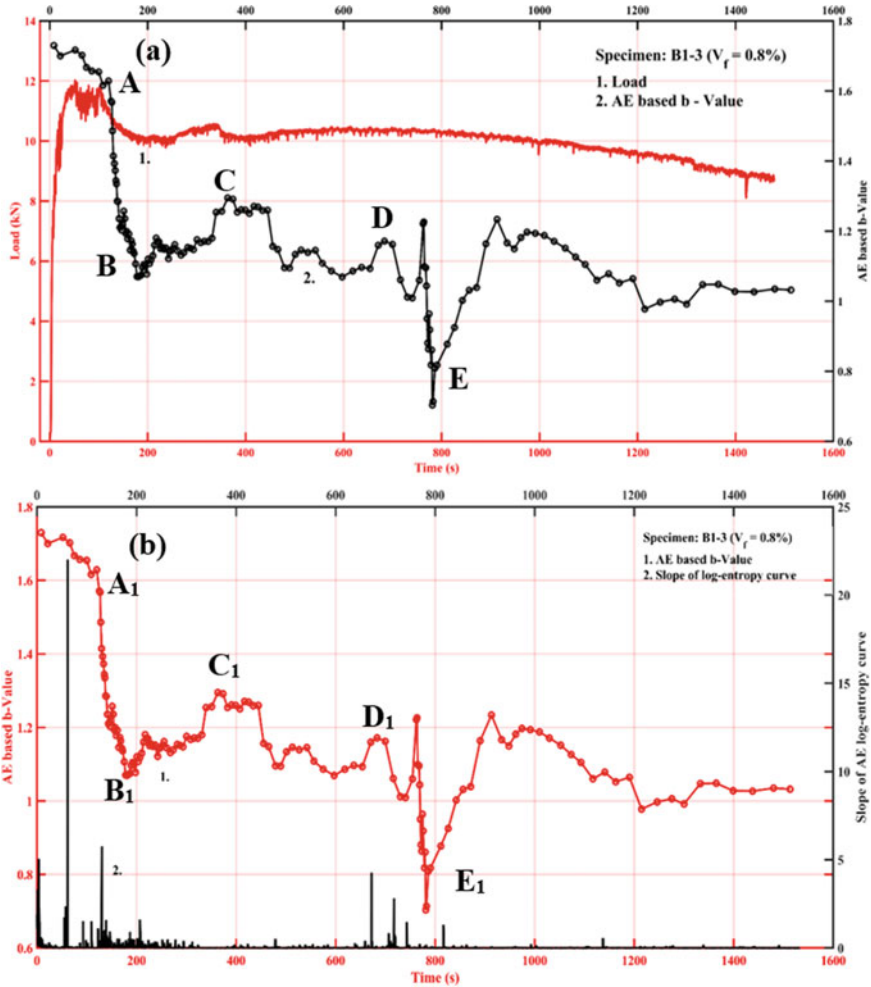


Fig. 10 Variation of b -value with **a** load **b** log-cumulative AE information entropy slope for $V_f = 0.8\%$

microcracking to macrocracking. However, as the beam transitions into the strain-softening region, the b -value can be seen to recover to a higher value. This recovery shown in Fig. 10a from B to C of the b -value is due to the crack-bridging effect of the steel fibres, which prevent the microcracks from transitioning into macrocracks. The slope change in the log-cumulative AE entropy curve has been compared to the AE based b -value in Fig. 10b. It can be observed that major slope change occurs in between A_1 and B_1 as just as the b -value drops. Also, spikes in the slope change can be observed in Fig. 10b wherever there is a fluctuation of the b -value variation such as between D_1 and E_1 as shown in Fig. 10b. This proves that the slope change of the log-cumulative AE entropy curve is an indicator of the damage in the material.

4.5 Variation of AE Information Entropy with AE Based Damage Index

Figure 11a shows the variation of load with time for SFRC specimen with $V_f = 0.8\%$. Figure 11b shows the variation of the AE based damage index (D) with b -value calculated by using the formulation introduced by Cox and Meredith [14],

$$D = \sum 10^{cm} \quad (4)$$

where c is a constant, whose value is 3 and m is a factor that is proportional to the amplitude of an AE event. Figure 11c shows the variation of AE entropy with D . In Fig. 11b it is observed at location A where the b -value drops, D starts increasing from that instant. The same observation was made under uniaxial compression of rock samples by previous researchers [15]. Correspondingly, in Fig. 11c at location A and A_1 , where there is a significant increase in the slope of cumulative AE information entropy, D also starts increasing. After comparison between Fig. 11b and 11c it can be observed that the location where D , b -value and cumulative AE information entropy starts increasing are same. In Fig. 11a at B a slope change θ_4 can be observed which causes a fluctuation in the b -value. At the same instant, a sudden jump in the AE entropy can be observed in Fig. 11c at B. Therefore, AE information entropy can be used as a parameter to detect the onset of damage in the material. Also, the AE it may be used to monitor the development of fracture process in the cementitious material.

4.6 Correlation of AE Information Entropy with AE Parameters

The information entropy of the AE waveforms has been compared with AE parameter such as AE counts, peak amplitude, and AE energy in Fig. 12. It can be observed in Fig. 12a, 12b and 12c, there is a large scatter in the data which indicates that there is no correlation between these parameters and AE information entropy. Thus, information entropy of the AE waveforms can be used as an independent AE parameter to study the fracture process in cementitious composites.

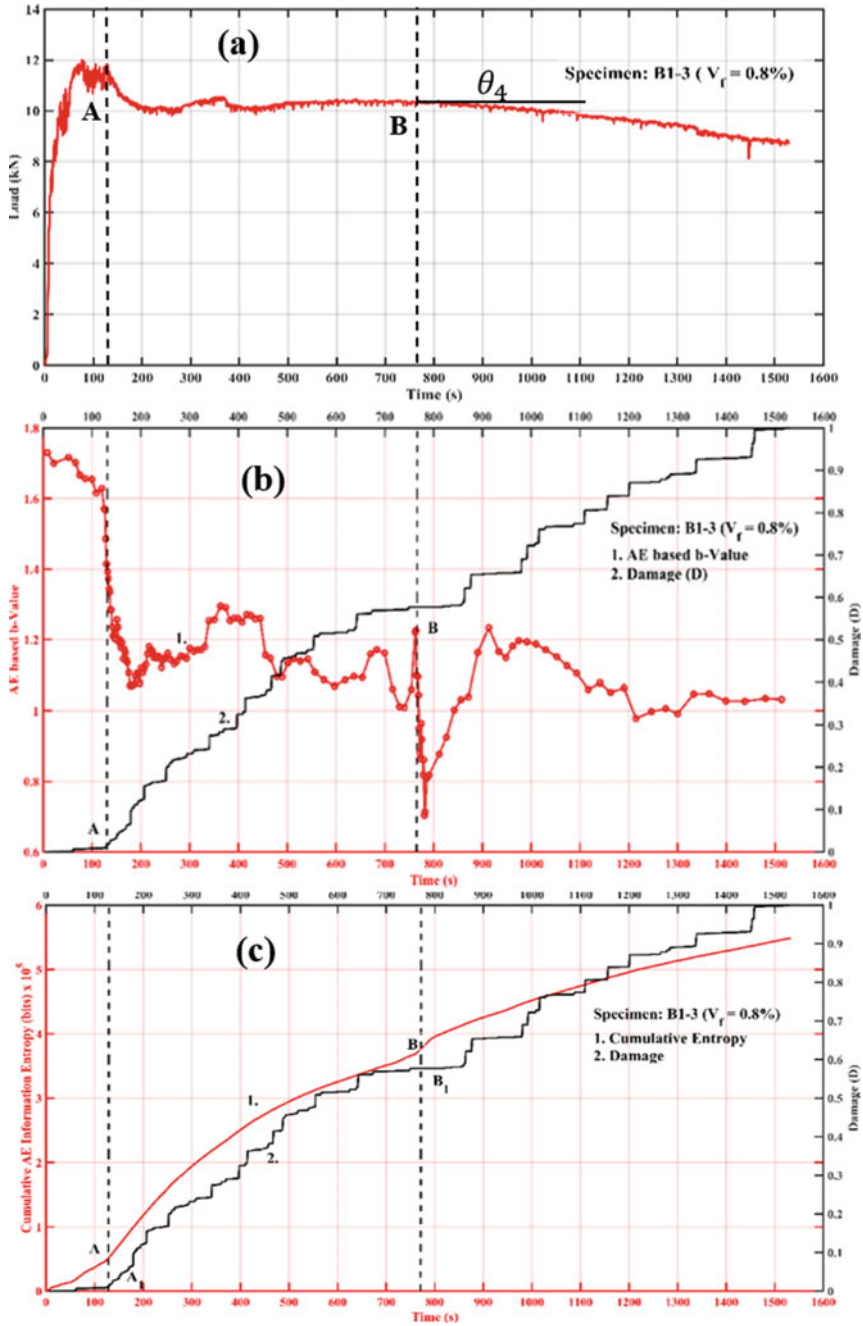


Fig. 11 Variation of a load with time b b-value with damage index (D) c cumulative AE information entropy with damage index (D)

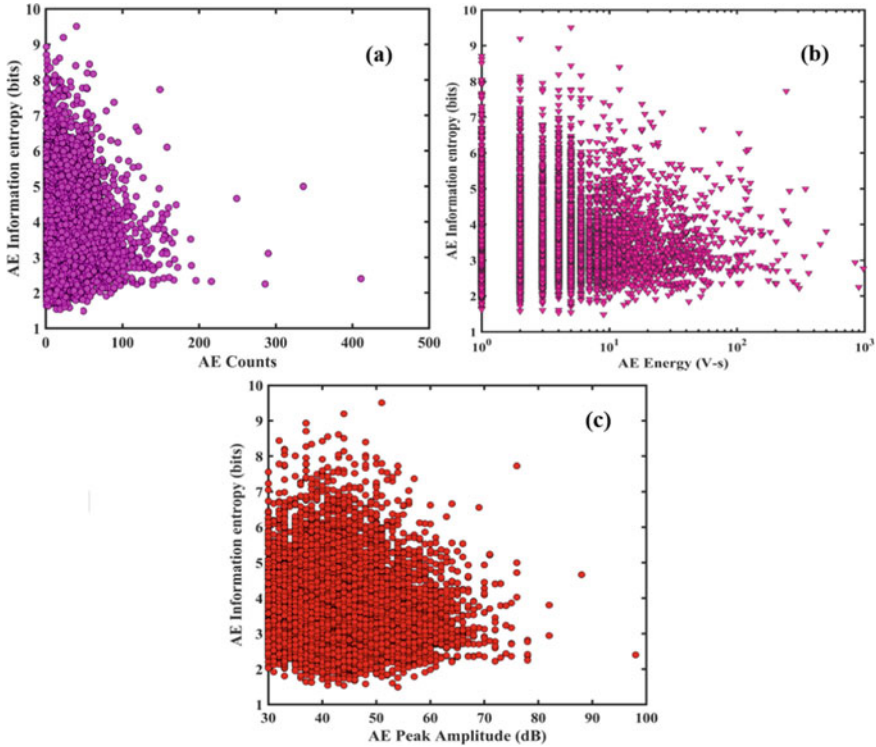


Fig. 12 Variation of AE information entropy with **a** AE counts **b** AE energy **c** AE peak amplitude for $V_f = 0.8\%$

5 Summary

In this experimental study, three-point bend specimens cast with steel fibre reinforced concrete ($V_f = 0.0, 0.8$ and 1.6%) were tested by following the EN-14651: 2005, in Mode I fracture. Simultaneously, during the fracture process in the specimens, the released acoustic emissions were recorded. Based on the experiments, it was observed that the log-cumulative AE entropy curve becomes parallel to the time axis as the damage in the material progresses. However, for SFRC specimens, an increasing slope was noticed which was because of steel fibre pullout. The onset of nonlinear behaviour of the material is detected by a sudden decrease in the slope of the AE waveform entropy curve for all the V_f . The slope change of in the log-cumulative AE entropy curve shows significant spikes when there is a fluctuation in the AE based b -value. This property may be useful to predict the failure of a concrete structure made with SFRC, as the slope becomes less with the development of damage. The variation of the AE information entropy with the AE based damage index shows that there exists a direct relation between the development of AE information entropy and the development of damage. Also, it was observed that for SFRC there was no significant

AE signals in the pre-peak region, but for plain concrete specimen significant AE activity was observed in the pre-peak region. In the mechanical response it was observed that the three-point bend specimens with $V_f = 1.6\%$ showed a strain hardening behaviour which was not observed in the specimens with $V_f = 0.8\%$.

References

1. Buratti N, Mazzotti C, Savoia M (2011) Post-cracking behaviour of steel and macro-synthetic fibre-reinforced concretes. *Const Build Mat* 25:2713–2722
2. Barile C, Casavola C, Pappaletta G, Vimalathithan PK (2019) Experimental wavelet analysis of acoustic emission signal propagation in CFRP. *Eng Fract Mech* 210:400–407
3. Sauerbrunn C, Kahirdeh A, Yun H, Modarres M (2017) Damage assessment using information entropy of individual acoustic emission waveforms during cyclic fatigue loading. *App Sci* 7(6):562
4. Chai M, Zhang Z, Duan Q (2018) A new qualitative acoustic emission parameter based on Shannon's entropy for damage monitoring. *Mech Sys Sig Proc* 100:617–629
5. Chai M, Zhang Z, Duan Q, Song Y (2018) Assessment of fatigue crack growth in 316LN stainless steel based on acoustic emission entropy. *Int J Fat* 109:145–156
6. Das AK, Leung CKY (2019) Power spectral entropy of acoustic emission signal as a new damage indicator to identify the operating regime of strain hardening cementitious composites. *Cem and Conc Comp* 104
7. Karimian SF, Modarres M, Bruck AH (2020) A new method for detecting fatigue crack initiation in aluminium alloy using acoustic emission waveform information entropy. *Eng Fract Mech* 223
8. Cover TM, Thomas JA (2006) *Elements of Information Theory* (Wiley Series in Telecommunications and Signal Processing), Wiley, Hoboken
9. Shannon CE (1948) A mathematical theory of communication. *Bell Syst Tech J* 27(3):379–423
10. Unnthorsson R, Runarsson TP, Jonsson MT (2008) AE entropy for the condition monitoring of CFRP subjected to cyclic fatigue. *J Acoust Emi* 26:262–269
11. Qi G, Fan M, Lewis G, Wayne SF (2012) An innovative multi-component variate that reveals hierarchy and evolution of structural damage in a solid: application to acrylic bone cement. *J Mater Sci Mater Med* 23:217–228
12. Scott DW (1979) On optimal and data-based histograms. *Biometrika* 66(3):605–610
13. EN-14651 (2005) Test method for metallic fibered concrete - measuring the flexural tensile strength (limit of proportionality (LOP), residual).
14. Cox SJD, Meredith PG (1993) Microcrack formation and material softening in rock measured by monitoring acoustic emissions. *Int J Rock Mech Min Sci Geomech Absts* 30(1):11–24
15. Main IG, Meredith PG, Jones C (1989) A reinterpretation of the precursory seismic b -value anomaly from fracture mechanics. *Geo. J Int* 96(1):131–138

3D Non-linear Finite Element Analysis of a Naturally Corroded Beam



Ankita Suman Mohanty  and B. N. Rao 

Abstract Corrosion in steel reinforcement has a severe impact on the performance of the structures. It is one of the important factors for the degradation of structures. It leads to volume expansion due to corrosion products, cracking and splitting of concrete and degradation of bond between the steel reinforcement and concrete. Most of the numerical studies carried out are based on artificial corrosion but there is lack of study with respect to the 3D nonlinear finite element analysis of a naturally corroded beam. The concrete and reinforcement is modelled based on a constitutive model which is based on nonlinear fracture mechanics and von-mises plasticity yield criterion respectively. Bond and corrosion model which was previously developed is used in this analysis. Interface 2D elements are used for the surface between the concrete and steel reinforcement. The analysis results indicates that the beam analyzed shows a variation of around 20% with respect to the existing literature for a naturally corroded beam.

Keywords Corrosion · 3D Nonlinear finite element · Naturally corroded · Numerical analysis

1 Introduction

Steel corrosion is recognized as one of the leading cause of deterioration in concrete structures worldwide. It severely impacts the serviceability and load carrying capacity of the structure. Corrosion in Reinforced Concrete (RC) structures can be due to uniform corrosion i.e. corrosion induced due to carbonation and pitting corrosion i.e. corrosion due to chlorides. In general, the corrosion in RC structures has two phases—1. Corrosion initiation phase and 2. Corrosion propagation phase [1]. The initiation phase refers to the time during which the chlorides enter into the concrete but no damage is being observed. The propagation phase is that period of time during

A. S. Mohanty (✉) · B. N. Rao

Department of Civil Engineering, Indian Institute of Technology Madras, Chennai 600036, India

B. N. Rao

e-mail: bnrao@iitm.ac.in

which the accumulation of corrosion products around the interface between the rebar and concrete takes place leading to ultimate failure. The corrosion initiation phase is relatively longer as compared to the corrosion propagation phase [2–4].

As the reinforcement gets corroded both steel and surrounding concrete gets damaged. The corrosion initiation is followed by rust formation causing volume expansion as 2 to 6 times the original volume thereby inducing splitting stresses in concrete around the rebars [5–7]. As the corrosion propagates cracking and spalling of the concrete cover occurs thereby decreasing the bond strength between the rebars and the concrete. In the meantime the corrosion penetration reduces the cross sectional area of the rebars and also affects the mechanical properties of the bar [8–10]. The expansion due to corrosion products formed causes concrete cracking which has an added effect on the bond between the concrete and the reinforcement [11–13]. Corrosion affects the mechanical behavior of Reinforced Concrete structures and the load carrying capacity. It also effects both the force and stiffness redistribution in the concrete structure [14, 15].

Most of the numerical studies conducted involve the use of artificially corroded specimens because of the shortest time taken for completing the corrosion process [16, 17]. Naturally corroded specimens undergo the natural destruction process in the real structure and the main issue with that is it requires several decades until some changes are being noticed. To avoid this issue specimens subjected to artificial corrosion techniques are generally used.

Many numerical analysis studies have been carried out on artificially corroded specimens and there exists uncertainty whether the results so obtained from it is reliable enough for the evaluation of the already existing structures. Hence for good understanding of the behavior of the structure with respect to corrosion numerical analysis should involve the use of naturally corroded specimen results.

2 Numerical Analysis

Three-dimensional non-linear finite element analysis is done using DIANA 10.2 which is a finite element analysis software on a corroded RC beam from previous literature [18, 19]. The dimensions of the beam taken into consideration is as shown in the Fig. 1. The 3D finite element model mesh for the beam is shown in the Fig. 2.



Fig. 1 Longitudinal and cross-sectional view of corroded beam specimen [19]

Table 1 Material properties of concrete

Specimen	f_c (Compressive strength of concrete in MPa)	f_{ct} (tensile strength of concrete in MPa)	G_F (Fracture energy of concrete in N/m)	Average concrete cover (mm)	Average weight loss of bars (%)
Beam	46.1	2.8	86.9	50.8	3.2

Table 2 Material properties of steel

E_s (Young's modulus in GPa)	f_y (Yield strength in MPa)	ν (Poisson's ratio)
220	650	0.3

Table 3 Material properties of the interface element

f_{cm} (Mean concrete strength in MPa)	f_{ctm} (Mean concrete tensile strength in MPa)	E_c (Young's modulus in GPa)	r (Radius in mm)	x (Corrosion penetration in μm)
46.1	2.8	24	8	149

Half of the beam is modelled due to symmetry. The cross section of the main steel bars is modelled as octagon. The reinforcement is modelled as embedded assuming perfect bond conditions between the rebars and concrete. In general, for simplicity translation in x direction was restricted and the nodes for the centerline of the section was also restricted in the y and z directions. For the meshing of concrete and reinforcement (TE12L) which is a 3D 4 noded isoparametric solid tetrahedron element was used. For the interface element (T18IF) which is a 6 noded plane triangle element was used only for the bottom reinforcement as they only used the bond and corrosion model [20, 21]. Triangular prism element (TP18L) which is a 6 noded isoparametric solid wedge element and (HX24L) which is a 8 noded isoparametric solid brick element were used for the meshing of wood and steel plates respectively (Tables 1, 2 and 3).

The bond properties of rebar and the swelling effect of corrosion is modelled by bond and corrosion model by Lundgren 2005a [20]. In this model to describe the relation between the displacement and the traction 2D interface element was used. 2D interface element were used to describe the bond behavior between the steel and the concrete. This model is limited by two yield functions F1 and F2. The limitations of both the functions is described by the Fig. 3. In the corrosion model the volume of rust with respect to the uncorroded steel was taken as an input and the corrosion penetration (x) was applied as a function of time which is being described by Fig. 4.

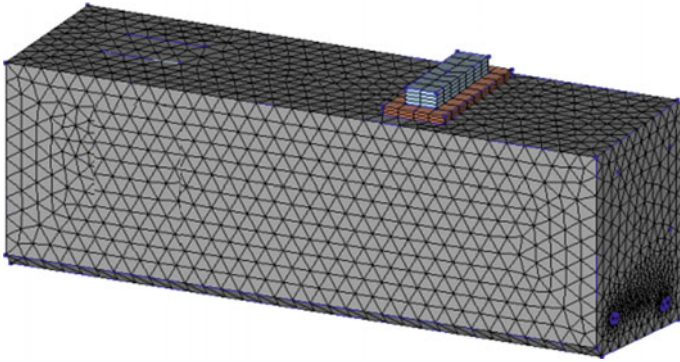
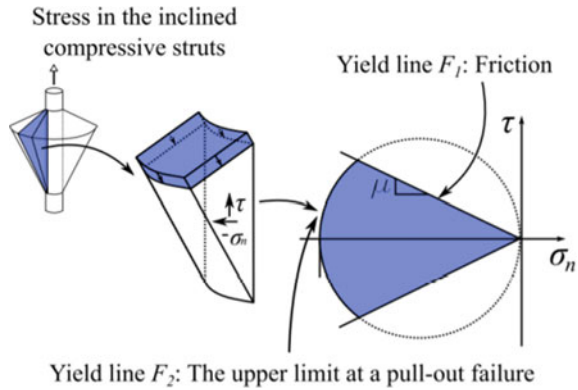


Fig. 2 3D finite element model mesh

Fig. 3 Two yield functions, F_1 and F_2 , limiting the yield surface from Lundgren (2005a) [20]



The concrete was modelled using smeared rotating crack model and the reinforcement is based on von mises plasticity yield criterion. The interface between the steel and concrete is modelled using the 2D interface element which is based on a friction model which considers both bond and corrosion. The analysis was carried out first as corrosion phase in which time steps was applied to follow splitting cracks in concrete and secondly as mechanical phase with displacement steps which is being described by Table 4.

Table 4 Analysis procedure with different time steps and iteration method

Model	Iteration method mechanical	Iteration method corrosion	Step size corrosion (μm)	Step size mechanical (mm)	Convergence criterion (force/disp.)	Analysis time (hr)
Beam	Quasi-Newton	NR-regular	1(150)	0.1(100)	0.01	4

3 Results and Discussion

The variation of bond stress with end slip is as described by Fig. 5. The average bond stress increases in the beginning with a small increment in the end slip. Once the maximum bond stress is reached then it decreases with the further increment in end slip. The maximum bond stress for the numerical analysis is around 5.5 MPa and for the experiment is around 6.9 MPa. Hence the bond stress is underestimated at around 20.28%. The average bond stress in case of the numerical analysis was calculated as the force divided by the circumference of the rebar where the crack crosses it for various load steps applied to it and in case of experiment it was calculated as the highest of the average values of bond stress of all the rebars subjected to corrosion.

The applied load to the beam with respect to the mid span deflection is plotted in Fig. 6. Linear behavior was observed till 80 kN load for both the numerical analysis and experimental values. After the load crossed 80 kN change of stiffness for both continues to follow the same trend. The maximum load for the numerical analysis is around 370 kN and for the experiment it is around 310 kN. The beam fails after 9 mm of deflection as per the numerical analysis but as far as the experiment is concerned it fails before 8 mm. Hence the load capacity was overestimated at around 19.35%. In case of the experiment the longitudinal rebars along with the stirrups had a difference in corrosion level due to the atmospheric conditions, crack width and stochastic nature of corrosion but in case of the numerical analysis it was considered subjected to uniform corrosion for all the rebars.

For the different stages on the load vs displacement curves the crack pattern are shown in Figs. 7 and 8. Around 90 kN after the linear behavior bending cracks start to appear. Around 190 kN shear cracks starts to appear. After a slight increment in the load, the second shear crack appears and is fully visible when the maximum load reaches around 370 kN. The splitting cracks also increases and spalling of concrete cover is prominent in the post peak branch. Overall, the cracks propagate in a similar pattern as that of the experiment in the literature. The mesh sensitivity analysis is done such that the maximum load is plotted with respect to the mesh size. Mesh size of 10 mm is considered as appropriate for the analysis. The plot is as shown in Fig. 9.

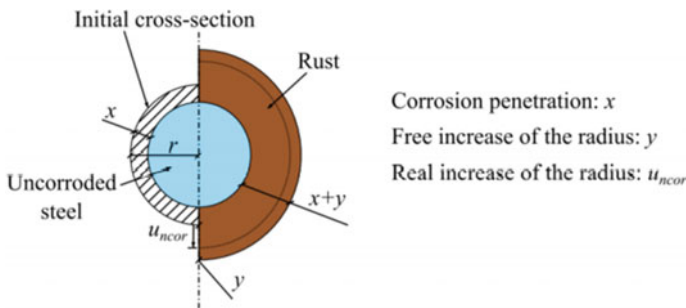


Fig. 4 Different parameters of corrosion model from Lundgren (2005b) [21]

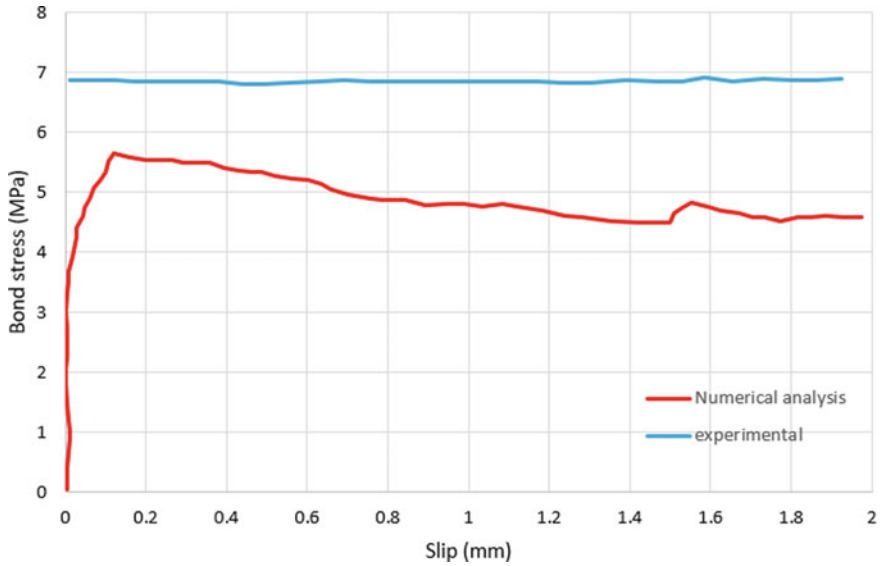


Fig. 5 The maximum average bond stress from the experiment is plotted together with the average bond stress from numerical analysis vs end slip

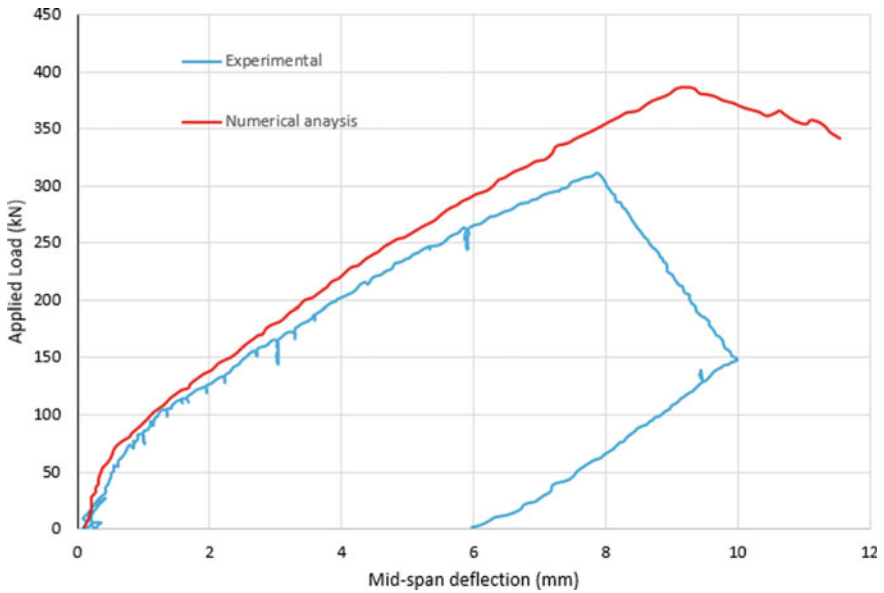


Fig. 6 The applied load vs mid-span deflection for the experimental data and numerical analysis

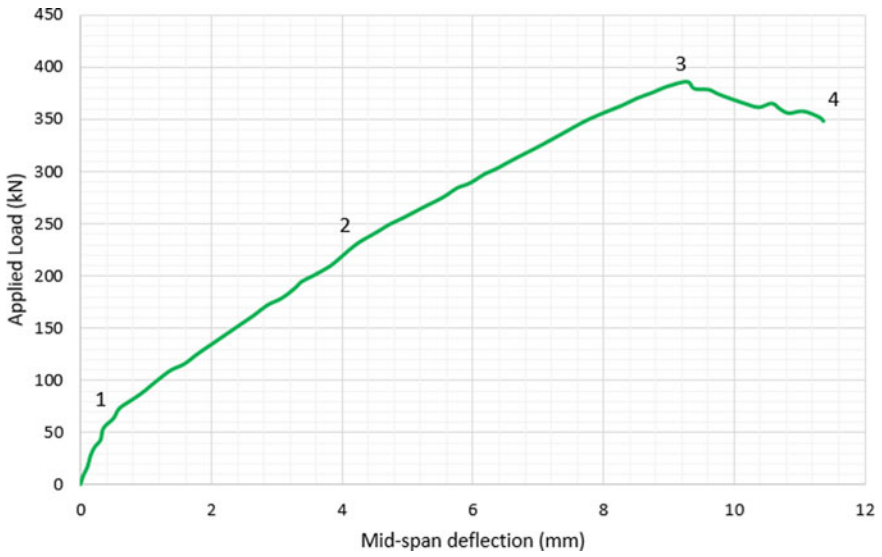


Fig. 7 Load vs displacement curve for different points for crack pattern estimation

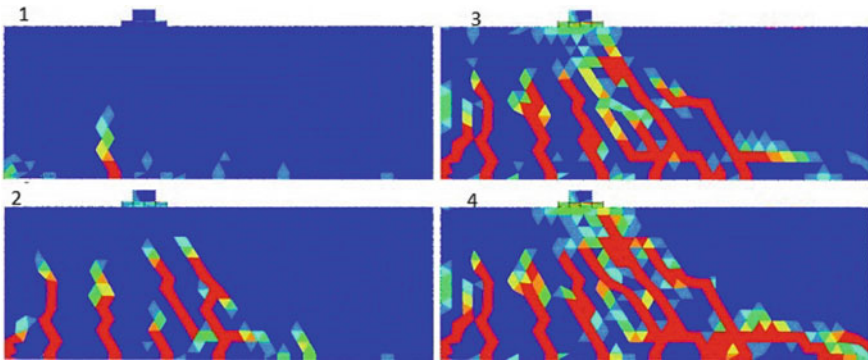


Fig. 8 Various crack patterns corresponding to the points on the load vs displacement curve

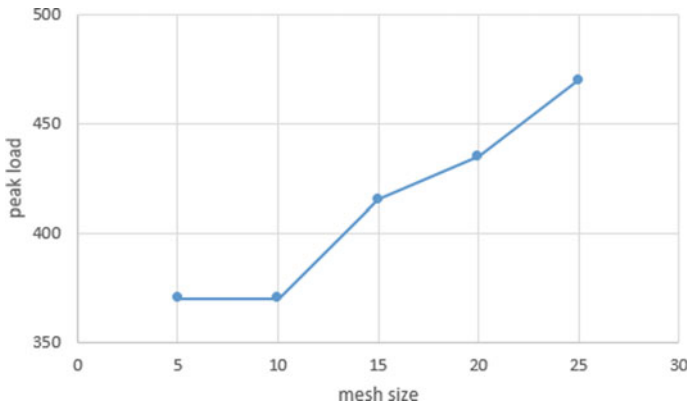


Fig. 9 Variation of maximum load as a function of mesh size

4 Conclusion

The numerical analysis and experimental data showed similar structural behavior leading to anchorage failure of the beam. The maximum load was overestimated as 60 kN (19.35%). After reaching maximum load and bond stress the end slip started to increase both for the numerical analysis as well as the experiment. That signifies a loss in the bond which indicated anchorage failure as a governing failure mode. The variation in the bond stress for the numerical analysis and the experiment corresponds to the variation in the anchorage length which is 460 mm for the numerical analysis and 473 mm for the experiment and also the bond stress is compared to the maximum average bond stress. The variation in the load displacement values between the experimental results and numerical analysis corresponds to the difference in the application of corrosion to the rebars as in case of experiment some rebars had very high corrosion compared to others which could not be implemented in the analysis.

References

1. Tuutti K (1982) Corrosion of steel in concrete
2. Coronelli D, Gambarova P (2004) Structural assessment of corroded reinforced concrete beams. *Model Guide* 130(8):1214–1224. [https://doi.org/10.1061/\(ASCE\)0733-9445\(2004\)130:8\(1214\)](https://doi.org/10.1061/(ASCE)0733-9445(2004)130:8(1214))
3. Du Y (2001) Effect of reinforcement corrosion on structural concrete ductility. Ph.D. dissertation, University of Birmingham
4. Hanjari KZ, Kettil P, Lundgren K (2013) Modelling the structural behavior of frost-damaged reinforced concrete structures. *Struct Infrastruct Eng* 9(5):416–431. <https://doi.org/10.1080/15732479.2011.552916>
5. Rodriguez J, Ortega L, Casal J (1997) Load carrying capacity of concrete structures with corroded reinforcement. *Constr Build Mater* 11(4):239–248. [https://doi.org/10.1016/S0950-0618\(97\)00043-3](https://doi.org/10.1016/S0950-0618(97)00043-3)

6. Zhang R, Castel A, Francois R (2009) Serviceability limit state criteria based on steel concrete bond loss for corroded reinforced concrete in chloride environment. *Mater Struct* 42(10):1407–1421. <https://doi.org/10.1617/s11527-008-9460-0>
7. Lundgren K (2007) Effect of corrosion on the bond between steel and concrete: an overview. *Mag Concr Res* 59(6):447–461. <https://doi.org/10.1680/macrc.2007.59.6.447>
8. Lundgren K, Kettil P, Hanjari KZ, Schlune H, Roman ASS (2012) Analytical model for the bond-slip behaviour of corroded ribbed reinforcement. *Struct Infrastruct Eng* 8(2):157–169. <https://doi.org/10.1080/15732470903446993>
9. Molina FJ, Alonso C, Andrade C (1993) Cover cracking as a function of rebar corrosion. II: numerical model. *Mater Struct* 26:532–548. <https://doi.org/10.1007/BF02472864>
10. Coronelli D, Gambarova P (2004) Structural assessment of corroded reinforced concrete beams: modeling guidelines. *ASCE-J Struct Eng* 130(8):1214–1224. [https://doi.org/10.1061/\(ASCE\)0733-9445\(2004\)130:8\(1214\)](https://doi.org/10.1061/(ASCE)0733-9445(2004)130:8(1214))
11. Devi AK, Ramajaneyulu K, Sundarkumar S, Ramesh G, Kumar BB, Moorthy TK (2017) Ultimate load behaviour of reinforced concrete beam with corroded reinforcement. *J Instit Eng (India) Ser A* 98(4):525–532. <https://doi.org/10.1007/s40030-017-0239-6>
12. CEB-fib (2000) Bond of reinforcement in concrete. state-of-art report, fédération internationale du béton. Bulletin 10, prepared by task group bond models. lausanne, swetzerland. <https://doi.org/10.35789/fib.BULL.0010>
13. Torres-Acosta AA, Martinez-Madrid M (2003) Residual life of corroding reinforced concrete structures in marine environment. *J Mater Civ Eng* 15(4):344–353. [https://doi.org/10.1061/\(ASCE\)0899-1561\(2003\)15:4\(344\)](https://doi.org/10.1061/(ASCE)0899-1561(2003)15:4(344))
14. Ou Y-C, Susanto YTT, Roh H (2016) Tensile behavior of naturally and artificially corroded steel bars. *Constr Build Mater* 103:93–104. <https://doi.org/10.1016/j.conbuildmat.2015.10.075>
15. Du Y, Clark L, Chan A (2005) Residual capacity of corroded reinforcing bars. *Mag Concr Res* 57(3):135–147. <https://doi.org/10.1680/macrc.2005.57.3.135>
16. Gestsdóttir E, Gudmundsson T (2012) Bond behaviour of naturally corroded reinforcement in concrete structures, experimental and numerical study. Master Thesis, Chalmers University of Technology
17. Khan I, François R, Castel A (2014) Experimental and analytical study of corroded shear-critical reinforced concrete beams. *Mater Struct* 47(9):1467–1481. <https://doi.org/10.1617/s11527-013-0129-y>
18. Diana T (2017) Finite element analysis user's manual-release 10.2, TNO DIANA
19. Zhu W, Francois R (2014) Corrosion of the reinforcement and its influence on the residual structural performance of a 26-year-old corroded RC beam. *Constr Build Mater* 51:461–472. <https://doi.org/10.1016/j.conbuildmat.2013.11.015>
20. Lundgren K (2005a) Bond between ribbed bars and concrete. Part 1: Modified model. *Mag Concr Res* 57(7): 371–382. <https://doi.org/10.1680/macrc.2005.57.7.371>
21. Lundgren K (2005b) Bond between ribbed bars and concrete. Part 2: The effect of corrosion. *Mag Concr Res* 57(7), 383–396. <https://doi.org/10.1680/macrc.2005.57.7.383>

A Review of Stage Separation Systems for Launch Vehicles



Shyamala Iyer and V. Narayanamurthy

Abstract Stage separation system in a launch vehicle helps to physically separate the burnt stage of the vehicle from the subsequent live stage located towards the fore end. There are several stage separation systems and they differ from their principle of operation, construction, generated impulse or the shock levels, the type of mechanism and the operational duration. This paper provides a brief review of several stage separation systems being adopted in launch vehicles. It explores the adopted methods, design specifications, and identifies the problems and challenges.

Keywords Separation system · Actuators · Release devices · Separation · Impulse devices · Pyrotechnics

1 Introduction

The launch vehicles are featured with more than one or two multiple stages in order to increase the range and performance of the flight vehicle. Once the operation of one lower stage towards the aft direction is completed, it is detached from the subsequent live stage to reduce unwanted mass of the vehicle and to increase the momentum. The separation of two adjacent stages can be approached in two ways, designing a continuous structure that carries loads and then adding a device that cuts the structure cleanly upon actuation, or designing two separate structures attached at a mating surface until the separation is initiated [1, 2].

The jettisoning of devices is accomplished by hot or separation. The hot separation is accomplished by the action of gas jet from the engine of the upper stage which begins ignition when the two stages are connected together. The lower stage sends forth a command for cut-off of engine ignition to reduce the thrust, and when its thrust is reduced to a certain value, the upper stage engine ignites. The exhaust ports at the

S. Iyer (✉)

Amrita School of Engineering, Vishva Vidyapeetham, Coimbatore, Tamil Nadu 641112, India

V. Narayanamurthy

Research Centre Imarat, Hyderabad, Telangana 500069, India

e-mail: v.narayanamurthy@rcilab.in

inter-stage sector are opened so as to expel the hot gas stream and when it reaches a certain value, separation ensues. Advantages include high separation force, high reliability and short time of no-control. Disadvantages include high disturbances and the need for providing a heat insulation layer at the top of the lower stage tank to prevent damage by high pressure and by heat of the engine exhaust of the upper stage. Sufficient space needs to be maintained to avoid shock wave penetration which could affect normal operation of the upper stage engine. This results in a layout with increased length and weight of the rocket. In cold separation, the upper stage engine ignites only after the two stages have separated. The separation relies on the addition of auxiliary force and on the reverse thrust of solid fuel rockets. Reverse thrust rockets push the lower stage away and auxiliary force accelerates the upper stage. Separation with a relatively small active force, small disturbances, steady operation process, no heat insulation and no required exhaust ports at the inter-stage sector are some of the advantages.

The mechanisms and the system used are designed based on factors such as stiffness, physical and functional interfaces, and dynamic characteristics between the separation bodies, their mass, applicable range-safety standards and requirements and anticipated operating conditions [3]. The connections undergo extreme conditions during take-off and hence need to be extremely stable but at the same time should ensure quick and reliable separation, accompanied by minimum changes in rotational rates and attitude. Structural integrity, load path continuity until separation, adequate clearance between the separating bodies, fault tolerance, damage, and contamination by debris are important considerations to be taken into account. The system should not produce high shock capable of destroying the components of the spacecraft. A typical stage separation system is shown in Fig. 1.

2 Comprehensive Design Requirements

Staging mechanism includes *i) actuators, ii) release devices, iii) separation impulse devices and iv) auxiliary devices*. Actuation is the initiation of the separation process accomplished by devices called actuators. Actuation can be electric or pyro-based e.g. pyro-bolt cutting actuation. The physical separation is accomplished by severance or release mechanism which is of two types: (a) mechanical systems and (b) pyrotechnic devices. In the former, two separate structures are attached to each other by means of clamps, diaphragms and/or point release devices. The latter is accomplished by the use of explosive released devices which sever along a line or shape, e.g. mild detonating fuze (MDF) and linear shaped charge (LSC). The first stage is the heaviest part and should impart the initial thrust required to overcome the earth's gravity and take-off. Separation impulse devices provide the impulse to avoid re-contact, e.g. springs, thrust reversal and auxiliary rockets. Auxiliary devices assist the separation maneuver by severing electric and hydraulic connections between stages and guiding/changing the rate of rotation or spin rate of the continuing stage, e.g. de-spin mechanisms, yo-tumble system and tumble rockets.

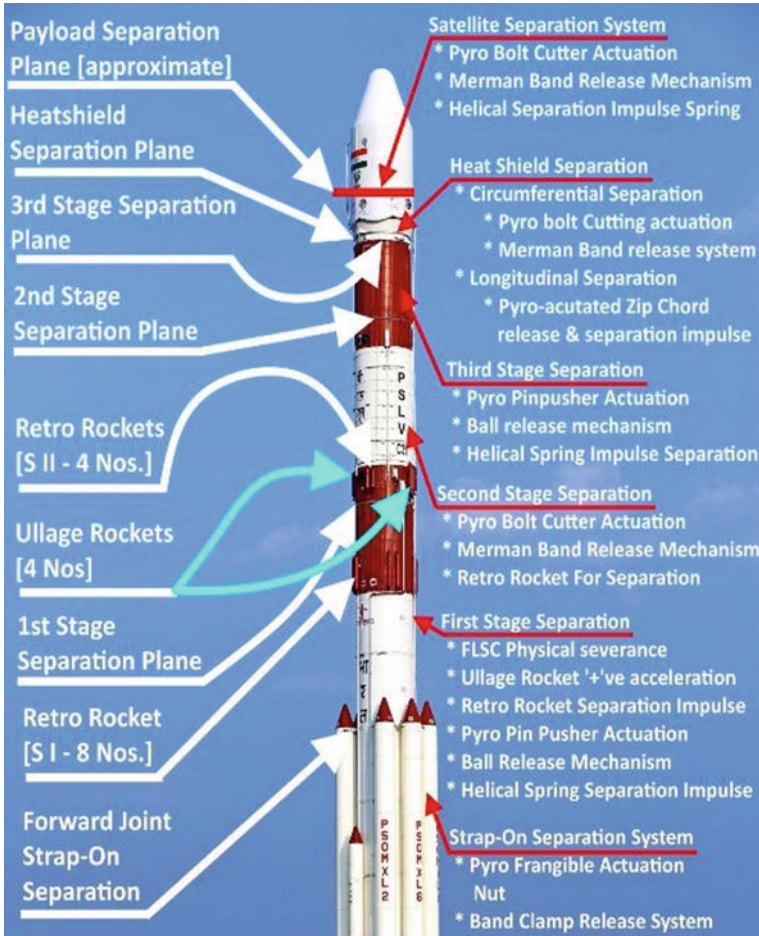


Fig. 1 A typical stage separation system [3]

The stage has to be releasably connected to the launch vehicle. The means for separating the components are decided based on multiple design factors and requirements.

- i. Asymmetry of thrust causes deviations that need to be corrected.
- ii. Wind disturbance in atmospheric separation
- iii. Shifting of the center of gravity to be considered and play an important role in rocket separation.
- iv. For minimum tip-off errors, the separation should be accomplished within a short span of time, especially at low altitudes since the aerodynamic forces might cause a relatively high drift.

- v. The tip-off rate should be minimal after separation and sufficient velocity should be imparted so that both the separating bodies do not enter the collision space between them.
- vi. The separation should happen during the minimum amount of time so that the “no-control duration” is minimum.
- vii. The separating bodies should not re-contact and hence there should be adequate clearance.
- viii. The fragments following detonation should not be excessive or cause damage to the instrument and equipment.
- ix. The collision of the surfaces is to be avoided at all costs which call for the requirement of motion between the stages.
- x. No detrimental shock loads should be induced in the structures and the effect of shock transmission to the rest of the structure is, therefore, to be taken into account.
- xi. The allowable shock levels and contamination are important aspects to be taken care of.
- xii. The structure should be able to withstand shocks and impulses without undergoing premature separation or failing.
- xiii. Reliability of the separation system is an important factor that can be ensured to some extent by making sure that the flight load stiffness and dynamic characteristics are intact.
- xiv. The mechanism should also be able to withstand the natural and induced environment.
- xv. It is essential that the separated bodies undergo joint rotation and simultaneity.
- xvi. The Spacecraft Separation system needs to survive extremely high or low temperatures and should be able to survive a nuclear environment with some amount of fault-tolerance.
- xvii. Parts of the separation system should have almost the same coefficient of thermal expansion.
- xviii. The stage separation system should not be too heavy or too big and it must have a long storage life.
- xix. The materials used in the separation system should be devoid of fault and should be of good quality.
- xx. A stiff connection is to be retained until deployment even under the worst case load conditions, capable of release upon command with minimal imparted shock.

The complexity of the separation model necessitates a robust design following a unified design approach catering almost all the above requirements.

All manufacturing and joining processes result in the increase of strain energy and hence can warp structures. The adjoining vehicles should be flat at the interface. If they are too warped, stress may get built in it resulting in breakage while joining. Load peaking i.e. concentration of load in areas of high stiffness like corners, edges and areas of reinforcement needs to be taken care of. Tip-off might be beneficial

to produce even solar heating or stabilizing the vehicle dynamically. It is important that the structural integrity be preserved under loads on ground and in-flight and the payload should be protected during separation. ‘Chuffing’ is where the expended stage overtakes and bumps into the continuing stage due to small positive thrust by solid propellant which continues to burn after separation. This can be overcome by the use of auxiliary devices. In the case of liquid propellant motors, a similar problem known as ‘burp’ is encountered. Pyro-technics release a high amount of energy but the major drawback is the shock produced during the separation event. They need to be actuated and synchronized within a short span (which results in high investments). The tip-off disturbances occur not only in cases where the upper stage is fired in the presence of a lower stage, but also are present when no obstructions exist rearward of the nozzle exit plane during upper stage ignition and burning, which calls for a guidance system.

3 Principles of Separation Systems

The principles behind the mechanisms used in the separation systems of the launch vehicle are to be devised based on the application and environmental conditions. Pyrotechnics provide separation events with a high ratio of separation force versus system weight, which result in less consumption of fuel. They release a high amount of energy but the major drawback is the shock produced during the separation event. Some of the separation systems discussed in this paper are LSC, MDC, fragmenting explosive bolts and nuts, non-fragmenting explosive nut, pyro-fuze, pin-pushers and pin-pullers. While mechanical systems produce relatively less shock, the separation event relatively takes more time. Example: V-clamp bands, pneumatic lock, springs, and ball lock pins.

3.1 *Types of Separation Systems*

Some of the separation systems for launch vehicles [4] are:

- i. Separation by fluid communication of pressurized gas
- ii. Separation by pressure rise
- iii. Micro-cylinder separation system
- iv. Fastening and separating system
- v. Latching separation system
- vi. Confined linear explosion separation system
- vii. Pyro-fuze separation system
- viii. Explosively actuated separable structure
- ix. Explosive separation device
- x. Shear pin pyro-mechanical mechanism.

There are certain specific advantages and challenges associated with each and every type of stage separation system.

3.2 Working Principles of the Mechanisms

The working principles of some common components of separation systems are explained here.

- i. **LSC** is an explosive technique where the structure along the metal sheath is cut through the unnotched structural skin. Explosive energy is enclosed in a seamless metal sheath which upon detonation results in a uniform cutting in the shape of the sheath. This is based upon the ‘Munroe effect’ according to which the severance by an explosive into a surface is increased and made as a deeper indentation by shaping a conical or hemispherical hollow in the forward end of the cartridge.
- ii. **MDC** is a confined linear explosive technique where an explosive charge is used to fracture a joint. MDC is a metal-clad explosive drawn or extruded on the separating body in a favorable position.
- iii. **Fragmentive explosive bolts** and nuts contain explosives that detonate internally. Explosive bolt is a technology in which a pyrotechnic fastener is initiated electrically and the charge breaks the bolt at notches where the severance should occur.
- iv. **Electro explosive devices** are devices that can be detonated with electricity or electrostatic charge. These ordnance devices can be ignited by radio frequency as well.
- v. **Non-fragmenting explosive nut** is a sealed explosive technique where the bolt is freed upon initiation followed by the ejection of the bolt by a piston.
- vi. **V-clamp band** consists of an upper ring attached to the spacecraft, a lower ring attached to the launch vehicle and a clamp band circumferentially tensioned to both rings. The clamp band is tensioned by bolts and explosive cutters that sever the bolts.
V-clamp bands are attached to severable load-carrying devices and provide a field joint.
- vii. **Frangible nut** is an explosively splittable nut in which the bolt remains intact but the nut splits upon detonation. The fragments are captured by energy absorption material.
- viii. **Pyrofuze** is a sandwich construction where a sheet of aluminum is held between two sheets of Palladium. This is initiated by applying sufficient heat to melt down the aluminum which causes the palladium to alloy. This reaction is exothermic and is violent and continues till it cools down or till all the materials are consumed, whichever is earlier. A detonating device is introduced which is capable of increasing the temperature making it an alloy.

- This alloy lacks structural capabilities and hence the structure will reduce to component parts and separate.
- ix. Some explosive type separations tend to produce deformation at the edges known as flowering which impairs the aerodynamic stability of the next stage.
 - x. **Pin pullers** are linear actuators in which a pin or a piston remains in a position in which it blocks a deployable element. On activation, it retracts releasing the mobile element.
 - xi. **Pin pushers** are actuators where a connection link is released upon initiation and the gas pressure pushes the pin forward.
 - xii. **Diaphragms** include a T-flange on the outer petals of the central disc which connects the stages and is a one-piece circular coupling.
 - xiii. **Springs** convert potential energy to kinetic energy. If the bodies are spinning, a single spring is adequate but for non-spinning separations or when allowable tip-off errors are small, three or more springs are to be used.
 - xiv. **Pneumatic lock and release mechanisms** include the use of pressurized gases for the separation event. Gas-operated pistons force the continuing body by gas pressure generated in a cylinder. It provides reliability.
 - xv. **Bellows** expand to separate the stages and provide release, and may be preloaded in a compressed position or activated at the time of separation.
 - xvi. **Stage ignition** refers to the motors of the continuing stage being fired upon disconnection of stages. Exhaust-gas pressure creates a separation force and also accelerates the continuing stage.
 - xvii. **Auxiliary rockets** can be located on continuing or jettisoning stage and provide separation when fired.
 - xviii. **Thrust reversal** refers to a pressure-venting device in front of the solid-propellant rocket motor which reverses thrust of the expended stage on signal. The exhaust gases impart some separation impulse to the continuing stage.
 - xix. Yo-tumble system causes weight on cable located off the center of gravity of expended stage to unwrap a spinning body and cause it to de-spin and tumble due to unbalanced forces.

3.3 Challenges in Separation Systems

The challenges faced during previous launches help in refining the design of stage separation systems [5]. Some of the perceivable challenges in the design of stage separation systems are discussed here.

3.3.1 Shock and Vibration

Pyro shock-induced vibration environments may damage vulnerable components in the vicinity of the separation system joint. Pyro-shock vibrations and aero-thermal

environments induced by small solid motors and pyrotechnics, can damage avionics or lead to upper stage engine over pressure and over temperature. The release system is complicated and the extra parts increase the system weight. Safety concerns for unintended release persist.

3.3.2 Space Environmental Effects

Space environment effects pose a questionable problem on ordnance devices. There isn't enough data on the effects of radiation on detonating cords and shaped charges which pose a risk of outgassing/subliming of the explosive. Spacecraft separation systems face different environments and circumstances and they need to be able to get through them without failure. The structure should be able to withstand flight loads under extreme conditions and be able to survive contamination/debris and be lightweight.

3.3.3 Tension, Friction and Loadings in Mechanical Systems

V-bands have high tension requirements due to the combined weight of the belt, clamps and ancillary devices such as springs and often required specialized equipment to tension the band, which increases the overall weight. High tension and release shock limits the life of the components and hence limits the testing. The use of mechanical systems, though over pyrotechnics is much preferred, posed a problem of discharge of solid matter (slugs, springs, pressure cans). Load peaking i.e. concentration of load in areas of high stiffness should be taken care of. Friction control is an important factor between moving surfaces and is to be taken into consideration. The system becomes susceptible to high friction when the lubricated surface finishes wear away and it is imperative that a low friction is maintained. The system should be able to withstand random or sinusoidal vibration, rocket-thrust misalignments, acoustic noise, humidity and pressure.

3.3.4 More Separation Time

Mechanical systems are usually more complex and require more time to separate completely. In the case of abnormal separation, there is a fine chance for the system to collide. To obtain a positive velocity in the minimum time, requires the use of pyrotechnic devices but they produce shock waves and "no-control duration" is increased though less, but significantly upon the usage of mechanical systems. Collision between the stages can occur due to aerodynamic wake behind the continuing body. Ball lock pins cause problems including alignment, friction, binding and tip-off. Pneumatic lock and release contain compressed gases which is compressed energy and hence pose safety concerns.

3.3.5 Stress Corrosion and Gas Corrosion

Immediate failure in preloaded systems has caused stress-corrosion cracking which can be controlled by minimizing the potential stress concentrations. Ignition of the upper stage liquid fuel engine under conditions free of thrust will result in the carrier rocket propellants moving forward from the bottom of the fuel tank which results in the production of gas bubbles at the turbine pump opening. This phenomenon is known as 'gas corrosion' and results in unsteady combustion which might lead to a dangerous explosion. The systems often include auxiliary devices such as extra drag flaps, single-yo tumble systems, tumble motors etc., to alter the trajectory of the expended stage.

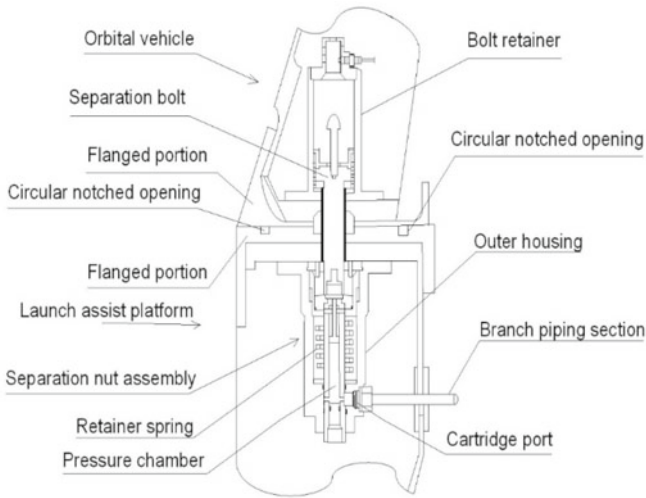
3.3.6 Safety and Related Problems in Pyro-devices

Electro-explosive devices or EEDs may be accidentally ignited by electrostatic charges and cannot be stated safe as sometimes RF (radio frequency) could set it off. The buildup of static electricity in the body ignites these devices upon contact. Diaphragms are used for small-diameter solid-propellant boosters. They can be used with success within the atmosphere as the spinning of the vehicle may cause the separation joint to be keyed preventing the stages from premature separation. Pin-pullers or pushers cause design problems including alignment and matching of force, displacement and time characteristic of pin units and lateral loads. LSC causes severe blast, contamination and fragmentation, and may require blast shielding. Springs add to the weight and complexity of the system and are costly. FLSC generates high levels of shock. MDF may cause higher fragmentation than LSC. Many launch vehicles have been lost due to failure in the explosive system and many more due to pyrotechnic shock.

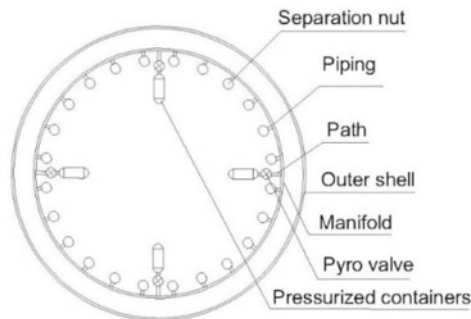
4 Design Configurations

4.1 Separation by Fluid Communication of Pressurized Gas

This separation system contains separation nut assemblies actuated by fluid communication of pressurized gas [5]. The cross-section connecting orbital vehicle and launch assist platform is as shown in Fig. 2. A flanged portion of the upper orbital vehicle connects to the flanged portion of lower launch assists platform using separation nut assembly. This includes an outer housing surrounded by retainer spring. A cartridge port connects branch piping section. Fluid communication path between branch piping section and separation bolt is provided by pressure chamber. A plurality of these separation nut assemblies are used to decouple launch assist platform and orbital vehicle. Upon actuation of pyrotechnic valves in right side of Fig. 2, fluid



(a) Partial cross-section illustrating juncture between launch assist platform and orbital vehicle



(b) Cross-section of a portion of the separation system

Fig. 2 Separation by fluid communication of pressurized gas

communication is established between pressurized containers and manifold. Manifold is a circular hollow tube. This allows trapped gas to travel through pyrotechnic valves through branch piping sections, fully charging manifold. Pressurized gas proceeds through branch piping sections into separation nut assembly via cartridge port causing the release of retainer spring. Bolt retainer is used to capture separation bolt. The objectives of this design are to use limited number of pyrotechnics whereby the structural damage and flying debris are reduced, and to prevent unwanted side velocities, uneven separation and structural damage. This method is safe, reliable and cost-effective. The disadvantages are that in case of a leak or a rupture, the pressurized gases can lead to a catastrophic failure. High force is required to maintain

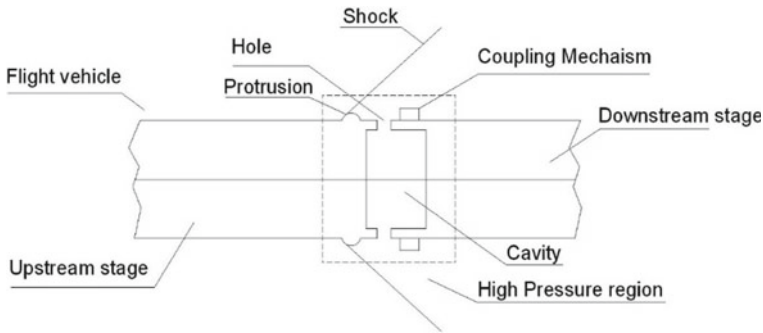


Fig. 3 Cavity pressure rise stage separation system connecting forward and aft part

and seal the frictional grip. The use of pyrotechnics, though limited, still causes significant shock.

4.2 Separation by Holes in Fluid Communication

This separation system contains one or more holes in fluid communication with a cavity between upstream portion and downstream stage of the flight vehicle [6]. Local variations in the form of protrusions or tabs are used to produce shocks and which lead to an increased pressure in the regions in Fig. 3. One or more holes are provided for fluid communication with the cavity. The elevated pressure in the cavity facilitates the separation of upstream and downstream portions. This system could be improved by increasing the effective area of the cavity, by coupling it with explosive bolts, releasable latches or other mechanisms and/or by including a series of protrusions. The holes should be close to the shocks since the pressure decreases as we move aft of the launch vehicle. Some of the advantages of this mechanism are reduced weight, cost and complexity. The major drawback is the increase in drag which implies a greater fuel consumption. The shock produced is also not desirable.

4.3 Micro-cylinder Pyrotechnic Gas Actuated Separation System

The system comprises of a hub with multiple components of micro cylinders 3 arranged radially [7] as shown in Fig. 4. A cylindrical casing extends across the section which has housings for receiving the outwardly directed fingers of micro cylinders in an assembled position. In hub is the housing of a cartridge pyrotechnic which distributes pressure uniformly to annular chamber. The fingers of the micro-cylinders are directed outwards and are housed in corresponding radial housings of

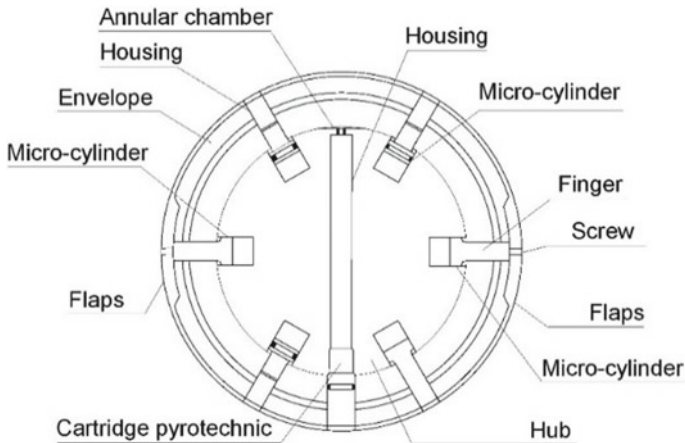


Fig. 4 Sectional view of micro-cylinder separation system

a cylindrical envelope extending to the other section of the separation system. These fingers lock both sections before actuation. When the operation of the cartridge is triggered, the pressurized gas generated by pyrotechnic means actuates the micro-cylinders whose fingers retract inside thus unlocking the two sections. Flaps 5, two in number, are mounted on the aft section, fixed in the retracted position to the finger vis-à-vis by a rupture screw. During unlocking, the movement of removal of the fingers 7 ensures the breaking of the screws which releases the flaps. The forward section continues its movement due to the initial speed of the machine while the latter is braked aerodynamically by the flaps ensuring separation. This mechanism is desirable due to the absence of shock wave and the risk due to splinters. The system is designed for missiles.

4.4 Fastening and Separating System

This system for satellites comprises a fastening piece screwed to upper ring of adapter of launch vehicle [8] as shown in Fig. 5. The tensioning strip consists of a metal band in two parts which surround clamps which serves to fasten satellite. They have thin walled cylindrical body with rotational shaft in its lower part formed by several lugs. These clamps surround and press resting via their upper part on lower ring. Each clamp is allocated at least one pressing cam, of which shaft is fixed and shift is movable and describes a circumference on moving. This forces deformation of piece as shown in Fig. 5, which presses against satellite and against adapter. On applying tension to strip, hook zone of satellite is deformed, separating from catch to which they were joined in open position. Catch is applied to cams and pushes till they come in contact with catch as in the closed position. Tensioning strip is released and

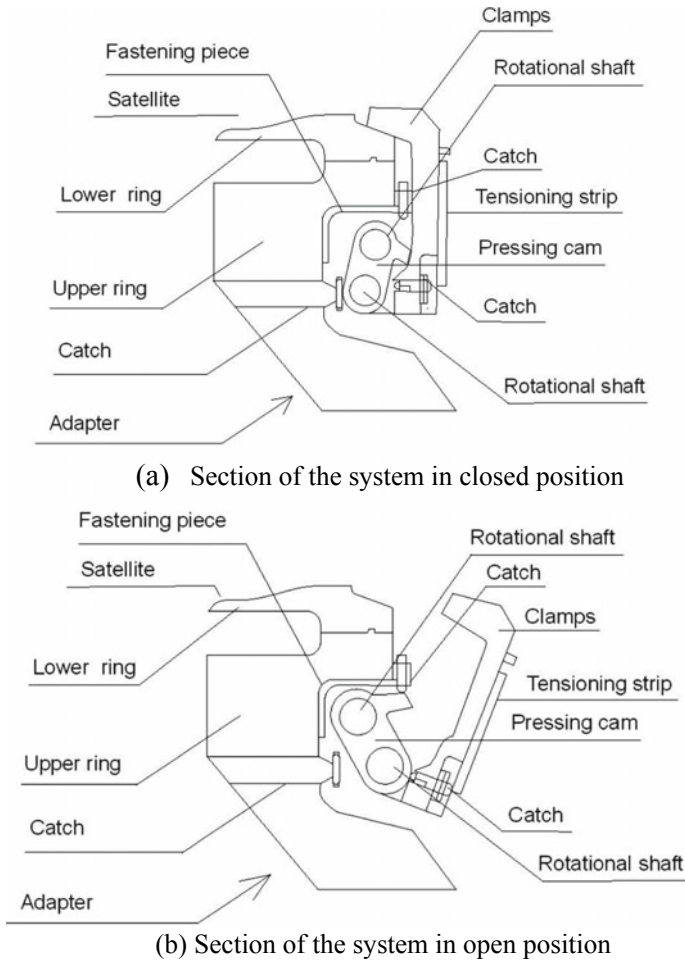


Fig. 5 Fastening and separating system

satellite is released with the assistance of pyrotechnics. Unlike majority of known systems, there is no excessive tension that may lead to seize-up effects resulting in violent satellite release. This system is simple, cost effective and highly reliable. It can be applied to satellites of any size. This system has significant strain energy stored and it might not work through partial failure mode.

4.5 Latching Separation System

This separation method includes latches which rotate about bearing [9]. Lateral member is coupled with latches for synchronized rotation as shown in Fig. 6. Member is held by pins. A pair of lateral members may be used to prevent unwanted torque while using more latches. Outer surface of must be made of deformable material while the hook of the latches must be made of non-deformable material for stable latching. Application of force in the lateral member in the direction decouples the latch and the bearing separating from the launch vehicle. Lower structure and upper structure are formed preferably by extruded aluminum. A motor can be used to provide lateral forces to rotate the latches. This invention is non-explosive, reusable, simple, light weight and inexpensive. This system can be tested and it can be modified depending

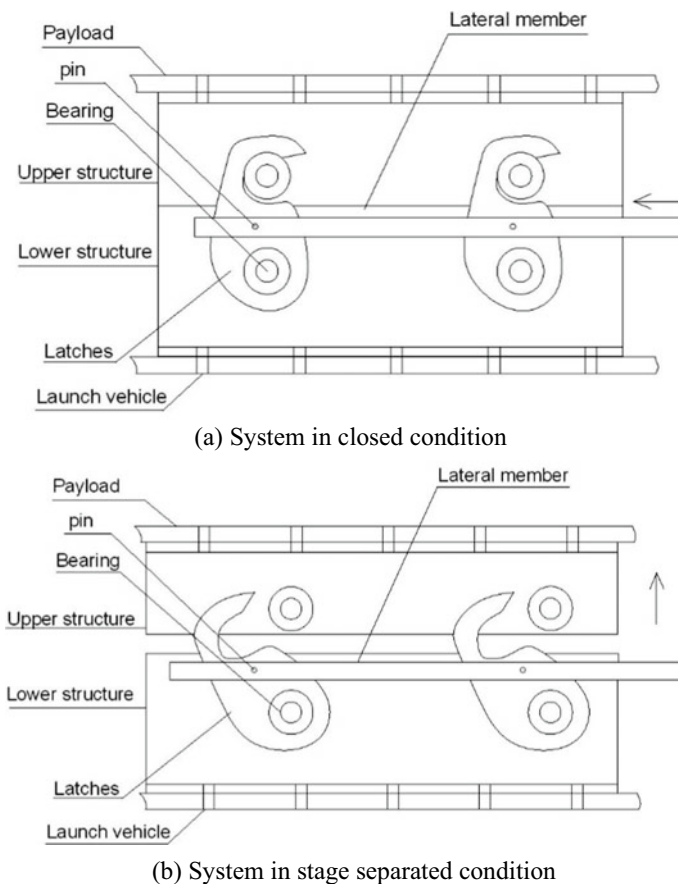


Fig. 6 Latching/coupling separation system

upon the size of the spacecraft, small and large. Possibility of heating due to friction, mechanical shock and high stress are some disadvantages.

4.6 Confined Linear Explosion Separation System

This method uses confined linear explosive for separation [10] as shown in Fig. 7. The female member has a cross section view similar to a clevis. Located in the outside surfaces of the flanges and generally aligned with the fillets are an opposing pair of shear lip grooves. Mounting the female member to the forward section is accomplished by fastener assemblies, each consisting of a nut and bolt. Female member of the separation joint assembly consists a pair of opposite spaced flanges having outside surfaces 18 and inside surfaces 15 intersecting with bottom portion to form a fillet. Shear lip groove pair are aligned with outside flanges. Female member is mounted onto a forward section by fastener assembly containing nut and bolt. Linear explosive is embedded in elastomer contained in a metal tube. After firing explosive, gases of detonation inside elastomer surrounds the tube due to the pressure of explosive gases, forcing shear at plane which is the centerline of groove. This system is light-weight, non-contaminating and has a structurally efficient separation joint which results in a continuous fracture. This system produces shock, causes permanent deformation to the structure and cannot be tested due to use of ordnance devices.

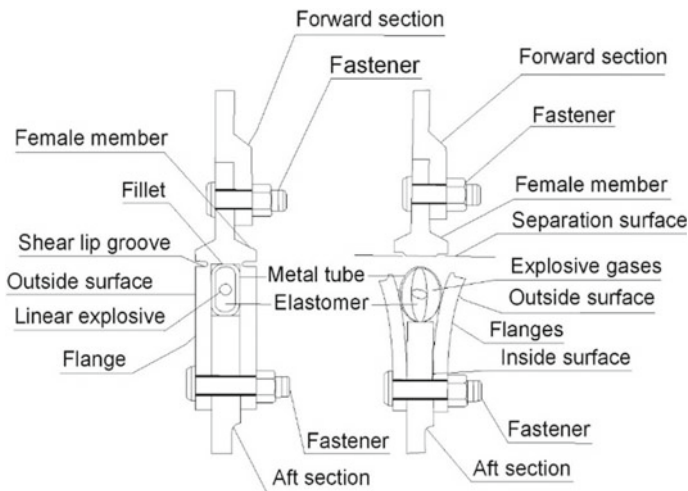


Fig. 7 Section view through the separation joint before and after separation

4.7 Pyrofuze Separation System

Pyrofuze is a sandwich construction where a sheet of aluminum is held between two sheets of palladium [11] as shown in Fig. 8. This system is initiated by applying sufficient heat to melt down the aluminum which causes the palladium to alloy. This reaction is exothermic, violent and continues till it cools down or till all the materials are consumed, whichever is earlier. A detonating device is introduced which is capable of increasing the temperature making it alloy. In this separation system, pyrocore fuse is positioned in close contact with pyrofuze sandwich by means of a U clamp, capable of being ignited by electrical or non-electrical means with detonation ignition core. Pyrofuze has sufficient thickness to maintain structural integrity of 11 and 12 by means of connecting bolts. Parts 1 and 2 are formed by aluminum extrusions of which their ends define chamber. The said chamber accepts pyrocore and holder, and holds expanding gases generated by initial detonation of pyrocore by ignition. Once pyrofuze sandwich alloys, bond between parts 1 and 2 is broken, as the alloy lacks structural capabilities and hence the structure will reduce to component parts and separate. Pressure build up in chamber will push part 1 and part 2 away ensuring fairing. This mechanism provides simultaneously and quick fairing in addition to being light weight, strong and offers minimum air resistance. The use of pyrofuze makes the system impossible to be tested and reused, and causes significant shock.

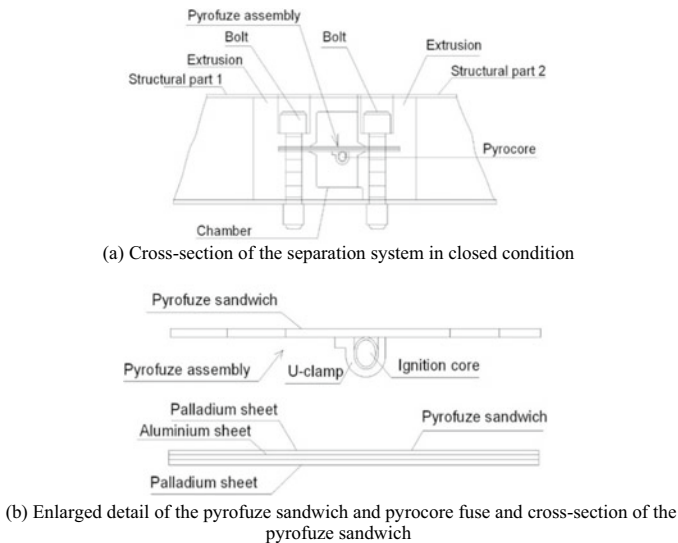


Fig. 8 Pyrofuze separation system

4.8 Linear Explosive Separation Device

This separation device as shown in Fig. 9 utilizes a detonating shaped charge to separate severed sections [12]. The separation device comprises an annular strap or ring having inner diameter closely fitting the casing section of forward section and rearward section. Strap overlaps abutting the end portions so that the cleavage plane is located between the ends of the straps. The strap is attached to forward and rearward section by circumferentially placed rivet. The strap has an annular flange at one end surrounding the end portion of forward section with holes through which the rivets extend. Shaped explosive charge is mounted in the closed annular chamber which comprises an annular ring of MDF type explosive having outer shape and V-Shaped recess which is flexible. It collapses the metal liner upon detonation. A row of rivets inserted to attach the strap. A length of FLSC is inserted in the annular recess. Flange of annular strap and end portion of the rearward section, join forward and rearward sections through the strap. FLSC is detonated upon actuation which causes a shock and pressure build up in the closed chamber. Simultaneously metal line cut thin wall around the periphery of the strap. Cover plate prevents explosive damage to regions opposite to thin section. The energy generated is used in cutting the reduced section and separating the sections. This system is advantageous as it eliminates flowering or deformation at least one edge, is simple, compact, lightweight, easy to manufacture and is reliable. Significant shock is produced. Shock loading depends upon the type

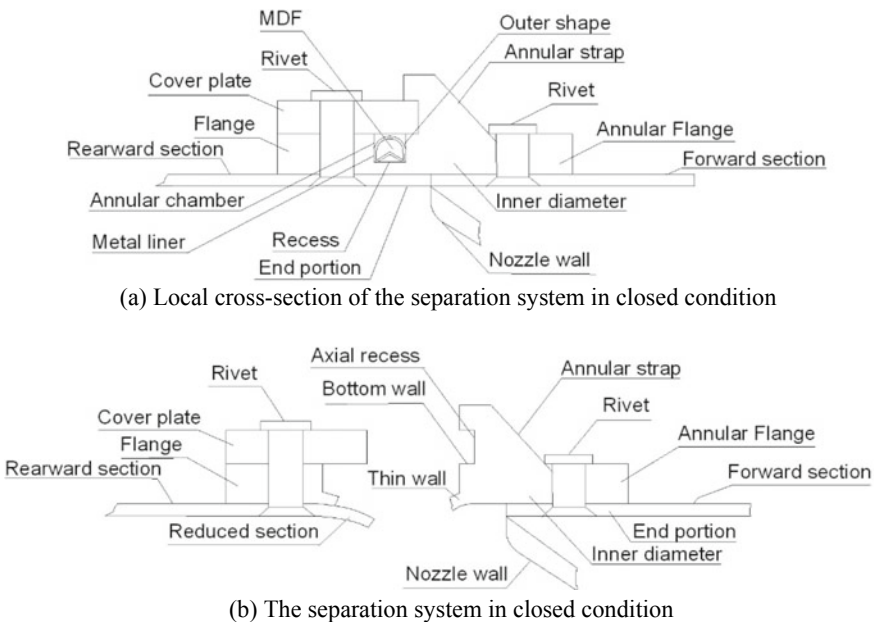


Fig. 9 Thin wall section of the separation device cut by the shaped charge

of material to be cut. Fragmentation and debris from the severance is relatively high and might cause damage to the continuing structure.

4.9 Shear Pin Pyro-Mechanical Mechanism

Load is mechanically released from the structure by the use of shear pin [13] as shown in Fig. 10. A quick-release disconnect device having a load bearing bolt is positioned vertically in a central opening in a main body. A frangible shear pin positioned across the upper part of the central opening prevents vertical movement of an upwardly biased retainer member which retains the load bearing bolt in position. This is accomplished by preventing inward movement of a combination of balls positioned through the wall of the load bearing bolt. Each ball is provided with holder, screw threaded to body and bearing against side of the ball. Thus balls are prevented from moving horizontally and held in position to prevent vertical movement of the bolt. Destruction of the shear pin permits upwardly biased movement of the retainer member allowing the balls to drop inward and release the bolt from the main body. This device produces a mechanical release of a load carrying element without directly subjecting the element to shock due to pyro-initiation. It is lightweight, highly reliable, simply constructed and operates in an efficient and positive manner. There is fragmentation and the debris which might damage to the structure.

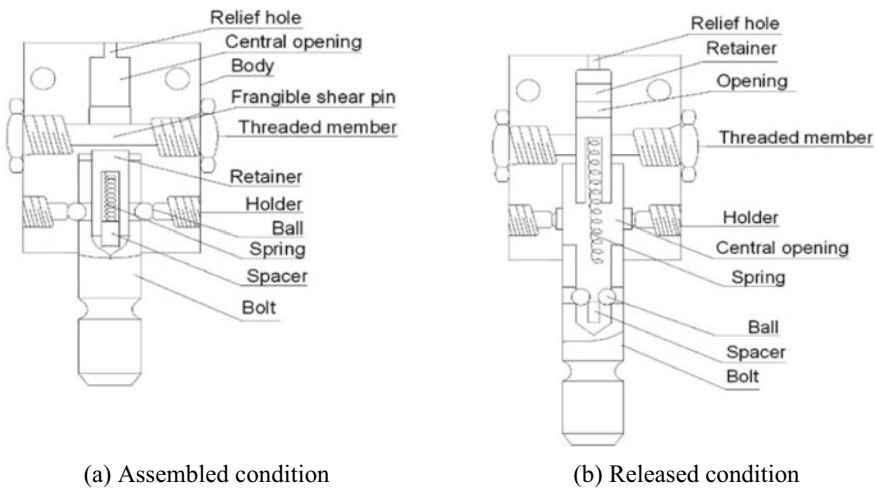


Fig. 10 Longitudinal view in partial cross section of a pyro-mechanical release device

4.10 Explosively Actuated Separable Structure

Areas of weakness are provided to ensure separation by explosive actuation [14, 15] as shown in Fig. 11. The invention contains two structural parts connected together by a pair of separation plates affixed by suitable fastener pins. An explosively actuated expandable tube is positioned in the space between both plates and ends of the structural parts. The tube includes an explosive cord within a metal tube which is oval shaped. Between the rounded sides of the metal tube and the ends of structural parts, a cushioning material is provided to protect the soft rounded sides of the expandable tube. Each separation plate has two areas of weakness at the notches. Plates at the notch affixed to separation plate 1 are weaker than plates 2 and upon explosive actuation, weaker plates formed by notches or grooves sever when the stronger plates bend. Location of notches or grooves is important for proper operation. The areas of weakness which act as hinges about which the severed portions of the plates can bend or rotate more easily upon explosive actuation, reduce the amount of explosive energy needed to sever and rotate the plates. This method can be employed for stronger structures and is capable of carrying higher structural loads at the exact

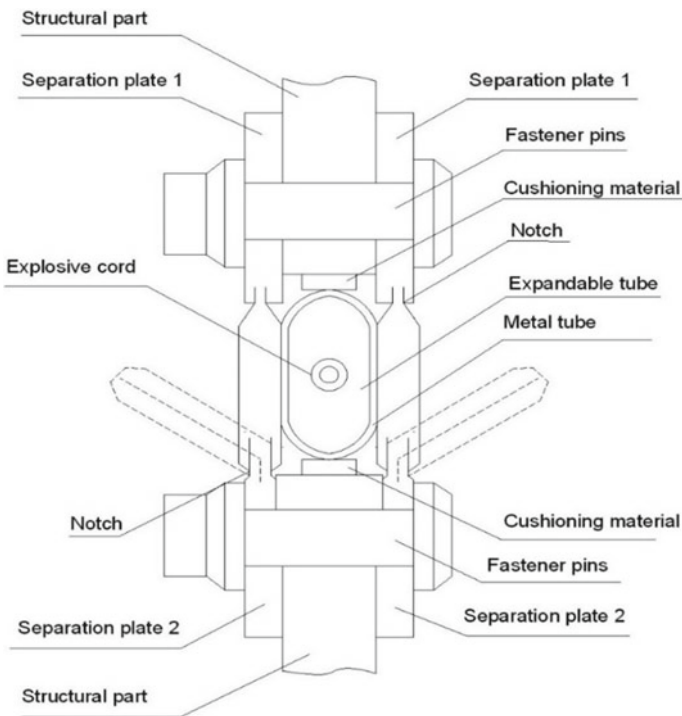


Fig. 11 Fragmentary sectional view of explosively separable structures

time. Explosive energy required to sever the plate causes high shock and vibration. This system produces fragmentation and debris.

5 Conclusion and Future Work

The separation systems discussed pose a problem in one way or other. While choosing the separation system for a particular launch vehicle, it becomes imperative that one consider the purpose and analyze the aspects involved. Almost all of the pyrotechnic devices cause major shock which is capable of damaging the payload after release. Reliability is an important factor and it is advisable to have redundant features in the system so that the release doesn't cause any significant damage to the system even in partial-failure mode. High separation force versus system weight is achieved by pyrotechnics as they release a high amount of energy while being compact, but they need to be synchronized and actuated with high accuracy. Mechanical systems can be tested multiple times while pyrotechnic systems cannot be. Pyro shock, mechanical shock, fragmentation, tip-off and contamination are faced while using almost the systems. A separation system should be chosen for a purpose after considering all the advantages and disadvantages and suitability. The system should be able to function even in partial failure mode and hence most systems have redundant features. Future attempt is to develop a new stage separation system to achieve relatively low shock levels <2000 g for @ <5 ms.

References

1. Mitchell DH, NASA (1970) Flight separation mechanisms. Langley Research Center, Hampton, Virginia, pp 2–63
2. Yu X (1983) Separation between stages of multistage carrier rocket, China, Air Force Systems Command
3. Subhankar D (2017) Mechanisms facilitating stage separation & satellite (D, 2017) deployment with the PSLV. India. <https://www.spansen.com/2017/02/pslv-stage-separation-case-for-launch.html>
4. Hopkins J Jr, Hopkins J, Isakowitz S (2004) international reference guide to space launch systems, American Institute of Aeronautics and Astronautics, Inc. pp 3–357
5. Lucy MH, Hardy RC, Kist EH Jr, Watson JJ, Wise SA (1996) Report on alternative devices to pyrotechnics on spacecrafts. In: 2010 annual AIAA/USU conference on small satellites, Virginia
6. Mueller GE, Cochran DB (2001) WA (US), Stage separation system and method-US6289818B1
7. Daniel D, Jeffery R, Charles M, Robert D (2017) Stage separation mechanism and method-EP3663704A1. US, Raytheon Company
8. Denis JF, Fourniols J, Laurend P, Lienard A (1996) Device separation system with mechanical unlocking and aerodynamic exhaust-FR2741710A1
9. Miguel V, Fernando J (1997) Madrid, fastening and separating system for satellites-EP0768241A1
10. Holemans W (2011) MD (US), latching separation mechanism-US007861976B2

11. Noel R, Shouvrouek BV (1987) CA Separation System-USPatent-4685376
12. Stefano MN, Rush SH, Green SL (1967) CA, High speed low shock separation system-US3319520A (1967)
13. Weber WL, Dattilo AW, Bristol UK (1963) Explosive separation device- US3863570A
14. Eaton B (1972) CA, Pyromechanical release device-USPatent-3640174
15. Olcer NY (1992) CO, Explosively actuated separable structure-US005109749A

Testing and Numerical Simulations on Fracture Behavior of Fresh Quartzite Rock Using the Discrete Element Method



G. V. Ramana , Jaisingh Verma , and P. Ravi Prakash 

Abstract Discontinuities play a significant role in the analysis and design of rock structures, e.g., tunnels, stability of slopes, blocky rock masses, etc. Therefore, the following study is conducted using a discrete element method (DEM) model in Universal Distinct Element Code (UDEC) software which takes into consideration the discontinuities present in the material medium, both load-induced as well as inherent discontinuities. The DEM model in UDEC is used for the study to simulate the Uniaxial Compressive test response of Fresh Quartzite Rock. The Quartzite Rock is taken for this study because the same rock was encountered at a project site Saundatti, Karnataka, which has been identified as an amenable place to develop an integrated project by Greenko Group. In this study, all the laboratory experiments are performed on the Quartzite rock, and its behaviour is understood with those experimental results. Out of all the experiments, Uniaxial Compressive Strength (UCS) Test is chosen for the simulation purpose. The specimen model used for simulation of UCS is 110 mm in height and 54 mm in width. The specimen is further subdivided into around 900 smaller deformable blocks to simulate the field condition accurately. The model is bounded at the top and bottom by steel platens to ascertain relatively uniform load transfer across the specimen cross-section. The contact points between the deformable blocks are characterized with the normal and shear stiffness, with their nonlinear behaviour modelled from Mohr–Coulomb failure envelope (shear regime) and Rankine tension cutoff (tension regime). These micro-mechanical parameters to the DEM model are characterized by the obtained macro-level parameters from laboratory experiments. The simulation of UCS using UDEC is carried out to quantify the deformability characteristics, fracture patterns, and the stress–strain curve of the rock specimen. The deformability characteristics obtained from the numerical model

G. V. Ramana (✉) · J. Verma
National Institute of Technology, Warangal, India
e-mail: gvramana@nitw.ac.in

J. Verma
e-mail: verma_ce19221@student.nitw.ac.in

P. Ravi Prakash
Indian Institute of Technology, Jodhpur, India
e-mail: rp@iitj.ac.in

are quite consistent with that of experimental observations and is mainly due to the precisely chosen micro-mechanical parameters. Moreover, the cracks initiation and propagation, stress profiles and deformation patterns obtained in the simulation are studied intricately.

Keywords Fracture behavior · Discontinuities · Distinct element code · Uniaxial compressive strength

1 Introduction

Quartzite is a non-foliated metamorphic rock, an excellent medium for constructing dams and tunnels across the flowing stream of irrigation projects. Moreover, the rock is a naturally occurring geological material characterized by discontinuities in the form of joints, fissures, and inclusions. Therefore, representative design parameters of rock play a critical role in engineering design practices. In the past several decades, many research investigations have been undertaken to understand the fracture behaviour of rock specimens under various stress states. Many researchers have studied the deformation, peak and post-peak strength characteristics of rock specimens from their comprehensive experimental campaigns [1]. It should be mentioned that in the recent decades, there has been increased attention among the researchers on investigating the multi-scale behaviour of various rock specimen and the subsequent application in the performance-based design of engineered structures. Such studies are usually supported by physics-based numerical models, which account for the inherent as well as load-induced discontinuities along with relevant experimental studies [1].

Discontinuities play a vital role in the analysis of rock structures, especially for tunnels, caverns, blocky rock masses, slope stability problems, etc. Inherent discontinuities expected in rock masses (also referred to as joints, contacts) is a surface or plane that represents a change in the physical or chemical characteristics of a rock. The discontinuity can be in many forms, such as bedding, foliation, cleavage, crack, fissure, joint, or fault plane. These discontinuities affect the rock's response as they reduce its strength and induce nonlinearities in their deformation characteristics by altering the stress–strain response [2]. The other form of discontinuities expected in rock masses corresponds to load-induced discontinuities, which might result from various natural hazards (earthquakes, avalanches, etc.) It is to be noted that there are different techniques available to study such discontinuities [3–5], and notable mentions include traditional FEM, DEM, MPM, etc. Although conventional FEM has been well explored for solving various rock mechanics problems, they result in inaccurate model predictions, especially while handling discontinuities [6]. One potential alternative in this context includes the DEM, which has been utilized in the present study. In the case of DEM, complete detachment of particles is allowed and therefore, inherent discontinuities and load-induced discontinuities expected in rock masses can be modelled precisely.

The present study is conducted using a discrete element method (DEM) model in Universal Distinct Element Code (UDEC) software which takes into consideration the discontinuities expected in the material medium, both load-induced as well as inherent discontinuities. Different rock samples from the site were collected, and all the laboratory experiments were performed on the collected samples to characterize the Quartzite rock. The data collected from the laboratory experiments were used as input parameters in the numerical simulation. The Unconfined Compressive strength (UCS) test was chosen to carry out the numerical simulation, with emphasis on deformability characteristics, stress–strain response and fracture patterns, respectively.

2 Discrete Element Method

Discrete Element Method, also known as Distinct Element Method, is a discrete particle-based numerical technique and has been well explored for discontinuum simulations on rocky medium after it was first introduced by Cundall [7]. In the present study, a plane stress-based modelling strategy is chosen for the UCS test. The material medium in DEM is modelled as an assemblage of numerous small discrete semi-rigid 2-D polyhedral blocks. The mathematical foundations for such DEM framework can be seen in Cundall [7], and not repeated herein for the sake of brevity.

The blocks are connected to the neighbouring particles through contacts (See Fig. 1), and these contacts are treated as boundary conditions during the simulation. Moreover, the new contacts generated during the deformation are identified, and their forces and displacements are updated at each step. DEM allows translation motion and a rotational motion to the particles, which are again updated at each time step.

The assumptions pertaining to the present DEM framework is discussed herein. Firstly, the polyhedral blocks are semi-rigid with finite inertia (inertia of mass and rotation) and can be described analytically. The blocks can translate and rotate, and their interaction with neighbouring blocks will be governed by the contact algorithm. The interaction between the corners of a block is depicted by the contact behaviour, which is governed by the normal and shear contact springs and is assumed to be decoupled in the present study. The normal spring is assumed to be elastic in the compression regime, whereas in the tension regime, simple Rankine tension cutoff in normal tensile stress (σ) is considered and is mathematically written as

$$\sigma \leq f_t, \quad (1)$$

where, f_t corresponds to the Rankine cutoff tensile strength. In the case of the shear regime, the failure envelope is governed by Mohr-Columb failure envelope (see Fig. 1) and is mathematically written as

$$\tau \leq c + \sigma \tan \varphi, \quad (2)$$

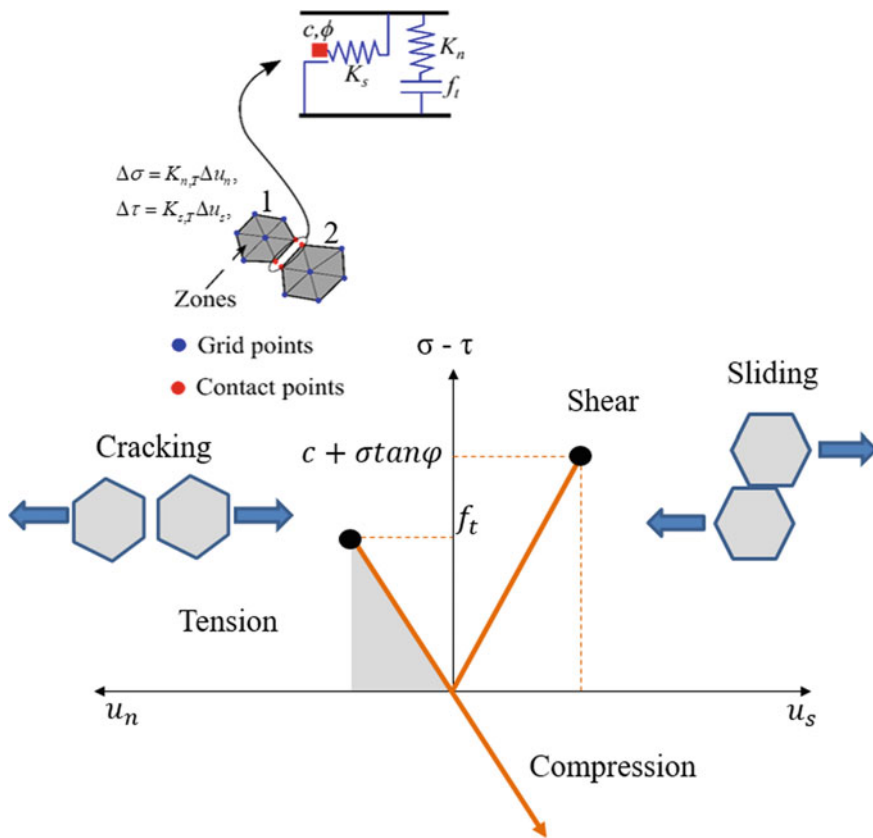


Fig. 1 2-D DEM model

where, τ , c and ϕ represent shear stress, cohesion and friction angle, respectively.

Blocks 1 and 2 represent the two semi-rigid connected by springs. The spring stiffness K_n and K_s acts in the normal and tangential direction, respectively. The friction coefficient μ represents the friction between the particles.

3 Sample Preparation and Testing

The rock samples were collected from the project site, Saundatti, Belagavi, Karnataka and the specimens were prepared as per the IS: 9179–1979 according to the requirement of the laboratory experiments. After the specimen preparation, laboratory experiments, namely: Bulk density test, Brazilian Test, Triaxial Compression and UCS test, were conducted. UCS of the Quartzite Rock was conducted to determine the peak strength, Modulus of Elasticity (E), and Poisson’s ratio (μ). The parameters obtained

Table 1 Properties of quartzite rock obtained from the experimental investigation

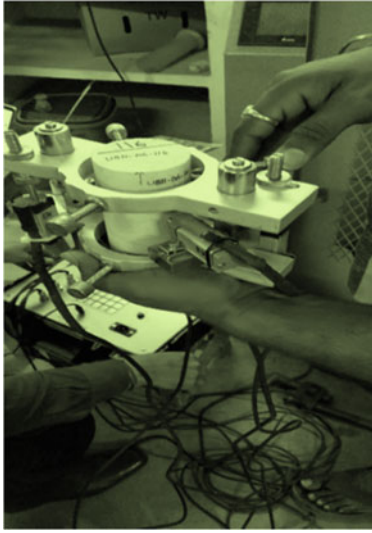
Parameters	Experimental values
Density	2807 kg/m ³
Tensile strength	14 MPa
Cohesion	3 MPa
Friction angle	55°
UCS	57.8 MPa
Modulus of elasticity (E)	41.5 GPa
Poisson's ratio (μ)	0.24
Shear modulus (G)	16.73 GPa

during the UCS testing were later compared with the Numerical Results. Moreover, the fracture patterns obtained during the experiments were also compared with the fracture patterns obtained numerically during DEM simulations. The values obtained experimentally are shown in Table 1.

3.1 Uniaxial Compressive Strength

Uniaxial Compressive Strength (UCS) is performed in the laboratory to quantify the deformability characteristics of the rock. The deformability characteristics of the rock include Modulus of Elasticity, E and Poisson's ratio, μ . The specimen with an L/D ratio of 2.0 is placed in the loading frame bounded at the top and bottom by steel platens. Four strain gauges, two vertical and two circumferential, are wound around the specimen, as shown in Fig. 2(a).

These strain gauges are further connected to the Wheatstone bridge circuit of the Multi-point Measuring Unit, as shown in Fig. 2(b). The axial, as well as lateral strains, are recorded from this unit. After the setup is ready, the specimen is loaded axially between the platens in the UTM, and the failure stress is recorded as the failure load per unit area of the cross-section of the specimen. The rate of loading should be such that the specimen fails in about 5 to 10 min. In other words, the stress rate should be in the range of 0.5–1.0 MPa/s. In order to determine the deformability characteristics of the rock, the sample is not loaded to failure at once. It is performed in two cycles of loading and unloading. During the first cycle, the sample is loaded up to half of the expected UCS value and then unloaded to the initial or seating load. This is done in order to know the irrecoverable strain or permanent set of the specimen. The sample is loaded again, and the load is increased till the specimen fails. During the process of loading and unloading, the strains, both axial and lateral, are being recorded in the Measuring Unit at fixed intervals. These strains are used for plotting stress–strain curves and calculating the Modulus of Elasticity, E and Poisson's ratio, μ . These parameters are calculated at 50% of the UCS value and not up to the full UCS value.



(a) Strain Gauges



(b) Multi-point Measuring Unit

Fig. 2 Experimental setup of UCS. **a** Strain gauges **b** Multi-point measuring unit

4 Simulation Framework

For the previously discussed Quartzite sample, DEM analysis is performed in a plane-stress setting in UDEC. The principal reason for such an assumption is to facilitate computationally efficient numerical modelling, and such modelling strategies have been well established by earlier studies [6, 8]. The DEM model employs a two-level discretization strategy, as shown in Fig. 1, wherein the sample is discretized with 2-D polyhedral blocks, and the blocks are further discretized into zones. For the present simulation framework, the zones are assumed to be elastic, and a tension-shear mode of failure is considered at the contact points. Moreover, such nonlinear failure modes are characterized in an iterative manner from the obtained macro experimental properties discussed in the previous section.

4.1 Model Geometry

The Quartzite specimen used for the UCS experiment was 54 mm in diameter and 110 mm in height, as shown in Fig. 3. Using aforementioned sample dimensions, the 2-D DEM model (Sample dimensions: width = 54 mm; height = 110 mm) is created in a plane-stress setting as discussed previously. The specimen is bounded at

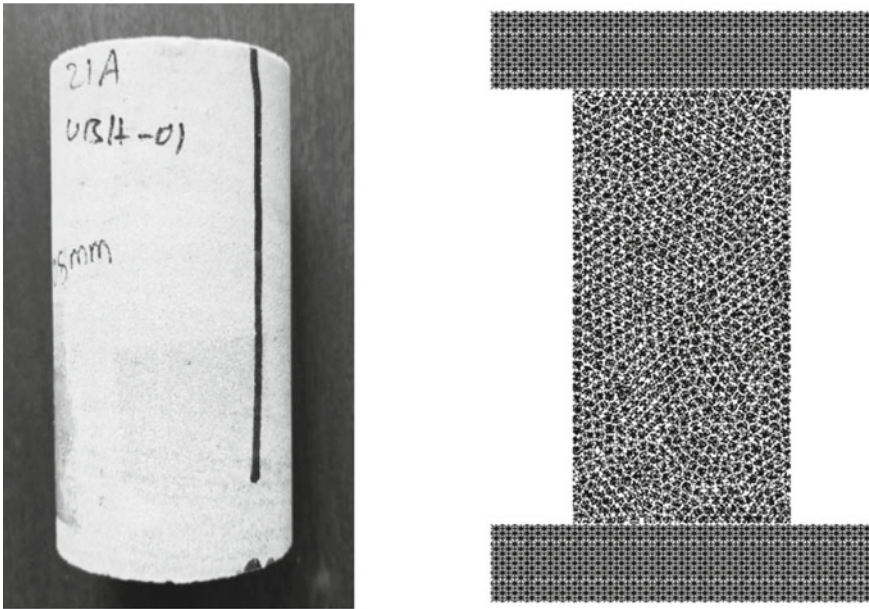


Fig. 3 Quartzite specimen and the corresponding DEM model

the top and bottom by steel platens to ascertain uniform load distribution throughout the specimen, as shown in Fig. 3.

The height and width of the steel platen are 20 and 94 mm, respectively. The Quartzite model bounded between the steel platens is discretized into 900 polyhedral deformable blocks. Subsequently, each block is further discretized into three zones. The experimental UCS test for the chosen Quartzite specimen is strain-controlled. Accordingly, such physical boundary conditions are replicated in the numerical model by fixing the bottom platen and application of velocity of 0.05 mm/s at the top platen. The fracturing process is expected to take place along the contact points. The edge length of each deformable block is 2.55 mm. The chosen block sizes and the number of zones within each block are based on relevant convergence studies and not repeated herein for the sake of conciseness.

4.2 Input Parameters

For the developed DEM model, the input parameters are chosen in an iterative manner from the macro-level experimental observations. The summary of such macro-level experimental observations are shown in Table 1. The elastic properties (Modulus of

elasticity (E), Modulus of rigidity (G) and Poisson's ratio) of the zones within the blocks are directly taken from the macro-level elastic properties of the sample. In the case of the contact points, the normal stiffness (K_n) and shear stiffness (K_s) are calculated using the empirical relation shown below, which is taken from the work of Prakash et al. [6] as

$$K_n = \frac{E_m}{t_b}, \quad (3)$$

$$K_s = \frac{G_m}{t_b}, \quad (4)$$

where, E_m and G_m represent the modulus of elasticity and shear modulus of the Quartzite sample obtained at the macro-level (see Table 1); t_b represents edge length of blocks (2.55 mm in present DEM model). In scenarios where the modulus of elasticity departs from its experimental counterpart, the values obtained in Eqs. (3) and (4) are slightly adjusted for accurate model predictions. The values of f_i , c and φ required for the nonlinear contact behaviour in tension and shear regimes are taken from the macroscopic observations as depicted in Table 1. Upon building the DEM model, gravity analysis is first executed, followed by UCS test simulations, and the corresponding results are discussed in the subsequent sections.

5 Results and Discussions

Table 2 shows the comparison of the macro-level response entities, namely: modulus of elasticity (E), UCS and Poissons's ratio against their experimental counterparts. The results indicate that the DEM based simulation framework is reasonably accurate in simulating the UCS test setup. The obtained stress–strain curve corresponding to the UCS test in the DEM simulation is depicted in Fig. 4. The stress–strain curve indicates elastic response followed by strain-softening as expected in quasi-brittle materials like Quartzite.

The fracture patterns obtained numerically as well as experimentally are presented in Fig. 5. However, it is observed that the obtained fracture patterns in DEM model are inconsistent with respect to its experimental counterpart. This limitation can be partly alleviated with more sophisticated contact models.

Table 2 Comparison of experimental and numerical results

Parameters	Experimental	Numerical
UCS	57.8 MPa	55 MPa
Modulus of elasticity, E	41.5 GPa	41.4 GPa
Poisson's ratio, μ	0.24	0.25

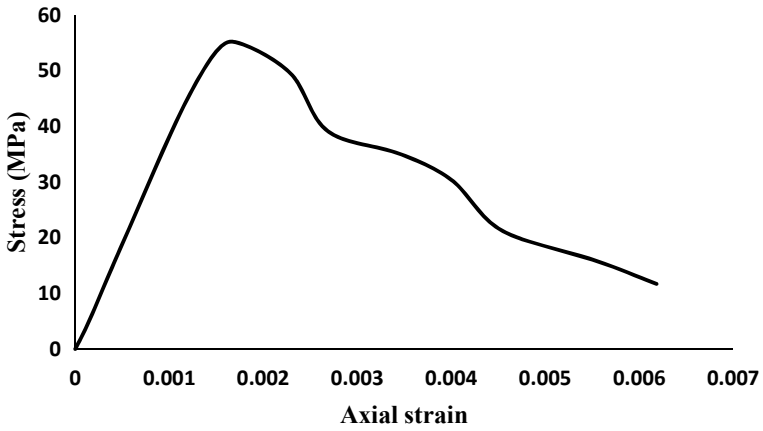
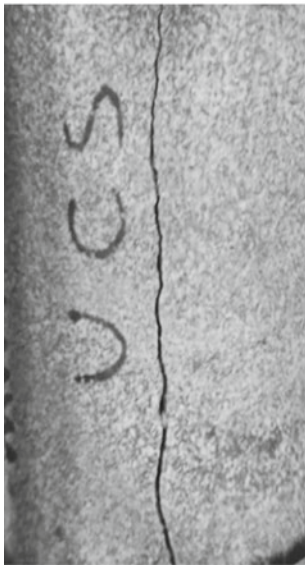
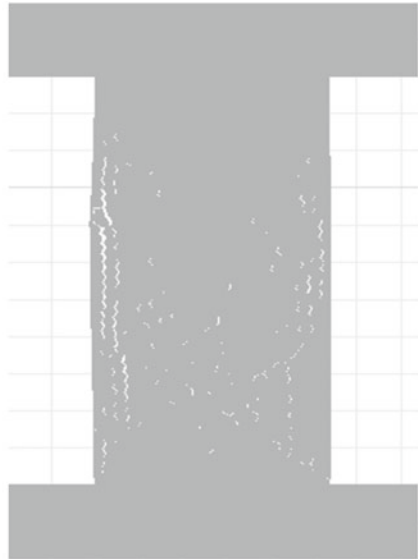


Fig. 4 Stress versus axial strain curve obtained from the numerical analysis



(a) Experimental



(b) Numerical model

Fig. 5 Fracture patterns obtained for the chosen quartzite rock. **a** Experimental. **b** Numerical model

6 Conclusions

In the present study, experiments and numerical simulations were carried out on Quartzite Rock, and the following conclusions are drawn.

1. The stress–strain curve obtained from the Numerical simulation was validated with the experimental results, and the values of deformability characteristics were compared. The UCS value of the rock obtained numerically was 55 MPa which was in close agreement with the experimental UCS value of 57.8 MPa. The Modulus of Elasticity and Poisson's ratio obtained numerically were also consistent with the experimental results. The Modulus of Elasticity, E and the Poisson's ratio, μ obtained numerically were 41.4 GPa and 0.25, respectively. These numerically obtained values were consistent with the experimental results, which produced E and Poisson's ratio of 41.5 GPa and 0.24, respectively.
2. The Uniaxial Compressive Strength (UCS) test was conducted on Quartzite Rock and the crack patterns developed in the specimen during the loading was observed. The crack patterns obtained in the specimen model during the numerical simulation was also observed and compared with those obtained in the laboratory during the experiments. The cracks obtained numerically followed more or less the same patterns as were obtained experimentally.
3. It is sometimes challenging to measure the stress and displacement fields inside a rock specimen during laboratory experiments. These stress and displacement fields play a very vital role in understanding the fracture mechanisms occurring inside the rock. Therefore, in order to gather such information related to fracture mechanisms, numerical techniques like Discrete Element Method (DEM) are adopted which can simulate the field conditions of the rock when they are subjected to different kinds of loading.

Acknowledgements This research work was supported by Civil Engineering Department of National Institute of Technology, Warangal, India. The authors would also like to express their sincere gratitude to the editor and anonymous reviewers for their valuable comments, which have greatly improved this paper.

References

1. Zhao C, Niu J, Zhang Q, Yu S, Morita C (2019) Numerical simulations on cracking behavior of rock-like specimens with single flaws under conditions of uniaxial and biaxial compressions. *J Mater Civ Eng* 31:04019305. [https://doi.org/10.1061/\(asce\)mt.1943-5533.0002967](https://doi.org/10.1061/(asce)mt.1943-5533.0002967)
2. Lisjak A, Grasselli G (2014) A review of discrete modeling techniques for fracturing processes in discontinuous rock masses. *J. Rock Mech Geotech Eng* 6:301–314. <https://doi.org/10.1016/j.jrmge.2013.12.007>
3. Zhang XP, Wong LNY (2012) Cracking processes in rock-like material containing a single flaw under uniaxial compression: a numerical study based on parallel bonded-particle model approach. *Rock Mech Rock Eng* 45:711–737. <https://doi.org/10.1007/s00603-011-0176-z>
4. Tang CA, Lin P, Wong RHC, Chau KT (2001) Analysis of crack coalescence in rock-like materials containing three flaws - Part II: numerical approach. *Int J Rock Mech Min Sci* 38:925–939. [https://doi.org/10.1016/S1365-1609\(01\)00065-X](https://doi.org/10.1016/S1365-1609(01)00065-X)
5. Hoek E, Martin CD (2014) Fracture initiation and propagation in intact rock - a review. *J Rock Mech Geotech Eng* 6:287–300. <https://doi.org/10.1016/j.jrmge.2014.06.001>

6. Prakash PR, Pulatsu B, Lourenço PB, Azenha M, Pereira JM (2020) A meso-scale discrete element method framework to simulate thermo-mechanical failure of concrete subjected to elevated temperatures. *Eng Fract Mech* 239:107269. <https://doi.org/10.1016/j.engfracmech.2020.107269>
7. Cundall AP (1971) A computer model for simulating progressive, large-scale movement in blocky rock system. In: *Proceedings of the international symposium on rock mechanics 1971 (1971)*
8. Kazerani T, Zhao J (2010) Micromechanical parameters in bonded particle method for modelling of brittle material failure. *Int J Numer. Anal Methods Geomech* 34:1877–1895. <https://doi.org/10.1002/nag.884>

Feasibility of Composite Compressor Blade Using Sub-element Level Bird Strike Tests and Analysis



Prakash Jadhav

Abstract As part of the composite compressor blade of aircraft engine concept study, a technical feasibility of replacing the current Titanium blades with fiber reinforced composite ones is evaluated here. This can result into substantial weight saving and may result in some cost saving too. In addition to the regular design criteria like stress and frequencies, survival under bird strike loading is also most important criteria. To evaluate composite blades made with different possible material systems under bird strike loading, is a time consuming and expensive task. In order to come up with a simplified method to evaluate the various possible cases, flat sub-element coupons are designed, fabricated and tested under bird strike loading in a real test facility. This simplified method is easy to use, fast and cost effective. This method generates strain allowable for different cases under bird strike loading using the combination of actual bird strike tests and the bird strike analysis of the same panel models in LS-Dyna software. This paper presents the results of the analysis and testing of these laminated composite panels and test analysis correlation. It is shown that strain allowable are easy to extract from the test-analysis correlation data.

Keywords Composite compressor blade · Bird strike · Strain allowable

1 Introduction

Many attempts are on to introduce lightweight fiber reinforced composites into the aircraft engine since last many years. There are a few researchers who worked on the improvement of composite components in the aircraft engine. Composite compressor blades were evaluated for the vibration criteria and it was shown that they can meet the criteria successfully [1]. A NASA study indicates that ply by ply composite blade for aero engines can be built and it is proved through the simulation that it will sustain the loading successfully [2]. Structural design and analysis procedures for fan blades that are followed by the manufacturers recently is also discussed and

P. Jadhav (✉)

School of Engineering and Sciences, SRM University-AP, Mangalgiri 522240, Andhra Pradesh, India

e-mail: prakash.j@srmmap.edu.in

© The Author(s), under exclusive license to Springer Nature Singapore Pte Ltd. 2022

T. Tadepalli and V. Narayanamurthy (eds.), *Recent Advances in Applied Mechanics*,

Lecture Notes in Mechanical Engineering, https://doi.org/10.1007/978-981-16-9539-1_14

presented [3]. Effect of stacking sequence in the composite fan blade was studied and it was found that the 0/45/0/-45 ply lay-up show least chance of failure through simulation results i.e margins to failure plots [4]. One such attempt discusses the use of sandwich composite fan blade replacing the metal blade and by doing that 72% weight saving was demonstrated without affecting the mechanical performance [5]. Enhanced numerical simulation capability was demonstrated through the advanced bird strike analysis of composite blades and deformation/damage characterization methodologies were developed [6]. It is a big challenge to redesign these engine components with composite materials and to prove the feasibility of it for the stress, frequency and other bird strike requirements. Author and his team have been part of many such attempts [7–17]. This work is a part of the investigation to make compressor blades of aircraft engine lightweight and cost effective. Although current Titanium compressor blades are working fine, even a small amount of weight reduction can make a huge impact. The most critical design criteria for these blades is the survival under bird strike loading. Pieces of the bird may escape from the gaps in the fan blade and then enter the compressor or booster blade assembly and may cause big damage. Flat panels are designed here with different layups of laminated carbon composite material and fabricated/tested under bird strike loading.

2 FEA Analysis

3D non-linear explicit dynamic finite element analysis (LS-Dyna) is conducted on these representative panel models. Bird properties are used as found in the literature. The flat panel models were created to be exactly similar size to that of the real compressor blades. Bird size was designed as per the guidelines for aircraft engine which specifies the mass of the bird which can escape from gap in the fan blades and reach the compressor blades. The material considered for compressor blades is IM7/8551 laminated carbon composites with different possible lay ups.

Figure 1 shows the actual compressor blade design which is used in the aircraft engine. The individual blade and the assembly of blades is also shown. Figure 2 shows the representative flat compressor blade panel model and bird hitting on the one corner of it. The current Titanium material for booster blades is proposed to be replaced with the suitable composite material. Although there are many other design criteria (like stress, frequency etc.) for the booster blade, the expected limiting design criteria for a composite booster blade is survival under bird strike loading. Figure 1 also shows the booster blade rotor assembly bird strike simulation model, where it can be seen that the partial (or sliced) bird comes out from the fan blade and hits on one of the booster blades. It is very cumbersome and time consuming to run these simulations for the whole booster assembly, particularly if it is just for some material evaluations. Hence, it was proposed to come up with a methodology which includes simple flat composite plates (representative of booster blades) subjected to bird strike loading conditions (both test and analysis) to judge the feasibility of bird strike test on real assembly. From the design trade of studies performed by aviation

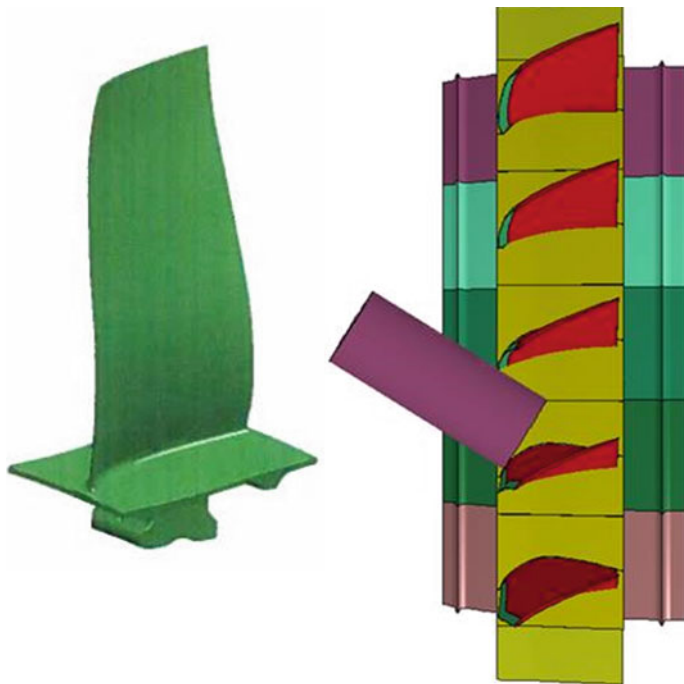


Fig. 1 Actual compressor blade design and assembly

Fig. 2 Representative flat panel and bird FEA model



experts, it was concluded that the design requirement is, the survival of the booster blade under 165 g bird hitting with approximately 110 m/s velocity at 32° angle for rotating impact (rotor is rotating while bird is hitting). Based on the proposal that the plate level impact be carried out under static condition (plate is fixed and not rotating) the design criteria has been revised to same size bird hitting at approx. 130 m/s. Based on the bird material density, the bird size has been calculated as 48 mm dia and approx. 100 mm long. The bird was modeled as per the exact properties that were used in the standard aviation fan blade bird strike analysis. Based on the actual booster blade size, the flat plates of size 125 mm × 67 mm × 16 plies thick are used for both analysis model and test specimens. The plates are used in cantilever boundary condition while bird hits at an angle. Two types of laminated composite materials are proposed here for flat plates, symmetric and balanced quasi-isotropic layup and proposed fan blade lay-up consisting of 0 and 45° fibers. The material used here is IM7/8551 carbon composite material. The flat plates that we have used here are constant thickness plates as against the actual blade which has varying thickness over the spanwise and chordwise direction. The average thickness was computed by measuring thickness profile all over blade and was used here for plates.

Figure 2 shows the meshed 3D FEA simulation model for the bird and flat plate. A ply by ply model has been created for this purpose with effective orthotropic material property being assigned to each and every carbon (IM7-8551) ply. For 45 and -45 orientation plies, effective properties were computed using the in-house excel based tools. One element is modeled through one ply thickness, so overall 16 elements are there in the model through thickness. One particular size (block volume) of the bird was chosen for impacting on the composite plate in cantilever configuration. The mass of this bird happens to be around 165 g based on the density of the bird. The velocity of impact was varied from 50 m/s to 130 m/s to check and see the stress/strain level generated in the model. Automatic node to surface contact was used in the analysis with soft option on to avoid penetration problem of the bird. Hourglass option is used for bird material to control the excessive distortion of the bird elements. In the current bird strike analysis, it is observed that the stress/strain hot spots do occur near the fixity. Figure 3 shows the analysis result comparison of the actual rotor assembly bird strike and the flat plate level bird strike. Please note that the rotor assembly model has the blade with smeared properties (average) and 3 elements through thickness. In-plane element size also is very big. Hence special plate level model (same mesh size as the assembly model blade mesh) is created to check the strain levels. The longitudinal and inter-laminar strain levels are comparable in both cases, while max strain locations are also near fixity. Based on this, it was decided to perform mesh sensitivity studies on the flat plate model (all cases at 165 g bird at 110 m/s velocity). Figure 4 shows pictures of some of the mesh types that were used for plate and the table shows the difference in results (longitudinal and inter-laminar strains) for the models with different mesh sizes. First two rows show the comparison of the smeared models (3 element through thickness) that we have talked about from Fig. 3. The strain results compare well for the actual blade and the flat plate. The third row talks about the 16 ply thick model with in-plane mesh size same as that in blade model. Longitudinal strains get elevated slightly but inter-laminar strains

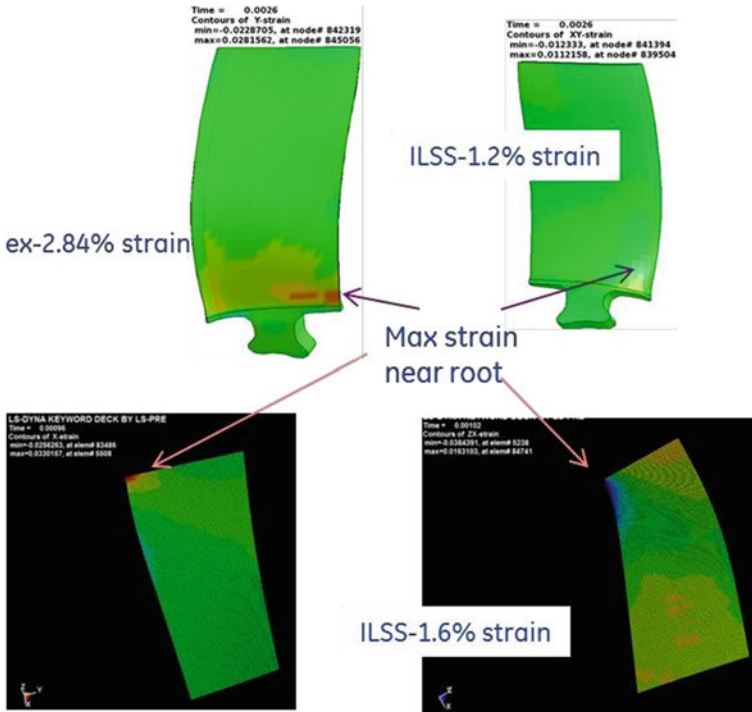
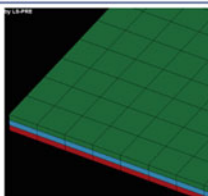
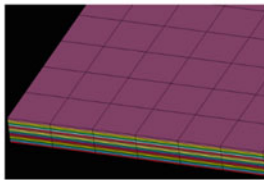


Fig. 3 Actual blade FEA vs representative flat plate FEA

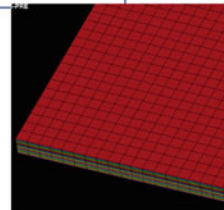
case	Max longitudinal strain ex %	Max inter-laminar strain exz %	Comment
BEC blade bird strike results- coarse mesh-smeared properties-3 elem	2.84	1.2	Vh-2003, Vv-4035
Plate level bird strike-Smeared properties-coarse mesh- 3 elem	3.19	1.6	Mesh size similar to blade mesh
Plate level bird strike-Only in plane coarse mesh- 16 plies	3.4	6.0	In-plane blade like mesh
Plate level bird strike- tapered root-coarse mesh- 3 elem	2.05	1.5	Thickness double
Plate level bird strike- increased width at root-coarse mesh- 3 elem	1.9	1.0	32% higher width
Plate level bird strike-ply by ply model- 16 plies	3.2	6.0	16 plies thro thk



Blade like mesh
3 ply thro thk



Blade like in-plane mesh
16 ply thro thk



Refined mesh-16 ply thro thk

Fig. 4 Mesh sensitivity study

really jump up at very high level. This happens due to the use of ply by ply plate model instead of smeared one.

The fourth and fifth row in Figure 4 shows the effect of change in thickness of plate. The plate thickness near root is artificially increased either by using thickness-wise taper or widthwise taper. This is done to match higher root thickness in the real blade. It can be seen that the inter-laminar strain reduced drastically while longitudinal strain reduced up to some extent. The fifth row shows the smeared model (3 element thro thickness) with increased root width, which also shows reduction in longitudinal strain and similar inter-laminar strain when compared with the blade model. The last row shows the constant thickness 16 ply thick plate analysis results which show higher longitudinal and inter-laminar strains. For all these cases, the locations of max strains were near fixity.

Table 1 shows the analysis results of different bird impact locations and different bird impact velocities on the flat plate. Case 1, 2 and 3 shows results of the analysis cases where the bird is impacting at increasing velocities 57, 86 and 114 m/s near the tip location at an angle of 32° . As the bird velocity increases, longitudinal and inter-laminar strain also jumps up to higher level. Interestingly, the ratio of ILS/tensile strain stabilizes at higher velocities, indicating that there are chances that the specimens may fail by inter-laminar mode of failure at higher velocities. While at lower velocity, it is clearly fiber failure by first bending mode. Case 4 and 5 shows the effect of changing the bird impact location to mid-length instead of at tip. The individual longitudinal and inter-laminar strains and also the ratio of ILS/tensile strain jumps up to higher level compared to the similar cases at tip impact indicating that there is more chance of having inter-laminar failure in mid-length impact compared to the tip impact. Case 6, 7 and 8 shows the effect of the change in angle of impact. Case 6 is the perpendicular impact to the plate, case 7 is at very acute angle impact and case 8 is almost like sliding impact on the plate (all cases at approx. 50 m/s velocity). The perpendicular impact shows the higher strain levels; and acute angle and sliding impact shows lower levels of longitudinal and inter-laminar strain levels as expected. Case 9 shows the tip impact at much lower velocity of 40 m/s which of course shows much lower levels of longitudinal and interlaminar strains. Case 10 shows the effect of using half bird mass by just tweaking the density of the bird material and it does not show significant changes in the longitudinal and inter-laminar strains as compared to the full mass bird impact at same velocity.

Case 11, 12 and 13 shows all mid-length impact; with case 11-very low velocity perpendicular impact to the plate, case 12-low velocity inclined impact and case 13-medium velocity perpendicular impact. Case 14 and 15 shows very low bird mass mid length impact; with case 14-angle of impact 32° and case 15-angle of impact 60° . The main reason for trying out all these different cases in analysis is to come up with suitable test configurations where there are higher chances of interlaminar shear failure than the fiber breakage. All the cases where the ILSS/tensile ratio is higher than 1.4 are assumed to be promising, so based on these results and actual test conditions/difficulties probable test configurations are decided.

Table 1 FEA simulation cases and the results

Case	Vh m/s	Vv m/s	Angle degree	Bird impact location	Axial strain max%	ILS strain max %	Ratio ILS/tensile
1	25.0	-51.7	32	Near tip	2.2 near support	1.85 away from support	0.84
2	37.5	-77.5	32	Near tip	3.5 near support	5.1 away from support	1.45
3	50.0	-103.3	32	Near tip	4.2 near support	6.0 away from support	1.42
4	25.0	-51.7	32	Mid length	3.0 near support	4.0 away from support	1.33
5	50.0	-103.3	32	Mid length	4.0-5.0 near support	8.0 to 9.0 near support	2.0
6	0.00	-50.0	90	Mid length	2.5 near support	3.5 away from support	1.41
7	50.0	-25.0	10 to 15	Mid length	1.2 near support	0.5	0.41
8	50.0	-0.00	0	Mid length	0.4 to 0.6 near support	0.1	0.2
9	18.7	-38.3	32	Near tip	1.5 near support	1.0 away from support	0.7
10	50.0	-103.3	32 (half mass)	Mid length	4.0 near support	7.0 away from support	1.75
11	0.00	-25	90	Mid length	1.5 near support	1.4 away from support	0.93
12	18.7	-38.3	32	Mid length	2.0 near support	1.75 away from support	0.875
13	0.00	-75	90	Mid length	3.5 near support	5.0 away from support	1.42
14	50.0	-103.3	32 (1/8 th mass)	Mid length	2.01 near support	2.7 away from support	1.34
15	25.0	-110.0	60 (1/8 th mass)	Mid length	1.6 near support	0.9 away from support	0.56

3 Bird Strike Tests

It was decided to conduct the bird strike tests at the facility in National Aerospace Laboratory, Bangalore. As shown in Figure 5, the test configuration was decided based on earlier FEA analysis. The specimen size used was 175 mm × 67 mm × 16 plies with bottom 50 mm length used for bonding tabs on both sides for good hold in the clamp. For most of the cases tested here, bird was impacted near tip and at an angle of 60° as shown in the figure. The strain gages were installed on both sides (tension and compression) of the specimens near fixity as shown in the figure. The strain gages were slightly away from the edge and also from fixity as shown in the figure. The bird used was of slightly different dimensions (40 mm dia × 90 mm length) than the one used in analysis due to the test machine (gun) limitations. The two types of layup configurations that were used here for tests i.e quasi-isotropic and fan blade lay-ups. 10 specimens each were used with symmetric and balanced lay-ups. The carbon composite prepreg material (IM7-8551) was used to manufacture these specimens using autoclave curing. Plastic tabs were later bonded on both sides of the specimens to have better grip in the clamp.

Figure 6 shows the high speed camera pictures at different stages of impact for fan blade layup specimens; top pictures for a specimen which did not fail and bottom pictures are for the specimen which failed. Bottom pictures show fiber breakage at the bottom of the blade and permanent deformation; while top picture blade just bends without any failure and comes back to the original position. Similarly in the high speed camera pictures at different stages of impact for quasi-isotropic blade layup specimens show fiber breakage at the bottom of the blade and delamination after certain velocity range is reached.

Table 2 tabulates the test results for these two lay-up materials. The fan blade lay-up specimens were subjected to the increasing velocity bird impact, varying from

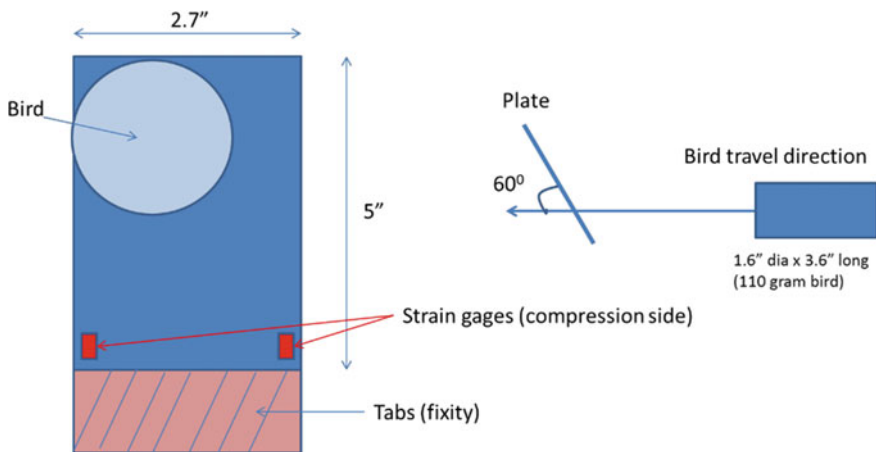


Fig. 5 Test coupon design and configuration

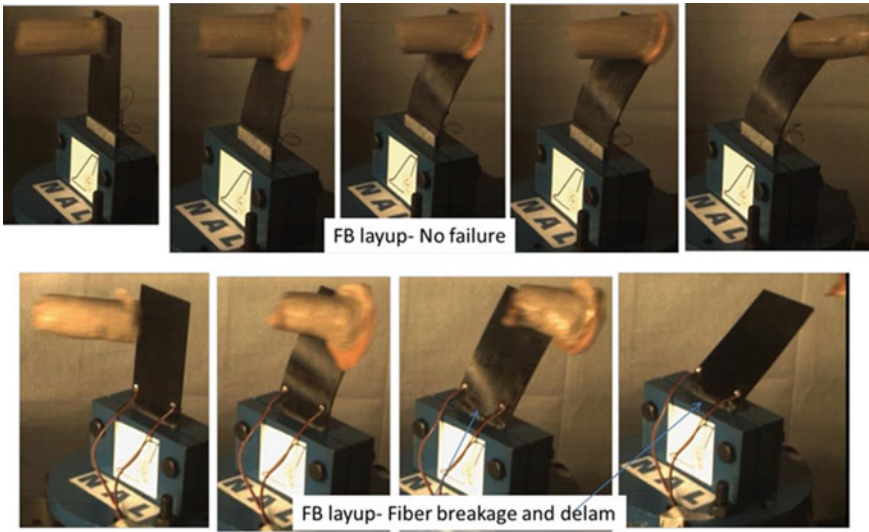


Fig. 6 High speed camera pics of bird strike test

66 m/s to the 90 m/s. Up to 71 m/s velocity impact, specimens did not fail and all specimens failed at higher velocity impact than 71 m/s. The failure mode observed was mostly fiber breakage and some delamination for the failed specimens. The compression side gage strain seems to reach 1.3% approximately; while tension side gage strain seems to reach 1.25% approximately before it fails. Failed specimens seem to show lower strain readings. QI lay-up specimens are subjected to increasing velocity impact i.e from 55 m/s to 92 m/s and also some offset/mid-length impacts. Here except the first one (55 m/s impact), in all other higher velocity impact cases, specimens are failing. Here also compression side gage strain seems to reach 1.35% approximately and tension side gage strain seems to reach 1.25% approximately before failure. Failed specimens show large fluctuations in the strain readings. The offset tip impact i.e half bird outside the edge shows twist dominant delamination type of failure mode, while offset mid-length impact also shows twist dominant delamination type failure mode.

To validate these test cases, LS-Dyna bird impact analysis was again performed for the correct size bird and the correct velocity of the bird (at, just before and just after the failure velocity from tests-threshold velocity). Figure 7 shows axial/longitudinal strain response of the fan blade specimens from tests and FEA (QI lay up-55 m/s-no specimen failure). As can be seen the test-analysis strain results at gage location compare well. Here the FEA strain is computed as the average of the element strains located exactly at the same location as the gage was in experiment. The FEA strain levels at fixity location are much higher than the gage location strains. Figure 8 shows the similar test-analysis result comparison for the QI lay-up at 65 m/s (specimens failed). Here also the test-analysis axial strain results at gage location compare well. However as seen earlier, the strain levels at fixity are very high compared to the gage

Table 2 Bird strike test cases and the results

Test no	Velocity m/s	Plate lay up	Compression side strain gages %	Tension side strain gages %	Damage
1	66 m/s	Fan blade type	1.2/1.15		No visual damage
2	71 m/s	Fan blade type	1.3/1.2	1.25	No visual damage
3	71 m/s	Fan blade type	1.34/No reading		No visual damage
4	75 m/s	Fan blade type	1.3/1.2	1.2	Fiber breakage
5	85 m/s	Fan blade type	1.2/0.65		Fiber breakage /delamination
6	85 m/s	Fan blade type	No strain readings		Fiber breakage
7	90 m/s	Fan blade type	1.35/1.1		Fiber breakage
8	55 m/s	Quasi isotropic	1.2/1.1		No visual damage
9	65 m/s	Quasi isotropic	1.35/1.25		Fiber breakage+delam
10	68 m/s	Quasi isotropic	1.7/1.34		Fiber breakage+delam
11	77 m/s	Quasi isotropic	1.1/No reading		Fiber breakage+delam
12	83 m/s	Quasi isotropic	1.9/1.2		No visual damage
13	85 m/s	Quasi isotropic	No reading		Fiber breakage+delam
14	92 m/s	Quasi isotropic	1.35/1.0		Fiber breakage+delam
15	70 m/s offset impact	Quasi isotropic	0.8/0.82	1.2	Twist dominant, delam
16	69 m/s offset+mid length	Quasi isotropic	No reading		Twist dominant, delam+fiber breakage

location strain. Figure 9 shows the similar test-analysis result comparison for the QI lay-up at 75 m/s (specimens failed). Here also the test-analysis axial strain results at gage location compare well and the strain levels at fixity are very high compared to the gage location strain. The similar test-analysis result comparison for the fan blade lay up (at 65, 75 and 85 m/s velocities respectively) was also performed. Here also the test-analysis axial strain results at gage location compare well. The strain levels at fixity are very high compared to the gage location strain.

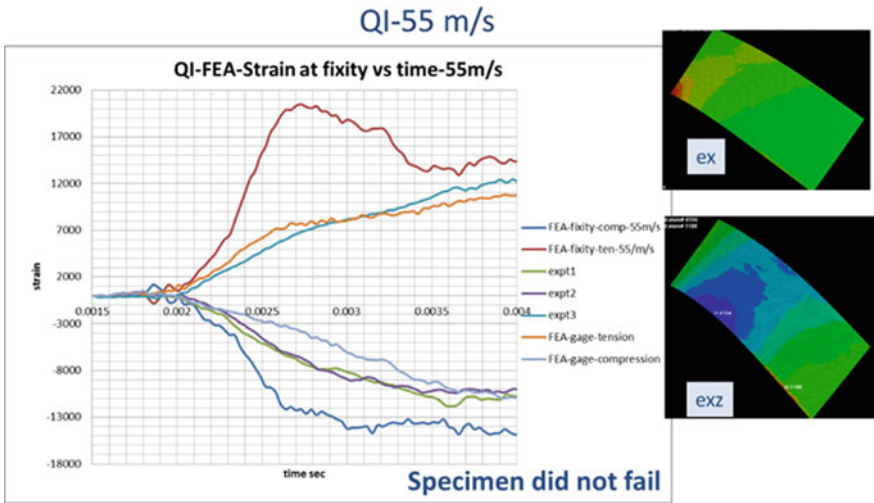


Fig. 7 Test vs FEA results comparison (55 m/s velocity)

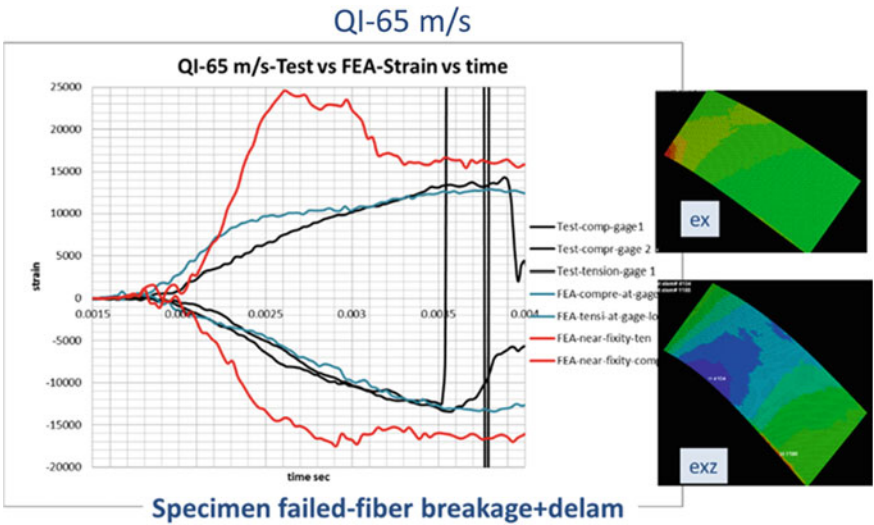


Fig. 8 Test vs FEA results comparison (65 m/s velocity)

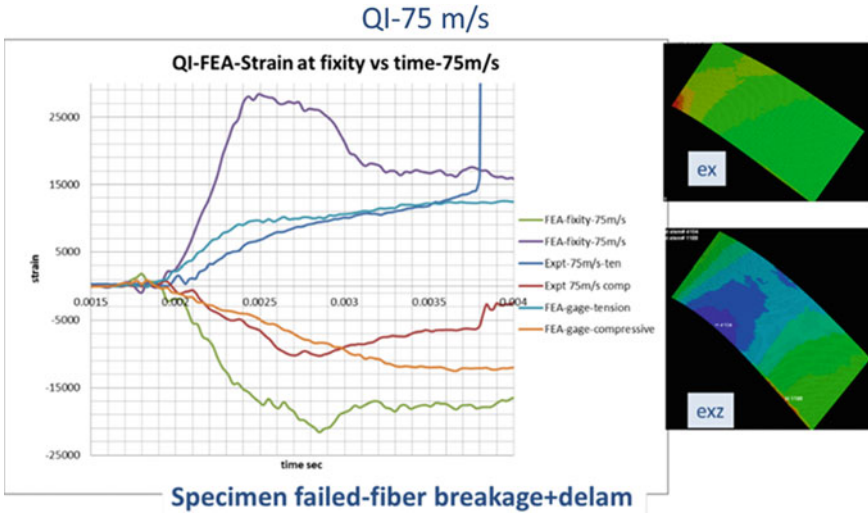


Fig. 9 Test vs FEA results comparison (75 m/s velocity)

4 Strain Allowable Computation

Table 3 lists the max longitudinal/axial strain level seen in each case at 3 velocities in fan blade and QI lay ups. As can be seen, FEA and Test gage location strain levels

Table 3 Test vs FEA failure strain mapping

Plate lay up/velocity	Expt max ex gage %		FEA max ex gage location %		FEA max ex fixity location %	
	Tension	Compression	Tension	Compression	Tension	Compression
Fan blade type layup						
65 m/s		1.2		1.15	2.28	1.95
75 m/s	1.23	1.28	1.18	1.27	2.49	2.14
85 m/s		1.22		1.31	2.88	2.31
QI lay up						
55 m/s	1.25	1.2	1.08	1.07	2.05	1.5
65 m/s	1.42	1.35	1.28	1.33	2.47	1.75
75 m/s	1.25	1.1	1.25	1.25	2.83	2.15
70 m/s offset	1.2	0.91	1.25	1.2	2.35	1.88
70 m/s offset mid length	–	–	–	–	3.06	3.14

Table 4 Strain allowable computation

Plate lay up/velocity	FEA max ex fixity location%		FEA max exz-ILS
	tension	compression	
Fan blade lay upg			
65 m/s- no failure	2.28	1.95	2.49
75 m/s fiber breakage/delam	2.49	2.14	2.81
85 m/s fiber breakage/delam	2.88	2.31	3.41
Strain allowable	2.4	2.0	>2.5
QI lay up			
55 m/s no failure	2.05	1.5	2.01
65 m/s fiber breakage/delam	2.47	1.75	2.48
75 m/s fiber breakage/delam	2.83	2.15	3.05
70 m/s offset- delam	2.35	1.88	3.5
70 m/s offset mid length-fiber breakage/delam	3.06	3.14	3.55
Strain allowable	2.4	2.0	2.5-3.5

match very well. Max strain levels which occur near fixity are higher than the gage location strains. Table 4 shows the allowable strain calculation for fan blade lay-up specimens. The max strain numbers in red are for failed specimens while max strain numbers in blue are for un-failed specimens. The average of max strain for un-failed specimen and max strain for failed specimen is taken as allowable strain which is 2.4% for tension and 2.0% for compression as shown in the table. For the case of inter-laminar strains, as the most specimens failed in fiber dominated mode and unfailed specimen shows 2.49% strain, the allowable is computed as >2.5%. This is because the upper strain limit of ILS failure is not seen in specimens as they failed in fiber breakage mode. Similarly, we can see the behavior for the strain allowable computation for QI lay-up specimens under longitudinal and inter-laminar cases. Offset impact cases are also added here for validation purpose. Under offset impact, the failure mode is twist dominated i.e mostly delamination. Therefore it helps to derive inter-laminar shear allowable from the offset impact cases. As can be seen, strain allowable for QI lay up specimens are 2.4% for tension, 2% for compression and between 2.5 to 3.5% for inter laminar shear. Appendix shows the micrographs of the tested specimens where the region near fixity is highlighted. Fan blade layup specimens show mostly fiber breakage type of failure mode and QI layup specimens show mostly fiber breakage and some delamination type of failure mode. The offset QI specimens show mostly delamination dominated failure mode. Lastly the comparison of FEA and test failure

mode location is shown for offset impact case. As can be seen, the FEA shows delamination happening near surface while tested specimen show delamination near surface and also deep in the thickness.

5 Summary

Strain allowable for the laminated composite compressor blade were obtained using the bird strike analysis and test correlation of the results. These allowable can be used to properly design the laminated composite compressor blade and the objective of reducing the weight of compressor blade assembly can be achieved. From the plate test-analysis work that is performed here, some important conclusions are drawn here. 1. Using the combinations of plate level bird strike test and analyses, the strain allowable for the material under consideration were obtained 2. 70 to 100% higher strain allowable compared to that under static tests 3. Methodology is established 4. More offset impact test needed to develop confidence level in ILS allowable.

References

1. Wollmann T, Modler N, Dannemann M, Langkamp A, Nitschke S, Filippatos A (2017) Design and testing of composite compressor blades with focus on the vibration behavior. *Compos Part A Appl Sci Manuf* 92:183–189
2. Abumeri GH, Kuguoglu LH, Chamis CC (2004) Composite fan blade design for advanced engine concept. NASA/TM-2004-212943
3. Amoo LM (2013) On the design and structural analysis of jet engine fan blade structures. *Prog Aerosp Sci* 60:1–11
4. Xiao J, Chen Y, Zhu Q, Lee J, Ma T (2017) A general ply design for aero engine composite fan blade. In: *Proceeding of ASME turbo expo technical conference*. <https://doi.org/10.1115/GT2017-64377>
5. Coroneos RM, Gorla RSR (2012) Structural analysis and optimization of a composite fan blade for future aircraft engine. *Int J Turbo Jet Eng* 29(3):131–164
6. Nishikawa M, Hemmi K, Takeda N (2011) Finite element simulations for modeling composite plates subjected to soft body high velocity impact for application to bird strike problem of composite fan blades. *Compos Struct* 93:1416–1423
7. Jadhav P (2020) Effect of ply drop in aerospace composite structures. *Key Eng Mater* 847:46–51
8. Jadhav P (2020) Innovative designs of embedded foam inserts in aerospace composite structures. *Mater Today Proc* 21, Part 2:1164–1168
9. Spoonire RA, Lin W, Schilling J, Shim DJ, Gemeinhardt GC, Jadhav PK (2016) Hybrid turbine blade including multiple insert sections. US Patent US 9309772B2
10. Shim D-J, Finn SR, Kray NJ, Sinha VK, Jadhav PK, Zheng L (2013) Fan blade. US Patent US 2013/02875588A1
11. Jadhav P, Li Z, Prasad S (2016) Cohesive zone modeling to model delamination in composite structures under static and dynamic loading. In: *Proceedings of SAMPE conference, May 2016, California*
12. Jadhav P, Li Z, Prasad S (2015) Evaluation of ply drop allowable in composites. In: *Proceedings of COMTEST conference, April 2015, IMDEA, Spain*

13. Jadhav P (2021) Passive morphing in aerospace composite structures. *Key Eng Mater* 889:53–58
14. Jadhav P, Gruha LY (2021) Design and optimization of hybrid interface joint in a composite fan blade of aircraft engine. In: *IOP conference series, material science and engineering*, vol 1126, p 012036
15. Jadhav P (2021) Failure criteria for composite blades with wavy edge in aerospace applications. In: *Advanced in materials and mechanical engineering. Lecture notes in mechanical engineering*. Springer, pp 113–121
16. Kray JN, Gemeinhardt GC, Jadhav P, Klei DE, Nandula P, Subramanian S (2019) Composite compressor blade and method of assembling. US Patent 10247014 B2
17. Jadhav P (in press) Design methodologies for composite structures in aircraft engines. *Advanced composites in aerospace engineering application*. Springer

Influence of Invertube's Thickness on Crash Energy Absorption



Velugubantla Dushyanth Rudra Mahesh  and V. Narayanamurthy 

Abstract Invertubes are crash energy absorbing structures incorporated in automobiles for frontal crash protection. Researchers have proposed various designs of crush tubes, some of which outperform others in terms of crashworthiness parameters. Invertube provides excellent crashworthiness due to its unique mode of deformation i.e. tube inversion which controls high initial peak forces resulting in attenuating the forces transmitted to the passenger during vehicular collisions. This paper explores the requirement of optimum thickness of an invertube for maximum energy absorption and better crashworthiness. Non-linear explicit FEA simulations are adopted and the result is validated with experimental result in the literature for a nominal thickness.

Keywords Invertube · Impact · Crashworthiness · Energy absorption · Thickness

1 Introduction

Compartment crushing, internal injuries and fatalities during collision is mainly due to high deceleration levels and crash-impact energy transmission, which is often experienced during a head-on collision. In order to protect the occupants from injuries, the energy generated during the collision must be absorbed using various energy absorbers like crush tubes, bumper, and bumper reinforcements of multiple geometries, including circular tubes, square tubes, spherical shells, frusta [1–15]. They absorb impact energy through different means like tube splitting, friction fracture, plastic bending, crushing, cyclic plastic deformation and metal cutting. This plastically deformable type of energy absorbing structure enables the vehicle to minimize impact-induced decelerations to occupants by providing them with a few extra milliseconds for the impact wave to reach the occupants, thereby reducing the intensity of injuries.

V. Dushyanth Rudra Mahesh (✉)

Mechanical Engineering, Vidya Jyothi Institute of Technology, Hyderabad 500075, India

V. Narayanamurthy

Research Centre Imarat, Hyderabad 500069, India

e-mail: v.narayanamurthy@rcilab.in

1.1 Brief About Crush Tube

A crush tube is an energy-absorbing (EA) structure employed to absorb impact energy generated during collision through plastic deformation, thereby attenuating the intensity of impact forces to occupants. An effective EA structure should exhibit the following properties, (1) it should deform at optimum initial crush force within the human tolerance limit of 20 g, (2) it should delay the transfer of impact-induced decelerations into occupants cell, (3) it should exhibit a uniform crush force during the entire stroke length, and (4) it should convert impact energy to plastic deformation of EA structure.

The deformation mechanism in cylindrical shells or general crush tubes is initially due to plastic buckling, followed by crushing [1–4]. Deformation modes are generally governed by geometric parameters of the tube and material properties. Usually, EA structures made of ductile materials are preferred as energy absorbers and are widely used in automobiles for structural safety and spaceships for soft landing applications.

An ideal EA structure should exhibit maximum total energy absorption (TEA) with higher stroke efficiency (SE) and crush force efficiency (CFE) with minimum mass to achieve utmost specific energy absorption (SEA). An ideal crush tube requires some initial force to trigger plastic deformation, and the force required is the peak force. This peak force induces plasticity in the crush tube and is followed by tube crushing. For an ideal EA structure, the complete length is utilized, thereby maximizing TEA by increasing the area under a curve, and for an ideal EA structure, CFE should tend to unity. In later phases, the tube gets completely deformed by absorbing maximum possible energy and starts transmitting forces directly to occupants. Figure 1 shows a graphical representation of an ideal EA structure's crashworthiness performance.

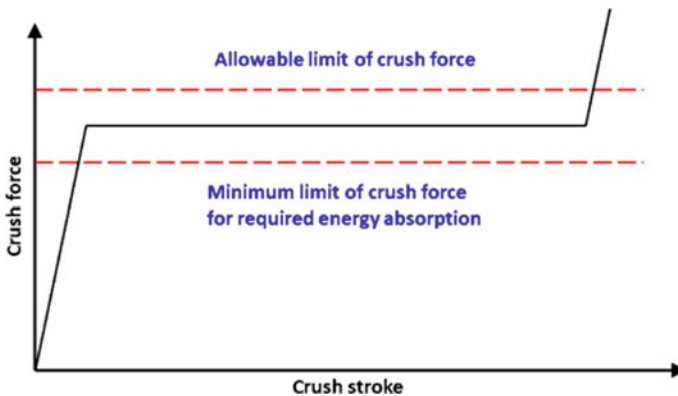


Fig. 1 Ideal energy-absorption curve

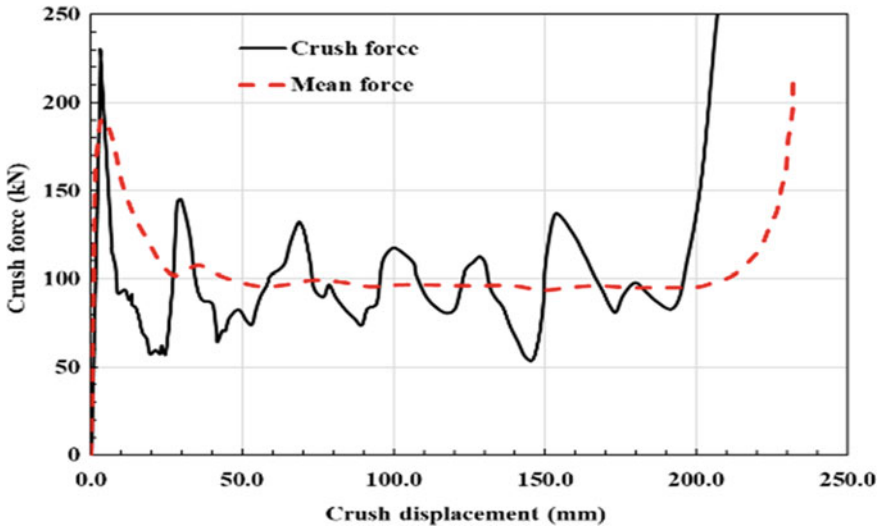


Fig. 2 Behaviour of a typical crush tube

1.2 Crashworthiness

Crashworthiness is a measure of the ability of the structure to protect occupants during a collision. Due to strict laws, car makers must implement agile safety systems, preventing the occupant from being intruded by engine block and crumpling the occupant’s compartment while keeping the impact-induced deceleration levels within human tolerance. There are two types of crashworthiness parameters, namely primary and secondary. Primary crash parameters are mass (m), mean force (F_{mean}), peak force (F_{peak}), and stroke length (δ). Secondary parameters are derived from primary parameters, they are TEA, SEA, CFE, and SE. Figure 2 [2] depicts the variation of crush force versus crush displacement of a typical crush tube, an initial peak of 225 kN is developed, and a mean of 125 kN is generated over length, making it not an ideal choice for energy absorption.

1.3 Crashworthiness Parameters

TEA of EA structure is not the only key measure of crashworthiness; there are many critical parameters, which should be taken care of for the occupant safety. These parameters are given below.

$$F_{peak} = \max[F(l)] \tag{1}$$

$$SE = \frac{l}{L} \times 100 \tag{2}$$

$$TEA = \int_0^l F(x)dx \tag{3}$$

$$CFE = \frac{F_{mean}}{F_{peak}} \times 100 \tag{4}$$

$$SEA = \frac{TEA}{m} \tag{5}$$

$$\text{Total efficiency, } TE = CFE \times SE \tag{6}$$

$$\text{Specific total efficiency, } STE = \frac{TE}{m} \tag{7}$$

1.4 Tube Inversion

Tube inversion is an excellent choice for energy absorption with near-ideal behaviour [2]. Tubes deforming by inversion phenomena are referred to as invertube. Tube inversion controls high initial peak crush force and helps achieve nearly 100% stroke and crush force efficiencies leading to near ideal energy absorption. In addition, they avoid bending and operate under constant load, helping in maximizing the energy absorption through its complete stroke deformation, as shown in Fig. 3.

Conventional crush tubes attain densification earlier than invertubes due to their mode of deformation and geometry, leading to transmission of very high impact forces directly into the occupant’s cell. Furthermore, proper utilization of the crush tube’s stroke length can be achieved by using guides.

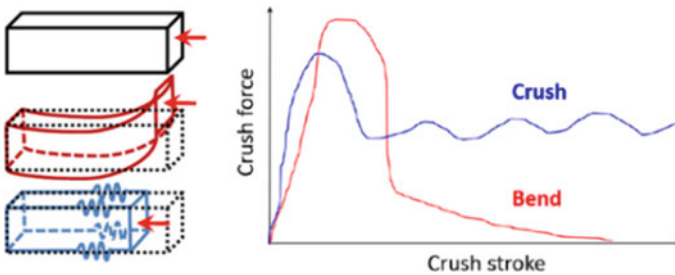


Fig. 3 Variation in energy absorption pattern due to crushing and bending

The race to find inversion loads has begun in late 1960 by Guist and Marble [5] for soft landing. Later in 1992, an attempt was made by Reddy [6] to improve the natural knuckle radius predicted by Guist and Marble [6]. The present research has taken a new face of development where retractable crush tubes [7], crush tubes made of other materials, alloys, different shapes, sizes are appreciated. In 2019, Reddy *et al.* [2] proposed an invertube that exhibit near-ideal crash energy absorption. Previous research outputs from geometric data to inversion load prediction are widely accepted and used for the present research. This research is done by assuming the crush tube to be free from geometric imperfections, and it is assumed that the crush tube is manufactured to given dimensions.

Researchers have always tried to find inversion loads, geometric requirements for proper inversion, including knuckle radius and other dimensional parameters, design for multiple inversions or progressive crushing, the effect of material change, deformation models and mechanisms, free inversions, guided inversions, strain rate effects on inversion and crashworthiness parameters of foam-filled tubes, honeycomb structures, composite materials and alloys [1–20]. Ignoring the effect of imperfections in geometry, and effect of optimum thickness on crashworthiness during production will seriously affect the predicted energy absorption [1–7]. Minimal experimentation and numerical investigation are available on optimum thickness required for an invertube. Therefore, the present research is focused on finding an optimum thickness and its effects on crashworthiness on the invertube demonstrated by Reddy *et al.* [2].

2 Methodology and Numerical Simulations

2.1 Methodology

The final profile of tube geometry mentioned as variant-5 in Reddy *et al.* [2] and as shown in Fig. 4 is chosen for this study. This invertube profile has the following geometric parameters viz. thickness = 1.0 mm; length of crush tube = 90 mm; the diameter of upper circular section = 76 mm integrated with various circular arcs of radius 328 and 12 mm; and diameter of bottom circular section = 160 mm. Model is created in ABAQUS and numerically investigated for its crashworthiness parameters.

In the first phase of this work, finite element simulation is compared with the experimental results of [2] for validating the numerical model and analysis procedure. Subsequently in the second part, the numerical procedure thus validated is extended in analyzing the effect of thickness on crashworthiness and studied for different thicknesses such as 0.5, 1.0, 1.25, 1.75 and 2 mm. The study is done for an axial impact with a velocity of 15 m/s. After analyzing merits and demerits through numerical simulation, optimum thickness is recommended.

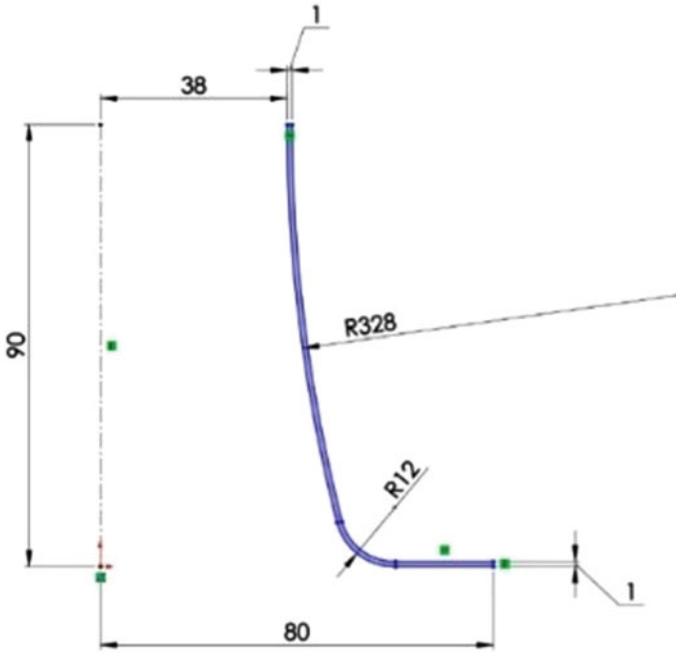


Fig. 4 Geometry of invertube

2.2 Material Properties

Material test conducted by Reddy *et al.* [2] on SS304 stainless steel resulted in following material properties which are used in numerical simulations: Young's modulus (E) = 210 GPa; Poisson's ratio (μ) = 0.29; yield strength = 280 MPa; ultimate tensile strength = 600 MPa; density = 8000 kg/m³; and elongation at break = 55%. The stress-strain curve in Fig. 5 is considered for numerical simulation.

2.3 FEA Model

A 3D deformable shell model, as shown in Fig. 6(a), is considered and discretized with four-node linear quadrilateral elements (S4R) in ABAQUS. This resulted in 42,245 elements and 42,600 nodes and the mass of the specimen is 0.291 kg. The crush tube's material is modelled by through stress-strain data shown in Fig. 5. A time step of 0.006 s is adopted using the dynamic explicit procedure, and a general contact interaction with tangential behaviour of 0.2 penalty friction coefficient and normal behaviour with hard contact. After studying mesh convergence with various element sizes, an element edge length of 1 mm is adopted to capture the plastic

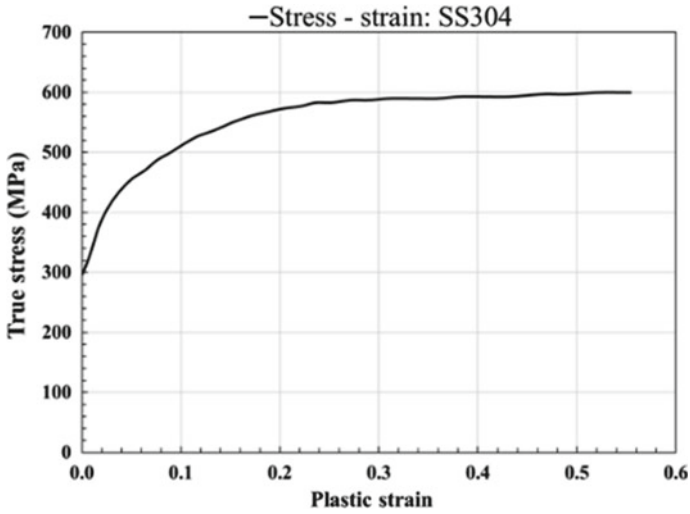


Fig. 5 Stress-strain curve of 304 stainless steel

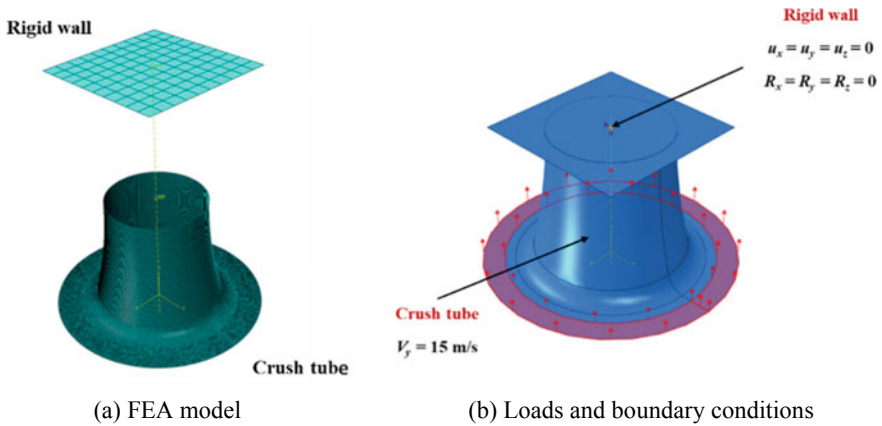


Fig. 6 Details for FEA simulation

deformation through inversion. A rigid body (an impactor) is modelled using the discrete rigid type option in ABAQUS. The impactor is constrained in all degrees of freedom to acts as a barrier.

The specimen is given a velocity of 15 m/s, equivalent to 56 kmph, as in Fig. 6(b) and is chosen explicitly due to NCAP i.e. national crash analysis programme (frontal impact) safety standards, whereas FMVSS 208 (federal motor vehicle safety standards) rigid barrier test is conducted at speeds up to 48 kmph. The crush tube with specified velocity travels toward the impactor and collides, absorbing kinetic energy through plastic deformation by the inversion phenomenon.

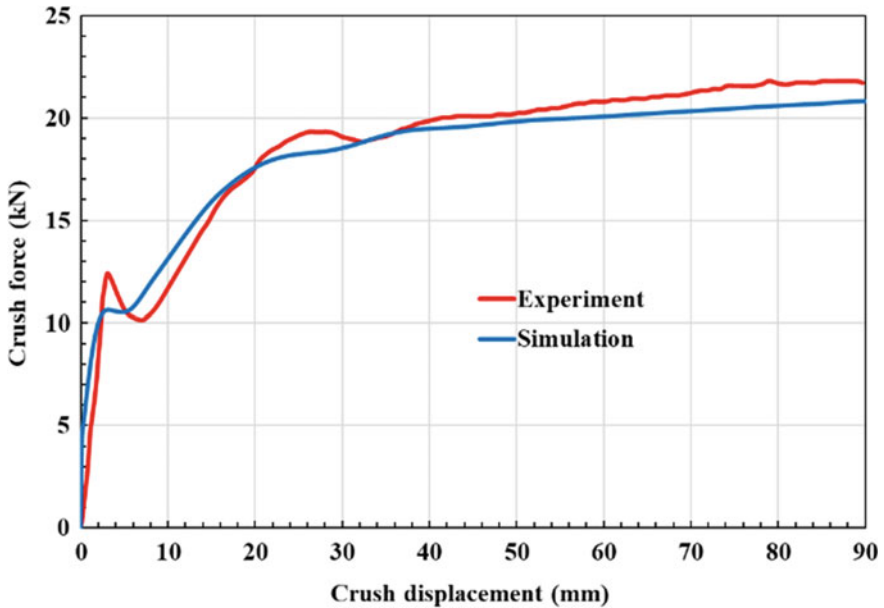


Fig. 7 Comparison of crush force versus crush displacement between experiment and present simulation of 1 mm thick invertube

2.4 Comparison Between Simulation and Experiment

The simulation is carried out with 1.0 mm thickness of invertube. The results from present numerical simulation is compared with experiment [2] as shown in Fig. 7 which shows a good agreement between them and thereby validating the numerical simulation.

3 Effect of Thickness Variation

In order to find the optimum thickness of the crush tube, various thickness (t) values such as 0.5, 1.0, 1.25, 1.75 and 2 mm are assigned to geometry and evaluated the primary and secondary crashworthiness parameters and the results are provided in Tables 1 and 2 respectively. A comparison of crush force versus crush displacement curves for different thicknesses of invertube is shown in Fig. 8 which shows that with the increase in thickness of the tube, the materials failure strain is reached prior to 100% SE or before complete stroke deformation leading to premature failure for the corresponding geometry. Therefore, optimum thickness is arrived at carefully by keeping the induced plastic strains within the materials limit of elongation at

Table 1 Primary crashworthiness parameters of invertubes

t (mm)	m (kg)	F_{peak} (kN)	F_m (kN)	δ (mm)
0.50	0.1460	2.83	4.35	90.00
1.00	0.2910	17.30	17.90	90.00
1.25	0.3640	25.38	28.23	87.04
1.75	0.5100	44.83	47.37	48.91
2.00	0.5820	47.35	48.75	13.65

Table 2 Secondary crashworthiness parameters of different invertube

t (mm)	TEA (kJ)	SEA (kJ/kg)	CFE %	SE %
0.50	0.90	6.16	153.71	100.00
1.00	1.63	5.60	103.47	100.00
1.25	2.29	6.29	111.23	93.38
1.75	2.08	4.08	105.67	54.34
2.00	0.58	1.00	102.96	15.17

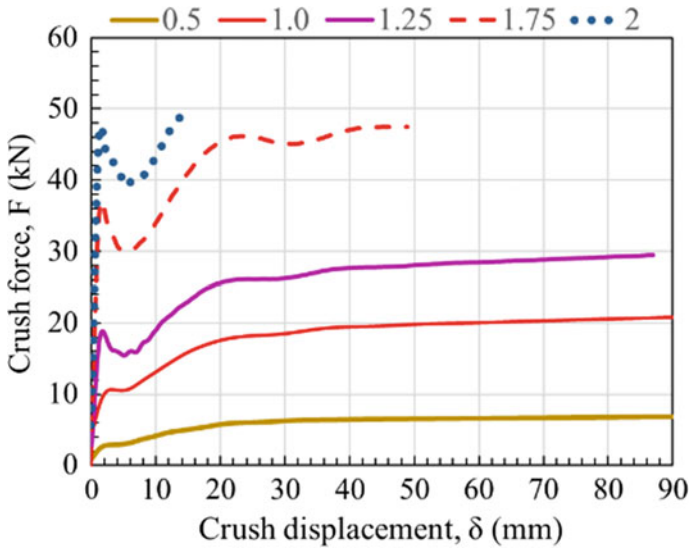
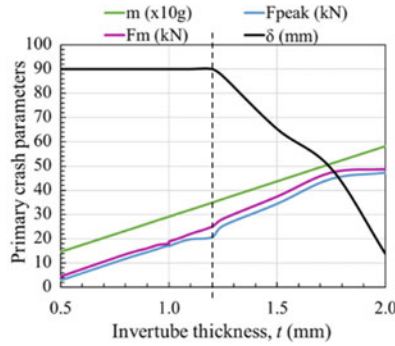
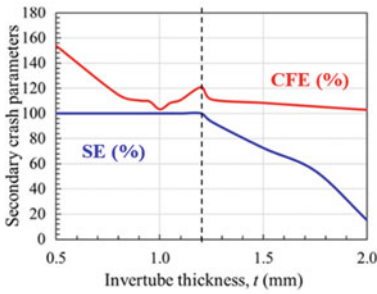


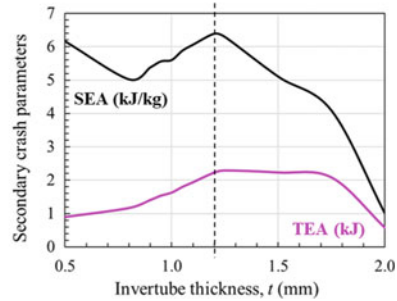
Fig. 8 Comparison of crush force versus crush displacement curves of 0.5 to 2.0 mm thick invertubes



(a) Variation in primary crash parameters



(b) Variation in secondary crash parameters - CFE and SE



(c) Variation in secondary crash parameters - TEA and SEA

Fig. 9 Variation in primary and secondary crashworthiness parameters for different thicknesses of invertube

break. Figure 9 shows the comparison of primary and secondary crashworthiness parameters and reveals that the optimum thickness for invertube is about 1.2 mm.

4 Results and Discussion

The variation of primary crashworthiness parameters shown in Fig. 9(a) provides significant inference about the contribution of invertube's thickness. The mean force and peak force increase with increase in thickness from 0.5 to 1.75 mm only and they stabilize for $t > 1.75$ mm. On the other hand, the crush length is constant at 90.0 mm up to $t = 1.20$ mm only exhibiting SE of 100%. For $t > 1.20$ mm, the crush length decreases leading to steady drop in SE from 100% for 1.20 mm thickness to less than 20% at 2.0 mm thickness as shown in Fig. 9(b). The CFE is highest at $t = 0.5$ mm, decreases to 100% at $t = 1.0$ mm, increases to 120% at $t = 1.2$ mm and beyond

which it decreases to 100% at $t = 2.0$ mm. The SEA decreases from 6.2 to 5.0 kJ/kg for $0.5 < t < 0.8$ mm and for $t > 0.8$ mm, it increases and reaches its maximum value of 6.4 kJ/kg at $t = 1.20$ mm. For $t > 1.20$ mm, the SEA decreases and reaches to 1.0 kJ/kg at $t = 2.0$ mm as seen in Fig. 9(c). Interestingly, the TEA increases from 1.0 kJ to 2.3 kJ for $0.5 < t < 1.20$ mm and it remains constant up to $t = 1.75$ mm and beyond which it decreases to 0.6 kJ at $t = 2.0$ mm.

The TEA initially increases with increase in thickness and upon further increase in thickness, the specified geometry does not support the free inversion, leading to prior failure without reaching the materials failure strain and results in decrease in TEA. The reduction of TEA implies a transfer of higher energy into the occupant's compartment. The SEA may initially increase due to less thickness (also means less mass). More the CFE, safer is the vehicle under frontal impact. Achieving CFE more than 100% is possible through tube inversion as compared to other crush tubes. With an increase in thickness, the force required to initiate deformation is very high, leading to a decrease in CFE. SE depicts the deformability of the structure and more than 100% can be achieved through inversion. Conventional crush tubes attain densification without exhibiting 100% deformation. An increase in thickness till 1.20 mm for the particular geometry, the SE tends to unity, leading to 100% utilization of the crush tube for energy absorption. With a gradual increase in thickness, the stiffness increases, leading to premature failure of energy absorption structure without utilizing its complete stroke length. The CFE depends upon the stiffness of the invertube, stiffer the structure greater will be the initial peak developed leading to reduction in CFE. Therefore, the stiffness of the invertube is directly affected by thickness variation which influences the entire tube inversion behavior and affects the crashworthiness parameters.

5 Conclusion

This paper, numerically examined the effect of thickness variations (0.5 to 2.0 mm) in invertube on its crashworthiness performance. The simulation is validated by comparison with experimental result and a good agreement is observed for the one with standard thickness of 1.0 mm. The crash performance of the invertube investigated at different thicknesses revealed that a thickness of 1.2 mm results in best possible crash performance. This thickness exhibited 100% SE, 120% CFE, 6.4 kJ/kg of SEA and 2.3 kJ of TEA.

References

1. Tarlochan F (2013) Design of thin wall structures for energy absorption applications: design for crash injuries mitigation using magnesium alloy. *Int J Res Eng Technol* 2(7):24–36. <https://doi.org/10.15623/ijret.2013.0207004>

2. Reddy TJ, Narayanamurthy V, Rao YVD (2019) Evolution of a new geometric profile for an ideal tube inversion for crash energy absorption. *Int J Mech Sci* 155:125–142. <https://doi.org/10.1016/j.ijmecsci.2019.02.024>
3. Salehghaffari S, Tajdari M, Panahi M, Mokhtarnezhad F (2010) Attempts to improve energy absorption characteristics of circular metal tubes subjected to axial loading. *Thin-Walled Struct* 48(6):379–390. <https://doi.org/10.1016/j.tws.2010.01.012>
4. Guist LRR, Marble DP (1966) Prediction of the inversion load of a circular tube. National Aeronautics and Space Administration, Washington, D.C
5. Reddy TY (1992) Guist and marble revisited—on the natural knuckle radius in tube inversion. *Int J Mech Sci* 34(10):761–768. [https://doi.org/10.1016/0020-7403\(92\)90040-n](https://doi.org/10.1016/0020-7403(92)90040-n)
6. Zhang X, Cheng G, Zhang H (2009) Numerical investigations on a new type of energy-absorbing structure based on free inversion of tubes. *Int J Mech Sci* 51(1):64–76. <https://doi.org/10.1016/j.ijmecsci.2008.11.001>
7. Wood DP, Veyrat N, Simms C, Glynn C (2007) Limits for survivability in frontal collisions: theory and real-life data combined. *Accid Anal Prev* 39(4):679–687. <https://doi.org/10.1016/j.aap.2006.10.014>
8. Wierzbicki T, Bhat SU, Abramowicz W, Brodtkin D (1992) Alexander revisited—a two folding elements model of progressive crushing of tubes. *Int J Solids Struct* 29(24):3269–3288. [https://doi.org/10.1016/0020-7683\(92\)90040-z](https://doi.org/10.1016/0020-7683(92)90040-z)
9. ABAQUS Analysis Users Manual (2017) Dassault systemes. ABAQUS version 2017. Dassult Systèmes, Providence
10. Qiu X, Yu X, Li Y, Yu TX (2016) The deformation mechanism analysis of a circular tube under free inversion. *Thin-Walled Struct* 107:49–56. <https://doi.org/10.1016/j.tws.2016.05.019>
11. Qiu X, He L, Gu J, Yu X (2013) A three-dimensional model of circular tube under quasi-static external free inversion. *Int J Mech Sci* 75:87–93. <https://doi.org/10.1016/j.ijmecsci.2013.06.009>
12. Hamada H, Nakatani T (1997) Analysis of crushing mechanism on composite tube under axial load. SAE Technical Paper Series. <https://doi.org/10.4271/970247>
13. Composite materials and structures (2003) Energy absorption of structures and materials, pp 317–350. <https://doi.org/10.1201/9780203484128.ch11>
14. Reddy TJ, Rao YVD, Narayanamurthy V (2017) Thin-walled structural configurations for enhanced crashworthiness. *Int J Crashworthiness* 23(1):57–73. <https://doi.org/10.1080/13588265.2017.1306824>
15. Reddy S, Abbasi M, Fard M (2015) Multi-cornered thin-walled sheet metal members for enhanced crashworthiness and occupant protection. *Thin-Walled Struct* 94:56–66. <https://doi.org/10.1016/j.tws.2015.03.029>
16. Jones N (1998) Some recent developments and future trends in thin-walled sections for structural crashworthiness. *Thin-Walled Struct* 32(1–3):231–233. [https://doi.org/10.1016/s0263-8231\(98\)00033-0](https://doi.org/10.1016/s0263-8231(98)00033-0)
17. Beik V, Fard M, Jazar R (2016) Crashworthiness of tapered thin-walled S-shaped structures. *Thin-Walled Struct* 102:139–147. <https://doi.org/10.1016/j.tws.2016.01.013>
18. Li J, Gao G, Yu Y, Guan W (2019) Experimental and numerical study on splitting process of circular steel tube with enhanced crashworthiness performance. *Thin-Walled Struct* 145:106406. <https://doi.org/10.1016/j.tws.2019.106406>
19. Zhang H, Zhang X (2016) Crashworthiness performance of conical tubes with nonlinear thickness distribution. *Thin-Walled Struct* 99:35–44. <https://doi.org/10.1016/j.tws.2015.11.007>
20. Acar E, Altin M, Güler MA (2019) Evaluation of various multi-cell design concepts for crash-worthiness design of thin-walled aluminum tubes. *Thin-Walled Struct* 142:227–235. <https://doi.org/10.1016/j.tws.2019.05.012>

Maximizing the Energy Absorption Capacity of Thin Walled Box Structures Using Ultra High Strength Steels (UHSS) at Sensitive Zones



Peddi Sai Rama Narayana, Raghu V. Prakash, Srinivas Gunti,
and Kanugula Raghu

Abstract Thin walled front-end box structures play a significant role in absorbing the collision energy in case of frontal impacts. Maximizing energy absorption within the constraints of available space, weight, cost and the average impact force that will not deteriorate occupant safety is challenging. Past research suggests that the structural shape, the use of high strength materials, and a combination of foam filled structures significantly improve the energy absorption capacity. This paper presents a new methodology to maximize the energy absorption capacity by means of optimum material combinations of low and high strength steels at sensitive locations. A Finite Element Analysis (FEA) methodology has been formulated with a simple square shaped crush box of a mild steel material and subsequently with combination of mild steel and high strength steels at sensitive zones of the crush box to improve the energy absorption capacity. Similar set of simulations are repeated with circular shape and the results are compared. The significant factors affecting the energy absorption which are critical to occupant safety has been compared between the simulations. It is noted that more than 90% of specific energy absorption capacity can be increased by using the optimum combination of mild and high strength steels at the sensitive zones of the structure. The methodology has been applied on the full vehicle crash simulation and demonstrated the benefits in reducing the structural intrusions. This proposed methodology has potential to be used in low-cost, lightweight applications.

Keywords FEA · Lightweight · LS DYNA · Specific energy · Crush box · Crush force

P. S. R. Narayana (✉) · S. Gunti · K. Raghu
Mahindra Research Valley, Chennai, India
e-mail: narayana.peddi@mahindra.com

R. V. Prakash
Indian Institute of Technology Madras, Chennai, India

1 Introduction

Vehicle weight reduction, reduced costs and improved safety performance are the main driving forces behind today's automotive industry. The continuous enhancements of safety norms across the globe has resulted in heavier vehicles, on the other hand, every gram of weight saved reduces CO₂ emissions and thus makes the vehicles eco-friendly and more fuel efficient. It has been estimated that for every 10% of weight reduction from vehicle's total weight, fuel economy improves by ~7%. Efficient dissipation of crash energy is one of the fundamental requirements that govern the vehicle body design to meet crashworthiness requirements. For optimal frontal crash behavior, all kinetic energy of the vehicle should be dissipated by the frontal structure by utilizing the available deformation length efficiently without deforming the passenger compartment. The collision energy absorption through plastic deformation mechanism of thin-walled box structure under axial compressing load is a well proven concept and is widely accepted.

To achieve both light weight and crash & safety performance, the application of advanced high strength steels as well as cross section optimization of the structure is essential. Chen et al. [1] found that 12-sided cross-section with the use of DP980 gives significant mass and cost savings compared to square cross-section. Reddy et al. [2] showed that circular, or Hybrid cross-sections exhibit better crashworthiness when compared with cross-sections made of basic shapes. Geometries with continuously varying cross sections can offer better control over deformation trends for enhanced crashworthiness. Jang HH et al. [3] proposed a process to determine the dimensions of crush box cross section to improve the energy absorption efficiency. Jie L et al. [4] studied the influence of several types of materials and showed that the material properties have influence to automobile energy - absorbing components crashworthiness. Zheng et al. [3] introduced the ridgeline strengthening technology applied to the square tube by using special laser heat treatment and concluded that the thin-walled box structure with selective strengthened ridgelines can significantly increase the SEA capacity.

The thin walled bx structures made of Advanced/Ultra high strength steels (AHSS) play a vital role in meeting the vehicle safety targets, by absorbing large amounts of impact energy, as well as by withstanding higher impact loads that occur due to vehicle collisions. However, the use of high or advanced high strength steels is always associated with higher costs and manufacturing issues. The current work proposes a new methodology for optimum usage of high strength steels in combination with mild steels to increase the energy absorption of thin walled box structures under axial compressive loads. Numerical simulation of crash analysis is carried out for this study.

2 Crush Box

A simple square shaped crush box with a section of 56×56 mm and with a length of 200 mm as shown in Fig. 1 is considered for the study. A rigid plate of 500 kg mass is added at one end of the box to represent the mass of the system as shown in the Fig. 1. Initial thickness of the component is considered as 1.0 mm and the high strength material grade DP980 with yield ~ 980 MPa. The crush box is impacted to a rigid wall with a velocity of 56 kmph to determine the Specific Energy Absorption (SEA) capacity of the box. SEA is defined as the ratio between the total energy absorption to its mass.

To understand the effect of cross section on the SEA values, the square section is replaced by the circular section of 56 mm diameter by keeping all the boundary same as in the case of square section. Table 1 shows the detailed SEA results obtained from square and circular section crush boxes. Results clearly indicate that there is an increase of 20% in the energy absorption capacity by just changing the square cross section to circular section.

The same square and circular section simulations are repeated by changing the material grade of the crush box to understand the effect of material on the specific energy absorption. Three grades of steel, viz., Mild steel (Yield strength ~ 170 MPa), DP 980 steel (Yield strength ~ 980 MPa) and Ultra High Strength Steels (UHSS) (Yield strength ~ 1200 MPa) were chosen to represent various strength categories of the steels. The summary of the results is shown in the Fig. 2. It is observed from the figure that the percentage change in the energy absorption capacity between square and circular sections is varying. As the material grade changes from lower to upper grade, the percentage change is in increasing trend and UHSS material shows 30.6% increase as compared to mild steel which is 8% between square and circular sections.

Fig. 1 FE model setup of square crush box

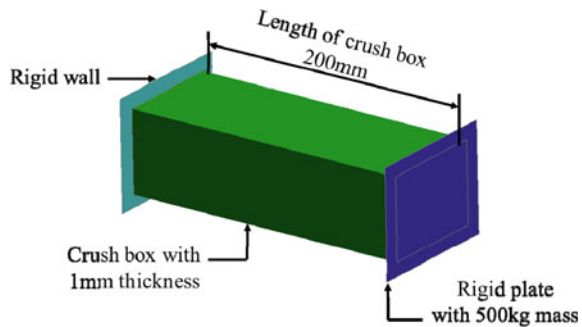
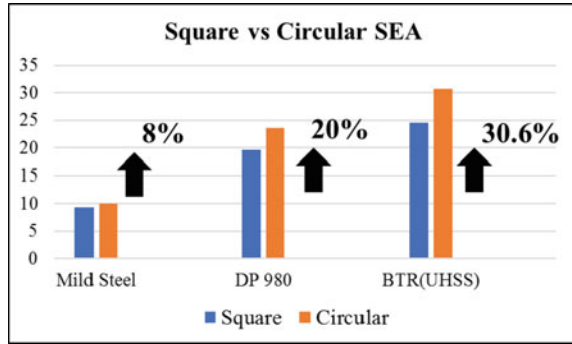


Table 1 Comparison of specific energy absorption between square and circular sections

Shape	Energy (kJ)	Weight (kg)	Specific energy absorption (kJ/kg)
Square	6.69	0.341	19.62
Circle	6.44	0.273	23.59 (~20% higher)

Fig. 2 Comparison of specific energy absorption between square & circular cross sections for Mild, DP980 & UHSS material



3 Crush Box with Combination of Mild Steel and UHSS at Sensitive Zones

Since the corner zones of the crush box are stiffer and offer higher resistance to impact forces as compared to side zones, the material combination of mild steels at sides and ultra high strength steels at corners were considered to enhance the energy absorption capacity of the crush box. The corners of the crush box are changed into Ultra High Strength Steel (UHSS) with yield strength of ~1180 MPa, and at sides with a mild steel of Yeild strength ~170 MPa as shown in Fig. 3.

Similar study has been done by changing the shape of the crush box to circular section of 56 mm diameter as shown in Fig. 4.

The simulations with square and circular sections with the combination of mild and UHSS were carried out and the results are tabulated. The significant energy

Fig. 3 Square crush box with UHSS material at corners

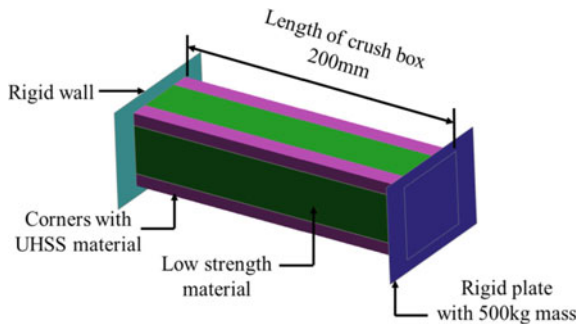
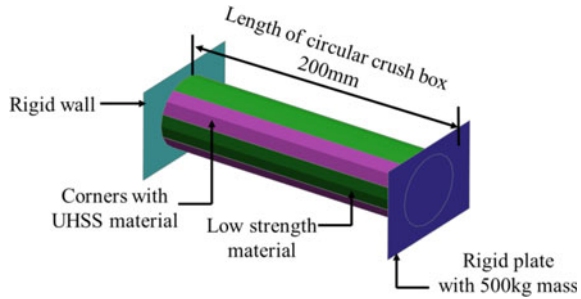


Fig. 4 Circular crush box with combination of UHSS material



absorption parameters like Peak Force (F_{peak}), Mean Force (F_{mean}), TEA (Total Energy Absorption), Delta (Crush Displacement), CFE (Crush Force Efficiency), SE (Stroke Efficiency), SEA (Specific Energy Absorption) that influence the occupant safety were compared for both square and circular section. The brief description of these parameters is given below.

Initial peak crush force (F_{peak}): It is the peak impact crush force that is required to trigger the plastic deformation in the structure.

Stroke efficiency (SE): It is the ratio of the length of an Energy Absorbing Structure (EAS) (l) crushed by plastic deformation (i.e. effective crush stroke) to its initial total length (L).

Total energy absorbed (TEA): It is the total energy absorbed by an EAS by plastic deformation during the impact. It is the area under the crush force (F) versus crush stroke (δ) curve.

Specific energy absorption (SEA): It is the ratio of the TEA by an EAS through plastic deformation to its total mass (m).

Crush force efficiency (CFE): It is the ratio of mean crush force (F_{mean}) to the F_{peak} .

Table 2 shows the comparison of results for square and circular sections. The results indicate that there is a 67% increment (From 14.32 kJ/kg to 23.92 kJ/kg) in the SEA values between the Single mild steel square crush box and the Hybrid model with corners changed to UHSS material. Similarly, in case of circular cross section, the SEA values rose to 91% (From 14.01 kJ/kg to 26.84 kJ/kg). The crush box resistance force to the impact which is represented by Peak (F_{peak}) and Mean (F_{mean}) forces has improved tremendously in Hybrid model when compared to mild steel material model. The circular shape factor further enhancing this resistance and thus the energy absorption levels are significantly improved.

The comparison of percentage change in the energy absorption parameters between Single mild steel and Hybrid models for square and circular sections are shown in the Fig. 5.

Table 2 Comparison of energy absorption parameters between square and circular sections

Section	Material	F-peak (kN)	F-mean (kN)	TEA (kJ)	Delta (mm)	CFE (%)	SE (%)	SEA (kJ/kg)
Square	Single material (mild steel)	78.89	30.20	5.05	167.20	38.28	83.60	14.32
	Hybrid material (mild steel +UHSS)	170.57	51.15	8.39	164	30	82	23.92
Circle	Single material (mild steel)	60.39	22.98	3.86	168	38.05	84	14.01
	Hybrid material (mild steel +UHSS)	130.55	44.28	7.35	166	34	83	26.84

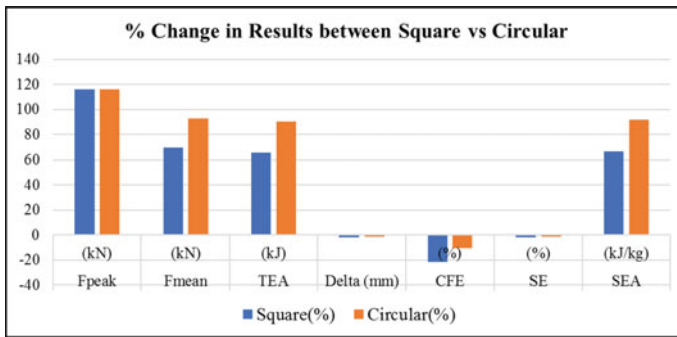


Fig. 5 Comparison of % change in the energy absorption parameters between square and circular sections

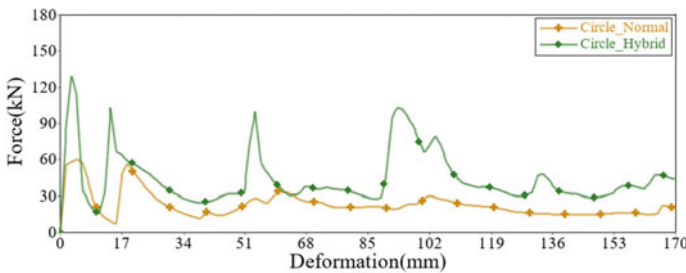


Fig. 6 Comparison of Force vs Deformation plot of Hybrid and Single mild steel material models for circular section

Figure 6 shows the comparison of Force vs Deformation (FvsD) plots of single and Hybrid models for circular section. It is noted from the plot that Hybrid model is showing higher forces throughout the deformation range and thus absorbing more energy compared to single material model.

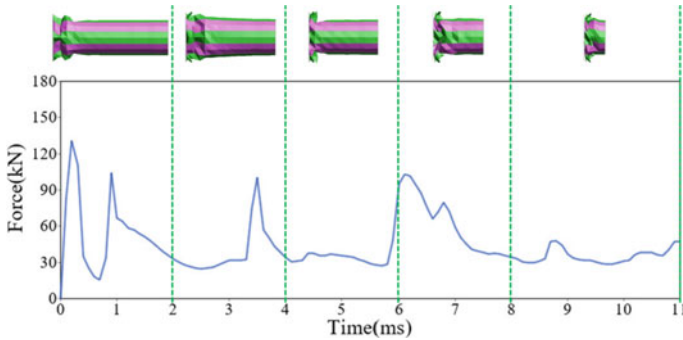


Fig. 7 Overlay of crush deformation with respect to Force vs Time plot of Hybrid material model for circular section

Figure 7 shows the crush deformation of Hybrid model of circular section overlaid on the Force vs Time (FvsT) plot. As shown in the figure, the time axis is divided into five time zones represented by vertical lines. The deformation of crush box is captured at the end of each time zone and overlaid on FvsT plot. It is observed from the figure that the crush mode is purely axial in nature as the simulation carried out at a component level, with an assumption of initial velocity acting in a purely axial direction. However when it is assembled in a vehicle, there is a possibility of observing both axial and bending deformation due to interaction with other components of the vehicle. In a full vehicle crash, it is essential that the supporting structure of the crush box in the vehicle, to be strong enough to sustain the higher impulse loads transferred to it to see a predominant axial collapse. It is to be noted that the current research focussed mainly on the maximizing the crushbox energy absorption by considering the component level analysis.

4 Crush Box with Combination of High Strength Steel and UHSS

A study has been conducted by changing the material combinations of the crushbox with High Strength Dual Phase (DP) steel grades DP590 (~590 Mpa) and DP 980 (~980 Mpa) in combination with UHSS materials of the circular cross section as indicated in the Fig. 8. The results have been compared with single material results of either DP590, DP980 or Mild Steel.

Table 3 shows the comparison of percentage increase in SEA values of Hybrid material combination with UHSS, for mild steel and DP grades of materials with respect to single material models. It is observed from the figure that the combination of mild steel and UHSS gives highest increase in the energy absorption as compared to DP grades of materials. Both DP 590 and DP 980 materials with combination of UHSS gives similar values of percentage of change from single material results. The

Fig. 8 Circular crush box with combination of DP & UHSS material

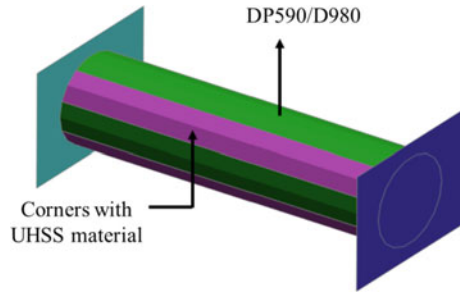


Table 3 Comparison of specific energy absorption between single and hybrid material combinations for circular section

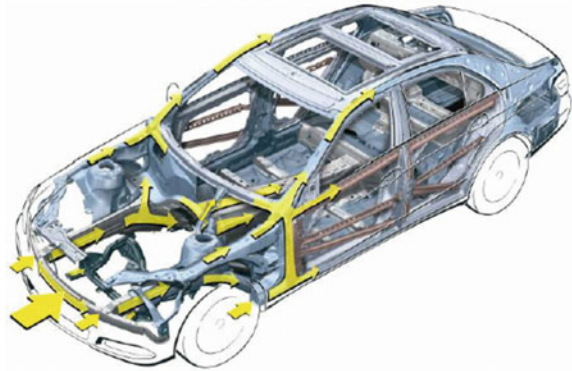
Material grade	Specific energy absorption with UHSS combination (kJ/kg)	% Increase with single material
Mild steel	26.84	91.6
DP590	30.86	40.9
DP980	45.47	41.6

results indicate that the maximum benefit can be achieved by combining the mild steel and UHSS materials as compared to high strength DP grade steels with UHSS materials.

The results demonstrate that mild steel materials with combination of UHSS materials at sensitive zones has good potential to replace the expensive high strength materials for increasing energy absorption. In practical application, the two materials can be combined using Laser Welded Blanks (LWB) or crush box corners can be adhesively bonded with UHSS materials, about which experimental investigations need to be conducted. Continuously joined structures with adhesives are generally better than spot-welded/Laser welded structures in terms of energy absorption and stability [6, 7]. This methodology has better potential to save the weight and cost in the design of automotive structures.

Figure 9 shows the distribution of collision load during the frontal crash. For optimal frontal crash behavior, all kinetic energy of the vehicle should be dissipated by the front structure by utilizing the available deformation length efficiently without deforming the passenger compartment. The increasing trend observed in the peak and mean resistance forces indicate that the combination of mild and UHSS materials can also be used in the passenger compartment zones like A pillar, Sill, Mid rail regions where higher reaction forces are required to resist the collision force.

Fig. 9 Front crash load path



5 Application to Full Vehicle Crash Analysis

To demonstrate the benefits of the proposed method on the full vehicle crash analysis, a monocoque vehicle is considered as a case study. Full vehicle analyses for Frontal Offset Deformable Barrier (FODB) load case is considered for the study as shown in the Fig. 10. In an offset impact, the passenger compartment intrusions play a significant role along with the deceleration pulse, in reducing the occupant injuries during the vehicle collisions. For optimal frontal crash behavior, the kinetic energy of the vehicle should be dissipated efficiently by the front end structure without deforming the passenger compartment.

The passenger compartment zone should be strong enough to sustain and support the higher impulse forces transmitted from the front-end structure. Figure 11(a) shows front end structure highlighting the mid rail component of the passenger compartment which plays a vital role in supporting the front-end structure to dissipate the collision energy efficiently.

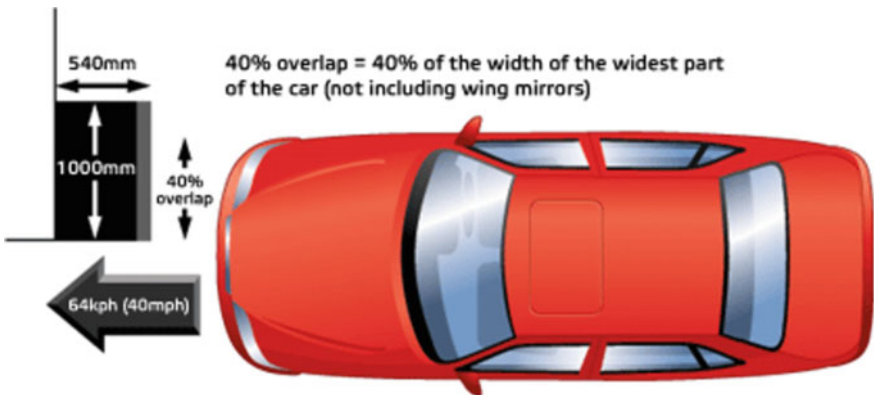


Fig. 10 Frontal Offset Deformable Barrier (Odb) crash test configuration

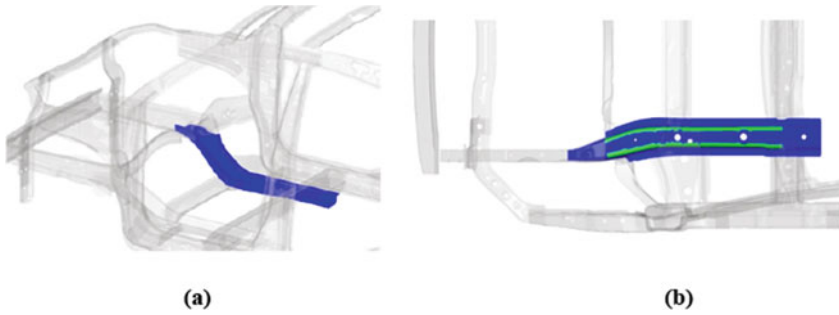


Fig. 11 a Front structure of the vehicle highlighting mid rail part b mid rail component with combination of mild steel and UHSS material at corners

A study has been conducted initially by assigning single material grades of mild steel, DP590 and DP980 separately to the mid rail component, and subsequently the hybrid combination of mild steel and UHSS at corners of the part as shown in the Fig. 11(b). The structural intrusions at footwell and toe pan regions of the passenger compartment are evaluated from the full vehicle crash simulations using LS-DYNA.

Figure 12 shows the comparison of key results between Single material and Hybrid models. It is to be noted that the results shown are scaled results, and the lower the value is better the performance. The Hybrid model results show that there is a significant drop in the intrusion values with respect to both mild and DP steel results. The footwell region shows more than 41% reduction from 5.05 mm to 2.96 mm when compared with mild steel model results. Also, it is observed that there is no change in the peak deceleration values 3.86 g, which is well within targets, while reducing the intrusions in the occupant compartment.

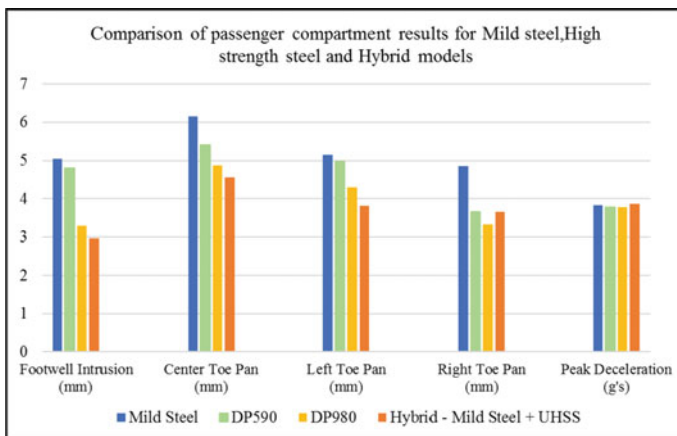


Fig. 12 Comparison of passenger compartment intrusions for Mild, HSS & Hybrid models

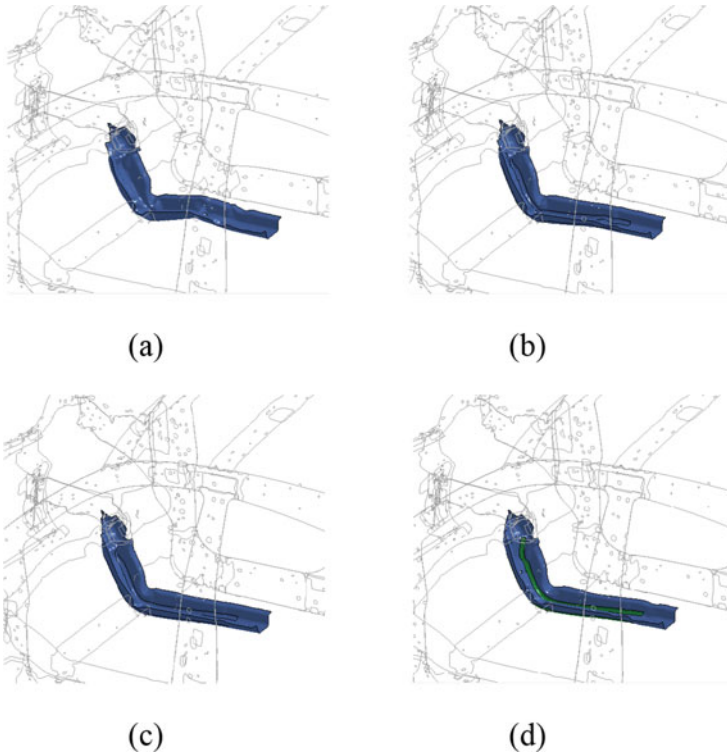


Fig. 13 Comparison of mid rail deformation **a** Mild steel **b** DP590 **c** DP980 **d** Hybrid Model-Mild steel + UHSS

Figure 13 shows the comparison of the mid rail deformation modes of single material and Hybrid models. It is observed that mild steel and DP HSS models show higher deformation leading to higher intrusions in the compartment whereas the Hybrid model shows stable and lesser deformation resulting in the reduction of intrusions.

The mid rail component plays a vital role in supporting the front-end structure to dissipate the collision energy efficiently. It needs to be strong enough to resist and sustain the higher impulse loads transmitted from the front end structure. The increased peak and mean resistance forces observed in Hybrid models shown in Sect. 3 indicate that this material combination can also be used in the passenger compartment zones like A pillar, Sill, Mid rail regions where higher reaction forces are necessary. Infact it is observed from the above results that the combination is more effective even compared with single HSS like DP590 & DP980 leading to oppertunities for higher cost saving avenues.

6 Conclusions

The present work demonstrated the methodology to maximize the energy absorption capacity by means of optimum shape and material combinations of mild and UHSS steels at sensitive locations.

Thin-walled box structures made out of mild steel with corners strengthened by ultra-high strength steel (UHSS) has higher potential to increase the SEA values. By combing the shape and multi material, it is observed that the SEA values can increase by more than 90%.

The increasing trend observed in the peak and mean resistance forces indicate that the combination of mild and UHSS materials can also be used in the passenger compartment zones like A pillar, Sill, Mid rail regions, where higher reaction forces are required to resist the collision force.

This method of multi steel material combination provides greater opportunities to reduce the vehicle weight and cost in the design of automotive structures.

Acknowledgements The authors would like to thank Professor Lakshman Rao, Dr. Vijay Bhaskar and Mr. Noushad for their invaluable inputs provided during this work.

References

1. Chen G, Shi MF, Tyan T (2008) Cross-section optimization for axial and bending crushes using dual phase steels, no. 2008-01-1125, Copyright © 2008 SAE International
2. Reddy TJ, Narayanamurthy V, Rao YVD (2020) Study on crush tube geometric cross sections and topology for axial crashworthiness. *Defence Sci J* 70(3):249–259. <https://doi.org/10.14429/dsj.70.14345>
3. Jang HH, Lee H-A, Yi S-I, Kim DS, Yang HW, Park G-J (2011) Cross-section design of the crash box to maximize energy absorption, no. 2011-28-0110, Copyright © 2011 SAE International
4. Jie L, Lin D (2014) Influence of material properties on automobile energy-absorbing components crashworthiness. *Open Mech Eng J* 8:113–116
5. Zheng Y, Zhu X, Dong X (2016) Energy absorption behavior and application of thin-walled box structure with higher strength in ridgelines. SAE technical paper 2016-01-0398. <https://doi.org/10.4271/2016-01-0398>
6. Conrads L, Liebsch C, Hirt G (2017) Increasing the energy absorption capacity of structural components made of low alloy steel by combining strain hardening and local heat treatment. In: International conference on the technology of plasticity, ICTP 2017, 17–22 September 2017, Cambridge, United Kingdom
7. Peroni L, Avalle M, Belingardi G (2009) Comparison of the energy absorption capability of crash boxes assembled by spot-weld and continuous joining techniques. *Int J Impact Eng* 36(3):498–511

A Non-model Damage Diagnostic Technique for Online Structural Health Monitoring



K. Lakshmi 

Abstract Early diagnosis of structural damages in engineering structures helps in reducing the maintenance cost of structures and increases their life span, reliability, and safety. This paper addresses the damage diagnosis of civil engineering structures like bridges and buildings by employing an energy-based model-free technique with output-only measurements. The proposed diagnostic algorithm is highly amenable for online monitoring and requires only acceleration time history measurements. The damage localization is attempted by extracting the damage feature from the acceleration time history measurements. The damage feature employed here is the nodal curvature of the continuous waveform of energy associated with a jolt, evaluated from the acceleration responses of the structure. A novel damage index is proposed using the above feature to detect the presence of damage as well as localization to handle the hidden factors like operational and environmental variability and the inevitable presence of measurement noise. Numerical investigations have been carried out by considering a scaled-down model of a real bridge in operation, across river Amaravathy at Dharapuram, Tamil Nadu of India to demonstrate the practical viability of the proposed damage diagnostic technique.

Keywords Structural health monitoring · Damage detection · Model-free techniques · Damage localization · Energy-based diagnostics · Bridge structure · Nodal curvature

1 Introduction

The rapid advancements in sensor technologies and data-analysis techniques have promoted structural health monitoring (SHM) as an active research area for monitoring the civil engineering structures and it is fast becoming an effective alternative to the old-fashioned periodic manual inspections of the structures. The availability of low-cost ubiquitous sensors has also immensely helped the rapid development of

K. Lakshmi (✉)
CSIR-Structural Engineering Research Centre, CSIR Campus, Taramani,
Chennai 600113, Tamilnadu, India
e-mail: lakshmik@serc.res.in

© The Author(s), under exclusive license to Springer Nature Singapore Pte Ltd. 2022
T. Tadepalli and V. Narayanamurthy (eds.), *Recent Advances in Applied Mechanics*,
Lecture Notes in Mechanical Engineering, https://doi.org/10.1007/978-981-16-9539-1_17

235

structural health monitoring technology. Online SHM is an effective means of evaluating the condition of the structure and it will ensure safe and sustainable operations of in-service civil infrastructures.

Damage diagnostics is the core component of structural health monitoring and several researchers have worked on it and developed several algorithms for this purpose and well compiled review papers are available in the literature detailing several of these techniques [1–5]. However, the quality of damage diagnostics depends rather heavily on the quality of information gathered from the structures. The more the number of sensing units mounted on the structures, the better will be the information. However, high fidelity sensing is extremely expensive as it requires a large number of sensors especially on the spatial large civil infrastructure, and also expensive dataloggers with a sufficient number of data ports to collect the measured data.

In view of this, optimal sensor placement algorithms which can help to place the sensors judiciously on the structure to obtain maximum information without redundancies have become an integral component of the SHM [6–8]. Once the sensors are placed optimally, another problem arises due to faulty sensors which are not uncommon. These faulty sensors may give a faulty diagnosis of the structure. In view of this, sensor fault detection and sensor data correction algorithms also have an important role to play in the SHM schemes to avoid false positive or negative diagnosis [9, 10]. The major focus in this paper is on damage detection and localization of large civil engineering structures using the measured time-history data.

Vibration-based damage diagnostic techniques are popular among various methods proposed in the literature. The majority of these damage diagnostic techniques developed earlier are based on natural frequencies, vibration modes, and their associated features like structural flexibility, modal curvatures, and modal strain energies. Even though these techniques look theoretically very impressive, there are several practical problems in the field implementation of these techniques. Since mode shapes present only the global state of the structure in contrast to the damage which is very local it poses a natural problem in diagnosing damages with the first few modes. On the other hand, extracting higher modes is practically rather difficult from low energy responses due to operational traffic load. Apart from this, it is difficult to handle the confounding factors associated with environmental and operational variability (EoV) on the civil engineering structures due to continuous variations in operational loads and also temperature [11].

To overcome the limitations of modal based damage diagnostic techniques, several popular signal processing techniques using time-frequency analysis [12, 13], time series analysis [14–17], multi-variate analysis [18, 19], modal filters [20], multi-modal techniques [21–23] have been developed and are found to be more successful in handling the confounding factors associated with environmental and operational variability.

An effective structural health monitoring technique should ideally address the following characteristics.

- i. Model-free methods do not need a correlated finite element model of the measured structure. Many civil engineering structures are spatially large and complex, thus obtaining the correlated numerical model and maintaining these correlations throughout the service life of the structure is very difficult.
- ii. Output-only techniques are preferable, as measuring the operational loads like traffic and seasonal variations of wind on structures is always a very difficult task.
- iii. The Structural Health Monitoring (SHM) techniques should be able to handle the confounding variables such as environmental and operational variabilities of the structure. It is shown in several earlier investigations that these confounding factors unless handled properly can result in misleading diagnostics.
- iv. The SHM techniques should be amenable for online monitoring with less computational complexity so that the diagnosis can be performed relatively faster.

Keeping these things in view, a model-free approach based on the ‘energy associated with jolt’ of response is explored which can be amenable for online SHM. Damage detection and localization procedure, based on the difference of normalized curvature of waveform energy associated with jolt, is proposed. A novel damage index is proposed which can handle environmental and operational variabilities effectively. The performance of the proposed method is numerically verified by considering a practical example of a real bridge across river Amaravathi near Dharapuram, Tamil Nadu, India. The investigations carried out and presented in this paper demonstrates that the proposed method has good accuracy, handles effectively the EoV, and is robust to measurement noise.

2 Energy Extraction from Acceleration Measurements

The jolt response, $V(t)$, from the measured acceleration time history, can be extracted as the rate of change of acceleration.

$$V(t) = \frac{d\ddot{y}(t)}{dt} \quad (1)$$

where $V(t)$ is the calculated jolt response, $\ddot{y}(t)$ is the measured acceleration time history.

Jolt energy is given by:

$$\text{Jolt_E}_s = \log \sum_{t=\Delta t}^{(N-1)\Delta t} \left[\frac{\ddot{y}_s(t + \Delta t) - \ddot{y}_s(t)}{\Delta t} \right] \quad (2)$$

where Δt is the sampling interval., \ddot{y}_s is the acceleration at the measured node 's', and N is the total number of measured samples at the sensor node. Once the Jolt energy at each sensor node is evaluated, the continuous waveform of energy is formed by connecting these energy values at each node. Once the jolt energy spatial profile is formed, the central difference approximation can be used to arrive at the curvature of the waveform of the jolt energy.

The curvature difference ΔC_{pq}^s of waveform of the jolt energy between two different sets of measurements taken on the structure, for any typical sensor node s , can be written as

$$\Delta C_{p,q}^s = C_p^s - C_q^s \quad (3)$$

where C^s represents the curvature of the waveform for sensor node s , subscripts p and q refer to two distinct sets of measurements taken at a particular instant or different instants of time.

3 Damage Diagnostic Technique

The proposed model-free, output-only damage diagnostic is organized into two phases namely 'First Phase' and 'Diagnosis Phase'. The step-by-step procedures to execute the two phases associated with the proposed energy-based damage diagnostic algorithm are presented in this section.

3.1 First Phase

The first phase is carried out on the targeted structure when it is in a healthy state to establish the control limits for future damage diagnosis handling the environmental and operational variability. The excitations from the ambient conditions, due to environmental/operational loads like varied temperature levels and varied levels of operational load, are simulated while generating the rich number of instances of acceleration time history responses. Using a MATLAB script, the acceleration time history datasets are partitioned into several sub-datasets, with a reasonable number of predetermined data samples/points. The total number of sub-datasets is named 'numsets'. The changes in the dynamic state of the structure due to environmental and operational variabilities like temperature, operational loads are absorbed by establishing a control limit, using the sub-datasets formed in the previous steps. This control limit is essential to distinguish the actual damage from these confounding factors. The step-by-step procedure to establish the control limit is as follows:

- a) The acceleration time history responses at all N_d sensor locations of the first sub-dataset, 'SUBSET-1' are used to evaluate curvature ordinate at each node

- say C_1^s , $s = 1$ to Nd . Similarly, for the ‘SUBSET-2’, say C_2^s , $s = 1$ to Nd . Using these curvature values of these sub-datasets, the curvature difference ΔC_{12}^s , $s = 1, \dots, nd$ at each sensor node s , is evaluated using Eq. (3).
- b) Repeat step(a), by using the ‘SUBSET-1’ against the rest of the other available i.e., (numsets-2) sub-datasets (i.e., excluding sub-dataset-1 and sub-dataset-2) in the baseline pool and extract the curvature differences $\Delta C_{1,2}^s$, $s = 1, \dots, nd$ using Eq. (3) for each combination and normalize the curvature difference.
 - c) In this fashion, each sub-dataset will form [numsets – 1] combinations and thereby gives rise to [numsets – 1] values of the curvature difference $\Delta C_{p,q}^s$, $s = 1, \dots, nd$. Here subscripts p and q refer to two distinct sub-datasets. With this, the total number of ΔC vectors for all the sub-datasets works out to be [numsets * (numsets – 1) * Nd].
 - d) The control limit of a subdomain is established with the assumption that changes in the dynamic state due to environmental and operational variabilities follow the normal distribution. Accordingly, the control limit vector, L , can be established as.

$$L_s = [\text{mean}(\Delta C^s) + 3 * (\text{standard deviation}(\Delta C^s))] \tag{4}$$

- e) These control limits vector is subsequently used during the next phase i.e., the diagnosis phase while evaluating the damage indices at each sensor node, s .

3.2 Diagnosis Phase

In this second phase, a new unknown (current) state of the same structure is diagnosed by the following steps.

- i. The time history acceleration responses of the structure, recorded from the unknown state of the structure, are partitioned into several sub-datasets.
- ii. Each newly recorded current sub-dataset is paired with a randomly chosen sub-dataset in the baseline pool of the specific subdomain being investigated for damage.
- iii. The responses of the randomly chosen baseline sub-dataset say h is combined with the current subset, c to evaluate the normalized curvature differences at each sensor node s as $\Delta C_{c,h}^s$, $s = 1, \dots, nd$
- iv. The damage indicator DI_s is computed for the sensor node of the sub-dataset of current data.

$$\text{Damage index, } DI_s = \Delta C_{c,h}^s - L_s \tag{5}$$

where $\Delta C_{c,h}^s$ is the curvature difference between the current sub-dataset and the randomly chosen sub-dataset of the pristine state. The superscripts c and h stand for the current sub-dataset number and baseline sub-dataset number, respectively. The subscript c will act as a count of the current sub-dataset number and will help to

evaluate the exact time instant of damage from the sub-dataset count, c and number of samples in each sub-dataset, and the sampling frequency.

When the state of the structure is healthy and in the presence of environmental/operational variability, the damage indices at all sensor nodes are expected to be within the established control limits of the respective sensor node. When the damage is present in the structure, the damage index corresponding to sensor nodes will indicate a positive value signifying the damage, while the damage indices of the rest of the nodes, of the structure, will either be zero or negative. Therefore, positive damage index values of a typical sensor node(s) in the structure under consideration indicate the spatial location of the damage. The time instant of the damage can be arrived at by counting the current sub-dataset number indicated by superscript c of the damage index DI of the current data in which the damage is identified.

The complete procedure of the proposed technique is shown in the form of a flowchart in Fig. 1.

4 Numerical Investigation

Extensive numerical investigations have been carried out considering bridge girder, truss bridge, and also multi-storey framed structures. However, in this paper, numerical investigations have been presented by considering a real example of an existing Reinforced Concrete road bridge in Tamilnadu, India, across river Amaravathi. Investigations have been carried out with different levels of measurement noise and also simulating environmental variability.

For the investigations carried out for damage diagnostics in this paper, a typical span of the said bridge is considered. Since damage diagnostic studies on any live bridge cannot be carried out by physically inducing damage on the structure and usually conducted by simulating damage on correlated finite element models, this paper also it is proposed to simulate damage numerically in the finite element model in the present investigations. The commercial FE software, ANSYS is used to model the middle span of the bridge considered for numerical investigations in the present work. The longitudinal beams, cross girders as well as the deck of the bridge are discretized using 8 noded brick elements. Figure 2 shows the finite element idealization of the central span of the Amravati bridge. The boundaries are considered to be simply supported, in the present idealization of the bridge span. The initial five natural frequencies of the middle span of the Amaravathi bridge are worked out to be 5.3 Hz, 21.2 Hz, 47.7 Hz, 84.8 Hz, 132.5 Hz.

Each of the three girders is discretized using 25 brick elements. In the proposed numerical simulations, it is assumed that sensors are located at each alternative node of the beam. Accordingly, in the numerical simulations, the time history data at only 12 equally spaced nodes on each girder are considered in the present damage

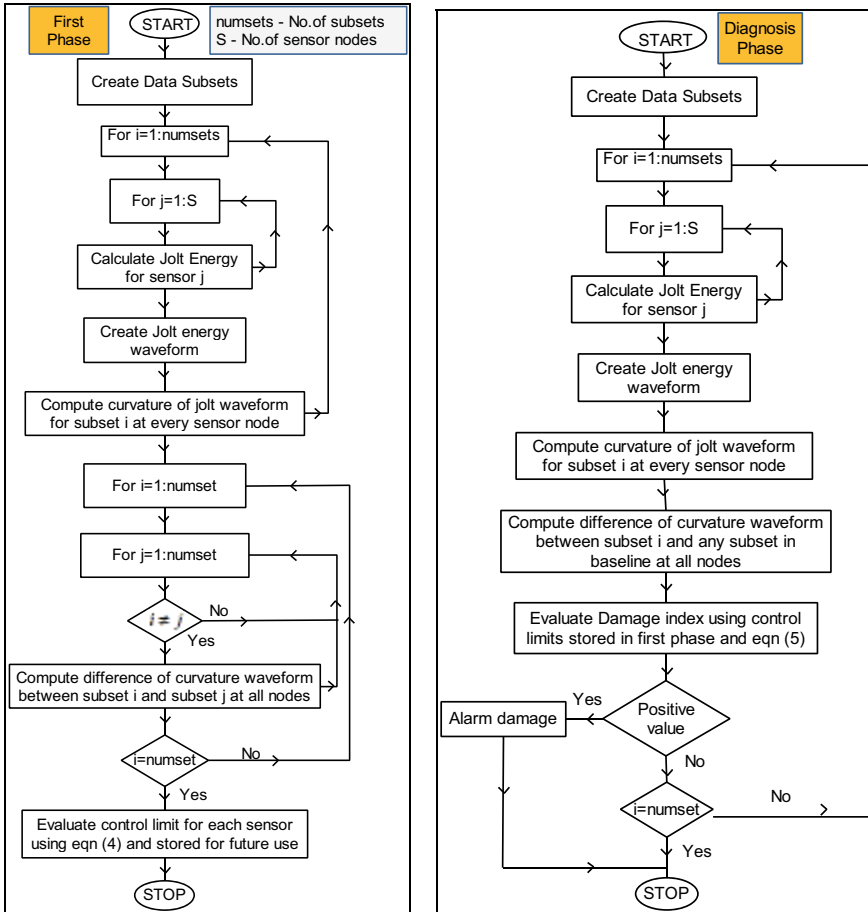


Fig. 1 Flowchart of the proposed damage diagnostic technique

diagnosis. The bridge is excited with random white Gaussian noise and dynamic analysis of the bridge is carried out using the Newmark time marching scheme. Rayleigh damping is assumed in the present investigations. The time step length for the dynamic simulations is taken as 0.001 s and it works out to the sampling rate of 1000 Hz.

An important issue in the practical implementation of SHM is the measurement noise. Hence, the sensitivity of the proposed algorithm with measurement noise is investigated by corrupting the computed acceleration time history measurements using white Gaussian noise whose mean statistic is zero, through a MATLAB script. Accordingly, the noise-free acceleration time-history responses are modified by adding a Gaussian random component to generate noisy measurements.

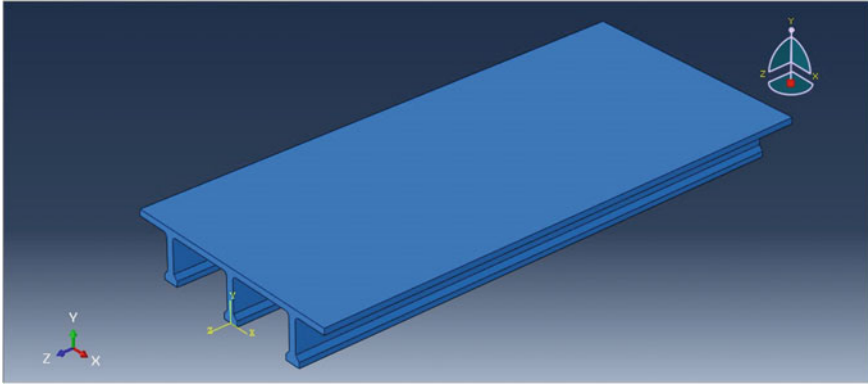


Fig. 2 Numerical model of existing RCC bridge at Dharapuram

$$\ddot{y}_m = \ddot{y} + \zeta_p N_{\text{noise}} \sigma(\ddot{y}) \tag{6}$$

where the subscript m refers to the noise corrupted acceleration measurements, N_{noise} is the standard normal distribution, ζ_p is the noise percentage, $\sigma(\ddot{y})$ is the standard deviation of the computed uncorrupted time-history response. In this numerical investigation, the random noise levels are altered as 2, 4 and 6%. Additionally, a severe experimental scenario is simulated due to the uncorrelated noisy sequences affecting different nodes.

As the longitudinal girders are the primary load-carrying components of a bridge, they have a higher probability of occurrence of damage. Therefore, the simulation of damage is focused on the middle longitudinal girder of the bridge. In the proposed numerical simulations, the damage simulation is carried out by decreasing the stiffness of elements 8 and 16, of the middle longitudinal girder (i.e. girder-2). The intensities of damage simulated are 8%, and 6% stiffness reduction, in elements 8 and 16, respectively.

Element-level parametric modeling of the structural damage is achieved by representing the stiffness matrix of the damaged j^{th} element as

$$k_j^d = \alpha_j k_j^u \tag{7}$$

where the scalar $\alpha_j \in [0, 1]$ defines the reduction in the stiffness matrix of the j^{th} element. The global stiffness matrix is given by

$$K = \underset{j=1}{\overset{n}{\mathbf{A}}} k \tag{8}$$

where A indicates the assembly operator in the finite element method.

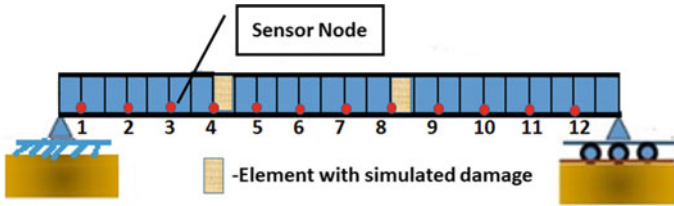


Fig. 3 A schematic diagram of the side view of the middle girder indicating the locations of sensor nodes and the simulated damages

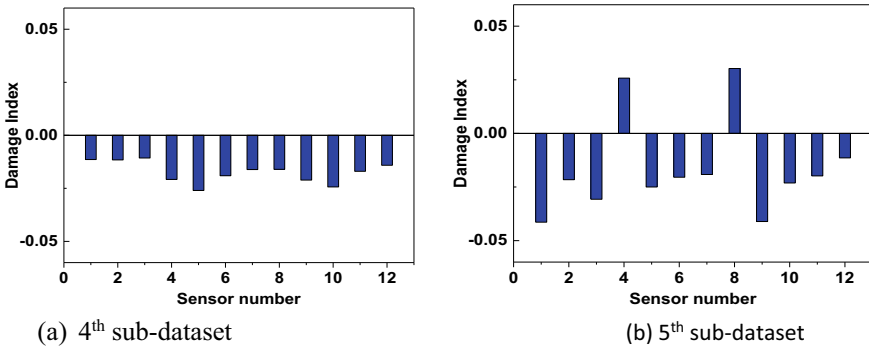


Fig. 4 Damage indices using the proposed damage diagnosis algorithm with noise-free measurements

The schematic diagram of the side view of the middle girder with the locations of sensor nodes and the simulated damage elements is shown in Fig. 3.

Both the first and the second phases are carried out by following the process discussed in Section-3. Accordingly, by employing the healthy sub-dataset and current sub-dataset, the jolt energy, curvature of the waveform, control limit, and the damage indices are evaluated, using Eqs. 2–5. The damage indices are presented in Fig. 4 for noise-free measurements and Fig. 5 for varied levels of measurement noise. It can be observed from the plots shown in Figs. 4 and 5 that the positive damage indices indicate the presence of damage in the structure.

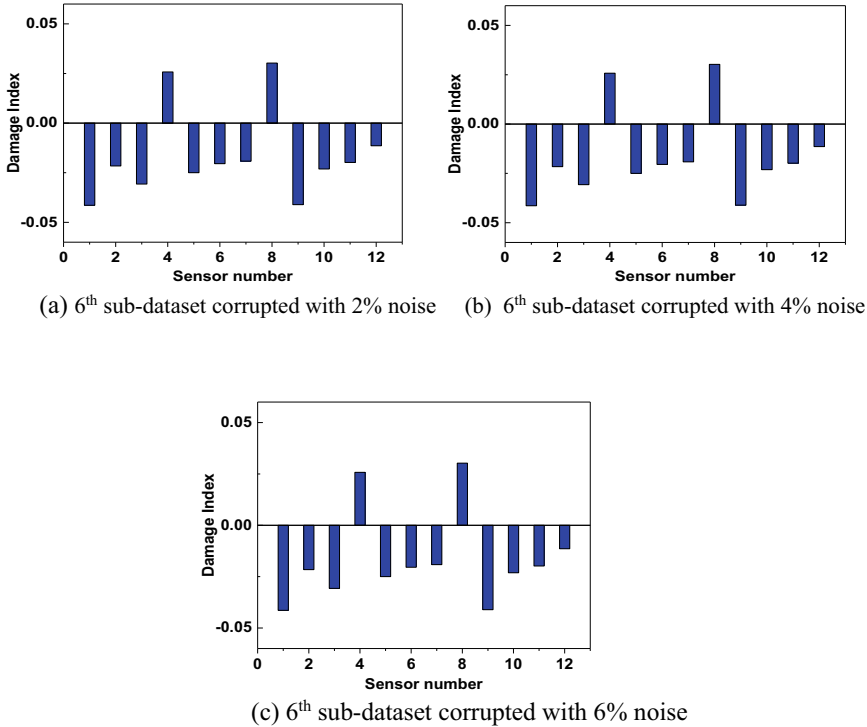


Fig. 5 Damage indices using the proposed damage diagnosis algorithm using time history data corrupted with varying levels of noise

5 Conclusion

A new online damage diagnostic technique, using the energy evaluated from jolt, is proposed in this paper. The proposed damage diagnostic procedure is modal-free and works only with output-only measurements. The damage localization is carried out by using the curvature difference of the jolt energy profiles of the structure evaluated from the acceleration time history measurements of the current and pristine structure. Numerical investigations have been carried out by considering a practical example of a real bridge in operation, across the river Amaravathi, near Dharapuram, Tamil Nadu, India. Based on the investigations presented in this paper, it can be concluded that the proposed algorithm can precisely identify the presence of damage, its exact time instant, and also can effectively localize the damage. It is also shown through the numerical investigations that the proposed damage diagnostic algorithm can handle the environmental and operational variabilities effectively apart from measurement noise. The proposed algorithm involves very few computations and the spatial profiles of jolt energy can be evaluated using the acceleration time history measurements, it is highly amenable to online structural health monitoring.

Acknowledgements This paper is being published with the permission of the Director, CSIR-SERC.

References

1. Fan W, Qiao P (2011) Vibration-based damage identification methods: a review and comparative study. *Struct Health Monit* 10(1):83–111. <https://doi.org/10.1177/1475921710365419>
2. Das S, Saha P, Patro SK (2016) Vibration-based damage detection techniques used for health monitoring of structures: a review. *J Civ Struct Heal Monit* 6(3):477–507. <https://doi.org/10.1007/s13349-016-0168-5>
3. Alvandi A, Cremona C (2006) Assessment of vibration-based damage identification techniques. *J Sound Vib* 292(1–2):179–202. <https://doi.org/10.1016/j.jsv.2005.07.036>
4. Deraemaeker A, Worden K (eds) (2012) *New trends in vibration-based structural health monitoring*, vol 520. Springer, Vienna. <https://doi.org/10.1007/978-3-7091-0399-91>
5. Avci O, Abdeljaber O, Kiranyaz S, Hussein M, Gabbouj M, Inman DJ (2021) A review of vibration-based damage detection in civil structures: From traditional methods to Machine Learning and Deep Learning applications. *Mech Syst Sig Process* 147:107077. <https://doi.org/10.1016/j.ymsp.2020.107077>
6. Kammer DC (1991) Sensor placement for on-orbit modal identification and correlation of large space structures. *J. Guidance Control Dyn* 14:251–259
7. Rao ARM, Anandakumar G (2007) Optimal placement of sensors for structural system identification and health monitoring using a hybrid swarm intelligence technique. *Smart Mater Struct* 16(6):2658
8. Rao ARM, Lakshmi K, Krishnakumar S (2014) A generalized optimal sensor placement technique for structural health monitoring and system identification. *Procedia Eng* 86:529–538
9. Rao ARM, Kasireddy V, Gopalakrishnan N, Lakshmi K (2015) Sensor fault detection in structural health monitoring using null subspace-based approach. *J Intell Mater Syst Struct* 26(2):172–185
10. Rao ARM, Kumar SK, Lakshmi K (2012) Sensor fault detection in large sensor networks using PCA with a multi-level search algorithm. *Struct Durability Health Monit* 8(3):271
11. Deraemaeker A, Worden K (2018) A comparison of linear approaches to filter out environmental effects in structural health monitoring. *Mech Syst Sig Process* 105:1–15
12. Rao ARM, Lakshmi K (2015) Damage diagnostic technique combining POD with time-frequency analysis and dynamic quantum PSO. *Meccanica* 50(6):1551–1578
13. Chen B, Zhao SL, Li PY (2014) Application of Hilbert-Huang transform in structural health monitoring: a state-of-the-art review. *Math Probl Eng* 2014:1–22. Article ID 317954
14. Lakshmi K, Rama Mohan Rao A (2014) A robust damage-detection technique with environmental variability combining time-series models with principal components. *Nondestr Test Eval* 29(4):357–376
15. Lakshmi K, Rao ARM, Gopalakrishnan N (2017) Singular spectrum analysis combined with ARMAX model for structural damage detection. *Struct Control Health Monit* 24(9):e1960
16. Lakshmi K, Rao ARM (2016) Structural damage detection using ARMAX time series models and cepstral distances. *Sādhanā* 41(9):1081–1097
17. Lakshmi K, Rao ARM (2015) Damage identification technique based on time series models for LANL and ASCE benchmark structures. *Insight-Non-Destructive Test Condition Monit* 57(10):580–588
18. Rao ARM, Lakshmi K, Venkatachalam D (2012) Damage diagnostic technique for structural health monitoring using POD and self-adaptive differential evolution algorithm. *Comput Struct* 106:228–244

19. Rao ARM, Lakshmi K, Kumar SK (2015) Detection of delamination in laminated composites with limited measurements combining PCA and dynamic QPSO. *Adv Eng Softw* 86:85–106
20. Lakshmi K (2021) Detection and quantification of damage in bridges using a hybrid algorithm with spatial filters under environmental and operational variability. *Structures* 32:617–631
21. Lakshmi K, Rao ARM (2019) Baseline-free hybrid diagnostic technique for detection of minor incipient damage in the structure. *ASCE J Perform Constr Facil* 33(2):04019018
22. Lakshmi K, Rao ARM (2018) A hybrid structural health monitoring technique for detection of subtle structural damage. *Smart Struct Syst* 22(5):587–609
23. Lakshmi K, Rao ARM, Gopalakrishnan N (2018) An improved damage diagnostic technique based on singular spectrum analysis and time series models. *Struct Infrastruct Eng* 4(10):1412–1431

Simulation of Mixed-Mode Fracture in a Single Phase and Two-Phase Composite Material



Subrat Senapati, Anuradha Banerjee, and R. Rajesh

Abstract In the present study, we focus on the deformation and mixed-mode fracture of a single phase and two-phase system. A square domain with an edge crack is discretized using a square lattice to develop a random spring network model. The model is based on each lattice point interacting with nearest and next nearest neighbours using extensional and torsional springs. From the mixed-mode fracture simulations, we show that the lattice architecture results in anisotropic fracture behaviour locally which we resolve by incorporating disorder in the failure strain threshold of the springs. Further, we show for a crack propagating in a two-phase solid, the inherent differences in the two phases result in an inclined crack path in mixed mode loading and additional disorder in the individual phases are not vital for realistic simulations of the fracture process.

Keywords Two phase material · Mode-I fracture · Mixed-mode fracture

1 Introduction

Heterogeneous biological materials such as bone, wood, tooth, nacre, etc., as well as man-made composite materials like concrete, reinforced plastics, etc., exhibit complex fracture processes that are a consequence of the disorder in their composition and local material behaviour. Damage, in a disordered material, is known to nucleate at multiple locations in the form of micro cracks. These micro cracks grow and interact leading to formation of macroscopic cracks and subsequent failure of the solid. Conventional continuum mechanics based approaches such as finite element modelling are ill-suited for modelling such discontinuous and discrete damage growth.

S. Senapati · A. Banerjee (✉)
Department of Applied Mechanics, IIT Madras, Chennai 600036, India
e-mail: anuban@iitm.ac.in

R. Rajesh
The Institute of Mathematical Sciences, C.I.T. Campus, Taramani, Chennai 600113, India
e-mail: rrojesh@imsc.res.in

Lattice based models, adopted widely in statistical physics, provide a suitable alternative for studying fracture in heterogeneous material [2, 4, 11, 16]. These investigations primarily focused on simulating the avalanche statistics of the fracture process in a bulk solid to identify universal characteristics like power-law behaviour with similarities to volcanic and seismic activities [1, 13, 14]. There has also been significant effort in simulations of growth of a pre-existing macro crack using lattice based models to identify factors that influence the resistance to crack growth in multi phase material [3, 5, 12, 15]. More recently, the model has been shown to well reproduce experimental macroscopic response of compressive fracture of bone, honeycombs, etc. [6, 8, 9]. Most investigations have, however, primarily examined the propagation under remote tensile load that locally results in opening mode, i.e., mode-I fracture. There has been comparatively much less effort in understanding the role of disorder on fracture behaviour under more realistic loads that are a combination of opening and sliding modes.

In the present work, we develop a random spring network model (RSNM) on a square lattice with nearest and next-nearest neighbour interactions using linear springs. To simulate growth of a macroscopic crack under mode-I as well as mixed mode loads, the lattice domain is connected to a loading pin arrangement through truss elements. The suitability of the loading arrangement is verified in its ability to generate mixed mode stress fields at the crack tip. From the fracture simulations, the lattice architecture was found to result in anisotropic fracture behaviour locally which was resolved by incorporating disorder in the failure strain threshold of the springs. Further, crack propagation in a two-phase solid shows that the inherent differences in the two phases result in an inclined crack path in mixed mode loading and additional disorder in the individual phases are not vital for realistic simulations of the fracture process.

2 The Random Spring Network Model (RSNM)

A square domain of size $L^2 = 25 \times 25 \text{ mm}^2$ is discretized by 50×50 elements or particles that are initially placed in equally spaced lattice points (Fig. 1a). The lattice size falls in the recommended range of representative volume element sizes for different heterogeneous materials, which varies between 0.1 mm for metals to 10 mm for wood [7]. A particle is connected to its neighbours and next nearest neighbours through extensional springs. The torsional deformation θ_{ijk} , as shown in Fig. 1c, is resisted by torsional springs. A lattice point along with its connected springs form a unit cell (Fig. 1c) and these unit cells form a network of springs as shown in Fig. 1b. A crack of length $a = 0.6L$ is inserted in the mid plane of the domain by removing the springs that fall in the crack plane.

When deformed from its initial configuration, the potential energy ϕ can be divided into extensional energy, ϕ_{ext} , and torsional energy, ϕ_{tor} :

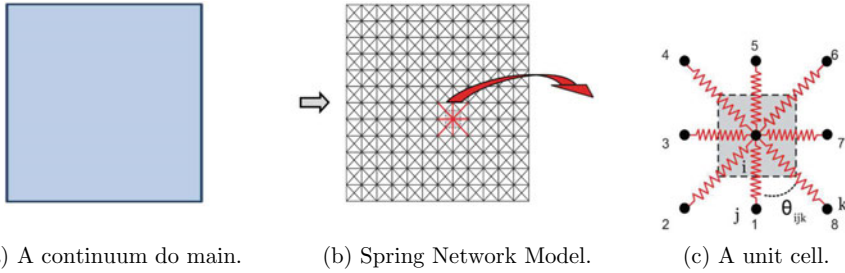


Fig. 1 The discretisation of a homogeneous elastic medium using RSNM

$$\phi = \phi_{ext} + \phi_{tor}. \tag{1}$$

The extensional energy stored in the domain of N lattice points is

$$\phi_{ext} = \sum_{i=1}^N \sum_{j=1}^4 \frac{1}{2} k_{ij} (|\vec{r}_i - \vec{r}_j| - a_{ij})^2, \tag{2}$$

where k_{ij} is the stiffness of the spring between particles i and j whose coordinates are denoted by \vec{r}_i and \vec{r}_j , and a_{ij} is the undeformed distance between them. The torsional component of the potential energy stored is

$$\phi_{tor} = \sum_{\langle ijk \rangle} \frac{1}{2} c_{ijk} \left(\theta_{ijk} - \frac{\pi}{4} \right)^2, \tag{3}$$

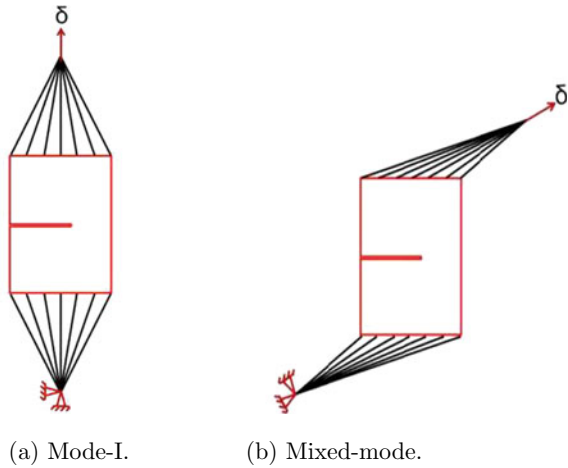
where c_{ijk} is the torsional stiffness between the lattice point i and two adjacent neighbours j and k as shown in Fig. 1c. The summation of $\langle ijk \rangle$ is done over the 8 angles formed around the lattice point i . In the undeformed state the angles are $\pi/4$.

In an uniform system, the constants k_{ij} and c_{ijk} do not depend on the spatial location. On equating the strain energy density of linear elastic continuum with the energy (stored in the extensional and torsional springs) density of a unit cell, the elastic material constants, Young’s modulus (E) and Poisson’s ratio (ν) are expressed in terms of spring constants [2, 10] as

$$E = \frac{8k \left(k + \frac{c}{a_0^2} \right)}{3k + \frac{c}{a_0^2}}, \tag{4}$$

$$\nu = \frac{\left(k - \frac{c}{a_0^2} \right)}{3k + \frac{c}{a_0^2}}, \tag{5}$$

Fig. 2 Schematic diagram of the loading fixtures for the different fracture modes. One end is loaded while the other end is fixed



where k is the spring constant for the next nearest neighbour springs, $2k$ is the spring constant for the nearest neighbour springs, and $c_{ijk} = c$.

The RSNM formulation for the homogeneous system, described above, is extended to a two phase system as follows. Given the elastic modulus and Poisson’s ratio for the two materials, the corresponding spring constants are obtained from Eqs. 4 and 5. A fraction r of the particles, chosen at random, are labelled as soft phase and the remaining as hard phase. According to the phase of a particle, the four springs labelled as 1, 2, 3, 4 in Fig. 1c are assigned the corresponding spring constants. All the 8 torsional spring constants c_{ijk} associated with a particle is assigned according to its phase.

To simulate mode-I and mixed-mode fracture, separate loading fixtures are attached to the RSNM, as shown in Fig. 2. The loading pin and fixed pin are connected to the domain through stiff trusses. Let β denote the angle that the line joining the pins makes with the normal to the crack plane. $\beta = 0$ corresponds to mode-I (Fig. 2a) while $\beta \neq 0$ corresponds to mixed-mode (Fig. 2b).

A quasi static displacement of $\delta = 3.5$ mm is applied to the loading pin in 350 steps. In each step the loading pin is displaced and the spring network deforms through the connecting trusses. To reach static equilibrium, the system is evolved using Newton’s equation of motion with an additional dissipative term. The acceleration \vec{a}_i of the site i due to interaction with other sites is expressed as:

$$\vec{a}_i = -\nabla_{\vec{r}_i} \phi - \gamma \frac{d\vec{r}_i}{dt}, \tag{6}$$

where mass has been set to one and γ is a damping coefficient. We choose $\gamma = 0.85$ for our simulations. Using velocity-Verlet algorithm, the position vector $\vec{r}_i(t + \Delta t)$ depends on the positions at earlier times as

$$\vec{r}_i(t + \Delta t) = \vec{r}_i(t) (2 - \gamma \Delta t) - \vec{r}_i(t - \Delta t) (1 - \gamma \Delta t) + \vec{a}_i(\Delta t)^2. \quad (7)$$

The positions are iterated using Eq. 7, until static equilibrium is reached.

The Young's modulus for hard and soft phases are chosen to 100 GPa and 20 GPa respectively, while ν for both phases is chosen to be 0.3. A bond fails or breaks when the stress in the bond exceeds a threshold σ^* . As the hard bonds are stiffer, a soft bond fails at a higher strain compared to that for a hard bond. Once a spring fails, it does not carry any further load and the load gets redistributed among the remaining springs. It is to be noted that the failure criterion used here is system size dependent. Brittle materials are known to have strong size effects in which the strength of brittle materials decrease with system size, and hence the failure threshold that we choose will also depend on system size.

3 Results

Initially, to verify the mode-mixity in the stress-field generated by the application of mixed-mode loading using the loading-pin arrangement described in previous section, three configurations with the loading angle, β , defined as the angle between the loading axis and the normal to initial crack plane, were analysed ($\beta = 0^\circ, 22.5^\circ, 45^\circ$). The contour plots of the opening stress, $\sigma_{\theta\theta}$, for each lattice point is calculated using its corresponding displacement field and elastic properties and the stress field is compared in Fig. 3 for the remote load of 1 kN at the loading pin. As expected, the opening stress field exhibits intensification near the crack tip and is symmetric about the initial crack plane for mode-I loading. With increasing loading angle the orientation of the maximum opening stress appear to be inclined away from the initial crack plane as shown in Fig. 3b and 3c. Further, to identify the direction of maximum opening stress, for all lattice sites in the region around the crack tip, the opening stress and the associated angle subtended by the lattice site with the origin at the crack tip are shown as point-plots in Fig. 4. The highest opening stresses occur along the direction of $\theta = 0^\circ, -20^\circ$ and -40° for the loading angle of $\beta = 0^\circ, 22.5^\circ$ and 45° respectively.

For simulation of the crack growth, the failure stress threshold was taken to be a gaussian distribution with a mean σ^* and standard deviation ϕ . For the simulations shown in Fig. 5 the mean failure stress threshold was arbitrarily taken to be 2.5 and a range of standard deviations $\phi = 2\%, 5\%$ and 10% of the mean, were used to understand the effect of disorder on the mode-I macroscopic response and crack path. For each case of non-zero disorder, 10 different realisations of the network were analysed. Resulting broken bonds are shown in colours green, black, magenta and yellow for probability of failure in % being (76–100), (51–75), (26–50), (1–25) respectively. In absence of disorder, the crack continues to propagate along the expected ($\theta = 0^\circ$) plane and with increasing disorder there are a few extra bonds broken in the neighbourhood of the ($\theta = 0^\circ$) plane suggesting minor deviations compared to the 0% disorder case.

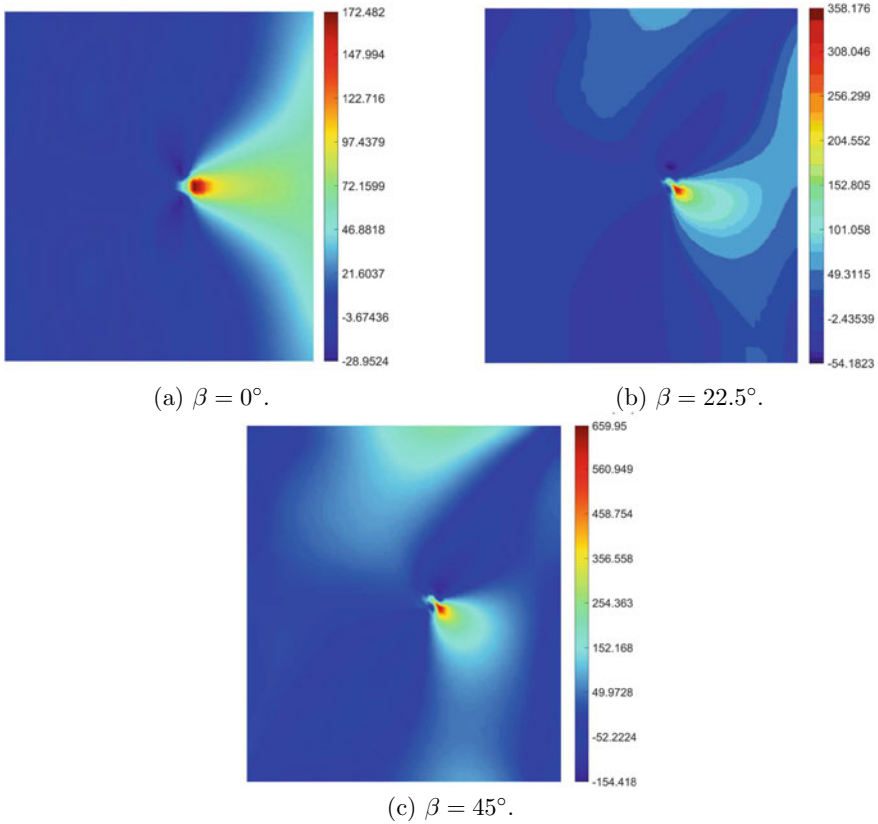


Fig. 3 Constant $\sigma_{\theta\theta}$ (MPa) contours for the different loading conditions

Similar simulations were performed for $\beta = 22.5^\circ$ and 45° , and the crack paths are presented in Figs. 6 and 7. For both mixed-mode loading angles, in absence of disorder ($\phi = 0\%$) the crack propagation is not along the expected path as per the maximum opening stress direction. The initial path is observed to be along $\theta = 0^\circ$ plane, followed by a minor deviation and finally back to a plane parallel to the $\theta = 0^\circ$ plane. This is an artefact of the lattice anisotropy resulting from its regular architecture as fewer bonds need to be broken when propagation of crack is along the $\theta = 0^\circ$ plane. However, with increase in disorder such anomalous crack propagation is averted and crack increasingly tends towards path as per maximum opening stress direction. Disorder of 5–10% results in more realistic crack propagation direction for all loading angles.

The effect of disorder in the failure strain threshold on the macroscopic response for the three loading configurations is presented in Fig. 8. In absence of disorder (Fig. 8a) the crack propagation is a single event with a large number of bonds being broken simultaneously whereas with higher disorder the peak load is achieved after

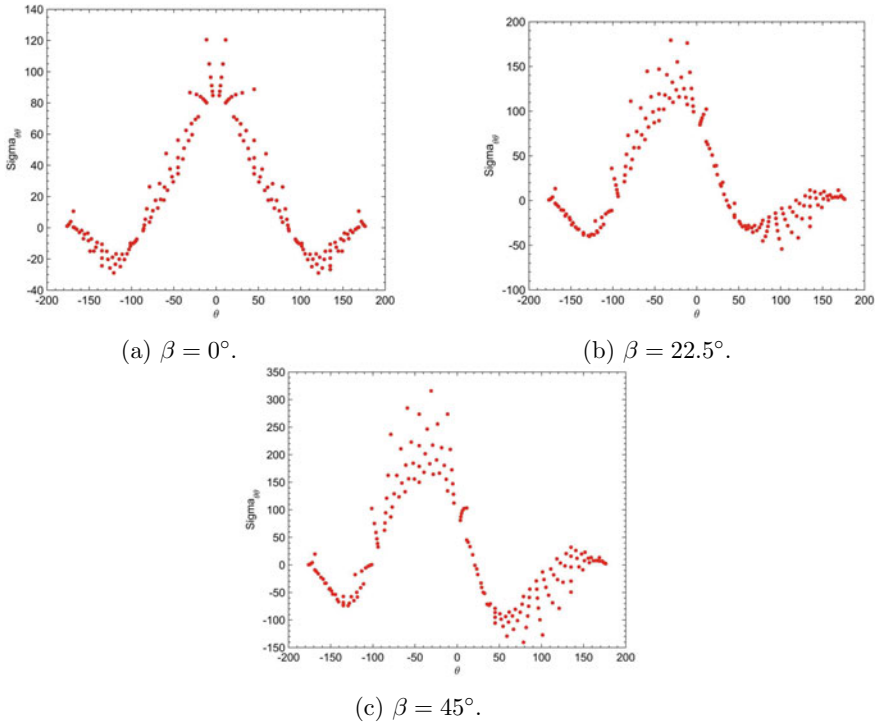


Fig. 4 Variation of $\sigma_{\theta\theta}$ with θ for the different loading conditions

a few failure events resulting in noticeable but limited non-linearity in the response prior to load drop. The load drop is more gradual for higher disorder which is consistent with the crack path being more tortuous as observed earlier in Fig. 5. For higher mixity, a similar trend is observed. The average of peak strength over 10 simulations are tabulated in Table 1. Increasing disorder results in a monotonic increase in the peak strength for mode-I, in contrast, the effect on the $\beta = 45^\circ$ loading, it is a monotonic decrease for the range of disorder considered.

We next examine effect of disorder on crack propagation in a two-phase composite material. The elastic behaviour of the phases, the hard and soft phase, are described by modulus E_h and E_s , respectively, with the ratio arbitrarily chosen to be 5. For simplicity the Poisson's ratio is kept a constant at 0.3. The failure strain thresholds are chosen such that the ratio is $\epsilon_h^f / \epsilon_s^f = E_s / E_h$. Similar to the single phase analysis, a range of disorder in the failure strain threshold is taken for each of the phases. From the simulations of 10 realisations of the network, the effect of disorder on the averaged macroscopic response is presented in Fig. 9. The effect was observed to be marginal for both $\beta = 0^\circ$ and 45° as the averaged peak strengths tabulated in Table 2 show less than 8% variation for $\beta = 0^\circ$ while the variation is within 2% for $\beta = 0^\circ$. The spatial distribution of broken bonds for mode-I and mixed mode show

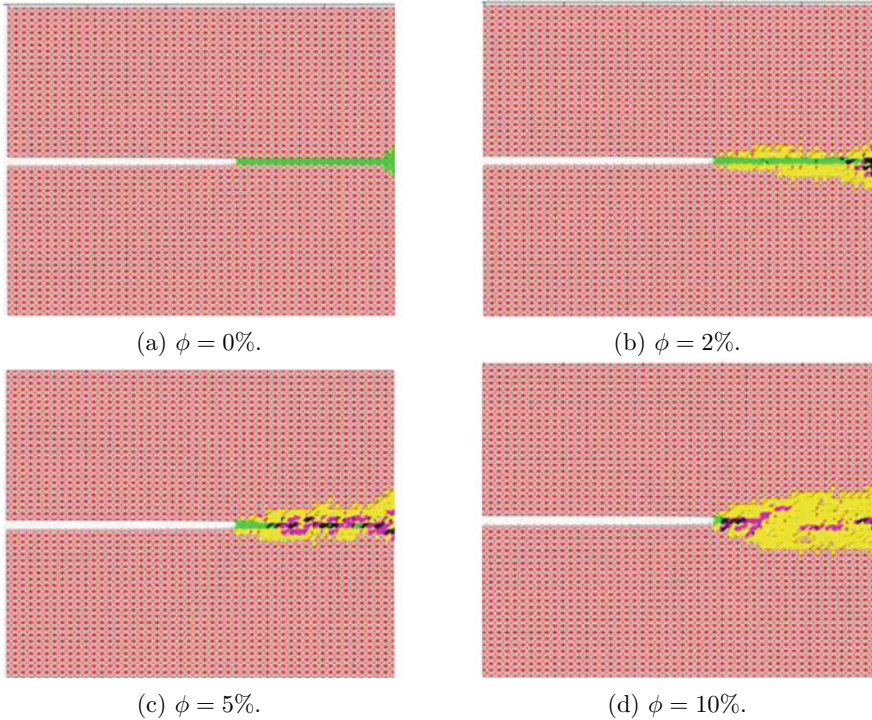


Fig. 5 Effect of disorder ϕ on the mode-I fracture path

no noticeable effect of lattice architecture on the crack path even when there is no disorder in the individual phases ($\phi = 0$).

Comparing Tables 1 and 2 we can conclude that presence of heterogeneity in a system enhances both mode-I and mixed-mode strength for all the disorders considered here. The enhancement is most pronounced for $\phi = 0$. The reason behind the increment in strength can be addressed by looking at the respective fracture path. The mode-I and mixed-mode fracture paths are averaged over 10 realisations and those are presented in Figs. 10 and 11 respectively. If we compare the fracture paths for homogeneous and heterogeneous system by looking at Figs. 10 and 5 for mode-I and Figs. 11 and 6 for mixed-mode, then it can be observed that the spread of the bond breakage is larger in the later system. A larger spread implies the crack paths are more tortuous. Which is the reason behind increment in heterogeneous fracture strength.

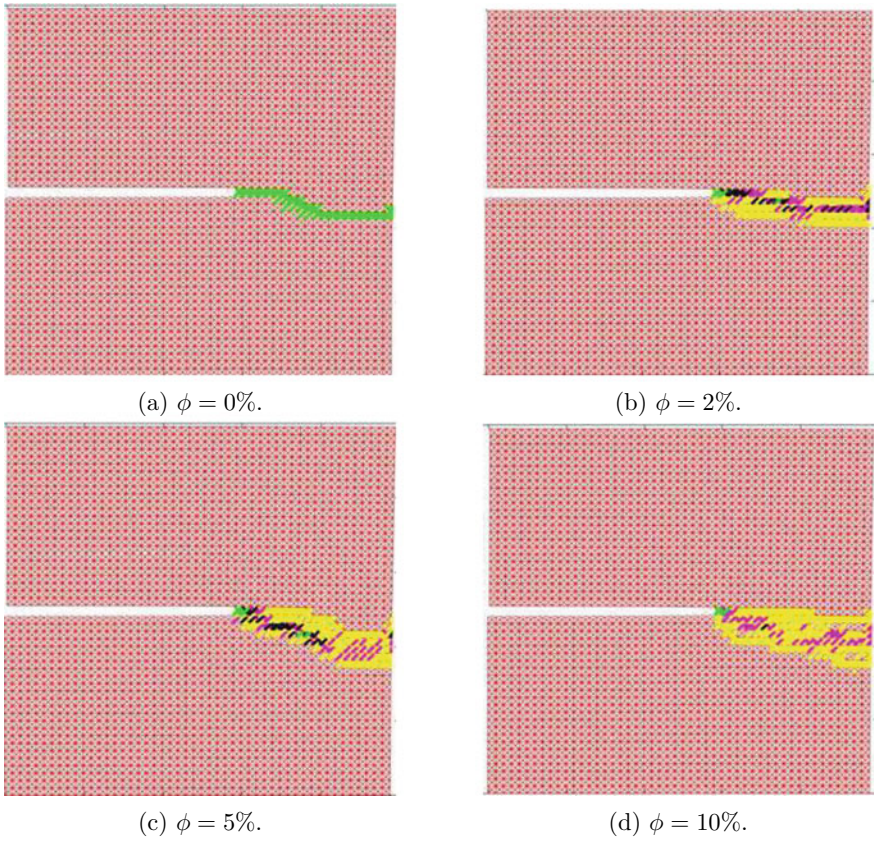


Fig. 6 Effect of disorder ϕ on the mixed-mode ($\beta = 22.5^\circ$) fracture path

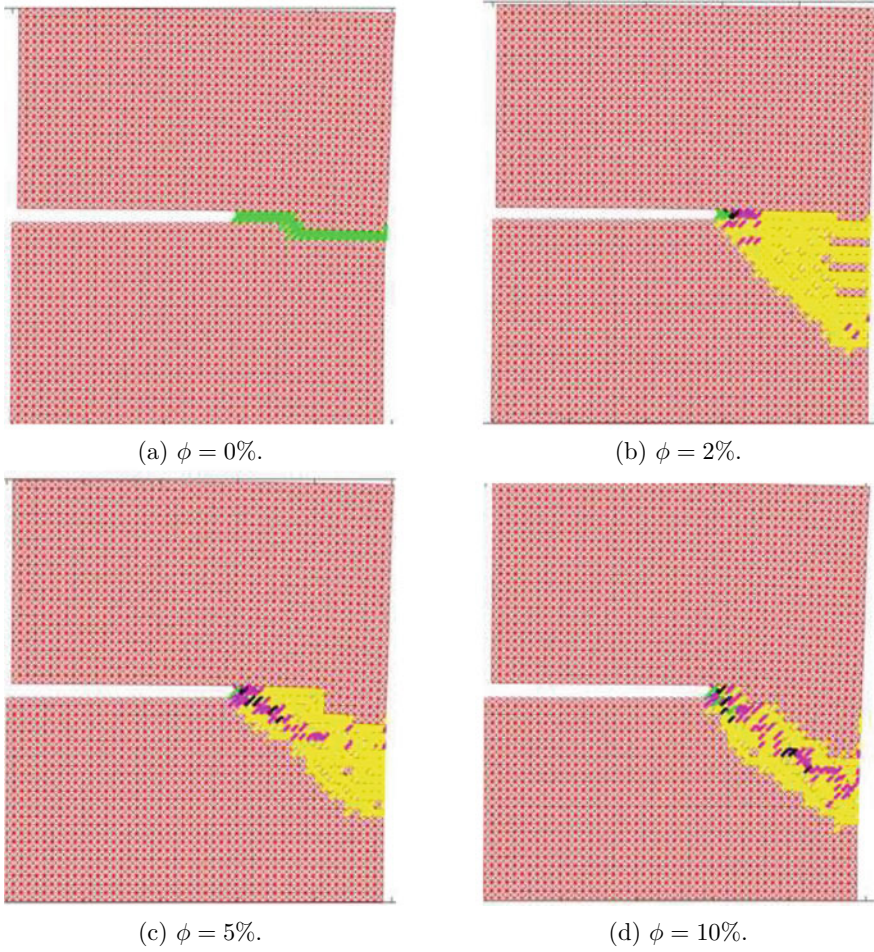


Fig. 7 Effect of disorder ϕ on the mixed-mode ($\beta = 45^\circ$) fracture path

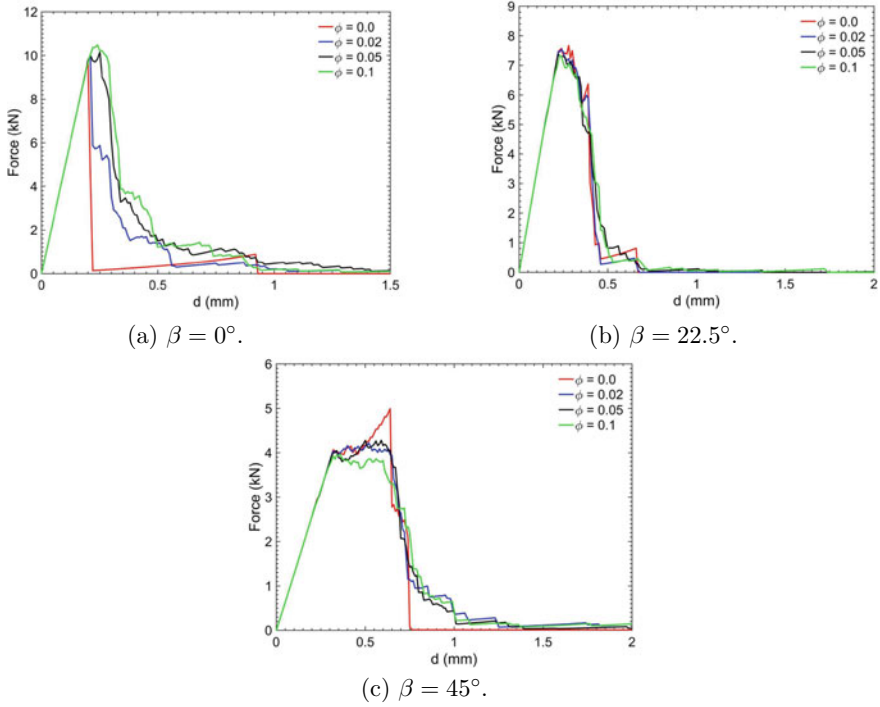


Fig. 8 The mean force deflection curve for various loading conditions

Table 1 Homogeneous Fracture strengths (kN) tabulated for various ϕ values

Fracture modes	$\phi = 0\%$	$\phi = 2\%$	$\phi = 5\%$	$\phi = 10\%$
Mode-I	9.786	10.492	10.587	11.366
Mixed-mode ($\beta = 22.5^\circ$)	7.671	7.741	7.755	7.712
Mixed-mode ($\beta = 45^\circ$)	4.993	4.878	4.726	4.405

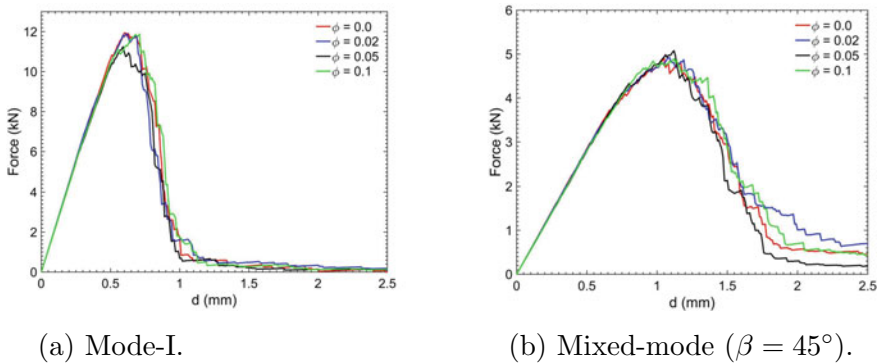
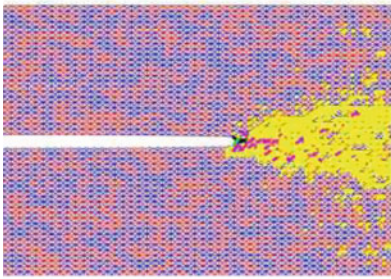
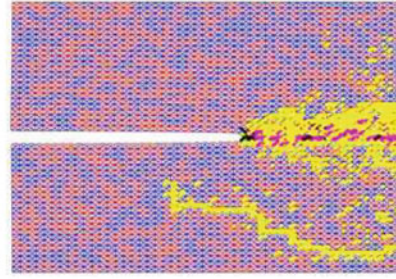
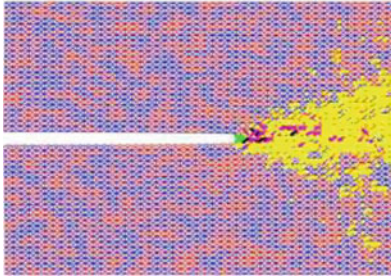
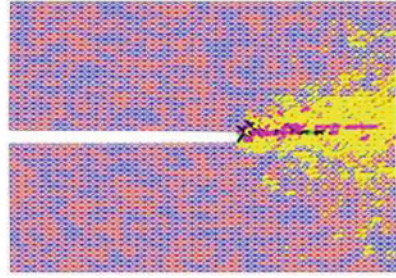


Fig. 9 Force deflection variation for the chosen range of ϕ and $r = 0.5$

Table 2 Fracture strengths (kN) tabulated for various ϕ values and $r = 0.5$

Fracture modes	$\phi = 0\%$	$\phi = 2\%$	$\phi = 5\%$	$\phi = 10\%$
Mode-I	12.917	12.578	12.104	12.459
Mixed-mode ($\beta = 45^\circ$)	5.362	5.326	5.306	5.386

(a) $\phi = 0\%$ (b) $\phi = 2\%$ (c) $\phi = 5\%$ (d) $\phi = 10\%$ **Fig. 10** Mode-I fracture path in the two phase system for various ϕ

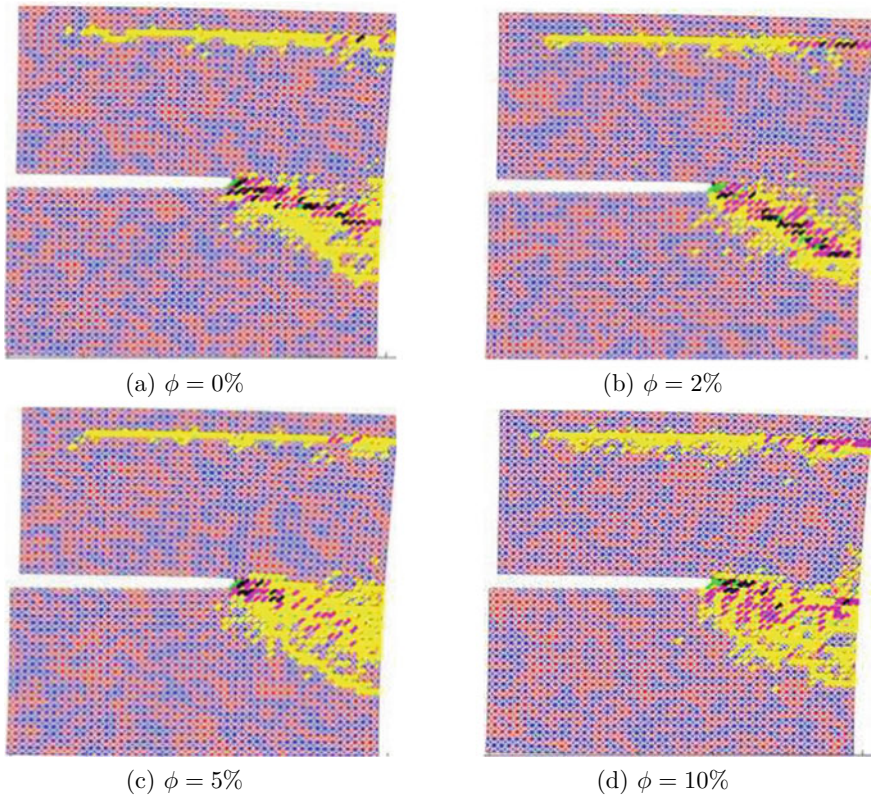


Fig. 11 Mixed-mode ($\beta = 45^\circ$) fracture path in the two phase system for various ϕ

4 Conclusion

Development of discrete element models is of particular importance in simulation of fracture processes in brittle heterogeneous materials. In the present work we develop random spring network model to simulate mixed-mode crack growth in a single phase as well as two-phase solid. In an isotropic brittle solid, the expected crack path is known to be along the maximum opening stress. We show that in a random spring network based on a square lattice with nearest and next-nearest neighbour interactions, the orthotropic architecture of the lattice results in crack propagation along the initial plane in spite of mixity in remote load. We resolve the discrepancy by incorporating a disorder in the failure strain threshold and we show that the disorder mitigates the dominance of the lattice anisotropy and results in more realistic crack paths. Further, crack propagation in a two-phase solid shows that the inherent differences in the two phases result in an inclined crack path in mixed mode loading and additional disorder in the individual phases are not vital for realistic simulations of the fracture process. Based on the results of the present

study, we are currently studying in detail the role of proportion of the two phases on the mechanisms of crack growth under mixed mode loading.

References

1. Acharyya M, Chakrabarti BK (1996) Growth of breakdown susceptibility in random composites and the stick-slip model of earthquakes: Prediction of dielectric breakdown and other catastrophes. *Phys Rev E* 53:140–147
2. Alava MJ, Nukala PKVV, Zapperi S (2006) Statistical models of fracture. *Adv Phys* 55(3–4):349–476
3. Boyina D, Kirubakaran T, Banerjee A, Velmurugan R (2015) Mixed-mode translaminar fracture of woven composites using a heterogeneous spring network. *Mech Mater* 91:64–75
4. Curtin WA, Scher H (1990) Brittle fracture in disordered materials: a spring network model. *J Mater Res* 5(3):535–553
5. Dimas LS, Giesa T, Buehler MJ (2014) Coupled continuum and discrete analysis of random heterogeneous materials: elasticity and fracture. *J Mech Phys Solids* 63:481–490
6. Kumar D, Banerjee A, Rajesh R (2021) Crushing of square honeycombs using disordered spring network model. *Mech Mater* 160:103947
7. Lemaitre J (1986) Local approach of fracture. *Eng Fract Mech* 25(5–6):523–537
8. Mayya A, Banerjee A, Rajesh R (2018) Role of porosity and matrix behavior on compressive fracture of Haversian bone using random spring network model. *J Mech Behav Biomed Mater* 83:108–119
9. Mayya A, Praveen P, Banerjee A, Rajesh R (2016) Splitting fracture in bovine bone using a porosity-based spring network model. *J Roy Soc Interface* 13(124):20160809
10. Monette L, Anderson MP (1994) Elastic and fracture properties of the two-dimensional triangular and square lattices. *Modell Simul Mater Sci Eng* 2(1):53
11. Pan Z, Ma R, Wang D, Chen A (2018) A review of lattice type model in fracture mechanics: theory, applications, and perspectives. *Eng Fract Mech* 190:382–409
12. Parihar RPS, Mani DV, Banerjee A, Rajesh R (2020) Role of spatial patterns in fracture of disordered multiphase materials. *Phys Rev E* 102(5):053002
13. Ray P, Date G (1996) Spatial scaling in fracture propagation in dilute systems. *Phys A* 229(1):26–35
14. Tzschichholz F, Herrmann HJ (1995) Simulations of pressure fluctuations and acoustic emission in hydraulic fracturing. *Phys Rev E* 51:1961–1970
15. Urabe C, Takesue S (2010) Fracture toughness and maximum stress in a disordered lattice system. *Phys Rev E* 82(1):016106
16. Zapperi S, Ray P, Stanley HE, Vespignani A (1997) First-order transition in the breakdown of disordered media. *Phys Rev Lett* 78:1408–1411

Comparable Safety Margins of the Ulnar Fingers When the Thumb Remains on an Unsteady Slider



Banuvathy Rajakumar and S. K. M. Varadhan

Abstract Among various daily life activities, grasping an object is a common task performed by all healthy individuals. For a stable grasp of an object, fingertip force distribution plays a major role. In the current study, an instrumented handle was designed on which five-fingertip force/torque measuring sensors were mounted. A vertical railing was provided on the left surface of the handle, and a slider platform with a force sensor to measure the forces from the thumb was placed over the railing. The present study focuses to investigate how the fingertip forces varied to keep the handle in equilibrium when the slider platform was made unsteady. The experiment involved two conditions. In one condition, the platform was fixed, and in the other condition, the platform was mobile. The participants had to lift the handle and match the flat mark on the platform to the mark on the handle during “fixed” and “free” condition. As a consequence of reduction in the thumb load force during the “free” condition, grip forces of ring and little fingers increased together, and they were statistically equivalent. We hypothesized that the load force exerted by the ring finger would be larger than the small finger, and the “safety margin” of the little finger would be greater than ring. However, both the tangential forces and safety margin of the ulnar fingers were found to be “comparable” during the free condition, while they were significantly different during the fixed condition.

Keywords Stabilization · Grasping · Safety margin

1 Introduction

Safe handling of objects is crucial in the successful grasp. Fine adjustment of fingertip forces plays a major role in achieving stabilization of the grasped object. Normal and tangential forces are the two important fingertip forces required for the static grasping of the object. A skilful adaptation of the grip force to the load force variations is essential for attaining grasp stability. The grip force produced by the fingers should

B. Rajakumar · S. K. M. Varadhan (✉)
Department of Applied Mechanics, Indian Institute of Technology Madras, Chennai, India
e-mail: skm@iitm.ac.in

not be too large to cause damaging of the object or too small to result slipping of the object from hand. Maintaining a proper safety margin is essential to avoid the chances of any hazard caused due to crushing or slipping. The safety margin is an index to measure the performance in prehension tasks [1] and is defined as the “normalized difference between the applied normal force and the minimal normal force to prevent slipping” [2, 3]. A minimal safety margin is observed when there is a simultaneous modification in the grip force due to the tangential force variation occurring due to the manipulation of the object [4].

There were studies performed in the past to investigate the safety margin of all participating fingers while grasping a handle by means of precision grip [2, 4] (using index and thumb) and prismatic precision grip [5–7] (using all fingers and thumb). In a study by Aoki [8], friction between the finger-object interface was varied, and the safety margin of the thumb and virtual finger [9] (includes fingers except thumb) was investigated. The surface friction of the thumb and other fingers was altered by using different materials such as rayon and sandpaper. It was found that the tangential (or load) force at the rayon side (thumb) was smaller than the tangential force at the sandpaper side (virtual finger). Similarly, the safety margin was also found to be lower at the rayon side than at the sandpaper side, as the low friction coefficient of rayon reduced the safety margin further along with the decrease in the load force.

However, in the current study, rather than changing the surface friction between finger-object interfaces, the friction between the object-handle interface was reduced by mounting a slider platform (object) on a railing fitted over the left surface of the grasped handle [10]. Since the thumb was positioned on the slider platform, we refer to it as thumb platform henceforth. Since we come across objects like retractable ballpoint pens and pipette controllers having sliding mechanisms towards the thumb side, we intended to understand the individual fingertip forces and safety margin while attempting to establish grasp stability during their operation. Although our experimental handle does not exactly mimic these objects, their working mechanism inspired us to provide liberty to the thumb in the up and down direction. Thus, the aim was to investigate the strategy employed by our central nervous system in controlling the fingertip forces to achieve an optimal safety margin while establishing static equilibrium in the handle with the thumb sliding mechanism.

From our work on investigating the fingertip forces of the individual fingers, where an unsteady platform was to be held firmly at the HOME position (midway of “middle and ring” fingers), there occurs a reduction in the load force of the thumb. As a consequence of this drop, grip forces of the ulnar fingers (“ring and little”) increased. It was found that the grip forces contributed by these fingers were equivalent. However, the load force distribution and safety margin in these fingers were not examined in detail when the movable platform was to be grasped firmly at the HOME. Therefore, in this manuscript, we focussed on investigating the safety margin of the ulnar fingers while the platform was held firmly at the HOME position.

Apart from the normal forces, the safety margin also changed depending on the tangential forces. Therefore, it is important to investigate on the tangential force sharing between these fingers. There exist three possible options for the tangential force distribution among the ulnar fingers. The first option will be to produce

comparable load forces by the ulnar fingers. The second option will be to produce significantly greater load force by the ring when in comparison to the small finger. The latter option will be to exert greater load force by the small finger in comparison to the ring finger. Based on these options for the tangential forces, the safety margin also varies accordingly.

Since the ring finger load force was greater than the small finger when the unsteady thumb platform was mechanically fixed [10], we expected the same result even when the platform was not mechanically fixed. The reason is that the ring finger exerts greater grip strength than the little finger among the ulnar fingers during the examination of the involvement of each finger to the overall grip [11, 12]. So, we expected that the “stronger” ring finger would be capable enough to share greater tangential force than the “weaker” little finger. Therefore, we hypothesized that the ring finger tangential force would be larger than the small finger (H1). Perhaps, if the ring finger shares greater tangential force than the little finger, it was expected that the safety margin of the little finger would be greater than the ring finger (H2).

2 Methods and Materials

2.1 Participants

Fifteen right hand dominant male volunteers performed this experiment. The average and standard deviation of the hand length, hand width, weight, age and height of the participants were measured as 18.6 ± 0.9 cm, 8.7 ± 0.3 cm, 73.3 ± 9.6 kg, 25.6 ± 2.7 years and 172.6 ± 3.9 cm. The participants with no history of neurological diseases and hand injuries participated in this experiment. Written informed consent were obtained from all the participants. The experiment methodology was sanctioned by the Institutional Ethics Committee of IIT Madras (Approval number: IEC/2016/02/VSK-2/12) before the start of the experiment.

2.2 Experimental Setup

A prehensile handle was designed and built with a vertical railing of length 7 cm fitted on the left surface of the handle upon which a slider platform was mounted. Six-component force and torque sensors (Nano 17, ATI Industrial Automation, NC, USA) were mounted on the handle to measure the forces and moments exerted by the individual fingers and thumb. The force produced by thumb was measured by mounting the sensor on the platform. The thumb platform could move freely in the up and down direction over the railing fitted on the thumb side.

At the upper end of the handle, an acrylic block was placed over which a position sensor (Liberty Standard sensor, Polhemus Inc., USA) was mounted. It measured the

position and orientation of the handle with respect to the electromagnetic transmitter. Next to the position sensor, a spirit level was placed for the participant to sustain the equilibrium of the handle. A detailed description of the experimental handle can be seen in our previous publication [10].

2.3 Experimental Procedure

Prior to the prehension experiment, a fingertip friction measuring experiment was performed.

Friction Experiment

A device was designed and built to mount a force sensor on top of the aluminum platform, as shown in Fig. 1. The platform could translate in the horizontal direction with the help of a pulley and belt activated by a motor. A grip force of 6N has to be produced by the participant's finger continuously for 3 s to initiate the horizontal motion of the motor. The grip force exerted by the participants was shown as visual feedback on the computer monitor. We collected data from the individual finger and thumb. Single-trial was conducted for each finger. The friction coefficient was obtained using following equation.

$$\text{Friction coefficient } (\mu) = \frac{\text{Load force}}{\text{Grip force}} \quad (1)$$

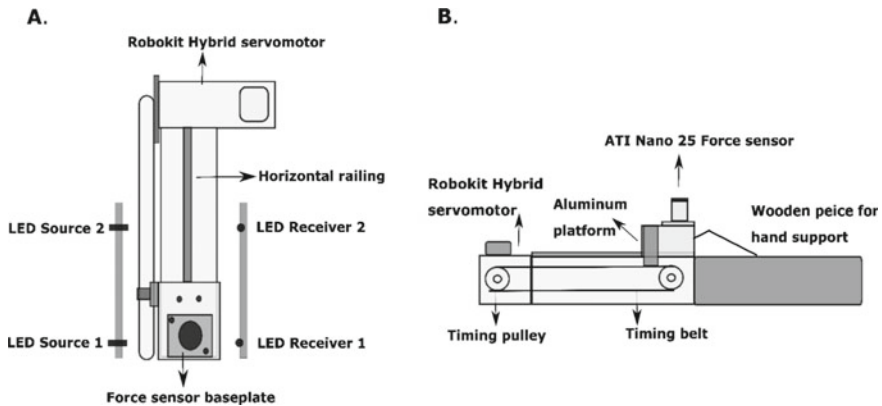


Fig. 1 Schematic diagram of the Friction experimental apparatus A. Top view of the friction setup with LED source (includes LED Source 1 and 2) and receiver (includes LED Receiver 1 and 2) to detect the position of the aluminum platform on the linear horizontal railing. B. Side view of the friction setup showing an ATI Nano-25 force sensor, timing pulleys, and belt powered by a servomotor

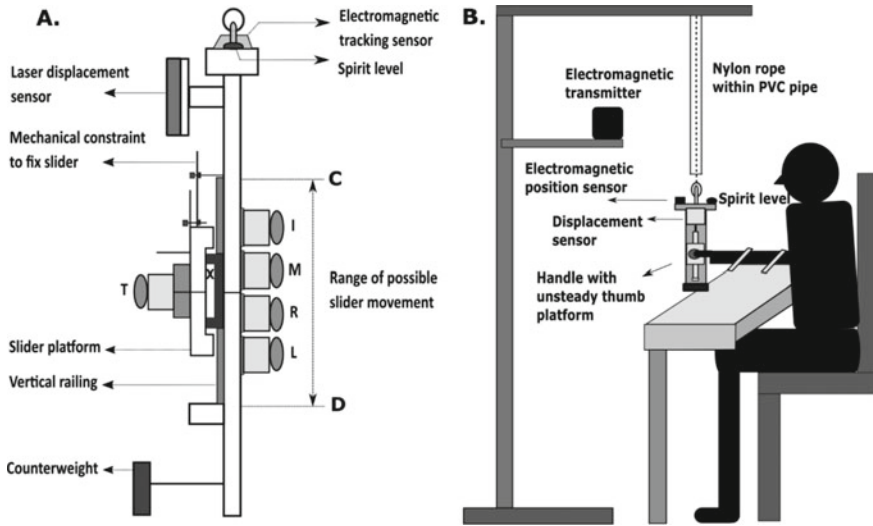


Fig. 2 Schematic diagram of the Experimental Apparatus A. Schematic diagram of the Experimental handle is shown. ATI Nano 17 force sensors were mounted on the handle frame ($20 \times 1 \times 3$ cm) to measure the forces of fingers (I-Index, M-Middle, R-Ring, Little-L, Th-Thumb). The geometric centre of the handle is represented by the symbol ‘X’ on the slider. The centres of the force sensors (excluding the thumb) were placed at a distance 2 cm apart from each other. Two solid horizontal lines were drawn (one on the slider and the other on the handle frame between middle and ring fingers). In free condition, the slider platform can translate over vertical railing such that it can theoretically move from point C to point D. B Schematic diagram of the participant holding the handle. Thumb side of the handle is shown. The handle setup was suspended from a wooden frame using nylon rope passing through a hollow PVC pipe. The PVC pipe allowed slight movement of the rope (and handle) but not undesirable large amplitude movement of the handle. The participant was required to lift the handle from its suspended position by 2 cm vertically, thus causing a slack of the nylon rope during the trial recording. The transmitter of the electromagnetic tracking system was placed few cm away from the handle to avoid distortion (Image adapted from the article: Rajakumar B, SKM V. 2020. Comparable behaviour of ring and little fingers due to an artificial reduction in thumb contribution to hold objects. PeerJ 8:e9962 <https://doi.org/10.7717/peerj.9962>)

Prehension Experiment

Participants performed the prehension experiment by placing their forearm on the table, as shown in Fig. 2. The experiment was carried out by performing a task that involves the following conditions: “Fixed” and “Free” condition. In the “fixed” condition, a screw was used to fix the position of the slider at the HOME. In the “free” condition, a screw was not used to fix the thumb slider. Therefore, the slider could slide over the railing. However, in both conditions, the participants were told to grasp the handle and match the line at the center of the platform to the line at the center of the central fingers on the handle. In addition, the handle has to be held in equilibrium during the entire trial. The position of the bubble in the spirit level provided feedback on the handle inclination to the participant. The trial commenced after the participants confirmed the comfortable holding of the handle. Also, the participants were provided

with familiarization trials before the start of the experiment. Both conditions were conducted as separate sessions. There was a total of thirty trials per condition. The trial duration was 10 s. A sufficient break was provided between the trials.

3 Data Analysis

Offline data analysis was performed in Matlab. Prior to the data analysis, the force data was low pass filtered with a cut off frequency of 15 Hz. Five seconds of data in the mid of the trial was considered for analysis.

3.1 Magnitude of Grip and Load Forces

Grip and Load forces exerted by the fingers and thumb were averaged across the time duration of 5 s for each trial separately and then averaged across 30 trials for each participant. Finally, it was averaged across 15 participants. We also computed the standard error of the mean (SEM) across participants.

3.2 Safety Margin

“The safety margin is the amount of extra normal force applied above the minimally required normal force to prevent slipping” [2, 13, 14]. It was computed for all the fingers and thumb by using the below equation.

$$SM(t) = \frac{\left[F_n - \frac{|F_t|}{\mu} \right]}{F_n} \quad (2)$$

where μ is the friction coefficient between the fingertip and sandpaper, t refers to the 5 s time interval, F_n is the grip force, and F_t is the load force applied to the object. The safety margin was computed by using the coefficient of friction values of each participant obtained from the friction experiment data. The friction coefficient of individual finger and thumb were averaged across 15 participants, and they were 0.9689 ± 0.0054 and 0.9745 ± 0.0109 , respectively. Fisher’s Z transform was performed for the safety margin values using the following equation prior to the statistical analysis.

$$SM_z = 0.5 * \ln\left(\frac{1 + SM}{1 - SM}\right) \quad (3)$$

3.3 Statistics

Statistical analyses were performed using R. Two two-way repeated-measures ANOVA was performed on the Load forces and Safety margin with the factors such as condition (2 levels: fixed and free) and fingers (levels: index, middle, ring, little, and thumb). The data was subjected to sphericity test, and the number of degrees of freedom was adjusted using the Huynh–Feldt (H-F) criterion wherever required. Pairwise Post Hoc Tukey tests were performed to check the significance within the factors. Equivalent tests were performed using the Two One-Sided T-test (TOST) approach [15] to check for equivalence between the ring and little fingers tangential forces and safety margin during the free condition. The TOST-T test approach was performed with the desired statistical power of 95%, having a sample size of 15.

4 Results

4.1 Task Performance

All the participants were able to complete the task successfully as per the instruction of holding the handle in static equilibrium throughout the trial. In the case of free condition, the participants were able to grip the thumb platform firmly at the HOME position by having the “flat” line drawn at the platform to the line on the handle.

4.2 Tangential Force

A two-way repeated-measures ANOVA on average tangential force with factors condition and finger showed a significant main effect of condition ($F_{(0.91,12.74)} = 13.77$; $p < 0.001$, $\eta_p^2 = 0.50$). Similarly, there was a significant main effect of the finger ($F_{(3.8,53.2)} = 46.875$; $p < 0.0001$, $\eta_p^2 = 0.77$) corresponding to a significantly greater tangential force for the thumb when compared to other fingers. The interaction condition \times finger was also significant ($F_{(3.64,50.96)} = 127.54$; $p < 0.0001$, $\eta_p^2 = 0.90$). The pairwise comparison confirmed that the tangential force of the ring finger (0.74 N) during the fixed condition was significantly ($p < 0.05$) greater than the tangential force of the little finger (0.41 N) during the same condition as shown in Fig. 3. Whereas, during the free condition, ring finger tangential force (1.25 N) was not statistically different ($t(14) = 0.789$, $p = 0.443$) from the little finger tangential force (1.14 N). Therefore, an equivalence test was performed to check whether the ulnar fingers have exerted comparable tangential forces during the free condition. The TOST procedure confirmed that the comparison was statistically equivalent ($t(14) = -2.813$, $p = 0.00691$), as the observed effect size ($d_z = 0.36$) of the dependent means was within the equivalence bounds of $\Delta_L = -0.93$ and $\Delta_U = 0.93$.

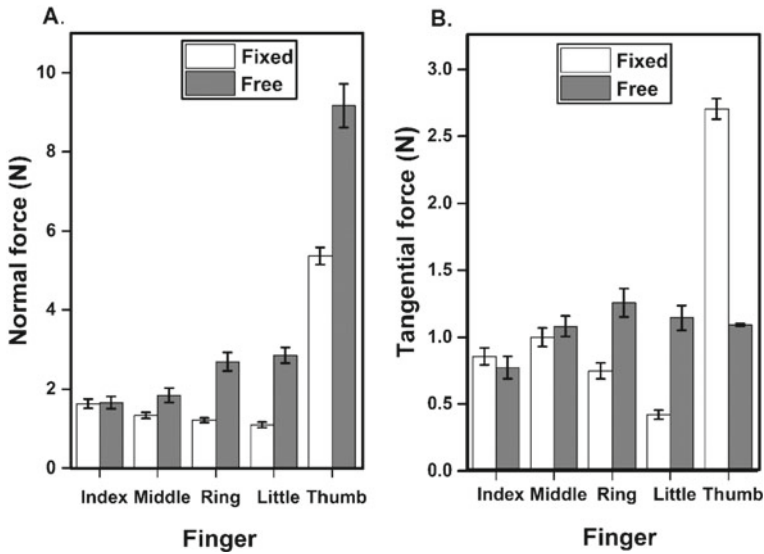


Fig. 3 Average Normal and Tangential forces of the individual fingers and thumb during the fixed and free condition A. Average normal force of the index, middle, ring, little and thumb during fixed (white) and free (grey) condition is shown in the left panel. Average normal force of the ring (2.69 N) and little (2.86 N) fingers were statistically equivalent ($t(14) = 3.059$, $p = 0.00425$) during free condition. B. Average tangential force of the index, middle, ring, little and thumb during fixed (white) and free (grey) condition is shown in the right panel. During the fixed condition, average tangential force of the ring (0.74 N) finger was significantly ($p < 0.05$) greater than the little finger (0.41 N). However, average tangential force of the ring (1.25 N) and little (1.14 N) fingers were found to be statistically equivalent ($t(14) = -2.813$, $p = 0.00691$) during the free condition (Image adapted from the article: Rajakumar B, SKM V. 2020. Comparable behaviour of ring and little fingers due to an artificial reduction in thumb contribution to hold objects. PeerJ 8:e9962 <https://doi.org/10.7717/peerj.9962>)

4.3 Safety Margin

Safety margin was different between two conditions. We observed a significant main effect of the condition ($F_{(0.89,12.46)} = 50.401$; $p < 0.0001$, $\eta_p^2 = 0.78$) and finger ($F_{(3.44,48.16)} = 29.26$; $p < 0.0001$, $\eta_p^2 = 0.67$) on the safety margin of the individual fingers and thumb. Interaction effects were significant ($F_{(3.56,49.84)} = 66.11$; $p < 0.0001$, $\eta_p^2 = 0.82$) for condition x finger. During the fixed condition, the safety margin of the little finger (0.70) was significantly ($p < 0.01$) greater than the ring finger (0.37) as shown in Fig. 4. However, during the free condition, the safety margin of the ulnar fingers (Ring finger: Mean = 0.56, SD = 0.18; Little finger: Mean = 0.66, SD = 0.20, $t(14) = -1.425$, $p = 0.176$, $d_z = 0.36$) were not statistically different. Therefore, we tested for statistical equivalence. By employing the TOST procedure, with equivalence bounds of $\Delta_L = 0.93$ and $\Delta_U = 0.93$, for a desired statistical power of 95%, dependent samples of safety margin of the ulnar fingers were found

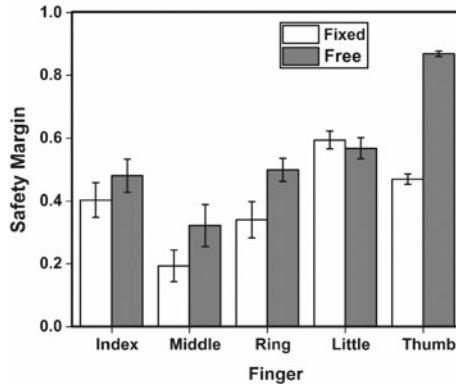


Fig. 4 Average Safety Margin of the individual fingers and thumb during the fixed and free condition In the fixed condition, the safety margin of the little finger (0.70) was significantly ($p < 0.01$) greater than the ring (0.37) finger. In the free condition, the safety margin of the ring (0.56) and little (0.66) fingers were found to be statistically equivalent ($t(14) = 2.17, p = 0.02$) (Image adapted from the article: Rajakumar B, SKM V. 2020. Comparable behaviour of ring and little fingers due to an artificial reduction in thumb contribution to hold objects. PeerJ 8:e9962 <https://doi.org/10.7717/peerj.9962>)

to be statistically equivalent ($t(14) = 2.17, p = 0.02$). As the observed effect size ($d_z = 0.36$) falls within the equivalence bounds, this comparison was deemed to be equivalent.

5 Discussion

In the current study, the participants performed the task of grasping the handle in equilibrium during both conditions. In the “fixed” condition, with the help of a screw, the movement of the thumb platform was arrested. Whereas, in the free condition, due to the absence of the screw, the platform was held by using the thumb in such a way that the line drawn on the platform coincides with the line drawn on the handle. During the entire trial in both conditions, the participants preserved the bubble at the center of the bull’s eye. Since the load of the platform was 0.101kg, the load force produced by the thumb to hold the platform dropped to 1 N. Thus, the contribution of the other fingers in establishing the handle stabilization was studied.

During the fixed condition, the load (or tangential) force was equally shared by the virtual finger and thumb. Followed by the thumb (2.70 N), the load force produced by the middle finger (1 N) was greater, then index (0.85 N), ring (0.74 N), and little (0.41 N) (see Fig. 3). However, in some studies that examined tangential force distribution during the static holding [5, 14], the order of sharing was slightly different. The small finger load force was lesser than the middle and index fingers but larger than the ring finger. For grip force, the order was as follows: Thumb (5.36 N),

Index (1.63 N), Middle (1.33 N), Ring (1.21 N), and Little (1.09 N). Thus, the results were in agreement with the results of the prehension studies [5, 16, 17].

During the free condition, there was a decline in the load force of the thumb that was accompanied by an rise in the load forces of the virtual finger to keep the object in equilibrium. Thus, resulting in the anti-clockwise tilt of the handle. Therefore, in order to retain the rotational equilibrium, a compensatory clockwise moment was required. This clockwise moment was produced by the ulnar finger grip forces. "With regard to the Mechanical advantage hypothesis, during the moment production tasks, it was expected that the small finger with a longer moment arm for grip force would produce higher normal force than the ring finger with a smaller moment arm for the normal force" [18]. Contrary to the expectation, the ulnar fingers produced an equivalent normal force during the free condition [10]. Since the grip forces exerted by the ring and little fingers should neither be too large to cause crushing of the object or fatigue in the hand muscles nor too low to cause slipping of the finger from the handle, proper regulation of normal forces is essential for achieving a stable grasp. Therefore, it is necessary to investigate the safety margin of these fingers so as to understand the strategy adopted by our controller in controlling the forces.

With respect to Eq. (2), the safety margin depends on the grip (or normal) force, the load force of the fingers, and the friction coefficient. Having comparable normal forces and the same friction coefficient by ulnar fingers, the next question would be to examine how the load force of these fingers varied? Whether it would be statistically equivalent or different? Suppose, if the ulnar fingers load forces were comparable, then the safety margin would also be comparable. In contrast, if the load forces were different, then the safety margin would also be different.

When there was a reduction in the load force of the thumb, during the "free" condition, an increase in the load force of the virtual finger could have been equally shared among the other fingers. However, our central nervous system (CNS) did not prefer to share the increase in the load forces among all the fingers equally. In case if there was a load force increase seen only in the index and middle finger, there should also be a rise in the grip force of the same fingers to avoid slipping. A simultaneous rise in the grip and load forces of the index and middle could cause a greater anti-clockwise tilt. As the instruction was to sustain the equilibrium of the handle, the possibility of increasing the radial fingers forces does not happen. Thus, the CNS has employed the strategy of increasing load forces of the ulnar fingers as there was a necessity to increase the grip forces of the same to compensate for the reduction in the thumb load force.

Among the ulnar fingers, tangential force sharing within ulnar fingers became a critical part. The magnitude of the force shared within the ulnar fingers might be comparable (Option 1), or the ring finger might share greater force than the little (Option 2), or the little finger might exert greater tangential force than the ring (Option 3) (see Fig. 5). From the literature, it is found that the ring finger is stronger than the small finger from the grip strength assessing tasks [12, 19]. In addition to this, from the results of the current study, during the fixed conditions, it was observed that the ring finger tangential force was greater than the little finger tangential force.

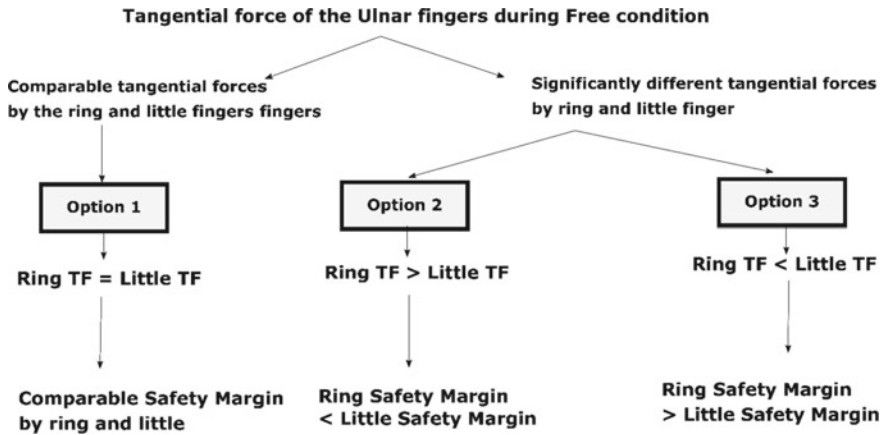


Fig. 5 Different possibilities of tangential force distribution and safety margin among the Ulnar fingers (ring and little) Three different possible ways by which tangential force (TF) among the ring and little fingers can vary are shown. Option 1: To produce comparable tangential forces by the ring and little fingers, Option 2: To produce significantly greater tangential force by the ring finger than the little finger, Option 3: To produce significantly greater tangential force by the little finger than the ring finger. If Option 1 is preferred by our CNS, the safety margin of the ring and little finger will also be comparable. If Option 2 is chosen, the safety margin of the ring finger would be lesser than the little finger. If Option 3 is selected, the safety margin of the ring finger would be greater than the little finger

Therefore, we expected the CNS to choose the second option of sharing greater tangential force by ring finger than the small finger during the “free” condition.

In contrast, there were few other studies that examined the load force distribution among the fingers during the grasping of a handle [5, 14]. According to their results, the little finger exerts greater load force than the ring finger. In a prehension study by Aoki (2007), when the surface friction at the thumb-object interface was reduced by using low friction contact material such as rayon, the little finger showed a rise in the load force that reached statistical significance. Similarly, middle and ring fingers also showed a rise in the load force, but they failed to reach statistical significance. Based on Aoki’s study, it is probable that the CNS could even choose the third option. However, this was not supported by our own previous findings. As our result on normal forces does not comply with the mechanical advantage hypothesis [18], the suspicion on the little finger sharing greater load force than the ring finger narrowed. Because if there is a greater load force exerted by the little finger, in order to maintain the safety margin of the same finger, the grip force of the little finger also tends to increase, which would probably be greater than the ring finger. But, in contradiction, the grip force of the ulnar fingers was comparable. So, it was thought that the chances of the little finger producing greater tangential force than the ring finger was lesser.

In reality, the tangential forces of the ulnar fingers were statistically comparable (i.e., Option 1). The reason for adopting the first option could have been due to the position of the thumb platform while grasping. This could be explained from a

biomechanical standpoint. Followed by the current study, there was another study performed with the same handle [20]. The participants were asked to trace the “trapezoid” and “inverted trapezoid” pattern displayed on the monitor by translating the thumb in the vertical direction, either upwards or downwards from the HOME. The amount of displacement of the thumb remained the same (1.5 cm) in both directions from HOME. During the trapezoid tracing condition, when the thumb reached 1.5 cm above the HOME, it was found that the load force of the ring finger was greater than the little finger. Similarly, during inverted trapezoid tracing condition, when the thumb reached 1.5 cm below the HOME, the little finger load force was greater than the ring finger. During both the conditions, they were required to keep the handle in equilibrium (even when there is a shift in the thumb position). We speculated that the biomechanical association between the little finger and thumb might have caused significant changes in the ulnar finger load forces.

When the thumb was translated upwards, there occurs an abduction of the carpometacarpal joint (CMC) of the thumb [21, 22]. The abduction movement of the thumb might have resulted in the radial deviation of the wrist, which could be restricted by an ulnar deviation (resisting action) caused by the abduction of the little finger [23, 24]. Thus, the abduction might have been accompanied by the abduction of the little finger, which occurs in the form of rotation towards medial side while grasping. Therefore, the location of force application of the little finger tends to shift downwards. Hence, we speculated that the reason for the greater reduction in the load force of the small finger (compared to other fingers) might be due to the resisting action of the little fingertip in the downward direction. Likewise, when the thumb was translated downwards, the opposition movement of the CMC joint of the thumb could be accompanied by an opposition act of a little finger that occurs in the form of lateral rotation [23, 25]. Therefore, the little finger exhibiting a rise in tangential force when compared to the other fingers.

However, when the thumb remained at the HOME, there was no necessity for the resisting action to be produced by the little finger, which might be a reason for the little finger to exert a comparable load force. Thus, we understood that our central nervous system was involved in activating the resistive reaction in the little finger when there was an active action of the thumb. This was visible from the fingertip forces of the respective fingers. Since there was a comparable tangential and grip force produced by the ulnar fingers, the safety margin was also statistically equivalent. This shows that the system does not consider the strength of the finger to share the forces in this particular task. Instead, it adapts to choose an economical way of sharing the forces when the thumb is comfortably positioned at the HOME.

6 Conclusion

In the current study, during the “free” condition, the decrease in the load force of the thumb was overcome by an increase in the load and grip forces of the ulnar fingers so as to establish static equilibrium. It was found that the load forces of the ulnar

fingers were statistically comparable. Also, the safety margin of the ulnar fingers showed a statistical equivalence when the thumb platform was held at HOME during the free condition. Thus, the controller has opted to vary the forces and safety margin in an economical way of sharing it equally among the ulnar fingers to preserve the equilibrium of the handle.

Acknowledgements We thank the Department of Science and Technology, Government of India, for supporting this work, vide Reference Nos SR/CSRI/97/2014 & DST/CSRI/2017/87 under Cognitive Science Research Initiative (CSRI) (awarded to Varadhan SKM), American Express (funding awarded to DART lab, IIT Madras) and “Women leading IIT Madras (WLI)” grant (awarded to Banuvathy Rajakumar). The funders had no role in study design, data collection, and analysis, decision to publish, or preparation of the manuscript.

References

1. Amis AA (1987) Variation of finger forces in maximal isometric grasp tests on a range of cylinder diameters. *J Biomed Eng* 9:313–320. [https://doi.org/10.1016/0141-5425\(87\)90079-3](https://doi.org/10.1016/0141-5425(87)90079-3)
2. Aoki T, Latash ML, Zatsiorsky VM (2007) Adjustments to local friction in multifinger prehension. *J Mot Behav* 39:276–290. <https://doi.org/10.3200/JMBR.39.4.276-290>
3. Aoki T, Niu X, Latash ML, Zatsiorsky VM (2006) Effects of friction at the digit-object interface on the digit forces in multi-finger prehension. *Exp Brain Res* 172:425–438. <https://doi.org/10.1007/s00221-006-0350-9>
4. Barakat MJ, Field J, Taylor J (2013) The range of movement of the thumb. *Hand (N Y)* 8:179–182. <https://doi.org/10.1007/s11552-013-9492-y>
5. Burstedt MKO, Flanagan JR, Johansson RS (1999) Control of grasp stability in humans under different frictional conditions during multidigit manipulation. *J Neurophysiol* 82:2393–2405. <https://doi.org/10.1152/jn.1999.82.5.2393>
6. Hermsdörfer J, Hagl E, Nowak DA, Marquardt C (2003) Grip force control during object manipulation in cerebral stroke. *Clin Neurophysiol* 114:915–929. [https://doi.org/10.1016/s1388-2457\(03\)00042-7](https://doi.org/10.1016/s1388-2457(03)00042-7)
7. Hirt B, Seyhan H, Wagner M (2016) *Hand and Wrist Anatomy and Biomechanics: A Comprehensive Guide*. Thieme, Stuttgart
8. Houglum PA, Bertoti DB (2012) *Brunnstrom’s Clinical Kinesiology*. F.A. Davis, Philadelphia
9. Iberall T (1987) The nature of human prehension: Three dextrous hands in one. In: 1987 IEEE international conference on robotics and automation proceedings, pp 396–401
10. Johansson RS, Westling G (1984) Roles of glabrous skin receptors and sensorimotor memory in automatic control of precision grip when lifting rougher or more slippery objects. *Exp Brain Res* 56(3):550–564. <https://doi.org/10.1007/BF00237997>
11. Kinoshita H, Kawai S, Ikuta K (1995) Contributions and co-ordination of individual fingers in multiple finger prehension. *Ergonomics* 38:1212–1230. <https://doi.org/10.1080/00140139508925183>
12. Li Z-M (2002) Inter-digit co-ordination and object-digit interaction when holding an object with five digits. *Ergonomics* 45:425–440. <https://doi.org/10.1080/00140130210129673>
13. MacDermid JC, Lee A, Richards RS, Roth JH (2004) Individual finger strength: are the ulnar digits “powerful”? *J Hand Ther* 17:364–367. <https://doi.org/10.1197/j.jht.2004.04.006>
14. Marshall VC, Marshall RD (1963) Movements of the thumb in relation to peripheral nerve injuries. *Postgrad Med J* 39:518–525
15. Lakens D (2017) Equivalence tests: a practical primer for t tests, correlations, and meta-analyses. *Soc Psychol Pers Sci* 8:355–362. <https://doi.org/10.1177/1948550617697177>

16. Pataky T, Latash M, Zatsiorsky V (2004) Tangential load sharing among fingers during prehension. *Ergonomics* 47:876–889. <https://doi.org/10.1080/00140130410001670381>
17. Radwin RG, Oh S, Jensen TR, Webster JG (1992) External finger forces in submaximal five-finger static pinch prehension. *Ergonomics* 35:275–288. <https://doi.org/10.1080/00140139208967813>
18. Rajakumar B, Skm V (2020) Comparable behaviour of ring and little fingers due to an artificial reduction in thumb contribution to hold objects. *PeerJ* 8:e9962. <https://doi.org/10.7717/peerj.9962>
19. Rajakumar B, Varadhan SKM (2021) Distinct behavior of the little finger during the vertical translation of an unsteady thumb platform while grasping. *bioRxiv* 2021.05.28.446096. <https://doi.org/10.1101/2021.05.28.446096>
20. Singh T, Ambike S (2017) A soft-contact model for computing safety margins in human prehension. *Hum Mov Sci* 55:307–314. <https://doi.org/10.1016/j.humov.2017.03.006>
21. Skm V, Zhang W, Zatsiorsky VM, Latash ML (2012) Age effects on rotational hand action. *Hum Mov Sci* 31:502–518. <https://doi.org/10.1016/j.humov.2011.07.005>
22. Talsania JS, Kozin SH (1998) Normal digital contribution to grip strength assessed by a computerized digital dynamometer. *J Hand Surg Br* 23:162–166. [https://doi.org/10.1016/s0266-7681\(98\)80165-4](https://doi.org/10.1016/s0266-7681(98)80165-4)
23. Westling G, Johansson RS (1984) Factors influencing the force control during precision grip. *Exp Brain Res* 53:277–284. <https://doi.org/10.1007/BF00238156>
24. Zatsiorsky VM, Gregory RW, Latash ML (2002) Force and torque production in static multi-finger prehension: biomechanics and control. *I Biomech Biol Cybern* 87:50. <https://doi.org/10.1007/s00422-002-0321-6>
25. Zatsiorsky VM, Latash ML (2008) Multi-finger prehension: an overview. *J Mot Behav* 40:446–476. <https://doi.org/10.3200/JMBR.40.5.446-476>
26. Opponens digiti minimi muscle of hand (2021) Wikipedia

Identification of Crack Parameters Using XFEM-QPSO



M. Surendran , J. Prawin , and S. Natarajan 

Abstract The extended finite element method (XFEM) combined with a meta-heuristic optimization algorithm namely Quantum Particle Swarm Optimization (QPSO) is proposed in this paper for the identification of crack parameters (crack position) in plate structures. The XFEM is employed to solve the forward problem of strain estimation in a cracked plate due to its advantage of a fixed mesh for any crack geometry and configuration. Four different objective functions that compare the measured and the predicted strains from the XFEM model of the cracked plate specimen with known properties of material, geometry and loads are considered to solve the inverse problem. Numerical investigation has been carried out on a plate with single interior crack at different orientations and a compact tension specimen with different crack lengths subjected to tensile loading to demonstrate the potential of the proposed XFEM-QPSO approach for crack identification problems.

Keywords XFEM · PSO · QPSO · Objective function · Inverse problem · Crack identification

1 Introduction

Material failures due to fatigue account to as high as 50% of total failures [1]. The cyclic stresses weaken the material and the size and position of cracks greatly influence these local stresses. Hence, identifying and characterizing cracks and their severity is of both industrial and academic interest. Inverse problem formulation in the studies of crack identification assumes the existence of crack, and usually use

M. Surendran · J. Prawin (✉)

CSIR-Structural Engineering Research Center, CSIR Campus, Chennai, Tamil Nadu, India

e-mail: prawinj@serc.res.in

M. Surendran

e-mail: surendran@serc.res.in

S. Natarajan

Department of Mechanical Engineering, IIT Madras, Chennai, Tamil Nadu, India

e-mail: snatarajan@iitm.ac.in

the structural response as reference. The goal is to find the crack characteristics that corresponds to a particular response. These problems are challenging because in many cases the cracks with very different characteristics may correspond to close measurements in the structural response, which is very complex from the inverse problem perspective. Finding the position of the crack is an inverse problem and is generally achieved through optimization algorithms. Solution to the inverse crack identification by any optimization algorithms requires the forward problem to be solved iteratively by a numerical model of the structure several times for different configurations. The Finite element method (FEM) is the most commonly used numerical method for solving elasticity problems. However, modelling singular problems using the FEM is a challenging task, since a conforming mesh is needed and also due to the requirement of special crack tip elements for accurate representation of the crack tip fields [2, 3]. The FEM also requires re-meshing the computational domain for each new crack configuration. If the cracks are not straight, the quality of the mesh could also be affected. And this in turn affects the accuracy of the solution. Hence, the difficulties increase when we are dealing with inverse problems which require solving a problem with a discontinuity several times iteratively. However, the extended finite element method (XFEM) allows modelling arbitrary discontinuities independent of the mesh and also avoids re-meshing altogether [4, 5]. Hence, various researchers have employed the XFEM in tandem with optimization algorithms, some of them include: XFEM-GA [6] and XFEM-meta heuristic algorithms such as XFEM-PSO, XFEM-Jaya, XFEM-ABC, XFEM-AFS [7] to solve the inverse problem of crack identification that include multiple cracks and as well as regular and irregular shaped cracks and investigated the convergence, accuracy and computational time. In the present study, XFEM is combined with an improved variant of PSO algorithm namely, QPSO and is employed for identification of crack parameters.

In the present study, an attempt is made to identify crack tip coordinates of straight and inclined cracks with in hand the dimensions of the plate, material properties, loading (with on hand XFEM model of the plate with crack). The scope of the present work is limited to detection and localization of different position of flaws in two-dimensional structures using static strain measurements and plate components subjected to axial loading.

2 XFEM Formulation for the Forward Problem

Consider a linear elastic body with a discontinuity. Let the domain be $\Omega \in \mathbb{R}^d$ bounded by $\Gamma \in \mathbb{R}^{d-1}$. In case of cracked domains, the boundary has three parts namely Γ_u , corresponding to displacement boundary conditions $\bar{\mathbf{u}}$, Γ_t , corresponding to tractive boundary conditions $\bar{\mathbf{t}}$ and Γ_c , corresponding to the discontinuity, such that $\Gamma = \Gamma_u \cup \Gamma_t \cup \Gamma_c$ and $\Gamma_u \cap \Gamma_t = \emptyset$. In the absence of body forces, the discretised version of the problem to be solved in a Galerkin framework [4, 5] is to find $\mathbf{u}^h \in \mathcal{U}^h$, such that $\forall \mathbf{v}^h \in \mathcal{V}^h$

$$\int_{\Omega} \boldsymbol{\varepsilon}(\mathbf{u}^h) : \mathbf{C} : \boldsymbol{\varepsilon}(v^h) d\Omega = \int_{\Omega} \bar{\mathbf{t}} \mathbf{v}^h d\Gamma \tag{1}$$

The above trial and test functions are continuous functions and thus cannot represent the singularity and discontinuity introduced by a crack. This is overcome by employing the XFEM framework. In XFEM, the crack is modelled implicitly as shown in Fig. 1. Within the XFEM framework, an enriched displacement field is used. The enriched displacement field has two components, a crack tip singularity at the crack tip and a discontinuity along the crack face. In linear elastic fracture mechanics (LEFM), the near-tip asymptotic displacement fields are spanned by the following crack tip enrichment functions given by [4, 5]

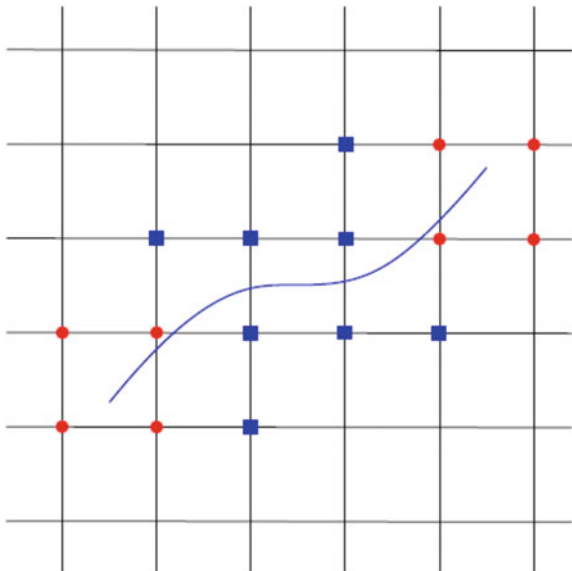
$$\mathbf{F}_n(r, \theta) = \left\{ \sqrt{r} \sin \frac{\theta}{2}, \sqrt{r} \cos \frac{\theta}{2}, \sqrt{r} \sin \theta \sin \frac{\theta}{2}, \sqrt{r} \sin \theta \cos \frac{\theta}{2} \right\} \tag{2}$$

For a point $x_i \in \Omega$, the discontinuity is introduced by employing the Heaviside enrichment functions given by

$$H = \begin{cases} +1, & (\mathbf{x}_i - \mathbf{x}^c) \cdot \mathbf{n} > 0 \\ -1, & (\mathbf{x}_i - \mathbf{x}^c) \cdot \mathbf{n} \leq 0 \end{cases} \tag{3}$$

This is achieved by using the level set method [8]. The XFEM is based on the partition of unity framework developed by Melenk [9] and Babuška [10]. Thus, the enriched displacement field is given by

Fig. 1 XFEM discretisation of a cracked domain. The curve represents the discontinuity. The red circles represent crack tip enriched nodes, blue squares represent Heaviside enriched nodes



$$\mathbf{u}^h(\mathbf{x}) = \sum_{I \in M_{std}} \mathbf{N}_I \mathbf{u}_I + \sum_{J \in M_{Hev}} \mathbf{N}_J(\mathbf{x}) H(\mathbf{x}) \mathbf{a}_J + \sum_{K \in M_{Tip}} \mathbf{N}_K(\mathbf{x}) \left(\sum_{n=1}^4 F_n(r, \theta) \mathbf{b}_K \right) \tag{4}$$

where, M_{std} , M_{Hev} , M_{Tip} are the set of all nodes, Heaviside function enriched nodes and Tip function enriched nodes in the domain. When this enriched displacement equation is introduced in Eq. 1, we arrive at a set of linear algebraic equations. This contains terms additional to the conventional stiffness matrix due to the enrichment terms as shown in Eq. 5. The stiffness matrix is obtained by numerical integration based on the enriched displacement field. In this work 4 noded quadrilateral elements are employed. The enriched elements are sub-triangulated and the standard Gauss integration is used over the sub-triangles.

$$\mathbf{K} = \begin{bmatrix} \mathbf{K}_{uu} & \mathbf{K}_{ua} & \mathbf{K}_{ub} \\ \mathbf{K}_{au} & \mathbf{K}_{aa} & \mathbf{K}_{ab} \\ \mathbf{K}_{bu} & \mathbf{K}_{ba} & \mathbf{K}_{bb} \end{bmatrix} \tag{5}$$

3 Quantum Particle Swarm Optimization (QPSO) for the Inverse Problem

Particle swarm optimisation (PSO) belongs to the well-known and established swarm intelligence group of meta-heuristic algorithms in the literature and has been widely applied for solving the problem of function optimization. PSO was proposed by Eberhart and Kennedy in 1995 [11, 12] which is stochastic in nature. PSO algorithm incorporates mathematical models that inspired from the observation of natural and social behaviour of swarm of birds in search of food sources.

PSO is initialized with multiple particles located in random positions. Each particle represents a flock member, travel across the search space and evaluate the quality of its current position. The main idea of the PSO algorithm is that, at each iteration, each one of the particles remembers the best position it had in the past, and replace it if a better position is found. These best points are called personal bests (pb_{ij}), and the absolute best point among them is called the global best (gb_j). This point is the key element of the collaboration between the flock. Because it helps to determine the direction in which the particles should move next and with what magnitude. The update equation is given by

$$x_{ij}^{k+1} = x_{ij}^k + \omega v_{ij}^k + c_1 r_1 (pb_{ij} - x_{ij}^k) + c_2 r_2 (gb_j - x_{ij}^k) \tag{6}$$

where the current velocity and current position of each particle (v_{ij}^k & x_{ij}^k) are used as a base for next position (x_{ij}^{k+1}). The index 'k' is for iterations, i is for indexing

the particles and j is the dimension of the particle. The last two terms of the above equation guide the particles to go simultaneously towards their personal best position (pb_{ij}) and towards the global best (gb_{ij}). In other words, the particles update their positions based on: 1) their own/personal best solution from the past and 2) global best solution achieved so far by any particle through communication in the population. The magnitude is determined by how far these two points are from the current position. $c1$ and $c2$ are algorithm parameters, and $r1$ and $r2$ are random values between 0 and 1. This will create the variation aspect between the particles, which helps to explore each space better. And finally, the w is a factor that decreases as iterations proceed. The parameter ‘ w ’ forces the reduction of the velocity magnitude at the later stages of the search, making the flock members move with smaller steps, thus focusing the search in a small area. This idea assumes that at the later stage, the search space is well explored, and the algorithm has likely found the global optimum.

It should be mentioned here that by adaptively tuning the parameter ‘ P ’, the weight coefficients $c1$ and $c2$ are fixed. The parameter P is mathematically given by

$$P = \frac{2 \cdot |gb - x|}{c_1 \cdot |pb - x| + c_2 \cdot |gb - x|} \tag{7}$$

It should be mentioned here that low and high values of P diversifies and intensifies the search. The parameter P should be chosen such that there exists good balance between intensification and diversification [13–15]. The updation of the position of all the particles in the population is repeated (iterations) until most of the particle converge to the same position (best solution). Further, each single solution is called a particle which update their position and velocity until the error is minimized or maximum number of iterations is reached or the solution is achieved, which is decided by the fitness/objective function.

Even though PSO has been widely used for solving many optimization problems due to its easy implementation and faster convergence, it is not a global search algorithm and has many control parameters.

Inspired by the concept of both quantum mechanics and PSO algorithm, Quantum-behaved particle swarm optimization (QPSO) was developed by David and Roger (1985) and Sun et al. (2004) [13–15] to improve PSO. It should be mentioned here that when compared with PSO, QPSO has fewer control parameters, guaranteed global convergence and the advantage of waiting phenomena among the particles.

Unlike PSO, QPSO determines the state of the particle by the wave function $\psi(x, t)$ instead of the position and velocity. The probability of appearance of particle at a certain position is employed to determine the next position. It is defined using the probability density function $|\psi(x, t)|^2$. The current position of the particle is updated by using Monte-Carlo technique. QPSO process starts by defining the initial population of the particles ‘ M ’ and maximum number of iterations ‘ N ’ and then the best solution ‘ pb ’ and ‘ gb ’ are identified similar to PSO. QPSO uses the current position along with information from the search results, to determine the positions of next iteration, calculated as in

$$\begin{aligned}
 x_{ij}^{k+1} &= p_{ij}^t + \beta \left| mb_{ij}^k - x_{ij}^k \right| * \ln(1/u_{ij}) \text{ if } r > 0.50 \\
 x_{ij}^{k+1} &= p_{ij}^t + \beta \left| mb_{ij}^k - x_{ij}^k \right| * \ln(1/u_{ij}) \text{ if } r \leq 0.50 \\
 \beta^k &= \beta_{\max} - \frac{(\beta_{\max} - \beta_{\min})}{k} \times \text{max_iterations}
 \end{aligned}
 \tag{8}$$

where $p_{ij}^k = \varphi_{ij}^k pb_{ij}^k + (1 - \varphi_{ij}^k).gb_j^k$ is the local attractor and the contraction–expansion coefficient β decide the convergence speed. The parameter mb is defined as the mean best of all the particles and given by

$$mb_{ij}^k = \left(\frac{1}{M} \sum_{i=1}^M P_{i1}^k, \frac{1}{M} \sum_{i=1}^M P_{i2}^k, \frac{1}{M} \sum_{i=1}^M P_{i3}^k, \dots, \frac{1}{M} \sum_{i=1}^M P_{iD}^k \right)
 \tag{9}$$

This parameter ensures the convergence to the global best solution only after considering its colleagues because ‘mb’ decides the particle’s position at next iteration. The other parameters are random values between 0 and 1.

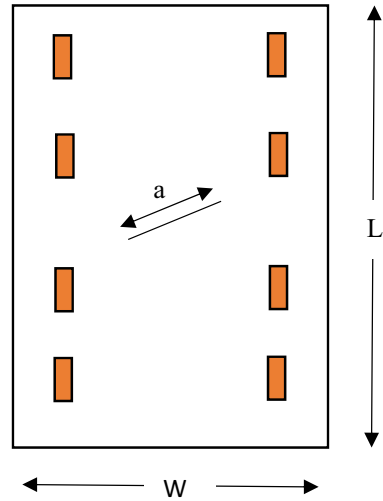
4 Methodology of Crack Tip Identification Using the XFEM-QPSO

The step by step procedure of the inverse problem of crack identification using XFEM-QPSO is given below.

1. Create an XFEM model of the plate with known dimensions, material properties and loading. In the present study regular 4-noded plane strain elements were used.
2. Through numerical experiments for the cracked plate subjected to quasi-static loading, estimate the strain components at 8 locations as shown in Fig. 2.
3. Solve the problem of crack identification by minimising the objective function based on the reference strains through numerical experiments and the predicted strain for randomly assumed crack location using the XFEM model and QPSO algorithm. The direction of cracks and orientation of the strain gauges, different components of strain tensor will influence the identification. Hence, following four objective functions based on norm of relative error in strain between the reference and predicted values are considered.

- Objective function 1, $f(\epsilon_x) = \left\| \frac{\epsilon_{x,ref} - \epsilon_{x, XFEM}}{\epsilon_{x,ref}} \right\|$
- Objective function 2, $f(\epsilon_y) = \left\| \frac{\epsilon_{y,ref} - \epsilon_{y, XFEM}}{\epsilon_{y,ref}} \right\|$
- Objective function 3, $f(\gamma_{xy}) = \left\| \frac{\gamma_{xy,ref} - \gamma_{xy, XFEM}}{\gamma_{xy,ref}} \right\|$
- Objective function 4 (combined criteria) $\left\| \frac{\epsilon_{x,ref} - \epsilon_{x, XFEM}}{\epsilon_{x,ref}} \right\| + \left\| \frac{\epsilon_{y,ref} - \epsilon_{y, XFEM}}{\epsilon_{y,ref}} \right\| + \left\| \frac{\gamma_{xy,ref} - \gamma_{xy, XFEM}}{\gamma_{xy,ref}} \right\|$

Fig. 2 Finite Plate with an interior crack. The plate dimensions are $W = 100$ mm and $L = 200$ mm. The length of the crack is a



4. Identify the best solution i.e. crack parameters once convergence is achieved

5 Numerical Investigations

5.1 Finite Plate with an Interior Crack at Different Orientations Subject to Tensile Stresses

A finite plate with a center crack, subjected to known tensile loading shown in Fig. 2 is considered as the numerical example for the inverse problem of crack identification. The dimensions are $W = 100$ mm and $L = 200$ mm. The material properties are Young’s modulus, $E = 2 \times 10^5$ MPa and Poisson’s ratio, $\nu = 0.3$. The plate is fixed vertically at the bottom edge. The top edge is subjected to uniaxial loading of $\sigma = 100$ Mpa. The plate is discretized with 10 elements \times 20 elements. The x-coordinates along the plate are 0 to 100 mm; while the y-coordinates extend from -100 to 100 mm. The crack is modelled based on the level set method. 4 noded quadrilateral plane strain elements are employed.

Three different crack configurations are considered by varying the length (a) and inclination (β): straight crack, Counter ClockWise(CCW) inclined crack and ClockWise (CW) inclined Crack. The crack configurations and strain sensor locations are given in Table 1. Strains at 8 specified locations are computed based on the XFEM and stored as reference values equivalent with experiments. They are presented in Table 2. Four different objective functions based on the strains that minimizes the error between the predicted values by XFEM model of the cracked plate and the reference/measured values are considered to evaluate the efficiency of the proposed XFEM-QPSO algorithm in identifying the crack parameters.

Table 1 Damage scenarios of a plate with one interior crack

Crack configuration	Coordinates of interior crack tips	Strain measurement locations
D1	[(25, 0) (75, 0)]	8 locations: (10, -20); (10, -40); (10, 20); (10, 40); (90, -20); (90, -40); (90, 20); (90, 40)
D2	[(25, -20) (75, 20)]	
D3	[(25, 20) (75, -20)]	

For QPSO, the following parameters are considered: Population Number 20; Generation number 20. Design variables are the crack tip coordinates (X_1, Y_1); (X_2, Y_2). The efficiency and accuracy of the predicted crack tip coordinates depend on the initial search space. Hence, two different search spaces were considered for the study. In the first search space, SP1, X coordinates lies in the range of 20 to 80 mm and Y coordinates lies in the range of -40 to 40 mm. In the second search space, SP2, X coordinates lies in the range of 15 to 90 mm and Y coordinates lies in the range of -80 to 80 mm. The initial crack tip coordinates are chosen randomly. The predicted crack tip coordinates for different objective functions and different search space are presented in Tables 3, 4 and 5.

It can be concluded from the results presented in Table 3, Table 4 and Table 5 that the Objective function based on shear strain and combined strain are effective. This is evident from the variations of the shear strain values at the considered 8 locations presented in Table 2. Also, Horizontal strain is not effective (as strains are very low in direction orthogonal to loading). With larger search space (i.e., an increase in the range of design variables) the accuracy decreases.

In order to demonstrate the efficiency of QPSO over PSO for the current problem of inverse problem of crack identification of finite plate subjected to axial loading, the first crack configuration is considered. The best objective function based on combined criteria i.e. objective function 4 is considered for comparison of PSO and QPSO in terms of computational cost and convergence. The convergence plot is presented in Fig. 3. It can be concluded from Fig. 3 that the Convergence of QPSO is rapid when compared to the traditional PSO.

The results of computational efficiency of QPSO and PSO for the first crack configuration with narrow and wider search space is presented in Table 6. Table 6 illustrates that the Number of iterations and computational time to convergence increases with increase in the size of search space. QPSO depicts less computational cost when compared to PSO. Therefore, from the numerical investigations carried out in this paper, it can be concluded that the proposed XFEM-QPSO identifies the crack coordinates using the four different objective functions based on strain measured at 8 locations. Further, the crack parameters (i.e. crack position and crack length/x and y coordinates) are identified with maximum error of 1% and is also computationally efficient.

Table 2 The reference strain ($\epsilon_x, \epsilon_y, \gamma_{xy}$) values at different locations (x, y) on the plate are considered for three cases. In the finite element mesh, x varies from 0 to 100 mm and y axis varies from -100 to 100

Case (i) A straight center crack of length a= 50mm. Coordinate of tips are Left (25,0) and Right (75,0)

Location		Strain components		
x	y	ϵ_x	ϵ_y	γ_{xy}
10	40	-249.13	579.25	111.54
10	20	-309.61	671.25	-34.28
10	-20	-309.84	671.92	35.391
10	-40	-249.86	581.27	-108.85
90	40	-249.23	579.48	-111.9
90	20	-309.91	671.65	35.06
90	-20	-310.14	672.32	-36.17
90	-40	-249.96	581.5	109.21

Case (ii) A CCW inclined center crack of length with coordinate of tips as Left (25, -20) and Right (75,20)

Location		Strain components		
x	y	ϵ_x	ϵ_y	γ_{xy}
10	40	-259.53	607.16	135.5
10	20	-312.1	701.73	71.8
10	-20	-213.15	590.48	1.84
10	-40	-275.13	603.55	8.45
90	40	-273.96	601.07	0.19
90	20	-218.04	597.93	2.48
90	-20	-313.63	705.51	72.78
90	-40	-261.21	611.81	132.72

Case (iii) A CW inclined center crack of length with coordinate of tips as Left (25,0) and Right (75, -20)

Location		Strain components		
x	y	ϵ_x	ϵ_y	γ_{xy}
10	40	-273.94	600.19	-3.88
10	20	-212.74	589.42	0.32
10	-20	-312.50	702.93	-70.20
10	-40	-260.75	610.57	-130.98
90	40	-259.98	608.39	-137.26
90	20	-313.23	704.30	-74.47
90	-20	-218.46	599.00	-4.65
90	-40	-275.15	604.42	-4.74

Table 3 Predicted crack tip coordinates for crack configuration 1

Objective function	Crack tip predicted for Search Space SP1	Crack tip predicted for Search Space SP2
$f(\epsilon_x)$	[(25, 0) (75, 0)]	[(25, 0) (75, 0)]
$f(\epsilon_y)$	[(25, 0) (75, 0)]	[(25, 0) (75, 0)]
$f(\gamma_{xy})$	[(25, 0) (75, 0)]	[(25, 0) (75, 0)]
Combined	[(25, 0) (75, 0)]	[(25, 0) (75, 0)]

Table 4 Predicted crack tip coordinates for crack Configuration 2

Objective function	Crack tip predicted for Search Space SP1	Crack tip predicted for Search Space SP2
$f(\epsilon_x)$	[(25, -19) (75, 18)]	[(27, -19) (74, 21)]
$f(\epsilon_y)$	[(25, -20) (75, 21)]	[(28, -21) (74, 21)]
$f(\gamma_{xy})$	[(25, -20) (75, 20)]	[(25, -20) (74, 18)]
Combined	[(25, -20) (75, 20)]	[(25, -20) (75, 21)]

Table 5 Predicted crack tip coordinates for crack configuration 3

Objective function	Crack tip predicted for Search Space SP1	Crack tip predicted for Search Space SP2
$f(\epsilon_x)$	[(25, 19) (75, -18)]	[(30, 16) (73, -28)]
$f(\epsilon_y)$	[(25, 20) (75, -21)]	[(27, 21) (76, -23)]
$f(\gamma_{xy})$	[(25, 20) (75, -20)]	[(29, 20) (74, -18)]
Combined	[(25, 20) (75, -20)]	[(25, 21) (75, -21)]

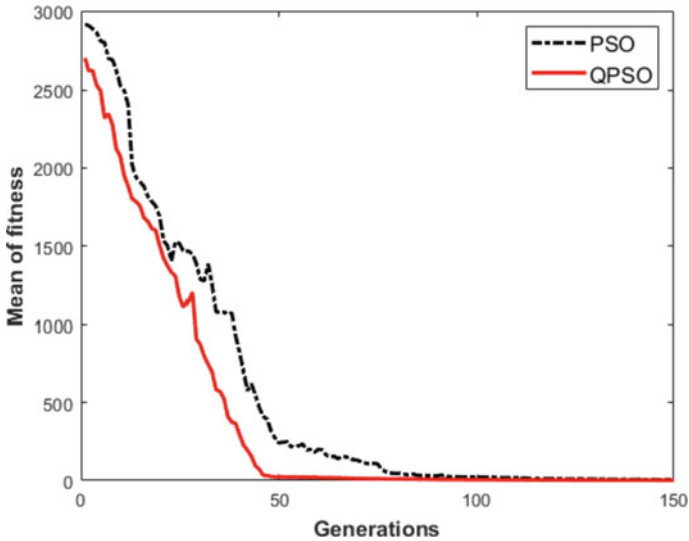


Fig. 3 Comparison of convergence for QPSO and PSO

Table 6 Comparison of computational efficiency of QPSO and PSO for different search spaces SP1 and SP2

Search Space	Method	Search Space SP1	Search Space SP2
Number of iteration	QPSO	10	46
	PSO	28	82
Computational time	QPSO	13.725	58.664
	PSO	32.568	118.452

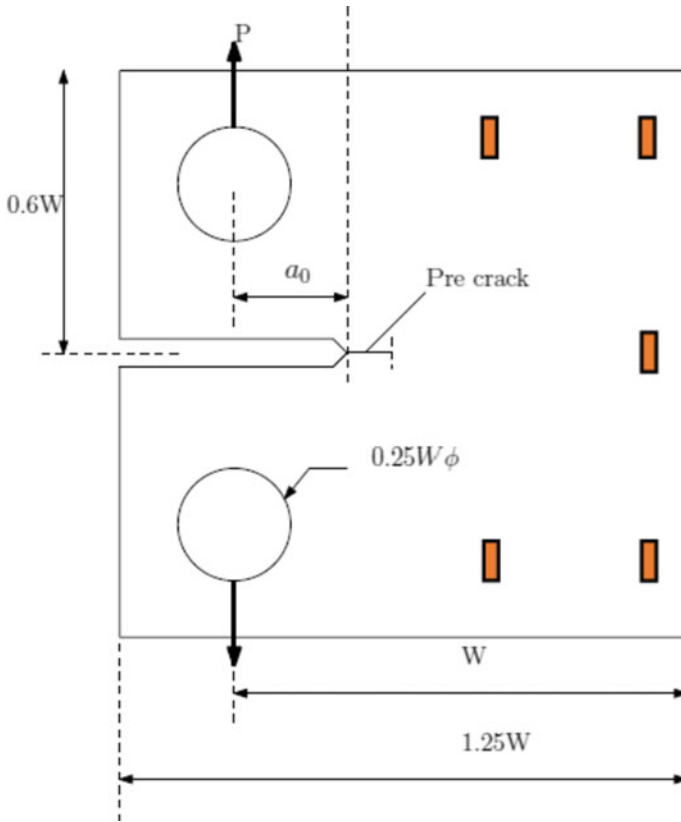


Fig. 4 A schematic of CT specimen asper ASTM E647 with a precrack/crack from the notch

5.2 Numerical Investigations—Compact tension (C(T)) Specimen Under Action of Tensile Loading

Compact tension (C(T)) specimens are widely used for characterization of fatigue and fracture properties such as fracture toughness and Paris crack growth parameters. The experimental investigations involve continuous monitoring of the crack growth in the specimen in order to obtain the required parameters. This becomes

even more cumbersome in case of cyclic tests where the number of cycles go up to 5 million. In such cases it would be useful to automate the recording of strains and inverse identify the crack tip locations from the collected strain data. Hence, a C (T) specimen of overall dimension 62.5×60 mm consisting of an initial notch of length 22.5×3 mm thick with a 45° v-notch tip (shown in Fig. 4) is considered as the second example. The dimensions are: $W = 50$ mm, $a_0 = 10$ mm. The starting notch portion is about 22.5 mm. The material properties are Young’s modulus, $E = 2.067 \times 10^5$ MPa and Poisson’s ratio, $\nu = 0.3$. Two point loads are considered as shown in Fig. 4. A mesh consisting of 7800 linear quadrilateral elements as shown in Fig. 5 is used. The x-coordinates along the plate are 0 to 62.5 mm; while the y-coordinates extend from 0 to 60 mm. In the XFEM model the notch is not modelled explicitly. The length of the notch and the pre-crack length is taken as the initial crack length. Two cases (CT1 and CT2) are considered with different crack lengths. The total crack length (including notch) in the two cases are 23.75 and 43.75 mm. The crack configurations and strain sensor locations are given in Table 7. Strains and displacements at five specified locations are computed based on the XFEM as a forward problem and stored as reference values equivalent with experiments. They are presented in Table 8.

Fig. 5 Mesh employed for simulating the CT specimen. The bold red line represents the crack segment used for level sets

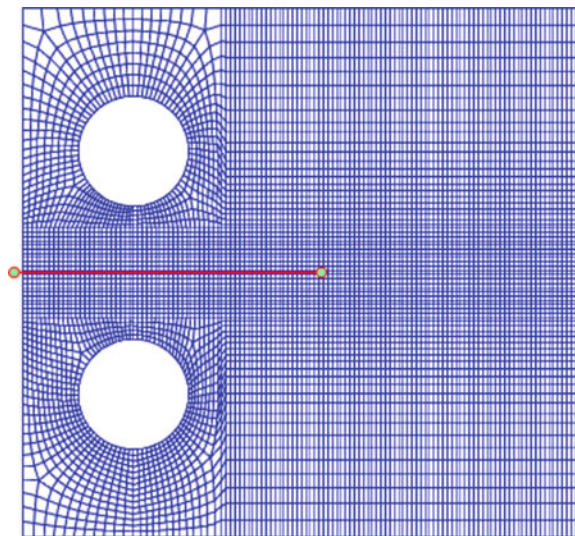


Table 7 Damage scenarios of CT specimen

Crack configuration	Coordinates of crack tip	Strain measurement locations
CT1	(23.75, 30)	5 locations: (40, 50); (55, 50); (55, 30); (40, 10); (55, 10)
CT2	(43.75, 30]	

Table 8 The reference strain ($\epsilon_x, \epsilon_y, \gamma_{xy}$) values at different locations (x, y) on the CT specimen are considered for two cases. In the finite element mesh, x varies from 0 to 62.5 mm and y axis varies from 0 to 60 mm

Case (i) A crack of length of 23.75mm. Coordinate of tips are (23.75, 30)

x	y	ϵ_x	ϵ_y	γ_{xy}
40	50	-38.54	23.01	255.25
55	50	9.11	-39.85	165.20
55	30	73.74	-125.5	-0.003
40	10	-38.79	23.29	-255.16
55	10	9.10	-39.84	165.19

Case (ii) A crack of length of 43.75mm. Coordinate of tips are (43.75, 30)

x	y	ϵ_x	ϵ_y	γ_{xy}
40	50	-271.56	256.97	-25.57
55	50	-49.18	-73.02	850.95
55	30	538.06	-616.73	0.065
40	10	-271.79	257.23	25.53
55	10	-49.19	-73.02	-850.97

For QPSO, the following parameters are considered: Population Number 20; Generation number 20. The design variable for this problem is the crack length. The search space is chosen between the range 10 mm to 60 mm. The predicted crack length for different objective functions for the two different configurations of Table 7 is presented in Table 9.

It can be concluded from Table 9 that the proposed XFEM-QPSO approach identifies crack length reasonably well with maximum error of 1% for CT specimen through inverse problem identification.

Table 9 Predicted crack length for CT Specimen

Objective function	CT1	CT2
$f(\epsilon_x)$	23.707	43.649
$f(\epsilon_y)$	23.707	43.911
$f(\gamma_{xy})$	23.707	43.646
Combined	23.897	43.7841

6 Conclusion

A meta-heuristic optimisation algorithm namely QPSO is used in this paper to solve the inverse problem of crack identification in plate structures. In each iteration of the optimisation problem, XFEM is used to solve the forward problem for assumed various combinations of crack positions and lengths and minimization is performed between the predicted strain/displacement from the numerical model and reference data. It should be mentioned here that in the XFEM based strain prediction of cracked plate specimen, the mesh remains unchanged in all iterations and thereby considerably reduces computational time. Numerical investigations carried out on a cracked plate specimen and compact tension specimen in this paper concludes that the proposed XFEM-QPSO approach identifies both crack position and crack length with excellent accuracy. The convergence can be improved with variants of QPSO for larger search space of design variables. Further, if fixed mesh of model of XFEM of plate with crack is smaller, accuracy will be higher especially in the case of larger search space. Future studies may be attempted towards varying the strain measurement locations to evaluate the efficiency of the proposed algorithm, problem involving multiple cracks, both load and crack locations as unknowns.

Acknowledgements The first two authors acknowledge the support of professional and technical help received from CSIR-SERC, Chennai.

References

1. Stephens RI, Fatemi A, Stephens RR, Fuchs HO (2000) *Metal Fatigue in Engineering*. Wiley, Hoboken
2. Henshell RD, Shaw KG (1975) Crack tip finite elements are unnecessary. *Int J Numer Meth Eng* 9(3):495–507
3. Barsoum RS (1977) Triangular quarter-point elements as elastic and perfectly-plastic crack tip elements. *Int J Numer Meth Eng* 11(1):85–98
4. Belytschko T, Black T (1999) Elastic crack growth in finite elements with minimal remeshing. *Int J Numer Meth Eng* 45(5):601–620
5. Moës N, Dolbow J, Belytschko T (1999) A finite element method for crack growth without remeshing. *Int J Numer Meth Eng* 46(1):131–150
6. Rabinovich D, Givoli D, Vigdergauz S (2007) XFEM-based crack detection scheme using a genetic algorithm. *Int J Numer Meth Eng* 71(9):1051–1080
7. Khatir S, Wahab MA (2019) A computational approach for crack identification in plate structures using XFEM, XIGA, PSO and Jaya algorithm. *Theor Appl Fract Mech* 103:102240
8. Ventura G, Budyn E, Belytschko T (2003) Vector level sets for description of propagating cracks in finite elements. *Int J Numer Meth Eng* 58(10):1571–1592
9. Melenk JM, Babuška I (1996) The partition of unity finite element method: basic theory and applications. *Comput Methods Appl Mech Eng* 139(1–4):289–314
10. Babuška I, Melenk JM (1997) The partition of unity method. *Int J Numer Meth Eng* 40(4):727–758
11. Kennedy J, Eberhart RC (1995) Particle swarm optimization. In: *Proceedings of IEEE international conference on neural networks*, Piscataway NJ, pp 1942–48

12. David D, Roger P (1985) Quantum theory, the Church-Turing principle and the universal quantum computer. *Proc R Soc Lond A Math Phys Sci* 400:97–117
13. Sun J, Feng B, Xu W (2004) A global search strategy of quantum behaved particle swarm optimization. In: *IEEE conference on cybernetics and intelligent Systems*, pp 111–116
14. Sun J, Feng B, Xu W (2004) Particle swarm optimization with particles having quantum behavior. In: *IEEE congress on evolutionary computation*, pp 325–331
15. Luitel B, Venaygamoorthy GK (2010) Particle swarm optimization with quantum infusion for system identification. *Eng Appl Artif Intell* 23:635–649

Computational Study of Hydrodynamics of Mixing Tank with Non-Newtonian Fluids



Aishwarya Mulampaka  and Rajmohan Soundararajan 

Abstract Mixing is an essential and age-old industrial operation commonly in use by industries such as Chemical, Petro-chemical, Bio-chemical, Food, and Polymer industry. It is vital to understand the hydrodynamics of the mixing tank and the mixing behavior of the fluids to assess the quality of mixing. There are plenty of experimental and computational studies done on Newtonian fluids, and only limited studies related to non-Newtonian fluids have been reported. The turbulence effect around the region of the impeller, pumping capacity, and power consumption can be studied better with the help of Computational Fluid Dynamics. The simulation of the mixing process is studied using ANSYS Fluent. In this, velocity vector plots, contours, and streamlines are performed and analyzed to optimize the design. In the current research work, study related to various turbulence models and rotating approaches in the CFD, prediction of hydrodynamic behavior of Newtonian and non-Newtonian fluids is performed to validate the model. Modifications in the Rushton turbine impeller are carried out by introducing cuts in the blade of the Rushton Turbine impeller. The blade geometry is modified by introducing cuts names V-cut blade turbine, U-cut blade turbine, W-cut blade turbine. Moreover, the hydrodynamics study and mixing behavior in the modified blades are studied using carboxy methylcellulose solution as mixing fluid. Comparison of the results regarding power consumption and mixing time are made to identify the optimum design with less power consumption and shorter mixing time for shear-thinning fluids. The trade-off between power consumption and mixing time to select the best design for efficient mixing is analyzed.

Keywords CFD · Non-Newtonian fluids · Power consumption · ANSYS fluent

Nomenclature

K Consistency index ($\text{kg s}^{n-2}/\text{m}$)
 D_i impeller diameter (m)

A. Mulampaka · R. Soundararajan (✉)
Department of Chemical Engineering, National Institute of Technology Warangal, Warangal
506004, Telangana, India
e-mail: rajmohan@nitw.ac.in

N	impeller rotational speed (rps)
N_p	Power number
n	Flow behavior index
P	power required for running agitator (W)
N_q	Flow number

Greek letters

ϕ_v	viscous dissipation function (s^2)
ρ	density (kg/m^3)
ϵ	dissipation due to turbulence kinetic energy (m^2/s^3)
μ	viscosity (Pa s)
η	apparent viscosity (Pa s)
k	specific turbulent kinetic energy (m^2/s)

1 Introduction

Mixing is a significant age-old operation with its applications in almost every chemical, food processing, polymer industry, etc. It involves blending of two immiscible fluids, homogenization, dispersion of solids into liquids, gases in liquids. Based on the type of operation they are classified as batch, continuous, and semi-batch. It is essential to study the hydrodynamics of the mixing tank and the mixing behavior to assess the quality of mixing and the energy consumption to optimize the mixing process. There are plenty of experimental and computational studies done on Newtonian fluids, and only limited studies related to non-Newtonian fluids are reported. Non-Newtonian fluids are of vital importance in the food and pharmaceutical industries. The mixing operation depends mainly on the geometry of the impeller, the number of baffles present, type of tank, presence of draft tubes. The turbulence effects around the region of the impeller can be best studied with help of CFD. The simulation of the mixing process is studied using ANSYS Fluent. In this, velocity vector plots, contours, and streamlines are performed and analyzed to optimize the design. In the current research work, study related to various turbulence models and rotating approaches in the CFD, prediction of hydrodynamic behavior of Newtonian and non-Newtonian fluids is performed to validate the model. Reduction in power consumption is the most concerning aspect in mixing operation.

Many studies have been done to study the effect of impeller geometry on power Consumption [1]. The power draw depends greatly on the impeller blades, blade spacing, clearance, disc thickness, shaft inclination, eccentricity [2]. Modifications in the Rushton turbine impeller made but limited to Newtonian fluids [3]. Both experimental and simulation work has been reflected. This research work has adapted

the modification in Rushton Turbine blades to viscoelastic fluids from the literature data mentioned [4]. The studies show that the cavern size (well mixed) region is great for standard Rushton turbine but with additional power consumption when compared to blades with cuts [5]. In this work, the idea of modified blades from [3] is to be adapted to test the effect of power consumption when shear-thinning fluids (Pseudo-plastic) are to be utilized. The velocity flow field, power number, and mixing time are to be compared. Subsequently, the best design with less power consumption and shorter mixing time are predicted with the help of Computational Fluid Dynamics. Studies on the mixing behavior and hydrodynamic behavior and fluid flow that is affected by impeller characteristics on CSTR are studied using CFD [12]. A detailed description of tank geometry, baffles, impeller, draft tubes are given with a description of experimental and computational techniques are provided with classification on types of discretization schemes and modeling approaches [13]. Modifications in the Rushton turbine impeller are made by introducing cuts in the blade of the Rushton Turbine impeller. The blade geometry is modified by introducing cuts names V-cut blade turbine, U-cut blade turbine, W-cut blade turbine. Comparison of the results regarding power consumption and mixing time to identify the optimum design with less power consumption and shorter mixing time for shear-thinning fluids was performed. The trade-off between power consumption and mixing time to select the best design for efficient mixing is analyzed.

2 System Specification

The geometry of the mixing tank is created using Spaceclaim tools, with standard dimensions. Data validation is performed with Newtonian fluid (water) [6]. The dimensions of the standard Rushton blade turbine are mentioned in Table 1. Modification in the blade design is done with [3], the dimensions are taken from reference, mentioned in Table 1. The rheological properties of working fluids are mentioned in Table 2 [11, 14]. To predict how to flow pattern, power consumption, and mixing time vary when the blade geometry is modified is the main idea. This paves a way for selecting the best design suitable for the mixing operation with less power consumption and shorter mixing time.

Table 1 Tank and blade dimensions

Tank	Dimensions
Tank height (H)	270 mm
Tank diameter (D)	270 mm
Diameter of impeller ($D_i = D/3$)	90 mm
Blade height ($D_i/5$)	18 mm
Blade length ($D_i/4$)	22.5 mm
Baffle width ($D/10$)	27 mm

Table 2 Rheological properties of working fluids

Working fluid	Wt%	Fluid consistency index (K)[kg sn-2/m]	Power law index (n)
Carboxy methyl cellulose	0.1	13.2	0.85
Xanthum gum	0.045	9.5	0.8
Xanthum gum	0.08	34.0	0.64
Natrosol	1	10.8	0.59

2.1 Mathematical Model

A fluid that deviates from “Newton’s law of viscosity” is termed non-Newtonian fluids. For a non-Newtonian fluid, the viscous behavior is variable i.e., may vary with stress, with time, or with a combination of both. Based on this behavior the fluids are classified as Pseudoplastic, Thixotropic, Rheopectic, and Dilatant. The different non-Newtonian fluids as jam, butter, Carboxymethyl cellulose, Xanthum gum, sauces, yogurt, detergents, etc. [7].

2.2 Governing Equations

Anslys Fluent, is a CFD tool that utilizes a Finite Volume Method (FVM). It solves the corresponding equations of conservation of mass, energy and momentum [8].

$$\frac{\partial \rho}{\partial t} + \nabla \cdot (\rho \bar{v}) = 0 \tag{1}$$

$$\frac{\partial}{\partial t} (\rho \bar{v}) + \nabla \cdot (\rho \bar{v} \bar{v}) = -\nabla P + \nabla \cdot (\bar{\bar{\tau}}) + \rho \bar{g} \tag{2}$$

$$\rho C_p \frac{\partial T}{\partial t} + \rho C_p \nabla \cdot (\bar{v} T) = k e_{ff} \cdot \nabla^2 T - \phi_v \tag{3}$$

Here P is the static pressure, \bar{v} is velocity vector, $\bar{\bar{\tau}}$ is the stress tensor, \bar{g} is the gravitational body force, T is temperature, $k e_{ff}$ is an effective thermal conductivity. The stress tensor $\bar{\bar{\tau}}$ is denoted as

$$\bar{\bar{\tau}} = \eta [\nabla \bar{v} + \nabla \bar{v}^T] - \frac{2}{3} \nabla \cdot \bar{v} I \tag{4}$$

Here I is the unit tensor and turbulence created by the impeller, can be modeled by a standard k-ε turbulence model.

$$\nabla \cdot (\rho k \bar{v}) = \nabla \cdot \left[\left(\mu + \frac{\mu_t}{\sigma_k} \right) \nabla \cdot k \right] + G_k - \rho \varepsilon \quad (5)$$

$$\nabla \cdot (\rho \varepsilon \bar{v}) = \nabla \cdot \left[\left[\mu + \frac{\mu_t}{\sigma_\varepsilon} \right] \nabla \cdot \varepsilon \right] + C_2 \rho \frac{\varepsilon'}{k + \sqrt{\nu \varepsilon}} \quad (6)$$

in which C_2 is a constant [8].

$$C_2 = 1.92, \sigma_k = 1.0, \sigma_\varepsilon = 1.2.$$

σ_k and σ_ε are the turbulent Prandtl numbers for k and ε respectively.

G_k is generation of turbulence kinetic energy

$$G_k = -\overline{\rho u'_i u'_j} \frac{\partial u_j}{\partial x_i} \quad (7)$$

The turbulent or eddy viscosity, μ_t is calculated as follows [8]

$$\mu_t = \rho c \mu_\varepsilon \frac{k^2}{\varepsilon} = \mu_t s^2 \quad (8)$$

Reynolds number of the impeller for the mixing tank with Newtonian fluids is

$$Re = \frac{\rho N D_i^2}{\mu} \quad (9)$$

Here N is the impeller rotational speed.

For modeling the viscosity of the fluid, non-Newtonian pow law is:

$$K = \dot{\gamma}^{n-1} \quad (10)$$

Here, K is fluid consistency index and n is the power law index.

The Reynolds number for pseudo-plastic fluids is calculated by Metzner-Otto method [9]

$$Re = \frac{\rho N^{2-N} D_i^2}{K \cdot k_s^{n-1}} \quad (11)$$

where k_s is impeller geometry constant, the value of $k_s = 11.5$.

Dimensionless power number for calculating the power consumed is given as

$$N_p = \frac{P}{\rho N^3 D_i^5} \quad (12)$$

3 Numerical Method

Using Ansys Workbench 17.2 the geometry is created using Space claim CAD tools Fig. 1a and the mixing tank computational domain is discretized with tetrahedral mesh depicted in Fig. 1b. Grid independence test is conducted and the results prove that the generated mesh yields result that is independent of the mesh size. The results are tabulated in Table 3. First Order Upwind Scheme has been utilized to discretize the momentum equations. The SIMPLE algorithm was used for solving Pressure–Velocity Coupling.

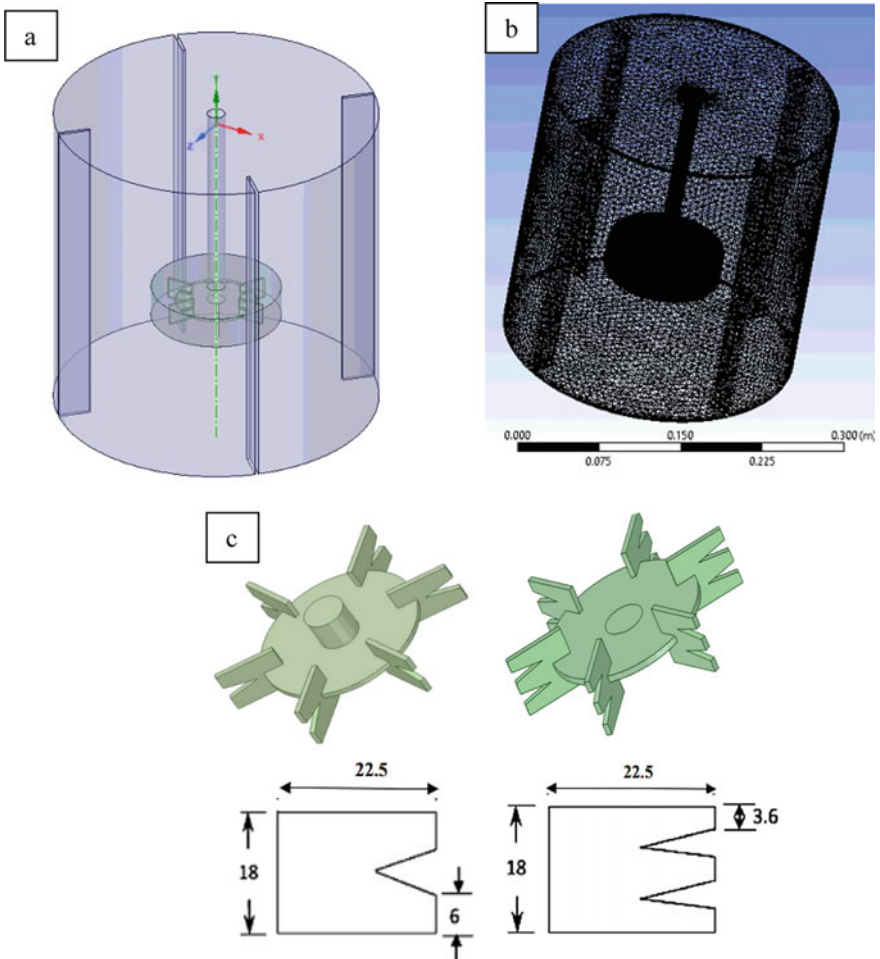


Fig. 1 a Geometry of the mixing tank b Tetrahedral meshing of mixing tank c Dimensions of modified blades (V-cut blade turbine and W-cut blade turbine)

Table 3 Grid independence test results

Element size (m)	No. of nodes	No. of elements	Velocity (m/s)
4e-003 (fine)	475,647	2,325,578	0.960531
5e-003 (medium)	278,179	1,331,897	0.958653
6e-003 (coarse)	188,757	895,474	0.960149

In this study we are using the Standard $k-\epsilon$ model, it is robust and with less computational cost, and has been useful in the engineering community for many years. It gives stable calculation and very suitable, especially for high Reynolds number.

Multiple Reference Frames model (MRF) modified form of the Rotating Frame model, uses several rotating and non-rotating frames. In the MRF approach for the rotating frame, the impeller does not move. In a stationary frame with tank walls and baffles, the wall and baffles do not move. The rotating frame is under motion.

The non-Newtonian power-law model is activated by writing console code and the materials are created with the corresponding rheological properties of the working fluids. The Convergence criteria of 0.000001 are defined for continuity and x-&y-components of velocity.

The blade geometry of the conventionally used Rushton blade turbine is termed as Std. Rushton Blade turbine is modified by introducing cuts in the blade. The dimensions of the cuts and the three-dimensional images of the V-cut blade turbine and W-cut blade turbine are depicted in Fig. 1c.

4 Validation

Computational Fluid Dynamics uses the FVM technique for solving the governing equations for mass, energy, and momentum. Solving these partial differential equations analytically is an extremely tough task. CFD discretizes these equations from non-linear termed equations to linear algebraic form, which are further solved to get accurate results for the corresponding fluid domain [10]. Most industrial operations deal with the turbulent conditions of fluid.

Therefore, it is vital to study the turbulence effect on the mixing phenomena to understand the mixing process better. Many studies have been done with various impellers to observe the power consumption and flow field inside the mixing tank system.

The geometric model is first validated with the literature data available from the experiments done by Venneker et al. [11], for the same fluids as taken by the authors. Khapre and Munshi [6] used the same system for validation but had conducted studies to understand the thermodynamic and hydrodynamic behavior of the fluids

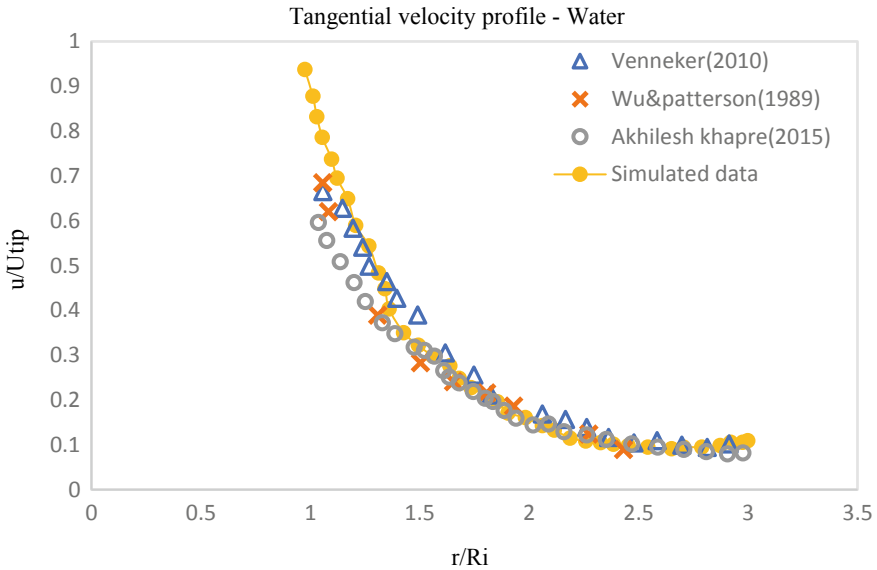


Fig. 2 Axial velocity Vs normalized radial distance for water

in the mixing tank for the Rushton blade turbine impeller and Helical screw impeller. The effect of blade width on entropy generation has been studied. Velocity profiles of Newtonian fluid (water), both experimental data and present simulated data are plotted in a graph as shown in Fig. 2. The comparison of the predicted results with the experimental data shows good agreement.

5 Results and Discussions

5.1 Effect on Power Consumption

Every impeller has a unique power curve. From the literature, data is verified that the power curve obtained by simulation is in agreement with the unique power curve of the Rushton turbine impeller. The hydrodynamics and mixing behavior are largely affected by the impeller design and fluid properties. The power consumption is one of hugely concerned factor. To minimize the power consumption and to study the effect of blade design, cuts have been introduced into the standard Rushton blade turbine impeller. The power curves for each type of impeller have been observed, by calculating torque at different rotational speeds. The dimensionless Power number versus Reynolds number curves of different working fluids for all the three types of impeller design have been plotted on logarithm plot. With comparison to the CMC solution the power number reported by each type of impeller can be inferred

from Fig. 3a–c. The std. Rushton blade turbine reports the power number of CMC solution at Reynolds number of 100,000 as 4.33, for V-cut blade turbine and W-cut blade turbine it is reported to be 3.910 and 3.115 respectively.

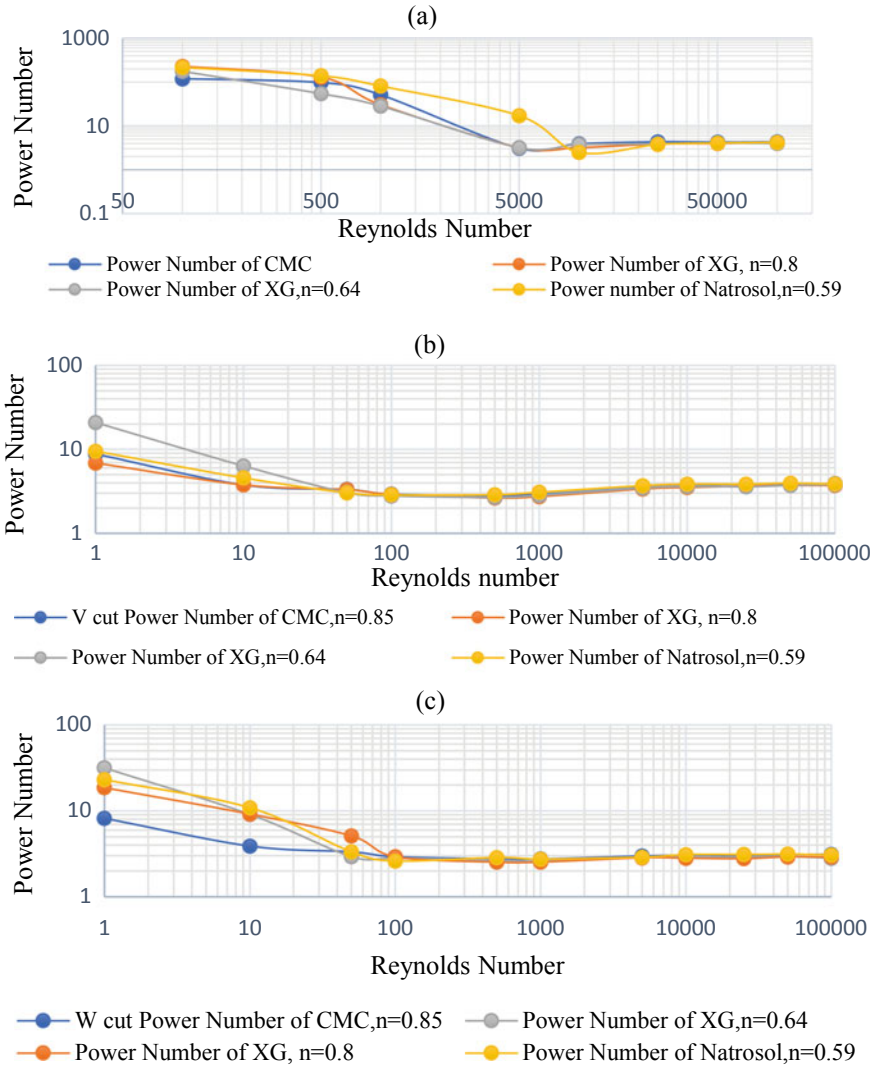
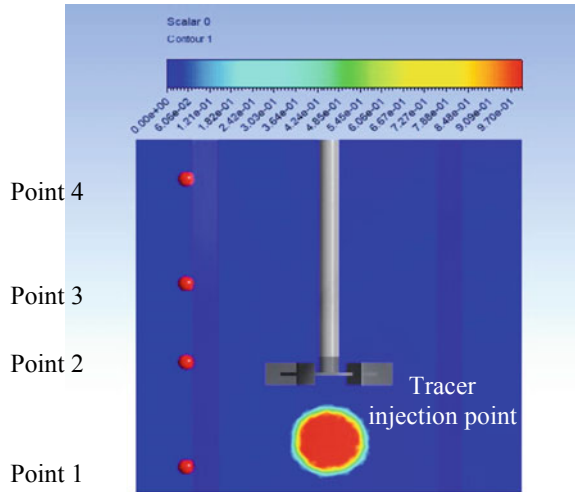


Fig. 3 a Power curves for Std. Rushton Blade turbine b Power curves for V-cut Blade turbine c Power curves for W-cut Blade turbine

Fig. 4 Tracer injection and probe points inside the tank



5.2 Effect on Mixing Time

Mixing time or Blending time is one of the important parameters to characterize the performance of the mixing tank. It is the time taken to achieve the maximum (99%) of the steady state concentration. Mixing/Blending time was predicted using “Transient transport of a neutrally-buoyant tracer (Scalar)”. The method to find the mixing/blending time is by injecting a tracer at particular position in tank & estimating the concentration at different probe positions, of the injected tracer with respect to time. The probe positions at Point 1, at Point 2, at Point 3, and at Point 4 is depicted in Fig. 4.

The response curves for CMC at 180 rpm for Std. Rushton blade turbine, V-cut blade turbine and W-cut blade turbine are shown in Fig. 5a–c respectively.

The mixing time that is estimated from the response curves for Carboxy Methyl Cellulose (CMC) fluid at 180 rpm for the four types of impellers (Std. Rushton blade turbine, V-cut, W-cut blade turbines) is listed in Table 4. The highest mixing time is observed for the Std. Rushton blade turbine, followed by W-cut blade turbine and the least time is taken by the V-cut blade turbine.

The reason for this order could be, the strong impinging flow of fluid by the V-cut blade turbine allows the flow radially with stronger recirculation loops that are reaching the top surface of the tank. Though Std. Rushton blade turbine has better radial flow with maximum cavern size, the time taken to reach the homogeneity is greater. Though the results of mixing time are differed by the value of one to two seconds, to find the best compromise among the mixing time power consumption, the studies of mixing time are considered here.

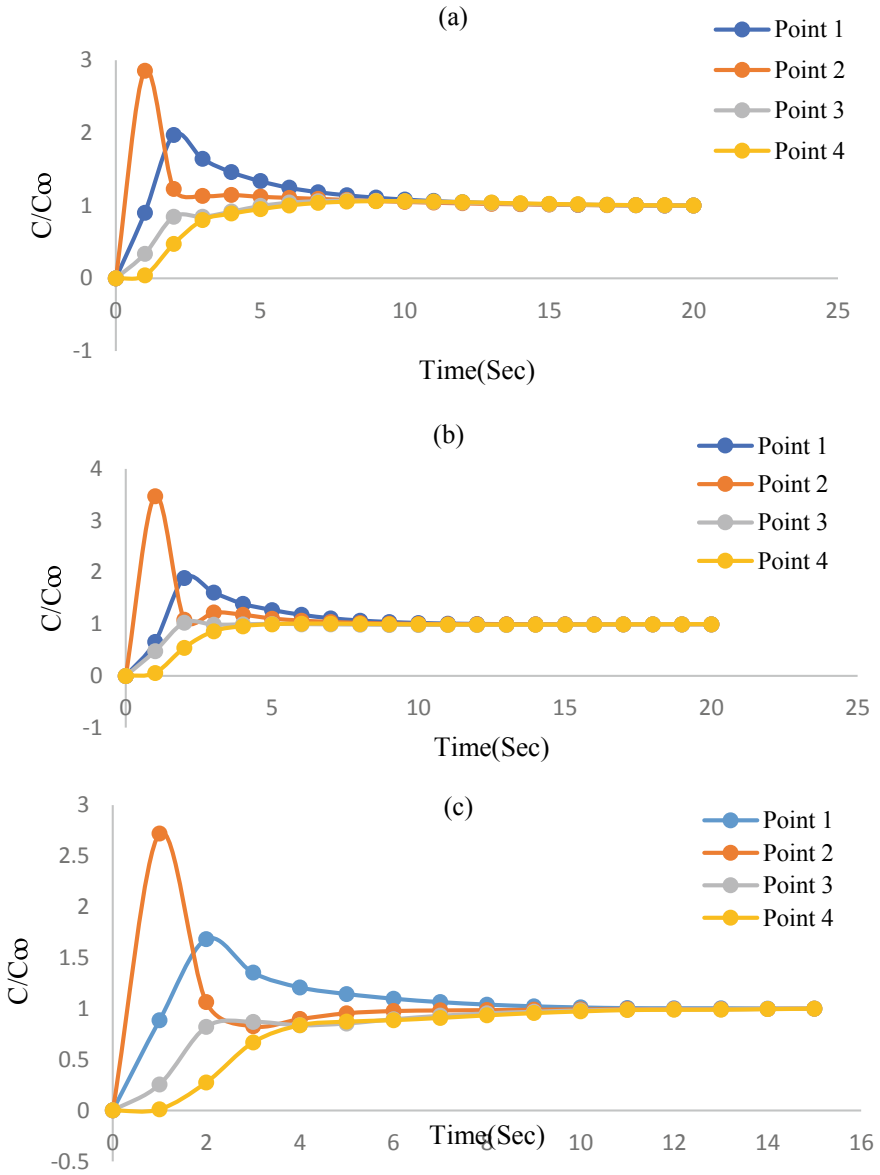


Fig. 5 a Response curve of CMC at 180 rpm for Std. Rushton Blade turbine b Response curve of CMC at 180 rpm for V-cut blade turbine c Response curve of CMC at 180 rpm for W-cut blade turbine.

Table 4 Mixing time reported for different impellers

Type of blade design	Mixing time (sec)
Std. Rushton Blade turbine	12
V-cut blade turbine	10
W-cut blade turbine	13

6 Conclusions

- The importance of mixing in the chemical industries is highlighted. A geometric model has been created using Ansys Fluent.
- The simulated results of the Newtonian fluid system–water, have good agreement with the literature data. Grid independence test has been conducted and it is proven that the results are independent of the mesh size.
- The power number results for Standard design and modified (V-cut design and W-cut design) are observed. It shows that the Std. Rushton turbine has consumed power of 10.7% more than that of V-cut turbine. When compared with the W-cut turbine, it consumed 39% more power.
- Based on the mixing time observations it is found that for Std. design, V-cut, W-cut turbines it is 12, 10 and 13 s respectively.
- The conventionally used Std. Rushton Blade turbine gives better mixing results but with greater power consumption. A compromise on both power consumption and mixing time gives us the following order of preference for efficient mixing operation.

Std. Rushton blade turbine > V-cut blade turbine > W-cut blade turbine.

References

1. Taghavi M, Zadghaffari R, Moghaddas J, Moghaddas Y (2011) Experimental and CFD investigation of power consumption in a dual Rushton turbine stirred tank. *Chem Eng Res Des* 89(3):280–290
2. Wang S, Wu J, Ohmura N (2013) Inclined-shaft agitation for improved viscous mixing. *Ind Eng Chem Res* 52(33):11741–11751
3. Rao DA, Sivashanmugam P (2010) Experimental and CFD simulation studies on power consumption in mixing using energy saving turbine agitator. *J Ind Eng Chem* 16(1):157–161
4. Cortada-Garcia M, Dore V, Mazzei L, Angeli P (2017) Experimental and CFD studies of power consumption in the agitation of highly viscous shear thinning fluids. *Chem Eng Res Des* 1(119):171–182
5. Ameer H (2018) Modifications in the Rushton turbine for mixing viscoplastic fluids. *J Food Eng* 1(233):117–125
6. Khapre A, Munshi B (2015) Numerical investigation of hydrodynamic behavior of shear thinning fluids in stirred tank. *J Taiwan Inst Chem Eng* 1(56):16–27
7. Tavlarides LL, Stamatoudis M (1981) The analysis of interphase reactions and mass transfer in liquid-liquid dispersions. In: *Advances in chemical engineering*, vol 11, pp 199–273. Academic Press, 1 January 1981

8. Ansys Fluent 13 (2011) User's Guide Ansys Inc., U.S.A
9. Metzner AB, Otto RE (1957) Agitation of non-Newtonian fluids. *AIChE J* 3(1):3–10
10. Ferziger JH, Perić M, Street RL (2002) Computational methods for fluid dynamics. Springer, Cham, December 2002. <https://doi.org/10.1007/978-3-319-99693-6>
11. Venneker BC, Derksen JJ, Van den Akker HE (2010) Turbulent flow of shear-thinning liquids in stirred tanks—The effects of Reynolds number and flow index. *Chem Eng Res Des* 88(7):827–843
12. Rajavathsavai D, Khapre A, Munshi B (2011) Study of hydrodynamic behaviour of a CSTR using CFD. In: Conference Paper, March 2011. <https://doi.org/10.13140/RG.2.1.2270.8161/1>
13. Ochieng A, Onyango M, Kiriamiti K (2009) Experimental measurement and computational fluid dynamics simulation of mixing in a stirred tank: a review. *S Afr J Sci* 105(11–12):421–426
14. ASI. <https://www.brenntag.com.ashland>, https://www.brenntag.com/media/documents/bsi/product_data_sheets/material_science/ashland_cellulose_rheology_modifiers/natrosol_250_pds.pdf

Development of a 100 mm-Diameter Split-Hopkinson Pressure Bar for High Strain Rate Characterization of Concrete



S. Ranjithkumar , S. N. Khaderi , and S. Suriya Prakash 

Abstract The Split-Hopkinson Pressure Bar (SHPB) is an experimental technique used to examine the behavior of materials at high strain rates. The aim of this paper is to present the development of a SHPB for the testing of concrete at high strain rates. The construction of the SHPB is detailed, including the important decisions made during its development. The basic calibration of the setup has been performed. The ordinary and fiber reinforced concrete (FRC) specimens (M30) with a diameter of 100 mm and L/D ratio of 0.5 are tested at a strain rate of about 50 to 65 s⁻¹. The comparison of the results from the SHPB test and the quasi-static test is also presented. From the results, it is concluded that the developed SHPB is giving consistent results for the ordinary concrete, whereas for FRC specimens, there is a difference in the peak stress, which could be the variabilities in the dispersion of fibers in the concrete.

Keywords Split-Hopkinson Pressure Bar · SHPB · High strain rate · Pulse shaping · Ordinary concrete · Fiber reinforced concrete

1 Introduction

Concrete is the most commonly used material in Civil Engineering applications due to its cost-effective, durable, and sustainable end products. During the service life of concrete structures, it can be exposed to vehicular collisions, blasts, explosions, and other complicated dynamic loads. For example, the concrete structure for nuclear

S. Ranjithkumar (✉) · S. S. Prakash
Department of Civil Engineering, Indian Institute of Technology, Hyderabad 502285, Telangana, India
e-mail: ce20mtech12006@iith.ac.in

S. S. Prakash
e-mail: suriyap@ce.iith.ac.in

S. N. Khaderi
Department of Mechanical and Aerospace Engineering, Indian Institute of Technology, Hyderabad 502285, Telangana, India
e-mail: snk@mae.iith.ac.in

power stations must be designed to withstand the dynamic loads due to explosions and impacts. Hence, understanding concrete’s behavior and mechanical properties under complex dynamic loads are essential to design such structures.

As concrete is a heterogenic material, the mechanical characteristics are complex. Nowadays, the mechanical properties of concrete are well understood because of the extensive research carried out in the past. However, the mechanical characteristics of concrete are studied by employing quasi-static tests whose strain rates are usually in the ranges of 10^{-6} to 10^{-5} s^{-1} . The behavior of concrete at high strain rates is different from that of quasi-static loading conditions. Abrams in 1917 [1] initially observed the rate-sensitive behavior of concrete. Many researchers studied the behavior of concrete at high strain rate loadings [1, 2]. Still, the advanced research on the behavior of different types of concrete at high strain rates is going on [3–5]. Our research focus is on the development of Ultra-High-Performance Concrete (UHPC) for blast resistance applications. For such applications, it is essential to understand the behavior of concrete at high strain rates. Hence, it is essential to develop the SHPB to characterize the concrete at high strain rates.

The strain rate is defined as the rate at which the strain changes with respect to time. Let us consider 50-mm long specimen deforms at a speed of 5–500 m/s, then the strain rate in the specimen is 10^2 – 10^4 s^{-1} . Typically blast kind of loading conditions generates such amplitudes of strain rates. The concrete structures will experience different strain rates during the service life ranging from 10^{-4} to 10^4 s^{-1} . Usually, high strain rates are defined as the strain rates ranges from 10^2 to 10^4 s^{-1} [6]. Figure 1 shows the ranges of strain rates encountered in the different loading conditions [7].

Various kinds of specialized machines are used to test the specimens with different strain rates. Usually, quasi-static tests can be performed by using conventional quasi-static testing machines. Special servo-hydraulic machines can be able to achieve strain rates of 10^1 s^{-1} . Drop weight machines can produce strain rates ranges between 10^0 to 10^2 s^{-1} [6]. The most commonly used experimental technique for the strain rate range of 10^2 to 10^4 s^{-1} is SHPB [8]. Kolsky [9] developed the first prototype of the modern SHPB by splitting the Hopkinson’s [10] pressure bar into two units (i.e., incident bar and transmission bar) and placing the specimen in between the units.

In the early stages, SHPB was used to characterize the strain rate behavior of metal-like materials using small diameter bars, called conventional SHPB. Unlike metals, quasi-brittle materials like concrete exhibit minimal strain in the range of 1 to 2% before failure. This low failure stain imposes the non-uniform stress state

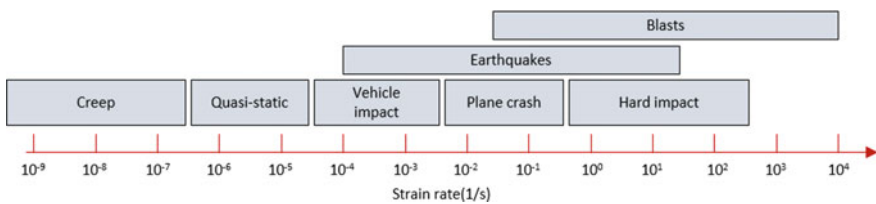


Fig. 1 Typical ranges of strain rates for different loading conditions (Recreated from Pajak [7])

within the specimen in the case of conventional SHPB. SHPB requires large diameter bars for testing concrete specimens, which will introduce wave dispersions. Hence proper modifications should be made in the SHPB as well as the testing procedure to ensure the accuracy and reliability of the test results. This paper mainly focuses on developing the 100 mm diameter SHPB to test concrete at high strain rates.

2 Basic Description

SHPB is the widely used technique to determine the dynamic behavior of materials at high strain rates. The primary mechanism of the SHPB is to use two lengthy rods as the transducers with a specimen size substantially smaller than the length of the pulse.

Figure 2 shows the schematic representation of the SHPB. The SHPB consists of the gas gun, incident, transmission, and striker bars. Typically all the bars are physically straight and have equal diameters. All three bars are made up of the same material with high yield strength. The gas gun comprises of pressure accumulator, double-acting valve, and barrel. In between the incident and transmission bar, the specimen is placed.

The gas gun is triggered by using the operating panel once upon reaching the particular pressure in the accumulator. The sudden release of the pressurized gas in the gas gun propels the striker bar. The propelled striker bar impacts against the incident bar. The velocity of the striker bar is measured by employing the velocity sensors at the end of the barrel. The collision of the striker bar on the incident bar generates the compressive stress pulse. An incident pulse is the stress pulse generated in the incident bar. The incident pulse is regularized by the pulse shaper placed in between the incident and striker bar. The incident pulse passes through the

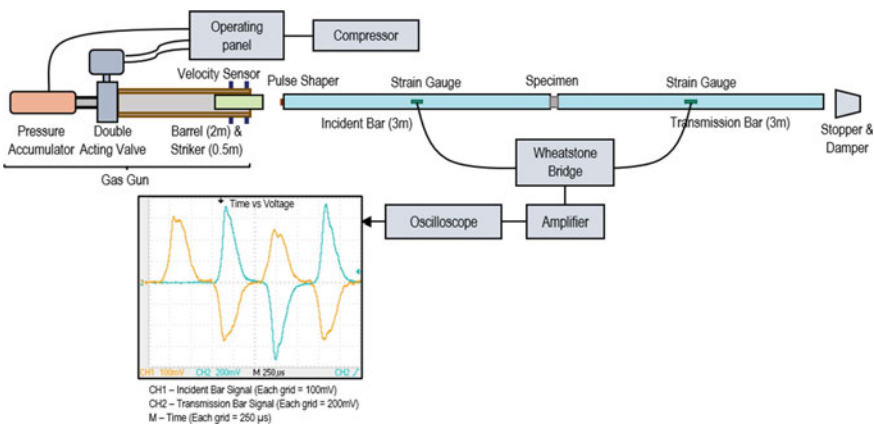


Fig. 2 Schematic representation of SHPB

incident bar and reaches the interface between the incident bar and specimen. The impedance mismatch between the incident bar and specimen generates the reflection and transmission of the incident pulse (i.e., reflected and transmitted pulse).

Two strain gauges are placed diametrically opposite on the surface of the incident, as well as transmission bars. The strain gauge captures the incident, transmitted, and reflected pulses, and the pulses are recorded on a digital oscilloscope through the Wheatstone bridge and amplifier. The recorded pulses are used to calculate the stress, strain, and strain rate in the specimen during high strain rate loading based on the one-dimensional wave propagation theory. The followings are the assumptions made in the determination of dynamic properties [11],

- During the deformation, the specimen is under a uniform and uniaxial state of stress.
- During the experiment, the incident and transmission bars should be within the elastic limit at all times. The end surfaces of the incident and transmission bars should be parallel and flat.
- The incident reflected and transmitted waves undergo minimal dispersion as they travel along the length of the bar. (i.e., the lateral dispersion of the wave should be minimal in order to make sure the one-dimensional wave propagation).
- The stress distribution should be uniform across the cross-section of the incident and transmission bars. (i.e., the strains measured on the surface of the bars should be the representative data of the stress in the elastic bars).
- The accumulated strain in the specimen is calculated solely based on the single incident stress pulse. (i.e., the subsequent loading pulses are not considered in the calculation).

The following Eqs. (1) (2) (3) are employed to determine the stress, strain, and strain rate in the specimen during the experiment [6].

$$\dot{\varepsilon}_s(t) = -\frac{2c_b}{l_0} \varepsilon_R(t) \quad (1)$$

$$\varepsilon_s(t) = \int_0^t \dot{\varepsilon}_s(t) dt \quad (2)$$

$$\sigma_s(t) = \frac{E_b A_b}{A_s} \varepsilon_T(t) \quad (3)$$

c_b, E_b, A_b are the wave velocity, Elastic modulus, and cross-sectional area of the bar. A_s, l_0 are the cross-sectional area and length of the specimen. $\varepsilon_R, \varepsilon_T$ are the reflected and transmitted pulse. $\sigma_s, \varepsilon_s, \dot{\varepsilon}_s$ are the stress, strain, and strain rate in the specimen, respectively.

3 Challenges Involved

The conventional SHPB is usually used to characterize the mechanical behavior of metal-like ductile materials where the primary interest is the plastic strains. The stress, strain, and strain rate results calculated from SHPB signals involve several assumptions. However, for quasi-brittle material like concrete, the specimen fails at very low strains. As a consequence, few of the assumptions will be violated at high strain rate testing of concrete. Hence, to test the concrete-like materials at high strain rates, the protocols of operating the conventional SHPB have to be modified to achieve proper results. The followings are the challenges involved in developing the SHPB for concrete materials.

Specimen and Bar Diameter: The selection of the diameter of the specimen and the rod is a crucial step in the high strain rate testing. Typically, concrete is a heterogenic mixture of cement, fine aggregate, coarse aggregate, and water. The nominal size of the coarse aggregates used in conventional concrete is 10–20 mm. According to ASTM standards, the diameter of the specimen should be at least three times the size of the coarse aggregate to get the representative test data. As a result, the minimum specimen diameter required is 75 mm. The specimen diameter should be equal to the bar diameter to minimize the stress concentration in the specimens. Hence, to test the concrete like quasi-brittle materials at high strain rates, the diameter of the SHPB should be large enough. On the other hand, increasing the diameter of the bar will lead to an increase in the wave dispersion, and it will also impose difficulties in achieving the velocity of the striker. We, therefore, choose a diameter of 100 mm for our SHBP.

Uniform Stress State: The first assumption made in the SHPB analysis is the uniform stress state within the specimen before it reaches the failure point. Stress equilibrium within the specimen can be achieved by choosing the duration of the incident pulse sufficiently longer. During this time, wave reflections within the specimen occur, after which the state of uniform stress is expected to prevail. Ravichandran and Subash [12] did extensive research on the uniform stress state of ceramics at high strain rates and stated that 4 to 8 reflections within the specimen are required to achieve the stress equilibrium. However, in conventional SHPB, the planar impact of the striker bar on the incident bar produces the trapezoidal incident pulse whose raising time is usually in the range of 10 to 30 μ s. This trapezoidal pulse could be used for metal-like material where the plastic strains are of most importance. But for concrete, in most situations, the trapezoidal incident pulse causes the fracture in the incident end of the specimen, whereas the other end could be intact. Hence, the triangular incident pulse with a longer duration is recommended for concrete materials, and it can be achieved by changing the shape of the striker bar. As an alternative solution, the energy absorbing material (i.e., pulse shaper) can also be placed at the impact end of the incident bar to modify the shape and duration of the incident pulse.

Pulse Shaping: Major issue with the large diameter bars is the wave dispersion due to radial inertia. As the diameter increases, the material acceleration in the lateral direction is also increasing. The acceleration in the lateral direction produces additional axial stresses due to inertia. As a consequence, wave dispersion happens, and it accumulates over the length of the bar. Gong et al. [13] investigated the dispersion of elastic wave propagation in 76.2 mm diameter SHPB and developed an algebraic formulation on wave dispersion correction. The formulation was used by Lok et al. [14] to calculate the relationship between C_n/C_0 and $a/\lambda n$. The finding drawn from the calculation is that there are no dispersions when $a/\lambda n$ is less than 0.1. Here, a is the diameter of the bar, and λn is the wavelength. As the diameter of the bar is fixed, the only way to eliminate the wave dispersion is to increase the wavelength. Consequently, the high-frequency oscillations have to be eliminated, and it is achieved by placing a pulse shaper at the impact end of the incident bar. In our SHPB, square copper plates of size 15 mm and thickness 1 mm are used as a pulse shaper. Figure 3 shows the time histories of incident pulse with and without pulse shaper for the average striker velocity of 9.1 m/s. From the figure, it is well understood that the pulse shaper increases the loading duration of the incident pulse by four times, and it also eliminates the high-frequency oscillations.

Maximum Strain Rate: The maximum strain rate is the strain rate at which the specimen experiences the non-uniform stress state, and hence the data acquired from the experiment becomes invalid. As discussed, the uniform stress distribution within the specimen will occur only after enough wave reflections within the specimen. As a consequence, the duration of the incident pulse or the specimen length needs to be limited. Ravichandran and Subash [12] developed the formulation to determine the achievable maximum strain rate in the SHPB for brittle materials based on the constant stress state conditions. The formulations show that the maximum strain rate is a function of the failure strain (ϵ_f), specimen length (l_s), and wave velocity of the specimen (C_s). These quantities are related by the Eq. (4)

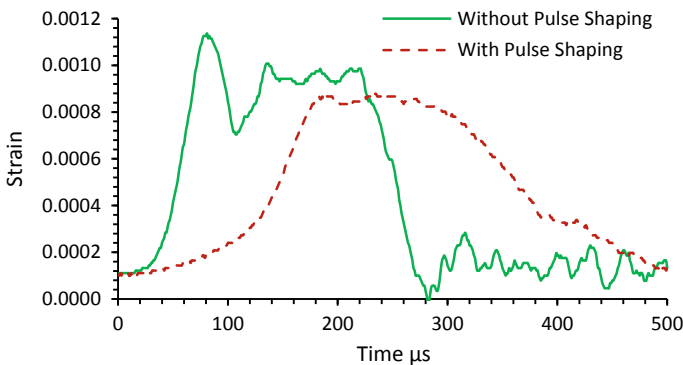


Fig. 3 Time history of incident wave with and without pulse shaper

$$\dot{\varepsilon}_l = \frac{\varepsilon_f C_s}{\alpha l_s} \quad (4)$$

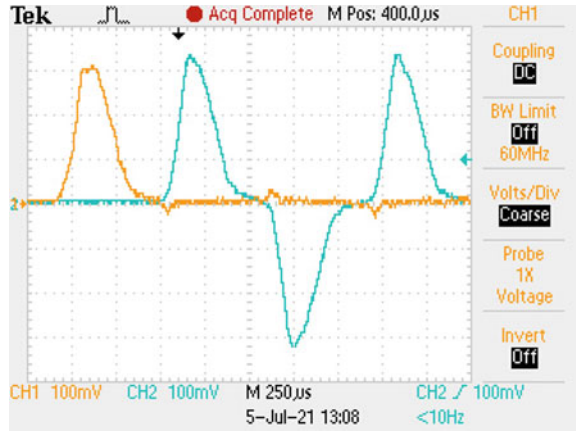
Here, α denotes the number of wave reflections within the specimen to achieve stress equilibrium. Hence, for the failure strain of 1%, specimen length of 75 mm, and the wave velocity of 3350 m/s, the maximum strain rate of 111.67 s⁻¹ can be allowed. If the striker velocity leads to a strain rate higher than this value, we would see local deformations, and the sample will not be in equilibrium.

Material Selection of Rods: The dynamic properties of the concrete are evaluated based on the strain measurement in the incident and transmission bars. Hence, during the experiment, the incident and transmission bars should be within the elastic region at all times. The end surface of the bars which would be in contact with the specimen should remain parallel and flat during the deformation of the samples. Care should be taken in the selection of bar material such that in any circumstance, the incident and transmission bars should not be damaged during the testing especially testing of a special type of concrete (i.e., Ultra-High-Performance Concrete (UHPC) whose quasi-static compressive strength is usually greater than 150 MPa). The bars used in our setup have a yield strength of 900 MPa, which can allow an incident velocity of up to 24 m/s.

Alignment: Alignment of the striker, incident, and transmission bars is a crucial part of the SHPB test setup. A slight deviation in the alignment will adversely affect the incident, transmitted, and reflected pulses. These pulses are the representative data of the specimen at high strain rates. Consequently, the stress, strain, and strain rate calculated using the pulses will be erroneous and will not give the actual material properties. Alignment tests are often conducted by directly butting the incident bar against the transmission bar with no specimen in between. This will produce an incident pulse in the incident bar, which gets transmitted to the transmission bar without any reflection. If the alignment were not proper, we would observe a reflected pulse as well. Figure 4 shows the signals captured during the alignment test. The reflected pulse having a magnitude of 5% of the incident pulse is observed from the test, and it is well within the permissible limit. A special alignment fixture has been made so that a horizontal alignment can be easily performed, while the vertical alignment is performed using shims.

Frequency Response of the Measurement System: The voltage output from the strain gauges in the SHPB experiment is too small to record, often in the order of millivolts. Hence, a signal amplifier with an oscilloscope is required to record the low-amplitude voltage accurately. On the other hand, the total duration of the experiment is in the order of micro-seconds. Hence, both the oscilloscope and the amplifier should have a higher frequency response to record the output pulses accurately. An amplifier with an oscilloscope is used in our SHPB experiment to record the signal from the strain gauge. The frequency response of the oscilloscope used to record the signals is 1 MHz.

Fig. 4 Alignment test signal



4 Description of Apparatus

Our SHPB consists of three bars (i.e., striker, incident, and transmission bars) of a uniform cross-section of diameter 100 mm and the gas gun. The length of the striker bar is 500 mm, and the length of the incident and transmission bars is 3 m each. All three bars are made up of EN24 steel with Young’s modulus of 200 GPa and a density of 7850 kg/m³. Table 1 shows the material, diameter, and length of the striker bar, incident bar, and transmission bar. The incident and transmission bars are mounted on the frictionless linear graphite lubricating brass bearing having an inner diameter of 100 mm. The gas gun consists of a pressure accumulator, a Double-acting Y valve, and a barrel. The pressure accumulator is capable of accumulating 300 bar pressure. A Double-acting Y valve with the working pressure of 10 bars is controlled by a 24 V dc solenoid valve with a maximum working pressure of 8 bars. The barrel has an inner diameter of 100 mm, and a length of 2 m, is connected to the Y valve. The laser-based velocity sensors having two pairs of emitter and transmitter spaced at 150 mm distance are fixed at the end of the barrel to measure the striker bar velocity. The 15 × 15 mm square copper plate with 1 mm thickness is used as a pulse shaper. Two diametrically opposite strain gauges of 5 mm gauge length and 120 Ω resistance are mounted on the surface of the incident and transmission bars. The strain gauges are located at the mid-length of the bars. The strain gauges are connected to the amplifier through half circuit Wheatstone bridge. The amplifier is having a low pass filter of 100 kHz that amplifies the signal by 100 or 1000 times. Finally, the amplified

Table 1 Details of the components of SHPB

Component	Diameter (mm)	Length (mm)	Material
Striker bar	100	500	EN24
Incident bar	100	3000	EN24
Transmission bar	100	3000	EN24

signal is recorded by Tektronix TDS oscilloscope with a sampling rate of one million samples per second.

5 Experimental Setup and Specimen Preparation

The experimental test setup of the Split Hopkinson Pressure Bar is shown in Fig. 5. The alignment test is carried out on SHPB by launching the striker bar on the incident bar without the specimen in between. The signals captured during the alignment test indicate the presence of a reflected pulse. However, the magnitude of the reflected pulse is 5% of the magnitude of the incident pulse, and it is well within the permissible limit. The cylindrical concrete specimens are tested to verify the performance of the SHPB test setup, and the results from the SHPB test are compared with the quasi-static test results. For this purpose, the M30 grade ordinary concrete cylinders (i.e., Control specimen) and fiber reinforced concrete (FRC) cylinders are cast. The dimensions of the cylinders are 100 mm diameter, 200 mm height, and 150 mm diameter, 300 mm height. The fiber-reinforced concrete cylinders are having a combination of micro steel and polyolefin fibers, and each type of fiber has about 0.5% volume fraction. The quasi-static tests are performed with 150 mm diameter cylinders by using a displacement control CTM of about 5000 kN capacity, and the resulting stress-strain curves are plotted. As per ASTM standard, the L/D ratio of 2 is maintained in the quasi-static tests.

The SHPB tests are performed with concrete cylinders having a diameter of 100 mm and an L/D ratio of 0.5. The 200 mm height cylinders are cut into 50 mm thick cylinders by using a cutting machine with a diamond cutting blade. The cut cylinders are ground to reduce the unevenness in the thickness of the cylinders. The concrete specimens are sandwiched between the incident and transmission bar with a thin layer of grease to reduce the friction between the two surfaces. Figure 6 shows the concrete specimen sandwiched between incident and transmission bars. A small cardboard sheet is provided as temporary support to avoid the slippage of the specimen. The gas gun is operated with 1.5 bar pressure, which produces the average striker velocity of 9 m/s. Table 2 shows the description and test results of concrete cylinders at high strain rates as well as quasi-static strain rates.



Fig. 5 Experimental test setup (SHPB)

Fig. 6 Specimen sandwiched between incident and transmission bars

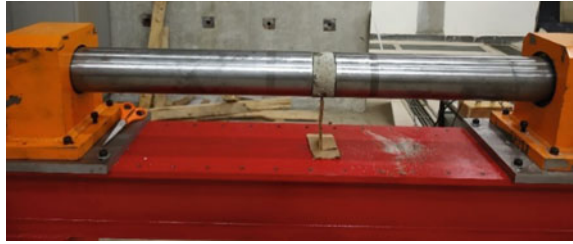


Table 2 Specimen details, quasi-static and dynamic test results

Type	Specimen details	Diameter (mm)	Thickness (mm)	Strain rate (s ⁻¹)	Dynamic strength (MPa)	Quasi-static strength (MPa)
Ordinary concrete	Specimen 1	100	50.55 ± 0.20	54.25	40.40	28.42
	Specimen 2	100	50.15 ± 0.10	56.50	40.40	
Fiber reinforced concrete	Specimen 1	100	49.50 ± 0.40	67.50	52.19	24.16
	Specimen 2	100	48.90 ± 0.50	52.75	42.65	

6 Results and Discussion

The SHPB test setup is validated by performing the high strain rate testing on the ordinary and fiber reinforced concrete specimens. The test results of quasi-static and SHPB tests are tabulated in Table 2. Figure 7 shows the typical strain gauge signals captured during the test of ordinary concrete and FRC specimens. Figure 8 shows the stress histories at the two ends of the specimen, which are calculated from incident, transmitted and reflected signals. From the figure, it can be understood that the stress differences between the two ends of the specimen are high at the initial stages.

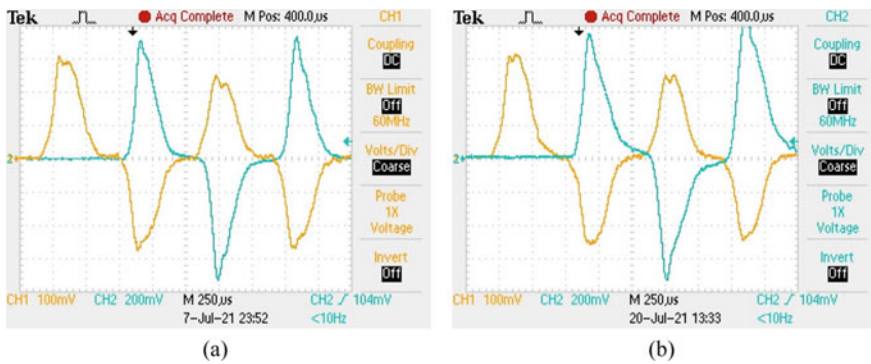


Fig. 7 Typical SHPB test signals **a** Ordinary/control concrete specimen **b** FRC specimen

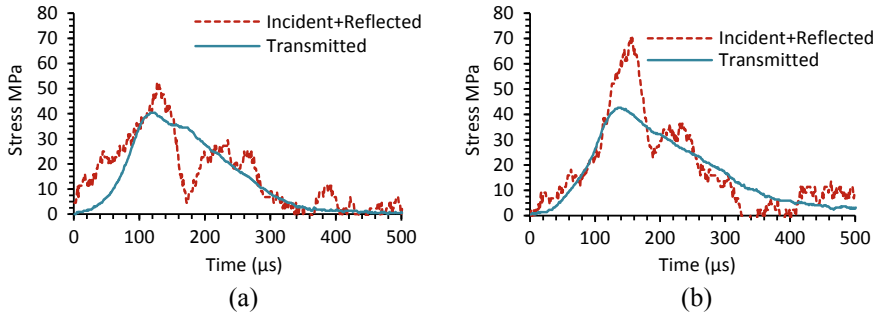
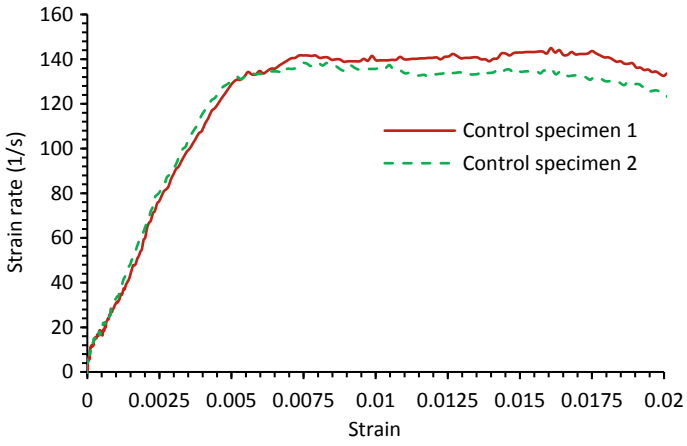
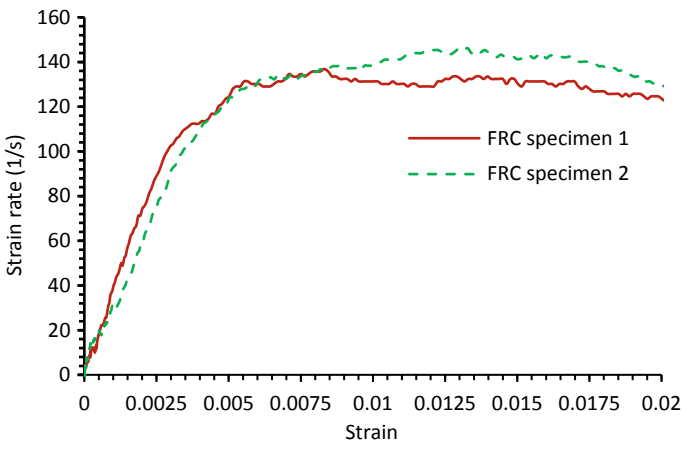


Fig. 8 Stress histories at the ends of the specimen calculated from the incident, transmitted and reflected pulse **a** Ordinary/control concrete specimen **b** FRC specimen

Approximately at $75 \mu\text{s}$, the stresses at the two ends of the specimen are almost equal, attributing to the uniform stress state of the specimen. As the specimen undergoes the deformation, the post-peak regions have high-stress differences. The same trend of stress histories can be found in both types of concrete specimens. Figure 9 shows the strain vs. strain rate curves for ordinary concrete and FRC specimens with the average striker velocity of 9.10 m/s . Both types of specimens are following the same trend in the strain vs. strain rate curve. The strain rates increase linearly up to the strain of 0.005 , and then it reaches the constant strain rate. On the other hand, at the strain of 0.0025 , the specimen starts deforming. Hence the strain rates between the strains corresponding to 80% to 100% of the peak stress are considered, and the average value is reported. Figure 10 shows the stress-strain plots of SHPB tests in comparison with the quasi-static stress-strain behavior. Stress-strain plots of ordinary and FRC specimens attribute the strength increase in high strain rates tests. The dynamic increase factor (i.e., the ratio of dynamic strength to that of quasi-static strength) is found to be 1.42 in the case of ordinary concrete specimens, whereas for FRC specimens, it is in the range of 1.76 to 2.16 . The SHPB tests on concrete provided consistent results. However, a marginal difference in the peak stress was observed in FRC, which could be due to variabilities in the dispersion of fibers in concrete.



(a)



(b)

Fig. 9 Strain vs. strain rate plot for average striker velocity of 9.10 m/s **a** Ordinary/control concrete specimen **b** FRC specimen

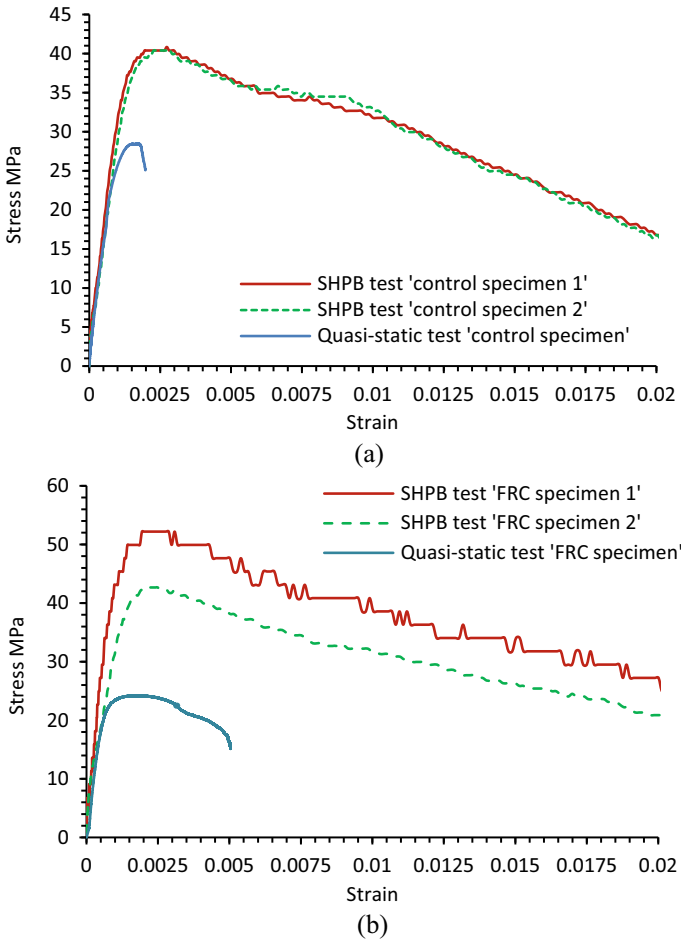


Fig. 10 Stress-strain plots **a** Ordinary/control concrete specimen **b** FRC specimen

7 Summary

SHPB setup is conventionally used to test ductile materials that involve several assumptions in the calculation of stress, strain, and strain rate. While testing quasi-brittle materials like concrete using SHPB, there is a possibility of a non-uniform stress state within the specimen which can violate the assumptions. A large diameter SHPB has been developed to get the representative test data of quasi-brittle materials like concrete. Consequently, the dispersion of the waves along the length of the bar has to be eliminated. Considering all the merits and demerits of SHPB, a 100 mm diameter SHPB is developed to test concrete-like brittle materials at high strain rates. Ordinary concrete with no fibers and FRC concrete specimens were tested at a strain

rate of about 50 to 65 s⁻¹ by using the developed SHPB. Based on the test results, the following can be summarized.

1. The uniform stress state within the specimen was achieved, and the high-frequency oscillations due to wave dispersion were eliminated.
2. The strain rates achieved during testing were consistent for ordinary and FRC specimens.
3. The strength of the concrete increased with an increase in high strain rates.
4. SHPB test setup provides consistent results for ordinary concrete. For FRC specimens, there is a variation of peak stress due to variation in the distribution of fibers.

Further studies on concrete using SHPB can be carried out by varying shapes and dimensions of the specimen. The effect of size and shape of the concrete specimen and its influence would be interesting and is scope for future work. The developed SHPB can also be modified to perform the Brazilian test on concrete specimens.

References

1. Bischoff PH, Perry SH (1991) Compressive behaviour of concrete at high strain rates. *Mater Struct* 24(6):425–450. <https://doi.org/10.1007/BF02472016>
2. Ross CA, Thompson PY, Tedesco JW (1989) Split-Hopkinson pressure-bar tests on concrete and mortar in tension and compression. *ACI Mater J* 86:475–481. <https://doi.org/10.14359/2065>
3. Xiong B, Demartino C, Xiao Y (2019) High-strain rate compressive behavior of CFRP confined concrete: large diameter SHPB tests. *Constr Build Mater* 201:484–501. <https://doi.org/10.1016/j.conbuildmat.2018.12.144>
4. Pham TM et al (2020) Dynamic compressive properties of lightweight rubberized geopolymer concrete. *Constr Build Mater* 265:120753. <https://doi.org/10.1016/j.conbuildmat.2020.120753>
5. Liu G-J, Bai E-L, Xu J-Y, Yang N, Wang T (2020) Dynamic compressive mechanical properties of carbon fiber-reinforced polymer concrete with different polymer-cement ratios at high strain rates. *Constr Build Mater* 261:119995. <https://doi.org/10.1016/j.conbuildmat.2020.119995>
6. Ramesh KT (2008) High rates and impact experiments. In: Sharpe WN (ed) *Springer handbook of experimental solid mechanics*. SHB, pp 929–960. Springer, Boston. https://doi.org/10.1007/978-0-387-30877-7_33
7. Pajak M (2011) The influence of the strain rate on the strength of concrete taking into account the experimental techniques. *Archit Civ Eng Environ* 4:77–86
8. Chen W, Song B (2011) *Split Hopkinson (Kolsky) Bar*. MES. Springer, Boston. <https://doi.org/10.1007/978-1-4419-7982-7>
9. Kolsky H (1949) An investigation of the mechanical properties of materials at very high rates of loading. *Proc Phys Soc Sect B* 62(11):676–700. <https://doi.org/10.1088/0370-1301/62/11/302>
10. Hopkinson B (1914) X. A method of measuring the pressure produced in the detonation of high, explosives or by the impact of bullets. *Philos Trans R Soc Lond Ser A Containing Pap Math Phys Charact* 213(497–908):437–456. <https://doi.org/10.1098/rsta.1914.0010>
11. Nemat-nasser S, Diego S (2018) Introduction to high strain rate testing. *Mech Test Eval* 8:427–428. <https://doi.org/10.31399/asm.hb.v08.a0003293>
12. Ravichandran G, Subhash G (1994) Critical appraisal of limiting strain rates for compression testing of ceramics in a split Hopkinson pressure bar. *J Am Ceram Soc* 77:263–267. <https://doi.org/10.1111/j.1151-2916.1994.tb06987.x>

13. Gong JC, Malvern LE, Jenkins DA (1990) Dispersion investigation in the split Hopkinson pressure bar. *J Eng Mater Technol Trans ASME* 112:309–314. <https://doi.org/10.1115/1.2903329>
14. Lok TS, Li XB, Liu D, Zhao PJ (2002) Testing and response of large diameter brittle materials subjected to high strain rate. *J Mater Civ Eng* 14(3):262–269. [https://doi.org/10.1061/\(ASCE\)0899-1561\(2002\)14:3\(262\)](https://doi.org/10.1061/(ASCE)0899-1561(2002)14:3(262))

Numerical Investigation of Bistable Laminates on Geometric Scaling



G. S. Srikanth, S. Scheffler, P. M. Anilkumar, B. N. Rao, and R. Rolfes

Abstract Bistable laminates are finding applications at various scales. They are being used in energy harvesting, sensors and morphing structures. It is crucial to understand the theoretical and practical scale bounds of bistable laminates. Variations of curvatures, snap-through loads, strain energies and planar stresses for a [0/90] cross-ply laminate upon geometric scaling are investigated in the paper for two plan sizes and various edge length to thickness ratios. Governing scaling law for isometric geometrical scaling is determined. 3-dimensional finite element analysis using solid-continuum elements is presented to predict possible delamination at the free edge. By characterizing the laminate behavior, the paper aims to reduce the numerical and experimental effort in investigating large numbers of individual specimens.

Keywords Bistability · Cross-ply laminates · Curvatures · Scaling law · Distributed compliance · Continuum analysis

1 Introduction

Multistable structures are treated as morphing adaptive structures which can attain multiple stable configurations with respect to the changes in the environment. The ability of these multistable structures to stay in their attained stable configurations without any need of external energy makes research on multistable structures interesting. By definition, any structure is defined as a multistable structure when it can attain two or more equilibrium shapes in distinct configurations. The property

G. S. Srikanth (✉) · P. M. Anilkumar · B. N. Rao
Structural Engineering Division, Department of Civil Engineering, Indian Institute of Technology Madras, Chennai 600036, India
e-mail: garigipatis@IISc.ac.in

S. Scheffler · R. Rolfes
Institute of Structural Analysis, Leibniz Universität Hannover, Appelstraße 9A, 30167 Hannover, Germany

of multistability in any structure depends on how the material anisotropy distorts the symmetry of potential energy of the structure under uniform deformation and thereby seeding preferential directions for minimum stored energy [1]. Structure which possesses two stable configurations is the simplest form of the multistable structure and is called a bistable structure. Prior to the development and usage of bistable laminates, unsymmetric composite laminates were not considered as a viable material for many engineering applications. This is especially because of the bending-stretching component in the stiffness matrix of the laminate. According to Classical Laminate Plate (CLT) theory, bending-stretching components results in undesirable saddle shape after curing for the unsymmetric laminate [2, 3].

Unsymmetric composite laminates exhibit bistability due to a mismatch in their thermal expansion coefficients along the thickness of the laminate, where thermal strains will be induced in the laminate and result in two stable shapes [4]. These stable shapes have large curvatures, and require external energy to overcome the energy barriers for shape-changing action. Hyer [5] was the first one to identify this bistable behaviour in the year 1981.

Hyer performed his research on the deformation shapes of different unsymmetric cross-ply laminates and found that thin unsymmetric laminates can have two stable semi-cylindrical shapes at room temperature. Due to the presence of bistable room-temperature configurations, bistable laminates find applications in morphing applications. They can be snapped from one shape to the other by the application of a sufficient external force. Shape change due to residual thermal stresses post cooldown can lead to either a monostable saddle shape or cylindrical bistable shape depending upon the material, geometry, ambient moisture, temperature and boundary conditions. Laminate behavior is characterized by its edge length (L) to thickness (t) ratio, also termed as aspect ratio (L/t). Thicker laminates generally do not exhibit bistability [6]. The dependence of laminate behavior on aspect ratio can be understood by looking at variation in either curvature or strain energy (SE) with change in aspect ratio. In a bistable laminate, the two cylindrical states have lower SE than the SE of the saddle shape. The laminate loses its bistability as the energy difference between cylindrical and saddle shapes disappears. The aspect ratio value above which bistability is observed is called bifurcation point. Brampton et al. [6] reported the bifurcation point of a square [0/90] laminate by reporting the curvature in one of the principal directions. Although the saddle shape cannot be obtained experimentally in a thin bistable laminate because of instability, as opposed to the cylindrical shapes, comparing the two shapes is helpful. Unstable saddle shape can be analyzed either numerically or analytically.

Geometric scaling is the scaling of the dimensions of the laminate. If isometrically scaled, all the dimensions are scaled equal times. The dependence of curvatures, snap-through loads, strain energies and stresses on dimensions of a laminate needs to be studied. In order to design bistable laminates in practical morphing applications, it is important to understand the effect of geometric scaling while preparing the

prototypes for the intended application. It is important to predict the size limitations of laminates by studying the magnification of properties upon geometric scaling. The paper presents a numerical study on the variation of laminate properties for a [0/90] cross-ply laminate to achieve this aim. The analysis is performed for two laminate plan sizes to understand the effect of isometric geometric scaling on the magnification of its properties, while the aspect ratio is varied for both the plan sizes. Knowledge of magnification of stresses upon geometric scaling is useful in stress-based design methodologies. Out-of-plane normal stress can cause delamination of the composite. Location of maximum out-of-plane stress and the effect of geometric scaling is explored.

2 Methodology

In this paper, square [0/90] cross-ply thermally cured graphite-epoxy composite laminates have been investigated. The reason behind selecting the square cross-ply ([0/90]) laminate is to particularly verify the bifurcation point (from the finite element model) with the result reported in Brampton et al. [6]. Figure 1 shows a representative diagram of the laminate. Numerical analyses using a commercially available FE package (*ABAQUS*) have been performed. Dimensional analysis is performed by changing the laminate edge length (L) and thickness (t). Two plan

Fig. 1 Square laminate of size $L \times L \times t$ is fixed at the center to prevent rigid body motions. A location of interest is marked and numbered

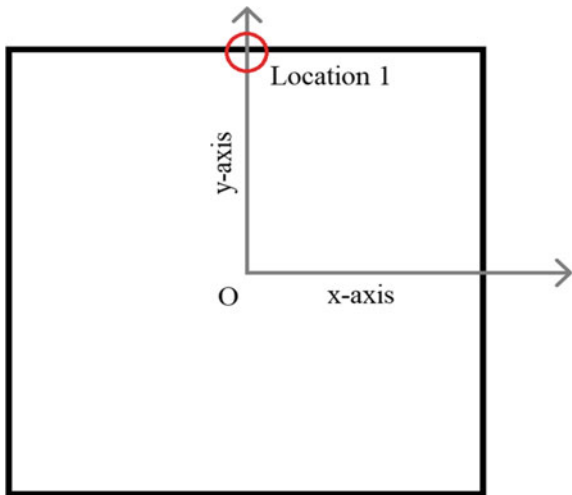


Table 1 Elastic properties of T300/5028 graphite-epoxy ply [6]

Property	E_{11} (GPa)	$E_{22} = E_{33}$ (GPa)	$\nu_{12} = \nu_{13}$	ν_{12}	$G_{12} = G_{13}$ (GPa)	G_{23} (GPa)	$\alpha_{11} = \alpha_{33}$ ($^{\circ}\text{C}$)	α_{22} ($^{\circ}\text{C}$)
Value	161	10	0.308	0.17	6.95	5	2.48×10^{-6}	2.65×10^{-5}

sizes, 150×150 mm (size 1) and 300×300 mm (size 2) are used in this study. The thickness of the laminate is altered by varying edge length to thickness ratio (L/t). Separate 2-dimensional shell analysis and 3-dimensional continuum analysis have been performed. The laminate is cured at 180°C in an initially flat configuration. The temperature is specified by applying a uniform temperature field. The temperature is then reduced to 20°C and the laminate is allowed to deform into one of the stable shapes. The material properties for the lamina used (Table 1) are taken from Brampton et al. [6]. The lamina used is T300/5028 graphite-epoxy composite. The numerical model is verified by comparing the bifurcation points. Curvatures, the angle subtended, elastic strain energies, snap-through forces, in-plane and out-of-plane normal stresses are analyzed, and magnification of these properties due to isometric geometric scaling is reported.

2.1 2D Modelling

Finite element modelling is performed with the aid of a commercially available FE software (*ABAQUS*). The laminate stacking ($[0/90]$) is specified by the use of composite shell sections. The laminate is modelled using quadrilateral four-node shell elements (*S4*) [7]. A mesh convergence study has been performed by considering out-of-plane displacements as a governing criteria. Based on the mesh convergence study, mesh characteristics with suitable mesh types are used to discretize the investigated laminate to achieve a good compromise between computational time and accuracy of the solution. With the increase in mesh density from a coarse mesh to a finer mesh, the obtained solution converges toward a unique value, and the finer mesh size has been used for the subsequent analysis. A static nonlinear analysis is performed. A temperature field difference of $\Delta T = -160^{\circ}\text{C}$ is imposed to simulate the cool down after the thermal curing. In order to simulate the snap-through action, static transverse point loads are applied at the corners of the laminate. The load applied to the laminate should be higher than the snap-through force to deform the laminate to the other stable shape.

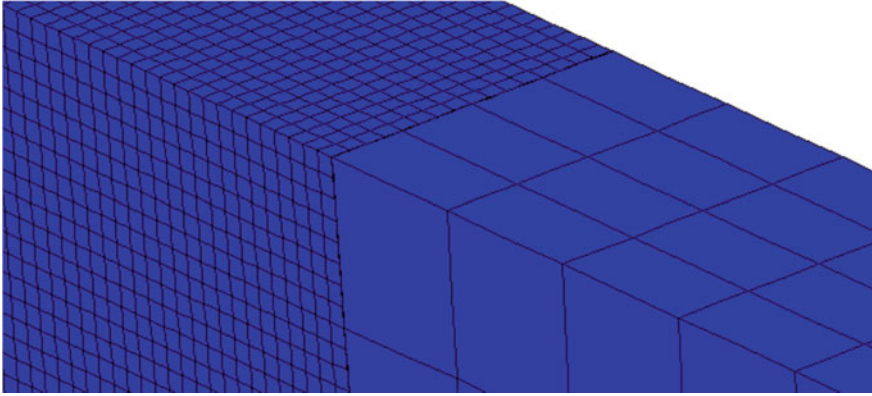


Fig. 2 Mesh refinement at location 1 used for the 3-dimensional study

2.2 3D Modelling

Linear 8-node C3D8 elements are known to be much stiffer in flexure in comparison to planar S4 elements. Quadratic elements can take up curved profiles. Hence, 20-node fully integrated hexagonal brick elements (C3D20) have been used for modeling accurate bending behavior. Only a quarter panel of the laminate is modeled by making use of symmetry about the x -axis and the y -axis to reduce computational effort. In order to plot accurate variation of the stresses in the edge region, local mesh refinement has been carried out. A coarse mesh size of $300 \times 300 \times 4$ and a fine mesh size having 16 elements in the thickness are used as shown in Fig. 2. The plan and out-of-plane dimension of fine elements is kept similar to form cubical elements. The mesh size has been selected after performing detailed mesh convergence studies, where out-of-plane displacements have been compared with the results of shell analysis.

3 Results and Discussions

3.1 Curvature

The bistable laminate can be characterized by its principal curvature in the given directions. Gigliotti et al. [8] reported a study on bifurcation by plotting principal edge curvature against aspect ratio for square plates, where the critical aspect ratio for which the plate loses bistability has been reported similar to Brampton et al. [6]. Figure 3 depicts the curvature of selected laminates with respect to different (L/t)

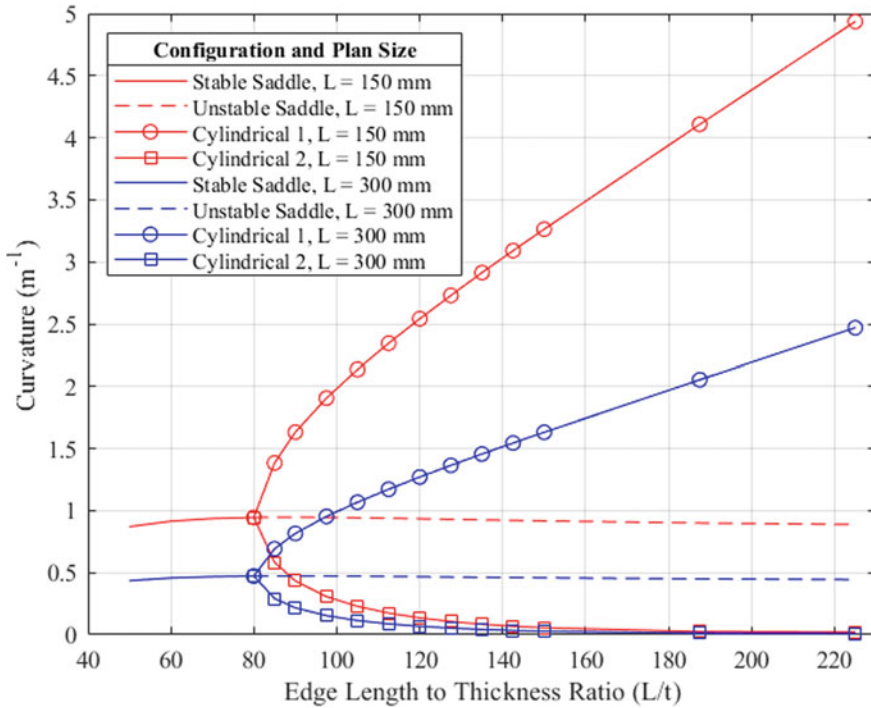


Fig. 3 x-curvature plotted against aspect ratio (L/t)

ratios as obtained in the current study. It has been noticed that thick laminates, having low L/t ratios, do not exhibit bistability and exhibit a saddle shape. The curvatures associated with the unstable saddle shape are represented by dashed lines, and the curvatures associated with stable shapes are represented by solid lines. The trend of the curvature plots for laminate size 1 and laminate size 2 are similar, exhibiting the same L/t ratio at bifurcation. Bifurcation is observed at an L/t ratio of 80, recreating the results of Brampton et al. [6]. Magnification of curvature values, upon isometric geometric scaling of 2, is half.

As the laminate exhibits a cylindrical shape, the path along which curvature is measured forms an arc of a circle. The radius of this circle is inverse of the laminate curvature. The curved profiles of a laminate can also be characterized by measuring the angle subtended by the arc. The arc subtends an angle θ at its center as shown in Fig. 4. Figure 5 depicts the variation in arc angle. The plot is a similar trident shape, although unmagnified by isometric geometric scaling. Bifurcation is observed at an L/t ratio of 80.

Fig. 4 Angle θ , subtended by the curved laminate in cylindrical configuration 1

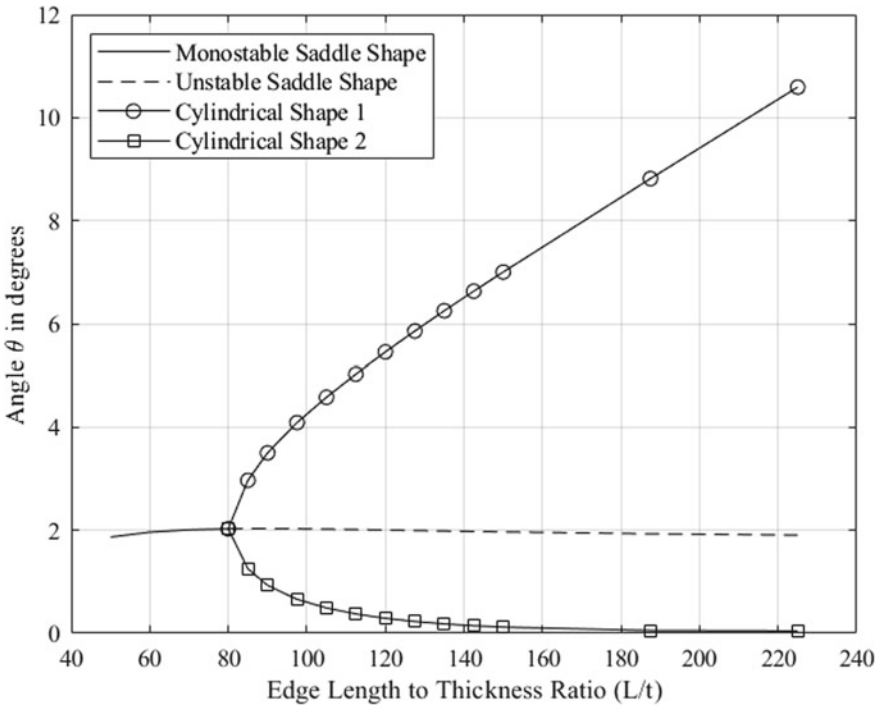
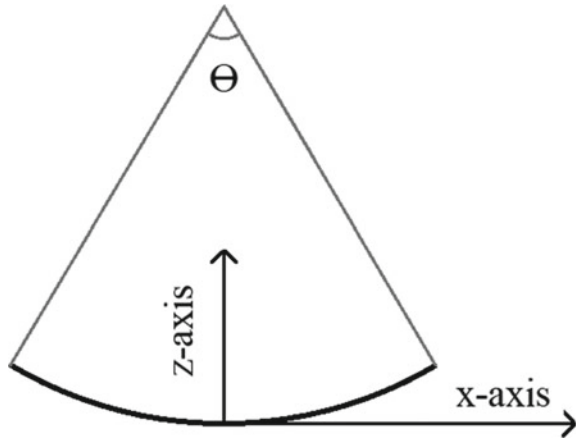


Fig. 5 Angle θ plotted against aspect ratio (L/t) for both plan sizes

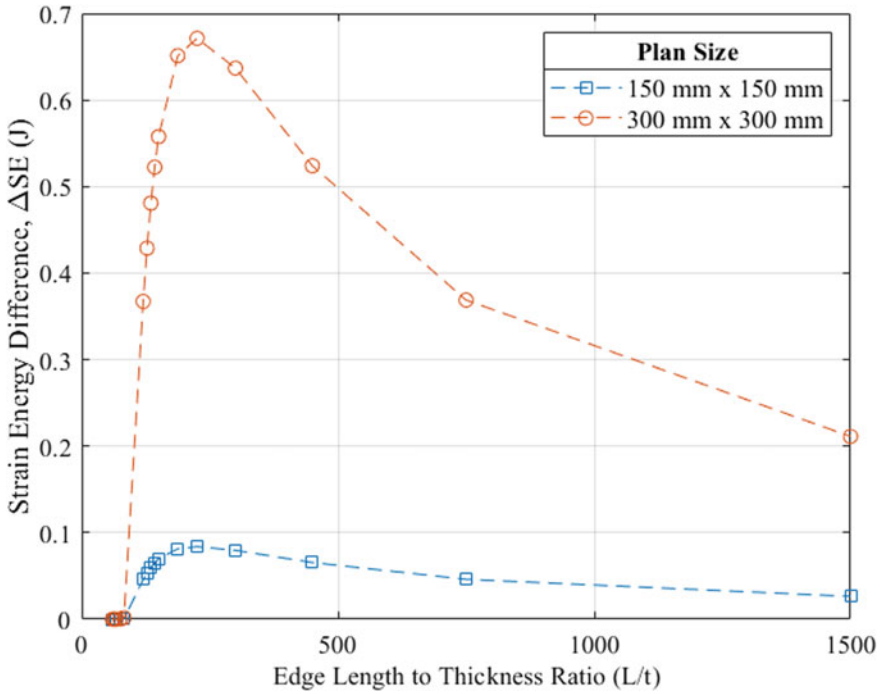


Fig. 6 ΔSE is plotted against aspect ratio (L/t)

3.2 Strain Energy

The stable shapes of a laminate can be studied using the strain energy values corresponding to the saddle and cylindrical shapes. Stable shape corresponds to the state which has a lower potential energy.

Bistability is exhibited when the saddle shape has a higher strain energy than the two cylindrical shapes. At the bifurcation point, the saddle and cylindrical shapes must have the same strain energy. The strain energy difference between the saddle shape and the cylindrical shape, ΔSE, is plotted in Fig. 6. The values represent the total elastic strain energy obtained from the ALLSE history output in the Abaqus FE package. This plot serves as a measure of the extent of bistability in a laminate. The bifurcation point is observed at an L/t value of 80, same as in the case of curvatures.

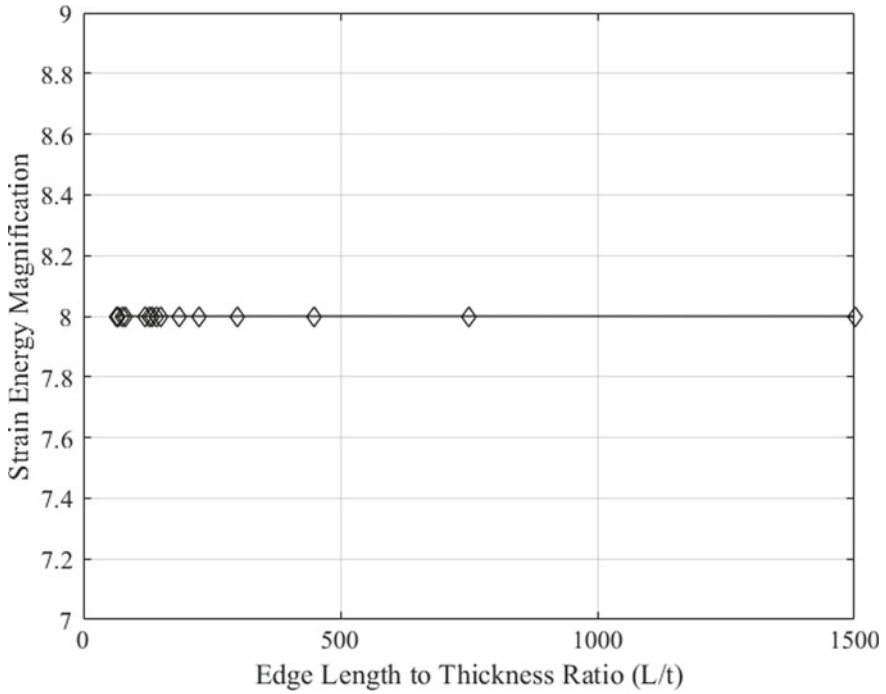


Fig. 7 Magnification of strain energy against aspect ratio (L/t)

The shapes of plots for laminate size 1 and laminate size 2 seem identical. The peak Δ SE values are observed at an L/t value of 225 for both laminates plan sizes. As high L/t values indicate lower thickness values, the reduction in volume is reflected in lower strain energies at the tail end of the plot. The magnification of strain energies upon isometric geometrical scaling is plotted in Fig. 7.

3.3 Snap-Through Force

A concentrated load is applied normally to the surface at the corners on the bistable laminates to trigger snap-through while the center of the laminate is fixed.

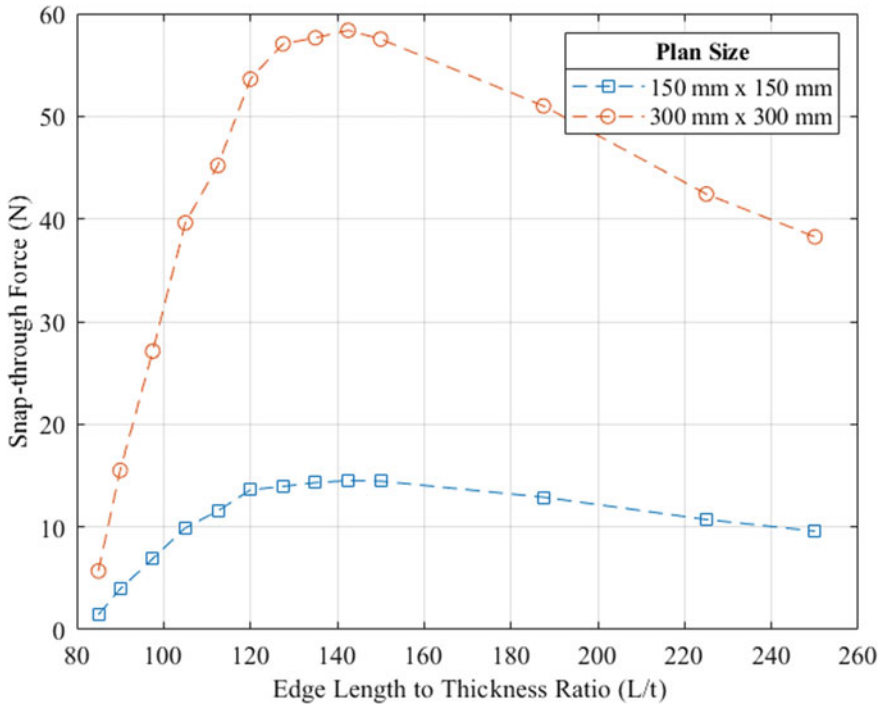


Fig. 8 Snap-through force is plotted against aspect ratio (L/t)

The analysis is performed in a force-controlled step. The result of dimensional analysis of snap-through forces is plotted in Fig. 8. The snap-through force approaches zero near the bifurcation point. As the two shapes of a bistable laminate attain distinct curvatures, their out-of-plane displacements increase. This results in an increase in snap-through force. The reduction in snapping force at the tail end of the plot is due to reduction in flexural stiffness of the laminate as the thickness decreases. A peak is obtained at an L/t value of 142.5. The magnification of snap-through forces upon isometric geometric scaling is plotted in Fig. 9.

3.4 In-Plane Stresses

A shell analysis using S4 elements assumes a plane state of stress. The in-plane normal stresses σ_{11} and σ_{22} are plotted along the y-axis in Figs. 10 and 11 respectively. At the curved edge, the in-plane normal stresses in the direction perpendicular to the

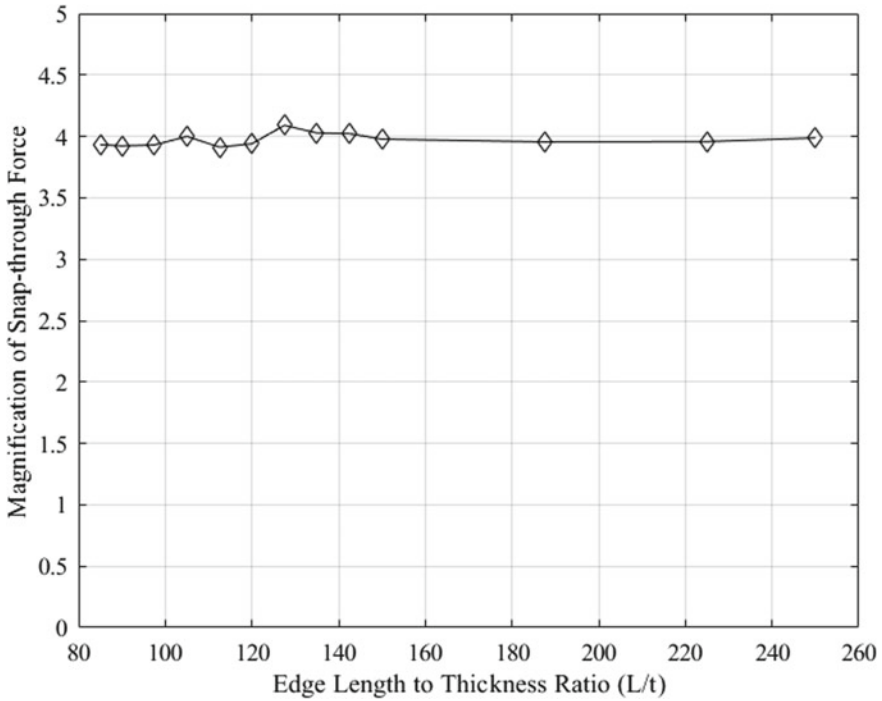


Fig. 9 Magnification of snap-through loads against aspect ratio

edge are maximum. The maximum values of stresses are the same for both the plan sizes. The pattern of both the stress fields is similar, and the stresses are not magnified upon isometric geometric magnification. The maximum σ_{11} and σ_{22} are 150.8 and 45.1 MPa respectively at an aspect ratio of 150 for both the plan sizes.

3.5 3D Analysis

Out-of-plane delamination stress (σ_{33}) can be obtained by modeling using solid continuum elements. Higher delamination stresses are observed near the curved edges (Location 1) in a cylindrical configuration. Solid continuum analysis is expected to

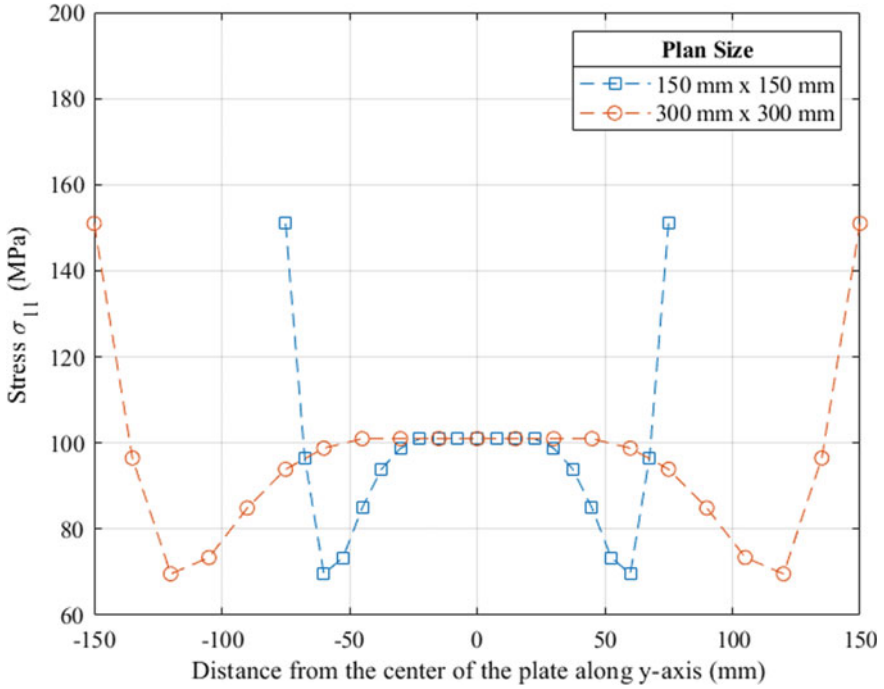


Fig. 10 Variation of normal stress σ_{11} along y-axis in cylindrical configuration shown in Fig. 3 for $L/t = 150$

recreate the curvature plots obtained through shell analysis, as out-of-plane deflections were accurately modelled. The variation of normal stress σ_{33} through the thickness at the middle of the curved edge (Location 1) for configuration 1 (refer Fig. 4) is plotted in Fig. 12 for laminates of both plan sizes. Due to different orientations of the plies, the thermal residual stresses are different in the two layers. This results in a discontinuity in σ_{33} at the interface of the two layers. The stresses in the 90° layer are higher than the stresses in the 0° layer. The out-of-plane stresses do not magnify upon isometric geometric scaling. The maximum σ_{33} stress value is 55.6 MPa for both the laminate plan sizes, for the given aspect ratio of 150 in configuration 1.

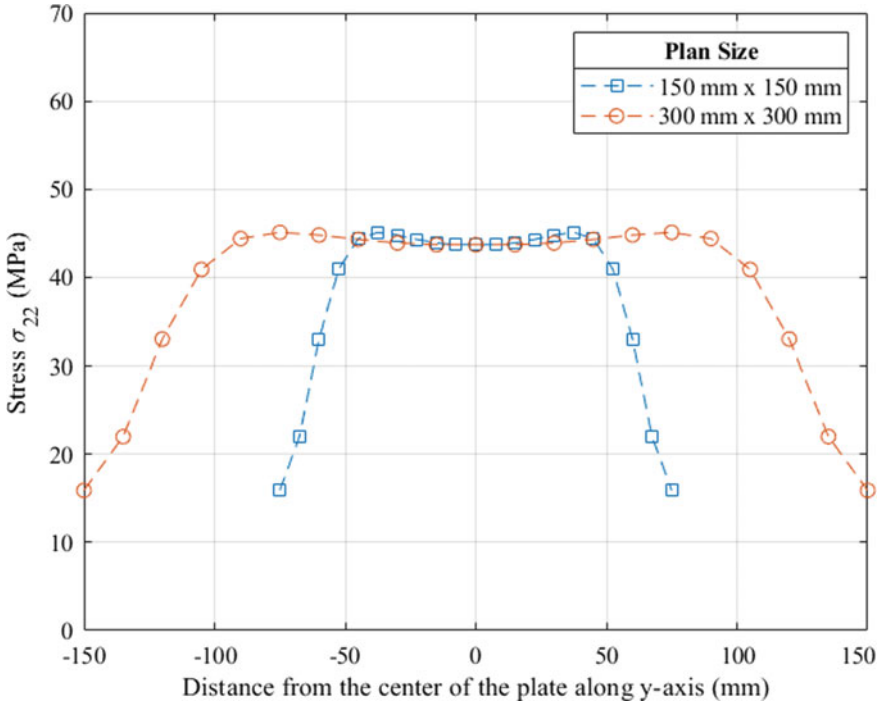


Fig. 11 Variation of normal stress σ_{22} along y-axis in cylindrical configuration 1 (refer Fig. 4) for $L/t = 150$

3.6 Magnification and Scaling Law

The magnification of properties upon isometric geometric scaling explored in Sects. 3.1, 3.2, 3.3, 3.4 and 3.5 can be summarized by a generalized scaling law in Eq. 1.

$$F_m = F_g^{m+n} \tag{1}$$

F_m = Magnification factor of a property

F_g = Isometric geometric scaling factor

m, n and p = Power of mass (M), length (L) and time (T) in the dimensional formula of the given property, respectively

An F_g value of 2 is used in the study. When the dimensions of the laminate are scaled by F_g , the properties are magnified by F_m . The observed values of F_m seem to obey Eq. 1 as summarized in Table 2.

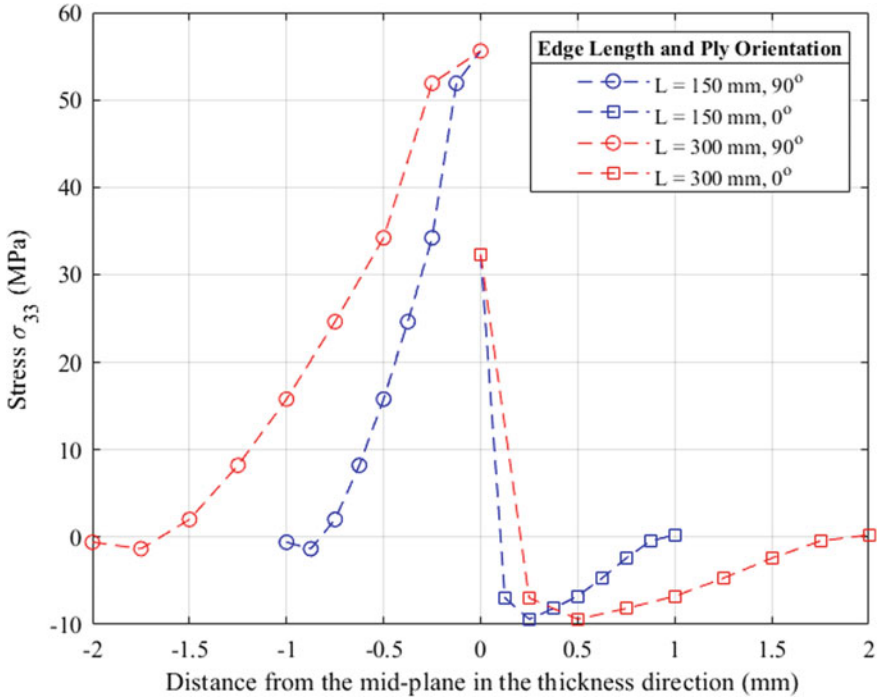


Fig. 12 Normal stress σ_{33} variation in the thickness direction, at location 1 (refer Fig. 1) in cylindrical configuration 1 (refer Fig. 4)

Table 2 Magnification factor F_m summarized for the study

Property	Dimensional Formula ($[M^m L^n T^p]$)	m value	n value	F_m
Curvature	$[M^0 L^{-1} T^0]$	0	-1	0.5
Arc angle	$[M^0 L^0 T^0]$	0	0	1
Strain energy	$[M^1 L^2 T^{-2}]$	1	2	8
Snap-through force	$[M^1 L^1 T^{-2}]$	1	1	4
Plane stress	$[M^1 L^{-1} T^{-2}]$	1	-1	1
Out-of-plane stress	$[M^1 L^{-1} T^{-2}]$	1	-1	1

4 Concluding Remarks

The existence of laminate bistability is explored through curvatures and strain energies, both of which lead to the same conclusions. Upon isometric geometric scaling, the stress field pattern is unaltered in a given stable shape. The maximum values of stresses do not magnify, which suggests that the laminate can be scaled without changing its stress-based failure criteria. With a geometric scaling factor of 2, the total volume of the laminate increases eight times, which leads to a large increase

in the strain energy of the laminate (eight times). The associated forces, like the snap-through forces, quadruple. Curvatures reduce by half. Peak values of snap-through forces and strain energy difference, ΔSE , are observed at an L/t of 142.5 and 225 respectively, for the given laminate material, ply orientation and temperature difference. Knowledge of variation of snap-through force against aspect ratio (L/t) values is useful in dimensioning laminates in morphing applications where snap-through forces are tailored to needs. The out-of-plane normal stress (σ_{33}) is useful if delamination stress is a governing failure criterion. In a cylindrical configuration, the location of maximum out-of-plane normal stress (σ_{33}) is at the curved free edge, in the ply layer having a perpendicular orientation to the edge.

Acknowledgements The first author would like to acknowledge the Combined Study and Practice Stays for Engineers from Developing Countries (KOSPICE) with Indian IITs fellowship, funded by German Academic Exchange Service: Deutscher Akademischer Austauschdienst–DAAD, during the course of this research.

References

1. Seffen K (2007) ‘Morphing’ bistable orthotropic elliptical shallow shells. *Proc R Soc A Math Phys Eng Sci* 463(2077):67
2. Reddy JN (2013) *Mechanics of composite materials: selected works of Nicholas J. Pagano*. SMIA, vol 34. Springer, Dordrecht. <https://doi.org/10.1007/978-94-017-2233-9>
3. Hasselman DP, Heller RA (2012) *Thermal stresses in severe environments*. Springer, Boston. <https://doi.org/10.1007/978-1-4613-3156-8>
4. Emam SA, Inman DJ (2015) A review on bistable composite laminates for morphing and energy harvesting. *Appl Mech Rev* 67(6):2037
5. Hyer MW (1981) Some observations on the cured shape of thin unsymmetric laminates. *J Compos Mater* 15(2):175–194
6. Brampton CJ (2013) Sensitivity of bistable laminates to uncertainties in material properties, geometry and environmental conditions. *Compos Struct* 102:276–286
7. Anilkumar PM, Haldar A, Jansen E, Rao BN, Rolfes R (2019) Design optimization of multistable variable-stiffness laminates. *J Mech Adv Mater Struct* 26(1):48–55
8. Gigliotti M, Wisnom MR, Potter KD (2004) Loss of bifurcation and multiple shapes of thin [0/90] unsymmetric composite plates subject to thermal stress. *Compos Sci Technol* 64(1):109–128

Theory of Shape for Living and Non-living Things–Based on Thin Fluid Flows in Hele-Shaw Cell



Vijayakumar Mathaiyan, R. Vijayanandh, S. Srinivasamoorthy,
Tharika Ramesh Kumar, Sivaranjani Sivalingam, and Dong Won Jung

Abstract The liquid flow inside the Hele-Shaw cell can be used to explain the shape of snowflake, rupture nucleation shape in bubble, shape of leaf, shape of cells in Plants and Animals, etc. When the pressure is applied on the thin layer of liquid, the liquid flow happens only in the edges. In addition to this, the liquid flow inside the Hele-Shaw will stop when there is no more fluid to be distributed. The brilliant patterns were based on the paradigm inside the thin cells, in which the fluid flow. Detailed study is presented in this paper.

Keywords Hele Shaw cell · Snowflake · Cells · Shape of living and non-living things

1 Introduction

Hele-Shaw used the thin sheet to visualize the flow of fluids [1]; Hele-Shaw cell-based geometry of a microfluidic device can be used to study the effect of fluid shear stress in animal cells [2]. The similarities of the shapes in living and non-living things are quite fascinating. The formation of fern like ice formation, the brilliant patterns in snowflake, the shape of jelly fish, and so on is alike because of the fluid. Though we have a theory of evolution to categories all these similarities, there is a limited research on this.

Cytoplasmic Streaming is the movement of cytoplasm inside the cell [3]. Tomi-naga et al. [4] proved that cytoplasmic streaming is responsible for the growth factor of the plant. If the cytoplasmic streaming is responsible for the growth of the plant,

V. Mathaiyan (✉) · S. Srinivasamoorthy
Department of Mechanical Engineering, Jeju National University, Jeju si 63243, South Korea

R. Vijayanandh
Department of Aerospace Engineering, Kumaraguru College of Technology, Coimbatore 641049, India

T. R. Kumar · S. Sivalingam · D. W. Jung (✉)
Department of Aerospace Engineering, Auburn University, Auburn 36849, USA
e-mail: jungdw77@naver.com

then the cellular division is also because of it. Indirectly the nuclear wall collapse is also based on the cytoplasmic streaming. Detailed analysis shows that the flow velocity is not sufficient enough to break the nuclear wall; we believe the collapse is because of increased fluid absorption of nucleus. We have found that the placement of daughter nuclei after separation from the nucleus is based on the flow physics of the cytoplasmic streaming.

Liu et al. stated that the turgor pressure decides the cell wall formation [3]. It is noted that the velocity of cytoplasmic streaming is almost stagnant in middle of two newly separated nuclei. This let us conjecture that the cell wall may form, only if the cytoplasmic streaming velocity is low in a region. Detailed information regarding the same is discussed in this paper.

2 Theory of Shape for Fluid Flow in Thin Cells

We propose the commonly observed phenomena to create a theory which fits for all thin geometry flow mechanics. When the thin fluid flows in the Hele-Shaw cell [1], the pattern inside the Hele-Shaw cell decides the pattern of the thin fluid flows and vice versa. The fluid need not to fully fill the Hele-Shaw cell to attain its paradigm, and the fluid flow happens only in the edges of the cell. We call this commonly observed behavior as thin cell flow theory. Note that the Hele-Shaw Cell can be artificial and or naturally available cell structure and it can be with or without the closed space.

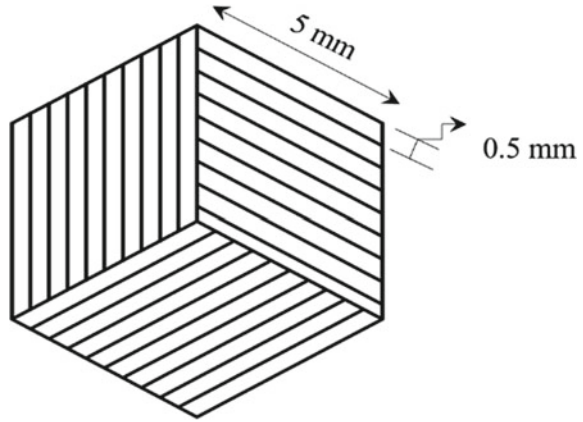
Experimental Setup and Results

A simple experimental setup is used to study the phenomena. Thin lines of 0.5 mm thickness were imprinted on the thin plastic sheet forming a rhombus of sides with 5 mm in a defined pattern throughout the entire sheet. We name the thin sheets with imprints as imprinted board. Figure 1 shows the block of pattern which is repeated several times to cover the entire sheet of dimension $0.2 * 0.3 \text{ m}^2$.

The imprinted board with a defined pattern is coated with the powder (fine-grained white concrete). A drop of water is placed on the surface of the imprinted board at various points. After several minutes, we observed the pattern formed by the water droplets. Observation shows that complete profile formed even without the wetting the entire surface of the imprinted board. If the experiment is carried in a closed Hele-Shaw cell, these surfaces will be filled with air gap. When the same experiment is carried with different pattern on the surface of imprinted board, we have found different shapes on the surface of it.

The Fig. 2(a) and (b) shows the results from the experiment. The brilliant star shape is formed on surface of powder coated imprinted board, when the water droplet is let to flow. The observation shows that the thin fluid is flowing only in the edges of the Hele-Shaw Cell. It is notable that the three rhombuses in Fig. 1 were united to

Fig. 1 Shows the block of pattern used for the experimental study



(a)



(b)

Fig. 2 **a** shows the pattern formed by water on the surface of the imprinted board. **b** shows the pattern on the imprinted board coated with powder

form a block of pattern which has 6 edges. The number of sides in the stars formed on the sheet depends upon the number of edges.

From the simple experiment, it is evident that the thin cell flow theory is valid to explain the brilliant patterns found in thin fluid flows. We also can correlate paradigm from Fig. 2 with the brilliant patterns in snowflakes. Ripples and Acceleration due to gravity predominantly changes the patterns in snowflakes. Similar results were found in the Schutzius research [5], the hydrophilic material in the shape of Swiss flag could hold the fluid onto its surface.

In addition to this, if the cross section of the parts in living things is fit in a pipe, the outer appearance looks alike. In our simple study, we have created the cross section of pineapple and fitted in the pipe, the resultant appearance is same. We call the pineapple like appearance in water as fluid pineapple. The phenomena are due to

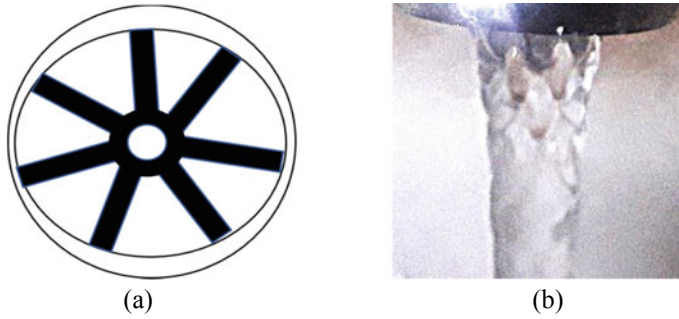


Fig. 3 **a** Cross section of Pipe, **b** Fluid pineapple

the coalescence and non-coalescence of the jet. Detailed study of this phenomenon will be presented elsewhere (Fig. 3).

3 Observations

The rod-shaped pattern was observed in the internodal cells in the *Nitella Flexilis*. The pattern gives the cylindrical shape to the cells, and the cytoplasmic streaming happens mostly in edges. This verifies the proposed theory for the fluid flow inside a Hele-Shaw cell. From the Literature review, Fanalista et al. [6] emphasized the importance of pattern inside the cell to determine the shape of it. Szymanski et al. [7] works also suggest the shape of the cell is based on cytoskeleton. If the pattern inside the cell can be altered, the shape of the cell can be changed. The shape of cells determines the shape of leaf; In other words, we can say there is a possibility of altering the shape of leaf as desired. Note that according to the theory, the flow happens only in the edges, and need not to be fully filling the cell with fluid to form a shape. Vacuole does exist in the cells of *Nitella Flexilis*.

The number of cells in a newly generated leaf will never change, and the size of it depends only on the amount of fluid flowing in it. From Ozturk et al. [8] the study of fluid inside the Hele-Shaw cell shows the pattern like *Riccia Heubeneriana*. Similarly, there is a formation of fern like shapes in the ice bubble. Thus, if the pattern inside the cell is same, the shape of the objects will be same (Fig. 4).

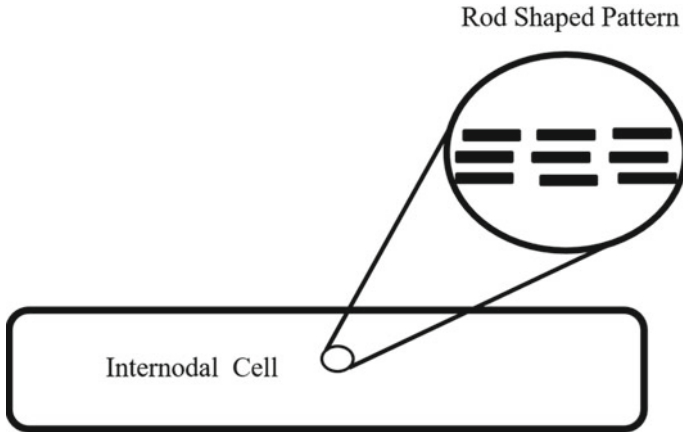


Fig. 4 Shows a typical cell with vacuoles

4 Theory of Conservation of Energy for Thin Fluid Flow

From Mathaiyan et al. [9] the theory of conservation of energy can be applied to the micro fluidics irrespective of the size. Thus, we believe that three laws of conservation are applicable even to micro scale study of thin fluid flow.

Shape of Rupture Nucleation in Bubbles

The pressure acts inside, and outside of the thin layer in bubble. From the observation, there is a pattern inside the top and bottom layer of the thin film. When the rupture nucleates the non-uniform thin film of liquid flows in cracks of the rupture. The shape of the bubble ruptures has shape of the snowflakes. The Reynolds number determines the definition star shape bubble rupture nucleation [10].

Let us consider the bubble as a structure made of brittle material which ruptures and initiates the crack. When the crack propagates in the bubble, it releases the liquid entrapped that should flow based on theory of thin fluid flow. From Brian Lawn [11], the dynamic fracture for brittle materials is derived from the energy equation. The kinetic energy plays a major part in unstable crack propagation. Considering the potential energy as constant, the kinetic energy U which can describe the dynamic fracture is modified to derive the following term,

$$dU = \frac{\pi c^2 \sigma^2}{E} \left(1 - \frac{c_o}{c}\right) \tag{1}$$

where c_o and c is the length of crack initiated at time $t = 0$ and at t_1 seconds. The equation is derived for the brittle materials, but the assumption and methodology used makes the equation a valid candidate for the derivation of crack in bubbles. The normal stress σ is the force per unit area and E is stress parallel to the plane. Let us take a small area under consideration in bubbles; the normal stress can be replaced

by surface tension T per unit length. The plane stress can be replaced by the kinetic energy of the crack propagation in bubble. Note the kinetic energy is the only source which can run parallel to the plane for the problem mentioned. The potential energy of the thin film of water in bubble is almost constant throughout the surface, and pressure acting on the bubble varies at every location during the crack propagation. Change in pressure energy dP is because of the kinetic energy of the air moving inside out of bubble. The volume of the air released out from the bubble at different points are not constant.

From the conservation of energy, for a system in flowing fluid per unit volume,

$$dU = \frac{2\pi c^2 T^2}{\rho v^2} \left(1 - \frac{c_o}{c}\right) = -dP \quad (2)$$

where v is the velocity of the crack propagation and ρ is the density of the liquid. The above equation is an attempt to derive a relation for a crack in the bubble. The crack propagation in bubble can also be visualized as a flow of thin liquid under the Hele-Shaw Cell and will obey thin cell fluid flow theory. The ice formed in the bubble under frozen temperature proves that there is a defined pattern in between the layers of the bubble.

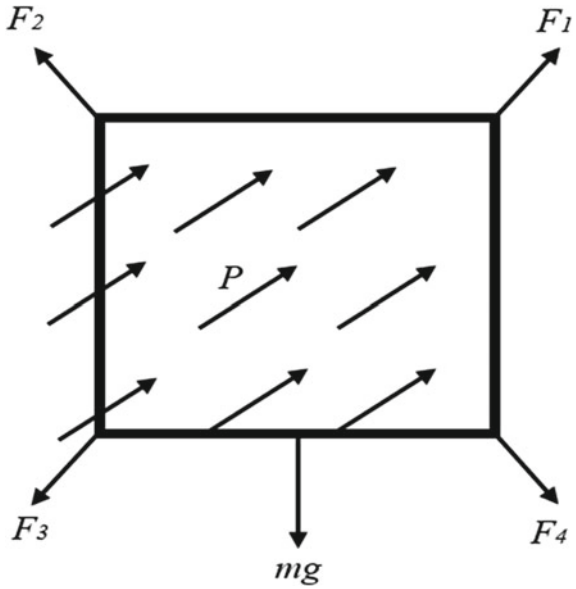
Shape of the Snowflake

Consider a certain mass of fluid from the cloud which will become a snowflake. The fluid undergoes the crystallization because of the decrease in temperature. If the fluid temperature is decreased, the density of the fluid increases resulting in increased pressure. According to thin cell flow theory, the pressurized fluid flows only in edges of the Hele-Shaw cell. It is observed that all the snowflakes grow only in the edges. The brilliant pattern is based on the flow inside the cell. From the infamous sandbag experiment, the Lissajous curve is formed when movement of sandbag with mass reduction is visualized. In addition to this, the snowflake images captured in Schaeffer et al. [12] matches with water surface under vibration. We also believe the same happens in the snowflake; hence we use the force equilibrium for the study. The pressure applied on the snowflake distributes the pressurized fluid in the edges at a mass flow rate.

If we consider fluid trapped inside the snowflake of a rectangular shape with mass m falls from the cloud undergoes the ripple due to acceleration due to gravity g . The mass flow rate of ice growth and acceleration due to gravity creates the brilliant pattern in the snowflake. Pressure acting on the snowflake is from various sources in the atmosphere. Some of the sources are ice crystallization growth, wind force, and so on. If u is the velocity at which the mass flow rate dm/dt takes place in edges, the pressure applied is force per unit area. The summation of forces at various edges of the four-sided rectangular snowflake may not be equal to 0, because of the non-uniform pressure distribution.

In the Fig. 5 below, the pressure is applied on both sides of the snowflake perpendicularly. The pressure applied will result in flow of fluid at a mass flow rate; the edge effect causes the flow only in the sides. Thus, the force is a function of mass

Fig. 5 Pressure applied on the Assumed small amount of fluid resulting in a certain mass flow rate in the edges



flow rate \dot{m} and velocity u in the sides as show in equation.

$$\frac{\sum F - mg}{dA} = dP \tag{3}$$

The summation of the forces can be written in terms of the mass flow rate and velocity as in equation.

$$\sum F = \sum \dot{m}u \tag{4}$$

If the change in pressure is zero, the force term is equal to 0. The resultant equation will be as shown below.

$$mg = \sum \dot{m}u \tag{5}$$

This shows that even the variable, acceleration due to gravity, affects the fluid flow. The displacement x of the fluid flow in the edges, for this condition, at time t from 0 can be written as

$$x = \frac{gt^2}{2 \ln m} \tag{6}$$

The constants were not included in the above equation. In other words, the ripple creates the pattern inside the snowflake, the pressure on it induces the thin fluid flows.

The growth of snowflake follows edge effect with air gaps in it following the theory. The resultant is a brilliant-patterned snowflake.

Shape of Plant and Trees

If we consider that there is a connection in shape between the fern like formation inside the snow bubble and fern. The major factor in common for the ice formation and shape of the plant parts is the fluid flow and acceleration due to gravity. Since the acceleration due to gravity remains almost same for both phenomena, the only factor which gives the similarity is the fluid. Stephanie et al. [13] review states that Acyl chains in membrane lipids are responsible for the membrane fluidity. In plants, the fluid flow or cytoplasmic streaming is studied in terms of pressure. Tominaga et al. [4] work shows that the pressure of the liquid absorbed decides the size of the plant. The study from the Petro et al. [14] also proved the importance of fluid content for the shape of leaf. Detailed study about the shape of leaf was carried out by Dhkar et al. [15] if the pressure contributes for the growth of plants, the same pressure is responsible for the cellular reproduction.

Shape of Organs

When water flows from a cross section with holes in shower head, the outflow shape will be similar to the shape of wing. The wings of the birds also follow the same principle. The part connecting the wings to body has different outflow velocities at different localized position which decides the shape of the wing. The pressure of the blood flow is a dominant factor in wing size and shape. Study on the position of the heart in the bird, and the cross section where the wing is attached with body can be used to predict the size and shape of a wing.

Shape of heart and all organs depends on the flowing inside and outside of it. The pressurized blood flow inside the organ shapes it. When the blood flows inside any organ, blood inflates it. In real world environment, if the fluid flows on a surface. The surface always ends up with a circular cross section. This is the reason behind the circular cross section in all the organs including nerves. The folds in the brain are also because of fluid inside and outside of it. Cerebral fluid plays a major role in the creation of folds in the brain. Brain and gut connection were spoken in plenty of research work, but most of them have not considered the permeability of gut. We believe that permeability of gut plays major role in the connection between both the organs. The connection can even create grunting in the brain. Draining of the cerebral fluid followed by the pressure difference from the gut in connection can generate this noise. Detailed research can help the patients avoid brain problems because of the gut issues. Note that it is possible to have grunting sound in the head.

Shape of Leaf

Thin sheet of liquids form when two similar laminar liquid jets made to interact with each other at a certain angle and the fluid flows in edge as mentioned before. [16] The shape of the liquid sheet formed looks like the shape of a leaf. Since the shape of the liquid sheet formed is based on the annulus through which the fluid flow, the shape of the leaf should also because of the cross-sectional shape of the

petiole. Kolmogorov model for the fragmentation is used to simulate the segregation in the bubble rupture. The paradigm formed by the rupture can be explained from the Smoluchowski's kinetic aggregation. [17] We believe the same can be used to simulate the fragmentation in the leaf.

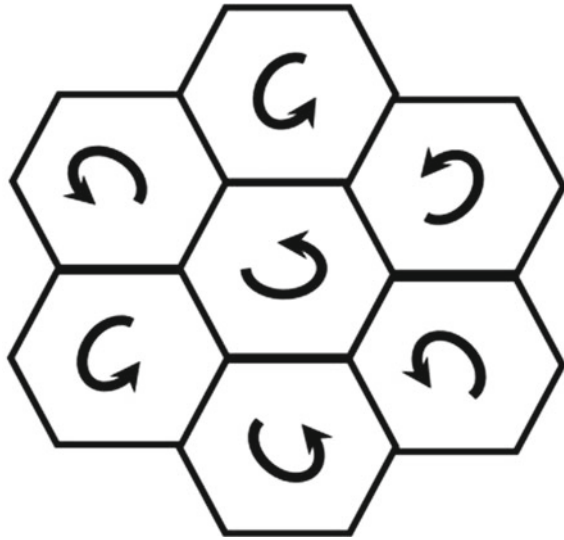
5 Theory of Conservation of Energy for Thin Fluid Flow

Density of the water decides the crystal structure of ice [18]. Reference table in Brini et al. shows the structure for the respective density of water. Heyden et al. [19] assumed the mass density of cytoplasm as 1 gm/cm^3 . Wayne et al. [20] and Schwuchow et al. [21] measured the cytoplasmic streaming in *Nitellopsis* and Apical cells. The density of both the cells is almost 1.05 g/cm^3 and their shape is rectangular. Tetrahedral arrangement of the hydrogen bonds in the water is because of its property. The disordered, cage like structure is found in the water. With increase in density, the distinct hexagonal shaped molecular arrangement is seen. [18] The observation of bath under vibration with a droplet on top of it shows that the pressure variations can provide the same results as in snowflakes. Some of the commonly observed polygons are in the triangular, square, hexagon, octagon and dodecagon shapes. If the molecular structure decides the shapes in snowflakes, then the same is responsible for the shape of cells.

The shape of the cell in almost all living organism is polygonal in shape. Polygonal shape is because of the molecular arrangement of water. The osmotic pressure inside the cell changes with variation in the velocity of liquid flowing in it. Change in pressure will result in ordered hexagonal or polygonal shape of the fluid. If the fluid has the shape of polygon on it, the cell wall or distinct separation happens in the location of low pressure around it. Thus, we conclude the brilliant polygonal shape of the cell is because of the molecular arrangement of the water.

The molecular arrangement in the ice and lattice formation from Eddi et al. [22] are almost similar. Though temperature plays a major role in ice formation, it is evident the pressure change can create a similar pattern. The change in cytoplasmic streaming each cell may be different. Thus, the shape and size need not be same. Moreover, the density gives the clue about the shape of the cell. The usage of Fibonacci spheres made the water molecules evenly distributed [23]. We believe that the Fibonacci series in the living things is because of chemical properties of fluids. Thus, the molecular structure of the fluid is the responsible for the presence of Fibonacci series. Note Keyzer et al. [40] stated that the Fibonacci series fits at the molecular level in nature. This proves that the molecular structure of water is responsible for the shape of cell and the presence of Fibonacci series. Figure in ref. [24] shows the hexagonal structure of the leaf cells from *Lophozia Silvicola*. The hexagonal structure is common in the snowflakes because of water molecular structure. The same is reflecting in the cells

Fig. 6 Schematic of the fluid flow in cells



as shown in the Fig. 7. Corneal Endothelium cells in rabbit are also in hexagonal shape [25].

Cellular Flow Physics

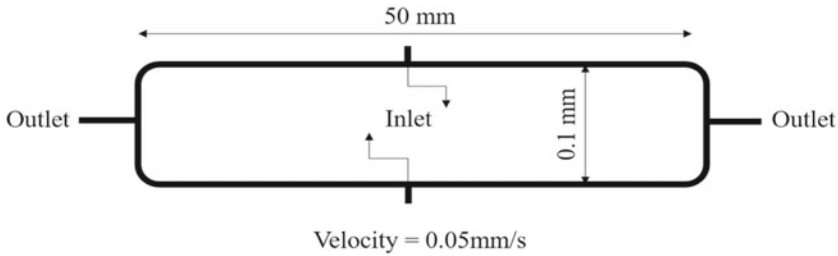
Howard et al. wrote about the fluid circulation noticed in epithelial cells. If the fluid flow in a cell flows in clockwise direction, transport of fluid in the nearby cell are in anticlockwise direction. Thus, the flow direction in the cells can be represented as shown in Fig. 6. If the vibration due to the heart is not considered, then the fluid circulation Γ inside the cell can be written as follows from [26]. Vorticity is infinite at the center, and it is called as Vortex Center. Note that the nucleus is at the center of the cell.

$$\Gamma = \oint v_{\theta} ds = \int_0^{2\pi} \frac{K}{r} r d\theta = 2\pi K \quad (7)$$

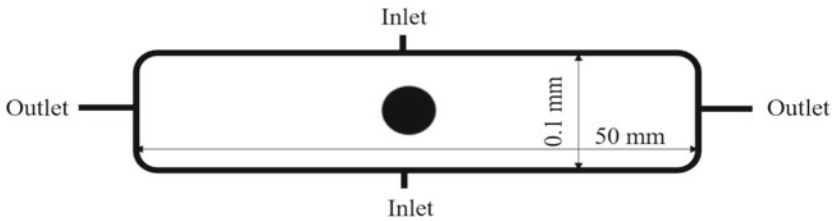
where r is the radius of the circular path formed around the vortex center, K is the vortex strength, and v_{θ} is the velocity distribution.

6 Theory Numerical Simulation and the Results

No changes in the governing equations were done for the computational study in Howard et al. [27] for microscale flow field. Hence no change is done to the governing equation in our work. Computational domain used for the numerical analysis to study the flow dynamics is shown below.



(a) Computational domain without the nucleus with velocity inlets and pressure outlets



(b) Computational domain with the nucleus having pressure inlets and outlets

Fig. 7 Computational domain used for the flow physics visualization for cells of Nitella. **a** Computational domain without the nucleus with velocity inlets and pressure outlets **b** Computational domain with the nucleus having pressure inlets and outlets

Figure 7 shows the computational domain used to study the flow physics of Cytoplasmic streaming inside the internodal cell of Nitella Flexilis. The domain is changed to simplify the complexity behind natural flow process in the cell and note that cytoplasmic streaming is the reason for cellular reproduction. Position of inlet is right above and below the nucleus to study the maximum possible effect of streaming. Based on this, pressure rise inside cell is expected to break the nucleus wall. It is predicted that the cell wall formed inside cell during mitosis is also based on cytoplasmic streaming. Numerical values required for the study in Nitella cell is taken from Kikuchi et al. [28].

Observation shows that there is a possible effect of cavitation, and localized turbulence because of cavitation. Meairs et al. [29] wrote a detailed review which confirms the possibility of microbubble inside the cells. Effects of micro bubbles are more than that of the macro bubbles [28], and the turbulence depends on the size scale function [31]. Cavitation with bubble–bubble interaction can be used for a treatment. [32] The effects of the bubbles and other flow phenomena associated with the cell division were not considered in the numerical simulation.

In order to analyze the above theory, a numerical study in 2D is carried out using Ansys Fluent [33]. From the Foisner et al. [34] the nucleus of internodal cell is in the range of 22 to 56 μm . The domain dimension of $50 * 0.1 \text{ mm}^2$ is set with pressure inlet and outlet as the boundary condition shown in the Fig. 7. The setup is

numerically studied with and without nucleus for a velocity range. The results were analyzed to know the impact of cytoplasmic streaming on nucleus wall.

Numerical results show that the velocity of flow streaming is high at a certain distance from the nucleus to the cell sides. The low-pressure regions are on the sides of nucleus because of this, the daughter nucleoli will move only in its sideward. Though the increase in streaming velocity cannot generate enough force required for the rupture of nucleus wall, we believe that the nucleus may observe the fluid in excess and swell. The increase in size of the nucleus and pressure difference from inside out may collapse the nucleus wall. When the rupture happens, the nucleoli will move to the low-pressure region in the cell. Cell wall is made up of Polysaccharide which is secreted by the components in the cell [35]. It is noted that the cell wall is formed in the region of low pressure. From Fig. 9, the flow analysis of the domain without nucleus shows the low-pressure region is exactly in the place of nucleus. Increase in nucleus size increased the flow velocity in the domain.

The plant resembles like a water fountain with the trunk, and top at which water distributes. Growth of the plant keeps on increasing with increase in osmotic pressure. It is noted that almost all the trees have the leaves only on the top following the fountain phenomena. Cytoplasmic streaming which controls the cellular division and cell wall formation decides the fountain phenomena in plants. Even growth of branches depends on the cytoplasmic streaming. The shape of leaf depends on the cells in it, if the pattern inside the cell can be changed, there is a possibility that the leaf shape can also be changed.

The theories can be used to change the property of any cells for its growth or destruction. If the cell number is limited with increase in fluid flow, the cells must reproduce or die. If the fluid flowing inside the organism is modified by changing flow pattern, the property of the cell may change. We believe the same concept can be used to cure the cancer. There is a notable change in Cytoplasmic streaming of the cancer cell when compared to the healthy cell [36]. The flow dynamics inside the cancer cells can be determined with the pattern inside it. The changes in the pattern may kill the cell or reduce the nucleus division. The viruses were detected using nucleic acid and the effective methodology is to target it [37]. Making changes to the nucleic acid of the virus may result in its destruction. Even in the field of Cryogenics, the theory may give better understanding of ice formation.

Results

See Figs. 8 and 9.

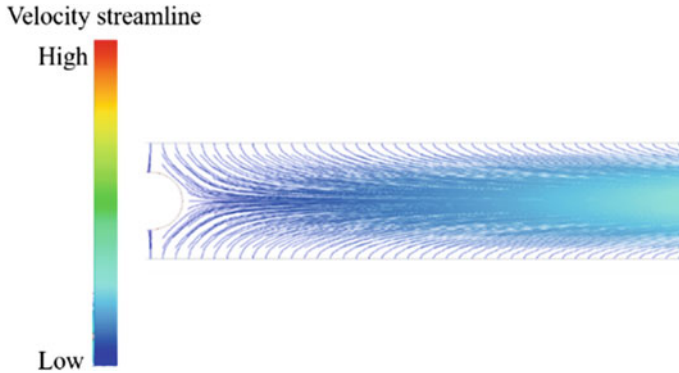


Fig. 8 Velocity streamline for the computational domain with nucleus diameter of 0.05 mm for velocity 0.05 mm/s

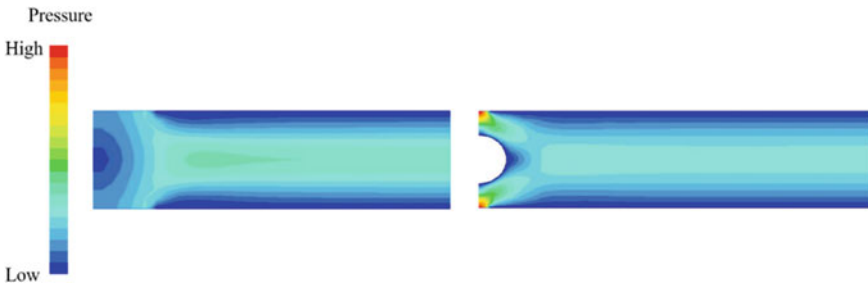


Fig. 9 Pressure contour for the computational domain for velocity 0.05 mm/s. **a** without nucleus **b** with nucleus diameter of 0.05 mm

7 Conclusion

Thin cell flow theory shows the physics behind the formations of brilliant pattern in thin fluid flow. This theory can explain the shape of snowflakes, cells of plants and animals, etc. Acceleration due to gravity, ripple, and mass flow rate creates patterns in the Hele-Shaw cell, which ends up as the brilliant symmetrical paradigm in living and non-living things. We have found that the cytoplasmic streaming decides the placement of daughter nuclei in the respective positions and cell wall formation. Due to this, the shape of the liquid in its various dynamical behavior is reflecting in all living and nonliving things. Mammary glands of human being are a good example. The shape of the mammary glands is same as the shape of droplet on the smooth surfaced wall. The application of the theory can even be used to cure cancer and virus infection.

Shape of animals like jelly fish, parts of the human beings, and so on depends on the fluid flowing in it. The fluid flow decides the cellular division and gives the shape to it. There is an asymmetrical cellular division following Fibonacci series in

plants [Fleming] [38] and animals [Willie] [39]. The presence of asymmetrical cell division following Fibonacci, or any other series can also be explained using the theory. Properties of fluid is responsible for the presence of Fibonacci series in the living and non-living thing. Note that Keyzer et al. also observed the molecular level fit of Fibonacci series in nature.

The shape of the water molecular structure is explained in correlation with the shape of snowflake. Their shapes depend on the molecular structure of water which is always polygonal in shape [Brini][18]. The shape of the cell also depends on the fluid flow inside it. If the molecular structure of water changes the shape of snowflake, then the same is responsible for polygonal shape of the cells. Moreover, the lattice arrangements of the series of droplets in Eddi et al. may be reason behind the organized growth of the normal cells in living things. The images from the Howard et al. [27] and Saenz et al. [41] shows the presence of circulation inside the cell. The snowflake, and cells like Squamous Epithelia cells of the frogs, Corneal Endothelium cells of rabbit, etc. are hexagonal in shape.

After a certain age of the cell in plants, the vegetative reproduction does not happen even with increase in cytoplasmic streaming. Endoplasmic Reticulum (ER) is the responsible for the nuclear wall formation [Lu] [43], so there is a good chance that the ER may be protecting the nucleus from streaming. If ER safeguards the nucleus from the streaming after a certain age, the artificial detachment of the ER from nucleus with increased cytoplasmic streaming may induce the reproduction. Information regarding the ER removal is provided in the study of Schwarcz et al. [42].

If the fluid flow influences the growth and various factors in the plants, and animals. Mutation of DNA is because of the fluid flowing in or around it. Fluid flow in the earth may have experienced serious changes with its climatic change for millions of years. The evolution may have happened because of the gradual changes in environment of living organism. Similar study from Sarkar et al. [44] shows the climatic change plays major role in evolution. Arumuganathan et al. [45], provided the contents of the Nuclear DNA which provided better insight of the resemblance in plant species.

Acknowledgements Our sincere thanks to Assistant Professor Sivanesan Iyyakannu, Konkuk University, South Korea for his valuable suggestions. We also would like to thank Prof. V. R. Sanal Kumar from Kumaraguru College of Technology, India and Prof. Sunghwan Jung from Dankook University, South Korea for their continuous support to finish the work.

References

1. Shaw H (1898) The flow of water. *Nature* 58(1489):34–36
2. Delon LC et al (2020) Hele Shaw microfluidic device: a new tool for systematic investigation into the effect of the fluid shear stress for organs-on-chips. *MethodX* 7(100980):1–17
3. Liu S et al (2017) Intracellular microfluid transportation in fast growing pollen tubes. In: *Modeling of microscale transport in biological processes*, pp 155–169

4. Tominaga, M et al (2013) Cytoplasmic Streaming Velocity as a Plant Size Determinant. *Cell Press* 345–352
5. Schutzius TM et al (2014) Morphing and vectoring impacting droplets by means of wettability-engineered surfaces. *Sci Rep* 4(7029):1–7
6. Fanalista F et al (2019) Shape and size control of artificial cells for bottom-up biology. *ACS Nano* 13:5439–5450
7. Szymanski D et al (2018) The actin cytoskeleton: functional arrays for cytoplasmic organization and cell shape control. *Plant Physiol Am Soc Plant Biol* 176(1):106–118
8. Ozturk D et al (2005) Flow-to-fracture transition and pattern formation in a discontinuous shear thickening fluid. *Commun Phys* 3(1):1–9
9. Mathaiyan V et al. Theoretical Modelling of Thin Air Film Thickness in Miscible Liquids. In: *Advances in Mechanical and Materials Technology*, pp 817–824
10. Thoroddsen ST (2012) *Micro-Bubble Morphologies Following Drop Impacts onto a Pool Surface*. 708:469–479. Cambridge University Press
11. Lawn B (1993) *Fracture of Brittle Solids*, 2 edn. Cambridge University Press, pp 86–105
12. Schaefer VJ (1946) The production of ice crystals in a cloud of supercooled water droplets. *Science* 456–459
13. Ballweg S et al (2017) Control of membrane fluidity: the OLE pathway in focus. *Biol Chem* 398(2):215–228
14. Petrov P et al (2018) Relationship between leaf morpho-anatomy, water status and cell membrane stability in leaves of wheat seedlings subjected to severe soil drought. *J Agron Crop Sci* 219–227. Wiley Publication
15. Dhkar J et al (2014) What determines a leaf's shape? *EvoDevo* 1–19
16. Bush JWM et al (2004) On the collision of laminar jets: fluid chains and fishbones. *J Fluid Mech* 511:285–310. Cambridge University Press
17. Eggers J, Villermaux E, *Physics of Liquid Jets*. Rep Prog Phys 1–79. IOP Publishing
18. Brini E et al (2017) How water's properties are encoded in its molecular structure and energies. *Chem Rev* 12385–12414. American Chemical Society
19. Heyden S et al (2016) Investigation of the influence of viscoelasticity on oncotripsy. *Comput. Methods Appl Mech Eng* 1–9.
20. Wayne R et al (1991) The Density of the Cell Sap and Endoplasm of *Nitellopsis* and *Chara*. *Plant Cell Physiol* 32(8):1137–1144
21. Schwuchow JM et al (2000) The density of apical cells of dark-grown protonemata of the moss *ceratodon pupureus*. *Protoplasma* 225–233
22. Eddi A et al (2009) Archimedean lattices in the bound states of wave interacting particles. *Lett J Exploring Front Phys* 56002:1–6
23. Kildgaard JV et al (2018) Hydration of atmospheric molecular clusters: a new method for systematic configurational sampling. *J Phys Chem A* 1–11
24. Arizona State University, USA. <https://askabiologist.asu.edu/chlorophyll-and-chloroplasts>
25. Koudouna E et al (2017) Immune cells on the corneal endothelium of an allogenic corneal transplantation rabbit model. *IOVS* 58:242–251
26. White FM (2018) *Fluid Mechanics - 8th Edn*. Mc Graw Hill Publications
27. Howard, R et al (2019) Cytoplasmic convection currents and intracellular temperature gradients, *PLOS Comput Biol* 1–17
28. Kikuchi K et al (2015) Diffusive promotion by velocity gradient of cytoplasmic streaming in nitella internodal cells. *PLOS One* 1–12
29. Meairs S et al (2007) Ultrasound, microbubbles and the blood-brain barrier, *Progr Biophy Mol Biol* 354–362
30. Brennen C (1995) *Cavitation and Bubble Dynamics*. Cambridge University Press
31. Harlow FH et al (1968) *Transport of Turbulence Energy Decay Rate*, United States Atomic Energy Commission, pp 1–11
32. Yuan F et al (2015) Cell Membrane deformation and bioeffects produced by tandem bubble-induced jetting flow. *Appl Phy Sci PNAS PLUS* E7039–E1047
33. Fluent (2014) *Fluent Simulation Software Package*, Ansys Inc., Pennsylvania, USA

34. Foissner I et al (2014) Characean internodal cells as a model system for the study of cell organization. *Ine Rev CellMol Biol* 311:308–353
35. Lampugnani ER et al (2018) Building a plant cell wall at a glance, *J Cell Sci* 1– 6
36. Sherwin RP et al (1967) The occurrence of a cyclosis-like phenomenon in human lung cancer cells in vitro, *Cancer Res* 152–158
37. Shen M et al (2020) Recent advances and perspective of nucleic acid detection for coronavirus. *J Pharm Anal* 97–101
38. Fleming AJ (2002) Plant mathematics and fibonacci's flowers. *Nature* 18:1–1
39. Willie JJ (2012) Occurrence of fibonacci series in development and structure of animal forms: phylogenetic observations and epigenetic significance. *Nat Sci* 4(4):1–8
40. Keyzer H et al (2015) Molar ratios of therapeutic water-soluble phenothia-zine.water-insoluble phospholipid adducts reveal a fibonacci correlation and a putative link for structure-activity relationship. *RSC Adv* 20865–20877
41. Saenz PJ et al (2018) Spin lattices of walking droplets. *Phy Rev Fluids Gallery Fluid Motion* 100508:1–3
42. Schwarz DS et al (2016) The endoplasmic reticulum: structure, function and response to cellular signaling. *Cellular Mol Life Sci* 73:79–94
43. Lu L et al (2009) Cisternal organization of the endoplasmic reticulum during mitosis. *Mol Biol Cell* 3471–3480
44. Sarkar P et al (2009) Plant cell walls throughout evolution: towards a molecular understanding of their design principles. *J Exp Bot* 3615–3635. Advance Access Publication
45. Arumuganathan K et al (1991) Nuclear DNA content of some important plant species. *Plant Mol Biol Rep* 208–218

Investigation on Impact Characteristics of Concrete Under Varying Drop Height of Pendulum Impact



K. Senthil, R. Sharma, A. Thakur, M. A. Iqbal, and A. P. Singh

Abstract The experiments and simulations were performed on concrete cylinders by impacting varying drop weight with hemisphere shape nose under angular motion. The dynamic compression tests were studied under pendulum impact testing frame. The aspect ratio (l/D) of concrete cylinder (100×200 mm) and mass of impactor was kept constant i.e., 2 and 60 kg respectively, whereas drop angle of dynamic tests were varied as 13, 20, 28, 36, 46 and 58° corresponding drop height was varied as 49–941 mm. The numerical investigations have been carried out on concrete cylinders using ABAQUS/Explicit finite element program. A well-known rate dependent constitutive model Concrete Damage Plasticity model (CDP) available in ABAQUS was used to model the inelastic response of concrete. The numerical results in light of peak force and failure pattern were investigated and compared with the experimental results. It was also observed that the material parameters affect the response history significantly with varying drop angle. The subjective CDP parameters predict the behaviour of concrete strength very well as compare to original parameters. Overall, the results thus obtained were found in good agreement with the experimental results. The results revealed that the uniaxial compressive strength of cylinder was sensitive to rate of loading which can be characterized by modifying the failure parameters under CDP.

Keywords Dynamic strength · Experiment · Simulations · CDP model

1 Introduction

Concrete is widely used material in structural components is often subjected to dynamic loadings, therefore its mechanical properties under different rate of loading

K. Senthil (✉) · R. Sharma · A. Thakur · A. P. Singh
Department of Civil Engineering, National Institute of Technology Jalandhar, Jalandhar 144011,
Punjab, India
e-mail: kasilingams@nitj.ac.in

M. A. Iqbal
Department of Civil Engineering, Indian Institute of Technology Roorkee, Roorkee 247667,
Uttarakhand, India

© The Author(s), under exclusive license to Springer Nature Singapore Pte Ltd. 2022
T. Tadepalli and V. Narayanamurthy (eds.), *Recent Advances in Applied Mechanics*,
Lecture Notes in Mechanical Engineering, https://doi.org/10.1007/978-981-16-9539-1_25

353

are of great significance. Watsteint [1] investigated 3×6 -in. cylinders using drop hammer machine for a maximum strain rate of 10 in. per in. per second. The compressive strength of concrete enhanced with higher strain rate loadings with maximum ratio of dynamic to static compressive strength of about 1.8 for a straining rate of 10 in. per in. per sec. The resistance of concrete to impact was also enhanced with increase in rate of application of load. Weidner et al. [2] performed a series of drop test on $\phi 100 \times 200$ cylinders from a height of 8 and 16 ft. Test data was acquired and compared between the strain gage and load cell data. The dynamic strength of concrete in compression was between 1.1 and 3.2 times the static strength; the dynamic strength of concrete in tension was between 1.0 and 4.1 times greater the static strength. Ross et al. [3] found that dry concrete has negligible sensitivity towards strain rate below the transition strain rates $(1-10) \text{ s}^{-1}$. However, for wet concrete there is considerable rise in strength even at lower transition strain rates. Lee et al. [4] found that the inertial effect because of strain acceleration, density and geometry of specimen produces non conservative results when applied in relation to dynamic increase factor (DIF's) of ACI and other fib models whereas considering pure rate effects improved the predictions of dynamic strength enhancement of concrete. Pajak [5] stated that the dynamic tensile strength of concrete can achieve the value of 13 times its quasi-static strength. The tests conducted using hydraulic and drop hammer machine have lesser scattering than research data obtained using split Hopkinson pressure bar (SHPB). However, due to the lesser test duration the results obtained using technical scopes of the measure can have additional distortions.

Mellinger and Birkimer [6] conducted test on cylinders under end impact concluded that the compression wave from impact propagate along the specimen and the reflected wave at other end gets propagate as tension wave. When total stress from reflected wave minus incident compression wave exceeded its tensile strength, the concrete sample would fail. Kaneko et al. [7] states that the parameters for failure criteria can be determined from the experimental results on scaled down cylinders. The parameters were defined such that it would represent a decrease in shear modulus and failure strength, and can be decided so that experimental and numerical results can match with each other. Elfahal et al. [8] found that the size effect has a significant effect on the time to reach the peak stress in concrete cylinder as generally for lower sized specimens takes longer time to reach peak stress. The materials models available in ABAQUS are simplified uniaxial models and may not be suitable for studying compressive dynamic failure of concrete because of stress triaxiality under dynamic conditions. Williams [9] found that the important parameter for concrete in tension include the tensile strength and the post cracking tension stiffening behaviour. Neglecting tension-stiffening effects in finite element method (FEM) models by using a simple tension cut off result in tensile stresses in the region of a crack having a spurious dependency on the mesh size. Wang et al. [10] found that the short autoclave aerated concrete (AAC) cylinders had compressive failure mode characterized by parallel vertical cracks and exhibited excellent energy

absorbing ability. Strain rate sensitivity in shear failure mode is much greater than that in splitting failure mode.

From the past literature, it was observed that there is no standard procedure mentioned to test the dynamic response of concrete as compared to static testing. Previous testing results showed high variations in the results due to testing difficulties associated with dynamic loadings due to different method of loading and different energy loss mechanisms involved. Therefore, this study is an attempt to study the dynamic response of concrete under different impact energies. In order to understand the effect of varying rate of loading, experimental and numerical investigations have been carried out on concrete under varying rate of loadings. The experiments were carried out on conventional plain concrete cylinder of M40 grade and tested against varying drop height, see Sect. 2. Also, the finite element simulations were performed using ABAQUS finite element software and the Concrete Damage Plasticity (CDP) model was used in order to predict the behaviour of concrete, see Sect. 3. The material parameters of CDP model were investigated thoroughly and subjective parameters were presented in order to predict the response history of target, see Sect. 4. The effect of drop height on the concrete specimens in light of dynamic characteristics were studied in Sect. 5.

2 Experimental Investigations

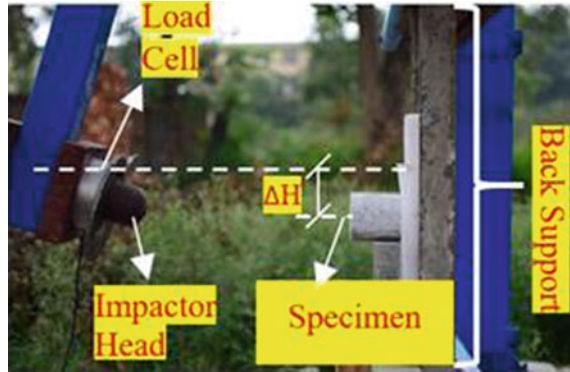
The concrete specimens were prepared as per the conventional approach and the mix design was carried out as per IS 10262:2019 [11]. The source materials such as cement, sand, coarse aggregate and fine aggregates were tested as per the standard procedures. The samples were cured for 90 days and it was dried before testing.

The experiments were performed using pendulum impact testing frame having capacity of 250 kN, see Fig. 1. The concrete cylinders were tested under varying drop weight with hemisphere shape nose under angular motion. The aspect ratio

Fig. 1 Pendulum impact testing frame



Fig. 2 Testing on concrete cylinders



(I/D) of concrete cylinder (100×200 mm) and mass of impactor was kept constant i.e., 2 and 60 kg respectively, whereas drop angle of dynamic tests were varied as 13, 20, 28, 36, 46 and 58° corresponding drop height was varied as 49–941 mm. The samples were placed at right position in order to avoid any eccentricity and the overall arrangement of the experiment is shown in Fig. 2. The ensure the fixity, the concrete cylinder were packed with help of the cushion materials. The pendulum was released with help of the steel rope which are connected with the winch. The winch was designed for manual operations and having 8 mm diameter ropes. The translational velocity was measured from the experiment using Tracker software's.

3 Constitutive Modelling

The behavior of concrete have been incorporated using CDP constitutive model. The model is able to reproduce the key characteristics of concrete, primarily the asymmetric strength behaviour in tension and compression, pressure sensitivity associated with yielding and stiffness degradation associated with damage in tension and compression. The model is idealized as homogeneous and isotropic due to the simplicity of modelling technique and similar elastic moduli observed in compression and tension stress–strain diagrams. The elastic parameters as well as the CDP parameters available in [12–17] were shown in Table 1. The concrete damage plasticity model parameters such as (d_t) tension damage, compression damage (d_c), $\tilde{\varepsilon}_t^{pl}$ and $\tilde{\varepsilon}_c^{pl}$ along with tension recovery were shown in Table 2. The parameters corresponding to 36° were modified slightly which were available in literature [15] and these parameters were treated as Set 1. Whereas the remaining parameters corresponding to 13, 20, 36, 46 and 58° were subjective parameters proposed in the present study.

Table 1 Material model parameters

Elastic parameters [12]				
ρ	E	ν		
2300 kg/m ³	20.82 GPa	0.15		
CDP parameters				
σ_{b0}/σ_{c0} [13]	ψ [14]	ϵ [15]	K_c [15]	μ [16]
1.16	32°	0.1	0.67	0.0001

Table 2 Set 1 and set 2 parameters

Drop height (m) and drop angle	Parameters				
	$\tilde{\epsilon}_t^{pl}$	$\tilde{\epsilon}_c^{pl}$	d_t	d_c	Tension recovery
0.035-13° (Set-2)	0.028	0.012	0.96	0.90	0.00015
0.109-20° (Set-2)	0.020	0.024	0.96	0.90	0.00015
0.223-28° (Set 2)	0.060	0.048	0.96	0.90	0.00016
0.382-36° (Set-1)	0.198	0.121	0.96	0.90	0.01800
0.605-46° (Set-2)	0.300	0.500	0.96	0.90	0.02000
0.927-58° (Set-2)	1.100	0.300	0.98	0.95	0.02500

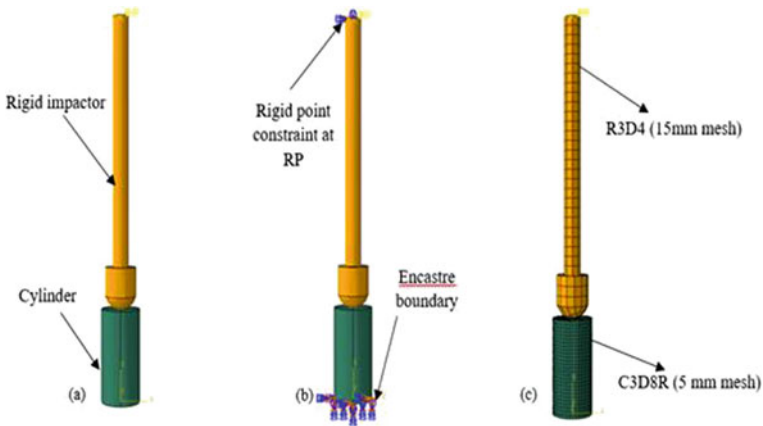


Fig. 3 Modelling of **a** impactor **b** boundary conditions **c** mesh size

The finite element simulations were performed using ABAQUS/CAE. The concrete target modelled as deformable body and the impactor was modelled as discrete rigid body. The height and diameter of the concrete cylinder was 200 and 100 mm respectively. The target as well as impactor is shown in Fig. 3(a). The base of target in the experiment was held in place using steel support assembly. Therefore, to

match the boundary conditions, fixed boundary was assigned. A reference point was assigned to the impactor to measure the force versus time response, see Fig. 3(b).

The mesh convergence was not performed however, the sensitivity of mesh would be considered in the future study. The mesh size in the concrete target 5 mm as C3D8R type was considered in the present study. Similarly, the 15 mm mesh size of R3D4 type was considered for the impactor, see Fig. 3(b). The translational velocity was measured from the experiment and the same velocity was defined on the impactor. The contact between the impactor and concrete cylinder was modelled as hard contact and tangential contact was modelled with classical Coulomb friction model with a friction coefficient of 0.1.

4 Validation of Model

The results in terms of impact force against varying drop height were predicted and compared, see Table 3. The parameters were such as (d_t) tension damage, compression damage (d_c), $\tilde{\epsilon}_t^{pl}$ and $\tilde{\epsilon}_c^{pl}$ along with tension recovery were modified slightly over the original static parameters, see Fig. 4 i.e., Set 1. The failure criteria adopted in simulations are based on non-physical criteria which needs to be calibrated for a specific case to delete distorted mesh element which can otherwise induce artificial stiffness to the model. The set 1 parameters were based on the failure criteria that inelastic strain at failure for compression and tension has a value of 0.121 and 0.198 respectively as per available literature. The response history on targets with set 1 parameters found to be over predicted in case of low angle of hit whereas the same was found to be under predicted at higher angle of hit hit may be due to the

Table 3 Comparison of experimental and simulation results

Drop height (mm)	Angle of hit	Peak force (kN)		
		Experiment	Simulation	
			Parameter (Set 1)	Parameter (Set 2)
49	13°	7.00	29.08	8.41
123	20°	14.61	32.10	18.04
237	28°	22.71	42.69	0.78
396	36°	43.08	44.11	44.11
619	46°	52.85	40.97	56.29
941	58°	68.79	45.19	59.47

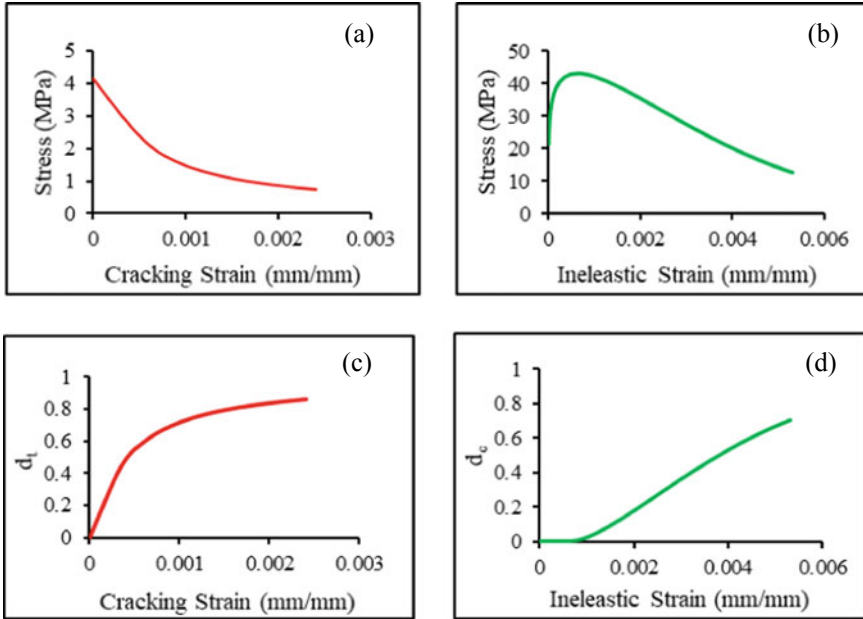


Fig. 4 Static response under **a** tension **b** compression and **c** tensile damage **d** compression damage [17]

strain rate sensitivity of concrete in tension and compression which was not explicitly modelled. In order to overcome the difference between the experimental and numerical simulations, the parameters were such as (d_t) tension damage, compression damage (d_c), $\tilde{\epsilon}_t^{pl}$ and $\tilde{\epsilon}_c^{pl}$ along with tension recovery were modified i.e., Set 2, as shown in Table 2. The predicted force-time history response of target was found to be in close agreement with the experimental results in case of set 2 parameters.

The response of target in terms of force versus time against varying drop angle is shown in Fig. 5. Overall, the predicted response of target with set-2 parameters were found in good agreement with the experimental results. The peak force was found to be 10, 15, 22, 48, 58 and 75 kN against 13, 20, 28, 36, 46 and 58° drop angle, respectively.

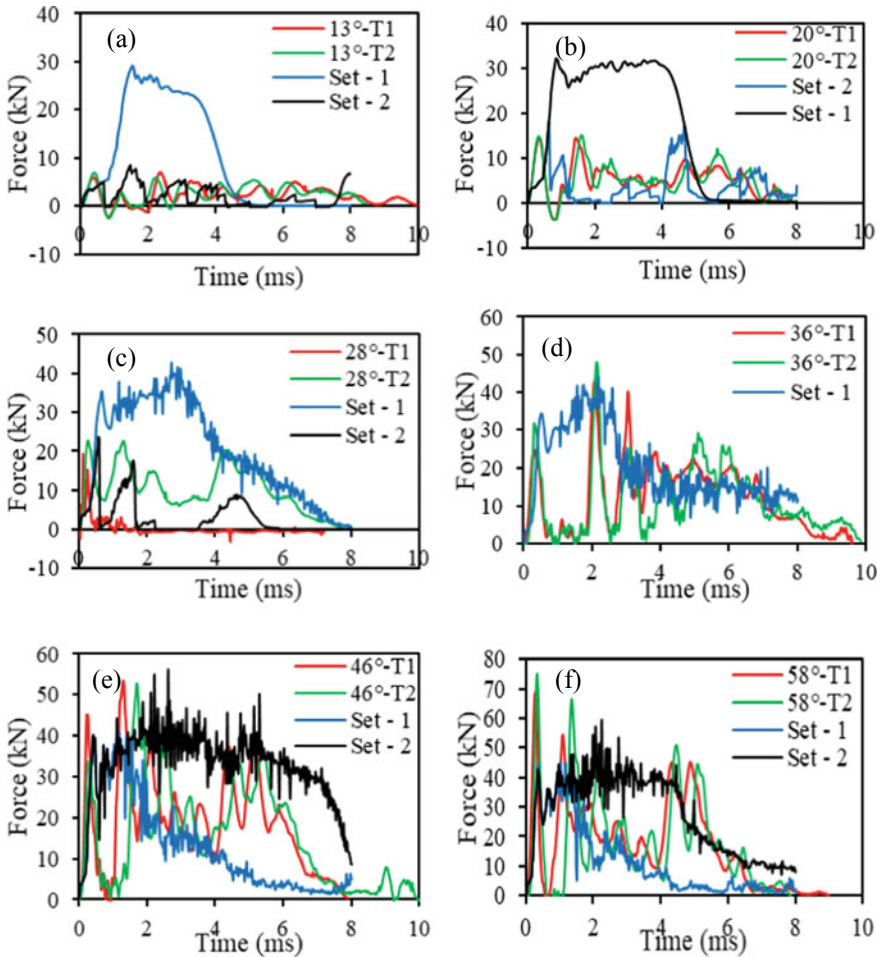


Fig. 5 Response history of a 13° b 20° c 28° d 36° e 46° f 58° drop angle

5 Dynamic Characteristics of Concrete

The dynamic characteristics of the concrete was studied under varying drop height. The Mises stresses (MPa) in the concrete against varying drop height is shown in Figs. 6, 7, 8, 9, 10 and 11. The von-Mises stress shows an increase in stress response of concrete cylinders under dynamic loading. With an increase in angle of drop, the von-Mises stress increases specifying the enhanced behavior of specimens. For 13–58° drop angle, the Mises stress increases with time resulting of localized stress concentrations at the point of impact and thereafter decreases due to the stress wave propagation as compressive wave and gets reflected as tensile wave further increasing the stress concentrations at the other segments of the cylindrical specimen

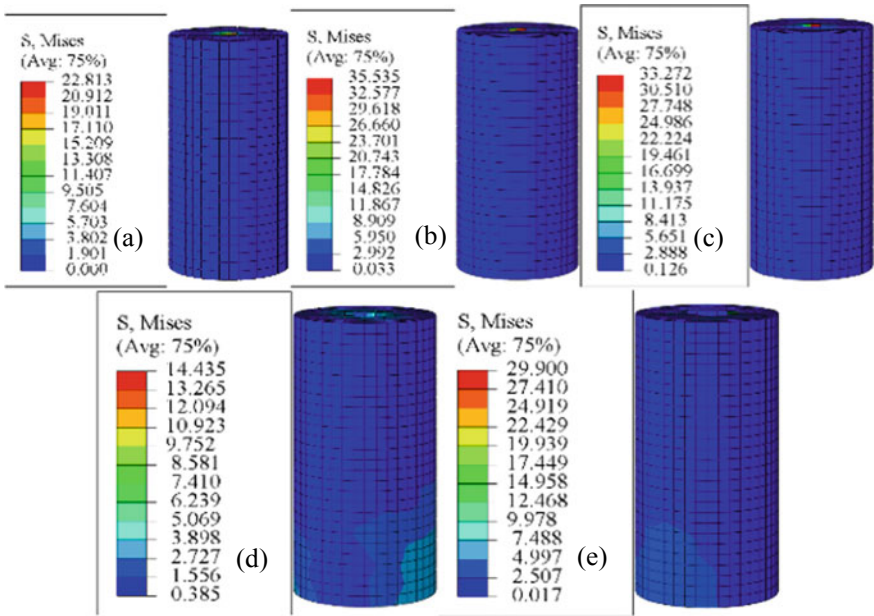


Fig. 6 Stress wave propagation in cylinder at a 0.1 b 0.4 c 1 d 2 e 3 ms during 13° pendulum drop

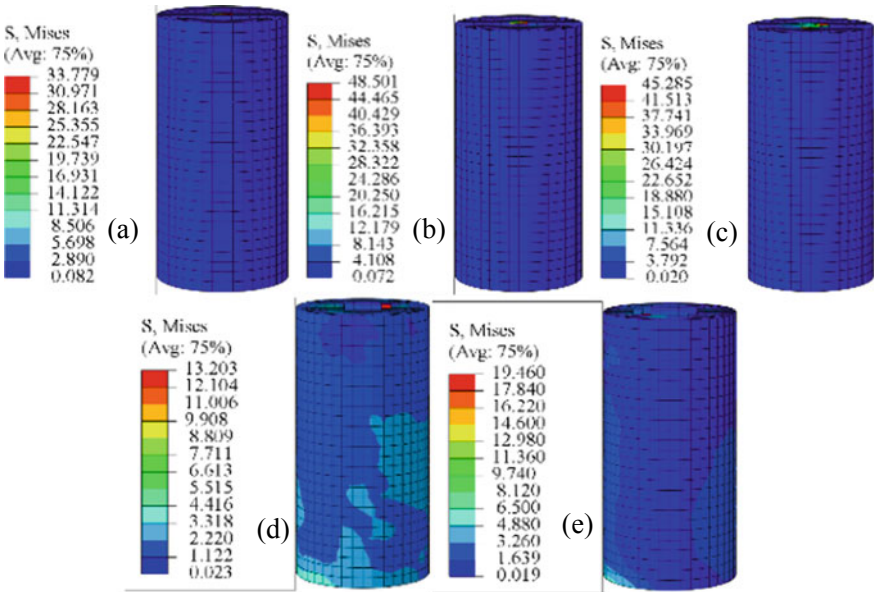


Fig. 7 Stress wave propagation in cylinder at a 0.1 b 0.4 c 1 d 2 e 3 ms during 20° pendulum drop

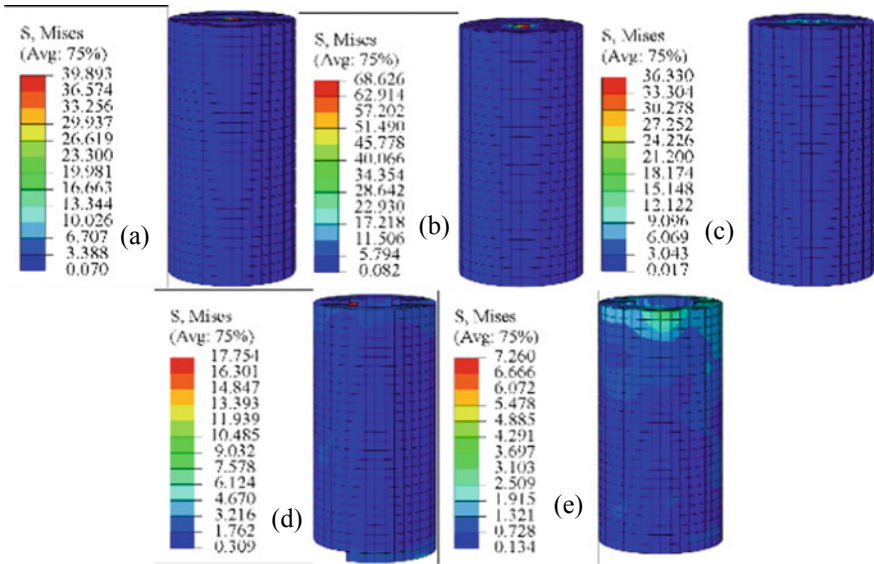


Fig. 8 Stress wave propagation in cylinder at a 0.1 b 0.4 c 1 d 2 e 3 ms during 28° pendulum drop

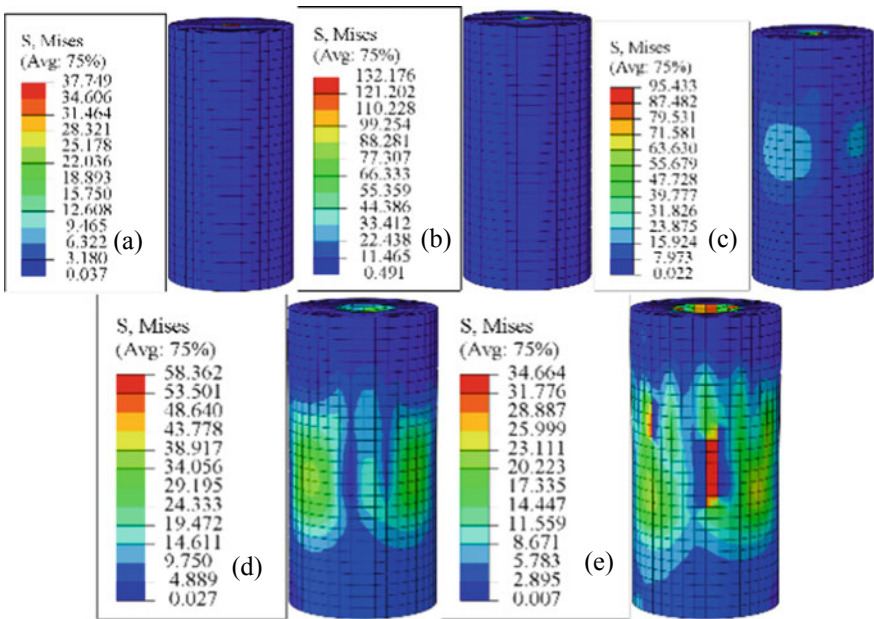


Fig. 9 Stress wave propagation in cylinder at a 0.1 b 0.4 c 1 d 2 e 3 ms during 36° pendulum drop

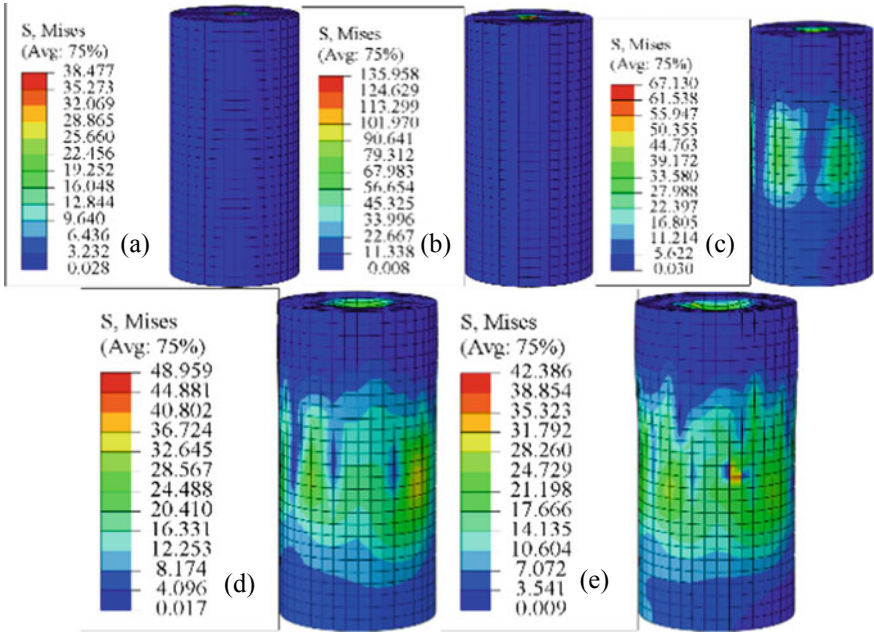


Fig. 10 Stress wave propagation in cylinder at i 0.1 ii 0.4 iii 1 iv 2 v 3 ms during 46° pendulum drop

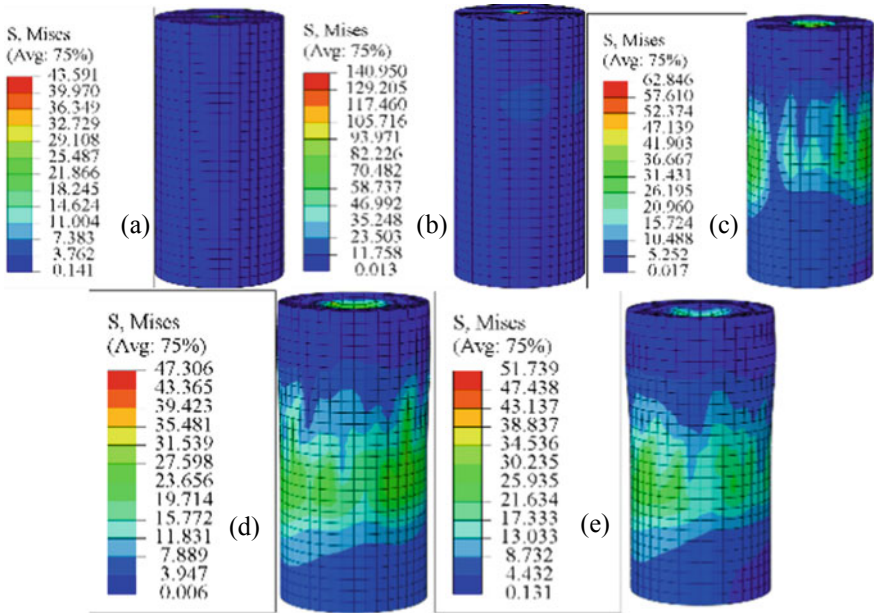


Fig. 11 Stress wave propagation in cylinder at i 0.1 ii 0.4 iii 1 iv 2 v 3 ms during 58° pendulum drop

at later stage. As the drop angle of impactor increases, the von-mises stress increases, which further increased the intensity of reflective tensile stress wave. Therefore, the corresponding stress concentrations were found to be increasing in the periphery of the back face of the specimens, see Figs. 6, 7, 8, 9, 10 and 11. The cylinders showed an enhanced response against dynamic loading with increasing von Mises stress from 35.535 MPa for 13° drop angle to a stress of 140.950 MPa for 58° that indicating a strain rate dependency of concrete under dynamic loading. The (Dynamic increase factor) DIF of concrete defined as ratio of uniaxial stress under dynamic to the uniaxial stress under quasi-static loading is used to define the enhanced response of concrete. As reported by [17], the DIF value of concrete under compression can be higher than 2 whereas it is higher than 6 in case of tension.

The mode of failure of concrete was quite different as compared to quasi-static loading. Under pendulum drop impact, the concrete cylinders showed more localized failure with more stress concentration under the point of impact, Figs. 6, 7, 8, 9, 10 and 11. The strain dependent concrete failure criteria was adopted using ABAQUS/EXPLICIT showed elements failed under mixed mode failure i.e., under compression near the point of impact and under tension at the far end of the impact specimen due to reflective tensile stress wave. As the drop angle of impactor increases, the concrete specimens fail under increased tensile cracking and crushing compressive strain and due to the absence of strain rate data for CDP the model fails to capture proper response using calibrated parameters. The subjective parameters for such conditions with increased tensile cracking and crushing compressive strains to properly capture the force–time response of concrete cylinders under increased strain rate may be recommended.

6 Conclusion

The following conclusions have been drawn based on the experimental and numerical investigations;

- The peak force was found to be increasing with increase of angle of drop revealing that higher impact energy tend to generate higher impulses in the target specimen.
- The von-Mises stress was obtained under numerical simulations showed an increment with the increase in angle of drop stating the strain rate dependency of concrete.
- The subjective parameters for element removal based on inelastic strain at failure under tensile cracking and crushing compressive strains slightly over predicts the peak force for 13–46° drop angle and under predicts for 58° pendulum drop.

References

1. Watsteint BD (1953) Effect of straining rate on the compressive strength and elastic properties of concrete. *ACI J Proc* 49(4):11850. <https://doi.org/10.14359/11850>
2. Weidner AM, Pantelides CP, Richins WD, Larson TK, Blakeley JE (2012) Drop hammer test of concrete cylinders considering fiber reinforcement and elevated temperature. INL/EXT-13-28118 Revision 1. Idaho National Laboratory
3. Ross CA, Jerome DM, Tedesco JW, Hughes ML (1996) Moisture and strain rate effects on concrete strength. *ACI Mater J* 93:293–300. <https://doi.org/10.14359/9814>
4. Lee S, Kim K-M, Cho J-Y (2017) Investigation into pure rate effect on dynamic increase factor for concrete compressive strength. *Procedia Eng.* 210:11–17. <https://doi.org/10.1016/j.proeng.2017.11.042>
5. Pajak M (2011) The influence of the strain rate on the strength of concrete taking into account the experimental techniques. *Archit Civ Eng Environ* 2:231–253
6. Mellinger FM, Birkimer DL (1968) Measurements of stress and strain on cylindrical test specimens of rock and concrete under impact loading. Technical Reporting Army Department, Ohio
7. Kaneko T, Ujihashi S, Yomoda H, Inagi S (2008) Finite element method failure analysis of a pressurized FRP cylinder under transverse impact loading. *Thin Walled Struct* 46:898–904. <https://doi.org/10.1016/j.tws.2008.01.016>
8. Elfahal MM, Krauthammer T, Ohno T, Beppu M, Mindess S (2005) Size effect for normal strength concrete cylinders subjected to axial impact. *Int J Impact Eng* 31:461–481. <https://doi.org/10.1016/j.ijimpeng.2004.01.003>
9. Williams MS (1994) Modeling of local impact effects on plain and reinforced concrete. *ACI Struct J* 91:178–187. <https://doi.org/10.14359/4603>
10. Wang B, Chen Y, Fan H, Jin F (2019) Investigation of low-velocity impact behaviors of foamed concrete material. *Compos Part B Eng* 162:491–499. <https://doi.org/10.1016/j.compositesb.2019.01.021>
11. IS: 10262 (2019) Concrete Mix Proportioning-Guidelines. Bureau of Indian Standard, Delhi, New Delhi
12. EN1992-1-2 (2004) Eurocode 2: Design of concrete structures. Part 1–2: General rules–Structural Fire Designing Communication European Communities, Brussels
13. Kupfer H, Hilsdorf HK, Rusch H (1969) Behaviour of concrete under biaxial stresses. *ACI J Proc* 66:656–666
14. (Lambert) Li X-X, Wang C, Sato J (2020) Framework for dynamic analysis of radioactive material transport packages under accident drop conditions. *Nucl Eng Des* 360:110480. <https://doi.org/10.1016/j.nucengdes.2019.110480>
15. Birtel V, Mark P (2006) Parameterised finite element modelling of RC beam shear failure. In: Abaqus user's conference, pp 95–108
16. Szczecina M, Winnicki A (2017) Relaxation time in CDP model used for analyses of RC structures. *Procedia Eng* 193:369–376. <https://doi.org/10.1016/j.proeng.2017.06.226>
17. Malvar LJ, Crawford JE (1998) Dynamic increase factor for concrete. Twenty-Eighth DDESB Seminar Orlando, FL, August 98

Axial Stiffness of a Slot-Nut Type Conformal Segment Joint



M. Umakanth, P. Uday Kumar, V. Narayanamurthy, and S. Korla

Abstract Slot-nut type of joint is adopted in integrating two axially adjacent curved cylindrical shell segments. The fasteners in this joint are concealed within the slot in one of the shell segments, which do not project externally and conforms within the curved outer profile of the shell segments. This paper presents the experimental and numerical investigations for evaluating the axial stiffness of this joint. The shell segments made of aluminum alloy have been fabricated and joined using an alloy steel fastener, tensile experiments were conducted at displacement-controlled loadings until the joint deflection reaches a maximum of 2.0 mm at the joint interface. The numerical simulations have been conducted and a good agreement is obtained with the experimental results. It is found that the component tensile stiffness of this kind of joint is less than 70% of that in compression.

Keywords Joint stiffness · Finite Element Analysis (FEA) · Stud and nut · Shell · Displacement · Deflection · Universal Testing Machine (UTM)

1 Introduction

There are several types of joints for axially integrating any two curved cylindrical shell segments or two cylindrical shells such as pipes [1–3]. Majority of these joints protrude from the external curved surface of the shells which may not be a problem to shell joints adopted in general engineering practices [4–10]. Theoretical, numerical and experimental studies on bolted circular flange joints where the joint protrudes from external curved surface have been studied [11–26]. But when a design requirement imposes this joint to be concealed within the curved shell's external profile,

M. Umakanth (✉) · P. Uday Kumar · V. Narayanamurthy
Research Centre Imarat, Hyderabad 500069, Telangana, India
e-mail: masuram.umakanth@rcilab.in

V. Narayanamurthy
e-mail: v.narayanamurthy@rcilab.in

S. Korla
Department of Mechanical Engineering, NIT-Warangal, Hyderabad 506004, Telangana, India

without any external projection from the shell surface, the conventional joints become a challenge. Notwithstanding this specific requirement, even the select conventional pipe threaded joints, flange joints, spigot joints with a cotter, etc., can be designed to be conformal within the external shell surface. But when (a) the size i.e., the diameter of the cylindrical shell segments varies from a nominal value of 300 to 5000 mm or more, (b) there is a need for high joint stiffness of more than 10 kN/mm, (c) the shear load at the joint is significantly higher and (d) leak-proof or sealing requirements, are to be met additionally, even these select joints become a difficult choice. The slot-nut type conformal segment joint discussed in the paper can meet all these requirements.

The axial joint stiffness is one of the prime requirements for this joint and its determination from experimental and numerical methods is discussed in this paper. The concepts adopted in axial stiffness determination can be extended to other similar joints in full geometric form i.e. with shells of revolution such as tubular flanged joints adopted in chimneys, masts and other applications. The details of the geometric model with dimensions for a typical slot-nut type of a conformal joint adopted in present study and the fabricated joint is shown in Fig. 1. End of one shell segment i.e. member-1 is provided with a thick internal flange and a radial slot with an axial hole. The adjacent shell segment i.e. member-2 is featured with a similar thick internal flange having a stud at the end face. When both the shell segments are brought together axially, the stud in member-2 enters the axial hole in the slot of member-1 and then the nut is tightened and torqued to make this joint.

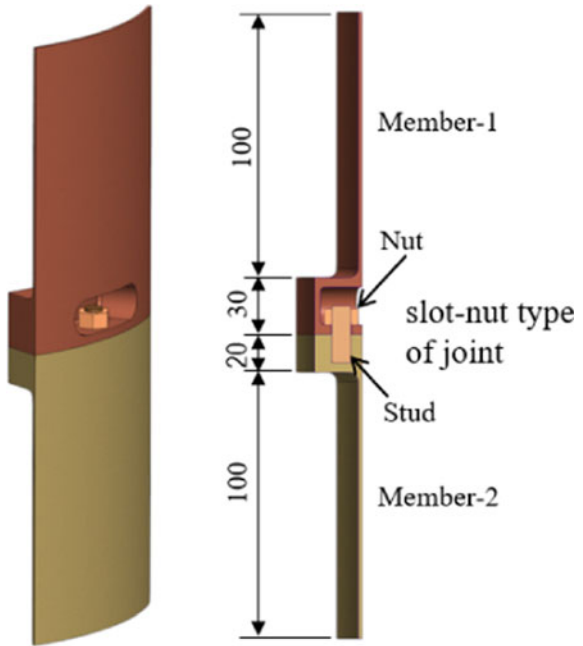
2 Numerical Simulations and Experiments

2.1 Numerical Simulation

The numerical simulation to evaluate the joint stiffness is carried out for both the tension and compressive loadings. The joint members-1 and 2 are made of aluminum alloy with Young's modulus $E = 61$ GPa and Poisson's ratio $\nu = 0.32$. The stud and nut are made of alloy steel with $E = 200$ GPa and $\nu = 0.3$. The stress-strain behaviour of both the shell segments and fastener materials are obtained from tensile tests of dog-bone shaped specimens shown in Fig. 2 with dimensions provided in Table 1. The stress-strain behaviors shown in Fig. 3 are used as input for the material model in FEA. The material properties of the test specimens are given in Table 2.

The geometry of members 1 and 2, stud and nut are discretised with 20 node hexahedral elements with an element size of 1 mm. The contact interface between the external surface of stud and inner surface of member-2 and inner surface of nut are bonded to simulate the screwed joint. Frictional contacts with a friction coefficient of 0.5 is established between 1) the mating surface of the nut against the flat vertical face in the slot of member-1; and 2) the two contacting flat end surfaces of both the shell segments. A pretension of 20,000 N [4] is applied by using bolt-pretension tool in ANSYS [27] to simulate the effect of pre-tightening torque of 40 Nm. This bolt

Fig. 1 Geometry model of a slot-nut type conformal segment joint



(a) Geometric model



(b) Physical model

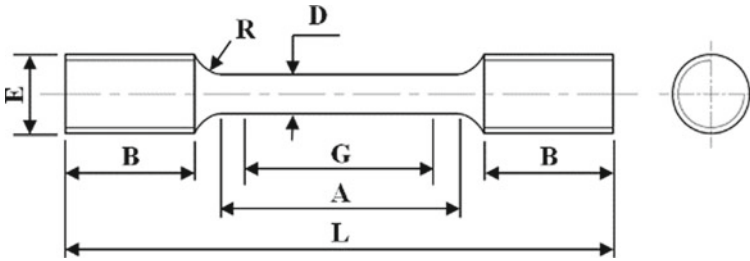
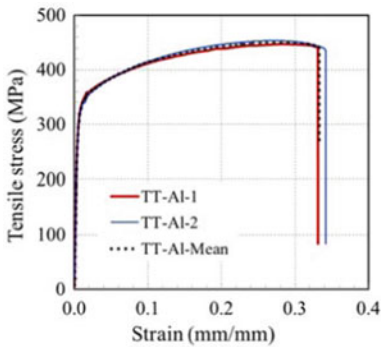


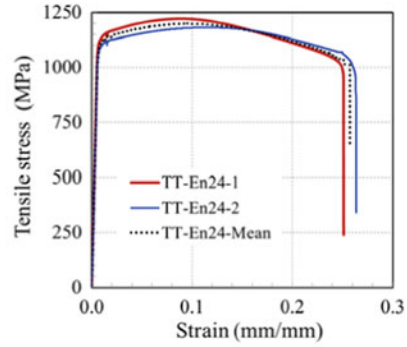
Fig. 2 Tensile test specimen

Table 1 Dimensions of tensile test specimens

Specimen	L	A	G	B	D	R	E
Aluminum alloy	85	38	24	20	6.0	6 ± 0.1	M12 × 1.75
Alloy steel	85	34	25	20	6.25	5 ± 0.12	M12 × 1.75



(a) Aluminum alloy



(b) Alloy steel

Fig. 3 Stress–strain curves of segment shells and fastener

Table 2 Material properties from tensile tests

Material	E (GPa)	UTS (MPa)	0.2% Proof strength (MPa)	% Elongation
Aluminium alloy	61.10	447.25	312	19.2
Alloy steel	187.6	1221.9	1084	18.4

pretension creates an equivalent compressive force on the mating surfaces of the joint members 1 and 2. The bottom face of the member-2 is constrained in all degrees of freedom. The FEA plot with boundary conditions is shown in Fig. 4. A displacement u_y of 2.5 mm is applied in steps of 0.1 mm on the free end of the member-1 until a non-linear joint deflection $\delta \geq 2.0$ mm.

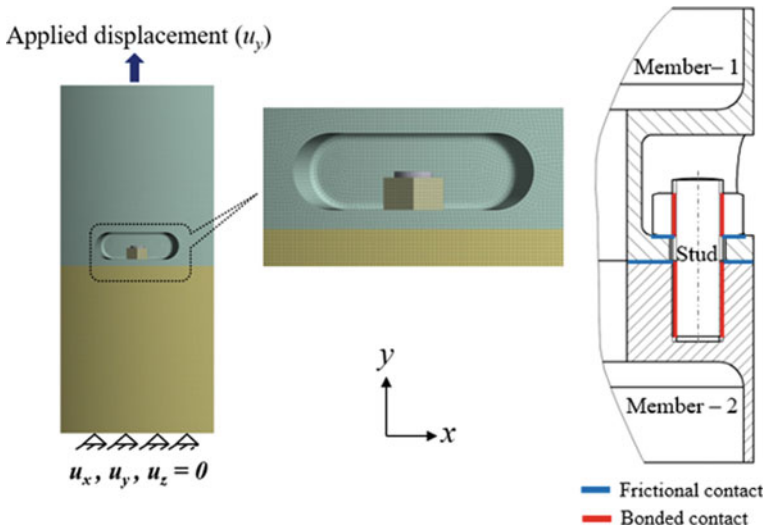


Fig. 4 FE model with loading and boundary conditions

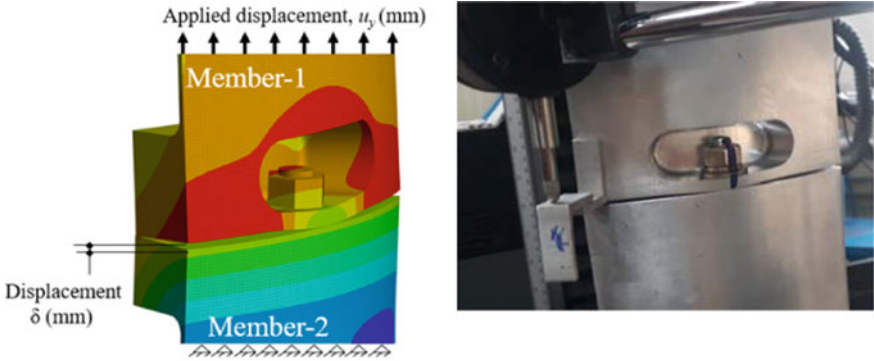
The predicted results obtained from the FEA for the joint under tension is shown in Fig. 5. The axial displacement behaviour of the joint due to the displacement applied on the loading attachment is shown in Fig. 5(a). The stiffness of the joint under tensile loading is the initial slope of the force–displacement curve shown in Fig. 5(b). The slope of the force–displacement curve yields a joint stiffness of 16 kN/mm in tension.

Similarly, the predicted results obtained from the FEA for the joint under compression is shown in Fig. 6. The axial displacement behaviour of the joint due to the displacement applied on the loading attachment is shown in Fig. 6(a). The stiffness of the joint under compressive loading is obtained as the initial slope of the force–displacement curve as shown in Fig. 6(b). The slope of the force displacement curve yields a joint stiffness of 50 kN/mm in compression.

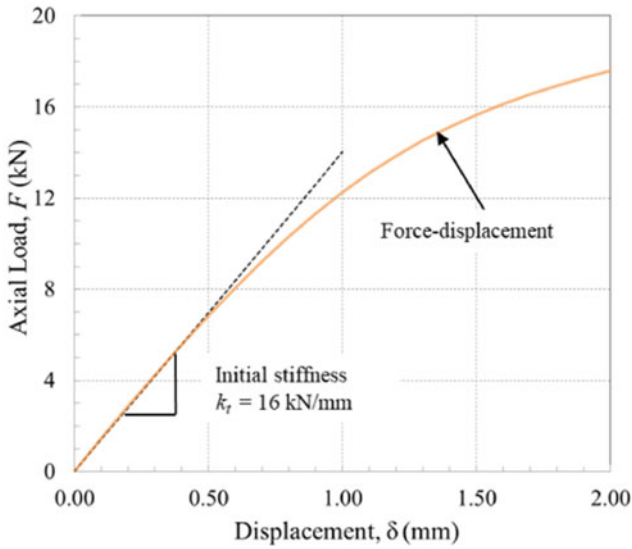
2.2 Experiments

Two experimental specimens were realised along with end attachments for holding the joint at the bottom side and for applying the load on the top side. These loading attachments are fastened to the joint specimen using M6 screw and nut (13 Nos) as shown in Fig. 7 on top and bottom ends.

The two joint specimens are mounted in an Instron Universal Testing Machine (UTM) and subjected to a displacement-controlled loading as shown in Fig. 8. A displacement u_y of 2.5 mm is applied in steps of 0.1 mm on the free end of the member-1 until a non-linear joint deflection $\delta \geq 2.0$ mm.



(a) Deformation of joint



(b) Force-displacement behaviour

Fig. 5 Prediction of joint stiffness under tension

The force–displacement curves obtained from the two specimens and their averaged results under tension loading from the experiment is shown in Fig. 9.

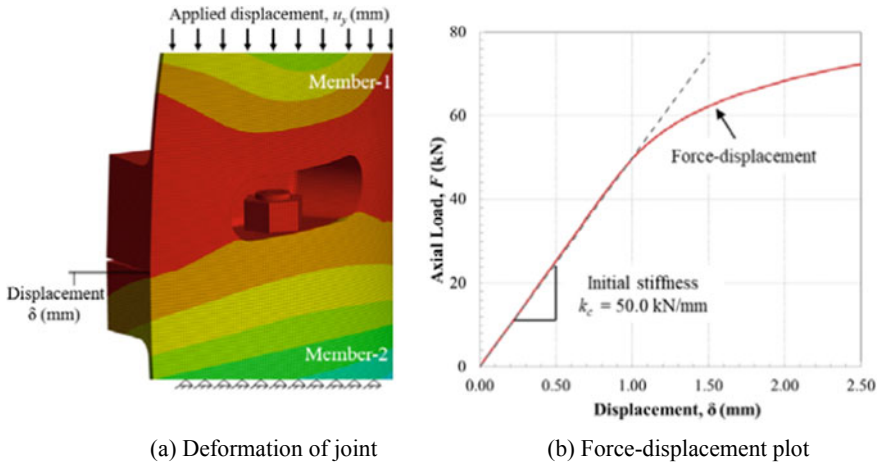


Fig. 6 Prediction of joint stiffness under compression

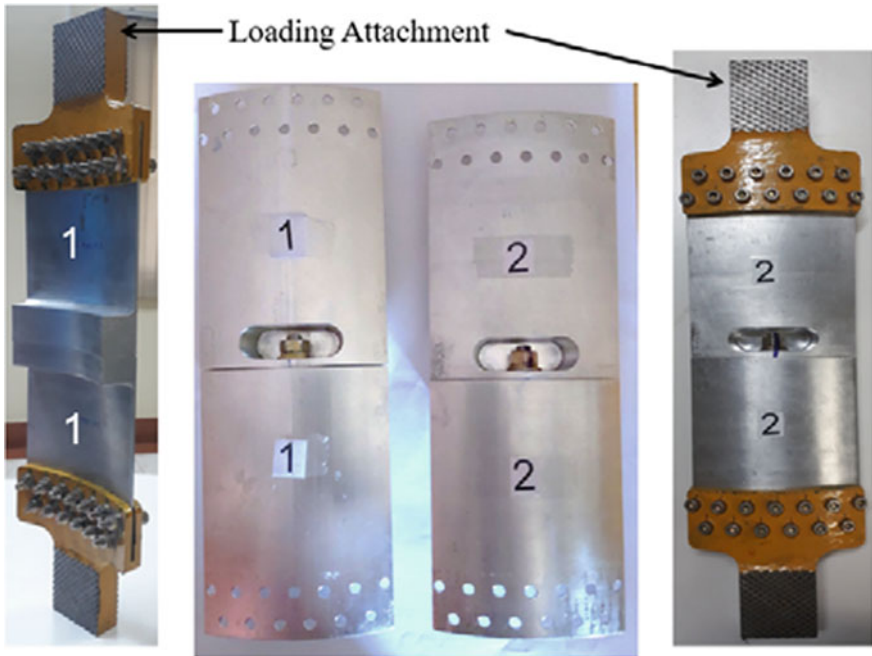


Fig. 7 Experimental joint specimens

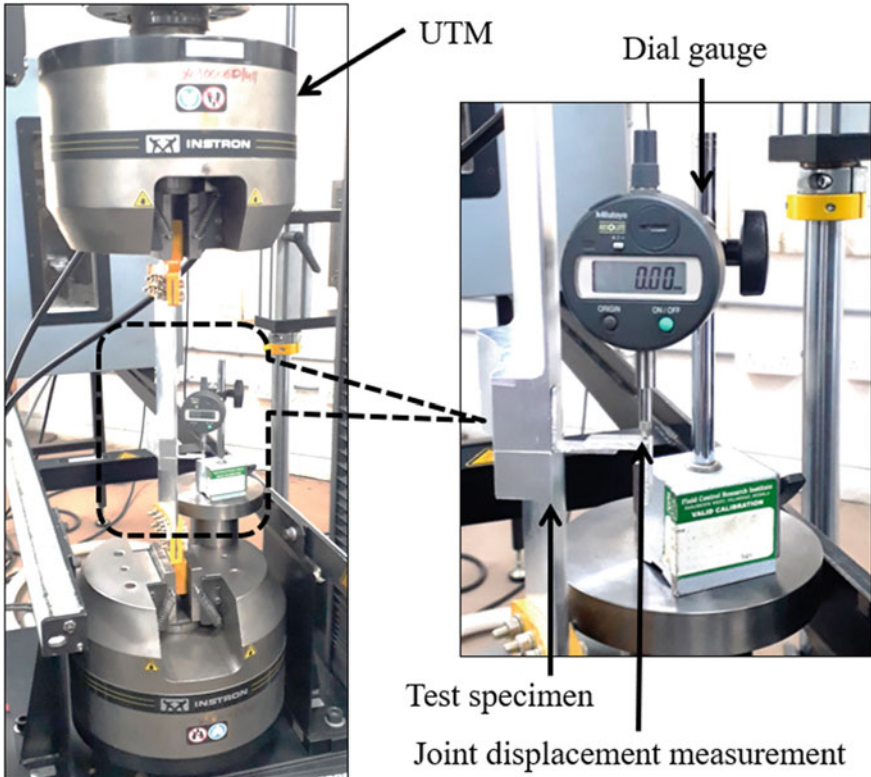
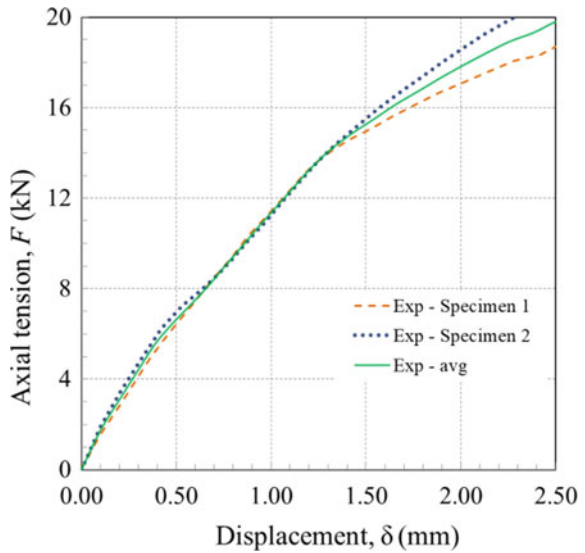


Fig. 8 Experiment on slot-nut type conformal segment joint

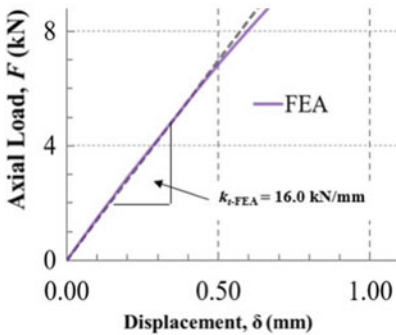
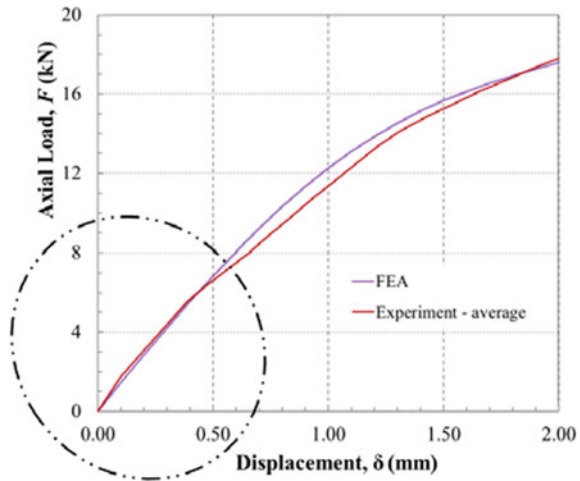
Fig. 9 Experimentally obtained force–displacement behavior under tension



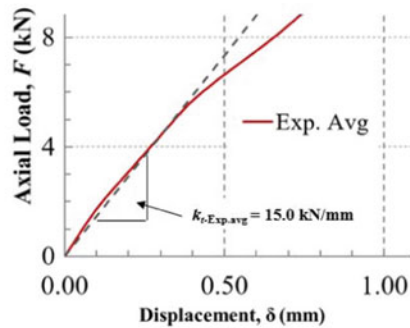
3 Results and Discussions

A comparison between the joint displacement δ and the axial reaction F due to the applied displacement u_y for the FEA and experiment is shown in Fig. 10. The initial slope of these F - δ curves represent the axial joint stiffness k_t in tension, as shown in phantom lined circle. The behavior is non-linear beyond this boundary. The axial joint stiffness obtained from FEA is 16 kN/mm and from the experiment is 15 kN/mm as depicted in Figs. 11(a) and (b).

Fig. 10 Graphical comparison between FEA and experiment



(a) FEA



(b) Experiment

Fig. 11 Axial joint stiffness

4 Conclusions

The slot-nut type of a conformal segment shell joint provides high joint stiffness besides resisting considerable shear loads. This joint is investigated numerically and experimented to determine the axial joint stiffness. An axial joint stiffness of 16 kN/mm is predicted in FEA and 15 kN/mm is obtained in experiment under tension. A difference of 6.25% between the prediction and experiment divulges a good agreement between FEA and experiment. An axial joint stiffness of 50 kN/mm is predicted in compression. Based on close agreement of the results in tension, the experimental results for the compression loading will be similar and will be in close agreement with predictions.

References

1. Umakanth M, Narayanamurthy V, Korla S (2021) Review of flight intersection joints. *Int Rev Aero Eng* 14(3):131–146. <https://doi.org/10.15866/irease.v14i3.19401>
2. Nassar SA, Yang X, Gandham SVT, Wu Z (2011) Nonlinear deformation behavior of clamped bolted joints under a separating service load. *J Pres Ves Tech* 133(2):1–9. <https://doi.org/10.1115/1.4002674>
3. Wojnar A, Kozłowski A, (2006) Mechanical model for assessment of the stiffness of bolted flanged joint. In: *Proceedings of the 11th International Conference on Metal Structures*, Taylor and Francis, Rzeszów, Poland, pp 188–189
4. Bolted tension flange joint research (ring flanges joining CHS), British Steel Corporation Tubes Division, Research Report CE 71/46, Corby, UK (1974)
5. BS 8100 Lattice towers and masts, British Standards Institution, London, UK (1988)
6. Hollow structural sections design manual for connections, 2nd Ed., Stelco Design Manual, Hamilton, Canada (1981)
7. Igarashi S, Wakiyama K, Inoue K, Matsumoto T, Murase Y (1985) Limit design of high strength bolted tube flange joints (Part 1). *J Struct Const Eng* 354:52–66
8. Igarashi S, Inoue, K, Matsumoto T (1987) Limit design of bolted circular tube flange joint subjected to tension. In: *Proceedings of the International Conference on Steel and Aluminium Structures*, Cardiff, UK, pp 825–834
9. Kato B, Hirose R (1984) Bolted tension flanges joining circular hollow section members. *J Constr Steel Res* 5(2):79–101
10. CIDECT13 (1984) Construction with hollow steel sections, British Steel Corporation, Corby, UK
11. Cao JJ, Bell AJ (1994) Finite element analysis of circular flange joints under tension forces. In: *Proceedings of 9th UK ABAQUS User Group Conference*, Exeter College, Oxford, UK
12. Cao JJ, Bell AJ (1996) Experimental study of circular flange joints under tension forces. *J Strain Anal Eng Des* 31(4):259–267. <https://doi.org/10.1243/03093247V314259>
13. Cao JJ, Packer JA (1997) Design of tension circular flange joints in tubular structures. *Eng J* 34(1):17–23
14. Stamatopoulos G, Ermopoulos J (2008) Interaction curve for non-preloaded bolted connections in tubular members. In: *Proceedings of Eurosteel 2008, 5th Conference on Steel and Composite Structures*, Graz, Austria, pp 27–35
15. Couchaux M, Hjiatj M, Ryan, I (2010) Static resistance of bolted circular flange joints under tensile force. In: *Proceedings 13th International Symposium on Tubular Structures*, Hong-Kong <https://doi.org/10.1201/b10564-6>.

16. Wojnar A, Kozłowski A (2006) Mechanical model for assessment of the stiffness of bolted flanged joint. In: Proceedings of the 11th International Conference on Metal Structures, Taylor and Francis, Rzeszów, Poland, pp 188–189
17. Kozłowski A, Wojnar A, Slecza L (2007) Influence of flanged bolted joints stiffness on the behaviour of steel chimneys. In: Proceedings of the 3rd International Conference on Structural Engineering, Mechanics and Computation, Cape Town, South Africa
18. Kozłowski A, Wojnar A (2008) Initial stiffness of flange bolted joints and their influence on the behaviour of steel chimneys. In: Proceedings of Eurosteel 2008, 5th Conference on Steel and Composite Structures, Graz, Austria
19. Couchaux M, Hjjaj M, Ryan I (2011) Behaviour of bolted circular flange joints subjected to a bending moment and an axial force. In: Proceedings of Eurosteel 2011, 5th Conference on Steel and Composite Structures, Budapest, Hungary, pp 219–224
20. Azim MR (2013) An analytical investigation on bolt tension of a flanged steel pipe joint subjected to bending moments. *Int J Eng App Sci* 2(3):2305–8269
21. Emara M, Ahmed ES, Soliman E, Azhar A (2019) Numerical analysis of CHS unstiffened bolted circular flange connection. *Univ Civil Eng Res Mag* 41(1)
22. Zhang O, Poirier JA (2004) New analytical model of bolted joints. *ASME J Mech Des* 126(4):721–728. <https://doi.org/10.1115/1.1760777>
23. Grosse IR, Mitchell LD (1990) Nonlinear axial stiffness characteristics of axisymmetric bolted joints. *ASME J Mech Des* 112(3):442–449. <https://doi.org/10.1115/1.2912628>
24. Kim J, Yoon JC, Kang BS (2006) Finite element analysis and modelling of structure with bolted joints. *J App Math Model* 31(5):865–911. <https://doi.org/10.1016/j.apm.2006.03.020>
25. Wileman J, Choudhury M, Green I (1991) Computation of member stiffness in bolted connections. *ASME J Mech Des* 113(4):432–437. <https://doi.org/10.1115/1.2912801>
26. Rasti N (2007) Comparative study of joint stiffness calculations using finite element analysis, M.S. Thesis, University of Windsor, Canada
27. ANSYS Workbench Documentation Manual, ANSYS Corp USA (2021)

Simulation and Analysis of Natural Gas Pipe Network for MNNIT (Allahabad) Staff Colony



Ashwin Pandey, Ankit Prakash, Ramesh Pandey, and Anubhav Rawat

Abstract In most of the developed countries and also in few of the metro cities of India, transportation and distribution of gas is through complex arrangement of pipe networks. These pipe networks handle wide range of pressures and flow rates of the fluids. The Pipe networks are more convenient, efficient and economical mode of transportation systems compared to the surface transport systems viz. Rail wagon, trucks etc. This fact is much more important for B class metropolitan cities like Prayagraj. Therefore, present study focuses on design, simulation and analysis of a pipe network for a small colony (MNNIT-Allahabad staff colony) of Prayagraj city. It first emphasizes on an optimum design of pipe network for proper supply of natural gas to the staff colony residents at low system operating cost. For simulation and analysis of the pipe network, two mathematical models i.e., Newton-Loop Method (Multidimensional) (N-L-M) and Newton-Loop Method (One-Dimensional) or Hardy-Cross Method (H-C-M) are implemented to find out the value of flow rate in each individual pipe and value of pressure at each node and further are compared to find out the best method out of the two to transport the LNG in the colony. The values of operating parameters obtained from both of the models are plotted to visualize the convergence rate and it is found that the N-L-M gives better convergence rate compared to H-C-M.

Keyword Gas distribution networks · Pipe network optimization · LNG · Pressure and flow rates

A. Pandey (✉) · A. Prakash · R. Pandey · A. Rawat
Applied Mechanics Department, Motilal Nehru National Institute of Technology-Allahabad,
Prayagraj 211004, Uttar Pradesh, India

R. Pandey
e-mail: ramesh@mnnit.ac.in

A. Rawat
e-mail: Anubhav-r@mnnit.ac.in

Nomenclature

Δ	Difference
ΔP	Pressure difference (mBar)
∂q	Correction in loop flow (m^3/h)
D	Diameter of the pipe (mm)
$F(q)$	Loop Error
f	Friction factor
JK	Loop Jacobi matrix
K	Pipe constant
L	Length of the pipe (m)
P_n	Standard pressure (≈ 0.1 MPa)
Q	Flow rate in pipes (m^3/h)
Q_c	Corrected flow rate in pipes (m^3/h)
q_A	Loop flow in Loop A (m^3/h)
q_B	Loop flow in Loop B (m^3/h)
R_{air}	Characteristic gas constant of air (KJ/Kg-K)
S	Specific gravity (Kg/m-s)
T	Temperature (K)
T_n	Standard temperature (≈ 288 K)
z	Compressibility factor

1 Introduction

In India, the natural gas is supplied and distributed as per the guidelines related to pricing and utilization policies issued by Government of India from time to time. Supply and distribution of natural gas is accomplished by pipeline networks which are the most economical and safe mode for transportation of the natural gas compared to surface transport system by connecting gas sources to gas consumption market. Initial cost of laying pipelines is high but the subsequent running costs are minimal. It rules out trans-shipment losses or delays. Pipelines can also be laid through difficult steep areas as it involves very low energy-consumption and need very little maintenance.

Liquefied natural gas (LNG) is natural gas that is allowed to cool down to liquid form for the sake of ease and safety during transportation. The first part of LNG supply chain is exploration and production. The natural gas is firstly pretreated for the removal of the contaminants from it. Later on, for the prevention of freezing of it, heavier hydrocarbons are removed when the gas is cooled down to -256 °F and to meet the standard specifications at the delivery points of LNG.

If the above properties of LNG are compared to LPG, LNG is cleaner fossil fuel which produces slightly less CO₂ when burned and doesn't require door to door delivery in cylinders. Also, from the safety point of view, LNG is lighter than air and will disperse quickly in air in the event of a leak.

There are many important studies existing in the literature for the simulation and analysis of these kinds of Gas Pipeline Network system. In earlier developments, Hardy and Cross [1] gave an analytical method for the flow of gases in networks of pipes and it was the very first method which incorporated engineering aspects in the field of pipe network calculations. Prior to their method only electrical analogs of hydraulic network were existing.

Hyman and Jones [2] talked about a number of iterative methods for determining the solution of pipeline networks, such as Newton-Nodal, Newton-Loop, Hardy-Cross method etc. Similarly, Boyne [3] also designed and analyzed various pipe networks for gas flows. Hamam [4] described flow equations to calculate the pressure drop in the individual pipes of a pipe network. Jeppson [5] compared the linear theory method, Newton-Raphson method and Hardy-Cross method to analyze the pipe networks. Mah [6] explained that the status of relevant technology is assessed with particular reference to formulation of problems and methods of solution. Aylmer [7] described the flow equations and efficiency factor. Osiadacz [1] explained mathematical models for complex networks i.e., networks consisting larger number of nodes and loops and further compared the results of nodal method and loop method applied to a particular pipe network. Adewumi and Tian [8] used step-forward algorithm, which doesn't require the matrix algebra. Cohelo [9] focused on discussions on the particularities of pressure drop equations being used in the design. Swamee [10] analyzed the pipe network for water flow using Hardy-Cross method. Brkic' [11] explained about development of centralized system fueled by Natural Gas. Gonzalez [12] focused on modelling and simulation of a gas distribution pipeline network with a special emphasis on gas ducts. Brkic' [13] further emphasized on comparative study of all the iterative method i.e., nodal method, Hardy-cross method, node-loop method, modified Hardy-Cross method etc. Lukman [14] proposed Hardy-cross method for analysis of flow in pipe networks based on FORTRAN & VISUAL BASIC programming language. Sharma [15] analyzed the pipe network using Linear Programming technique. Niazkar and Afzali [16] analyzed simple pipe networks using MATLAB and EXCEL. Kar [17] explained insights into development of gas market and evolution of city gas distribution business in India. Bianchini [18] studied about safety measures in Natural gas pipelines. Brkic' [19] also summarized the whole history of work done on pipe network i.e., they reviewed the status on development of the H-C-M for computation in piped distribution networks. Similarly, Pandey and Rawat [20] solved the sanitization pipe network using mathematical models and EPANET software.

The above brief literature survey reveals that although the pipe network system is better system but their analysis for optimized operations is very complex. Further, for the analysis of pipe networks, amongst of all the methods, Newton-Nodal methods (Multi-dimensional and One-dimensional) and Newton-Loop methods (Multi-dimensional and One-dimensional) are one of the efficient methods to obtain better convergence results. But Newton-Loop method results in better convergence than Newton-Nodal method due to less sparsity coefficient values. Thus, in the current study two Newton-Loop methods i.e., Newton-Loop method (Multi-dimensional) and Newton-Loop method (One-dimensional) or Hardy-Cross method are analyzed and compared to find out the best one for the optimization of the pipe gas distribution network selected in the current study.

2 Numerical Strategy

At the outset, to reduce the computational complexity, it is assumed that the flow is steady, isothermal, having negligible kinetic energy change with constant compressibility of the gas over the entire length of the pipe, validity of the Darcy-Weisbach' relationship along the pipe, and constant friction coefficient.

Under these considerations, the general flow equation for steady-state gas flow is given as [1]–

$$Q = C \frac{T_n}{P_n} \sqrt{\frac{2P_n(P_1 - P_2)D^5}{fSLTZ}} \quad (1)$$

Where, C is a constant value which shall be explained later in subsequent section, Q is Flow rate, T_n and P_n are temperature and pressure respectively at standard condition, (P₁ – P₂) is pressure difference, D is diameter, f is friction factor, s is specific gravity, L is length, T is temperature and Z is compressibility factor.

2.1 Flow Equation

As mentioned in previous section, many flow equations are given in literature out of which the equation best suitable for our work is selected. For low gas pressure systems: $T \approx T_n$, $Z \approx 1$ and $C = \sqrt{\frac{\pi^2 R_{air}}{64}}$, where $R_{air} = 287$ J/kg-k.

For LNG taking density as 0.722 kg/m³, Specific weight S as 0.589 and friction factor of pipe f as 0.0065 [1] and after putting all these values in Eq. (1), we get

$$\Delta P = (P_1 - P_2) = K \times Q^2 \quad (2)$$

Where, $K = 11.7 \times 10^3 \times L/D^5$ (K is known as Pipe constant).

Equation (2) is known as Lacey’s Low-Pressure Equation [1], which has been used to calculate the pressure-difference between two nodes in both of the methods selected for current study.

2.2 Design Details of the LNG Pipe Network

Based on the physical survey and drawings of the MNNIT staff colony, a Pipe network as shown in Fig. 1 is designed for the 3 Wings of MNNIT Staff Colony i.e. A-Wing, B-wing and C-wing which consists of 36 nodes, 37 pipes and 2 loops. Each node (●) represents a house in a wing. Therefore, the Pipe Network has been designed for 5 houses in A-Wing, 10 houses in B-wing and 20 houses in C-Wing. The distance between two houses is taken as 5 m and distance between two wings is taken as 15 m with every pipe in the loop having diameter (D) as 1.25 in. (31.75 mm). Load (m^3/h) on each node in the network is represented by an arrow (→) and the value of loads are taken as three average values of the practical Natural gas consumption in households. These three values of load 0.099 m^3/h , 0.67 m^3/h and 0.10 m^3/h are randomly put on each 36 nodes. The input flow rate (load) at node 1 is initially

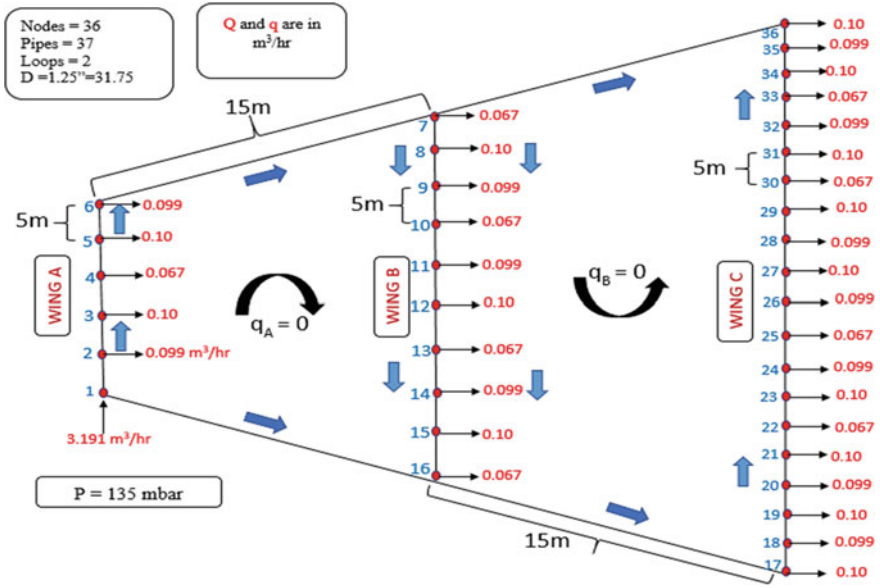


Fig. 1 Design of the pipe network

assumed as summation of load values of all the nodes. Therefore, Input load at node1 is taken as 3.191 m³/h. Further, Input pressure at node1 is taken as P1 = 135 mBar, which is very close to the practical LNG networks. Initial Loop flows q_A and q_B (as shown in Fig. 1) are assumed for the two loops to obtain the correct values of branch flows as branch flows are initial approximations to the true values. For the sake of simplicity initially both q_A and q_B are taken as zero.

The above initial design parameters are defined based on the objectives of the current study i.e., to calculate the value of flow rate in each individual pipe and value of pressure at each individual node.

2.3 Optimization Techniques Used for the LNG Pipe Network

As mentioned in the literature survey, a lot of good numerical methods are available to solve the gas network problems. But for kind of the networks as designed in Fig. 1 two methods namely N-L-M (Multi-Dimensional) and N-L-M (One-Dimensional) or H-C method are selected for comparative study in current work. The two of the methods have been explained in the subsequent sections.

2.3.1 Newton-Loop Method (Multi-dimensional)

Newton-Loop multidimensional method is based on Kirchhoff’s second law, according to which the summation of pressure-drops around any loop is zero. The steps followed in the Newton-Loop method for the desired solution of the pipe network are summarized in a flowchart as shown Fig. 2.

2.3.1.1 Loop Jacobi Matrix [1]

The loop Jacobi matrix as mentioned in Fig. 2 is shown in Eq. 3.

$$J^k = \begin{bmatrix} \frac{\delta f1}{\delta q1} & \frac{\delta f1}{\delta q2} & \dots & \frac{\delta f1}{\delta qk} \\ \frac{\delta f2}{\delta q1} & \frac{\delta f2}{\delta q2} & \dots & \frac{\delta f2}{\delta qk} \\ \vdots & \vdots & \ddots & \vdots \\ \frac{\delta fk}{\delta q1} & \frac{\delta fk}{\delta q2} & \dots & \frac{\delta fk}{\delta qk} \end{bmatrix} \tag{3}$$

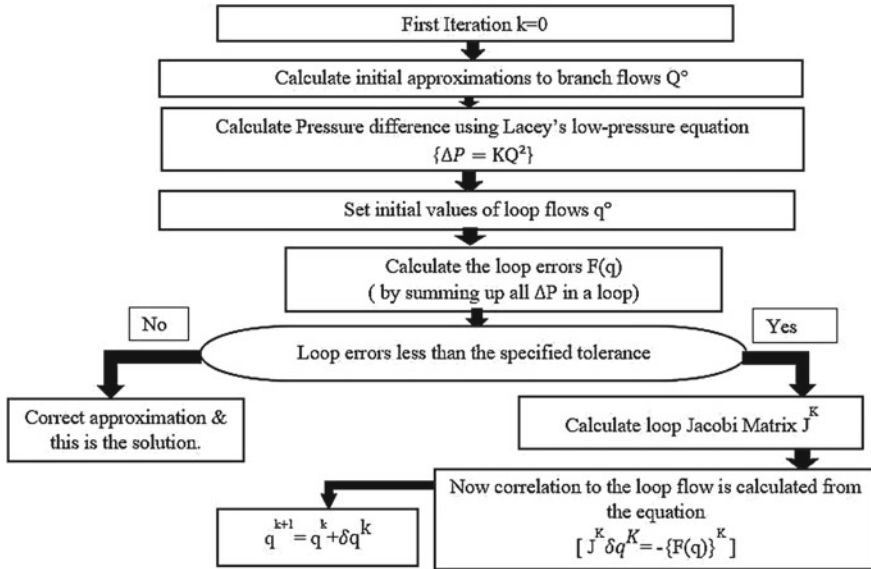


Fig. 2 Flowchart of the N-L (Multi-D) method

Where, f is the loop error, which is defined as:

$$f = \sum (Sign) S_i K_i [S_i Q_c]^m \tag{4}$$

f is calculated for all the loops. Where, i represents the branch in a loop and Q_c is the corrected flow rate for a branch i.e., $Q_c = Q_k \pm$ loop flow (Q_k is the branch flow).

[+ve sign if branch flow follows the direction of loop flow otherwise -ve sign] (Sign) in summation (Σ) will also be +ve if branch flow follows the direction of loop flow otherwise -ve sign.

$S = +1$ if Q_c is positive

$S = -1$ if Q_c is negative

$$m = \left\{ \begin{array}{ll} 2 & \text{for low-pressure networks} \\ 1.858 & \text{for medium range pressure networks} \\ 1.854 & \text{for high range pressure networks} \end{array} \right\}$$

2.3.2 Newton-Loop Method (One-Dimensional)/Hardy-Cross Method

Similar to the Newton-Loop method (Multi-dimensional), Hardy-Cross method also solves the similar set of equations but solves each set individually. Various steps followed in the Hardy-Cross method are summarized in a flowchart as shown below in Fig. 3.

3 Results and Discussion

The aim of the study is to calculate the value of flow rate in each individual pipe and value of pressure on each node. For simulation and analysis of the designed pipe network, N-L-M (Multi-dimensional) and N-L-M (One-dimensional) are used and further results obtained with both of the method are compared.

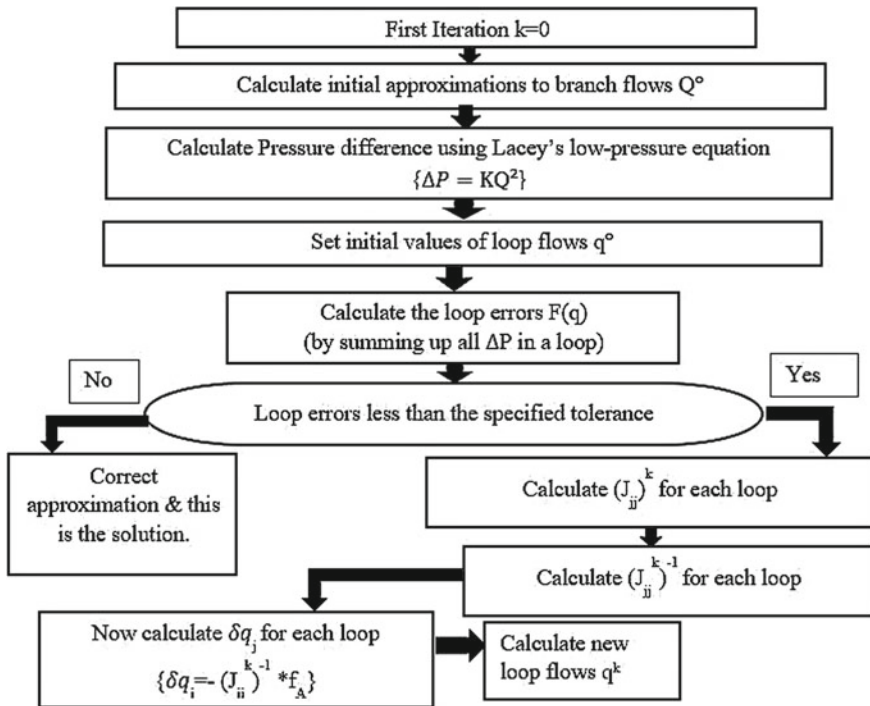


Fig. 3 Flowchart of the N-L (One-D) method

3.1 Newton-Loop Method (Multi-dimensional)

The N-L-M (Multi-Dimensional) is applied to the designed pipe network. Initially loop flows q_A and q_B are assumed to be zero i.e., $q_A = 0$ and $q_B = 0$ and the direction assumed is shown in the network. Input pressure at node 1 is taken as 135 mBar. Input flow rate is taken as 3.191 m³/h. The initial values of flow rates and pressure difference are mentioned in Table 1 for all pipes and nodes of the pipe network shown in Fig. 1.

Initially, $q_{A0} = 0$ and $q_{B0} = 0$

$$q = \begin{bmatrix} 0 \\ 0 \end{bmatrix} \tag{5}$$

Table 1 Initial values of flow rate and pressure difference

Pipe	Q	Qc	Δ(P) (mbar)
1	3.191	3.191	0.018462514
2	3.092	3.092	0.017334694
3	2.992	2.992	0.016231565
4	2.925	2.925	0.015512756
5	2.825	2.825	0.014470186
6	2.726	2.726	0.040421291
7	0	0	0
8	2.659	2.659	0.012819583
9	2.559	2.559	0.011873474
10	2.46	2.46	0.010972547
11	2.393	2.393	0.010382994
12	2.294	2.294	0.009541662
13	2.194	2.194	0.008727914
14	2.127	2.127	0.00820299
15	2.028	2.028	0.007457154
16	1.928	1.928	0.006739866
17	1.861	1.861	0.018838713
18	1.761	1.761	0.005622843
19	1.662	1.662	0.005008403
20	1.562	1.562	0.004423839
21	1.463	1.463	0.003880841
22	1.363	1.363	0.003368441
23	1.296	1.296	0.00304542
24	1.196	1.196	0.00259358
25	1.097	1.097	0.002181979
26	1.03	1.03	0.001923586
27	0.931	0.931	0.00157158
28	0.831	0.831	0.001252101
29	0.732	0.732	0.000971537
30	0.632	0.632	0.000724221
31	0.565	0.565	0.000578807
32	0.465	0.465	0.000392052
33	0.366	0.366	0.000242884
34	0.299	0.299	0.000162099
35	0.199	0.199	7.18031E-05
36	0.1	0.1	1.81316E-05
37	0	0	0

Loop errors for both of the loop's A and B can be calculated from the equations as shown below-

$$F_A = \Delta P_1 + \Delta P_2 + \dots + \Delta P_{16} - \Delta P_7 = 0.20915119 \quad (6)$$

$$F_B = \Delta P_8 + \Delta P_9 + \dots + \Delta P_{36} - \Delta P_{37} = 0.143591044 \quad (7)$$

Where, F_A & F_B are loop error in loop A and B respectively.

$$\text{Loop error matrix } F(q^0) = \begin{bmatrix} F_A \\ F_B \end{bmatrix} = \begin{bmatrix} 0.20915119 \\ 0.143591044 \end{bmatrix} \quad (8)$$

From Eq. (3)-

$$\text{Loop Jacobi Matrix (J)} = \begin{bmatrix} \frac{\partial f_A}{\partial q_A} & \frac{\partial f_A}{\partial q_B} \\ \frac{\partial f_B}{\partial q_A} & \frac{\partial f_B}{\partial q_B} \end{bmatrix} \quad (9)$$

$$\frac{\partial f_A}{\partial q_A} = 2[K_1|Q_{c1}| + K_2|Q_{c2}| + \dots + K_{16}|Q_{c16}|] = 0.1589964 \quad (10)$$

$$\frac{\partial f_B}{\partial q_B} = 2[K_8|Q_{c8}| + K_9|Q_{c9}| + \dots + K_{37}|Q_{c37}|] = 0.158743 \quad (11)$$

$$\frac{\partial f_A}{\partial q_B} = \frac{\partial f_B}{\partial q_A} = 2[K_8|Q_{c8}| + K_9|Q_{c9}| + \dots + K_{16}|Q_{c16}|] = 0.07485469 \quad (12)$$

$$J = \begin{bmatrix} 0.1589964 & 0.07485469 \\ 0.07485469 & 0.158743 \end{bmatrix} \quad (13)$$

$$J^0 * \partial q^0 = -F(q)^0 \Rightarrow \partial q^0 = \begin{bmatrix} -1.14343 \\ -0.36537 \end{bmatrix} \quad (14)$$

$$q^1 = q^0 + \partial q^0 \Rightarrow q^1 = \begin{bmatrix} -1.143432 \\ -0.36537 \end{bmatrix} \quad (15)$$

Initial assumption of flow rate in pipes is shown in Fig. 4 and Table 1.

Further four more iterations are carried out to obtain the most accurate values of pipe flow and optimized value of pipe flow rate. After iteration 5 the values are presented in pipe network as shown in Fig. 5.

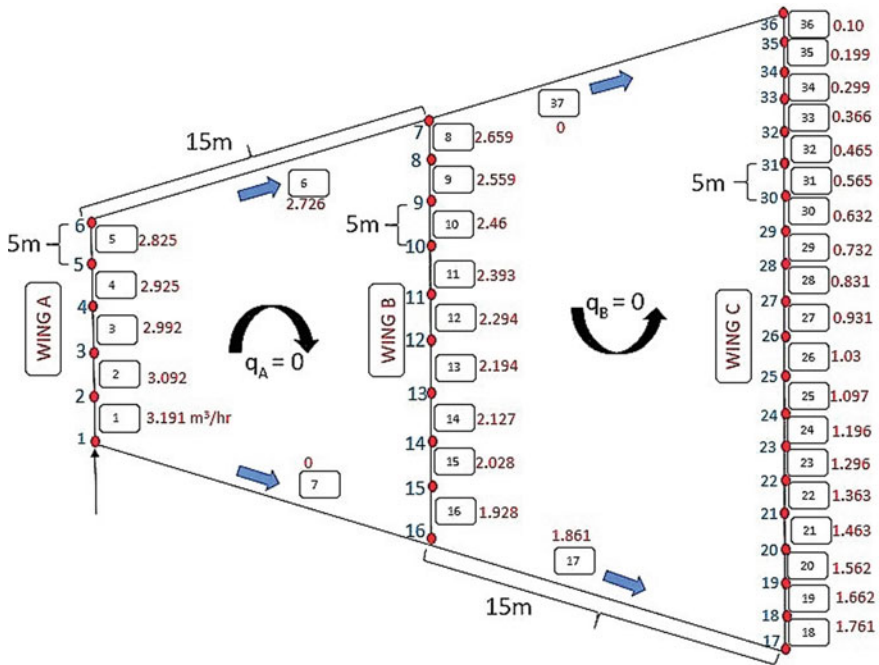


Fig. 4 Initial values of pipe flow rate for both N-L-M and H-C-M

3.1.1 Convergence Criteria

The convergence criteria for loop errors to stop the iterations in this study is taken in the range of 10^{-2} .

After five iterations, obtained values of loop error are in the range of 10^{-3} which fulfills the convergence criteria. The graphs for loop errors F_A and F_B , loop flow correction Δq_A and Δq_B with respect to number of iterations are as shown in Fig. 6 for N-L-M and Fig. 8 for H-C-M.

3.2 Newton-Loop Method (One-Dimensional)/Hardy-Cross Method

Now H-C-M is used over the pipe network as shown in Fig. 1 and the initial approximations are kept as same as for the N-L-M (Multi-dimensional) as shown in Fig. 4 and Table 1. In Hardy-Cross method, each set of equations is solved individually. So, in this method only diagonal elements of the matrix are calculated as shown below:

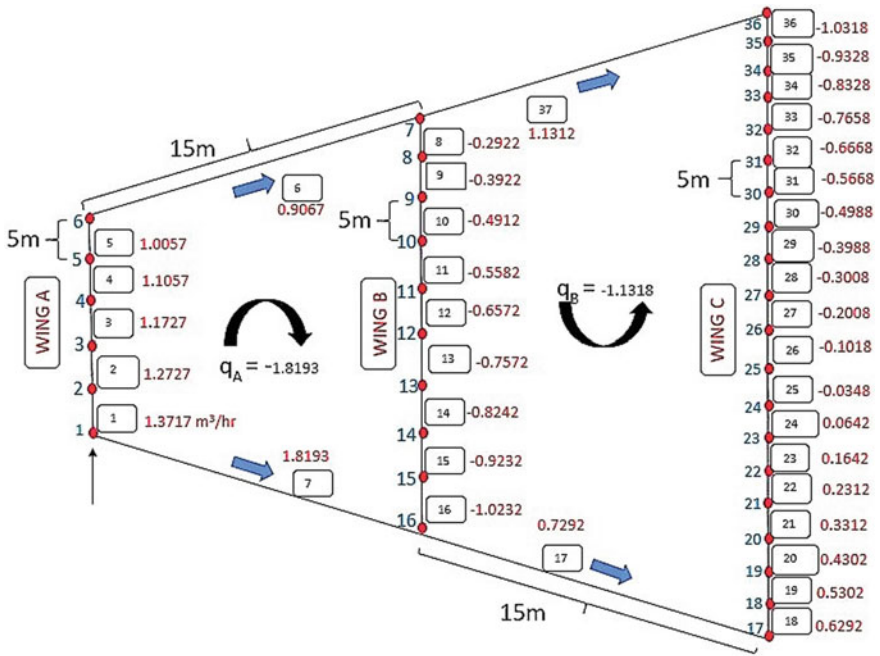


Fig. 5 Optimized pipe flow rate values obtained by N-L-M

Initially, $q_{A0} = 0$ and $q_{B0} = 0$

$$q^0 = \begin{bmatrix} 0 \\ 0 \end{bmatrix} \tag{16}$$

$$J_{AA}^0 = \frac{\partial f_A}{\partial q_A} = 2[K_1|Q_{C1}|+K_2|Q_{C2}|+\dots\dots\dots+K_{16}|Q_{C16}|] = 0.158996399$$

$$J_{BB}^0 = \frac{\partial f_B}{\partial q_B} = 2[K_8|Q_{C8}|+K_9|Q_{C9}|+\dots\dots\dots+K_{16}|Q_{C16}|] = 0.158742556$$

$$J_{AA}^0 \partial q_A^0 = -f_A^0 \triangleright \partial q_A^0 = -1.31544608$$

$$J_{BB}^0 \partial q_B^0 = -f_B^0 \triangleright \partial q_B^0 = -0.90455293$$

$$q_A^1 = q_A^0 + \partial q_A^0 = -1.31544608$$

$$q_B^1 = q_B^0 + \partial q_B^0 = -0.90455293$$

Initial approximation of flow rate in pipes is shown in Fig. 4.

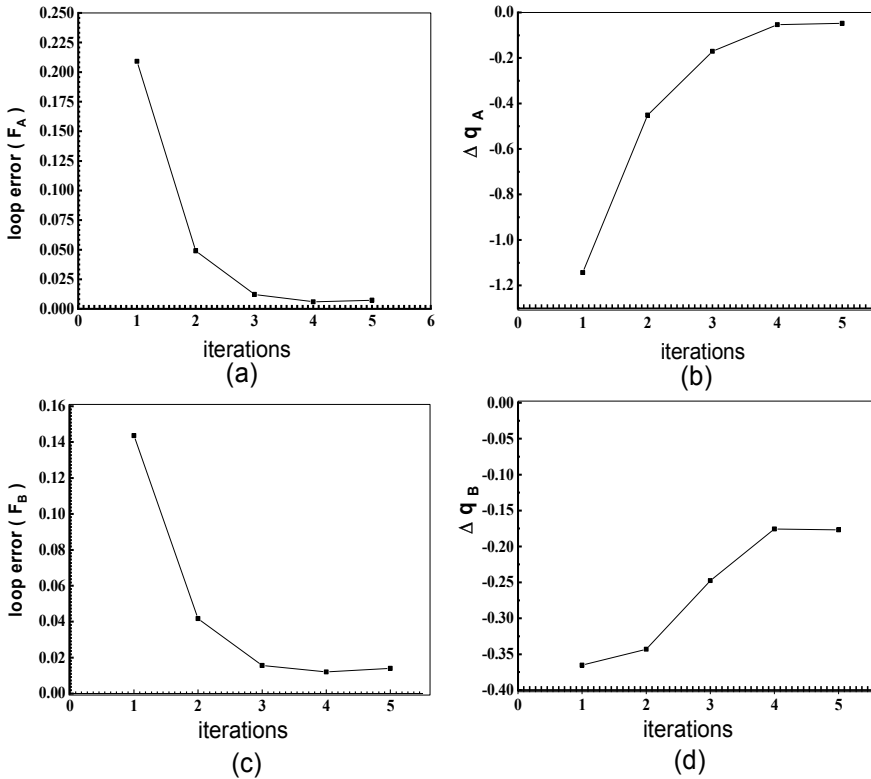


Fig. 6 a F_A vs iterations b Δq_A vs iterations c F_B vs iterations d Δq_B vs iterations (for N-L-M)

Also in this case, the same convergence criteria are applied and Optimum value of pipe flow rate is shown below at the pipe network in Fig. 7.

Further the graphs for loop errors F_A and F_B , loop flow corrections Δq_A and Δq_B with respect to the number of iterations for H-C-M are as shown in Fig. 8. The Figure clearly depicts that the solution gets converged after 5 iterations.

3.3 Node Pressure (for Both N-L-M and H-C-M)

The Pressure at each node is calculated by, $P_j = \Delta P_k - P_i$ (in each individual iteration). Where P_i is pressure at sending node and P_j is pressure at receiving node. The calculated values of pressure for both of the methods are as shown in Table 2.

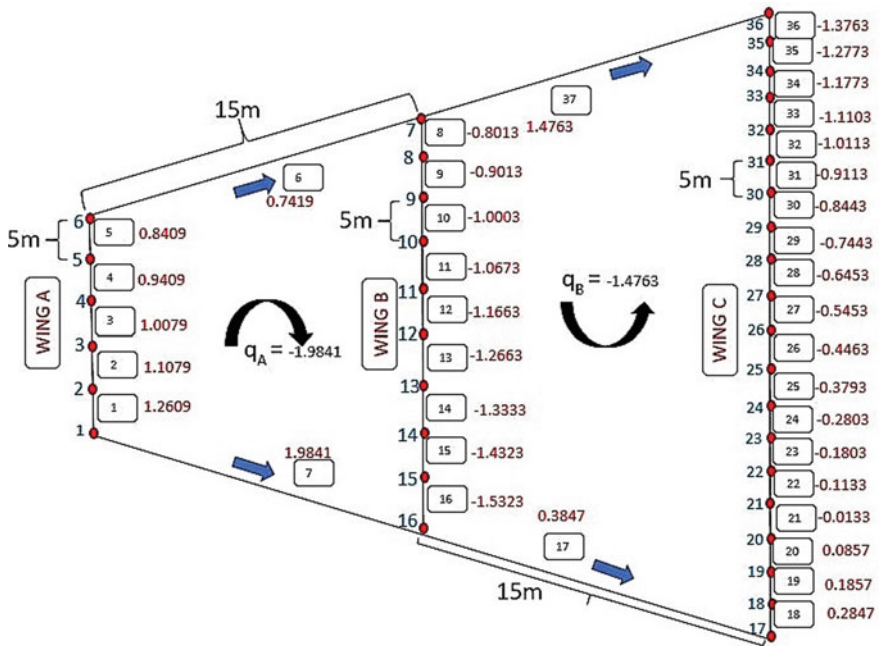


Fig. 7 Optimized pipe flow rate values obtained by H-C-M

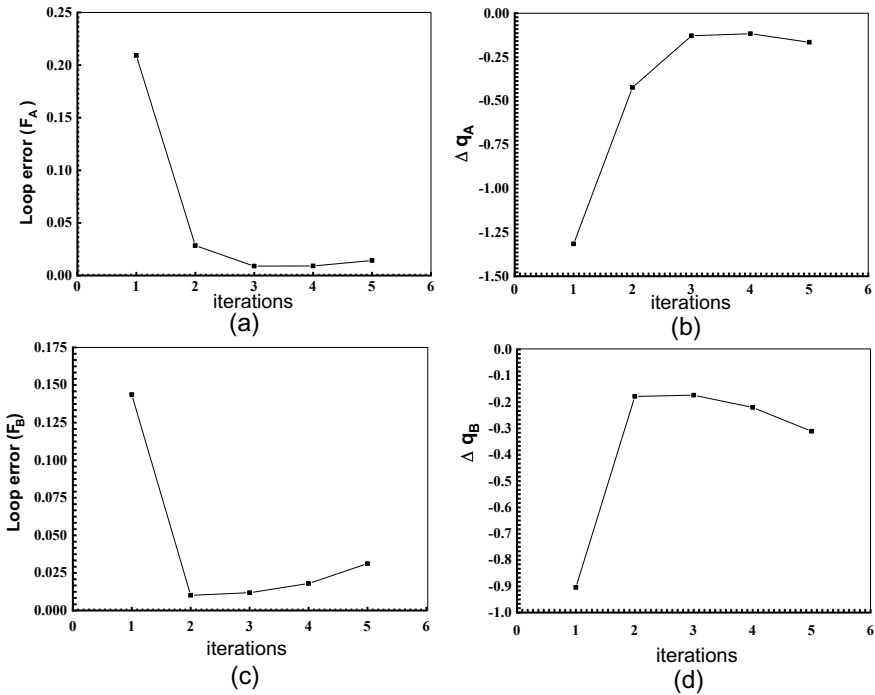


Fig. 8 a F_A vs iterations b Δq_A vs iterations c F_B vs iterations d Δq_B vs iterations (for H-C-M)

Table 2 Pressure at nodes obtained by both N-L-M and H-C-M

Node	Pressure (mbar) (N-L-M)	Pressure (mbar) (H-C-M)	Node	Pressure (mbar) (N-L-M)	Pressure (mbar) (H-C-M)
1	135	135	19	134.9705834	134.963302
2	134.9965885	134.9973587	20	134.9702479	134.9632887
3	134.9936517	134.995133	21	134.9700491	134.9632884
4	134.9911583	134.9932909	22	134.9699522	134.9632651
5	134.9889416	134.9916856	23	134.9699033	134.9632062
6	134.9871078	134.9904033	24	134.9698959	134.9630637
7	134.9826361	134.987409	25	134.9698937	134.9628029
8	134.9824814	134.9862447	26	134.9698749	134.9624418
9	134.9822025	134.9847716	27	134.9698017	134.9619026
10	134.9817651	134.9829572	28	134.9696376	134.9611477
11	134.9812002	134.9808916	29	134.9693477	134.9601432
12	134.9804172	134.9784251	30	134.9688947	134.9588508
13	134.9793777	134.9755174	31	134.9683121	134.957345
14	134.9781461	134.972294	32	134.9675058	134.9554907
15	134.9766009	134.9685741	33	134.9664424	134.9532555
16	134.9747027	134.9643166	34	134.9651847	134.9507425
17	134.9718107	134.9635115	35	134.9636069	134.9477844
18	134.971093	134.9633646	36	134.9616764	134.9443499

3.4 Comparison of Newton-Loop Method (Multi-D) and Hardy-Cross Method

Now for finding the best method of solution of the gas flow pipe network shown in Fig. 1, a comparative study between N-L-M and H-C-M is conducted in the current section as shown below in Fig. 9.

The graph in Fig. 9 shows that the values of loop error and loop flow corrections converge faster in Newton-Loop (Multi-D) method compared to the Hardy-cross method. The reason being the Hardy-Cross method neglects the off-diagonal elements of the Loop-Jacobi Matrix by treating each loop individually. The off-diagonal elements show the interconnections between two loops which are ignored in Hardy-Cross Method, thus resulting in poor convergence characteristics.

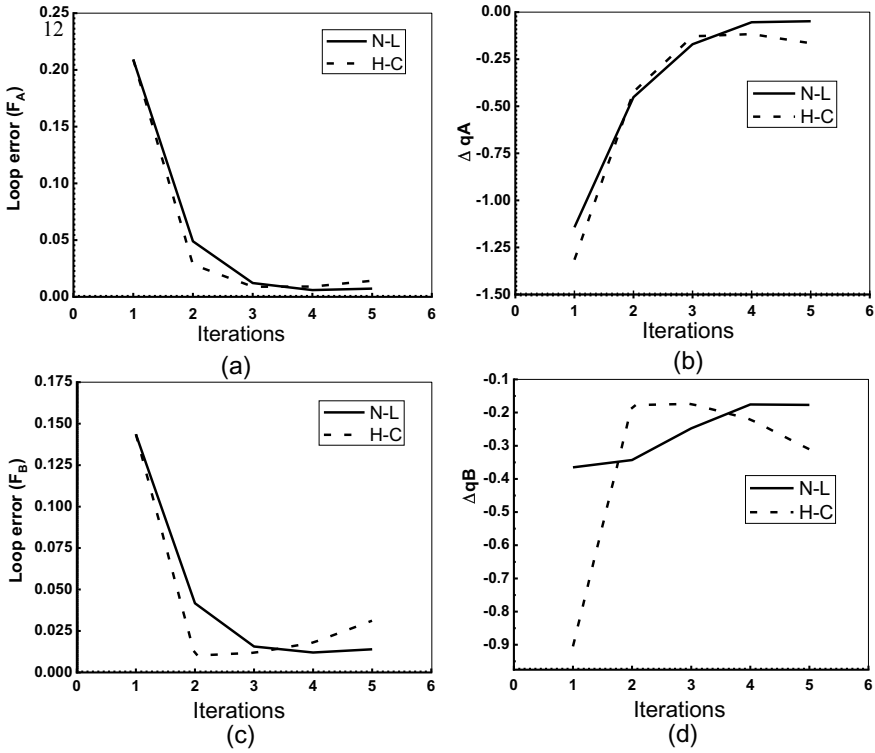


Fig. 9 a F_A vs iterations b F_B vs iterations c Δq_A vs iterations d Δq_B vs iterations

4 Conclusion

The study provides an optimized solution for the problem considered in the current work. The optimized pressures at each node for the initial conditions given in the gas pipe network as shown in Fig. 1, using both (N-L-M) and (H-C-M) methods are been given in Table 2 and Figs. 5, 6 and 7. The study also establishes that Newton-Loop (Multi-dimensional) method is a better method for the optimization of the LNG pipe distribution network.as shown in Fig. 1.

References

1. Osiadacz A (1987) Simulation and analysis of gas networks
2. Hyman SI, Jones RI (1967) Loop defining techniques for gas distribution network analysis. In: American gas association workshop on computer application to distribution designs problems, Washington, DC
3. Boyne GG (1970) The design & analysis of gas distribution networks. Ph.D. dissertation, Heriot-Watt University

4. Hamam YM, Brameller A (1971) Hybrid method for the solution of piping networks. In: Proceedings of the institution of electrical engineers, vol 118, no 11. IET Digital Library, pp 1607–1612
5. Jeppson RW (1974) Steady flow analysis of pipe networks: an instructional manual
6. Mah RSH, Shacham M (1978) Pipeline network design and synthesis. *Adv Chem Eng* 10:125–209
7. Aylmer S (1981) Interactive gas flow analysis
8. Tian S, Adewumi MA (1993) A simple algorithm for analyzing gas pipeline networks. In: SPE production operations symposium. Society of Petroleum Engineers. <https://doi.org/10.2118/25475-MS>
9. Coelho PM, Pinho C (2007) Considerations about equations for steady state flow in natural gas pipelines. *J Braz Soc Mech Sci Eng* 29(3):262–273. <https://doi.org/10.1590/S1678-58782007000300005>
10. Swamee PK, Sharma AK (2008) Design of water supply pipe networks. Wiley, Hoboken
11. Brkić D, Tanasković TI (2008) Systematic approach to natural gas usage for domestic heating in urban areas. *Energy* 33(12):1738–1753
12. Herrán-González A, De La Cruz JM, De Andrés-Toro B, Risco-Martín JL (2009) Modeling and simulation of a gas distribution pipeline network. *Appl Math Model* 33(3):1584–1600
13. Brkić D (2011) Iterative methods for looped network pipeline calculation. *Water Resour Manag* 25(12):2951–2987
14. Lukman S, Ismail A, Ibrahim A, Saulawa BS (2012) Development, utilization and statistical evaluation of Hardy Cross pipe network analysis softwares. *Int J Water Resour Environ Eng* 4(8):252–262
15. Sharma AK, Swamee PK (2013) Application of linear programming for looped water supply pipe network design. *Water Sci Technol Water Supply* 13(5):1195–1201
16. Niazkar M, Afzali SH (2017) Analysis of water distribution networks using MATLAB and Excel spreadsheet: h-based methods. *Comput Appl Eng Educ* 25(1):129–141
17. Kudaisya SK, Kar SK (2017) A comprehensive review of city gas distribution in India. In: Natural gas markets in India, pp 113–165
18. Bianchini A, Guzzini A, Pellegrini M, Saccani C (2018) Natural gas distribution system: a statistical analysis of accidents data. *Int J Press Vessels Pip* 168:24–38
19. Brkić D, Praks P (2019) Short overview of early developments of the Hardy Cross type methods for computation of flow distribution in pipe networks. *Appl Sci* 9(10):2019. <https://doi.org/10.3390/app9102019>
20. Pandey A, Rawat A (In preparation) Numerical pipe network analysis for sanitization to fight COVID-19

To Predict Frictional Pressure-Drop of Turbulent Flow of Water Through a Uniform Cross-Section Pipe Using an Artificial Neural Network



Vaibhav Srivastava, Ankit Prakash, and Anubhav Rawat

Abstract The current work uses an Artificial Neural Network (ANN) approach to determine the friction factor for turbulent flows of water in a pipe of uniform circular cross-section. The Colebrook equation which is the most fundamental equation in the context of this problem and combines the available data for transition and turbulent flow in pipes is implicit in the friction factor. Also, some approximations of the Colebrook equation, explicit in friction factor developed using an analytical approach, introduce some significant additional errors in the solution. The most popular approach today used by engineers is the Moody Chart, which relates friction factor as a function of Reynolds number and relative roughness. However, referring to the chart repeatedly is a time-consuming activity. Besides these conventional approaches, neural networks (a subset of artificial intelligence) can be applied as they have in recent time matured to a point of offering practical benefits in many of their applications. In this study, the best performance in terms of Mean Absolute Percentage Error and R^2 Score was achieved by 2-6-6-6-6-1 network with tanh, sigmoid, tanh, tanh, sigmoid functions respectively for hidden layers and ReLU for output layer, which was around 0.59% in terms of Maximum Error and Explained Variance Score. The 2-6-8-6-8-6-1 architecture with sigmoid, tanh, sigmoid, tanh, sigmoid for hidden layers and ReLU output performed slightly better with a Maximum Error of 0.0008 and Explained Variance Score of 0.99985. This study also sought to discover a relationship between the number of data points and the accuracy of Artificial Neural Networks tested.

Keywords Friction factor · Colebrook equation · Artificial Neural Networks

V. Srivastava (✉) · A. Prakash · A. Rawat
Applied Mechanics Department, Motilal Nehru National Institute of Technology-Allahabad,
Prayagraj 211004, Uttar Pradesh, India

A. Rawat
e-mail: anubhav-r@mnnit.ac.in

1 Introduction

For the design of a pipeline system, Pressure-Drop is the most important criterion. The major factor contributing to the Pressure-Drop is the friction factor and the Pressure-Drop for all types of fully developed internal flows can be expressed as (Cengel [1]):

$$\Delta P = f \frac{L}{D} \frac{\rho V^2}{2} \quad (1)$$

where f is the Darcy friction factor, and $\frac{\rho V^2}{2}$ is the dynamic pressure. L and D simply refer to the length and diameter of the pipe respectively. This friction factor for turbulent flow is controlled by the Reynolds Number (Re) and relative roughness (ϵ/D) parameters, where ϵ is the mean height of roughness. Numerous experiments, using artificially roughened surfaces were conducted for transition as well as turbulent flows, and f was calculated by measuring the Pressure-Drop and discharge. Notably, most of such experiments were conducted by Nikuradse [2] in 1933 and covered a large range of roughness values. The data obtained through these experiments was brought into a functional form in 1939 by Colebrook et al. [3], now famously known as the Colebrook equation:

$$\frac{1}{\sqrt{f}} = -2.0 \log \left(\frac{\epsilon}{3.7D} + \frac{2.51}{Re\sqrt{f}} \right) \quad (2)$$

This relation can also be used for noncircular pipes by replacing the diameter D with the hydraulic diameter and it is implicit in the friction factor. This implies that f can only be obtained via an iterative solution. The final results may have errors based on the initial guess values and solving this equation using numerical methods is tedious, especially if friction factors for a lot of input pairs of Re and ϵ/D are needed. So, various explicit approximations of this equation were developed. One of them was given by Haaland [4] in 1983:

$$\frac{1}{\sqrt{f}} \cong -1.8 \log \left[\frac{6.9}{Re} + \left(\frac{\epsilon}{3.7D} \right)^{1.11} \right] \quad (3)$$

This explicit approximation of the Colebrook equation developed using an analytical approach will also introduce some additional error lying within 2% of the solution given by the Colebrook equation given that the Reynolds number is greater than 3000 [5]. This additional error can be reduced using ANNs.

Moody diagram [6] is the most popular method used today for friction factor estimation, where friction factor is plotted against ϵ/D and Re . However, it is quite tedious if required to look upon multiple times and there will be some error in reading this chart manually. This also can be avoided using Artificial Neural Networks (ANNs) as will be explained further in this paper.

In the present scenario, Artificial Intelligence (AI) has proved its superiority not only in areas such as image recognition, chatbots, and cybersecurity, but is also being applied beyond computer science to solve countless intractable practical engineering problems. ANNs are a subset of AI. Hence this study aims to discover how well are ANNs able to solve this problem of finding friction factors if they are trained using some data samples as input. More precisely, this approach can give insight on how accurately and quickly friction factor can be obtained for a large dataset, which using conventional approaches is tedious and time-taking either because of numerous iterations of Colebrook equations or looking at Moody's chart repeatedly. In addition, this network can then possibly be used to find friction factor in more complex problems (like Non-Newtonian Fluid Flow) using approaches like Transfer Learning.

The application of neural networks to solve fluid flow problems is a relatively new field of analysis. Among the initial attempts to find friction factor using ANN, one was given by Shayya and Sablani [7] in 1998 and the trained network was able to predict the response with a mean relative error of less than 1.25%. Data was generated by solving the Colebrook equation using the Regula-Falsi method.

Recently, Yazdi and Bardi [8] attempted this problem in 2011. Dataset used by them for training the network consisted of 2000 values. They used techniques like normalization to improve the performance of the network and found that if the acceptance criterion for training neural networks was Maximum Percentage Error (MPE) being less than 1%, then the best choice was '2-10-20-1' structure if training time was a consideration with 0.98% MPE. If not, the '2-20-25-1' structure gave the best performance with 0.35% MPE. Fadare and Ofidhe [9] developed an ANN with a 2-20-31-1 configuration trained with the Levenberg-Marquardt training algorithm gave a better performance with R-value = 0.999 and Mean Absolute Percentage Error (0.68%). Note that the same training algorithm was used by Yazdi and Bardi [8].

Another attempt for predicting friction factor using ANN was done by Sahai et al. [10]. In their work, ANN modeling was carried out based on 378 samples extracted from the Moody chart, out of which 70% data was used for training the model, 15% data was used for model validation, and the rest 15% data was used for testing purpose. The developed ANN model had less than 5% error in the prediction.

Brkić and Cojbasić [11] also developed an ANN model for predicting friction factor, a total of 90,000 datasets were used for a 2-50-1 network topology with an error of 0.07%. In order to generate the training set for the ANN model, they also solved the Colebrook equation iteratively.

The Multi-Layer Perceptron (MLP) neural network by Offor and Alabi [12] in 2016 with two hidden layers having 30 neurons each had relative error up to a maximum of 0.004% when compared with the Colebrook equation. This was evidently better than all explicit models and also one of the most accurate ANN models available for friction factor estimation of turbulent flow of pipes.

Although all of the above models were accurate, the dataset used had a wide range. According to Andrew et al. [13] for superior performance of any ANN, two requirements are the ability to train a big enough neural network for the data, and

second is the amount of data itself. In other words, if more data is used to train a network of suitable size, then the network will be able to predict better. Also, a skillfully designed small ANN can do better than a larger ANN for the same dataset. Hence, not only the accuracy of the network is important, but the amount of data being used to train the network is also important. This approach is similar to the work by Sethi et al. [17], in which they have predicted the impact of wall parameters on plug – 1 flow characteristics through pipelines. They have varied two wall parameters (wall friction coefficient and wall cohesion coefficient) and then predicted the Pressure-Drop for Plug - 1 flow using 3 datasets having 50,000, 250,000, and 500,000 samples. The best architecture was found to be t50-t40-r1 architecture with ‘adamax’ optimizer, with Mean Absolute Percentage Error (MAPE) being close to 0.00402% when tested on the 500,000 samples dataset.

Consequently, this study not only aims to develop a network that is more accurate than both the explicit approximations of the Colebrook equation or finding it through a Moody’s chart manually but also to determine what order of dataset can make that network do this task.

It must also be noted that the objective of this research is not to give a replacement for the Colebrook equation but to observe how well this flourishing area of Artificial Neural Networks applies to this problem. This will give insight regarding other such problems of more complex fluid flows that might be tackled easily using this powerful tool where large experimental datasets are not available, by selecting the established accurate models and generating required dataset using suitable mathematical applications viz. MS-Excel, or MATLAB, or Python code itself.

2 Methodology

2.1 Activation Functions and Optimizers Used

The algorithm used for the current work possesses different neuron pairs in every layer which are connected either through a ‘tanh’ function or through a ‘sigmoid’ function to produce new neurons in subsequent layers which leads to the formation of the model to map the input to output. ReLU function is used in the output layer to have positive values of friction factor at the output.

Sigmoid function is an activation function with a mathematical expression given as:

$$A = \frac{1}{1 + e^{-z}} \quad (4)$$

where A is the activation value. $Z = WX + b$. (W = weight matrix, X = input matrix and b = bias). The graph is as shown below in Fig. 1(a).

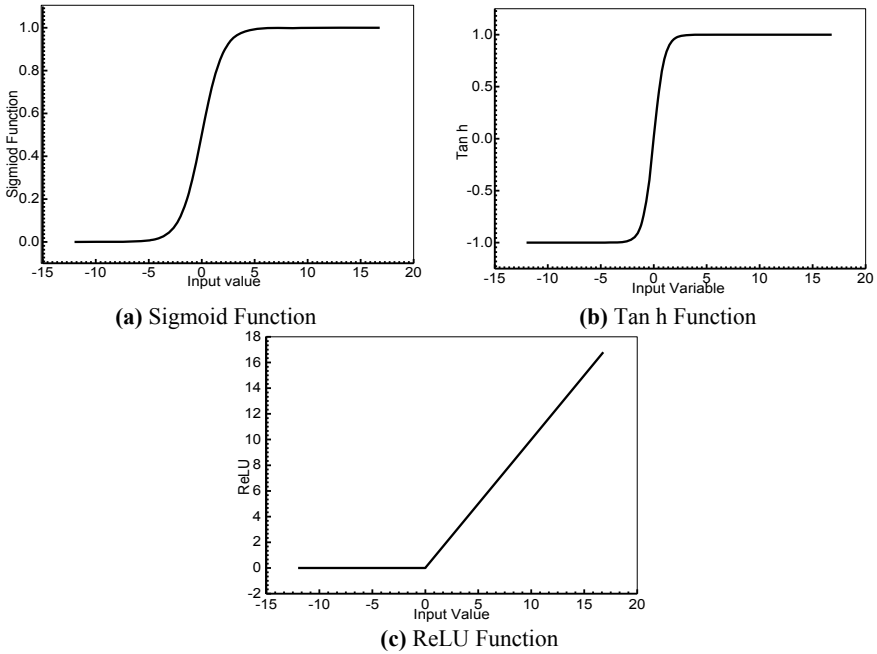


Fig. 1 Activation functions used in the study

The tan h function refers to the hyperbolic tan function. This function has the effect of centering the data to 0 rather than 0.5 as in sigmoid. This has a normalizing effect and makes learning for the next layer easier. The graph of tanh function is shown in Fig. 1(b).

Since the output of this ANN (Friction factor) is always positive, ReLU (Rectified Linear Unit) function is used which is given as:

$$A = \max (0, Z) \tag{5}$$

which is always positive as shown in graph (Fig. 1(c)).

Various optimizers used in the current work are SGD, Adam optimization algorithm, Adagrad optimization algorithm, and Adamax optimization algorithm. Stochastic Gradient Descent (SGD) (with momentum) optimizer involves computing the weighted averages of gradients and then using them to update weights. This technique almost always gives faster convergence than SGD without momentum because it smoothens the steps of gradient descent as the cost gets closer to the optimal value.

Adam’s optimization algorithm combines SGD with momentum and Root mean square propagation (RMSprop) algorithm, and hence most of the time works better than these two. RMSprop can be described as an exponential moving average applied to the square of gradient steps in backward propagation. This is helpful because adjusting the gradient without squaring can be noisy in the case of mini-batch gradient

or stochastic gradient descent. Hence this smoothens the gradient descent steps and makes the cost convergence faster.

In Adagrad optimization algorithm, the learning rate is based on the parameters themselves. Parameters related to frequently occurring features have a low learning rate while those related to infrequent features have a higher learning rate. Using this algorithm, the need to manually tune the learning rate is eliminated.

Whereas, the Adamax optimization algorithm is a small variation of the Adam algorithm, which uses a special case of L infinity norm instead of L2 norm while calculating gradient velocity, resulting in a stable and well-performing algorithm.

2.2 Artificial Neural Network Approach

An artificial neural network learning algorithm, or neural network, is a computational system that learns using a network of functions to understand a data input of one form into the desired output.

To solve a problem using this approach, various steps are involved. Firstly, the generation of a dataset that can be split to train and test the neural network and preprocessing. Secondly, developing a neural network code and training and then testing the network and tuning hyperparameters for better accuracy. At the end observing and tabulating the variation in the accuracy of the results with and selection of optimal ANN Architecture.

These steps shall be explained in detail in the subsequent sections. For reference, one of the many ANN structures used in the current study, an ANN structure (2-6-8-6-8-6-1) is represented in Fig. 2 above which is obtained using NN-SVG tool. Where in input layer 2 neurons are selected, in output layer 1 neuron is selected and in the hidden layers from left to right 6-8-6-8-6 neurons are selected to construct the 2-6-8-6-8-6-1 ANN structure.

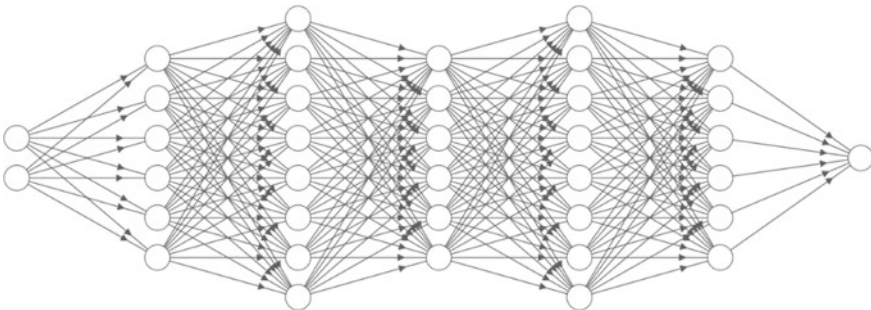


Fig. 2 One of the ANNs used in the current study, with 2-6-8-6-8-6-1 architecture visualized using NN-SVG tool

Dataset Generation and Pre-processing. The data generation is done in three steps to find the order or amount of data needed using this approach for reliable accuracy. The three datasets used consisted of 3000, 6000, and 10,000 samples and were generated using a Microsoft Excel spreadsheet. Datasets were generated by solving Colebrook et al. [3] equation iteratively. An initial guess value of friction factor was chosen using Haaland [4] equation. Newton-Raphson method [14] as shown below was the numerical method used to achieve the solution.

$$f_{n+1} = f_n - \frac{g(f_n)}{g'(f_n)} \tag{6}$$

where, f_n is the friction factor in n^{th} iteration, and $g(f_n)$:

$$g(f_n) = \frac{1}{\sqrt{f_n}} + 2.0 \log \left(\frac{\frac{\epsilon}{D}}{3.7} + \frac{2.51}{\text{Re} \sqrt{f_n}} \right) \tag{7}$$

and $g'(f_n)$:

$$g'(f_n) = -\frac{1}{2} \frac{1}{f_n^{-3/2}} \left[\frac{\left(1 + 2 \times \frac{2.51}{\log_e 10 \times \text{Re}} \right)}{\left(\frac{\epsilon}{3.7 D} + \frac{2.51}{\text{Re} \sqrt{f_n}} \right)} \right] \tag{8}$$

The values of $g(f_n)$ and $g'(f_n)$ are found using Colebrook et al. [3] equation as shown above. Here subscript n refers to the iteration number. Seven iterations of the Newton-Raphson method were carried out although most of the values converged to the estimated error of the order of 10^{-14} in just 3 to 4 iterations. This can be attributed to the choice of better initial guess value. The test set split was 0.05 for the dataset of 3000 samples, 0.025 for 6000 samples, and 0.015 for 10,000 samples. This was done for keeping uniformity as all test sets would contain 150 samples even if belonging to different datasets. *Feature scaling* [15] was applied to inputs to standardize them at the beginning of the code. The standard score of an input x_1 is found using the formula below:

$$z_1 = \frac{(x_1 - u_1)}{s_1} \tag{9}$$

where u_1 is the mean of all input samples and s_1 is the standard deviation.

Development of ANN Code and Training. The ANN code used in this research was generated using Python 3 programming language. Sophisticated machine learning libraries and frameworks like TensorFlow (version 2.1.0), Keras (version 2.3.1), and Scikit-learn (version 0.23.2) were used. This resulted in faster, vectorized code without involving any ‘for’ loops. The first layer consisted of Re and ϵ values as input parameters to the ANN. Feature scaling [15] method was applied so that the large value of one input doesn’t overshadow the other input. Which means that the discrepancies due to the difference in the order of inputs were avoided in this network.

Different combinations of hyperparameters like the number of layers, number of units in each layer, and type of activation functions were tested on sample datasets. The number of hidden layers was varied from 1 to 5, while the number of units in a layer ranged from just 4 to 84. The “tanh” and “sigmoid” activation functions were used for the hidden units while the “ReLU” function was used in the output layer as it outputs only positive values. Different optimizers namely Adam, Adagrad, Adamax, and Stochastic Gradient Descent are used and selected depending upon their suitability to different networks, The Mean Square Error was the cost function to be minimized. Mini Batch [16] sizes were 30, 60, and 100 for 3000, 6000, 10,000 samples respectively for the sake of consistency. The codes were run up to 100,000 epochs. Mean Absolute Percentage Error (MAPE), Maximum Error, Explained Variance Score, and R^2 Score were chosen as the metrics to test the accuracy of the network. A common test set was assigned for each dataset so that the ANNs are tested on the same values of friction factor. These many different combinations of network architectures on three different datasets were tried as there is no single established procedure for choosing these parameters and it comes only by prior experience. Hence, the exercise was also important to get a complete idea of the problem.

Testing Network and Tuning Hyperparameters. Choice of optimization algorithm, Number of hidden layers, Number of neurons, and activation function in each hidden layer were the hyperparameters considered in this problem. The approach used to tune these hyperparameters were similar to Coarse-to-Fine sampling scheme [16]. After getting a rough idea of the problem by trying 18 randomly chosen networks for the 3000-sample dataset (coarse sampling), the hyperparameters were tuned in the region where previously the results were more accurate. The dataset was increased to observe the variation in accuracy even after trying various ANN combinations.

Observation of Results and Selection of Optimal ANN Architecture. Four metrics are used in this study to evaluate the ANNs on test sets namely MAPE, ME, EVS, and R^2 Score.

Mean Absolute Percentage Error (MAPE). The MAPE is defined as

$$MAPE = \frac{1}{m} \sum_{n=1}^m \left| \frac{A_n - F_n}{A_n} \right| \quad (10)$$

where m is the number of test examples and A_n and F_n refer to the actual and forecasted values of friction factor respectively.

Maximum Error (ME). Maximum Error is the maximum deviation of predicted friction factor from actual friction value among all test examples.

$$ME = \max(|A_n - F_n|) \quad (11)$$

Explained Variance Score (EVS). This score measures the proportion to which any ANN accounts for the variation of a given dataset. This regression score's best possible value is 1.0 and lower values are worse.

$$EVS = 1 - \frac{Var\{A - F\}}{Var\{A\}} \quad (12)$$

R² Score. This score represents the segment of variance of actual friction factor values that has been explained by the independent variables of the ANN. It indicates how well new samples are likely to be predicted by the model. Note that since variance is dataset dependent, it is not recommended to compare R² scores across different datasets. The best possible score is 1.0 and it can also take negative values.

$$R^2 = 1 - \frac{\sum_{n=1}^m (A_n - F_n)^2}{\sum_{n=1}^m (A_n - \bar{A})^2} \quad (13)$$

where $\bar{A} = \frac{1}{m} \sum_{n=1}^m A_n$.

Hence, *MAPE* and *ME* will be used to compare networks in general, especially with different input different datasets. While R² and EVS will be used to compare networks with the same input dataset so as to give a better idea of how well the model shall predict new values.

Algorithm for ANN Code. The flowchart in Fig. 3 shows the algorithm for the ANN code used in the current work in the Python language.

3 Results and Discussion

In the current work, initially 18 random ANN architectures were trained on the dataset with 3000 samples (3000 series). The results helped give the idea of what kind of architectures can work on the problem well. Consequently, in the second stage, a lesser number of more effective variations were tried (Coarse-to-Fine sampling [16]) while the number of data samples were increased to 6000 to achieve better accuracy but no architecture could do that. In the third stage, the dataset was increased to 10,000 samples and better architectures were tried based on the experience. Finally, the 2-6-6-6-6-6-1 network with tanh, sigmoid, tanh, tanh, sigmoid functions respectively for hidden layers was found to give the best performance in overall MAPE, ME, and the two variance scores. However, it must also be mentioned that these performances of ANNs may vary based on the initialization of weights and biases (done randomly by the system for each iteration) and the number of iterations for which the model is trained. It is assumed that these factors affect accuracy only to a limit so that the final results do not vary.

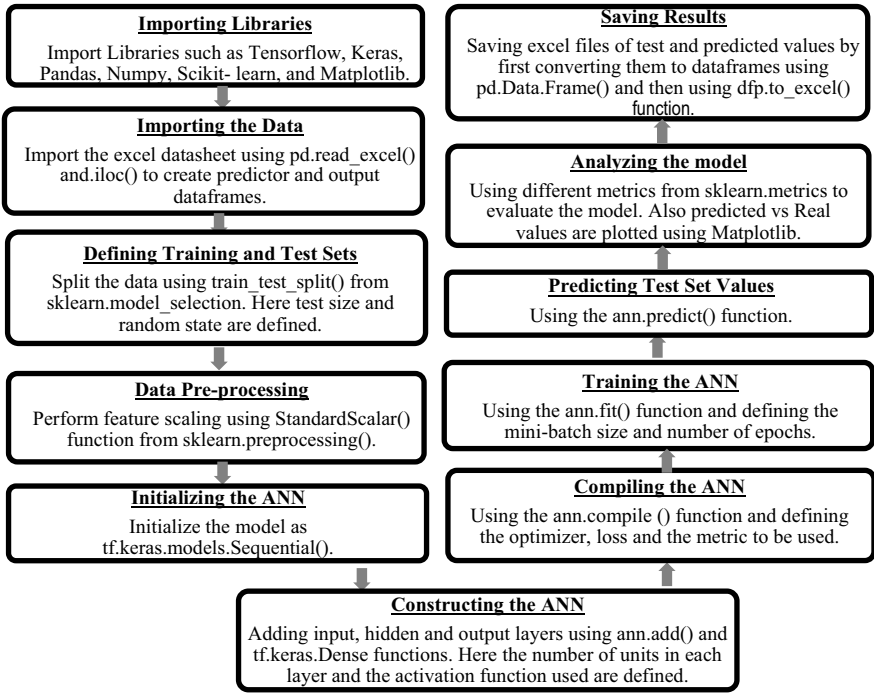


Fig. 3 Algorithm for ANN code

3.1 Initial Attempt with Dataset Having 3,000 Values

Table 1 is the record of observations of the 18 different ANN architectures tested in this stage. The t34-t42-t62-r1 architecture with ‘adamax’ optimizer was found to be the best performer in this stage with MAPE around 0.62%, ME of 0.00278, and best EVS and R² Scores. While the worst performance was of t16-s18-t22-s14-r1 with ‘adagrad’ optimizer with MAPE about 14.9%. It can be concluded at this stage that ‘adagrad’ optimizer was slow compared to ‘adam’, ‘adamax’, and ‘sgd’. This optimizer was hence not used for the next stage. Single hidden layer networks were all having the most error (more than 5%) hence they were also dropped for the next stage. Further, a need was felt to increase the number of data points for these networks to perform better. Hence dataset was doubled. Results of first stage convergence criteria for loop errors to stop the iterations in this study are given in Table 1 and are taken in the range of 10⁻².

Table 1 Results of the first stage

3000 series ANNs										
H1	H2	H3	H4	H5	O	MAPE (%)	ME	EVS	R ² Score	Optimizer
t4					r1	7.955244	0.016152404	0.94513131	0.94512981	adamax
s14					r1	8.784752	0.018032692	0.932019237	0.93144027	adamax
t22					r1	7.5946665	0.016104244	0.949788589	0.949747	adamax
s84					r1	12.671642	0.014549844	0.943718201	0.92491532	adamax
t6	s8				r1	3.1250322	0.003577541	0.994832313	0.99336738	adam
s16	t35				r1	4.2574477	0.009596571	0.986796194	0.98665214	adamax
t82	s44				r1	2.598253	0.003649143	0.998475113	0.99741134	adamax
s6	s8				r1	3.5338814	0.011761293	0.98219569	0.98149351	adamax
t12	s16	t12			r1	1.7217108	0.002913788	0.9989418	0.99849078	adamax
t34	t42	t62			r1	0.6169763	0.002782238	0.99936924	0.99936034	adamax
s6	t8	s6			r1	2.0092845	0.003053321	0.997467335	0.99663334	adamax
t30	s20	t10			r1	11.430753	0.018586047	0.908334871	0.90827551	sgd
s6	s8	s6			r1	6.3537397	0.014552714	0.965335857	0.96461574	adamax
t16	s18	t22	s14		r1	14.896118	0.019691803	0.880391082	0.88008869	adagrad
s6	t8	s6	t8		r1	0.9343764	0.002479619	0.998464237	0.99834078	adamax
t62	s34	t56	s74		r1	11.802379	0.019982927	0.898936995	0.89542847	sgd
t4	t5	t6	t7		r1	1.534904	0.002814705	0.997907192	0.91431646	adamax
s6	t8	s6	t8	s6	r1	14.37397	0.020864651	0.874257901	0.87420876	sgd

where, in columns H heading represents the hidden layer number, O represents output layer, and MAPE, ME, EVS, and R² Score are the evaluation matrix used. Optimizers used are given in the last column. The ‘t’, ‘s’, and ‘r’ imply tanh, sigmoid, and ReLU activation function respectively in the above table. The number of units in the corresponding layer is also given with the letter denoting function. A layer denoted as t4 means that it has four neurons/hidden units and the activation function for all those four units is tanh. Together many such layers will make a complete ANN structure, having notations like t16-s18-t22-t14-r1. Whereas, each row represents one complete ANN architecture.

3.2 Second Attempt with the Dataset Having 6,000 Values

Table 2 is the record of the observations of the 12 different ANN architectures tested in this stage. The s6-t8-s6-t8-s6-r1 architecture with ‘adamax’ optimizer was found to be the best performer in this stage in terms of MAPE which was around 0.63% while the t5-t6-t7-t8-r1 was seen to have the best ME, EVS, and R² Scores and hence the best predictability. The worst performance was of s4-t3-s4-t3-r1 architecture with ‘sgd’ optimizer with MAPE about 10.1%. It can be concluded at this stage that ‘sgd’ optimizer was slow compared to ‘adam’ and ‘adamax’. This optimizer was hence not used for the next stage. Single hidden layer networks were all having most error

Table 2 Results of the second stage

6000 Series ANNs										
H1	H2	H3	H4	H5	O	MAPE (%)	ME	EVS	R ² Score	Optimizer
t4	s7				r1	1.9860829	0.005642699	0.996098269	0.996079643	adamax
s19	t14				r1	3.979229	0.00729883	0.98900903	0.984711116	adamax
s5	s9				r1	5.446821	0.01287415	0.972474958	0.972459111	adamax
t32	t44	t66			r1	8.4045515	0.017279638	0.94024097	0.939738462	sgd
t32	t44	t66			r1	0.6846988	0.003037612	0.999012764	0.999006358	adamax
s7	s9	s7			r1	2.86578	0.006640287	0.991553085	0.991530728	adamax
t34	s42	t62			r1	8.643547	0.018133338	0.936963338	0.935493346	sgd
t30	s20	t10			r1	0.937442	0.003432269	0.998401771	0.998212514	adamax
s4	t3	s4	t3		r1	10.0944395	0.018892224	0.92302338	0.921448578	sgd
t5	t6	t7	t8		r1	1.1181109	0.001581904	0.999536404	0.999213943	adamax
s6	t8	s6	t8		r1	0.9185886	0.004378153	0.998218486	0.998062673	adam
s6	t8	s6	t8	s6	r1	0.6325457	0.003091732	0.999185386	0.999151189	adamax

hence they were also dropped for the next stage. Further, a need was felt to increase the number of data points for these networks to perform better. Hence dataset was doubled.

3.3 Third Attempt with the Dataset Having 10,000 Values

Table 3 is the record of observations of the 6 different ANN architectures tested in this stage. The t6-s6-t6-t6-s6-r1 architecture with ‘adamax’ optimizer was found to be the best performer in this stage in terms of MAPE and R² Score, which was around 0.59% while in terms of ME and EVS, the s6-t8-s6-t8-s6-r1 architecture performed slightly better. The worst performance was of s8-s8-r1 architecture with ‘adamax’ optimizer with MAPE about 4.5%. It can be concluded at this stage that in this stage even the worst performance had less than 5% error. All the networks showed good performance and deep networks performed better in general and had better predictability. The accuracy for best networks was increasing very little with the multiplication of data.

Table 3 Results of the third stage

10000 Series ANNs										
H1	H2	H3	H4	H5	O	MAPE (%)	ME	EVS	R ² Score	Optimizer
t5	s6				r1	2.8072114	0.00502236	0.995469406	0.9949289	adamax
s8	s8				r1	4.5352154	0.00923053	0.986209238	0.98586908	adamax
t35	t47	t59			r1	1.3656207	0.00425203	0.998342417	0.99803778	adamax
t6	s6	t6	t6	s6	r1	0.5903617	0.00142839	0.999839133	0.99982988	adamax
s9	t9	s9	t9	s9	r1	0.6953561	0.0025123	0.999609633	0.9996035	adamax
s6	t8	s6	t8	s6	r1	0.8200564	0.0008073	0.999853228	0.99979674	adamax

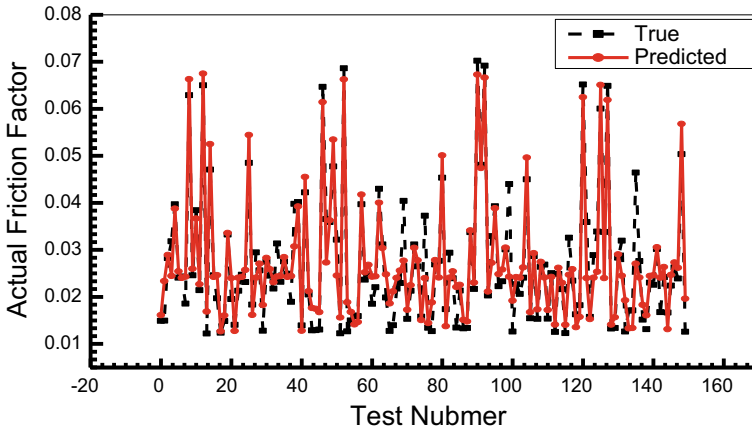


Fig. 4 Predicted vs Real values for the t16-s18-t22-t14-r1 architecture trained on 2850 datapoints (They are so close that the graphs overlap). This was the worst performance of all the networks

3.4 Comparison Between the Predicted Values and the True Values of the Friction Factor

In this section, a detailed comparison between the predicted values of the friction factor obtained using the optimum ANN structure (2-6-8-6-8-6-1) and the value of friction factor obtained from the Colebrook white equation (True/real values) is done. The comparison for two structures t16-s18-t22-t14-r1 architecture trained on 2850 data points and t6-s6-t6-t6-s6-r1 architecture trained on 9850 data points is done in Figs. 4 and 5 respectively.

It can be seen from Figs. 4 and 5 for t16-s18-t22-t14-r1 that the variations from real values are as high as $\pm 45\%$. This was the worst performance among all of the networks tested. Whereas, in the Figs. 6 and 7 the variations are within $\pm 0.5\%$ for t6-s6-t6-t6-s6-r1 architecture. This was the best performing network among all other networks tested. Even in Fig. 6 the true value and predicted data for friction factor from the optimum ANN almost overlap with each other. Therefore, the ANN structure (2-6-8-6-8-8-1) with t6-s6-t6-t6-s6-r1 architecture is the optimum architecture for the calculation of the friction factor of the flow of water through pipes in the turbulent regime.

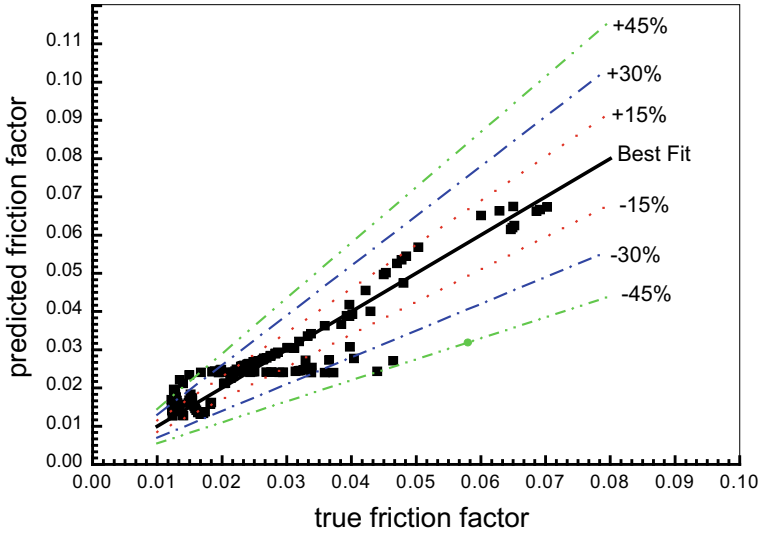


Fig. 5 Comparison between True value and predicted value of friction factor t16-s18-t22-t14-r1 architecture

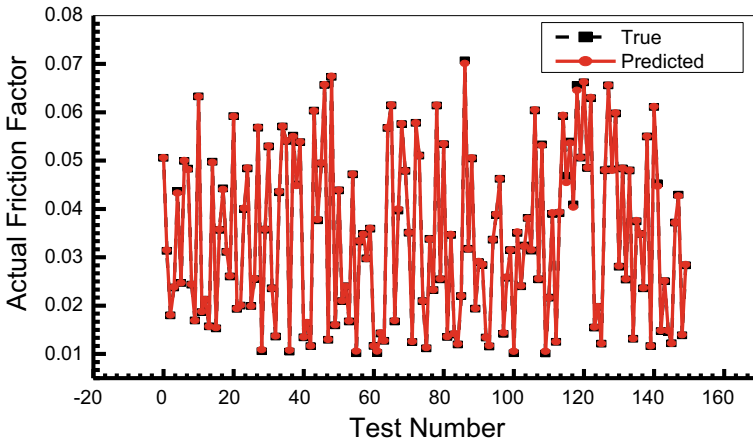


Fig. 6 Predicted vs Real values for the t6-s6-t6-t6-s6-r1 architecture trained on 9850 datapoints (They are so close that the graphs overlap). This was the best performance among all of the networks.

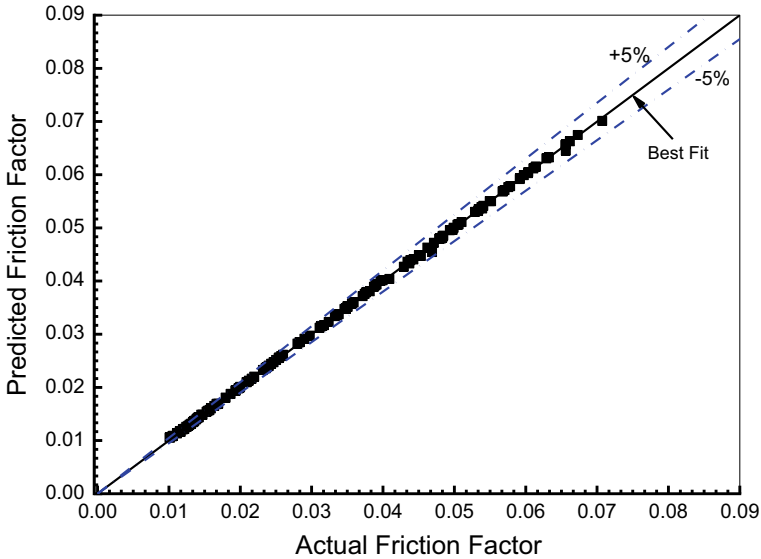


Fig. 7 Comparison between actual and predicted friction factor of t6-s6-t6-t6-s6-r1 architecture

4 Conclusions

In the current work, the analysis of the performance of 36 ANN architectures to find the friction factor for turbulent flow in a pipe of water is done. And some important inferences could be drawn from the present study where, the focus was on finding the appropriate volume of data to solve the problem accurately with the best ANN architecture. The Training time was not a priority as once trained the input data need not be changed for a network as input data always comes from the Colebrook equation. The Training time can also be important for problems with dynamic data as there is a need to train the network repeatedly. But it was observed to have a very small increase in accuracy of best networks with the amount of data. Contrary to estimate, minimum error from 3000 to 6000 sample dataset was seen to increase from 0.61% to 0.63% which can be attributed to the fact that the networks were different and the error is dependent on initialization of weights and biases [13] which was done randomly by the system. However, it decreased for 10,000 sample datasets to 0.59%. Also, in general, the error was seen to decrease with the amount of data.

Further, ‘adamax’ optimizer was able to train networks better in comparison to ‘adagrad’ and ‘sgd’ and ‘adam’. Also, a general increase in accuracy was observed by using the Coarse-to-Fine [16] scheme along the stages and the maximum error for the architectures decreased with stages and it was evident that the search for better ANN architecture moved in the right direction. Deeper networks in the same stage performed well than the networks with fewer hidden layers in general, given that the optimizer was the same, especially in terms of R^2 scores. Best performance in terms

of MAPE and R^2 Score was achieved by t6-s6-t6-t6-s6-r1 architecture/2-6-6-6-6-6-1 network with the tanh, sigmoid, tanh, tanh, sigmoid functions respectively for hidden layers and ReLU function for output, which was around 0.59%. While in terms of ME and EVS, the s6-t8-s6-t8-s6-r1/2-6-8-6-8-6-1 architecture with sigmoid, tanh, sigmoid, tanh, sigmoid for hidden layers and ReLU output performed slightly better with ME of 0.0008 and EVS Score of 0.99985.

References

1. Yunus AC (2010) Fluid mechanics: fundamentals and applications (SI units). Tata McGraw Hill Education Private Limited, New York
2. Nikuradse J (1933) Stromungsgesetze in rauhen Rohren [Laws of flow in rough pipes]. Forschung Auf dem Gebiete des Ingenieurwesens. NACA Technical Memorandum 1292 (in German) 361. NAID 10024691252
3. Colebrook CF, Blench T, Chatley H, Essex EH, Finnicome JR, Lacey G, Williamson J and MacDonald GG (1939) Correspondence. Turbulent flow in pipes, with particular reference to the transition region between the smooth and rough pipe laws (includes plates). J Inst Civil Eng 12(8):393–422. <https://doi.org/10.1680/ijoti.1939.14509>
4. Haaland SE (1983) Simple and explicit formulas for the friction factor in turbulent pipe flow. J Fluids Eng 105:89–90. <https://doi.org/10.1115/1.3240948>
5. Fox W, Pritchard P and McDonald A (2010) Introduction to fluid mechanics, 7th edn. Wiley, New York
6. Moody LF (1944) Friction factors for pipe flow. Trans ASME 66:671–684
7. Shayya WH and Sablani SS (1998) An artificial neural network for non-iterative calculation of the friction factor in pipeline flow. Comput Electron Agric 21(3):219–228. [https://doi.org/10.1016/S0168-1699\(98\)00032-5](https://doi.org/10.1016/S0168-1699(98)00032-5)
8. Yazdi M and Bardi A (2011) Estimation of friction factor in pipe flow using artificial neural networks. Can J Autom Control Intell Syst 2(4):52–56
9. Fadare DA and Ofidhe UI (2009) Artificial neural network model for prediction of friction factor in pipe flow. <http://ir.library.ui.edu.ng/handle/123456789/1924>. Accessed 25 Nov 2020
10. Sahai S, Kulkarni T, Tikhe S and Mathpati CS (2017) Use of artificial neural network to predict Pressure-Drop in rough pipes. In: Paper presented at the 2017 international conference on computing methodologies and communication (ICCMC), pp 452–455. IEEE, 18 July 2017
11. Brkić D and Čojbašić Ž (2016) Intelligent flow friction estimation. Comput Intell Neurosci 2016:1–10 (2016). <https://doi.org/10.1155/2016/5242596>
12. Offor UH and Alabi SB (2016) Artificial neural network model for friction factor prediction. J Mater Sci Chem Eng 4(7):77–83. <https://doi.org/10.4236/msce.2016.47011>
13. Ng A, Katanforoosh K and Mourri YB (2020) Neural networks and deep learning [MOOC]. Coursera. <https://www.coursera.org/learn/neural-networks-deep-learning/>. Accessed 3 July 2020
14. Newton method for finding roots (2020). http://en.wikipedia.org/wiki/Newton's_method. Accessed 10 Nov 2020
15. Eremenko K and Ponteves H (2020) SuperDataScience team. Deep learning A–Z™: Hands-on artificial neural networks [MOOC]. Udemy. <https://www.udemy.com/course/deeplearning/> (2020). Accessed 28 Nov 2020
16. Ng A, Katanforoosh K and Mourri YB (2020) Improving deep neural networks: hyperparameter tuning, regularization and optimization [MOOC]. Coursera. <https://www.coursera.org/learn/neural-networks-deep-learning/>. Accessed 28 Aug 2020
17. Sethi A, Rawat A and Srivastava V (2022) Artificial neural network models for wall parameters on plug-1 flow characteristics through pipelines. J Eng Res (in Press)

Dynamic Analysis of 3D Printed Polylactic Acid Bolted Joint Beams



K. P. Sibivivek and Ashok Kumar Pandey

Abstract This study shows an experimental method and a finite element model for modal analysis of 3D printed Polylactic acid (PLA) bolted joint beams. Three test samples are 3D printed with 20% infill density and tested with scanning head Laser Doppler Vibrometer (LDV) for its natural frequencies and mode shapes. The test specimens are a monolithic beam, a lap joint beam and a reduced Brake Reuβ beam. Since the material properties like Young's modulus and density of 3D printed structures are not exactly known, we develop a parameter estimation method to calculate these values. Using these estimated values, a prestressed nonlinear finite element model is created by taking the effect of friction in contacting interfaces. Ansys software is used to create the finite element models. The natural frequencies and mode shapes from experiment and finite element model match with an error less than 10%. This model and estimated parameters can be used for further studies with 3D printed polylactic acid material and in contacting interface modelling.

Keywords Modal analysis · Nonlinear finite element model · 3D printing · Natural frequency · Mode shapes · Polylactic acid (PLA) · Bolted joint

1 Introduction

Bolted joints are present in many mechanical and civil structures. Bolted joints are threaded fasteners used to connect homogeneous or non-homogeneous parts. The main function of a bolted joint is to hold the parts together and transmit loads. In many scenarios, bolted joints are subjected to dynamic loading. The type and number of joints highly influence the structural vibration of the system. Reducing the structural vibrations and avoiding resonance conditions are some of the major objective in mechanical system design. The failure of bolted joint in systems like aircrafts,

K. P. Sibivivek (✉) · A. K. Pandey
Indian Institute of Technology Hyderabad, Kandi, Sangareddy 502284, Telangana, India
e-mail: me19mtech01003@iith.ac.in

A. K. Pandey
e-mail: ashok@mae.iith.ac.in

© The Author(s), under exclusive license to Springer Nature Singapore Pte Ltd. 2022
T. Tadepalli and V. Narayanamurthy (eds.), *Recent Advances in Applied Mechanics*,
Lecture Notes in Mechanical Engineering, https://doi.org/10.1007/978-981-16-9539-1_29

bridges, buildings, etc., may cause life and money. Hence, there is a necessity of studying the behaviour of bolted joints under different conditions. With the help of additive manufacturing, rapid prototyping has gained much attention than ever before. Using this method, it is possible to make a scale model of the original system and can perform necessary tests for further development. 3D printing is one of the types of additive manufacturing methods. This method is widely used by various industries and researchers because of its speed and cost efficiency. The number of studies that have been conducted on the 3D printed components is very less and there exists a lack of understanding on the behaviour of 3D printed parts under dynamic loading conditions. These components are partially hollow in section based on the printing orientation and set up, which makes them even difficult to predict under different conditions. This study focuses on the combination of 3D printed and bolted joint beams under dynamic loading conditions. The material used here for 3D printing is Polylactic acid (PLA) material. This material is widely used in automobile, medical and health care, food packaging and textile industries. The importance of mechanical joints is discussed by Brake et al. [1]. Stiffness, damping, and other dynamic properties of the structure are highly affected by the process of joining [2]. A previous study shows the modal analysis of monolithic and jointed cantilever beams with nonuniform sections [3]. The authors used a Laser Doppler Vibrometer (LDV) to find the natural frequencies and mode shapes of non-uniform cantilever beams. Two researchers, Matthew R. W. Brake and Pascal Reuß developed Brake Reuß beam [4]. This beam helps to study the nonlinear dynamics of the bolted structures effectively. Some of the properties of Polylactic acid (PLA) material is described by Farah et al. [5]. Pawlak studied the effect of wear and frictional effects of PLA material used for 3D printing technology [6]. Gusztáv Fekete conducted a numerical wear analysis on PLA based spur gears with respect to friction and temperature [7].

However there exist no study regarding the dynamics of PLA made bolted joints. Also there is a lack of understanding on how the type of joint affects the natural frequencies of the system. The present study helps to understand more about the 3D printed and PLA made bolted joint dynamics. Three different type of 3D printed beams are used here. The monolithic beam helps to understand the behaviour of beams without any joint. Lap joint beam and reduced Brake Reuß beam show the effect of joint on the natural frequencies and mode shapes of the system. All the beams are 3D printed with PLA material and tested with a Laser Doppler Vibrometer for their natural frequencies and mode shapes. A finite element model is developed with frictional contacts and prestressed conditions to compare the obtained experimental results.

2 Methodology

The specimens are modelled by CAD software and 3D printed using Polylactic acid (PLA) material with 20% infill density and diamond fill orientation. All the specimens are of 287 mm × 25 mm × 5 mm dimensions. Specimens differ by the type of joint

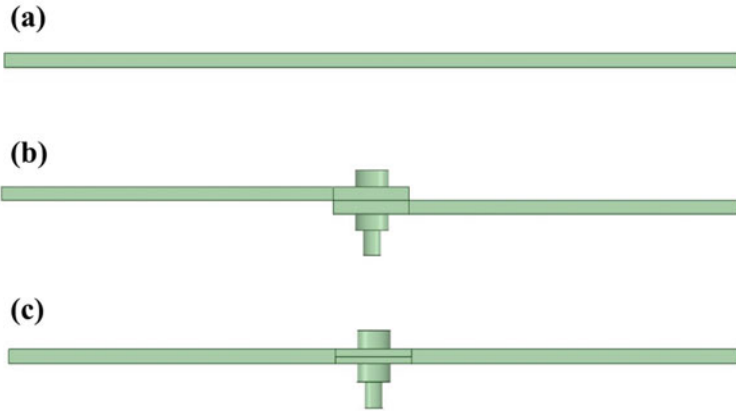


Fig. 1 (a) Monolithic beam, (b) Lap joint beam, (c) Reduced Brake Reuβ beam

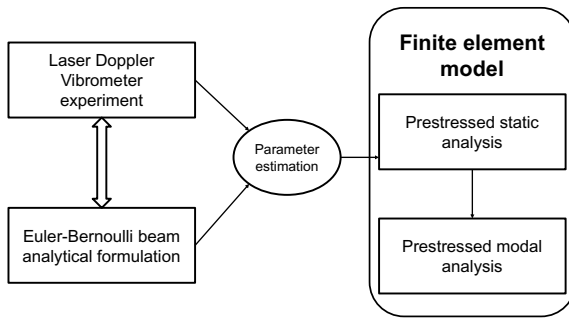


Fig. 2 Model outline

present in it. Figure 1 shows all three types of specimens. All the specimens are subjected to fixed-free boundary conditions and excited with an electromagnetic shaker. Polytec PSV 500 non-contacting scanning head Laser Doppler Vibrometer (LDV) is used for finding the experimental natural frequencies and mode shapes. M6 hexagonal nut and bolt is used to fasten the samples. The bolt selection is based on the dimensions and weight of plates. We compare the experimental natural frequencies with the Euler-Bernoulli beam model to estimate the unknown parameters and use them to create a prestressed finite element model as shown in Fig. 2. The experimental set up from LDV scanning is given below Fig. 3. First four bending mode shapes and the corresponding natural frequencies are obtained.

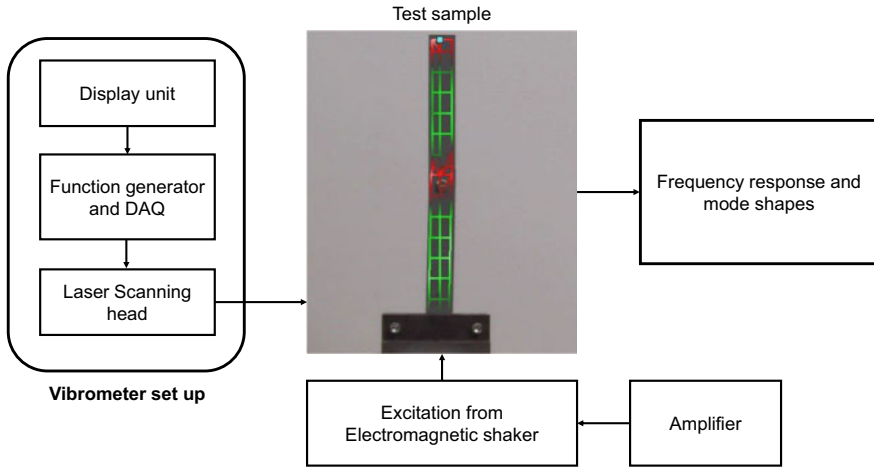


Fig. 3 Experimental set up for LDV scanning

3 Results and Discussion

This section deals with the results obtained from the experimental as well as the prestressed finite element model. The section starts with the experimental results of monolithic beam, lap joint beam and reduced Brake Reu β beam followed by the detailed results of respective prestressed finite element model. A parameter estimation method is used to calculate the Young's modulus (E) of the 3D printed parts for comparing the experimental natural frequencies with the Euler-Bernoulli beam model.

3.1 Experimental Results

Natural frequencies and mode shapes are obtained from Polytec PSV 500 scanning Laser Doppler Vibrometer. The obtained frequency response function (FRF) and mode shapes for all three specimens are given below Figs. 4, 5, and 6.

3.2 Parameter Estimation

Since the material properties like Young's modulus of 3D printed parts are not known, we use a parameter estimation method by comparing obtained experimental natural frequencies with analytical models based on the Euler-Bernoulli beam. 3D printed components are not always solid in cross section. Since they are used in rapid

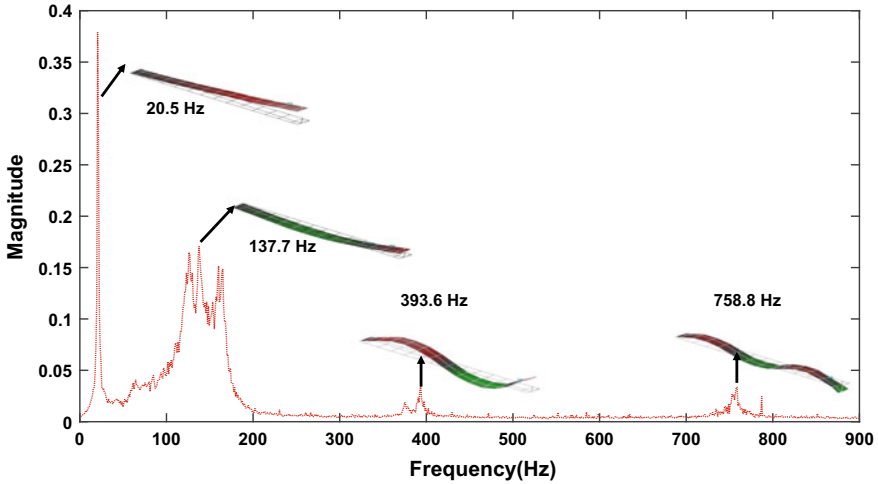


Fig. 4 FRF, Natural frequencies and mode shapes for monolithic beam

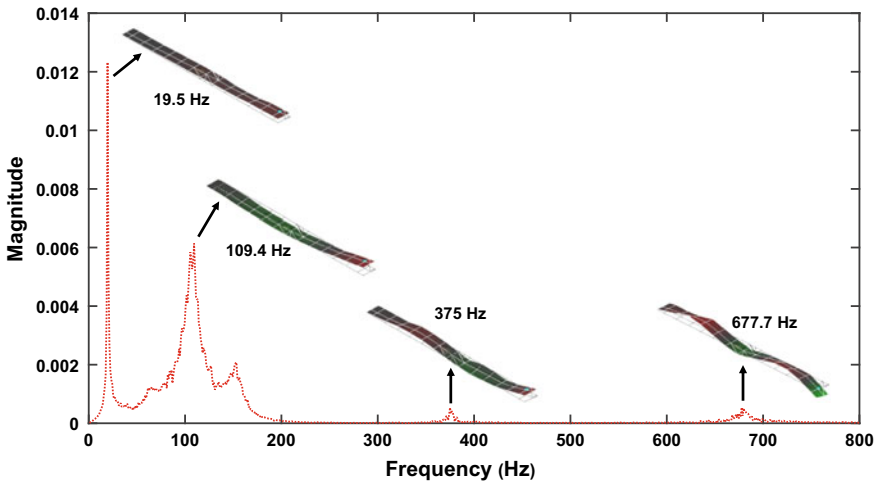


Fig. 5 FRF, Natural frequencies and mode shapes for lap joint beam

prototyping, the time taken for printing each component is very important. We can either print a solid component or a component with voids. Printing a solid component consumes more time than the component with voids. The material properties are well defined for a solid component. But when it comes to a component with voids this properties changes based on the structure inside. Infill density and type of infill pattern surely affects the Young's modulus of 3D printed components. Experimental testing for each combination of infill density and infill pattern might be a tedious task. So we can use the parameter estimation method to calculate the Young's mod-

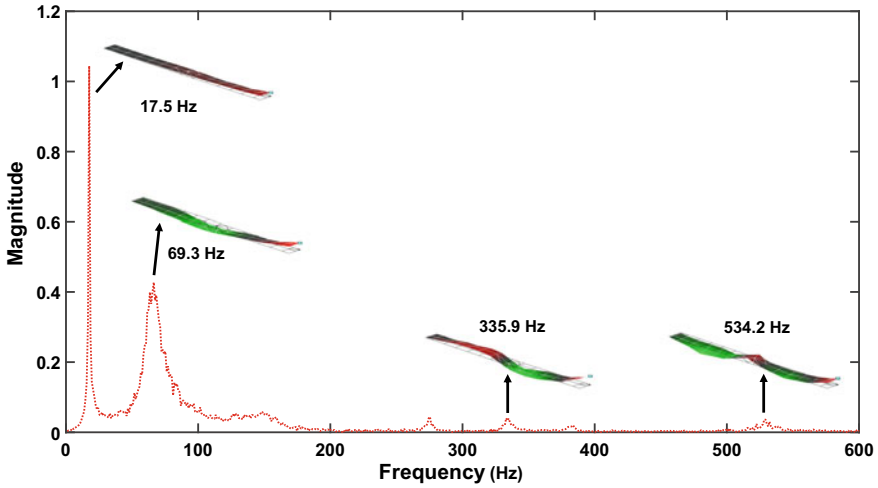


Fig. 6 FRF, Natural frequencies and mode shapes for Reduced Brake Reuβ beam

ulus without consuming much time and effort. Therefore we can use the this method when a combination of infill density and infill pattern is used to print the component.

The governing differential equation for the Euler-Bernoulli beam can be written as

$$\frac{d^2}{dx^2}[EI(x)\frac{d^2Y}{dx^2}] = \omega^2m(x)Y(x). \tag{1}$$

Considering $m(x)$ and $EI(x)$ as constant, for instance, in the above equation, we get

$$\frac{d^4Y}{dx^4} = \frac{\omega^2m}{EI}Y(x). \tag{2}$$

Assuming the frequency parameter as β , we get

$$\beta^4 = \frac{\omega^2m}{EI}. \tag{3}$$

Substituting Eqs. (3) to Eq. (2), the governing differential equation now becomes,

$$\frac{d^4Y}{dx^4} - \beta^4Y = 0. \tag{4}$$

The solution for Eq. (4) is assumed as,

$$Y(x) = A \sin \beta x + B \cos \beta x + C \sinh \beta x + D \cosh \beta x \tag{5}$$

and boundary conditions for cantilever are

Table 1 βL values for first four natural frequencies

Modes	First	Second	Third	Fourth
βL	1.875104069	4.69409113	7.854757438	10.99554073

Table 2 $\sqrt{\frac{EI}{mL^4}}$ values extracted from first four natural frequencies

Modes	First	Second	Third	Fourth
$\sqrt{\frac{EI}{mL^4}}$	36.6338	39.26546	40.08384	39.43428

$$x = 0 : Y(0) = 0 \text{ and } Y'(0) = 0$$

$$x = L : Y''(L) = 0 \text{ and } Y'''(L) = 0.$$

Solving Eq. (5) with the above boundary conditions, we get the frequency equation as,

$$1 + \cos \beta L \cosh \beta L = 0. \quad (6)$$

For a given $\beta_n L$ for n^{th} , we get the expression of frequency as,

$$\omega_n = (\beta_n L)^2 \sqrt{\frac{EI}{mL^4}}. \quad (7)$$

For the first four natural frequencies, the values of $\beta_n L$ are given in Table 1,

Now, to calculate Young's modulus, we extract the term $\sqrt{\frac{EI}{mL^4}}$ from four modal frequencies obtained by the experiment. Since, frequency ω is given by

$$\omega_n = (\beta_n L)^2 \left[\sqrt{\frac{EI}{mL^4}} \right]_n = 2\pi f_n. \quad (8)$$

the values of extracted term $\sqrt{\frac{EI}{mL^4}}$ from the first four natural frequencies can be obtained as mentioned in Table 2.

Taking the average value from the above term we get, $[\sqrt{\frac{EI}{mL^4}}]_{avg} = 38.85366$, where $m = \rho A$ and $I = \frac{bh^3}{12} = 2.60416 \times 10^{-10} \text{ m}^4$. Thus, the mean value of Young's modulus (E_{avg}) for 3D printed specimen is obtained as 2.23 Gpa.

3.3 Damping Ratios

To find damping ratios, we measure the quality factor based on the half power bandwidth method from the frequency response function. Quality factor is a dimensionless

Table 3 Damping ratios obtained using half power bandwidth method

Damping ratios			
	Monolithic beam	Lap joint beam	Reduced Brake Reu β beam
First mode	0.0357	0.02496	0.02777
Second mode	0.02659	0.03794	0.0772
Third mode	0.003101	0.00127	0.005132
Fourth mode	0.001929	0.0007203	0.00277

Table 4 Contact friction conditions

Contact surfaces	Coefficient of friction
PLA - PLA	0.492
PLA - Steel	0.4

parameter which describes the under damping characteristics of a vibrating system. For higher values of quality factor, the damping will be less with lower rate of energy loss. The formulation for quality factor is given below Eq. (9).

$$Q = \frac{f_n}{f_2 - f_1} = \frac{1}{2 \times \zeta}. \quad (9)$$

Q = Quality factor, f_n = Natural frequency, $f_2 - f_1$ = Band width, ζ = Damping ratio.

The obtained values of damping ratios for first four modes of all three samples are given in below Table 3.

3.4 Finite Element Model

Using the estimated and known parameters, a finite element model is created for all three test samples. The FEM model made using Ansys Workbench software with prestressed modal analysis. Hexagonal brick elements are used to mesh the models for better speed and accuracy. Figure 7 shows the transverse bending mode shapes of monolithic, lap joint and reduced Brake Reu β beams.

Frictional and Prestress Analysis.

All the contacting interfaces are simulated as frictional contacts and the coefficient of friction for different contacting interfaces are mentioned in Table 4 [5–7]. A preload of 2.5N is applied on the bolts of lap joint and reduced Brake Reu β beam. Bolts are modelled as solid body in Ansys finite element software and preload is applied on bolt shank between contacting interfaces.

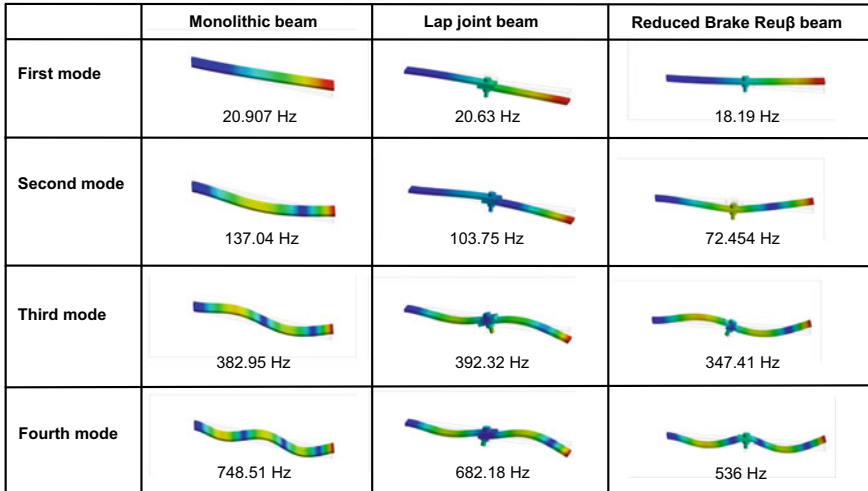


Fig. 7 Natural frequencies and mode shapes obtained from prestressed finite element model

Table 5 Comparison of Natural frequencies

Mode No.	Monolithic Beam			Lap joint beam			Reduced brake reuβ beam		
	Experimental	FEM	Error(%)	Experimental	FEM	Error(%)	Experimental	FEM	Error(%)
First	20.5 Hz	20.907 Hz	1.98	19.5 Hz	20.63 Hz	5.9	17.6 Hz	18.19 Hz	3.35
Second	137.7 Hz	137.04 Hz	0.479	109.4 Hz	103.75 Hz	5.1	69.3 Hz	72.454 Hz	4.55
Third	393.6 Hz	382.95 Hz	2.7	375 Hz	392.32 Hz	4.61	335.9 Hz	347.41 Hz	3.42
Fourth	758.8 Hz	748.51 Hz	1.35	677.7 Hz	682.18 Hz	0.66	534.2 Hz	536 Hz	0.337

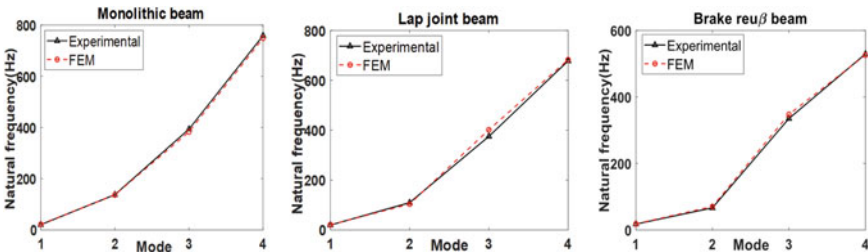


Fig. 8 Comparison of experimental and finite element model natural frequencies

3.5 Comparison

In this section, we compare the experimentally measured and numerically computed natural frequencies of monolithic beam, lap joint beam and reduced Brake Reuβ beam. Table 5 shows the comparison and respective percentage errors. Figure 8 shows the comparison of first four transverse bending natural frequencies from the experiment and the prestressed finite element analysis.

4 Conclusions

Based on the studies performed on bolted joint samples, there is a significant effect of joints on the dynamic characteristics of the beams in terms of natural frequencies and the corresponding mode shapes. The natural frequencies are found to be reducing in bolted joint structure as compared that of a monolithic beam. The joint under tension leads to variation in stiffness and damping of the beam. This creates a variation in natural frequencies. It also increases the mass of the system. From the testing and simulation of lap joint beam and reduced Brake Reu β beam, it is clear that the type of joint affects natural frequencies and mode shapes. Due to the pretension condition, stresses generate on both plates and bolt. These stresses induces small deformation to these components. The comparison of experimental and finite element results of natural frequencies gives good conformation with a percentage error less than 10% for all three cases.

Acknowledgements First author acknowledge the fellowship received from the Ministry of Education, India. The work is also partially supported by AR&DB, India, with project number 1824.

References

1. Brake MRW, Ewins DJ, Wynn, CB (2018) Are joints necessary?. In: *The Mechanics of Jointed Structures: Recent Research and Open Challenges for Developing Predictive Models for Structural Dynamics*. Springer, Cham, pp 25–36. <https://doi.org/10.1007/978-3-319-56818-8-3>
2. Brake MRW (2018) Introduction to research on the mechanics of jointed structures. In: Brake MRW (ed) *The Mechanics of Jointed Structures*. Springer, Cham, pp 3–10. https://doi.org/10.1007/978-3-319-56818-8_1
3. Purohit B, Jain PC, Pandey AK (2016) Modal analysis of monolithic and jointed type cantilever beams with non-uniform section. *Exp Mech* 56(6):1083–1094. <https://doi.org/10.1007/s11340-016-0149-y>
4. Brake MRW, Reu β , P (2016) The Brake-Reu β Beams: a system designed for the measurements and modeling of variability and repeatability of jointed structures with frictional interfaces. In: *The Mechanics of Jointed Structures: Recent Research and Open Challenges for Developing Predictive Models for Structural Dynamics: Brake MRW, CONFERENCE 2018*, pp 99–107, Springer, Cham, <https://doi.org/10.1007/978-3-319-56818-8-9>
5. Farah S, Anderson DG, Langer R (2016) Physical and mechanical properties of PLA, and their functions in widespread applications - a comprehensive review. *Adv Drug Delivery Rev* 107:367–392. <https://doi.org/10.1016/j.addr.2016.06.012>
6. Pawlak W (2018) Wear and coefficient of friction of PLA graphite composite in 3D printing technology. In: *Engineering Mechanics 24th International Conference*, pp 649–652, Institute of Theoretical and Applied Mechanics of the Cech Academy of Sciences, Prague, Svratka, Czech Republic
7. Fekete G (2021) Numerical wear analysis of a PLA-made spur gear pair as a function of friction coefficient and temperature. *Coatings* 11(4):409. <https://doi.org/10.3390/coatings11040409>

Effect of Longitudinal Unstiffened Cut-Outs on Buckling Behavior of Metal-FRP Hybrid Airframe Shell



G. Vamsi Krishna, V. Narayanamurthy, and C. Viswanath

Abstract Cutouts are an integral part of airframe shells. Understanding the effect of cutouts on the buckling behavior of FRP stiffened airframe shells is an essential part of designing these hybrid shell structures. This paper investigated the effect of centrally located unstiffened longitudinal rectangular cutouts with varying size on the buckling behavior of an elastically buckling hybrid airframe shell of a high radius to thickness ratio (r/t) and equipped with end bulkheads. The effect of cutouts on shells is a function of initial geometric imperfections, predominantly in elastically buckling shells. So, the above investigations are carried out both for shells with very small and relatively large imperfection magnitudes. It is brought out that pre-buckling deformations and stress concentration play a dominant role in deciding the buckling pattern and buckling load of shell structures with cutouts.

Keywords Metal-FRP hybrid shell structures · Elastic buckling · Unstiffened cutouts

1 Introduction

Shell buckling modes are the mode of failure for shell structures subjected to axial compression. Plain metallic shells exhibit a variety of buckling modes which is a function of r/t ratio of shells and initial geometric imperfections. FRP strengthening is very effective against different shell buckling modes exhibited by plain metallic shells, viz. elephant foot axisymmetric buckling [1] and elastic asymmetric buckling

G. Vamsi Krishna (✉)
Advanced Systems Laboratory, Hyderabad, India
e-mail: me14m16p000004@iith.ac.in

V. Narayanamurthy
Research Center Imarat, Hyderabad, India
e-mail: v.narayanamurthy@rcilab.in

C. Viswanath
Indian Institute of Technology Hyderabad, Kandi, Sanga Reddy, India
e-mail: viswanath@mae.iith.ac.in

[2]. Krishna et al. [3] brought out the effectiveness of FRP strengthening methods for plain metallic shells undergoing a variety of buckling modes. Shells equipped with cut-outs of various sizes, shapes, and configurations viz. unstiffened, stiffened, stiffened with closure are employed in industrial/ aerospace applications. The study of the cut-out effect on the buckling behavior of shell structures is an integral part of the design of these structures. Extensive studies were carried on the effect of cut-outs in metallic [4] and composite shell structures [5] subjected to axial compression. Though much research has been carried out on the effect of unstiffened cut-outs and stiffened cut-outs in metallic and composite shells, no reported literature has been found on the effect of cut-outs on FRP stiffened metallic shell structures. This study has numerically explored the effects of the unstiffened centrally located longitudinal cut-out of various sizes on the buckling behavior of elastically buckling aerospace shell structures equipped with end bulk heads. The effect of cut-outs on shells is a function of initial geometric imperfections, predominantly in elastically buckling shells. So, all the above investigations are carried out for shells with very small and relatively large imperfection magnitudes.

2 Numerical Simulation Model

Typical elastically buckling smaller diameter aerospace AA2014 metallic shell structure of high r/t ratio equipped with integral end bulkhead (BH)s is employed in this study. The geometric details of the shell structure are shown in Fig. 1(a). Shell is of outer diameter $d = 300$ mm, thickness $t = 1$ mm, shell length $L = 260$ mm, integral end BHs length and thickness = 20 mm and equipped with centrally located cut-out. The cut-out dimensions, L corresponds to the longitudinal length of cut-out size, and C corresponds to the circumferential length of cut-out size. Cut-outs are named $C \times L$ in this study. Fillet radius = 1/5th of smallest cut-out dimension is employed FRfor different cut-out sizes studied.

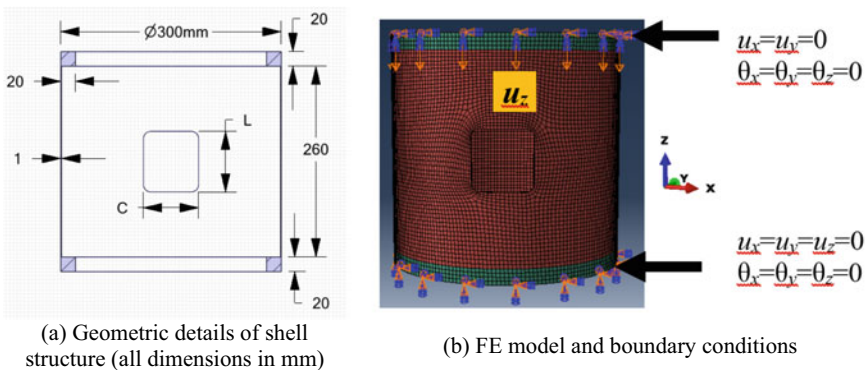


Fig. 1 Geometric and FE details of the model employed for study

Typical mechanical properties of AA2014 material in T652 condition viz. Young's modulus $E = 71$ GPa; Poisson's ratio $\nu = 0.33$; yield strength $\sigma_y = 380$ MPa; and tangent modulus $E_t = 780$ MPa are employed [6]. The L/λ for the plain metallic shell = 12.2, where λ represents the linear half-wavelength of meridional bending, given by

$$\lambda = \frac{\pi}{\sqrt[4]{12(1 - \nu^2)}} \sqrt{rt} \quad (1)$$

So, L/λ is ensured much higher than the minimum requirement of 2 to be categorized as medium length cylinder. These shells are short enough and do not fail by Euler's buckling mode, and long enough so that end boundary conditions do not influence their buckling load [7]. Elastic buckling and yield capacities of the plain metallic shell obtained by multiplying the critical elastic buckling stress σ_{cl} and yield strength with the shell cross-section area is 273 kN and 358 kN, respectively. The σ_{cl} of a bare metallic shell is given as [7]

$$\sigma_{cl} = \frac{E}{\sqrt{3(1 - \nu^2)}} \frac{t}{r} \quad (2)$$

The elastic buckling nature of the plain metallic shell is confirmed by the fact that the elastic buckling load being much smaller than its yield load.

FRP strengthening of metallic shell structure by wrapping externally with one layer of unidirectional carbon fiber reinforced polymer (CFRP-UD) wrap in hoop direction is considered. The properties of CFRP wrap of high modulus carbon epoxy pre-peg employed in the present study are [6]: elastic modulus along (a) fiber direction $E_1 = 209$ GPa, (b) transverse direction $E_2 = 9.5$ GPa, and (c) thickness direction $E_3 = 9.5$ GPa; Poisson's ratio, $\nu_{12} = \nu_{13} = 0.27$, and $\nu_{23} = 0.4$; shear modulus, $G_{12} = G_{13} = 5.5$ GPa, and $G_{23} = 3.9$ GPa; and thickness of one layer of CFRP wrap = 0.17 mm. FRP strengthening along the hoop direction has already been established to be relatively more effective for elastically buckling shells compared to strengthening along other directions [3]. The finite element (FE) modeling and analysis are carried out in ABAQUS [8]. FE model and boundary conditions are shown in Fig. 1(b). This work adopts the FE model and solution methodology similar to Krishna et al. [3] developed for metal-FRP hybrid shell structures. The two end bulkheads and the cylindrical shell showed in Fig. 1(a) are modeled as three cylindrical shell surfaces that share the topology at butting interfaces.

The FRP wrap is modeled as another shell surface with the same diameter of 300 mm and length equal to 300 mm. Bonded constraint is assigned between the metallic cylindrical shell's outer surface and the FRP wrap's inner shell surface. Linear quadrilateral reduced integration, S4R shell elements are used for discretization of all shell surfaces. Composite layup definition is employed for defining the following section properties of shell elements: 1) bi-linear isotropic strain hardening material model for the metallic shell surface; 2) linear elastic orthotropic material model for FRP shell surface; 3) orientation of the circumferential direction of element

co-ordinate system of CFRP shell surface along fiber direction of FRP wrap; and 3) nine and five integration points across the thicknesses of metallic and FRP wrap's shell surfaces, respectively. An element size of 3 mm \times 3 mm is employed for better representation of local buckles around the cut-out as well as global buckles over the entire length of the shell structure. Discretized FE model with boundary conditions is showed in Fig. 1(b). The rotation θ about and displacement u along three co-ordinate directions x , y and z are fixed at the top and bottom edges, except the displacement in z , *i.e.*, the axial direction at top edge, along which a displacement-controlled loading is enforced.

Buckling behavior of shell with rectangular cut-out with varying cut-out size along the longitudinal direction is studied. The cut-out dimension along the circumferential direction is held constant at 75 mm.

The method of linear buckling mode-shape imperfections (LBMI) proposed by Khot and Venkayya [9] is employed to introduce initial imperfections in the model. This method is based on seminal work by Koiter [10], who revealed that imperfections in the form of perfect shell buckling mode shape are the most deleterious forms of imperfections. For each shell structure, either bare or with one layer of hoop wrapping, with different orientations of the cut-out configurations, employing perfect geometry, linear perturbation buckling analysis is carried out initially. 'Lanczos' Eigen solver in ABAQUS [8] is used to extract the first 30 buckling mode shapes. Among these mode shapes, the first few are local mode shapes that involve buckles only around the cut-out region. The rest of the higher modes are global mode shapes involving the buckles spread over the full circumference and length of the shell.

It is found from the non-linear analysis carried out that employing different tuned local buckling mode shapes with a particular magnitude of imperfection leads to the value of buckling loads with less than 5% scatter [11]. Similarly, non-linear analysis employing different tuned global buckling mode shapes with the same value of the magnitude of imperfection leads to a relatively much lower buckling load. But the scatter in buckling loads with different global buckling mode shapes is less than 5%. Since the imperfection should trigger any possible buckling modes, one of the higher modes of buckling is employed for non-linear analysis. Regarding the choice from among different higher buckling modes that follow normal probability density function, the stochastic method developed by Behrooz et al. [11] is employed to select the mode shape that has maximum possibility of occurrence for each configuration of the shell structure. Subsequently, the chosen mode shape is used as initial geometric imperfection for carrying out non-linear standard implicit analysis employing *Static Riks* solver. The mode shape selected is tuned by using the scaling factor. The ratio of maximum radial deviation of imperfect geometry, *i.e.*, mode shape chosen from perfect geometry (w_0) to the shell thickness is employed as a scaling factor. Two different values of this fraction ($w_0/t = I$) viz. 0.02 and 0.2 are employed. $I = 0.02$ corresponds to a relatively perfect shell where imperfection will only act as a trigger for shell buckling. $I = 0.2$ corresponds to the critical value of imperfection magnitude in the LBMI method, at which buckling load suddenly drops to a lower value [11] and represents a relatively imperfect shell. At each of these values of imperfection

magnitude (w_0/t), the buckling behavior of every shell structure is predicted using *Static Riks* solver.

3 Results and Discussion

3.1 Buckling Patterns

The typical buckle patterns exhibited by relatively perfect and imperfect shells with an unstiffened longitudinal cut-out of varying sizes is depicted in Fig. 2. The evolution of the buckling pattern in the perfect shells ($I = 0.02$) exhibiting ‘corner buckles’ is depicted in Fig. 2(a-b). Perfect shells with a longitudinal cut-out size ≥ 25 mm exhibit lip opening along the longitudinal edge of the cut-out. Lip opening along the two longitudinal edges of cut-out leads to the formation of dimples on either side of lips, as shown in Fig. 2(a). These dimples become probable locations for buckle formation, leading to the formation of ‘corner buckles’ as depicted in Fig. 2(b), which is followed by sequential initiation and growth of ‘circumferential buckles’. But for perfect shells with larger longitudinal cut-out size (≥ 150 mm), ‘adjacent buckles’ are formed at the lip opening hinges as shown in Fig. 2(c) instead of ‘corner buckles’. These ‘adjacent buckles’ are followed by sequential initiation and growth of ‘circumferential buckles’ as in shells exhibiting ‘corner buckles’. Buckle pattern exhibited by imperfect shells ($I = 0.2$), with longitudinal cut-out size < 150 mm is shown in Fig. 2(d). No ‘corner buckles’ around cut-out is observed; instead, simultaneous initiation of ‘opposite buckles’ diametrically opposite to cut-out is observed after very little lip opening.

Unlike perfect shells, initiation of many simultaneous ‘opposite buckles’ is observed for imperfect shells. But even imperfect shells with longitudinal cut-out size ≥ 150 mm, exhibit a similar buckling pattern of that of the perfect shell, as shown in Fig. 2(c). For these shells, lip opening is happening readily with the least resistance, forcing the formation of ‘adjacent buckles’ even dominating the effects of large surface imperfection. These ‘adjacent buckles’ are followed by sequential initiation of ‘circumferential buckles’ both for the case of perfect and imperfect shells. For cut-out sizes < 25 mm both along longitudinal and circumferential directions, no buckles around the cut-out are observed. These shells fail by global shell buckling modes.

3.2 $P - \delta$ Buckling Behavior

FRP stiffened metallic shell structure with one layer of CFRP-UD wrap along hoop direction is termed ‘H1’. Bare shell structure without any FRP strengthening is termed ‘B’. Shells modeled with very small initial surface imperfections of 0.02 are termed ‘ $I = 0.02$ ’, while those modeled with the relatively large initial surface

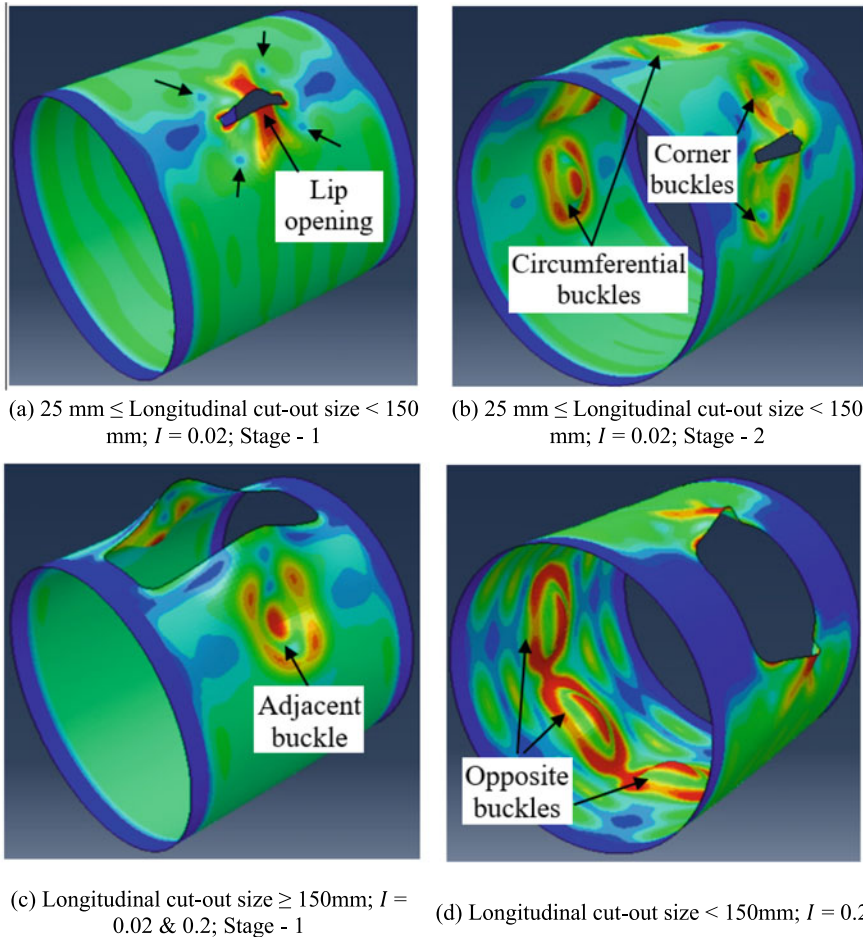


Fig. 2 Buckling patterns exhibited by bare aluminum shells with variations in longitudinal cut-out size, and imperfection magnitude

imperfection of 0.2 are termed ' $I = 0.2$ '. The $P - \delta$ buckling behavior exhibited by 'B' and 'H1' shells with unstiffened longitudinal cut-outs of small viz. 10 mm and relatively large viz. 225 mm sizes are brought out in Fig. 3. Circumferential cut-out size is held constant at 75 mm. For a particular cut-out size, all four variations in shell configuration viz. i) B; $I = 0.02$, ii) B; $I = 0.2$, iii) H1; $I = 0.02$, and iv) H1; $I = 0.2$ are shown in Figs. 3(a) and (b).

Snap through buckling behavior is exhibited by both B and H1 perfect shells ($I = 0.02$) for all cut-out sizes as shown in red solid and dashed lines in Figs. 3. All these shells display significant axial load increase after initial snap-through behavior. Due to the sequential appearance of circumferential buckles as explained in Fig. 2(b), zig-zag $P - \delta$ behavior is displayed. The appearance of each buckle results in a drop

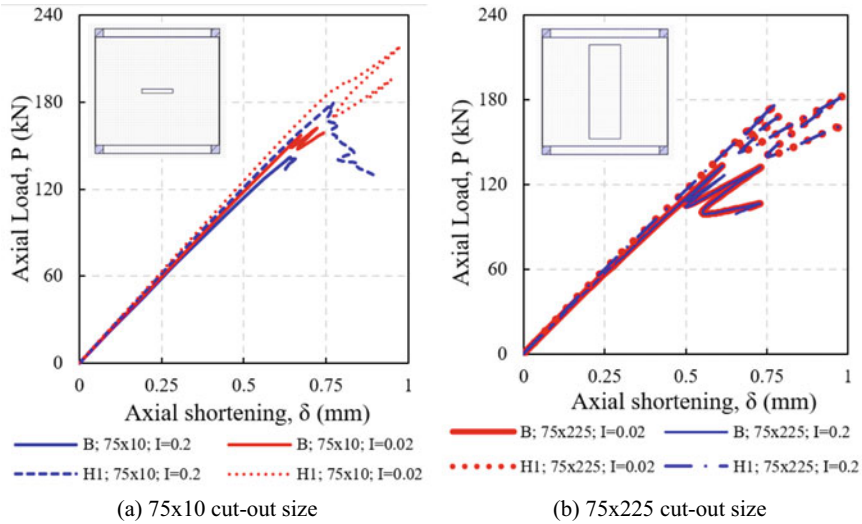


Fig. 3 Buckling behavior of bare (B) and one-layer FRP wrapped (H1) shells with very small and relatively large longitudinal cut-outs with $I = 0.02$ and 0.2

in load followed by an increase in load during the buckle growth stage. More the delay between each buckle formation, more pronounced would be the snap-through behavior. Lesser delay or near-simultaneous appearance of buckles would result in steadily dropping scribbling $P - \delta$ behavior. All imperfect shells ($I = 0.2$) as shown in solid and dotted blue lines in Fig. 3(a) display this kind of buckling behavior except for large longitudinal cut-out sizes ≥ 150 mm viz. Figure 3(b). For large longitudinal cut-out sizes, buckling behavior and buckle pattern remain the same for both perfect and imperfect shells, as observed from overlapping curves in Fig. 3(b) for both perfect and imperfect bare and FRP stiffened shells. Initiation of adjacent buckles in FRP stiffened shells happens at a later point of loading due to resistance offered by FRP against the lip opening. It can be noticed that for all the cut-out sizes, FRP stiffened shells buckle at higher loads than their bare counterparts.

4 Conclusions

This work reveals the effect of cut-outs of rectangular cut-out in longitudinal orientation and varying cut-out sizes on the elastically buckling airframe metal-FRP hybrid shell. It is brought out that:

- The cut-out effect is only felt as an increase in stress concentration for smaller cut-out sizes up to 25 mm. Local buckling around cut-out is not observed for these

cut-out sizes. It would even increase the buckling load with an increase in cut-out sizes up to 25 mm for imperfect shells.

- Larger longitudinal cut-out size ≥ 150 mm forces the formation of adjacent buckles even in the presence of large imperfections leading to a steady increase in buckling load with an increase in longitudinal cut-out size.
- FRP strengthening is also more effective in resisting pre-buckle deformations, i.e., lip opening, as well as alleviating stress concentration effects leading to a higher increase in P_u for larger longitudinal as well as for smaller cut-out sizes.

References

1. Teng JG, Hu YM (2007) Behaviour of FRP-jacketed circular steel tubes and cylindrical shells under axial compression. *Constr Build Mater* 21(4):827–838. <https://doi.org/10.1016/j.conbuildmat.2006.06.016>
2. Haedir J, Zhao XL (2011) Design of short CFRP-reinforced steel tubular columns. *J Constr Steel Res* 67(3):497–509. <https://doi.org/10.1016/j.jcsr.2010.09.005>
3. Krishna GV, Narayanamurthy V, Viswanath C (2021) Effectiveness of FRP strengthening on buckling characteristics of metallic cylindrical shells. *Compos Struct* 262:113653. <https://doi.org/10.1016/j.compstruct.2021.113653>
4. Jullien JF, Limam A (1998) Effects of openings of the buckling of cylindrical shells subjected to axial compression. *Thin-Walled Struct* 31(1):187–202. [https://doi.org/10.1016/S0263-8231\(98\)00003-2](https://doi.org/10.1016/S0263-8231(98)00003-2)
5. Hilburger MW, Starnes JH Jr (2005) Buckling behavior of compression-loaded composite cylindrical shells with reinforced cutouts. *Int J Non-Linear Mech* 40(7):1005–1021. <https://doi.org/10.1016/j.ijnonlinmec.2005.02.001>
6. Zhao XL (2014) FRP-strengthened metallic structures. CRC Press, Boca Raton
7. Teng JG, Rotter JM (2004) Buckling of thin shells - an overview. In: Teng JG, Rotter JM, eds. *Buckling of thin metal shells*, London, New York, Spon Press
8. Dassault System's Simulia Corp (2018) ABAQUS 2018 User's Manual. Providence, RI, USA
9. Khot NS, Venkayya VB (1970) Air Force Flight Dynamics Laboratory (US). Effect of fiber orientation on initial postbuckling behavior and imperfection sensitivity of composite cylindrical shells. Wright-Patterson Air Force Base, Ohio: Air Force Flight Dynamics Laboratory, Air Force Systems Command, United States Air Force
10. Koiter WT (1970) On the Stability of Elastic Equilibrium, HJ Paris Publ., Amsterdam 1945, English translation: Report nr. AFFDL-TR-70-25, Air Force Flight Dynamics Lab., Wright Patterson AFB, OHIO
11. Taheri-Behrooz F, Omidi M, Shokrieh MM (2017) Experimental and numerical investigation of buckling behavior of composite cylinders with cutout. *Thin-Walled Struct* 116: 136–144. <https://doi.org/10.1016/j.tws.2017.03.009>

Vibration Perception Threshold Tuning Curve Towards Early Diagnosis of Diabetic Peripheral Neuropathy



V. Madhan Kumar, S. Natarajan, and M. Manivannan

Abstract Diabetic Peripheral Neuropathy (DPN) is a severe complication of Diabetic Mellitus (DM) that causes the multisensory disorder. It is well-known that the Pacinian Corpuscle (PC), a mechanoreceptor responsible for vibration sensation, begins to deteriorate and degenerate first under DPN condition. Therefore, the vibration perception threshold (VPT) test is the most commonly used diagnostic method for the DPN. The VPT tests are made (clinically and in research) only 50 Hz and 120 Hz stimulus frequencies. However, the resonant frequency of human PC falls 200 Hz to 300 Hz, far away from what is being used in the current diagnostic method. In this work, we propose a VPT “curve” analysis of DM participants for six different frequencies, 50, 100, 200, 300, 400, 500 Hz at four points on the foot. The observed VPT curves of the DM participants are compared with the average VPT curves of normal (non-DM) participants for each point on foot. We observed that, unlike non-DM participants, the VPT curves for DM participants do not follow the conventional tuning curve shape. Instead, the VPT curves of DM participants are shifted up in most cases, indicating that the sensitivity of DM participants for the vibration stimulus is more inadequate. Furthermore, the vibration stimulus of frequencies 200 to 300 Hz gives a more apparent distinction of VPT than other frequencies.

Keywords Pacinian Corpuscle · Mechanoreceptor · Tactile · VPT

1 Introduction

One of the most common long-term complications of Diabetes mellitus (DM) is Diabetic peripheral neuropathy (DPN) which is affecting 50% of the people having it [17]. Diabetic neuropathies are the severe complication of DM [17] with increased

V. Madhan Kumar (✉) · M. Manivannan
Indian Institute of Technology Madras, Chennai 600036, India
e-mail: mani@iitm.ac.in

S. Natarajan
Central Council for Research in Siddha, Chennai 600106, India
e-mail: s.natarajan78@gov.in

© The Author(s), under exclusive license to Springer Nature Singapore Pte Ltd. 2022
T. Tadepalli and V. Narayanamurthy (eds.), *Recent Advances in Applied Mechanics*,
Lecture Notes in Mechanical Engineering, https://doi.org/10.1007/978-981-16-9539-1_31

risk of foot ulceration and amputation. Among various diabetic neuropathies listed by Pop-Busui et al. [12], the most common (75% of all neuropathies) is Distal Symmetric Polyneuropathy (DSP) which affects sensory nerves predominantly. The DSP may give rise to positive (involving C fibers leading to pain, pricking, and tingling) or negative (affecting large fibers causing sensory losses) symptoms in diabetic patients. The ultimate therapy for DSP is glycemic control. The standard diagnosis method for the DSP is the objective quantification of Nerve Conduction (NC) abnormality. According to Tesfaye et al. [17] the NC value that determines the severity of DSP (Grade scores - 0, 1a, 1b, 2a, and 2b) provides a DSP diagnosis (possible, probable, and confirmed). Several other methods for checking the severity are proposed in the literature.

If the NC values are normal and still the patient suffers from symptoms, then the density of intraepidermal nerve fiber is measured through biopsy. The Sympathetic Skin Response (SSR) test is commonly used for the diagnosis of diabetic neuropathies. It is the potential generated in skin sweat glands due to the activation of the reflex arch using various stimulus modalities - commonly, electrical stimulation. This electrical stimulation activates all the sensory fibers, especially the afferent part of the reflex arch. And it is not considering the somatic sensory tracts [8] such as tactile, kinesthetic, and thermal. The tactile afferent fibers emerge from four major mechanoreceptors: Merkel, Meissner, Ruffini, and Pacinian Corpuscles (PC). Among these four, PC is the most sensitive and responsible for the vibration sensation.

Vibrotactile (Vibration) perception threshold (VPT) analysis has become one of the quantifiable early diagnostic tools [14] for the DPN/DSP [15]. VPT is included as one of the quantitative sensory testings in the diagnosis of DPN as per consensus recommendations [1]. Although many works have been done in diagnosing the DPN, to our knowledge, none of them generates the entire psychophysical VPT curve for diabetic patients. In general, biopsies have shown denervation and neuronal structural changes, especially the PC axon [16]. Therefore, instead of stimulating all the nerve fibers, we can selectively stimulate the Pacinian axon for the early diagnosis, which is why the VPT test is popular in the DSP diagnosis [7]. According to Park and Kim [10], the combination of multiple testing methods can help with earlier diagnosis. They combined monofilament examination, the 128-Hz tuning-fork, ankle-reflex, and pinprick tests; the Total Symptom Score and the 15-item self-administered questionnaire of Michigan Neuropathy Screening Instrument for the early detection of DPN. Furthermore, other tactile sensory tests include two-point discrimination [11] and the verification of law of mobility using VPT [9]. Both these tests show significant difference for DM patients.

Although the VPT test is well known clinically and in the literature, the test is performed only 50 Hz or 120 Hz (depending on the biothesiometer or a tuning fork) [5]. Since we know that the PC axon is the first receptor to get denervated and the most responsive frequency band for PC falls 200 Hz and 300 Hz [4, 13, 18–21], we can focus our diagnosis on this frequency range along with other clinical frequencies. Furthermore, the proposed VPT curve analysis can be combined with conventional DPN diagnosis methods. The hypothesis we are testing here is that the VPT curve shifts upwards (lesser sensitive) for the DM subjects compared to the non-DM (nDM)

subjects. The main objective of this work is to identify the differences in the VPT curve for various vibration frequencies at four different measurement sites in the sole and ankle for the normal and DM subjects.

2 Methods

To assess vibration perception threshold (VPT) curves of non-diabetic and diabetic for set of frequencies, we conducted a psychophysical experiment. The experiment with diabetic patients is conducted at the Department of clinical research, Siddha Central Research Institute, CCRS, Chennai, India.

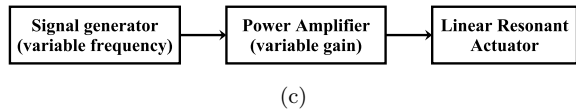
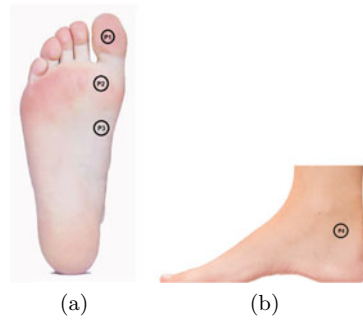
2.1 *Experimental Specifics*

We performed the experiment with twelve participants including eight diabetic (DM) and four non-diabetic (normal: non-DM) participants. The age of the participants ranges from 21 to 65 in which DM subjects age lies between 35 to 65 years and nDM subjects age lies between 21 to 35 years. Participants do not report any kind of pain and stress while conducting the experiment. They are in a fully comfortable position for the entire course of the experiment and breaks are given accordingly. We conducted the experiment at an average room temperature of 27°C. Some of the DM participants are maintaining physical exercise regularly with proper food. All the DM participants are taking diabetic medicine for at least 3 years minimum. We used Linear Resonant Actuator (LRA: C10-100) to deliver vibratory stimulus to the participants and the vibration intensity, duty-cycle, and frequency are controlled by the driver setup.

2.2 *Experimental Task*

In this experimental study, we used one of the well-known classical psychophysical methods [6] referred to as Method of Limits. For a fixed frequency, the intensity of the vibration is increased in steps until the participant reports that the vibration is felt and that particular intensity level is recorded. This is the detection task in which the participants need to detect the presence of a vibratory stimulus applied through vibration motors placed at specific points on foot (Fig. 1) to apply vibrations of variable frequency and intensity. We considered six different vibration frequencies in this study which are 50, 100, 200, 300, 400, 500 Hz at four different locations in the foot. The psychophysical specifications of the experiment are as follows:

Fig. 1 a,b Various points on the foot where VPT is measured for all the normal and DM participants. P1 - first phalanx; P2 - first metatarsal; P3 - lateral cuneiform; P4 - lateral talus bone. **c** Block diagram of the vibrotactile actuator setup. We used standard electronic driver circuit to excite the linear resonant actuator (LRA: C10-100)



- Task: Detection
- Stimulus: Cutaneous tactile vibration
- Measure: Absolute threshold
- Method: Staircase (method of limits)
- Analysis: Vibration perception threshold (VPT) curve

The data collected from the DM and non-DM participants are plotted in a logarithmic scale as represented conventionally in the literature [3, 21] to obtain VPT curves.

2.3 Experimental Protocol

The protocol of the experiment is as follows:

1. Participants are instructed about the experiment with a consent form and questionnaire.
2. Participants are asked to lay comfortably on a bed and the room temperature is maintained between 24°C and 28°C.
3. Three measurement sites (first phalanx (P1), first metatarsal (P2), lateral cuneiform (P3)) are marked on the sole and one point (Lateral of Talus bone (P4)) is marked in the ankle of the participant's foot as shown in Fig. 2.
4. The LRA is placed on the first point with the vibration frequency kept constant 100Hz and the vibration amplitude is slowly increased from zero volts in a step of 0.1 V until the participant informs the experimenter that the vibration is detected.

5. Once the participant reports the detection of vibration, the vibration amplitude is decreased with the same step size until the participant reports the complete loss in vibration sensation.
6. This trial is repeated thrice and the average value is considered as a threshold for the vibration detection in the particular frequency.
7. This procedure (steps 4–6) is repeated for different constant values of vibration frequencies such 200 Hz and 300 Hz.
8. The entire procedure (steps 4–7) is repeated for all the remaining four points marked on the foot of the participant.
9. Intermittent breaks are given to the participants so that there is no numbness or loss of concentration reported.
10. All the values are tabulated and the average value of VPT is calculated for each frequency and for each point.

3 Results and Discussion

In this section, we presented the results using VPT curves and the raw data in form of tables, for each points chosen on the foot for individual DM subjects. We have VPT curves of four normal participants (Fig. 2) in which four different plots (a-d) represents four different points on the foot. Since the VPT curves of non-DM participants follow conventional VPT curves reported in the literature, we consider only the averaged curves (and VPT values) of non-DM participants for the comparison of VPT for individual DM participants.

VPT curves of normal and DM participants are compared in Fig. 3a–h. Plots in the first row of Fig. 3 represents the average VPT curves of normal participants, whereas the plots in the second row indicate the VPT curves of DM participants. Since all the DM participants struggled to detect vibrations of all frequencies due to their condition, we plotted only those points which could be detected by them. The raw data is shown in the tabular form by comparing with the average VPT data of normal participants, as shown in Tables 1, 2, 3, and 4. In these tables, each value except first row represents the vibration intensity, and ND denotes not detected.

Comparison of VPT Curves of Normal Participants with Experimental Literature and Model Results: Figure 2 shows the VPT curves for four subjects measured in four different points on foot. These VPT curves can be compared with the curves reported in the literature (add adapted figures in chap 2) [2, 4, 21]. It is observed that the curve matches with the experimental data available from the literature. Furthermore, the measured VPT curves can be compared with the various computational model results reported in the literature [3, 20]. The major difference from the literature is that the resonant frequency (the frequency at which the lowest threshold occurs) point differs at different points on the sole. This is also evident as the resonant frequency depends on the thickness of the skin and the PC properties as reported in the literature [3].

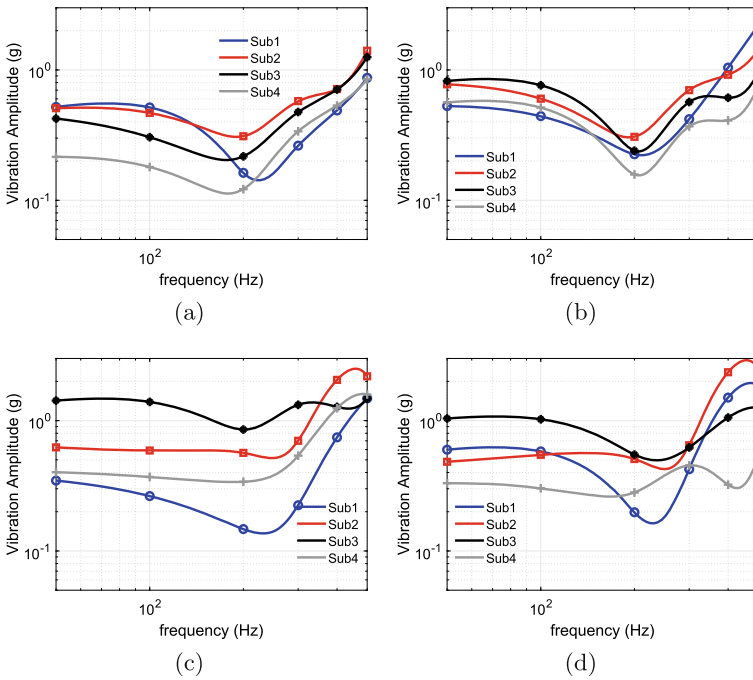


Fig. 2 Vibration Perception Threshold (VPT) of normal participants measured at four different points **a-d** on the foot

Comparison of Psychophysical and Neurophysiological Thresholds: Psychophysical threshold represents the human perception, that is, the minimum stimulus amplitude required to elicit the sensation. Whereas, the neurophysiological threshold represents the minimum stimulus amplitude required to elicit Action Potentials (neural impulses). Verrillo [21] proposed the first comparison between the psychophysical and neurophysiological threshold curves in which the neurophysiological thresholds are measured from the electrophysiological recordings and the psychophysical thresholds are measured through perceptual experiments. In our study, we can compare the threshold curves resulted from the proposed computational models based on neurophysiology with the threshold curves that we measured through psychophysical experiments.

Variations in VPT Between Normal and DM Participants: It is observed from Fig. 3 that the deviation (error bars) can be considered as an early diagnostic tool for DPN. The deviation is more for DM participants compared to that of the normal participants in all the cases.

SSR test can be time-effective, but it measures the response due to the activation of several nerve fibers. However, the method described above selectively focuses on the Pacinian channel and characterizes the patient’s vibration sensation limit.

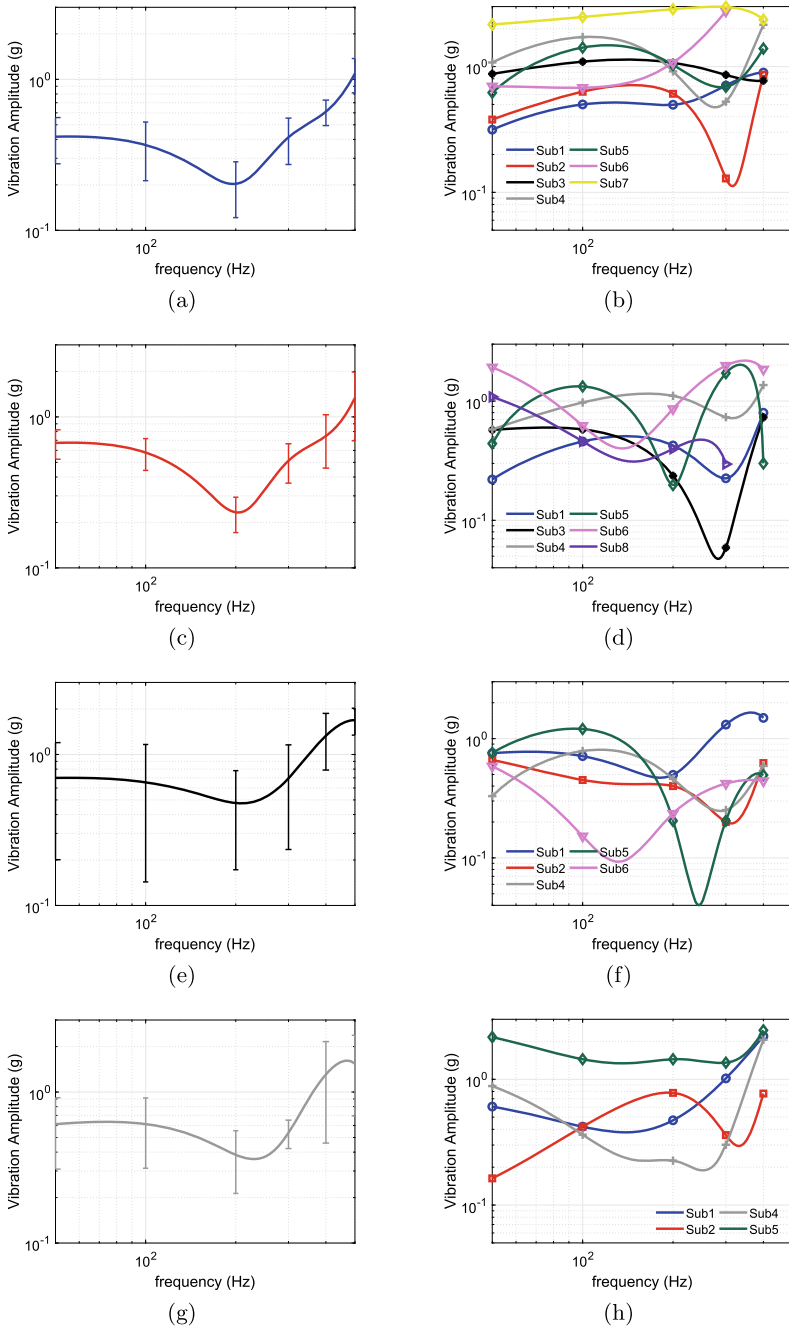


Fig. 3 (a,c,e,g) The average VPT curve of all four normal participants (as shown in Fig. 2) for four points on the foot. (b,d,f,h) VPT curves of individual DM participants for the same points. The amount of deviation in terms of vibration amplitude in the VPT curves is evident in each row. Error bars indicate standard deviation

Table 1 For single point on the sole (P1), average VPT of normal participants is used to compare the VPT of individual DM participants

Frequency	Normal	DM1	DM2	DM3	DM4	DM5	DM6	DM7	DM8
50Hz	0.42 ± 0.14	0.32	0.38	0.88	1.08	0.62	0.70	2.16	2.15
100Hz	0.37 ± 0.15	0.50	0.63	1.09	1.72	1.42	0.68	2.48	0.90
200Hz	0.20 ± 0.08	0.50	0.61	1.07	0.92	1.03	1.07	2.86	ND
300Hz	0.41 ± 0.14	0.71	0.13	0.86	0.53	0.69	2.76	2.98	2.13
400Hz	0.61 ± 0.11	0.90	0.86	0.77	2.15	1.39	ND	2.36	2.08
500Hz	1.09 ± 0.28	ND	ND	ND	ND	ND	ND	ND	ND

Table 2 VPT comparison for point P2

Frequency	Normal	DM1	DM2	DM3	DM4	DM5	DM6	DM7	DM8
50Hz	0.67 ± 0.14	0.22	0.12	0.57	0.58	0.44	1.92	ND	1.08
100Hz	0.58 ± 0.14	0.46	0.16	0.58	0.97	1.33	0.62	0.87	0.46
200Hz	0.23 ± 0.06	0.42	0.02	0.24	1.11	0.20	0.86	0.76	0.40
300Hz	0.51 ± 0.15	0.23	0.06	0.06	0.73	1.71	1.98	ND	0.30
400Hz	0.75 ± 0.29	0.80	0.89	0.73	1.36	0.30	1.84	ND	ND
500Hz	1.34 ± 0.64	ND	ND	ND	ND	ND	ND	ND	ND

Table 3 VPT comparison for point P3

Frequency	Normal	DM1	DM2	DM3	DM4	DM5	DM6	DM7	DM8
50Hz	0.70 ± 0.49	0.76	0.66	ND	0.33	0.76	0.59	ND	ND
100Hz	0.65 ± 0.51	0.71	0.45	ND	0.79	1.21	0.15	2.28	ND
200Hz	0.48 ± 0.30	0.50	0.40	ND	0.46	0.20	0.24	ND	0.28
300Hz	0.70 ± 0.46	1.31	0.20	ND	0.25	0.20	0.42	ND	ND
400Hz	1.33 ± 0.54	1.49	0.62	ND	0.59	0.49	0.44	ND	ND
500Hz	1.68 ± 0.34	ND	ND	ND	ND	ND	ND	ND	ND

Given that the Pacinian axon is affected even before the first symptom occurs, a simple VPT test for several frequencies will be the effective method for the early diagnosis of DSP.

Once we validate the diagnosis method, we can improve the diagnosis method’s effectiveness with better design and time-effectiveness. However, we need to do an extensive study with the selective diabetic patients in the early stage of hyperglycemia for the initial validation. The assessment needs to be carried out along with the patient questionnaire and their HbA1c test report.

Table 4 VPT comparison for point P4

Frequency	Normal	DM1	DM2	DM3	DM4	DM5	DM6	DM7	DM8
50Hz	0.61 ± 0.30	0.61	0.16	ND	0.88	2.17	0.76	ND	0.97
100Hz	0.61 ± 0.30	0.42	0.42	ND	0.36	1.44	ND	ND	1.24
200Hz	0.38 ± 0.17	0.47	0.78	ND	0.23	1.44	0.47	ND	1.25
300Hz	0.54 ± 0.11	1.02	0.36	ND	0.30	1.35	ND	ND	ND
400Hz	1.31 ± 0.85	2.20	0.77	ND	2.06	2.45	ND	ND	ND
500Hz	1.54 ± 0.84	ND	ND	ND	ND	ND	ND	ND	ND

4 Summary

Measuring VPT for the set of frequencies and visualizing them as a VPT curve gives a better insight into the diagnosis of DPN. The VPT curves from the normal subjects are validated using the psychophysical VPT curve from the literature. The degree of shifts in the VPT curve for the DM participants reported in this study can be predicted as the diagnosis for diabetic peripheral neuropathy (DPN). Therefore, the method introduced in this study can serve as an early diagnostic parameter for the diagnosis of diabetic peripheral neuropathy. The future studies include conducting the VPT curve experiment with large sample of DM participants along with their HbA1c report and use it for the comparison to get more accurate prediction of DPN. This method proposed in this study can be combined with the existing DPN diagnostic procedures to improve the accuracy and precision of the early diagnosis of DPN.

Acknowledgement The authors thank the Department of clinical research, Siddha Central Research Institute, CCRS, Chennai for their support in conducting this study. The authors would like to thank the participants who took part in the experiment. The authors would also like to thank the members of Haptics Lab at the Indian Institute of Technology Madras for providing valuable feedback regarding this study.

References

1. Association AD et al (1988) Report and recommendations of the san Antonio conference on diabetic neuropathy. *Diabetes* 37(7):1000–1004
2. Bell J, Bolanowski S, Holmes MH (1994) The structure and function of Pacinian corpuscles: a review. *Progress Neurobio.* 42(1):79–128
3. Biswas A, Manivannan M, Srinivasan MA (2015) Vibrotactile sensitivity threshold: nonlinear stochastic mechanotransduction model of the Pacinian corpuscle. *IEEE Trans. Haptics* 8(1):102–113
4. Bolanowski S Jr, Zwislocki JJ (1984) Intensity and frequency characteristics of Pacinian corpuscles I action potentials. *J. Neurophys.* 51(4):793–811
5. Boulton A, Betts R, Franks C, Newrick P, Ward J, Duckworth T (1987) Abnormalities of foot pressure in early diabetic neuropathy. *Diabetic Med.* 4(3):225–228
6. Gescheider GA (2013) *Psychophysics: The Fundamentals.* Psychology Press

7. Gregersen G (1968) Vibratory perception threshold and motor conduction velocity in diabetics and non-diabetics. *Acta Med. Scandinavica* 183(1–6):61–65
8. Kucera P, Goldenberg Z, Kurca E (2004) Sympathetic skin response: review of the method and its clinical use. *BRATISLAVSKE LEKARSKE LISTY* 105(3):108–116
9. Manivannan M, Periyasamy R, Narayanamurthy V (2009) Vibration perception threshold and the law of mobility in diabetic mellitus patients. *Primary care Diabetes* 3(1):17–21
10. Park JH, Kim DS (2018) The necessity of the simple tests for diabetic peripheral neuropathy in type 2 diabetes mellitus patients without neuropathic symptoms in clinical practice. *Diabetes Metabolism J.* 42(5):442
11. Periyasamy R, Manivannan M, Narayanamurthy V (2008) Correlation between two-point discrimination with other measures of sensory loss in diabetes mellitus patients. *Int. J. Diabetes Develop. Countries* 28(3):71
12. Pop-Busui R, Boulton AJ, Feldman EL, Bril V, Freeman R, Malik RA, Sosenko JM, Ziegler D (2017) Diabetic neuropathy: a position statement by the American diabetes association. *Diabetes care* 40(1):136–154
13. Sato M (1961) Response of Pacinian corpuscles to sinusoidal vibration. *J. Phys.* 159(3):391–409
14. Shy M, Frohman E, So Y, Arezzo JC, Cornblath D, Giuliani M, Kincaid J, Ochoa J, Parry GJ, Weimer L (2003) Quantitative sensory testing: report of the therapeutics and technology assessment subcommittee of the American academy of neurology. *Neurology* 60(6):898–904
15. Sorensen L, Molyneaux L, Yue DK (2006) The level of small nerve fiber dysfunction does not predict pain in diabetic neuropathy: a study using quantitative sensory testing. *Clinic. J. Pain* 22(3):261–265
16. Spencer PS, Schaumburg HH (1975) Nervous system degeneration produced by acrylamide monomer. *Environ. Health Perspect.* 11:129–133
17. Tesfaye S, Boulton AJ, Dyck PJ, Freeman R, Horowitz M, Kempner P, Lauria G, Malik RA, Spallone V, Vinik A et al (2010) Diabetic neuropathies: update on definitions, diagnostic criteria, estimation of severity, and treatments. *Diabetes Care* 33(10):2285–2293
18. Vasudevan MK, Ray RK, Muniyandi M (2020) Computational model of a Pacinian corpuscle for an electrical stimulus: spike-rate and threshold characteristics. In: Nisky I, Hartcher-O'Brien J, Wiertelowski M, Smeets J (eds) *EuroHaptics 2020*, vol 12272. LNCS. Springer, Cham, pp 203–213. https://doi.org/10.1007/978-3-030-58147-3_23
19. Madhan Kumar V, Sadanand V, Manivannan M (2021) Computational model of a Pacinian corpuscle for hybrid-stimuli: spike-rate and threshold characteristics. In: Manocha AK, Jain S, Singh M, Paul S (eds) *Computational Intelligence in Healthcare. HIS*. Springer, Cham, pp 379–396. https://doi.org/10.1007/978-3-030-68723-6_21
20. Vasudevan MK, Sadanand V, Muniyandi M, Srinivasan MA (2020) Coding source localization through inter-spike delay: modelling a cluster of Pacinian corpuscles using time-division multiplexing approach. *Somatosensory Motor Res.* 37(2):63–73
21. Verrillo RT (1966) Vibrotactile sensitivity and the frequency response of the Pacinian corpuscle. *Psychon. Sci.* 4(1):135–136

Effect of Elevated Finger Temperature on Active Force JND



V. Madhan Kumar, A. Ashwath, and M. Manivannan

Abstract Many studies have focused on the sensory interaction between thermal and haptic perception. However, the quantification of influence of temperature on force discrimination is not studied so far. This study aims to measure the active force Just Noticeable Difference (JND) of right forefinger at an elevated temperature. We have conducted an active force discrimination experiment through the forefinger of twenty-one participants at two different fingertip temperatures (33 and 40 °C). We have used a classical psychophysical method for the forces from 3.05 to 3.95 N with an interval of 0.15 N (reference force = 3.5 N), and the two-alternative forced-choice paradigm. The participant has to apply the force to match the target that is visually displayed and compare the two forces given in two different intervals. Sixteen out of twenty-one participants' JND is found to be reduced for the fingertip temperature of 40 °C. On an average, the active force JND is 7.3% at 33 °C and 5.5% at 40 °C which shows a 25% reduction in the JND. We conclude that the force discrimination ability can be enhanced by elevating the fingertip temperature.

1 Introduction

Alteration of a tissue temperature has proven to be one of the best ways for the tissue therapy by constricting (cold) or dilating (hot) the blood vessels. Especially for the skin surface, the thermal gradient has been shown to influence the perception of other haptic modalities such as tactile and kinaesthetic sensations. Many studies have been conducted for understanding the influence of temperature on the haptic sensation. Green et al. [8] showed that the roughness perception of the surfaces is reduced when the skin temperature falls below 32 °C and enhanced when the skin temperature is above 32 °C. Moreover, works of Bolanowski, Verillo and Green [3, 8] have reported an increase in vibro-tactile threshold for high-frequency stimulus (200–350 Hz) applied over the skin which is cooled. Lederman and Jones [6] reviewed

V. Madhan Kumar (✉) · A. Ashwath · M. Manivannan
Touch Lab, Department of Applied Mechanics, Indian Institute of Technology Madras,
Chennai 600036, India
e-mail: mani@iitm.ac.in

thermal grill illusion which is a burning pain sensation while touching surface that alternates between hot and cold temperatures. It is not clear that the perception of haptic sensations influenced by the temperature changes, is either due to the changes in the tactile or kinaesthetic receptor activity due to local blood flow or due to the combined activity of the thermal, tactile and kinaesthetic receptors. The efforts being made in obtaining the human specification in terms of force sensation and perception are enormous [11].

Force discrimination in milli Newtons is vital in many situations such as microsurgical procedures and clinical diagnosis, for example palpating and suturing in case of surgery, sensing vein and GI tract in case of diagnosis. Jones [11] reviewed the force perception in detail, and along with Galie [6] they studied the influence of thermal cues for force perception. In the latter work, they have shown that the perceived force magnitude through index finger is not dependent on the temperature which varied from 22 to 38 °C. There are works [4] suggesting that inducing cold temperature to the skin degrades the haptic perception, whereas the higher temperatures improves the haptic perception. It is clear from the literature that there is a huge influence of temperature changes on other haptic sensations. However, the quantification of force discriminability under the temperature change is not reported.

Unlike other senses, touch is the only sensory modality that includes active manipulation of the objects to be sensed. Touch modality involves sensing of vibration, pressure, temperature, displacement and also force, either actively or passively (each involves unique receptor kind and separate channel to the central nervous system). Active touch is where the motor system is involved to manipulate the object. Active Force sensing involves tactile receptors and Golgi tendon organs to sense the force that is being applied through the fingers by motor system. Whereas, passive involves only tactile receptors without any kinesthetic receptors.

Measurement of active force JND (Just Noticeable Difference) by psychophysics [7] deals with the measurement of mental events that is responsible for the perception of stimulus. The ability of the human to detect smallest difference in the stimuli range is called Just Noticeable Difference (JND) in psychophysical terms. In case of force as a stimulus, we have active force JND and passive force JND. Since our primary interest lies in active manipulation tasks, we have considered only active force JND in this work.

The inter-modality dependencies on the perception of haptic sensations are well studied [6, 12]. JND, considered as the perceptual resolution, is found to be 7% for force and elastic stiffness [13, 17]. Simulated environments where the haptic feedback is vital (epidural injection simulators), can be designed better if we know more about the perceptual measurement of vibration, force and stiffness [16]. Force control psychophysical experiment conducted by Allin et al. [1] yielded higher force JND of 10%. In a force matching task [15] (bimanual task), for a right index finger, the force JND is reported as 10%. The force JND can be manipulated using other factors such as visual illusions, or temperature. This influence on force perception can be utilized to fine-tune the user performance and experience in the simulated environments, such as virtual surgical simulators, and so on. Force JND is also influenced by the rate of change of stimulus [2]. Knorlein et al. [12] reported improved

perception of stiffness due to visual delays. Ho and Jones [9, 10] modeled the process of heat transfer (fingertip), and explained how the contact skin temperature changes is essential for apparent temperature.

Temperature effects of force while grasping [4, 5] are well studied without involving psychophysics. Carnahan et al. [4] reported that the haptic system consistently manages the sensory and motor components of cold object perception. They investigated the perception of moisture illusion as a coefficient of friction between the surface and finger by monitoring the force. Dizmen et al. [5] reported degradation in haptic parameters such as dexterity, reaction time and grip span for lower temperatures (10°C) than at higher temperatures (20 and 30°C). It is essential to analyze the human force perception by using the thermal changes of the fingertip through which the force is sensed actively or passively.

The aim of this study is to find whether there is an influence of temperature elevation of fingertip in active force JND. This classical psychophysical study includes the comparison of active force JND of right forefinger in room temperature (33°) with that of elevated temperature (40°). Applications of this study could be surgical and clinical diagnosis where the physician has to sense finer differences of force. Moreover, we have used naive participants in our experiments to measure the active force JND. This work can be extended to measure the active force JND of the experienced and novice surgeons for surgical tasks, or any other tasks where active force discrimination is vital.

2 Methodology

To determine the active force JND, we have conducted a classical psychophysical experiment of discrimination task. We have used the constant stimuli method in which we have chosen set of six forces and one reference force in an equal interval, and we have chosen two-interval two-alternative forced choice paradigm (2I-2AFC) in which the forces to be discriminated are given in two different times and the response is forced towards only two options, either greater or smaller. There are two versions of the experiment, one at the normal temperature (NT) of the forefinger 33°C, and another one at the elevated temperature (ET) of 40°C.

2.1 Experiment Specifications

To measure the force, we have used ATI-Nano 17F/T sensor along with its signal conditioner which amplifies the strain gauge outputs from the sensor. The force signal is given to the data acquisition system (NI DAQ 6221) which inputs the force data to the computer. Initially, the force sensor is calibrated with the known weights. We have used NI device monitor for the DAQ interface and Visual studio 2017 to create the visual setup. We have used IR lamp to increase the temperature of the fingertip,

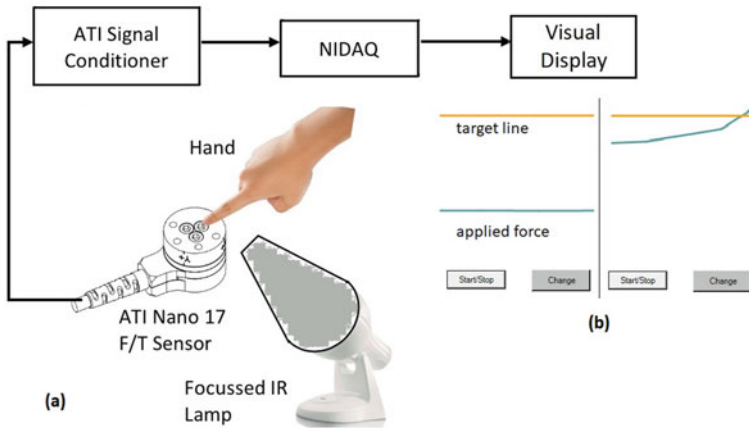


Fig. 1 **a** Experimental setup which shows the participant actively applying force on the sensor in presence of IR lamp focused towards the finger. The target line and applied force line are displayed so that the participant tries to match in each trial, and compares two different forces (one is reference force 3.5 N, and another one is actual force, 3.05, 3.2, 3.35, 3.65, 3.8, or 3.95 N). **b** Initially, two lines are shown to the participants so that they apply force on the sensor using their finger tip in order to match the target line (yellow) with the force line (blue). Once the participants reach the target line, they are asked to hold for 3 s. This is to avoid the random guessing of the response

and an IR camera is used to monitor the temperature of the fingertip continuously. IR camera is from Sonel[®] and the model is NT-150. We made sure that the temperature change of a strain gauge sensor doesn't affect the resolution requirements of our force range. The force difference that we are using is 0.15 N, and the accuracy error of the sensor over 15 °C change is given as 0.5% and the resolution of sensor is given as 1/320 N which is well inside our resolution requirements even with temperature change.

2.2 Participant Specifics

With informed consent, twenty one healthy naive participants in the age range of 19–28 years were chosen for the active force discrimination task. Participants reported no abnormalities in their sensory or motor systems. They are all right handed, and moreover they are normal in terms of temperature sensation. The experimental protocol was explained to all the participants clearly, and they were given a trial before the start of the actual experiment. The study is approved by the Institute Ethics Committee (Reference number IHEC/2021-01/MM/02/14).

2.3 Active Force Discrimination Task

The setup for Active Force Discrimination (AFD) at NT and ET tasks is shown in Fig. 1 in which the ATI-Nano 17 F/T sensor indicates the strain gauge type force sensor which is connected to the ATI signal conditioner for amplification of force signal. The display is provided to visualize the target line and applied force, so that the participants get the visual cues, as shown in Fig. 1b.

Experimental Procedure. The experiment has two versions AFD-NT and AFD-ET, and the participant has to perform both forms of the experiment. Initially, the participants are divided into two groups A and B. Group A performed initially AFD-NT task and then AFD-ET, and Group B performed the reverse order. This is to check whether there is a learning effect and its influence on JND measurement. The target line is displayed so that the participant has to match the applied force with the target line for each force, as shown in Fig. 1b. The task is conducted such that the participant applies force isometrically through forefinger, and the entire arm is rested. One trial includes, discriminating the actual and reference forces given in two different intervals. The reference force is chosen to be 3.5 N, and the actual force is chosen from the set of forces, 3.05, 3.2, 3.35, 3.65, 3.8, or 3.95 N. Each pair of force is repeated for 8 times, and a single AFD task includes 48 trials of force discrimination. The task of the participant is to compare the reference force with the actual force and inform which is greater. The actual force is chosen in a random order, and the order of reference and actual forces is also randomized for each trial. Focused IR lamp is used to apply the IR light to the finger through which the participant applies force, and enough time is allowed for achieving the steady state temperature (40°). IR camera is used to measure the temperature of the finger, so that the constant temperature is maintained in both task. The room temperature is maintained at 26°C in both NT and ET cases.

AFD Task Protocol

- Initially, the participant is asked to sit comfortably with arms resting, and the experiment protocol is explained to the participant.
- Sample trials were given to the participant to get used to the NT and ET tasks, and then the actual experiment is started.
- In each version of the experiment, two forces are given: one reference force and one of the actual forces, in a random order.
- The participant has to compare these forces using the right forefinger, and report which among them is greater.
- IR camera is used, in case of ET task, to measure the temperature of the finger region through which the participant applies force.
- During the sample and actual trials, the participants are inquired about their comfort, especially the finger temperature.

2.4 Quantification of AFD Tasks

We have used constant stimuli method of psychophysics [7] with 2I-2AFC paradigm, as mentioned previously in this section. The response from twenty-one subjects are collected and analyzed to calculate the active force JND. We have used two methods to calculate the average %JND. One is by plotting psychometric function for each participant, and from the psychometric function 75 and 25% values are used to calculate the JND as given in Eq. 1 and then individual JNDs are averaged to find the overall JND.

$$JND = \frac{S_{75} - S_{25}}{2} \quad (1)$$

where S_{75} indicates the 75% response force stimulus value and S_{25} indicates the 25% response force stimulus value.

Another method of finding %JND is by plotting the average psychometric function considering all the participants together and then calculating the JND. Other quantification includes the distribution analysis and statistical significance tests. The normal distribution of JNDs of each task is then plotted for the comparison. Paired t-test is used to check the influence of order of the experiment on JND. Moreover, z-score analysis is used to check the significance between the JNDs of AFD-NT and AFD-ET tasks.

3 Results and Discussion

Although it is clear from the literature that there is a huge influence of temperature changes on haptic perceptions, there are no studies that quantifies the force discrimination under the influence of temperature.

In our study, the active force JND is calculated from the first method as 7.3% for the task AFD-NT and 5.51% for the task AFD-ET. We can observe around 25% decrease in the JND for the ET task compared to NT on an average. This implies that the elevated finger temperature makes the participant more sensitive towards the finer changes in the force levels. The percentage JNDs of individual participants are compared in Fig. 2, which shows that the ET JND is lesser for 16 subjects out of twenty-one. Five participants have shown the opposite effect which is increase in JND for the ET case, and one has shown negligible change. The reason for this increase could be either the temperature elevation is not sufficient for the participant since we have maintained constant temperature elevation of 40°C for all the participants, or the participants themselves are insensitive to the temperature change for the force perception.

Initially, to check whether the order of the task, ET or NT, is influencing the JND, all the participants were grouped into A and B. Group A performed task AFD-NT first and then AFD-ET, and group B performed the reverse order. The data from these

Fig. 2 Comparison of active force JND of individual participants in AFD-NT and AFD-ET cases. The reduction in percentage force JND is observed in nine participants out of fourteen, in case of AFD-ET task

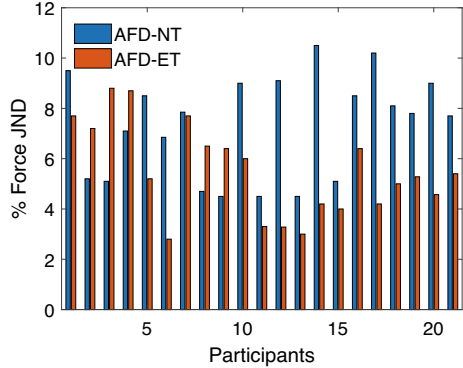
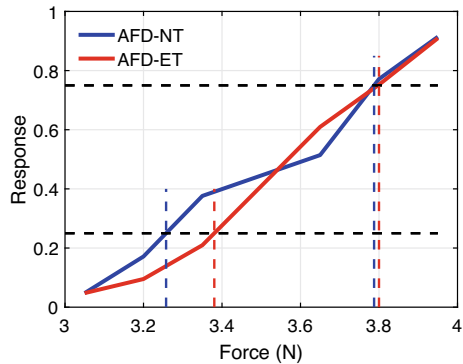


Fig. 3 Comparison of psychometric functions of AFD-NT and AFD-ET tasks. This function is plotted with the average responses for each force, and then the active force JND is calculated using the 75 and 25% values



two groups were analyzed to check whether there is a significant difference due to the order of the tasks. The t-test analysis has shown that the comparison of JND between these two groups is insignificant ($p = 0.82$, for $\alpha = 0.05$). Therefore, we have combined all the data together for the calculation of mean active-force JND.

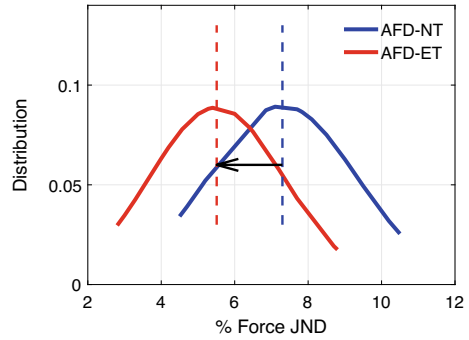
The z-score analysis between the active JND of AFD-NT and AFD-ET tasks has shown that there is a significant ($p(z) = 0.0025$, for $\alpha = 0.05$) difference between the these two tasks.

The psychometric functions of each task are plotted as shown in Fig. 3, from which the average active force JNDs are calculated to be 7.6 and 6% for AFD-NT and AFD-ET, respectively. The force JND calculated from averaging individual participants' JNDs, and from the averaged the psychometric function are similar.

Based on the percentage increment (25%) of %JND that we observe from AFD-NT to AFD-ET tasks, we strongly recommend the accompaniment of thermal sensation to the kinesthetic sensation, wherever the force discrimination improvement is required. Also, as mentioned in literature [4, 5], we can expect better perception of haptic sensation with the assistance of thermal sensation.

The result from our study is in contradiction with the result of Galie and Jones [6] in which they have shown that the perception of force is not the function of

Fig. 4 Distributions (solid lines) of active force JND for AFD-NT (blue) and AFD-ET (red) cases. The dotted lines indicate the peak JND value of each tasks, and the arrow head indicates the direction of shift of the percentage force JND from 7.3 to 5.51%. Around 25% reduction in percentage force JND is observed in case of AFD-ET task



temperature of the contact surface which varied from 22 to 38 °C, and they have given a linear relation between reference and matching forces with almost no shift for each temperature levels considered by them. We studied only the force discrimination rather than the force magnitude itself. Also the reference force is fixed in our case, whereas they had variable reference force. From our results, we suggest that there is a strong influence of temperature on the perception of force discrimination.

While conducting experiment, we have inquired participants to know the perceptual sensitivity change subjectively. All the participants who have shown decreased JND have expressed that they felt easier to discriminate the reference and actual forces in case of AFD-ET task compared to AFD-NT task. Moreover, the participant felt comfortable in the discrimination task without any ambiguities in their decision for the response. Adding to this, we have also visualized the raw-data from the force sensor. Due to the high precision of the sensor, we have visualized the minute changes of the force applied (tremors) by the participants. As compared to the tremors of AFD-NT task, the force signal of AFD-ET task had lesser tremors for the participants whose JND are lower for elevated finger temperature. This observation is supported by Dizmen et al. [5] and Uppangala et al. [18] which have shown that the haptic performance is highly degraded by the cold temperature and improved by the temperatures slightly higher than the room temperature.

If we observe Fig. 4, there is a shift in distribution towards left from AFD-NT task to the AFD-ET task. However, the variance of the distribution remains almost same. The shift in the mean of the distribution indicates that the participants performed well in discrimination task especially in the AFD-ET task. This implies that their force perception is enhanced by the thermal perception, in the order 25% for 7 °C change in temperature.

It is well known in the literature that studying temperature influence on perception of haptic sensations has more potential benefits in many situations. The force discrimination is one such important haptic sensation especially for the surgeons, and clinicians. We intended to assess their force JND (thereby increasing sensitivity) by introducing elevated finger temperature during grasping tasks [20] in surgical training [19]. As a future study, the temperature influence can be observed on various haptic submodalities such as tactile, kinesthetic, and proprioception. For instance,

tactile illusions [14] reported in the literature can be extended to study under changes in the temperature.

4 Conclusion

In this study our objective is to find whether the active force JND is influenced by temperature elevation of fingertip. We used classical psychophysical method and measured the active force JND of right forefinger as 7.3% for the AFD-NT task (33°C) and 5.51% for the AFD-ET task (40°C). Our current work implies that the temperature change in the fingertip highly influences on the active force JND. This can be applied to the situations where the force discrimination ability of the human needs to be improved. For example in surgical training simulations, minute force differences can be simulated and the novice surgeons can be asked to discriminate them with and with out temperature elevation. This performance can be quantified again by the psychophysical methods. The future works can include repeating the same procedure and finding the JND values at elevated temperatures for all fingers, and also by finding the JND values for different fingertip temperatures. The latter one which gives the JND as a function of fingertip temperature has more clinical importance.

Acknowledgements The authors would like to thank the participants who took part in the experiment. The authors would also like to thank the members of Haptics Lab at the Indian Institute of Technology Madras for providing valuable feedback regarding this study.

References

1. Allin S, Matsuoka Y, Klatzky R (2002) Measuring just noticeable differences for haptic force feedback: implications for rehabilitation. In: Proceedings 10th symposium on haptic interfaces for virtual environment and teleoperator systems, HAPTICS 2002. IEEE, pp 299–302
2. Bhardwaj A, Chaudhuri S (2014) Does just noticeable difference depend on the rate of change of kinesthetic force stimulus? In: International conference on human haptic sensing and touch enabled computer applications. Springer, pp 40–47
3. Bolanowski S Jr, Verrillo RT (1982) Temperature and criterion effects in a somatosensory subsystem: a neurophysiological and psychophysical study. *J Neurophysiol* 48(3):836–855
4. Carnahan H, Dubrowski A, Grierson LE (2010) Temperature influences both haptic perception and force production when grasping. *Int J Ind Ergon* 40(1):55–58
5. Dizmen C, Man K, Chan A (2015) The effect of temperature on manual dexterity, reaction time, and optimum grip-span. In: Proceedings of the international multicongress of engineers and computer scientists, vol 2, pp 1–5
6. Galie J, Jones LA (2010) Thermal cues and the perception of force. *Exp Brain Res* 200(1):81
7. Gescheider GA (2013) *Psychophysics: the fundamentals*. Psychology Press
8. Green BG, Lederman SJ, Stevens JC (1979) The effect of skin temperature on the perception of roughness. *Sens Processes* 3(4):327–333

9. Ho H, Jones L (2004) Material identification using real and simulated thermal cues. In: The 26th annual international conference of the IEEE engineering in medicine and biology society, vol 1. IEEE, pp 2462–2465
10. Ho HN, Jones LA (2006) Contribution of thermal cues to material discrimination and localization. *Percept Psychophys* 68(1):118–128
11. Jones LA (1986) Perception of force and weight: theory and research. *Psychol Bull* 100(1):29
12. Knorlein B, Di Luca M, Harders M (2009) Influence of visual and haptic delays on stiffness perception in augmented reality. In: 2009 8th IEEE international symposium on mixed and augmented reality. IEEE, pp 49–52
13. Pang XD, Tan HZ, Durlach NI (1991) Manual discrimination of force using active finger motion. *Percept Psychophys* 49(6):531–540
14. Patel P, Ray RK, Manivannan M (2019) Power law based “out of body” tactile funneling for mobile haptics. *IEEE Trans Haptics* 12(3):307–318
15. Prasad MR, Purswani S, Manivannan M (2013) Force JND for right index finger using contra lateral force matching paradigm. In: ICoRD 2013. Springer, pp 365–375
16. Ravali G, Manivannan M (2017) Haptic feedback in needle insertion modeling and simulation. *IEEE Rev Biomed Eng* 10:63–77
17. Tan HZ, Durlach NI, Beauregard GL, Srinivasan MA (1995) Manual discrimination of compliance using active pinch grasp: the roles of force and work cues. *Percept Psychophys* 57(4):495–510
18. Uppangala C, Krishnamoorthy P, Vishrutha K, Prarthana K (2019) Effect of temperature on muscle endurance in healthy adults. *Natl J Physiol Pharm Pharmacol* 9(7):583–585
19. Vasudevan MK, Isaac JH, Sadanand V, Muniyandi M (2020) Novel virtual reality based training system for fine motor skills: towards developing a robotic surgery training system. *Int J Med Robot Comput Assisted Surg* 16(6):1–14
20. Wils S, Mathew G, Manivannan M, Devasahayam SR et al (2013) A comparison of pinch force between finger and palm grasp techniques in laparoscopic grasping. *Engineering* 4(10):46

Fatigue Crack Growth Study in Miniature Single Edge Notch Tension Specimen Using Acoustic Emission Technique



Raghu V. Prakash , Prathmesh Pokharkar ,
and Chandan K. Mukhopadhyay 

Abstract Understanding fatigue crack growth (FCG) characteristics is essential to predict the useful life of components. In this context, miniature specimens are considered as potential geometries for materials extracted from in-service components because a small volume of material is required. In this study, FCG rate of an Inconel alloy miniature single edge notch tension (SEN(T)) specimen of 30 mm in length \times 10 mm wide and 1 mm in thickness is monitored at two load ratios 0.1 and 0.7 using visual and acoustic emission technique (AE). A Ws α wide band AE sensor placed on the fixture is used to acquire acoustic emission waveform parameters such as counts, absolute energy, hits, peak amplitude, and duration. The exponent of AE cumulative absolute energy with ΔK is found to be higher than the Paris exponent in FCG. AE technique was found to be useful to correlate transition in stages of fatigue crack growth in miniature specimens.

Keywords Fatigue crack growth · Miniature single edge notch tension specimen · Acoustic emission monitoring · Inconel alloy

1 Introduction

Fatigue is considered one of the critical factors for the failure of structures. Fatigue crack initiates due to stress concentration at notches and grows until the critical stress intensity factor is reached when the fast fracture occurs. In case of ductile materials, considerable fraction of fatigue life is spent in crack propagation; hence, fatigue crack growth study is important to predict the failure of a component containing defects. Generally, there are three stages in the fatigue crack growth (FCG) rate curve of most materials: crack initiation (stage 1), stable crack growth (stage 2), and fast fracture failure (stage 3). Various factors like microstructure, load ratio, environment, and

R. V. Prakash (✉) · P. Pokharkar
Department of Mechanical Engineering, IIT Madras, Chennai 600036, India
e-mail: raghuprakash@iitmadras.ac.in

C. K. Mukhopadhyay
HBNI/IGCAR, Kalpakkam 603102, India

thickness influence the different stage of the FCG rate curve [1, 2]. Monitoring of fatigue crack growth helps to avoid catastrophic failure of a component. For monitoring crack growth, several techniques, including active and passive nondestructive evaluation (NDE) techniques are employed. Acoustic emission (AE) is a passive NDE technique used to monitor defects in components. AE sensor coupled to a component captures the stress wave generated from damage zone of a component, which when recorded and processed further helps in damage prognosis. Several researchers have used AE to study FCG, crack closure, and fracture mechanism of various steels [3–10]. In the study conducted on compact tension (CT) specimen made from ASTM A572 Grade 50 material, AE waves close to peak loads were considered for analysis by Yu et al. [3]. They reported a linear relation between AE count rates dC/dN (counts/cycles) and stress intensity factor range (ΔK) for the entire Paris region. Roberts et al. [4] investigated FCG in CT specimens made of grade S275 JR steel for different load ratios and calculated constants relating acoustic emission count rate with ΔK considering AE activity for different percentage of the load range. They found that AE behavior is independent of loading parameters. Kumar et al. [5] reported that AE behavior for HSLA steel is dependent on load ratio, and higher number of AE events was recorded for a higher load ratio. Studies conducted by Kumar et al. [5] and Han et al. [6] observed that AE activity recorded at higher values of stress intensity factor is helpful to describe the changeover from stage 2 to stage 3 of fatigue crack growth. Baldev Raj et al. [7] studied AE activity for austenitic stainless steel and observed that the ring down count (RDC) reduced by 2 to 3 times in 2 h aged samples and 20 to 25 times for 8 h aged samples in comparison to solution annealed specimens. Han et al. [6] reported that inclusions and precipitates promoted the formation of micro-voids, thus leading to early AE activity change and intense AE activity during fatigue. AE activity was found to be strongly influenced by microstructure of the specimen. Moorthy et al. [8] stated that for ductile materials, acoustic emission activity generated during the whole fatigue cycle should be considered to get insights about all sources of AE. Analyzing only peak load activity may not be helpful to study overall acoustic emission sources contributing to the damage mechanism. For austenitic stainless steel [7, 8] and HSLA steel [5], it was observed that the variation in the slope of cumulative count and absolute energy vs. stress intensity factor range (ΔK) in stage 2 shows a two-slope behavior compared to the log-linear growth of (da/dN) vs. ΔK in stage 2 of FCGR curve; this points to a change in crack growth mechanism and presence of two sub-stages, stage 2a (plane strain dominant) and stage 2b (plane stress dominant), within the linear Paris region. Babu et al. [10] reported that for decreasing ΔK test, AE count rate (dC/dN) did not decrease continuously with ΔK ; instead, intermittent increase at various values of ΔK was observed for SS316LN and P91 steels.

Previous studies performed to study FCG by AE have used standard specimens and are performed on different grades of steel [3–10]. If a large volume of material is not available for testing, fabrication of standard size specimens may not be possible. In such a case, miniature specimens may be used to study FCG behavior [11, 12]. Miniature specimens require a small volume of material for fabrication due to their reduced size. This implies that the microstructure could play a significant role, as

the specimen size becomes comparable to the grain size of the material. Prakash et al. [11] studied the size scale on FCG characteristics of aluminum alloy and concluded that FCG of the alloy depends on the size scale of test specimen used, and specimen configuration affects the FCG behavior of the alloy. Shin et al. [12] compared C(T) and miniature SEN(T) specimen FCGR curve and observed that a conservative estimate of fatigue life from miniature specimen data could be drawn if (da/dN) was plotted against effective stress intensity factor range ΔK_{eff} , that is free from crack closure.

In general, the use of the AE technique to monitor FCG on miniature SEN(T) specimens is less explored in the literature. Compared to AE monitoring of standard specimens, AE setup for miniature specimens requires modification, as AE sensor cannot be placed directly on the specimen due to the size of the specimen; it has to be mounted on the fixture or away from the specimen and suitable wave guide will have to be employed. Under such scenario, low peak amplitude AE hits during FCG in miniature specimen may not get recorded due to the threshold value set during AE monitoring. Further, AE waves may get deflected or lost at the specimen–fixture interface. The objective of the present study is to monitor AE signals to study the FCG behavior of the Inconel alloy miniature SEN(T) specimen and to relate AE cumulative absolute energy with ΔK values. It is noted that relatively less literature is available on the AE characteristics of Inconel alloy from FCG response.

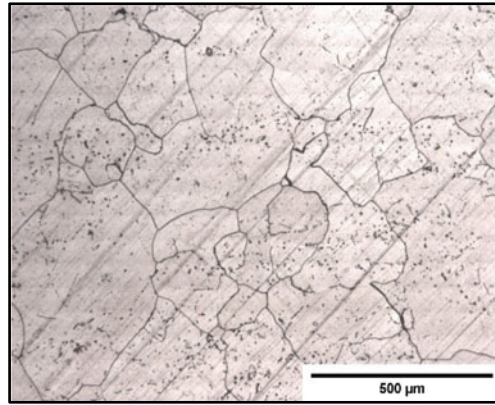
2 Materials and Methods

An Inconel alloy used in power plant applications is the material chosen for this investigation. The chemical composition was estimated by electron dispersive spectroscopy (EDS) point analysis and expressed as wt % as shown in Table 1. The alloy conforms to a commercial grade Inconel 617 alloy [13]. The microstructure of the alloy was obtained after immersion etching of the specimen for 75 s in Marble solution; Fig. 1 presents the optical and scanning electron microscope image obtained using Inspect F50 FEI model. The average grain size of alloy calculated by using the mean lineal intercept method is estimated as 134 μm . The microstructure images show randomly distributed precipitates within the matrix and along the grain boundaries. EDS study showed these precipitates to be Cr-rich $M_{23}C_6$ carbides and Ti-rich Ti(C, N) carbides.

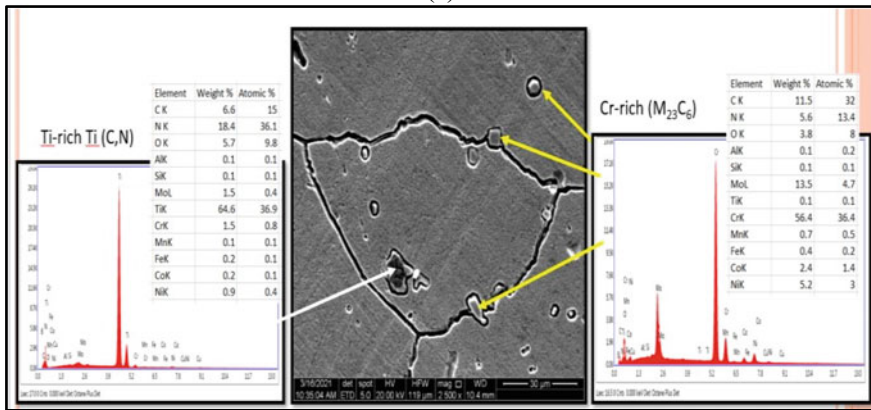
Single edge notch miniature specimens of 30 mm length \times 10 mm wide and 1 mm thickness were used for testing. An edge notch of length 1 mm was fabricated on the edge of a specimen by wire electric discharge machining (EDM) method. Miniature

Table 1 Weight % of elements in IN617 alloy

Element	Cr	Co	Mo	Al	Fe	Mn	Ti	Cu	Ni
Weight %	22.1	11.5	7.6	1.5	0.7	0.2	0.3	0.3	Bal.



(a)



(b)

Fig. 1 **a** Microstructure image from the optical microscope, **b** Energy Dispersive Spectroscopy (EDS) spot analysis results. Particles (indicated by yellow arrow) have a high percentage of Chromium followed by Molybdenum, Cr-rich $M_{23}C_6$ carbides. Particles (indicated by white arrow) are black colored and having a high percentage of Titanium followed by Nitrogen, Ti-rich Ti (C, N) carbides

specimens were gripped using an in-house developed friction pad fixture for the fatigue crack growth test. The grip length was maintained as 10 mm for the top and bottom grip and the un-gripped length was 10 mm, as shown in Fig. 2. Increment in crack length due to fatigue cycling was monitored using a traveling microscope having a least count of 0.01 mm. FCG tests were performed at two load ratios (R) (minimum to maximum load), 0.1 and 0.7 for three specimens each. All specimens were tested till failure. ΔK values for miniature SEN(T) Specimen are expressed using Eq. (1) [12].

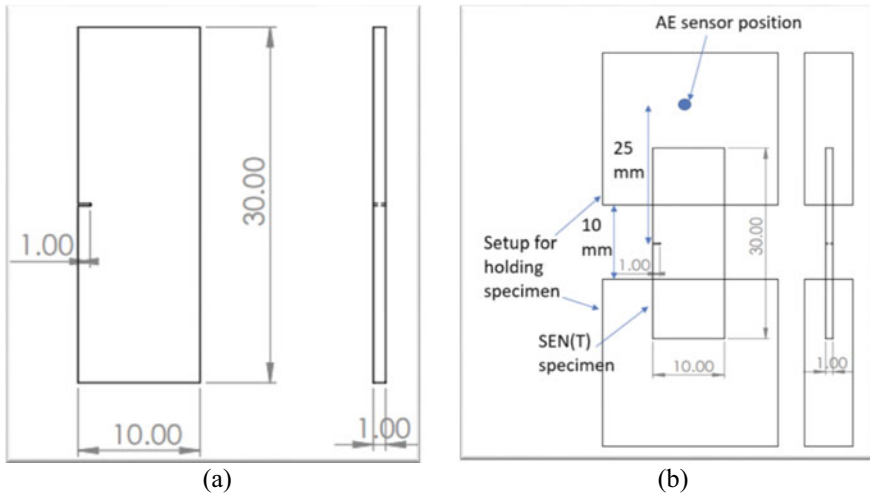


Fig. 2 a Dimension of specimen b Setup to hold the specimen and AE sensor position (all dimension are in mm)

$$\Delta K = \Delta\sigma\sqrt{\pi a}\left(\frac{1}{\left(1 - \frac{a}{W}\right)^{\frac{3}{2}}}\right)\left(1.122 - 1.302\frac{a}{W} + 0.988\left(\frac{a}{W}\right)^2 - 0.308\left(\frac{a}{W}\right)^3\right) \quad (1)$$

Where ‘W’ is width of SEN(T) specimen, ‘a’ is crack length, and ‘Δσ’ is applied stress range.

AE signals were recorded using a wideband single-ended (Wsa) acoustic emission sensor supplied by Physical Acoustics Corporation (PAC) having a dimension 19 mm outer diameter and 21.4 mm height. The AE sensor has frequency limit of 100 to 1000 kHz. Preamplifier with a gain of 40 dB was used. AE sensor was placed on the fixture used to hold miniature specimen using vacuum grease as couplant at the sensor location shown in Fig. 2. Verification tests were performed before starting the test each time to identify external noise levels. Based on these noise levels, the threshold value of 35 ± 5 dB and frequency filter of 100–600 kHz was applied while recording AE activity. Recorded AE waves were processed in AEwin® software to extract AE parameters.

3 AE Data Filtering

AE data filtering is essential in the study of acoustic emission waveform, as noise is embedded with acoustic signals from fatigue damage during the test. It is noted that AE sensor picks up signals from the environment, external noise, machine setup noise, reflections from edges, and waves from the crack tip area, which may fall in the selected frequency range and above the threshold. Various data filtering techniques

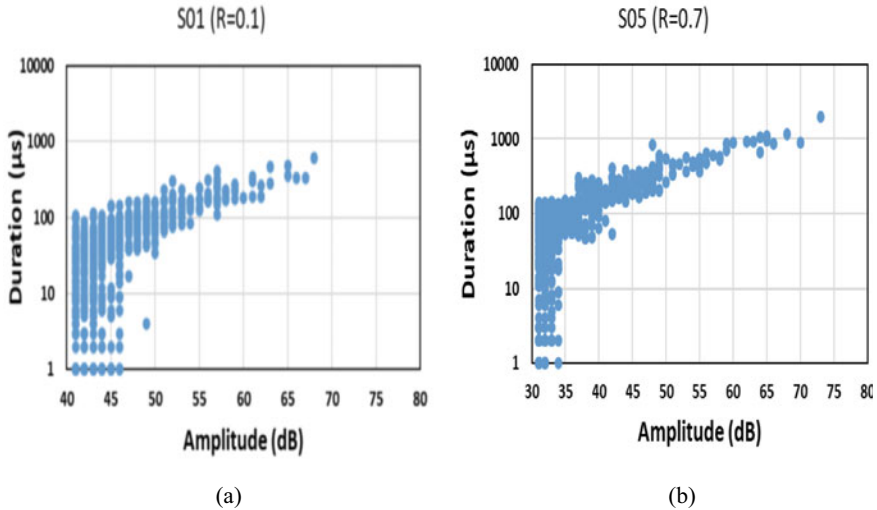


Fig. 3 Amplitude duration plot for specimen **a** S01 and **b** S05

are used to filter noise. Earlier studies [3, 4] suggested that AE waves occurring close to peak load to be related to crack growth. To ensure AE waves are coming from the crack area, a linear source location filter was used [3, 5]. In this study, frequency filter and amplitude threshold were set such that there is minimum interference of noise waves with genuine waves. Peak amplitude and duration parameters were used to differentiate noise and reflection signals. Amplitude-duration filter is used in studies [3, 9] for filtering recorded data. Peak amplitude is less dependent on threshold and is related to the AE source. Duration is defined as the time for which wave is above the threshold. Thus, hits within the banded region of the peak amplitude-duration plot were considered; high duration low amplitude hits and low duration high amplitude hits were removed. Figure 3 shows amplitude duration plots for S01 specimen ($R = 0.1$) and S05 specimen ($R = 0.7$). It was observed that the high number of hits of the same AE parameter was recorded in a short interval of time. These hits were considered as noise and were removed.

4 Results and Discussion

4.1 Variation of Crack Growth Rate with ΔK

Figure 4a shows the crack length versus the number of cycles plot for typical fatigue crack growth experiments performed on SEN(T) specimens at $R = 0.1$ and 0.7 . Fatigue crack growth rate (da/dN) was calculated using a 5-point incremental polynomial method, similar to the 7-point incremental polynomial method suggested by

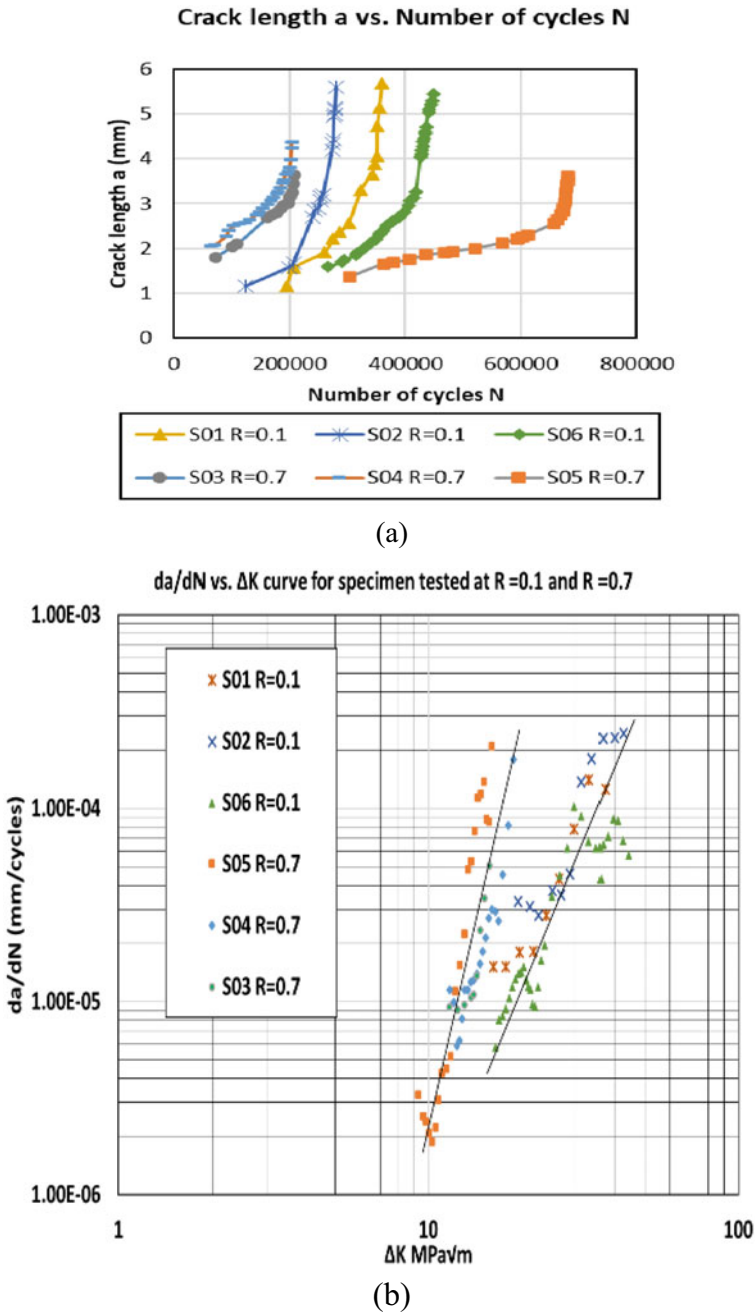


Fig. 4 **a** Crack length versus fatigue cycles plot **b** FCGR curve for SENT specimens tested at R = 0.1 and 0.7

ASTME647-15 [14], and the (da/dN) vs. ΔK plot is shown in Fig. 4b. 5-point method was resorted to as the total data points were much less for miniature specimen FCGR testing; use of 7-point method would imply leaving 3 points each at the start and end of the experiment. Higher scatter is observed at low crack growth rate values. The Paris exponent (which is the slope of the FCGR curve in log-log plot) for specimens tested at $R = 0.7$ was observed to be higher than that tested at $R = 0.1$.

4.2 AE During Fatigue Crack Growth Propagation

Figure 5 shows a plot of a normalized cumulative count, absolute energy, and cumulative hits versus number of cycles for specimens S01 and S05 tested at load ratios 0.1 and 0.7 respectively. AE cumulative count and absolute energy increased exponentially with the number of cycles, much similar to the way crack length increased. Cumulative AE hit represents total AE Hits recorded during the monitoring period. The curve of cumulative AE hits shows a slow upward trend for the initial cycles, and the slope of the curve rapidly increases at higher cycles. High AE activity is observed as the specimen approached failure. The increase in the cumulative AE hits, count and absolute energy values is observed at the critical crack level, which is helpful to determine the critical level of crack growth and provide a warning for damage evaluation.

4.3 Variation of Cumulative Absolute Energy and Count with Stress Intensity Factor Range

AE parameter cumulative absolute energy was plotted with ΔK to study the variation of acoustic emission activity during FCG study in the miniature specimen of Inconel alloy. Figure 6 shows the plot of (da/dN) (mm/cycles), Cumulative count, and Cumulative absolute energy versus ΔK for specimens tested at a load ratio of 0.1 and 0.7. Normalized values of cumulative count and absolute energy values are considered; normalization is done by dividing cumulative values by maximum cumulative value at the end of the test. Change in the slope of cumulative count and absolute energy with ΔK was observed for the fatigue crack growth ΔK range. Two slope behavior was observed, which could indicate a change in FCG mechanism. This change is not observed from (da/dN) vs. ΔK plot for the corresponding ΔK range. An initial increase in slope is observed till $27.69 \text{ MPa}\sqrt{\text{m}}$; after that, till $42.6 \text{ MPa}\sqrt{\text{m}}$, a reduced increase in cumulative absolute energy is observed. After $42.6 \text{ MPa}\sqrt{\text{m}}$, the slope increased for specimen tested at load ratio = 0.1. Change in AE activity was observed at ΔK values of $13.33 \text{ MPa}\sqrt{\text{m}}$, and $15.38 \text{ MPa}\sqrt{\text{m}}$ for specimen tested at load ratio 0.7. Similar behavior was observed for the cumulative count parameter.

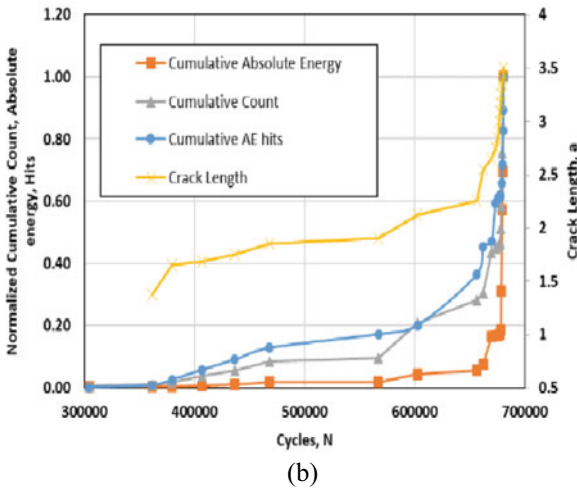
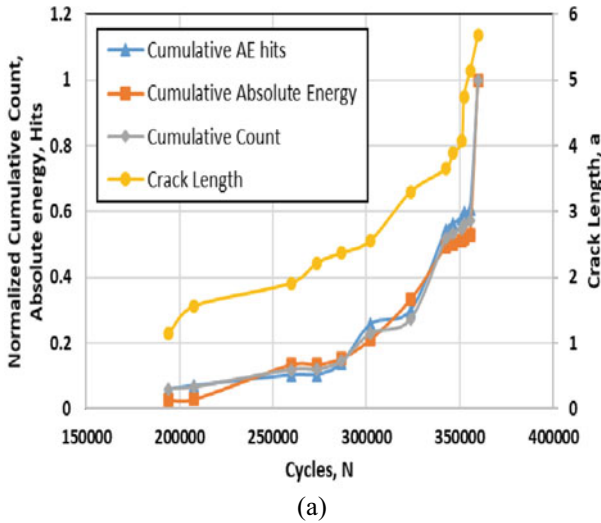
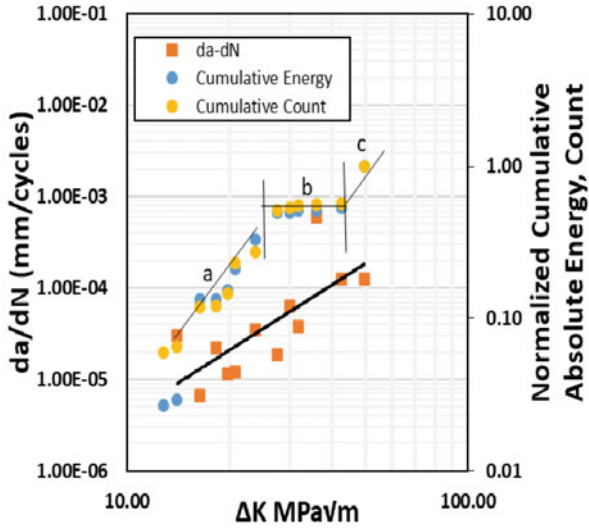


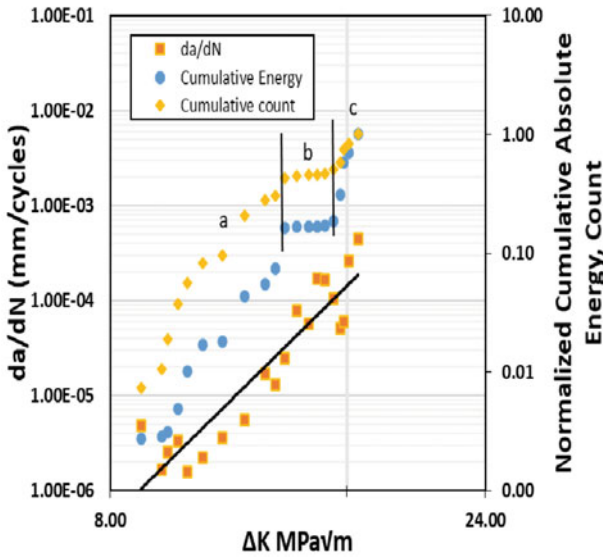
Fig. 5 Normalized cumulative absolute energy, counts, AE hits, and crack length versus load cycles for **a** specimen S01 and **b** specimen S05

Thus, AE parameters cumulative absolute energy and count are more sensitive to the crack growth mechanism and could indicate transition within stage 2 of FCG.

During FCG test on ductile material, sources of AE activity are plastic deformation within the monotonic plastic zone (MPZ), cyclic plastic zone (CPZ), crack closure, and crack extension. If the crack extension occurs at the peak load, a linear increase in the slope of the AE parameter within the FCG ΔK range would have been observed, irrespective of load ratio; however, as crack extension takes place during entire cyclic loading, the variability of AE signature was observed for tests



(a)



(b)

Fig. 6 da/dN , normalized cumulative absolute energy, count vs. ΔK plot **a** specimen S01 **b** specimen S05

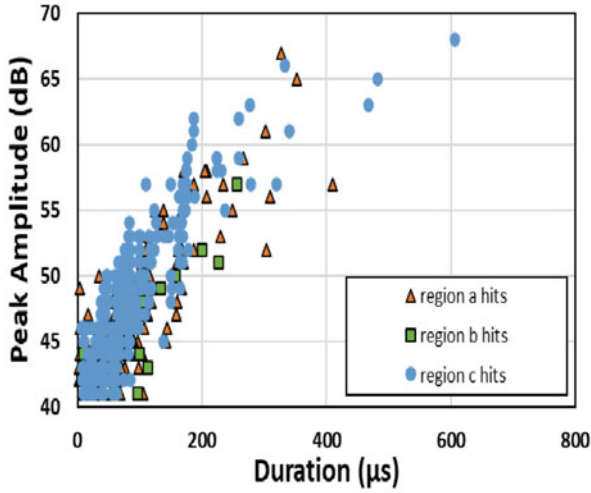
conducted at two load ratios. It may be noted that the effect of crack closure is less at higher R ratio; hence, the change in AE parameter slope is observed for specimen tested at $R = 0.7$. It has been stated in the literature that during stage 2 of FCG for ductile materials, dislocations during cyclic plasticity within the CPZ are the main source of AE activity compared to ductile crack extension due to monotonic loading, MPZ, and crack closure [7, 8]. Plastic deformation takes place in every fatigue cycle in CPZ. As number of cycles increase, damage accumulation in CPZ is more than MPZ because cyclic plastic deformation occurs within the MPZ [15]. The initial increase in AE activity may be attributed to an increase in MPZ and an increase in cyclic plasticity within MPZ. During stage 2b, the crack front remains more or less plane perpendicular to the direction of loading. At larger crack size, the shear lips are formed, which may be the reason for a decrease in AE activity. Similar AE behavior was observed in works of Ref. [5, 7–9] and was attributed to a change in a stress state and the size of CPZ. A rise in the cumulative count and absolute energy values at higher ΔK was observed as the specimen failed.

4.4 Variation of AE Parameters for Different Regime of Fatigue Crack Growth

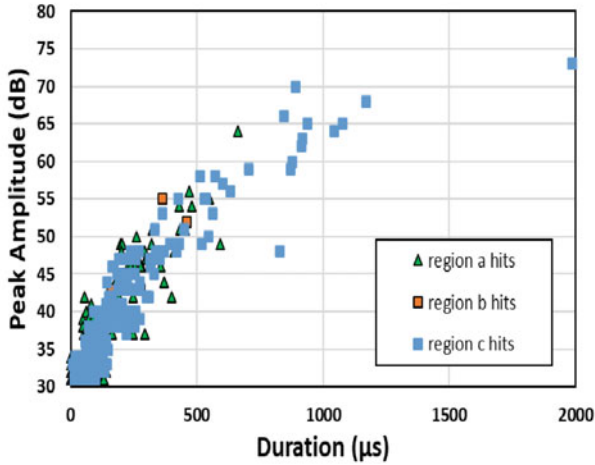
The peak amplitude vs. duration plot is shown in Fig. 7 for three different regions observed from Fig. 6. An overlap was observed for different regions. Due to the small size of the specimen, the number of hits recorded is less, and these are primarily low amplitude hits. More hits are recorded in region c and have amplitude ranging from threshold to peak amplitude. More high amplitude and high duration hits are recorded in region c. Fewer hits are recorded in region b compared to the other two regions for both the specimens. Also, high duration hits are recorded in the S05 specimen tested at $R = 0.7$ compared to the S01 specimen tested at $R = 0.1$. It is observed that high rise time AE hits are recorded for the S05 specimen compared to the S01 specimen.

4.5 Relation Between AE and Stress Intensity Factor Range

Earlier investigations [3, 4] have considered AE activity within 10–30% of peak load and used it to correlate with ΔK . For ductile material under fatigue loading, the damage is due to both maximum stress intensity factor K_{max} and ΔK [8]. Hence acoustic emission activity during the entire fatigue cycle should be considered. Moorthy et al. [8] found that cumulative ring down count is more appropriate to relate with ΔK than AE count rate (dC/dN). AE signals accumulate with crack growth; hence in this study, AE cumulative absolute energy and cumulative count calculated from complete cycle AE activity are considered to relate with ΔK .



(a)



(b)

Fig. 7 Peak amplitude vs. duration plot for a S01 (R = 0.1) and b S05 (R = 0.7) specimens

The AE parameter (cumulative absolute energy and count) is correlated with ΔK as given by Eq. (2).

$$\text{Cumulative Absolute energy/Count} = Be(\Delta K)^p \tag{2}$$

Table 2 presents the values of the AE exponent and Paris exponent. AE exponent value is obtained from Eq. (2) by correlating cumulative absolute energy and count with ΔK values for the initial increase of slope, till $\Delta K = 27.69 \text{ MPa}\sqrt{\text{m}}$ for S01 R

Table 2 AE exponent and Paris exponents values for IN 617 alloy

Specimen	Load ratio (R)	Paris exponent (m)	AE exponent Cum. Abs. Energy (pe)	AE exponent Cum. Count (pc)
S01	0.1	2.37	3.9	2.75
S05	0.7	8.14	9.7	9.35

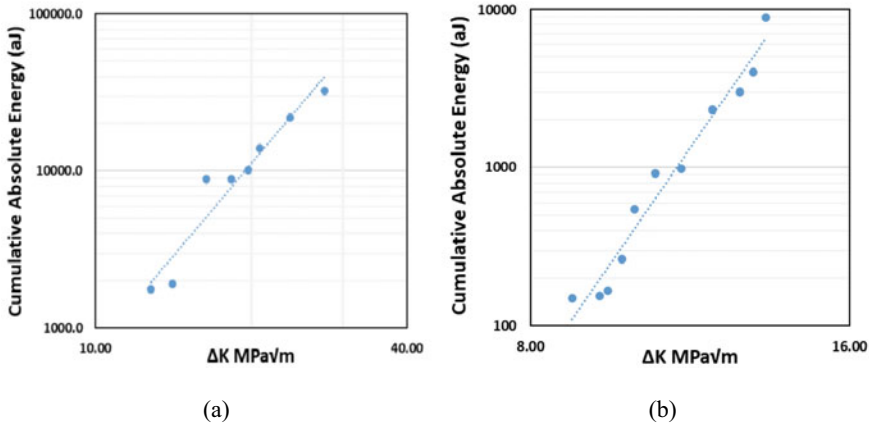


Fig. 8 Cumulative absolute energy and ΔK plot of **a** S01 and **b** S05 specimen

= 0.1 specimen and $\Delta K = 13.33 \text{ MPa}\sqrt{\text{m}}$ for S05 R = 0.7 specimen as shown in Fig. 6. AE cumulative absolute energy and ΔK relation fit is shown in Fig. 8.

It is observed that the value of the AE constant is higher for specimen tested at a higher load ratio compared to specimen tested at a lower load ratio. It may imply that K_{max} as well as crack closure has an effect on AE activity during FCG. Higher AE constants for higher load ratio was observed in the study [16] conducted on modified SE[T] specimens. AE exponent calculated from cumulative absolute energy and cumulative count are higher than Paris constants.

5 Summary and Conclusion

FCG behavior of Inconel alloy miniature specimens has been studied using acoustic emission technique. An amplitude duration filter is useful to filter the AE data for miniature specimens. A sharp increase in cumulative absolute energy, cumulative count, and cumulative AE hit parameters increases with an increase in crack length; thus, these parameters could be helpful as a warning for evaluation. It is observed that the slope of cumulative absolute energy and cumulative count changes for the FCG stress intensity factor range. Cumulative absolute energy increases initially;

thereafter, it is less in stable crack growth region, and near final fracture, an increase is observed. An intermediate change in the AE activity at lower ΔK values is related to the major AE activity source. AE activity due to cyclic plasticity within the monotonic plastic zone could be the major AE source during FCG of Inconel alloy. The exponent values from AE signature are higher than Paris law exponents.

References

1. Suresh S (1991) *Fatigue of materials*. Cambridge University Press, Cambridge
2. Ritchie RO (1999) Mechanisms of fatigue-crack propagation in ductile and brittle solids. *Int J Fract* 100(1):55–83. <https://doi.org/10.1023/A:1018655917051>
3. Yu J, Ziehl P, Zárate B, Caicedo J (2011) Prediction of fatigue crack growth in steel bridge components using acoustic emission. *J Constr Steel Res* 67(8):1254–1260. <https://doi.org/10.1016/j.jcsr.2011.03.005>
4. Roberts T, Talebzadeh M (2003) Acoustic emission monitoring of fatigue crack propagation. *J Constr Steel Res* 59(6):695–712. [https://doi.org/10.1016/S0143-974X\(02\)00064-0](https://doi.org/10.1016/S0143-974X(02)00064-0)
5. Kumar J, Ahmad S, Mukhopadhyay CK, Jayakumar T, Kumar V (2016) Acoustic emission studies for characterization of fatigue crack growth behavior in HSLA steel. *Nondestruct Test Eval* 31(1):77–96. <https://doi.org/10.1080/10589759.2015.1070850>
6. Han Z, Luo H, Zhang Y, Cao J (2013) Effects of micro-structure on fatigue crack propagation and acoustic emission behaviors in a micro-alloyed steel. *Mater Sci Eng A* 559:534–542. <https://doi.org/10.1016/j.msea.2012.08.138>
7. Raj B, Mukhopadhyay CK, Jayakumar T (March 2003) Acoustic emission technique for characterizing deformation and fatigue crack growth in austenitic stainless steels. In: AIP conference proceedings, vol 657, no 1. American Institute of Physics, pp 1439–1446. <https://dx.doi.org/10.1063/1.1570300>
8. Moorthy V, Jayakumar T, Baldev R (1994) Acoustic emission behaviour during stage II fatigue crack growth in an AISI type 316 austenitic stainless steel. *Bull Mater Sci* 17(6):699–715. <https://doi.org/10.1007/BF02757552>
9. Chai M, Zhang J, Zhang Z, Duan Q, Cheng G (2017) Acoustic emission studies for characterization of fatigue crack growth in 316LN stainless steel and welds. *Appl Acoust* 126:101–113. <https://doi.org/10.1016/j.apacoust.2017.05.014>
10. Babu MN, Mukhopadhyay CK, Sasikala G (2019) Fatigue crack growth study in p91 and 316LN steels using acoustic emission. *Trans Indian Inst Met* 72(12):3067–3080. <https://doi.org/10.1007/s12666-019-01773-2>
11. Prakash RV, Sathesh Kumar S (November 2012) Investigation of size scale effects on the fatigue crack growth characteristics of an aluminum alloy. In: ASME international mechanical engineering congress and exposition, vol 45196. American Society of Mechanical Engineers, pp 641–648. <https://doi.org/10.1115/IMECE2012-87717>
12. Shin CS, Lin SW (2012) Evaluating fatigue crack propagation properties using miniature specimens. *Int J Fatigue* 43:105–110. <https://doi.org/10.1016/j.ijfatigue.2012.02.018>
13. Special Metals Corporation (March 2005) Limiting chemical composition, %, of INCONEL alloy 617 Publication Number SMC-029 Copyright © Special Metals Corporation
14. American Society for Testing and Materials (ASTM) (2015) ASTM E647: standard test method for measurement of fatigue crack growth rates. In: Annual book of ASTM standards, vol 03.01. American Society for Testing and Materials (ASTM), West Conshohocken
15. Paul SK, Tarafder S (2013) Cyclic plastic deformation response at fatigue crack tips. *Int J Press Vessels Pip* 101:81–90. <https://doi.org/10.1016/j.ijpvp.2012.10.007>
16. Nemati N, Metrovich B, Nanni A (2016) Acoustic emission assessment of fatigue crack growth from a transverse weld toe. *J Mater Civ Eng* 28(2):04015103. [https://doi.org/10.1061/\(ASCE\)MT.1943-5533.0001340](https://doi.org/10.1061/(ASCE)MT.1943-5533.0001340)

Numerical Investigations on the Pelton Turbine Jet



Firoz Khan and Arun Kumar

Abstract The quality of the water jet emerging out from the Pelton turbine injector is an important factor for the performance of the Pelton turbine. Especially at part load operation the efficiency of the Pelton turbine decreases due to the poor quality of the jet. The jet surface deformation, deviation, and dispersion are the qualitative parameters of the jet. A careful description of the boundary layers and turbulence model is required to capture the flow patterns properly. A study aiming for further insight into the flow in the jet has been carried out using CFD analysis. A reference geometric model of the Pelton turbine injector (90° nozzles and 60° needle angle) based on the external servomotor control having supporting ribs is developed. For the CFD simulations, Tetra-meshing is done in ICEM CFD with proper boundary layer resolution. The free surface and multiphase flow of the jet are modeled using the Volume of Fluid (VOF) model. Commercial CFD software Ansys-CFX has been used with turbulence closure. Reynolds averaged Navier stokes equation (RANS) based turbulence model $k-\epsilon$ has been selected. Discharge characteristics and velocity distributions for the different openings of the nozzle at different distances along the jet have been plotted. The energy loss in the injector is found about 1% and the hydraulic force on the needle differs by 6.85% on comparison of analytical and CFD results.

Keywords Pelton turbine injector · Multi-phase · Jet quality · and CFD

1 Introduction

The Pelton turbine invented in the 1870s is a mature hydraulic turbine for hydropower generation and is in use globally. It is an impulse-type tangential flow turbine that

F. Khan (✉) · A. Kumar

Hydraulic Turbine Laboratory, Department of Hydro and Renewable Energy, Indian Institute of Technology Roorkee, Roorkee, India

e-mail: fkhan@ah.iitr.ac.in

A. Kumar

e-mail: arun.kumar@hre.iitr.ac.in

is generally installed at high head and low discharge. It is a low specific speed (it is the speed of the turbine which produce the unit power under operating with unit head) turbine in the range of 35 to 60 for a single jet to multi-jet. The experiences and findings achieved during a long time improved the hydraulic and mechanical performance of the turbine. The injector consisting of a nozzle and needle, is the most important component in this turbine where nozzle converts the pressure energy into kinetic energy and flows are controlled by the movement of the needle through the servomotor [1].

Flows in the Pelton turbine are having different regimes, single-phase water flows in the injector, the free jet flow after emerging out from the nozzle, free-surface flows over the buckets, and then two-phase dispersed flows in the casing [2]. The quality of the water jet is an important factor for the performance improvement of the Pelton turbine. To evaluate the jet quality and injector characteristics CFD analysis and experimental test were performed in [3–5] and the impact of secondary flows due to upstream piping geometry was discussed.

The paper, [6] verified the physical consistency of the outcomes of the VOF method for the two-phase free surface flow of the jet. The six-jet Pelton turbine modeled and investigated for the velocity distribution and found non-uniform as compared to the ideal jet velocity profile [7]. In [8], worked on the design optimization of the nozzle and the investigation found that the injector losses can be reduced by up to 0.5% when using the improved $110^\circ/70^\circ$ nozzle/spear angle design instead of the $90^\circ/50^\circ$ design. Nesiadis et al., evaluated the Pelton turbine injector geometry using a numerical algorithm that solves only for the liquid phase [9]. The study helps finding optimum nozzle geometry modifications. Staubli et al., has investigated the governing effects on the quality of jet-like jet dispersion, jet deviation, and jet deformation [4].

The study was performed for the improvement and rehabilitation projects in large hydropower plants. It is remarked that Pelton jets depend on complex flow behavior related to both upstream piping geometry and operating head [5]. Zhang & Parkinson; observed that the impacting process of the free surface jet on the running Pelton bucket depends on the jet quality which is given by the jet pattern and the jet stability [10]. In the present study, a highly accelerated multi-phase flow of the Pelton jet has been analyzed and the injector characteristics are performed using CFD analysis.

2 Injector Model and Computational Domain

The external servomotor control injector model shown in Fig. 1 has been designed according to the jet diameter of 30 mm. Nozzle and needle angles are 90° and 60° respectively. The Reynolds number 1.6×10^6 and specific hydraulic energy of the injector is 725.94 J/kg as per available head and discharge at the test rig. These data were used for the numerical analysis.

Based on the design parameters of nozzle and needle (90° & 60°), the computational model has been generated in the design modeler of Ansys. The diameter of the nozzle is 36.3 mm. and the needle has three ribs to support the needle and to

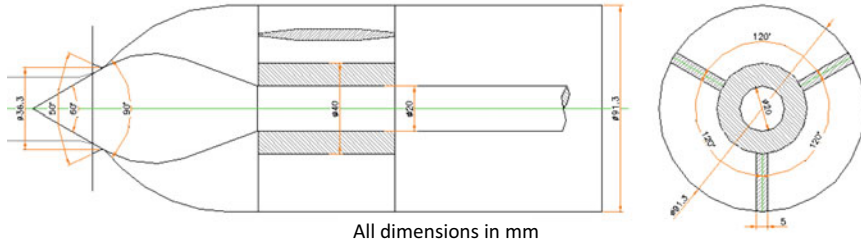


Fig. 1 Pelton turbine injector

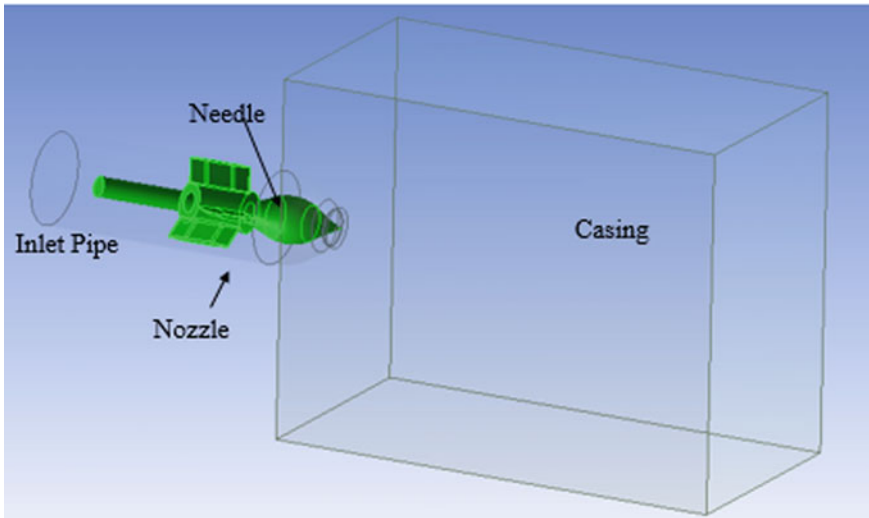


Fig. 2 3D model of Pelton turbine injector based on external servomotor

make the flow axis symmetric. The pipe diameter of 91.3 mm is the inlet pipe of the nozzle. The geometry of the injector is based on an external servomotor. The nozzle geometry with the simulated flow domain is shown in Fig. 2. The dimension of the flow domain of casing length, width, and height is 12, 6, and 6 times of jet diameter respectively.

3 Numerical Model

The 3D, two-phase numerical simulation is realized using the Reynolds averaged Navier stokes (RANS) equation. Two fluids, water and air, were taken at 25 °C temperature for the cell zone condition of flow domain. The flow model used for the

CFD simulation is based on the homogenous multiphase model given by the Ishii [11]. The volume of fluid method adopts to solve the free surface flow inside the casing. It is assumed that there no mass transfer takes place between the phases and both phases share the common flow field. The Volume of Fluid method (VOF) is a universal technique in monitoring the two-phase flow interfaces and free surface flow. It is based on volume fraction and its values is in between 0 and 1. The momentum and continuity equations for the homogenous multi-phase flow are as given in Eqs. (1), (2) respectively and the density of mixture is defined in Eq. (3):

$$\rho \frac{\partial u}{\partial t} + \rho \nabla \cdot uu = -\nabla p + \rho g + \nabla \mu (\nabla u + \nabla^T u) + f \quad (1)$$

$$\frac{\partial \rho}{\partial t} + u \cdot \nabla \rho = 0 \quad (2)$$

$$\rho = r_\alpha \rho_l + r_\beta \cdot \rho_g \quad (3)$$

With r_α and r_β are the volume fractions for water and air phase, ρ is the mixture density, ρ_g is the air density, f is the surface tension force, and u is the velocity of flow.

The surface tension model given by Brackbill et al. [12] is used in the CFX solver, according to this the surface tension force in two immiscible fluids is as per Eq. (4).

$$f = -\sigma_{\alpha\beta} \kappa_{\alpha\beta} n_{\alpha\beta} \quad (4)$$

$$\kappa_{\alpha\beta} = \nabla \cdot n_{\alpha\beta} \quad (5)$$

where $\sigma_{\alpha\beta}$ is the surface tension coefficient between water and air, $n_{\alpha\beta}$ direction normal vector water to air, and $\kappa_{\alpha\beta}$ is the constant for curvature.

The used mesh is shown in Fig. 3. The tetrahedral mesh is built in the ICEM CFD. The bottom-up technique is used for the meshing. In the bottom-up technique, surface meshing is done followed by volume meshing. For the volume mesh, the Delaunay method is used. In order to confirm that the results are independent of the number mesh elements, a grid independency test was done for the three meshes at the particular needle travel. The average jet velocity at the nozzle outlet is plotted with number of element in Fig. 4. It is observed that, there is a 1.1 and 0.74% difference in the average velocity at nozzle outlet for consecutive meshes therefore the second mesh was chosen for this study, the qualitative parameter of the mesh can be seen in Table 1. Another Meshes for the different openings of the nozzle were created accordingly.

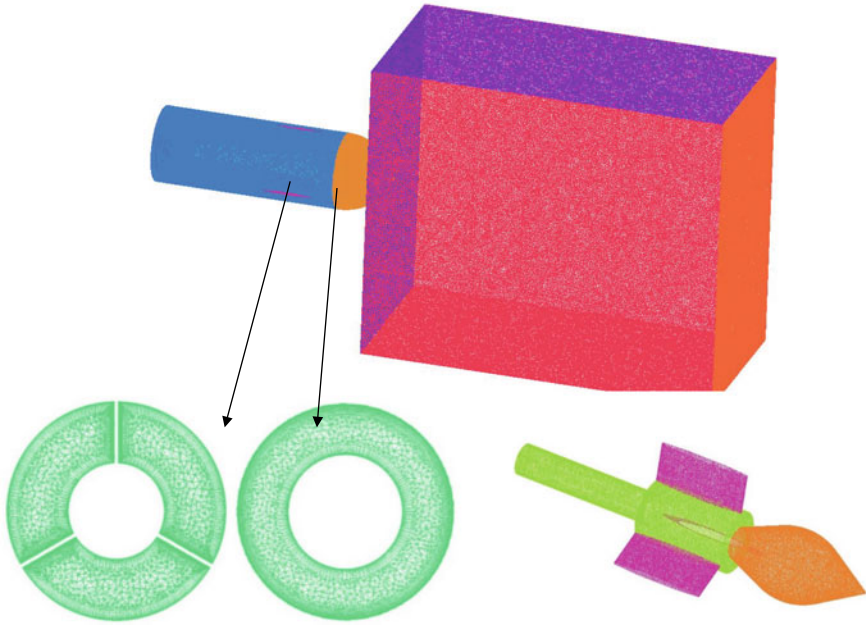


Fig. 3 Meshing of injector model and casing

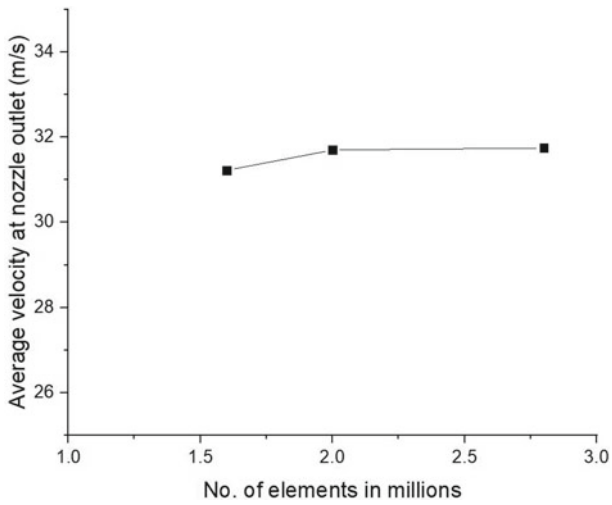


Fig. 4 Grid independency test

Table 1 Mesh quality

Number of nodes	349,376		
Number of element	2,001,845		
Parameter	Min.	Max.	Mean.
Equiangle skewness	0.282104	0.999555	0.718523
Orthogonal quality	0.431369	1	0.8638488
Aspect ratio	1.001	3.322	15.9232

Table 2 Input to CFX solver

Parameter	Input
Inlet	Total pressure inlet (74 m head) 725,672 Pa, water volume fraction = 1
Outlet	0 Pa, opening
Turbulence model	K-ε
Multiphase	The volume of fluid, homogenous, two phases (water and air), Free surface Flow
Wall setting for needle and nozzle	Stationary wall, non-slip
Discretization scheme	Second-order upwind scheme
Convergence criterion	10^{-5}
Casing walls	Opening at 0 Pa
Stroke to nozzle diameter (s/d)	0.1, 0.2, 0.3, 0.4, 0.5

3.1 Discretization and CFD Code Validation

The CFD simulation has carried out using the Ansys CFX code. The momentum and continuity equations are discretized using a second-order upwind scheme. The boundary condition for the input of the solver has defined in Table 2. At the inlet, the water volume fraction is 1 with total pressure of 725,672 Pa and the outlet is open to the static pressure of 0 Pa. The Reynolds no. in the domain is $\sim 1.6 \times 10^6$. Turbulence is solved by using the k-ε model. As the mass-momentum is solved by total pressure at the inlet, and zero-gauge pressure at the outlet so the mass flow rate is calculated for a particular stroke of the needle by the convergence of the solution.

For the validation of the CFX solver code, the non-dimensionalized jet velocity profile at the 50% of needle stroke has been compared with the literature data. Although the design of every Pelton turbine injector differs from each other due to the different operating conditions like head and discharge, but the trend of the jet velocity profile can be compared. In the Fig. 5 the non-dimensionalized jet velocity profile has compared with investigation done in literature for Pelton turbine injector of diameter 36 mm which is nearly same as the injector designed for this study and the results matched well.

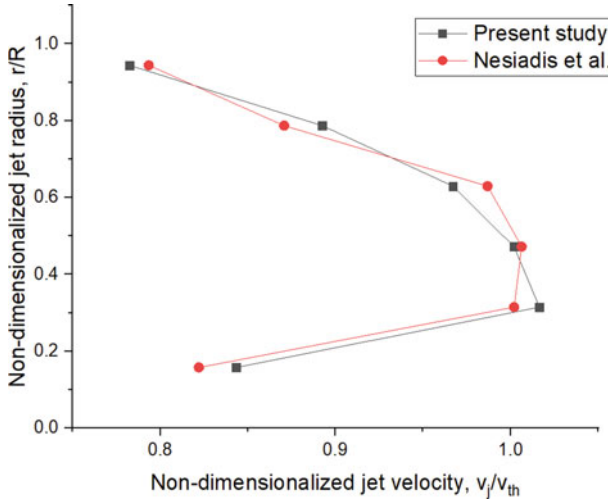


Fig. 5 Comparison of non-dimensionalized jet velocity for this study with Nesiadis et al. [9]

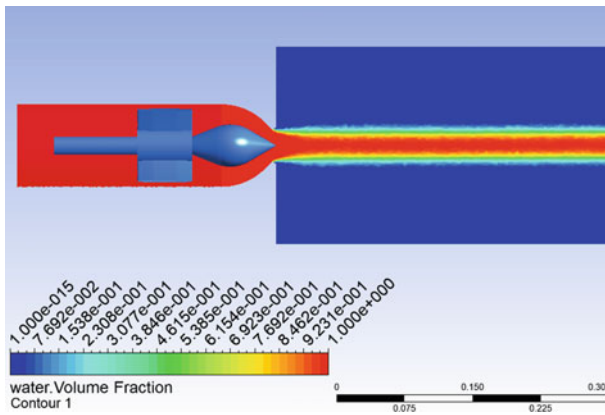


Fig. 6 Water volume fraction

4 Results and Discussion

4.1 Volume Fraction and Jet Velocity

Figure 6 shows that the contour of water volume fraction, the volume fraction is 1 where the water phase is present and shown by the red color and vice versa for air. The surface of the water jet has deformed due to the entrainment of air into the highly turbulent water jet and this give rise to the instability of the jet. In Fig. 7

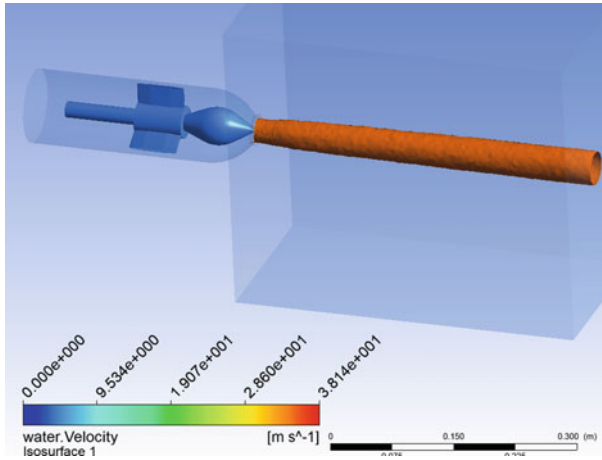


Fig. 7 Jet velocity iso-surface

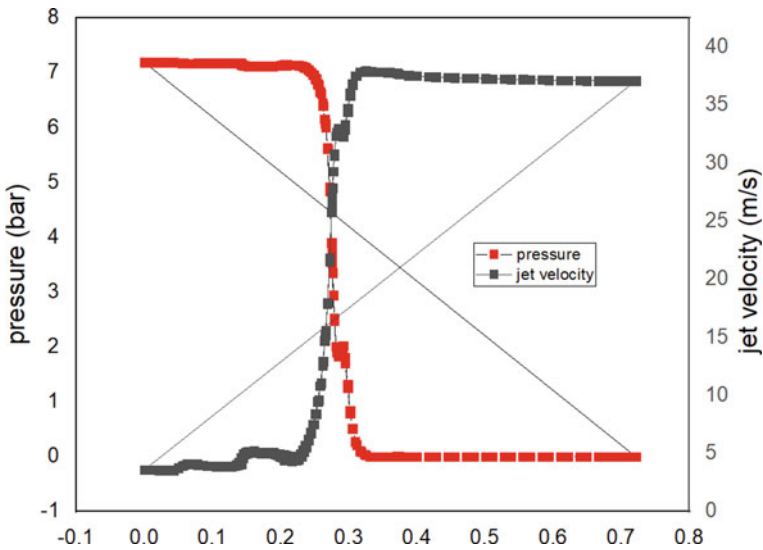


Fig. 8 Pressure and velocity distribution along with the flow streamline

the iso-surface of jet velocity has shown, the jet velocity is the same throughout the circumference at a particular radius of the jet.

Figure 8 shows the conversion of the pressure energy of water into the kinetic energy along the flow streamlines. Jet flow streamlines can be seen in Fig. 9. The streamlines follow the curvature of the nozzle and all streamlines are parallel and symmetric. The water flow inside the injector is incompressible so the density of water is constant and according to Bernoulli's equation flow energy is constant. The

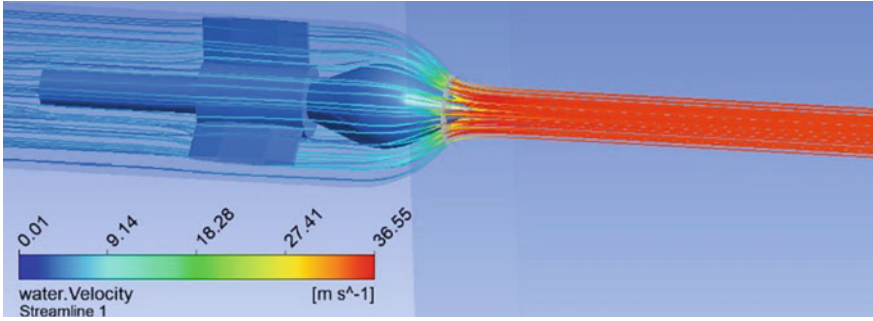


Fig. 9 Jet flow streamlines

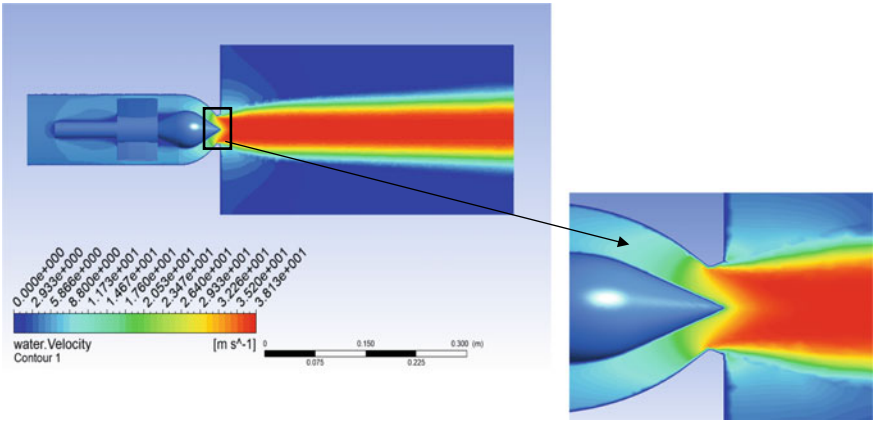


Fig. 10 Jet velocity contour

flow velocity is increasing in the convergent part of the nozzle and accelerated as per Eq. (6), where u is the flow velocity in the direction of x and A is the opening area of the nozzle.

$$\frac{du}{dx} = -\frac{u}{A} \frac{dA}{dx} \tag{6}$$

Due to the boundary layer formation on the needle, the clear separation of the jet core at the centerline can be seen in the velocity contour Fig. 10. Therefore, velocity deficit occurs towards the jet core and static pressure increases while the total pressure is constant.

Jet velocity profile for different s/d (needle stroke to nozzle diameter), along the length of the jet, has been drawn with non-dimensionalized jet radius (r/R) vs jet velocity. Figure 11a–d show the jet velocity profile in the direction of jet flow at the distance of 0.5, 1, 2, and 3 times of jet diameter respectively. The comparison

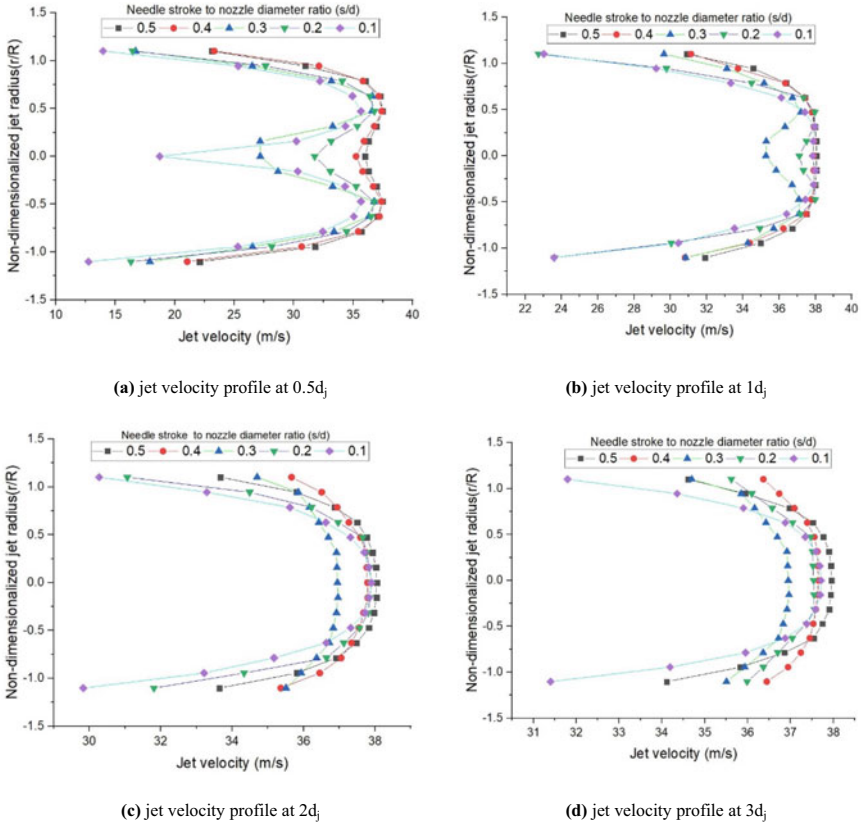


Fig. 11 Velocity profile of the jet at a different location for different openings of nozzle

shows that the jet velocity profile is more developed as going through the length of the jet. The velocity profile of the jet emerging out from the nozzle outlet is in the developing stage in Fig. 11a, b however the velocity profile is fully developed at the inlet of the injector.

4.2 Injector Characteristics

Figure 12 shows the energy loss in the injector at different s/d ratios. Energy loss is calculated based on Eq. (7). To analyze the injector loss nozzle outlet is considering as the outlet. According to Eq. (8), the discharge coefficient of the injector is calculated and plotted in Fig. 13. Where Q_{jet} is the discharge through the nozzle, d is the nozzle diameter and H is the head.

Fig. 12 Energy loss in the injector

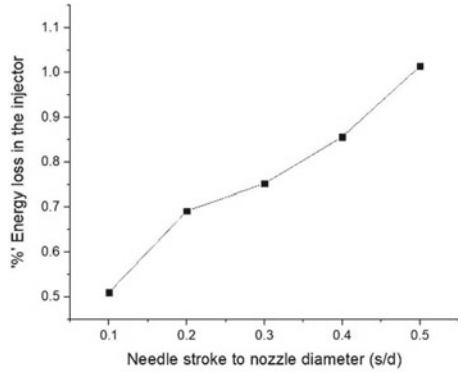
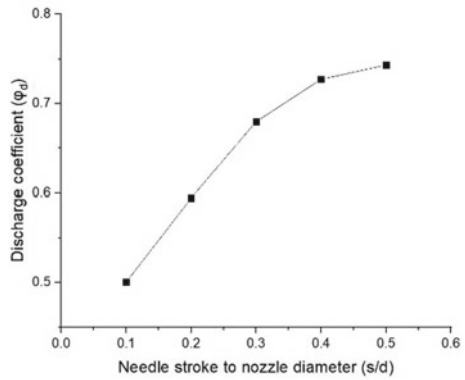


Fig. 13 Discharge coefficient of the injector



$$E = \sum_1^n (P_i + \rho u_i^2/2) u_i A_i \tag{7}$$

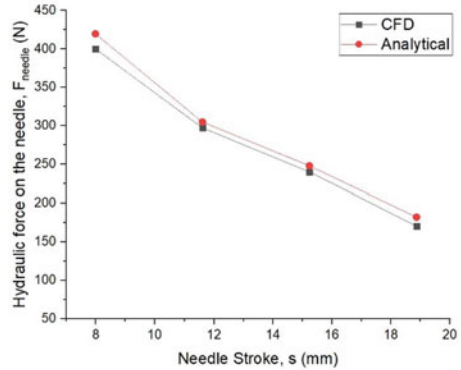
$$\phi_d = \frac{4Q_{jet}}{\pi d^2 \sqrt{2gH}} \tag{8}$$

4.3 Hydraulic Force on the Needle

The control of the needle is performed by the servomotor which operates by the oil pressure. Therefore, it is necessary to know the force required to control it at each position of the needle. The hydraulic force produces by the flow and acting on the needle is equals to the integration of the pressure force on its surface. The hydraulic force of the needle is given as per Eq. (9).

$$F_{needle} = \sum_{i=1}^m p_i A_i \sin \theta_i \tag{9}$$

Fig. 14 Hydraulic force on the needle



Where p_i is the static pressure at a point on the needle, A_i is the surface area on which pressure is acting and θ_i is the needle angle at a particular position on the needle. The hydraulic force calculated analytically and compared with CFD results which is presented in Fig. 14.

5 Conclusion

Turbulent flow inside the nozzle leads to energy losses due to the formation of secondary flows which further dissipate the energy. The non-uniform velocity distribution in the region outside the jet core is revealing of curved streamlines in the jet. Circumferential shape, velocity distribution, and dispersion of jet are influenced by nozzle and upstream piping geometry. Velocity contours show that the RANS model does not predict the anisotropic turbulence at the surface of the jet adequately. The energy loss in the injector is found about 1% and the analytical hydraulic force on the needle is well-matched with CFD results.

Acknowledgements The authors wish to acknowledge with thanks for the design and dimensions of jet injector provided by Flovel Energy Pvt. Ltd., Faridabad India, turbine manufacturer for the collaboration in this research work.

References

1. Zhang Z (2016) Pelton turbines. Springer. <https://doi.org/10.1007/978-3-319-31909-4>
2. Perrig A, Avellan F, Kuenny JL, Farhat M, Parkinson E (2006) Flow in a Pelton turbine bucket: numerical and experimental investigations. J Fluids Eng Trans ASME 128:350–358. <https://doi.org/10.1115/1.2170120>

3. Jo IC, Park JH, Kim JW, Shin Y, Chung JT (2016) Jet quality characteristics according to nozzle shape of energy-recovery Pelton turbines in pressure-retarded osmosis. *Desalin Water Treat* 57:24626–24635. <https://doi.org/10.1080/19443994.2016.1152641>
4. Staubli T, Abgottspon A, Weibel P, Bissel C, Parkinson E, Leduc J, Leboeuf F (2009) Jet quality and Pelton efficiency. *Hydro 2009 Progress - Potential – Plans*, Lyon, France
5. Peron M, Parkinson E, Geppert L, Staubli T (2008) Importance of jet quality on Pelton efficiency and cavitation. In: *International conference on hydraulic efficiency measurements*, pp 1–9
6. Avellan F, Dupont P, Kvicinsky S, Chapuis L, Parkinson E, Vullioud G (1998) Flow calculations in Pelton turbines. Part 2: free-surface flows. In: *Proceedings of the 19th IAHR symposium on hydraulic machinery and systems*, vol 1, pp 294–305
7. Kumashiro T, Alimirzazadeh S, Maertens A, Jahanbakhsh E, Leguizamón S, Avellan F, Tani K (2019) Numerical investigation of the jet velocity profile and its influence on the Pelton turbine performance. *IOP Conf Ser Earth Environ Sci* 240. <https://doi.org/10.1088/1755-1315/240/7/072006>
8. Benzon D, Židoniš A, Panagiotopoulos A, Aggidis GA, Anagnostopoulos JS, Papantonis DE (2015) Impulse turbine injector design improvement using computational fluid dynamics. *J Fluids Eng Trans ASME* 137:1–9. <https://doi.org/10.1115/1.4029310>
9. Nesiadis AV, Papantonis DE (2011) Numerical study of the effect of spear valve design on the free jet flow characteristics in impulse hydro turbines. In: *7th GRACM international congress on computational mechanics*
10. Zhang Zh, Parkinson E (2002) LDA application and the dual-measurement-method in experimental investigations of the free surface jet at a model nozzle of a Pelton turbine. In: *11th international symposium on applied laser anemometry to fluid mechanics*, pp 1–7
11. Ishii M, Hibiki T (2011) *Thermo-fluid dynamics of two-phase flow*. Springer, New York. <https://doi.org/10.1007/978-1-4419-7985-8>
12. Brackbill JU, Kothe DB, Zemach C (1992) A continuum method for modeling surface tension. *J Comput Phys* 100:335–354. [https://doi.org/10.1016/0021-9991\(92\)90240-Y](https://doi.org/10.1016/0021-9991(92)90240-Y)

Electromechanical Modelling of Ring Type of MEMS Gyroscopes



Sunrit Samanta and Ashok Kumar Pandey 

Abstract A new mathematical model for the combined slanting and scalloping defect, seen in the microelectromechanical systems (MEMS), has been suggested. This defect is observed in the high aspect ratio systems that are generally manufactured using the ‘Bosch Process’. Prior to this, the analytical model of a vibratory ring gyroscope (VRG), including the nonlinear terms, is delved into, considering the outer thin ring resonator. Its linear form is compared and analyzed with the finite element analysis in ANSYS. The impact of the aforesaid defect on the dynamics of a VRG is plotted with the help of MATLAB, applying the linear form of the expressions.

Keywords MEMS · Vibratory ring gyroscope · Combined slanting and scalloping

1 Introduction

MEMS vibratory gyroscopes are one of the emerging sensors, which are extensively used at present, to measure the angular rate of a system. In these gyroscopes, elements such as beams, disk, ring, etc. are used as the resonating structures. They follow the principle of “Coriolis Effect”. When an object is set into motion in a direction, as soon as it experiences rotation about a direction perpendicular to its motion, an inertial force is developed, called “Coriolis Force”. This force tends to deviate the object in the third mutually perpendicular direction, which is known as the “Coriolis Effect”. These types of gyroscope have great importance in navigation as well as in various applications, like aerospace, military, etc.

A simple MEMS vibratory gyroscope consists of a vibrating structure, that works according to the principle of the Coriolis Effect, [1]. In [2, 3], the author provides detailed insight into MEMS devices and their design principles. In [4] and [5], mechanics and dynamics of MEMS are explained. MEMS gyroscopes with axisymmetric resonating structures, i.e., ring and disk vibratory gyroscopes, offer significant advantages over the other ones. It is because of the inherent geometrical symmetry.

S. Samanta (✉) · A. K. Pandey
Indian Institute of Technology Hyderabad, Kandi, Sangareddy 502284, India
e-mail: ashok@mae.iith.ac.in

As a result, the two modes of vibration display symmetry in their frequencies too. Consequently, sensitivity to change in orientation of a ring gyroscope increases. Also, it has good long-term stability. In [6, 7], the linear and non-linear vibrations of axisymmetric systems like shells, membranes, tubes, rings, etc. have been studied thoroughly. In [8], the author has looked into nonlinear flexural vibrations and in [9], the author has studied the dynamics of free-vibrations, of thin circular ring. In [10], the author studied the resonant frequencies with their mode shapes of a SCS vibratory ring resonator. In [11], a new method is proposed for decreasing the frequency split of two modes of vibration of a (100) SCS ring resonator.

It is essential to control the dimensions of a specific MEMS gyroscope in order to obtain consistency in the quality of its performance. During the manufacturing of these gyroscopes, some defects occur which alter the dimensions of them. The major defects due to the DRIE fabrication process are scalloping and slanting. Some of the previous works on these defects are discussed here. In [12], the usual DRIE process is improved by proposing a new procedure called DREM, which resulted in the distribution of uniform scallops on the walls of the structures of high thickness. In [13], a mathematical formulation for predicting the effect of scalloping on the electrostatic actuating force has been developed. In [14], the effects of major manufacturing defects on the dynamics (i.e., stiffness, resonant frequency, etc.) and performance parameters of a vibratory gyroscope have been studied.

In this paper, the non-linear analytical model of a vibratory ring gyroscope is obtained by considering the model of a thin ring resonator. Subsequently, the non-linear equations have been simplified to its linear form. This linear form has been compared by creating a solid model in ANSYS SCDM and analyzing it through modal analysis in ANSYS Mechanical. Furthermore, considering the linear form of the non-linear equations of motion, combined slanting and scalloping defect is modeled in a new way and their effects on stiffness, electrostatic actuation force, equivalent mass, etc. have been examined. This work has been a part of the thesis work, [15], for the degree of Master of Technology from Indian Institute of Technology Hyderabad.

2 Vibratory Ring Gyroscope

2.1 Design and Working Principle

The vibratory ring gyroscope is designed referring to [11] with the dimensions mentioned in the Table 1. A thin ring is designed at first. A circular anchor is placed and fixed at the center of the circular ring. 8 supporting beams connect the ring to the anchor. This results in a resonating structure that has two in-plane “wine-glass” modes of vibration.

Working Principle. The resonating structure is electrostatically vibrated and set into motion or oscillation in one direction (suppose, along the x-axis) forming the drive mode of vibration. As soon as it is subjected to external rotation about another

Table 1 Values of the parameters

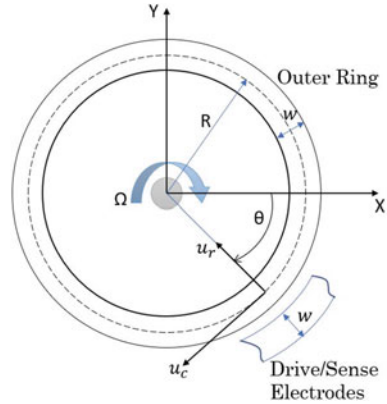
Parameter	Value
Mean radius (R) of the ring	1004 μm
Outer radius of the ring	1008 μm
Inner radius of the Ring	1000 μm
Width (w) of the ring and each suspended beam	8 μm
Thickness (H) of the ring and each suspended beam	22 μm
Inner radius of each curved suspended beam	900 μm
Outer radius of each curved suspended beam	908 μm
Angle subtended by the center line of each curved suspended beam at the center	44°
Gap (a) between the ring and each electrode	4 μm
Density of the material (ρ)	2330 kg/m^3
Young's Modulus (E) of the material	166 GPa
Actuating voltage (V_{AC})	0.1 V
Bias or Tuning voltage (V_{DC})	5 V
Permittivity of free space (ϵ_0)	$8.85e - 12 \frac{\text{s}^4\text{A}^2}{\text{m}^3\text{kg}}$

direction (suppose, about the z-axis), a pseudo-force known as the Coriolis force develops in the third direction (i.e., in the y-axis) and starts oscillating in this 3rd direction forming the sense mode. The amplitude along this sense mode is sensed through the capacitive sensors, generally. Sensing this amplitude helps us to calculate the external angular velocity and accordingly, we can adjust and orient the system into its original configuration. A vibratory ring gyroscope also follows the same principle. In this case, two “wine-glass” modes of vibration are of importance. The first one is called the drive mode, in which the ring is electrostatically actuated. The second one is known as the sense mode. Due to the rate of angular displacement experienced by the vibrating ring, it starts vibrating into the sense mode. In the case of a ring-resonator, it is located 45° away from the drive mode. Through capacitive sensing, the amplitude of the vibration in the sense direction is sensed by the electrodes placed around the periphery of the ring-resonator.

2.2 Mathematical Model

In this section, we have looked into the derivation of non-linear equation of motion of a vibratory ring gyroscope. We have considered a cylindrical coordinate system. It consists of the coordinates r , θ and z . r and θ are the in-plane coordinates. The outer ring of the gyroscope is considered for this study. The suspended beams are not considered in the derivation. The ring has two elliptical modes. We denote the

Fig. 1 Schematic representation of the system under study



modes with modal coordinates r_A and r_B . The nodal diameters of the mode shapes are separated by 45° . Thus, they are denoted by $\Psi_A(r, \theta) = \zeta(r)\cos 2\theta$ and $\Psi_B(r, \theta) = \zeta(r)\sin 2\theta$. The alphabets A and B represent the drive and sense modes respectively. The resonating structure experiences two types of displacements (u_r and u_c). One of them acts in the radial direction of the ring. The other one is acting in the tangential or circumferential direction. We assumed these displacements to be independent of z-coordinate.

The outer ring has a very less thickness. Thus, the mode shapes become independent of the radius ‘r’ of the ring, [7]. Thus, they can now be expressed as $\Psi_A(\theta) = \cos 2\theta$ and $\Psi_B(\theta) = \sin 2\theta$ for the two modes. Considering the case of a thin ring, u_r can be expressed as, [7]:

$$u_r = u_r(\theta, t) = r_A(t)\cos 2\theta + r_B(t)\sin 2\theta, \tag{1}$$

Now, as per [8], u_r can further be expressed as:

$$u_r = u_r(\theta, t) = r_A\cos 2\theta + r_B\sin 2\theta - \frac{r_A^2 + r_B^2}{R}, \tag{2}$$

where $-(r_A^2 + r_B^2)/R$ represents the pure radial vibration of the ring; r_A and r_B are the generalized coordinates and R is the mean radius of the ring, as shown in Fig. 1.

The unit elongation of the mean radius of the ring at any point is given by, [7]: $\epsilon_{\theta\theta}^0 = -\frac{u_r}{R} + \frac{\delta u_c}{R\delta\theta}$.

Assuming $\epsilon_{\theta\theta}^0 = 0$, i.e., inextensible mean radius of the ring, we can obtain the value of $u_c(\theta, t)$ as:

$$u_c = u_c(\theta, t) = \frac{1}{2}(r_A\sin 2\theta - r_B\cos 2\theta) - \left(\frac{r_A^2 + r_B^2}{R}\right)\theta, \tag{3}$$

The potential energy (P.E.) of the system is, $P.E. = (P.E.)_p + (P.E.)_e$; where $(P.E.)_p$ = elastic potential energy, can be expressed as, [7]:

$$(P.E.)_p = \frac{EI}{2R^3} \int_0^{2\pi} [u_r + \frac{\delta^2 u_r}{\delta \theta^2}]^2 d\theta \quad (4)$$

Substituting, u_r in the above equation:

$$(P.E.)_p = \frac{EI}{2R^3} [9\pi r_A^2 + 9\pi r_B^2 + 2\pi \frac{r_A^4 + r_B^4}{R^2} + \frac{4\pi r_A^2 r_B^2}{R^2}] \quad (5)$$

The electrodes are placed around outer periphery of the ring at a very small distance a . We can consider them as parallel plate capacitor. Generally, the potential energy for this type of capacitor can be expressed as: $\frac{\epsilon_o(\text{Voltage})^2(\text{Area})}{2(\text{Gap})}$. In this case, Voltage = $V_{DC} + V_{AC} \cos 2\theta$, Area = $HR d\theta$ and the ring displaces by u_r in the radial direction during vibration. Thus the electrostatic potential energy $((P.E.)_e)$, can be expressed as:

$$(P.E.)_e = - \int_0^{2\pi} \frac{\epsilon_o [V_{DC} + V_{AC} \cos 2\theta]^2 (RH)}{2(a - u_r)} d\theta \quad (6)$$

The above equation can further be expressed as:

$$(P.E.)_e = - \frac{\epsilon_o RH}{2a} \int_0^{2\pi} [V_{DC} + V_{AC} \cos 2\theta]^2 (1 - \frac{u_r}{a})^{-1} d\theta \quad (7)$$

As we know, generally $u_r \ll a$, thus by applying Taylor's Series Expansion:

$$(P.E.)_e = - \frac{\epsilon_o RH}{2a} \int_0^{2\pi} [V_{DC} + V_{AC} \cos 2\theta]^2 [1 + \frac{u_r}{a} + (\frac{u_r}{a})^2 + (\frac{u_r}{a})^3 + (\frac{u_r}{a})^4] d\theta \quad (8)$$

The terms up to 4^{th} power are considered in order to maintain similarity with the expression of $[(P.E.)_p]$ that contains terms (r_A, r_B) up to 4^{th} power. Similarly, after performing the integration, the terms (r_A, r_B) above 4^{th} power are neglected. Now, the kinetic energy (K.E.) of the system is given by, [6]:

$$K.E. = \frac{\rho A_{cs} R}{2} \int_0^{2\pi} [(\dot{u}_r - u_c \Omega)^2 + (\dot{u}_c + (R + u_r)\Omega)^2] d\theta \quad (9)$$

where, $\dot{u}_r = \frac{du_r}{dt}$, $\dot{u}_c = \frac{du_c}{dt}$, Ω = external angular velocity and ρ = density of the material.

Now, applying Lagrange's Equation:

$$\frac{d}{dt} \left[\frac{\delta(K.E.)}{\delta \dot{q}_i} \right] - \frac{\delta(K.E.)}{\delta q_i} + \frac{\delta(P.E.)}{\delta q_i} = 0 \quad (10)$$

After solving the above equation, the non-linear equation of motion of the drive mode is:

$$\begin{aligned}
 & m\left\{1 + \frac{32}{5R^2}\left(1 + \frac{4\pi^2}{3}\right)r_A^2 + \frac{8}{5R}r_A\right\}\ddot{r}_A + m\{2\omega_d\xi_A + \frac{64}{5R^2}\left(1 + \frac{4\pi^2}{3}\right)r_B\dot{r}_B + \frac{4m}{5R}\dot{r}_A\}r_A \\
 & + \left\{\frac{9\pi EI}{R^3} - \frac{\pi\epsilon_0 V_{DC}^2 RH}{a^3} + \left(\frac{4\pi EI}{R^5} - \frac{3\pi\epsilon_0 V_{DC}^2 RH}{2a^5}\right)r_A^2 + \left(\frac{4\pi EI}{R^5} - \frac{3\pi\epsilon_0 V_{DC}^2 RH}{2a^5}\right)r_B^2\right\}r_A \\
 & + \frac{\rho A_{cs}}{2}\left[\left\{\frac{11}{2}\pi R - \frac{8\pi}{R}\left(1 + \frac{4\pi^2}{3}\right)(r_A^2 + r_B^2) - 3\pi r_A\right\}\Omega^2 + 8\pi r_B\Omega\right. \\
 & \quad \left. + \frac{16\pi}{R}\left(1 + \frac{4\pi^2}{3}\right)(r_A^2 + r_B^2 + r_B\ddot{r}_B)\right]r_A \\
 & = \frac{\rho A_{cs}}{2}(\pi\Omega^2 r_B^2 - 2R\Omega r_B - 2\pi r_B^2 - 2\pi r_B\ddot{r}_B) + \frac{\pi\epsilon_0 V_{AC} V_{DC} RH}{a^2}\left(1 + \frac{3}{4}\frac{r_B^2}{a^2} + \frac{9}{4}\frac{r_A^2}{a^2}\right) \\
 & \quad + \frac{\pi\epsilon_0 V_{AC}^2 RH}{4a^3}\left(3 + 3\frac{r_B^2}{a^2} + 5\frac{r_A^2}{a^2}\right)r_A \tag{11}
 \end{aligned}$$

Where, $m = \frac{5}{4}\pi\rho A_{cs}R$ is the equivalent mass and $A_{cs} = wH$ is the cross-sectional area of the ring. Keeping in mind the negligible effect of few terms (like, $\frac{hr_A r_B^2}{Ra^3}$, $\frac{hr_A^2 r_B}{a^3}$, etc.) on the expression of $\frac{\delta(P.E.)_e}{\delta q_i}$, those terms are not considered before applying Lagrange's equation.

Similarly, the non-linear equation of motion of the sense mode is:

$$\begin{aligned}
 & m\left\{1 + \frac{32}{5R^2}\left(1 + \frac{4\pi^2}{3}\right)r_B^2 + \frac{8}{5R}r_B\right\}\ddot{r}_B + m\{2\omega_s\xi_B + \frac{64}{5R^2}\left(1 + \frac{4\pi^2}{3}\right)r_A\dot{r}_A + \frac{4m}{5R}r_B\dot{r}_B\}r_B \\
 & + \left\{\frac{9\pi EI}{R^3} - \frac{\pi\epsilon_0 V_{DC}^2 RH}{a^3} + \left(\frac{4\pi EI}{R^5} - \frac{3\pi\epsilon_0 V_{DC}^2 RH}{2a^5}\right)r_B^2 + \left(\frac{4\pi EI}{R^5} - \frac{3\pi\epsilon_0 V_{DC}^2 RH}{2a^5}\right)r_A^2\right\}r_B \\
 & + \frac{\rho A_{cs}}{2}\left[\left\{\frac{11}{2}\pi R - \frac{8\pi}{R}\left(1 + \frac{4\pi^2}{3}\right)(r_A^2 + r_B^2) - 3\pi r_B\right\}\Omega^2 + 8\pi r_A\Omega\right. \\
 & \quad \left. + \frac{16\pi}{R}\left(1 + \frac{4\pi^2}{3}\right)(r_A^2 + r_B^2 + r_A\ddot{r}_A)\right]r_B \\
 & = \frac{\rho A_{cs}}{2}(\pi\Omega^2 r_A^2 - 2R\Omega r_A - 2\pi r_A^2 - 2\pi r_A\ddot{r}_A) + \frac{3\pi\epsilon_0 V_{AC} V_{DC} RH}{2a^4}r_A r_B \\
 & \quad + \frac{\pi\epsilon_0 V_{AC}^2 RH}{4a^3}\left(1 + \frac{r_B^2}{a^2} + \frac{3r_A^2}{a^2}\right)r_B \tag{12}
 \end{aligned}$$

Excluding the non-linear terms and the coupled terms, the linear equation of motion of drive mode:

$$\begin{aligned}
 & \frac{5}{4}\pi\rho wHR\ddot{r}_A + c_A\dot{r}_A + \left[\frac{9\pi EI}{R^3} - \frac{\pi\epsilon_0 V_{DC}^2 RH}{a^3} + \frac{11}{4}\pi\rho wHR\Omega^2\right]r_A \\
 & = -\rho wHR\Omega r_B + \frac{\pi\epsilon_0 V_{AC} V_{DC} RH}{a^2}\cos\omega t \tag{13}
 \end{aligned}$$

The linear equation of motion of sense mode:

$$\begin{aligned} \frac{5}{4}\pi\rho wHRr\ddot{r}_B + c_B\dot{r}_B + \left[\frac{9\pi EI}{R^3} - \frac{\pi\epsilon_o V_{DC}^2 RH}{a^3} + \frac{11}{4}\pi\rho wHR\Omega^2\right]r_B \\ = -\rho wHR\Omega(r_A)_{amp}\omega_d\cos\omega t \end{aligned} \quad (14)$$

where, drive (k_d) and sense stiffness (k_s) expressions are same,

$$k_d = k_s = \frac{9\pi EI}{R^3} - \frac{\pi\epsilon_o V_{DC}^2 RH}{a^3} + \frac{11}{4}\pi\rho wHR\Omega^2 \quad (15)$$

drive resonant frequency, $\omega_d = \sqrt{\frac{k_d}{m}}$ and sense resonant frequency, $\omega_s = \sqrt{\frac{k_s}{m}}$ and electrostatic actuating force, $F = \frac{\pi\epsilon_o V_{AC}V_{DC}RH}{a^2}$.

3 Finite Element Analysis

The model of a VRG referring to the shape described in [11] and using the dimensions stated in Table 1, is designed using ANSYS R18.0 Space Claim Design Modeler (SCDM) and the properties of Silicon Anisotropic material are assigned to it, and then the modal analysis is carried out using finite element simulation in ANSYS Mechanical with fixed support (of diameter 50 μm) at the center as shown in the following figures. The 3D model, without the drive and sense electrodes, is meshed with an element size of 4.86e-6 m using tetrahedron patch conforming method. In Fig. 2, the drive mode and sense mode of the aforesaid gyroscope are shown side by side. Including the slanting effect with a slant angle of 0.1°, a ring gyroscope is modelled having similar dimensions. Also, the meshing is done with the similar size of the elements. Its drive and sense modes of vibration are shown in Fig. 3. The direction of the vibrations for each mode is shown by blue arrows in the figures.

After completing the modal analysis, the resonant frequency of the drive mode is obtained as 7943.9 Hz and that of the second “wine-glass” mode is obtained as 7944.2 Hz. The size of the element during meshing was decreased from 7.86e-6 m to 4.86e-6 m. Due to this, the number of finite elements of the meshed model changes from 75,380 to 2,56,115. As a result, 0.157% of change is seen in the resonant frequency of the drive mode of vibration and 0.161% of change is seen in that of the other mode of vibration. Thus, it can be inferred that convergence has been achieved. The theoretical value of the two resonant frequencies obtained from the linear form of the analytical model are equal, i.e., 8027.6 Hz. The deviation in both the values of the frequencies from the calculated value are 1.054% and 1.05%. Similarly, considering the effect of slanting, the numerical values of drive and sense mode resonant frequencies are 7980.6 Hz and 7981 Hz, respectively. The increase in the number of elements during meshing of the model, from 73,646 to 2,56,094 resulted in a change of 0.155% in both the resonant frequencies. The calculated theoretical value is 8062.73 Hz. In this

Table 2 Values of resonant frequencies for the two 3D solid models

Modes of vibration	3D model without any defect	3D model with slanting effect ($\beta = 0.1^\circ$)
Drive	7943.9 Hz	7980.6 Hz
Sense	7944.2 Hz	7981 Hz

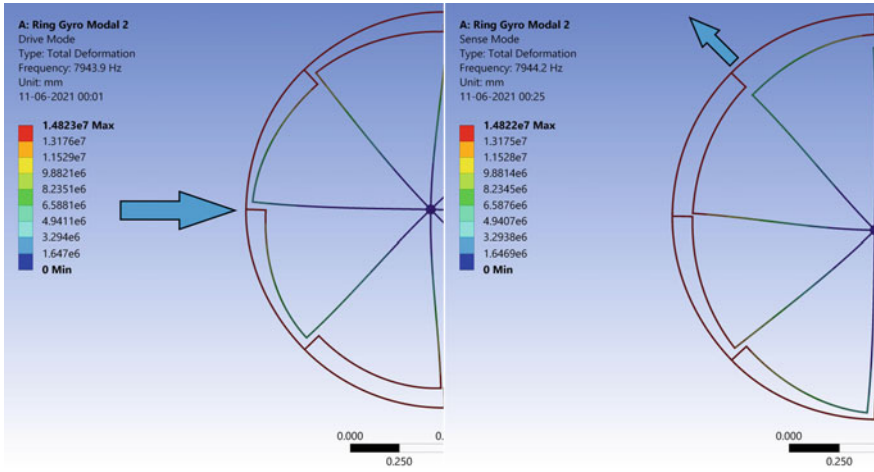


Fig. 2 Drive and sense mode in ANSYS (front view)

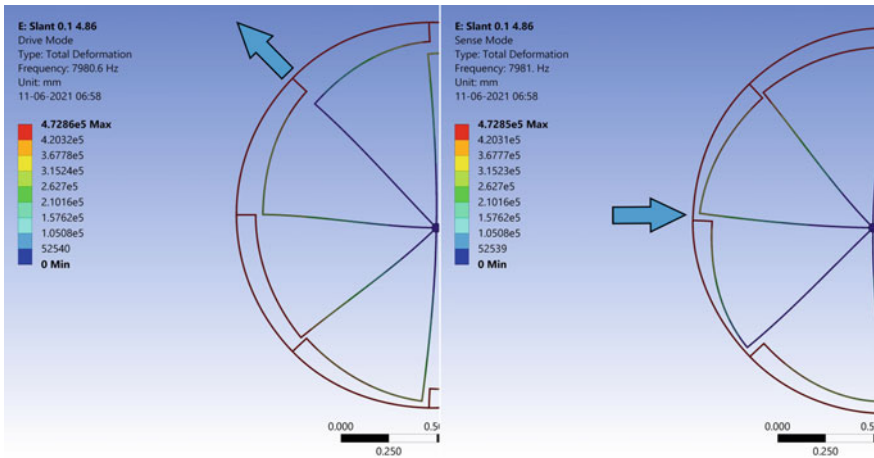


Fig. 3 Drive and sense mode in ANSYS (with $\beta = 0.1^\circ$)

case, the difference between the theoretical and the numerical values of the frequencies are 1.03% and 1.024%. The values of the frequencies are listed in the Table 2.

Without considering the electrical term ($V_{DC} = 5\text{ V}$) in the stiffness expression, the theoretical value of resonant frequency for the 1st model is 8258.37 Hz. This deviates from the simulated value of 7943.9 Hz by 3.95%. The theoretical value for the 2nd model is 8311.36 Hz. In this case, the deviation from the simulated value is 4.15%.

4 Combined Slanting and Scalloping Defect

4.1 Fabrication Process

The basic processes of the fabrication of MEMS structure are (a) Deposition Processes, (b) Patterning, (c) Etching Processes. In etching, the material is removed from the silicon wafer selectively to make a specific geometry as required. Wet etching and dry etching are the two basic types of etching. Dry etching consists of vapour phase etching, reactive ion etching, etc. One of the mostly used dry etching, i.e., the deep reactive ion etching (DRIE) is usually preferred while fabricating high aspect ratio MEMS. The most popular DRIE is the “Bosch process”. An etch cycle of this process consists of three steps: (1) Isotropic Etching, (2) Side-wall Passivation, and (3) Anisotropic Etching for floor cleaning.

Fabrication Defects. A number of etch cycles is performed continuously to get the deep vertical structures. But, often the vertical walls have undulations on their surfaces, which is known as “scalloping”. Also, the walls tend to deviate from the vertical line causing a taper or slant angle with it, known as “slanting”. Their effects are mostly tangible in the moment of inertia, area, stiffness, the resonant frequency of the structures and the electrostatic actuating force.

4.2 Analytical Model

For the combined slanting and scalloping cases, the scallops tend to vary as we go downwards as shown in Fig. 4. The centre of the ellipse changes along with the variation of its minor axis. Thus, to get the total effect on a certain parameter like area, the summation of each area (A_p) corresponding to a particular scallop should be done. The p represents the p^{th} scallop, i.e., $p = 1$ represents the 1st scallop and so on.

Previous Work. As discussed in [13], the actual model showed the combined slanting and scalloping defect, in which the semi-minor axis of the ellipse is changing from 0.52 μm to 0.02 μm along the thickness, as we go downwards. The main assumption

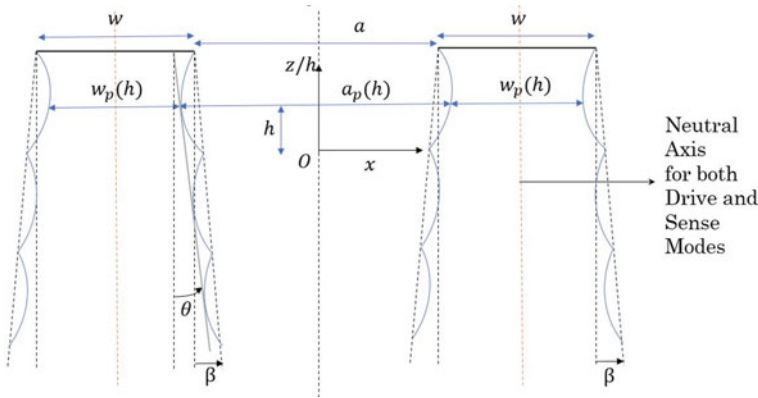
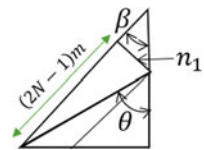


Fig. 4 Schematic representation of the defect according to the original profile

Fig. 5 For the calculation of θ



made in [13] is that the semi-minor axis of the ellipse is horizontal for all the scallops, which is not the case for the actual profile obtained during manufacturing. The shape of the scallop has been represented as a semi-ellipse. The semi-minor axis is gradually varying as we go downwards.

New Formulation. The main drawback of the previous assumption is that for large deviation, i.e., slant angle, the results from the previous model will not at all be comparable with the actual ones. The differences between them will increase. Thus, for this study, we have analytically modeled the defect according to the original profile obtained during manufacturing, where the semi-minor axis of the elliptical scallop remains inclined to the horizontal by a certain angle. In the Fig. 4, ‘O’ is the origin with x and z or h as the horizontal and vertical axis respectively. The value of semi-major axis has been assumed to be constant throughout the thickness H and the semi-minor axis is gradually varying according to the angle θ . The angle θ can be calculated referring to Fig. 5 as:

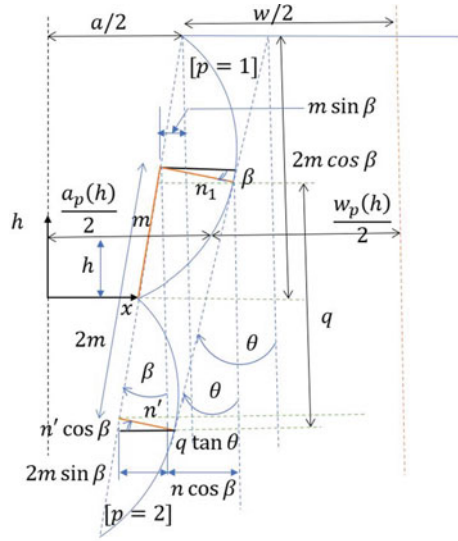
$$\cos\theta = \frac{2mN \cos\beta - (m \cos\beta + n_1 \sin\beta)}{[(2N - 1)m]^2 + n_1^2} \tag{16}$$

where, $n = n_1$ is the semi-minor axis of the 1st elliptical scallop.

From the Fig. 6, q can be expressed as:

$$q = 2m \cos\beta + (n' - n_1) \sin\beta \tag{17}$$

Fig. 6 Modeling of the defect



Also,

$$2m \sin\beta + n_1 \cos\beta = q \tan\theta + n' \cos\beta \tag{18}$$

Using the above two equations, the semi-minor axis of the 2nd scallop can be calculated from:

$$n' = n_1 + \frac{2m(\sin\beta - \cos\beta \tan\theta)}{\cos\beta + \sin\beta \tan\theta} \tag{19}$$

Thus, for the p^{th} scallop,

$$n_p = n_1 + \frac{2m(p - 1)(\sin\beta - \cos\beta \tan\theta)}{\cos\beta + \sin\beta \tan\theta} \tag{20}$$

The centre of the ellipse, in the original case, gets shifted by $(m \sin\beta)$ in x-direction towards the origin, when we proceed to 2nd scallop from the 1st one. Thus, for the p^{th} scallop, the centre shifts by $[(2p - 1)m \sin\beta]$. The new centre of the ellipse, with m and n_p as the major and minor axis for the p^{th} scallop respectively, will then be given by (x_1, h_1) , as:

$$x_1 = \frac{a}{2} - (2p - 1)m \sin\beta$$

$$h_1 = m \cos\beta$$

Now, the ellipse is rotated by an angle β , as shown in Fig. 6, in the clockwise direction. Thus, we need to apply the rotation matrix as follows, to get the equation of the elliptical curve:

$$T(\beta) = \begin{bmatrix} \cos\beta & -\sin\beta \\ \sin\beta & \cos\beta \end{bmatrix}$$

The x and h coordinates of the rotated and translated ellipse are given by x' and h' , as:

$$\begin{Bmatrix} x' \\ h' \end{Bmatrix} = T(\beta) \begin{Bmatrix} x - x_1 \\ h - h_1 \end{Bmatrix}$$

$$x' = (x - x_1)\cos\beta - (h - h_1)\sin\beta$$

$$h' = (x - x_1)\sin\beta + (h - h_1)\cos\beta$$

Thus, the equation of ellipse for this case can be written as:

$$\frac{[(x - x_1)\cos\beta - (h - h_1)\sin\beta]^2}{n_p^2} + \frac{[(x - x_1)\sin\beta + (h - h_1)\cos\beta]^2}{m^2} = 1 \quad (21)$$

From the above equation, the x coordinates of the ellipse can be expressed as:

$$x = x_1 + \frac{-B_b \pm \sqrt{B_b^2 - 4A_a C_c}}{2A_a} \quad (22)$$

where,

$$A_a = m^2\cos^2\beta + n_p^2\sin^2\beta$$

$$B_b = -(h - h_1)(m^2 - n_p^2)\sin 2\beta$$

$$C_c = (h - h_1)^2(m^2\sin^2\beta + n_p^2\cos^2\beta) - m^2n_p^2$$

The variation of width ($w_p(h)$) of the ring and the gap ($a_p(h)$) between the ring and the electrode for p^{th} scallop are given by:

$$a_p(h) = 2x$$

$$w_p(h) = (a + w) - 2x$$

Area. The total cross-sectional area (A) can be obtained from:

$$A = \sum_{p=1}^N A_p, \text{ where } A_p = \int_0^{2m} w_p(h)dh \quad (23)$$

where, N = number of scallops = $\frac{H}{2m}$

Mass. The equivalent mass in this case can be calculated from:

$$M = \frac{5\pi\rho R}{4}A \quad (24)$$

Electrostatic Force. The total electrostatic actuating force can be expressed as:

$$F = \sum_{p=1}^N F_p, \text{ where } F_p = \pi\epsilon_o V_{DC} V_{AC} R \int_0^{2m} \frac{dh}{(a_p(h))^2} \quad (25)$$

Stiffness. The moment of inertia about z-axis is calculated from:

$$I = \sum_{p=1}^N \left[\int_0^{2m} \frac{w_p(h)^3}{12} dh \right] \quad (26)$$

Now, the stiffness can be calculated from:

$$k = \frac{9\pi EI}{R^3} - \sum_{p=1}^N \left[\pi\epsilon_o V_{DC}^2 R \int_0^{2m} \frac{dh}{(a_p(h))^3} \right] \quad (27)$$

5 Results

This section shows the results from the analytical modelling of the defects by plotting their effects on four different parameters, i.e., stiffness, electrostatic force, resonant frequency and equivalent mass of the vibratory ring gyroscope.

5.1 Effects of Fabrication Defects

Combined Slanting and Scalloping. For the combined slanting and scalloping defect, two different cases are considered as follows:

Case-1: The slant angle varies according to the thickness of the structure, which can be obtained from the fitted curve in [14]. Considering thickness $H = 22 \mu\text{m}$, semi-minor axis of the first scallop ($p = 1$) $n_1 = 0.2 \mu\text{m}$ and varying slant angle β from 0° to 0.1° , the graphs in Fig. 7 and Fig. 8, are obtained for stiffness, resonant frequency, equivalent mass, and electrostatic force, respectively, showing the comparison of the old and new formulations.

Case-2: Similarly, for $H = 80 \mu\text{m}$, $n_1 = 0.5 \mu\text{m}$, and varying slant angle β from 0° to 0.3° , the graphs in Fig. 9 and Fig. 10, are obtained for stiffness and electrostatic force, respectively. The results for (a) $H = 22 \mu\text{m}$, $n_1 = 0.2 \mu\text{m}$ and $\beta = 0.1^\circ$, and (b) $H = 80 \mu\text{m}$, $n_1 = 0.5 \mu\text{m}$ and $\beta = 0.3^\circ$ are shown in the Table 3 and Table 4, respectively along with the changes (in %) in the values with respect to those obtained using old formulations.

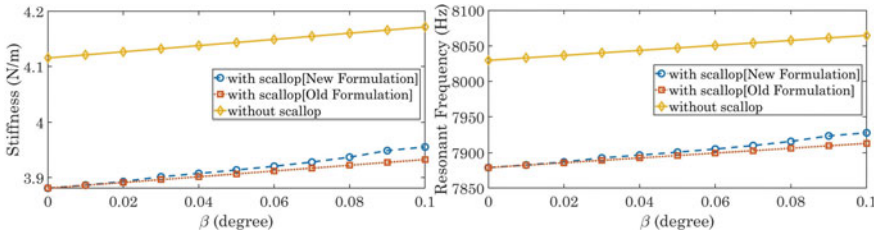


Fig. 7 Variation of stiffness and frequency with slanting angle for $H=22 \mu\text{m}$.

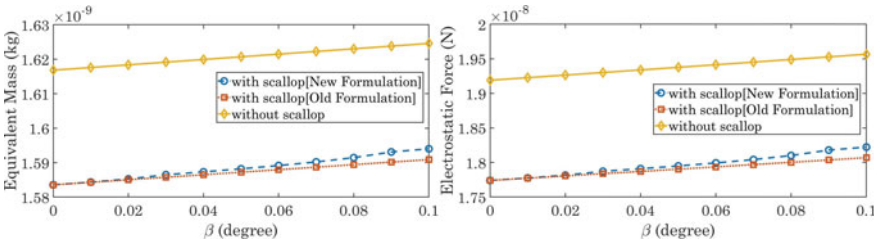


Fig. 8 Variation of equivalent mass and electrostatic force with slanting angle for $H=22 \mu\text{m}$.

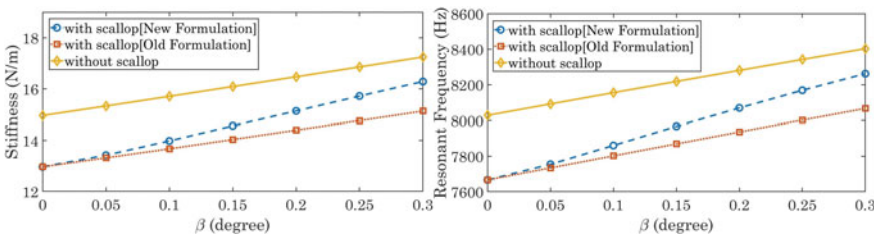


Fig. 9 Variation of stiffness and frequency with slanting angle for $H=80 \mu\text{m}$.

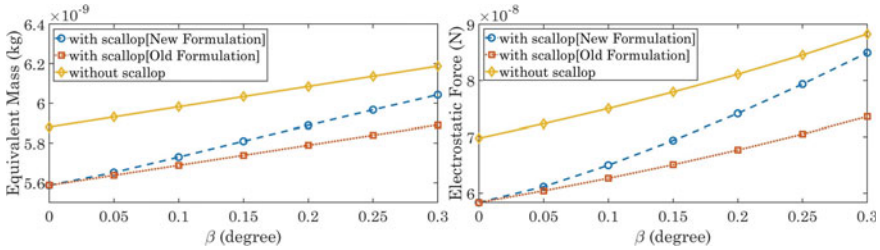


Fig. 10 Variation of equivalent mass and electrostatic force with slanting angle for $H=80\mu\text{m}$.

Table 3 Comparison of the two formulations for $H=22\mu\text{m}$

Parameter	With old formulation	With new formulation	Change (%)
Stiffness (N/m)	3.93092	3.95357	0.58
Electrostatic force (N)	1.80688e-8	1.8222e-8	0.85
Resonant frequency (Hz)	7911.30	7926.26	0.19
Equivalent mass (kg)	1.59088e-9	1.59042e-9	0.20

Table 4 Comparison of the two formulations for $H=80\mu\text{m}$

Parameter	With old formulation	With new formulation	Change (%)
Stiffness (N/m)	15.1308	16.2819	7.61
Electrostatic force (N)	7.35867e-8	8.49496e-8	15.44
Resonant frequency (Hz)	8066.49	8261.50	2.42
Equivalent mass (kg)	5.89023e-9	6.04265e-9	2.59

In both the cases, the effects show gradual increase in the values with increase in the slant angle. It can be inferred that for the high aspect ratio structure, the change in the values calculated using old and new formulations becomes significant.

6 Conclusions

The effect of combined slanting and scalloping defect on stiffness, electrostatic actuating force, etc. can be seen in the graphs plotted using MATLAB. The difference between new and old formulations is prominent in the structures of large aspect ratio. Thus, the new analytical model of the combined slanting and scalloping defect, can be very helpful in deciding the appropriate dimensions while designing gyroscopes for specific performance requirements. Also, the mathematical formulations for a

VRG have been completed to express the non-linear equation of motions for its drive and sense mode of vibration.

Acknowledgements I, Sunrit Samanta, acknowledge the Ministry of Education (MoE), formerly known as the Ministry of Human Resource Development (MHRD), New Delhi, India, for the fellowship provided to me for pursuing master of technology from Indian Institute of Technology Hyderabad.

References

1. Apostolyuk V (2007) Theory and design of micromechanical vibratory gyroscopes. In: MEMS/NEMS, pp 173–195. https://doi.org/10.1007/0-387-25786-1_6
2. Bao M (2005) Analysis and design principles of MEMS devices, 1st edn. Elsevier Science, Amsterdam
3. Bao M (2000) Micro mechanical transducers: pressure sensors, accelerometers, and gyroscopes, 1st edn. Elsevier Science, Amsterdam
4. Lobontiu N, Garcia E (2005) Mechanics of microelectromechanical systems. Springer, Boston
5. Lobontiu N (2007) Dynamics of microelectromechanical systems. Springer, Boston
6. Soedel W (2005) Vibrations of shells and plates. Marcel Dekker Inc., New York
7. Timoshenko S (1937) Vibration problems in engineering. D. Van Nostrand Company Inc., New York
8. Evensen DA (1966) Nonlinear flexural vibrations of thin circular rings. *J Appl Mech* 33(3):553–560. <https://doi.org/10.1115/1.3625121>
9. Natsiavas S (1994) Dynamics and stability of non-linear free vibration of thin rotating rings. *Int J Non-Linear Mech* 29(1):31–48. [https://doi.org/10.1016/0020-7462\(94\)90050-7](https://doi.org/10.1016/0020-7462(94)90050-7)
10. Chang CO, Chang GE, Chou CS, Chien WTC, Chen PC (2008) In-plane free vibration of a single-crystal silicon ring. *Int J Solids Struct* 45(24):6114–6132. <https://doi.org/10.1016/j.ijsolstr.2008.07.033>
11. Shu Y, Hirai Y, Tsuchiya T (2019) Tabata O (2019) Geometrical compensation for mode-matching of a (100) silicon ring resonator for a vibratory gyroscope. *Jpn J Appl Phys* 58:SDDL06. <https://doi.org/10.7567/1347-4065/ab0dee>
12. Chang B, Leussink P, Jensen F, Hübner J, Jansen H (2018) DREM: infinite etch selectivity and optimized scallop size distribution with conventional photoresists in an adapted multiplexed Bosch DRIE process. *Microelectron Eng* 191:77–83. <https://doi.org/10.1016/j.mee.2018.01.034>
13. Pawar VS, Menon PK, Murty AL, Pal P, Pandey AK (2019) Influence of scalloping on electrostatic forces in comb drive microdevices. *ISSS J Micro Smart Syst* 8(2):127–134. <https://doi.org/10.1007/s41683-019-00042-0>
14. Biswas A, Pawar VS, Menon PK, Pal P, Pandey AK (2020) Influence of fabrication tolerances on performance characteristics of a MEMS gyroscope. *Microsyst Technol* 27(7):2679–2693. <https://doi.org/10.1007/s00542-020-05059-2>
15. Samanta S, Pandey AK (2021) Electromechanical modelling of ring type of MEMS gyroscopes. M.Tech thesis, IIT Hyderabad, India

Material Parameter Identification for Brain Tissue Using Open-Source Platforms - GIBBON and FEBio



Abhilash Awasthi, Umesh Gautam, and Sitikantha Roy

Abstract An accurate estimation of the constitutive response of brain tissue is a crucial requirement for the development of a neurosurgical simulation framework. In this work, open-source platforms named GIBBON and FEBio have been utilized to solve an inverse finite element-based optimization problem for calibrating the material parameters for the brain tissue. The *ex-vivo* uniaxial force-displacement data for the goat brain tissue has been used for calibration. The objective of the study is to demonstrate the differences in material parameters calibrated using standard least-square curve fitting and inverse finite element method. Although a close agreement between the stress-strain curves from experimental data, curve fitting and inverse finite element method was observed, however, a significant deviation was found between the material parameters extracted from both the methods. The extracted material parameters could then be used to represent brain tissue for developing and solving boundary value problems concerning neurosurgical procedures.

Keywords Brain tissue testing · Inverse finite element method · Ogden model · FEBio · GIBBON

1 Introduction

Neurosurgical procedures are the most complex processes and need highly skilled hand-eye coordination during surgery. The computer-aided practice is an advisable alternative solution to eliminate human errors by performing surgical procedures on a virtual head model [1]. Apart from ensuring a detailed anatomical description, the reliability of a virtual head model is also guaranteed by an accurate prediction of material properties [2].

A. Awasthi · U. Gautam · S. Roy (✉)

Department of Applied Mechanics, Indian Institute of Technology Delhi, Hauz Khas,
New Delhi 110016, India

e-mail: sroy@am.iitd.ac.in

URL: <https://sites.google.com/view/sitilab-iitd/>

© The Author(s), under exclusive license to Springer Nature Singapore Pte Ltd. 2022

T. Tadepalli and V. Narayanamurthy (eds.), *Recent Advances in Applied Mechanics*,

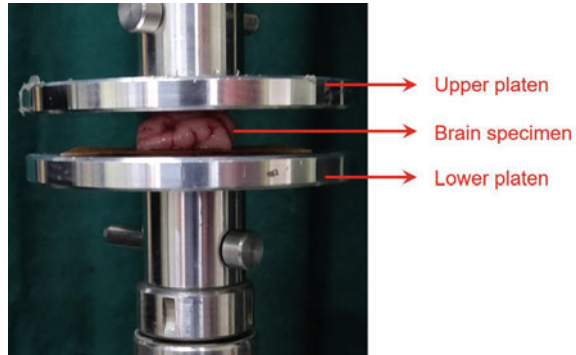
Lecture Notes in Mechanical Engineering, https://doi.org/10.1007/978-981-16-9539-1_36

Material parameter calibration is one of the essential parts of a virtual neurosurgical training platform. The standard way of calibrating the material parameters is to use a least-square approach to fit the mathematical model representing material behavior with experimental data. The standard curve fitting technique is quite robust and is used most of the time to calibrate the material parameters against the experimental data [3]. However, this method has some significant limitations which might affect the accuracy of calibrated material parameters. One of the limitations is the absence of geometrical considerations. Sometimes the method leads to physically unsound but mathematically accurate values of material parameters, possibly due to the assumptions and simplifications used in mathematical modeling. For instance, the assumption of a homogeneous state of deformation leads to various unexpected errors during the calibration [4]. Also, with the requirements of constant stress or strain field, representing the whole specimen with a single value of the elastic field poses a significant challenge to the realistic material parameter estimation. The curve fitting method also becomes cumbersome in finding the analytical solution when one tries to incorporate complexity in terms of loading modes such as biaxial, multiaxial, indentation, or incorporation of anisotropic material behavior [5].

Alternatively, the inverse finite element (FE) method is more advantageous. It aims to replicate the experimental boundary value problem using an FE model and minimize the error between the test and simulation results in an iterative loop for the optimal set of material parameters. The advantage of using the inverse FE method is that the physics of the problem in terms of either material behavior, geometry, or realistic boundary conditions, is captured more accurately than the curve fitting method. Also, the complexity, either in terms of loading or material behavior, could be easily implemented in the FE framework. The strict requirements for material homogeneity and a constant elastic field could then be relaxed and, in some cases, completely avoided.

In this work, a one-term Ogden hyperelastic material model has been used to extract the constitutive material parameters of goat brain tissue in a compression test. The constitutive parameters have been compared by extracting them using the standard curve fitting least-square approach and later inverse FE method using open-source platforms viz. GIBBON [6] and FEBio [7]. The present study is a part of a long-term goal to develop an *in-silico* training platform for neurosurgical procedures, which inevitably needs a computer model with accurate material physics. *In-silico* modeling involves developing a computational framework, such as a virtual surgical platform, to model and study different physical processes by combining the advantages of both *in-vivo* and *ex-vivo* experimentation. The material parameter extraction from experimentally extracted data, whether *in-vivo* or *ex-vivo*, is one of the several challenges of the modeling framework. Such *in-silico* platforms help in developing a better understanding of the diagnosis, progression and treatment of various diseases at a reduced overall cost.

Fig. 1 Representative mixed white and grey matter brain tissue specimen glued to the lower platen of experimental setup ready for testing



2 Materials and Methods

2.1 Specimen Preparation and Experimental Setup

One 10-month-old intact goat brain was obtained from a local slaughterhouse and stored in a Phosphate Buffer Saline (PBS) solution at 4°C temperature. Cuboid-shaped specimens of mixed white and grey matter were excised from cerebrum regions of both hemispheres with the help of a surgical scalpel. The specimens were 30 × 26 mm² in cross sectional area and 10 mm in height.

All the experiments were performed on 5 kN DAK UTM (DAK Inc.) equipped with a load cell of 50N capacity. The bottom face of the specimens was glued to the lower load platen with cyanoacrylate adhesive (see Fig. 1). A piece of sandpaper was used between the platen and specimen to increase the glued area. The specimens were hydrated with PBS solution throughout the experiment to avoid dehydration. A quasi-static compression test was conducted by applying strain up to 28%. The extracted load versus stretch data was converted to engineering stress versus stretch data by dividing the load with the undeformed cross-sectional area of the specimen (see Fig. 2(b)).

2.2 Constitutive Modeling and Data Analysis

The deformation map for a homogeneous, isotropic, incompressible continuum solid subjected to uniaxial compression is given by:

$$x_1 = \lambda_1 X_1; \quad x_2 = \lambda_2 X_2; \quad x_3 = \lambda_3 X_3 \quad (1)$$

where x_i and X_i denote the coordinates in current and undeformed configurations, respectively, and λ_i is the stretch. In uniaxial compression, the stretch can be

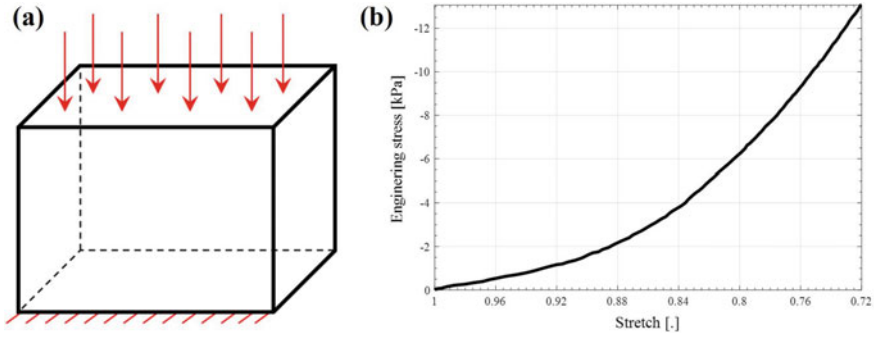


Fig. 2 **a** Representative boundary value problem for the experimental setup along with prescribed boundary conditions; **b** nominal stress versus stretch behaviour of a brain tissue sample in compressive loading

calculated from the relation, $\lambda = 1 - \Delta h/H$, where Δh and H are the actuator displacement in one of the orthogonal directions and original length of the specimen, respectively. The first Piola Kirchhoff stress can be calculated by dividing the force data by the undeformed area of the specimen.

Assuming $\lambda_3 = \lambda$ as applied stretch, for an incompressible material, the volume of the specimen under deformation should not change, which can be written mathematically as:

$$J = \lambda_1 \lambda_2 \lambda_3 = 1 \tag{2}$$

Further, for a homogeneous specimen undergoing uniaxial deformation, the principal stretches can be re-written as (using Eq. 2):

$$\lambda_1 = \lambda_2 = \lambda^{-1/2} \text{ and } \lambda_3 = \lambda \tag{3}$$

Thus, for homogeneous and incompressible deformation, one can write the deformation gradient tensor, \mathbf{F} , as:

$$\mathbf{F} = \begin{bmatrix} 1/\sqrt{\lambda} & 0 & 0 \\ 0 & 1/\sqrt{\lambda} & 0 \\ 0 & 0 & \lambda \end{bmatrix} \tag{4}$$

Since brain tissue shows nonlinear mechanical response, the same has been modeled using a hyperelastic material model. In the present work, a one-term Ogden model was considered with strain energy function (W), expressed in terms of principal stretches as:

$$W = \frac{2\mu}{\alpha^2} (\lambda_1^\alpha + \lambda_2^\alpha + \lambda_3^\alpha - 3) \tag{5}$$

where λ_1, λ_2 and λ_3 are the principal stretches, and μ and α are the material parameters. Further, the principal Cauchy stresses (σ_i) can be expressed in terms of strain energy function (W) as:

$$\sigma_i = \lambda_i \frac{\partial W}{\partial \lambda_i} - p, \quad i = 1, 2, 3 \quad (6)$$

where p is the reactive hydrostatic pressure due to the incompressibility of the material. For the present case, a homogeneous specimen modeled as Ogden incompressible material undergoing uniaxial deformation (in direction - 3) along with traction free boundary conditions for the lateral directions ($\sigma_1 = \sigma_2 = 0$) has been considered. Therefore, the constitutive relation is given by (using Eqs. 5 and 6):

$$\sigma_3 = \sigma = \frac{2\mu}{\alpha} \left(\lambda^\alpha - \lambda^{-\frac{\alpha}{2}} \right) \quad (7)$$

The first Piola-Kirchhoff stress (the engineering stress) in the loading direction can be computed as:

$$P_3 \text{ or } P = \frac{\sigma_3}{\lambda_3} \text{ or } \frac{\sigma}{\lambda} \quad (8)$$

Finally, to calibrate the constitutive model given in the above equation, the *lsqcurvefit* algorithm in MATLAB® was used for the curve fitting using the least square approach.

2.3 Inverse FE Analysis

The inverse FE approach is based on replicating the experimental setup in a boundary value problem. The sample was modeled as a cuboid with dimensions $30 \times 26 \times 10 \text{ mm}^3$ and meshed using hexahedral elements (see Fig. 2(a)). The bottom face of sample in contact with the lower loading platen was constrained to move in x, y and z -directions similar to what has been observed during the experiments. The top face of the specimen was applied with displacement boundary condition to compress the sample to 28% of engineering strain (or $\lambda = 0.72$). For demonstrating the complete framework, a one-term Ogden model was considered to capture the material physics. A MATLAB-based open-source package named GIBBON was used for optimization purposes, including creating the FE model and post-processing the FE analysis results. An open-source FE solver - FEBio was used for conducting the simulations and getting the results in a specified format. The FEBio was coupled to MATLAB using the GIBBON, and an optimization routine was employed to calibrate the material parameters by using the objective function in terms of absolute error (Err), defined by:

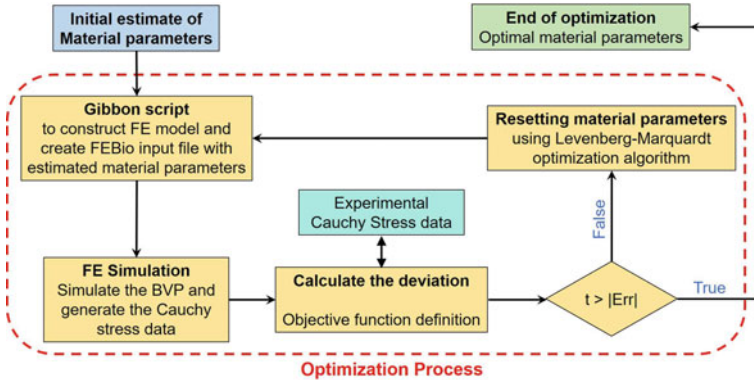


Fig. 3 Flowchart of the optimization procedure for calibrating optimum Ogden hyperelastic material parameters using inverse FE method

$$Err = \sum_{i=1}^N (P_{exp} - P_{comp})^2 \tag{9}$$

where P_{exp} and P_{comp} are the first Piola Kirchoff stress values from the experiments and computed from the FE analysis, respectively, and N are the number of data points. At a particular stretch value, the computed stress value P_{comp} from the FE model was obtained by taking the mean of all elemental stress values. This helps in accounting for the uncertainties, whether in terms of inhomogeneous material response or experimental boundary conditions. The workflow of the optimization procedure using the open-source platforms is shown in Fig. 3.

3 Results and Discussion

Figure 4 reports the results of the optimization routine and their comparison with the experimental data. A close agreement between the curves from experimental data, curve fitting, and inverse FE method can be observed. The optimal set of material parameters for the Ogden hyperelastic model calibrated using the inverse FE analysis and the least square curve fitting is presented in Table 1. The deviation between the stiffness parameter (μ) extracted from both approaches is significant. The discrepancy between the two values could be explained using many assumptions considered for curve fitting, most of which could be omitted using the FE approach. One simplification in terms of experimental boundary conditions is to assume the samples to be glued to the platens. This induces stresses in the transverse direction, which ultimately violates the assumption of the uniaxial nature of the test [5].

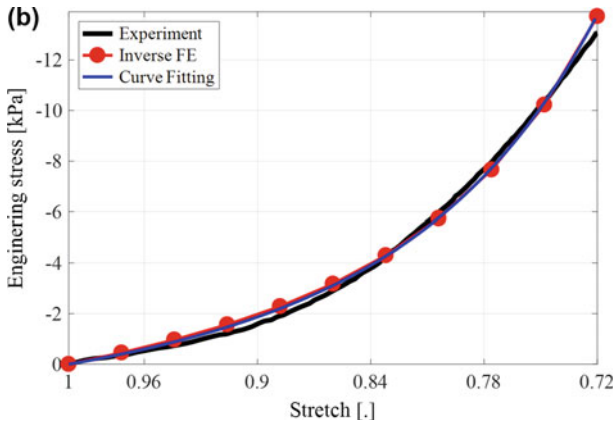


Fig. 4 Comparison of the *ex-vivo* nominal stress versus stretch data in compression with model data from curve fitting and inverse FE method

Table 1 Extracted Ogden parameters from curve fitting and inverse FE method

Procedure	μ (kPa)	α
Least square curve fitting	4.37	-6
Inverse finite element method	3.73	-6.06

The brain tissue has also been found to exhibit compressibility and viscoelasticity as its material characteristics [3]. The present FE framework can be extended to include the brain tissue’s compressibility and its viscoelastic nature. Further, experimental data acquired using other loading modes such as uniaxial tension, simple shear or biaxial could be used to redefine the objective function. A unique set of material parameters could then be extracted, representing the material’s behavior in the possible loading or boundary modes. The pipeline demonstrated in the present study has been developed for simple loading modes only. Further studies could be carried out for data acquisition under complicated deformation modes.

Further, testing soft tissues under the ideal uniaxial deformation conditions is practically very difficult. Setting up a testing procedure that yields ideal uniaxial conditions while testing the soft tissue specimen faces significant challenges. One of the challenges is difficulty gripping the specimen between the loading platens because of the soft and slippery nature of the tissue. A thin liquid film is used for the compression mode between the tissue surface and loading platen to reduce the friction between the two. This procedure, however, worsens the testing procedure.

Similarly, for the tensile testing, clamping the sample using grips is not a feasible idea. Lastly, excising a long enough dog-bone-shaped specimen from tissues such that the middle portion of the specimen away from the boundaries could be assumed to be

in the state of pure uniaxial deformation is practically impossible. Also, as reported previously, the brain tissue behaves like a biphasic material with solid and fluid domains [8]. The FE framework can further be extended to incorporate a poroelastic material model with relevant experimental results.

4 Conclusion

The presented framework for material parameter calibration using the inverse FE method was found to be more robust than the standard least square curve fitting method. The framework could be applied to any soft material provided the experimental data is available. The framework also offers the flexibility to amend the workflow at any stage, such as adapting different FE material models, objective function definitions based on the availability of the experimental data, and optimization algorithms. The method could also be combined with physics-informed neural networks using machine learning based approaches to replace the computationally costly FE simulations.

Acknowledgements This project is supported by the Department of Health Research, Ministry of Health and Family Welfare, Government of India, through grant number DHR-ICMR/GIA/18/18/2020.

References

1. Awasthi A, Gautam U, Bhaskar S, Roy S (2020) Biomechanical modelling and computer aided simulation of deep brain retraction in neurosurgery. *Comput Methods Programs Biomed* 197:105688. <https://doi.org/10.1016/j.cmpb.2020.105688>
2. Delorme S, Laroche D, DiRaddo R, Del Maestro RF (2012) NeuroTouch: a physics-based virtual simulator for cranial microneurosurgery training. *Oper Neurosurg* 71(suppl_1):ons32–ons42. <https://doi.org/10.1227/NEU.0b013e318249c744>
3. Budday S et al (2017) Mechanical characterization of human brain tissue. *Acta Biomater* 48:319–340. <https://doi.org/10.1016/j.actbio.2016.10.036>
4. Miller K (2005) Method of testing very soft biological tissues in compression. *J Biomech* 38(1):153–158. <https://doi.org/10.1016/j.jbiomech.2004.03.004>
5. Voyiadjis GZ, Samadi-Dooki A (2018) Hyperelastic modeling of the human brain tissue: effects of no-slip boundary condition and compressibility on the uniaxial deformation. *J Mech Behav Biomed Mater* 83:63–78. <https://doi.org/10.1016/j.jmbbm.2018.04.011>
6. Moerman KM (2018) GIBBON: the geometry and image-based bioengineering add-on. *J Open Source Softw* 3(22):506. <https://doi.org/10.21105/joss.00506>
7. Maa, SA, Ellis BJ, Ateshian GA, Weiss JA (2012) FEBio: finite elements for biomechanics. *J Biomech Eng* 134(1). <https://doi.org/10.1115/1.4005694>
8. Ehlers W, Wagner A (2018) Multiscale aspects in the multiphase modelling of human brain tissue. In: *Biomedical technology. Lecture notes in applied and computational mechanics*, pp 3–13. Springer, Cham. https://doi.org/10.1007/978-3-319-59548-1_1

Porosity/Distributed Resistance (PDR) Modelling in the CFD Solver PDRFOAM



Manish Dhiman , V. Meysiva, P. Sathiah,
and Vagesh D. Narasimhamurthy 

Abstract The accidental release of hazardous gases might happen in various chemical plants, storage tanks, or in their transportation. The gas when released, interacts with the surrounding structures, i.e. vessels and pipelines, etc. It is also established that the objects of varying sizes do have an impact on the flow turbulence and combustion phenomena in gas explosions (Hjertager., Modelling, Identification and Control, 1985). The prediction of such explosions due to accidental leakage is usually modelled through computational fluid dynamics (CFD) approach. Porosity/distributed resistance (PDR), a pragmatic approach that takes into consideration the effects of numerous complicated geometries in a CFD solution, is a natural choice for this purpose. Sub-grid models for quantification of objects, that are smaller than the grids are formulated to integrate the under resolved nature of the simulations. In the current study, a PDR based CFD solver, PDRFOAM is used to explore non-reactive flows over pipe bundles of various configurations. We compared the modelled mean velocities and fluctuations with the experimental results to seek the efficacy of the solver. It is observed that the qualitative trends for the quantities are captured even for low mesh resolutions, which is in contrast to the standard body fitted mesh approach. Further, the solver is able to predict the maximum turbulent kinetic energy levels in the vicinity of the pipe/obstacle appreciably. The efficacy for the solver in congested environment is also explored for the cases where pipes are placed side-by-side to each other.

M. Dhiman (✉) · V. D. Narasimhamurthy
Department of Applied Mechanics, Indian Institute of Technology Madras, Chennai 600036, India
e-mail: am21ipf01@smail.iitm.ac.in

V. D. Narasimhamurthy
e-mail: vagesh@iitm.ac.in

V. Meysiva
Department of Chemical Engineering, Indian Institute of Technology Madras, Chennai 600036,
India
e-mail: ch17b008@smail.iitm.ac.in

P. Sathiah
Shell Technology Centre Bangalore, Shell India Markets Private Limited, Bangalore 562149,
Karnataka, India
e-mail: pratap.sathiah@shell.com

Keywords PDR modelling · Open-source · Sub-grid models

1 Introduction

In various industrial applications, the hazardous chemical leak may happen while producing, transporting or storing flammable gases. The released gases, after interacting with the surrounding structures, can get ignited immediately leading to a jet fire or vapour cloud explosion. Thereby, to predict the extent of the damage and to minimize the harm, it is a prerequisite, to pre-empt the assessment and prepare the emergency response plan for the concerned establishment. Industrial combustion problems are intricate due to the presence of the various obstacles in the flow domain (pipes and blocks etc.). The effect of an obstacle of few millimetres in a domain of several meters can be significant in examining the flame propagation [1, 2]. Consequently, various mathematical models are employed to simulate and predict the explosion of gases, when they form flammable mixture and get ignited after certain time delay. Unfortunately, the standard CFD solvers for turbulent combustion become impractical owing to the high computational requirements for the fully resolved simulations. Therefore, commercial CFD solvers such as FLACS [3] is predominantly considered to predict the explosion of gases around the confined domains. The effect of release rate and obstacles on the release of carbon dioxide in a confined framework employing Ansys FLUENT [4] have been explored [5]. Similarly, Kassomenos *et al.* [6] studied the dispersion of vinyl chloride in an industrial establishment and assessed its impact on the workers. There have been many studies in the past decade which demonstrated a reasonable agreement between the CFD assessments and the experimental measurements in this field [7, 8].

The efficacy of a model is always a major concern in CFD investigations. In order to use a prescribed model with confidence, the veracity of the simulated results must be achieved with the standard experimental observations [9]. Many studies in the past have suggested that the Reynolds averaged Navier-Stokes (RANS) models are able to predict the gas dispersion effectively [7, 8, 10]. Few studies [10, 11] have indicated that the standard $\kappa - \epsilon$ and shear stress Transport (SST) $k - \omega$ models over-predicts the concentrations at various probe points. Although there have been another set of studies [12, 13], which proposed that the results from $\kappa - \epsilon$ models are acceptable. However, for realistic modelling of the physical phenomena, the consideration of small scale obstacles is absolutely important. The models based on PDR (Porosity/distributed resistance) approach have been found to be a good option for estimating the extent of a gas release in industrial set ups [14–16]. In this approach, the RANS approach $\kappa - \epsilon$ model is modified with sub-grid models in order to take into account the drag and turbulence generated by obstacles that are smaller than the grid cells. It is worth mentioning here that one should not confuse or infer sub grid models for obstacles in PDRFOAM as that of sub-grid models in *Large Eddy simulations* (LES).

PDRFOAM (based on Porosity/distributed resistance methodology) [14], a variant of open-source CFD software OPENFOAM [17], is considered in the present study. Here, we have tried to assess the efficacy of this solver by comparing the modelled quantities such as mean velocity and fluctuations, with the results from the various *non-reacting* flows over pipe bundles [15, 18, 19].

2 Porosity/Distributed Resistance

2.1 Brief History

The introduction of PDR approach for simulating the fluid flow was taken up, by Patankar and Spalding [20]. The gradual extension of this method to the turbulent flows was then carried forward [21]. Further, Hjertager [22] adopted this PDR approach in the software FLACS for simulating the gas explosions. Thereafter, Christian Michelson Institute (CMI) extended the applicability of the solver to various off-shore facilities which also led to the updated versions of FLACS. Recently, Shell started [14] the development of the open source platform PDRFOAM, which is of interest in this study.

2.2 Numerical Methodology

The PDRFOAM solver, deciphers the Favre averaged Navier-Stokes governing equations for fluids. The model incorporates the equations for mass, momentum, enthalpy, fuel mass fraction and mixture fraction simultaneously. Turbulence model based on Eddy viscosity, such as, the standard $\kappa - \epsilon$ model with certain modifications is considered. However, in the present study, the reacting and heat transfer flows are not considered and therefore, the equations related to them are not presented.

$$\frac{\partial}{\partial t}(\beta_v \rho) + \frac{\partial}{\partial x_j}(\beta_j \rho u_j) = \frac{m}{V} \quad (1)$$

$$\frac{\partial}{\partial t}(\beta_v \rho u_i) + \frac{\partial}{\partial x_j}(\beta_j \rho u_i u_j) = -\frac{\partial}{\partial x_j}(\beta_v p \delta_{ij}) + \frac{\partial}{\partial x_j}(\beta_j \tau_{ij}) - F_{o,i} + \beta_v(\rho - \rho_o) \quad (2)$$

Equations (1) and (2) shows the transport equations for conservation of mass and momentum respectively. Here, ρ is the fluid density, u_i is the fluid velocity in the x_i direction, τ_{ij} is the stress tensor, p is the pressure. The fluid density (ρ) is shown for the general uniformity. $\frac{m}{V}$ denotes the source term for mass. These Eqs. (1) and (2) are generic equations except for the introduction of terms β_v and β_j . These terms portray

the PDR concept in the transport equations. β_v is the volume fraction engaged by the fluid in the control volume, and β_j is the area fraction accessible for the flow. These are the quantities computed for a particular mesh. $F_{o,i}$ is the sub-grid drag source term which is considered as the momentum loss. Gravity (g_o) is not considered in this study and thereby, not shown in the standard equations.

$$\tau_{ij} = \mu_{eff} \left(\frac{\partial u_i}{\partial x_j} + \frac{\partial u_j}{\partial x_i} \right) - \frac{2}{3} \left(\rho k + \mu_{eff} \frac{\partial u_k}{\partial x_k} \right) \delta_{ij} \quad (3)$$

$$\frac{\partial}{\partial t} (\beta_v \rho k) + \frac{\partial}{\partial x_j} (\beta_j \rho u_j k) = \frac{\partial}{\partial x_j} \left(\beta_j \frac{\mu_{eff}}{\sigma_k} \frac{\partial k}{\partial x_j} \right) + \beta_v \rho P_k - \beta_v \rho \epsilon \quad (4)$$

$$\frac{\partial}{\partial t} (\beta_v \rho \epsilon) + \frac{\partial}{\partial x_j} (\beta_j \rho u_j \epsilon) = \frac{\partial}{\partial x_j} \left(\beta_j \frac{\mu_{eff}}{\sigma_\epsilon} \frac{\partial \epsilon}{\partial x_j} \right) + \beta_v \rho P_\epsilon - C_{2\epsilon} \beta_v \rho \frac{\epsilon^2}{k} \quad (5)$$

$$P_k = \frac{\tau_{ij} \partial u_i}{\partial x_j} - \mu_{eff} \frac{1}{\rho} \frac{\partial \rho}{\partial x_i} + G_w + G_o \quad (6)$$

$$P_\epsilon = \frac{C_{1\epsilon} \epsilon}{\kappa} (1 + C_{3\epsilon}) \quad (7)$$

The $\kappa - \epsilon$ model is framed as Eqs. (3 to 7) in PDRFOAM. The stress term is modelled through Boussinesq hypothesis and Eq. (3) also manifests the effective viscosity (μ_{eff}) term. The production term P_ϵ , is also shown in Eq. (7). Production rate of turbulence kinetic energy (P_k), takes into consideration the effect of fluid strain, wall function (G_w), and sub-grid objects (G_o) respectively. It is to be noted that the model constants are represented as C_μ , $C_{1\epsilon}$, $C_{2\epsilon}$ and $C_{3\epsilon}$. Similarly turbulence Schmidt numbers are represented as σ_k and σ_ϵ respectively.

The PDR based CFD tools employ structured Cartesian grids as shown in Fig. 1. This is where sub-grid models in PDR concept come to the forefront. There are objects which produces drag and turbulence and their contribution must be taken into account. The drag $F_{o,i}$ provided by the sub-grid objects is denoted as Eq. (8), where C_D and A are the drag coefficient and area, respectively. The methodology suggested by Sha and Launder [21], is considered for the turbulence generated by such objects. Here, C_o is considered as a constant with f_i as the geometry parameter. This Eq. (9), constitutes the sub-grid turbulence model in PDRFOAM.

$$F_{o,i} = \frac{1}{2} \rho C_D A u_i |u_i| \quad (8)$$

$$G_o = C_o \beta_v \rho |\vec{u}| u_j^2 f_j \quad (9)$$

Figure 1 shows the mesh formulation in the PDR methodology. In the CAD/PDR set fields directory of PDRFOAM, the inclusion of volume porosity (β_v), and the area porosity, (A_w), for a given configuration (mesh and geometry) is computed. CADPDR/PDR set fields takes input a series of files (“obstacle files”) describing

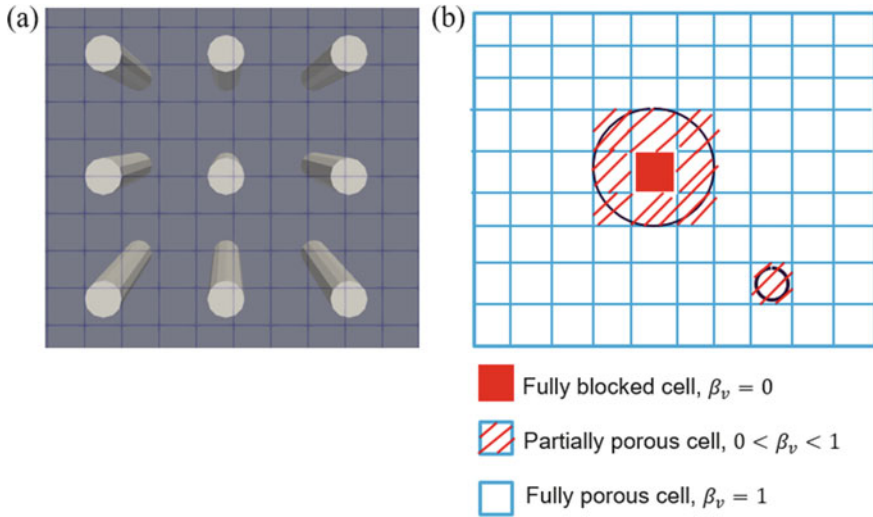


Fig. 1 a Mesh representation for obstacle is portrayed b Plot showing porosities for the Cartesian grid cells

3D CAD geometry of a problem containing pipes, blocks, walls or other obstacle. From these it generates the fields needed by PDRFOAM; such as set of geometrical obstructions to determine the equivalent blockage effects when setting the cases for PDRFOAM. The fields such as Lobs (representative diameter for obstacles) are obtained. Finally, output fields are availed. Figure 1(b) shows the representation of the porosity pattern for any obstacle immersed in a Cartesian mesh.

3 Test Cases

3.1 Problem Definition

Primarily, the 2D non-reacting flows in references [15, 18, 19] are examined. Four different flow geometries are considered as shown in Fig. 2. Firstly, flow over a cylindrical obstacle is considered, as exhibited in Fig. 2(a). The initial fluid velocities are taken as 25 m/s for both the cases in Fig. 2(a and b). The diameter (D) of the obstacle is considered as 0.5 m, however, for 5 obstacle case (b), diameter of 0.17 m is undertaken for each pipe. The measurements are taken at a distance of 1 m, and 0.66 m downstream of the obstacle centreline, respectively for both the cases as in (a) and (b). The dotted line indicates the probe location, from where the statistical data is reported. The comparison for the quantities with the conventional simpleFOAM solver in OPENFOAM is also examined [17]. The test cases are also extended to one column of 5 obstacles and two columns of 5 obstacles each as shown in Fig. 2(c) and

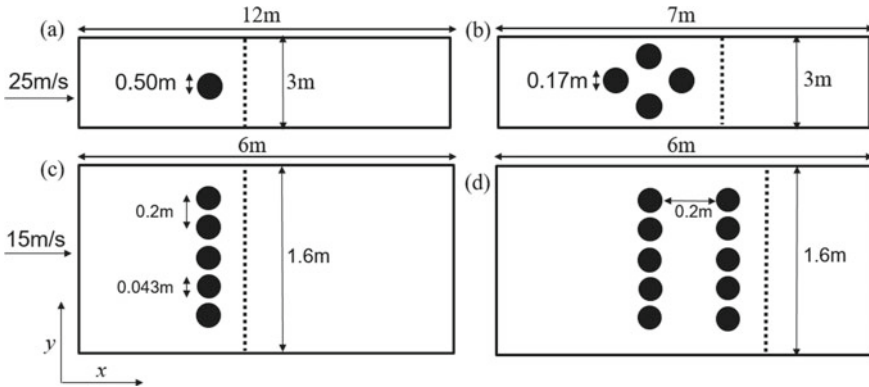


Fig. 2 Schematic of the geometries considered in this study; **a** Single obstacle **b** 5 obstacle in a star-like configuration **c** single column of obstacles, and **d** two columns of obstacles. Dashed line denotes the probe point for reporting quantities. Axes are given as a guide to the eye

Table 1 Reynolds number for the different test cases. Re_o is based on obstacle diameter

Test case	(a)	(b)	(c), (d)
Re_o	1,531,250	520,625	79,012.5

(d), as considered in British gas report from project **EMERGE** [19]. The Reynolds number based on obstacle diameter for all the configurations is also expressed in Table 1.

3.2 Boundary Conditions

As mentioned above, the effect of congestion (number of obstacles) is investigated to assess the capability of the solver. In the current non-reacting flow study, air is considered as the working fluid. Free slip boundary condition is employed on the bottom and top walls with zero-gauge pressure at the outlet. Uniform inlet velocity is considered for all the cases. Bluff bodies are represented by the sub-grid models.

4 Results and Discussion

4.1 Single obstacle

The modelled mean velocities and fluctuations for a single pipe case (Fig. 3(a)), are compared with the CMR results as reported in Ref. [15]. The data obtained from

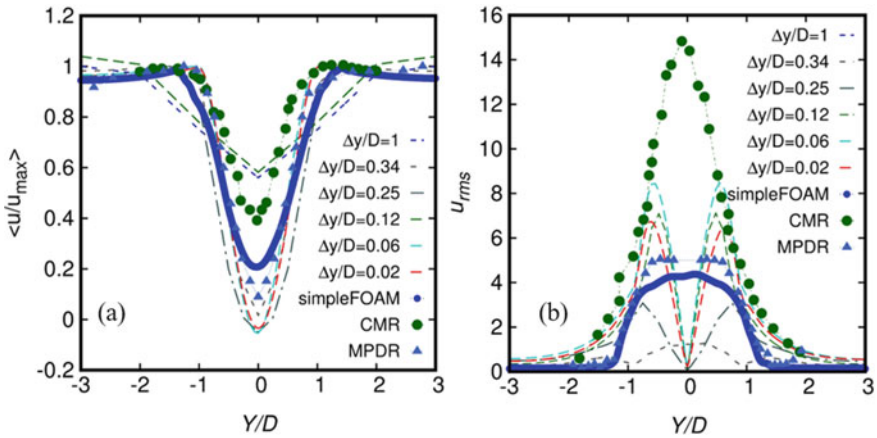


Fig. 3 a Normalized mean velocity b U_{rms} , for different grids, in comparison with the numerical and experimental results

the body fitted approach (simpleFOAM solver) for the finer grid ($\Delta y/D = 0.02$) is also plotted against the results procured through different grid sizes employing the PDRFOAM approach. The comparison is also extended to the results obtained using the McUNewt-MPDR approach [23]. Figure 3 demonstrate that the trends for mean velocities, and u_{rms} can be readily captured with over-prediction in the plots at moderate to higher grids can be sighted. Moreover, Fig. 3(a), suggests that there is no significant variation in mean velocities for a coarser grid ($\Delta y/D = 0.1$) in PDRFOAM while comparing with the CMR data. The similar trend is also observed for fluctuating velocities. The under prediction in the plot is visible for all the grid sizes especially in the rear side of the obstacle in the downstream where a dip in the plots can be seen due to the interstitial velocities induced by the obstacle.

It can be depicted that the sub-grid models are sensitive to the grid resolution. However, it is also established that, when the length scale of the obstacle is much smaller than the cell width (Δy), evaluation of PDR is satisfactory [15]. This is in contrast to the case when the cell width (Δy), is small compared to the obstacle diameter; the usual approach (body fitted grids) in standard CFD solvers. Though, the results from the simpleFOAM solver captures the trends, but it captures the trend at a significant computational cost. This suggests that the PDRFOAM is viable for configurations where the obstacle size is small compared to the cell size. Furthermore, computational cost is also reduced significantly.

Figure 4 shows the instantaneous x -velocity distribution plot for the single obstacle at different grid resolutions. The solver is able to capture the unsteadiness in the flow with the increment in grid resolution. Nevertheless, the modelled mean velocities are able to imitate the trends even at lower grids as is evidenced from Fig. 3(a). The top panel ($\Delta y/D = 1$) suggests that further refinement is required to capture the flow fields correctly. The unsteadiness in the flow is captured with the increase in mesh resolution.

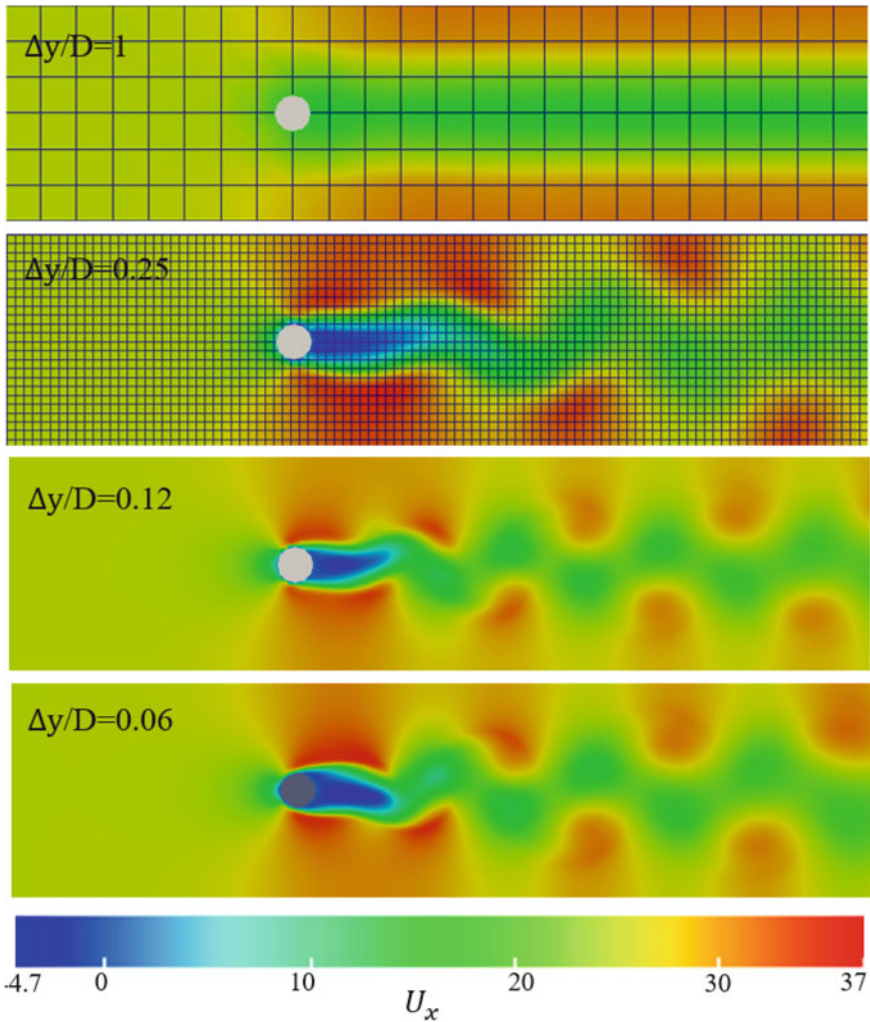


Fig. 4 Instantaneous x -velocity contours, along with the representation of the mesh considered for the single obstacle case

Figure 5 shows the turbulent kinetic energy contours for the single obstacle case. The instantaneous turbulent kinetic energy contours suggest that the turbulent kinetic energy (TKE) from the fluid flow velocity is significantly high in the vicinity of the obstacle (especially in the first panel, $\Delta y/D = 1$). Nonetheless, the panel is significantly coarser. TKE is produced by the shearing of fluid layers, which in turns form a cascade sort of system in the fluid layers before dissipating to low scales. It is understood that for the rate of combustion the instantaneous TKE in the vicinity of the obstacle plays a key role in the flame propagation [14, 15]. It is also observed from the panels that the maximum TKE increases with the increment in the grid

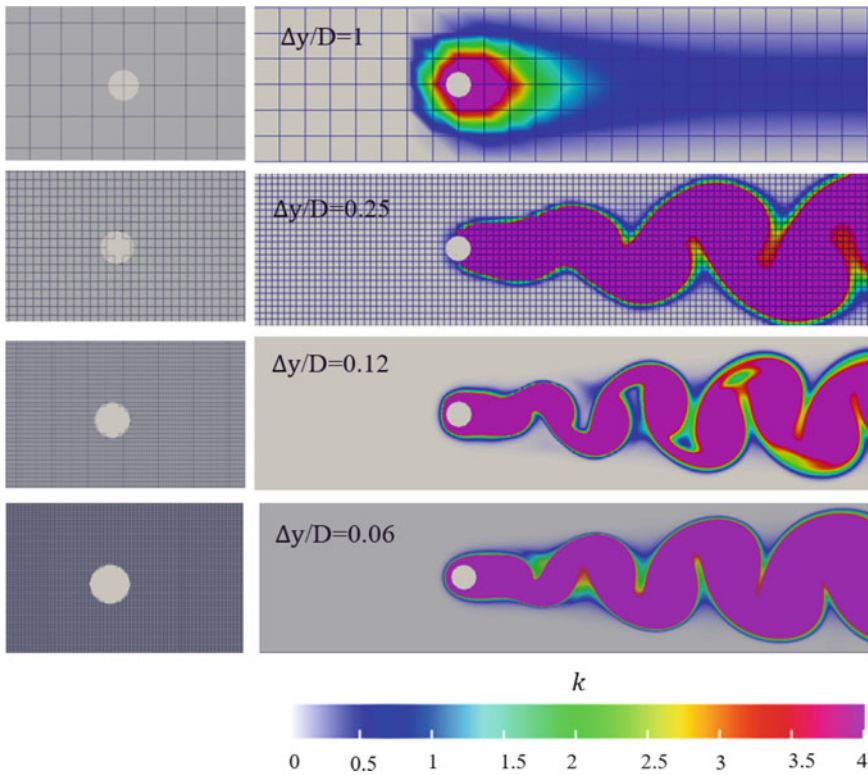


Fig. 5 The corresponding instantaneous turbulent kinetic energy ($k, m^2/s^2$) contours computed in PDRFOAM. The panels in the right side shows the mesh resolution for the corresponding grid sizes ($\Delta y/D$)

resolutions suggesting that the models based on sub-grid are also able to forecast the maximum levels with precision (though varying with refinement). The peak values of turbulent kinetic energy zone are found in the recirculating region in the vicinity of the obstacle which is also observed in a similar study [16].

4.2 Star-like Five obstacles

The accuracy and efficacy of the solver is also explored for the case when more than one obstacle (congestion) is present in the flow. Figure 6 shows the mean velocities and fluctuations for the schematic shown in Fig. 2(b). The dip in the velocity field is also observed (as in the line for single obstacle case) in the downstream with the increment in the grid resolution. However, the dip is not significantly appreciable for low mesh resolutions. Qualitatively, the trends are readily captured for mean velocities with both the experimental as well as modified porosity distributed resistance

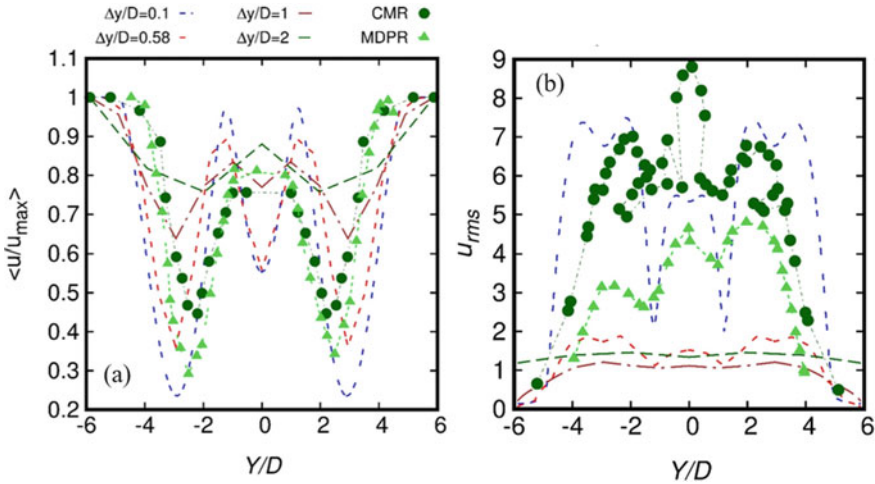


Fig. 6 **a** Normalized mean velocity **b** U_{rms} , for different grids, in comparison with the numerical and experimental results for five obstacles in a star-like configuration. Symbols mean the same in **b** as in **a**

code as in [23]. Whilst the smallest grids are inherently showing under-prediction with the experimental values, higher grid sizes still resemble the trends. The similar course is also observed for fluctuating velocities (Fig. 6(b)). The smaller resolution is having under prediction, whereas higher grid does resemble the trends of CMR experiments qualitatively.

The instantaneous TKE contour plot for star-like configuration is shown in Fig. 7. Whereas the top panel ($\Delta y/D = 2$) is significantly coarser, still the instantaneous TKE contour plots suggests that for coarser grids, maximum TKE levels ($\Delta y/D = 2, 1, 0.58$) are in the similar range at the vicinity of the obstacle across all the panels.

4.3 Obstacles in a single column

The effect of congestion is also expanded to configurations where obstacles are placed in-line in a single column. The schematic shown in Fig. 2(c) portrays the configuration considered in this section. The experimental data from Project EMERGE of the British gas experiments [19] is contemplated, and an attempt has been made to validate them with PDRFOAM solver.

In Fig. 8, five obstacles are placed side-by-side to each other and likewise, as in the previous figures, the quantities such as mean velocities and fluctuating velocities are reported. Likewise in the single obstacle case, the trends are readily captured at higher refinements ($\Delta y/D = 0.12$). At low mesh resolution, the dips in the flow profile induced by the obstacles, is not observed appreciably. There is, again a significant under-prediction at smaller grid resolutions. The similar regime is also exhibited

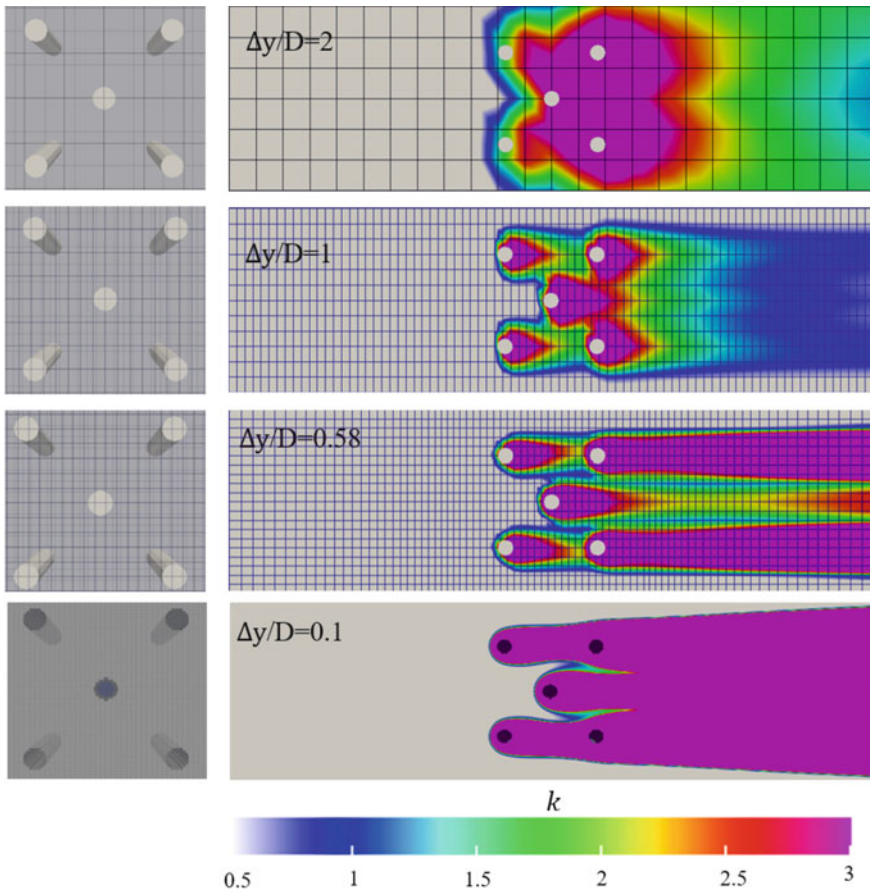


Fig. 7 The instantaneous turbulent kinetic energy ($k, m^2/s^2$) contours computed in PDRFOAM. The panels in the right side shows the mesh resolution for corresponding ($\Delta y/D$)

from the velocity fluctuation plots with ready capture at higher refinements ($\Delta y/D = 0.12$). It is to be noted here that Fig. 8(a, b) shows the quantities at a distance of “2D” from the obstacle centreline in the downstream, whereas figures (c, d) resembles them at a “4D” distance. It is clearly visible that at a further distance in the downstream the veracity in the trends deviates to a certain extent which is in contrast to what is observed at probe points closer to the obstacle (Fig. 8a and b). The recirculation in the flow is also observed, and is captured only at higher grid resolutions.

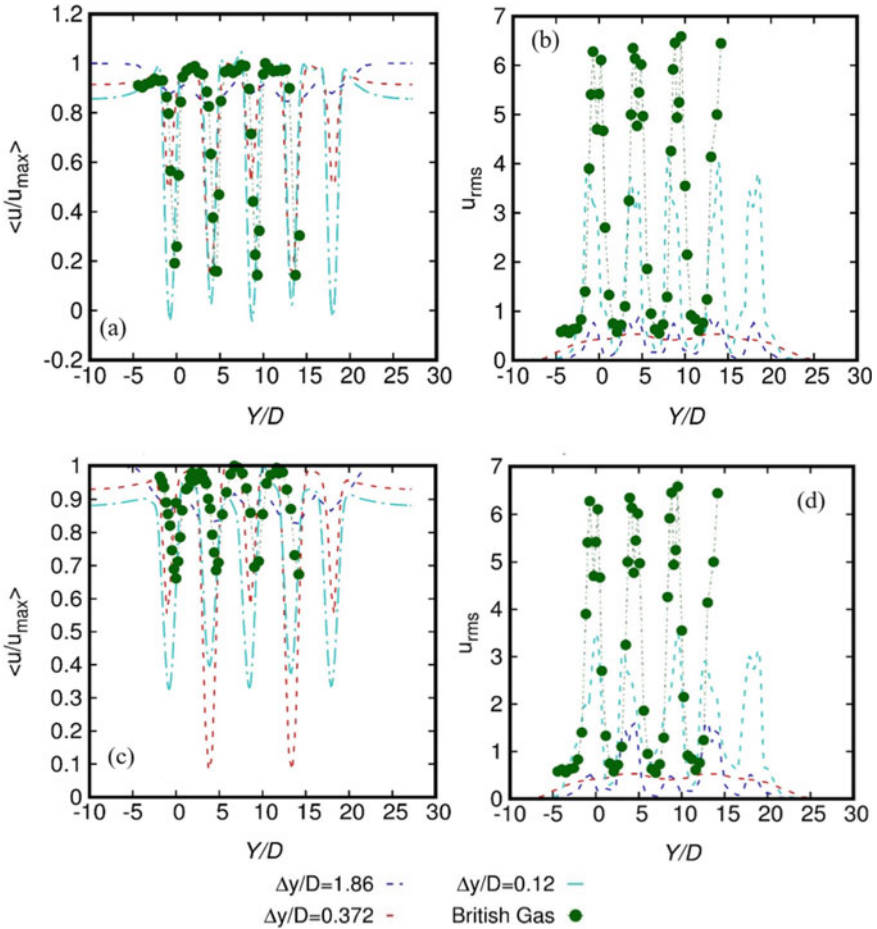


Fig. 8 **a** Normalized mean velocity **b** U_{rms} , for different grids, in comparison with the experimental results for five rows of obstacles in a single column at distance of “2D” from the centre of the obstacle in downstream. Similarly, **c** and **d** for mean velocity and fluctuations, at a distance “4D” from the obstacle in the downstream

The instantaneous TKE (k) contour plot for obstacles placed in a single column is shown in Fig. 9. The top panel with coarser mesh is depicting a low TKE in comparison to the moderate to higher TKE observed in the vicinity of the obstacle for finer grid resolutions. The variation in TKE is more pronounced at ($\Delta y/D = 0.12$), with oscillating fumes in the downstream. Thereby, comprehensive apprehension is evidenced in mean velocities for such a grid resolution.

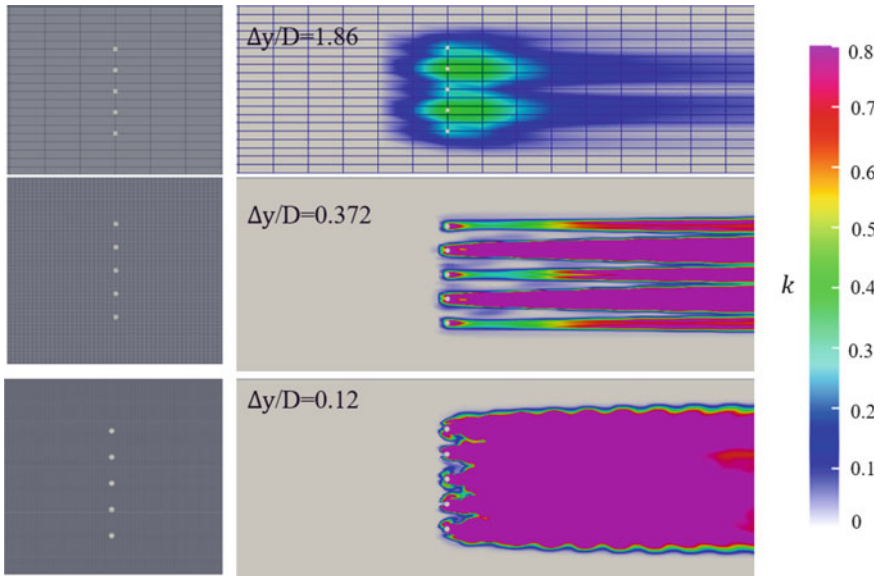


Fig. 9 Instantaneous turbulent kinetic energy ($k, m^2/s^2$) contours for single column of obstacles computed in PDRFOAM. The panels in the right side shows the mesh resolution for corresponding ($\Delta y/D$)

4.4 Obstacles in two columns

Out stretching the previous case to a scenario, where obstacles are placed side-by-side to each other in two columns so as to assess the solver for rigorous congestion, is also undertaken. The schematic for such configuration can be envisioned from Fig. 2(d). Unlike that in previous sub-section, the coarser mesh ($\Delta y/D = 1.86$) is also able to establish the veracity with the British gas results as can be observed from Fig. 10. The dips in the flow profile is clearly visible suggesting that at higher congestion, the solver is able to predict the trends with an appreciable level of precision. The trends are captured thoroughly with the quantitative resemblance as well. The accuracy in the prediction is also visible at probes located “4D” distance from the obstacle centreline (Fig. 10c and d). Moreover, there is no appreciable difference in the fields at both the probe points; the trend which is also observed in British gas experiments.

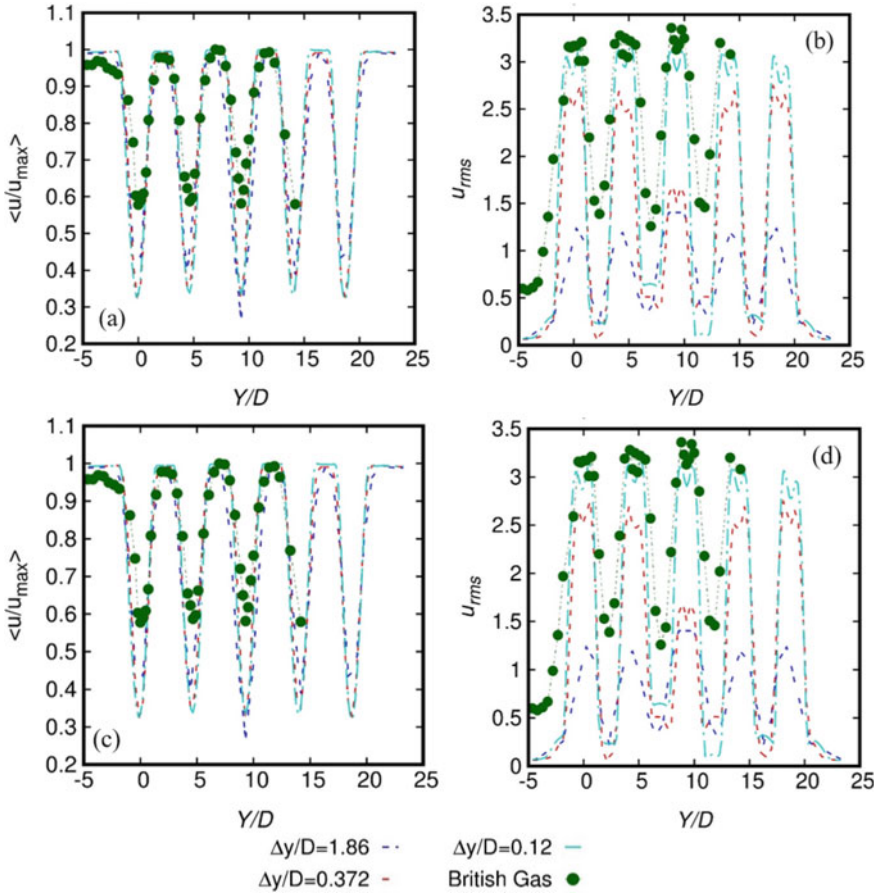


Fig. 10 a Normalized mean velocity, b U_{rms} , for different grids, in comparison with the experimental results for five rows of obstacles in two columns at distance of “2D” from the centre of the obstacle in downstream, c, d at a distance “4D”

The instantaneous TKE (k) contour plot for obstacles is shown in Fig. 11. Unlike that in previous sub-section, the top panel with coarser mesh is also depicting the moderate to higher TKE in the vicinity of the obstacle; however, not so appreciably as in finer grid resolutions. The variation in TKE is more pronounced at ($\Delta y/D = 0.12$), with fumes in the downstream. It can also be observed from the panels in Fig. 11 that the maximum TKE increases with the increment in the grid resolutions suggesting that the models based on sub-grid are able to forecast the maximum levels with certain degree of obscurity. Nonetheless, the solver is still capable to assess the quantities and showcase that by and large, this solver holds true in embracing congestion in the flow domain.

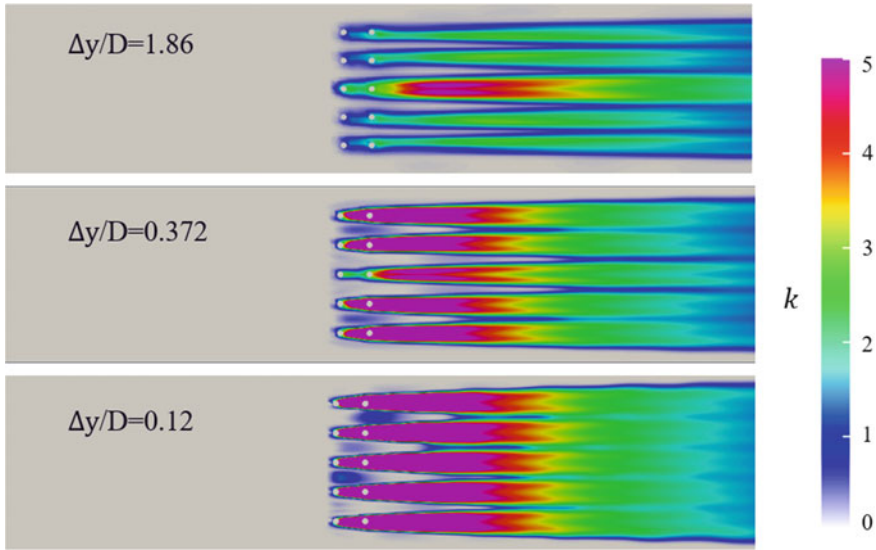


Fig. 11 Instantaneous turbulent kinetic energy ($k, m^2/s^2$) contours for two columns of obstacles computed in PDRFOAM. Refer to Fig. 9 for mesh representation

5 Conclusions

In this study, the assessment and the accuracy of the solver PDRFOAM is investigated for non-reacting flows over various pipe bundles. Overall, it is observed that the solver is able to predict the quantities such as mean velocities and fluctuations, for the cases considered at a significantly low computational cost. For each case, there is an optimal grid size after which the quantities does not deviate. At higher congestion, the solver scrutinizes the effect of obstacles efficiently at a reasonably small grid resolution (especially for the case when the obstacles are placed in two columns). For lower grid resolutions, the turbulent kinetic energy (TKE) trends suggests that the solver is able to capture the maxima in the vicinity of the obstacle. This observation would be handy for the cases while incorporating the combustion in the domain (reacting flows). The solver indicates that PDR methodology can be a good alternative to the standard body fitted mesh approach.

Acknowledgements Authors would like to express gratitude to Douglas Michael Johnson, DNV, for providing the report from Project **EMERGE**.

References

1. Skjold T, Pedersen H, Bernard L, Middha P, Narasimhamurthy VD, Landvik T, Lea T, Pesch L

- (2013) A matter of life and death: validating, qualifying and documenting models for simulating flow-related accident scenarios in the process industry. *Chem Eng Trans* 31:187–192. <https://doi.org/10.3303/CET1331032>
2. Hisken H, Enstad GA, Narasimhamurthy VD (2016) Suppression of vortex shedding and its mitigation effect in gas explosions: an experimental study. *J Loss Prev Process Ind* 43:242–254. <https://doi.org/10.1016/j.jlp.2016.05.017>
 3. Gexcon AS (2020) FLACS v20. <https://www.gexcon.com/products-services/flacs-software/>
 4. ANSYS (2019) ANSYS academic research fluent, release 19.2, help system, theory guide. ANSYS Inc., Canonsburg
 5. Dong L, Zuo H, Hu L, Yang B, Li L, Wu L (2017) Simulation of heavy gas dispersion in a large indoor space using CFD model. *J Loss Prev Process Ind* 46:1–12. <https://doi.org/10.1016/j.jlp.2017.01.012>
 6. Kassomenos P, Karayannis A, Panagopoulos I, Karakitsios S, Petrakis M (2008) Modelling the dispersion of a toxic substance at a workplace. *Environ Model Softw* 23(1):82–89. <https://doi.org/10.1016/j.envsoft.2007.05.003>
 7. Moen A, Mauri L, Narasimhamurthy VD (2019) Comparison of k-ε models in gaseous release and dispersion simulations using the CFD code FLACS. *Process Saf Environ Prot* 130:306–316. <https://doi.org/10.1016/j.psep.2019.08.016>
 8. Gant SE, Narasimhamurthy VD, Skjold T, Jamois D, Proust C (2014) Evaluation of multi-phase atmospheric dispersion models for application to Carbon Capture and Storage. *J Loss Prev Process Ind* 32:286–298. <https://doi.org/10.1016/j.jlp.2014.09.014>
 9. Chen Q, Srebric J (2002) A procedure for verification, validation, and reporting of indoor environment CFD analyses. *HVAC&R Res* 8(2):201–216. <https://doi.org/10.1080/10789669.2002.10391437>
 10. Tauseef SM, Rashtchian D, Abbasi SA (2011) CFD-based simulation of dense gas dispersion in presence of obstacles. *J Loss Prev Process Ind* 24(4):371–376. <https://doi.org/10.1016/j.jlp.2011.01.014>
 11. Sklavounos S, Rigas F (2004) Validation of turbulence models in heavy gas dispersion over obstacles. *J Hazard Mater* 108(1–2):9–20. <https://doi.org/10.1016/j.jhazmat.2004.01.005>
 12. Xing J, Liu Z, Huang P, Feng C, Zhou Y, Zhang D, Wang F (2013) Experimental and numerical study of the dispersion of carbon dioxide plume. *J Hazard Mater* 256–257:40–48. <https://doi.org/10.1016/j.jhazmat.2013.03.066>
 13. Cheng C, Tan W, Liu L (2014) Numerical simulation of water curtain application for ammonia release dispersion. *J Loss Prev Process Ind* 30:105–112. <https://doi.org/10.1016/j.jlp.2014.05.003>
 14. Puttock JS, Chakraborty D, Farmayan W (2014) Gas explosion modelling using PDRFoam. In: 10th international symposium on hazards, X ISHPMIE, Bergen, Norway, 10–14 June 2014
 15. Vianna S, Cant R (2010) Modified porosity approach and laminar flamelet modelling for advanced simulation of accidental explosions. *J Loss Prev Process Ind* 23:3–14. <https://doi.org/10.1016/j.jlp.2009.08.002>
 16. Narasimhamurthy VD, Hisken H, Atanga, G, Skjold T (2015) Porosity/distributed resistance modelling for industrial CFD applications. In: 8th national conference on computational mechanics (MekIT 2015), Trondheim, Norway
 17. Weller HG, Tabor G, Jasak H, Fureby C (1998) A tensorial approach to computational continuum mechanics using object-oriented techniques. *Comput Phys* 12:620. <https://doi.org/10.1063/1.168744>
 18. Arntzen BJ (1998) Modelling of turbulence and combustion for simulation of gas explosion in complex geometries. Ph.D. thesis, The Norwegian University of Science and Technology, Division of Applied Mechanics, Thermodynamics and Fluid Dynamics
 19. Rogers M (1995) Project EMERGE measurement of turbulent characteristics and drag loads on pipework obstacles in steady unidirectional flows. British Gas Research and Technology, GRCR, 0610
 20. Patankar SV, Spalding DB (1974) A calculation procedure for the transient and steady state behavior of shell-and-tube heat exchangers. In: Afgan NH, Schlunder EV (eds) *Heat exchangers—design and theory source book*. McGraw-Hill, New York, pp 155–176

21. Sha WT, Launder BE (1979) A model for turbulent momentum and heat transport in large rod bundles. Report ANL-77-73. Argonne National Laboratory, Illinois
22. Hjertager BH, Solberg T, Nymoer KO (1992) Computer modelling of gas explosion propagation in offshore modules. *J Loss Prev Process Ind* 5(3):165–174. [https://doi.org/10.1016/0950-4230\(92\)80020-9](https://doi.org/10.1016/0950-4230(92)80020-9)
23. Dawes WN (1992) The solution-adaptive numerical simulation of the 3D viscous flow in the serpentine coolant passage of a radial inflow turbine blade. In: International gas turbine and aeroengine congress and exposition, Cologne, Germany, Paper no: 92-GT-193

Design of Experimental Setup for Investigation of Leakage in O-Rings



Amrish Biredar , Sri Krishna Sudhamsu Kambhammettu ,
and Lakshmana Rao Chebolu 

Abstract Elastomeric O-ring seals play a critical role in sealing fluids in variety of applications across the industries. In spite of their importance, systematic experimental leakage investigations on O-ring seals have been rarely conducted. In this paper, we design an experimental setup to conduct leakage experiments on O-ring seals at different amounts of compression and different gas pressures. The experimental setup is designed to measure different aspects of leakage such as leak initiation pressure, leak rate and circumferential leak distribution. Preliminary experiments are also conducted to measure leak initiation pressures for O-ring seals made of Nitrile Butadiene Rubber (NBR), Hydrogenated Nitrile Butadiene Rubber (HNBR) and fluoro elastomer (FKM). The test setup is expected to allow experimental investigations that help in modelling leakage and also in evaluating the performance of new, old and damaged seals

Keywords Sealing · Gas pressure · Leakage · Experimentation · Elastomer · O-ring

1 Introduction

O-ring seals are commonly used elastomeric seals that prevent leakage of fluid from one compartment [1] of equipment to another. They are generally classified into static O-ring seals and dynamic O-ring seals, depending on their application. Seals that do not have any relative motion with the surrounding interfacing components are called static seals as shown in Fig. 1a. Such static seals are widely used in pressure cookers, pressure vessels and storage casks of nuclear waste etc. Seals that experience relative motion with their interfacing components while preventing fluid leakage are called dynamic seals as shown in Fig. 1b. Such seals are used in pistons and cylinders of compressors, hydraulics arms etc.

A. Biredar (✉) · S. K. S. Kambhammettu · L. R. Chebolu
Department of Applied Mechanics, Indian Institute of Technology Madras, Chennai 600036, India

L. R. Chebolu
e-mail: lakshman@iitm.ac.in

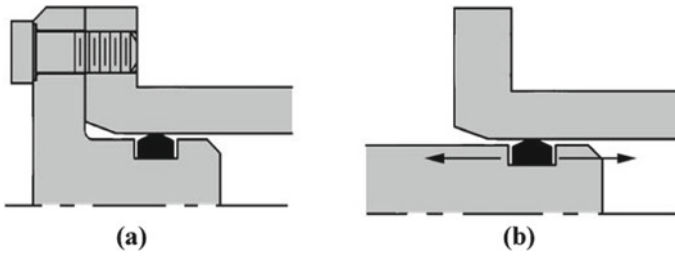


Fig. 1 a Static seal [13], b Dynamic seal [13]

In static seals sealing is achieved by compressing the O-ring in the fixture between the flanges, as shown in Fig. 2b. Such compression develops contact pressure at the sealing interface (O-ring-surrounding component interface), causing a preliminary sealing action at low pressures. When pressurized fluid is introduced, the contact pressure at the interface increases, preventing leakage, as shown below in Fig. 2c.

Generally, O-rings are known for their efficient sealing abilities. However, over time, due to degradation in bulk material properties by the aging of the elastomer, the contact pressure often decreases, leading to leakage [2] as shown in Fig. 2d. Hence, investigating the relationship among contact pressure, applied gas pressure and leakage is important and such investigation has been attempted by some researchers.

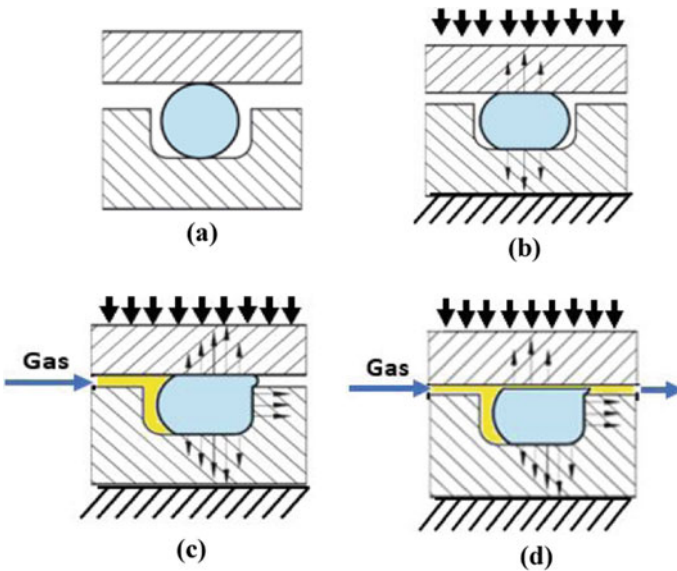


Fig. 2 a Cross-section of an O-ring seal, b Compression, c Application of gas pressure, d Leakage of the seal

Experimental literature regarding O-ring seals can be broadly classified into two categories. Literature of the “first category” investigate the changes in the material properties and its effects on contact pressure of the O-rings when subjected to working conditions. This corresponds to investigation of process-A in Fig. 3. For example, Kommling et al. [2] monitored material properties of O-ring samples made up of HNBR, FKM, NBR over a period of five years in suitable fixtures in a compressed state without applying any gas pressure. The measured mechanical properties were compared with critical values to predict the lifetime of the O-rings. Literature of the “second category” monitor the presence of leakage through O-rings from time to time at elevated temperatures or after a material damage inducing loading. These investigations correspond to process-B in Fig. 3. For example, Momon et al. [3] used standard FKM and EPDM O-rings for conducting the leakage experiment by injecting helium at varying temperatures. They characterized the leak tightness of elastomeric O-rings at varying temperatures. Kommling et al. [4] conducted leakage experiments on EPDM and HNBR aged O-ring seals. A modified leakage test was used which involved measuring leakage after a rapid decompression of the seal. The leakage values observed were compared with pre-defined critical values to estimate the life of the seal. Battani et al. [5] conducted leakage experiments on EPDM O-ring seals using a helium leak detector equipped with a customized holding device for O-rings. The leak rate was observed at various compression percentages of O-rings.

It is to be noted that since leakage is a direct consequence of reduced contact pressure, the mechanics of process-C in Fig. 3 should be investigated. However, most existing literature attempted to relate leakage directly to material degradation [2] i.e., process-B in Fig. 2. This resulted in unscalable empirical relations that are useful in a very narrow context. In this paper, we design an experimental setup for studying process-C i.e., the effect of contact pressure on the leakage at different gas pressures.

In order to design such an experiment, we go through the existing experimental setups in the literature. As we shall see, many researchers have designed leakage experiments on O-rings. However, most of them are designed for specific objectives that do not completely match with our goals discussed above. For example, Kommling et al. [4] designed experiments to measure leakage through seals that seal vacuum

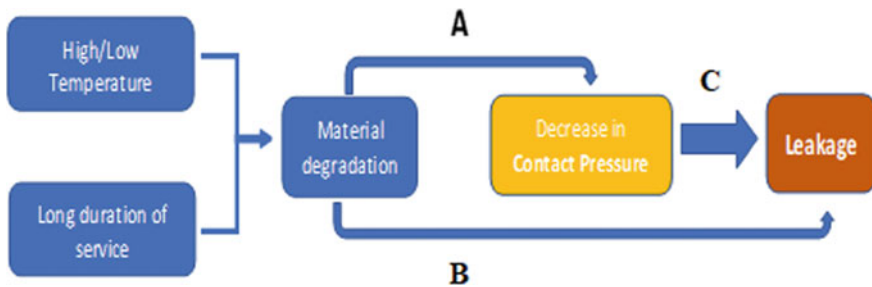


Fig. 3 Literature summary

pressure. Hence in this experiment, there is no variation of gas pressure. However, for the scenario in our context, gas pressure variation is a required feature. Similarly, each of the many experiments conducted in the literature has different objectives and cannot be applied directly to our context. Table 1 lists out such examples in detail.

In order to satisfy the requirements specified in Table 1, an experimental setup with the following features is required.

- a. Control over compression percentage of the O-ring: Standard O-ring cross-sections (torus cross-section diameter) vary from 1 to 20 mm O-rings are generally compressed from 1 to 20% depending on the application. If an O-ring with cross-section 5 mm is to be compressed say, in steps of 1% compression (for the sake of investigating leak characteristics at different contact pressures), then an incremental compression of 0.05 mm is to be applied. This is too small a distance to be controlled accurately on many machines. Hence, an appropriate mechanism to control the compression increment and selection of an appropriate O-ring size is crucial to the design of the experiment.
- b. Measuring the spatial field of leakage in an O-ring: Most investigations on leakage of seals treat leakage as an axisymmetric problem modelling homogeneous leakage throughout the circumferential length of the interface. However, recent experiments on leakage on different seals showed scattered patches of interface exhibiting leakage. In this paper, we would like to observe the leak and no-leak areas on the circumference of the O-ring. This is not possible in most fixtures as the primary test O-ring is neither accessible nor visible from the outside during the test. In this paper, we design a fixture that allows for such monitoring.
- c. Leak initiation and Leak rate measurements are set up by directly measuring the volumetric leak rate: Most existing setups use pressure drop criteria to measure leakage. However, such a system is not useful when small leaks are to be measured in short amount of time. Sudhamsu et al. [6] has developed a water-column displacement based real-time leakage measurement system. In this paper, we shall adapt and improve this for our purpose.

2 Design of the Setup

2.1 Conceptual Design

Static O-ring seals are generally used in two different configurations: face type configuration and annular configuration. In face type configuration leakage in radial direction is prevented while in annular type configuration leakage in longitudinal direction is prevented by the O-ring as shown in Fig. 4.

In annular seals shown in Fig. 4a, compression of the O-ring can only be varied by changing the geometry of the mating parts. However, in face seals shown in Fig. 4b, it is possible to easily vary the O-ring compression by moving the mating parts

Table 1 Leakage experiments

Authors	Objectives	Leak detection mechanism	Fixture design	O-ring material
S. Momon et al.	To find the critical temperature for leakage at low temperature conditions and time taken for seals to leak at higher temperature conditions	Inner chamber is filled with helium gas and, gas leaks to the outer chamber, leak is detected by helium mass spectrometer	Two chambers are created using two O-rings, a primary O-ring (test specimen) is kept inside and a secondary large O-ring is kept outside. Whole fixture is placed in a thermal enclosure	F.K.M, EPDM and HNBR O-rings
Kommling et al.	To measure lifetime of aged seals at low and high temperature conditions	The atmospheric air leaks inwards through an O-ring seal, the volumetric leak rate is calculated by measuring the rise in pressure of the leaked air in the inside chamber by a pressure sensor	The aged O-ring sample to be tested, is compressed between the flanges	Aged EPDM and HNBR aged O-rings
D Battani et al.	To find the minimum compression percentage for O-ring subjected to different radiation levels to avoid leakage	Leak tests were carried out using a Helium leak detector. O-rings are squeezed and helium is sprayed from outside	O-rings are held at varying squeezes in the fixture	EPDM O-rings subjected to various levels of radiation dosage are used
K Sudhamsu et al.	To find leak initiation pressure and leak rate for elastomer-metal interface	Pressurized gas is passed to the inside chamber, the leak starts from the metal-elastomer interface to the outer chamber. The leaked gas is then measured using inverted flask method	Elastomeric sheet sits between the bottom and top fixture. Inside chamber is subjected to high pressure and gas leaks through the interface to outer chamber	FKM, HNBR and NBR elastomeric sheets

(continued)

Table 1 (continued)

Authors	Objectives	Leak detection mechanism	Fixture design	O-ring material
Requirements for experiments in this work	To find leak initiation pressure and leak rates for elastomeric O-rings at different contact pressures and gas pressures	Spatial measurement of Leak initiation and leak rate measurements	Designing the Fixtures which allow the accurate compression percentage control	FKM, HNBR and EPDM O-rings

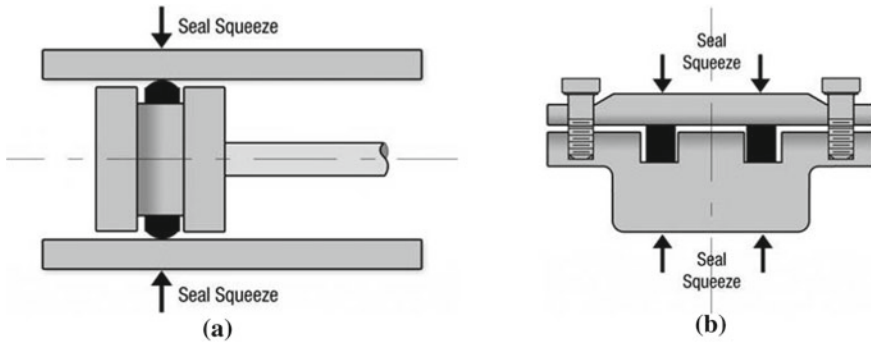


Fig. 4 a Radial seal [13], b Face seal [13]

towards or away from each other. Hence, in this design we choose face type O-ring seal setup for experimentation. Figure 5 shows the conceptual design of the setup, based on a conventional design commonly found in the literature [3]. The primary O-ring sample for testing is kept inside (as shown in Fig. 5), and another secondary

Fig. 5 Conventional conceptual design

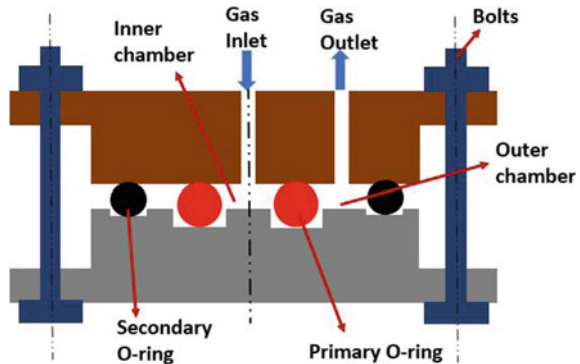
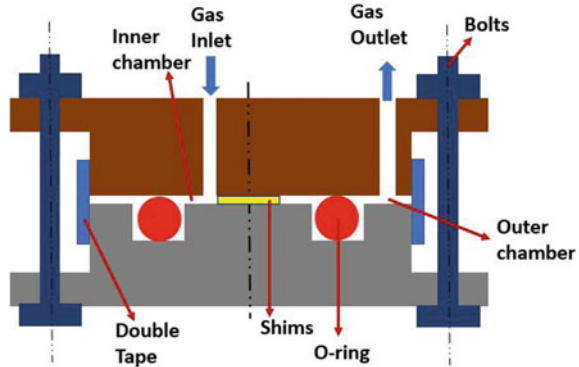


Fig. 6 Final conceptual design



O-ring sample is used to create an outer chamber as shown in the Fig. 5. Compression of O-rings is achieved by tightening the bolts. Once the seal is compressed in this manner, pressurized gas is released into the inner chamber. If the gas leaks through the primary O-ring, it will be trapped in the chamber created by the secondary O-ring. While the construction of a conventional setup is easier the investigation of spatial location of leakage is not possible. In addition, the accurate control of compression of the O-ring by bolt tightening is not possible.

To overcome these limitations, we tweak the standard design and come up with a new design shown in Fig. 6. In this design, shims are placed between the top and bottom bodies to maintain uniform and controlled compression on the O-ring once the bolts are completely tightened or when the top and bottom bodies are compressed towards each other by means of a compression machine. The compression of the O-ring is varied by using shims of different thicknesses. The secondary seal in Fig. 5 is replaced with a industrial grade transparent double tape. Since the gas pressure in the secondary chamber is only slightly above atmospheric pressure (due to constant outflow of gas through the “Gas Out” port for measurement), the double tape should be sufficient enough to maintain the outer chamber sealing. In addition, the thickness of the outer body (beyond the O-ring) is reduced to the minimum possible value. This allows for visual monitoring of the outer circumference of the interface. If markers like soap bubble water are applied at the outer circumference of the interface, locations of leak can be easily observed during the experiment.

2.2 Detailed Design

As discussed in Sect. 1, an O-ring of higher cross-section allows for higher resolution of control on the compression percentage. For this reason, a standard O-ring with a large cross-section is sought after in this work.

The O-ring of dimensions shown in Fig. 7a is selected for the same reason. With O-ring of 20 mm cross-section and shims of 0.2 mm, a resolution of 1% compression

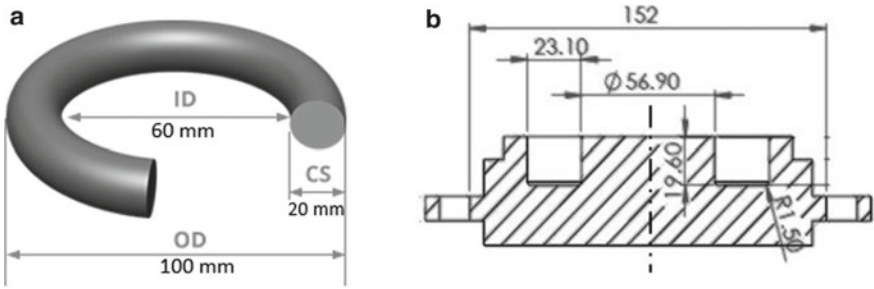


Fig. 7 a O-ring cut-section, b Cross-section of bottom fixture

percentage can be achieved easily. The Fig. 7b shows the cross-section of the bottom groove. The groove and O-ring dimensions based upon on AS.568A [14] standard. It has a depth of 19.60 mm, width of 23.10 mm and an inner diameter of 56.9 mm. Figure 8a shows the machined fixture assembly consisting of a top die and a bottom die made up of SS-316 material. An elastomeric O-ring seal and metal shims are placed in between the dies and industrial tape is pasted on the periphery to arrest the leakage.

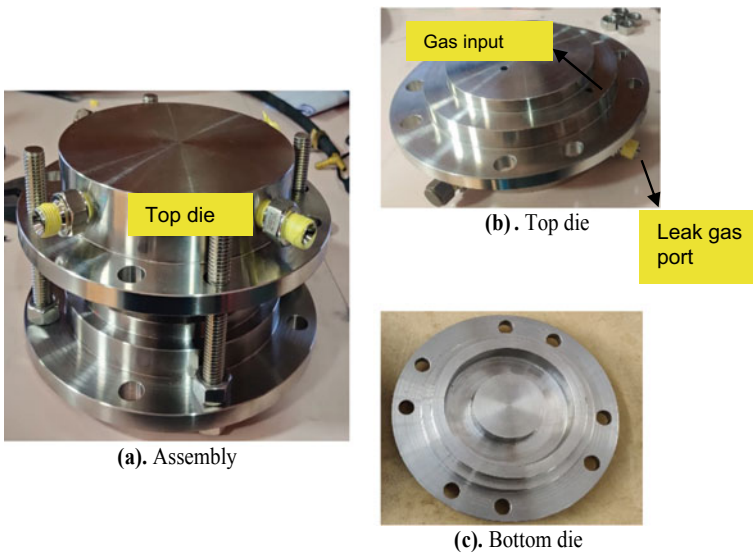


Fig. 8 a Assembly, b Bottom die

3 Experimental Setup

As discussed, the important functionalities of required experimental setup are compression of O-ring, gas pressure application, identifying circumferential leak distribution and measurement of leakage. In this section we will separately discuss each of these functional components.

3.1 Compression of O-Ring and Gas Pressure Application

Figure 9 shows the schematic of the complete experimental setup. The nitrogen cylinder is attached with a pressure regulator, giving output pressure up to 30 bar. The nitrogen gas from the cylinder is sent to the inlet port of the O-ring fixture. The designed O-ring fixture sits in a compression machine. The entire O-ring fixture assembly can be compressed using the displacement-controlled compression testing machine. Alternatively, bolts can be also used to compress the O-rings. In addition, shims can be placed between top and bottom body to accurately control the applied compression. Leaked gas from the O-ring fixture will be sent to the leakage measuring cylinder setup.

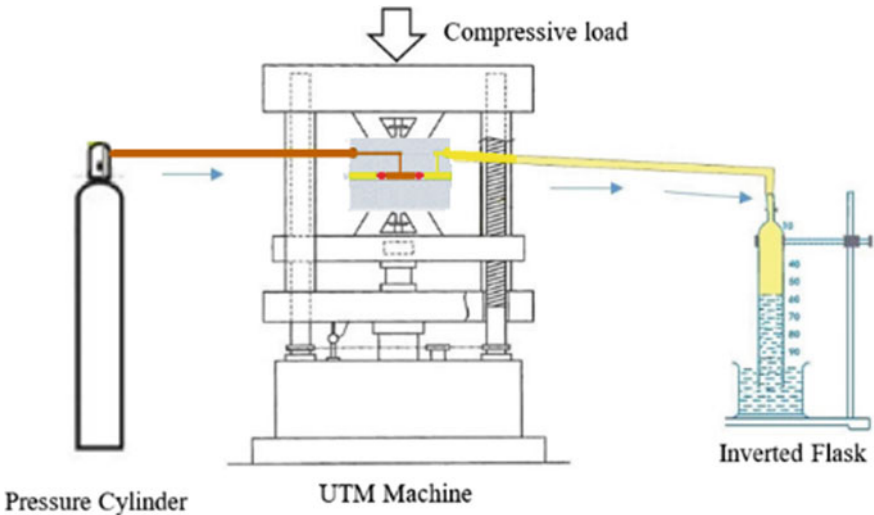


Fig. 9 Schematic of the setup

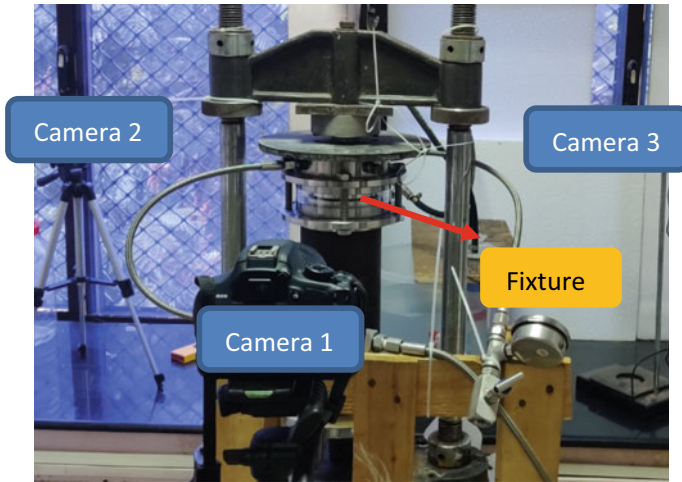


Fig. 10 Camera setup

3.2 Identifying Circumferential Distribution of Leakage

In order to investigate the leak initiation from the O-ring assembly, the bottom fixture of the assembly is marked with symbols to detect the direction of start of leak. 3 cameras are placed at 120° apart to have the whole circumference captured at once. Camera positions are shown in Fig. 10. Using this setup, the spatial and temporal leak initiation can be investigated more precisely.

3.3 Design of Leakage Measurement Setup

The trapped gas in the outer chamber will be sent to leakage measuring setup. An inverted flask setup can be used, in which the leakage of the gas is measured through the change in the height of the water column. The fluctuations in the water column by putting the floater can be captured using taking photographs at regular intervals. Image processing methods can be used to accurately calculate the movement of floater which in turn gives the leak rate (ml/sec). The schematic of the design and photograph of the setup is shown in Fig. 11.

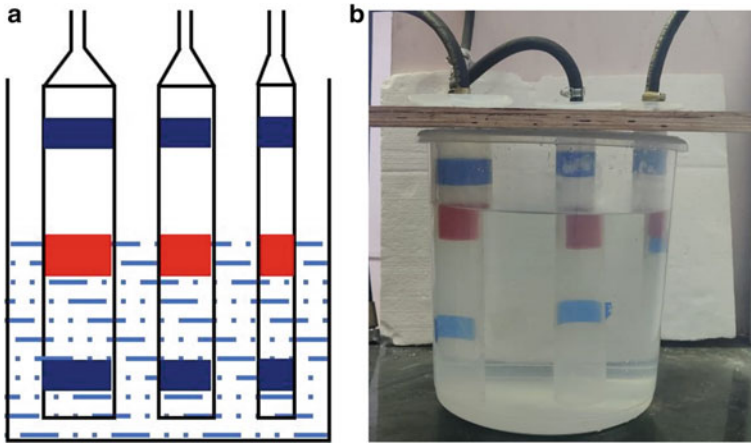


Fig. 11 **a** Schematic of the leakage measuring cylinders with red floaters, **b** Photograph of the leakage measuring with red floaters

4 Preliminary Experiments and Discussion

Preliminary experiments were conducted on O-rings made of Nitrile Butadiene Rubber (NBR), Hydrogenated Nitrile Butadiene Rubber (HNBR) and Fluoro elastomer (FKM) to verify and ensure smooth functioning of the test setup. Each material sample has been tested up to gas pressure of 14 bar at different compression percentages that varied from 1 to 5% to measure leak initiation pressures.

The results obtained from such preliminary experiments are shown in Figs. 12, 13 and 14. It was observed that leakage initiation pressure increased with increase in compression percentage for all the specimens. This also means that higher compression percentage is required to seal gases of higher pressure. This is similar to the results observed in leak experiments in Sudhamsu et al. [6] on elastomeric sheet seals where leak initiation pressure was found to be monotonously increasing with compression induced contact pressure. However, unlike Sudhamsu et al. [6], the trends observed in Figs. 12, 13 and 14 are nonlinear. This can probably be attributed to the geometric non-linearities and boundary non-linearities associated with the O-ring seal. However, such causation can only be confirmed after further experimentation with multiple specimens to ensure repeatability. Such experiments should also measure the leak rates at gas pressures higher than leak initiation pressure and should even investigate the circumferential distribution of leakage through the seal-surrounding material interface. The fixture designed in this paper is capable of handling such experimentation.

It should be noted that although the fixture is designed to test new O-rings, it could be put to a greater and more readily helpful use by testing aged seals. Aged seals are known to lose their elastic properties due to material degradation [2]. This is known to reduce their sealing efficacy. By comparing leak initiation pressures of new and aged

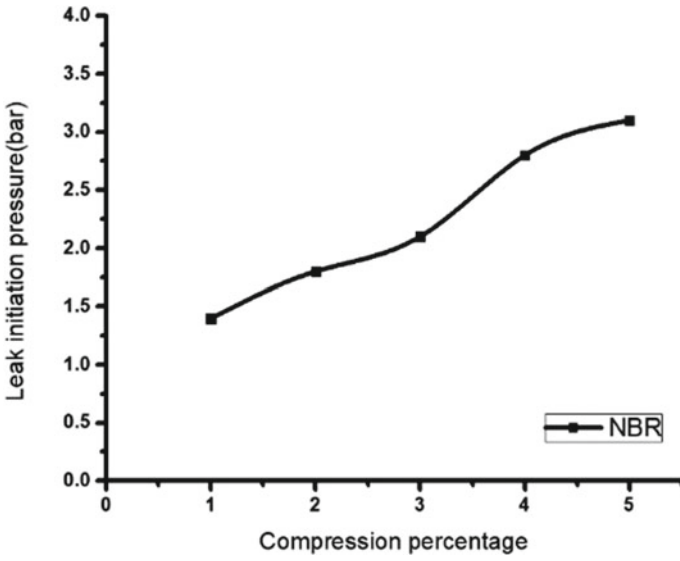


Fig. 12 Leak initiation pressure vs compression percentage for NBR

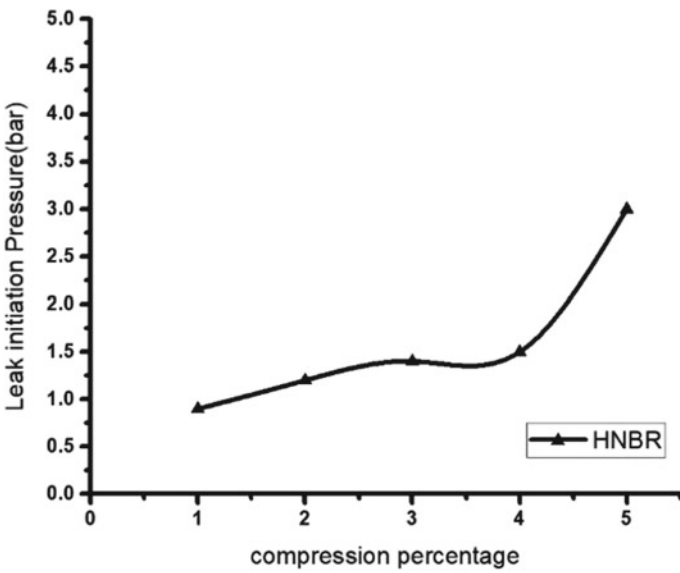


Fig. 13 Leak initiation pressure vs compression percentage for HNBR

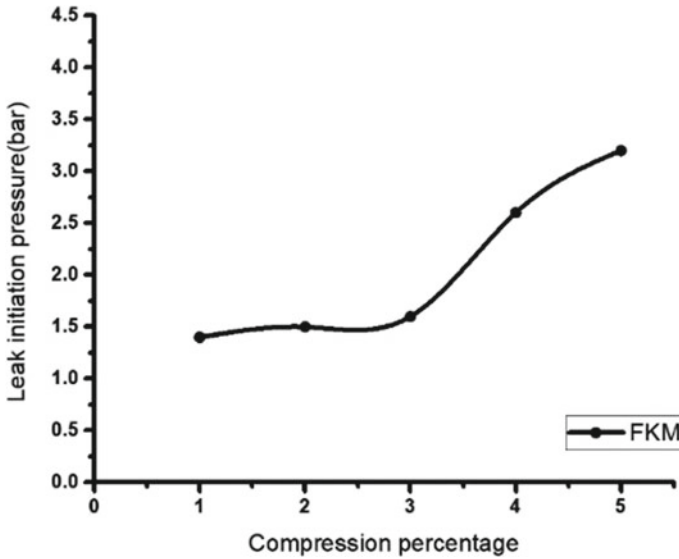


Fig. 14 Leak initiation pressure vs compression percentage for FKM

seals at different amounts of compressions, the effect of aging on seal performance can be accurately characterized. This solves vast literature of inconclusive results obtained by testing new and aged seals at only one compression [3, 7, 8]. In addition, as discussed, using this test setup, experiments can also be conducted to measure leak rate and circumferential leak distribution by the setup discussed in the Sect. 3. These experiments may be further used to validate models [9–12] that describe leakage.

5 Summary and Conclusions

In this work a new test fixture that can measure leak initiation pressure, leak rate and circumferential leak distribution of leakage through O-rings at different gas pressures and compressions has been developed. Preliminary experiments to verify the functioning of the setup were conducted using NBR, HNBR and FKM based O-rings. The functional flexibility of this fixture in characterizing leakage in different ways in different conditions allows for accurate estimation of seal damage caused by various phenomena such as material degradation, rapid gas decompression, extrusion damage etc., In addition, valuable data that can verify the functioning of different leak predicting models can be generated using this fixture. Although such investigations are out of the scope of the current work, efforts to fulfil them shall prove to be helpful for the design of better seals.

References

1. Druecke B, Dussan EB, Wicks VN, Hosoi AE (2015) Large elastic deformation as a mechanism for soft seal leakage. *J Appl Phys* 117(10). <https://doi.org/10.1063/1.4914523>.
2. Anja Kömmling MJ, Wolff D (2015) Aging of elastomeric seals for storage casks – 15080. *Acta Univ Agric Silv Mendelianae Brun* 16(2), 39–55. <https://doi.org/10.1377/hlthaff.2013.0625>
3. Momon S, Garcia J, Issard H (2013) Leak tightness of O-rings for transport of radioactive material. *Packag Transp Storage Secur Radioact Mater* 24(1):3–9. <https://doi.org/10.1179/1746510913Y.0000000033>
4. Kömmling A, Jaunich M, Pourmand P, Wolff D, Hedenqvist M (2019) Analysis of O-ring seal failure under static conditions and determination of end-of-lifetime criterion. *Polym (Basel)* 11(8). <https://doi.org/10.3390/polym11081251>
5. Battini D et al (2018) Experimental testing and numerical simulations for life prediction of gate valve O-rings exposed to mixed neutron and gamma fields. *Mater Des* 156:514–527. <https://doi.org/10.1016/j.matdes.2018.07.020>
6. Sudhamsu KSK, Lakshmana Rao C, Deshpande AP, Devan J (2019) Experimental characterisation of leak through elastomer-metal interface. *Int J Mater Struct Integr* 13(1–3):186–199. <https://doi.org/10.1504/IJMSI.2019.100435>
7. Gillen KT, Celina M, Bernstein R (2003) Validation of improved methods for predicting long-term elastomeric seal lifetimes from compression stress-relaxation and oxygen consumption techniques. *Polym Degrad Stab* 82(1):25–35. [https://doi.org/10.1016/S0141-3910\(03\)00159-9](https://doi.org/10.1016/S0141-3910(03)00159-9)
8. Kuran S, Gracie BJ, Metcalfe R (1995) Low pressure sealing integrity of o-rings based on initial squeeze and counterface finish. *Tribol Trans* 38(2):213–222. <https://doi.org/10.1080/10402009508983398>
9. Kambhammettu SKS, Chebolu LR, Deshpande AP (2020) A wedge penetration model to estimate leak through elastomer–metal interface. *Int J Adv Eng Sci Appl Math* 12(1):65–72. <https://doi.org/10.1007/s12572-020-00262-w>
10. Kambhammettu SKS, Deshpande AP, Chebolu LR (2021) A compressible porous media model to estimate fluid leak through a metal-elastomer interface. *Transp Porous Media* 136(1):191–215. <https://doi.org/10.1007/s11242-020-01507-9>
11. Persson BNJ, Yang C (2008) Theory of the leak-rate of seals. *J Phys Condens Matter* 20(31), <https://doi.org/10.1088/0953-8984/20/31/315011>
12. Biredar A, Kambhammettu SKS (2021) Numerical simulation of leakage initiation in face-type static O-ring seals. *NMIMS Eng Technol Rev* III(1):108–124
13. Hannifin P (2018, March 16) A Simple guide to radial seals | sealing fundamentals, parker Hannifin Seal. <http://blog.parker.com/a-simple-guide-to-radial-seals-sealing-fundamentals>
14. Hannifin, P. (2020). *Parker O-Ring Handbook* ORD 5700. Parker Hannifin Corporation, Lexington, KY

Development of Digital Twin for Polycrystalline BCC α -Fe



Gopi Gulivindala , Madhu Kiran Karanam ,
and Viswanath Chintapenta 

Abstract In the current study, crystal plasticity based finite element model is proposed to predict the flow stress behavior of the BCC α -Fe. The deformation behavior of the single crystal is predicted from crystal plasticity simulations and compared with experimental results on BCC α -Fe from the literature. Further, the flow stress behavior of polycrystalline BCC α -Fe is obtained using a simple four-grain model. Insights into interaction effects between grains due to different orientations on the global deformation behavior of bi-crystal are also presented.

Keywords Crystal plasticity · Flow stress · Grain-grain interactions · BCC α -Fe

1 Introduction

Ferritic steels consisting of α -Fe are among the most widely used engineering material, as they possess good ductility and corrosive resistance. Its applications include automobile parts, industrial machines, etc. Therefore, continuous improvement in these materials is required to meet the demanding service conditions. The experimental approach for predicting the mechanical behavior of advanced material is daunting due to the difficulty in specimen preparation and constructing experimental setup. These drawbacks can be overcome using a virtual representation of the physical process and material. This representation of real time physical process or material is called as a digital twin. Multi-scale modeling is usually employed for developing a digital twin in such materials.

In this paper, an attempt has been made to develop a digital twin for BCC α -Fe using the crystal plastic finite element method (CPFEM). The developed model is

G. Gulivindala · M. K. Karanam · V. Chintapenta (✉)
Micro Mechanics Lab, IIT Hyderabad, Hyderabad, India
e-mail: viswanath@mae.iith.ac.in

G. Gulivindala
e-mail: me18resch11008@iith.ac.in

M. K. Karanam
e-mail: me15resch11006@iith.ac.in

used for understanding anisotropic mechanical properties, such as flow behavior and the effect of grain interaction between randomly oriented crystals. Towards this, three sets of studies were conducted, namely, single crystal studies to calibrate the model, bi-crystal studies to understand grain interactions, and a four-grain model to estimate the flow behavior.

A simplistic single crystal model was considered for testing the effect of initial crystallographic orientation (ICO) of grain on flow stress and to calibrate with experiments from the literature [2]. Three different grain ICOs, i.e., $\langle 100 \rangle$, $\langle 110 \rangle$, and $\langle 111 \rangle$ were explored. In bi-crystal studies, two grains of all possible combination ICOs listed above were explored to understand the effects of the grain-grain interaction on the deformation mechanism. Finally, a representative of polycrystalline material was considered as a unit cell with four grains of different ICOs to predict the effect of local properties on the global deformation behavior of polycrystalline. That is, using the polycrystalline model, a comprehensive comparison of the flow stress behavior, plastic strain, and slip system activation in BCC α -Fe was studied.

Some of the assumptions used in the study are: i) The grain boundary effects, such as grain boundary sliding and diffusion, were not included in the model. ii) The grain shape was simplified to a cuboid. iii) The ICOs were limited to $\langle 100 \rangle$, $\langle 110 \rangle$, and $\langle 111 \rangle$ iv) Only $\{110\}\langle 111 \rangle$ and $\{112\}\langle 111 \rangle$ slip systems were considered. v) Non-Schmid effects were not included in this study.

Based on the above assumptions, the sharp grain boundary was modeled between the grains by direct merging the elements of adjacent grains. And, the chosen ICOs represent the vertices of the standard stereographic triangle; in the literature above mentioned ICOs are often considered [6, 7]. Further, slip system $\{123\}\langle 111 \rangle$ was not considered as it is active only at higher temperatures [1].

The rest of the paper is organized as follows. In Sect. 2, a description of possible BCC slip systems is presented. And, Sect. 3 details the numerical model, constitutive behavior, and material properties used in this study. Model calibration is presented in Sect. 4, along with results of grain-grain interaction, active slip systems, and flow stress behavior of polycrystalline BCC α -Fe. Finally, in Sect. 5, conclusions and future scope are discussed.

2 BCC Slip Systems

BCC slip systems are not well defined compared to FCC. In literature, most of the time, two different sets of slip systems were considered, either $\langle 111 \rangle \{ \{110\}/\{112\} \}$ (see Ref. [1, 2]) or $\langle 110 \rangle \langle 111 \rangle$ (see Ref. [8]). This ambiguity comes from the fact that the slip systems in BCC metals are selectively active. Since the analysis is performed at room temperature, $\langle 111 \rangle \{ \{110\}/\{112\} \}$ slip systems are active. The slip direction in BCC metals is always along the diagonal direction $\langle 111 \rangle$, but these directions are possible in three different slip planes $\{110\}/\{112\}/\{123\}$. Hence, the slip is also possible in any of these planes through a cross-slip. However, the limitation of the

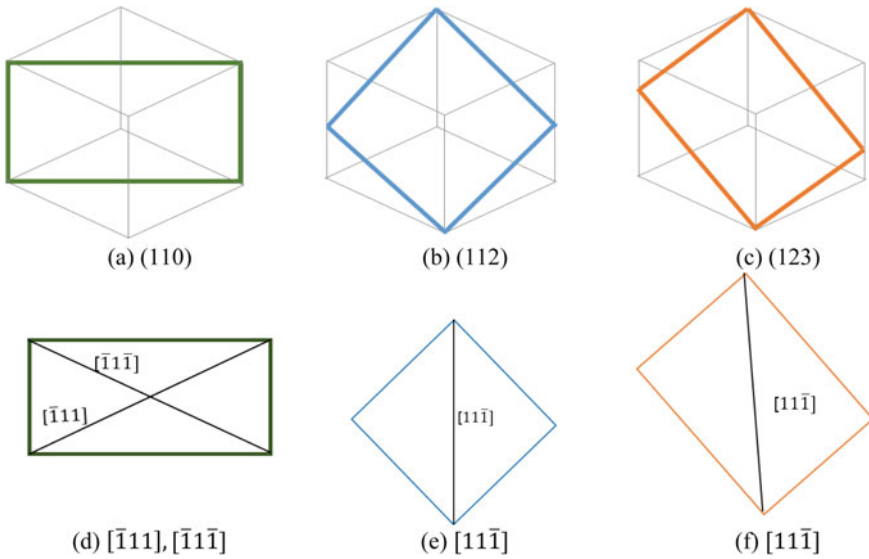


Fig. 1 Schematic representation of BCC slip systems; **a-c** slip planes, **d-f** slip directions

current study is it does not consider non-Schmid effects to capture the mechanisms such as cross-slip.

In Fig. 1 a–c, typical slip planes in BCC metals are shown. Recognizing the specific planes on which slip occurs in BCC metals is less straightforward [9]. Because BCC metals neither show stable stacking fault energy nor the splitting of a screw dislocation. And, experimental studies to understand the slip in BCC metals are not effective as the cross slip occurs due to subsurface dislocation activity [10]. Further, experimental observations only show slip traces on the exposed free surfaces. Hence, this causes ambiguity of slip systems in BCC.

Figure 1 d–f shows the slip directions on the slip planes $\{110\}$, $\{112\}$, and $\{123\}$, respectively for BCC. However, in this study, two families of slip systems $\langle 111 \rangle$ $\{\{110\}/\{112\}\}$ are considered. This constitutes of 24 slip system considering both positive and negative shear as equivalent. The insights on the slip systems and their activation are presented in Sect. 4.3.

3 Methodology

This section explains the numerical model, constitutive behavior, and material parameters used in this study.

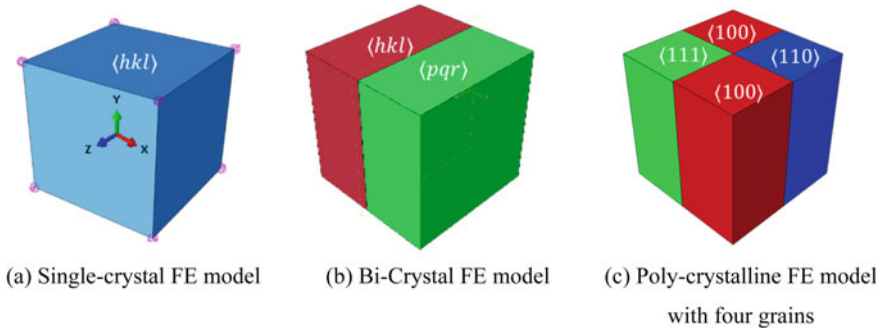


Fig. 2 Details of the numerical model

3.1 Numerical Model

The unit cells shown in Fig. 2a–c represent single crystal, bi-crystal, and four-grain model, respectively. All the models were meshed with fully integrated linear hexahedral elements (C3D8). The boundary condition applied for the above models was uniaxial tension; i.e., on the top-face, a macroscopic strain was applied, and the bottom-face was constrained (Y direction). Due to which, the side faces of the unit cell remained traction-free, and they expand/contract in the X and Z directions. Further, along global X and Z directions, grounded-springs with a small stiffness value of $1\text{E}-3$ N/mm were added to avoid over constraining the model. This additional small stiffness usually does not cause any reaction force in the model.

The unit cell shown in Fig. 2a represents a single crystal that was used to calibrate the model qualitatively with the available literature on the BCC α -Fe (Zhang et al. [2]). Later, the effect of ICOs on the deformation mechanism was also studied. The unit cell shown in Fig. 2b was for bi-crystal consisting of two combinations of the ICOs. This was used to understand the effect of the inter grain interaction, grain deformation, and the intergranular shear strains. Finally, the model was extended for a four-grain model with arbitrary orientations to demonstrate the scalability of the proposed numerical model.

3.2 Constitutive Model

The macro-scale aspect of polycrystalline metal was included by considering multiple grains using bi-crystal and four-grain models. And, the micro-scale phenomenon of slip in finite strain rate-dependent viscoplastic material was captured through the crystal plasticity framework. The power-law based hardening model was used to account for the strain hardening [3].

Table 1 Material parameter values used for the study

Parameters	C_{11} (GPa)	C_{12} (GPa)	C_{44} (GPa)	h_0 (MPa)	τ_s (MPa)	τ_0 (MPa)	q	q_1	m	$\dot{\gamma}_0$ (s^{-1})
{110}[111]	230.1	134.6	116.6	180	148	65	1	1.4	0.1	0.001
{112}[111]	230.1	134.6	116.6	300	150	100	1	1.4	0.1	0.001

Table 2 Initial crystallographic orientation definition

Initial crystallographic orientation/Grain orientation	Crystallographic orientation on global coordinates X–Y–Z
$\langle 100 \rangle$	$[00\bar{1}]$ - $[100]$ - $[0\bar{1}0]$
$\langle 110 \rangle$	$[0\bar{1}\bar{1}]$ - $[011]$ - $[100]$
$\langle 111 \rangle$	$[11\bar{2}]$ - $[111]$ - $[1\bar{1}0]$

3.3 Material Parameters

The material properties used in this study are referred from Zhang et al. [2]. Table 1 lists various parameters used in the study. In this study, three ICOs: $\langle 100 \rangle$, $\langle 110 \rangle$, and $\langle 111 \rangle$ were considered. The ICO represents the crystal lattice direction parallel to the principal loading direction of the specimen. The relation between local (crystal lattice) and global (specimen) coordinate systems for each crystallographic orientation is presented in Table 2.

4 Results and Discussion

4.1 Model Calibration

The proposed model is first calibrated with experimental and numerical results from Zhang et al. [2] on BCC α -Fe for ICOs: $\langle 100 \rangle$, $\langle 110 \rangle$, and $\langle 111 \rangle$. Figure 3 shows the applied strain vs. equivalent stress graph for three ICOs, numerical and experimental, from the literature [2]. It is observed that at low applied strain, equivalent stress for all the orientations was in line with the experiments [2], and the deviation starts at an applied strain of $\epsilon = 0.003$. This results show a good qualitative match with [2]. All the ICOs used in this study have multiple slip systems; therefore, the stress–strain behavior is different from the typically observed stress–strain behavior of a single crystal with a single slip system. However, it should be noted that Zhang et al. [2] study was for polycrystalline metal, and hence a quantitative comparison is not possible.

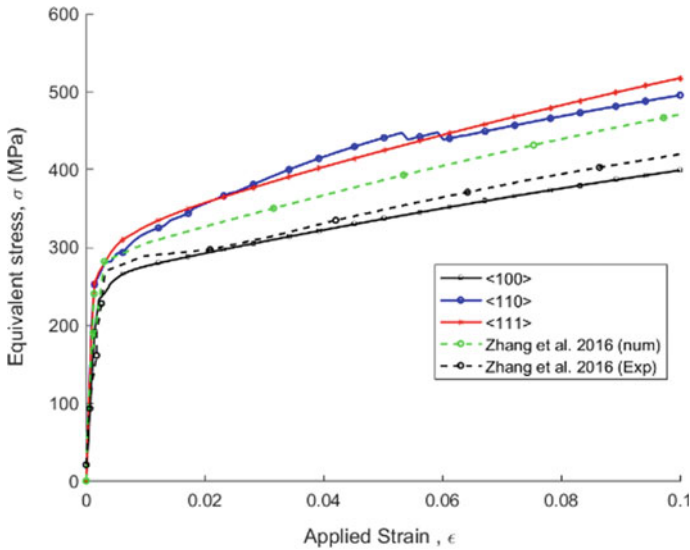


Fig. 3 Correlation of flow stress behavior with Zhang et al. 2016 [2]

4.2 Active Slip Systems and Their Dependence on the Grain Orientation

Unlike for FCC metals, where the number of active slip systems is well defined with respect to the ICO and can be schematically represented using Thomson tetrahedron. For BCC metals, this information is not straightforward, and no such simplistic representation is possible. This is primarily due to the presence of non-Schmid stresses in BCC α -Fe [4, 5]. The active slip systems are identified as the slip system on which the resolved shear stress (Schmid stress) is higher than the critical resolved shear stress (CRSS). The non-Schmid effects were not included in this model and will form part of future study. For BCC, as discussed in Sect. 2, there are three potential families of slip systems ($\{110\}$ [111], $\{112\}$ [111], and $\{123\}$ [111]) and out of these three, at room temperature, two slip systems ($\{110\}$ [111] and $\{112\}$ [111]) are more relevant. Each family of slip systems can have different CRSS.

Figure 4a and b shows the resolved shear stress vs. applied strain graph for slip system family-1 ($\{110\}$ [111]) and family-2 ($\{112\}$ [111]), respectively for ICO $\langle 100 \rangle$. The resolved shear stress on the slip system increases with applied strain due to material hardening. The value of CRSS for the slip system family-1 is 65 Mpa, and for slip system family-2 is 100 MPa. These values are represented with a black dotted line in Fig. 4. Similarly, Fig. 5 and Fig. 6 shows the resolved shear stress vs. applied strain graph for ICOs $\langle 110 \rangle$ and $\langle 111 \rangle$, respectively. Table 3 summarizes active slip systems for all three ICOs. In the table, cells are marked from one to twelve

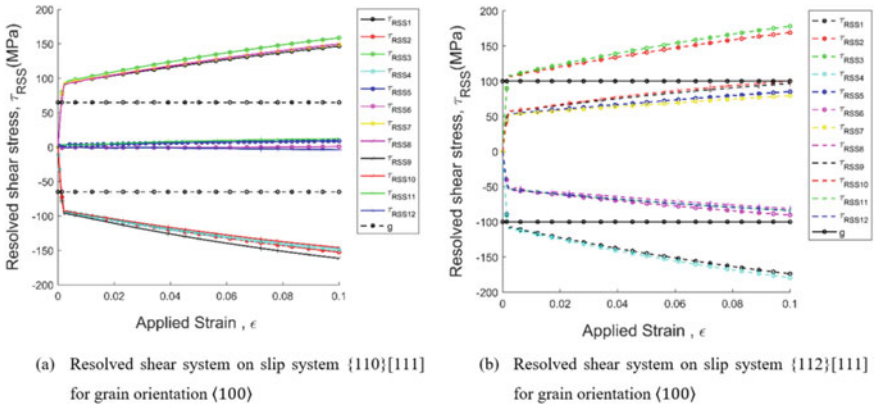


Fig. 4 Resolved shear stress for identifying the active slip system for grain orientation (100)

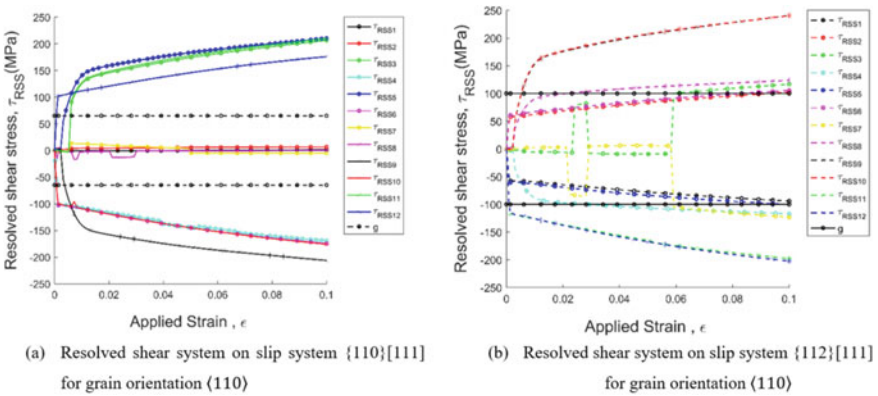


Fig. 5 Resolved shear stress for identifying the active slip system for grain orientation (110)

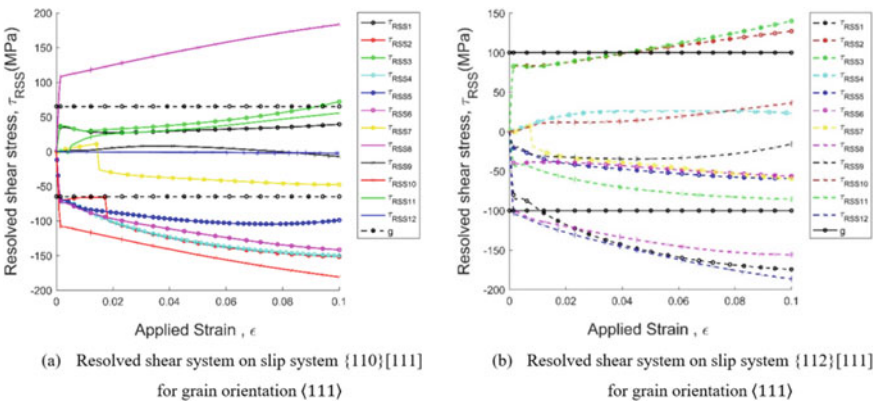


Fig. 6 Resolved shear stress for identifying the active slip system for grain orientation (111)

Table 3 Active slip systems in each of the slip system families for grain orientation $\langle 100 \rangle$, $\langle 110 \rangle$ and $\langle 111 \rangle$

$\langle 100 \rangle$	Slip system family 1 : $\{110\}[111]$, active slip systems - grey color box											
	1	2	3	4	5	6	7	8	9	10	11	12
	Slip system family 2 : active slip systems – grey color box											
$\langle 110 \rangle$	Slip system family 1 : $\{110\}[111]$, active slip systems –grey color box											
	1	2	3	4	5	6	7	8	9	10	11	12
	Slip system family 2 : $\{112\}[111]$, active slip systems - grey color box											
$\langle 111 \rangle$	Slip system family 1 : $\{110\}[111]$, active slip systems - grey color box											
	1	2	3	4	5	6	7	8	9	10	11	12
	Slip system family 2 : $\{112\}[111]$, active slip systems are - grey color box											
$\langle 111 \rangle$	Slip system family 1 : $\{110\}[111]$, active slip systems - grey color box											
	1	2	3	4	5	6	7	8	9	10	11	12
	Slip system family 2 : $\{112\}[111]$, active slip systems are - grey color box											
$\langle 111 \rangle$	Slip system family 1 : $\{110\}[111]$, active slip systems - grey color box											
	1	2	3	4	5	6	7	8	9	10	11	12
	Slip system family 2 : $\{112\}[111]$, active slip systems are - grey color box											

representing all the slip systems of the family. In here, all the active slip systems are highlighted by shaded cells. It is observed that the number of active slip systems of the ICOs $\langle 100 \rangle$, $\langle 110 \rangle$, and $\langle 111 \rangle$ are twelve, seventeen, and eleven, respectively.

4.3 Study of Grain-Grain Interaction and Its Effect on Flow Stress

A bi-crystal model was used to study the interaction between grains by modeling two grains with different ICOs. The interface was simplified as a sharp grain boundary by directly merging elements from the adjacent grains. This modeling approach captures elastic and plastic mismatches between the grains. This model gives useful insights into grain-grain interaction by studying the cumulative shear strain at the interface. The cumulative shear strain (γ') was obtained as the sum of shear strains from all active slip systems. Figure 7 shows the cumulative shear strain plots over all the slip systems for a single and bi-crystal at an applied strain of $\epsilon = 0.1$

Figure 7a–d are for single crystal and Fig. 7e–f for the bi-crystal. The cumulative plastic strain over all the slip system is comparable for bi-crystal $\langle 100 \rangle$ – $\langle 110 \rangle$ w.r.t the respective plastic strain in the individual grains. Thus, they were indicating a lesser-stressed interface. Whereas, for the bi-crystal with grain orientations of $\langle 110 \rangle$ – $\langle 111 \rangle$, for which significantly higher cumulative plastic strain value w.r.t individual single grains was noticed. This behavior can be observed clearly in the flow stress plots shown in Fig. 8.

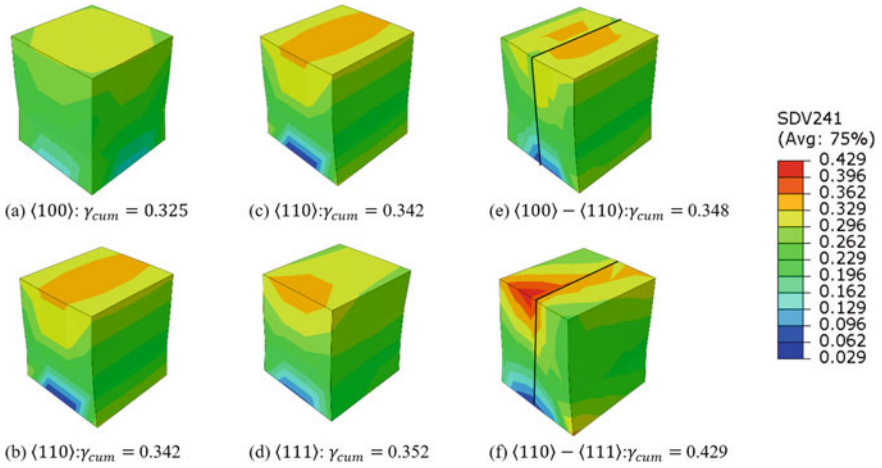


Fig. 7 Cumulative shear strain over 24 slip systems for single and bi-crystals at 0.1 applied strain

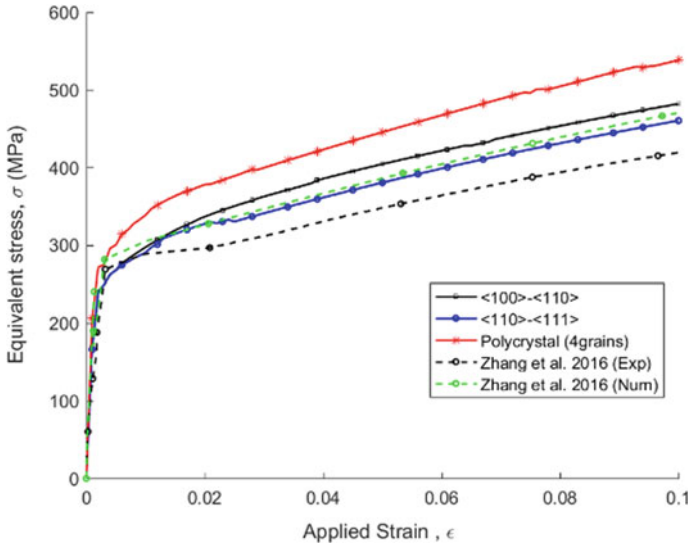


Fig. 8 Flow stress comparison of polycrystalline modeled using four cubic grains with Zhang et al., 2016 numerical and experimental results

4.4 Flow Stress Behavior of Polycrystalline α -Fe (4 Cubic Shaped Grains)

The polycrystalline BCC α -Fe was modeled using four grains, with each grain oriented in one of three ICOs, as shown in Fig. 2(c). The grain orientation for the four grains was selected arbitrarily. The interface between the grains was modeled by the direct merging of element's from the adjacent grains, representing a sharp grain boundary. The unit cell is loaded uniaxially, and flow stress behavior is studied.

Figure 8 shows the applied strain vs. equivalent stress graph for the four-grain model described above, along with experimental and numerical results from Zhang et al. [2]. The results from this study show a good qualitative comparison: a) initial yield stress from this study is 274 MPa, and experimental from [2] is 257 MPa showing a deviation of 6%. b) slope of the flow stress curve showed similar behavior in both the results. The four-grain model showed higher strain hardening compared to Zhang et al. [2]. Further, Fig. 8 also shows the results from two bi-crystal models ($\langle 110 \rangle - \langle 111 \rangle$ and $\langle 110 \rangle - \langle 100 \rangle$). It is observed that the bi-crystal models show a lower value of initial yield compared to the four-grain model and similar material hardening behavior.

5 Conclusion

A digital twin model was developed to simulate the mechanical behavior of polycrystalline BCC α -Fe. Single crystal studies showed a good qualitative match with experimental results from Zhang et al. [2]. Further, the strong dependency of flow stress on ICOs was observed: ICO $\langle 111 \rangle$ has higher material hardening than the remaining ICOs ($\langle 100 \rangle$ and $\langle 110 \rangle$). The results from the bi-crystal model showed that the flow stress behavior varies based on the selection of orientation of constituent grains. That is the bi-crystal model $\langle 110 \rangle - \langle 111 \rangle$ has stronger material hardening compared to $\langle 100 \rangle - \langle 110 \rangle$ model. Further, it was observed that the grain-grain interface for the bi-crystal model shows a significant difference in the shear strain values compared to the corresponding single crystals. This, in turn, resulted in a flow stress behavior with a higher hardening rate for the bi-crystal models. Effect of ICOs on slip system activation showed that the number of active slip systems for the ICOs $\langle 100 \rangle$, $\langle 110 \rangle$, and $\langle 111 \rangle$ were twelve, seventeen, and eleven, respectively. Results from the four-grain model showed the feasibility of extending the use of the proposed model for polycrystalline material. The model, though good for the prediction of the flow stress behavior, needs a further extension to include realistic grain shapes and non-Schmid effects.

Acknowledgements Authors GG, MK, and VC would like to thank the Science and Engineering Research Board (SERB) for funding through the Early Career Research grant ECR/2016/002063.

References

1. Yalcinkaya T, Brekelmans W, Geers M (2008) BCC single crystal plasticity modeling and its experimental identification. *Model Simul Mater Sci Eng* 16:085007. <https://doi.org/10.1088/0965-0393/16/8/085007>
2. Zhang C, Zhang L, Shen W, Xia Y, Yan Y (2016) 3D Crystal plasticity finite element modeling of the tensile deformation of polycrystalline ferritic stainless steel. *Acta Metallurgica Sinica (English Letters)* 30:79–88. <https://doi.org/10.1007/s40195-016-0488-9>
3. Peirce D, Asaro R, Needleman A (1982) An analysis of nonuniform and localized deformation in ductile single crystals. *Acta Metall* 30:1087–1119. [https://doi.org/10.1016/0001-6160\(82\)90005-0](https://doi.org/10.1016/0001-6160(82)90005-0)
4. Lim H, Hale L, Zimmerman J, Battaile C, Weinberger C (2015) A multi-scale model of dislocation plasticity in α -Fe: incorporating temperature, strain rate and non-Schmid effects. *Int J Plast* 73:100–118. <https://doi.org/10.1016/j.ijplas.2014.12.005>
5. Savage D, Beyerlein I, Knezevic M (2017) Coupled texture and non-Schmid effects on yield surfaces of body-centered cubic polycrystals predicted by a crystal plasticity finite element approach. *Int J Solids Struct* 109:22–32. <https://doi.org/10.1016/j.ijsolstr.2017.01.003>
6. Yerra S, Tekoglu C, Scheyvaerts F, Delannay L, Van Houtte P, Pardoën T (2010) Void growth and coalescence in single crystals. *Int J Solids Struct* 47:1016–1029. <https://doi.org/10.1016/j.ijsolstr.2009.12.019>
7. Ha S, Kim K (2010) Void growth and coalescence in f.c.c. single crystals. *Int J Mech Sci* 52:863–873. <https://doi.org/10.1016/j.ijmecsci.2010.03.001>
8. Gröger R, Vitek V (2019) Impact of non-Schmid stress components present in the yield criterion for bcc metals on the activity of $\{110\}\langle 111\rangle$ slip systems. *Comput Mater Sci* 159:297–305. <https://doi.org/10.1016/j.commatsci.2018.12.021>
9. Taylor G (1938) Plastic strain in metals. *J Inst Met* 62:307–324
10. Christian J (1983) Some surprising features of the plastic deformation of body-centered cubic metals and alloys. *Metall Trans A* 14:1237–1256. <https://doi.org/10.1007/BF02664806>

Interaction of Shock Waves in a Multi-material System



Satyendra Pratap Singh, Harpreet Singh, and Puneet Mahajan

Abstract High-velocity impacts produce high pressures and strain rates, which results in shock waves. Shock wave propagating in a heterogeneous medium interacts with material interfaces and the boundaries resulting in change of state of the system. Different shock interactions taking place in layered medium have been numerically simulated using ABAQUS FE package. The interaction of shock with material interface, with boundary, interaction of two shock waves, and interaction of two rarefaction waves have been studied using a layered medium composed of two materials. The shock generated due to high velocity impact has been applied in the form of pressure pulse on the layered medium. Shock front pulse, and square shock pulse has been used for simulation of different interactions of shock, and interaction of rarefaction waves respectively. The pressure and particle velocity plots have been studied. The materials have been considered to behave hydrodynamically under high velocity impact. The Us-Up Equation of State (EoS) has been used. The numerical results for each of the shock interaction have been compared with analytical result. It has been found that numerical and analytical results are in good agreement. The study of different interactions undergone by shock wave in a heterogeneous medium captured the change in material response due to scattering of shock waves.

Keywords Shock wave · Shock wave interactions · Heterogeneous medium · Impact

1 Introduction

Composite materials are used in wide applications because of their lightweight and high specific stiffness and strength properties that are critical to the design. Their application ranges from structures in aerospace and automotive industries to backing materials in ballistic armours and blast-resistant structures in defence. In ballistic

S. P. Singh (✉) · P. Mahajan
Indian Institute of Technology Delhi, Delhi, India

H. Singh
Indian Institute of Technology Goa, Ponda, India

and blast applications where strain rate is of the range of $10^4/s$ or more, materials are subjected to high-pressure dynamic loads, and operate in the hydrodynamic regime. Material in a hydrodynamic regime behave like a compressible viscous fluid, and result in the propagation of shock wave through the material. The stress–strain response is divided into deviatoric and hydrostatic parts. The relation between pressure and volume changes is given by Equation of State (EoS). The nonlinear nature of EoS is responsible for generation of shock when material experiences large deformation at high strain rates. The characterization of material response under shock loading is done experimentally under the uniaxial strain state, using flyer plate test [1]. The non-feasibility of performing experiments because of the high cost involved, theoretical and numerical attempts have been made by researchers to understand the response of composites under shock loading. Composites being heterogeneous and anisotropic in nature, analysing the wave scattering due to multiple interactions, becomes very complicated and difficult. In heterogeneous materials wave scattering occurs due to multiple wave interactions at interfaces and affect the material response to the dynamics loading.

In general, many computational simulations use homogenized properties of the composites while considering various material components. Modelling high velocity impact problems interfaces should be considered as they are the root causes for scattering. Researchers used periodically layered system of materials to study the heterogeneity offered by composites. Shock wave propagation and interaction at individual interfaces has been studied in Davison [2] and Cooper [3]. Tarin [4] simulated the elastic plastic wave propagation generated due to low velocity impact. Sve [5] and Chen [6] found the analytical solution for stress time history at a particular position in a periodically layered material system subjected to unit step loading. Zahunag [7] studied influence of interface scattering effect on shock waves by impacting flyer plates onto periodically layered composites. Chandra [8] examined the response of shock wave on its interaction with an interface and computed the multiple reflection and transmissions. Chen [9] studied the effect of heterogeneity in the form of impedance mismatch, interface density, and thickness ratio on plane wave propagation through layered composites and on the wave structure. Vinamra [10] studied the plate impact problem on layered medium by tracing all the ways propagating in the system and solving them to get the overall response of heterogeneous medium to shock loading. The effect of interfacial (density, structure and strength) and material properties on dissipation and dispersion of shock wave traveling parallel to layers was studied by Specht [11]. Hui [12] and Fernando [13] showed that continuous impedance graded materials with decreasing impedance can be used for the purpose of mitigation of shock. Recently, Fernando [13] studied the shock propagation in impedance graded multi-metallic system. Shock wave interaction at the free surface leading to tensile stress generation was simulated and the features of free surface velocity were explained using the interaction of waves.

Studying the response of shock on propagation in heterogeneous material analytically is complex making the numerical study a more adopted method for charactering the response of the material under shock loading. Simulation of stress wave propagation in elastic solids has been done. However, all the interactions shock undergoes

during propagation in a heterogeneous medium have not been studied. The scattering of waves in the layered material affects the material response thus all the possible interactions of shock in layered medium have been simulated. The numerical results have been compared with the analytical values for each of the interaction.

Interaction of shock with material interface across which the shock impedance is increasing and decreasing have been studied. Interaction of two shock waves and two rarefaction waves have been simulated. Shock interaction with a fixed and a free boundary have been modelled. The study of different interactions provide more understanding of the scattering of waves taking place in the medium and change in material response due to these interactions.

2 Analytical Study

Hypervelocity impact leads to formation of shock wave in the impacted material. The material behaves in a uniaxial strain manner under shock loading. For high velocity impact the hydrostatic stress is very large in comparison to strength of solid and hydrodynamic assumption have been considered. Hydrodynamic assumption neglects the formation of elastic precursor and propagation of only shock wave takes place in the medium. The hydrostatic stress is given by a relation between pressure, specific volume, and specific internal energy known as Equation of State (EoS). Mie-Gruneisen EoS [14] represented in Eq. (1) is used. The Hugoniot relation between any two of 5 shock parameters (pressure, density, specific volume, particle velocity, shock speed and specific internal energy) represent partial EoS. One Hugoniot relation can be converted into another with the help of mass and momentum conservation equation across shock. The Mie-Gruneisen EoS for the isothermal case reduces to pressure–volume ($p - v$) Hugoniot relation represented in Eq. (2). Equation 3 represents the shock-particle velocity Hugoniot ($U_s - u_p$) relation. The pressure-particle velocity ($p - u_p$) Hugoniot represented by Eq. (4) is used in solving the shock interaction problems.

$$p = \frac{\rho_0 C_0^2 \eta}{(1 - s\eta)^2} \left(1 - \frac{\Gamma_0 \eta}{2}\right) + \Gamma_0 \rho_0 E_0 \quad (1)$$

$$p = \frac{\rho_0 C_0^2 \eta}{(1 - s\eta)^2} \quad (2)$$

$$U_s = C_0 + s u_p \quad (3)$$

$$p = \rho_0 C_0 u_p + \rho_0 s u_p^2 \quad (4)$$

where $U_s, u_p, C_0, s, \eta = 1 - \frac{\rho_0}{\rho}, E_0, \Gamma_0$ represents shock velocity, particle velocity, y intercept of $U_s - U_p$ graph, material constant, nominal volumetric strain measure vol , specific internal energy, and Gruneisen constant respectively.

The changes in stress and particle velocity during shock wave interactions are found using the pressure-particle velocity Hugoniot relationship for the transmitted and reflected shock wave respectively. The pressure-particle velocity Hugoniot relationship for the transmitted shock (moving towards the positive z axis) and reflected shock (moving towards the negative z axis) is represented in Eqs. 5 and 6 respectively.

$$P_{transmitted} = \rho_0 C_0 (u_1 - u_0) + \rho_0 s (u_1 - u_0)^2 \quad (5)$$

$$P_{reflected} = \rho_0 C_0 (u_0 - u_1) + \rho_0 s (u_0 - u_1)^2 \quad (6)$$

where ρ_0, C_0, s represents the previously defined quantities. u_0, u_1 are the particle velocity before and after the interaction. The pressure and particle velocity at the interface is same for both the materials forming the interface due to equilibrium and contact constraint. Thus, the pressure for transmitted and reflected shock is equated to get the pressure and particle value after the interaction.

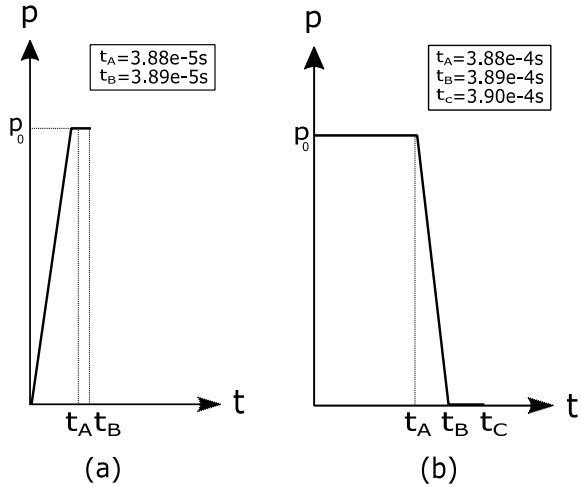
Shock impedance is defined as product of initial density and shock speed ($Z = \rho_0 U$). The final pressure and particle velocity after the interaction of shock with material interface can higher or lower than the values before interaction depending on the change in impedance (Z) of the two materials forming the interface.

3 Numerical Study

Numerical simulations have been carried out Abaqus Explicit Finite element package. A layered material system composed of two materials has been modelled. The two materials in the layered system are tied to each other to make them perfectly bonded. The aim is to study the material response due to scattering of shock wave in the layered material system and compare its result with the analytical calculated results for each interaction. Z axis is the axis of the bar and the wave travels longitudinally in that direction. A 3 dimensional C3D8R an 8 noded brick-element with reduced integration having hourglass control has been used to model the layered material system.

The impact of flyer on the layered material system generating shock has been modelled by applying the shock in the form of pressure pulse on the front face of the layered material system. The shock pulse applied on the layered system has been shown in Fig. 1. The material deforms in a state of uniaxial strain on shock loading. The uniaxial strain behaviour has been modelled by allowing only the translation along z axis. The other degrees of freedom along other 2 axis are constrained by applying the boundary conditions on the four faces of the bar (Top, Bottom, Left, and Right). The end face of the layered material is kept fixed or free depending upon

Fig. 1 Pressure pulse used as input (a) Shock front pulse (b) Square shock pulse



the type of interaction studied. During hyper velocity impacts the hydrostatic stress exceeds the material strength and the contribution of deviatoric stress is neglected treating the solid as fluid, known as Hydrodynamic assumption [10]. The analysis has been considered to take place isothermally, thus shock-particle velocity Hugoniot ($U_s - u_p$) relation has been used to define the material. The material properties considered for the simulation purpose have been shown in Table 1. The material properties have been taken from Cooper [6].

Linear artificial viscosity is kept as 0.06 to dampen out the oscillations in the result and the bulk viscosity parameter as zero as the shock pulse applied as input is given very small thickness to not make it a discontinuity. Fixed time increment of $1e-6$ s and the mesh size is used keeping in mind the Courant-Friedrichs-Lewy condition (CFL condition). Figure 2 shows the mesh sensitivity analysis done to identify the level of mesh refinement required to achieve accurate results from the numerical models. For this purpose, a 25 GPa pressure pulse with amplitude variation as shown in Fig. 1a is applied on the bar made of Aluminium with 10 m length. Pressure variation with time in an element at the centre of the bar ($z = 5$ m) has been recorded. The mesh size in the bar is gradually reduced, starting from 0.2 m, until the pressure pulse accurately compared with the analytical solution of pressure pulse with steep front and no oscillation. It is observed that a pulse with steep front and least oscillations about the mean pressure of 25 GPa is recorded for mesh sizes less

Table 1 Material properties used [6]

Material	Density (Kg/m ³)	C ₀ (m/s)	s
Aluminium	2833	5041	1.420
Copper	8930	3940	1.489
Steel	7896	4569	1.4
Brass	8450	3726	1.434

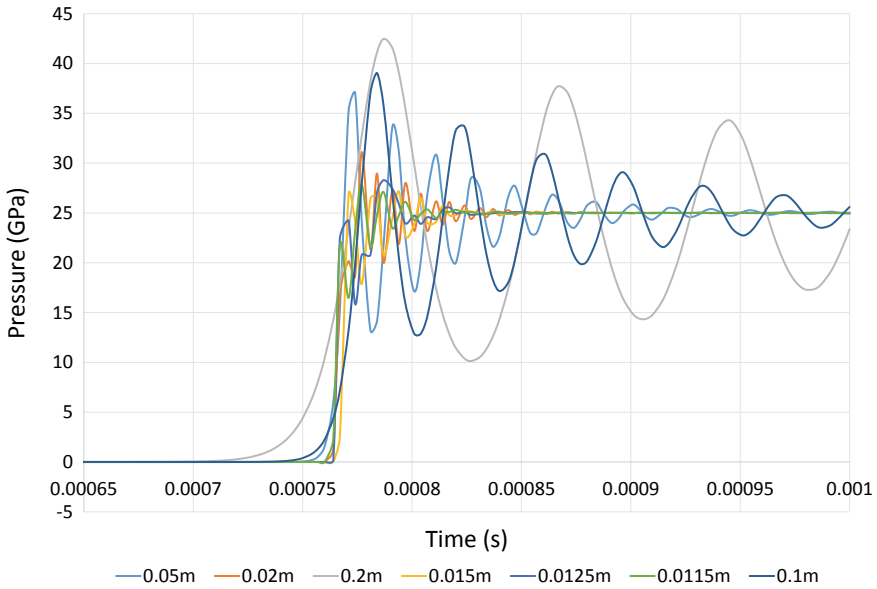


Fig. 2 Pressure variation with time for different mesh sizes

than 0.02 m. Hence, based on the results from the mesh convergence study, a mesh size of $0.015 \times 0.015 \times 0.015$ m is used for the bar in all the case of numerical study.

The pressure pulse in Fig. 1a is used to model the shock. Pressure pulse in Fig. 1a represents the shock front and doesn't contain the back part of the square shock pulse to avoid rarefaction wave. Interaction of two rarefaction leads to the formation of tensile stress in the material. The pressure pulse in Fig. 1b, represents the square shock pulse with rarefaction, is used to simulate the collision of two rarefaction waves. The schematic diagrams for the different interactions of shock wave that have been studied are shown in Fig. 3.

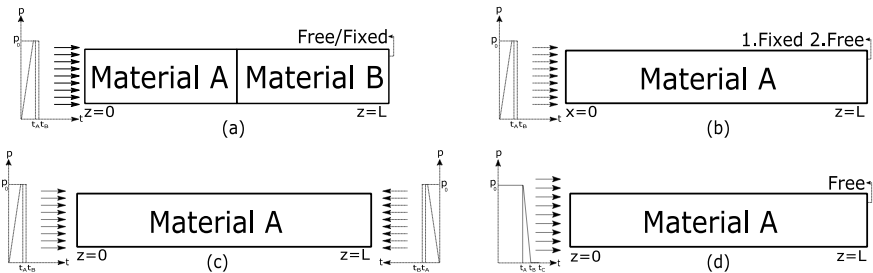


Fig. 3 Schematic diagram for studying the shock interaction (a) at the interface of two materials (b) with boundary (fixed and free) (c) with opposite moving shock (d) study of interaction of two rarefaction waves

4 Results and Discussion

4.1 Interaction of Shock at Material Interface

Interaction of shock with material interface having increasing and decreasing shock impedance across it has been studied here.

Shock at Material Interface with Decreasing Impedance $Z_A > Z_B$

Layered material is made of Copper as material A and Aluminium as material B. Copper has more shock impedance than aluminium making impedance decrease across the material interface on going from material A to material B. From Fig. 4 it is observed that stress decreases from 25 to 14.2 GPa, and Fig. 5 shows that initial particle velocity of 582.44 m/s increases to 807.45 m/s, after interaction with material interface. It is observed that interaction of shock with material interface across which the shock impedance decrease results in the reduction and increment in the shock pressure and particle velocity respectively.

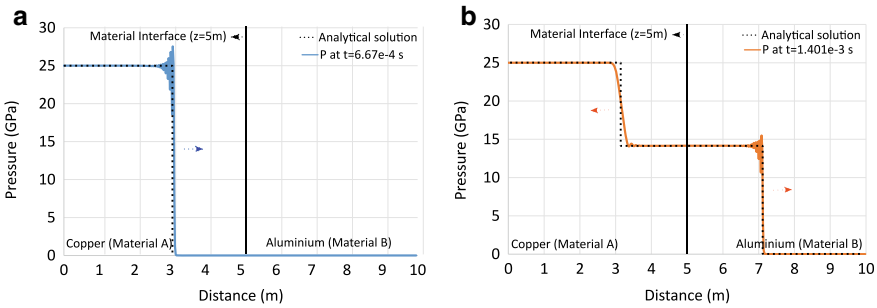


Fig. 4 Pressure v/s Distance for $Z_a > Z_B$ (a) before interaction (b) after interaction

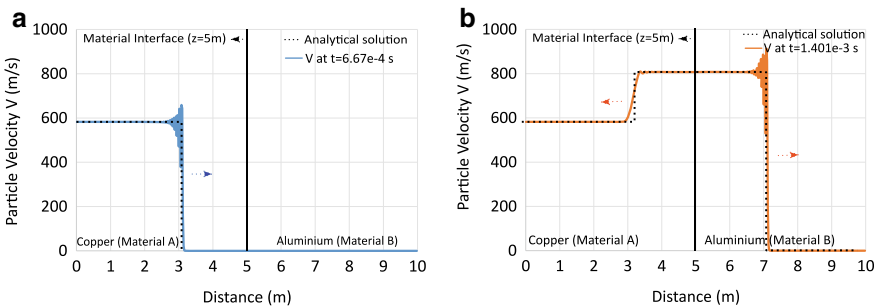


Fig. 5 Particle velocity v/s Distance for $Z_a > Z_B$ (a) before interaction (b) after interaction

Shock at Material Interface with Increasing Impedance $Z_A < Z_B$

Layered material is made of Aluminium as material A and Copper as material B. Copper has more shock impedance than aluminium making impedance increase along the material interface on going from material A to material B. From the Fig. 6 it is observed that stress increases from 25 to 37.9 GPa and Fig. 7 shows that initial particle velocity of 1280 m/s decreases to 821.842 m/s after interaction with material interface. It is observed that interaction of shock with material interface across which the shock impedance increases results in the increment and reduction in the shock pressure and particle velocity respectively.

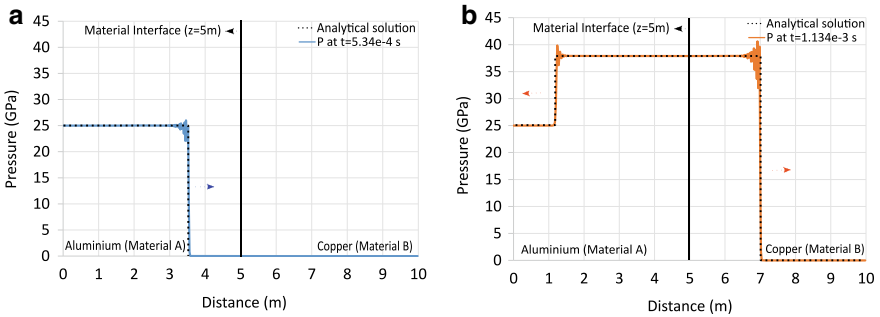


Fig. 6 Pressure v/s Distance for $Z_a < Z_B$ (a) before interaction (b) after interaction

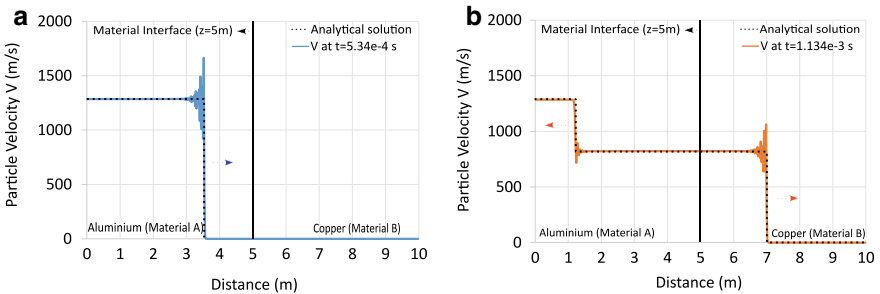


Fig. 7 Particle velocity v/s Distance for $Z_a < Z_B$ (a) before interaction (b) after interaction

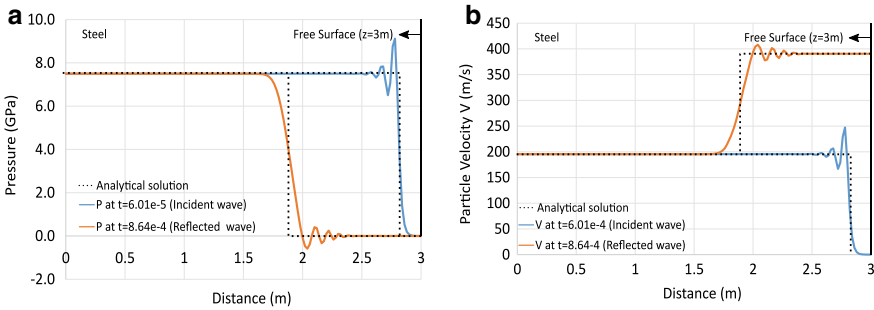


Fig. 8 Shock wave interaction with fixed boundary (a) Pressure v/s distance (b) Particle velocity v/s distance

4.2 Interaction of Shock with Boundary

Shock wave interaction with boundary have been considered in a single material with free and fixed constraint.

Interaction of Shock with Fixed Boundary

The rear face ($z = 3\text{ m}$) of the bar has been fixed and a pulse of 7.5 GPa has been applied on the front face of the bar ($z = 0$). From the Fig. 8b it is observed that initial particle velocity of 195 m/s becomes zero as the surface is fixed, and Fig. 8a shows that stress gets doubled from 7.5 GPa to around 16 GPa after the interaction with fixed surface. It is observed that interaction of shock with fixed surface results in a reflected wave with double the initial stress and same particle velocity in opposite direction making the overall particle velocity zero with the fixed surface.

Interaction of Shock with Free Boundary

The rear face ($z = 3\text{ m}$) of the bar has been made free and a pulse of 7.5 GPa has been applied on the front face of the bar ($z = 0$). From the Fig. 9 it is observed that initial particle velocity of 195 m/s becomes 390 m/s and stress reduces from 7.5 GPa to 0 after the interaction with free surface. It is observed that interaction of shock with free surface results in a reflected wave with zero stress (as free surface has zero stress) and double the initial particle velocity releasing the compressed material to make the stress zero.

4.3 Collision of Two Shock Waves

Collision of two shock wave have been simulated by applying one shock pulse on the front face ($z = 0$) moving in the positive z direction and other shock pulse on the rear face ($z = 10\text{ m}$) moving in the negative z axis towards the front shock. Shock pulse of 12 GPa has been applied on front face and 18 GPa on the rear face. From

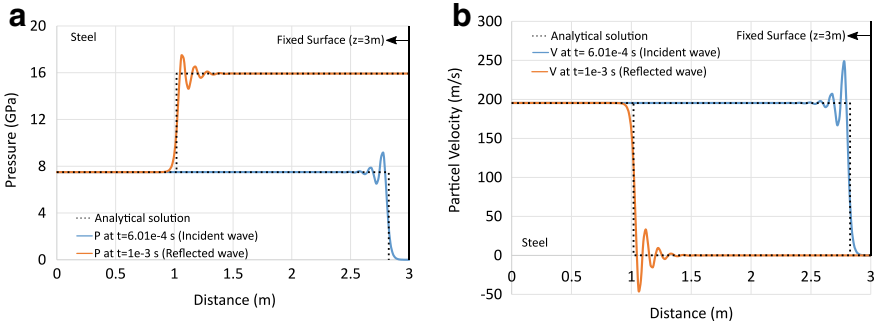


Fig. 9 Shock wave interaction with free boundary (a) Pressure v/s distance (b) Particle velocity v/s distance

the Fig. 10 it is observed that the stress after the collision of these two shocks is 34.3 GPa. Figure 11 shows the particle velocity is -144.72 m/s after the interaction between two shocks. It is observed that the pressure after the collision of two shocks is greater than the sum of individual shock pressure. The particle velocity is negative

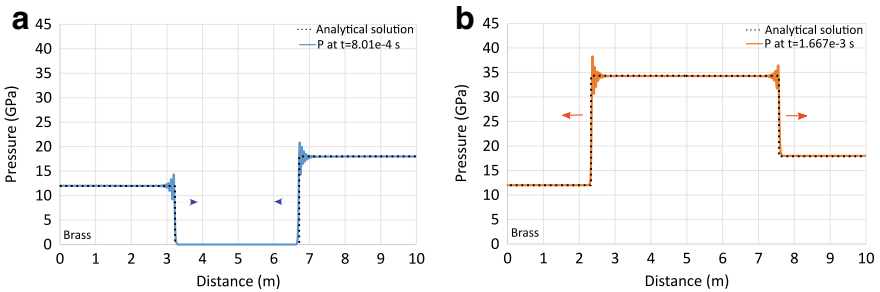


Fig. 10 Pressure v/s Distance for collision of two shocks (a) before interaction (b) after interaction

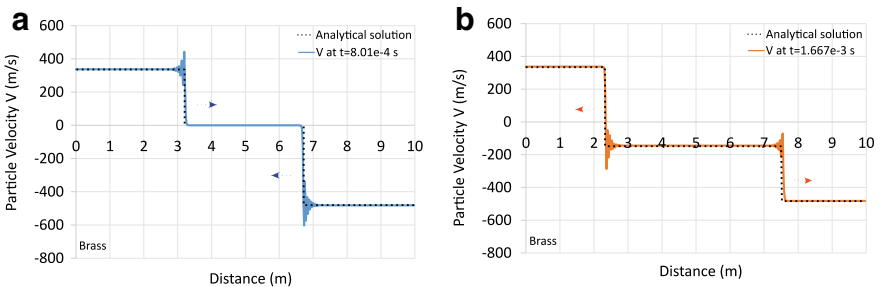


Fig. 11 Particle velocity v/s distance for collision of two shocks (a) before interaction (b) after interaction

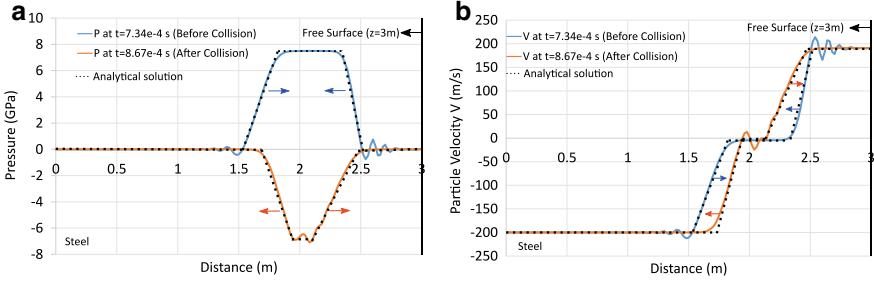


Fig. 12 Interaction of two rarefaction waves (a) Pressure v/s Distance (b) Particle velocity v/s Distance

as the shock pulse moving in negative z axis was more in magnitude than the shock moving in positive z axis.

4.4 Collision of 2 Rarefaction Waves

The pressure pulse used here is the one shown in Fig. 1b which represents the square shock pulse with rarefaction behind the shock front. The magnitude of the pulse applied is 7.5 GPa. The shock front of the square shock pulse interacts with the free surface and generates a rarefaction wave travelling in the opposite direction of the interacting shock front. The duration of the pulse used for the simulation has been kept long to make possible the interaction of two rarefaction waves: rarefaction at the back of square shock pulse, and rarefaction generated after the interaction of shock with the free surface. The interaction of two rarefaction waves moving opposite to each other results in the formation of tensile stresses in the material. In Fig. 12 the blue profile shows two rarefactions moving towards each other before interaction, and the orange profile represents the tensile wave formed after the interaction of two rarefaction waves. Material failure occurs when the magnitude of tensile stress generated is more than the tensile strength of the material. The analytical results for the pressure and particle velocity, before and after interaction are in good agreement with the numerical simulation results.

5 Conclusion

Numerical and analytical study of different interactions a shock wave undergoes on propagation in a layered medium has been done. A layered medium composed of two materials has been used for the purpose of the simulation. Shock interaction at material interface, shock interaction at boundary, collision of two opposite moving shocks, and collision of two rarefaction waves have been simulated. The comparison

of numerical and analytical simulation results show that the both the results are in very good agreement and suggest that the numerical methodology adopted to study change in material response due to scattering of shock from interfaces and boundaries is accurate.

The methodology can be applied to a multi-material layered medium composed of more than two materials, to study the effect of heterogeneity offered by the layered material system.

Acknowledgments This work was supported by a start-up research grant (SRG/2020/000480) of the Science and Engineering Research Board of India. The content is solely the responsibility of the authors and does not necessarily represent the official views of the funding organization.

References

1. Field JE, Walley SM, Proud WG, Goldrein HT, Siviour CR (2004) Review of experimental techniques for high rate deformation and shock studies. *Int J Impact Eng* 30:725–775. <https://doi.org/10.1016/j.ijimpeng.2004.03.005>
2. Davison L (2008) *Fundamentals of shock wave propagation in solids*. Springer Science & Business Media, New York
3. Cooper PW (2018) *Explosives engineering*. John Wiley & Sons, New York
4. Vanichayangkuranont T, Maneeratana K, Chollacoop N (2005, October). Simulations of stress wave propagation from dynamic loads. In: Proceedings of the 19th conference of mechanical engineering network of Thailand (ME-NETT19), Phuket, Thailand, October, pp 19–21
5. Sve C (December 1, 1972) Stress Wave Attenuation in Composite Materials *ASME J Appl Mech* 39(4):1151–1153. <https://doi.org/10.1115/1.3422852>
6. Chen X, Chandra N, Rajendran AM (2004) Analytical solution to the plate impact problem of layered heterogeneous material systems. *Int J Solids Struct* 41(16–17):4635–4659. <https://doi.org/10.1016/j.ijsolstr.2004.02.064>
7. Zhuang S, Ravichandran G, Grady DE (2003) An experimental investigation of shock wave propagation in periodically layered composites. *J Mech Phys Solids* 51(2):245–265. [https://doi.org/10.1016/S0022-5096\(02\)00100-X](https://doi.org/10.1016/S0022-5096(02)00100-X)
8. Chandra N, Chen X, Rajendran AM (2002) The effect of material heterogeneity on the shock response of layered systems in plate impact tests. *J Compos Tech Res* 24(4):232–238. <https://doi.org/10.1520/CTR10929J>
9. Chen X, Chandra N (2004) The effect of heterogeneity on plane wave propagation through layered composites *Compos Sci Technol* 64(10–11), 1477–1493. <https://doi.org/10.1016/j.compscitech.2003.10.024>
10. Agrawal V, Bhattacharya K (2014) Shock wave propagation through a model one dimensional heterogeneous medium. *Int J Solids Struct* 51(21–22):3604–3618. <https://doi.org/10.1016/j.ijsolstr.2014.06.021>
11. Specht PE, Weihs TP, Thadhani NN (2016) Interfacial effects on the dispersion and dissipation of shock waves in Ni/Al multilayer composites. *J Dyn Behav Mater* 2(4):500–510. <https://doi.org/10.1007/s40870-016-0084-0>
12. Hui D, Dutta PK (2011) A new concept of shock mitigation by impedance-graded materials. *Compos B Eng* 42(8):2181–2184
13. Fernando PLN, Mohotti D, Remennikov A (2019) An innovative approach of using continuous impedance-graded metallic composite system for attenuation of stress waves. *J ApplMech* 86(6):061002. <https://doi.org/10.1115/1.4042681>

14. Fernando, PLN, Mohotti D, Remennikov A, Hazell PJ, Wang H, Amin A (2020) Experimental, numerical and analytical study on the shock wave propagation through impedance-graded multi-metallic systems. *Int J MechSci* 178:105621. <https://doi.org/10.1016/j.ijmecsci.2020.105621>
15. Meyers MA (1994) *Dynamic behavior of materials*, John Wiley & Sons, New York

Analytical Modeling of Electro-Mechanical Linear Actuator for Control Pedal of Unmanned Ground Vehicle



R. Prem Chand, P. Chellapandi, and C. Lakshmana Rao

Abstract The recent development of actuation system is applied in various areas like automation of vehicle system and robotics system. The driver's control of a manned vehicle can be automated to make them an unmanned ground vehicle (UGV) along with a control system and remote station. The electro mechanical actuator plays a major role to convert a manned vehicle into UGV to operate the driver control pedals like accelerator, brake, steering and gear shifter. To design and develop an actuator prototype, analytical modeling of electro mechanical actuator is very much necessary to derive a valid design. In this paper, an analytical model is proposed and developed using principle of virtual work applying quasi static condition for a linear electro-mechanical actuator which operates a control pedal of UGV. The actuation of control pedal by the actuator is considered as single degree of freedom. The empirical correlation between the two parameters torque and force are derived correlation from virtual work principle and variation due to other parameters such as spring stiffness, leverage length or actuation height of actuator on pedal are quantified and the variation has been understood. Based on that, the empirical correlation has been developed which will be used for controlling system, particularly for the understanding the perturbation at every configuration selected. In the present paper, a particular configuration 45° theta has been taken for the case study.

Keywords Electro mechanical actuation · Unmanned ground vehicle · Actuator · Analytical model · Principle of virtual work · Quasi static condition · Control pedal

1 Introduction

Unmanned ground vehicles (UGV) application in various fields like transportation and military fields for different missions is very much essential in near future.

R. P. Chand (✉) · P. Chellapandi · C. L. Rao
Department of Applied Mechanics, IIT Madras, Chennai 600 036, India
e-mail: am19m011@smail.iitm.ac.in

C. L. Rao
e-mail: lakshman@iitm.ac.in

The challenges faced in the development of UGV are conversion of manned military vehicle into remotely operated unmanned vehicle, design of suitable electro-mechanical actuator for each driver’s control in the available space without removing the existing mechanical system which is essential for manual override and mathematical model for validating and design modification of actuators. The driver’s control of a manned vehicle can be automated to make to them an unmanned ground vehicle along with a control system and remote station. A set of electro-mechanical actuators can be incorporated in the vehicle for different driver’s controls like accelerator, brake, steering, gear shifter and parking brake. These controls in the vehicle may be pedal operated or hand lever operated. A rotary or linear electro-mechanical actuator shall be incorporated for each of the single degree of freedom actuation.

The electro mechanical actuator application has been prompted by the significant benefits deriving from the replacement of the traditional mechanical-hydraulic systems with electric systems: higher efficiency, lower maintenance requirements, better dynamic response and accuracy, much higher overall design flexibility far easier integration with control and monitoring systems, unprecedented levels of drive assistance functions, and so on. The keys components of an automated system are electric actuator, rotary to linear movement mechanism, control pedal and feedback sensors [1–4].

In [5], the robust control scheme with partially known dynamics was proposed for steer by wire system. It was shown that an steer by wire system is considered as a partially known system with an unknown lumped uncertainty. The dynamic equation of the steering motor was given to relate the steering wheel rotation to the torque transmitted to the steering shaft. In [6], the application of energy method to the real world problem with the classical approach principle of virtual work. The system with single degree of freedom can be solved without the differential equation and this gives simpler equation which relates input and output quantities with different design parameters. In [7], a virtual simulation system model was proposed for two axis CNC machine which has x and y axis movements. A linear dynamic mathematical model gives transfer function between the torque input and the angle output of the servo motor unit.

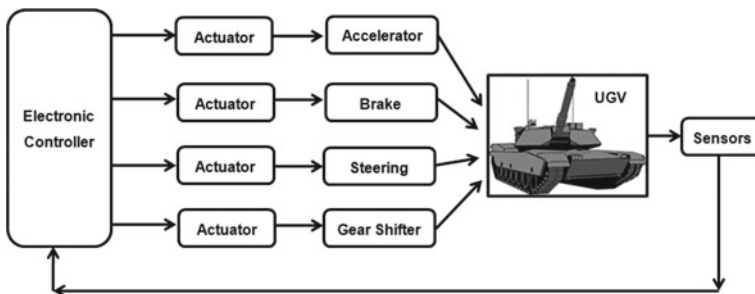


Fig. 1 Drive by wire system to remotely operate UGV

In this paper, a simpler analytical model is proposed for the linear electro mechanical actuation system which has ball screw assembly and the control pedal connected together with roller contact to allow linear horizontal movement of ballscrew nut with push bar and rotary motion of control pedal. This analytical model using this energy method with quasi static condition gives simpler equation without differential equation. The input force and torque requirement of the system is related to angle output of control pedal. As the torque value is used for control system, the quasi static analysis is more appropriate.

The objective is to develop analytical model of linear electro mechanical actuator with control pedal. This model includes a ball screw and nut mechanism with a push bar to operate the rotary control pedal which has pin joint support at base. A closed coil helical spring element is connected to the control pedal at a distance L_2 from the pivotal point as shown in Fig. 3. The analytical model is developed using energy method, principle of virtual work by applying quasi static condition of system which includes the ball screw system integrated with the control pedal. A roller contact is provided at the point L_4 between the linear actuator and the control pedal instead of pivotal joint to provide manual override option. In this analytical model, the force and torque required at the actuator side is determined for quasi static angular position of control pedal.

The Sect. 2 describes the methodology and approach of developing the analytical model. It briefly tells about the various parameters incorporated in the analytical model. The free body diagram analysis is shown to describe various forces acting on the control pedal of actuation system at various points. The Sect. 3 shows the force and torque results got from the analytical model using principle of virtual work with quasi static condition. The parameters are kept as variables to generate different plots for study and analysis of force and torque with respect to the angular position of the control pedal. The Sect. 4 covers the overall summary of the work and gives conclusion related to the analytical model and the work.

2 Analytical Model

2.1 Specifications and Assumptions

The electro mechanical actuator consists of DC servo motor to deliver torque, ball screw and nut mechanism to convert rotary motion of screw into translator movement of nut. A push bar with roller is connected to the ball screw nut to push a rotary driving control pedal of UGV. The objective is to derive equation for force and torque with respect to angular displacement of pedal by applying quasi static condition. The elements are modeled as rigid bodies and the parameters in the model can be varied according to the requirement of simulation.

The assumptions are listed below

- Single degree of freedom system

- Frictional forces are not considered
- All bodies are assumed as rigid bodies
- Variation as $\delta\theta$
- Maximum angular displacement of pedal is 45°
- Quasi static condition

The quasi static assumption is made with the main objective of finding the force - torque relation for every configuration and ignoring all the other dynamic effects.

2.2 Modeling of Actuation System

The accelerator pedal of Unmanned Ground Vehicle (UGV) is having pin joint with the base as shown in Fig. 2. The pedal rotates about the point A. The ball screw mechanism converts the rotary motion of DC servo motor to linear motion and the force ‘F’ is transferred horizontally to the pedal at point D. There is a roller contact between the push bar and the pedal to avoid sliding friction. A closed helical coil spring is connected to the pedal at point B and the spring will be in unstretched position when the pedal is in vertical position. The mass of the pedal is acting vertically downwards at the point C. As the rigid bodies in the system are connected mechanically, the rotary displacement of motor shaft at input end leads to angular displacement of pedal. This actuation system can be modeled as single degree of freedom system.

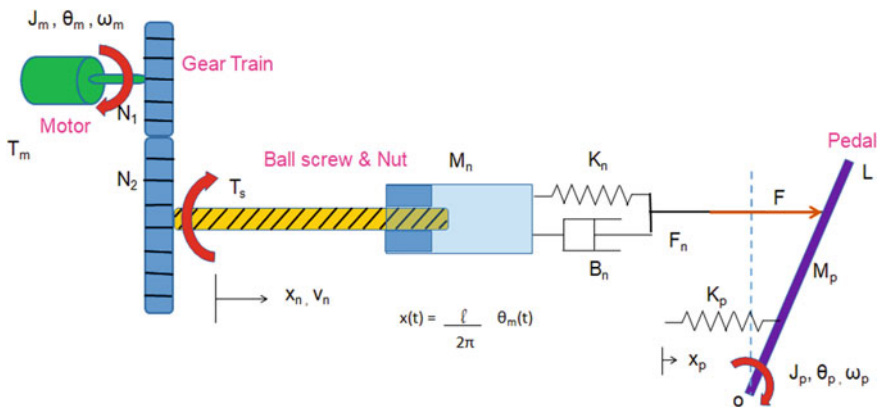


Fig. 2 Schematic representation of actuator and the pedal assembly

2.3 Principle of Virtual Work

The classical approach principle of Virtual work shall be used for single degree of freedom (DOF) system of rigid bodies. This is a energy method which use the concepts of work and energy which are scalars by nature. In this, all the rigid bodies are connected and static equilibrium condition is applied. The application of equilibrium conditions for a system of bodies requires a free-body diagram analysis. The force 'F' does the work 'W' when the point of application of the force moves through a distance. Hence, the effect of an external force, i.e., the displacements of the points of application of the forces, will naturally be involved in any statement involving energy (Fig. 3).

An infinitesimal imaginary displacement ' $\delta\theta$ ', called as virtual displacement, will be given to the system about a point and not considering the motions of the bodies. Self-equilibrating forces that exist in the system will do work only when their points of application are subjected to virtual displacements, and this work is called virtual work. This is applied to determine equilibrium configuration, unknown forces and reactions in rigid body assembly.

For body with static equilibrium, δW is always zero as $\sum_i^n M_i = 0$, M_i is the moment of force F_i , and is independent of the applied virtual rotation, $\delta\theta$. The total work done by the equilibrating external forces is always zero for any arbitrary infinitesimal virtual displacements (Fig. 4) [6].

Let the net work done is equal to zero

$$\delta W = F\delta_{x_D} - K\Delta\delta_{x_B} + mg\delta_{y_C} = 0 \tag{1}$$

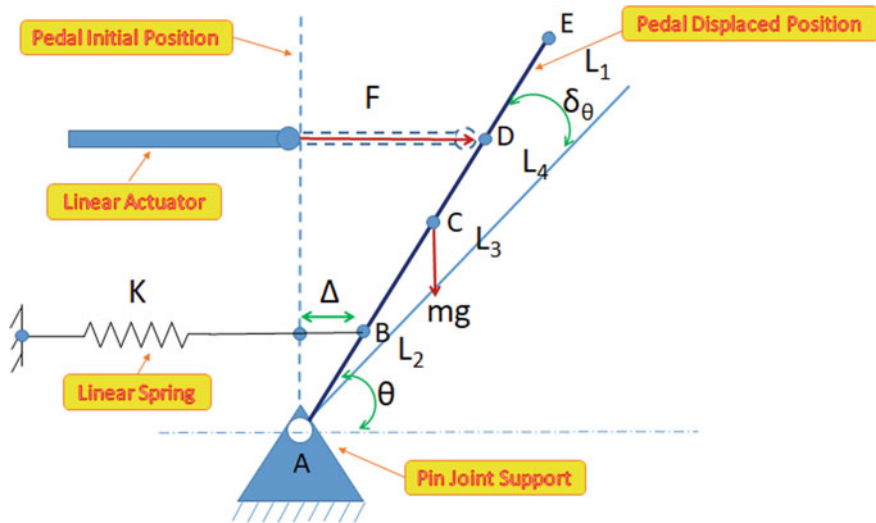
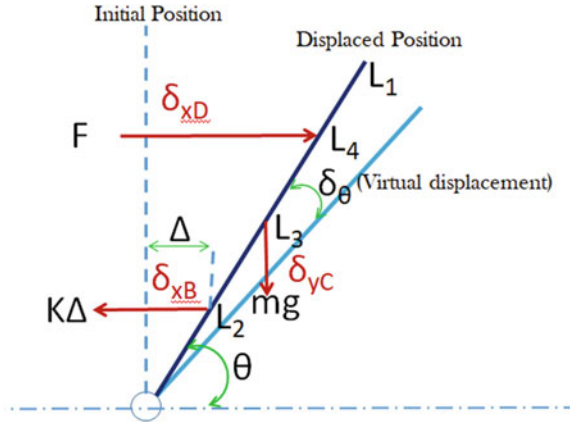


Fig. 3 Schematic representation of actuator pushing the rotary pedal and Forces acting at different locations on the pedal

Fig. 4 Free body diagram of the pedal



The displacement δ_{xD} is along the direction of F, therefore positive sign
 The displacement δ_{xB} is opposite to the direction of K, therefore negative sign
 The displacement δ_{yC} is along the direction of mg, therefore positive sign
 For point 'B', the x and y coordinate values are

$$x = L_2 \cos \theta \quad \text{and} \quad y = L_2 \sin \theta \tag{2}$$

$$\delta x_B = -L_2 \sin \theta \delta \theta$$

For point 'C', the x and y coordinate values are

$$x = L_3 \cos \theta \quad \text{and} \quad y = L_3 \sin \theta \tag{3}$$

$$y_C = L_3 \cos \theta \delta \theta$$

For point 'D', the x and y coordinate values are

$$x = L_4 \cos \theta \quad \text{and} \quad y = L_4 \sin \theta \tag{4}$$

$$\delta x_D = -L_4 \sin \theta \delta \theta$$

$$\Delta = L_2 \cos \theta$$

Substituting the displacement values in Eq. 1, we get

$$\delta W = F \delta x_D - K \Delta \delta x_B + mg \delta y_C = 0 \tag{5}$$

$$F L_4 \sin \theta \delta \theta - K L_2 \cos \theta L_2 \sin \theta \delta \theta + mg L_3 \cos \theta \delta \theta = 0$$

$$F L_4 \sin \theta - K L_2^2 \sin \theta \cos \theta + mg L_3 \cos \theta = 0 \tag{6}$$

$$F = \frac{\cos \theta (K L_2^2 \sin \theta - mg L_3)}{L_4 \cos \theta}$$

The horizontal Force applied by the linear actuator on the pedal,

$$F = \frac{KL_2^2 \sin\theta - mgL_3}{L_4 \tan\theta} \tag{7}$$

Solving the equation, we get the mathematical relation between angular displacement theta and Force to be applied on the pedal. The torque on ball screw can be calculated using below mentioned relation by substituting lead and efficiency values of ball screw.

The Torque applied by the DC servo motor to the ball screw,

$$T = \frac{Fl}{2\pi\eta} \tag{8}$$

where,

l = pitch of the ball screw

η = efficiency of the ball screw assembly

3 Results and Discussion

In this design, the total angular displacement of pedal is taken as 45°. This angular displacement value is sufficient for most of the pedal actuation system. The parameter study has been done by changing the system parameters like spring stiffness k , the length L_4 which is the vertical height of contact of actuator on control pedal, and the efficiency of ball screw system η . The various graphs are plotted for the input and output values by varying the system parameters.

The force to be applied by the linear actuator on pedal with respect to angular displacement of pedal from 0° to 45° for $k = 2.5$ N/mm is plotted as a graph and shown in Fig. 5(a).

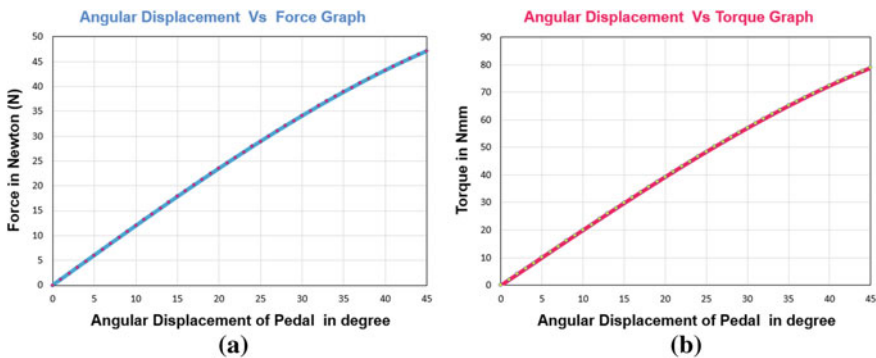


Fig. 5 a Angular displacement of pedal vs force and b Angular displacement of pedal vs Torque

The torque to be applied at the input side of ball screw by the motor with respect to angular displacement of pedal from 0° to 45° for $k = 2.5 \text{ N/mm}$ is plotted as a graph and shown in Fig. 5(b).

This study of parameters helps to determine the Force and Torque requirement of the system. The system parameters can be varied according to the specification of the elements in the system to evaluate input force and torque at actuator end to get the required angular displacement of control pedal. As we are going to use the system for every discrete position, we want to find out the force and torque distribution for displacement pattern. At every configuration what will be the force and torque relation. At every discrete configuration from 0 to 45°, we are trying to understand the relation between the force and torque. Since the torque value is the input to control system of the actuation, the value derived from the equation Eq. 8 using virtual work gives the balancing torque to maintain the control pedal at particular discrete angular position. The slope of the torque vs force curve is related to the factor, $\sqrt{2\pi} \eta$. The stiffness of the spring and the leverage length L_4 are measurable parameters and the

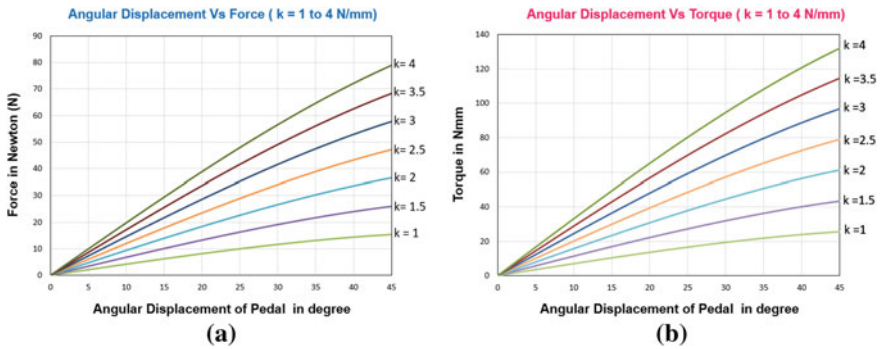


Fig. 6 a Angular displacement of pedal vs Force and b Angular displacement of pedal vs Torque for different spring stiffness ‘k’

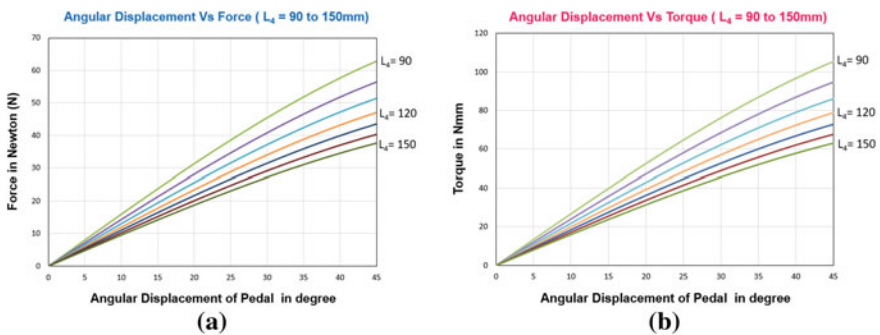


Fig. 7 a Angular displacement of pedal vs Force and b Angular displacement of pedal vs Torque for different leverage length ‘L₄’ on pedal

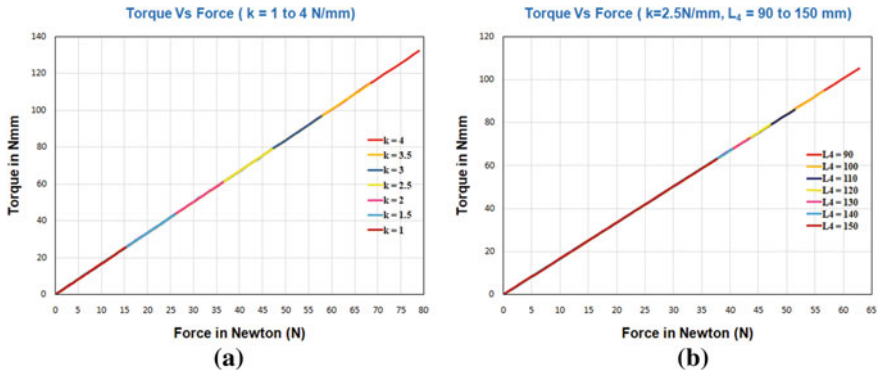


Fig. 8 **a** Torque vs Force for different spring stiffness ‘k’ and **b** Torque vs Force for different leverage length ‘L₄’ on pedal

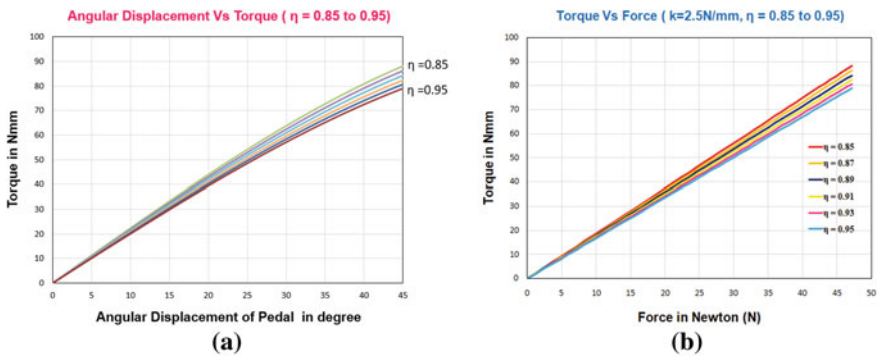


Fig. 9 **a** Angular displacement of pedal vs Torque and **b** Torque vs Force for different efficiency values of ball screw system ‘η’

force can be measured only by experimentation. If the torque—force curve is given, then the slope can be matched and used to find the efficiency of the ball screw system.

4 Conclusion

For a typical electromechanical actuator system, an analytical relation among the applied torque to lead screw, linear force transmitted and resulting angular displacement of control pedal is derived for quasi static condition. From the derived formula, the torque required at the input side of ball screw by the motor and angular displacement of control pedal is obtained. Results of parametric study are plotted in Figs. 6, 7, 8 and 9. Since the torque value is the basic input for the present control system, the quasi static analysis is more appropriate. The established correlation derived

from empirical relation is adequate and applicable for the control of the system. The analytically derived torque—force relation can be compared using experimental model of actuator and further used for assessing the efficiency of the system. Further validation of the empirical correlation through experimental mock up is planned by the authors at the institute.

References

1. Ilene J. Busch-Vishniac, (2012) *Electromechanical Sensors and Actuators*, Springer New York, 987654321 ISBN 0-387-98495-X
2. Bertoluzzo M, Bolognesi P, Bruno O, Buja G, Landi A, Zuccollo A (2004) Drive-by-wire systems for ground vehicle. In: 2004 IEEE international symposium on industrial electronics, IEEE
3. Bolognesi P, Bruno O, Landi A, Sani L, Taponecco L (2003) Electric machines and drives for X-by-wire systems in ground vehicles. In: 10th European conference on power electronics and applications, 2003, France
4. Wang X, Liao R, Shi C, Wang S (2017) Linear extended state observer-based motion synchronization control for hybrid actuation system of more electric aircraft, 2017. *Sensors* 7(11):2444
5. Wang H, Man Z, Shen W, Cao Z, Zheng J, Jin J, Tuan DM (2014) Robust control for steer-by-wire systems with partially known dynamics. *IEEE Trans Industr Inf* 10(4):2014
6. Lakshmana Rao C, Lakshminarasimhan J, Sethuraman R, Sivakumar SM (2003) *Engineering Mechanics Statics and Dynamics*. Prentice-Hall of India, New Delhi
7. Guo H, Li J, Meng T, Li Z (2016) The research on virtual simulation of lead screw system. In: *Proceedings of the IEEE international conference on information and automation Ningbo, China, August 2016*

Evaluation of Population-Based Metaheuristic Methods for Optimization of Truss Structures



K. Akanksh and B. N. Rao

Abstract This research critically compares the water evaporation optimization metaheuristic, the tug-of-war optimization metaheuristic, the vibration particle system metaheuristic, the cuckoo search metaheuristic, and the imperialist competition algorithm for truss sizing optimization problems which includes node displacements and member stress constraints. The evaluation is based on benchmarks with different design variables and static indeterminacy. A strict statistical study was conducted on a large sample size and events occurring through the optimization exercise was observed. This shows and explains the convergence performance of each algorithm. The results show that Cuckoo Search is the best metaheuristic in terms of robustness, performance, and ability to scale.

Keywords Truss weight minimization · Water evaporation optimization algorithm · Tug of war optimization algorithm · Vibrating particles system algorithm · Cuckoo search algorithm · Imperialist competitive algorithm

1 Introduction

Optimization of truss structures involves all or part of the difficulties faced in real-world optimization problems such as non-convexity of functions, discrete requirements of variables, and the uncertainty of a global optimum. Hence, researchers explored mathematical programming methods (MIP in particular) and optimality criteria (OC) methods to optimize truss structures.

MIP can guarantee a global optimum or a solution within an acceptable tolerance range but there are a few key disadvantages with this approach. Firstly, it requires a clearly explained model of all equations of problems with linear relations, and this requirement cannot always be fulfilled as most real-world problems are non-linear in nature. In such cases, the linearization will bring in more complexity and a significant

K. Akanksh (✉) · B. N. Rao

Department of Civil Engineering, Indian Institute of Technology Madras, Chennai 600036, India

B. N. Rao

e-mail: bnrao@iitm.ac.in

degree of error which may not be trivial. Another shortcoming of this approach is the non-polynomial relationship between problem execution, problem dimensions and design variables. This proves to be a hindrance in large-scale problems [1].

In the OC method, simple recursive formulas are derived from assumptions about the best designs. These formulae can be practical and straightforward, but they generally don't converge for statically indeterminate structures. Also, they do not solve the problem precisely in operational research terms [2].

Considering the disadvantages of traditional methods, the implementation of soft computing optimization methods has shown exponential growth in recent years. These methods have the following advantages over traditional methods:

- Meta-heuristics do not need a precise mathematical model of the problem being discussed.
- They provide an exciting platform to solve practical design problems, in which field knowledge and experience plays a crucial role.
- They uncover many ground-breaking and successful results in numerous fields of engineering and technology that are in great need of optimization.

Based on the advantages offered by meta-heuristic algorithms while solving optimization problems, it is necessary to compare and evaluate the meta-heuristic algorithms being developed by researchers worldwide.

2 Problem Statement

The main purpose of the truss structure sizing optimization design is to obtain the configuration corresponding to the minimum mass of the structure while also satisfying some or all of member stresses and nodal deflection constraints. In this set of problems, the area cross-section of individual members is considered as design variables. The most satisfactory proposal of the truss configuration can be signified as:

$$\text{Find } A = [A_1 \cdots A_n]$$

$$\text{To minimize } W(A) = \sum_{i=1}^n \gamma_i A_i L_i$$

Which are subject to the below-mentioned constraints:

$$\sigma_i^c \leq \sigma_i \leq \sigma_i^t, \quad i = 1, 2, 3, 4, 5, n$$

$$A_{min} \leq A_j \leq A_{max}, \quad j = 1, 2, 3, 4, 5, n$$

$$\delta_{min} \leq \delta_k \leq \delta_{max}, \quad k = 1, 2, 3, 4, 5., d$$

where A comprises the area of each member; n is the number of bars in the truss; $W(.)$ is the mass of truss, γ_i is the density of the bar i ; A_j is area cross-section of the member j which takes a value sandwiched between A_{min} and A_{max} ; L_i is the length dimension of the bar i ; d is the number of end connections; σ^c and σ^t are the permissible compressive and tensile stresses for member i , respectively; δ_i is the displacement of end connection i ; δ_{min} and δ_{max} are the lower and upper limits of displacement in a particular direction.

The violations are handled by a penalty function. A fitness function is defined to evaluate the solution. Constraint violation operator is defined as follows:

$$v_n^j = v_o^j / v_a^j - 1$$

where v_n^j is the normalization of the violation of the j^{th} constraint, v_o^j is the value computed for a particular member, and v_a^j is the pre-defined limiting value. The following cost function is computed for every solution:

$$F_{fitness} = W(A) + f_{penalty}$$

$$f_{penalty} = \sum_{j=1}^{N_c} \delta_j (A v_n^j + B)$$

where A and B are sufficiently large, N_c is the total amount of restrictions, and δ_j is the Kronecker delta defined as:

$$\delta_j = \begin{cases} 1, & v_n^j > 0 \\ 0, & v_n^j \leq 0 \end{cases}$$

3 Benchmark Problems

The following benchmarks are chosen to observe the performance of the meta-heuristic algorithms. Both cases are analyzed without grouping:

3.1 10-BAR 2D TRUSS (10 Design Variables, Degree of Static Indeterminacy: 2)

The following figure depicts the configuration & loads acting on a cantilever truss beam comprising ten bars and six nodes (Fig. 1).

The members' lengths are $1-6 = 360$ in. and $7-10 = 360\sqrt{2}$ in., and the cross-section areas are A_{1-10} . Node 5 and node 6 are fixed by the hinges.

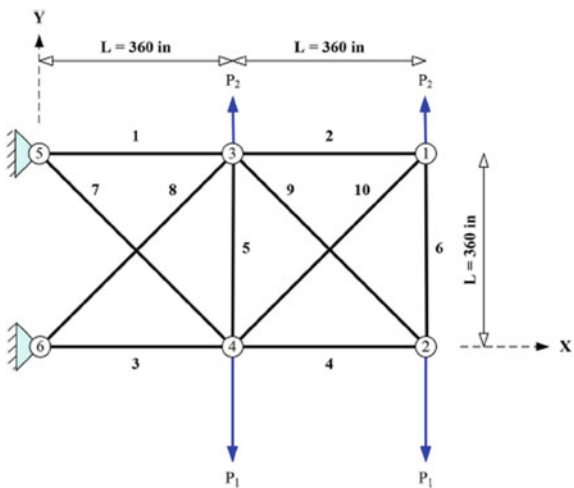
The algorithms are evaluated on two load cases (I) P_1 is 100 kips; P_2 is 0 kips; (II) P_1 is 150 kips; P_2 is 50 kips. Material with modulus of elasticity value of 10,000 ksi and density of material value of 0.1 lb/in.^3 is used throughout. The area of each member takes a value anywhere between 0.10 and 35 sq.in. Limit on bar stresses is set to 25 ksi in both possible cases, while the displacement of the end connections does not exceed 2 in. in any given direction.

3.2 25-BAR 3D TRUSS (25 Design Variables, Degree of Static Indeterminacy: 7)

The following figure shows the configuration of a space truss which comprises of 25 bars (Fig. 2).

The modulus of elasticity value is 10,000 ksi and density of material is chosen to be 0.1 lb/in.^3 . The structure is subject to two sets of loads which is tabulated in Table 1. The allowable compressive stress values are depicted in Table 2. The displacement of end connections in all directions is restricted to ± 0.35 in. The least value of cross-section area for each member is 0.01 sq. in., and the highest value is 3.4 sq. in.

Fig. 1 10-bar cantilever planar truss



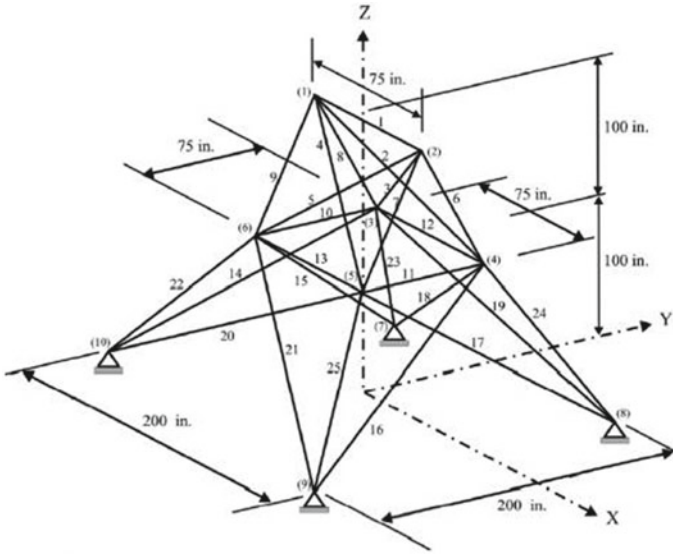


Fig. 2 25-bar space truss

Table 1 Loading specifications for 25-bar space truss

Case	Node number	Load (lb/sq.in.)		
		P_x	P_y	P_z
I	1	1000	10,000	-5000
	2	0	10,000	-5000
	3	500	0	0
	6	500	0	0
II	1	0	20,000	-5000
	2	0	-20,000	-5000

Table 2 Compressive stress limits imposed on the 25-bar truss

Area member	Compressive stress limits (in psi)
1 st	35,092
2 nd _5 th	11,590
6 th _9 th	17,305
10 th _11 th	35,092
12 th _13 th	35,092
14 th _17 th	6759
18 th _21 st	6959
22 nd _25 th	11,080

4 Scope of this Study

Any minimization problem can be classified into single objective and multiple objective optimization problems. Practical optimization problems have some set of meaningful and necessary restrictions or constraints. Hence, minimization problems can also be grouped into unconstrained and constrained optimization. In this study, only single-objective constrained optimization problems are considered. Also, only truss sizing optimization is considered. Constraints on bar stresses and nodal displacements are imposed, and these constraints are problem-specific.

Problems with discontinuous variables are discrete optimization problems, and problems with continuous variables are continuous optimization problems. In this study, every design variable is presumed to be continuous design variables for the sake of uncomplicatedness. A suitable metric can be applied without any hassles while discretizing the members.

5 Basic Features of This Study

The below-mentioned ground rules were imposed during this study:

1. Same unbiased setup was incorporated for every metaheuristic in all benchmarks. For established algorithms, parameters were taken from literature. For new algorithms, the ideal combination was defined from trial and error.
2. The maximum number of times an objective function can be evaluated is capped at 20,000, and the standard deviation of outcomes attained is considered the appropriate metric to compare algorithms of diverse nature and setups.
3. Fifteen autonomous runs were conducted for separate cases and individual optimization algorithm in order to procure statistically significant data.
4. The unit system utilized is the imperial unit's system. This is done to avoid any approximation errors during comparisons. The results obtained are rounded-off to 3 significant digits after the decimal point.
5. All algorithms are written in MATLAB™ 2021a and are evaluated in a workstation with the Intel® Core™ i5-6200U CPU @ 2.30 GHz running on 8 GB of RAM.

6 Description of the Algorithms Considered

The five metaheuristics that are evaluated in this study are: (1) Water Evaporation optimization algorithm, (2) Tug-of-War Optimization Algorithm, (3) Vibrating Particles System algorithm, (4) Cuckoo Search Algorithm, (5) Imperialist Competitive Algorithm.

6.1 *Water Evaporation Optimization Algorithm (WEO Algorithm)*

The phenomenon of Water Evaporation is studied extensively in biology and environmental science and engineering. Evaporation of water molecules from a surface, such as ponds or streams, is different from the evaporation of restricted water molecules on a solid surface. In this metaheuristic, water molecules are regarded as entities of the algorithm. A solid surface with varying wetting abilities is reflected as the domain. Decreasing the surface wetting ability will cause the accumulation of water from a single layer to regroup into sessile droplets. This observation is consistent with how the individual design responds as the algorithm progress. The decline in surface wetting ability represents a decrease in the objective function of minimization problems. The change in flux due to evaporation of water molecules is considered the best update metric of individual solutions. Variability of evaporation flux is very consistent with the algorithm's global & local searching power. This makes the algorithm perform well while displaying good convergence with an easy-to-comprehend structure. In this algorithm, each search cycle includes three steps: (i) single layer evaporation stage, which is the global search prowess (ii) droplet evaporation stage, which can be considered as local search prowess (iii) the renewal of water molecules, which is the update mechanism of candidate solutions. The specifics of this particular optimization algorithm are well presented in [3].

6.2 *Tug-of-War Optimization Algorithm (TWO Algorithm)*

Tug-of-war is a show of strong competition in rope pulling. Two teams are battling to pull a rope to bring it and the competing team to their side. Obviously, the movement of the losing team regulates the amount of rope moved. Like other meta-heuristics, TWO begins with a random set of solution candidates. Solution candidates are participating teams, and the entire group forms a league. After evaluating each iteration of the algorithm, the team will be assigned a weight that is proportional to its strengths.

Consequently, the best-performing team will have the maximum weight, and the worst-performing team will have the minimum weight. Look at any two solutions as two opposites of the pulling rope. Generally speaking, the weaker team will lose the game and accelerate towards the stronger team. The algorithm incorporates the ideal game scenario to determine the net force of the interaction between the weaker team with the stronger team. As a consequence of Newton's second law, the weaker team rushes towards the stronger team, and the displacement rate is based on the equations of motion. TWO also adds randomness to the framework based on Newton's rules of mechanics. In each cycle, the league will be reorganized through a sequence of rope pulling games, with the intention of positioning the team to the best position. This dictates convergence of the algorithm. The specifics of this particular optimization algorithm are well presented in [4].

6.3 Vibrating Particles Search Algorithm (VPS Algorithm)

The vibrating Particles Search algorithm is a swarm-based algorithm that simulates the unrestricted vibration of an SDOF setup with viscous damping. Like every other swarm-based technique, VPS begins with an initial set of random solutions and treats them as viscous damped SDOF free vibration particles. Observing the underdamped condition, each unrestricted particle undergoing vibration will oscillate and return to a specific equilibrium. Combining random nature and exploiting the results obtained, the algorithm constantly improves the set of particles by pushing particles towards equilibrium as the search for optimum progress. Any given particle's equilibrium comprises three parts; the best position attained until that point in the search space, the good particle, and the bad particle (HP, GP and BP respectively). VPS includes the following concepts; self-adaptation (particle movement towards the best), cooperation (influence of good and bad on the new location), and competition (extra effect of good). VPS uses the knowledge gained from the harmony search technique to rectify the location of particles ejected out of the search space. The specifics of this particular optimization algorithm are well presented in [5].

6.4 Cuckoo Search Algorithm (CS Algorithm)

Observing the freeloading routines of cuckoo species and invasion of them by host animals, a population-based meta-heuristic method was developed that would mimic this biological system present in nature. All nests or eggs, irrespective of whether

they are cuckoos or not, represent a solution candidate in search space. Cuckoo and host birds compete to foster its own species.

Individual egg in a given nest is a candidate solution, and the cuckoo egg is viewed as a novel solution. The objective is to substitute the sub-standard egg in the nest with a new and potentially better egg (solution). In its modest form, the individual nest has an egg. The algorithm can be stretched to more compound circumstances, where individual nests have numerous eggs that denote a set of solutions.

Three rules that direct the Cuckoo Search algorithm are itemized underneath:

1. The individual cuckoo lays one egg at a time and then tosses its egg into a haphazardly nominated nest. Characteristically, this randomization is governed by Lévy flights.
2. All the nests or eggs, excluding the finest ones, are passed on based on their superiority by novel cuckoo eggs formed by manipulating the current solutions towards the good nest concurrently with Lévy flight.
3. The available host nests are pre-defined, and the host bird discovers cuckoo eggs laid with a certain probability. In this case, the host bird can abandon the eggs and shape a fresh nest.

The specifics of this particular optimization algorithm are well presented in [6].

6.5 *Imperialist Competitive Algorithm (ICA)*

The Imperialist Competitive Algorithm is enthused by the historical spectacles of expansionism and interventionism. By looking at settler rivalry in anthropological civilization, a similarity can be initiated to motivate researchers to develop a swarm-based metaheuristic. This metaheuristic initially creates a random set of contender solutions in the pre-defined search space. The arbitrary point created is termed the starting (initial) country. The country in this algorithm is a collection of candidate solution values. The penalized objective function of the optimization exercise regulates the asset of individual realm. Depending on their supremacy, some of the finest starting (initial) countries (the countries with the lowest penalized objective function value) become imperialists and begin to regulate other countries (called colonies) and form the early kingdoms.

The two fundamental driving forces of this algorithm are assimilation and revolution. Assimilation makes the colony of individual kingdom approach the imperialist country in the socio-political distinctive space (optimization of the search space). Revolution causes abrupt and arbitrary changes in the location of certain countries in the search space. In the pursuit of the above-mentioned steps, a colony can gain an

improved spot and have the prospect to control the complete empire and substitute the current imperialist empire. The imperialist struggle is a further vital part of this algorithm. All empires attempt to win this sport and conquer the colonies of other empires. At separate steps of the algorithm, depending on one’s strength, all realms have a fair chance to keep one or more regions of the punier realm. The algorithm endures iteratively till a stopping norm is fulfilled. The specifics of this particular optimization algorithm are well presented in [7].

7 Results Obtained

The results obtained after running each algorithm 15 times are tabulated below. Note that the mean refers to the mean weight obtained after 15 runs of the code; best and worst weight refers to the lowest and highest value of weight obtained during the 15 runs; min and max corresponds to the area obtained for the best and worst weight respectively (Tables 3, 4, 5 and 6).

Table 3 Evaluation of algorithm performance in 10-bar truss problem (Load Case I)

Weight (lbs)	CSA		ICA		TWO		WEO		VPS	
	Mean	St. Dev.	Mean	St. Dev.	Mean	St. Dev.	Mean	St. Dev.	Mean	St. Dev.
	Best	Worst	Best	Worst	Best	Worst	Best	Worst	Best	Worst
	Min.	Max.	Min.	Max.	Min.	Max.	Min.	Max.	Min.	Max.
A_1	30.138	29.989	31.993	21.734	30.345	29.429	30.374	29.613	30.821	29.626
A_2	0.100	0.102	0.100	9.827	0.100	1.139	0.101	0.100	0.107	0.112
A_3	23.431	22.590	22.462	35.000	23.192	29.429	23.400	22.514	23.030	24.209
A_4	15.263	15.551	17.686	10.281	15.991	14.731	14.955	14.996	14.932	14.907
A_5	0.100	0.100	0.169	7.278	0.100	0.100	0.100	0.100	0.100	0.100
A_6	0.556	0.527	0.393	9.233	0.552	1.091	0.562	0.742	0.565	0.167
A_7	7.446	7.540	7.507	29.396	7.457	11.368	7.480	7.471	7.504	8.358
A_8	21.177	21.270	22.095	6.761	21.094	19.051	20.945	20.268	20.696	21.767
A_9	21.485	21.863	19.177	13.494	21.093	19.447	21.781	23.851	22.024	20.812
A_{10}	0.100	0.100	0.100	12.434	0.100	2.041	0.100	0.100	0.102	0.135

Table 4 Evaluation of algorithm performance in 10-bar truss problem (Load Case II)

Weight (lbs)	CSA		ICA		TWO		WEO		VPS	
	Mean	St. Dev.	Mean	St. Dev.	Mean	St. Dev.	Mean	St. Dev.	Mean	St. Dev.
	Best	Worst	Best	Worst	Best	Worst	Best	Worst	Best	Worst
	Min.	Max.	Min.	Max.	Min.	Max.	Min.	Max.	Min.	Max.
A_1	4680.559	1.313	4815.820	98.454	4696.036	15.245	4700.085	8.607	4696.630	9.299
A_2	0.100	0.104	0.100	0.100	0.100	0.100	0.101	0.167	0.111	0.215
A_3	25.155	24.990	28.156	25.163	24.388	22.230	24.439	23.251	24.857	26.159
A_4	14.091	13.857	14.357	15.243	13.975	12.432	14.651	16.038	14.772	13.792
A_5	0.100	0.101	0.100	1.388	0.100	0.100	0.104	0.100	0.106	0.118
A_6	1.972	1.993	2.035	1.969	1.971	2.089	2.120	2.058	1.968	2.375
A_7	12.492	12.679	12.256	8.663	12.757	13.169	12.578	13.290	12.436	12.403
A_8	12.917	13.257	14.571	15.922	13.291	12.917	13.221	13.928	13.033	12.760
A_9	20.101	19.838	19.212	20.699	19.997	22.331	20.830	18.871	20.816	19.379
A_{10}	0.101	0.100	0.100	0.100	0.100	0.100	0.100	0.100	0.102	0.104

Table 5 Evaluation of algorithm performance in 25-bar truss problem (Load Case I)

Weight(lbs)	CSA		ICA		TWO		WEO		VPS	
	Mean	St. Dev.	Mean	St. Dev.	Mean	St. Dev.	Mean	St. Dev.	Mean	St. Dev.
	Best	Worst	Best	Worst	Best	Worst	Best	Worst	Best	Worst
	501.358	517.353	534.315	598.375	518.320	548.314	517.063	538.229	499.560	525.392
A₁	Min	Max	Min	Max	Min	Max	Min	Max	Min	Max
A ₁	1.683	1.571	1.473	1.433	1.712	1.659	1.606	1.588	1.463	2.001
A ₂	1.126	1.009	1.419	3.216	1.079	2.232	1.767	1.925	0.582	1.153
A ₃	1.134	0.807	1.766	2.781	1.183	1.946	0.808	1.744	0.878	1.236
A ₄	0.010	1.041	1.981	1.944	0.579	0.633	1.691	2.033	0.083	3.369
A ₅	0.111	1.467	1.276	1.953	1.548	1.397	1.803	1.617	0.620	1.644
A ₆	3.319	3.400	3.397	2.655	3.291	2.451	3.388	2.786	3.304	3.249
A ₇	3.400	2.863	1.829	1.570	2.758	2.722	2.559	1.963	3.311	2.517
A ₈	3.330	3.400	3.400	1.861	2.993	2.529	2.672	2.621	3.300	3.202
A ₉	2.883	2.975	2.110	2.225	3.155	2.871	2.153	1.946	3.128	2.229
A ₁₀	0.072	0.010	0.096	0.581	0.514	1.502	0.054	0.01	0.334	0.026
A ₁₁	0.167	0.097	0.010	2.002	0.019	1.016	0.022	0.076	0.102	0.158
A ₁₂	1.004	1.716	0.833	0.630	1.068	0.931	1.329	0.639	1.398	1.601
A ₁₃	2.189	0.855	0.028	0.191	1.344	1.016	1.948	0.275	1.884	1.003
A ₁₄	0.886	1.276	0.994	1.344	0.728	0.672	1.079	1.403	1.564	0.783
A ₁₅	0.754	0.888	0.506	0.387	0.984	1.054	0.929	0.941	0.850	0.748
A ₁₆	0.892	0.847	0.938	2.641	0.826	1.732	0.951	1.196	0.978	1.176
A ₁₇	0.818	1.024	0.733	0.552	0.702	0.139	0.601	0.688	0.779	0.799
A ₁₈	1.339	1.155	1.534	1.822	0.890	0.959	1.163	1.168	1.009	0.984
A ₁₉	1.088	0.826	1.212	2.032	1.357	1.337	0.844	1.094	0.975	0.513
A ₂₀	0.254	0.333	1.307	1.231	0.689	1.022	0.231	1.329	0.036	0.164
A ₂₁	0.201	0.557	1.255	0.711	0.853	0.935	0.096	1.045	0.144	0.111
A ₂₂	3.378	3.210	2.864	2.725	3.059	2.780	3.296	3.111	3.277	3.204
A ₂₃	3.400	3.092	3.383	2.027	3.390	3.391	3.335	3.175	3.327	3.354
A ₂₄	3.373	3.355	3.243	3.127	3.386	3.173	3.364	3.335	3.375	3.399
A ₂₅	3.400	2.998	2.766	3.354	2.782	3.103	3.397	2.605	3.381	3.348

Table 6 Evaluation of algorithm performance in 25-bar truss problem (Load Case II)

Weight(lbs)	CSA		ICA		TWO		WEO		VPS	
	Mean	St. Dev.	Mean	St. Dev.	Mean	St. Dev.	Mean	St. Dev.	Mean	St. Dev.
	Best	Worst	Best	Worst	Best	Worst	Best	Worst	Best	Worst
	405.616	413.477	415.182	512.446	411.728	452.929	413.399	438.524	400.780	418.049
A₁	Min	Max	Min	Max	Min	Max	Min	Max	Min	Max
A ₁	2.125	2.062	2.004	2.076	2.135	2.312	2.264	2.304	2.056	2.247
A ₂	1.962	2.724	1.948	3.307	2.296	1.961	2.252	2.025	1.925	1.928
A ₃	2.024	1.788	2.544	1.847	2.305	2.402	1.879	1.616	2.750	2.705
A ₄	2.198	1.665	2.565	0.605	1.900	2.332	2.732	2.068	1.947	3.073
A ₅	2.116	2.387	1.836	3.329	1.907	2.646	1.821	2.382	1.891	3.369
A ₆	3.018	2.287	2.026	2.086	2.371	2.195	2.766	2.597	2.486	3.230
A ₇	3.043	3.011	2.818	0.984	2.498	3.072	3.322	2.978	3.120	3.332
A ₈	2.326	2.861	3.337	3.399	2.995	2.651	2.506	2.385	3.253	3.064
A ₉	3.313	3.124	3.399	3.020	2.734	2.835	2.991	2.773	3.373	2.423
A ₁₀	0.114	0.161	0.066	0.819	0.444	1.424	0.093	0.929	0.167	0.058
A ₁₁	0.049	0.022	0.015	2.559	0.815	0.108	0.010	0.442	0.197	0.058
A ₁₂	0.091	0.010	0.010	0.036	0.059	2.107	0.555	0.412	0.024	0.117
A ₁₃	0.028	0.492	0.304	2.531	0.123	0.125	0.096	0.483	0.117	0.073
A ₁₄	0.555	0.458	0.297	1.182	0.514	0.352	0.620	0.418	0.393	0.238
A ₁₅	0.077	0.169	0.435	0.010	0.076	0.069	0.052	0.116	0.130	0.063
A ₁₆	0.124	0.202	0.387	0.024	0.010	0.081	0.199	0.244	0.092	0.224
A ₁₇	0.368	0.273	0.355	1.114	0.475	0.329	0.285	0.340	0.349	0.162
A ₁₈	1.740	1.749	1.600	2.618	1.528	1.812	1.969	1.974	1.544	1.380
A ₁₉	1.873	2.002	1.579	3.400	2.119	1.672	1.768	2.187	1.712	1.719
A ₂₀	2.352	1.979	2.004	2.447	2.188	1.886	1.732	2.456	1.884	1.746
A ₂₁	1.261	1.712	1.449	1.276	1.641	1.676	1.549	1.523	1.486	1.263
A ₂₂	0.010	0.010	0.114	0.349	0.325	0.416	0.260	0.053	0.069	0.027
A ₂₃	0.047	0.010	0.011	0.050	0.090	1.354	0.010	0.256	0.040	0.021
A ₂₄	0.155	0.399	0.559	0.423	0.098	0.308	0.133	0.577	0.029	0.095
A ₂₅	0.010	0.010	0.101	0.194	0.010	0.010	0.010	0.328	0.027	0.043

The mean values of the minimum weights obtained after 15 runs of each algorithm are plotted against the function evaluations (Figs. 3, 4, 5 and 6).

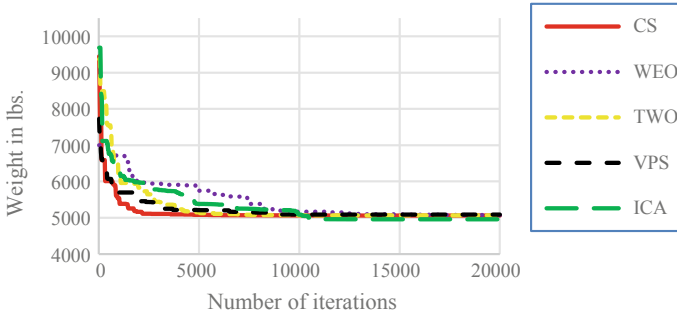


Fig. 3 Variation of the values for minimum weight vs Number of objective function assessments for the algorithms pertaining to the 10-bar truss problem for Load Case I

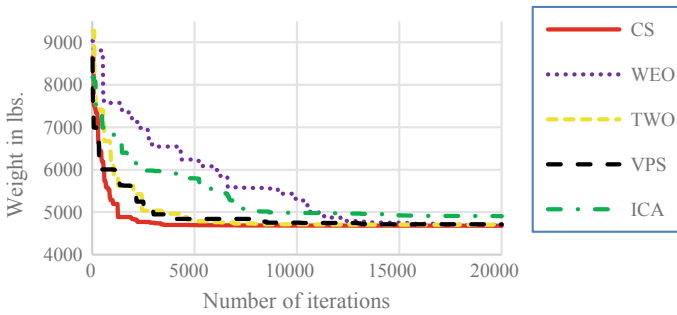


Fig. 4 Variation of the values for minimum weight vs Number of objective function assessments for the algorithms pertaining to the 10-bar truss problem for Load Case II

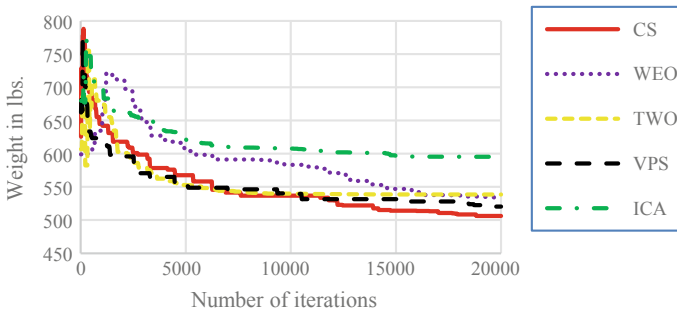


Fig. 5 Variation of the values for minimum weight vs Number of objective function assessments for the algorithms pertaining to the 25-bar truss problem for Load Case I

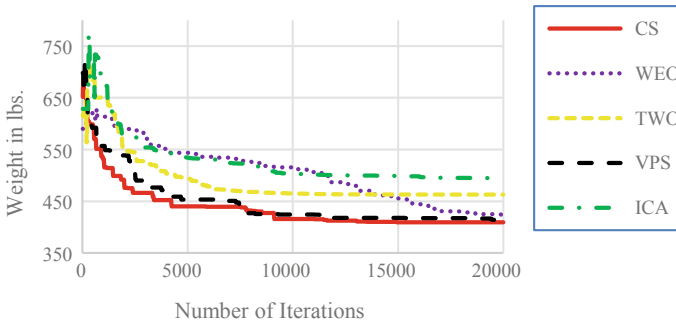


Fig. 6 Variation of the values for minimum weight vs Number of objective function assessments for the algorithms pertaining to the 25-bar truss problem for Load Case II

8 Concluding Remarks

The best result was obtained by Cuckoo Search, which obtained the value of 5061.387 lbs. for the cantilever 10-bar truss problem for Load Case I and obtained the value of 4678.577 lbs. for Load Case II. For the 25-bar space truss, the Vibrating Particles search algorithm obtained the best result of 499.56 lbs. for Load Case I and obtained 400.780 lbs. for Load Case II. The time taken to obtain the results for the 10-bar truss benchmark problem for Cuckoo Search was around 10 s, and the rest of the algorithms took about 6 s, the fastest being WEO algorithm followed by TWO, VPS, and ICA. This pattern does not change much when the design variables are increased to 25 variables. In the 25-bar space truss case as well, the Cuckoo Search takes the longest, and all other algorithms take almost the same time to obtain the results. In terms of data variability, Cuckoo search has the least standard deviation for the results obtained for the cantilever 10-bar truss configuration, which suggests that Cuckoo Search algorithm is less vulnerable to getting trapped in a local optimum. This trend is also seen in the 25-bar truss case as well.


References

1. Nemhauser G, Wolsey L (1988) Integer and combinatorial optimization. <https://orcid.org/10.1002/9781118627372>
2. Feury C, Geradin M (1978) Optimality criteria and mathematical programming in structural weight optimization. *Comput Struct* 8:7–17. [https://orcid.org/10.1016/0045-7949\(78\)90155-4](https://orcid.org/10.1016/0045-7949(78)90155-4)
3. Kaveh A, Bakhshpoori T (2016). Water evaporation optimization: a novel physically inspired optimization algorithm. *Comput Struct* 167:69–85. <https://doi.org/10.1016/j.compstruc.2016.01.008>
4. Kaveh A, Bakhshpoori T (2019) Tug of war optimization algorithm. *Metaheuristics: Outlines, MATLAB Codes and Examples*, pp 123–135. https://doi.org/10.1007/978-3-030-04067-3_11

5. Kaveh A, Ilchi Ghazaan M (2017) A new meta-heuristic algorithm: vibrating particles system. *Sci. Iranica* 24(2):551–566. <https://doi.org/10.24200/sci.2017.2417>
6. Yang X (2010) *Nature-inspired metaheuristic algorithms*. Luniver Press, United Kingdom
7. Atashpaz-Gargari E, Lucas C (2017) Imperialist competitive algorithm: an algorithm for optimization inspired by imperialistic competition. In: 2007 IEEE congress on evolutionary computation. <https://doi.org/10.1109/cec.2007.4425083>

Effectiveness of Polyurea Based Foams as Seat Cushion to Reduce Spinal Compression Injury of Occupant in Vehicle During Mine Blast Using Finite Element Analysis



Basa Jsk Kalyan Subrahmanyam, Venkatesh Balasubramanian,
and C Lakshmana Rao 

Abstract This article shows the Excellent Protective capability of Armor Grade Steels in vehicle floor and Polyurea Foams as seat cushion when used in a vehicle—occupant system subjected to Undermine Blast Event Comparative Analysis involving other widely used Seat cushion material Polyurethane and Vehicle Floor plate made of Mild steel has been carried out using Explicit Dynamic Finite Element Code LS-DYNA, spinal Region in particular Lumbar spine experiences serious injury measured in terms of Dynamic Response Index (DRI) is found out for various masses of TNT (Tri Nitrotoulene) 1.5, 6, 8, 10 kg Following NATO STANAG AEP II Standards.

Keywords Polyurea and Polyurethane Foams · Hybrid-3Dummy · Spine injury · DRI LS-DYNA · Explicit finite element analysis · Modelling and simulation · Blast load

1 Introduction

Elastomeric foams have long been utilized in a variety of mechanical, aeronautical, and other constructions, as well as in personal protective equipment. By integrating foams into the systems of interest, protection levels can be enhanced since they function as superior energy absorption materials. In a situation like Vehicle under Mine Blast, such a necessity exists. The shock wave from an explosive blast travels through the air before impacting the vehicle chassis. When the crew makes contact with the vehicle's floor plate and the seat, dynamic impact loads of up to a few hundred

B. J. K. Subrahmanyam (✉) · V. Balasubramanian
Department of Engineering Design, Indian Institute of Technology Madras, Chennai 600036, India

V. Balasubramanian
e-mail: chanakya@iitm.ac.in

C. Lakshmana Rao
Department of Applied Mechanics, Indian Institute of Technology Madras, Chennai 600036, India
e-mail: lakshman@iitm.ac.in

“g” are transmitted to the floor and crew in a matter of milliseconds [1] Qitao Guo. As per the NATO AEP-55 standardisation agreement [2], vehicle reliability should be improved to deal with combat conditions, and occupant injury levels within the vehicle should not exceed the values indicated for specific areas on the body in a blast test. For this purpose, ATD’s Anthropomorphic Test Device (also referred to as dummy in the Automotive field) are used. In the present study, we demonstrated the effectiveness of Polyurea Foams, used as seat cushion and compared it with the traditionally and widely used Polyurethane Material in the seat subjected to the Blast loads. The relative assessment has been made Numerically and Compared Numerical results with the experimental Results for Validation purpose. Dynamic response Index is used as metric to understand the spinal compression injury. Further Parametric studies were conducted with variation in Blast load parameters such as mass varying from 6, 8, 10 kg (NATO-AEP standards) and the standoff distance using CONWEP Methodology (Figs. 1, 2 and 3).

Ballistic steel absorbs, reflects, as well as deflects shock induced wave to reduce impact, while mild steel undergoes plastic deformation and fails due to tearing, in a ductile manner as per the work carried out by Gs Langdon et al. (2015) [5]. Because armour steels have a higher strength, they store more elastic energy during deformation than mild steel. When steel plates are impulsively loaded, they show three failure modes: Mode I, which shows severe deformation in the plastic region, Mode II, which shows partial tearing, and Mode III, which shows capping in the central region, according to Olson (1993) [6].

Polyurea/Polyurethane coatings, sandwich plates, honeycombs and foams are examples of absorption mechanisms used to counter blast waves. Foams act as a

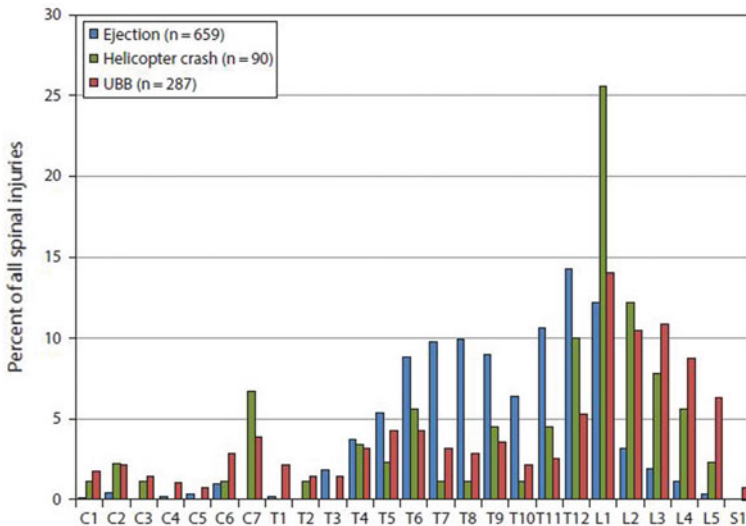


Fig. 1 Distribution of spinal injuries in military loading situations [2]

Fig. 2 Pelvis

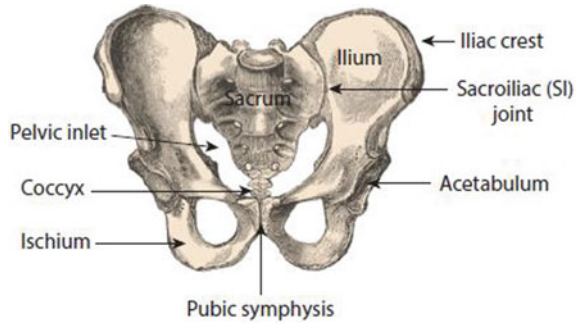
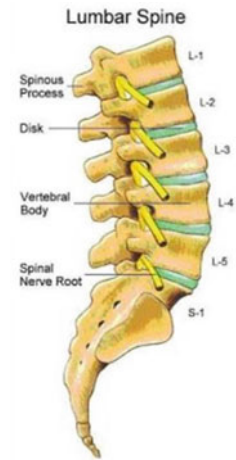


Fig. 3 Lumbar spine



defence mechanism against overpressures acceleration, according to Cendon et al. [3]. Local viscoelastic processes involving Twisting, Bending as well as struts buckling formed during the Fabrication Process are the mechanism of energy dissipation in foams [7–9]. A typical viscoelastic foam’s compressive stress–strain activity is divided into three distinct regions: bending of the cell walls in linear elastic region (ii) a plateau stress induced by the foam’s cellular structure collapsing over itself due to non-linear completely recoverable (viscoelastic foams) buckling of its struts. (iii) an area of densification where previously-collapsed cells starts to compress over one another to maximum density, which results in sharp rise in stress The energy consumed or dissipated by a foam is determined by the region under its stress–strain curve [7–9].

Elastomeric polymer Polyurea is created by the chemical reaction of an isocyanate ($N=C=O$) with amine whereas polyurethane is made from the reaction of an isocyanate with a polyol $(CHOH)_nH_2$.

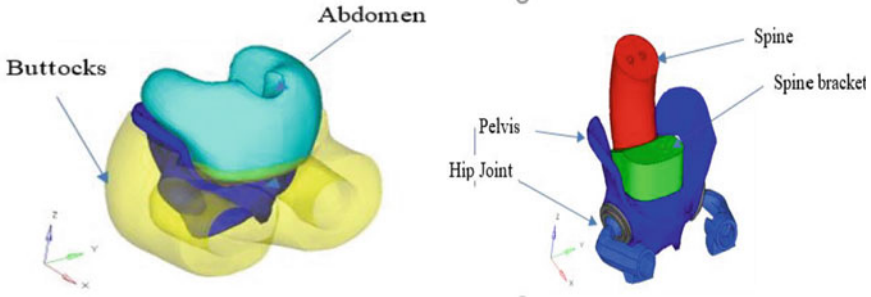


Fig. 4 Spine pelvis system numerical model

Fig. 5 Simplified spring mass damper to measure DRI

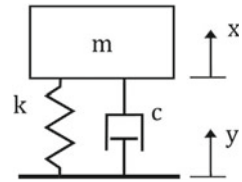
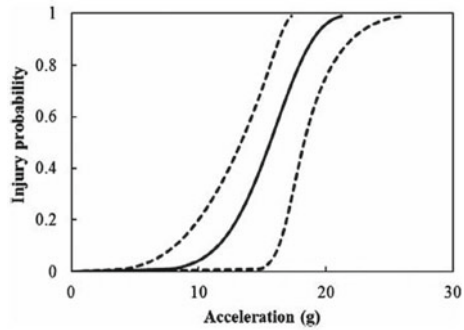


Fig. 6 Acceleration vs injury probability curve [15]



A good cushioning material or device absorbs great energy at the similar capacity or the same amount of energy at a lesser load. Foams are now used in nearly all industries. In spite of their widespread use and maturity, there are indeed regions in which foam technology can be improved, specifically in impact applications [9, 10].

The Dynamic Response Index (DRI) is a tool for predicting the likelihood of compression fractures in the lower region of the spine as a result of acceleration from the pelvis to the head [2]. Figure 5 shows a seated person with a mass m bound to a seat by a spring k and a dashpot c in a Single DOF Model.

$$\frac{\partial^2 \delta}{\partial t^2} + 2\zeta \frac{\partial \delta}{\partial t} + \omega^2 \delta = \frac{\partial^2 y}{\partial t^2} \tag{1}$$

Table 1 Showing the tolerance limits of Lumbar spine [15]

DRI	Risk category	Probability of serious injury
15.2	Low	0.5%
17.7	Medium	10%
21.3	High	50%

$$DRI = \frac{\omega^2 * \delta_{max}}{g} \tag{2}$$

$$\xi = \frac{c}{2 * \sqrt{mk}} \tag{3}$$

$$\omega = \sqrt{\frac{k}{m}} \tag{4}$$

x body displacement, y being seat displacement, δ stands for relative motion which is the difference between x and y displacement. Given the input acceleration one can calculate the Peak deflection δ_{max} and find the Dynamic Response Index. In the current model, the natural frequency is 52.9 rad/s and damping coefficient 0.224 respectively taken from reference [15] (Fig. 6 and Table 1).

2 Numerical Analysis

The 3D Finite Element Analysis is carried out in LS-DYNA CONWEP technique can be used to simulate the physical event of blast Basically CONWEP Generates the Pressure waves that are encountered in a typical Blast in the computer program Kingerly and Bulmash developed this model. Using the empirical equations given below, this method measures traditional blast loading effects on structures using *LOAD_BLAST_ENHANCED keyword formulation (Fig. 7 and Table 2).

Table 2 Showing the pressures generated using the CONWEP methodology

S.No	Mass of TNT (Kg)	Peak pressure (Mpa)
1)	1.5	7.6
2)	6	23
3)	8	28
4)	10	33

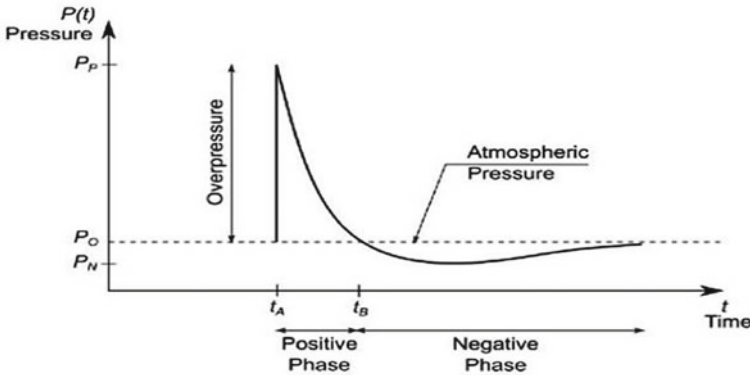


Fig. 7 Pressure time characteristics of a Blast wave [13]

As compared to mild steels, ArmoX steels have a higher hardness and toughness, ArmoX 500T (BHN 500) is Compared against Mild steels for assessment of performance through which better material can be selected for future designs that may be used as a deflection and absorption material in the event of a blast [14].

Vehicle Floor

The materials selected for the comparative assessment are mild steel and armour steels. Since ductility is critical in energy dissipation due to loading, steel with a good balance of ductility and adequate strength can be used. The Johnson Cook (JC) model [14] is widely used in the literature to deal with simulations of high strain rate and temperature effects.

The Von Mises flow stress is calculated using the JC model as

$$\sigma = [A + B \varepsilon^n][1 + C \ln \varepsilon^*][1 - T^{*m}] \tag{5}$$

Seat

Before Energy gets transferred to crew, Energy absorption take place in the seat cushion.

Stress strain graph for a particular density from the experiments [11] are applied as Input to the Load curve ID required in the Numerical material Model for Polyurea and Polyurethane Foams.

*MAT_57 Material Card in LS-DYNA Model is employed for cushion of the seat in order to model Foams. Other factors affecting the foam formation and its characteristics can be found from the references [4,12]The steps in the model design are presented below

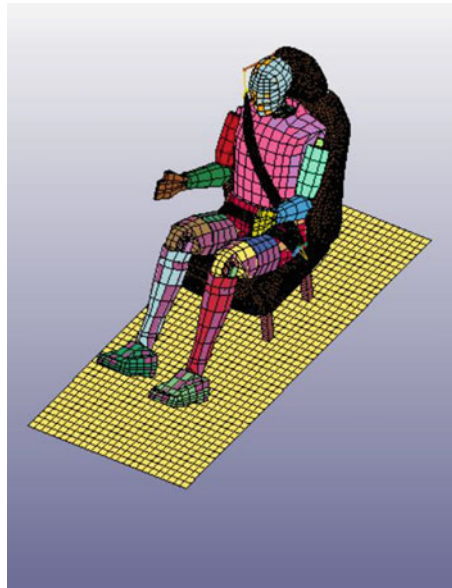
$$\sigma_{ij}^r = \int_0^t g_{ijkl}(t - \tau) \frac{\partial \varepsilon_{kl}}{\partial \tau} \partial \tau \tag{6}$$

$$\sigma_{ij} = \sigma_{ij}^f + \sigma_{ij}^{r*} \tag{7}$$

$$g(t) = \alpha_0 + \sum_{m=1}^N \alpha_m e^{-\beta t} \tag{8}$$

$$g(t) = E_d e^{-\beta_1 t} \tag{9}$$

$g_{ijkl}(t - \tau)$ is the relaxation function.
 Seat Cushion Dimensions are 600 * 500 * 75 mm (Table 3).



Mesh types used for the model:

For the Plate element length is varied from 30 to 10 mm and found that 20 mm mesh size capturing acceleration within tolerable limits.

Hexahedral mesh (Brick Element) was used for the seat and the no of elements through the thickness was chosen as 4 (Number of Elements in cushion 22,035) after varying the number of elements through thickness from 2 (Total Number of Elements in cushion 2825) to 8 (Total Number of Elements in cushion 68,140) error in acceleration measurement with 4 elements through thickness and 8 elements through thickness is negligible further with 8 elements through thickness computational time is 5 times that of 4 elements through thickness case (Figs. 8, 9, 10, 11 and Table 4).

Table 3 Material properties of various steel grades used as floor plate [3]

Steel type	A (MPa)	B (MPa)	C
Mild steel	325	275	0.076
Armored grade 1	792	510	0.014
Armored grade 2	1372	835	0.061

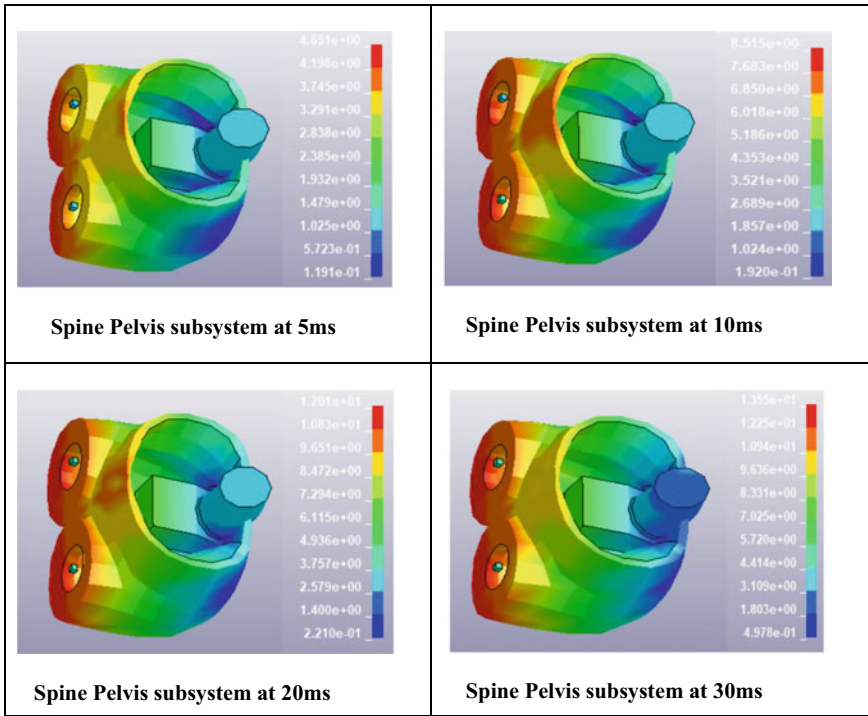


Fig. 8 Spinal compression contours (max 4.8 mm) DRI 1.3 for ArmoX 500T steel as floor plate and Polyurea as seat cushion, Blast load 1.5 kg at 1 m SOD

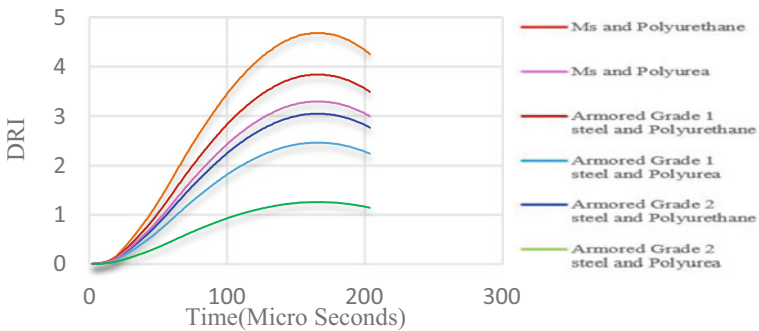


Fig. 9 DRI vs time curve for different configurations foam density 170 Blast Load 1.5 kg @ 1 m SOD

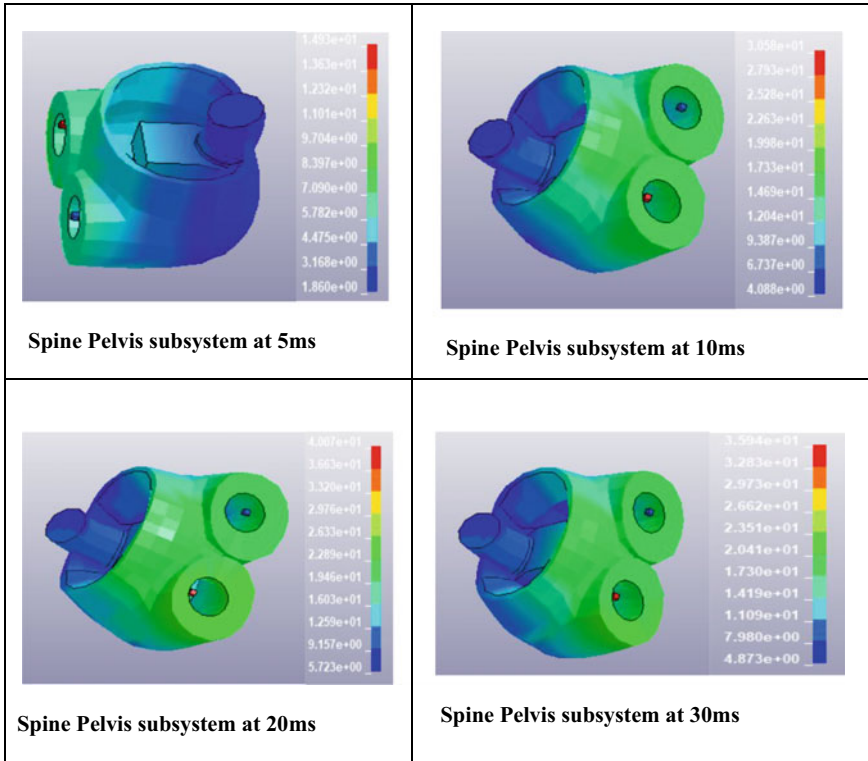


Fig. 10 Spinal compression contours (max 16.1 mm) DRI 4.7 for Mild steel as floor plate and Polyurethane as seat cushion, Blast load 1.5 kg @ 1 m SOD

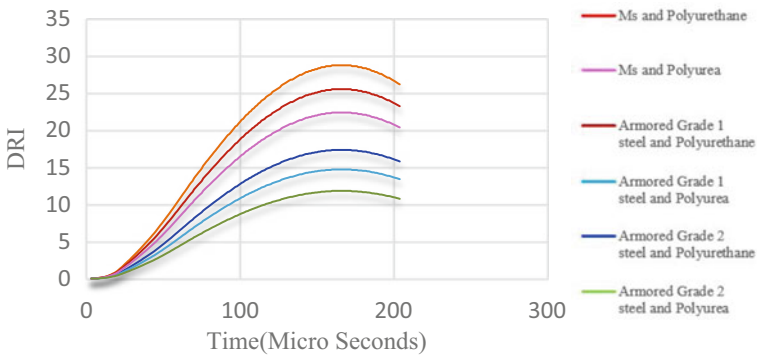


Fig. 11 DRI vs time curve for different configurations foam density 200 Blast load 10 kg TNT @ 1 m SOD

Table 4 Showing comparison of the DRI results for 6 to 10 kg

TNT (Kg)	Steel type	DRI spine with polyurethane as seat cushion	DRI spine with polyurea as seat cushion
6	MS	12.9	8.4
	Armored 1	10.7	6.8
	Armored 2	7.6	4.7
8	MS	20.1	12.2
	Armored 1	17.3	10.1
	Armored 2	14.2	7.8
10	MS	28.4	17.1
	Armored 1	25.2	14.5
	Armored 2	22.1	11.7

3 Results and Discussion

Spinal Injury Response is estimated Numerically for various parameters namely density of seat cushion, Mass of the TNT Explosive (corresponding pressure load) Distance from the Explosion point to the system under consideration. The validation of the Numerical work was compared to the experimental studies conducted by Guo et al. (2016). The DRI Value in the experiment is 2.1, in the current numerical study value obtained was 2 for density of 200 kg/m^3 which is very close to experimental Value. The variation of spinal compression with 1.5 kg Mass of the TNT (Pressure Load) is as described by Fig. 4. When 170 kg/m^3 Foam density is used for both Polyurethane and Polyurea, DRI (spinal compression levels of the order of 16.1 mm) maximum observed for the configuration with mild steel as floor plate and Polyurethane foams as seat cushion and least DRI (spinal compression levels approximate to 4.3 mm) for the configuration with Armored grade 2 steel (Armox 500T) and Polyurea Foams and the DRI Values for Other configurations lies between 1.3 and 4.7 as identified by the DRI vs Time Plot. Average Percentage Reduction in DRI when same grade of floor plate when used for Polyurea based foams as seat cushion compared to Polyurethane based seat cushion is 38%. As the Mass of the charge is increased from 6 to 10 kg Spinal compression levels increased in both the cases involving Polyurethane and Polyurea. However the Probability of risk of spinal injury using Polyurea foams is 10% whereas the Injury risk Probability was 50% when polyurethane seat cushion are used. This way massive reduction in acceleration achieved by Polyurea foams helped in Reducing the Spinal Injury risks associated with the occupant.

4 Conclusions

Numerical studies were conducted to understand the Protective capability of Polyurea based foams against widely used Polyurethane Foams as seat cushion in a typical vehicle-Occupant model subjected to Mine Blast pulses that originate from Explosives with masses ranging from 1.5 to 10 kg using Explicit Finite Element Code LS-DYNA. The following are the conclusions that can be drawn from the current study.

- i) Equal weights of Polyurea Foams and Polyurethane Foams in seat cushions when subjected to same blast load, Polyurea Foams performed better in Acceleration Mitigation leading to 40% reduction in spinal injuries of occupant.
- ii) When same stress field is applied DRI of spine measured with LS-DYNA ATD showed least value with Armox 500T Vehicle floor plate and Polyurea Foam as seat cushion Configuration when compared with other configurations.

References

1. Guo Q, Zhou Y, Wang X, She L, Wei R (2016) Numerical simulations and experimental analysis of a vehicle cabin and its occupants subjected to a mine blast. *Proc Inst Mech Eng Part D J Autom Eng* 230(5):623–631
2. Franklyn M, et al (2017) Military Injury Biomechanics
3. Langdon G, Lee W, Louca L (2015) The influence of material type on the response of plates to air-blast loading. *Int J Impact Eng* 78:150–160
4. Ramirez BJ (2019) Energy absorption and low velocity impact response of open-cell polyurea foams. *J Dyn Behav Mater* 5(2):132–142
5. Reed N et al (2020) Synthesis and characterization of elastomeric polyurea foam. *J Appl Polym Sci* 137(26):48839
6. Olson M, Nurick G, Fagnan J (1993) Deformation and rupture of blast loaded square plates—predictions and experiments. *Int J Impact Eng* 13:279–291
7. Gibson LJ, Ashby MF (1999) Cellular solids: structure and properties, 2nd edn. Cambridge University Press, Cambridge
8. Mills N (2007) Polymer foams handbook: engineering and bio- mechanics applications and design guide. Butterworth-Heinemann, Oxford
9. Rusch KC (1969) Load-compression behavior of flexible foams. *J Appl Polym Sci* 13:2297
10. Gupta V, Crum R, Gámez C, Ramirez B, Le N, Youssef G, Citron J, Kim A, Jain A, Misra U (2015) Adhesive and ultrahigh strain rate properties of polyurea under tension, tension/shear, and pressure/shear loadings with applications to multilayer armors. In: Barsoum R (ed) *Elastomeric polymers with high rate sensitivity*
11. Ramirez BJ (2017) Manufacturing and characterization of temperature-stable, novel, viscoelastic polyurea based foams for impact management. University of California, Los Angeles
12. Ramirez BJ, Gupta V (2018) High tear strength polyurea foams with low compression set and shrinkage properties at elevated temperatures. *Int J Mech Sci* 150:29–34
13. Hallquist J (2006) LS-DYNA theory manual. Livermore Software Technology Corporation
14. Neuberger A, Peles S, Rettel D (2007) Scaling the response of circular plates subjected to large and close range spherical explosions. Part II: buried charges. *Int J Impact Eng* 34(5):874–882
15. Ravi S (2014) Assessment of the accuracy of certain reduced order models used in the prediction of occupant injury during under-body blast events. *SAE Int J Transp Saf* 2(2):307–319

Numerical Analysis of a Vibration Isolator Under Shock Load



Ameena Nazeer, Rajesh P. Nair, and D. D. Ebenezer

Abstract Mechanical devices are used to isolate sea-going vessels from the forces generated by onboard machinery and the machinery from shock loads that are transmitted through the vessel. In this paper, the shock and vibration isolation characteristics of a quasi-zero-stiffness device are determined by using finite element models. The non-linear dome-shaped device is designed to have nearly zero stiffness when it is pre-compressed by machinery. Therefore, when the machinery vibrates, it has low resonance frequency and low force transmissibility at low frequencies. The shock isolation characteristics for various combinations of the peak shock levels and the shock duration are reported.

Keywords Visco-elastic · Quazi zero stiffness · Transmissibility

1 Introduction

Vibrations can cause severe damages to the structures. So its isolation became one of the important tasks nowadays. The natural frequency of isolator should be $\sqrt{2}$ times less than the frequency of vibrations to isolate machine vibrations. To have low natural frequency, vibration isolators for machines should have simultaneously low rigidity and high static loading. But this is impossible for traditional springs and rubber vibration isolators, because then they would have to have very large dimensions. In general, the issue of simultaneously obtaining low stiffness and high load capacity is a well-known problem. An overview of the latest achievements in this field shows that systems with quasi-zero stiffness may theoretically isolate vibration very well, but there are only few working models. The few available prototypes are unstable due to large number of elements, and this also lead to the high level of friction in the vibration isolator that ultimately degrades the system performance. Thus, it is required to develop quasi-zero stiffness isolators with minimum number of elements, preferably with only one that will provide the best simplicity, and thus high reliability.

A. Nazeer (✉) · R. P. Nair · D. D. Ebenezer
Department of Ship Technology,
Cochin University of Science and Technology, Cochin 682022, India

Then we chose a dome shaped vibration isolator made up of viscoelastic material called polyurethane. The rated load is the load that makes the isolator to attain quasi zero stiffness will be calculated and natural frequency of the model will be calculated. The model will be analyzed under the shock load that is corresponding to the rated load as specified by JSS-55555 and it will be validated using Von-Mises theory.

2 Objectives

Isolators are primarily designed to attenuate the periodic force due to machinery mounted on top of them and reduce the force that acts on the base on which the isolator is mounted. Isolators are also designed to attenuate the shock force that acts on the isolator through the base and reduce the shock force transmitted to the machinery. Quasi zero stiffness isolators have a non-linear load-deformation curve that has a nearly zero slope in the neighborhood of the rated static load. When the weight of the machinery mounted on them is equal to the rated load, they have a very low resonance frequency; and excellent linear vibration isolation characteristics even at low frequencies when the dynamic load is small enough to ensure that the deformation is only in the quasi zero stiffness regions. The objective of the present study is to analyze the vibration isolation and shock attenuation characteristics of quasi zero stiffness isolators. It is well known that they have excellent vibration isolation characteristics but their shock attenuation characteristics are less well known.

3 Numerical Model of Quasi Zero Stiffness Isolators

3.1 Modelling of a Vibration Isolator

The design of the mount was chosen from the literature (2). A quasi- zero stiffness system is adopted following the literature (Fig. 1).

Where

- r_2, r_1 are the outer and inner radii of the mount
- t is thickness of wall.
- h_s is height of vertical wall.
- d_2, d_1 are the outer and inner diameter of the mount.

3.1.1 Dimensions

- The inner and outer diameters of the isolator were taken 120 and 75 mm. Thickness of wall was taken 7 mm and height of vertical wall h_s was kept 15 mm. The height

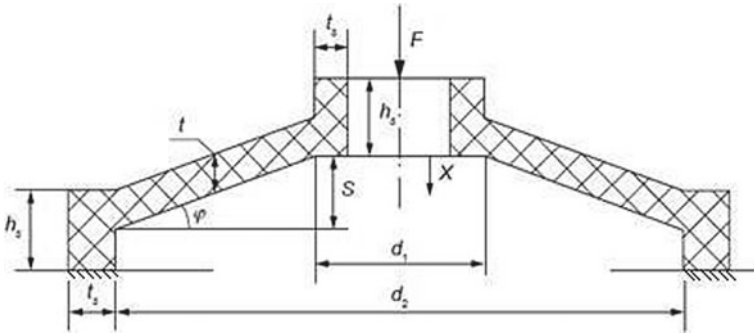
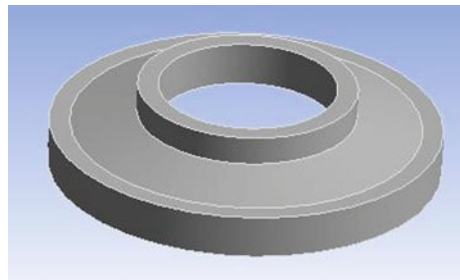


Fig. 1 Cross section of the dome shaped vibration isolator [Courtesy-(A. Valeev 2015)]

Table 1 Dimensions of the vibration isolator

Dimension	Value
Outer diameter	120 mm
Inner diameter	75 mm
Wall thickness	7 mm
Height of outer wall	15 mm
Inclination angle	12.5°
Inclined wall height	5 mm

Fig. 2 Modelled diagram of vibration isolator



of the inclined wall, S is obtained as 5 mm. This is the required deformation for the walls to become horizontal and the mount to act as QZS mount.

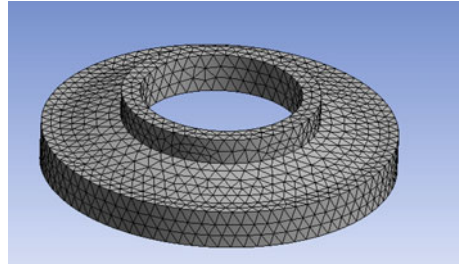
- The inclination angle of wall was calculated to be 12.5°
- The shape factor is $S = 0.63$. Shape factor or bulge factor is the ratio of area under load to area free to bulge. As this factor increases, stiffness increases and tendency to buckle decreases. The advisable range is between 0.5 to 1.

The dimensions for the vibration isolator are shown in Table 1.

With these dimensions, model of the isolator was modelled using design modeller Fig. 2 shows the modelled diagram of vibration isolator. Boundary condition has been provided as fixed support at the bottom ring of the isolator.

Table 2 Material properties of polyurethane

Data	Value
Density	1136.5 kg/m ³
Poisson ratio	0.48
Young's modulus	4.5 MPa
Damping coefficient	65%
Relaxation modulus	0.4723
Relaxation time	8.69 s

Fig. 3 Finite element model of the vibration isolator

3.2 Material Properties of Polyurethane

An isolation mount is provided with polyurethane material and is modeled using viscoelastic modeling to incorporate the large deflection behavior and also damping behavior. Table 2 shows the general material properties of polyurethane. For the viscoelastic modeling in ANSYS workbench platform, Prony shear relaxation model was chosen. For the Prony relaxation model, the two parameters or constants required are relaxation modulus and relaxation time. Parameters of these models are shown in Table 2. These values are inputted in the engineering data tool by creating a new material called polyurethane.

4 Numerical Results for Quazi Zero Stiffness Isolators

4.1 Mesh for Quazi Zero Stiffness Isolator

Meshing has been done first with coarse mesh. Then meshing has been done with finer mesh by inputting mesh size of 4 mm. And it results with nnumber of nodes as 25,758 and elements as 15,021. Meshed diagram of vibration isolator is shown in Fig. 3.

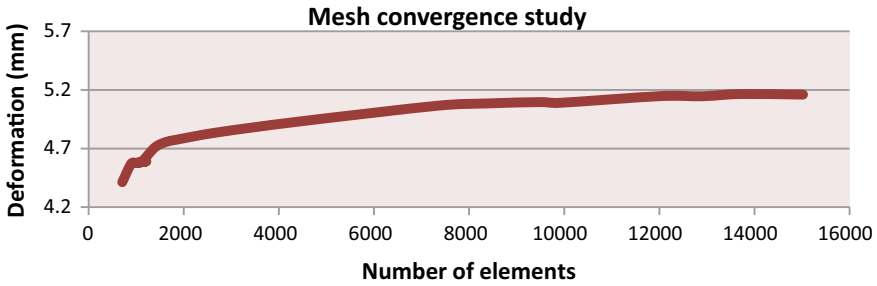


Fig. 4 Mesh convergence study

After creating mesh, mesh convergence study was done to find the optimum mesh size and number of elements. And shown in Fig. 4 at 15,021 elements and the result was constant independent of mesh size.

4.2 Static Structural Analysis

A **static structural analysis** determines the displacements, stresses, strains, and forces in structures or components caused by loads that do not induce significant inertia and damping effects. By using static structural analysis, load to define quazi zero stiffness or rated load is found out. Quazi zero stiffness is the property that is obtained when the load deformation graph gets a flat surface. By turning on large deformation ON, non linear effects in ANSYS have been activated and the presence of Visco elastic material is taken in to consider. For to study the differences between effects of large deformation OFF and ON case, load versus deformation about Y axis was plotted as shown in Figs. 5 and 6 respectively. In Fig. 5, large deformation off case, graph was turned to be a linear, even for the higher range of loads. And thus it shows that non linear effects have been not taken in to consider. In Fig. 6, large deformation ON case, graph was non linear and there by non linear effects has been taken into consider.

Fig. 5 Load v/s deformation graph of large deformation off case

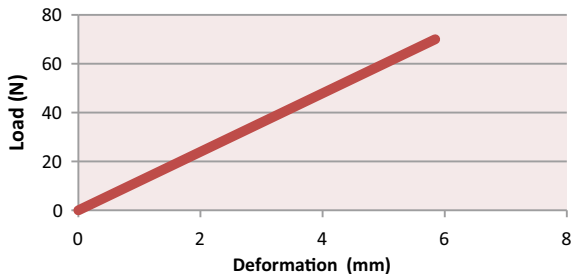
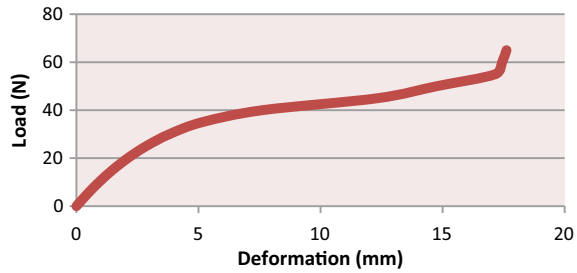


Fig. 6 Load v/s deformation graph of large deformation on case



Next step is to find rated load. For that a probe has been set up at the upper inner diameter of the conical frustum and its deformation about Y axis is checked and it is shown in Fig. 7. 5 mm is the dome height. When a load produces 5 mm deformation in the upper diameter of the conical frustum—the isolator acts as a single rubber plate—that load is taken as rated load and this result is shown in Table 3.

Thus 5 mm deformation was obtained for 35 N and taken as rated load. That means this 35 N weighing equipment which is topped over the isolator makes the isolator to enter the quazi zero stiffness state. So for the further analysis, a plate of very high young’s modulus such that it does not bend and of same diameter of upper ring of conical frustum is made and connected to the isolator. Bonded connection option is used for the connection between isolator top face and plate bottom face.

Fig. 7 Deformation probe on the vibration isolator

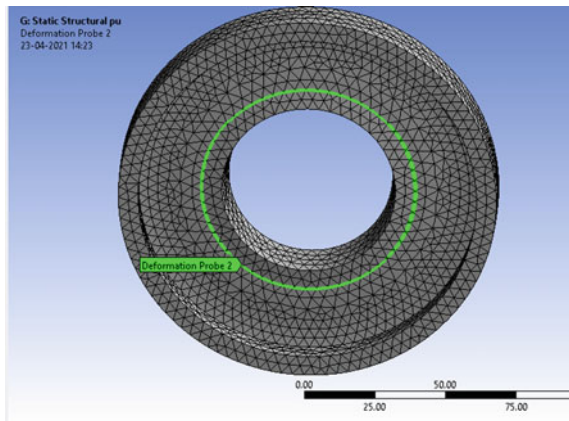


Table 3 Results of static structural analysis

Result of static structural analysis	
Deformation at probe	Solved
Directional deformation about axis	Y Axis
Maximum value	-5.1414 mm

Fig. 8 Modelled diagram of the vibration isolator with plate

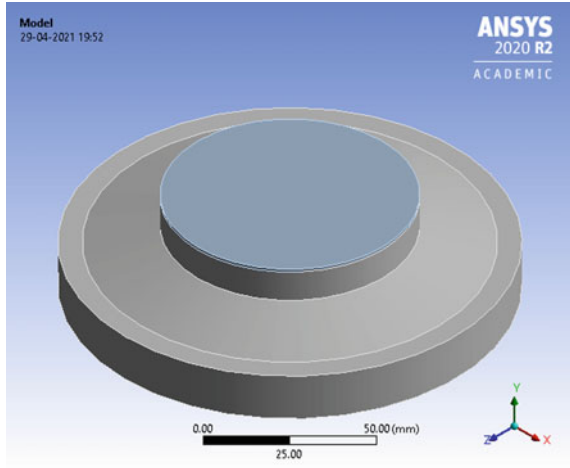


Table 4 Natural frequencies of the vibration isolator

Mode	1	2	3	4	5	6
Frequency (Hz)	10.139	14.086	14.096	18.732	18.733	29.905

This modified diagram of isolator is shown in Fig. 8. A new material was used for plate with following properties.

Since weight = $mg = 35 \text{ N}$,

Mass = $35/9.81 = 3.567 \text{ kg}$.

Thickness of the plate = 1 mm .

Volume of plate = $\pi r^2 h = 4417.864 \text{ mm}^3$.

So, density = $\text{mass/volume} = 807,403.76 \text{ kg/m}^3$.

4.3 Modal Analysis

Modal analysis is a technique to study the dynamic characteristics of a structure under vibration excitation. Natural frequencies, mode shapes and mode vectors of a structure can be determined using modal analysis. A graphical variation of number of modes vs. the frequency can also be obtained from ANSYS Workbench. Vibration is about frequencies. Frequency is defined as number of cycles in a given period of time. One cycle per second is equivalent to one Hertz. Fixed end is given as the boundary condition. Here modal analysis is performed and found first 6 natural frequencies and mode shapes with directional deformations. Natural frequencies varying from 10.13 to 29.905 Hz. Mode shapes corresponding to these frequencies are also obtained. Table 4 shows the mode frequencies. Since structure, boundary conditions, loading conditions etc. are ax symmetrical, only axisymmetrical mode

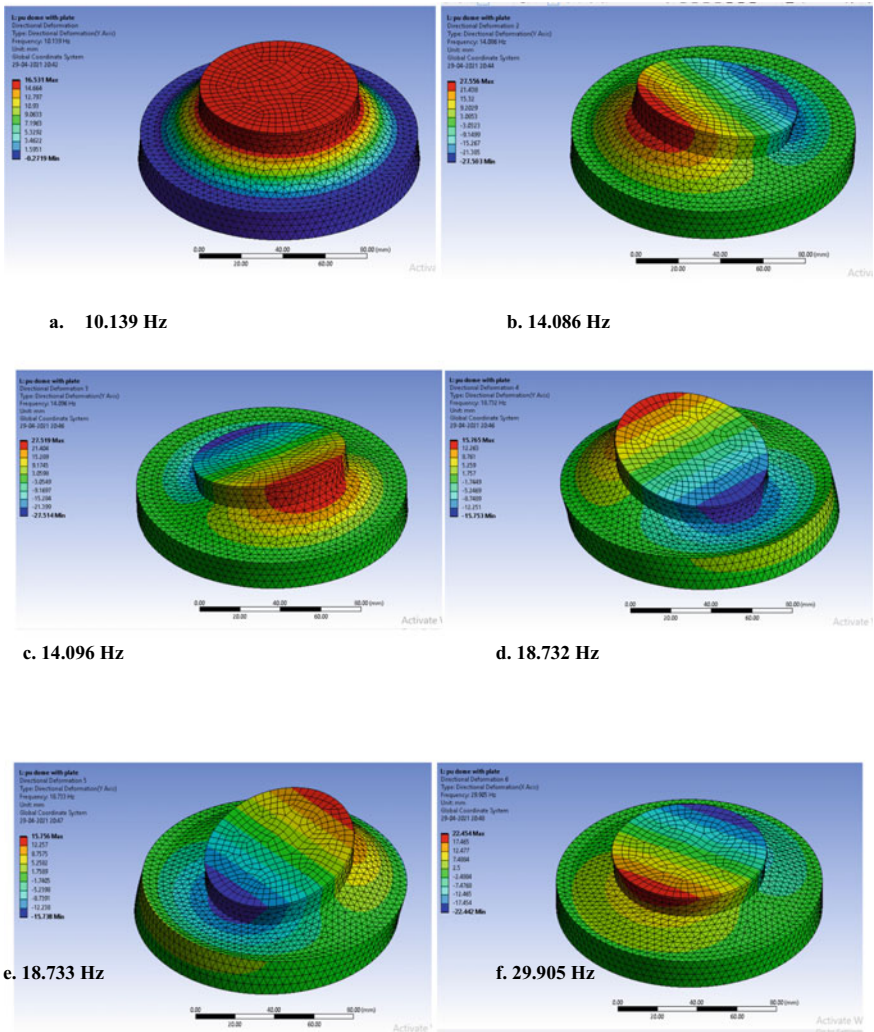


Fig. 9 Mode shapes of the vibration isolator

shapes is needed to be considered, so, mode 1 i.e.; 10.13 Hz is axisymmetrical and taken in to consideration and its mode shape is shown in Fig. 9(a) and it was matched with the analytical calculation result too. Other natural frequencies are non axisymmetrical and they occurs in pairs. Two resonances are rocking about X and Z axis. Rocking means all vibration on that axis is zero. If we cut the isolator on this axis, its displacement will be zero.

Table 5 Results of harmonic response analysis

Results of harmonic response analysis		
Damping	0	0.65
Maximum amplitude	10,512 mm	440.75 mm
Frequency	10. Hz	10 Hz
Phase angle	178.47°	92.416°
Real	-10,508 mm	-18.582 mm
Imaginary	280.76 mm	440.36 mm

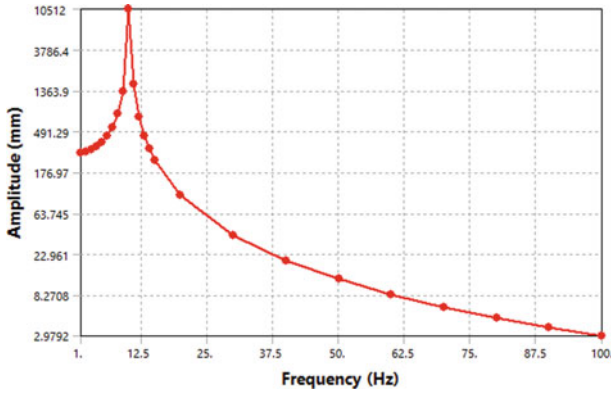


Fig. 10 Frequency response graph with zero damping

4.4 Harmonic Response Analysis

Harmonic Response Analysis is a linear dynamic analysis used to determine the response of a system to excitation at specific frequencies. It is also referred to as Frequency Response Analysis. A Harmonic Response Analysis is a linear-elastic dynamic analysis that cannot consider any non-linearity in the system. Here we have done full harmonic response analysis. Frequency has been set up from 1 to 100 Hz. Since natural frequency of isolator is 10 Hz, 1 Hz is set as interval for range between 1 to 20 Hz. then 10 Hz is set as the interval for range between 20 and 100 Hz. A pressure force of magnitude 1 MPa in Y direction is given in the top surface of the plate and frequency response at the centre of the plate and directional deformation about Y axis has been asked for the output. Result obtained was shown in Table 5. Here frequency at maximum amplitude obtained is 10 Hz and it matches clearly with modal analysis result. So, as per vibration isolation theory, vibrations of frequencies 1.414 times 10 Hz i.e.; 14.14 Hz will be isolated using this isolator. Amplitude at 10 Hz was obtained as 10.512 m i.e.; 2.33 mm per Newton displacement. These results are also shown in graph in Fig. 10. From the graph it is well much clear that at 10 Hz, maximum peak value is obtained. When a damping value of 0.65 is

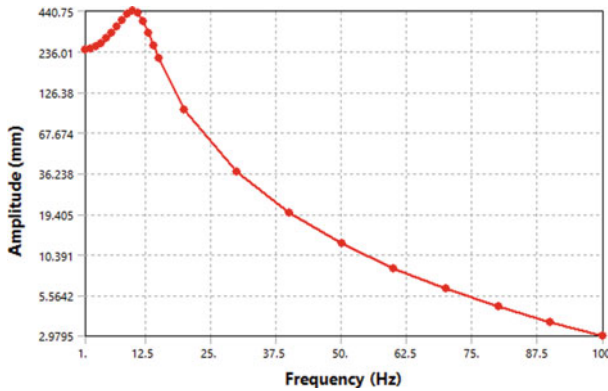


Fig. 11 Frequency response graph with 0.65 damping

considered, peak value is reduced to 0.4 m with displacement of 0.1 mm per Newton and it is shown in Fig. 11.

4.5 Transient Structural Analysis

Transient structural analysis is the process of calculating and determining the effects of loads and internal forces that are a function of time on a structure or an object. It is used to determine the dynamic response of a structure under the action of any general time-dependent loads. The shock is a transient excitation. Shock transmissibility is defined in this report as the maximum time-dependent output acceleration divided by the maximum time-dependent input acceleration. The details of the shock to be applied depend on the machinery that is being protected and the platform on which it is mounted. It will be defined by the users of the isolator. Triangular, half-sine, and more complex shocks are used in practice. The peak values of the shock and the total duration of the shock depend upon the application. Shocks with various peak values and various durations are used in practice. A peak value of 300 m/s² is used in some military tests. The shock pulse has a corresponding frequency spectrum. If the shock is a triangular pulse of total duration 2 T, the spectrum is

$$F(f) = \left[\frac{\sin(\pi f T)}{\pi f T} \right]^2.$$

The spectrum has a zero when $fT = 1$. If the frequency spectrum of the shock is zero at the frequency at which there is a peak in the isolator transmissibility, then the output is expected to have special characteristics. In this study, the vibration isolator has a resonance frequency of 10 Hz. The vibration transmissibility of the isolator is ≥ 1 in the 0 to 10 Hz band and it has a peak at the resonance frequency. The zero

in the shock spectrum will occur at 10 Hz when $T = 0.1 \text{ s} = 100 \text{ ms}$ and the total duration of the triangular shock pulse is $2 T = 200 \text{ ms}$. Therefore, the same isolator is subjected to shocks with various total durations. The effect of the duration on the transmissibility is studied. The duration varies from 30 to 200 ms. in order for the fast analysis; modal superimposed transient analysis is done. Then maximum stress obtained in the model is found out such that it is within the permissible limit validated by the Von Mises theory. As per von misses theory, maximum stress $[\sigma_1]$ acting upon the material must be less than allowable stress of the material $[\sigma]$.

Case 1: As per JSS-55555, environmental test methods for electronic and electrical equipment, it states that for the ground equipment and base design model, shock load of 30 g for 30 ms is taken in to the test. The time duration for the test has to be taken as per the code. So, here ending time for the analysis was chosen as 0.4 s with time step size of 1 ms. Shock load is given in the form of base excitation at the fixed end in the Y axis direction. Table 6 and Fig. 12 below shows how the shock load is distributed.

A probe has been set up at the centre of the plate and its directional acceleration about Y axis is asked for the output and so that finally transmissibility ratio was calculated as the ratio of output acceleration to the input acceleration. Then maximum equivalent stress at the isolator has been also asked for the result and it is verified such that it is within the permissible limit as per von misses theory. Results for maximum directional acceleration at the probe and maximum equivalent stress were calculated for 30 g in 30 ms and are shown in Table 7. Value of maximum acceleration was calculated as 220.56 m/s^2 and the transmissibility ratio was calculated as 0.75 and value of maximum equivalent stress was within the limit and so safe. It is seen that stress gets reduced with the course of time and shown in graph. Figure 14 shows contour diagram of output equivalent stress in dome isolator (Fig. 13).

Table 6 Shock load distribution-Case 1

Time (sec)	0	0.012	0.0195	0.027	0.0345	0.042	0.072	0.4
Acceleration (m/s^2)	0	0	147	294	147	0	0	0

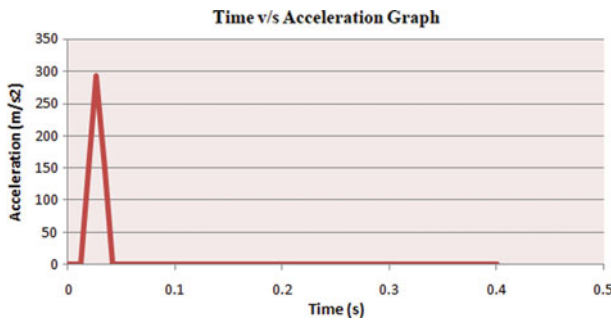


Fig. 12 Shock load of 30 g m/s^2 for 30 ms

Table 7 Results of transient analysis-Case 1

Results of transient analysis Case 1		
<i>Directional acceleration about Y axis</i>	<i>Equivalent stress 2</i>	<i>Transmissibility ratio</i>
@ centre of top plate	@ dome isolator	Transmissibility = $220.56/294 = 0.75$
220.56 m/s ²	5.1196 MPa	

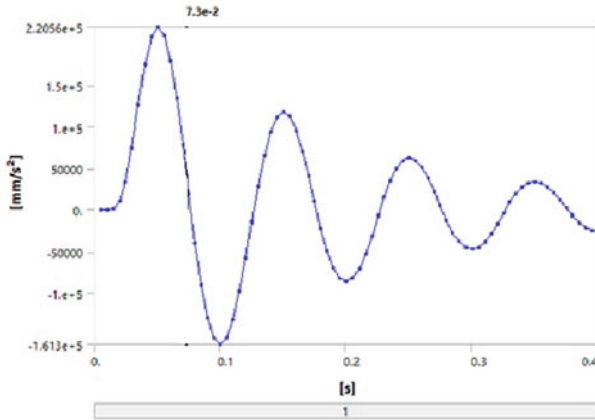


Fig. 13 Output acceleration v/s time graph

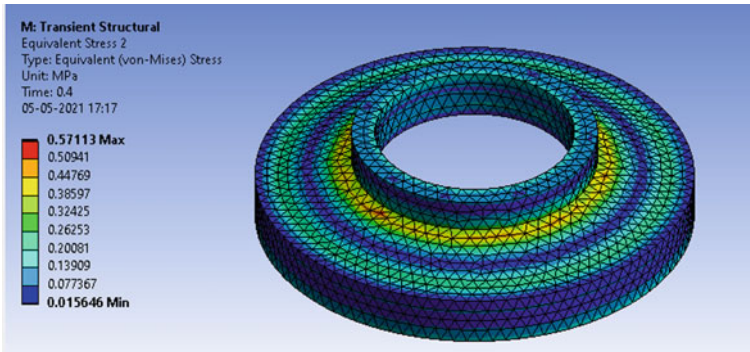


Fig. 14 Contour diagram of output equivalent stress in dome isolator

Case 2: a shock load of magnitude 30 g for 50 ms is considered in a triangular pulse form and step end time is 0.4 s and time step interval is 1 m. Results for maximum directional acceleration at the probe and maximum equivalent stress were calculated for 30 g in 50 ms and are shown in Table 8. Value of maximum acceleration was

Table 8 Results of transient analysis-Case 2

Results of transient analysis Case 2		
<i>Directional acceleration about Y axis</i>	<i>Equivalent stress 2</i>	<i>Transmissibility ratio</i>
@ centre of top plate	@ dome isolator	Transmissibility = $322.71/294 = 1.097$
322.71 m/s ²	7.5252 MPa	

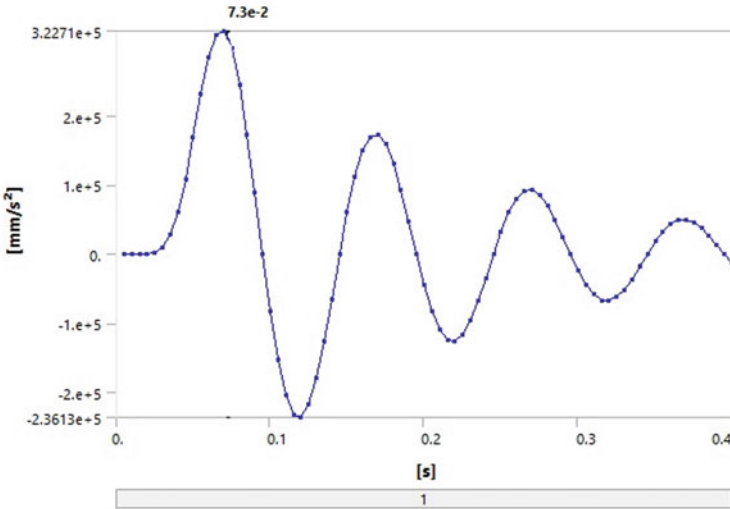


Fig. 15 Output acceleration v/s time graph

calculated as 322.7 m/s². And the transmissibility ratio was calculated as 1.097 and value of maximum equivalent stress was within the limit and so safe. It is seen that stress gets reduced with the course of time and shown in graph (Fig. 15).

Case 3: a shock load of magnitude 30 g for 100 ms is considered in a triangular pulse form and step end time is 0.6 s and time step interval is 1 ms. Results for maximum directional acceleration at the probe and maximum equivalent stress were calculated for 30 g in 100 ms and are shown in Fig. 16. Value of maximum acceleration was calculated as 391.06 m/s². And the transmissibility ratio was calculated as 1.33 and value of maximum equivalent stress was within the limit and so safe. It is seen that stress gets reduced with the course of time and shown in graph (Table 9).

Case 4: a shock load of magnitude 30 g for 200 ms is considered in a triangular pulse form and step end time is 0.6 s and time step interval is 1 ms. Results for maximum directional acceleration at the probe and maximum equivalent stress were calculated for 30 g in 200 ms and are shown in Fig. 17. Value of maximum acceleration was calculated as 301.06 m/s². And the transmissibility ratio was calculated as 1.02

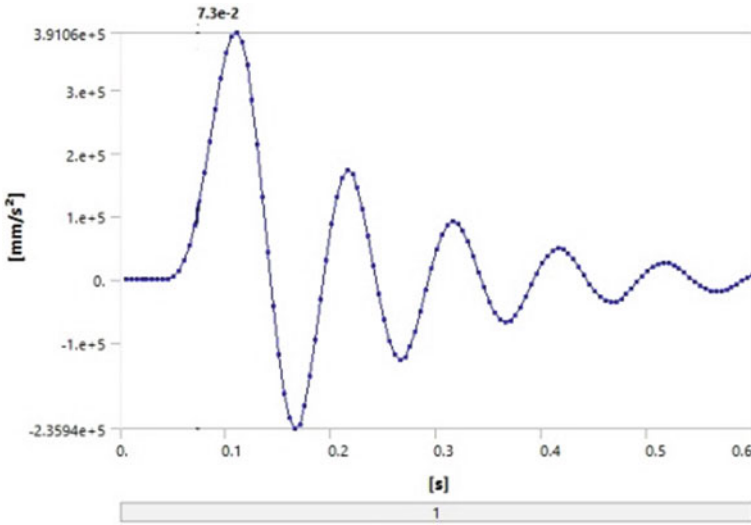


Fig. 16 Output acceleration v/s time graph

Table 9 Results of transient analysis-Case 3

Results of transient analysis Case 3		
<i>Directional acceleration about Y axis</i>	<i>Equivalent stress 2</i>	<i>Transmissibility ratio</i>
@ centre of top plate	@ dome isolator	Transmissibility = $391.06/294 = 1.33$
391.06 m/s ²	9.1266 MPa	

and value of maximum equivalent stress was within the limit and so safe. It is seen that stress gets reduced with the course of time and shown in graph (Table 10).

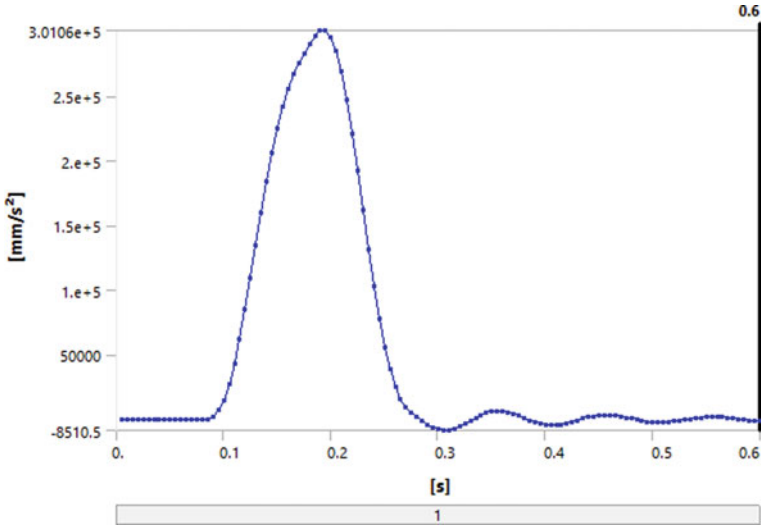


Fig. 17 Output acceleration v/s time graph

Table 10 Results of transient analysis-Case 4

Results of transient analysis Case 3		
<i>Directional acceleration about Y axis</i>	<i>Equivalent stress 2</i>	<i>Transmissibility ratio</i>
@ centre of top plate 301.06 m/s ²	@ dome isolator 7.0524 MPa	Transmissibility = 301.06/294 = 1.02

5 Conclusions

Vibration isolator of dome shaped with polyurethane material is modelled using design modeller tool in ANSYS. Mesh convergence study has been done and found 4 mm as the mesh size. Static structural analysis was done to find the rated load for the model and a plate of high stiffness and weight equal to rated load has been designed and placed over dome. Modal analysis was done and found as 10 Hz. So vibrations of frequency which is 1.2 times 10 Hz will be isolated using this isolator. Harmonic response analysis of isolator with 1 to 100 Hz frequencies vibration has run and got a peak response at 10 Hz. This conveys that structure is having its peak value at the natural frequency; thereby it will be lead to its resonance at this frequency. For the study of shock isolation by this isolator, transient structural analysis was done. Here shock load value from JSS 55,555 (30 g m/s² for 30 ms) was considered, analyzed and transmissibility ratio were calculated as 0.75. For to study the behaviour of structure with different shock loading condition the same isolator is subjected to shocks with various total durations and the effect of the duration on the transmissibility is studied.

The duration varies from 30 to 200 ms. It is seen from the numerical results that the output acceleration bears a small resemblance to the input acceleration when the total duration is 200 ms and the spectrum of the shock has a null at the frequency (10 Hz) at which the transmissibility of the isolator has a peak. The output acceleration is approximately a triangular pulse or a half-sine pulse with a low-level oscillating tail. If the peak in the frequency spectrum of the shock occurs at the frequency at which there is a peak in the isolator transmissibility, then the output acceleration will be high. The shock spectrum has a peak at 10 Hz when $fT = 0.5$. For $f = 10$ Hz, this corresponds to $T = 0.05$ s and a total duration of 100 ms. For a total duration of 100 ms, the shock transmissibility is higher than when the total duration is 30 and 50 ms. For these 3 durations, the output acceleration patterns are similar. However, when the total duration is 200 ms, the pattern is quite different. When the total duration is lesser than 200 ms, the initial positive response is followed by many oscillations. It rings at 10 Hz. From all these results, time period of the wave, i.e.; time between two adjacent peaks were calculated as 0.1 s. Then natural frequency is 10 Hz. So, by giving different excitation to the structure, response of the structure is primarily at its resonance frequency. In the design stage, the maximum output acceleration will have to be less than some specified value to prevent damage. The analysis done in this study with various shock durations gives insight into the shock response of vibration isolators. It will be useful for designing isolators with specified characteristics.

References

1. Valeev A, Zotov A, Kharisov S (2015) Designing of compact low frequency vibration isolator with quasi-zero stiffness. *J Low Freq Noise Vib Active Control* 34:459–474
2. ANSYS Inc. (2015) ANSYS Lectures. ANSYS
3. Valeev A (2017) Numerical and experimental analysis of metamaterial with quasi-zero effect for vibration isolation. In: International conference on functional materials, characterization, solid state physics, power, thermal and combustion energy
4. Valeev A, Kharisov S (2016) Application of vibration isolators with a low stiffness for the strongly vibrating equipment. In: International conference on industrial engineering. ICIE 2016, pp 641–646
5. Valeev A, Zotov A, Tokarev A (2017) Study of application of vibration isolators with quasi-zero stiffness for reducing dynamic loads on the foundation. *Dyn Vibro Acoust Mach (DVM2016) Procedia Eng* 176:137–143
6. Mohan A, Shajahan K, Nair RP (2020) Design and analysis of an optimised passive low frequency vibration isolator, M.Tech, Thesis, DST, CUSAT
7. Frankovich D (2009) The basics of vibration isolation using elastomeric materials, Indiana, pp 1–7
8. Temoshinko G (2015) Mechanics of materials
9. Manoj Kunnil SK (2012) Finite element analysis of elastomers using ANSYS. In: Proceedings of the 2012 20th international conference on nuclear engineering collocated with the ASME 2012 power conference
10. Alabuzhev PA, Gritchin L, Kim L, Stepanov CP (1989) *Vibration Protecting and Measuring Systems with Quasi-Zero Stiffness*. Hemisphere Publishing, New York

Finite Element Analysis of OGrid Lateral Bracing System



V. J. Farhana, Beena Mary John, and Rajesh P. Nair

Abstract Structures are to be designed to resist a set of external forces or physical conditions, so that the damages that occur to the structure is a minimum. Efficient structural design by changing its form and geometry, and by using better structural elements is a novel approach in the structural design of buildings. Braced circular frames are lateral load resisting systems which offer more ductility, appropriate stiffness and high performance. In this paper, a circular bracing system is analyzed and evaluated. Various geometries are analyzed to arrive at the best geometry and to evaluate the optimized geometry in a multistoried structure. The parametric study in this work has been conducted with the aid of a commercial FEM software package, ANSYS 2020 R2. Static structural analysis is done to find the deformations for lateral loads applied to frames with various geometries. The load and loading conditions are given as per Indian standards, considering a structure in Visakhapatnam, considering the severe condition. The wind load is given as per IS 875 (Part 111) and seismic load is given as per IS 1893 (Part 1). The results obtained are tabulated and thereafter represented graphically to understand and study the pattern exhibited and are then optimized. The optimized bracings are then analyzed within a five-storied steel structure and modal analysis of the same is carried out to find the natural frequencies and mode shapes.

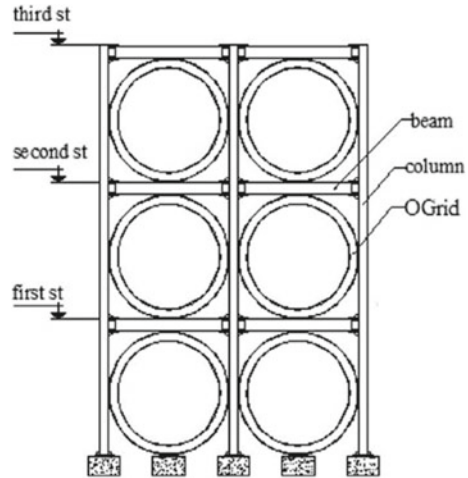
Keywords OGrid · Moment resisting frames · Lateral load resistance

1 Introduction

The OGrid bracing system is a novel lateral bracing system, which is represented by a braced frame with a circular brace connected by joint connections to a moment-resisting frame. The circular brace provides the lateral stiffness and the inelastic behavior of the braces leads to energy dissipation during seismic excitation. OGrid bracing systems are generally used in high-rise buildings as one circular brace in

V. J. Farhana (✉) · B. M. John · R. P. Nair
Department of Ship Technology, Cochin University of Science and Technology, Cochin, India

Fig. 1 OGrid bracing system



every two storeys. This helps in decreasing the weight and at the lowest story, this brace is connected to the foundation like the column [2].

The use of seismic response control systems, in the form of hysteretic dampers with high dissipative capacity and their performance for single as well as multi-storey frames are discussed in [1, 3, 9–11]. There are several other literature which discusses the use of hysteretic dampers. Unlike the use of the above dampers, the novel idea of using circular elements as passive energy dissipation systems proves advantageous because of the high performance, ductility and easy replacement of the damaged members (Murthy 2005).

The use of the novel O-shape system (OGrid) braces proves effective in the sense that it can be used in any part of the structure, with regard to the architectural expression of form and with due consideration of its functional requirements. The OGrid also acts as structural fuses during earthquake loading, so that it does not affect the main structural components, which eventually leads to easy retrofitting of the damaged member.

[7] presents a study on the determination of optimum type of bracing by applying topology optimization on a simple steel structure to find the minimum deformation under the effect of reversed wind load. [8] introduces the hexa-braced frame, an innovative concept, in which the hexagonal bracing configuration is formed by connecting the vertical structural elements to the bracings, for improved seismic response of the structure. Figure 1 shows the OGrid bracing system used for the present study.

2 Geometrical Modelling of OGrid Bracing System

The frame of the OGrid bracing system considered for this work, has a span and height of 3000 mm. The bracing is made of steel material with a yield stress of

Table 1 Sections of the column, beam, and bracing

Model	Details of column section	Details of beam section	Details of brace section
O-I-W	ISHB 150	ISMB 175	ISMB 125
O-I-F	ISHB 150	ISMB 175	ISMB 125
O-C	ISHB 150	ISMB 175	ISMC 125
O-R	ISHB 150	ISMB 175	122 × 61 × 4.5
O-Ci	ISHB 150	ISMB 175	122 Ø × 4.5

Table 2 Design wind load at various heights

Height	P_z	$F = A_e \times (f \times P_z)$ (N/m)	Wind load (kN/m)
0–10	1161.6	8363.52	8.36
10–15	1325.4	9542.88	9.54
15–20	1440.6	10,372.32	10.37
20–30	1591.35	11,457.72	11.45

Table 3 Design seismic load at various heights

h_i	Q_i (kN)
10	9.40
15	20.048
20	37.01
30	84.821

235 MPa, Poisson’s ratio of 0.3, and ultimate stress of 363 MPa. A structure of 24 × 15 × 30 m is taken with 3 m height for each storey. The various geometries considered in the present study are:

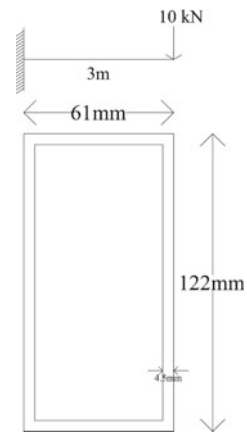
OGrid-I web connected section [O-I-W], OGrid-I flange connected section [O-I-F] OGrid-Channel section [O-C], OGrid-Rectangular section [O-R], OGrid-Circular section [O-Ci].The geometric sections for all the models are taken from IS 800:2007. Table 1 shows the sections of column, beam and bracing system.

To simulate the real conditions, OGrid bracing system is analyzed with a fixed support at two columns to restrain axial deformation whereas load is applied in one direction. Combined effects of the lateral loads are being given at loading. In most situations, the lateral loads represent live loads, the main component of which are horizontal forces or forces acting parallel to the x axis. The most common types of lateral loads are wind load and seismic load. The load and loading conditions are given as per Indian standards, considering a structure in Vishakapatnam, considering the severe condition. Wind load is calculated as per IS 875 (part III)–1987 and the seismic load is calculated as per IS 1893 (part I). Tables 2 and 3 shows the wind load and seismic load at various heights.

Table 4 Maximum values of deformation, stress and strain for the different OGrid models

Name of model	Max deformation (m)	Max stress (N/m ²)	Max strain
OGrid-I (web connected)	1.07×10^{-2}	3.50×10^8	1.78×10^{-3}
OGrid-I (flange connected)	0.75×10^{-2}	3.67×10^8	1.86×10^{-3}
OGrid-C	1.50×10^{-2}	3.46×10^8	1.76×10^{-3}
OGrid-R	1.46×10^{-2}	3.12×10^8	1.6×10^{-3}
OGrid-Ci	0.85×10^{-2}	2.83×10^8	1.43×10^{-3}

Fig. 2 Cantilever beam section



3 Analysis of OGrid Bracing System

A static structural analysis of the above models are carried out using ANSYS 2020 R2 software to determine the displacements, stresses and strains in each of these models. The parameters like maximum deformation, maximum stress, and maximum strain of all the analyzed models are listed and compared as shown in Table 4.

The optimum bracing type for minimum deformation under the effect of lateral load is determined based on obtained result parameters. A simple beam analysis based on the same loading and boundary conditions is carried out to validate the numerical model. Loads are applied in various directions to check the maximum deformation. The results are analytically compared to validate the numerical analysis. A cantilever beam with a rectangular cross-section, as shown in Fig. 2 is analyzed both numerically and analytically.

Figure 3 illustrates the results of the cantilever beam analyzed numerically, which shows a maximum deformation of 150 mm.

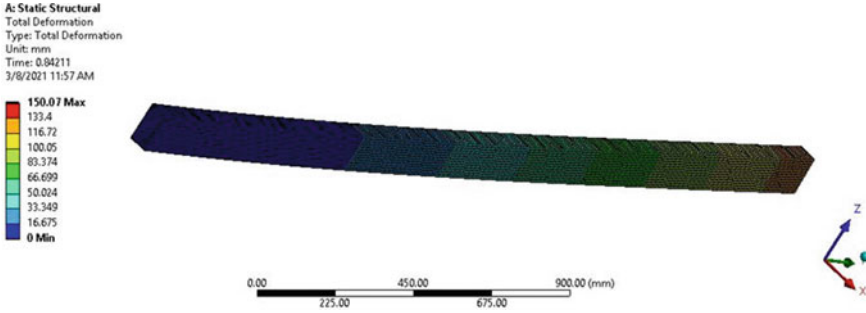


Fig. 3 Deformation for cantilever beam

The cantilever beam is analyzed analytically with the equations for maximum deflection and moment of inertia, given by Eqs. 1 and 2 below:

$$\Delta = \frac{WL^3}{3EI} \tag{1}$$

$$\begin{aligned} I &= \frac{BD^3}{12} - \frac{bd^3}{12} \\ &= \frac{61 \times 122^3}{12} - \frac{[[6-(2 \times 4.5)][12-(2 \times 4.5)]]^3}{12} \\ &= 2978007 \text{ mm}^4 \end{aligned} \tag{2}$$

The moment of inertia obtained is 2978007 mm⁴ with young’s modulus 2 × 10⁵, with a load of 10 kN at free end and beam span of 3 m,

$$\begin{aligned} \Delta &= \frac{wl^3}{3EI} \\ &= \frac{10 \times 10^3 \times 3000^3}{3 \times 2 \times 10^5 \times 2878007} \\ &= 151.10 \text{ mm} \end{aligned}$$

The maximum deflection values obtained using Eq. 1 is in good agreement with the deformation obtained in Fig. 3. Further, a beam with two different cross-sections is analyzed numerically by applying load in two different directions. I section and circular section is analyzed as it has least deformation values on frame analysis. The same load is applied in both z direction and x direction and results are obtained. For the I section, when the load is applied in z direction maximum deflection obtained is 15.881 mm and when applied in x direction maximum deflection obtained is 2.013 mm.

For the circular section, when the load is applied in z direction maximum deflection obtained is 3.046 mm and when applied in x direction maximum deflection obtained is 3.038 mm. Figure 4 represents the loads applied for the I section and the circular section.

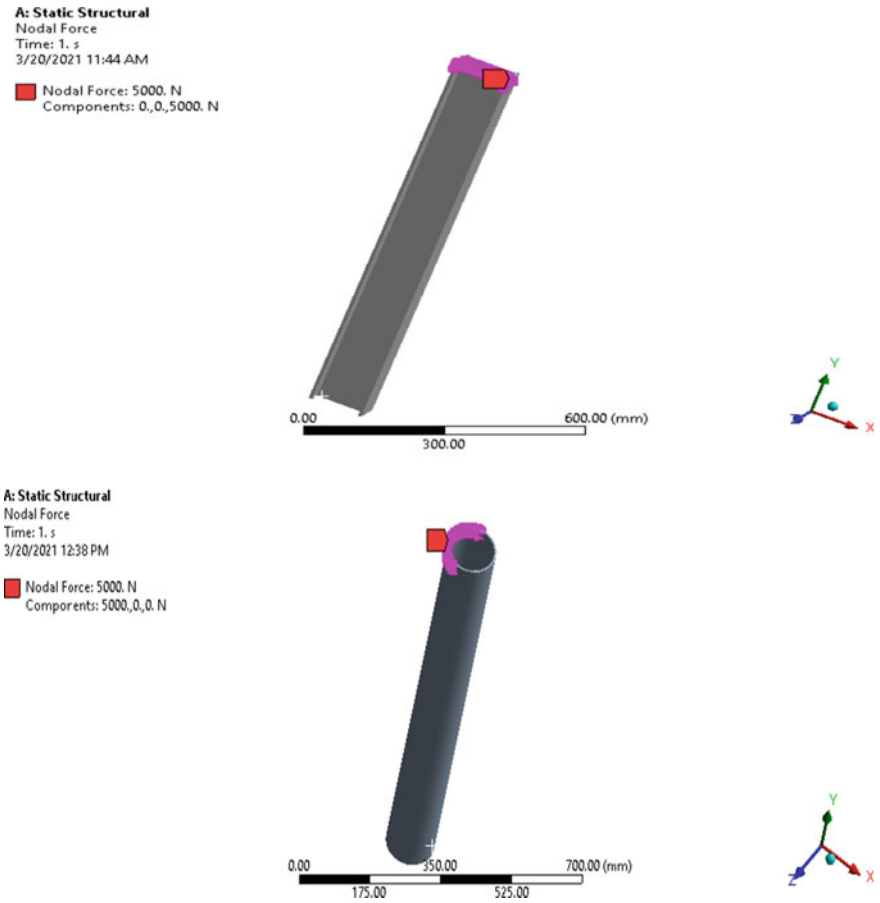


Fig. 4 Comparison models for I section and circular section

The bracing with I section (flange connected) shows the least and better deformation results on applying load and is therefore, considered as the optimized model. Also on comparing other sections circular OGrid shows better performance in parameters.

4 Analysis of OGrid Multistoried Structure

Novel housing solutions in India are shifting to multi-storey building construction, as it saves construction land area and are more affordable for individual buyers. Taking this into consideration, a five storied steel structure is modelled using the optimum model selected in Sect. 3, that is, OGrid with flange connected I section. The study is carried out by using ANSYS 2020 R2 software, by following provisions

and specifications as per IS 800. The dimensions of the model in the longitudinal and transverse directions are 30 m and 15 m, respectively. A height of 25 m (5 m of each story) is considered for the building (Fig. 5), with six spans in the longitudinal direction and three spans in a transverse direction.

Wide parallel flange beams (WPB) are used for both the columns and beams. The details of column section and beam sections are shown in Tables 5 and 6. Figure 6 represents model of the OGrid multistorey structure.

For this study, the wind and earthquake loads are calculated as set forth by the provision of IS codes, as discussed in Sect. 2. Figure 7 shows the boundary conditions used in the model runs of the multistoried building.

A modal analysis is performed to find the deformations and frequencies of both braced an unbraced structures and the results are shown below (Tables 7 and 8):

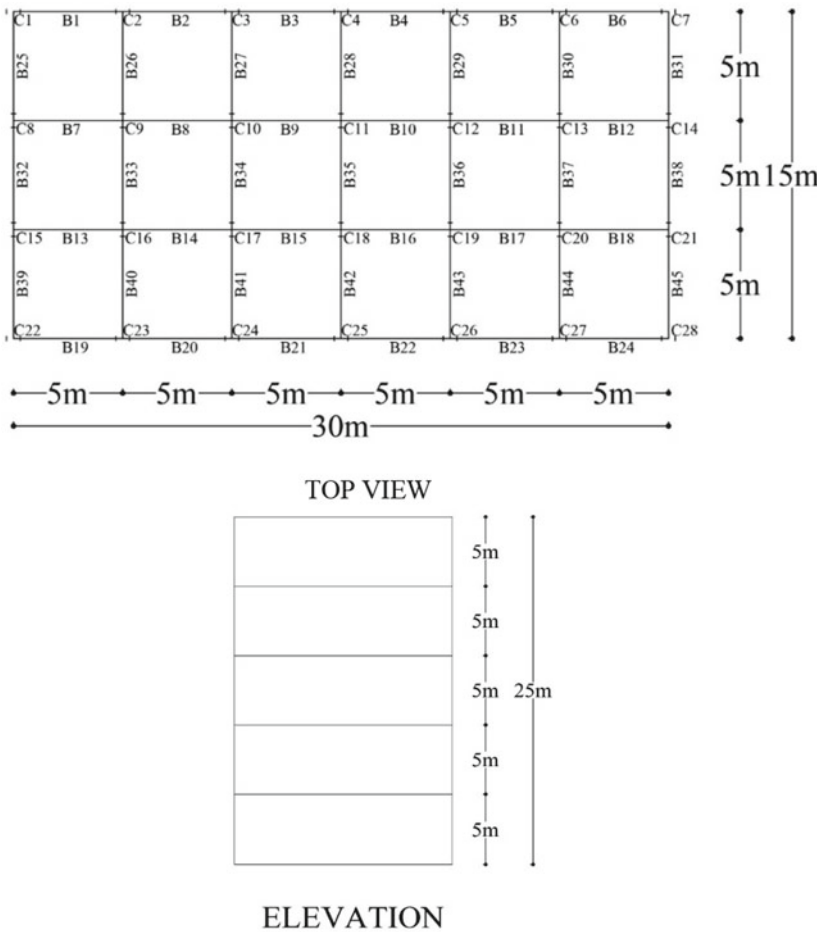


Fig. 5 Layout of multistoried building

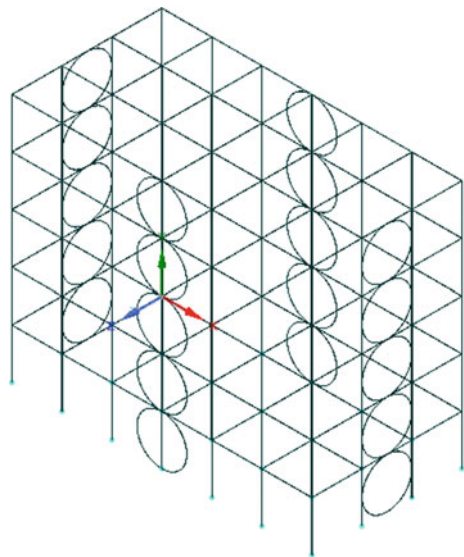
Table 5 Details of the column sections

Column ID	Wide flange section
C1, C2, C3, C4	WPB 700 × 300
C19, C20, C21, C22, C23, C24, C25, C26, C27, C28	WPB 550 × 300
C5, C6, C7, C8	WPB 800 × 300
C9, C10, C11, C12, C13, C14, C15, C16, C17, C18	WPB 900 × 300

Table 6 Details of the beam sections

Beam ID	Wide flange section
B13, B14, B15, B16,17, B18, B31, B32, B33, B34, B35, B36, B37, B38, B39, B40, B41, B42, B43, B44, B45	WPB 340 × 300
B2, B3, B4, B5, B8, B9, B10, B11	WPB 360 × 300
B1, B6, B7, B12, B20, B21, B22, B23, B26, B27, B28, B29	WPB 400 × 300
B19, B24, B25, B30	WPB 400 × 400

Fig. 6 Geometrical model of OGrid multistoried structure



After the modes are identified, the response in that mode is picked from the response spectrum. The total response of the structure is estimated from the peak responses obtained. The resulting plot is then used to pick the response of any linear system, given its natural frequency of oscillation. From this study, for an unbraced structure, the maximum amplitude obtained is 17.916 mm with a frequency of 0.0096 Hz and a phase angle of 180° as shown in Fig. 8. For a braced structure,

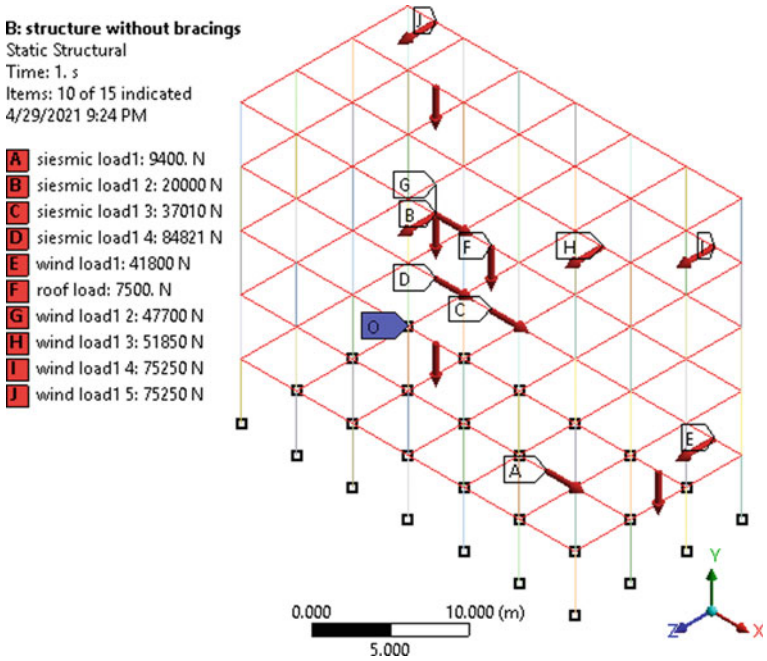


Fig. 7 Boundary conditions of multistoried building

Table 7 Deformation of multistoried building without bracings

Mode	Frequency (Hz)	Maximum deformation (mm)
1	9.9158e-002	1.761
2	0.105	3.389
3	0.124	2.083
4	0.149	2.068
5	0.161	15.807
6	0.173	48.782

Table 8 Deformation of multistoried building with bracings

Mode	Frequency (Hz)	Maximum deformation (mm)
1	8.5359e-002	1.614
2	8.8638e-002	2.469
3	9.545e-002	2.613
4	0.135	2.137
5	0.137	2.21
6	0.185	2.090

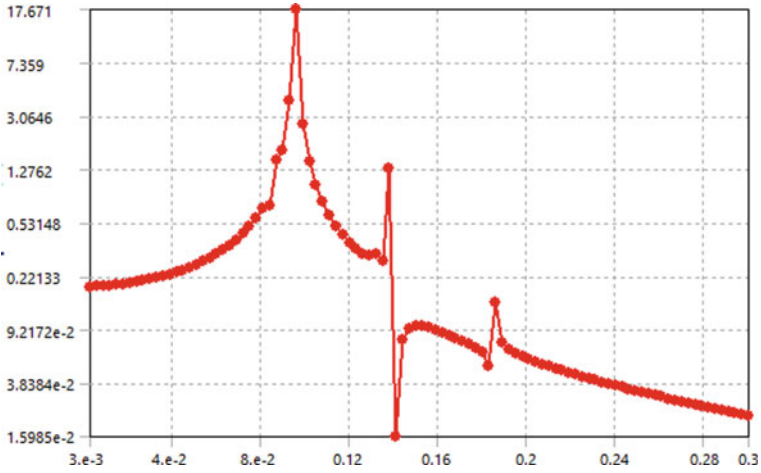


Fig. 8 Frequency response of unbraced structure

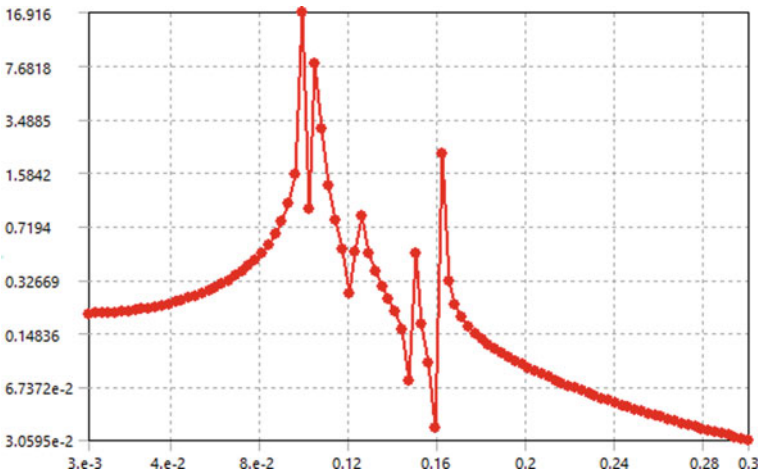


Fig. 9 Frequency response of braced structure

the maximum amplitude is obtained as 16.916 m with a frequency of 0.0099 Hz and a phase angle of 0° as shown in Fig. 9.

5 Conclusions

The lateral behaviour of a multistoried building with an OGrid bracing system is investigated in this work. The behaviour of different bracing models is first investigated and the optimum bracing model, in the form of OGrid bracing with I section (flange connected), with the least deformation characteristics is used to model the multistoried building. The results presented in this study also shows that the model with a circular cross-section gives better performance, conforming to the novel idea of using circular elements as passive energy dissipation systems which also proves worthwhile in offering more ductility, high performance, and easy replacement of damaged members without making use of specialized technologies. As seen from the present study, the placement of bracings in the central span leads to minimized deformations at various mode shapes. By changing the bracing positions and increasing the number of bracings with more enhanced sections might lead to further reduced deformation, which has not been studied in this work.

References

1. Benavent-Climent A (2010) A brace-type seismic damper based on yielding the walls of hollow structural sections. *Eng Struct* 32(4):1113–1122
2. Boostani M, Rezaifar O, Gholhaki M (2018) Introduction and seismic performance investigation of the proposed lateral bracing system called “OGrid.” *Arch Civ Mech Eng* 18:1024–1041
3. Colajanni P (1999) Braced frames with hysteretic dissipative devices: seismic response and design criteria. *J Earthq Eng* 3(01):33–57
4. IS 800 (2007) Indian Standard code of practice for general construction in steel (Third Revision), Bureau of Indian Standards, New Delhi
5. IS 1893 (part 1) (2002) Indian Standard criteria for earthquake resistant design of structures, Bureau of Indian Standards, New Delhi
6. IS 875 (part 3) (1987), Code of practice for design loads (other than earthquake) for building and structures, wind loads, Bureau Of Indian Standards, New Delhi
7. Kutuk MA, Gov I (2014) Optimum bracing design under wind load by using topology optimization. *Wind Struct* 18(5):497–510
8. Mashhadiali N, Kheyroddin A (2018) Seismic performance of concentrically braced frame with a hexagonal pattern of braces to mitigate soft-story behavior. *Eng Struct* 175:27–40
9. Mazza F, Vulcano A (2011) Control of the earthquake and wind dynamic response of steel-framed buildings by using additional braces and/or viscoelastic dampers. *Earthq Eng Struct Dyn* 40(2):155–174
10. Teruna DR, Majid TA, Budiono B (2015) Experimental study of hysteretic steel damper for energy dissipation capacity. *Adv Civ Eng* 2015:1–12
11. Tsai KC, Chen HW, Hong CP, Su YF (1993) Design of steel triangular plate energy absorbers for seismic-resistant construction. *Earthq Spectra* 9(3):505–528

Active Vibration Model Predictive Control for a Smart Flexible Beam



A. R. Prashant, Arun K. Tangirala, C. Lakshman Rao, and M. V. V. S. Murthy

Abstract The reaction wheel in satellites creates tonal and random disturbances which can jeopardize the functionality of certain electronic payloads. To dampen out these disturbances, passive or active mechanical isolators are used. The active mechanical isolators generally consist of flexible mechanical elements with collocated sensors and actuators along with a suitable controller which is generally referred as active vibration control (AVC). For space-based applications, the controller should be an optimal controller capable of controlling free and forced vibrations along with actuator constraints. In literature, most of the controllers adopt either state feedback or output feedback techniques. These control techniques have inherent drawbacks either in handling actuator constraints, modeling errors, or optimality. Model predictive control (MPC) is one control that can meet all the above-mentioned requirements. Hence, this paper proposes MPC for such space based applications. For study purposes, the active mechanical isolator is simulated using a flexible beam with collocated piezo sensors and actuator, which is referred to as a smart flexible beam (SFB). MPC is designed for this SFB. MPC being a model-based design, a finite element method (FEM) based state space approach is adopted to obtain the model of SFB. The model obtained using the FEM based state space approach is experimentally verified ensuring the correctness of the model. The simulation study of the proposed control under the framework of MPC for SFB has shown the effectiveness in attenuating the free vibrations to more than 50% at its first two resonant modes.

Keywords Model predictive control · Finite element method · State space model · Tonal disturbance · Prediction horizon

A. R. Prashant (✉) · M. V. V. S. Murthy
U R Rao Satellite Centre, Bangalore, Karnataka, India

A. K. Tangirala · C. L. Rao
Indian Institute of Technology Madras, Chennai, Tamil Nadu, India

1 Introduction

The reaction wheel in satellite creates tonal and random disturbances [1] which can jeopardize the functionality of certain electronic payloads in it. To dampen out these disturbance forces, passive isolators [2] and active isolators are proposed [3]. The active mechanical isolators generally consist of flexible mechanical elements with collocated sensors and actuators along with a suitable controller. Several controllers have been proposed in the field of active vibration control. The controllers in the area of active vibration control applications can be broadly classified under different categories. Linear (Linear Quadratic Regulator(LQR) [4] and nonlinear (Fuzzy [5]) control, model-based (Pole placement [6]) and model-free (Proportional Integral Derivative(PID) [7]), state feedback(LQR)and output feedback, based on feedback variable used: displacement (position) [8], strain (strain rate) [9],etc., based on robustness(H-infinity) [10] and prediction/optimality (MPC) [11]. Apart from these control design approaches, the problem of variable structural control is addressed by introducing adaptivity [12] into the control loop.

All these control approaches or techniques have their own merits and demerits. MPC has been generally applied in the process industry wherein the plant dynamics are much slower. With the advent of a faster digital signal processor, MPC is now being proposed in the area of active vibration control which has faster dynamics. Very few literatures are available on the implementation of MPC in the area of AVC application. MPC being a model-based controller, a mathematical model of the mechanical system (in our case, smart flexible beam) is essential for designing and for tuning purposes. Usually, finite elements based on Euler Bernouli theory [13] or the, Timoshenko beam theory [14] are adopted to model such SFB, depending on the thickness of the beam. In addition, data driven approach is also adopted when experimental data is available [15].

This paper proposes an Active vibration control under the framework of MPC, which we call here as, Active Vibration Model Predictive Control (AVMPC). First, the mathematical modeling of SFB is presented along with the control design and closed loop AVMPC simulations for harmonic and tonal type of disturbances. Later, the simulation results for control performance metrics for different prediction horizon are presented, demonstrating the effectiveness of AVMPC in attenuating the free vibration to more than 50% of SFB. For a fair comparison, the performance of AVMPC is compared with Linear Quadratic Gaussian (LQG) regulator.

2 Model for Controller: Finite Element-State Space Model

A smart flexible beam consists of a regular beam with piezoelectric material bonded on both sides of it in a collocated fashion at predefined locations of the beam. The piezo material can act both has sensor and actuator. All piezo actuators are bonded to one side and all piezo sensors to the other side of the SFB. The mathematical

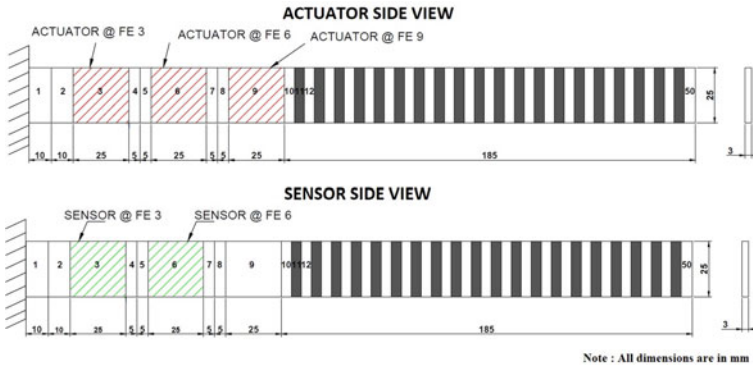


Fig. 1 Geometry of smart cantiliver beam with 50 finite elements

Table 1 Geometry and material property of beam and piezoelectric material

Physical parameter	Cantiliver beam	Piezomaterial (PZT) material	Unit
Length	$0.300(L_b)$	$0.025(l_p)$	m
Width	$0.025(w_b)$	$0.025(w_p)$	m
Thickness	$0.003(t_b)$	$0.0005(t_p = t_a)$	m
Density	$2700(\rho_b)$	$7500(\rho_p)$	kg/m^3
Modulus of elasticity	$6.9e10(E_b)$	$6.0e10(E_p)$	Nm^{-2}
PZT Strain Constant	—	$285e-12(d31)$	m/V
PZT Stress Constant	—	$9e-3(g31)$	Vm/N

model of the smart flexible beam is formulated using FEM based on Euler-Bernoulli theory and finally transformed into a state-space model, which is generally referred as FEM-SS approach in the literature. The geometry of the SFB is shown in Fig. 1 and Table 1 provides the material property of the beam and piezoelectric material.

2.1 Finite Element Model

The SFB (Fig. 1) is meshed into 50 Finite Elements (FE). The beam which is bonded with piezos on either side is termed as the smart beam (FE Number:3,6,9) element and the beam without piezos (FE Number: 1, 2, 4, 5, 7, 8, 10–50) are termed as regular beam element. Piezo material at FE number 3 and 6 of SFB is bonded in a collocated fashion. The piezo actuator mounted at FE number 9 of SFB is used to provide the disturbance for the SFB. The sensor mounted at FE number 3 and 6 is used to measure the disturbance. The actuator mounted on FE number 3 and 6 is used to provide the counter vibration to the SFB to minimize the vibrations generated due to the disturbances in the beam. The global mass matrix \mathbf{M} and global stiffness matrix

\mathbf{K} are obtained by assembling individual local mass and stiffness matrix respectively as presented in [14]. The local mass $[\mathbf{M}_r]$ and stiffness matrix $[\mathbf{K}_r]$ in an explicit form for a regular beam of length l_b is given by,

$$[\mathbf{M}_r] = \frac{\rho_b A_b l_b}{420} \begin{pmatrix} 156 & 22l_b & 53 & -13l_b \\ 22l_b & 4l_b^2 & 13l_b & -13l_b^2 \\ 54 & 13l_b^2 & 156 & -22l_b \\ -13l_b & -3l_b^2 & -22l_b & 4l_b^2 \end{pmatrix} \quad [\mathbf{K}_r] = \frac{E_b I_b}{l_b} \begin{pmatrix} \frac{12}{l_b^2} & \frac{6}{l_b} & -\frac{12}{l_b^2} & \frac{6}{l_b} \\ \frac{6}{l_b^2} & 4 & -\frac{6}{l_b} & 2 \\ -\frac{12}{l_b^2} & -\frac{6}{l_b} & \frac{12}{l_b^2} & -\frac{6}{l_b} \\ \frac{6}{l_b^2} & 2 & -\frac{6}{l_b} & 4 \end{pmatrix} \quad (1)$$

where $A_b = l_b \times w_b$ is the cross sectional area and $I_b = \frac{w_b^3 t_b^3}{12}$, moment of Inertia. Similarly, the local mass $[\mathbf{M}_s]$ and stiffness matrix $[\mathbf{K}_s]$ for smart beam element (top piezo actuator patch + middle regular beam element + bottom piezo sensor patch) of length l_p is given as,

$$[\mathbf{M}_s] = \frac{\rho_s A_s l_p}{420} \begin{pmatrix} 156 & 22l_p & 53 & -13l_p \\ 22l_p & 4l_p^2 & 13l_p & -13l_p^2 \\ 54 & 13l_p^2 & 156 & -22l_p \\ -13l_p & -3l_p^2 & -22l_p & 4l_p^2 \end{pmatrix} \quad [\mathbf{K}_s] = \frac{E_s I_s}{l_p} \begin{pmatrix} \frac{12}{l_p^2} & \frac{6}{l_p} & -\frac{12}{l_p^2} & \frac{6}{l_p} \\ \frac{6}{l_p^2} & 4 & -\frac{6}{l_p} & 2 \\ -\frac{12}{l_p^2} & -\frac{6}{l_p} & \frac{12}{l_p^2} & -\frac{6}{l_p} \\ \frac{6}{l_p^2} & 2 & -\frac{6}{l_p} & 4 \end{pmatrix} \quad (2)$$

where, $\rho_s A_s = w_b(\rho_b t_b + 2\rho_p t_p)$, $E_s I_s = E_b I_b + 2E_p I_p$, $I_p = \frac{w_b^3 t_b^3}{12} + w_p t_p (\frac{t_b + t_p}{2})^2$.

Actuator and Sensor Equation: For a two node finite element, the control force f_{ctrl} produced by the actuator that is applied on the beam and the strain rate sensor output voltage V^s is given by,

$$f_{ctrl} = \mathbf{h}u(t) \quad V^s(t) = \mathbf{p}^T \dot{\mathbf{q}} \quad (3)$$

where $u(t)$ is the control input (manipulated value) given to the actuator and $\mathbf{h}^T = E_p d_{31} w_p \bar{z} [-1 \ 0 \ 1 \ 0]$ and $\bar{z} = (\frac{t_a + t_b}{2})$ is the distance between neutral axis of the beam and the piezoelectric layer. $\mathbf{p}^T = G_c z e_{31} w_b [0 \ -1 \ 0 \ 1]$, where G_c is a signal conditioner gain and $z = (\frac{t_b}{2} + t_p)$. Here \mathbf{p} is a constant vector of size (4×1) and depends on the type of sensor, its characteristics, and its location on the beam. The $\dot{\mathbf{q}}$ is time derivative of the nodal co-ordinate vector \mathbf{q} .

2.2 Dynamic Equation and State Space Model

The equation of motion for SFB is given by,

$$\mathbf{M}\ddot{\mathbf{q}} + \mathbf{K}\mathbf{q} = f_{ext} + f_{ctrl} \quad y(t) = V^s(t) = \mathbf{p}^T \dot{\mathbf{q}} \quad (4)$$

where \mathbf{M} , \mathbf{K} , \mathbf{q} , $\ddot{\mathbf{q}}$, f_{ext} , f_{ctrl} and \mathbf{p}^T are global mass matrix, global stiffness matrix, displacement vector, acceleration vector, external force vector, controlling force vector and a constant vector of the beam. In our case, \mathbf{M} and \mathbf{K} are of size (100×100) and all other are of size (100×1) . Introducing generalized coordinates and using transformation $\mathbf{q} = \mathbf{T}\mathbf{g}$ and also considering Rayleigh's proportional damping we can obtain the dynamic equation as given in Eq. (5)

$$\mathbf{M}^* \ddot{\mathbf{g}} + \mathbf{C}^* \dot{\mathbf{g}} + \mathbf{K}^* \mathbf{g} = \mathbf{f}_{ext}^* + \mathbf{f}_{ctrl}^* = \mathbf{f}^* \quad y(t) = V^s(t) = \mathbf{p}^T \dot{\mathbf{q}} = \mathbf{p}^T \mathbf{T} \dot{\mathbf{g}} \quad (5)$$

where, $\mathbf{T}(100 \times 2)$, $\mathbf{M}^*(2 \times 2)$ ($\mathbf{M}^* = \mathbf{T}^T \mathbf{M} \mathbf{T}$), $\mathbf{K}^*(2 \times 2)$ ($\mathbf{K}^* = \mathbf{T}^T \mathbf{K} \mathbf{T}$), $\mathbf{f}_{ext}^*(2 \times 1)$ ($\mathbf{f}_{ext}^* = \mathbf{T}^T \mathbf{f}_{ext}$), $\mathbf{f}_{ctrl}^*(2 \times 1)$ ($\mathbf{f}_{ctrl}^* = \mathbf{T}^T \mathbf{f}_{ctrl}$) are modal matrix and generalised mass matrix, stiffness matrix, external force vector and control force vector respectively. \mathbf{C}^* is a generalised modal damping matrix (2×2) , given by $\mathbf{C}^* = \alpha \mathbf{M}^* + \beta \mathbf{K}^*$, where α and β are frictional and structural damping constant respectively.

For two vibratory modes, the state space model is obtained as follows: Let vector $\mathbf{g} = \mathbf{x}$, where $\mathbf{x}^T = [x_1 \ x_2]$ and let $\dot{\mathbf{x}}^T = [\dot{x}_1 \ \dot{x}_2] = [x_3 \ x_4]$, then Eq. (5) can be re-arranged as,

$$\begin{bmatrix} \dot{x}_3 \\ \dot{x}_4 \end{bmatrix} = -\mathbf{M}^{*-1} \mathbf{K}^* \begin{bmatrix} x_1 \\ x_2 \end{bmatrix} - \mathbf{M}^{*-1} \mathbf{C}^* \begin{bmatrix} x_3 \\ x_4 \end{bmatrix} + \mathbf{M}^{*-1} \mathbf{f}^* \quad (6)$$

The Eq. (6) can be written in the state space model as below,

$$\begin{bmatrix} \dot{x}_1 \\ \dot{x}_2 \\ \dot{x}_3 \\ \dot{x}_4 \end{bmatrix} = \begin{bmatrix} 0 & I \\ -\mathbf{M}^{*-1} \mathbf{K}^* & -\mathbf{M}^{*-1} \mathbf{C}^* \end{bmatrix} \begin{bmatrix} x_1 \\ x_2 \\ x_3 \\ x_4 \end{bmatrix} + \begin{bmatrix} 0 \\ -\mathbf{M}^{*-1} \mathbf{T}^T \mathbf{h} \end{bmatrix} u(t) + \begin{bmatrix} 0 \\ -\mathbf{M}^{*-1} \mathbf{T}^T \mathbf{f} \end{bmatrix} r(t) \quad (7)$$

The sensor voltage is taken as the output of the model (SFB) is given by,

$$y(t) = \mathbf{p}^T \mathbf{T} \dot{\mathbf{g}} = [\mathbf{p}^T \mathbf{T}] \begin{bmatrix} x_3 \\ x_4 \end{bmatrix} = [\mathbf{0} \ \mathbf{p}^T \mathbf{T}] \begin{bmatrix} x_1 \\ x_2 \\ x_3 \\ x_4 \end{bmatrix} \quad (8)$$

The continuous state space model and the output equation is given by Eq.(9),

$$\dot{\mathbf{x}}(t) = \mathbf{A}\mathbf{x}(t) + \mathbf{B}u(t) + \mathbf{E}r(t) \quad y(t) = \mathbf{C}^T \mathbf{x}(t) + \mathbf{D}u(t) \quad (9)$$

$$\mathbf{A} = \begin{bmatrix} \mathbf{0} & \mathbf{I} \\ -\mathbf{M}^{*-1} \mathbf{K}^* & -\mathbf{M}^{*-1} \mathbf{C}^* \end{bmatrix} \quad \mathbf{B} = \begin{bmatrix} \mathbf{0} \\ -\mathbf{M}^{*-1} \mathbf{T}^T \mathbf{h} \end{bmatrix}$$

$$\mathbf{C} = [\mathbf{0} \ \mathbf{p}^T \mathbf{T}] \quad \mathbf{D} = \mathbf{0} \quad \mathbf{E} = [\mathbf{0} \ -\mathbf{M}^{*-1} \mathbf{T}^T \mathbf{f}]$$

where $r(t)$, $u(t)$, \mathbf{A} , \mathbf{B} , \mathbf{C} , \mathbf{D} , \mathbf{E} , $\mathbf{x}(t)$ and $y(t)$ represents the external force input, the control input, system matrix, input matrix, output matrix, transmission matrix, external disturbance coupling matrix, state vector and system output (sensor output) respectively.

3 Active Vibration Model Predictive Control

Model predictive control(MPC) is an advanced optimal control method that minimizes a cost function comprising a vector of future errors. These errors are evaluated as the difference between the desired set point trajectory and the predicted dynamic behavior of the system to be controlled. The controller utilizes a model of the system that has been derived either by an analytical, empirical, or data-driven approach. The key feature that distinguishes MPC is the ability to predict the plant response, minimizes the tracking error with optimal control effort, and handles constraints. An MPC controller solves, at each sampling instant, a finite horizon optimal control problem, and only the first value of the resulting optimal control variable solution is then applied to the plant.

3.1 Controller Design

For MPC design, the Prediction model, Constraints, and Cost function need to be defined. The tuning parameters for MPC are Prediction Horizon, Control horizon, and weights applied in the cost function. Typical architecture of AVC-MPC is given in Fig. 2.

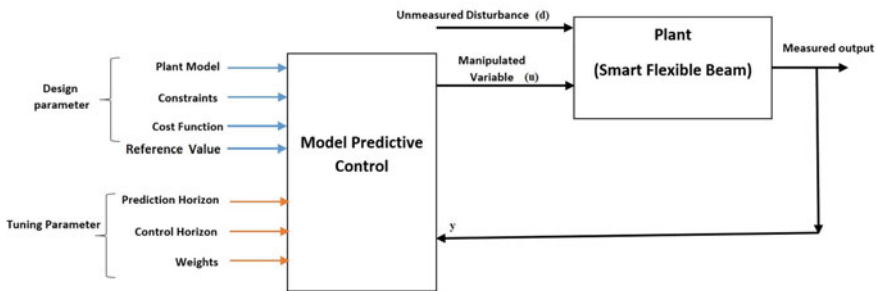


Fig. 2 Architecture for AVC-MPC

Prediction model in our case is the discretized state-space model obtained through the FEM-SS approach as stated in Sect. 2.2. It may be noted here that discretized state-space model is an reduced order model of SFB capturing the first two resonances. The discretized state-space model is given by,

$$\mathbf{x}[n + 1] = \mathbf{A}_d\mathbf{x}[n] + \mathbf{B}\mathbf{3}_d u[n] + \mathbf{B}\mathbf{9}_d d[n] \quad y[n] = \mathbf{C}_d\mathbf{x}[n] \quad (10)$$

with $\mathbf{D} = \mathbf{0}$. The sampling frequency for discretisation is set to $f_s = 1600$ Hz. It may be noted here that the disturbance to SFB is given at FE location 9. The external force is zero and hence $\mathbf{E} = \mathbf{0}$ (refer Eq. (9)). The $\mathbf{x}[n](4 \times 1)$, $\mathbf{A}_d(4 \times 4)$, $\mathbf{B}\mathbf{3}_d(4 \times 1)$, $\mathbf{B}\mathbf{9}_d(4 \times 1)$, $\mathbf{C}_d(1 \times 4)$, $u[n](1 \times 1)$, $d[n](1 \times 1)$ are state variable, system matrix, input matrix, disturbance influence matrix, output matrix, manipulated variable, and disturbance variable.

Constraints only on the manipulated variable is considered. The actuator constraint is ± 100 V. Since an external gain of 10 is provided by the power amplifier for the actuator, the constraint set during control design is ± 10 V.

Cost function is to defined for MPC. The cost function (J) considered in this paper is given in the Eq. (11)

$$J = (\hat{y}[n + 1] - r[n + 1])^T \mathbf{W}_y (\hat{y}[n + 1] - r[n + 1]) + \Delta u^T [n] \mathbf{W}_{\Delta u} \Delta u [n] \quad (11)$$

\mathbf{W}_y and $\mathbf{W}_{\Delta u}$ are positive semidefinite weighting matrices and usually chosen as diagonal matrices. $r[.]$ is the reference set value. It may be noted here that in AVC application, the objective is to achieve zero vibration. Hence, in our case $r[.]$ is set to 0.0001.

The **tuning parameters** for MPC are prediction horizon (P), control horizon (M), and the weights applied in the cost function. These parameters are tuned to have closed-loop control performance based on certain control metrics. For the control problem in our case, the tuning parameters are tuned such that for a simple harmonic disturbance of the first resonance of SFB, a minimum of 50% attenuation is to be achieved at its free vibration modes.

Disturbance Model: The reaction wheel creates tonal and random disturbance [1]. The steady state tonal disturbance model is provided in Eq. (12),

$$d(t) = \sum_{i=1}^n C_i \Omega^2 \sin(2\pi h_i \Omega t + \alpha_i) \quad (12)$$

where, $d(t)$ is the disturbance signal, n is the number of harmonics included in the model, C_i is the amplitude coefficient of the i -th harmonic, Ω is the wheel speed, h_i is the i -th harmonic number and α_i is a random phase (assumed to be uniform over $[0, 2\pi]$). From the controller perspective, this is an unmeasured disturbance signal.

4 Results and Discussion

The mathematical model of SFB is developed using Matlab. For implementing and for simulation purpose Matlab MPC toolbox and SIMULINK environment is used.

4.1 Verification of FEM-SS Model

The mathematical model obtained is verified against the experimental data obtained from the experimental smart beam with the same configuration as mentioned in Sect. 2. For the initial mathematical model, Rayleigh’s proportional damping was considered. Tuning of damping at first and second resonance is carried based on the data obtained through experimental results. The damping ratio for the first and second resonance set in the mathematical model is $\xi_1 = 0.0136$ and $\xi_2 = 0.0038$ respectively.

Discussion: Figure 3 shows the time domain response for the first two resonances of SFB. The first resonance of the flexible beam is 31 Hz and the second resonance is 167 Hz. The error between the experiment and FEM-SS model shows the deviation of **0.2%** in the first resonance and **0.4%** in the second resonance.

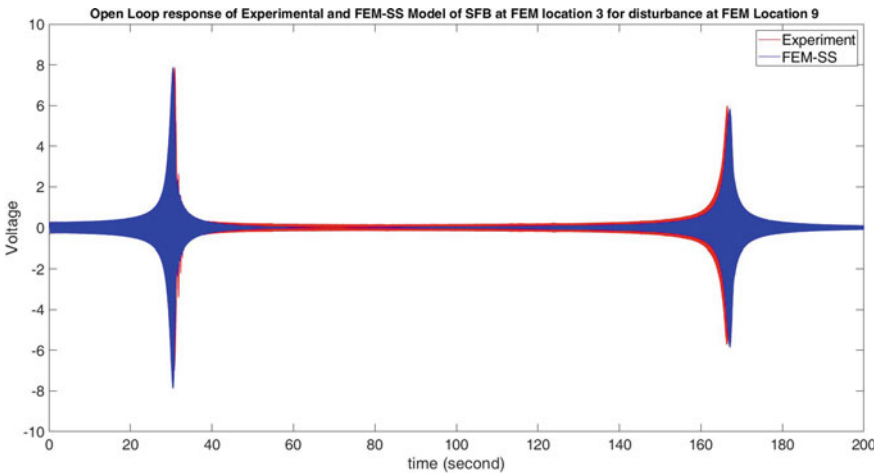


Fig. 3 Time domain response of Experiment and FEM-SS model

4.2 Controller Performance for Simple Harmonic Disturbance

The objective of the controller is to achieve nearly 50% attenuation at free vibration of SFB for a simple harmonic disturbance signal set to the first resonance frequency of SFB. Since LQR/LQG is one of the popular controllers used in the area of AVC, the performance of MPC is compared with LQG for a fair comparison.

The control horizon is kept at nearly around 20% of the prediction horizon. The Weights on input i.e. ($W_{\Delta u}$) is kept at unity and (W_y) is varied to achieve the closed-loop desired attenuation level. For implementing LQG control, the Kalman estimator is used to estimate the states. The state feedback gain is calculated using the 'lqrd' command in Matlab and the associated quadratic cost function in LQG control was tuned to achieve the closed-loop desired 50% attenuation level for harmonic disturbance signal set to the first resonance frequency of SFB. For control performance metrics, Sum Squared Control Error (SSCE) and Input Performance Index as given in Eq. (13) is used.

$$SSCE = \frac{1}{N} \sum_{k=1}^N (y[k] - r[k])^2 \quad IPI = \log\left(\frac{1}{N} \sum_{k=1}^N \Delta u^2[k]\right) \quad (13)$$

Discussion: Table 2 provides the control metrics for MPC and LQG controller respectively at steady-state output. The disturbance signal is set to harmonic signal at the first and second resonance of SFB. From the prediction horizon of 20 onwards, MPC can attenuate the vibration to 50% compared at first resonance. The associated weights set are $W_{\Delta u} = I_u$ and $W_y = I_y * 6e4$. Here I_u and I_y is a unity matrix of appropriate dimensions based on control and prediction horizon respectively. It can be seen from the Table 2, that the LQG performance at first resonance is similar to MPC (P=20, M=4). LQG performs better at second resonance. For a prediction horizon of 20, the SSCE is minimum and hence for further study of MPC, the prediction horizon and control horizon are set to 20 and 4 respectively. For the tuned parameters, MPC can meet the control objective of attenuating vibration more than 50% both at first (50%) and second resonance (72.63%).

4.3 Controller Performance for Tonal Plus Random Disturbance

As explained in Sect. 3.1, the reaction wheel produces tonal disturbance as given in Eq. (12). For simulation purpose, only 5 (i.e. $n = 5$) harmonic is considered. The relationship considered for amplitude coefficient C_i is given by $C_i = \frac{1}{\Omega_m^2}$, $i = 1, m = 1, 2$ and $C_i = \frac{1}{2} C_{i-1}$, $i = 2, 3, 4, 5$ where Ω is the fundamental frequency. (In our

Table 2 Control Metrics of LQG and MPC with different Prediction(P) and Control(M) horizon

MPC							
P	M	First resonance			Second resonance		
		SSCE	IPI	% Attn.	SSCE	IPI	% Attn.
10	2	0.237	8.406	20.00	0.0719	8.4203	28.35
15	3	0.202	3.470	48.73	0.0278	2.5377	72.64
20	4	0.187	3.555	50.70	0.0278	2.5374	72.63
30	6	0.192	3.529	50.00	0.0277	2.5394	72.70
40	8	0.194	3.694	49.80	0.0277	2.5394	72.70
50	10	0.190	3.612	50.27	0.0277	2.5392	72.69
500	100	0.186	3.559	50.77	0.0277	2.5387	72.68
LQG (Q=2.7, R=0.0001)							
-	-	0.193	3.550	50.00	.00045	3.105	95.99

Table 3 Control metrics for MPC and LQG controller for tonal and random disturbance

Only tonal disturbance							
$\Omega_1 = 30.95 \text{ Hz}$				$\Omega_2 = 167.66 \text{ Hz}$			
SSCE		IPI		SSCE		IPI	
MPC	LQG	MPC	LQG	MPC	LQG	MPC	LQG
0.187	0.193	3.556	3.558	0.0278	.00045	2.537	3.106
Tonal + Random Disturbance							
0.180	0.185	3.547	3.734	0.0310	0.0022	2.6560	3.444

simulation $\Omega_1 = 30.95 \text{ Hz}$ and $\Omega_2 = 167.66 \text{ Hz}$). The relationship considered for phase α_i is given by $\alpha_i = 0, i = 1$ and $\alpha_i = \frac{\pi}{i}, i = 2, 3, 4, 5$

Discussion: Table 3 provides the control metric for MPC and LQG control for only tonal disturbance as well as tonal plus random disturbance. The performance of MPC for a tonal disturbance with fundamental frequency ($\Omega_1=30.95 \text{ Hz}$) shows better performance than LQG control. LQG control performs better at higher frequency but with more control effort. The tonal disturbance signal as described in the Eq. (12) plus random signal is simulated. The random signal with zero mean and standard deviation of 1 is added to the tonal disturbance signal. Table 3 provides the control metrics for this type of disturbance. Both MPC and LQG performs in similar line and both the controller can attenuate the vibration at free modes of SFB.

5 Conclusion

Active Vibration Model Predictive Control for controlling the free vibration of smart flexible beam is demonstrated subjecting to tonal plus random disturbances. For a

fair comparison, performance of AVMPc is compared with LQG control and it is shown that the steady state performance of a closed loop AVMPc is better in low frequency region and LQG performs fairly better at higher frequency region. As AVMPc is able to handle actuator constraint and also meets the control objective of attenuating vibration to more than 50% in the first two resonant modes of SFB, AVMPc is a preferred controller over LQG.

Acknowledgement The author thanks Director, U R Rao Satellite Centre, Bangalore and Management of Facilities Area for providing the necessary support to carryout the work.

References

1. Masterson RA, Miller DW, Grogan RL (2002) Development and validation of reaction wheel disturbance models: empirical model. *J Sound Vibr* 249(3):575–598
2. Mou L, Yao Z, Youyi W, Quan H, Rui Q (2019) The pointing and vibration isolation integrated control method for optical payload. *J Sound Vibr* 438:441–456
3. Kamesh D, Pandian R, Ghosal A (2012) Passive vibration isolation of reaction wheel disturbances using a low frequency flexible space platform. *J Sound Vibr* 331(6):1310–1330
4. Tian J, Guo Q, Shi G (2020) Laminated piezoelectric beam element for dynamic analysis of piezolaminated smart beams and GA-based LQR active vibration control. *Compos Struct* 252:1–19
5. Mancang J, Shijie Z, Rongbo H (2019) Multi-mode optimal fuzzy active vibration control of composite beams laminated with photostrictive actuators. *Chin J Aeron* 32(6):1442–1450
6. Mohit K, Arun PP (2018) Modeling of low frequency dynamics of a smart system and its state feedback based active control. *Mech Syst Signal Process* 99:774–789
7. Erdi G, Mehmet C (2018) Active vibration control of a smart beam by a tuner-based PID controller. *J Low Freq Noise Vibr Active Control* 37(4):1125–1133
8. Saeed NA, Awwad EM, Abdelhamid T, El-Meligy MA, Sharaf M (2021) Adaptive versus conventional positive position feedback controller to suppress a nonlinear system vibrations. *Symmetry* 13(255):1–22
9. Riessom W, Prasad K, Gangadharan KV (2014) Vibration control of smart cantiliver beam using strain rate feedback. *Procedia Mater Sci* 5:113–122
10. Zhang XY, Zhang SQ, Wang ZX, Qin XS, Wang RX, Schmidt R (2019) Disturbance rejection control with H optimized observer for vibration suppression of piezoelectric smart structures. *Mech Ind* 20(202):1–13
11. Haijun P, Fei L, Ziyun K (2020) A novel distributed model predictive control method based on a substructuring technique for smart tensegrity structure vibrations. *J Sound Vibr* 471:1–26
12. Yuxue P, Huanlin Z, Zeng M (2019) Multi Channel adaptive active vibration control of piezoelectric smart plate with online secondary path modelling using PZT patches. *Mech Syst Signal Process* 120:166–179
13. Bandyopadhyay B, Manjunath TC, Umopathy M (2007) Modeling, Control and Implementation of Smart Structures: A FEM-State Space Approach, 1st edn. Springer, Heidelberg
14. Manjunath TC, Bandyopadhyay B (2009) Vibration control of Timoshenko smart structures using multirate output feedback based discrete sliding mode control for SISO systems. *J Sound Vibr* 326(1–2):50–74
15. Yangmin X, Chao W, Hang S, Junwei S (2018) A data driven control method for structure vibration suppression. *Acta Astronautica* 143:302–309

Effect of Notch-to-Depth Ratio and Steel Fiber Volume Fraction on Acoustic Emissions Generated During Mode I Fracture Process in Steel Fiber Reinforced Concrete



Sardar Abhijit Samadhan and R. Vidya Sagar

Abstract This article reports the effect of notch to depth ratio (α) and steel fiber volume fraction (V_f) on Acoustic Emissions (AE) generated during Mode I fracture process in Steel Fiber Reinforced Concrete (SFRC). The Plain Concrete (PC) and SFRC Three-Point Bend (TPB) specimens were tested by following EN: 14651-2005, RILEM TC 162-TDF, RILEM TC FMC-50 and JCI-S-001-2003 by CMOD control. Simultaneously, the AE signal waveforms were recorded by using eight AE channel monitoring system. The 2D surface strains and displacements were also recorded using Digital Image Correlation (DIC) technique. The spikes in the cumulative AE energy versus time plot were observed at the instants where sudden drops in the post peak load carrying capacity occurred. Peak load, Fracture energy, AE energy and post peak ductility decreased with increasing α value. The fiber bridging mechanism in SFRC was explored using the concept of crack kinematics with the DIC technique.

Keywords Steel fiber reinforced concrete · Notch to depth ratio · Acoustic emission · Digital image correlation

1 Introduction

It is known that when steel fibers are added to the concrete mixture, its post peak ductility increases [1, 4]. The study of the fracture process in Mode I is carried out by several researchers [1, 4]. The influence of notch to depth ratio (α) on the fracture parameters and generated Acoustic Emission (AE) is important to characterize the fracture process in SFRC [7–9]. Fiber pullout from the cementitious matrix works as a crack arrestor by preventing progression of further damage avoiding the catastrophic events. Hence, the identification of fiber pullout instant is important.

S. A. Samadhan (✉) · R. Vidya Sagar
Department of Civil Engineering, Indian Institute of Science, Bangalore 560012, India
e-mail: abhijits@iisc.ac.in

R. Vidya Sagar
e-mail: rvsagar@iisc.ac.in

Digital Image Correlation(DIC) is an optical technique capable of measuring full field one or two-dimensional surface deformations. AE method gives the information about damage progression with the help of parametric and waveform analysis. Combination of both these methods can be used as a robust tool to perform accurate damage assessment and subsequently increases the longevity of the pre-existing structures. Study of crack kinematics is important to understand the damage process in cementitious composites. Advanced crack tip tracking techniques can be implemented using DIC method and subsequent crack kinematics can be studied for different material and geometric parameters.

2 Literature Review

The effect of loading rate and α value in PC was studied, the peak loads and ductile behavior reduced with the increasing α value. Accurate fracture energy was also determined by tail modeling methods validated with FE and DIC results [7]. The effects on fracture and AE parameters due to loading rate and α value was studied using DIC and AE technique in self compacting concrete [8]. Effect of change in α values on the post peak behavior of SFRC was done and it was observed that hardening behavior increased till α value of 0.33. There was considerable increment in the post peak ductility with the increment in volume fraction of steel fibers [9]. Fracture energy, flexural strength decreased with the increasing α value in Ultra-High Performance Concrete(UHPC) specimens [10]. The fracture behavior for different types of fiber reinforced concrete was assessed using AE and DIC methods [11]. AE and DIC methods were used to study the fracture behavior in Berea sandstone. Relationship between AE and fracture energy was determined [12]. The combined usage of AE and DIC method together is more useful since the damage progression and surface strains and displacements can be recorded simultaneously. The Crack Tip Tracking (CTT) method was used to calculate the crack length in fly ash concrete material [13]. The effect of loading rate on the crack velocities was studied by using crack initiation technique [14].

3 Experimental Program

In the present study, PC and SFRC ($V_f = 1.5\%$) Three-Point Bend (TPB) specimen (260 mm \times 80 mm \times 80 mm) with a span of 240 mm were tested in MTS machine by following EN: 14651 - 2005, RILEM TC 162-TDF, RILEM TC FMC-50 and JCI-S-001-2003 standards. Eight AE channel monitoring system and two AE sensors (57 kHz) were used to record the AE signal waveforms. AE sensors were differential and resonant type and were placed at 40 mm around the notch and 40 mm from the top fiber of the beam. DIC technique was used to record the 2D surface strains and displacements. The concrete mix details are given in Table 1. The testing

Table 1 Concrete mix details

Material	Cement (Kg/m ³)	Fine aggregate (Kg/m ³)	Coarse aggregate (Kg/m ³)	Water (liter/m ³)	Steel fibers (%) (by volume)	w/c ratio (by weight)
PC	440.96	865.796	806.76	220.48	0	0.5
SFRC	440.96	865.796	806.76	220.48	1.5	0.5

Table 2 Testing procedure details

Material	Loading rate (mm/s)	Standard	Testing control
PC	0.0004	RILEM TC 50-FMC	CMOD control
SFRC	0.0008 till 0.1 mm 0.0033 till 4.0 mm	EN: 14,561, RILEM TC 162-TDF	CMOD control

procedure details are shown in Table 2. The experimental setup for testing TPB specimens is shown in the Fig. 1.

4 Results and Discussion

Figures 2a and Fig. 2b shows the load versus midspan displacement and Fig. 3a and Fig. 3b shows load versus CMOD for both PC and SFRC specimen tested under Mode I fracture. It can be observed that there is significant softening response in SFRC as compared to PC. This is reflected on the trends observed in the fracture energy. Softening phase for PC beams with largest α value ends faster than specimen with smaller α value as shown in Fig. 2 and Fig. 3. The softening phase for SFRC with different values of α is observed to continue till the tested CMOD value.

The loading response for PC is relatively smooth. The drops in the flexural load carrying capacity were observed in case of SFRC as shown in Fig. 2 and Fig. 3. These drops in the load value can be attributed to the failure mechanisms such as debonding of coarse aggregate and concrete matrix alongwith coarse aggregate crushing in PC. In case of SFRC, the drops might occur due to fiber pullout or fiber breakage. Figure 4a and Fig.4b shows the variation of load and cumulative AE energy with respect to time for both PC and SFRC specimens tested under Mode I fracture. In Fig. 4a, the cumulative AE energy rose immediately after the peak load in PC specimens. The relatively smooth curve of cumulative AE energy with time was observed in case of PC beams. Abrupt changes in the slope of load versus time curve and sudden drops in the post-peak load carrying capacity were observed at multiple inflection points in SFRC specimens. These inflection points were successfully identified at the position where there is a spike in cumulative AE energy. These kind of inflection points were not observed in the mechanical response of PC specimens. Hence, the reduction in post-peak load carrying capacity could be attributed only to the fiber pullout mechanism in SFRC. The least number

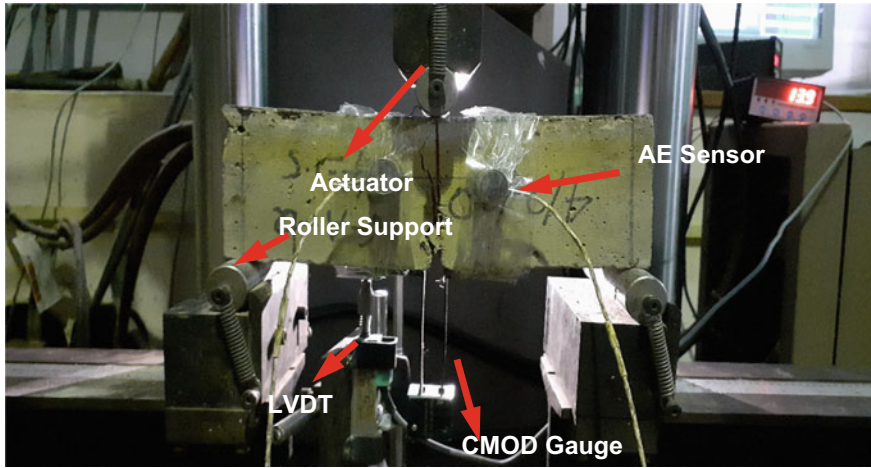
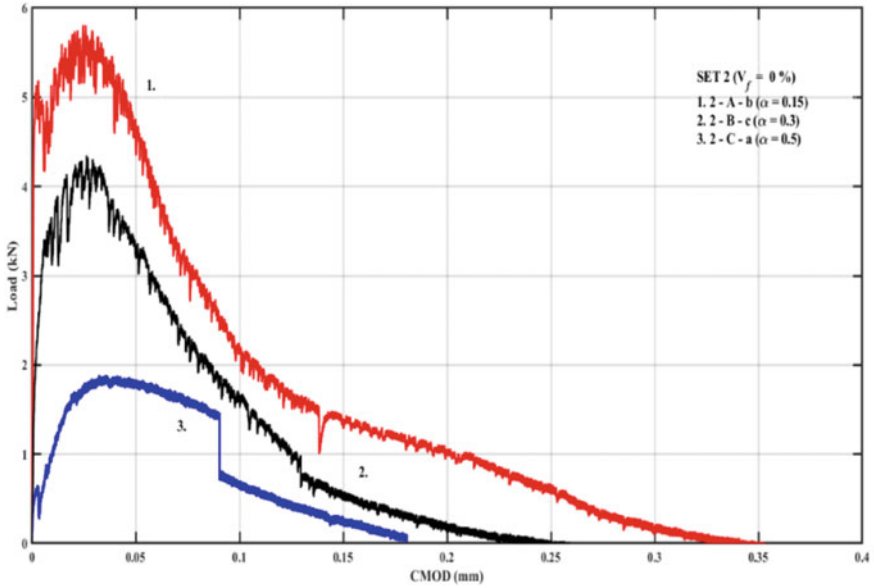


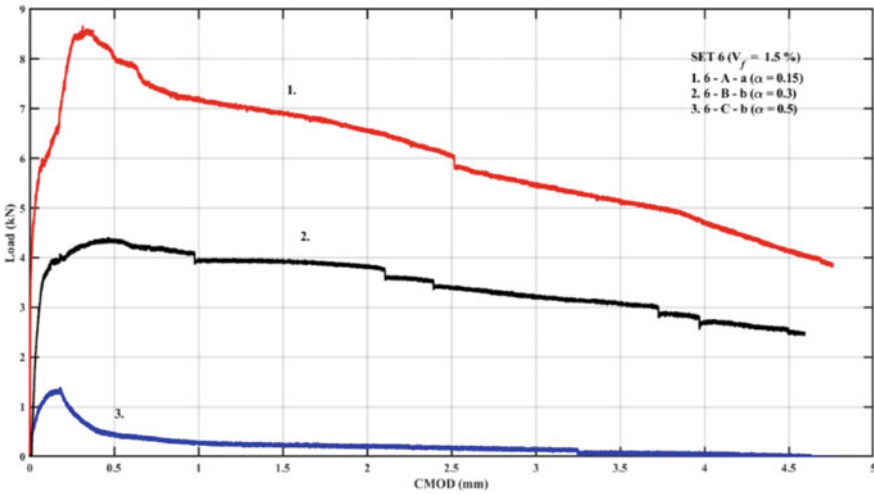
Fig. 1 Experimental setup in structures laboratory, Department of Civil Engineering, Indian Institute of Science, Bangalore, India

of inflection points were identified in specimen 6-C-a and in the corresponding load vs time curve there was a sudden drop in the post peak load carrying capacity. Specimen 6-C-a did not show a significant ductile behavior as compared to the specimens with higher α values. Hence the ductility was observed to reduce with increasing α value. In the specimen with α value of 0.3, a greater number of inflection points were observed which can be attributed to the occurrence of higher fiber pullout events ensuring that the fiber distribution was optimum in the ligament cross sectional area over the notch tip. The drop in post peak load carrying capacity was minimum for specimen with α value of 0.3 and the strain hardening behavior was observed out of all the three cases. Hence α value of 0.3 is the optimum value for a V_f of 1.5% to show the maximum ductile behavior for the given specimen geometry and material property.

In case of specimen 6-A-a, slope changes in the load versus time curve were also observed because of crack initiation, matrix cracking and fiber pullout events, which were identified with the positions of the cumulative AE energy spikes. To study the variation of strain fields at the inflection points, DIC technique was used. In Fig. 5, two major locations on the load versus time curve were identified, where the major changes were observed in the mechanical loading response of SFRC. Images extracted at these locations were given as an input to carry out the DIC analysis. The variations in contours of strains in x-direction (ϵ_{xx}) were shown at the location p and q in Fig. 6 At p, the entire localized region of suspected crack initiation and propagation is showing the highest ϵ_{xx} values indicated by yellow color and no stress concentration is visible indicating that the process of crack initiation and microcrack accumulation has just started. Hence there is a sudden change in the slope of loading response. At location q, a discontinuity can be observed to develop in ϵ_{xx} contour. At this instant, there is a generation of major macrocrack attributed to occurrence of fiber pullout event at the stage of sudden load drop. Point of crack initiation is

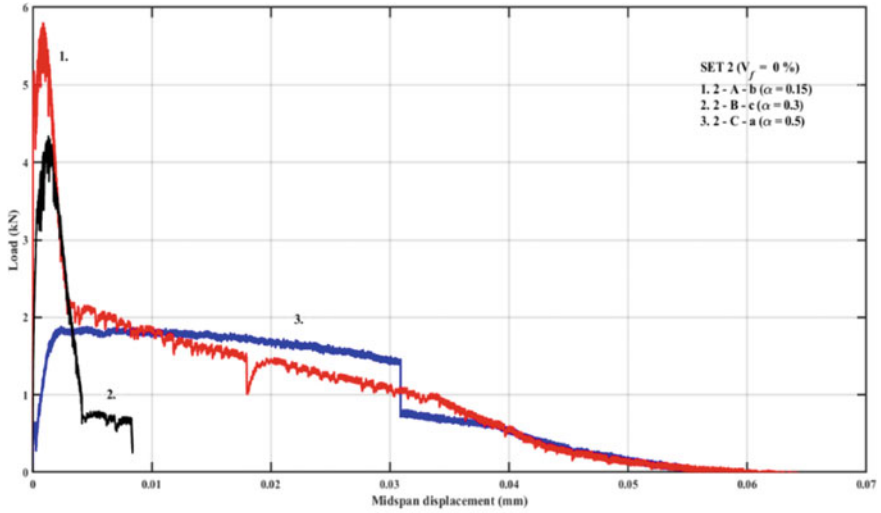


a. Load versus CMOD for PC

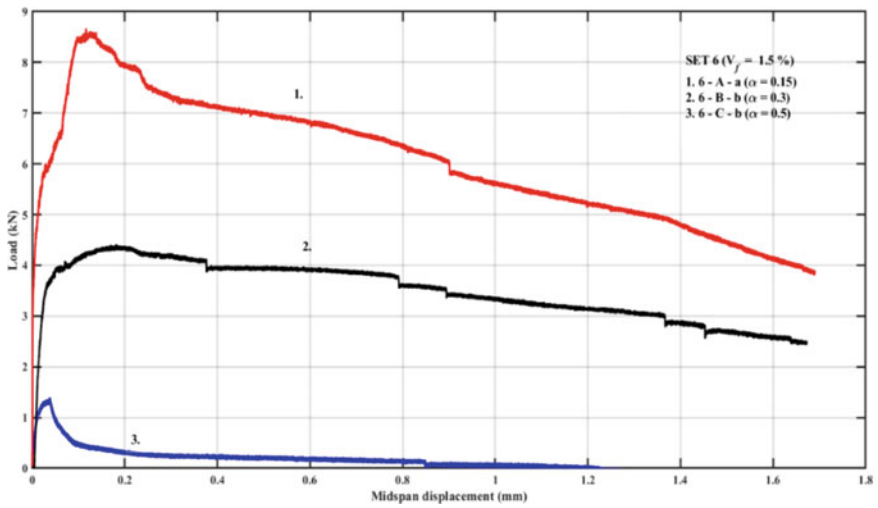


b. Load versus CMOD for SFRC

Fig. 2 a Load versus CMOD for PC, b Load versus CMOD for SFRC

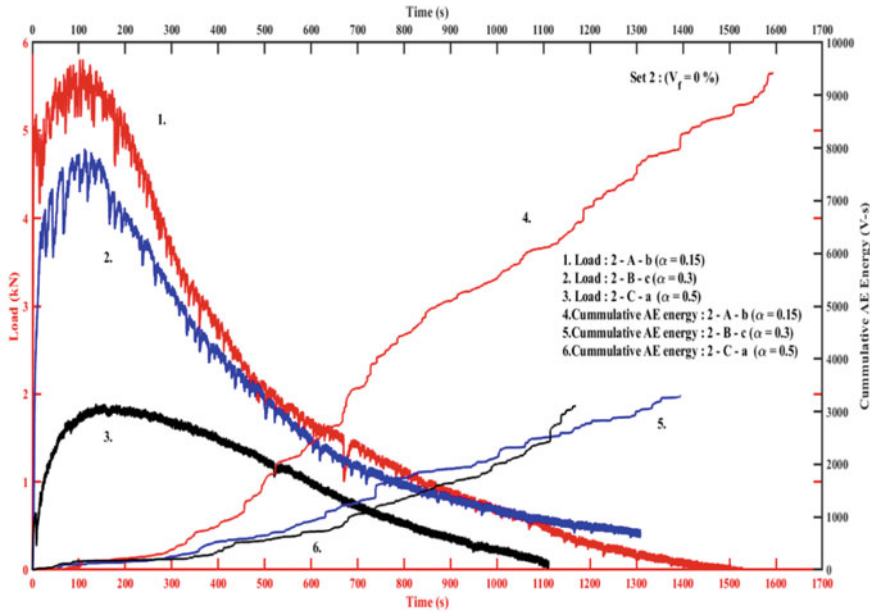


a. Load versus midspan displacement for PC

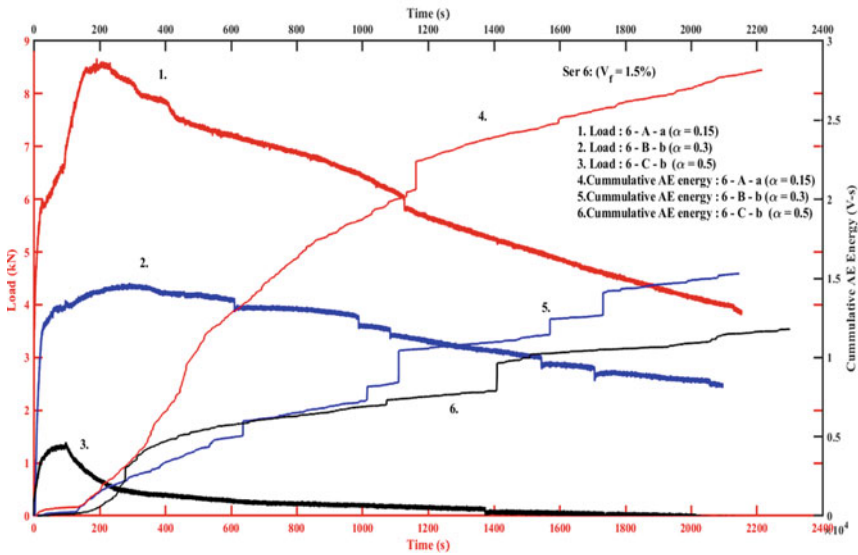


b. Load versus CMOD for SFRC

Fig. 3 a Load versus midspan displacement for PC, b Load versus CMOD for SFRC



a. Cumulative AE energy and loading response for PC



b. Cumulative AE energy and loading response for SFRC

Fig. 4 a. Cumulative AE energy and loading response for PC, b Cumulative AE energy and loading response for SFRC

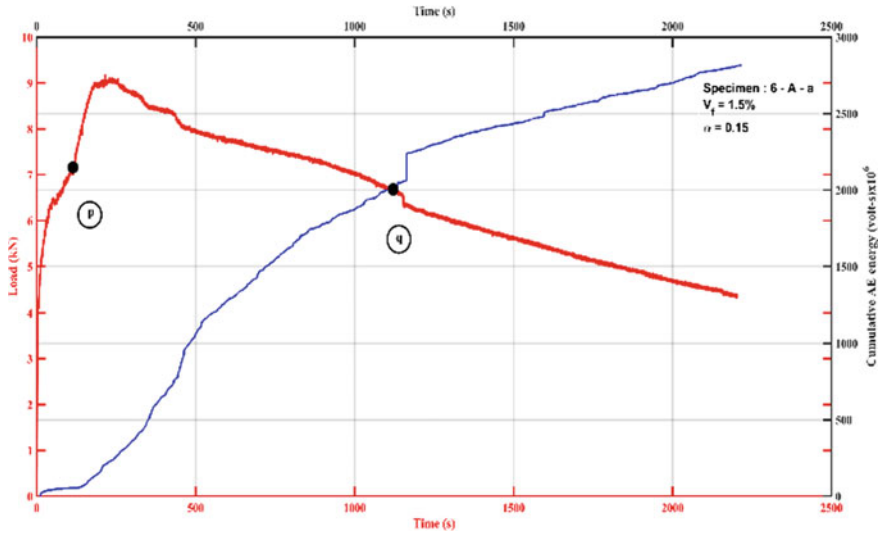
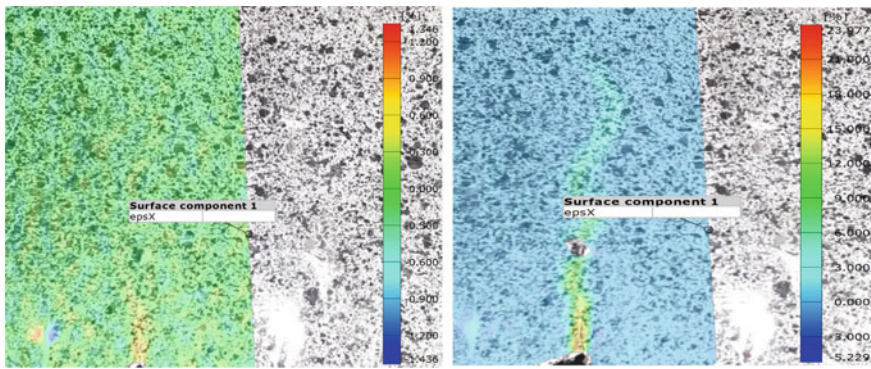


Fig. 5 Inflection points on load and cumulative AE energy versus time plot for specimen 6-A-a



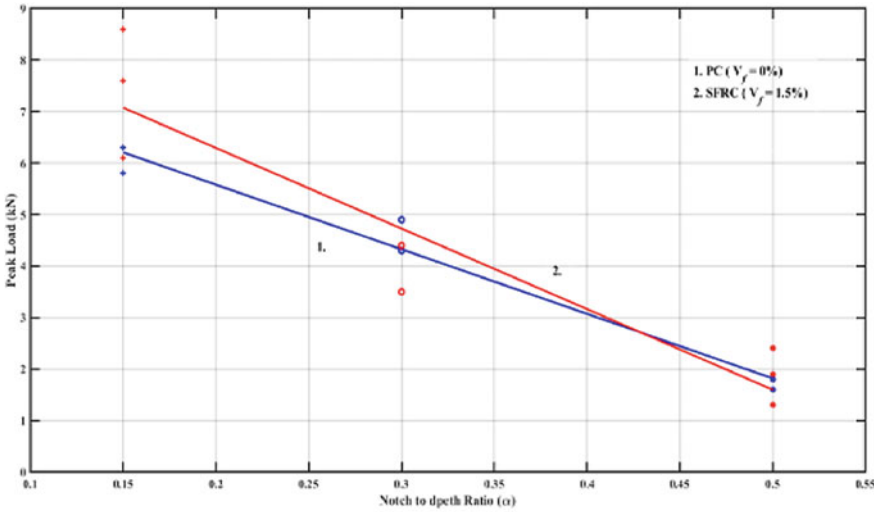
a. ϵ_{xx} contour at location p

b. ϵ_{xx} contour at location q

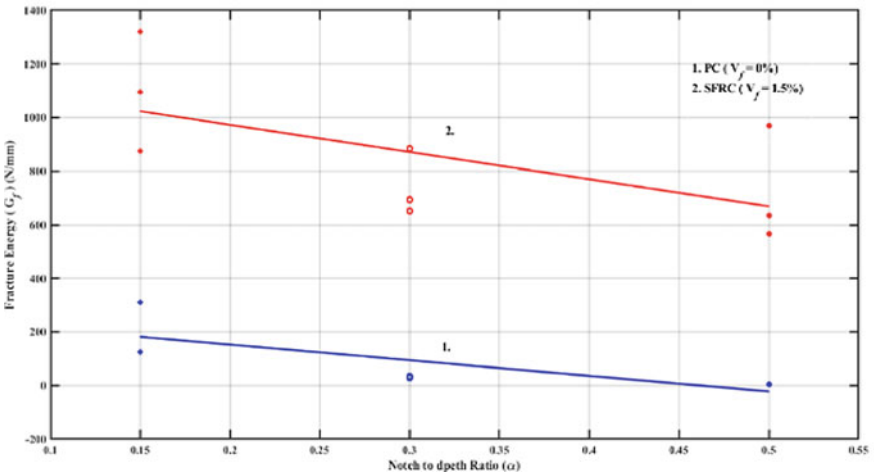
Fig. 6 a ϵ_{xx} contour at location p, b ϵ_{xx} contour at location q

observed to occur around the same position for all PC specimens. In case of SFRC, time for occurrence of crack initiation increases with the α value as seen in Fig. 4.

The variation of peak loads with the α values can be seen in the Fig. 7a. The peak loads are observed to reduce with the increasing α value. No significant changes were observed with peak loads in PC and SFRC. Fracture energy (G_f) for PC and SFRC was calculated using RILEM TC FMC-50 and JCI-S-001-2003 standards respectively. Figure 7b shows the variation of fracture energy with α values for both



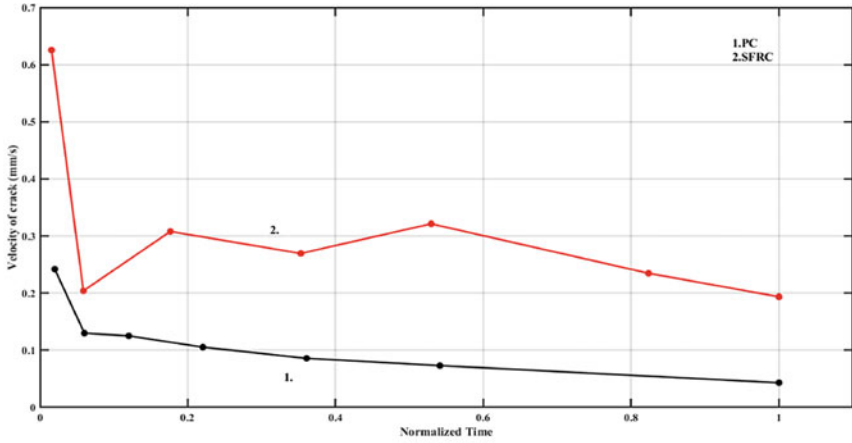
a. Peak load variation with notch to depth ratio



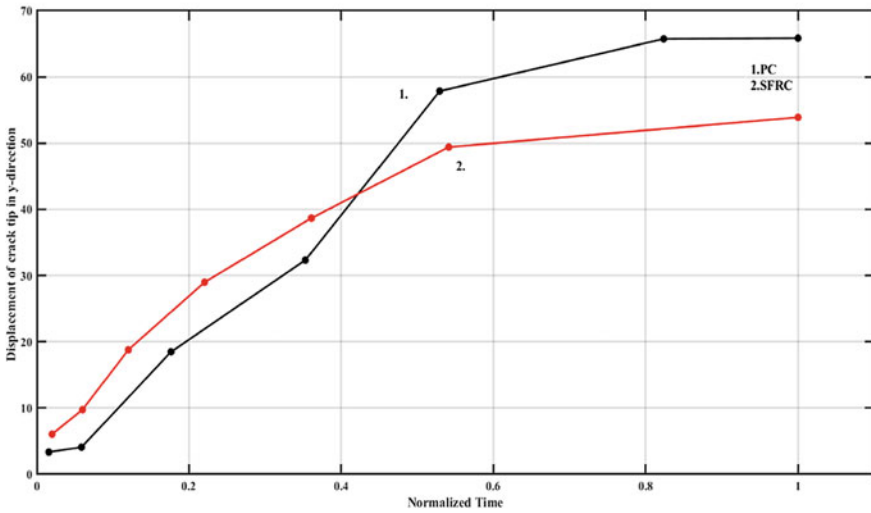
b. Fracture Energy variation with notch to depth ratio

Fig. 7 a Peak load variation with notch to depth ratio, b Fracture energy variation with notch to depth ratio

PC and SFRC. There was a significant increase in the fracture energy in SFRC as compared to that of PC thus making the SFRC material more ductile. The fracture energy was observed to reduce with increasing α values. Since the energy absorption capacity increased, the ductility also increased with increase in fiber volume fraction.



a. Crack velocity variation with normalized time



b. Displacement of crack tip in y-direction versus normalized time

Fig. 8 a Crack velocity variation with normalized time, b Displacement of crack tip in y-direction versus normalized time

The experimental observations for each specimen are shown in Table 3. AE Energy, hits and fracture energy are observed to decrease with increasing α value but increased with increase in V_f .

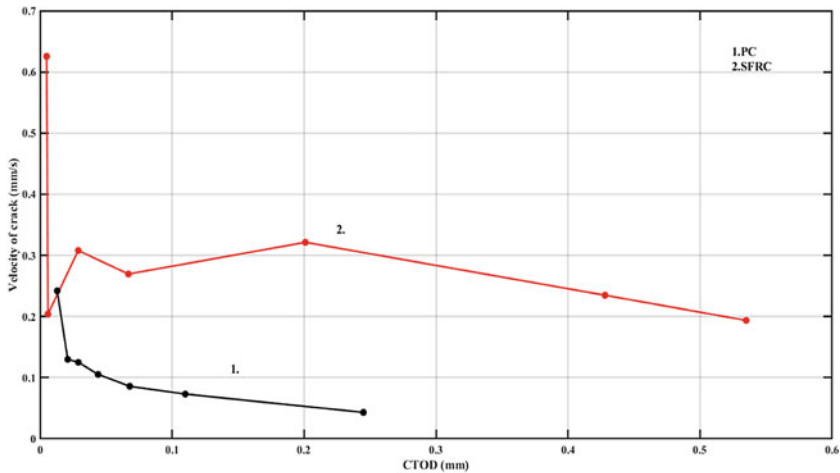
Table 3 Specimen details with mechanical response and AE parameters

Specimen name	Notch depth ratio (α)	Peak load (kN)	Fracture energy (N/mm)	Total AE parameters				
				Hits	Counts	Energy (v-s)	Absolute energy (aj)	Signal strength (pv-s)
2_A_a	0.15	**	24.79	2774	80,685	5694	712,084.9	43,151,916.1
2_A_b		5.8	12.35	5667	161,778	12,110	1,760,430.4	91,262,601.2
2_A_c		6.3	31.07	**	**	**	**	**
2_B_a	0.3	4.9	29.48	1640	44,692	2866	280,224.5	22,323,063.6
2_B_c		4.3	33.81	2004	52,840	3747	563,959.6	28,811,008.3
2_B_b		**	**	**	**	**	**	**
2_C_a	0.5	1.8	2.05	1818	46,059	3103	466,816.4	24,493,509.5
2_C_b		1.8	**	973	23,568	1310	82,492.2	10,748,169.6
2_C_c		1.6	5.61	**	**	**	**	**
6_A_a	0.15	8.6	1322.14	18,355	414,433	28,164	14,897,899.2	225,222,111.4
6_A_b		6.1	873.99	17,158	412,856	32,994	26,326,060.3	252,443,877.4
6_A_c		7.6	1095.05	**	**	**	**	**
6_B_a	0.3	3.5	465.01	4829	117,488	9216	10,073,035.1	70,448,971.5
6_B_b		4.4	884.04	7067	153,594	15,315	27,878,526.3	114,590,548.0
6_B_c		4.4	693.31	**	**	**	**	**
6_C_a	0.5	1.9	564.92	9044	226,429	28,803	64,918,018.1	204,888,159.5
6_C_b		1.3	970.63	5835	139,966	11,795	12,519,216.2	89,730,425.3
6_C_c		2.4	634.92	**	**	**	**	**

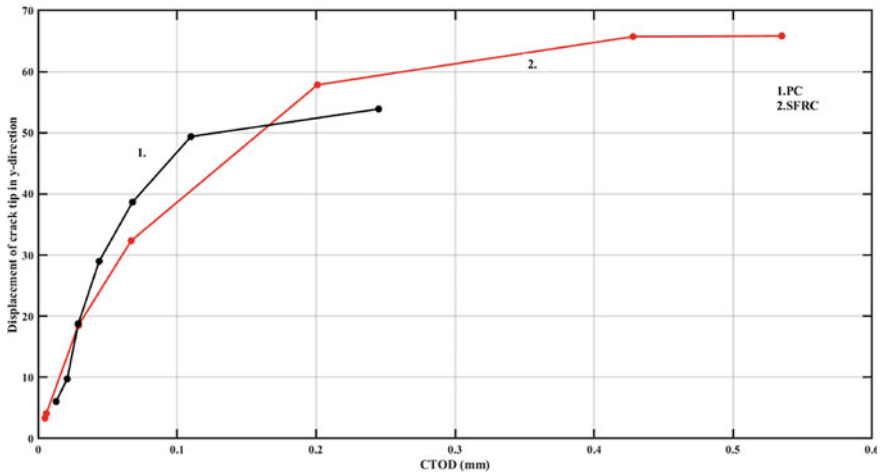
** indicates that the values were not recorded due to instrumental error

The study of dynamics of crack is crack kinematics. DIC is very useful tool to study the crack kinematics. It helps in locating the crack tip and study the progression of crack in the material. The GOM correlate software was used for doing the DIC analysis. The facet size was kept 19 mm and the point distance was set as 14 mm to create the accurate surface component. The CTT (Crack Tip Tracking) method was used to locate the crack tip [13]. The vertical displacement of crack tip in the y-direction at a given time is useful to calculate the crack velocity of a crack tip at that instant. A virtual extensometer was placed at the notch tip to calculate the CTOD values. Figure 8a and Fig. 8b shows the variation of crack velocity and vertical displacement of crack tip with respect to normalized time for PC and SFRC. The initial crack velocity and the immediate drop in the velocity for SFRC was much higher than PC from the point of crack initiation. The velocity decreased continuously for PC indicating that no stress transfer is taking place across the crack due to

the absence of stress transfer mechanism. In SFRC, the velocity is almost constant indicating that the fiber bridging is taking place and stress transfer is occurring across the crack. The crack is arrested due to the fiber bridging mechanism. In Fig. 8b, Crack is travelling faster in PC and reaches the top fiber earlier than SFRC indicating that this is brittle failure and crack arresting is not taking place. In SFRC, the crack is travelling uniformly with a decreasing speed and has still not reached the top fiber indicating the ductile behavior due to fiber bridging. Figure 9a shows the variation of



a. Crack velocity variation with CTOD



b. Displacement of crack tip in y-direction versus CTOD

Fig. 9 a Crack velocity variation with CTOD b Displacement of crack tip in y-direction versus CTOD

crack velocity with CTOD and it was observed that crack velocity is reducing with CTOD for both PC and SFRC. Crack velocity reduced from the identified point of crack initiation, indicating that the crack is still present in pre peak region. In SFRC, the velocity increased after the sudden drop and almost remained constant indicating the post – peak action of fiber bridging. Figure 9b shows the vertical displacement of crack tip with CTOD. It was observed that slope of displacement of crack tip with CTOD was more indicating that the crack was travelling faster in PC and reaching the top fiber earlier in PC than SFRC. The crack was still slowly moving with CTOD in SFRC. Figure 10 shows CTT method for tracking crack tip using ϵ_{xx} contours.

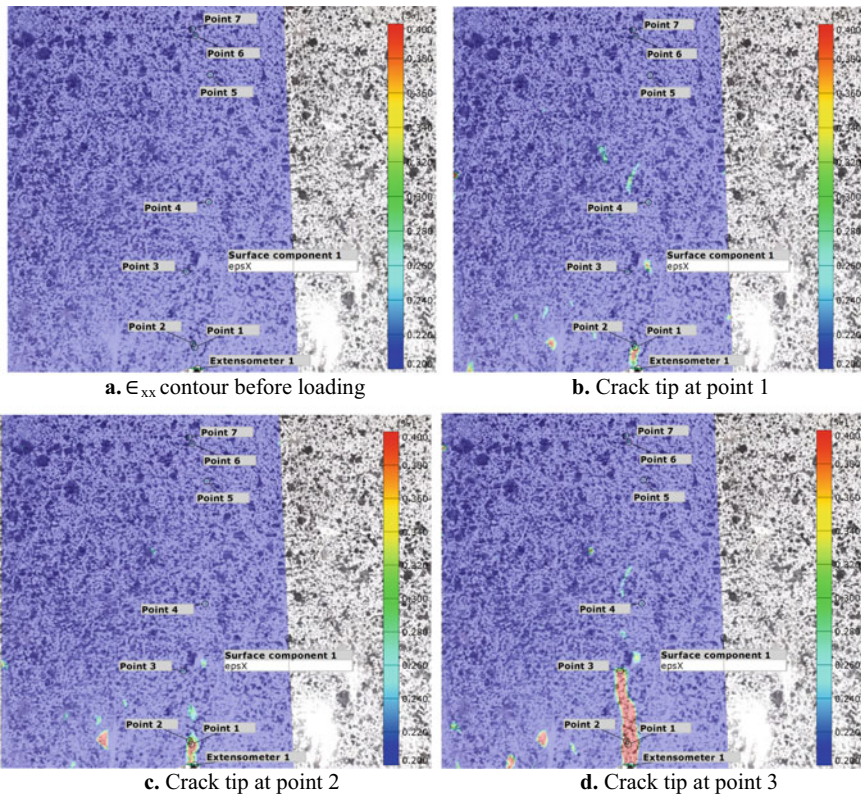


Fig. 10 a ϵ_{xx} contour before loading b Crack tip at point 1, c Crack tip at point 2, d Crack tip at point 3, e Crack tip at point 4, f Crack tip at point 5, g Crack tip at point 6, h Crack tip at point 7

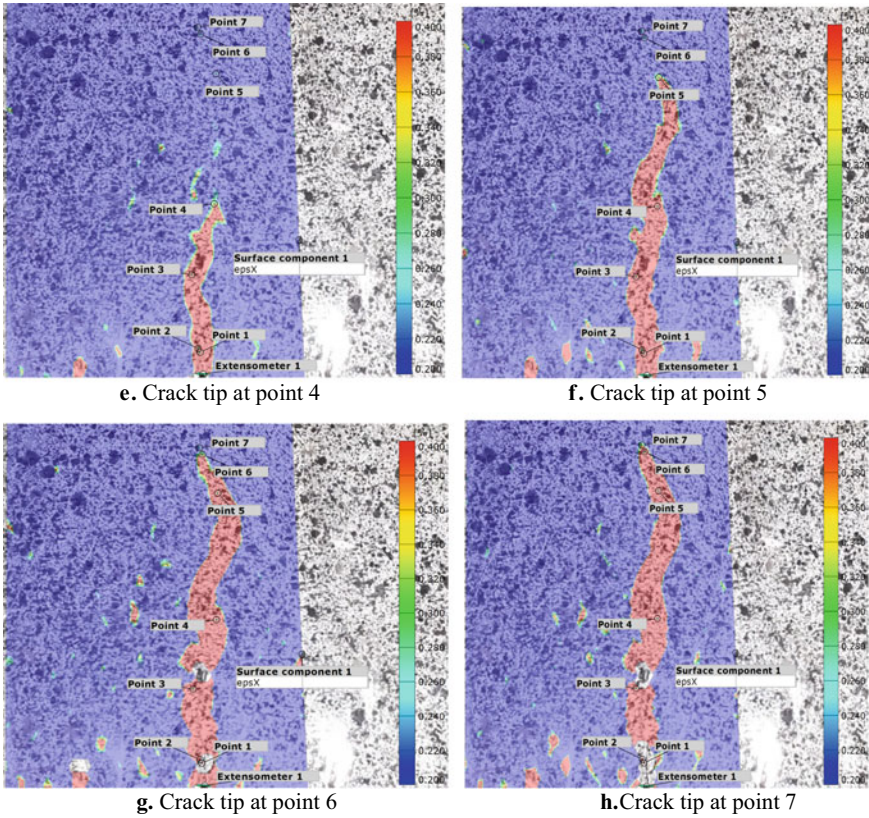


Fig. 10 (continued)

5 Conclusion

The DIC method combined with AE technique was used to identify points at which the sudden load drops occurred in the loading response with the help of corresponding cumulative AE energy spikes at these inflection points. As the α value increases, the peak load, AE energy, fracture energy and ductility of the SFRC reduces. The design of SFRC for the maximum ductility is not only dependent on optimum percentage of V_f but also is a specimen geometry and notch to depth ratio dependent property. Hence, these three parameters are needed to be simultaneously optimized to obtain maximum ductility for the given geometry of a structure. The crack kinematics studied using DIC helps in better visualization of contribution of steel fibers in fiber bridging mechanism of SFRC.

References

1. Buratti N, Mazzotti C, Savoia M (2011) Post-cracking behaviour of steel and macro-synthetic fibre-reinforced concretes. *Const Build Mat* 25:2713–2722
2. EN-14651: 2005, Test method for metallic fibered concrete - measuring the flexural tensile strength (limit of proportionality (LOP), residual)
3. Aggelis DG, Barkoula NM, Paipetis AS, Matikas TE (2012) Influence of fiber chemical coating on the acoustic emission behavior of steel fiber reinforced concrete. *Cement Concr Compos* 34(1):62–67
4. Aggelis DG, Soulioti DV, Sapouridis N, Barkoula NM, Paipetis AS, Matikas TE (2011) Acoustic emission characterization of the fracture process in fiber reinforced concrete. *Constr Build Mater* 25(11):4126–4131
5. Grosse CU, Ohtsu M (2008) *Acoustic emission testing*. Springer, Heidelberg. <https://doi.org/10.1007/978-3-540-69972-9>
6. Karihaloo BL (1995) *Fracture mechanics and structural concrete*, Longman Scientific & Technical
7. Zhu X, Chen X, Lu J, Fan X (2019) Analysis of notch depth and loading rate effects on crack growth in concrete by FE and DIC. *Comput Concr* 24(6):527–539
8. Chen X, Shi D, Zhang J, Cheng X (2020) Experimental study on loading rate and notch-to-depth ratio effects on flexural performance of self compacting concrete with acoustic emission and digital image correlation technologies. *J Strain Anal Eng Des* 1(13)
9. Aguilar JV, Alvarado CAJ, Rangel JMM, Torres BTT (2021) Effect of the notch-to-depth ratio on the post-cracking behavior of steel-fiber-reinforced concrete. *Materials* 14(2):445
10. Meng W, Yiming Y, Mobasher B, Khayat KH (2017) Effects of loading rate and notch-to-depth ratio of notched beams on flexural performance of ultra-high-performance concrete. *Cement Concr Compos* 83:349–359
11. Bhosale A, Rasheed MA, Prakash SS, Raju G (2019) A study on the efficiency of steel vs. synthetic vs. hybrid fibers on fracture behavior of concrete in flexure using acoustic emission. *Constr Build Mater* 199:256–268
12. Lin Q, Wan B, Wang Y, Lu Y, Labuz JF (2019) Unifying acoustic emission and digital imaging observations of quasi-brittle fracture. *Theor Appl Fract Mech* 103:102301
13. Golewski GL (2021) Validation of the favorable quantity of fly ash in concrete and analysis of crack propagation and its length – using the crack tip tracking (CTT) method – in the fracture toughness examinations under Mode II, through digital image correlation. *Constr Build Mater* 296:122362
14. Zhang X, Ruiz G, Elazim AMA (2015) Loading rate effect on crack velocities in steel fiber-reinforced concrete. *Int J Impact Eng* 76:60–66

Delamination Buckling of Composite Conical Shells



A. Nagendranath, Sanjay A. Khalane, R. K. Gupta, and C. Lakshmana Rao

Abstract Conical shells are most useful in primary aerospace structures owing to their aerodynamic shape and form the foremost portion of flight vehicles experiencing severest drag forces. Delamination raised during the production process or during usage would adversely affect the structural integrity of the shell structure. In the present paper, finite element modeling of delamination embedded in composite conical shells subjected to axial compression is carried out in line with the procedure available in published literature. Layered shell element has been used and the effect of delamination length & depth on the structural integrity of conical shell is studied. Study has been carried out for isotropic and orthotropic materials. Verification of the methodology is carried out by comparing with published literature on composite cylindrical shells. Global as well as local buckling mode shapes have been observed during the simulation. The linear bifurcation buckling load of first mode is considered as the critical load under axial compression. The critical load is normalized with respect to critical load of intact conical shell. The normalized critical load is illustrated graphically against the normalized length of delamination. Consistent pattern has been observed for isotropic and cross ply configurations. Further analysis is required for angle ply configuration.

Keywords Composite shells · Delamination · Buckling · Conical shells

1 Introduction

Composite material systems are prime choice of materials in design of aerospace structures owing to their high specific strength and stiffness. Shell structures form the main geometry of configuration design. Among the shell structures, conical shells are most useful in primary aerospace structures owing to their superior aerodynamic

A. Nagendranath (✉) · S. A. Khalane · R. K. Gupta
Advanced Systems Laboratory, DRDO, Hyderabad 500 058, India

C. Lakshmana Rao
Department of Applied Mechanics, IIT Madras, Chennai 600 036, India

shape and form the foremost portion of flight vehicles that experience severest drag forces.

Similar to majority of composite structures, defects in the form of delamination/de bond arise during realization stage or when in use. These defects would reduce the load bearing capability as there is no reinforcement in the thickness direction. The residual strength and stiffness depend on the size and location of the defect. Structural testing of composite conical shell subjected to axial compression is being planned as part of evolving acceptance criteria. Computational model is prepared in line with that of planned testing activity and the simulation is carried out to estimate the critical defect size and its location. These details will be used in realizing the prototype with embedded delamination.

2 Literature Survey

The presence of delamination will reduce buckling strength of shell structures [1]. Numerous analyses have been carried out by researchers on delaminated structures considering buckling behavior. Majority of the published research work deal with beams and flat plates. Limited information is available on shells and panels. Comprehensive analytical study on delamination buckling of cylindrical shells has been performed by Simitse et al. [2] and this analytical study does not incorporate contact conditions. Hence buckling modes may have penetration. Numerical analyses on delamination buckling of cylindrical shells under axial compression, external pressure, bending and combined loading conditions were carried out by Tafreshi [3, 4] involving contact feature. Increase in buckling load is the observation when contact feature is incorporated in the simulation. The majority of the reported work is on cylindrical shells with ply sequence as that of cross ply. Meager information is available on conical shells.

Large conical shells are realized by means of filament winding and at any cross section along the length the ply sequence is that of angle ply. Hence the study of conical shells with angle ply sequence would be of direct relevance. The learning is supplemented by performing the simulation for isotropic material (Aluminum) and cross ply sequence. In general, the cross ply sequence for axially loaded structure will of $(0^\circ, 90^\circ, 0^\circ)$ s where 0° is the axial direction and designated as crossply0 in this study. With an intuition that the higher number of 90° plies will offer higher buckling load as 90° ply being transverse to 0° thereby reducing out of plane deformation, cross ply sequence of $(90^\circ, 0^\circ, 90^\circ)$ s which is designated as crossply90 is also studied.

3 Finite Element Simulation Methodology

Compressive load causes failure of the shell structure not just by strength criteria but also by instability caused by buckling. Failure by buckling can be premature to failure by strength if the stiffness of structure is inadequate. Presence of delamination further compounds and significantly brings down the buckling factor. Sub-laminate behavior at the place of delamination causes it. Hence buckling factor is chosen as the metric for comparison.

Geometry of the delaminated composite (Carbon/Epoxy) conical shell (8.5° semi cone angle) is shown in Fig. 1. Studies have been carried out for axial compression with delamination present at $1/8$ th, $1/4$ th and mid thickness of the shell, denoted as delamination thickness: h of 0.125, 0.25 and 0.5 respectively (non-dimensional parameter; location of delamination/total thickness). The delamination is assumed to be located symmetrically from both the edges of the shell and progress equally to both the sides. The presence of delamination is considered from inner surface of the cone. The results would be either equal or higher in the case of outer surface, as the sub laminates of $h = 0.125$ & 0.25 would have higher moment of inertia.

For angle ply, the ply sequence considered is $\pm\theta^\circ$. The angle of winding varies along the length of the cone with $\pm 35^\circ$ at the center of the cone (geodesic winding) and is taken into consideration.

The conical shell is idealized with shell formulation using SHELL281, 8 node element [5]. The intact zone in the finite element model is meshed with single layer shell element with a size of 5 mm. The delaminated zone is meshed with double layer of shell elements and contact elements connecting the two layers for load transfer as well as penetration prevention. The contact elements behave as compression only elements which offer stiffness when compressive load exists across them and do not offer stiffness when tensile load exists across them; hence a non-linearity based on contact status arises. Transition zone is meshed with double layer of shell elements and multipoint constraint connecting the two layers. Section offset has been used to maintain the uniformity of mid surface along the length of the cone as shown

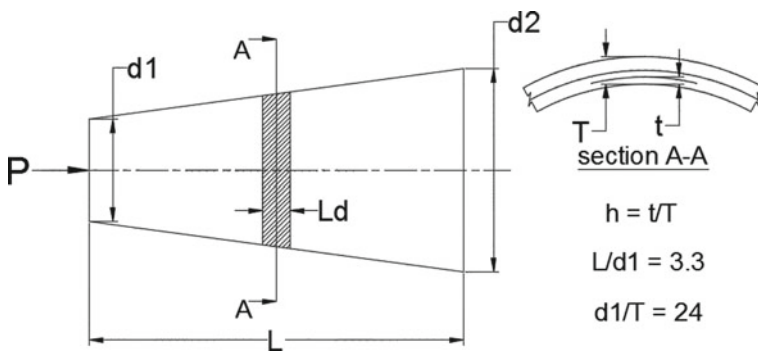


Fig. 1 Composite conical shell with delamination on the entire circumference

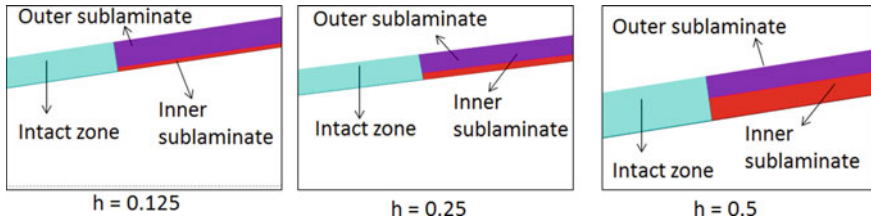
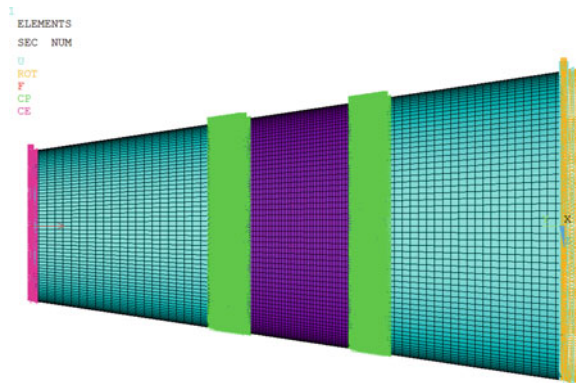


Fig. 2 Section offset for uniformity of mid surface for various depths of delamination

Fig. 3 Loads and boundary conditions on composite conical shell



in Fig. 2. The delaminated zone and the transition zone have been meshed with an element size of 2 mm.

Orthotropic material properties with stiffness ratio, EL/ET , of 20 have been considered.

Axial load is applied on the lower diameter end of the cone and other degrees of freedom are restrained. The other end of the cone is restrained completely simulating clamped condition. The boundary conditions are illustrated in Fig. 3.

4 Verification

A verification of the present methodology has been carried out by performing analysis of cylindrical shell made of isotropic material (Aluminum) with clamped ends under axial compression, identical to the model described by Tafreshi et al. [3]. Circumferential delamination in symmetry with both the shell ends and aspect ratios $L/R = 5$, $R/t = 30$ & $h = 0.5$ is considered for comparison. Critical loads are normalized with respect to critical load of ideal cylinder without delamination. Typical mode shape and comparison of normalized critical loads are as shown in Figs. 4 and 5 respectively. For the delamination length of 0.05, a maximum error of 3% is observed which perhaps is due to dissimilar mesh and time step sizes which were not reported in the

Fig. 4 Typical mode shape of isotropic cylinder with delamination at a depth of 0.5

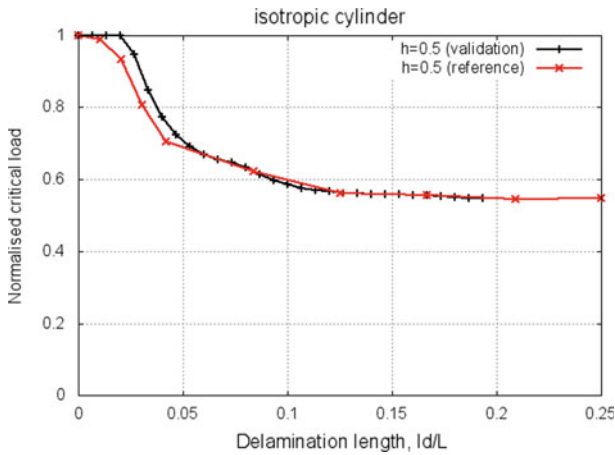
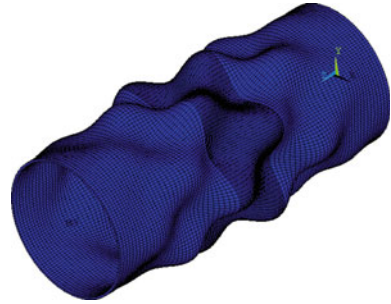


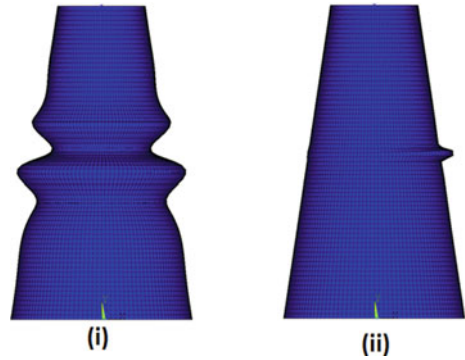
Fig. 5 Validation of isotropic cylinder with delamination at a depth of 0.5 with reference [3]

referred publication. There is good agreement with that of reference data beyond delamination length of 0.05 validating the methodology and to extend it for conical geometry.

5 Results

The linear bifurcation buckling load is considered as the critical load under axial compression. The first mode is chosen irrespective of the mode shape as any excessive deformation of the cone would alter the aerodynamic shape of the flight vehicle and is not desirable. Global & symmetric buckling mode shapes as well as local & asymmetric buckling mode shapes typically shown Fig. 6 has been observed during the simulation. Global modes are more noticeable for delamination depths of 0.25 and 0.5. The local modes are observed for delamination depth of 0.125.

Fig. 6 Typical global and local buckling mode shapes in conical shell



The critical load is normalized with respect to critical load of intact conical shell. The normalized critical load is illustrated graphically against the normalized length of delamination in Figs. 7, 8, 9 and 10 for isotropic, angle ply, crossply0 and crossply90 respectively for depths of delamination 0.125, 0.25 and 0.5.

For isotropic case (Fig. 7), similar to the published literature on cylindrical shell, as the delamination depth reduces, critical buckling load decreases. The reduction is severe when the delamination length is below 0.05 for depth of 0.125 and below 0.1 for depths of 0.25 & 0.5. For delamination lengths above 0.1, the buckling loads are almost independent of delamination length and the residual factors are 0.6, 0.3 and 0.2 for delamination depths of 0.5, 0.25 and 0.125 respectively.

For angle ply case (Fig. 8), consistent pattern is not obtained and needs further study. The curves of 0.25 are higher than that of 0.5. Similar results were reported in the referred literature for cross ply laminates on cylindrical shell. The reduction is severe when the delamination length is below 0.01 for depth of 0.125 and below

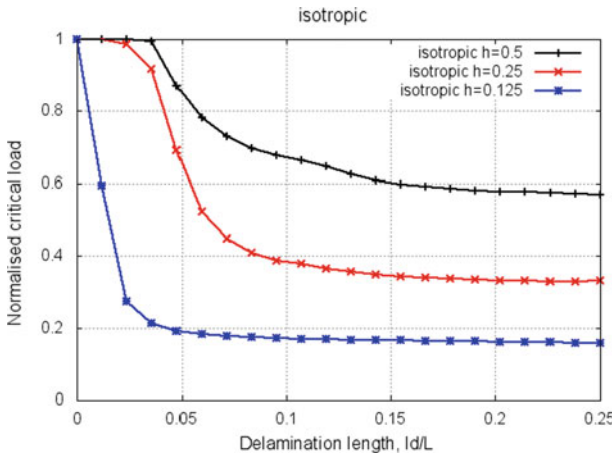


Fig. 7 Effect of defect length on critical buckling load of isotropic conical shell

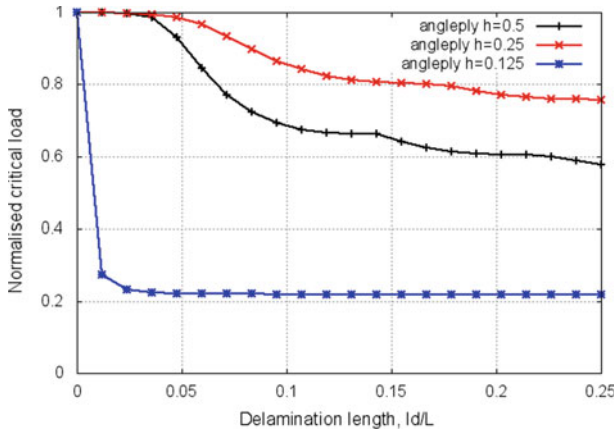


Fig. 8 Effect of defect length on critical buckling load of composite (angle ply) shell

0.1 for depths of 0.25 & 0.5. For delamination lengths above 0.1, the buckling loads are almost independent of delamination length and the residual factors are 0.6, 0.8 and 0.2 for delamination depths of 0.5, 0.25 and 0.125 respectively.

For cross ply cases (Figs. 9 and 10), consistent pattern is observed. Reduction in buckling load is more as the depth of delamination is reducing. The reduction is severe when the delamination length is below 0.05 for depths of 0.125 & 0.25 and below 0.1 for depth of 0.5. For delamination lengths above 0.1 and only for depths of 0.125 & 0.25, the buckling loads are almost independent of delamination length and the residual factors are 0.4, and 0.1 for delamination depths of 0.25 and 0.125 respectively. For depth of 0.5, such independence is not achieved in the span of study.

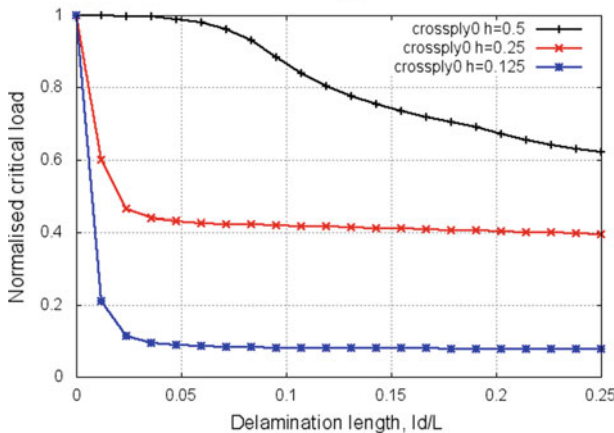


Fig. 9 Effect of defect length on critical buckling load of composite (crossply0) shell

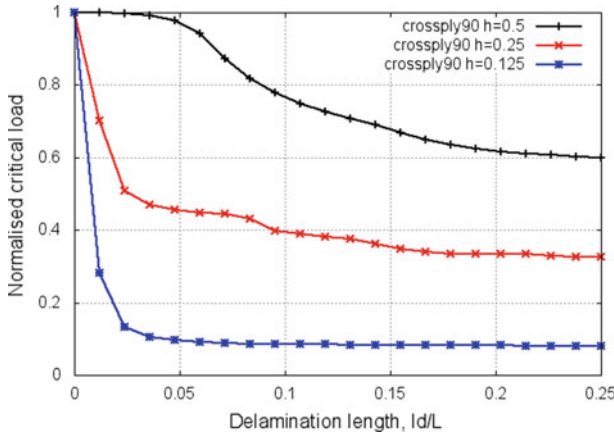


Fig. 10 Effect of defect length on critical buckling load of composite (crossply90) shell

The same data has been presented as function of delamination depth, comparing angle ply, crossply0 and crossply90 in Figs. 11, 12 and 13. For delamination depth of 0.5 (Fig. 11), crossply0 exhibits higher buckling load. For delamination depths of 0.25 & 0.125 (Figs. 12 and 13), angle ply exhibits higher buckling load. In these figures, crossply90 has higher buckling load than that of crossply0 until delamination length of 0.1.

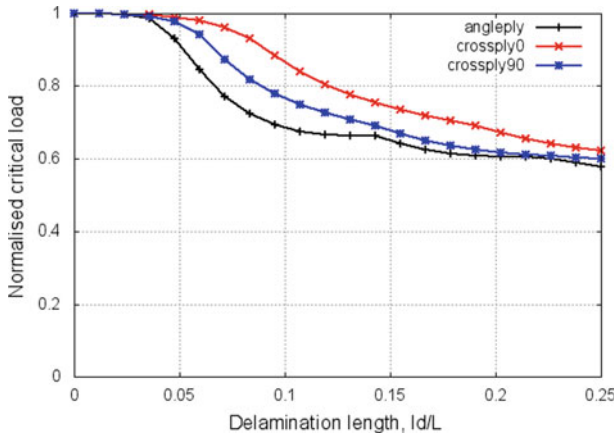


Fig. 11 Effect of defect length on critical buckling load for delamination at depth of 0.5

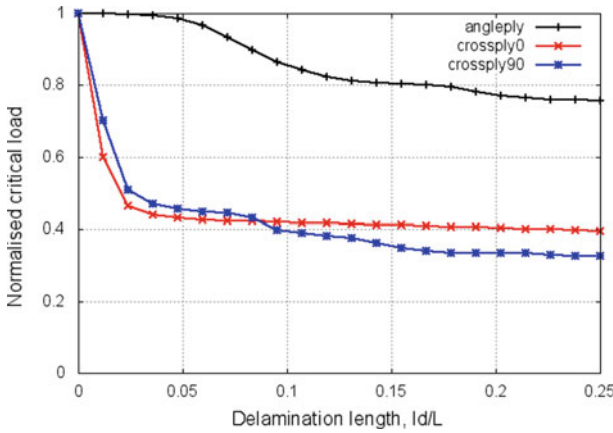


Fig. 12 Effect of defect length on critical buckling load for delamination at depth of 0.25

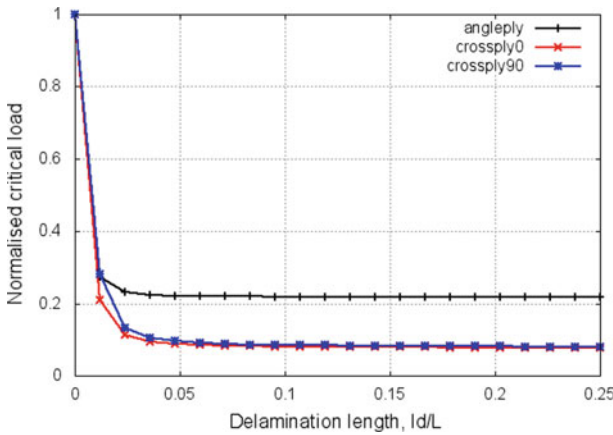


Fig. 13 Effect of defect length on critical buckling load for delamination at depth of 0.125

6 Conclusion

Methodology of estimating residual buckling load of conical shells with embedded delamination subjected to axial compression is established. A verification problem using this methodology has been carried out for cylindrical shell and compared with the published literature. Good comparison has been obtained. Further the study has been carried out with angle ply and two variants of cross ply. Consistent pattern of reduction in buckling load with reduction delamination depth (i.e. as the delamination moves from middle towards surface) has been observed for cross ply variants. Further examination is required in the case of angle ply configuration.

The bifurcation buckling results represent upper bounds of the estimates in view of the ideal linear elastic structure and stable crack considered in the present study. This preliminary study is adequate for planning a prototype testing. The finite element model will be supplemented with geometric non-linearity. A prototype of conical shell will be manufactured with embedded delamination based on the present results and validation of the numerical model will be carried out by testing with axial compression load.

References

1. Sridharan S (eds) Washington University in St. Louis, USA, Delamination behavior of composites (2008)
2. Sallam S, Simitses GJ (1991) Delamination buckling of cylindrical shells under axial compression. *Thin Walled Struct* 11:25–41
3. Tafreshi A (2004) Efficient modelling of delamination buckling in composite cylindrical shells under axial compression. *Compos Struct* 54:511–520
4. Tafreshi A (2004) Delamination buckling and post buckling in composite cylindrical shells under external pressure. *Thin Walled Struct* 42(10):1379–1404
5. Ansys documentation, Version 19.3

Comparative Study of 2D Heat Transfer Models for a Wankel Expander



Gautam Subburaj, Vipin V. Gopal, and Satyanarayanan Seshadri

Abstract Wankel expander are among the emerging technologies for use in cogeneration in process industries, ORCs, and other energy storage systems. Heat transfer and thermodynamic analysis is key to understand the expander and improve its performance. Previous investigations on heat loss models for Wankel expander were based on empirical models from canonical experiments such as flat-plate geometry. In this work, we have built a numerical model with the actual geometry to predict the temperature distribution along the periphery of the expander. Python was used to code and predict the temperature distribution of the expander which was compared with COMSOL solutions with close agreement (<1% variation). Hence, our numerical approach can be extrapolated to sale the Wankel prototype and also create a physics based digital twin.

Keywords Wankel expander · Heat loss · FDM · COMSOL · Comparative study

Nomenclature

Symbols	Description	Units
k	Thermal conductivity	W/m. K
α	Shaft angle	radians
β	Rotor angle	radians
C	Specific heat capacity	J/kg. K
T	Temperature	K

(continued)

G. Subburaj · V. V. Gopal · S. Seshadri (✉)
Energy & Emissions Research Group (EnERG), Department of Applied Mechanics, Indian Institute of Technology Madras, Chennai 600036, India
e-mail: satya@iitm.ac.in

G. Subburaj
e-mail: am19d204@smail.iitm.ac.in

V. V. Gopal
e-mail: am16d300@smail.iitm.ac.in

(continued)

Symbols	Description	Units
t	Time	sec
e	Eccentricity	mm
R	Radius of epitrochoid	mm
ρ	Density	Kg/m ³
q	Heat flux	W/m ²
x, y	Orthogonal coordinates	mm
r, θ	Cylindrical coordinates	mm, radians

1 Introduction

Positive Displacement expanders [1, 2] are preferred over turbines where working fluid is in saturation domain. These expanders find applications in process industries, ORC, and energy storage systems. Various expander options including reciprocating [1, 3], screw [4], scroll [4] and Wankel [5, 6] are investigated. In [7] authors suggest Wankel expander as an ideal option for wet expansion. Geometric parameters defining the performance of Wankel expander are studied in [2, 8].

The existing Wankel expander technology have poor exergy efficiency during part-loading [8–10]. EnERG lab IIT Madras, has developed a technology [5] to address this issue. It is developed on the principle that controlling the duration and timing of inlet and exhaust valves during part loading can yield higher exergy. To further improve the exergy efficiency, we need to further investigate the losses associated with the expansion system.

Previous studies on thermal heat loss in Wankel expanders have used empirical relations to determine the heat transfer coefficient [11]. This was further used in [10] with correction taking into account the geometry of the Wankel expander as two half-pipes with rectangular sections in between the pipes. However, this model [10] did not consider the wetness in the admission steam and thin water film between the steam and inner wall of the rotor housing. This thin film can increase or decrease the heat transfer coefficient that may invariably reduce or increase the heat loss from the expander.

This paper deals with the numerical model that can predict the temperature distribution and heat loss of the rotor housing in the Wankel expansion systems. Typically, the expansion process in these expanders is assumed to be adiabatic. However, the percentage heat loss from an expander is a function of its speed (rpm), exposed surface area, and material thermal properties. In this study, a heat transfer analysis using a user-defined Python model and COMSOL model is done on the geometry of Wankel expander developed in EnERG lab IITM.

2 Methodology

Epitrochoid profile for the Wankel expander is defined by parameters R and e . The x - y coordinates of the epitrochoid profile [12] are given by the Eqs. (1) and (2). The simplified geometry using lines and circles replaces the complex curves of the epitrochoid profile. This was done to simplify the structured meshing of the Wankel Expander. Figure 1 shows a graphical representation of the two boundaries that define the limits of the rotor housing, and the inner boundary is the simplified version of the epitrochoid profile.

$$x = e \cos \alpha + R \cos \beta \tag{1}$$

$$y = e \sin \alpha + R \sin \beta \tag{2}$$

Our Wankel geometry has radius, $R = 80$ mm and eccentricity, $e = 10.5$ mm. The material used for the manufacture of the expander is FG260 grey cast iron. The thermal properties of FG260 [13] are shown in Table 1. The thermal numerical model presented in this paper is based on the 2-D transient heat conduction equation. Equations (3) and (4) represent the transient heat conduction equation [14] in orthogonal and cylindrical coordinate systems, respectively.

Fig. 1 Epitrochoid profile and simplified geometry for the Wankel expander rotor housing

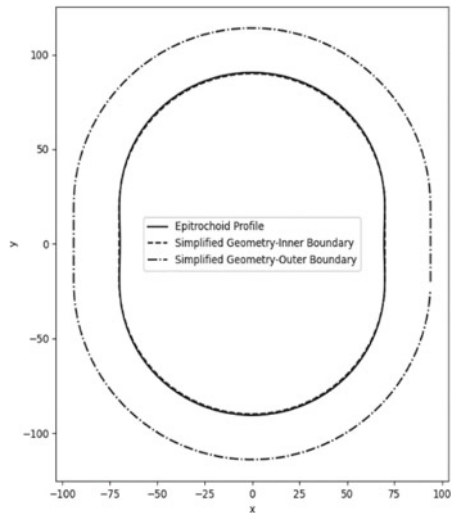


Table 1 Thermal properties for rotor housing

Material	k (W/m. K)	ρ (kg/dm ³)	C (J/kg. K)	α ($\times 10^{-6}$ /K)
FG260	48.8	7.2	460	11

$$k \frac{d^2T}{dx^2} + k \frac{d^2T}{dy^2} + q = \rho C_p \frac{dT}{dt} \tag{3}$$

$$k \frac{1}{r} \frac{dT}{dr} + k \frac{d^2T}{dr^2} + k \frac{1}{r^2} \frac{d^2T}{d\theta^2} + q = \rho C_p \frac{dT}{dt} \tag{4}$$

Equations (3) and (4) are used to create a thermal model for the epitrochoid profile of the Wankel expander incorporating the curved and straight geometries. The equations are discretized and solved using Finite Difference Method (FDM). The meshing for the geometry consists of both orthogonal and non-orthogonal structured meshing to compensate for the curved and straight geometries. Figure 2 shows the meshing for the simplified geometry for the Wankel expander, along with the enlarged Fig. 2(b) of the transition of orthogonal structured mesh to non-orthogonal structured meshing. The meshing also must consider the stability criteria of the solver since FDM explicit solvers are conditionally stable. Hence proper stability analysis is done to estimate the mesh sizes and time steps.

The resolved geometry of the Wankel expander has two boundaries, inner boundary and outer boundary. Isothermal boundary conditions and forced convective heat loss boundary conditions are set for the inner and outer boundaries respectively. The isothermal boundary condition is 133 °C, which corresponds to 3 bar saturated steam pressure. These fluid properties are used from the libraries of REFPROP [15]. The overall heat transfer coefficient, *h* for the forced convective heat loss for the above

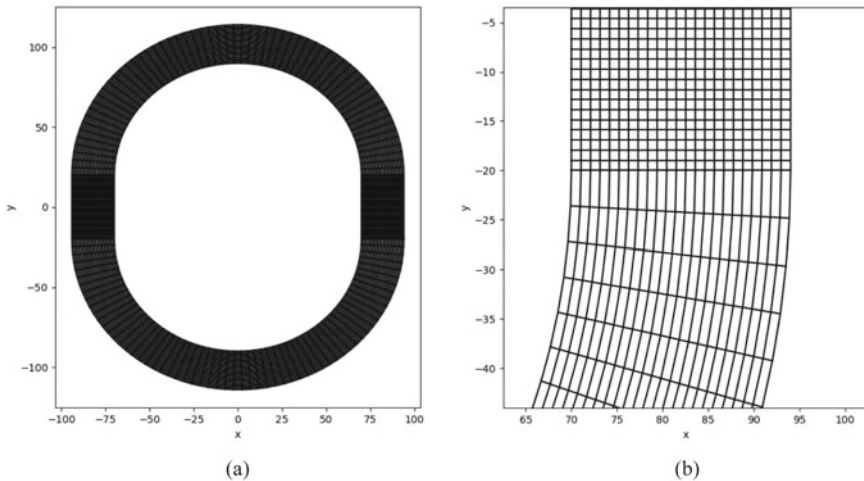


Fig. 2 (a) Structured meshing used in the thermal numerical model, (b) Zoomed image of the meshing at the transition between two different structured meshes

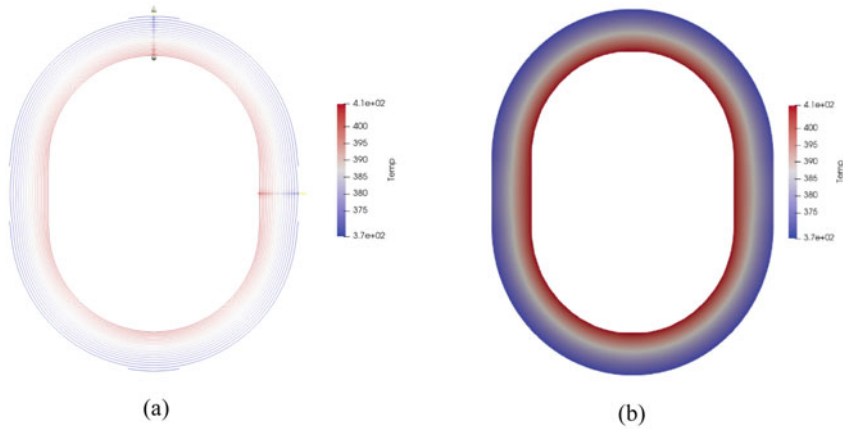


Fig. 3 (a) Contour plot and (b) Colour map of the temperature (K) distribution at the final time step for the expander

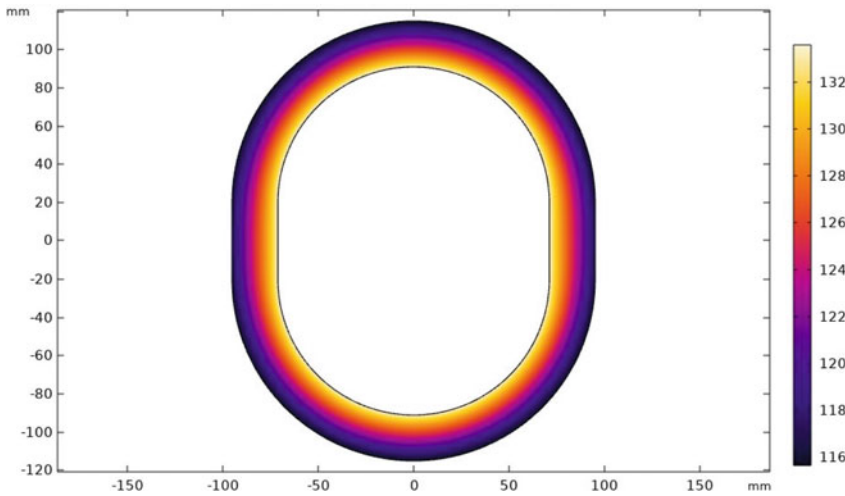


Fig. 4 Colour map of the temperature distribution at the final time step solved using COMSOL

condition was experimentally found out to be $370 \text{ W}/(\text{m}^2 \cdot \text{K})$. Initially, at $t = 0 \text{ s}$, the model is assumed to be at the atmospheric temperature of $30 \text{ }^\circ\text{C}$. The model is solved for different time steps to find the appropriate time step and compared with the results from COMSOL commercial software.

Post-processing of the results is done in Python along with ParaView software. ParaView software is used to generate the contour and colour map of the temperature distribution of the Wankel expander geometry at the final time step. The cross-sectional temperature distribution is also generated using this software that will be used to compare with the results from COMSOL as well.

3 Results and Discussion

The user defined thermal numerical model was solved from $t = 0$ to $t = 100$ s. Similarly, the COMSOL model was also solved for the defined geometry from $t = 0$ to $t = 100$ s. Figures 3 and 4 show the contour as well as the colour map of the temperature distribution in the Wankel expander for the final time step $t = 100$ s. The contour lines in the user defined model predict that there are constant temperature lines along the direction of the heat loss which follow the simplified epitrochoid profile. This is also predicted in the COMSOL model as well.

The temperature change with respect to time must be in acceptable range to accept the use of the model for further application. Figure 5 shows relative error change in the temperature at point (95, -20) for all time steps from $t = 0$ to 100 s. Similarly, for different time steps (Δt) of 0.01, 0.001 and 0.0001 s were also calculated. Figure 5(b) shows the comparison of this temperature distribution when compared with the COMSOL model. The relative error of the numerical model when compared with the COMSOL model is shown in Fig. 5(a). The results show that the relative error for $\Delta t = 0.01$ s is 22.8% whereas for $\Delta t = 0.001$ s it is 9.05%. But the results also predict that as time increases the temperature reaches stability and the relative error reduces to 0.5% for both the cases.

Thermal numerical model also predicted that the temperature distribution of the Wankel expander at the final time step of 100 s <1%, when compared with the COMSOL model. This is shown in Fig. 6, where the cross-sectional temperature distribution along X-axis and Y-axis is taken for consideration. COMSOL model has also predicted that there is variation between the two cross-sectional distributions of temperature in Wankel expander. Whereas in the user defined numerical model this variation is not considerable enough.

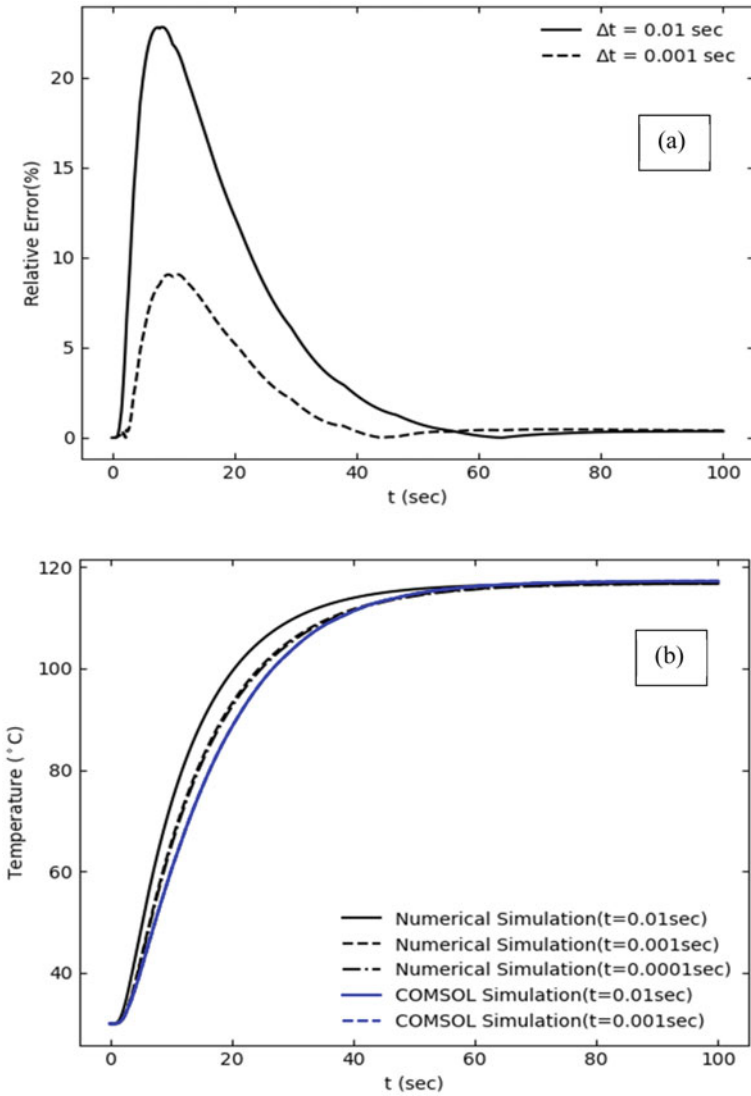
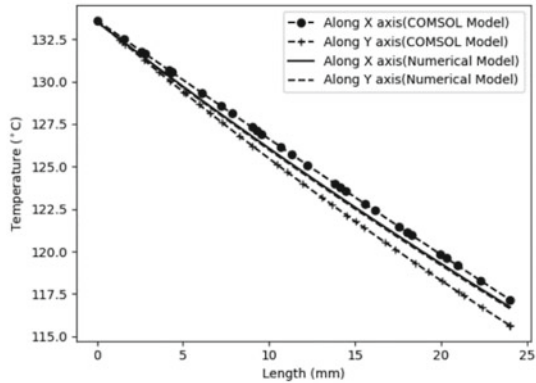


Fig. 5 (a) Relative error and (b) Temperature vs time plot at point (95, -20) using Numerical and COMSOL

Fig. 6 Comparison of temperature profiles along the x and y-axis cross-sections for $\Delta t = 0.001$ s



4 Conclusion

The numerical model for thermal analysis of the Wankel geometry closely matches the prediction obtained from commercial solvers like COMSOL. The relative errors for different time steps of 0.01 and 0.001 s are 22.8% and 9.05%. Hence the acceptable time step for the model is 0.001 s. Since the time step is changed the change in the meshing should also be taken into factor for stability criteria. The future scope of this model is to predict the outside temperature distribution and heat transfer of Wankel expander with pressure ratios as input conditions.

References

1. Gopal VV (2011) Thermodynamic analysis and performance evaluation of a heat (steam) engine
2. Badr O, Naik S, O'Callaghan PW, Probert SD (1991) Wankel engines as steam expanders: design considerations. *Appl Energy* 40:157–170. [https://doi.org/10.1016/0306-2619\(91\)90055-3](https://doi.org/10.1016/0306-2619(91)90055-3)
3. Badami M, Mura M (2009) Preliminary design and controlling strategies of a small-scale wood waste Rankine Cycle (RC) with a reciprocating steam engine (SE). *Energy* 34:1315–1324. <https://doi.org/10.1016/j.energy.2009.04.031>
4. Dumont O, Dickes R, Lemort V (2017) Experimental investigation of four volumetric expanders. *Energy Procedia* 129:859–866. <https://doi.org/10.1016/j.egypro.2017.09.206>
5. Venugopal V, Seshadri S (2019) Controlling admission volume of inlet gas for fixed rpm operation of rotary or reciprocating expander
6. Antonelli M, Baccioli A, Francesconi M, Desideri U, Martorano L (2014) Operating maps of a rotary engine used as an expander for micro-generation with various working fluids. *Appl Energy* 113:742–750. <https://doi.org/10.1016/j.apenergy.2013.08.003>
7. Badr O, Naik S, O'Callaghan PW, Probert SD (1991) Expansion machine for a low power-output steam Rankine-cycle engine. *Appl Energy* 39:93–116. [https://doi.org/10.1016/0306-2619\(91\)90024-R](https://doi.org/10.1016/0306-2619(91)90024-R)

8. Badr O, Naik S, O'Callaghan PW, Probert SD (1991) Rotary Wankel engines as expansion devices in steam Rankine-cycle engines. *Appl Energy* 39:59–76. [https://doi.org/10.1016/0306-2619\(91\)90063-4](https://doi.org/10.1016/0306-2619(91)90063-4)
9. Francesconi M, Caposciutti G, Antonelli M (2017) An experimental and numerical analysis of the performances of a Wankel steam expander. *Energy Procedia*. 129:395–402. <https://doi.org/10.1016/j.egypro.2017.09.118>
10. Antonelli IM, Desideri PU, Ulivi A (2015) Numerical and experimental analysis of a Wankel expander
11. Woschni G (1967) A universally applicable equation for the instantaneous heat transfer coefficient in the internal combustion engine. *SAE Tech Pap*. <https://doi.org/10.4271/670931>
12. Yamamoto K (1981) Rotary engine
13. Bureau of Indian Standards: IS 210: Grey Iron Castings (2009). <https://archive.org/details/gov.in.is.210.2009>
14. Holman J (2001) *Heat transfer*. McGraw-Hill
15. Lemmon EW, Bell IH, Huber ML, McLinden MO (2018) NIST reference fluid thermodynamic and transport properties Database (REFPROP), Version 10.0; standard reference data; National Institute of Standards and Technology, Gaithersburg, MD. NIST Stand. Ref. Databasev23, 288–290

A Novel Desiccant-Based Cooling System for Hot and Humid Climates



Sandeep Koundinya  and Satyanarayanan Seshadri 

Abstract A desiccant-based heat pump system along with a direct evaporative cooling system has been proposed as an alternative to the baseline cooling and dehumidifying system. Dynamic hourly simulation is performed for three consecutive summer days of Chennai to evaluate the performance of the proposed system. The proposed system achieves the comfort condition and is energy efficient. The results showed that the average COP of the proposed system is 2.62. The average COP improvement ratio compared to the baseline system is 1.52. A carbon emissions reduction of 48.2% is estimated by adopting the proposed system.

Keywords Dynamic hourly simulation · Desiccant cooling system · Decarbonisation · Direct evaporative cooling

Nomenclature

PDC	Proposed desiccant cooling
BS	Baseline system
COP	Coefficient of performance
SA	Supply air
OA	Outside air
Q	Capacity in KW
m	Mass flow rate in kg/s
T	Temperature in °C
w	Specific humidity in kg/kg of dry air
h	Enthalpy in KJ/kg

S. Koundinya · S. Seshadri (✉)
Energy & Emissions Research Group (EnERG), Department of Applied Mechanics, Indian Institute of Technology Madras, Chennai 600036, India
e-mail: satya@iitm.ac.in

S. Koundinya
e-mail: am18d033@smail.iitm.ac.in

c_p	Specific heat in KJ/kg K
ϕ	Relative humidity in %
C	Heat capacity in KJ/K s
ϵ	Effectiveness
f	Factor
η	Efficiency

List of Subscripts

<i>sen</i>	Sensible
<i>lat</i>	Latent
<i>dehum</i>	Dehumidification
<i>avg</i>	Average
<i>pro</i>	Process
<i>reg</i>	Re-generation
<i>exh</i>	Exhaust
<i>impr</i>	Improvement ratio
<i>elec</i>	Electrical
<i>wb</i>	Wet bulb
<i>g</i>	Saturated vapour

1 Introduction

Dehumidifying air in building ventilation systems is an important requirement to improve thermal comfort for the occupants. According to ASHRAE, dry bulb temperatures between 23–27 °C and relative humidity between 30 and 65% are considered comfort conditions during summer [1]. With the increase in the standard of living and affluence across the world, the demand for cooling is increasing at a rapid rate, especially in hot and humid climates [2]. Vapour compression systems is the technology of choice in hot and humid climates for space conditioning. In this system, the latent heat load in dehumidification is addressed by cooling air below the dew point temperature. In humid conditions, removal of moisture is very energy intensive and does not benefit much from current advancement such as inverter systems, as these are very effective mainly for sensible cooling. A schematic diagram of the baseline dehumidification and cooling system that is typically used in pharmaceutical company is shown in Fig. 1. The parameters considered for the components of the baseline system are listed in Table 1. Despite vast research in HVAC (heating ventilation and airconditioning) applications, researchers have not succeeded in decoupling the latent and sensible heat loads. Recent advancements in absorption cooling systems using desiccants have evolved as a solution [3]. But, to regenerate the water absorbed,

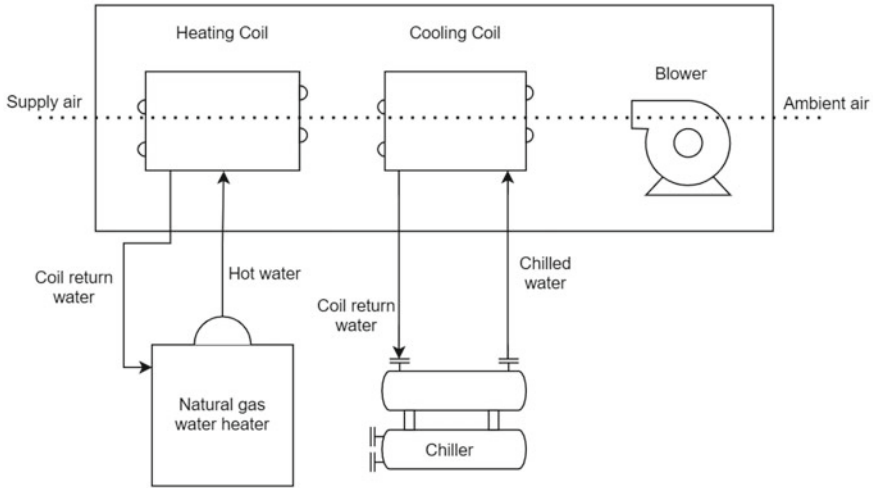


Fig. 1 Schematic diagram of the baseline dehumidifying and cooling system

Table 1 Parameters of the components of the baseline system

Component	Parameter	Value
Air blower	Nominal air flow rate	1934 kg/hr
	Nominal power	0.22 KW
Electric heating coil	Bypass fraction	0.15
Chiller cooling coil	Bypass fraction	0.15
Natural gas boiler	Rated capacity	90 °C
	Boiler efficiency	0.78
	Combustion efficiency	0.85
Chiller water pump	Water flow rate	5000 l/h
	Rated capacity	0.38 KW
Boiler water pump	Water flow rate	2000 l/h
	Rated capacity	0.28 KW
Chiller	Rated capacity	30 KW
	COP	3

natural gas-fired boilers are used, which makes the system inefficient and dependent of primary fuels, moving away from CO₂ reduction efforts.

Finocchiaro et al. [4] integrated a vapour compression system (VCR) and a solid desiccant system to improve the overall performance by decoupling the sensible load and latent load. This system is known as the hybrid cooling system. Also, this system is economically feasible as the low-grade energy sources such as the condenser heat was used to regenerate the water absorbed by the desiccant and the evaporator for further cooling the process air [5]. Worek and Moon [6, 7] performed numerical and

experimental study of a hybrid cooling system and compared the performance with the conventional VCR system. It was found that the COP of the hybrid system was 35% higher than the conventional VCR system. Dhar and Singh [8] used simulations to evaluate the performance of four different hybrid cooling cycles using the analogy method.

They concluded that the energy savings was marginal when the re-generation temperature was reduced from 135 to 80 °C. On further reducing the re-generation temperature to 60 °C, the energy consumption increased due to the increase of supply air flow rate because of high latent load. Jia et al. [9] performed an experimental study and found most of the evaporating surface remained dry due to the increase in the sensible heat factor of the evaporating coil.

As a result, the subsequent reheat can be avoided resulting in the reduction of electricity consumption. Jani et al. [10] experimentally investigated the performance of a hybrid cooling system and concluded that there was a significant reduction in the specific humidity in hot and humid climates. The same authors also did a TRNSYS simulation and studied the operating parameters and their influence on the performance for different hybrid cooling cycles [11]. Tu et al. [12] proposed a novel hybrid system with multi-stage air handling unit and discussed the optimum number of stages.

Desiccant cooling systems with different configurations have also been studied [13]. Pandelidis et al. [14] did a numerical study of evaporative air conditioning systems assisted by the solid desiccant. Ahn et al. [15] conducted experimental tests for the residential environment with a hybrid cooling system and showed that the energy consumption was not affected when the ambient humidity is low. Researchers in [16] performed thermal analysis for vehicle air conditioning. The air conditioner had direct evaporative coolers enhanced with desiccant dehumidification. Angrisani et al. [17] simulated a geothermal cooling system integrated with the desiccant system using TRNSYS. They concluded that the primary energy savings increased from 77 to 95%, and the pay-back period was reduced from 14 years to 1.2 years.

To the best of our knowledge, a hybrid cooling system enhanced with a direct evaporative cooling system has not been investigated yet, especially for hot and humid climates. Most of the earlier studies concentrated on the hybrid cooling system or evaporative cooling systems individually. A novel architecture is also proposed, and dynamic hourly simulation for the summer days of Chennai is performed using a program developed in python [18]. The main goal of this study is to propose a desiccant with direct evaporative cooling system integrated with a heatpump for additional sensible cooling and re-generation. We report the performance of the proposed system using dynamic hourly simulation and compare the results with the baseline system.

Section 2 explains the proposed system configuration. Section 3 describes the methodology adopted for the simulation and evaluation of performance of the proposed system. Simulation results are presented in Sect. 4 and summary along with conclusions in Sect. 5.

2 System Description

The schematic diagram and psychrometric chart of the proposed system is shown in Figs. 2 and 3. The components specification of the proposed system is listed in Table 2. The system consists of a desiccant wheel, heat pump, two sensible heat exchangers, direct evaporative cooler, an electric heater, a chiller and an air handling unit (AHU). The AHU has three air streams, which are discussed below.

1 to 2	Dehumidification process	3 to 4	Sensible cooling by the sensible heat exchanger 2
2 to 3	Sensible cooling by the sensible heat exchanger 1	4 to 5	Sensible cooling by the evaporator
5 to 6	Sensible cooling by chiller		

Re-generation air stream: The main purpose of this stream is to regenerate the water absorbed by the silica gel desiccant in the desiccant wheel. Ambient air enters a sensible heat exchanger 1, where the temperature of the re-generation air is increased

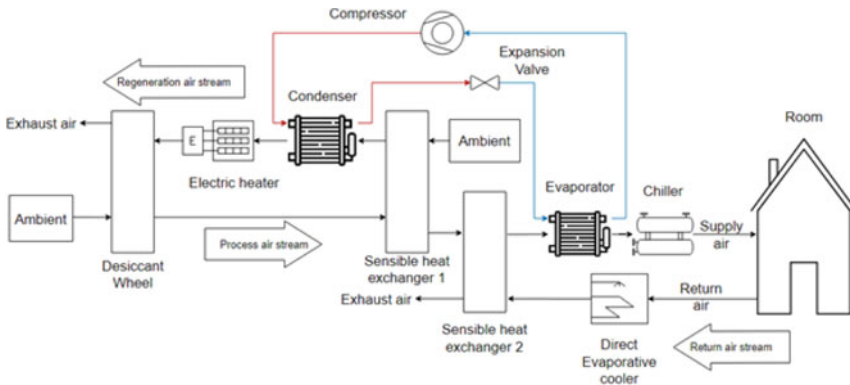


Fig. 2 Schematic diagram of the proposed system

Fig. 3 Psychrometric diagram of the proposed system

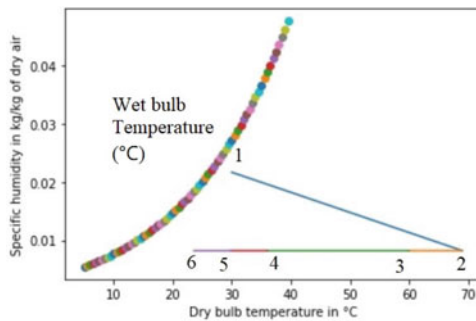


Table 2 Parameters of the proposed system components

Component	Parameter	Value
Regeneration air stream	Nominal air flow rate	677 kg/hr
	Nominal power	0.12 KW
Process air stream	Nominal air flow rate	1934 kg/hr
	Nominal power	0.22 KW
Return air stream	Nominal air flow rate	1900 kg/hr
	Nominal power	0.22 KW
Air to air sensible heat	Sensible heat transfer efficiency	0.6
Evaporative cooler	Saturation efficiency	0.9
	Pump nominal power	0.2 KW
Electric heating coil	Bypass fraction	0.15
Chiller cooling coil	Bypass fraction	0.15
Heat pump system	Condenser temperature	90 °C
	Condenser coil bypass fraction	0.15
	Evaporator temperature	25 °C
	Evaporator bypass fraction	0.15
	Compressor power	2.8 KW
	Refrigerant	R152a
Chiller	Condenser temperature	40 °C
	Evaporator temperature	15 °C
	Evaporator bypass fraction	0.15
	Compressor Power	0.568 KW
	Refrigerant	R407C
Silica gel desiccant wheel	Motor nominal power	0.05 KW

to around 58 °C by the process air stream coming out of the desiccant wheel. Later, hot air coming out of the heat exchanger passes over the condenser coil of the heat pump system, which is at 90 °C and gains heat. Then, the air passes over the electric heating coil, which heats the air to a re-generation temperature of around 105 °C. This hot re-generation air removes the water absorbed by the silica gel present in the desiccant wheel.

Process air stream: Humid ambient air enters the rotating desiccant wheel. Silica gel present in the desiccant wheel absorbs the water vapours present in the air and dehumidifies the air. The temperature of the air is increased because of the dehumidification process (also known as the sorption process). The hot and dry air coming out of the desiccant wheel is sensibly cooled by interacting with the ambient air of

the re-generation air stream and the air coming out of the direct evaporative cooler of the return air stream, in the sensible heat exchangers 1 and 2, respectively. The process air is further cooled by the evaporator coil of the heat pump system which is at 25 °C, and by the cooling coil of the chiller. After this, the process air at comfort condition is supplied to the room.

Return air stream: The return air from the room is passed to a direct evaporative cooler. Here, the relative humidity is increased, and the temperature is decreased. Humid, cool air is then passed through the sensible heat exchanger 2 to utilize this cool air to cool the process air.

3 Methodology

Dynamic hourly simulation is performed for three continuous summer (hot and humid) days of Chennai using in house developed python code. The historical weather data was retrieved from World Weather Online [19] through wwo-hist python package [20], which prints the data in CSV file. The psychrometric properties of air were retrieved from coolprop [21]. The flow diagram of the calculation is shown in Fig. 4. The mathematical models considered for the components of the proposed system are shown in Table 3. The sensible and latent heat loads to achieve the comfort conditions are calculated using the below Eqs. 1 and 2.

$$Q_{sen,dehum} = m_{air}c_{p,avg}(T_{OA} - T_{SA}) \quad (1)$$

$$Q_{lat,dehum} = m_{air}(w_{OA}h_{g,OA} - w_{SA}h_{g,SA}) \quad (2)$$

$$h_g \cong 2500.9 + 1.82 T$$

The performance of the proposed system is evaluated by the coefficient of performance (COP). The COP of the proposed system and the baseline system is given by the Eq. 3 and 4, respectively, and the performance improvement ratio is given by the Eq. 5.

$$COP_{PDC} = \frac{Q_{sen,dehum} + Q_{lat,dehum}}{P_{elec}} \quad (3)$$

$$COP_{BS} = \frac{Q_{sen,dehum} + Q_{lat,dehum}}{P_{elec} + P_{naturalgas}} \quad (4)$$

$$COP_{impr} = \frac{COP_{PDC} - COP_{BS}}{COP_{BS}} \quad (5)$$

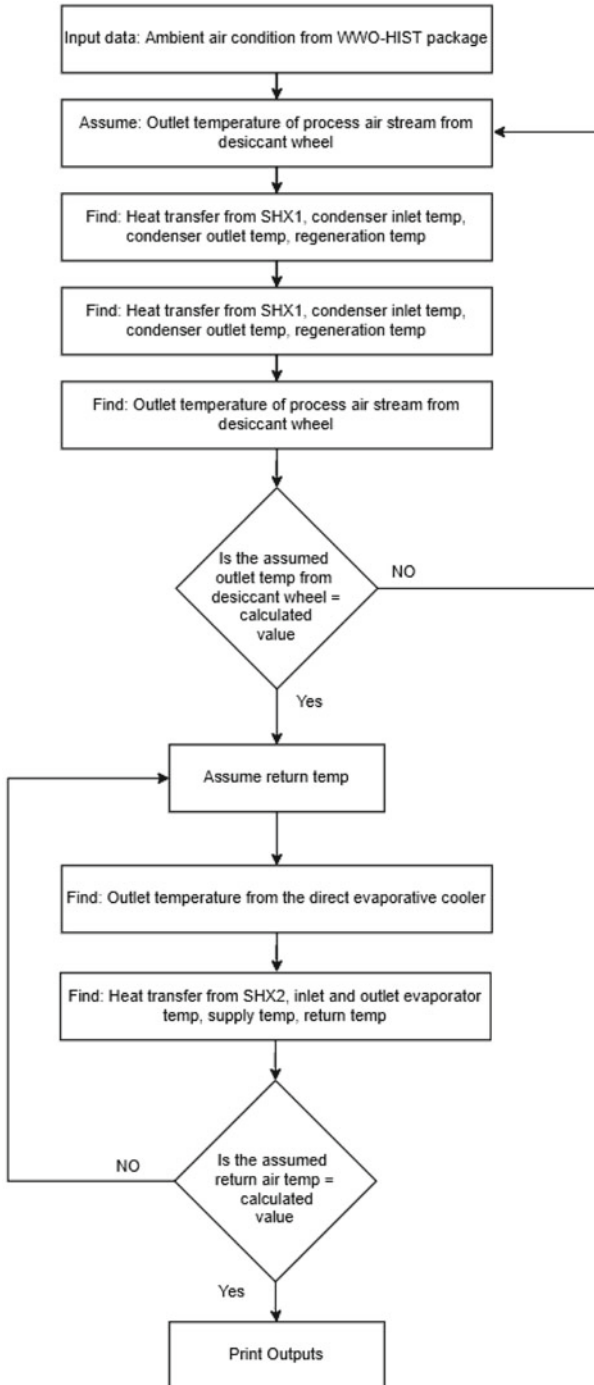


Fig. 4 Calculation flow diagram

Table 3 Mathematical model of the components

Component	Equation
Silica gel desiccant wheel	Ruivo et al. model [23]
	$\phi_{pro,out} = \phi_{pro,in} - 0.985(\phi_{pro,in} - \phi_{reg,in})$
	$h_{pro,out} = h_{pro,in} - 0.078(h_{pro,in} - h_{reg,in})$
Air to air sensible heat exchangers	Minimum capacitance
	$C_{min} = \min(m_{exh}c_{p,exh}, m_{fresh}c_{p,fresh})$
	Sensible heat transfer
Cooling and heating coils	Air heating rate
	$Q_{air} = m_{air}(1 - f_{bypass})(h_{air,in} - h_{air,out})$
	Evaporative cooler
Evaporative cooler	Air side heat transfer rate
	$Q_{air} = m_{air}(h_{air,in} - h_{air,out})$
	Outlet air temperature
	$T_{air,out} = T_{air,in} - \eta_{saturation}T_{wb}$

Table 4 Specific emissions for fossil fuel-fired stations

Coal	Diesel	Natural gas
0.98	0.59	0.45

The weighted average emission factor (β) is considered as 0.83 kg of equivalent CO₂ per kWh of electricity produced [22]. This is nearly the same from the year 2012 in India. The weighted average specific emissions for the fossil fuel-fired stations in the financial year 2016–17 in t CO₂/MWh is shown in Table 4. Using the above emission factors, the equivalent CO₂ emitted is calculated for the energy consumed (KWh) by the baseline and proposed system.

4 Results and Discussion

Dynamic hourly simulation is performed, and the performance is calculated. Figures 5 and 6 show the variation of ambient and supply temperature and ambient and supply relative humidity for three consecutive summer days, respectively. It is clearly observed that the supply conditions of the proposed system are within the range of comfort conditions. Figure 7 shows the coefficient of performances for the proposed and baseline system along with the COP improvement ratio. The average COP of the baseline system and the proposed system are 1.04 and 2.62, respectively. An average COP improvement ratio of 1.52 is observed. The baseline system has electricity consumption for running the chiller and auxiliaries to produce cold water, which is circulated in the cooling coil. Natural gas is used to generated hot water,

Fig. 5 Variation of temperature over the three summer days

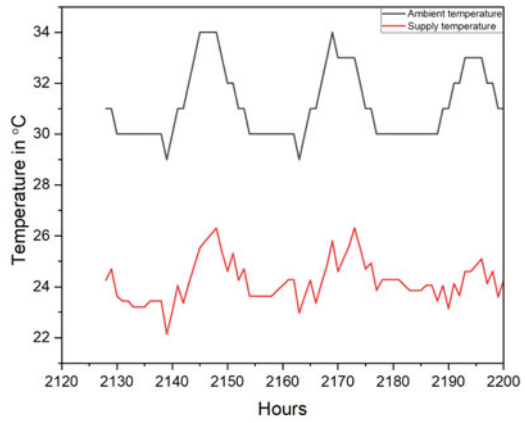


Fig. 6 Variation of relative humidity over the three summer days

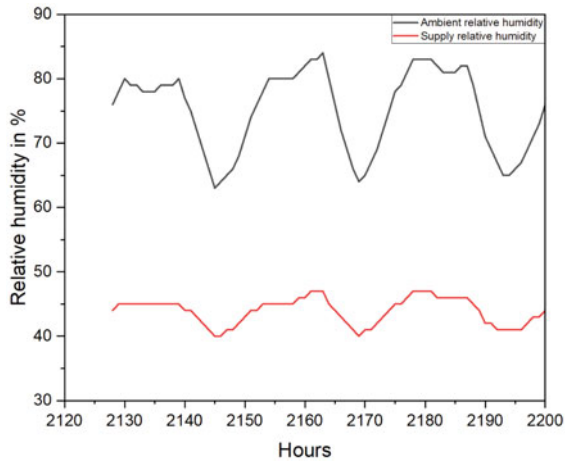


Fig. 7 Coefficient of performance

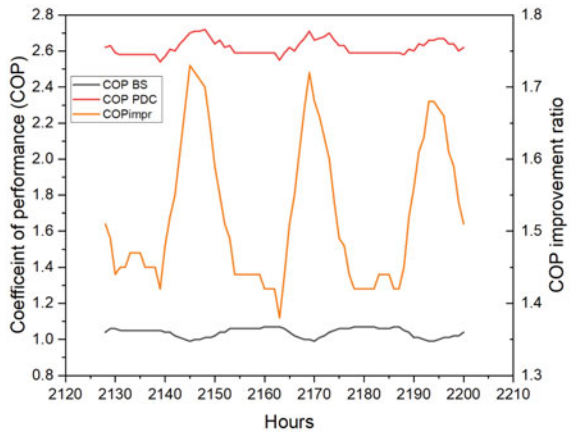


Fig. 8 Power consumption of the proposed and baseline system

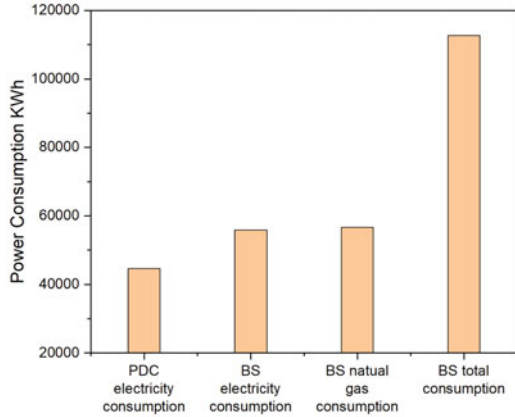
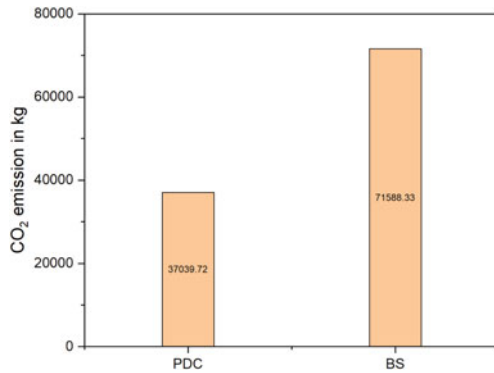


Fig. 9 Carbon emissions for the three summer days



which is circulated in the heating coil. Figure 8 shows the electricity and natural gas consumption for the proposed and baseline system for the three summer days.

The proposed system consumes 60.8% less power compared to the baseline system. On adopting the proposed system, 34,548.61 kg of CO₂ is eliminated for the observed three summer days, which is equal to 86,827 miles driven by an average passenger vehicle and a carbon emissions reduction of 48.26% is estimated. The baseline system emits 1.93 times more CO₂ than the proposed system. Figure 9 shows the CO₂ emissions for the proposed and the baseline system.

5 Conclusions

A desiccant based heat pump system along with direct evaporative cooling is proposed, and dynamic hourly simulation is performed for the three summer days

(hot and humid) of Chennai using an in house developed code in python. The simulation showed that the proposed system has a good ability to deliver air to the room in comfortable conditions. The power consumption is 60.8% less than the baseline system. This shows that the proposed system has a significant energy saving potential. An average COP of 2.62 is observed, and the average COP improvement ratio is 1.52. A CO₂ emissions reduction of 48.26% is estimated. An electric heater has been used since the re-generation temperature required for silica gel is more than 100 °C. Adoption of high-temperature heat pumps to the proposed system can further improve the performance by eliminating the electric heater. Further research is required in developing low re-generation temperature desiccants with better moisture removal capacity to improve the performance.

Acknowledgements The authors acknowledge the Ministry of Human Resource Development (MHRD), GOI, and Aspiration Energy Pvt Ltd for the financial support under grant number 35-8/2017-TS.1. Sandeep Koundinya is thankful to SERB-CII and Aspiration Energy Pvt Ltd for PM fellowship.

References

1. Turner SC, et al (1979) American society of heating, refrigerating and air-conditioning engineers. *Int J Refrig* 2:56–57. [https://doi.org/10.1016/0140-7007\(79\)90114-2](https://doi.org/10.1016/0140-7007(79)90114-2)
2. IEA (2018) The future of cooling
3. Ghosh TK, Hines AL (1999) Solid desiccant dehumidification systems. Elsevier Masson SAS
4. Finocchiaro P, Beccali M, Nocke B (2012) Advanced solar assisted desiccant and evaporative cooling system equipped with wet heat exchangers. *Sol Energy* 86:608–618. <https://doi.org/10.1016/j.solener.2011.11.003>
5. Sheridan JC, Mitchell JW (1985) A hybrid solar desiccant cooling system. *Sol Energy* 34:187–193. [https://doi.org/10.1016/0038-092X\(85\)90179-3](https://doi.org/10.1016/0038-092X(85)90179-3)
6. Worek WM, Chung-Ju M (1986) Simulation of an integrated hybrid desiccant vapor-compression cooling system. *Energy* 11:1005–1021. [https://doi.org/10.1016/0360-5442\(86\)90031-9](https://doi.org/10.1016/0360-5442(86)90031-9)
7. Worek WM, Moon CJ (1988) Desiccant integrated hybrid vapor-compression cooling: performance sensitivity to outdoor conditions. *Heat Recover Syst CHP* 8:489–501. [https://doi.org/10.1016/0890-4332\(88\)90010-5](https://doi.org/10.1016/0890-4332(88)90010-5)
8. Dhar PL, Singh SK (2001) Studies on solid desiccant based hybrid air-conditioning systems. *Appl Therm Eng* 21:119–134. [https://doi.org/10.1016/S1359-4311\(00\)00035-1](https://doi.org/10.1016/S1359-4311(00)00035-1)
9. Jia CX, Dai YJ, Wu JY, Wang RZ (2006) Analysis on a hybrid desiccant air-conditioning system. *Appl Therm Eng* 26:2393–2400. <https://doi.org/10.1016/j.applthermaleng.2006.02.016>
10. Jani DB, Mishra M, Sahoo PK (2016) Experimental investigation on solid desiccant-vapor compression hybrid air-conditioning system in hot and humid weather. *Appl Therm Eng* 104:556–564. <https://doi.org/10.1016/j.applthermaleng.2016.05.104>
11. Jani DB, Mishra M, Sahoo PK (2018) Performance analysis of a solid desiccant assisted hybrid space cooling system using TRNSYS. *J Build Eng* 19:26–35. <https://doi.org/10.1016/j.jobbe.2018.04.016>
12. Tu R, Hwang Y, Ma F (2017) Performance analysis of a new heat pump driven multi-stage fresh air handler using solid desiccant plates. *Appl Therm Eng* 117:553–567. <https://doi.org/10.1016/j.applthermaleng.2017.02.005>

13. Zouaoui A, Zili-Ghedira L, Ben Nasrallah S (2016) Open solid desiccant cooling air systems: a review and comparative study. *Renew Sustain Energy Rev* 54:889–917. <https://doi.org/10.1016/j.rser.2015.10.055>
14. Pandelidis D, Anisimov S, Worek WM, Drag P (2016) Comparison of desiccant air conditioning systems with different indirect evaporative air coolers. *Energy Convers Manag* 117:375–392. <https://doi.org/10.1016/j.enconman.2016.02.085>
15. Ahn J, Kim J, Kang BH (2016) Performance of a hybrid desiccant cooling system in a residential environment. *Heat Transf Eng* 37:633–639. <https://doi.org/10.1080/01457632.2015.1067036>
16. Alahmer A (2016) Thermal analysis of a direct evaporative cooling system enhancement with desiccant dehumidification for vehicular air conditioning. *Appl Therm Eng* 98:1273–1285. <https://doi.org/10.1016/j.applthermaleng.2015.12.059>
17. Angrisani G, Diglio G, Sasso M, Calise F, Dentice d'Accadia M (2016) Design of a novel geothermal heating and cooling system: energy and economic analysis. *Energy Convers Manag* 108:144–159. <https://doi.org/10.1016/j.enconman.2015.11.001>
18. Van Rossum G, Drake Jr, FL (1995) Python tutorial. cent. voor wiskd. en inform. Amsterdam, Netherlands
19. World weather online API. <https://www.worldweatheronline.com/developer/>
20. Viriyakovithya E. wwo-hist python package. <https://pypi.org/project/wwo-hist/>
21. Bell IH, Wronski J, Quoilin S, Lemort V (2014) Pure and pseudo-pure fluid thermophysical property evaluation and the open-source thermophysical property library CoolProp. *Ind Eng Chem Res* 53:2498–2508
22. GOI-MOP (2018) CO₂ baseline database for the indian power sector user guide. Rep by Minist Power Govt India 3:1–34
23. Ruivo CR, Costa JJ, Figueiredo AR, Kodama A (2012) Effectiveness parameters for the prediction of the global performance of desiccant wheels - an assessment based on experimental data. *Renew Energy* 38:181–187. <https://doi.org/10.1016/j.renene.2011.07.023>

Development of Heat Exchanger Models for Predicting Heat Transfer Behaviour of Mixed Refrigerants



Alfred Emmanuel , Satyanarayanan Seshadri ,
and Sandeep Koundinya 

Abstract The study analyses correlations used to determine the condensation heat transfer coefficient of refrigerant mixtures, R410A and R407C, in a tube in tube condenser. Shah [1], Jaster and Kosky [2], Thome et al. [3], and Dobson and Chato [4] correlations have been considered. The study identifies the flow parameters which influence the accuracy of correlations. The accuracy of the considered correlations is studied against the identified flow parameters. The flow parameters are used as a deciding criterion to select the most accurate correlation for a given case. This leads to a hybrid approach involving multiple correlations. The hybrid approaches are more accurate in comparison to the individual correlations.

Keywords Heat transfer coefficient · Condensation · Correlations · Refrigerant mixtures

1 Introduction

R22 is a Hydrochlorofluorocarbon (HCFC) that was widely used in the refrigeration and air-conditioning industry due to its excellent heat transfer characteristics. HCFC's have a high ozone depletion potential, and their release damages the ozone layer, which shields the earth from harmful ultraviolet radiation. The Montreal Protocol [5] led to the phase out of HCFC's due to their high ODP (Ozone depletion potential). Suitable alternatives to R22 were found in R410A and R407C. Both R410A and R407C have properties similar to R22 and have zero ODP.

However, being refrigerant mixtures, their heat transfer behaviour differs from R22. R410A is a nearly azeotropic refrigerant, which means that its dew point and bubble point temperature are nearly the same. But R407C is a zeotropic refrigerant,

A. Emmanuel · S. Seshadri (✉) · S. Koundinya
Energy & Emissions Research Group (EnERG), Department of Applied Mechanics, Indian
Institute of Technology Madras, Chennai 600036, India
e-mail: satya@iitm.ac.in

S. Koundinya
e-mail: am18d033@smail.iitm.ac.in

for which the dew point and bubble point temperature are different, leading to a temperature glide during the condensation process.

The heat transfer coefficient is a critical parameter for the design of a heat exchanger. It determines the overall heat transfer rate and the heat transfer area. Any error in its prediction may lead to the poor design of a heat exchanger. Heat transfer coefficient may be found either experimentally or through computational simulations, or through correlations. This study uses correlations for predicting the heat transfer coefficients and for analysing the heat transfer through a double pipe (tube-in-tube) counter flow condenser. A condenser encounters two-phase flow, containing vapour and liquid phase in the flow. There are separate correlations for two-phase flows.

Del Col D. [6] used the Thome et al. [3] correlation to study the heat transfer of zeotropic mixtures. He used the Silver [7] and Bell and Ghaly [8] correction to account for the mass transfer resistance. He compared the accuracy of the correlation against various parameters like Re_v , mass velocity, vapour quality and flow regime. D Jung et al. [9] studied the heat transfer of R22, R134A, R407C and R410A. They compared their experimental results against multiple heat transfer correlations. They studied the mean and average deviation of the predicted heat transfer coefficient against the experimental results. C. Aprea et al. [10] experimentally studied the heat transfer of R407C against R22 and compared the experimental results against correlations by Chato [11], Jaster and Kosky [2], Rosson and Myers [12], Singh et al. [13], and Dobson and Chato [4]. The study claims that Dobson and Chato correlation predicts the results best for both R407C and R22. D. Jung et al. [9] and C. Aprea [10] compared the accuracy of multiple heat transfer correlations by computing the mean and the average error. However, the influence of the flow variables on error has not been studied. Del Col D. [6] compared the accuracy of Thome et al. [3] correlation against flow parameters. Using only one correlation, it may not be possible to predict the heat transfer coefficient accurately for all cases. Thus, there is a need to compare the accuracy of multiple, prominent condensation heat transfer correlations against the flow parameters, for R410A and R407C.

The experimental results have been taken from literature. Table 1 gives a summary of the experimental data considered for the study. The study considers 184 data points for R410A and 114 for R407C.

2 Heat transfer Correlations

Specific correlations have been developed for predicting the condensation heat transfer coefficient of fluids. The study considers these four prominent correlations—Shah [1], Jaster and Kosky [2], Thome et al. [3], and, Dobson and Chato [4]. Except for Dobson and Chato, the rest of the correlations have been developed for pure fluids. Refrigerant mixtures encounter a mass transfer resistance during condensation. This

Table 1 Summary of experimental data taken from research papers

Sl. no	Author	Data points	Refrigerant	D (mm)	Tsat (°C)	G range (kg/m ² s)
1	M.K. Dobson [14]	117	R410A	7.04	35–45	27–651
2	A. Cavallini [15]	40	R410A	8	40	100–750
3	X. Boissieux [16]	14	R407C	8	24.2	175
4	Sweeney [17]	26	R407C	8	35	75–300
5	Apra [10]	55	R407C	20	37–39	47–115
6	D. Jung [9]	46	R410A/R407C	8.82	40	100–300

mass transfer resistance degrades the heat transfer coefficient of the fluid. To account for this mass transfer resistance, Bell and Ghaly [8] proposed a correction to the heat transfer coefficient found using correlations developed for pure fluids. In this study, this correction has been used to consider the effect of mass transfer resistance. The correction is given as,

$$\frac{1}{h_{tp,c}} = \frac{1}{h_{tp}} + \frac{dq_s}{dq_t} \frac{1}{h_v} = \frac{1}{h_{tp}} + \frac{x c_{pv} \Delta T_{gl}}{h_{fg} h_v} \tag{1}$$

$$h_v = 0.023 \frac{k_v}{D} Re_v^{0.8} Pr_v^{0.33} \tag{2}$$

$h_{tp,c}$ is the corrected value of heat transfer coefficient and h_{tp} is the value found using the correlation, h_v is the heat transfer coefficient considering the flow of the vapour phase, $\frac{dq_s}{dq_t}$ is the ratio of the sensible heat transfer to the total heat transfer.

3 Variables Influencing the Accuracy of the Correlations

In this study, we have compared the error in the correlations against these flow parameters- Re_v , Re_{vo} , J_v , Fr_{so} , Re_l , x , flow regime and void fraction. The flow regime is determined using either Thome et al. [18] and, Dobson and Chato [4] correlations. The study firstly analyses the influence of the flow parameters on the accuracy of the correlations. The expressions for these parameters are given below,

$$\text{Vapour only Reynolds number, } Re_{vo} = \frac{GD}{\mu_v} \tag{3}$$

$$\text{Vapour Reynolds number, } Re_v = \frac{GDx}{\mu_v \epsilon} \tag{4}$$

$$\text{Non dimensional vapour velocity, } J_v = \frac{xG}{\sqrt{gD\rho_v(\rho_l - \rho_v)}} \quad (5)$$

If $Re_l < 1250$,

$$\text{Modified Froude number (Soliman) [19], } Fr_{so} = .025Re_l^{1.59} \left[\frac{1 + 1.09X_{tt}^{0.039}}{X_{tt}} \right]^{1.5} \frac{1}{Ga^{0.5}} \quad (6)$$

else,

$$Fr_{so} = 1.26Re_l^{1.04} \left[\frac{1 + 1.09X_{tt}^{0.039}}{X_{tt}} \right]^{1.5} \frac{1}{Ga^{0.5}} \quad (7)$$

4 Methodology

The correlations were coded and analysed on Python 3.8 [20] with the following considerations,

- The flow of refrigerant in a straight, horizontal, tube-in-tube counterflow condenser.
- The refrigerant (condensing fluid) flows in the inner tube and the coolant (water) in the annulus.
- The assumptions involved in the analysis are,
 - fully developed flow,
 - outer tube is perfectly insulated,
 - the refrigerant is cooled using water in the annulus. The water temperature and pressure are taken as 20 °C and atmospheric pressure, respectively, unless mentioned otherwise in the literature.
 - the inner tube material is taken as copper.
- Friction factor has been calculated using Blasius equation for turbulent flow in smooth tubes.
- Void fraction has been calculated using the Steiner [21] horizontal version of the Rouhani-Axelsson [22] correlation.
- The frictional-pressure gradient is critical in determining heat transfer. It has been calculated using the Gronnerud [23] correlation.
- Four heat transfer correlations have been used, as discussed previously. With the help of these correlations, we can predict the heat transfer coefficient.
- The properties of the fluids are taken from NIST REFPROP version 10.0 [24].

- The heat exchanger is discretized along its length into multiple segments and for each segment the heat transfer coefficient, vapour quality, pressure gradient and fluid temperature are determined.
- The heat transfer analysis starts from the segment at the inlet of the condensing fluid, where the vapour quality and fluid temperature are known. The heat transfer and pressure drop are found using the correlations mentioned before. The vapour quality and fluid temperature at the outlet of this segment is determined using the heat transfer and pressure drop across the segment.
- The vapour quality and fluid temperature at the outlet of this segment are the inlet conditions for the next segment. In this manner, with a discretized approach, the heat transfer across the heat exchanger can be determined.
- The predicted heat transfer coefficients are then compared against the experimental results, and the error in predictions is found out.
- To analyse the influence of the variables on the accuracy of the correlations, plots of error versus variables are generated.

Thus, the heat transfer coefficients and the error in the predictions are calculated.

5 Results

The plots of absolute error for the four correlations versus variables are analysed. For certain variables, the plots do not exhibit any trend i.e., the error fluctuations are high all through the value of the variable. This indicates that the variable doesn't influence the error. But there are certain variables for which the plots show specific trends. For example, up to a certain value of the variable one correlation has the least error, but above this range, another correlation predicts better. Such plots suggest that a single correlation doesn't predict best all through the value of the variable. This leads to the concept of selecting a specific correlation based on the range of the variable. Such variables can be used as a criterion to select the appropriate correlation for a given case. This leads to a hybrid approach, where we select from multiple correlations, one that is most accurate for the given case. From the variables considered, the error is found to be dependent on Re_v , Re_{vo} , J_v , Fr_{so} and flow regime.

Figure 1 represents the absolute error of the correlations versus Re_{vo} . It suggests that from Re_{vo} value of 13,000 to 50,000, Dobson and Chato correlation has least error. From 50,000 to 1,00,000, Jaster correlation has the least error, then from 1,00,000 to 1,50,000, Shah has least error, and then till 4,00,000 Thome et al. is best. Thus, we now have a criterion to select an accurate correlation based on the Re_{vo} value. This forms the basis for the hybrid approach based on Re_{vo} . Similar inferences have also been drawn based on Re_v , Fr , J_v and flow regime. It basically involves dividing the range of the variable into subranges and selecting an appropriate correlation for each subrange. For each subrange, the correlation having the least error

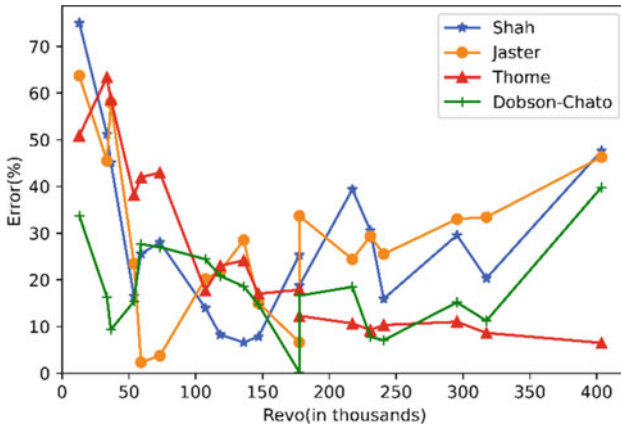


Fig. 1 Absolute error of correlations versus Re_{vo} for R410A

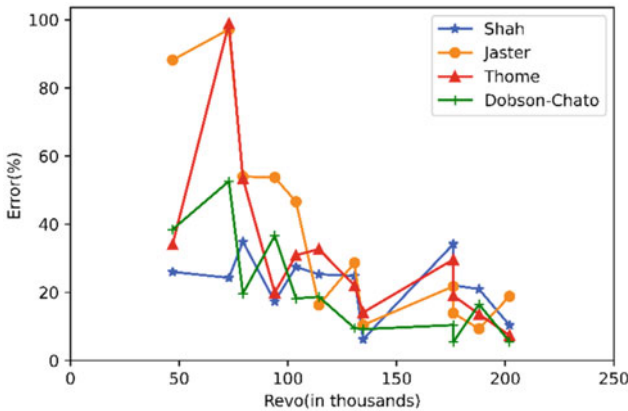


Fig. 2 Absolute error of correlations versus Re_{vo} for R407C

is selected. Since six variables have been found to influence the error, we develop six hybrid approaches using each of these variables. The hybrid approach based on Re_{vo} performs better than the other hybrid approaches for both R410A and R407C.

Figure 2 indicates that Re_{vo} also influences the error of the correlations for R407C. As for R410A, similar inferences have also been drawn for R407C. This forms the foundation of the hybrid approach, where we select from a set of multiple correlations, the one having the least error.

Tables 2 and 3 represent the mean and average error of all the data points for the hybrid approaches versus the individual correlations for R410A and R407C, respectively. Tables 2 and 3 indicate that for R410A and R407C, the mean error of

Table 2 Comparison of error of all data points for hybrid approaches and individual correlations considering R410A

Fluid	Hybrid approach based on						Individual correlations			
R410A	Re_{vo}	Re_v	J_v	Fr_{so}	Flow regime Thome	Flow regime DC	Shah	Jaster and Kosky	Thome et al.	Dobson and Chato
Mean error	10.72	14.15	15.03	15.47	17.48	16.03	27.08	28.29	26.10	18.05
Average error	-2.29	-7.84	-11.24	-11.22	-9.58	-12.95	-0.25	0.85	-19.70	-9.02

Table 3 Comparison of error of all data points for hybrid approaches and individual correlations considering R407C

Fluid	Hybrid approach based on						Individual correlations			
R407C	Re_{vo}	Re_v	J_v	Fr_{so}	Flow regime Thome	Flow regime DC	Shah	Jaster and Kosky	Thome et al.	Dobson and Chato
Mean error	17.01	18.98	19.55	19.95	19.30	21.01	22.25	39.62	32.72	21.01
Average error	-5.88	-11.65	-11.60	-11.13	-3.16	14.84	-13.59	30.64	9.99	14.84

the hybrid approach using Re_{vo} is the least. Among the four correlations considered, Dobson and Chato gives the least error for both R410A and R407C. The hybrid approach using Re_v performs better, leading to a reduction of over 7% and 4% in the mean error for R410A and R407C, respectively. The mean error and average error are calculated using below equations

$$Mean\ error = \sum \left| \frac{Predicted\ value - Experimental\ value}{Experimental\ value} \right| \times 100\% \quad (8)$$

$$Average\ error = \sum \frac{Predicted\ value - Experimental\ value}{Experimental\ value} \times 100\% \quad (9)$$

Figures 3 and 4 present the scatter plot of error for the hybrid approach using Re_{vo} for R410A and R407C, respectively. The scatter of the points seems to be uniformly distributed about the error axis.

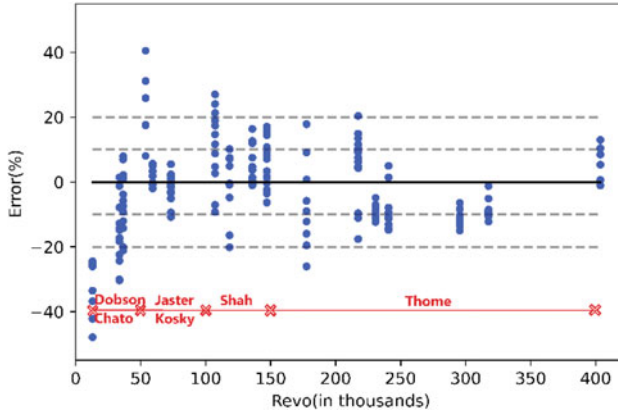


Fig. 3 Scatter plot of error of hybrid approach considering Re_{vo} for R410A (the best correlation based on the range is also depicted)

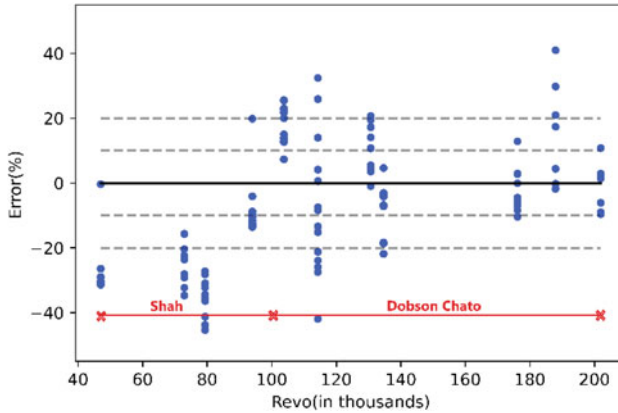


Fig. 4 Scatter plot of error of hybrid approach considering Re_{vo} for R407C

6 Discussion

The graphs of mean error versus the variables depict that each correlation has a range in which it seems to be predicting the results best, but outside that range, it may not predict well. The heat transfer correlations are developed considering a specific set of fluids and flow conditions. Generally, a statistical fit is performed to formulate a new correlation, such that it is in close agreement with the available experimental data. Thus, if this correlation is used to predict the heat transfer of a different fluid operating at different conditions, the correlation may not yield similar results. This drives the need to compare the correlations for different fluids and

different operating conditions. This is accomplished by comparing the correlations against multiple variables which, seem to influence the heat transfer.

The study compared the errors in the correlations against multiple variables and attempted to develop a hybrid approach using these variables. A hybrid approach based on Re_{vo} is found to be the best predictor of heat transfer for R410A and R407C. Using the hybrid approach the total error in the predictions can be significantly reduced.

The dependence of error on Re_{vo} is indicative of the influence that mass velocity has on error. Re_{vo} is a function of mass velocity, the dynamic viscosity of vapour and the diameter of the tube. In the experimental data collected, the variation of the viscosity of the fluid and the tube diameter are very low. Hence, mass velocity seems to be the most influential parameter on the error. In this study, it was found that the heat transfer coefficient is significantly dependent on mass velocity. Mass velocity is a dimensional parameter, but to get a comparison on a universal scale, we need to use a dimensionless parameter. This leads to the use of Re_{vo} instead of using mass velocity as a criterion.

7 Conclusion

Thus, as seen in Fig. 5, by adopting a hybrid approach based on Re_{vo} , we can achieve a significant reduction in the mean error of the heat transfer predictions for both R410A and R407C. This leads to a better prediction of the heat transfer coefficient of the flow and thereby helps in an efficient condenser design.

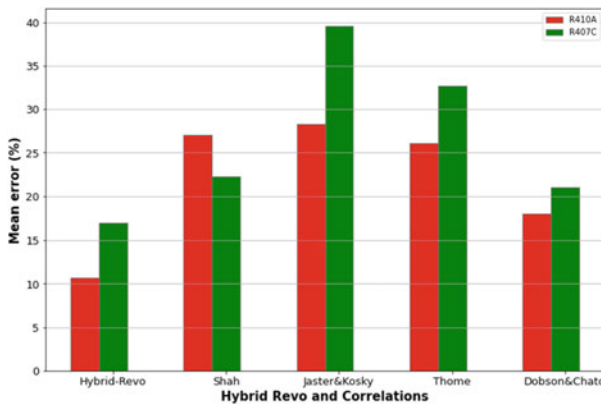


Fig. 5 Comparison of the Hybrid- Re_{vo} approach against individual correlations considering the mean error of all the data points

References

1. Shah MM (1979) A general correlation for heat transfer during film condensation inside pipes. *Int J Heat Mass Transf* 22:547–556. [https://doi.org/10.1016/0017-9310\(79\)90058-9](https://doi.org/10.1016/0017-9310(79)90058-9)
2. Jaster H, Kosky PG (1976) Condensation heat transfer in a mixed flow regime. *Int J Heat Mass Transf* 19:95–99. [https://doi.org/10.1016/0017-9310\(76\)90014-4](https://doi.org/10.1016/0017-9310(76)90014-4)
3. Thome JR, el Hajal J, Cavallini A (2003) Condensation in horizontal tubes, part 2: new heat transfer model based on flow regimes. *Int J Heat Mass Transf* 46:3365–3387. [https://doi.org/10.1016/S0017-9310\(03\)00140-6](https://doi.org/10.1016/S0017-9310(03)00140-6)
4. Dobson MK, Chato MAJC (1998) Condensation in smooth horizontal tubes
5. Montreal protocol on substances that deplete the ozone layer, Final Act: 1989. United Nations Environment Programme (2000)
6. del Col D, Cavallini A, Thome JR (2005) Condensation of zeotropic mixtures in horizontal tubes: new simplified heat transfer model based on flow regimes. *J Heat Transfer* 127:221–230. <https://doi.org/10.1115/1.1857951>
7. Silver L (1947) Gas cooling with aqueous condensation. *Trans. Inst. Chem. Eng* 25: 30–42
8. Bell KJ, Ghaly MA (1972) Approximate generalized design method for multicomponent/partial condensers. In: *AIChE Pap*
9. Jung D, Cho Y, Park K (2004) Flow condensation heat transfer coefficients of R22, R134a, R407C, and R410A inside plain and microfin tubes. *Int J Refrig* 27:25–32. [https://doi.org/10.1016/S0140-7007\(03\)00122-1](https://doi.org/10.1016/S0140-7007(03)00122-1)
10. Aprea C, Greco A, Vanoli GP (2003) Condensation heat transfer coefficients for R22 and R407C in gravity driven flow regime within a smooth horizontal tube. *Int J Refrig* 26:393–401. [https://doi.org/10.1016/S0140-7007\(02\)00151-2](https://doi.org/10.1016/S0140-7007(02)00151-2)
11. Chato JC (1962) Laminar condensation inside horizontal and inclined tubes. *ASHRAE J* 4
12. Rosson H, Meyers J (1965) Point of values of condensing film coefficients inside a horizontal tube. *Chem Eng Prog Symp Ser* 61:190–199
13. Singh A, Ohadi MM, Dessiatoun Sv (1996) Empirical modeling of stratified-wavy flow condensation heat transfer in smooth horizontal tubes. *ASHRAE Trans* 102
14. Dobson MK (1994) Heat transfer and flow regimes during condensation in horizontal tubes
15. Cavallini A, Col D del Doretto L, Rossetto L, Longo GA (2000) Purdue e-pubs condensation heat transfer of new refrigerants: advantages of high pressure fluids condensation heat transfer of new refrigerants: advantages of high pressure fluids
16. Boissieux X, Heikal MR, Johns RA (2000) Two-phase heat transfer coefficients of three HFC refrigerants inside a horizontal smooth tube, part II: condensation
17. Sweeney KA, Chato JC (1996) The heat transfer and pressure drop behaviour of a zeotropic refrigerant mixture in a micro finned tube. *ACRC Technical Report 95*, University of Illinois at Urbana-Champaign
18. el Hajal J, Thome JR, Cavallini A (2003) Condensation in horizontal tubes, part 1: two-phase flow pattern map. *Int J Heat Mass Transf* 46:3349–3363. [https://doi.org/10.1016/S0017-9310\(03\)00139-X](https://doi.org/10.1016/S0017-9310(03)00139-X)
19. Soliman HM (1982) On the annular-to-wavy flow pattern transition during condensation inside horizontal tubes. *Can J Chem Eng* 60:475–481
20. Van Rossum G, Drake FL (2009) Python 3 reference manual
21. Steiner D (1993) Heat transfer to boiling saturated liquids. *VDI-Warmeatlas*
22. Rouhani SZ, Axelsson E (1970) Calculation of void volume fraction in the subcooled and quality boiling regions. *Int J Heat Mass Transfer* 13. [https://doi.org/10.1016/0017-9310\(70\)90114-6](https://doi.org/10.1016/0017-9310(70)90114-6)
23. Gronnerud R (1979) Investigation of liquid hold-up, flow-resistance and heat transfer in circulation type evaporators, part IV: two-phase flow resistance in boiling refrigerants. International Institute of Refrigeration
24. Lemmon EW, Bell IH, Huber ML, McLinden MO (2018) NIST standard reference database 23: reference fluid thermodynamic and transport properties- REFPROP, Version 10.0

Dispersion of Love Waves in a Dry Sandy Layer Imperfectly Attached to a Microcontinuum Substrate: An Analysis with Stress-Free and Clamped Top Surface Conditions



Shikha Deep and Vikas Sharma

Abstract The present problem investigates the dispersion of Love waves in a dry sandy layer imperfectly attached to a microstructural substrate which is modeled through consistent couple stress theory. An analysis has been done in two cases, first, when the top surface of dry sandy layer is stress-free, and second, when it is clamped. Dispersion relations are derived for both the cases separately, using effective boundary conditions. A special case is also derived when dry sandy layer is perfectly attached to the substrate under both conditions. A detailed analysis has been done in both cases by studying the impacts of various parameters such as microstructural parameter associated with the half-space, sandiness parameter, thickness of the layer, imperfectness parameter on the propagation behavior of Love waves.

Keywords Dry sandy material · Consistent couple stress theory · Love waves · Clamped layer · Characteristic length · Imperfect interface

1 Introduction

Love waves are surface waves whose particle motion is purely horizontal along the surface of the medium and is normal to the direction of propagation of wave. These waves propagate through a layered structure, having a layer of finite thickness followed by a substrate. For the origination of these waves, the surface layer needs to be slower than the substrate. Love waves have numerous applications in various areas such as seismology, geology, geophysics, biosensors, and in SAW devices [1–3].

The presence of sandy soil, sandy rocks in the interior of Earth can influence the propagation of seismic waves. Weiskopf [4] pioneered the constituent relation for sandy materials and for such materials, $\frac{E}{\mu^d} > 2(1 + \sigma)$, where, $\sigma =$ Poisson's ratio, $\mu^d =$ Modulus of rigidity, and $E =$ Young's modulus. For sandy soil, the relationship between these material parameters is modified as $E = 2\eta_1(1 + \sigma)\mu^d$

S. Deep (✉) · V. Sharma

Department of Mathematics, Lovely Professional University, Phagwara, Punjab 144411, India
e-mail: shikhathakur493@gmail.com

V. Sharma

e-mail: vikas.sharma@lpu.co.in; vikassharma10a@yahoo.co.in

© The Author(s), under exclusive license to Springer Nature Singapore Pte Ltd. 2022

T. Tadepalli and V. Narayanamurthy (eds.), *Recent Advances in Applied Mechanics*,

Lecture Notes in Mechanical Engineering, https://doi.org/10.1007/978-981-16-9539-1_52

by introducing a parameter (η_1) called as sandy parameter. The inequality stated above holds, if the value of η_1 is greater than one and if $\eta_1 = 1$, then it corresponds to classical relationship between these parameters for an isotropic elastic material. Many researchers have theoretically investigated the problems of propagation of waves using sandy materials [5–7].

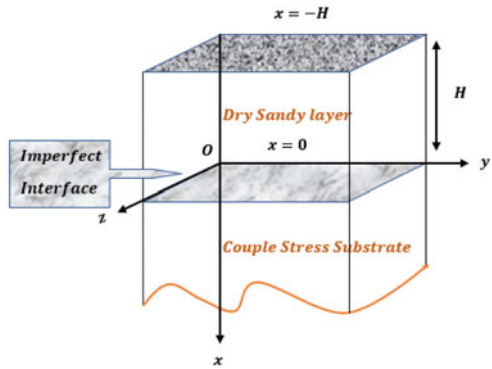
Microcontinuum theories are developed to understand the behavior of materials having internal microstructures, such as polymers, bones, and composites, etc. Voigt [8] originated the idea of couple stresses in materials and later, many researchers improvised this idea to propose various theories [9, 10]. Hadjesfandiari and Dargush [11] proposed consistent couple stress theory and introduced a new material constant called couple stress coefficient (η_2) other than classical Lamé's constants. This material constant is associated with shear modulus through a relation $\eta_2 = \mu_2 l^2$, where l is called characteristic length which is supposed to be of the order of cell size in composites or average spacing in fibrous composites. Couple stress theory has been incorporated by number of researchers in various problems [12–15]. Since, the interior of Earth is heterogeneous in nature, so to study any problem involving earth, there is a need to incorporate microcontinuum theories. Various layers inside Earth are not perfectly attached and imperfectness between layers can influence the propagation of waves. Perfect bonding between layers leads to continuity of field variables across the interface. For imperfect bonding between layers, the difference between displacement components is considered to be linearly proportional to traction vector. Many authors have modeled the idea of imperfectness at the interfacial surfaces in problems of wave propagation [16, 17].

Kaplunov et al. [18] have studied propagation of Love waves in a layered half-space with clamped surface. They stated that Love waves can exist in clamped layered structure, provided shear waves velocity of half-space exceeded the velocity of layer. Love waves are studied by many researchers in a stress-free layered structure, but authors haven't found much literature on Love waves in a clamped layered structure. In this problem, Love waves propagation is analytically investigated in a dry sandy layer which is attached imperfectly to a microstructural couple stress substrate. Propagation of Love waves is investigated in two scenarios, one when the top surface of attached layer is stress-free and the other, in which free surface of layer is clamped. Dispersion equations have been obtained by using effective boundary conditions and impacts of numerous parameters like imperfectness, thickness of layer, sandiness, and characteristic length have been investigated on the dispersion of Love waves.

2 Statement of the Problem

It is considered that a dry sandy layer of finite thickness H is imperfectly attached with a microstructural substrate as depicted in Fig. 1. The origin of coordinate system is assumed at the joining surface of two media. Further, x -axis is going vertically downward into the substrate and y -axis is along the direction of propagation of wave. The propagation of Love waves is causing displacement in z -direction only, and

Fig. 1 A geometry of the problem



displacement components for layer and microstructural substrate are (u_1, v_1, w_1) , (u_2, v_2, w_2) respectively. All field variables are independent of z -coordinate, that is $\frac{\partial}{\partial z} \equiv 0$ and for Love waves propagation in considered geometry, it is assumed $u_1 = 0, v_1 = 0, u_2 = 0, v_2 = 0, w_1 = w_1(x, y, t)$ and $w_2 = w_2(x, y, t)$.

3 Solution of the Problem

3.1 Solution of a Dry Sandy Layer

The equation of motion for a layer without body forces [19] is given by

$$\frac{\mu_1}{\eta_1} \left(\frac{\partial^2 w_1}{\partial x^2} + \frac{\partial^2 w_1}{\partial y^2} \right) = \rho_1 \frac{\partial^2 w_1}{\partial t^2} \tag{1}$$

where μ_1 is Lamé's constant, η_1 is sandiness parameter and ρ_1 is density of a material. The constitutive relation for a dry sandy medium is

$$\tau_{ij} = \lambda_1 e_{ii} \delta_{ij} + 2 \frac{\mu_1}{\eta_1} e_{ij} \tag{2}$$

τ_{ij} are stress components, δ_{ij} is Kronecker's delta, λ_1 is Lamé's constant, e_{ij} are strain components, where $i, j = 1, 2, 3$. Now, assume solution of Eq. (1) as $w_1(x, y, t) = f(x)e^{ik(y-ct)}$, where c is phase velocity and k is wave number, we get

$$\frac{d^2 f}{dx^2} + k^2 R^2 f(x) = 0, \text{ where } R = \sqrt{\frac{\eta_1 c^2}{\beta_1^2} - 1} \text{ and } \beta_1 = \sqrt{\frac{\mu_1}{\rho_1}} \tag{3}$$

Solution of Eq. (3) is

$$f(x) = A_1 \cos(kRx) + B_1 \sin(kRx) \tag{4}$$

where A_1 and B_1 are arbitrary constants.

Therefore, the non-vanishing displacement component of dry sandy layer becomes

$$w_1(x, y, t) = (A_1 \cos(kRx) + B_1 \sin(kRx))e^{ik(y-ct)} \tag{5}$$

The non-vanishing stress component for a dry sandy medium is

$$\tau_{13} = \frac{\mu_1}{\eta_1} (kR)(-A_1 \sin(kRx) + B_1 \cos(kRx))e^{ik(y-ct)} \tag{6}$$

3.2 Solution of Microstructural Substrate

The equation of motion for isotropic microstructural substrate described by consistent couple stress theory [11] is given as

$$(\lambda_2 + \mu_2 + \eta_2 \nabla^2) \nabla(\nabla \cdot \vec{w}) + (\mu_2 - \eta_2 \nabla^2) \nabla^2 \vec{w} = \rho_2 \frac{\partial^2 \vec{w}}{\partial t^2} \tag{7}$$

λ_2, μ_2 are Lamé’s parameters, ρ_2 is density, $\eta_2 = \mu_2 l^2$ is couple stress coefficient, l is the characteristic length, and $\vec{w} = (u_2, v_2, w_2)$ is the displacement vector.

The constitutive relations for microstructural substrate, are

$$\sigma_{ji} = \lambda_2 w_{k,k} \delta_{ij} + \mu_2 (w_{i,j} + w_{j,i}) - \eta_2 \nabla^2 (w_{i,j} - w_{j,i}) \tag{8}$$

$$\mu_{ji} = 4\eta_2 (\omega_{i,j} - \omega_{j,i}), \text{ where } \omega_i = \frac{1}{2} \epsilon_{ijk} w_{k,j} \tag{9}$$

σ_{ji} is non-symmetric stress tensor, w_i are displacement components, μ_{ji} is skew-symmetric couple stress tensor, ϵ_{ijk} is permutation tensor, and $i, j, k = 1, 2, 3$. By imposing conditions of Love waves propagation, equation of motion (7) reduces to

$$\left(\frac{\partial^2 w_2}{\partial x^2} + \frac{\partial^2 w_2}{\partial y^2} \right) - l^2 \left(\frac{\partial^4 w_2}{\partial x^4} + \frac{\partial^4 w_2}{\partial y^4} + 2 \frac{\partial^4 w_2}{\partial x^2 \partial y^2} \right) = \frac{1}{\beta_2^2} \frac{\partial^2 w_2}{\partial t^2}, \text{ where } \beta_2 = \sqrt{\frac{\mu_2}{\rho_2}} \tag{10}$$

Assume solution of Eq. (10) as $w_2(x, y, t) = g(x)e^{ik(y-ct)}$, where c is phase velocity and k is wave number, we get

$$\frac{d^4 g}{dx^4} - L \frac{d^2 g}{dx^2} + M g(x) = 0 \tag{11}$$

where $L = 2k^2 + \frac{1}{l^2}$ and $M = k^4 + \frac{k^2}{l^2} - \frac{(kc)^2}{l^2\beta_2^2}$

In elastic half-space, it is needed that amplitude of waves should decrease with an increase in depth. So, we get solution of Eq. (11) as $g(x) = A_2e^{-px} + B_2e^{-qx}$

where A_2 and B_2 are arbitrary constants and $p = \sqrt{\frac{L+\sqrt{L^2-4M}}{2}}$ and $q = \sqrt{\frac{L-\sqrt{L^2-4M}}{2}}$.

The displacement component of the microstructural substrate becomes

$$w_2(x, y, t) = (A_2e^{-px} + B_2e^{-qx})e^{ik(y-ct)} \quad (12)$$

The force stress and couple stress components for the substrate, are

$$\sigma_{13} = \mu_2[pA_2(l^2p^2 - l^2k^2 - 1)e^{-px} + qB_2(l^2q^2 - l^2k^2 - 1)e^{-qx}]e^{ik(y-ct)} \quad (13)$$

$$\mu_{12} = -2\mu_2l^2[A_2(p^2 - k^2)e^{-px} + B_2(q^2 - k^2)e^{-qx}]e^{ik(y-ct)} \quad (14)$$

4 Boundary Conditions

4.1 Stress-Free Boundary Conditions

- i. The stress component vanishes at the upper surface of layer, that is $\tau_{13} = 0$ at $x = -H$
- ii. Layer and microstructural substrate are not perfectly attached, so, difference in displacement components is proportional to stress tensor, that is $\tau_{13} = G(w_2 - w_1)$ at $x = 0$, G defines the degree of imperfectness
- iii. Stress components are continuous at the interface, so, $\tau_{13} = \sigma_{13}$ at $x = 0$
- iv. Couple stress coefficient vanishes at the interface, that is $\mu_{12} = 0$ at $x = 0$

By implementing the boundary conditions, we obtain following equations

$$A_1 \sin(kRH) + B_1 \cos(kRH) = 0 \quad (15)$$

$$GA_1 + \left(\frac{\mu_1 k R}{\eta_1}\right) B_1 - GA_2 - GB_2 = 0 \quad (16)$$

$$\left(\frac{\mu_1 k R}{\eta_1}\right) B_1 + (\mu_2 p - \mu_2 l^2 p^3 + \mu_2 l^2 p k^2) A_2 + (\mu_2 q - \mu_2 l^2 q^3 + \mu_2 l^2 q k^2) B_2 = 0 \quad (17)$$

$$(p^2 - k^2) A_2 + (q^2 - k^2) B_2 = 0 \quad (18)$$

For the non-trivial solution of the Eqs. (15)–(18), determinant of the arbitrary coefficients must vanish, so we get following dispersion relation for propagation of Love

waves, under stress-free conditions at top surface of layer, when layer and substrate are imperfectly attached.

$$\tan(kRH) = \frac{G((q^2 - k^2)T_1 - (p^2 - k^2)T_2)}{\left(\frac{\mu_1 k R}{\eta_1}\right)((q^2 - k^2)(T_1 + G) - (p^2 - k^2)(T_2 + G))} \quad (19)$$

where $T_1 = \mu_2 p - \mu_2 l^2 p^3 + \mu_2 l^2 p k^2$, $T_2 = \mu_2 q - \mu_2 l^2 q^3 + \mu_2 l^2 q k^2$.

If $G \rightarrow \infty$, interface between dry sandy layer and microstructural couple stress substrate becomes perfect in nature, so dispersion relation given in Eq. (19), reduces to

$$\tan(kRH) = \frac{(q^2 - k^2)T_1 - (p^2 - k^2)T_2}{\left(\frac{\mu_1 k R}{\eta_1}\right)(q^2 - p^2)} \quad (20)$$

Equation (20) shows dispersion relation for propagation of Love waves under stress-free conditions when layer and half-space are perfectly attached.

4.2 Clamped Boundary Conditions

In this case, all the conditions stated above will remain same, except the first condition. Here, it is assumed that top surface of layer is clamped, and for achieving this condition, displacement must vanish, therefore, first boundary condition will be taken as $w_1(x, y, t) = 0$ at $x = -H$. By imposing stated condition, we get following equation

$$A_1 \cos(kRH) - B_1 \sin(kRH) = 0 \quad (21)$$

By solving Eqs. (16), (17), (18) & (21) for a non-trivial solution, we get following dispersion relation for propagation of Love waves with clamped boundary conditions, when two materials are imperfectly attached.

$$\tan(kRH) = \frac{\left(\frac{\mu_1 k R}{\eta_1}\right)((q^2 - k^2)(T_3 + G) - (p^2 - k^2)(T_4 + G))}{G((p^2 - k^2)T_4 - (q^2 - k^2)T_3)} \quad (25)$$

where $T_3 = \mu_2 p - \mu_2 l^2 p^3 + \mu_2 l^2 p k^2$, $T_4 = \mu_2 q - \mu_2 l^2 q^3 + \mu_2 l^2 q k^2$.

If $G \rightarrow \infty$, layer and substrate will be in perfect mechanical contact and dispersion relation in Eq. (25) reduces to

$$\tan(kRH) = \frac{\left(\frac{\mu_1 k R}{\eta_1}\right)(q^2 - p^2)}{(p^2 - k^2)T_4 - (q^2 - k^2)T_3} \quad (26)$$

5 Numerical Results and Discussion

The material parameters for dry sandy layer are [20], $\mu_1 = 6 \times 10^9 \text{ N/m}^2$, $\rho_1 = 2300 \text{ kg/m}^3$ and for couple stress substrate are [21], $\mu_2 = 30.5 \times 10^9 \text{ N/m}^2$, $\rho_2 = 2717 \text{ kg/m}^3$. The impacts of various parameters are depicted on the phase velocity of Love waves, by considering initial mode ($n = 0$) of Love waves, when stress-free conditions prevail at the top surface of layer. It is found that initial mode ($n = 0$) of Love waves is not conclusive when the top surface of layer is clamped, so for this case, graphical results are depicted by considering the first mode ($n = 1$) of Love waves. In all Figs. 2, 3, 4, results are shown by considering two cases, firstly when a layer is perfectly attached to the half-space and secondly when two media are imperfectly attached. For all the Figs. 2, 3, 4, the value of the imperfectness parameter is considered as $G = 30.5 \times 10^9$. In all figures, dimensionless phase velocity is considered along y -axis, and dimensionless wave number is along x -axis.

5.1 The Impacts of Microstructural Parameter of Substrate

The effect of microstructures is revealed through characteristic length (l), which is supposed to be of order of internal cell size, on phase velocity of Love waves by assuming three values of the parameter as $l = 0.0001, 0.0004, 0.0006 \text{ m}$. For graphical illustrations, other parameters are considered as $H = 1.9 \text{ m}$ and $\eta_1 = 1.2$. Figure 2(a) is plotted for stress-free boundary conditions and Fig. 2(b) is plotted under clamped boundary conditions. Figures 2(a) and 2(b) reveal that characteristic length favors phase velocity and phase velocity of Love waves increasing, when the value of this parameter increases. Impacts of characteristic length parameter are meager and it is expected, as it is microstructural parameter. Results are depicted by considering both the cases, one when two media are mechanically in perfect contact and another when they are imperfectly attached. Although the pattern is same in both cases, but phase velocity is higher when layer and substrate are perfectly attached.

5.2 The Influence of the Sandiness Parameter (η_1)

Impacts of sandiness parameter are presented on phase velocity by considering three values as $\eta_1 = 1, 1.4, 1.6$. Other parameters are $l = 0.0004 \text{ m}$, $H = 1.9 \text{ m}$. Figure 3(a) is plotted, when top surface of layer is stress-free and in Fig. 3(b) layer is clamped. It can be noticed that phase velocity decreases, when the values of sandiness parameter increase and behavior is same, whether two media are perfectly/imperfectly attached. Therefore, sandiness parameter opposes phase velocity. For any given value of sandiness parameter, the phase velocity is maximum,

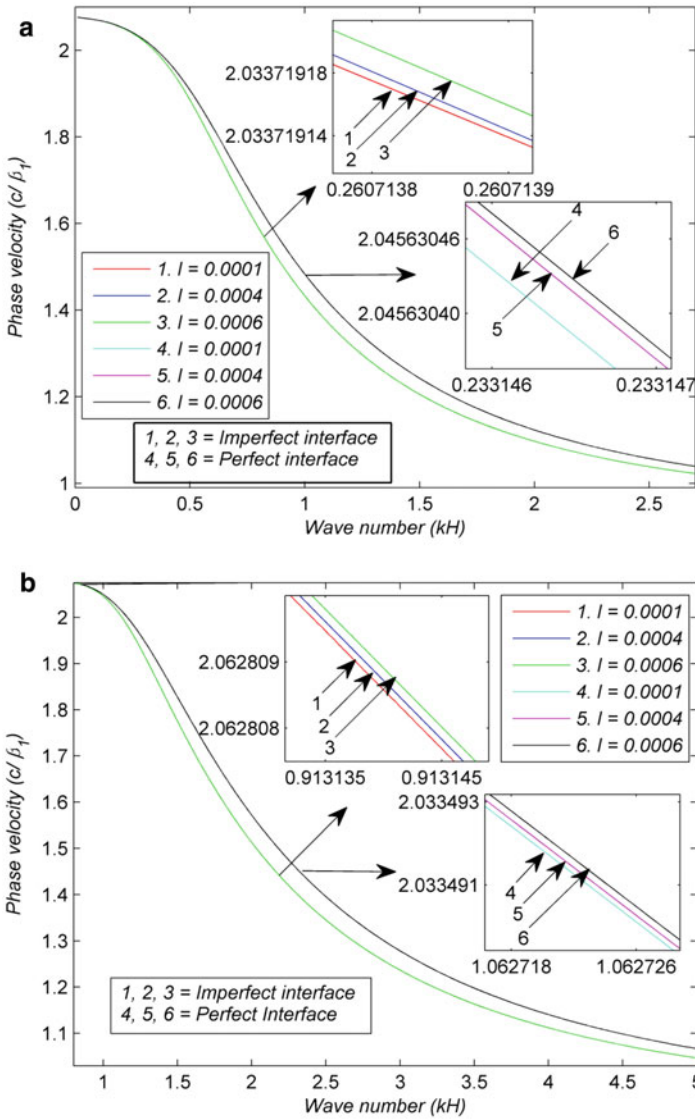


Fig. 2 a Dispersion profiles depicting impact of characteristic length parameter (l) under stress-free condition. **b** Dispersion profiles depicting impact of characteristic length parameter (l) under clamped condition

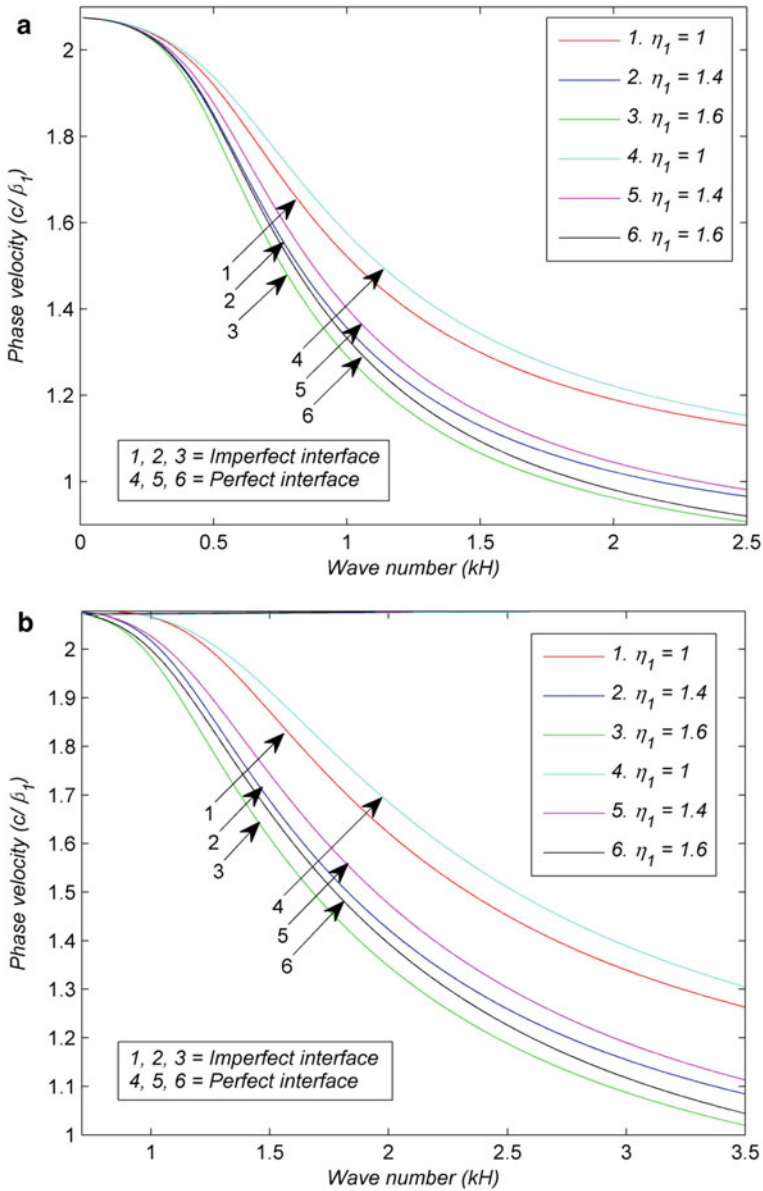


Fig. 3 **a** Dispersion profiles depicting impact of sandiness parameter (η_1) under stress-free condition. **b** Dispersion profiles depicting impact of sandiness parameter (η_1) under clamped condition.

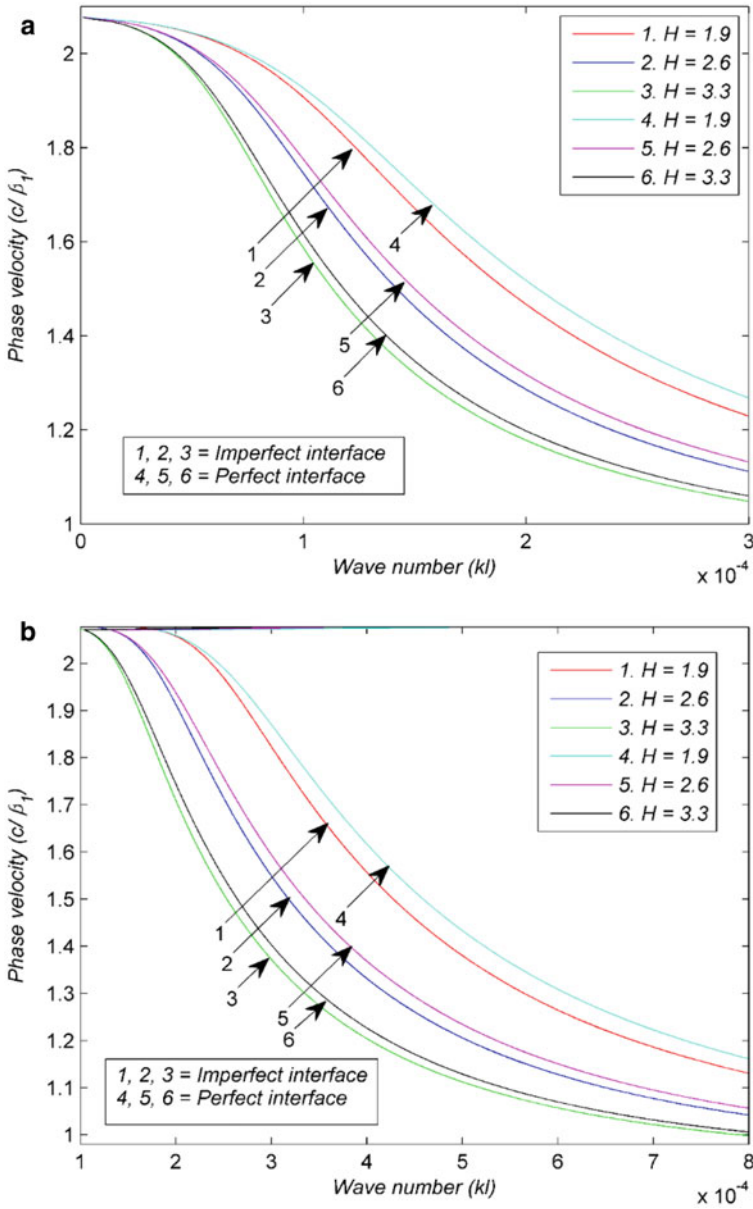


Fig. 4 **a** Dispersion profiles depicting impact of the thickness of the layer (H) under stress-free condition. **b** Dispersion profiles depicting impact of the thickness (H) under clamped condition.

when two media are attached perfectly as compared to when they are attached imperfectly.

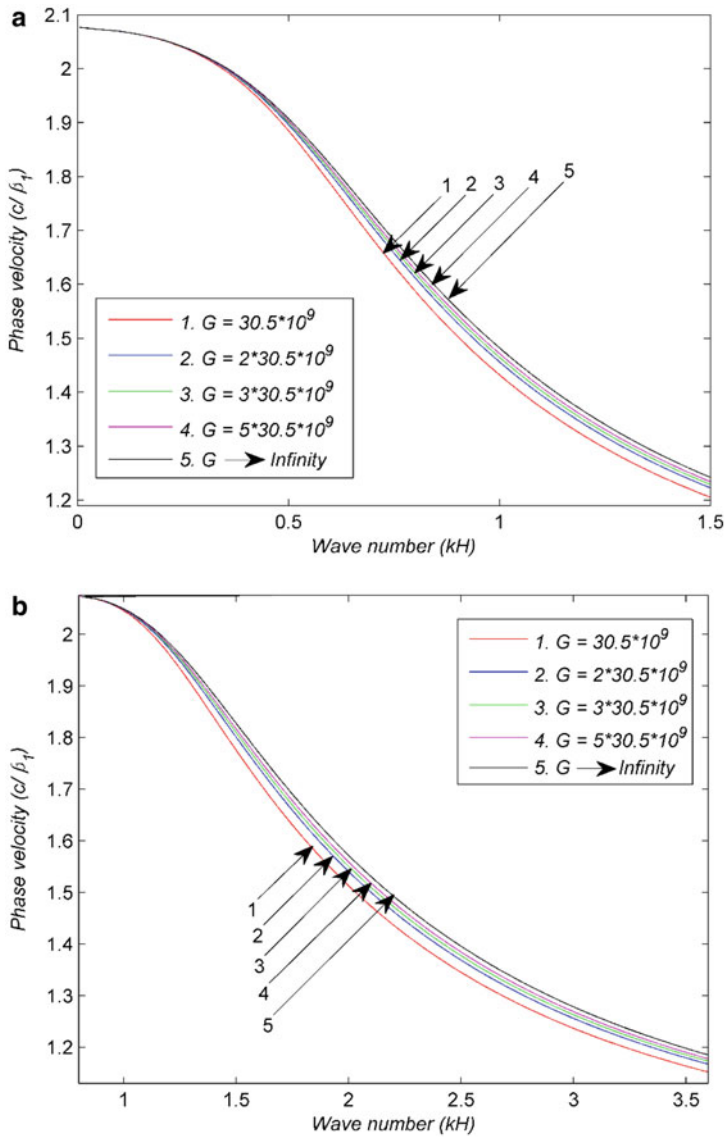


Fig. 5 **a** Dispersion profiles depicting impact of the imperfectness parameter (G) under stress-free condition. **b** Dispersion profiles depicting impact of the imperfectness parameter (G) under clamped condition.

5.3 The Influence of Thickness of the Layer (H)

To elucidate the effects of thickness of layer on phase velocity, graphs are shown by considering three values of thickness as $H = 1.9, 2.6, 3.3$ m. The values of other parameters are $l = 0.0004$ m and $\eta_1 = 1.2$. Figure 4(a) is drawn by taking stress-free conditions and for Fig. 4(b) layer is clamped. From both figures, it can be found that thickness of the layer works against the phase velocity that means phase velocity decreasing, when value of thickness parameter of layer increases. The pattern remains the same whether layer and half-space are perfectly attached, or they are imperfectly attached.

5.4 The Impacts of Imperfectness Parameter (G)

To find impacts of imperfectness parameter on phase velocity, Figs. 5(a)–(b) are shown by considering five values as $G = 30.5 \times 10^9, 2 \times 30.5 \times 10^9, 3 \times 30.5 \times 10^9, 5 \times 30.5 \times 10^9, G \rightarrow \infty$. Other parameters are kept as $H = 1.9$ m, $\eta_1 = 1.2$ and $l = 0.0004$ m. When $G \rightarrow \infty$, dry sandy layer and microstructural couple stress substrate are perfectly attached. Figure 5(a) is plotted under stress-free conditions at top surface of the layer, and for Fig. 5(b) layer is clamped. Since the degree of imperfectness and parameter G are inversely proportional, so from the trends, it is found that with the decrease in degree of imperfectness (increasing value of G) at the interface, phase velocity is increasing. Phase velocity is maximum, when degree of imperfectness is least ($G \rightarrow \infty$) and two media are in perfect contact.

6 Conclusions

The problem explores the possibility of existence of Love waves in dry sandy layer followed by a substrate which is described using consistent couple stress theory under two different sets of boundary conditions. In one case, it is assumed that upper surface of layer is stress-free, and in second case, it is considered that free surface of the layer is clamped. It is found that the initial mode of Love waves is not conclusive when top surface of layer is clamped, but higher modes are found clearly and hence all the graphical illustrations are given in this case using the first mode ($n = 1$) of Love waves.

In case of stress-free conditions at the top surface of layer initial as well as higher modes are clearly visible, so in this case, graphical results are given using initial mode of Love waves ($n = 0$). Results are further depicted when layer and substrate are perfectly/imperfectly attached. In general, it is found that phase velocity is higher when two media are in perfect contact as compared to when they are imperfectly attached.

Results of microstructural parameter characteristic length (l) associated with the substrate, are shown on the phase velocity and is observed that this parameter favors phase velocity of Love waves. Impacts of this parameter on phase velocity are meager, and it is quite obvious, as characteristic length parameter is supposed to be of the order of internal microstructure of the material.

It is noticed that the sandiness parameter (η_1) works against phase velocity and phase velocity decreases when value of this parameter increases. The impacts of thickness of layer (H) are also noticed on the phase velocity and it is seen that phase velocity of Love waves decreases with increase in the value of thickness of layer.

Impacts of imperfectness parameter (G) are observed on phase velocity of Love waves. When the value of imperfectness parameter (G) increases, the interface tends to become perfect that means bonding between two media becomes stronger and phase velocity is increasing with increasing value of the parameter (G). Phase velocity is maximum when layer and half-space are attached perfectly ($G \rightarrow \infty$).

The problem covers two major aspects, first the study of Love waves when top surface of layer is clamped, secondly the role of imperfectness which measures the nature of bonding between layer and substrate on propagation of Love waves. Further substrate is described using size-dependent couple stress theory, so it highlights the impact of order of inner microstructures of the material on phase velocity of Love waves. The findings of this paper can be useful for various areas involving applications of Love waves.

References

1. Kielczyński P (2018) Properties and applications of love surface waves in seismology and biosensors. *Surface Waves - New Trends Dev Intech Open*. <https://doi.org/10.5772/intechopen.75479>
2. Roach P, Atherton S, Doy N, McHale G, Newton M (2007) SU-8 guiding layer for love wave devices. *Sensors* 7(11):2539–2547
3. Du J, Harding G, Collings A, Dencher P (1997) An experimental study of Love-wave acoustic sensors operating in liquids. *Sens Actuators A* 60(1–3):54–61. [https://doi.org/10.1016/S0924-4247\(96\)01424-0](https://doi.org/10.1016/S0924-4247(96)01424-0)
4. Weiskopf WH (1945) Stresses in solids under foundation. *J Franklin Inst* 239(6):445–465. [https://doi.org/10.1016/0016-0032\(45\)90189-x](https://doi.org/10.1016/0016-0032(45)90189-x)
5. Deep S, Sharma V (2020) Love type waves in a dry sandy layer lying over an isotropic elastic half-space with imperfect interface. *J Phys Conf Ser* 1531:012069. <https://doi.org/10.1088/1742-6596/1531/1/012069>
6. Kundu S, Maity M (2017) Edge wave propagation in an initially stressed dry sandy plate. *Procedia Eng* 173:1029–1033
7. Pal PC, Kumar S, Bose S (2015) Propagation of Rayleigh waves in anisotropic layer overlying a semi-infinite sandy medium. *Ain Shams Eng J* 6(2):621–627. <https://doi.org/10.1016/j.asej.2014.11.003>
8. Voigt W (1887) *Theoretische Studien fiber die Elastizitatsverhiltnisse der Kristalle (Theoretical Studies on the Elasticity Relationships of Crystals)*, Abh. Gesch.Wissenschaften, 34
9. Toupin RA (1962) Elastic materials with couple-stresses. *Archive Rational Mech Anal* 11(1):385–414

10. Eringen AC (1968) Theory of micropolar elasticity, In: Liebowitz H (Ed) Fracture, Academic Press, New York. 2, pp 662–729
11. Hadjesfandiari AR, Dargush GF (2011) Couple stress theory for solids. *Int J Solids Struct* 48(18):2496–2510
12. Deep S, Sharma V (2021), Love wave propagation in viscoelastic layer sandwiched between fiber-reinforced layer and consistent couple stress substrate. *Iranian J Sci Technol Trans Mech Eng* doi: <https://doi.org/10.1007/s40997-020-00411-3>
13. Xu LM, Fan H (2018) Shear horizontal wave in a classical elastic half-space covered by a surface membrane treated by the couple stress theory. *J Appl Phys* 124(22):225303. <https://doi.org/10.1063/1.5040719>
14. Goyal R, Kumar S (2019) Quantifying viscoelastic, piezoelectric, and couple stress effects on love-type wave propagation. *Smart Mater Struct* 28(10):105021. <https://doi.org/10.1088/1361-665X/ab39bf>
15. Mandi A, Kundu S, Pati P, Pal PC (2020) An analytical study on the Rayleigh wave generation in a stratified structure. *Appl Math Mech* 41(7):1039–1054. <https://doi.org/10.1007/s10483-020-2625-9>
16. Goyal R, Kumar S (2021) Estimating the effects of imperfect bonding and size-dependency on Love-type wave propagation in functionally graded orthotropic material under the influence of initial stress. *Mech Mater* 155:103772. <https://doi.org/10.1016/j.mechmat.2021.103772>
17. Sharma V, Sharma V (2019) Love waves in fiber-reinforced layer imperfectly bonded to microstructural couple stress substrate. *J Theor Appl Mech* 58(1):221–232
18. Kaplunov J, Prikazchikov D, Sultanova L (2019) Rayleigh-type waves on a coated elastic half-space with a clamped surface. *Philosophical Trans Roy Soc A: Math Phys Eng Sci* 377(2156):20190111. <https://doi.org/10.1098/rsta.2019.0111>
19. Kar BK, Pala AK, Kalyani VK (1986) Propagation of Love waves in an irregular dry sandy layer. *Acta Geophysica Polonica* 34:157–170
20. Pal PC, Kumar S, Mandal D (2015) Surface wave propagation in sandy layer overlying a liquid saturated porous half-space and lying under a uniform liquid layer. *Mech Adv Mater Struct* 23(1):59–65
21. Vardoulakis I, Georgiadis HG (1997) SH surface waves in a homogeneous gradient-elastic half-space with surface energy. *J Elast* 47(2):147–165

Importance of Boundary Conditions in Multi-Physics Analysis of One-Dimensional ‘smart’ Beam



P. M. G. Bashir Asdaque  and Sitikantha Roy 

Abstract Dimensional reduction of the piezoelectric laminated smart beams led to the development of a two-dimensional cross-sectional analysis and later one-dimensional smart beam formulation. In this work, the contribution and effects of boundary conditions have been studied for multi-physics straight, one-dimensional beams. Here, Multiphysics refers to the coupled electro-elastic phenomena, exhibiting both direct and inverse piezoelectric effects on the straight ‘smart’ beam. The clamped-free and clamped–clamped type boundary cases were studied. It was found that the boundary conditions affect the behavior of the smart beams and their sensing capabilities. Such studies are important while designing ‘smart’ devices for monitoring and control purposes.

Keywords Smart structures · Slender beams · Composite · Piezoelectric

1 Introduction

The advance and major contribution of laminated and embedded piezoelectric in structures is the monitoring and control of the crucial structures. The slenderness parameter of engineering structures like wind turbines, helicopter blades, truss-links, and aero plane wings facilitates their mathematical modeling as ‘beams’. Monitoring and control of these structures are crucial and challenging task. One of recent challenges are attitude and maneuvering control of satellite bae, consisting of several links. Hodges [1] derived mixed variational principle for passive, slender beams. With the passage of time, this led to the development of a generalized and robust geometrically nonlinear analysis tool [2] for passive beams. Then the electro-elastic effects of piezoelectric based beams were included in the analysis, paving way for a theoretical modeling of smart beams, at cross-sectional level [3, 4], and one-dimensional ‘sensor’ beam [5]. In this work, both actuation and sensing physics are included in the theory and a straight beam compromised of actuation and sensing portions is studied for Clamped-Free (Cantilever) & clamped–clamped boundary conditions. The main

P. M. G. B. Asdaque (✉) · S. Roy
Department of Applied Mechanics, IIT Delhi, New Delhi 110016, India

purpose of this research work is to deliver a robust one-dimensional methodology to study both active and sensory piezoelectric physics simultaneously. The other fruitful outcome is the exploration of the type of boundary conditions depending upon the monitoring and control situations.

2 Methodology

The constitutive relations obtained from cross-sectional analysis by Roy et al. [3] for actuation, and Banerjee and Roy [4] for sensing were applied for theoretical formulation of a ‘smart’ beam. While the constitutive relation for actuation is one way coupled, for the sensing case it is a two-way fully coupled relation. The constitutive equations are then used in the Hamiltonian to obtain the mixed variational statement. From there, finite elements are derived. We present the flow chart of the whole methodology as follows:



The Hamiltonian is given as,

$$\begin{aligned}
 \int_{t_1}^{t_2} \int_0^l [\delta(K - U) + \overline{\delta W}] dx_1 dt &= \int_{t_1}^{t_2} \int_{\Omega_{Ac}} [\delta(K_{Ac} - U_{Ac}) + \overline{\delta W_{Ac}}] dx_1 dt \\
 + \int_{t_1}^{t_2} \int_{\Omega_{Sn}} [\delta(K_{Sn} - U_{Sn}) + \overline{\delta W_{Sn}}] dx_1 dt &= \overline{dA}.
 \end{aligned}
 \tag{1}$$

In Eq. (1), K and U represents the kinetic and potential energy whereas δW represents the virtual work equivalent. The subscripts ‘Ac’ and ‘Sn’ indicates the active and sensory portions. Also, dA represents the virtual action at the end of the beam and at the end of the time. Overbar indicates that they may not be the exact variation of the respective function. Readers are suggested to refer Banerjee and Roy [4], and Roy et al. [3] for constitutive relations and cross-sectional analysis. Proceeding with this Hamiltonian, as shown in flowchart, the final mixed variational statement obtained is given as follows,

$$\begin{aligned}
& \int_{\Omega_{Ac}} \left\{ \delta u'_g{}^T F_g^o + \overline{\delta \psi}'_g{}^T M_g^o + \right. \\
& \left. \overline{\delta \psi}'_g{}^T \left[\dot{H}_g + \tilde{\omega}_g H_g + \tilde{V}_g P_g - C^{gD} (\tilde{e}_1 + \tilde{\gamma}) F_D^o \right] \right. \\
& + \delta u'_g{}^T (\dot{P}_g + \tilde{\omega}_g P_g) - \overline{\delta F}'_g{}^T [C^{gD} (e_1 + \gamma) - C^{gb} e_1] - \overline{\delta F}'_g{}^T u_g \\
& - \overline{\delta M}'_g{}^T \theta_g - \overline{\delta M}'_g{}^T \left(\Delta + \frac{\tilde{\theta}_g}{2} + \frac{\theta_g \theta_g^T}{4} \right) C^{gb} \kappa \\
& + \overline{\delta P}'_g{}^T (V_g - v_g - \tilde{\omega}_g u_g - \dot{u}_g) \\
& \left. + \overline{\delta H}'_g{}^T \left(\Omega_D - \omega_D - C^{bg} \frac{\Delta - \tilde{\theta}_g/2}{1 + \theta_g \theta_g^T/4} \dot{\theta}_g \right) - \delta u'_g{}^T f_g - \overline{\delta \psi}'_g{}^T m_g \right\} dx_1 \\
& + \int_{\Omega_{Sn}} \left\{ \delta u'_g{}^T F_g + \overline{\delta \psi}'_g{}^T M_g \right. \\
& + \overline{\delta \psi}'_g{}^T \left[\dot{H}_g + \tilde{\omega}_g H_g + \tilde{V}_g P_g - C^{gD} (\tilde{e}_1 + \tilde{\gamma}) F_D \right] \\
& + \delta \phi^T Q + \delta u'_g{}^T (\dot{P}_g + \tilde{\omega}_g P_g) - \overline{\delta F}'_g{}^T [C^{gD} (e_1 + \gamma) - C^{gb} e_1] \\
& - \overline{\delta F}'_g{}^T u_g - \overline{\delta M}'_g{}^T \theta_g + \delta Q^T (\phi - \phi^C) \\
& - \overline{\delta M}'_g{}^T \left(\Delta + \frac{\tilde{\theta}_g}{2} + \frac{\theta_g \theta_g^T}{4} \right) C^{gb} \kappa + \overline{\delta P}'_g{}^T (V_g - v_g - \tilde{\omega}_g u_g - \dot{u}_g) \\
& \left. + \overline{\delta H}'_g{}^T \left(\Omega_D - \omega_D - C^{bg} \frac{\Delta - \tilde{\theta}_g/2}{1 + \theta_g \theta_g^T/4} \dot{\theta}_g \right) - \delta u'_g{}^T f_g - \overline{\delta \psi}'_g{}^T m_g \right\} \\
& dx_1 = \left(\delta u'_g{}^T \hat{F}_g + \overline{\delta \psi}'_g{}^T \hat{M}_g - \overline{\delta F}'_g{}^T \hat{u}_g - \overline{\delta M}'_g{}^T \hat{\theta}_g \right) \Big|_0'. \quad (2)
\end{aligned}$$

Subscripts and superscripts 'g' refer to the global body attached frame, while 'b' & 'D' represents the undeformed and deformed frame respectively. The terms ϕ and Q represents the voltage and charge respectively. Other terms and their meanings are same as provided in Hodges [1]. It can be observed that the maximum 1st order of the derivative occur in the mixed variational statement. Hence, by inspection, only linear and constant shape functions are used for approximation, hence paving for simple computation and avoiding numerical errors arising due to numerical integration process vastly used in displacement based finite element analysis. For example, the only linear shape functions used are given as follows [2],

$$\begin{aligned} \delta u_g &= (1 - \eta)\delta u_i + \eta\delta u_{i+1}, & \overline{\delta \psi}_g &= (1 - \eta)\overline{\delta \psi}_i + \eta\overline{\delta \psi}_{i+1}, \\ \overline{\delta F}_g &= (1 - \eta)\overline{\delta F}_i + \eta\overline{\delta F}_{i+1}, & \overline{\delta M}_g &= (1 - \eta)\overline{\delta M}_i + \eta\overline{\delta M}_{i+1}. \end{aligned} \tag{3}$$

In Eq. (3), η is the local coordinate system. Also, ‘i’ and ‘i + 1’ represents the starting and ending of any arbitrary beam finite element. Finally, finite element equations based on these shape functions are derived and Newton–Raphson method is used to find the unknowns from these equations.

3 Results and Discussion

Material properties of a vastly studied smart beam is considered [5, 6]. The material properties table is provided below in Table 1. Length of each portion, i.e., the actuator and the sensor part is 0.5 m. A schematic of the three layer smart beam consisting of both actuator and sensor portion is studied, as shown in Fig. 1. The actuation voltage applied on actuator link is 12.49 kV.

For ABAQUS® based simulation, a 3-D beam is created in part module. Then, a 3D partition of the part is done to create the PZT, and the adhesive portion. After that, PZT surfaces are again partitioned for active and sensing parts. The master and slave surfaces were defined on PZT and adhesive ‘interacting’ surfaces. A tie constraint is defined between these surfaces so that perfect bonding can be simulated.

Table 1 Material properties of three layer smart beam

Parameters	Gr/Epoxy	Adhesive	PZT-4
E_{11} (Pa) $\times 10^9$	126.00	6.90	68.90
E_{22} (Pa) $\times 10^9$	7.90	6.90	48.30
E_{33} (Pa) $\times 10^9$	7.90	6.90	48.30
Poisson’s ratio, $\nu_{12} = \nu_{13} = \nu_{23}$	0.275	0.40	0.25
G_{12} (Pa) $\times 10^9$	3.40	2.46	31.00
G_{13} (Pa) $\times 10^9$	5.65	2.46	31.00
G_{23} (Pa) $\times 10^9$	5.65	2.46	31.00
$e_{31} = e_{32}$ (Cm ⁻²)	0.00	0.00	-7.99
e_{33} (Cm ⁻²)	0.00	0.00	14.86
$e_{24} = e_{15}$ (Cm ⁻²)	0.00	0.00	15.37
g_{11} (F/m) $\times 10^{-11}$	3.089	542.90	542.90
g_{22} (F/m) $\times 10^{-11}$	2.560	542.90	542.90
g_{33} (F/m) $\times 10^{-11}$	2.560	532.00	532.00
Thickness, h (mm)	15.240	0.254	1.524
Width, b (mm)	25.40	25.40	25.40
Density, ρ (kg/m ³)	1527.00	1662.00	7600.00

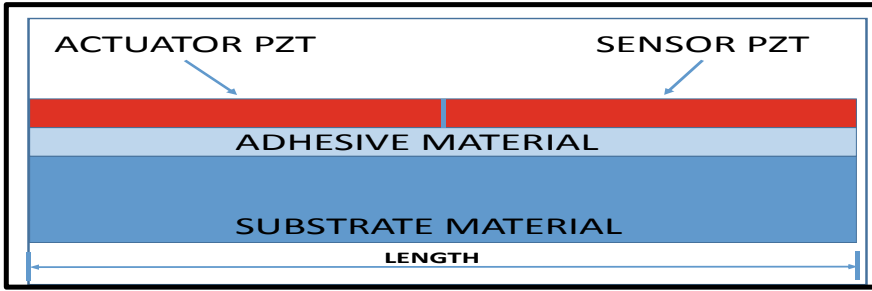


Fig. 1 A three layer smart beam

After that boundary conditions were provided. For mechanical boundaries, an end of the beam is ‘encastered’ while other is kept free to mimic the clamped-free or the cantilever type boundary conditions. Similarly, to study the clamped-clamped smart beam, all degrees of freedom are restricted or ‘encastered’ for both ends of the beam. Electrical boundaries in terms of voltages are provided for active portion. The surfaces of actuator and sensor PZT interacting with the adhesive surface is grounded, i.e., a zero-voltage boundary condition is provided. Upper PZT surface of sensor portion is divided in equipotential surfaces by equation constraints to mimic the separate electrodes. A high voltage of 12.49 kV is applied on the upper surface of the actuator PZT and the electric potential is recorded on sensor portion. Also, for recording mechanical outputs, a path is drawn through the beam. Mechanical and electrical responses are recorded and compared with the results obtained from the present analysis, as shown in Figs. 2, 3, 4 and 5.

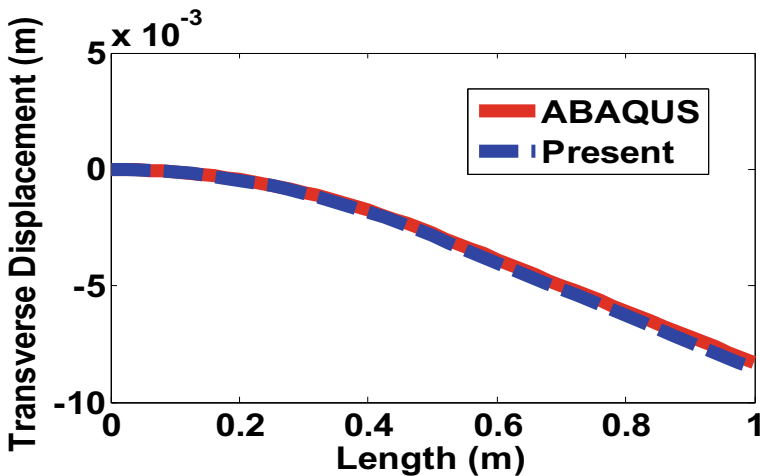


Fig. 2 Transverse displacement for Clamped-Free boundary

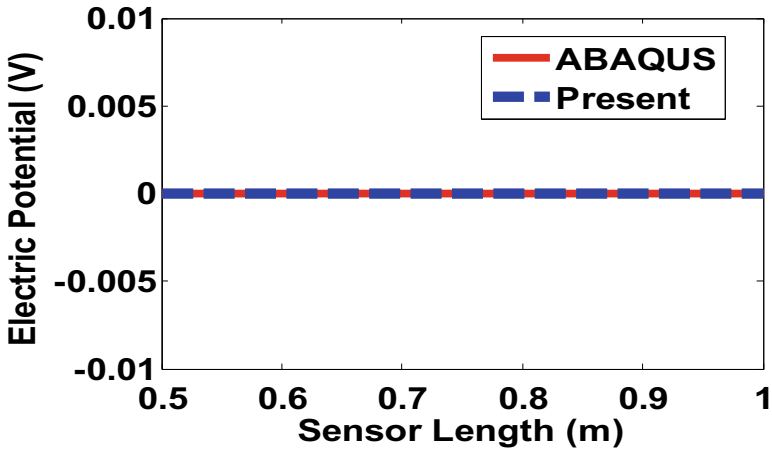


Fig. 3 Electric potential for Clamped-Free boundary

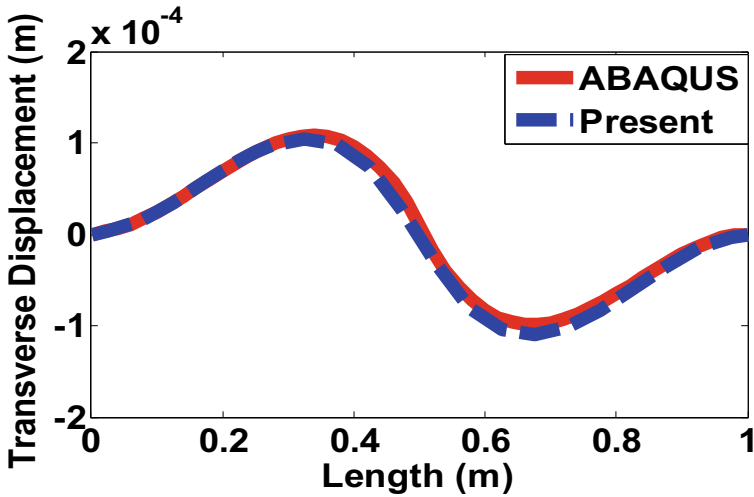


Fig. 4 Transverse displacement for Clamped-Clamped boundary

4 Conclusion

Two cases of clamped-free and clamped-clamped smart beams consisting of both active and sensory portions have been studied. The results obtained from the present theory are in very good agreement with those generated from 3D FE Software ABAQUS®. It is concluded that the type of boundary conditions are important, especially for the smart structures meant for monitoring and control. For instance, if one wants to monitor by sensed voltage, it is impossible with the cantilever type

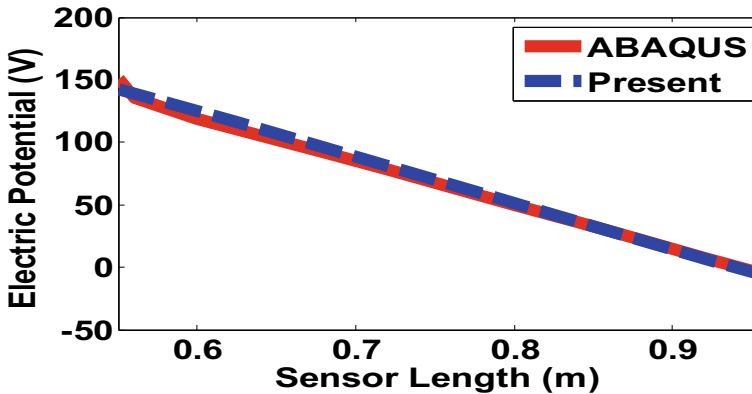


Fig. 5 Electric potential for Clamped–Clamped boundary

‘multi-physics’ structure, as shown in Figs. 2 and 3, since no voltage is generated on the sensor link, while only mechanical outputs are having non-zero values. While for clamped–clamped type boundaries, we obtain both mechanical as well as electrical outputs, as can be seen from Figs. 4 and 5.

References

1. Hodges DH (2006). Nonlinear composite beam theory. American Institute of Aeronautics and Astronautics, Reston, Virginia
2. Yu W, Blair M (2012) GEBT: A general-purpose nonlinear analysis tool for composite beams. *Compos Struct* 94:2677–2689. <https://doi.org/10.1016/j.compstruct.2012.04.007>
3. Roy S, Yu W, Han D (2007) An asymptotically correct classical model for smart beams. *Int J Solids Struct* 44:8424–8439. <https://doi.org/10.1016/j.ijsolstr.2007.06.028>
4. Banerjee S, Roy S (2018) A dimensionally reduced order piezoelectric energy harvester model. *Energy*. <https://doi.org/10.1016/j.energy.2018.01.116>
5. Asdaque PMGB, Banerjee S, Roy S (2019) An electromechanically coupled intrinsic, mixed variational formulation for geometrically nonlinear smart composite beam. *Appl Math Model* 65:549–565. <https://doi.org/10.1016/j.apm.2018.08.023>
6. Asdaque PMGB, Roy S (2019) Nonlinear dynamic analysis of slender, composite smart-structures under fixed and follower loads. *Compos Struct* 227:11269. <https://doi.org/10.1016/j.compstruct.2019.111269>

Numerical Investigation of Sweet Spot of Cricket Bat



Hari Vignesh , S. M. Srinivasan , and Ashish Pandey 

Abstract Collision and impact mechanics related to the cricket bat and ball is quite interesting to investigate. It has been observed that the exit velocity of the cricket bat depends on the location of the ball impact. The finite element method is employed to simulate the impact of cricket ball and bat. Exit velocities of the cricket ball have been plotted over the length of the bat to obtain the sweet spot of the cricket bat. This paper presents the response of the cricket bat for the different impact velocities and bowling methods and the exit velocities by using numerical methods that have been compared to get the response of the cricket bat.

Keywords Impact mechanics · Cricket ball-bat impact · Sweet spot

1 Introduction

Cricket is one of the most famous sports in the world and it is watched by billions of people all around the world. Cricket is a game conducted with the same rules and regulations recommended by MCC (Marylebone Cricket Club) for the past few centuries and technological advancements are significantly lesser in comparison to other sports which hampers improvement in the game [1]. If we compare baseball and tennis with cricket, baseball bats are made up of solid wood or hollow aluminium barrels and tennis rackets are made up of composites. All the batsmen know that there is a special spot on a cricket bat where the shots feel very smooth. It sometimes feels so good that there is almost no sensation at all that the bat hit the ball. It is the same with a tennis racquet or a baseball bat. These areas have been given various names such as sweet zone, sweet spot etc. A sweet spot is a position that is identified by the batsman at the best location of the bat with which the ball comes in

H. Vignesh (✉) · S. M. Srinivasan (✉) · A. Pandey (✉)

Department of Applied Mechanics, Indian Institute of Technology Madras, Chennai 600036, India
e-mail: am21s083@smail.iitm.ac.in

S. M. Srinivasan
e-mail: mssiva@iitm.ac.in

A. Pandey
e-mail: am17d031@smail.iitm.ac.in

contact and gives the maximum exit velocity. Initial researchers used experimental methods to obtain the optimal location for impact, later on, computational methods were adopted. Two methods have been discussed in the literature, depending on the definition of the sweet spot, vibrational and impact approach respectively. For vibration-based analysis of the cricket bat, when the ball strikes the bat, the contact lasts just a few seconds, and that the vibration detected during an impact on the sweet spot is practically zero throughout all three dimensions of the bat, which in turn results in maximum energy transfer to the ball. For the impact method, the prime objective is to obtain the highest coefficient of restitution irrespective of the vibration felt by the batsman. Brearley et al. [2] used rigid body models to explain that the optimal location for hitting the cricket ball is center of percussion (COP). Brody [3] countered that the point of maximum power was not necessarily at the COP, but it is between COP and the center of mass. Knowles et al. [4] described this point as the node of the first bending mode. Most of the researchers have used a vibrational approach in which the aim is to reduce the shock felt by the arm of the batsman. Gutaj et al. [5] developed a FE model for modal analysis and investigated the design characteristics of the bat. Hariharan et al. [6] gave three interpretations to sweet spot using numerical simulation of vibration of the bat during impact. The behavior of a cricket bat under the normal impact of a ball with different velocities was studied using numerical methods by Pandey and Rao [7]. Allen et al. [8] suggested that a rigid body model cannot accurately predict real exit ball velocities for all impact locations along the length of the blade. The exit velocity of the ball as a function of the impact location to confirm the region of maximum velocity is studied by Zandt [9]. Daish [10] analyzed the oblique ball impact considering the effect of frictional force and formulated the coefficient of restitution. Based on the distance from the toe end, the sweet spot has been classified into three different positions low, high and medium positioned sweet spot. In the present paper, the sweet spot of the cricket bat has been investigated by varying the ball velocity and the angle of impact.

2 Numerical Modeling

In this study, cricket bat and ball geometries are modelled based on the dimensions which are recommended by MCC in their laws and the law for the bat design comes under Law5-Bat. A cricket bat is the assembly of willow wood blade and cylindrical cane wood (Fig. 1). The material for the cricket bat is only willow wood and other materials are not allowed as per the rule of MCC. In the present study, the authors have taken the willow wood properties for the modelling.

CAD model of cricket bat and ball has been created using HYPERMESH. The finite element-based simulations were conducted using the ABAQUS FE package. The material used for the cricket bat modelling is willow wood having orthotropic properties. The cricket ball consists of multiple layers of materials (such as leather, cork and yarn) but in the present study, it is considered as an isotropic sphere. The material properties for willow wood [12] and cricket ball [13] are mentioned in Table 1.

Fig. 1 Geometry and dimensions of cricket bat

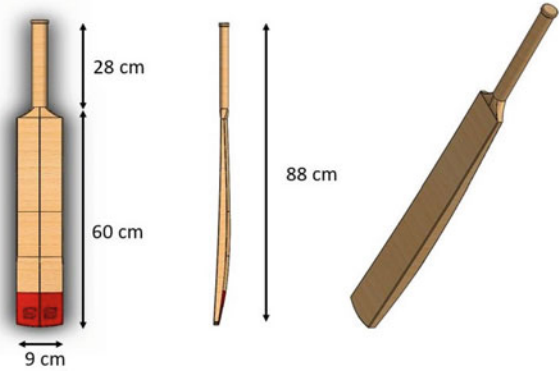


Table 1 Material properties of willow wood and ball

Material	Density (Kg/m ³)	Young's Modulus (GPa)			Poisson's ratio			Shear modulus (GPa)		
		E_1	E_2	E_3	μ_1	μ_2	μ_3	G_{12}	G_{23}	G_{31}
Wood	650	13.3	0.83	7.06	0.01	0.6	0.16	1.3	0.13	1.3
Ball	240	31			0.3			11.92		

The element type used for the modelling is C3D8 Hexahedral elements. Based on the mesh convergence, the element size for the bat is 5 mm and for the ball, 2 mm has been used for this modelling (Fig. 2). A numerical investigation is carried out for considering variation in velocity and angle of impact. In the present research work, all the cases analyzed are “pull shots” and the velocity ranges are taken as medium-fast bowling. The cricket bat is fixed at the handgrip region and frictionless contact is assumed between the bat and ball. Initially, simulation for the normal impact of the ball is performed for which the ball inlet velocities have been taken as 30 m/s and 45 m/s. Location of impact is varied over the length of the bat, starting from the

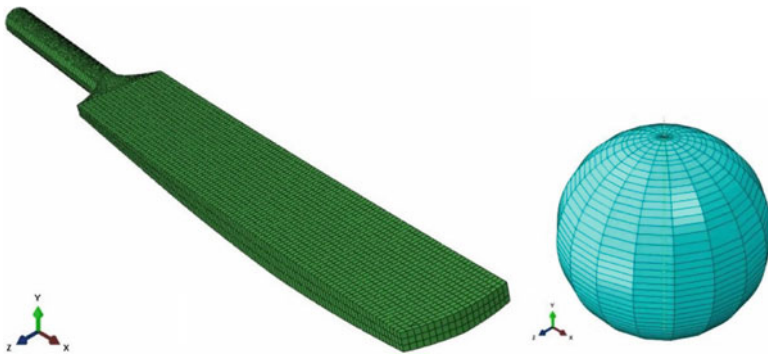


Fig. 2 FE model of cricket bat and ball

bat toe end to the handgrip end. Simulation of oblique impact with varying angles of impact is conducted for the same inlet velocity of 30 m/s. Exit velocities for the aforementioned cases have been obtained and will be explained in the next section.

3 Results and Discussion

To obtain the sweet spot of the cricket bat, the ball is impacted at different locations of the bat. Figure 3 shows the variation of the coefficient of restitution with three different ball inlet velocities 30 m/s, 37 m/s and 45 m/s respectively. Coefficient of restitution denotes the ratio between exit velocity and the inlet velocity of the cricket ball. It can be observed that exit velocities peak at a 200 mm distance from the toe end of the cricket bat and gradually decrease if the distance from the toe end is increased. The region from 150 mm–250 mm can be considered as the sweet zone where the higher exit velocities are obtained. The results from the numerical method are compared with an experimental investigation conducted by Bower on a qualitative basis. The sweet zone of 150 mm–200 mm is matching with the experimental results obtained by Bower.[11]

The effect of the angle of impact is also investigated and Fig. 4 shows the snapshots of the oblique impact (30°) of the cricket ball on the bat. Arrow marks the direction of the cricket ball. Peak stress noted after the ball impact is 16.49 kPa.

Figure 5 shows the variation of the exit velocities with varying angles of impact. The inlet velocity is kept constant at 30 m/s. It can be observed that higher exit

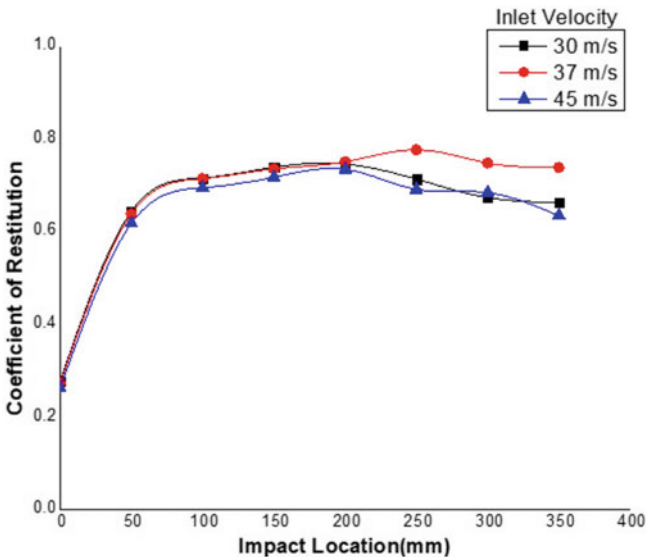


Fig. 3 Coefficient of Restitution vs Impact location for varying inlet velocity

Fig. 4 Snapshots of the oblique impact of the cricket ball for 30° impact

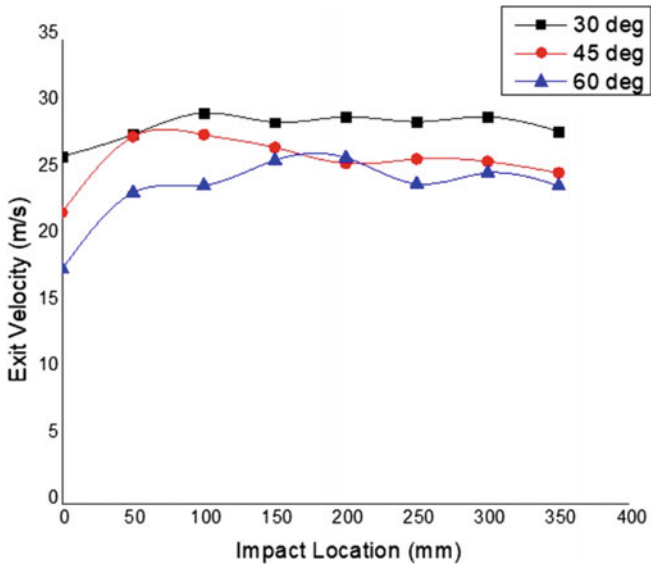
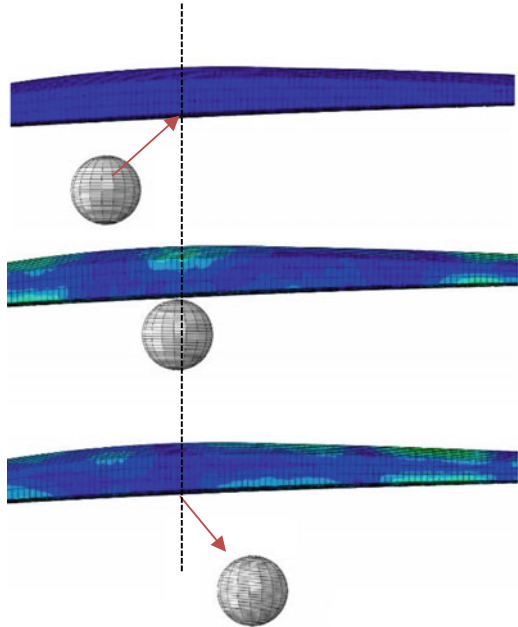


Fig. 5 Exit velocities of ball vs Impact location for varying angle of impact

velocities have been achieved for 30° impact in comparison with 45° and 60° inlet velocity.

4 Conclusion

Numerical simulation is used to obtain the ball exit velocity. Ball exit velocity is obtained for various impact locations and various angles of impact. It was observed that one-third of the bat towards the toe end is giving maximum exit velocity. It was also observed that the angle of impact also affects the location of the sweet spot. This approach can be used to improve the design of the cricket bat. Further studies by updating the material model of the cricket bat and cricket ball and by accurately modelling the handgrip can be conducted.

References

1. Marylebone Cricket Club (MCC) (2010) The laws of cricket (4th edn). London, Marylebone Cricket Club, London
2. Brearley MN, Burns JC, De Mestre NJ (1990) What is the best way to hit a cricket ball? *Int J Math Educ Sci Technol* 21(6):949–961
3. Brody H (1981) Physics of the tennis racket II: The “sweet spot”. *Am J Phys* 49(9):816–819
4. Knowles S, Mather JSB, Brooks R (1996) Cricket bat design and analysis through impact vibration modelling. In: *Engineering of Sport*, pp 339–346
5. Gutaj F (2004) A comparison of methods for modelling the dynamics of a cricket bat. *Proc Inst Mech Eng C J Mech Eng Sci* 218(12):1457–1468
6. Hariharan Ramasamy K (2012) Inertial and Vibration Characteristics of a cricket bat. <http://www.vibrationdata.com/>
7. Ashish Pandey C, Lakshmana R (2018) Numerical analysis of Bat and ball impact in Cricket, Symposium and Workshop for Analytical Youth in Applied Mechanics. BITS Pilani Goa
8. Allen T et al (2014) Finite element model of a cricket ball impacting a bat. *Procedia Engineering* 72:521–526
9. Van Zandt LL (1991) Dynamical theory of baseball bat. *Am J Phys* 60:172–181
10. Daish CB (1972) *The Physics of Ball games*. The English University Press, London
11. Bower R (2012) The sweet spot of a cricket bat for low speed impacts. *Sports Eng* 15(2):53–60
12. Kant A et al (2013) Dynamic analysis of impact of ball on cricket bat and force transfer to the elbow. In: *International Conference on Machines and Mechanisms*. IIT Roorkee
13. Pandey A, Rao CL (2020) Numerical simulation of ball-pitch impact in cricket. *Int J Adv Eng Sci Appl Math* 12:39–43

Comparative Study of Ballistic Performance Parameter of Kevlar/Epoxy Composite Laminate



A. Balaji Shunmugam  and R. Velmurugan 

Abstract In this paper, the authors study the impact of parabolic nose projectile on Kevlar/epoxy laminate with different orientations. Earlier work [17] on numerical analysis has been carried out with the projectile with conical nose and the analysis of the composite laminate is carried out using 3D solid elements. In this work, the authors use a more realistic parabolic nose model for the projectile. Moreover, 2D continuum shell elements for the composite with integrated Hashin damage model are used for damage initiation and linear fracture energy properties instead of 3D solid element. The residual velocities are qualitatively compared against the residual velocities obtained from FE analysis which was performed with 3D solid elements for laminate and conical projectile. The trend of the reduction in residual velocity for different orientations of the fibers is found to be in good agreement with the experimental results. This proposed analysis method using 2D continuum shell element could produce qualitatively comparable results of 3D solid elements by saving significant amount of run time in the analysis.

Keywords Ballistic impact · Composite laminate · Kevlar/epoxy · Numerical analysis · Parabolic projectile

1 Introduction

Kevlar based unidirectional composites are commonly used material for body armor due to their high failure strain, high modulus, and higher strength-to-weight ratio. A numerical model has been developed to determine the residual velocity of projectiles with parabolic nose for different fiber orientations.

A. Balaji Shunmugam (✉) · R. Velmurugan
Department of Aerospace Engineering, Indian Institute of Technology Madras,
Chennai 600036, India
e-mail: ae19s044@smail.iitm.ac.in

R. Velmurugan
e-mail: ramanv@iitm.ac.in

Numerous analytical and numerical studies have been carried out in the recent past. Morye et al. [1] have discussed a simple analytical model to determine the energy absorbed by composites under impact loading and also carried out ballistic impact tests on woven nylon, aramid and Dyneema composites to verify the results obtained from analytical study in the projectile strike velocity range of 500 to 600 m/s. Chocron-BenIouIo et al. [2] have derived a basic analytical model for ballistic impact on ceramic/composite armors and substantiated the results experimentally and numerically. All velocities of the projectile considered were above 1000 m/s. Bohong Gu [3] has framed analytical model to compute the reduction in kinetic energy and the residual velocity of the projectile on the woven fabric of Twaron and Kuralon. Naik et al. [4] have derived analytical expressions for each mechanism of energy absorption during impact, absorbed energy at different intervals of time during impact and the corresponding decrease in the projectile's velocity. Ganesh Babu et al. [5] have executed experimental and analytical works for the response of sandwich panels, subjected to the impact of heavy mass projectiles at low velocities. Zhu et al. [6, 7] have published an analytical derivation for normal impact and perforation of conical nose cylindrical projectile on laminated kevlar-29/polyester laminates and compared analytical results with experiments for velocity up to 200 m/s. Silva et al. [8] have performed experiments and numerical study of ballistic impact on thin kevlar-29 laminates of different thicknesses. AUTODYN-3D has been used to estimate the ballistic limit and damage area. Deka et al. [9] have analyzed the E-Glass/Polypropylene composites of different thickness values. For simulation of damage phenomenon explicit 3D code, LS DYNA, has been used. Experiments have been performed for the velocity range of 150 to 270 m/s. Sevkat et al. [10] have performed combined experimental and finite element study of angle ply glass/epoxy composites subjected to impact by deformable projectile. For simulation of ballistic limit, LS DYNA 3D code has been used. The velocity ranges considered are at ballistic limit and above. Gama et al. [11] have presented a full 3D finite element model of ballistic impact on thick composite sections. They have used LS-Dyna and progressive composite damage model MAT 162, which is linear elastic up to the initiation of damage and nonlinear softening thereafter. They have also validated the model with the ballistic experiments on glass/epoxy composites over a wide range of impact velocities from 50 to 1000 m/s. Garcia-Castillo et al. [12] have recommended non-dimensional parameters, namely, geometric ratio and density ratio, to estimate the projectile velocity and displacement during the perforation of thin plates made from woven glass/ polyester laminates. The results have been verified with experimental results of residual velocities, contact time and ballistic limit by these two parameters. Yeliz Pekbey et al. [13] have performed ballistic impact experimentally on Kevlar/epoxy composite with different fillers like Nano clay, Nano calcite and Nano carbon, to improve the ballistic impact resistance of Kevlar-epoxy composite at lesser weight. The addition of small amounts of Nano clay and Nano calcite distributed into the epoxy matrix enhanced the impact properties of the Kevlar/epoxy laminates. The laminates built with epoxy resin filled by 1 wt. % of Nano clay and 2 wt. % Nano calcite demonstrated the best ballistic performance. The presence of Nano carbon decreased ballistic performance of Kevlar-epoxy composites when

compared the results found for laminates with 0% Nano particles concentration. Nayak et al. [14] performed ballistic impact on aramid fabric-epoxy composite laminates at varying impact velocities with armor-piercing projectile experimentally and numerically. The simulated energy and stress distribution during impact of projectile on composite laminate showed marked difference with variation in impact velocities. The magnitude and duration of stress and the contact force were found to increase when projectile impacted at lower variations in impact velocities, thus enhancing the extent of delamination and the core damage area and the trend was reversed for higher variations in impact velocities. Kumar S et al. [15] have published numerical simulation for parametric study of ballistic impact with a cylindrical projectile. The influence of the projectile's mass and diameter on ballistic limit velocity was also discussed. Marcos Rodríguez Millán et al. [16] have performed the numerical simulation of the ballistic performance of Kevlar-29 under the impact of different double-nosed stepped cylindrical projectiles. The numerical simulation was carried out in order to find the failure mode of the laminate and the ballistic limit. The failure mode, ballistic limit and deformation of the targets by the impact of double-nosed projectiles were studied and related with those impact involved in penetration of single-nosed flat and conical projectiles. Substantial effect of the projectile geometry was proven: the lowest ballistic limit was found with the projectiles with conical nose shape.

Sikarwar et al. [17] have performed numerical simulation of ballistic impact with conical projectile and compared the residual velocities with experimental and analytical results [18]. Kevlar/epoxy laminate was modeled using 3D solid elements in Abaqus with subroutine usage as the Hashin failure model available within Abaqus is not compatible with 3D elements. The subroutine represented the Hashin failure model for the 3D solid elements. The numerically arrived results are in good agreement with his experimental and analytical results.

Hence in this research paper, a numerical model for a projectile with parabolic nose to represent the real projectile nose profile as in the experimentation and the laminate using continuum shell element has been analyzed. The Hashin damage initiation criteria and the linear fracture energy based damage evolution criteria have been used in this FE model. The results are comparable though the residual velocities from the newly built FE model with projectile of parabolic nose and the laminate modeled with continuum shell element are lesser.

2 Numerical Analysis

To model the laminate and the projectile, Abaqus/CAE has been used. The laminate is modeled with continuum shell element (SC8R) as a deformable body. The projectile is modeled with a Tetragonal element (C3D10M), and it was made rigid using interactions through a reference point created within the projectile. The dimension of the laminate is $0.3 \text{ m} \times 0.3 \text{ m}$. Number of layers considered are 8, 12, 15, and 19. The orientation of layers considered each laminate include (0/90), (0/90/30/-60), (0/90/45/-45), (30/-60/60/-30), (45/-45/0/90) and (0/45/-45/0). The projectile is

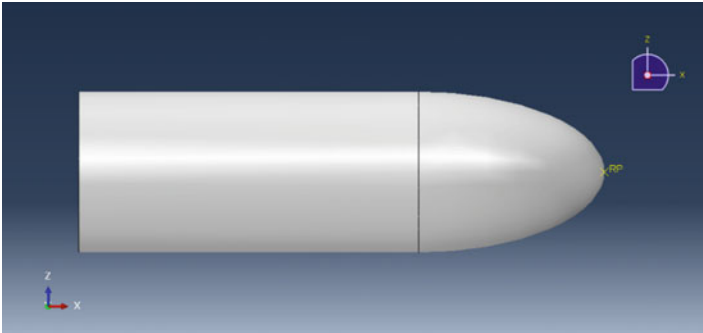


Fig. 1 Projectile with parabolic nose

assigned with 7.5 g of mass through a reference point created at the tip of the parabolic nose inertial property option. The shape of the projectile is cylindrical with parabolic nose $0.009 \text{ m} \times 0.029 \text{ m}$ per Fig. 1 as the original projectiles used in the experimental study by Sikarwar et al. [3] have a parabolic nose. The laminate and the projectile were assembled relative to each other with a gap of 0.0005 m. General contact is applied between the projectile and the laminate. The duration of the impact is set as 0.0003 s in all cases. Abaqus explicit solver has been chosen to solve the problem. The size of the mesh is 0.3 m for the laminate and 0.1 m for the projectile.

In the mesh module of the Abaqus explicit, under element controls choosing second-order accuracy has been helpful to fix the aborted simulation run with the excessively distorted element(s). Also, swapping the hourglass control option between default and enhanced has been useful to fix the aborted simulation run with excessively rotated element(s).

Material Model

The Hashin damage model, built within Abaqus, is chosen for the initiation of damage, and the linear fracture energy properties have been given for the damage progression model using the sub-option of damage evolution. The elastic material properties and the damage initiation criteria for the laminate are based on the work of Sikarwar et al. [17]. The damage evolution properties are based on the work by Yang et al. [19].

3 Results and Discussion

Table 1 compares the residual velocities from the above-mentioned FE analysis with experimental residual velocities from the work by Sikarwar et al. [18].

Table 2 compares the residual velocities from the above-mentioned FE analysis with both the FE-based and analytically calculated residual velocities from the work by Sikarwar et al. [17].

Table 1 Comparison of residual velocities from experimental and numerical results (with parabolic projectile)

Layup orientation	No. of layers	Thickness in mm	Initial Velocities in m/s	Experimental results [20]	Numerical results
				Residual average velocity in m/s	Residual velocity in m/s
0/90	8	2.4	378 ± 10	374 ± 10	366.3
	12	3.6	381 ± 8	374 ± 9	365.9
	15	4.5	378 ± 20	367 ± 18	357.5
	19	5.4	376 ± 9	360 ± 5	336.2
0/90/30/−60	8	2.4	386 ± 10	382 ± 11	375.1
	12	3.6	377 ± 10	372 ± 10	358.9
	15	4.5	385 ± 7	376 ± 6	364.5
	19	5.4	382 ± 6	370 ± 5	349.3
0/90/45/−45	8	2.4	386 ± 2	383 ± 3	372
	12	3.6	382 ± 13	376 ± 12	363.4
	15	4.5	375 ± 6	366 ± 9	349.4
	19	5.4	383 ± 8	371 ± 10	348.1
30/−60/60/−30	8	2.4	381 ± 10	378 ± 9	362.8
	12	3.6	386 ± 11	381 ± 11	366.3
	15	4.5	388 ± 8	381 ± 9	356.1
	19	5.4	390 ± 6	380 ± 10	358.4

Table 3 compares the residual velocities of parabolic projectile for different layup directions of laminate across a range of velocities from 200 to 600 m/s.

Wherever the projectile has plugged inside the target laminate, similar to Fig. 4, it has been mentioned as “Plugged” in Table 3.

The residual velocities calculated numerically from this research paper are comparatively less, which is mainly due to the following differences in the FE modelling approaches:

1. The FE model discussed in this research paper has been modeled with parabolic shaped projectile whereas the FE results from the work of Sikarwar et al. [17] was modeled with conical projectile Fig. 2.
2. The FE model of laminate discussed in this research paper was modeled with continuum shell elements whereas the FE model from the work of Sikarwar et al. [17] was modeled with solid elements.

However the trend in the residual velocities is found to be in good agreement with the residual velocities calculated from Experimental results, FE results with conical projectile, and the analytical results (Fig. 3).

Table 2 Comparison of residual velocities from numerical results (both parabolic projectile and conical projectile) and analytical results (with parabolic projectile)

Thickness of laminate	No. of layers	Projectile's Initial velocity (m/s)	FE based residual velocity (parabolic projectile) (m/s)	From the work by Sikarwar et al. [17] (m/s)	
				FE based residual velocity (conical projectile)	Analytically calculated velocity
2.4 mm	8	200	180.2	195.5	192.7
		250	236.3	245.7	244.5
		300	288.6	296.2	295.2
		350	335.7	346.5	345.8
		400	390.4	395.7	396.6
		450	441.1	Not available	Not available
		500	491.1		
		550	541.2		
600	591				
3.6 mm	12	200	176.2	188.7	187.8
		250	233	241.3	240.2
		300	282.2	290.1	292.8
		350	332.4	342.9	344
		400	382.9	392.3	394.5
		450	434.2	Not available	Not available
		500	484.5		
		550	534.9		
600	584.9				
4.5 mm	15	200	171.3	186.6	183.5
		250	222.6	238.1	237.5
		300	276.3	293.1	289.9
		350	329.4	343.3	341.5
		400	379.3	391.3	392.6
		450	430.7	Not available	Not available
		500	480.7		
		550	530.9		
600	580.3				
5.7 mm	19	200	149.1	182.6	178
		250	206.5	234.8	232.5
		300	260	289.9	285.7
		350	310.8	340.4	338.1

(continued)

Table 2 (continued)

Thickness of laminate	No. of layers	Projectile's Initial velocity (m/s)	FE based residual velocity (parabolic projectile) (m/s)	From the work by Sikarwar et al. [17] (m/s)	
				FE based residual velocity (conical projectile)	Analytically calculated velocity
		400	363.9	391.2	389.7
		450	419.2	Not available	Not available
		500	472.4		
		550	514.6		
		600	568.8		

All velocities are in m/s

Table 3 Comparison of residual velocities from numerical results (with parabolic projectile) for different lamina layup directions

Thickness of laminate	No. of layers	Projectile's initial velocity (m/s)	FE based residual velocity (parabolic projectile) for different lay up directions (m/s)			
			0/90	0/90/30/-60	0/90/45/-45	30/-60/60/-30
2.4 mm	8	200	180.2	162.5	167.5	175.1
		250	236.3	226.5	226.9	233.9
		300	288.6	283.7	280.7	286.7
		350	335.7	339.1	334.9	337.3
		400	390.4	389.7	386	388.5
		450	441.1	440.3	436.5	440.5
		500	491.1	490.4	486.4	490.5
		550	541.2	541.2	536.3	533.6
		600	591	587.9	586.8	584
3.6 mm	12	200	176.2	165.8	165.5	171
		250	233	219.4	216.5	217.7
		300	282.2	278.5	273.3	266
		350	332.4	330.9	330.9	328.8
		400	382.9	384.3	382.6	383.2
		450	434.2	435.3	434.3	431.7
		500	484.5	485.2	484.9	477.2
		550	534.9	535.6	535.6	531.4
		600	584.9	584.9	584.2	584.2

(continued)

Table 3 (continued)

Thickness of laminate	No. of layers	Projectile's initial velocity (m/s)	FE based residual velocity (parabolic projectile) for different lay up directions (m/s)			
			0/90	0/90/30/-60	0/90/45/-45	30/-60/60/-30
4.5 mm	15	200	171.3	156.8	151.7	Plugged
		250	222.6	222.2	210.7	206.1
		300	276.3	277.6	266.5	268.4
		350	329.4	329.7	320.4	319.2
		400	379.3	379.6	373.7	375.7
		450	430.7	429.6	430.2	424.5
		500	480.7	480.4	479	475.7
		550	530.9	531.3	529	529.4
		600	580.3	580	579.7	578.6
5.7 mm	19	200	Plugged	Plugged	Plugged	184.4
		250	206.5	186.436	188.131	233.4
		300	260	260.1	252.9	259.2
		350	310.8	316.4	314.6	314
		400	363.9	370.7	359.6	355.9
		450	419.2	420	413.3	410.8
		500	472.4	467.1	466.1	471.2
		550	514.6	517.3	515.3	523
		600	568.8	567.3	573.5	572.5

All velocities are in m/s

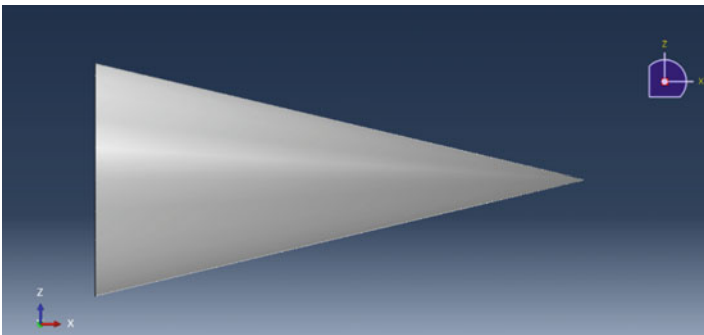


Fig. 2 Conical Projectile [17]

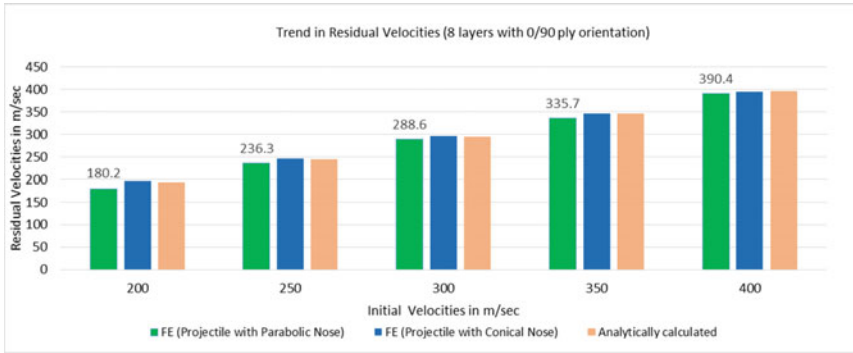


Fig. 3 Residual velocities (parabolic projectile, conical projectile, & analytical calculation) vs initial velocities

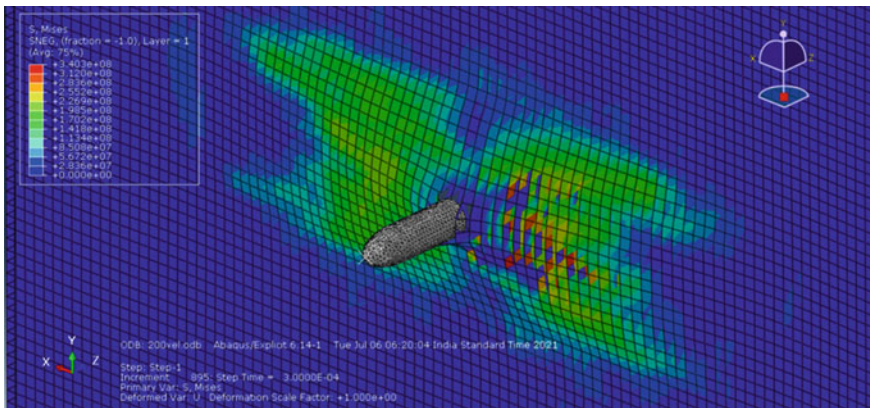


Fig. 4 Plugged projectile

Also, in this research paper residual velocities are calculated for initial projectile velocities up to 600 m/s whereas previously published paper [17] contains residual velocity calculations only up to 400 m/s.

4 Conclusion

Response of Kevlar/Epoxy laminates has been studied for a projectile with the parabolic nose, for different ply orientations and thicknesses numerically. The results are compared with numerical results with projectile of conical shape, experimental and analytical results. The residual velocities are qualitatively matching though they are slightly lesser than the residual velocities from the numerical model with conical projectile and analytical. The residual velocities for higher initial velocities are

numerically calculated in this research paper. Usage of continuum shell element enables us to leverage the Abaqus in-built failure model without any subroutines. Also modelling of the projectile with parabolic nose profile makes the numerical simulation comparatively realistic as the experimental tests were performed using parabolic shaped projectiles.

Also the run time for the numerical simulations is less as continuum shell elements have been used to model the composite laminate target with qualitatively matching results. Hence this FE modelling approach can be leveraged for design concept with reduced run time for a vast range of initial velocities and laminate layup directions.

Acknowledgements The authors would like to thank Professor. Lakshman Rao, Dr. Vijayabaskar and Mr. Noushad for their invaluable inputs provided during this work.

References

1. Morye SS, Hine PJ, Duckett RA, Carr DJ, Ward IM (2000) Modeling of the energy absorption by polymer composites upon ballistic impact. *Compos Sci Technol* 60(14):2631–2642
2. Benloulou ISC, Sanchez-Galvez V (1998) A new analytical model to simulate impact onto ceramic/composite armours. *Int J Solids Struct* 21(6):461–471
3. Bohong G (2003) Analytical modeling for the ballistic perforation of planer plain-woven fabric target by projectile. *Compos Part B* 34:361–371
4. Naik NK, Shrirao P (2004) Composite structures under ballistic impact. *Compos Struct* 66:79–590
5. Babu MG, Velmurugan R, Gupta NK (2006) Projectile impact on sandwich panels. *Int J Crashworthiness* 11(2):153–164
6. Zhu G, Goldsmith W, Dharan CHK (1992) Penetration of laminated Kevlar by projectiles-I. Experimental investigation. *Int J Solids Struct* 29(4):399–420
7. Zhu G, Goldsmith W, Dharan CHK (1992) Penetration of laminated Kevlar by projectiles-II. Analytical model. *Int J Solids Struct* 29(4):421–436
8. Silva MAQ, Cismasiu C, Chiorean CG (2005) Numerical simulation of ballistic impact on composite laminates. *Int J Impact Eng* 31:289–306
9. Deka LJ, Bartus SD, Vaidya UK (2009) Multi-site impact response of S2-glass/epoxy composite laminates. *Compos Sci Technol* 69:725–735
10. Sevkat E, Liaw B, Delale F, Raju BB (2009) A combined experimental and numerical approach to study ballistic impact response of S2-glass fiber/toughened epoxy composite beams. *Compos Sci Technol* 69:965–982
11. Gama BA, Gillespie Jr JW (2005) A quasi-static penetration model of ballistic penetration of thick-section composites. In: 20th annual technical conference, 7–9 September 2005. American Society for Composites, Philadelphia. Paper no: 52
12. García-Castillo SK, Sánchez-Sáez S, Barbero E (2012) Non-dimensional analysis of ballistic impact on thin woven laminate plates. *Int J Impact Eng* 39(1):8–15
13. Pekbey Y, Aslantaş K, Yumak N (2017) Ballistic impact response of Kevlar Composites with filled epoxy matrix. *Steel Compos Struct* 24(2):191–200
14. Nayak N, Banerjee A, Panda TR (2017) Numerical study on the ballistic impact response of aramid fabric- epoxy laminated composites by armor piercing projectile. In: 11th international symposium on plasticity and impact mechanics, Implast 2016. *Procedia Eng* 173:230–237
15. Kumar S, Gupta DS, Singh I, Sharma A (2010) Behavior of kevlar/epoxy composite plates under ballistic impact. *J Reinf Plast Compos* 29(13):2048–2064

16. Rodríguez Millán M, Moreno CE, Marco M, Santiuste C, Miguélez H (2016) Numerical analysis of the ballistic behavior of Kevlar® composite under impact of double-nosed stepped cylindrical projectiles. *J Reinf Plast Compos* 35(2):124–137. ISSN: 0731-6844
17. Sikarwar RS, Velmurugan R, Gupta NK (2013) Ballistic performance of Kevlar/epoxy composite laminates. *Proc Indian Natl Sci Acad* 79(4):789–799
18. Sikarwar RS, Velmurugan R, Madhu V (2012) Experimental and analytical study of high velocity impact on Kevlar/Epoxy composite plates. *Cent Eur J Eng* 2(4):638–650
19. Yang L, Yan Y, Kuang N (2002) Experimental and numerical investigation of aramid fiber reinforced laminates subjected to low velocity impact. *Polym Test* 32:1163–1173

Creep Failure Estimation of Nickel-Based Superalloys Using Unified Mechanics Theory (UMT)



Kambhammettu Sri Krishna Sudhamsu and Chebolu Lakshmana Rao

Abstract Failure modes of alloys such as creep failure, fatigue, fracture, etc., are generally treated as separate problems and are modelled separately using either empirical equations or based on the physics of individual failure mechanisms. However, modeling failure under the simultaneous action of different failure modes has been challenging for the engineering community. Unified Mechanics Theory (UMT) is an entropy-based failure model that uses entropy generated as a common “currency” to sum and determine the extent of damage and failure due to different modes. In this work, we use UMT to investigate creep failure in DZ125 nickel-based superalloy. We use the experimental data to calibrate and predict the failure strains (strain at the end of secondary creep) due to creep at different creep loads and temperatures.

Keywords Creep · Nickel based superalloys · Unified Mechanics Theory · DZ125

1 Introduction

The life of engineering materials has been an area of interest for metallurgists and mechanical engineers alike. Such life is generally estimated using models developed for loading conditions specific to each of the applications. For example, models used to predict fatigue life under cyclic loading are different from those used to predict ductile fracture under monotonous loading [1, 2]. Similarly, creep failure [3], corrosion damage [4], temperature-induced failure [5], etc., are all modelled separately based on the physics of the predominant mechanisms that cause such damage. Many times, they are also modeled using empirical relations. However, modeling failure under the simultaneous action of different failure modes has always been a challenging task [6]. For example, many components used in nuclear applications are known to undergo creep and fatigue simultaneously.

K. Sri Krishna Sudhamsu (✉) · C. Lakshmana Rao
Department of Applied Mechanics, Indian Institute of Technology Madras, Chennai 600036, India

C. Lakshmana Rao
e-mail: lakshman@iitm.ac.in

Similarly, turbine blades are also known to undergo failure due to multiple mechanisms such as creep, erosion, and fatigue. In order to describe simultaneous damage mechanisms, Unified Mechanics Theory (UMT) [7] has been formulated. This theory proposes that the total specific entropy generated in the material until rupture remains constant irrespective of the mode of failure. When multiple failure mechanisms act simultaneously, the entropy generated due to each of those mechanisms is summed to find the total entropy generated. The value of this total entropy forms a basis for evaluating a damage parameter that varies from 0 (virgin material) to 1 (fully damaged). This work uses this Unified Mechanics Theory (UMT) to investigate creep damage in Nickel-based superalloys.

Nickel-based superalloys are corrosion-resistant high-temperature alloys used in critical equipment like high-temperature turbines in industries such as the aerospace industry, nuclear industry, and oil/gas industry. Many such applications are often subjected to high temperatures up to 1000 °C [8]. For this reason, creep damage becomes one of the dominating failure modes in addition to other failure modes such as fatigue and erosion [9]. In order to quantify creep damage using Unified Mechanics Theory (UMT), entropy generated during creep loading due to dissipative processes such as inelastic work done on the material (area under stress-inelastic strain curve), heat generation, etc. should be estimated and summed to evaluate the net entropy generated in the material. Identifying entropy generation mechanisms and developing equations to estimate the entropy generated is the challenging aspect of Unified Mechanics Theory. As a first effort towards this, in this paper, we attempt to estimate creep in Nickel-based DZ125 alloy by considering that inelastic work as primary source the of entropy generation.

2 Equations

The Boltzmann equation for specific entropy (entropy per unit mass, s) is given by

$$s = \frac{R}{m_s} \ln W \quad (1)$$

Where

- m_s is molecular mass
- R is the universal gas constant
- W is the disorder parameter [10].

In Unified Mechanics Theory (UMT) a damage parameter known as the Thermodynamic State Index (TSI, ϕ) is defined as a function of the ratio of change in the disorder parameter to the reference (initial) disorder parameter) [7] as given by Eq. (2).

$$\phi = \phi_c \frac{W - W_o}{W} = \phi_c \left(1 - e^{-\Delta s \frac{m_s}{R}} \right) \tag{2}$$

Where

ϕ is the thermodynamic state index

Δs the change in specific entropy at the material point and is given by $\Delta s = s - s_o$

W and W_o are current and reference (initial) disorder parameters respectively

s and s_o are the current and reference (initial) specific entropies of the material

ϕ_c is a user-defined parameter representing a pre-defined failure criterion.

As discussed, Δs is the sum of entropy changes due to all the dissipative processes occurring in the material. As a preliminary effort, we consider in-elastic work as the only source of entropy generation in this work. The entropy generated due to in-elastic work (Δs_w) is given by Eq. (3).

$$\Delta s = \frac{1}{\rho T} \int_0^t \sigma : d\epsilon^p \tag{3}$$

Where

T is the temperature during an isothermal process.

t is the time elapsed from the beginning of the degradation process.

σ and ϵ^p are stress and the associated plastic strain tensors at the material point of interest.

ρ is the density and s is the specific heat of the alloy.

Experimental data on DZ125 Nickel-based superalloy is taken from [11]. The data is reproduced in Fig. 1 for the convenience of the readers. It can be observed that the primary creep is small and negligible when compared to the secondary and tertiary creep. This is a common occurrence in nickel based alloys especially at high temperatures beyond 1000 K. The tertiary creep is an unstable phase and

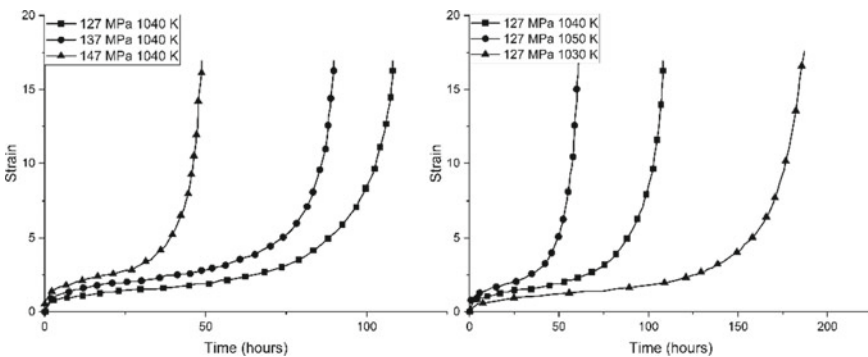
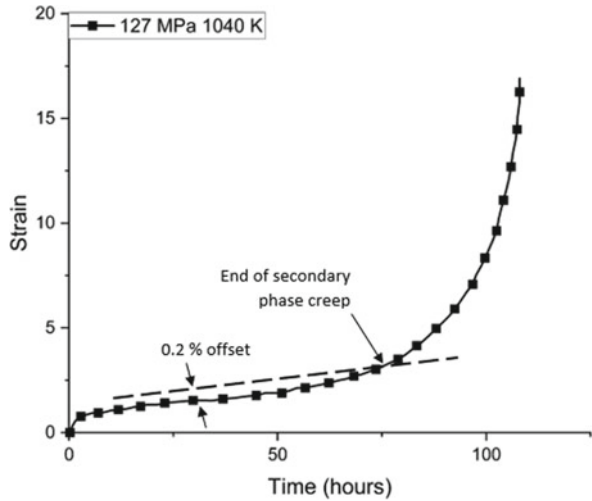


Fig. 1 Creep curves of DZ125 obtained from [11]

Fig. 2 Figure illustrating the identification of the end of secondary creep (offset not to scale)



for all engineering purposes, the end of secondary creep is considered as failure. The intersection of creep curve with a line parallel to the secondary creep line with 0.2.% strain offset is considered as the end of secondary creep phase. An illustrative example for such calculation is given in Fig. 2.

3 Results

In order ensure that the thermodynamic state index (ϕ) equals one at failure (end of secondary phase creep), the user-defined failure parameter ϕ_c should be appropriately calibrated. A single data point of failure strain at 1040 K temperature and 127 MPa creep stress is used along with Eqs. (2) and (3) and the value of ϕ_c is determined to be 142.5. This ϕ_c is then used to estimate the failure strains at other creep stresses and temperatures. The experimental and estimated failure strain at each data point are shown in Table 1.

Table 1 Experimental and estimated creep failure strains

S. no.	Tensile stress [MPa]	Temperature [K]	Failure strain (Experiment)	Failure strain (Estimated)	Error percentage [%]
1	127	1040	6.7	6.7	0
2	137	1040	6.25	6.22	0.48
3	147	1040	5.8	5.79	0.17
4	127	1030	7.01	6.64	5.20
5	127	1050	6.38	6.8	5.01

The results show that failure strain at different stresses is accurately estimated. However, to predict failure strains at different temperatures, additional entropy generation modes should be considered.

4 Discussion

In order to calculate the total entropy generated during creep deformation, the sum of entropy generated due to external sources (external to the specimen undergoing deformation) and internal sources should be added [12]. For a reversible process such as elastic deformation, such net entropy would be equal to zero [13]. In case of perfectly plastic deformation, net entropy will be equal to the entropy due to plastic work alone. However, in many cases, during deformation, several other internal processes also generate entropy. For example, self-heating of specimen during fatigue loading is one internal process that generates entropy. Entropy associated with such self-heating has been derived and used for estimating fatigue in solder alloys [14]. In creep process, self-heating of specimen is generally not reported/observed. However, external heating/cooling of specimen is required before subjecting the material to creep loading in order to bring the specimen to the operating temperatures such as those shown in Table 1. Such external heating or cooling processes are generally reversible and hence the net entropy generated in such processes is considered to be zero. However, heating at high temperatures such as those considered in this paper can irreversibly change the micro-structure of the material and are thus associated with non-zero net entropy. In addition, prolonged and simultaneous exposure to high temperature and creep loading can result in irreversible diffusion processes that contribute towards entropy generation. Although, few generic aspects of such mechanisms are modelled in [15], they are not in a form that can be used in this paper. Further, a detailed investigation is required to understand the nature of dissipation processes occurring in specific nickel based super alloys that are considered in this paper. For this reason, in this paper, such processes could not be considered while determining the total entropy generated. In the results shown by Table 1, we suspect that lack of accounting of such mechanisms resulted in a noticeable error percentage while calculating failure strains at temperatures other than 1040 K.

The failure strains predicted in this paper are the strains at the end of secondary creep phase. According to theory, UMT can also be used to predict rupture which is end of tertiary phase creep in creep failure. However, several challenges come in the way of its implementation in practice. Firstly, the failure described by UMT is failure at a material point. In extreme conditions near rupture, the homogeneity of damage is broken and several cracks/voids that are noticeable in the engineering length scale generally emerge [16, 17]. However, in standard creep tests, such moments are not generally identified. The inspection of the specimen is generally done after the entire sample splits into two separate pieces. This makes it difficult to identify the strains where observable cracks emerge. Secondly, due to the unstable nature of tertiary phase creep, it has been observed that the repeatability with respect to the rupture

strains especially at high temperatures is small [8]. Hence number of repeated experiments may be required to narrow down to a representative value of rupture strain. In view of these uncertainties associated with tertiary creep phase, end of secondary phase is used to estimate failure in all the engineering applications [18]. The same has been followed in this paper as well.

The unified mechanics theory framework discussed in this paper can be used to predict failure of materials subjected to variety of loads. However, the kinetics of such deformation and failure cannot be predicted using UMT. For example, although the failure strains at given creep loads and temperatures are predicted in this paper, the time for taken for failure could not be predicted. This is due to the limitation that the rate of a feasible process cannot be estimated using the second law of thermodynamics. Hence a separate law that describes the kinetics of creep should be modelled in order to complete the failure modelling. In spite of these limitations and challenges, the usability of UMT in describing any failure mechanism with ease make it uniquely useful.

5 Summary and Conclusions

In this paper, the failure strains of DZ125 nickel based super-alloy are estimated using UMT. The user-defined parameter ϕ_c of UMT is calibrated using one data point and the failure strains at other creep loads and temperatures are predicted using the calibrated model. The predicted failure strains are found to match the experimentally observed values when the temperature remained unchanged. However, when the experiments are conducted at other temperatures, an error of 5% is observed. These are attributed to the unmodelled irreversible internal processes associated with heating/cooling operations. Such processes are expected to be more pronounced especially due to high temperatures associated with the creep data. Once such processes are modelled, it is hoped that the resulting model can be used to predict not only creep but also a combination of several failure modes without a need for recalibration.

References

1. Bonora N (1997) A nonlinear CDM model for ductile failure. *Eng Fract Mech* 58:11–28
2. Liu Y, Kang G, Gao Q (2008) Stress-based fatigue failure models for uniaxial ratcheting–fatigue interaction. *Int J Fatigue* 30:1065–1073
3. Gaffard V, Besson J, Gourgues-Lorenzon A-F (2005) Creep failure model of a tempered martensitic stainless steel integrating multiple deformation and damage mechanisms. *Int J Fract* 133:139–166
4. Castorena-González JH, Martin U, Gaona-Tiburcio C et al (2020) Modeling steel corrosion failure in reinforced concrete by cover crack width 3D FEM analysis. *Front Mater* 7:41
5. Blish RC (1997) Temperature cycling and thermal shock failure rate modeling. In: 1997 IEEE international reliability physics symposium proceedings. 35th annual, pp 110–117

6. Dasgupta A, Pecht M (1991) Material failure mechanisms and damage models. *IEEE Trans Reliab* 40:531–536
7. Basaran C (2021) *Introduction to unified mechanics theory with applications*. Springer, Cham
8. Chavez SA, Korth GE, Harper DM, Walker TJ (1994) High-temperature tensile and creep data for Inconel 600, 304 stainless steel and SA106B carbon steel. *Nucl Eng Des* 148:351–363
9. Viswanathan R, Stringer J (2000) Failure mechanisms of high temperature components in power plants. *J Eng Mater Technol* 122:246–255
10. Dougherty JP (1964) *Lectures on gas theory*. By Ludwig Boltzmann. Translated by Stephen G. Brush. University of California Press, 490 pp. \$10.00 or 80s. *J Fluid Mech* 20:698–699
11. Sun H, Tian S, Tian N et al (2014) Microstructure heterogeneity and creep damage of DZ125 nickel-based superalloy. *Prog Nat Sci Mater Int* 24:266–273
12. Rao CL, Basaran C, et al (2021) A unified mechanics theory-based model for temperature and strain rate dependent proportionality limit stress of mild steel. *Mech Mater* 155:103762
13. Thomsen JS, Bers HC (1996) The reversible process: a zero-entropy-production limit. *Am J Phys* 64:580–583
14. Basaran C (2020) Entropy based fatigue, fracture, failure prediction and structural health monitoring
15. Mesarovic SD (2016) Lattice continuum and diffusional creep
16. Williams KR, Wilshire B (1977) Effects of microstructural instability on the creep and fracture behaviour of ferritic steels. *Mater Sci Eng* 28:289–296
17. Smallman RE (2016) *Modern physical metallurgy*. Elsevier
18. Lee Y, Basaran C (2011) A creep model for solder alloys

Experimental Studies on the Effect of Blast Loading on Scaled Down Plates



Agesh Markose and C. Lakshmana Rao

Abstract Quantification of effectiveness of protective structures under blast loads helps in optimizing its design. The selection of V-shaped plates in blast mitigation is acceptable for the design of protective hulls in armored personnel vehicles (APV). Still sufficient number of studies are not available, which focus on the quantification of effectiveness of those plates. Apart from the sheer size of full-scale model the variability in the response parameters also need to be addressed, for arriving at meaningful results. Hence it is attractive to carry out studies with scaled down plates which are subjected to controlled blast loads from a shock tube. This paper discusses an experimental study on V-shaped plates to assess the transmitted impulse, which is the parameter of interest. The plate with an optimized angle of 145° is used to assess the impulse transmitted when it is subjected to controlled blast loading from shock tube. A novel model of swing type impulse pendulum is used to measure the impulse. It was seen that; the net impulse could be measured with sufficient repeatability. The measurement technique using the pendulum is seen to be sufficient and as a suitable substitute for more costly sensor-based data acquisition system.

Keywords Blast mitigation · Shock tube loading · V-shaped plates · Repeatable experiments

1 Introduction

Threat from buried land mines and improvised explosive devices have evolved as a major threat to the life of soldiers and civilians. In this context blast resistant vehicles becomes important as they are the only means of mobility in these areas. The loading process and the response of the vehicle structure is difficult to analyze

A. Markose (✉)

Dept. of Mechanical Engineering, TKM College of Engineering, Kollam 691005, India
e-mail: agm@tkmce.ac.in

C. L. Rao

Dept. of Applied Mechanics, Indian Institute of Technology Madras, Chennai 600036, India
e-mail: lakshman@iitm.ac.in

and understand because of the large number of variables involved, like properties of soil, blast properties of explosive as well as the vehicle design parameters [1, 2]. The actual field test on these hulls may be expensive and time consuming and only limited number of experiments could be possible.

Energy based scaling laws have been widely adopted to predict the performance of full-scale models. It is seen that the parameters like displacement, velocity and acceleration for the full-scale models could be predicted accurately with these laws [3, 4]. Hence the design process is usually carried out with scaled down models of the actual vehicles. But it is seen that tests have been confined mostly to models with flat plate hulls [5]. Even though flat structural panels have been extensively used, other types of panels like V shaped panels are seen to be more advantageous. The V shaped panels are capable of deflecting a part of the blast load away from the vehicle hull, and thus reducing the blast loads. It was seen later from experimental and numerical analysis that V profiling can improve the blast mitigation considerably for scaled down models [6].

One of the main drawbacks with explosive loadings is the high variability associated with it [3]. Researchers have identified the variabilities associated with the different types of loadings like quasistatic, and dynamic loading [7]. The variability in parameters like blast pressure and loading duration have also been quantified [7, 8]. The variability for an important parameter like impulse transmitted has also been quantified to be as high as 50% [9]. The complications with the actual explosive loading process and the cost involved have made the testing with explosive loading less attractive.

In this context, the use of shock tubes to produce repeatable shock loads have gained popularity and has been used in this study. The shock tube produces uniform blast field with very low values of variability [10]. This is important for designing base line tests since the uncertainties from the loading process could be kept minimum. It is also relatively easy to measure the pressure field associated with the uniform blast wave, with the help of a single sensor mounted at the end of the shock tube. It was also seen that the transmitted impulse from the plates could be properly measured with the fabricated model of the impulse pendulum. Hence the objective of this experimental study is to evaluate and compare effectiveness of V shaped plates and flat plates subjected to shock loads generated from shock tubes.

2 Blast Loading

Blast loading generates a blast wave which propagates radially in all directions at a supersonic speed. The shock wave front is characterized by a thin layer of gases with a sudden jump in the parameters (like particle velocity, density, pressure and internal energy) compared to the surrounding air. It is also seen that the strength of the shock front decreases exponentially with time as it progresses towards the target. The shape of the wave front incident on the target depends on the standoff distance and the shape of the charge. The shock wave exerts a pressure, p_s which is much

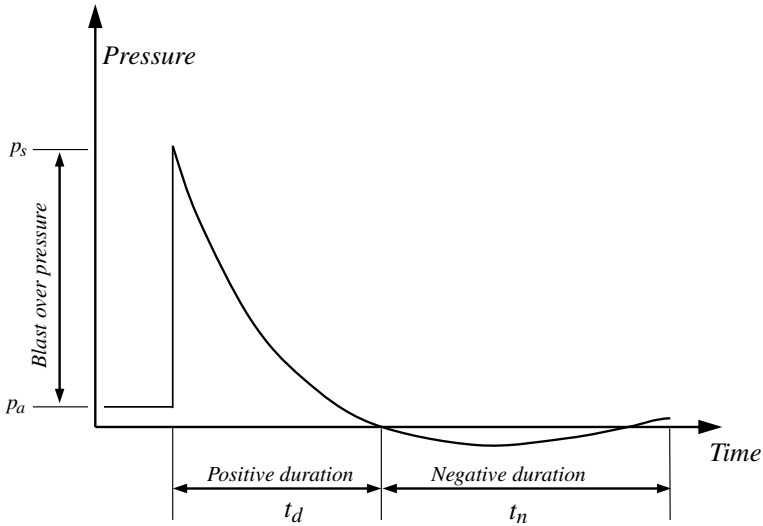


Fig. 1 Typical pressure time history of blast wave

higher than ambient pressure, p_a and the difference of these pressures is denoted by blast over pressure, $(p_s - p_a)$. The shock wave has a positive and negative phase associated with it and can be represented as shown in Fig. 1.

The pressure time history of the blast wave can be represented by the modified Friedlander equation [11].

$$p(t) = (p_s - p_a) \left(1 - \frac{t - t_a}{t_d} \right) e^{-\frac{(t-t_a)}{\theta}} \tag{1}$$

Here t_a is the time of arrival, t_d is the duration of the positive phase and θ is the decay constant. The loading due to detonation shock waves is complex and nonlinear. The imparted impulse (I) is obtained by integrating the pressure acting with respect to the time duration of the loading.

$$I = \int_0^{t_d} P(t) dt \tag{2}$$

Here P represents the applied pressure due to blast loading function and t_d is the duration of loading. The time evolution of pressure and calculation of impulses due to blast loading has been demonstrated by Aghesh et al. [12].

3 Experimental Studies

An experimental set up with shock tube, impulse pendulum mounted with test plates and camera for capturing the deflection of pendulum has been used in this study, Fig. 2. V-shaped plates and flat plates have been used for conducting separate set of experiments. The shock tube with aluminium diaphragms has been used to produce consistent blast waves. The shock waves falling on the plates transfers its momentum and the pendulum undergoes a deflection. The maximum deflection has been captured with a video camera working at 40 fps.

3.1 Shock Tube

A two-stage shock tube is used to generate the required shock waves with sufficient consistency, Fig. 3. The shock tube set up with the impulse pendulum is shown schematically in Fig. 4. The air pressure is used to rupture an aluminium diaphragm to create the shock waves inside the shock tubes. The shock waves are guided towards the plates mounted on impulse pendulum. On the target plate, these shock waves undergo a reflection process which involves the magnification of pressure of the waves. The pendulum shown in Fig. 4, is similar in construction to the model described in Fiserova [13].

In the rest position the pendulum is vertical. The impact from the blast wave transfers the momentum to the plate and the plate along with the pendulum swings up from its initial position at rest.

The calculation of the transmitted impulse is based on the angle of rotation between the initial and final position of the pendulum.

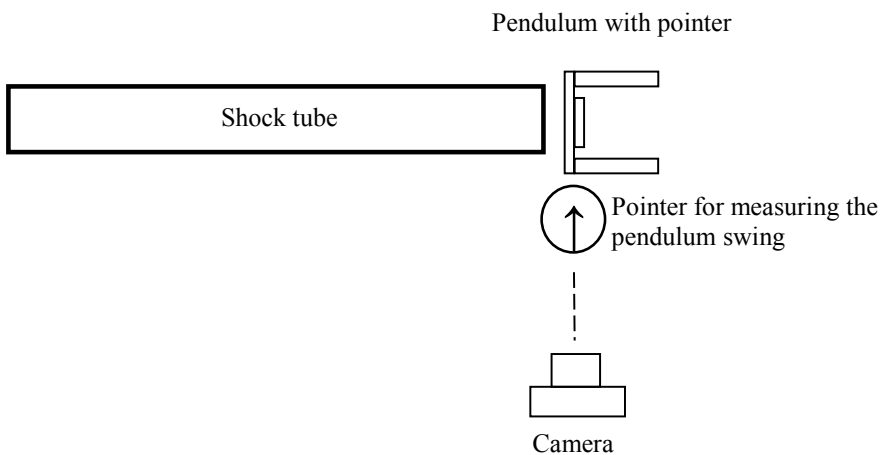


Fig. 2 Schematic representing the top view of the shock tube test setup

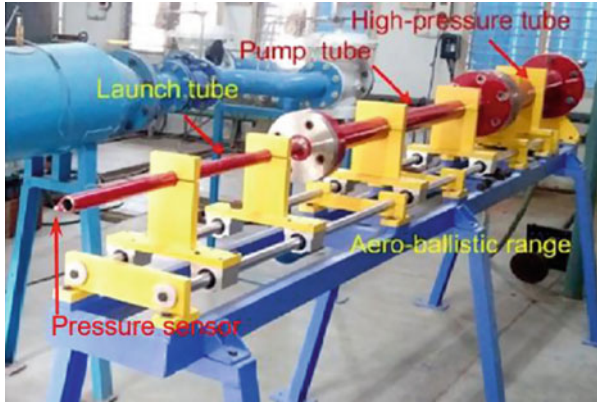


Fig. 3 Two stage shock tube test setup. (RGD lab, IIT MADRAS)

①	Primary section
②	Diaphragm
③	Secondary section
④	Diaphragm
⑤	Transition tube
⑥	Impulse pendulum

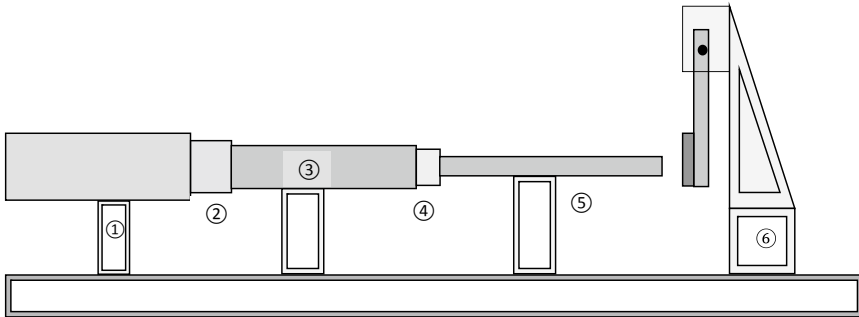


Fig. 4 Schematic of the shock tube with impulse pendulum

3.2 Details of Plates

The schematic representation of the plates is shown in Fig. 5, and its dimensions and other important parameters of the plates are shown in the Table 1. The plates are made of mild steel with sufficient thickness to resist any plastic deformation during the impact.

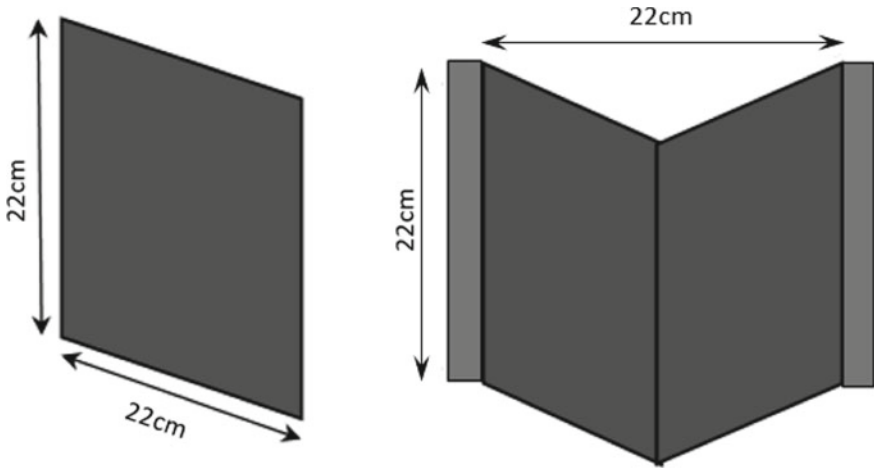
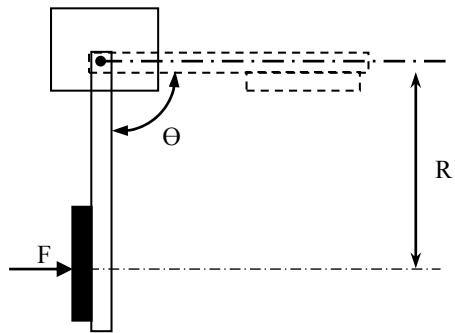


Fig. 5 Schematic of the square plate and V shaped plate with dimensions

Fig. 6 Schematic of mine impulse pendulum



3.3 Impulse Pendulum

The pendulum consists of a rotating arm fixed to a rigid structure, Fig. 6. The plates mounted on the free end of the pendulum are subjected to shock waves as discussed in the previous section.

The shockwaves were found to obey the Friedlander profile, which is typical for blast loading. The pendulum is allowed to swing due to the impact from of the shock wave and the maximum swing angle is captured with the help of the camera. The law of conservation of energy implies that the total energy (E) at any instant during the pendulum's motion equals the sum of kinetic energy ($E_{kinetic}$) and potential energy ($E_{potential}$).

$$E = E_{potential} + E_{kinetic}$$

When the impulse is transferred and pendulum is about to commence motion

$$E = 0 + \frac{J_0\omega^2}{2}$$

When the pendulum has reached the maximum height,

$$E = mgr(1 - \cos\theta_{max}) + 0$$

Equating the above energy equation gives the following result,

$$mgr(1 - \cos\theta_{max}) = \frac{J_0\omega^2}{2}$$

Momentum of the rotational motion is defined as,

$$I = \frac{J_0\omega}{R}$$

Hence the net impulse transferred (I) from the pendulum is,

$$I = \sqrt{\frac{2J_0mgr(1 - \cos\theta_{max})}{R^2}} \tag{3}$$

Here J_0 represents the polar moment of inertia of the pendulum arm and plate with respect to the pivot, I represent the impulse transmitted, θ_{max} represents the maximum swing angle of the arm, m represents the total mass of the pendulum, the dimensions r represents the distance between the pivot and center of gravity of the arm and R represents the distance between the pivot and point of application of load. The important parameters of the pendulum with plate is listed in the Table 1, below.

Table 1 Properties of the plates and pendulum

Mass of the flat plate(kg)	2030 g
Dimensions of the flat plate (mm)	22 cm × 22 cm
Dimensions of the V shaped plate(mm)	22 cm × 22 cm
Mass of the V shaped plate(kg)	2100 g
Dimensions of the pendulum rod (mm)	22.5 cm × 2 cm × 2 cm
Moment of inertia of the flat plate (J_0 , kgm ²) w.r.t axis of rotation	0.218 kgm ²
Moment of inertia of the V shaped plate (J_0 , kg m ²) w.r.t axis of rotation	0.192 kgm ²
Distance between the pivot and point of action of force (R)	0.372 m

3.4 Experimental Variables

The experiment is conducted to study the effect of V profiling while the variability due to the loading conditions have been kept at a minimum. The standoff distance is kept at 1 cm to reduce the effect of wave scattering. The uniform pressure wave is also ideal in reducing the variability during the loading. Identical diaphragms made with aluminium and having a thickness of 0.8 mm is used throughout and the operating pressure is maintained at 14 bars.

4 Results

The incident pressure was measured by using the piezoelectric pressure sensors mounted at the open end of the transition tube for finding the incident pressure. Readings were taken to ascertain the consistency of the readings. Figure 7, shows sensor reading for a reflected wave, captured with the pressure sensor. The readings were seen to be adequate without any filtration.

The deflections of the impulse pendulum were measured from the experiments. The transmitted impulse was calculated based on the Eq. (3) and is shown in Table 2. The comparison of the impulse shows that the transmitted impulses are generally lower for V shaped plates.

The V-shaped plates are better in blast mitigation as seen from the average value of transmitted impulse shown in Table 2. The reduction for the transmitted impulse is seen to be $\sim 27\%$. It is clear from the readings that the shock loaded V-plates impart lesser swing on the pendulum, corresponding to lesser momentum transfer to the pendulum. The results seem to suggest conclusively that the V-shaped plates can be used as a candidate structure for further development and research for blast mitigation. Almost all the reported studies have used strain gauges with high frequency measurement of the strains for the calculation of transmitted impulse. It may not be required in studies where the net transmitted impulse is the parameter of interest. In

Fig. 7 Pressure sensor data the end of the transition tube

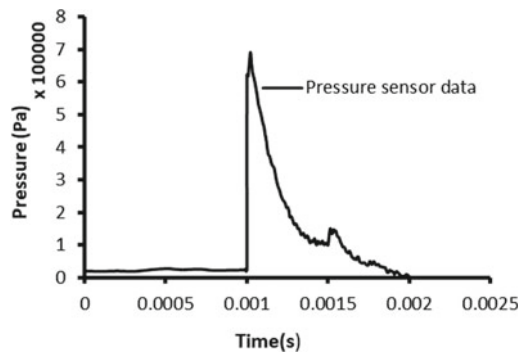


Table 2 Impulse calculated from experiments

Sl No	Plate type	Angular rotation (degrees)	Impulse (Ns),	Average Impulse (Ns)	Standard deviation of Impulse (Ns)
1	Flat plate	57.78	2.41	2.51	0.106
2		60.41	2.51		
3		60.97	2.53		
4		63.6	2.63		
5		55.7	2.33		
6		64.31	2.66		
7		60.17	2.50		
1	V shaped plate	46.62	2.12	1.81	0.417
2		41.42	1.89		
3		33.13	1.52		
4		50.19	2.27		
5		52.44	2.36		
6		25.47	1.17		
7		27.80	1.28		
8		41.08	1.88		

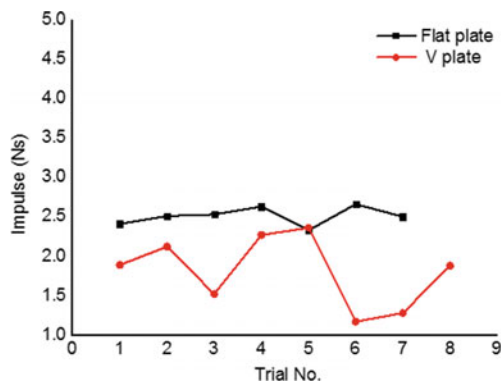
% variation indicating the difference in blast mitigation. $(I_f - I_v) * 100 / I_f = 27.77\%$

Here I_f and I_v is the transmitted impulse for flat plate and V shaped plate respectively

such situations it is always easy to use a small-scale impulse pendulum. It is seen in the experiment that use of small-scale pendulums models can deliver consistent and reliable data pertaining to the net impulse transmitted to the plates.

The variation in the transmitted impulse during the experiment for the same input conditions have been shown graphically in Fig. 8. it is clear that the variance in transmitted impulse for V plate is larger. But this is expected, since there could be slight variations in the loads acting on both sides of the plate during the impact.

Fig. 8 The variation in impulse transmitted by flat plate and V shape plate



5 Conclusion

An experimental study to observe the response of plates from shock loading under controlled conditions is presented. The response of the scaled down models of flat plates and V plates when subjected to shock loading is intended in this study. The effectiveness of the V shaped plate was demonstrated experimentally.

- A scaled down model of the impulse pendulum has been fabricated and used for calculation of impulse. As compared to sensor-based acquisition method, the pendulum can be used as a cost-effective solution, for the measurement of net impulse transferred.
- These studies demonstrate that experimental studies with controlled variability in loading can be performed on scaled down models with the help of a shock tube.
- The experimental studies are intended to represent the blast loading scenario underneath the hull of an APC, under conditions which reduce the variability of the results. The experimental study shows that the transmitted impulse for the V plate is lesser by about 27%, and hence more effective.

References

1. Peles S, Touati D, Azulay I, Neuberger A (2008) Numerical simulation of mine detonation beneath a generalized add-on armor structure. In: Proceedings 24th International Symposium of Ballistics, 1:439–447
2. Hlady SL (2004) Effect of soil parameters on land mine blast. In: 18th Military Aspects of Blast and Shock (2004)
3. Badgujar DP, Srinivasan K, Vasundhra P, Murugesan R, Rao LB (2017) Geometric Scaling of Plates Subjected to Mine Blast. *Def Sci J* 67(4):454. <https://doi.org/10.14429/dsj.67.11475>
4. Zhao X, Tiwari V, Sutton MA, Deng X, Fourney WL, Leiste U (2012) Deformation scaling of circular plates subjected to dynamic loading. *Procedia IUTAM* 4:196–205
5. Neuberger A, Peles S, Rittel D (2007) Scaling the response of circular plates subjected to large and close-range spherical explosions. Part II: buried charges. *Int J Impact Eng* 34(5):874–882
6. Yuen SCK, Langdon GS, Nurick GN, Pickering EG, Balden VH (2012) Response of V-shape plates to localised blast load: Experiments and numerical simulation. *Int J Impact Eng* 46:97–109
7. Twisdale LA, Sues RH, Lavelle FM (1994) Reliability-based design methods for protective structures. *Struct Saf* 15(1–2):17–33
8. Low HY, Hao H (2002) Reliability analysis of direct shear and flexural failure modes of RC slabs under explosive loading. *Eng Struct* 24(2):189–198
9. Roger E (2015) Mines buried in dry and saturated soils: blast experiments, soil modeling and simulations. Mechanical engineering [physics.class-ph], Université Grenoble, Alpes
10. Kleinschmit NN (2011) A Shock Tube Technique for Blast Wave Simulation and Studies of Flow Structure Interactions in Shock Tube Blast Experiments. MS thesis, University of Nebraska-Lincoln
11. Dharmasena KP, Wadley HN, Xue Z, Hutchinson JW (2008) Mechanical response of metallic honeycomb sandwich panel structures to high-intensity dynamic loading. *Int J Impact Eng* 35(9):1063–1074

12. Aghesh M, Lakshmana Rao C (2017) Mechanical response of V shaped plates under blast loading. *Thin-Walled Struct* 115:12–20
13. Fiserova D (2006) Numerical analysis of buried mine explosions with emphasis on effect of soil properties on loading. PhD thesis, Cranfield University